

Paramagnetic NMR in solution and the solid state

Andrew J. Pell ¹2, Guido Pintacuda ³, Clare P. Grey ⁴

May 12, 2018

¹Email: andrew.pell@mmk.su.se

²Department of Materials and Environmental Chemistry, Arrhenius Laboratory, Stockholm University, Svante Arrhenius väg 16 C, SE-106 91 Stockholm, Sweden

³Institut des Sciences Analytiques (CNRS UMR 5280, ENS de Lyon, UCB Lyon 1), Université de Lyon, 5 rue de la Doua, 69100 Villeurbanne, France

⁴Department of Chemistry, University of Cambridge, Lensfield Road, Cambridge, CB2 1EW, UK

Abstract

The field of paramagnetic NMR has expanded considerably in recent years, both in solution and the solid state. This review addresses both the theoretical description of paramagnetic NMR, and the way in which it is currently practised. We provide a review of the theory of the NMR parameters of systems in both solution and the solid state. Here we unify the different languages used by the NMR, EPR, quantum chemistry/DFT, and magnetism communities to provide a comprehensive and coherent theoretical description. We cover the theory of the paramagnetic shift and shift anisotropy in solution both in the traditional formalism in terms of the magnetic susceptibility tensor, and using a more modern formalism employing the relevant EPR parameters, such as are used in first-principles calculations. In addition we examine the theory first in the simple non-relativistic picture, and then in the presence of spin-orbit coupling. These ideas are then extended to a description of the paramagnetic shift in periodic solids, where it is necessary to include the bulk magnetic properties, such as magnetic ordering at low temperatures. The description of the paramagnetic shift is completed by describing the current understanding of such shifts due to lanthanide and actinide ions. We then examine the paramagnetic relaxation enhancement, using a simple model employing a phenomenological picture of the electronic relaxation, and again using a more complex state-of-the-art theory which incorporates electronic relaxation explicitly. An additional important consideration in the solid state is the impact of bulk magnetic susceptibility effects on the form of the spectrum, where we include some ideas from the field of classical electrodynamics. We then continue by describing in detail the solution and solid-state NMR methods that have been deployed in the study of paramagnetic systems in chemistry, biology, and the materials sciences. Finally we describe a number of case studies in paramagnetic NMR that have been specifically chosen to highlight how the theory in part one, and the methods in part two, can be used in practice. The systems chosen include small organometallic complexes in solution, solid battery electrode

materials, metalloproteins in both solution and the solid state, systems containing lanthanide ions, and multi-component materials used in pharmaceutical controlled-release formulations that have been doped with paramagnetic species to measure the component domain sizes.

Contents

1	Introduction	19
1.1	Paramagnetic NMR	19
1.2	New techniques for solid-state paramagnetic NMR	20
1.3	The paramagnetic shift and shift anisotropy	21
1.4	The paramagnetic relaxation enhancement	24
1.5	Bulk magnetic susceptibility effects	25
1.6	Paramagnetic NMR and dynamic nuclear polarization	26
1.7	What this review contains	29
2	Introduction to nuclear and electronic magnetism	33
2.1	Nuclear and electronic magnetic moments	33
2.2	Magnetic field, magnetization, and the magnetic susceptibility	35
2.3	The electronic and magnetic properties of periodic solids	38
2.3.1	Electronic energy levels and the density of states	38
2.3.2	Band structures of insulators, semiconductors, and metals	42
2.3.3	The free-electron model of metals	44
2.4	The nuclear and electronic Zeeman interactions	45
2.5	Irreducible spherical tensors and tensor operators	48
2.5.1	Cartesian tensor representation of the spin Hamiltonian	48
2.5.2	Irreducible spherical tensor representation of the spin Hamiltonian	49
2.6	Chemical shielding and chemical shift	53

2.6.1	The high-field approximation	55
2.6.2	The chemical shift	64
2.7	The spin interactions of quadrupolar nuclei	66
2.7.1	The nuclear quadrupole Hamiltonian	67
2.8	The hyperfine interaction	71
2.8.1	Interaction with a single delocalised electron	72
2.8.2	Interaction with a single localised electron	73
2.8.3	Interaction with a paramagnetic centre of multiple delocalised electrons	74
2.8.4	Interaction with a paramagnetic centre of multiple localised electrons	75
2.8.5	The hyperfine coupling constant	76
2.8.6	The hyperfine interaction in solid insulators	79
2.8.7	The hyperfine interaction in solid metals	79
2.8.8	Finite nucleus effects	80
2.9	Key concepts	81
3	The paramagnetic shift in electron spin-only systems	83
3.1	The origin of the paramagnetic shift	84
3.1.1	Two-spin system comprising two spin-1/2 heteronuclei	84
3.1.2	Two-spin system comprising one spin-1/2 nucleus and a free electron	89
3.2	The thermal average of the electron magnetic moment: the Brillouin function and the Curie spin	92
3.2.1	The Hamiltonian and the pseudo spin	92
3.3	The magnetic susceptibility	101
3.3.1	Magnetism of the bulk	101
3.3.2	The susceptibility in terms of the molecular/atomic-level parameters	102
3.3.3	Relating the paramagnetic shift to the magnetic susceptibility	103
3.4	The scaling factor	107
3.5	Key concepts	110

4	The paramagnetic shift due to <i>d</i>-block transition-metals with spin-orbit coupling	111
4.1	The EPR effective spin Hamiltonian	112
4.1.1	Derivation	112
4.1.2	The NMR and EPR tensors	120
4.2	The EPR formalism of the paramagnetic shielding	123
4.2.1	General derivation of the paramagnetic shielding tensor	123
4.2.2	The EPR formalism applied to <i>d</i> -block transition-metal systems	131
4.2.3	The EPR formalism in different temperature limits	133
4.3	The magnetic susceptibility tensor	141
4.3.1	Magnetism of the bulk	141
4.3.2	The susceptibility tensor in terms of the molecular/atomic-level parameters according to the EPR formalism	143
4.3.3	Relating the paramagnetic shift to the magnetic susceptibility tensor	144
4.4	The scaling factor revisited	147
4.4.1	The scaling tensor in the presence of magnetic susceptibility anisotropy	149
4.5	The Kurland–McGarvey formalism	150
4.6	Key concepts	153
5	The interpretation of the paramagnetic shielding tensor of <i>d</i>-block transition-metal ions	155
5.1	Correspondence between the EPR and susceptibility formalisms of the paramagnetic shielding tensor	156
5.2	Summary of the relevant tensor parameters	158
5.3	The paramagnetic shift in the susceptibility formalism	165
5.3.1	The contact shift and shift anisotropy	166
5.3.2	The spin-dipolar shift and shift anisotropy	167
5.3.3	The antisymmetric hyperfine shift anisotropy	175
5.3.4	Summary	176
5.4	The paramagnetic shift in terms of the molecular/atomic-level EPR parameters	178
5.4.1	Magnetically isotropic transition-metal ions in the absence of spin-orbit coupling	179

5.4.2	The contact shift and shift anisotropy	180
5.4.3	The spin-dipolar shift and shift anisotropy	184
5.4.4	The antisymmetric hyperfine shift anisotropy	188
5.4.5	Summary	188
5.5	Key concepts	191

6	The paramagnetic shift due metal ions with arbitrary spin-multiplicity and spin-orbit coupling strength: application to <i>d</i>-transition metals, lanthanides, and actinides	193
6.1	The crystal-field interaction and the effective spin	194
6.1.1	The effective spin	195
6.1.2	The crystal-field interaction	196
6.1.3	Crystal-field vs zero-field splitting	197
6.2	The generalized EPR spin Hamiltonian and paramagnetic shielding tensor	198
6.2.1	The electronic Zeeman interaction	199
6.2.2	The hyperfine interaction	200
6.2.3	The ZFS interaction	201
6.2.4	The EPR formalism of the paramagnetic shielding tensor	202
6.3	The paramagnetic shielding and magnetic susceptibility tensors due to a transition-metal ion with arbitrary spin multiplicity	204
6.3.1	The Bleaney expression for <i>d</i> -block metal ions revisited	206
6.3.2	The EPR formalism of the magnetic susceptibility tensor	208
6.4	Electronic properties of the lanthanide ions	210
6.4.1	The free lanthanide ions	210
6.4.2	The crystal-field interaction	213
6.5	The Bleaney theory of the paramagnetic shielding tensor due to lanthanide ions	215
6.5.1	The paramagnetic chemical shielding in terms of the magnetic susceptibility tensor	217
6.5.2	Contact shift contributions from excited states of different <i>J</i>	221
6.5.3	Pseudo-contact shift contributions from excited states of different <i>J</i>	222
6.5.4	The shortcomings of the Bleaney theory	224

6.6	The paramagnetic shielding due to actinides	226
6.6.1	Electronic structure of actinide ions	226
6.6.2	The EPR formalism for the paramagnetic shielding tensor	226
6.7	Key concepts	227
7	The paramagnetic shift in multi-metal-ion systems, and solid materials	229
7.1	The paramagnetic shift due to multiple non-interacting metal ions	230
7.2	The Heisenberg exchange Hamiltonian	231
7.2.1	The exchange interaction between two electronic spins 1/2	231
7.2.2	The exchange interaction between two arbitrary electronic spins	233
7.3	The paramagnetic shift due to a coupled electronic spin system	234
7.4	The general exchange Hamiltonian for transition metal ions subject to spin-orbit coupling	238
7.5	The paramagnetic shift due to a coupled electronic spin system subject to spin-orbit coupling	241
7.5.1	The EPR formalism	241
7.5.2	Example: two coupled electronic spins-1/2	244
7.6	Ferromagnetic and antiferromagnetic interactions in solid insulators: the Curie–Weiss law	247
7.6.1	The Weiss model of ferromagnetism	247
7.6.2	The Weiss model of antiferromagnetism	251
7.6.3	The magnetic susceptibility	253
7.6.4	The Néel temperature and Weiss constant in antiferromagnetic materials	255
7.6.5	The magnetic susceptibility in terms of the isotropic exchange coupling	257
7.7	The paramagnetic shielding tensor in solid insulator materials	261
7.7.1	The Curie–Weiss expression for the paramagnetic shielding tensor	261
7.7.2	The scaling factor	263
7.7.3	A word of caution	265
7.7.4	The magnetic susceptibility and paramagnetic shielding tensors in solid materials with more than one species of paramagnetic metal ion	266
7.8	Types of isotropic exchange interaction	268
7.8.1	Direct exchange	268

7.8.2	Superexchange	269
7.8.3	Double exchange	271
7.8.4	Ruderman–Kittel–Kasuya–Yosida exchange	272
7.9	Predicting the Fermi-contact shift with the Goodenough–Kanamori rules	272
7.10	The magnetic susceptibility and paramagnetic shielding tensors in solid materials due to metal ions with SO coupling	277
7.11	Exchange interactions between transition-metal ions and lanthanides	280
7.12	The paramagnetic shift in metals	281
7.12.1	The Knight shift	281
7.12.2	The Pauli magnetic susceptibility	285
7.12.3	Comparison between the paramagnetic shifts in metals and insulators	288
7.13	Key concepts	290
8	Relaxation in paramagnetic systems under fast-motional and high-field conditions	293
8.1	Overview of the models of electronic and nuclear relaxation	294
8.2	The Redfield theory of relaxation	297
8.2.1	The equation of motion	297
8.2.2	Relaxation by spatial reorientation of the interaction tensor	302
8.2.3	Relaxation by fast chemical exchange	304
8.2.4	The spin-dependent part	304
8.2.5	The nuclear relaxation superoperator	305
8.3	The correlation function and spectral density	307
8.3.1	A note on terminology for motional regimes	309
8.4	Electronic relaxation	310
8.4.1	Relaxation due to the transient ZFS	312
8.4.2	Relaxation due to the static ZFS	314
8.4.3	Beyond the simple Redfield approximation	315
8.4.4	Other electronic relaxation mechanisms involving spin-orbit coupling	316
8.5	Nuclear relaxation	318

8.6	The Solomon–Bloembergen–Morgan theory of paramagnetic nuclear relaxation	324
8.6.1	Relaxation due to the spin-dipolar interaction with delocalized electrons	324
8.6.2	Relaxation due to the spin-dipolar interaction with localised electrons (the Solomon mechanism)	325
8.6.3	Relaxation due to the Fermi-contact interaction (the Bloembergen mechanism) . . .	326
8.6.4	The Solomon–Bloembergen–Morgan equations	327
8.6.5	Shortcomings of the Solomon–Bloembergen–Morgan theory	328
8.7	Curie-spin relaxation	329
8.7.1	Relaxation due to the spin-dipolar interaction with delocalized electrons	331
8.7.2	Relaxation due to the spin-dipolar interaction with localised electrons	333
8.7.3	Relaxation due to the Fermi-contact interaction	334
8.7.4	Comparison of the Curie terms with the relaxation rate constants due to stochastic fluctuation of the paramagnetic chemical shielding interaction	335
8.7.5	The importance of the Curie term	337
8.8	Cross-correlation between the paramagnetic and diamagnetic relaxation mechanisms in solution	338
8.8.1	Nuclear–nuclear dipolar-coupling relaxation and cross-correlation with the Curie mechanism	341
8.8.2	Longitudinal relaxation	342
8.8.3	Transverse relaxation	344
8.9	Paramagnetic relaxation enhancements in non-dynamic solid insulators	350
8.10	Paramagnetic relaxation enhancements due to lanthanide ions	353
8.11	Relaxation properties of specific paramagnetic metal ions	355
8.11.1	The <i>d</i> -block transition-metal ions	356
8.11.2	The lanthanide ions	358
8.12	Key concepts	360
9	Relaxation in paramagnetic systems under general conditions	363
9.1	Introduction to the slow-motion theory of relaxation	364
9.1.1	The different approaches for slow relaxation dynamics	364

9.1.2	The Swedish slow-motion theory	367
9.2	The stochastic Liouville formalism	368
9.2.1	The Hamiltonian and Liouvillian	368
9.2.2	The density operator	371
9.3	Derivation of the stochastic Liouville equation	372
9.3.1	The relaxation superoperator	373
9.3.2	The longitudinal and transverse relaxation times	378
9.3.3	Summary of the formalism	380
9.4	Electronic relaxation in the Redfield limit	381
9.4.1	The spin system, lattice, and spin–lattice coupling	382
9.4.2	The electronic spin relaxation superoperator	384
9.5	The Solomon–Bloembergen–Morgan theory revisited	385
9.5.1	The lattice	385
9.5.2	The spectral densities	387
9.5.3	The Solomon–Morgan–Bloembergen equations	389
9.6	Low-field theory of the PRE in low-symmetry complexes in solution	392
9.6.1	Introduction	392
9.6.2	The lattice	393
9.6.3	The spectral densities	393
9.6.4	Electronic relaxation	397
9.6.5	Nuclear relaxation	400
9.7	The PRE under fast-rotation conditions in solution	403
9.7.1	Introduction	403
9.7.2	A simple model of inner- and outer-sphere relaxation	404
9.7.3	Inner-sphere relaxation at high field	406
9.7.4	Outer-sphere relaxation at high field	410
9.7.5	Inner- and outer-sphere relaxation at low field	414
9.8	The effect of vibrational motion on the PRE	416
9.8.1	Introduction	416

9.8.2	The vibrational subsystem	417
9.8.3	Electronic relaxation	420
9.8.4	The PRE	427
9.9	Longitudinal relaxation in metallic solids	428
9.9.1	Introduction	428
9.9.2	Longitudinal relaxation due to transitions between energy levels	429
9.9.3	The longitudinal PRE of nuclei in a metal	430
9.9.4	The Korringa relation	435
9.9.5	Comparison of the longitudinal PRE in solid insulators and metals	435
9.10	Key concepts	436
10	Inhomogeneous broadening due to the bulk paramagnetic susceptibility	439
10.1	The BMS shift in a single crystal	440
10.1.1	The demagnetising field in a single crystal	440
10.1.2	The BMS shift of a spherical crystallite	445
10.1.3	The IBMS and ABMS contributions to the paramagnetic shielding tensor	447
10.2	The BMS shift in a polycrystalline powder	450
10.2.1	The IBMS and ABMS contributions to the paramagnetic shielding	450
10.2.2	BMS inhomogeneous broadening	454
10.3	Key concepts	455
11	The NMR spectrum for non-interacting spins	457
11.1	The quantum mechanics of NMR	457
11.1.1	The Hamiltonian, propagator, and density operator	457
11.1.2	Radiofrequency pulses and sequences	460
11.1.3	The spin interactions	461
11.1.4	Basis operators	464
11.1.5	NMR frequencies and spin order	466
11.1.6	Solution NMR	470
11.1.7	Solid-state NMR of static powders	471

11.1.8	Solid-state NMR of spinning powders	472
11.2	The shift and shift anisotropy in paramagnetic NMR	477
11.2.1	The chemical shielding frequencies	477
11.2.2	Solution NMR	478
11.2.3	Solid-state NMR of static powders	482
11.2.4	Solid-state NMR of spinning powders	486
11.3	Paramagnetic NMR of integer-spin quadrupolar nuclei	490
11.3.1	Static solid powders	490
11.3.2	Solid powders under MAS	493
11.3.3	First-order quadrupolar and paramagnetic shift anisotropy interactions	493
11.4	Paramagnetic NMR of half-integer-spin quadrupolar nuclei	494
11.4.1	First-order quadrupolar interaction	494
11.4.2	Second-order quadrupolar interaction	497
11.4.3	Second-order quadrupolar and paramagnetic shift anisotropy interactions	499
11.5	Key concepts	501
12	A survey of NMR methods for paramagnetic systems	503
12.1	NMR pulse sequences	504
12.2	Solution NMR methods for paramagnetic systems	505
12.2.1	The general strategy	505
12.2.2	Small molecules	509
12.3	Solution NMR of paramagnetic proteins	526
12.3.1	General strategy for resonance assignment and structural restraints	526
12.3.2	Paramagnetic NMR methods	529
12.3.3	Paramagnetic structural restraints	534
12.3.4	Solvent PREs for measuring protein–solvent interactions	541
12.4	Measuring chemical exchange in solution NMR and MRI	542
12.4.1	Chemical exchange dependent saturation transfer (CEST)	542
12.4.2	Paramagnetic shift reagents in chemical exchange dependent saturation transfer (PARACEST)	544

12.5	Solid-state NMR methods for paramagnetic systems	546
12.5.1	The general strategy	546
12.5.2	One-dimensional NMR	550
12.5.3	Homonuclear through-space correlations	564
12.5.4	Homonuclear exchange correlations	566
12.5.5	Heteronuclear through-space correlations	567
12.5.6	Separation of shift and shift anisotropy interactions	568
12.5.7	Broadband NMR methods for spin-1/2 nuclei	578
12.5.8	Separation of shift-anisotropy and quadrupolar interactions	593
12.6	Solid-state NMR of paramagnetic proteins	611
12.6.1	General strategy	611
12.6.2	¹³ C-detection	613
12.6.3	¹ H-detection	616
12.6.4	Paramagnetic restraints	618
12.7	Key concepts	621
13	Case studies in paramagnetic NMR	623
13.1	Introduction	623
13.2	Transition-metal metallocenes M(C ₅ H ₅) ₂	627
13.2.1	Background	627
13.2.2	Paramagnetic shifts	629
13.2.3	Interpretation	632
13.2.4	The delocalization error	634
13.3	Co(II) pyrazolylborate complexes in solution	635
13.3.1	Background	635
13.3.2	The EPR tensor parameters	636
13.3.3	Paramagnetic shifts	636
13.4	Layered transition-metal oxides LiMO ₂	638
13.4.1	Background	638

13.4.2	Spin-transfer pathways in $\text{LiM}_y\text{Co}_{1-y}\text{O}_2$	640
13.4.3	^7Li contact shifts in $\text{LiM}_y\text{Co}_{1-y}\text{O}_2$	646
13.5	Prussian blue analogue materials $\text{A}_n\text{M}'_x[\text{M}(\text{CN})_6]_y \cdot z\text{H}_2\text{O}$	648
13.5.1	Background	648
13.5.2	Solid-state NMR spectra	652
13.5.3	Interpretation of the contact shifts	655
13.6	Olivine-type lithium transition-metal phosphate cathode materials LiMPO_4	656
13.6.1	Background	656
13.6.2	$^{6/7}\text{Li}$ NMR shifts and relaxation properties	658
13.6.3	^{31}P NMR shifts and relaxation properties	664
13.6.4	Shifts and shift anisotropies in the EPR formalism	667
13.6.5	Experiments and calculations on $\text{LiFe}_x\text{Mn}_{1-x}\text{PO}_4$	671
13.7	Contact shifts in ferredoxins due to coupled Fe_4S_4 clusters	673
13.7.1	Background	673
13.7.2	NMR spectroscopy and assignment	676
13.7.3	Temperature dependence of the contact shifts	678
13.7.4	Angular dependence of the contact shifts	680
13.8	Paramagnetic distance restraints in the metalloprotein superoxide dismutase (SOD)	683
13.8.1	Background	683
13.8.2	Resonance assignment and structure calculation using non-paramagnetic ^1H - ^1H distance restraints	684
13.8.3	Paramagnetic relaxation enhancement as structural restraints	685
13.8.4	Pseudo-contact shifts as structural restraints	687
13.9	Lanthanide stannates $\text{Ln}_2\text{Sn}_2\text{O}_7$ in the solid state	691
13.9.1	Background	691
13.9.2	Paramagnetic shifts	692
13.9.3	The $\text{Y}_{2-x}\text{Ln}_x\text{Sn}_2\text{O}_7$ materials with mixed composition	695
13.10	The interaction between guanidinium and tris-dipicolinate lanthanide ions in solution: $(\text{Gua})_3[\text{Ln}(\text{DPA})_3]$	696
13.10.1	Background	696

13.10.2 Pseudo-contact shifts	697
13.11 Paramagnetic effects of lanthanide ions in the dicalcium protein calbindin D_{9k}	700
13.11.1 Background	700
13.11.2 Pseudo-contact shifts	700
13.11.3 Extracting the crystal-field splitting parameters	704
13.12 Actinyl tris-carbonate complexes in solution	705
13.12.1 Background	705
13.12.2 Paramagnetic shifts	706
13.12.3 Interpretation	708
13.13 Solid actinide oxides	711
13.13.1 Background	711
13.13.2 Paramagnetic shifts	711
13.14 Probing the nanostructure of composite materials using relayed paramagnetic relaxation en- hancement	714
13.14.1 Background	714
13.14.2 The relay of the paramagnetic relaxation enhancement by spin diffusion	715
13.14.3 Measurement of domain sizes in ethyl cellulose/hydroxypropyl cellulose film coat- ings in pharmaceutical controlled-release formulations	717
13.15 Key concepts	720
14 Concluding remarks and the future of paramagnetic NMR	723
A The Wigner–Eckart theorem	729
A.1 The projection theorem	730
A.1.1 Magnetic moments due to ions subject to Russell–Saunders spin-orbit coupling . . .	731
B Relativistic corrections to the hyperfine coupling tensor	733
B.1 The vector potential	733
B.2 The non-relativistic hyperfine interaction	734
B.3 The spin-orbit-coupling correction to the hyperfine interaction	734

C	The Pennanen–Vaara formalism for the paramagnetic shift	737
C.0.1	The terms in the paramagnetic shift tensor	742
D	Derivation of the paramagnetic shielding tensor for arbitrary spin multiplicity to second order	745
E	Derivation of the paramagnetic shielding tensor for a system containing multiple, coupled paramagnetic centres of arbitrary spin multiplicity to second order	751
F	Simplification of the relaxation superoperator and spectral densities in the stochastic Liouville formalism	759
F.1	The relaxation superoperator	760
F.2	Symmetry properties of the spectral density	764

Chapter 1

Introduction

1.1 Paramagnetic NMR

Nuclear magnetic resonance (NMR) spectroscopy has become established as an essential method for structural characterisation in chemistry, biology, and the materials sciences [1, 2]. One area that has seen increased activity in recent years is the study of the structural and electronic properties of paramagnetic systems in both solution and the solid state [3–13]. Paramagnetic systems are defined as molecules or materials that contain one or more ‘paramagnetic centres’, which are atoms or ions possessing at least one unpaired electron. From the the point of view of NMR spectroscopy the important property of these systems is that there is a hyperfine interaction between the unpaired electrons and the observed nucleus, which is the origin of the paramagnetic shift and shift anisotropy (SA), the paramagnetic relaxation enhancement (PRE), and additional sources of substantial broadening due to bulk magnetic susceptibility effects. These interactions potentially yield important information about the system, including the bonding between the atoms and ions and their spatial arrangement, the delocalisation of the unpaired electrons onto the coordinating atoms and ligands, the dynamics of the system, and, in the case of lanthanide ions, details about the crystal-field splitting and consequent optical properties [14–17]. However the paramagnetism can also cause problems when attempting to both acquire and interpret the NMR data. The problem of acquisition arises because the paramagnetic shifts and SAs are often very large, with the result that excitation of the nuclei with practicable radio-frequency (RF) powers can be both inefficient and non-broadband, and the large PREs cause the coherences to decay rapidly

once they have been excited. The interpretation of the NMR data is not always intuitive, and usually requires the availability of reliable theoretical models. The research in the field of method development has therefore focused on two areas: the development of new and improved experimental NMR techniques for acquiring usable data, and the development of new theoretical techniques for calculating and interpreting the spectra.

1.2 New techniques for solid-state paramagnetic NMR

The development of new NMR techniques has focused on new methods for solid samples under magic-angle spinning (MAS). The motivation for this development arises from the observation that many conventional techniques that are standard for diamagnetic systems perform very poorly when applied to paramagnetic systems. In particular those techniques that require long periods of RF irradiation, such as cross-polarization (CP) [18] and heteronuclear decoupling [19] are found to be inefficient, due to RF field power not dominating the paramagnetic shift and SA interactions; in the worst cases this has a deleterious effect on the spectrum. The most successful techniques applied to paramagnetic solid-state NMR are generally those that employ short, high-power RF pulses, such as the spin-echo [20] and transferred-echo double-resonance (TEDOR) [21] sequences.

Clayton et al. showed that under slow-to-moderate MAS the linewidths in the ^{13}C spectra of paramagnetic complexes have a significant contribution due to the ^1H - ^{13}C dipolar couplings, and that attempts at conventional ^1H decoupling lead to no improvement [22]. However the problem can be alleviated by chemical substitution of ^2H for ^1H , which results in narrower lines due to the smaller heteronuclear dipolar interactions. These observations were later confirmed by Liu et al., who also showed that detection of ^2H leads to narrower lines than detection of ^1H , allowing the characterization of hydrogen environments closer to the metal ion [23]. One spectroscopic solution to the problem would be to design a new, more broadband, decoupling sequence, such as that proposed by Raleigh et al [24]. Their solution was to split the irradiation over multiple frequencies so that the RF power is distributed more evenly over the ^1H resonances. However this early method has not achieved widespread usage. Ishii et al. suggested a different approach using very fast MAS, under which conditions the dipolar-coupling contribution to the linewidths is sufficiently narrowed that the decoupling can be dispensed with [6, 25]. This approach has the advantage that the recycle delay can be shortened considerably, in the absence of a duty cycle limit, in order to exploit the PRE of the longitudinal

relaxation. Hence both the resolution and sensitivity are considerably enhanced. Very fast MAS is the foundation upon which all subsequent paramagnetic NMR methods have been based.

Further improvements in resolution and sensitivity have been made by using two-dimensional heteronuclear correlation experiments based on the TEDOR [7], dipolar insensitive nucleus enhanced by polarization transfer (DINEPT) [26], and dipolar heteronuclear single-quantum correlation (DHSQC) [27] experiments. These pulse sequences employ short, high-power pulses and have been shown to give superior results compared to the CP-based heteronuclear correlation (HETCOR) sequences. The use of such techniques is crucial if solid-state NMR is to yield unambiguous data for paramagnetic systems.

An additional avenue of enquiry is the development of new RF pulse schemes that are capable of delivering more broadband excitation, therefore making NMR applicable to more demanding paramagnetic systems experiencing larger interactions. The most promising schemes to have been proposed to date are those which employ adiabatic pulses, the most successful example of which is the family of short high-power adiabatic pulses (SHAP) [28]. It has been shown that the SHAPs are particularly versatile, and they have been incorporated into more sophisticated experiments to enhance sensitivity, such as the SHAP-CPMG sequence [29], and resolution, such as the adiabatic magic-angle turning (aMAT) experiment [30]. A second class of adiabatic scheme that has been proposed is the low-power single-sideband-selective adiabatic pulse (S^3AP) [31–33]. These pulses have been shown to achieve a broadband NMR response over a frequency range that is an order of magnitude larger than the applied RF field amplitude, and generally exhibit optimal performances at higher spinning frequencies. This field has been recently reviewed [34].

1.3 The paramagnetic shift and shift anisotropy

The interpretation of the paramagnetic shift and SA is aided by a number of different theories and formalisms that have been proposed over the years. Work in this area has been performed by theoretical physicists, researchers in quantum chemistry and density-functional theory (DFT), chemists, and biologists. As a result the different formalisms take different approaches, and often use different scientific language. It is one main purpose of this review to unify these different approaches, to identify the common ground, and to explain any differences. In brief the different approaches can be categorised into the groups described below, between which there is some overlap. For example some theories are designed for *d*-block transition-metal ions,

whilst others are specifically for lanthanide ions. There are also different ways of modelling the magnetic properties of the metal ions. In some cases the ions are described by their molecular/atomic-level electronic paramagnetic resonance (EPR) parameters, such as the g -tensor and zero-field splitting (ZFS), whilst in others the ions are described by their bulk magnetic susceptibility. Finally another important distinction that arises is whether the system being described contains non-interacting metal ions, such as complexes in solution, or an extended network of interacting metal ions, such as in periodic solid materials. The link between these cases is not always obvious.

The first contributions to understanding the paramagnetic shifts from d -block metal ions are due to McConnell in 1958, who identified two important contributions to the isotropic shift. These are the contact shift, which is due to through-bond transfer of the unpaired electron spin onto the nucleus [35], and the pseudo-contact shift (PCS), which arises from the through-space spin-dipolar coupling between the unpaired electrons and the nucleus [36]. Kurland and McGarvey generalized this formalism to include d -block metal ions with a more complex description of the magnetic properties [37]. More recently Moon and Patchkovskii have rejuvenated interest in this area by publishing a modern formalism describing the whole shift tensor, including the SA, for metal ions with a single unpaired electron [38]. This has since been extended to d -block metal ions with arbitrary electronic spin, and a small spin-orbit coupling parameter, by Pennanen, Vaara, et al., where the shift tensor is described in terms of the g -tensor, hyperfine tensor, and the ZFS [39, 40]. This formalism and its application in quantum chemistry and DFT calculations have been recently reviewed by Kaupp and Koehler [41].

An alternative description of the paramagnetic shift and SA due to d -block transition-metal ions has been given in terms of the bulk magnetic properties of an ensemble of such ions. Here the paramagnetic shift tensor is calculated from the magnetic susceptibility tensor and the and the hyperfine tensor [15, 16, 42]. This approach has been applied extensively to paramagnetic metalloproteins in both solution [43] and the solid state [44, 45], where the observed paramagnetic shifts are given entirely by the PCS. As a consequence of its origin from the through-space spin-dipolar interaction, the PCS has a very well-defined geometrical dependence that can be exploited to provide information on the position of the observed nuclei relative to the metal ion, and thence structural restraints [15]. The advantage of this susceptibility formalism is that it can be used to describe the paramagnetic shifts in materials with different magnetic properties by changing the form of the magnetic susceptibility accordingly. For example it has been used to describe

the shift due to a small cluster of paramagnetic *d*-block metal ions that are coupled together by exchange interactions [46, 47]. In addition this formalism has been used extensively to rationalize the paramagnetic shifts in periodic paramagnetic battery materials [48], glasses, and minerals [49–52]. For these systems it has been shown that the isotropic shifts are dominated by contact interactions, and the SAs are dominated by spin-dipolar interactions. One important observation is that the contact shifts can be broken down into a sum of contributions from the metal ions that transfer unpaired electronic spin density onto the nucleus, known as ‘pathway contributions’ [5]. This idea has been instrumental in allowing the analysis of the contact shifts of very complex battery materials which contain more than one type of metal ion [30, 53–59].

In parallel to these developments there has been some work, albeit less extensive, in rationalizing the form of the paramagnetic shift due to lanthanide ions. The first, and still principal, contributions to this were the Golding and Halton [60] and Bleaney [61] theories, which gives expressions for the contact shift and PCS respectively. For the latter the Bleaney theory links the PCS to the crystal-field splitting parameters of the metal ion [61]. These theories are considerably simpler than the formalisms for *d*-block metal ions described above, and depend on the assumption, which may not be universally valid [62], that the spin-orbit (SO) coupling interaction completely dominates the crystal-field splitting. Nevertheless they have been remarkably successful in rationalizing the observed shifts in both solid-state samples and in solution, and in pushing the field forward. An extension has been given by McGarvey, however the improvements are relatively modest and the theory is still subject to the same basic assumptions [63]. The basic forms of the Golding and Halton, and Bleaney theories have been instrumental in the rationalization of the shifts observed in lanthanide pyrochlores [64, 65], and more recently for the solid-state lighting materials, lanthanide-doped yttrium aluminium garnet [66, 67]. The Bleaney theory also allows the paramagnetic shift and SA due to lanthanides to be described in terms of the magnetic susceptibility [61]. This is an extension of the susceptibility formalism described above, and has been employed for materials in the solid state [66, 68–72], small molecules in solution [62, 73], and more extensively for proteins in solution including calcium-binding metalloproteins such as calbindin D_{9k} [74] and calmodulin [75, 76], and for many other proteins where the lanthanide ions have been introduced as attached tags [77–85].

Recently van den Heuvel and Soncini have introduced a formalism which describes the paramagnetic shift for any system with arbitrary SO coupling strength [86–88]. For *d* metal ions, lanthanides, and actinides the shift and SA can either be calculated directly from the electronic energy levels, or else via an intermediate

step where the EPR parameters are first determined. This is straightforward for $3d$ metals, but the equivalent description of lanthanides and actinides is more complicated due to the more complex electronic structure of these ions. This formalism has been explored for isolated d -block metal ions [87, 89, 90] and actinide ions [91, 92]. In the future it seems likely that this formalism will become more widely used.

1.4 The paramagnetic relaxation enhancement

The development of formalisms to describe the PRE, and their applications, have also been researched actively [93–95]. The earliest and most widely-used formalism is the Solomon–Bloembergen–Morgan theory, which describes the nuclear relaxation as the effect of stochastic fluctuations in the hyperfine interaction as a consequence of a combination of molecular dynamics, fast chemical exchange, and electronic relaxation [96–98]. This formalism is limited to applications in high external magnetic fields, and with fast molecular dynamics. Additionally, the electronic relaxation is only treated approximately, using phenomenological parameters. The theory has been extended to describe systems with molecular dynamics that are much slower than electronic relaxation, such as large biomolecules, adding an extra term known as the Curie relaxation rate [99, 100]. The Curie PRE is calculated by separating the slow molecular dynamics from the faster electronic relaxation, and treating the relaxation process as a hyperfine coupling to the average electronic magnetic moment. The Curie contribution has been shown to dominate the linewidths of nuclear spins in proteins in solution for paramagnetic metals with electron relaxation times much shorter than the reorientation times [15]. These formalisms have been widely used to interpret PREs as structural restraints, particularly for proteins [11, 17, 101].

Further developments have focussed on formalisms that treat the electronic relaxation explicitly, both in the fast- and slow-electronic dynamics regimes, and which are also applicable in low external magnetic fields. These formalisms have been developed mainly by research groups in Sweden, Grenoble, and Ann Arbor, and are consequently referred to as the Swedish slow-motion [93, 102–109], Grenoble [110, 111], and Ann Arbor [112–114] theories respectively. These theories are more complicated than the Solomon–Bloembergen–Morgan theory and Curie formalisms, but have also been shown to be more generally applicable. Explicit calculations of electronic relaxation have been incorporated, including mechanisms such as distortion of the metal-site geometry due to solvent collisions in solution samples [115, 116], and molecular vibrations in

solutions and solids [117–119]. The slow-motion theory has been used to describe the relaxation of solvent molecules in a solution of paramagnetic metal ions by the mechanisms of inner- and outer-sphere relaxation [120]. The former mechanism describes the relaxation of molecules in the solvation sphere of the metal ion that are in exchange with the bulk solvent, and the latter mechanism describes the PRE of solvent molecules that never coordinate to the metal ion. The theory that describes these effects, and the calculations it facilitates [121–124], are of importance to understanding and developing contrast agents in magnetic resonance imaging (MRI) [125–133]. In addition the studies of the PRE under low-field conditions enable the calculation of NMR dispersion (NMRD) profiles, which show how relaxation rates vary with field [134–144]. Such NMRD profiles are useful for studying dynamic processes such as protein folding [145, 146].

1.5 Bulk magnetic susceptibility effects

The final paramagnetic effects that are considered here are the bulk magnetic susceptibility (BMS) and anisotropic bulk magnetic susceptibility (ABMS). These are of particular importance in the solid-state NMR of paramagnetic single-crystal samples, powders, and complex and heterogeneous samples such as battery cells. The BMS effect involves the change in the bulk susceptibility at the surface of a crystal and in the surrounding medium, which gives rise to a demagnetizing field within the crystal leading in turn to changes in the measured paramagnetic shift and to inhomogeneous line broadening. For paramagnetic polycrystalline powder samples with an ABMS, the close packing results in each crystallite experiencing a demagnetizing field due to the neighbouring crystallites, which is also a source of inhomogeneous broadening. Importantly this ABMS broadening is not removed by MAS and can dominate the lineshapes and linewidths of spinning paramagnetic solids, and perturb the intensities of the spinning sidebands so that they can no longer be analysed in terms of a simple second-rank tensor. What this means in practice is that the BMS leads to NMR spectra with low resolution, which hinders the basic assignment, and also impedes the obtaining of accurate distance information from the analysis of sideband manifolds.

The BMS and ABMS broadening effects were first described by VanderHart [147], and Alla and Lippmaa [148]. The effects of the BMS on the linewidth and spinning sideband intensities were demonstrated on paramagnetic lanthanide stannates by Grey et al. [149], who also showed that it is possible to remove the perturbing effects on the spinning sidebands in materials with isotropic susceptibilities by immersing the

crystals in a medium with a matching magnetic susceptibility, thus removing the effects that are responsible for the BMS. A more complete theory of the BMS and ABMS broadening was proposed by Schwerk et al. [150], and extended by Kubo et al. [151]. More recently a practical method for calculating the broadening has been proposed by Dickinson et al., [152], who use ideas from classical electrostatics to calculate the demagnetizing fields due to a large bulk sample.

The BMS effect has been shown to be very important in the study of whole battery cells containing a paramagnetic material. In this case the linewidth varies with the orientation of the sample within the magnetic field, and so it is crucial that this be optimized in order to obtain the optimum data [153, 154].

1.6 Paramagnetic NMR and dynamic nuclear polarization

One area of magnetic resonance that is very closely related to paramagnetic NMR is dynamic nuclear polarization (DNP). The object of this method is to increase, or enhance, the nuclear polarization of a system that also contains unpaired electrons. The electrons have a larger gyromagnetic ratio than any nuclei and so the electrons also have a larger spin polarization. For example the electronic gyromagnetic ratio, and therefore the polarization in a magnetic field, is larger than that of the proton by a factor of 658. The DNP methods transfer this polarization to the nuclei via a number of mechanisms involving the coupling between the electronic and nuclear magnetic moments, by irradiating the electronic spin transitions with microwave radiation simultaneously to acquiring the NMR spectrum.

Dynamic nuclear polarization was first proposed as an enhancement method for metals by Overhauser [155], and was shortly after demonstrated experimentally by Carver and Slichter [156, 157]. In recent years, the field has been revolutionized by the development of polarization methods for frozen solutions at high magnetic fields [158, 159], and application to solids under MAS [160–162]. The best enhancements have generally been obtained on diamagnetic samples that have been impregnated with paramagnetic species based on organic nitroxide-based radicals, and frozen at low temperatures of around 100 K [163–170]. These radicals and conditions are chosen because the polarization transfer mechanisms are generally more efficient if the electrons have longer relaxation times, typically of the order of milliseconds. This approach has been shown to be very successful in NMR applications in both biology [162, 171–176] and materials science [177–179]. However it has also been demonstrated that DNP enhancements can be obtained on paramagnetic

samples containing high-spin transition metal ions, such as Mn^{2+} and Gd^{3+} which also have comparatively slow electronic spin relaxation since these ions have no orbital angular momentum [180, 181].

The field of DNP has much in common with that of paramagnetic NMR. The obvious similarity is that both fields are applicable to samples containing sources of unpaired electrons, and an understanding of both fields requires an appreciation of “paramagnetic NMR concepts” such as the hyperfine interaction, electronic relaxation, PRE, and BMS. Specifically to explain DNP fully, we need to understand these paramagnetic effects in samples that have been impregnated with many paramagnetic radical molecules. For example two paramagnetic effects that have consequences for DNP are quenching, and nuclear depolarization. The quenching effect is important for nuclei that are close to the radicals, and experience a large PRE or hyperfine coupling that renders them “invisible” in conventional NMR experiments. This effectively reduces the number of nuclei that contribute to the NMR signals, and acts to reduce the size of the DNP enhancement. The depolarization effect, described by Thurber and Tycko, is an interesting phenomenon where the impregnation of the sample with the radical has the effect of reducing the initial nuclear polarization in the absence of microwave irradiation [182]. With microwave irradiation depolarization is expected to reduce the enhancement. Thurber and Tycko showed that depolarization is more effective when the unpaired electrons have long electronic relaxation times, meaning that the effect is important for organic radicals at low temperature, and is increased at higher fields [182]. It was also shown that spinning samples experience larger depolarization than static samples, provided the electronic spin relaxation times are longer than the rotation period. Thurber and Tycko ascribed depolarization to the cross effect, which becomes more pronounced in spinning samples due to time-dependent spin-level crossings that occur in organic biradicals with spatially anisotropic electronic Zeeman interactions. It is currently unclear whether this effect is also important for paramagnetic samples containing metal ions at room temperature, although the indications so far are that depolarization is negligible for such samples under these conditions, as the metal ions generally have much shorter electronic relaxation times.

Both the fields of paramagnetic NMR and DNP have their origin in early contributions made from the 1950s onwards, but have only experienced an expansion into the mainstream relatively recently with advances in instrumentation and methodology. However there are also some subtle differences between the two fields. Firstly, most applications of DNP are to diamagnetic systems that have been impregnated with paramagnetic radicals specifically for the purpose of using the unpaired electrons to obtain the enhancement. For the

subsequent DNP study to be valid, it is clearly necessary to avoid any structural changes to the system on adding the radical, and so the impregnation is carried out in such a way that the part of the system of interest is sufficiently far from the unpaired electrons not to experience any direct paramagnetic NMR effects. Beyond experiencing an enhancement and any relayed paramagnetic effects transferred by spin diffusion, this part of the system is assumed to be unperturbed by the radical. The “paramagnetic” part of the sample that is close to the radical is usually not studied and, as has already been remarked, is often invisible under the experimental conditions. This is in contrast to the practice of paramagnetic NMR, where the unpaired electrons play a key role in the properties of the system, and it is of immense interest to probe the nuclei that are as close to the paramagnetic centre as possible. Secondly, the DNP radicals are designed so that the unpaired electrons have long electronic spin relaxation times, on the order of milliseconds at low temperature. By contrast paramagnetic NMR is applied to paramagnetic species with a broader range of electronic relaxation times, usually ranging from picoseconds to milliseconds, but most studies are performed on species with faster electronic relaxation than DNP. Thirdly, in paramagnetic NMR we usually model the shift and shift anisotropy by noting that the nuclear spin dynamics occur on a timescale that is much longer than the electronic relaxation times, meaning that the nuclear spin effectively interacts with the average electronic magnetic moment. This model is at the root of all the theories of the paramagnetic shift and shift anisotropy. We only model the electronic spin levels explicitly when we need to consider a process that occurs on a faster timescale, such as the processes leading to nuclear relaxation. In DNP, on the other hand, the polarization transfer mechanisms can only be understood from a full consideration of the electronic spin levels at all times. This difference from paramagnetic NMR is due both to the longer electronic relaxation times of DNP radicals, and to the fact that the microwave irradiation of the electronic spin transitions has a timescale that is shorter than, or comparable to, the electronic spin relaxation times.

The field of DNP is currently evolving very rapidly, and there are many details to be worked out and controversies to be resolved. Therefore a comprehensive review of the theory and applications of DNP is at the time of writing extremely difficult, and beyond the scope of the current review.

1.7 What this review contains

The purpose of this review is to unify the descriptions of paramagnetic effects in the literature, and set them out in the context of the most recent work, particularly the theoretical descriptions of the paramagnetic shift and SA, which have hitherto not been described in detail for the NMR community. In addition greater emphasis is placed on the form of the shifts obtained in solid materials, which has been somewhat neglected in comparison to paramagnetic molecules in solution. In all cases we pull out the key equations that are generally used to interpret the spectra so that the reader does not have to follow all of the derivations, which we hope makes the chapters more practically useful. We do not intend this to be comprehensive in terms of a review of the literature, but simply to review the different approaches and strategies, and their strengths and weaknesses.

This review is divided into five parts. Part I is the single chapter 2, which describes the basic concepts that are necessary for understanding paramagnetic effects on NMR. Part II comprises chapters 3–7, and contains a description of all the formalisms for the paramagnetic shift and SA under different conditions and in different systems. This part also attempts to provide a unified description of the different formalisms. Part III contains chapters 8 and 9, and describes the PRE in different regimes. Again a unifying description is provided. Part IV concerns the BMS and ABMS effects in single-crystal and powder samples, and is formed of the single chapter 10. Part V is chapter 11, and describes the quantum mechanics of the NMR experiment. It is shown how the different NMR interactions in paramagnetic systems change the observed spectral features in both solution and solid-state NMR. The final part VI, formed from chapters 12–14, is a practical guide to the NMR experiments that can be used on different paramagnetic systems in solution and the solid state, and includes a series of case studies of different systems.

Chapter 2 describes some basic concepts that are essential for understanding paramagnetic NMR. These include the basic theory of magnetism, the chemical shift, and the hyperfine interaction. This material forms the foundations of NMR [183] and EPR [184, 185] spectroscopy, and it will be seen that an understanding of paramagnetic effects in NMR can only be obtained through an understanding of EPR.

Chapter 3 describes the origin of the paramagnetic shift and SA for the simplest possible example of a spin-only transition-metal complex. The shift is described both in terms of the EPR parameters, and the bulk magnetic susceptibility, and the two formalisms are unified. The effects of SO coupling on the paramagnetic

shift and SA due to a *d*-block transition-metal ion are described in chapter 4 in terms of the EPR formalism of van den Heuvel and Soncini [86, 88]. The effect of SO coupling on the magnetic susceptibility and the susceptibility formalism, are given. This chapter concludes with the first description of a unification of the two formalisms. The interpretation of the various contributions to the shift and SA arising from these EPR and susceptibility formalisms is detailed in chapter 5. This chapter describes under which conditions the various contributions become important, and the different types of structural and electronic information that each can provide. The following chapter 6 provides an advanced description of the EPR formalism of van den Heuvel and Soncini [86, 88], and in particular the role of higher-order effects that may be present in the EPR description of the metal ion, and with arbitrary spin-orbit coupling strength. This description is first applied to *d*-block metal ions, and then extended to the shift and SA due to lanthanide ions in the Bleaney formalism [61]. The effect of interactions between neighbouring metal ions in transition-metal clusters and extended solids is described in chapter 7. It describes the role of low-temperature magnetic ordering, such as ferro- and antiferromagnetic ordering, in determining the sizes of the shifts and SAs. We also link the solid-state shift formalism described by Kim et al. [53] to the EPR formalism.

In chapter 8 we turn our attention to the PRE and the form that the relaxation rate constants take in different motional regimes, including rapidly-tumbling molecules in solution, large biomolecules, and rigid solids. This chapter presents the Solomon–Bloembergen–Morgan and Curie relaxation theories, which are used to interpret the PRE of small molecules and large biomolecules under conditions of high field, and with a phenomenological description of electronic relaxation. Chapter 9 extends the relaxation discussion to include explicitly the relevant mechanisms of electronic relaxation. The Swedish slow-motion formalism is used to describe the effects of slow electron dynamics, low field, and inner- and outer-sphere PREs [102–104, 107–109].

A feature of paramagnetic solid-state NMR that has hitherto been neglected by reviews is the presence of BMS effects in single-crystal and powder samples. However it is a very important effect as it leads to changes in the measured shift, and to broadening of the resonances which limits the available resolution. The BMS effects are described in chapter 10 in terms of the theory of classical electrodynamics [186].

The remainder of the review concentrates on how different paramagnetic effects appear in the NMR spectra of solutions, static, and spinning solids containing different metal ions. Chapter 11 describes the basic quantum mechanics of NMR. We examine how the appearance of the NMR spectrum varies with different

interactions due to paramagnetic metal ions, and how these effects combine with other interactions, such as the nuclear quadrupolar interaction, to give distinctive spectral features. Chapter 12 is a practical guide to the NMR pulse sequences that can be applied to paramagnetic systems. The survey has a wide scope, and encompasses small molecules in solution, solid materials, and proteins both in solution and the solid state. This chapter aims to find the general principles that govern the success or failure of particular NMR methods when applied to paramagnetic systems. This links to chapter 13, which presents a series of case studies in paramagnetic NMR. The examples that are presented include small molecules, biomolecules, and solid materials incorporating a wide range of unpaired electron species including $3d$ metal ions, lanthanides, and organic radicals. Finally we provide some concluding remarks, and offer a perspective on the future of paramagnetic NMR in chapter 14.

Each chapter ends with a summary of the salient points.

Chapter 2

Introduction to nuclear and electronic magnetism

This chapter introduces the basic concepts describing the magnetic properties of nuclei and electrons. Bulk properties, such as the magnetization and magnetic susceptibility, and molecular/atomic-level properties, such as magnetic moments, are presented. We employ Cartesian and spherical tensor formalisms for describing the spin Hamiltonians of the basic interactions that are relevant for the NMR of paramagnetic systems, namely the nuclear and electronic Zeeman interactions, the chemical shielding and shift, and the hyperfine interaction.

2.1 Nuclear and electronic magnetic moments

In quantum mechanics the magnetic dipole moment of a nucleus μ_I is proportional to the dimensionless nuclear spin angular momentum I ,

$$\mu_I = \hbar\gamma_I I, \quad (2.1)$$

where the constant of proportionality is the product of Planck's constant divided by 2π (\hbar), and the nuclear gyromagnetic ratio γ_I . Planck's constant is a fundamental physical constant, whereas γ_I takes different values depending on the nuclear species. It is important to note that γ_I is a signed quantity, i.e. it can take either positive or negative values. For example both ^1H and ^{13}C have positive gyromagnetic ratios, whereas ^{15}N has

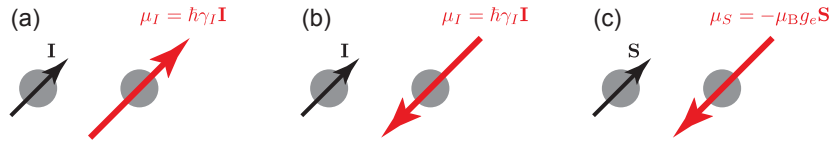


Figure 2.1: Illustration of the relationship between the spin and the magnetic dipole moment for nuclear and electronic spins. In (a) it is shown that a nuclear spin I with a positive gyromagnetic ratio γ_I possesses a magnetic moment μ_I that is parallel to the spin I . If instead the nuclear gyromagnetic ratio is negative, the spin and magnetic moment are antiparallel, as shown in (b). The free electron has a negative gyromagnetic ratio γ_S , and so the electronic magnetic moment μ_S is antiparallel to the electronic spin S .

a negative value. Figure 2.1 illustrates the relationship between the spin and magnetic moment vectors. The cases of positive and negative γ_I are shown in (a) and (b) respectively.

In describing the electronic magnetic moment we encounter a difference in the nomenclature used by the NMR and EPR communities. The definition of the nuclear magnetic moment in Equation 2.1, given in terms of \hbar and γ_I , is that most commonly employed by the NMR community. The EPR community, however, predominantly uses the alternative expression

$$\mu_I = \mu_N g_I \mathbf{I}, \quad (2.2)$$

where μ_N is the nuclear magneton, and g_I is the dimensionless nuclear g -factor. Like \hbar , μ_N is a physical constant; it can be related to other physical constants via the expression

$$\mu_N = \frac{e\hbar}{2m_p}, \quad (2.3)$$

where e is the elementary charge, and m_p is the rest mass of the proton. In this nomenclature different nuclear species have different values of g_I . The equivalence between the two sets of parameters describing the magnetic moment is concisely expressed as

$$\hbar\gamma_I = \mu_N g_I. \quad (2.4)$$

We note that g_I is also a signed quantity, and takes the same sign as γ_I .

In an analogous way the electron magnetic moment μ_S is proportional to the electron spin S , and can

also be written using two related constants of proportionality as follows:

$$\boldsymbol{\mu}_S = \hbar\gamma_S \boldsymbol{S} \quad (2.5)$$

$$= -\mu_B g_e \boldsymbol{S}, \quad (2.6)$$

where γ_S is the electron gyromagnetic ratio, g_e is the free-electron g -factor, and μ_B is a physical constant known as the Bohr magneton which can be calculated from the elementary charge and the rest mass of the electron m_e :

$$\mu_B = \frac{e\hbar}{2m_e}. \quad (2.7)$$

The relationship between the two sets of constants in the expression for the electronic magnetic moment is related in a similar way to Equation 2.4, but with an additional minus sign:

$$\hbar\gamma_S = -\mu_B g_e. \quad (2.8)$$

This awkward minus sign arises because the electron gyromagnetic ratio is actually negative, but it remains conventional to define g_e as a positive number with approximate value 2.0023. The relationship between the electronic spin and magnetic moment is illustrated in Figure 2.1 (c). In this review we adopt the convention that the angular momenta \boldsymbol{I} and \boldsymbol{S} refer to nuclear spins and electronic spins respectively.

2.2 Magnetic field, magnetization, and the magnetic susceptibility

In the literature one commonly encounters two definitions of the magnetic field, namely the magnetic field strength \boldsymbol{H} , and the magnetic induction, also known as the magnetic flux density, \boldsymbol{B} . When we are describing the application of a magnetic field to a material containing a large number of magnetic moments, the relationship between \boldsymbol{H} and \boldsymbol{B} is, in general, rather complicated. The field induces a net bulk magnetization \boldsymbol{M} which is the total induced magnetic moment per unit volume. The relationship between \boldsymbol{B} and \boldsymbol{H} is then [187]

$$\boldsymbol{B} = \mu_0(\boldsymbol{H} + \boldsymbol{M}), \quad (2.9)$$

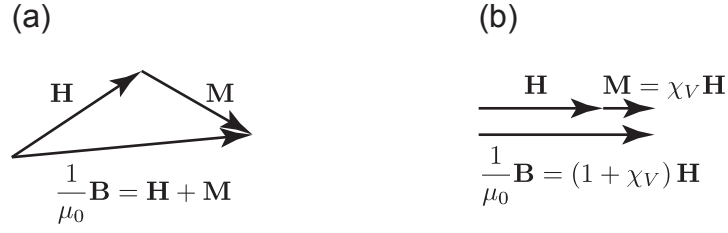


Figure 2.2: Illustration of the effect of applying a magnetic field to a magnetic material. The external magnetic field \mathbf{H} induces a response from the material in the form of a bulk magnetization \mathbf{M} . The vector sum of \mathbf{H} and \mathbf{M} is the total magnetic flux density \mathbf{B} . In general these three vector quantities are not parallel to each other, as shown in (a). The special case of a linear material with an isotropic volume magnetic susceptibility χ_V is shown in (b). Here \mathbf{M} is parallel to \mathbf{H} , and so both are parallel to \mathbf{B} .

where μ_0 is the permeability of free space. The magnetic field, magnetization, and flux density are not always parallel to each other, as illustrated in Figure 2.2 (a). Here we are concerned with *linear materials*, which are those materials for which the magnetization is proportional to the field strength [187]

$$\mathbf{M} = \chi_V \mathbf{H}, \quad (2.10)$$

where χ_V is a dimensionless scalar quantity called the volume magnetic susceptibility. Hence the flux density is given by

$$\mathbf{B} = \mu_0(1 + \chi_V)\mathbf{H}. \quad (2.11)$$

In this case the flux density is parallel to the field, as shown in Figure 2.2 (b). The scope of this review is restricted to paramagnetic systems which are linear, and for which the volume susceptibility is small, $|\chi_V| \ll 1$, and so the magnetic flux density and field strength are related by the simple relation

$$\mathbf{B} \approx \mu_0 \mathbf{H}. \quad (2.12)$$

Henceforth we use \mathbf{B} for the applied field, and refer to it simply as the ‘magnetic field’.

This review will focus on how the interaction between the nuclear and electronic spins in the presence of a magnetic field can be related to both the macroscopic and the molecular/atomic-level properties of the system. This link can be made by employing classical and statistical thermodynamics, and will be summarised here to facilitate the discussion. The first law of thermodynamics relates the infinitesimal change in the internal

energy U of a system to the energy supplied as heat and the work done by the system:

$$dU = TdS - pdV - VM \cdot dB. \quad (2.13)$$

The heat is equal to TdS , where T is the absolute temperature and S is the entropy of the system, and the work done by the system is $pdV + VM \cdot dB$ where p and V are the pressure and volume of the system. We define the Helmholtz free energy F as

$$F = U - TS. \quad (2.14)$$

The infinitesimal change in F that accompanies the infinitesimal change in U is

$$dF = dU - SdT - TdS \quad (2.15)$$

$$= -SdT - pdV - VM \cdot dB, \quad (2.16)$$

from which the components of the magnetisation are given by

$$M_i = -\frac{1}{V} \left(\frac{\partial F}{\partial B_i} \right)_{T,V}, \quad (2.17)$$

where the subscripts T and V indicate that the partial derivative is calculated at constant temperature and volume. This establishes the link between the bulk magnetization and the bulk thermodynamic properties of the system via the Helmholtz energy. It is also possible to establish a link to the molecular/atomic-level properties via statistical thermodynamics, from which it can be shown that F is given by

$$F = -NkT \ln Q, \quad (2.18)$$

where N is the number of particles, k is the Boltzmann constant, and Q is the partition function. This latter quantity is a sum over the molecular/atomic-level states $|n\rangle$ with energies E_n :

$$Q = \sum_n \exp(-E_n/kT). \quad (2.19)$$

Hence the expression for magnetization in terms of the molecular/atomic-level states is

$$M_i = \frac{NkT}{V} \left(\frac{\partial \ln Q}{\partial B_i} \right)_{T,V}. \quad (2.20)$$

This important link is used later to establish the forms of the chemical shielding and magnetic susceptibility tensors.

2.3 The electronic and magnetic properties of periodic solids

In chapter 7 we derive and discuss the form of the paramagnetic shielding tensor in periodic solid materials. In order to do so we must make a distinction between electronic insulators and metals, which have distinct electronic properties, and for which the contributions of the unpaired electrons to the NMR properties are very different. We therefore summarize the electronic properties of periodic solids here.

2.3.1 Electronic energy levels and the density of states

In finite systems, such as isolated molecules, the electronic energy levels form a discrete ladder with well-defined energies, and the wavefunctions may either be localized to certain atoms or delocalized to a limited extent across the molecule. However in an infinite periodic solid the energy spacing between levels is so small that the levels broaden into continuous bands [188]. The corresponding wavefunctions are delocalized across the entire material. In the absence of interactions between the electrons, the overall wavefunction can be approximated by a product of one-electronic wavefunctions $\phi(\mathbf{r})$ with energies E that are the solutions of the following Schrödinger equation:

$$\left(-\frac{\hbar^2}{2m_e} \nabla^2 + U(\mathbf{r}) \right) \phi(\mathbf{r}) = E\phi(\mathbf{r}), \quad (2.21)$$

where \mathbf{r} is the position of the electron. The potential $U(\mathbf{r})$ is due to the electrostatic attraction between the electron and all the nuclei distributed throughout the solid lattice. The potential is periodic over the lattice, and so satisfies the relation

$$U(\mathbf{r} + \mathbf{R}) = U(\mathbf{r}), \quad (2.22)$$

where the position vector \mathbf{R} is a linear combination of the three primitive vectors \mathbf{a}_i that span the lattice,

$$\mathbf{R} = n_1 \mathbf{a}_1 + n_2 \mathbf{a}_2 + n_3 \mathbf{a}_3, \quad (2.23)$$

and the n_i are integers. The energy levels $E_n(\mathbf{k})$ found by solving the Schrödinger equation can be characterized by a band index n , which is an integer defining the electronic band, and a wavevector \mathbf{k} which labels the levels within a particular band. Each corresponding one-electron wavefunction $\phi_{n\mathbf{k}}(\mathbf{r})$ is given by the product of a plane wave that depends on \mathbf{k} and is normalized over the sample volume V , and a normalized function $u_{n\mathbf{k}}(\mathbf{r})$ that depends on both n and \mathbf{k} :

$$\phi_{n\mathbf{k}}(\mathbf{r}) = \sqrt{\frac{1}{V}} \exp(i\mathbf{k} \cdot \mathbf{r}) u_{n\mathbf{k}}(\mathbf{r}). \quad (2.24)$$

The functions $u_{n\mathbf{k}}(\mathbf{r})$ have the same periodicity as the lattice, i.e. $u_{n\mathbf{k}}(\mathbf{r} + \mathbf{R}) = u_{n\mathbf{k}}(\mathbf{r})$, and the allowed values of \mathbf{k} satisfy

$$\exp(i\mathbf{k} \cdot \mathbf{R}) = 1. \quad (2.25)$$

If the electron-electron interactions are weak or absent we can write the normalized multi-electron wavefunction $\psi(\mathbf{r}_1, \mathbf{r}_2, \dots, \mathbf{r}_N)$ describing N electrons as the product of the N one-electron wavefunctions that have been properly symmetrized to satisfy the Pauli principle:

$$\psi(\mathbf{r}_1, \mathbf{r}_2, \dots, \mathbf{r}_N) = \sqrt{\frac{1}{N!}} \sum_P (-1)^P P \phi_{n_1 \mathbf{k}_1}(\mathbf{r}_1) \phi_{n_2 \mathbf{k}_2}(\mathbf{r}_2) \dots \phi_{n_N \mathbf{k}_N}(\mathbf{r}_N). \quad (2.26)$$

The operator P permutes the electron labels, the factor $(-1)^P$ is a plus or minus depending on whether an even or odd number of permutations is involved, and \mathbf{r}_i is the position of the i th electron.

It is frequently the case that we need to calculate certain general quantities that are the sums of contributions from the different electronic levels. For instance we may write a general quantity Q as the following sum of contributions $Q_n(\mathbf{k})$

$$Q = \sum_{n, \mathbf{k}} Q_n(\mathbf{k}), \quad (2.27)$$

where $Q_n(\mathbf{k})$ is the contribution from the level with wavevector \mathbf{k} in band n , and the sum runs over all bands n and the allowed values of \mathbf{k} within each band. In the limit where the volume of the system V becomes very

large the allowed values of \mathbf{k} become more closely spaced, and we can replace the sum over \mathbf{k} in Equation 2.27 with an integral. This allows us to calculate the value of the general quantity Q per unit volume, q , as

$$q = \lim_{V \rightarrow \infty} \frac{Q}{V} \quad (2.28)$$

$$= \frac{1}{(2\pi)^3} \sum_n \int Q_n(\mathbf{k}) d\mathbf{k}. \quad (2.29)$$

This expression is awkward to evaluate in practice, and so we replace it with an integral over the energies E . To do this we firstly calculate the average value of $Q_n(\mathbf{k})$ at constant energy E over all values of \mathbf{k} corresponding to that energy, denoted $\langle Q(\mathbf{k}) \rangle_E$. The value of q is then given by the following integral

$$q = \int \langle Q(\mathbf{k}) \rangle_E g(E) dE. \quad (2.30)$$

The function $g(E)$ is the density of states, which is given by the derivative of the number of electrons per unit volume $n = N/V$ with respect to energy:

$$g(E) = \frac{dn}{dE}. \quad (2.31)$$

Using this definition the number of electrons per unit volume with energies between E and $E + dE$ is $g(E)dE$. In the special case where $Q_n(\mathbf{k})$ depends on n and \mathbf{k} only through the energy $E_n(\mathbf{k})$, we can write Equation 2.30 as

$$q = \int Q(E)g(E)dE. \quad (2.32)$$

In the discussion so far we have focussed solely on the spatial properties of the electrons, and have made no reference to the spin. We account for the spin by multiplying the many-electron spatial wavefunction in Equation 2.26 with a properly symmetrized spin wavefunction. In addition we define separate density-of-state functions $g_\alpha(E)$ and $g_\beta(E)$ describing the electronic states of electrons in the α and β spin states. In the absence of an external magnetic field these functions are simply

$$g_\alpha(E) = g_\beta(E) = \frac{1}{2}g(E), \quad (2.33)$$

i.e. each is exactly half of the total density of states.

The density of states gives us the energies of the levels, but does not give us their populations. The average

occupancy of a level in band n with wavevector \mathbf{k} is given by the Fermi-Dirac distribution function $f_n(\mathbf{k})$. This distribution function is usually given in terms of the energy to give the following function $f(E)$,

$$f(E) = \frac{1}{\exp[(E - \mu)/kT] + 1}, \quad (2.34)$$

where μ is the chemical potential of the system. At zero temperature the Fermi-Dirac distribution function is a Heaviside step function [189], which is given by

$$f(E) = \begin{cases} 1, & E < \mu, \\ 0, & E > \mu, \end{cases} \quad (2.35)$$

i.e. the states with energies below the chemical potential are completely filled, and those with energies above the chemical potential are completely unfilled. Hence we see that at zero temperature the chemical potential is equal to the energy of the highest-energy occupied electronic level, which is referred to as the Fermi energy E_F , i.e. $\lim_{T \rightarrow 0}(\mu) = E_F$. The corresponding level is the Fermi level. At temperatures above zero the chemical potential deviates from the Fermi energy according to

$$\mu = E_F \left[1 - \frac{\pi^2}{12} \left(\frac{T}{T_F} \right)^2 + \mathcal{O} \left(\left(\frac{T}{T_F} \right)^4 \right) \right], \quad (2.36)$$

where T_F is the Fermi temperature which is defined via the relation $E_F = kT_F$. However the temperature-dependent correction can usually be neglected at typical temperatures from 100–1000 K, for example in the case of metals where T_F is of the order 10^4 – 10^5 K [183], and so we simply equate the chemical potential with the Fermi energy $\mu \approx E_F$. The Fermi-Dirac distribution function is plotted for different temperatures in Figure 2.3. It can be seen that the distribution is a step function at $T = 0$, with the discontinuity at $E = E_F$. However as the temperature increases we can clearly see the progressive population of states just above the Fermi level at the expense of those just below the Fermi level. The total number density of the electrons n is given by the integral expression in Equation 2.32, where the quantity $Q(E)$ is substituted for $f(E)$:

$$n = \int f(E)g(E)dE. \quad (2.37)$$

There are also analogous expressions for the separate number densities of α and β electrons.

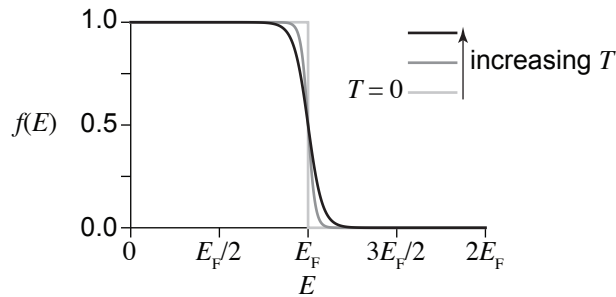


Figure 2.3: Plots of the Fermi–Dirac distribution function as a function of energy at different temperatures. At $T = 0$ (light grey curve) the distribution is a Heaviside step function with the discontinuity at E_F . As T increases (dark grey and black curves) the discontinuity is smoothed, and the states just above E_F are populated at the expense of those just below.

2.3.2 Band structures of insulators, semiconductors, and metals

We are now in a position to distinguish between the different types of periodic solid, namely insulators, semiconductors, and metals. The definitions of these materials are illustrated by the schematics of their band structures shown in Figure 2.4.

Insulators

We discuss the case of insulators first as this is the class of solid materials to which we devote the most time in this review. The band structure is shown in Figure 2.4 (a). The highest occupied band, called the valence band, is completely filled with electrons, and the next-highest, called the conduction band, is completely empty. There is an energy gap between the top of the valence band and the bottom of the conduction band called the band gap E_g , in the middle of which is the Fermi energy. This gives us our definition of a non-metallic system, which is a system for which the Fermi level lies in a band gap. Solid insulators have a band gap that is large compared to the thermal energy $E_g \gg kT$, so that the conduction band remains unpopulated. We note that such systems do not necessarily have equal numbers of α and β electrons, and that such systems behave as paramagnets. There is no mobility of electronic charge, and we can regard any unpaired metal electrons as being mainly localised on, for example, the metal ion. The paramagnetic NMR properties of these systems are discussed in section 7.7.

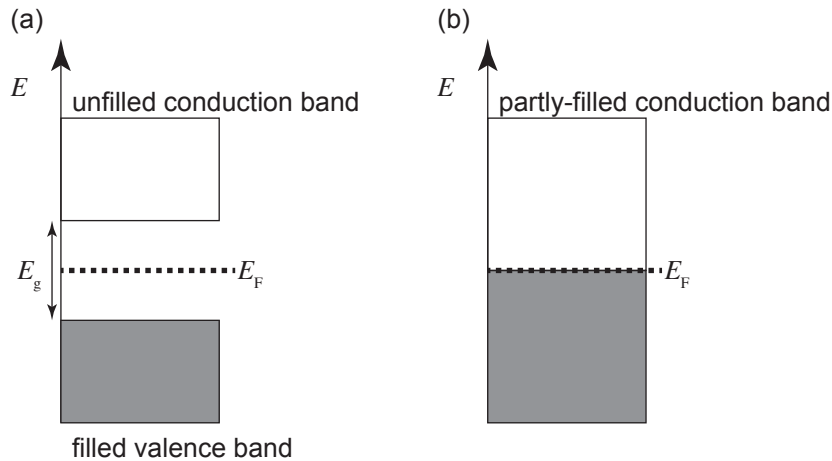


Figure 2.4: Schematic band structures of solid materials. The bands are shown for (a) an insulator with band gap $E_g \gg kT$, and (b) a metal. Intrinsic semi-conductors are also represented by (a), but now with $E_g \approx kT$

Semiconductors

Intrinsic semi-conductors are also described by the band structure in Figure 2.4 (a), with the Fermi level being located in a band gap. However the difference here is that the band gap is comparable to kT at room temperature, and not much greater, i.e. $E_g \approx kT$. Therefore there is some thermal population of the conduction band and the conduction electrons are delocalized over the whole lattice, rather than being localized to the paramagnetic centres. Hence the NMR properties are different to those of paramagnetic insulators, as discussed in section 7.12.

Metals

The final example we consider is the case of solid metals, the band structure of which is shown in Figure 2.4 (b). Here the highest-occupied band is only partly filled, and the Fermi level coincides with the highest-energy occupied level. Therefore at non-zero temperatures the levels just above the Fermi level become partly occupied and the material exhibits conductive behaviour. This has profound consequences for the NMR properties nuclei in such materials as the unpaired electrons, rather than being largely localised to the paramagnetic centres, are now delocalized across the whole lattice. These effects are discussed in section 7.12.

2.3.3 The free-electron model of metals

In order to facilitate a later discussion in section 7.12 comparing the NMR shifts observed in paramagnetic insulators and metals, we will use a simple model for the electronic structure of a metal referred to as a free-electron model. This model is summarized here.

The definition of a free-electron metal is a solid in which there is no attractive potential between the nuclei and the electrons, so that $U(\mathbf{r}) = 0$. The solid is also periodic in x , y , and z over a length L . Then the electronic levels are contained in a single band $n = 1$, and the one-electron wavefunctions $\phi_{\mathbf{k}}(\mathbf{r})$ are simply the normalized plane wave functions

$$\phi_{\mathbf{k}}(\mathbf{r}) = \sqrt{\frac{1}{V}} \exp(i\mathbf{k} \cdot \mathbf{r}), \quad (2.38)$$

i.e. $u_{\mathbf{k}}(\mathbf{r}) = 1$. The allowed values of the wavevectors are $\mathbf{k} = (2\pi/L)(n_1, n_2, n_3)$. The corresponding energies $E(k)$ depend only on the magnitude of the wavevector k , and are given by

$$E(k) = \frac{\hbar^2 k^2}{2m_e}. \quad (2.39)$$

The number density of electrons with wavevector magnitudes between k and $k + dk$ is given by the density of states $g(E(k))dk$ on the one hand. On the other the number density is equal to the volume of a spherical shell in wavevector space at radius k and thickness dk divided by the average volume per electron $(2\pi/L)^3$. Equating these two expressions we obtain

$$g(E(k)) dk = \frac{2}{V} \left(\frac{L}{2\pi}\right)^3 4\pi k^2 dk \quad (2.40)$$

$$= \frac{k^2}{\pi^2} dk, \quad (2.41)$$

where the extra factor of two accounts for double occupancy by electrons with paired spins. The number density of electrons $n(k, 0)$ with wavevector magnitudes between 0 and k is given by the integral

$$n(k, 0) = \int_0^k g(E(k')) dk' \quad (2.42)$$

$$= \frac{k^3}{3\pi^2}. \quad (2.43)$$

From this we can calculate an expression for the density of states as a function of energy:

$$g(E) = \frac{dn(k, 0)}{dk} \frac{dk}{dE} \quad (2.44)$$

$$= \frac{1}{2\pi^2} \left(\frac{2m_e}{\hbar^2} \right)^{3/2} E^{1/2} \quad (2.45)$$

We associate the Fermi level with a Fermi wavevector k_F , giving a Fermi energy of

$$E_F \equiv E(k_F) \quad (2.46)$$

$$= \frac{\hbar^2 k_F^2}{2m_e}. \quad (2.47)$$

Combining Equations 2.45 and 2.47, we obtain the following simple expression for the density of states at the Fermi level:

$$g(E_F) = \frac{3n}{2E_F}. \quad (2.48)$$

This expression will prove very useful when comparing the shifts in metals and paramagnetic insulators.

2.4 The nuclear and electronic Zeeman interactions

The energy of interaction E between a magnetic moment μ and a magnetic field B is given by the scalar product

$$E = -B \cdot \mu, \quad (2.49)$$

where the magnetic field can either be applied externally or be due to a second magnetic moment. Figure 2.5 (a) shows the variation of the interaction energy with the relative orientation of the magnetic moment with respect to the magnetic field. The corresponding Hamiltonian \hat{H} is given by the same expression with μ replaced with the equivalent operator $\hat{\mu}$:

$$\hat{H} = -B \cdot \hat{\mu}. \quad (2.50)$$

The interaction of the nuclear magnetic moment with an external magnetic field B_0 gives the nuclear

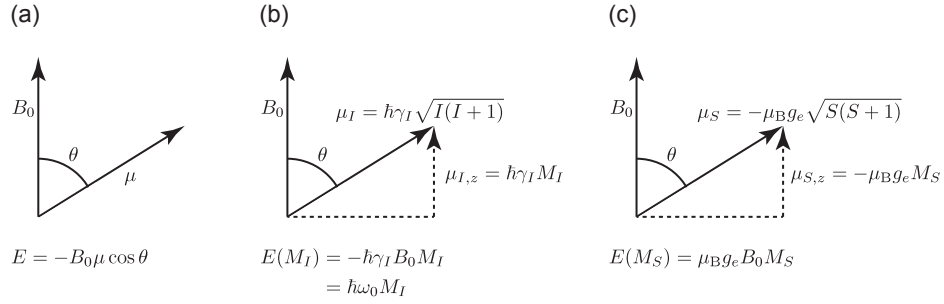


Figure 2.5: Illustration of the relationship between the spin, magnetic moment, external magnetic field, and Zeeman energy of interaction for nuclear and electronic spins. The classical description is illustrated in (a), with the energy of interaction between the magnetic moment and external field depending on the angle θ between the two vectors. The corresponding quantum-mechanical relationships are shown for the nuclear and electronic spins in (b) and (c), assuming that the external field is along z .

Zeeman Hamiltonian \hat{H}_{IZ}

$$\hat{H}_{IZ} = -\mathbf{B}_0 \cdot \hat{\boldsymbol{\mu}}_I \quad (2.51)$$

$$= -\hbar\gamma_I \mathbf{B}_0 \cdot \hat{\mathbf{I}}, \quad (2.52)$$

where $\hat{\mathbf{I}}$ is the nuclear spin operator. By convention the laboratory axis system is defined so that the external field is parallel to z . The nuclear Zeeman interaction is therefore given by

$$\hat{H}_{IZ} = -\hbar\gamma_I B_0 \hat{I}_z \quad (2.53)$$

$$= \hbar\omega_0 \hat{I}_z, \quad (2.54)$$

where \hat{I}_a is the operator representing the component of the spin along axis a , and $\omega_0 = -\gamma_I B_0$ is the nuclear Larmor frequency. Since γ_I is a signed quantity, so is ω_0 . For example we note that both ^1H and ^{13}C have a positive gyromagnetic ratio and a negative Larmor frequency, whereas ^{15}N has a negative gyromagnetic ratio and positive Larmor frequency. A nucleus of spin quantum number I has $2I + 1$ states $|IM_I\rangle$ which are labelled by the magnetic quantum number M_I which takes values from $-I$ to $+I$ in integer steps. Whilst this ‘complete notation’ is the one that is mainly used throughout this review, in some cases we also employ the more compact, and less crowded, notation $|M_I\rangle$ where the spin quantum number I is well defined. These

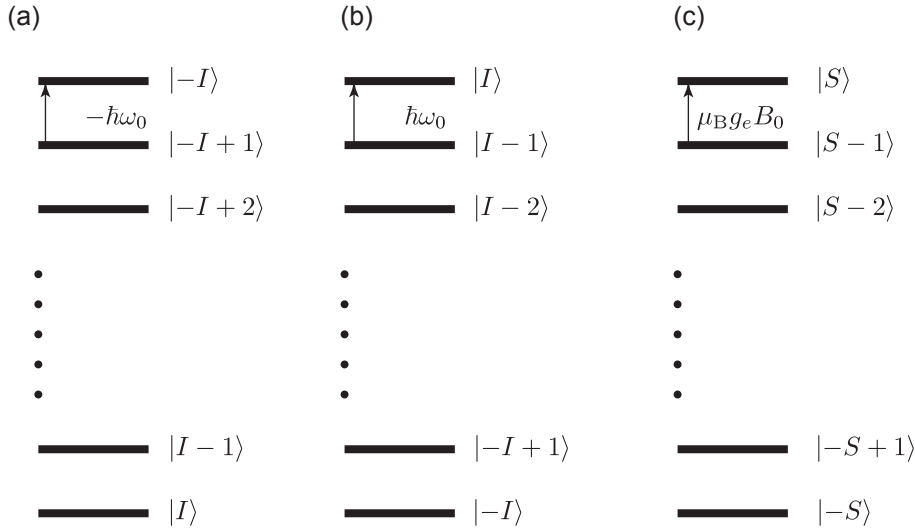


Figure 2.6: The ladder of energy levels due to the Zeeman interaction. The energy levels are shown for a general nuclear spin I with (a) a positive gyromagnetic ratio, and (b) a negative gyromagnetic ratio. The energy levels for an arbitrary electronic spin S are shown in (c). Note that the gyromagnetic ratio of the electron is negative. We employ the compact notation for the spin states, $|M_I\rangle$ or $|M_S\rangle$, rather than the complete notation. In each case the energies of the allowed transitions are shown.

states are the eigenstates of the Zeeman Hamiltonian, with the following energies $E(M_I)$:

$$E(M_I) = M_I \hbar \omega_0. \quad (2.55)$$

Figure 2.5 (b) illustrates the relationship between the nuclear spin vector, the external field, and the Zeeman energy of interaction. Note that for a nucleus with positive γ_I (and therefore negative ω_0), the lowest-lying state is $|I + I\rangle$, with energy $I\hbar\omega_0$, and the state with the highest energy is $|I - I\rangle$. Allowed transitions obey the selection rule $\Delta M_I = \pm 1$, and so the observed frequency of absorption is $-\omega_0$, as shown in Figure 2.6 (a). For nuclei with negative γ_I the energy order of the states is reversed with the lowest-lying state now being $|I - I\rangle$, with energy $-I\hbar\omega_0$, as shown in Figure 2.6 (b). The observed frequency of absorption for transitions obeying the selection rule $\Delta M_I = \pm 1$ is now $+\omega_0$. A nucleus with spin $I = 1/2$ possesses two states, which are conventionally labelled $|\frac{1}{2} + \frac{1}{2}\rangle \equiv |\alpha\rangle$ and $|\frac{1}{2} - \frac{1}{2}\rangle \equiv |\beta\rangle$.

The electron Zeeman interaction is described by the Hamiltonian \hat{H}_{SZ} which is given by

$$\hat{H}_{SZ} = -\mathbf{B}_0 \cdot \hat{\boldsymbol{\mu}}_S \quad (2.56)$$

$$= \mu_B g_e \mathbf{B}_0 \cdot \hat{\mathbf{S}}, \quad (2.57)$$

where $\hat{\boldsymbol{\mu}}_S$ and $\hat{\mathbf{S}}$ are the operators representing the electronic magnetic moment and spin respectively. When the applied magnetic field is along z the Hamiltonian becomes

$$\hat{H}_{SZ} = \mu_B g_e B_0 \hat{S}_z, \quad (2.58)$$

where \hat{S}_a is the operator representing the component of $\hat{\mathbf{S}}$ along axis a . The electronic spin states are now labelled $|S M_S\rangle$. A free electron has spin $S = 1/2$, and therefore two states with energies $E_\beta = -\frac{1}{2}\mu_B g_e B_0$ and $E_\alpha = +\frac{1}{2}\mu_B g_e B_0$. The relationship between the electronic spin, external magnetic field, and Zeeman energy of interaction is illustrated in Figure 2.5 (c). Note that as the electron has a negative gyromagnetic ratio, it is the $|\beta\rangle$ state that has the lower energy. Figure 2.6 (c) shows the ladder of Zeeman energy levels and energy of transition of an arbitrary electronic spin S .

2.5 Irreducible spherical tensors and tensor operators

2.5.1 Cartesian tensor representation of the spin Hamiltonian

This review makes extensive use of the various types of spin interactions that are present in both NMR and EPR spectroscopy, the basic ideas behind which are summarised here. All NMR and EPR interactions can be described as a coupling between two vectors, such as two spin vectors either belonging to two different spins or to the same spin, or a spin coupling to an external magnetic field, via a rank-two Cartesian tensor that contains all the information about the relevant spatial properties of the interaction. For example the nuclear Zeeman and chemical shielding interactions can be described by a Hamiltonian \hat{H}_{BI} of the form

$$\hat{H}_{BI} = \mathbf{B} \cdot \mathbf{K} \cdot \hat{\mathbf{I}}. \quad (2.59)$$

V_{10}	$V_{1\pm 1}$
V_z	$\mp \sqrt{\frac{1}{2}}V_{\pm}$

Table 2.1: Irreducible spherical tensor components of a vector \mathbf{V} in terms of the Cartesian components V_i , with $V_{\pm} = V_x \pm iV_y$.

The form of this Hamiltonian is instantly recognisable as a generalised scalar product of the external magnetic field vector \mathbf{B} with the spin vector $\hat{\mathbf{I}}$ via the real spatial tensor \mathbf{K} . As stated earlier in section 2 I refers to nuclear spins and S to electronic spins. Hence Equation 2.59 describes either a nuclear Zeeman or chemical shielding interaction, and the electronic Zeeman interaction can be obtained simply by replacing $\hat{\mathbf{I}}$ with $\hat{\mathbf{S}}$. Note that the information about the field, spatial orientation, and spin is neatly separated into the different parts of \hat{H}_{BI} , being represented by \mathbf{B} , \mathbf{K} , and $\hat{\mathbf{I}}$ respectively. Likewise a coupling between two spins S and I has the general Hamiltonian \hat{H}_{SI}

$$\hat{H}_{SI} = \hat{\mathbf{S}} \cdot \mathbf{K} \cdot \hat{\mathbf{I}}. \quad (2.60)$$

Finally the nuclear quadrupole interaction Hamiltonian is \hat{H}_{II} ,

$$\hat{H}_{II} = \hat{\mathbf{I}} \cdot \mathbf{K} \cdot \hat{\mathbf{I}}, \quad (2.61)$$

which mathematically appears to be the coupling of the spin vector of I with itself.

2.5.2 Irreducible spherical tensor representation of the spin Hamiltonian

In addition to the Cartesian representation of the interaction Hamiltonian, it sometimes proves convenient to adopt an irreducible spherical tensor representation of the field, spin, and spatial parts. A general irreducible spherical tensor is represented as P_{lm} , with l and m indicating the rank and order respectively. The order m takes values from $-l$ to $+l$ in integer steps. In the spherical tensor basis we write Cartesian vectors \mathbf{V} , such as the field and spin, as irreducible spherical tensors of rank 1. They have three components V_{10} , and $V_{1\pm 1}$, which are given in terms of the Cartesian components by the expressions in Table 2.1. It is usual to couple together the two vectors in the Hamiltonian to form either a mixed field-spin tensor operator, in the case of coupling the field to a spin operator, or a spin-spin tensor operator, in the case of coupling two spin operators. The coupling together of two rank-one tensors $\hat{U}_{1m'}$ and $\hat{V}_{1m''}$, both of which are in general operators, yields

the coupled tensor operator \hat{T}_{lm} via the expression [190]

$$\hat{T}_{lm} = \sum_{m'=-1}^{+1} \sum_{m''=-1}^{+1} \langle 11m'm''|lm \rangle \hat{U}_{1m'} \hat{V}_{1m''}, \quad (2.62)$$

where $\langle 11m'm''|lm \rangle$ is a Clebsch–Gordan coefficient, l takes the values 2, 1, and 0 according to the Clebsch–Gordan series, and $m = m' + m''$. Table 2.2 shows the tensor operators \hat{T}_{lm} formed by coupling together two rank-one spin tensors for interactions that are commonly encountered in NMR spectroscopy.

The real Cartesian spatial tensor \mathbf{K} can be broken down into an isotropic part K^{iso} , an anisotropic antisymmetric part \mathbf{K}^{asym} , and a traceless anisotropic symmetric part \mathbf{K}^{sym} :

$$\mathbf{K} = K^{\text{iso}} \mathbf{1} + \mathbf{K}^{\text{asym}} + \mathbf{K}^{\text{sym}}, \quad (2.63)$$

where $\mathbf{1}$ is the 3×3 identity matrix. These three parts are given by

$$K^{\text{iso}} = \frac{1}{3} \text{Tr}(\mathbf{K}), \quad (2.64)$$

$$\mathbf{K}^{\text{asym}} = \frac{1}{2} (\mathbf{K} - \mathbf{K}^T), \quad (2.65)$$

$$\mathbf{K}^{\text{sym}} = \frac{1}{2} (\mathbf{K} + \mathbf{K}^T) - \frac{1}{3} \text{Tr}(\mathbf{K}) \mathbf{1}. \quad (2.66)$$

We see that the nine independent components of \mathbf{K} are separated into these three parts as follows. The isotropic part K^{iso} contains a single component which corresponds to the orientation-independent part of \mathbf{K} . The anisotropic and antisymmetric part \mathbf{K}^{asym} contains three independent components, and is therefore equivalent to a so-called pseudo vector. The final part \mathbf{K}^{sym} , which is wholly anisotropic (i.e. traceless) and symmetric, contains five independent components. These five parts can be written in terms of the irreducible spherical tensors of ranks 0, 1, and 2 respectively as summarised in Table 2.3. The Hamiltonian written in the irreducible spherical tensor basis is

$$\hat{H} = \sum_{l=0}^2 \sum_{m=-l}^{+l} (-1)^m K_{lm} \hat{T}_{l-m}, \quad (2.67)$$

which is the form of the generalised scalar product [190].

It is conventional to parameterise the anisotropic parts of the spatial tensor according to their anisotropy

Interaction	\hat{T}_{00}	\hat{T}_{10}	\hat{T}_{1+1}	\hat{T}_{20}	\hat{T}_{2+1}	\hat{T}_{2+2}
Nuclear shielding (electronic Zeeman)	$-\sqrt{\frac{1}{3}}B_0\hat{I}_z$	0	$-\frac{1}{2}B_0\hat{I}_\pm$	$\sqrt{\frac{2}{3}}B_0\hat{I}_z$	$\mp\frac{1}{2}B_0\hat{I}_\pm$	0
Dipolar coupling (spin-dipolar hyperfine)	0	0	0	$\sqrt{\frac{1}{6}}(3\hat{I}_z\hat{S}_z - \hat{\mathbf{I}} \cdot \hat{\mathbf{S}})$	$\mp\frac{1}{2}(\hat{I}_z\hat{S}_\pm + \hat{I}_\pm\hat{S}_z)$	$\frac{1}{2}\hat{I}_\pm\hat{S}_\pm$
J -coupling (Fermi-contact hyperfine)	$-\sqrt{\frac{1}{3}}\hat{\mathbf{I}} \cdot \hat{\mathbf{S}}$	$-\frac{1}{2\sqrt{2}}(\hat{I}_+\hat{S}_- - \hat{I}_-\hat{S}_+)$	$\frac{1}{2}(\hat{I}_z\hat{S}_\pm - \hat{I}_\pm\hat{S}_z)$	$\sqrt{\frac{1}{6}}(3\hat{I}_z\hat{S}_z - \hat{\mathbf{I}} \cdot \hat{\mathbf{S}})$	$\mp\frac{1}{2}(\hat{I}_z\hat{S}_\pm + \hat{I}_\pm\hat{S}_z)$	$\frac{1}{2}\hat{I}_\pm\hat{S}_\pm$
Quadrupolar coupling (zero-field splitting)	0	0	0	$\sqrt{\frac{1}{6}}(3\hat{I}_z^2 - I(I+1)\hat{1})$	$\mp\frac{1}{2}(\hat{I}_z\hat{I}_\pm + \hat{I}_\pm\hat{I}_z)$	$\frac{1}{2}\hat{I}_\pm^2$

Table 2.2: Rank-two tensors formed by coupling two rank-one spin tensors, or a rank-one spin tensor to a rank-one magnetic field tensor for different internal spin interactions. The names of both the NMR interactions and their EPR equivalents (in parentheses) are given. The identity operator for the spin is written $\hat{1}$.

Rank	Expression in terms of K_{ij}	Expression in terms of K^{iso} , K_{ij}^{asym} , and K_{ij}^{sym}
0	$K_{00} = -\sqrt{\frac{1}{3}}(K_{xx} + K_{yy} + K_{zz})$	$-\sqrt{3}K^{\text{iso}}$
1	$K_{10} = -\frac{i}{\sqrt{2}}(K_{xy} - K_{yx})$ $K_{1\pm 1} = -\frac{1}{2}[K_{zx} - K_{xz} \pm i(K_{zy} - K_{yz})]$	$-i\sqrt{2}K_{xy}^{\text{asym}}$ $-[K_{zx}^{\text{asym}} \pm iK_{zy}^{\text{asym}}]$
2	$K_{20} = \sqrt{\frac{1}{6}}[3K_{zz} - (K_{xx} + K_{yy} + K_{zz})]$ $K_{2\pm 1} = \mp \frac{1}{2}[K_{xz} + K_{zx} \pm i(K_{yz} + K_{zy})]$ $K_{2\pm 2} = \frac{1}{2}[K_{xx} - K_{yy} \pm i(K_{xy} + K_{yx})]$	$\sqrt{\frac{3}{2}}K_{zz}^{\text{sym}}$ $\mp [K_{zx}^{\text{sym}} \pm iK_{zy}^{\text{sym}}]$ $\frac{1}{2}[K_{xx}^{\text{sym}} - K_{yy}^{\text{sym}} \pm 2iK_{xy}^{\text{sym}}]$

Table 2.3: Irreducible spherical tensor components of a matrix \mathbf{K} describing the spatial part of an interaction in terms of the Cartesian components K_{ij} . The isotropic part of the tensor is K_{iso} .

parameters in their respective principal axis frames (PAFs). The PAF of the antisymmetric rank-one tensor is defined as the coordinate system in which the irreducible spherical tensor components are given by

$$\bar{K}_{10} = -i\sqrt{2}\zeta, \quad (2.68)$$

$$\bar{K}_{1\pm 1} = 0, \quad (2.69)$$

where the overbar indicates that the tensor components are evaluated in the PAF of the antisymmetric part of the tensor. The antisymmetric anisotropy parameter ζ is defined as

$$\zeta = \sqrt{(K_{xy}^{\text{asym}})^2 + (K_{yz}^{\text{asym}})^2 + (K_{xz}^{\text{asym}})^2} \quad (2.70)$$

$$= \frac{1}{2}\sqrt{(K_{xy} - K_{yx})^2 + (K_{yz} - K_{zy})^2 + (K_{xz} - K_{zx})^2}. \quad (2.71)$$

The PAF of the symmetric part of the tensor is defined as the frame in which \mathbf{K}^{sym} is diagonal. Note that this frame does not, in general, coincide with the PAF of the antisymmetric part of \mathbf{K} . In the PAF of \mathbf{K}^{sym} the diagonal elements are ordered according to the Haeberlen convention so that $|K_{zz}^{\text{sym}}| \geq |K_{xx}^{\text{sym}}| \geq |K_{yy}^{\text{sym}}|$. The rank-two irreducible spherical tensor components are given by

$$\tilde{K}_{20} = \sqrt{\frac{3}{2}}\Delta K, \quad (2.72)$$

$$\tilde{K}_{2\pm 1} = 0, \quad (2.73)$$

$$\tilde{K}_{2\pm 2} = -\frac{1}{2}\eta\Delta K, \quad (2.74)$$

where the tilde indicates that the tensor components are evaluated in the PAF of the symmetric part of \mathbf{K} .

The symmetric anisotropy ΔK and asymmetry parameter η are given by

$$\Delta K = \tilde{K}_{zz}^{\text{sym}}, \quad (2.75)$$

$$\eta = \frac{\tilde{K}_{yy}^{\text{sym}} - \tilde{K}_{xx}^{\text{sym}}}{\Delta K}. \quad (2.76)$$

Before leaving this section we note that there are numerous examples of spatial interaction tensors \mathbf{X} , such as the nuclear quadrupolar interaction, zero-field splitting, and magnetic susceptibility tensors, which have an antisymmetric part of zero, i.e. $X_{10} = X_{1\pm 1} = 0$. In this case it is possible to define the rank-zero and rank-two tensors in terms of the components X_{ij} of the complete tensor:

$$X_{00} = -\sqrt{3}X^{\text{iso}}, \quad (2.77)$$

$$\tilde{X}_{20} = \sqrt{\frac{3}{2}}\Delta X, \quad (2.78)$$

$$\tilde{X}_{2\pm 1} = 0, \quad (2.79)$$

$$\tilde{X}_{2\pm 2} = -\frac{1}{2}\eta\Delta X, \quad (2.80)$$

where the anisotropy ΔX and asymmetry parameter η have modified expressions:

$$\Delta X = \tilde{X}_{zz} - X^{\text{iso}}, \quad (2.81)$$

$$\eta = \frac{\tilde{X}_{yy} - \tilde{X}_{xx}}{\Delta X}. \quad (2.82)$$

These definitions are completely equivalent to those in Equations 2.75 and 2.76.

2.6 Chemical shielding and chemical shift

The nuclear Zeeman Hamiltonian correctly describes the effect of an external magnetic field applied to an isolated nucleus. However when the nucleus is part of an atom, ion, or molecule, the Zeeman Hamiltonian no longer provides an adequate description, and we must account for the effect of the surrounding electrons. The external magnetic field causes the electrons to move in such a way that they produce their own induced magnetic fields that modify the actual field experienced by the nucleus. In diamagnetic systems the electronic

magnetic fields usually oppose the external field, thus *shielding* the nucleus from the external field. This effect is described by a chemical shielding tensor σ which can be included in the nuclear Zeeman Hamiltonian to give the correct overall description of the system:

$$\hat{H}_I = \hat{H}_{IZ} + \hat{H}_{IC} \quad (2.83)$$

$$= -\hbar\gamma_I \mathbf{B}_0 \cdot (\mathbf{1} - \sigma) \cdot \hat{\mathbf{I}}, \quad (2.84)$$

where $\hat{H}_{IC} = \hbar\gamma_I \mathbf{B}_0 \cdot \sigma \cdot \hat{\mathbf{I}}$ is the term in the Hamiltonian describing the chemical shielding, and $\mathbf{1}$ is the identity tensor.

The shielding tensor σ , which was first described theoretically by Ramsey [191], comprises isotropic, antisymmetric, and symmetric anisotropic parts. Ramsey showed that for diamagnetic systems the chemical shielding can be written as the sum of a “diamagnetic component” σ^{dia} and a “paramagnetic component” σ^{para} .

$$\sigma = \sigma^{\text{dia}} + \sigma^{\text{para}}. \quad (2.85)$$

Here we face our first difficulty with the terminology. The terms “diamagnetic” and “paramagnetic” do not refer to whether the *system* itself is dia- or paramagnetic, i.e. whether or not it has unpaired electrons. Rather, the former is the contribution to the shielding from the electronic ground state of the system, and the latter is due to the mixing of excited states with the ground state. Both contributions are present in both dia- and paramagnetic systems [88]. Pennanen and Vaara refer to the sum of these two terms as the *orbital* contribution to the shielding σ^{orb} [39]. In true paramagnetic systems we must add to the orbital contribution a second term that is due solely to the unpaired electrons σ^{S} to give the total shielding tensor

$$\sigma = \sigma^{\text{orb}} + \sigma^{\text{S}}. \quad (2.86)$$

It is σ^{S} that gives rise to the “paramagnetic shift”, and it is this that forms a central subject of this review.

The isotropic, antisymmetric, and symmetric parts of σ can be separated by rewriting \hat{H}_{IC} as the generalised scalar product of irreducible spherical tensors. This gives

$$\hat{H}_{IC} = \hbar\gamma_I \sum_{l=0}^{+2} \sum_{m=-l}^{+l} (-1)^m \sigma_{lm} \hat{T}_{l-m}, \quad (2.87)$$

where σ_{lm} is the component of the chemical shielding tensor with spherical rank l and order m , and contains the spatial dependence of the interaction. The rank l can take values of 0 (corresponding to the isotropic part of the tensor), 1 (antisymmetric anisotropic part), and 2 (symmetric anisotropic part), and m takes values from $-l$ to $+l$ in integer steps. The irreducible spherical components of σ are taken from Table 2.3. The irreducible spherical tensor operators \hat{T}_{lm} are formed by coupling together the components of the rank-one tensor representing the external magnetic field vector B_{1n} , and the rank-one tensor operator containing the components of the nuclear spin vector \hat{I}_{1n} where the order n takes the values $-1, 0$, and $+1$. These rank-one irreducible spherical tensor components are given in Table 2.1. The components of \hat{T}_{lm} that are formed by coupling the field and spin tensors are calculated from the formula [190]

$$\hat{T}_{lm} = \sum_n B_{1n} \hat{I}_{1,m-n} \langle 11n, m-n | lm \rangle \quad (2.88)$$

$$= B_0 \hat{I}_{1m} \langle 110m | lm \rangle \quad (2.89)$$

where the $\langle l_1 l_2 m_1 m_2 | LM \rangle$ are the Clebsch–Gordan coefficients, which are non-zero for values of L equal to $l_1 + l_2, l_1 + l_2 - 1, \dots, |l_1 - l_2|$, and for $M = m_1 + m_2$. To go to the last line we used the convention that the magnetic field is applied along z . The mixed field-spin second-rank tensor components formed by coupling the field and spin tensors in this manner are given in Table 2.2.

2.6.1 The high-field approximation

Conventional NMR experiments are performed in the high-field limit, where the Zeeman interaction of the spin with the external field dominates all internal interactions, including couplings between spins, and the interaction of the spin with the external field via the chemical shielding. In this limit we can simplify the form of the Hamiltonians describing these internal interactions by treating them as a perturbation to the Zeeman Hamiltonian. The perturbation expansion can be calculated by first transforming the Hamiltonian representing the interaction into the reference frame rotating at the Larmor frequency (simply referred to as the *rotating frame*) [183], and then computing the average Hamiltonian \bar{H} over one period of Larmor precession according to the Baker–Campbell–Hausdorff expansion, which can be written as $\bar{H} = \overline{H^{(1)}} + \overline{H^{(2)}} + \overline{H^{(3)}} + \dots$ where $\overline{H^{(i)}}$ is the i th-order term [192, 193].

The transformation of the chemical shielding Hamiltonian in Equation 2.87 into the rotating frame gives

a time-dependent Hamiltonian $\tilde{H}_{IC}(t)$ which is equal to

$$\tilde{H}_{IC}(t) = \hbar\gamma_I \sum_{l=0}^{+2} \sum_{m=-l}^{+l} (-1)^m \sigma_{lm} \hat{T}_{l-m} \exp(-im\omega_0 t) \quad (2.90)$$

$$= \hbar\gamma_I B_0 \sum_l \sum_m (-1)^m \langle 110 - m | l - m \rangle \sigma_{lm} \hat{T}_{l-m} \exp(-im\omega_0 t). \quad (2.91)$$

The first-order average Hamiltonian $\overline{H^{(1)}}$ is given by the time-average over one period of Larmor precession $\tau_0 = 2\pi/|\omega_0|$:

$$\overline{H^{(1)}} = \frac{1}{\tau_0} \int_0^{\tau_0} dt_1 \tilde{H}_{IC}(t_1) \quad (2.92)$$

$$= \hbar\gamma_I \sum_{l=0}^{+2} \sigma_{l0} \hat{T}_{l0}, \quad (2.93)$$

where we recall that only those terms with $m = 0$ contribute. For the chemical shielding interaction, and indeed all interactions apart from the coupling of the nuclear quadrupolar moment to the electric-field gradient, it is sufficient to truncate the average Hamiltonian series at the first-order term. We can now substitute in the expressions for the \hat{T}_{l0} in Table 2.2, noting that $\hat{T}_{10} = 0$ and that both \hat{T}_{00} and \hat{T}_{20} are proportional to $B_0 \hat{I}_z$. The result is

$$\overline{H^{(1)}} = -\hbar\omega_0 \left(-\sqrt{\frac{1}{3}}\sigma_{00} + \sqrt{\frac{2}{3}}\sigma_{20} \right) \hat{I}_z. \quad (2.94)$$

We can rewrite Equation 2.94 in terms of a high-field chemical shielding $\sigma^{(1)}$ as follows:

$$\overline{H^{(1)}} = -\hbar\omega_0 \sigma^{(1)} \hat{I}_z, \quad (2.95)$$

$$\sigma^{(1)} = -\sqrt{\frac{1}{3}}\sigma_{00} + \sqrt{\frac{2}{3}}\sigma_{20}. \quad (2.96)$$

We see that, in this high-field regime, the chemical shielding tensor contains only terms of spherical ranks zero and two, i.e. we only observe the symmetric part of the tensor. The isotropic term can be simplified easily by noting, with reference to Table 2.3, that $\sigma_{00} = -\sqrt{3}\sigma_{\text{iso}}$. The rank-two term is more complex to write out, as σ_{20} , by definition, varies with the orientation of the system. However we can separate the size of the anisotropy and the orientation dependence in the PAF. According to the Haeberlen convention the diagonal

elements $\tilde{\sigma}_{ii}$ are ordered as follows: $|\tilde{\sigma}_{zz} - \sigma_{\text{iso}}| \geq |\tilde{\sigma}_{xx} - \sigma_{\text{iso}}| \geq |\tilde{\sigma}_{yy} - \sigma_{\text{iso}}|$. The irreducible spherical tensor components of the chemical shielding tensor in the laboratory frame σ_{2m} can now be written in terms of the components in the PAF $\tilde{\sigma}_{2m}$ using the following relationship:

$$\sigma_{2m} = \sum_{m'=-2}^{+2} \tilde{\sigma}_{2m'} D_{m'm}^{(2)}(\alpha_{\text{PL}}, \beta_{\text{PL}}, \gamma_{\text{PL}}), \quad (2.97)$$

where the $D_{m'm}^{(l)}(\alpha, \beta, \gamma)$ are the Wigner rotation matrix elements of rank l , and the Euler angles $(\alpha_{\text{PL}}, \beta_{\text{PL}}, \gamma_{\text{PL}})$ give the orientation of the PAF in the laboratory frame. The Wigner rotation matrix elements can be written in terms of the reduced matrix elements $d_{m'm}^{(l)}(\beta)$ by separating the dependence on each Euler angle into three separate factors:

$$D_{m'm}^{(l)}(\alpha, \beta, \gamma) = \exp(-im'\alpha) d_{m'm}^{(l)}(\beta) \exp(-im\gamma). \quad (2.98)$$

The complete set of reduced Wigner rotation matrix elements are tabulated up to rank $l = 2$ in Table 2.4, along with the single fourth-rank element $d_{00}^{(4)}(\beta)$. Substituting the matrix elements into Equation 2.94 we obtain

$$\overline{H^{(1)}} = -\hbar\omega_0 \left(\sigma_{\text{iso}} + \sqrt{\frac{2}{3}} \sum_{m=-2}^{+2} \tilde{\sigma}_{2m} \exp(-im\alpha_{\text{PL}}) d_{m0}^{(2)}(\beta_{\text{PL}}) \right) \hat{I}_z. \quad (2.99)$$

Note that the anisotropic part of the chemical shielding interaction only depends on two Euler angles. This is because the application of the large magnetic field means that only the shielding spherical tensor components with $m = 0$ in the laboratory frame are retained in the Hamiltonian, as seen in Equation 2.93. Therefore the orientation dependence is described purely by the Wigner matrix elements $D_{m0}^{(2)}(\alpha_{\text{PL}}, \beta_{\text{PL}}, \gamma_{\text{PL}})$ in which the second index is zero, and so the dependence γ_{PL} is removed. The symmetric part of the chemical shielding tensor is conventionally represented as a chemical-shielding ellipsoid, as shown in Figure 2.7. Here the value of the chemical shielding tensor is plotted as $1/\sqrt{\sigma}$ as a function of orientation in a Cartesian coordinate system. The tensor has the shape of an ellipsoid when plotted as $1/\sqrt{\sigma}$. By convention the ii principal component is located along the i -axis, and is plotted as $1/\sqrt{\tilde{\sigma}_{ii}}$.

We can now use Table 2.3 to write down expressions for the rank-two chemical shielding terms in the PAF of the symmetric part of the shielding tensor, and substitute these into the Hamiltonian to give it an explicit

$l = 1/2$	expression
$d_{+1/2,+1/2}^{(1/2)}(\beta)$	$\cos(\beta/2)$
$d_{-1/2,+1/2}^{(1/2)}(\beta)$	$\sin(\beta/2)$
$l = 1$	expression
$d_{+1,+1}^{(1)}(\beta)$	$\cos^2(\beta/2)$
$d_{-1,+1}^{(1)}(\beta)$	$\sin^2(\beta/2)$
$d_{0,+1}^{(1)}(\beta)$	$\sin(\beta)/\sqrt{2}$
$d_{0,0}^{(1)}(\beta)$	$\cos(\beta)$
$l = 3/2$	expression
$d_{+3/2,+3/2}^{(3/2)}(\beta)$	$\cos^3(\beta/2)$
$d_{+1/2,+3/2}^{(3/2)}(\beta)$	$\sqrt{3} \cos^2(\beta/2) \sin(\beta/2)$
$d_{-1/2,+3/2}^{(3/2)}(\beta)$	$\sqrt{3} \cos(\beta/2) \sin^2(\beta/2)$
$d_{-3/2,+3/2}^{(3/2)}(\beta)$	$\sin^3(\beta/2)$
$d_{+1/2,+1/2}^{(3/2)}(\beta)$	$\cos(\beta/2) (3 \cos^2(\beta/2) - 2)$
$d_{-1/2,+1/2}^{(3/2)}(\beta)$	$-\sin(\beta/2) (3 \sin^2(\beta/2) - 2)$
$l = 2$	expression
$d_{+2,+2}^{(2)}(\beta)$	$\cos^4(\beta/2)$
$d_{+1,+2}^{(2)}(\beta)$	$\sin(\beta) (1 + \cos(\beta)) / 2$
$d_{0,+2}^{(2)}(\beta)$	$\sqrt{\frac{3}{8}} \sin^2(\beta)$
$d_{-1,+2}^{(2)}(\beta)$	$\sin(\beta) (1 - \cos(\beta)) / 2$
$d_{-2,+2}^{(2)}(\beta)$	$\sin^4(\beta/2)$
$d_{+1,+1}^{(2)}(\beta)$	$(2 \cos(\beta) - 1) (1 + \cos(\beta)) / 2$
$d_{0,+1}^{(2)}(\beta)$	$\sqrt{\frac{3}{2}} \sin(\beta) \cos(\beta)$
$d_{-1,+1}^{(2)}(\beta)$	$(2 \cos(\beta) + 1) (1 - \cos(\beta)) / 2$
$d_{0,0}^{(2)}(\beta)$	$(3 \cos^2(\beta) - 1) / 2$
$l = 4$	expression
$d_{0,0}^{(4)}(\beta)$	$(35 \cos^4(\beta) - 30 \cos^2(\beta) + 3) / 8$

Table 2.4: Expressions for the set of unique reduced Wigner rotation matrix elements $d_{m'm}^{(l)}(\beta)$ for ranks $l = 1/2, 1, 3/2,$ and $2,$ and the single fourth-rank element $d_{00}^{(4)}(\beta)$. Additional elements are generated using the symmetry relations $d_{mm'}^{(l)}(\beta) = (-1)^{m-m'} d_{m'm}^{(l)}(\beta)$ and $d_{-m'-m}^{(l)}(\beta) = (-1)^{m-m'} d_{m'm}^{(l)}(\beta)$.

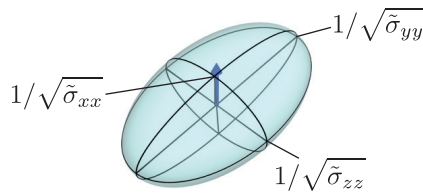


Figure 2.7: The chemical-shielding ellipsoid. The symmetric part of the chemical shielding tensor is plotted on three-dimensional Cartesian axes as $1/\sqrt{\sigma}$, with the three ii principal components plotted as $1/\sqrt{\sigma_{ii}}$ along the i -axes.

form. Remembering that the off-diagonal elements are zero in the PAF, the $\tilde{\sigma}_{2m}$ are [194]:

$$\tilde{\sigma}_{20} = \sqrt{\frac{3}{2}}\Delta\sigma \quad (2.100)$$

$$\tilde{\sigma}_{2\pm 1} = 0 \quad (2.101)$$

$$\tilde{\sigma}_{2\pm 2} = -\frac{1}{2}\eta\Delta\sigma, \quad (2.102)$$

where $\Delta\sigma$ and η are the chemical shielding anisotropy and asymmetry parameter respectively. They are defined according to the Haeberlen convention as

$$\Delta\sigma = \tilde{\sigma}_{zz} - \sigma_{\text{iso}} \quad (2.103)$$

$$\eta = \frac{\tilde{\sigma}_{yy} - \tilde{\sigma}_{xx}}{\Delta\sigma}. \quad (2.104)$$

For completeness we can also give explicit expressions for the unobservable antisymmetric part of the shielding tensor. The PAF of the antisymmetric tensor is the reference frame in which

$$\bar{\sigma}_{10} = -i\sqrt{2}\zeta, \quad (2.105)$$

$$\bar{\sigma}_{1\pm 1} = 0, \quad (2.106)$$

where the antisymmetric anisotropy parameter ζ is

$$\zeta = \frac{1}{2}\sqrt{(\sigma_{xy} - \sigma_{yx})^2 + (\sigma_{yz} - \sigma_{zy})^2 + (\sigma_{zx} - \sigma_{xz})^2}. \quad (2.107)$$

The σ_{ij} in Equation 2.107 are those in the laboratory frame. We recall that the PAF of the antisymmetric part *does not* in general coincide with that of the symmetric part, and that tensor components in the former are represented with a tilde, whereas those in the latter are shown with an overbar. In terms of these parameters

the Hamiltonian is

$$\overline{H^{(1)}} = -\hbar\omega_0 \left[\sigma_{\text{iso}} + \Delta\sigma \sqrt{\frac{2}{3}} \left\{ \sqrt{\frac{3}{2}} d_{00}^{(2)}(\beta_{\text{PL}}) - \frac{1}{2}\eta \left(\exp(2i\alpha_{\text{PL}}) d_{-20}^{(2)}(\beta_{\text{PL}}) + \exp(-2i\alpha_{\text{PL}}) d_{+20}^{(2)}(\beta_{\text{PL}}) \right) \right\} \right] \hat{I}_z \quad (2.108)$$

$$= -\hbar\omega_0 \left[\sigma_{\text{iso}} + \frac{1}{2}\Delta\sigma \left\{ 3 \cos^2(\beta_{\text{PL}}) - 1 - \eta \cos(2\alpha_{\text{PL}}) \sin^2(\beta_{\text{PL}}) \right\} \right] \hat{I}_z. \quad (2.109)$$

A nuclear spin with positive gyromagnetic ratio in a crystallite of a well-defined orientation $(\alpha_{\text{PL}}, \beta_{\text{PL}})$ will therefore resonate in the rotating frame at a single well-defined frequency $\Omega(\alpha_{\text{PL}}, \beta_{\text{PL}})$ which is given by

$$\Omega(\alpha_{\text{PL}}, \beta_{\text{PL}}) = \omega_0 \left[\sigma_{\text{iso}} + \frac{1}{2}\Delta\sigma \left\{ 3 \cos^2(\beta_{\text{PL}}) - 1 - \eta \cos(2\alpha_{\text{PL}}) \sin^2(\beta_{\text{PL}}) \right\} \right]. \quad (2.110)$$

In a polycrystalline powder, in which crystallites of all orientations are present with a random statistical distribution, each crystallite is represented by a sharp peak at a particular frequency. These peaks combine to give a broad resonance referred to as a powder pattern, an example of which is shown in Figure 2.8. Superimposed upon this powder pattern are the positions of five single-crystallite spectra (a)–(e) of representative orientations. The lineshape has two discontinuities, which are located at frequencies $\omega_0\tilde{\sigma}_{zz}$ and $\omega_0\tilde{\sigma}_{xx}$, with the former frequency defined as being the one that is further from the isotropic frequency $\omega_0\sigma_{\text{iso}}$. In addition there is a cusp at frequency $\omega_0\tilde{\sigma}_{yy}$. In principle, measuring these three positions is sufficient to obtain the three principal values of the symmetric part of the CSA tensor.

Second-order effects in the high-field approximation

In the majority of known cases the first-order approximation as presented in the previous section is sufficient for the description of the chemical shielding under high-field conditions. However for very large shifts and shift anisotropies, such as those that may be encountered in superparamagnetic systems [195–197], it may be necessary to include higher-order terms. We will calculate the second-order term here as an example, following the protocol of Ashbrook et al [193].

We proceed by calculating the second-order average Hamiltonian term in the Baker–Campbell–Hausdorff expansion, given by

$$\overline{H^{(2)}} = -\frac{i}{2\hbar\tau_0} \int_0^{\tau_0} dt_2 \int_0^{t_2} dt_1 \left[\tilde{H}_I(t_2), \tilde{H}_I(t_1) \right], \quad (2.111)$$

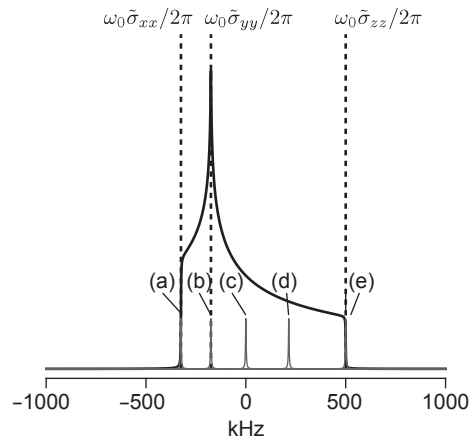


Figure 2.8: Simulated NMR ‘powder pattern’ spectrum of a static polycrystalline powder of a system containing a single spin-1/2, with positive gyromagnetic ratio, which experiences a CSA interaction. The three principal components of the CSA tensor are labelled, and correspond to the high- and low-frequency discontinuities, and the cusp in the powder pattern. Superimposed are the five spectra (a)–(e) corresponding to five representative crystallites of well-defined orientations. The chemical shielding isotropic and anisotropy parameters used are $\omega_0\sigma_{\text{iso}}/2\pi = 0$, $\omega_0\Delta\sigma/2\pi = 500$ kHz, and $\eta = 0.3$, which correspond to principal components of $\omega_0\tilde{\sigma}_{xx}/2\pi = -325$ kHz, $\omega_0\tilde{\sigma}_{yy}/2\pi = -175$ kHz, and $\omega_0\tilde{\sigma}_{zz}/2\pi = 500$ kHz. The single-crystallite spectra have orientations $(\alpha_{\text{PL}}, \beta_{\text{PL}})$ equal to (a) $(0^\circ, 90^\circ)$, (b) $(0^\circ, 64.74^\circ)$, (c) $(45^\circ, 54.74^\circ)$, (d) $(0^\circ, 36^\circ)$, (e) $(0^\circ, 0^\circ)$, and resonance frequencies $\Omega(\alpha_{\text{PL}}, \beta_{\text{PL}})/2\pi$ of (a) -325 kHz, (b) -175 kHz, (c) 0 kHz, (d) 215 kHz, (e) 500 kHz.

and extracting the secular terms. Substituting Equation 2.91 into the commutator we obtain

$$\left[\tilde{H}_I(t_2), \tilde{H}_I(t_1)\right] = \hbar^2 \gamma_I^2 B_0^2 \sum_{l_1, l_2} \sum_m \langle 110 - m | l_1 - m \rangle \langle 110 m | l_2 m \rangle \sigma_{l_1 m} \sigma_{l_2 - m} \left[\hat{I}_{1m}, \hat{I}_{1-m}\right] \exp(-im\omega_0(t_1 - t_2)), \quad (2.112)$$

where we have retained only the secular terms with $m_1 = -m_2 = m$. Inserting this expression into Equation 2.111 and computing the integral yields the second-order average Hamiltonian:

$$\overline{H^{(2)}} = \frac{1}{2} \hbar \omega_0 \sum_{l_1, l_2} \sum_{m \neq 0} \frac{1}{m} \langle 110 - m | l_1 - m \rangle \langle 110 m | l_2 m \rangle \sigma_{l_1 m} \sigma_{l_2 - m} \left[\hat{I}_{1m}, \hat{I}_{1-m}\right]. \quad (2.113)$$

The commutator of rank-one irreducible spherical tensor operators can be simplified after some tedious algebra by using the mathematical tools of quantum angular momentum, giving

$$\left[\hat{I}_{1m}, \hat{I}_{1-m}\right] = 2\sqrt{3}(-1)^{2I+1} \sqrt{I(I+1)(2I+1)} \langle 11m - m | 10 \rangle \left\{ \begin{array}{ccc} 1 & 1 & 1 \\ I & I & I \end{array} \right\} \hat{I}_z \quad (2.114)$$

$$= (-1)^m m \hat{I}_z, \quad (2.115)$$

where the array in braces is a Wigner $6j$ symbol [190]. Finally we use the explicit expressions for the Clebsch–Gordan coefficients to give the following second-order chemical shielding Hamiltonian:

$$\overline{H^{(2)}} = \frac{1}{2} \hbar \omega_0 \sum_{l_1, l_2} \sum_{m \neq 0} (-1)^m \langle 110 - m | l_1 - m \rangle \langle 110 m | l_2 m \rangle \sigma_{l_1 m} \sigma_{l_2 - m} \hat{I}_z \quad (2.116)$$

$$= \frac{1}{2} \hbar \omega_0 [\sigma_{1-1} \sigma_{1+1} - \sigma_{2-1} \sigma_{2+1} + \sigma_{1-1} \sigma_{2+1} - \sigma_{2-1} \sigma_{1+1}] \hat{I}_z. \quad (2.117)$$

In analogy to the first-order interaction, we can reformulate Equation 2.117 in terms of the second-order chemical shielding:

$$\overline{H^{(2)}} = -\hbar \omega_0 \sigma^{(2)} \hat{I}_z, \quad (2.118)$$

$$\sigma^{(2)} = -\frac{1}{2} [\sigma_{1-1} \sigma_{1+1} - \sigma_{2-1} \sigma_{2+1} + \sigma_{1-1} \sigma_{2+1} - \sigma_{2-1} \sigma_{1+1}]. \quad (2.119)$$

The spin part of this Hamiltonian is simply \hat{I}_z , which is the same as for the first-order high-field chemical

shielding interaction. The second-order term therefore indicates that the resonance frequency experienced by a nuclear spin is simply shifted from the frequency in Equation 2.94 by the correction term in Equation 2.117. This correction term is also proportional to the external magnetic field B_0 , and therefore the Larmor frequency ω_0 . The spatial dependence of this correction term is complicated as it is the sum of four terms, each of which is a product of two irreducible spherical tensor components, $\sigma_{l_1-1}\sigma_{l_2+1}$. It should be noted that only the antisymmetric and symmetric anisotropic parts of the shielding tensor contribute to the second-order interaction; no contribution is made by the isotropic shielding. The spatial dependence is more easily understood by writing the products $\sigma_{l_1m}\sigma_{l_2-m}$ in terms of the coupled spatial tensors $W_{L0}^{(l_1l_2)}$ as follows:

$$W_{L0}^{(C_1,C_2)} = \sum_m \langle l_1 l_2 m - m | L0 \rangle \sigma_{l_1m} \sigma_{l_2-m}. \quad (2.120)$$

The tensor $W_{L0}^{(l_1l_2)}$ is of rank L , which takes values according to the Clebsch–Gordan series from $l_1 + l_2$ down to $|l_1 - l_2|$ in integer steps. We will see that the only coupled tensors we need consider are those of ranks 0, 2, and 4. The rank-zero tensors correspond to spatially isotropic shielding components, the rank-two tensors to the symmetric shielding anisotropy, and the rank-four tensors to an additional shielding anisotropy with a different angular dependence. The coupled tensor components have the following symmetry with regard to the order in which the σ_{l_1m} are coupled together:

$$W_{L0}^{(C_1,C_2)} = (-1)^{L-l_1-l_2} W_{L0}^{(C_2,C_1)}. \quad (2.121)$$

In order to write the second-order shielding Hamiltonian in terms of the $W_{L0}^{(l_1l_2)}$ tensors, we invert Equation 2.120 to give an expression for $\sigma_{l_1m}\sigma_{l_2-m}$:

$$\sigma_{l_1m}\sigma_{l_2-m} = \sum_{L=|l_1-l_2|}^{l_1+l_2} \langle l_1 l_2 m - m | L0 \rangle W_{L0}^{(C_1,C_2)}, \quad (2.122)$$

which we substitute into Equation 2.117. The final expression is

$$\begin{aligned} \overline{H^{(2)}} = & \frac{1}{2}\hbar\omega_0 \left[\sqrt{\frac{1}{3}}W_{00}^{(C1,C1)} + \sqrt{\frac{1}{5}}W_{00}^{(C2C,2)} \right] \hat{I}_z \\ & + \frac{1}{2}\hbar\omega_0 \left[\sqrt{\frac{1}{6}}W_{20}^{(C1,C1)} - \sqrt{2}W_{20}^{(C1,C2)} - \sqrt{\frac{1}{14}}W_{20}^{(C2,C2)} \right] \hat{I}_z \\ & - \sqrt{\frac{2}{35}}\hbar\omega_0 W_{40}^{(C2,C2)} \hat{I}_z. \end{aligned} \quad (2.123)$$

The Hamiltonian in Equation 2.123 comprises three terms. The first is spatially isotropic, as it depends on $W_{00}^{(C1,C1)}$ and $W_{00}^{(C2,C2)}$ which are formed by coupling together two antisymmetric and two symmetric shielding tensor components respectively. It will therefore manifest itself as a change in the measured isotropic chemical shielding. The second term contains coupled tensors of rank 2, formed from coupling two antisymmetric, one symmetric and one antisymmetric, or two symmetric shielding components, and therefore contributes to the symmetric shielding anisotropy in the same way as the rank-two tensor in Equation 2.94. One intriguing aspect of these two terms is that both depend on the antisymmetric part of the shielding tensor, which is not observable in the conventional high-field (first-order) limit. The final term is new: it has a rank-four spatial dependence through $W_{40}^{(C2,C2)}$, which is due to the coupling of two symmetric shielding tensor components. It is spatially anisotropic, but with a different angular dependence to the ‘conventional’ shielding anisotropy. Such rank-four spatial terms are well known from the NMR of quadrupolar nuclei, where they are formed from the coupling together of two spatial components from the quadrupolar coupling Hamiltonian or the quadrupolar Hamiltonian with the CSA Hamiltonian [193], and are known to lead to broadening of the resonance [198] as well as being sources of information about the tensor parameters.

2.6.2 The chemical shift

So far we have formulated the discussion in terms of the chemical shielding. We now introduce the chemical shift convention, limiting ourselves to the high-field limit where only the first-order interaction is retained. In experimental NMR we actually measure the *chemical shift tensor* δ , the isotropic value of which is equal to the difference between the isotropic shielding of a reference system $\sigma_{\text{iso}}^{\text{ref}}$ and the system of interest:

$$\delta_{\text{iso}} = \sigma_{\text{iso}}^{\text{ref}} - \sigma_{\text{iso}}. \quad (2.124)$$

Using the shift convention we define the diagonal components (or principal values) of the symmetric part of the tensor in the PAF as $\tilde{\delta}_{ii}$, and write the chemical shift anisotropy (CSA) $\Delta\delta$, and asymmetry parameter η as:

$$\Delta\delta = \tilde{\delta}_{zz} - \delta_{\text{iso}} \quad (2.125)$$

$$\eta = \frac{\tilde{\delta}_{yy} - \tilde{\delta}_{xx}}{\Delta\delta}, \quad (2.126)$$

where we have used the Haeberlen convention to order the principal values: $|\tilde{\delta}_{zz} - \delta_{\text{iso}}| \geq |\tilde{\delta}_{xx} - \delta_{\text{iso}}| \geq |\tilde{\delta}_{yy} - \delta_{\text{iso}}|$. To obtain the isotropic chemical shift and the CSA in frequency units, we multiple δ_{iso} and $\Delta\delta$ by the Larmor frequency ω_0 . Note that for nuclei with a positive gyromagnetic ratio, and therefore a negative Larmor frequency, a positive value of either δ_{iso} or $\Delta\delta$ implies a negative frequency.

Finally, when we discuss the paramagnetic contribution to the chemical shielding σ^S we can also define a paramagnetic shift tensor. If our reference system is diamagnetic the total isotropic chemical shift is

$$\delta_{\text{iso}} = \sigma_{\text{iso}}^{\text{ref,orb}} - \sigma_{\text{iso}}^{\text{orb}} - \sigma_{\text{iso}}^S, \quad (2.127)$$

where $\sigma_{\text{iso}}^{\text{ref,orb}}$ is the orbital contribution to the isotropic shielding of the reference compound. The total chemical shift is therefore the sum of the orbital contribution $\delta_{\text{iso}}^{\text{orb}}$ and the paramagnetic shift δ_{iso}^S :

$$\delta_{\text{iso}} = \delta_{\text{iso}}^{\text{orb}} + \delta_{\text{iso}}^S, \quad (2.128)$$

where

$$\delta_{\text{iso}}^{\text{orb}} = \sigma_{\text{iso}}^{\text{orb,ref}} - \sigma_{\text{iso}}^{\text{orb}} \quad (2.129)$$

$$\delta_{\text{iso}}^S = -\sigma_{\text{iso}}^S. \quad (2.130)$$

This implies that the paramagnetic part of the isotropic shift is simply given by minus the isotropic part of the paramagnetic shielding tensor.

2.7 The spin interactions of quadrupolar nuclei

We now extend the previous discussion of nuclear spin interactions to quadrupolar nuclei, which are defined as nuclei with spin $I > 1/2$. Quadrupolar nuclei also experience nuclear Zeeman \hat{H}_{IZ} and chemical shielding \hat{H}_{IC} interactions, which have the same form as for spin-1/2 nuclei. However there is an additional term in the Hamiltonian, known as the nuclear quadrupolar interaction \hat{H}_{IQ} , which describes the interaction of the nuclear quadrupole moment with the gradient of the electric field due to the electrons. The total nuclear spin Hamiltonian \hat{H}_I is therefore

$$\hat{H}_I = \hat{H}_{IZ} + \hat{H}_{IQ} + \hat{H}_{IC}. \quad (2.131)$$

Under high-field conditions the magnitudes of the three interactions are generally ordered as follows: $|\hat{H}_{IZ}| \gg |\hat{H}_{IQ}| > |\hat{H}_{IC}|$, i.e. the nuclear Zeeman interaction dominates the chemical shielding and quadrupolar interactions. In some cases the magnitudes of the shielding and quadrupolar interactions may be opposite, for example for nuclei with small quadrupolar moments such as ${}^{6/7}\text{Li}$ and nuclei in a cubic environment. The dominance of the Zeeman interaction means that the internal spin interactions may be treated as perturbations, as we have already seen for the chemical shielding interaction. Hence we can write down a high-field internal spin interaction $\bar{H}_I^{(2)}$ with the following form:

$$\bar{H}_I^{(2)} = \bar{H}_{IQ}^{(1)} + \bar{H}_{IC}^{(1)} + \bar{H}_{I,Q \times Q}^{(2)} + \bar{H}_{I,Q \times C}^{(2)} + \bar{H}_{I,C \times C}^{(2)}. \quad (2.132)$$

In order of decreasing magnitude the interactions in Equation 2.132 are the first-order quadrupolar interaction $\bar{H}_{IQ}^{(1)}$, the first-order chemical shielding interaction $\bar{H}_{IC}^{(1)}$, and the second-order interactions due to the nuclear quadrupole $\bar{H}_{I,Q \times Q}^{(2)}$, the cross-terms between the quadrupole and chemical shielding $\bar{H}_{I,Q \times C}^{(2)}$, and the chemical shielding $\bar{H}_{I,C \times C}^{(2)}$. The two Hamiltonians for the chemical shielding $\bar{H}_{IC}^{(1)}$ and $\bar{H}_{I,C \times C}^{(2)}$ have already been determined for spin-1/2 nuclei in Equations 2.109 and 2.123, and have exactly the same form for a quadrupolar nucleus. However for quadrupolar nucleus there is the additional complication in that there are $2I + 1$ spin states, between which there are $I(2I + 1)$ transitions in which the magnetic quantum increases. Each transition has an associated frequency for each interaction. For example the first-order chemical shielding transition

frequency for a transition from state $|IM_1\rangle$ to $|IM_2\rangle$ is

$$\Omega_{IC}^{(M_1 \rightarrow M_2)}(\alpha_{PL}, \beta_{PL}) = -\omega_0 \left[\sigma_{\text{iso}} + \frac{1}{2} \Delta\sigma \left\{ 3 \cos^2(\beta_{PL}) - 1 - \eta \cos(2\alpha_{PL}) \sin^2(\beta_{PL}) \right\} \right] (M_2 - M_1). \quad (2.133)$$

We have already fully examined the chemical shielding interaction. The remainder of this section is devoted to the quadrupolar interaction under high-field conditions.

2.7.1 The nuclear quadrupole Hamiltonian

The nuclear quadrupolar Hamiltonian describes the interaction between the quadrupolar moment of the nucleus and the electric-field gradient (EFG) due to the surrounding electrons. The EFG is calculated from the electric scalar potential of the electrons V by taking the second derivative with respect to the position coordinates x_i . There are therefore nine components of the EFG, which takes the form of a symmetric and traceless tensor (rank two) with components $V_{ij} = \partial^2 V / \partial x_i \partial x_j$. We define the PAF of the EFG tensor as the reference frame in which the tensor is diagonal with principal components \tilde{V}_{ii} . These components are ordered as $|\tilde{V}_{zz}| \geq |\tilde{V}_{yy}| \geq |\tilde{V}_{xx}|$, and are written in terms of the EFG anisotropy eq and asymmetry η^Q parameters as follows:

$$\tilde{V}_{zz} = eq, \quad \eta^Q = \frac{\tilde{V}_{xx} - \tilde{V}_{yy}}{\tilde{V}_{zz}}. \quad (2.134)$$

The Euler angles giving the orientation of the PAF relative to the laboratory frame are $\Omega_{QL} = (\alpha_{QL}, \beta_{QL}, \gamma_{QL})$.

The nuclear quadrupolar Hamiltonian is given by

$$\hat{H}_{IQ} = \frac{eQ}{2I(2I-1)} \hat{\mathbf{I}} \cdot \mathbf{V} \cdot \hat{\mathbf{I}}, \quad (2.135)$$

where eQ is the nuclear quadrupole moment. Note that although \hat{H}_{IQ} appears to have the form of an interaction of the nuclear spin with itself, this is not the correct physical interpretation. As we have stated, the interaction is between the nuclear quadrupolar moment and the EFG. By convention we define the quadrupolar coupling constant C_Q (in Hz) and quadrupolar splitting frequency ω_Q (in rads^{-1}) as

$$C_Q = \frac{e^2 q Q}{h}, \quad \omega_Q = \frac{3\pi C_Q}{2I(2I-1)}. \quad (2.136)$$

In terms of these quantities we can rewrite \hat{H}_{IQ} as

$$\hat{H}_{IQ} = \frac{2\hbar\omega_Q}{3eq} \hat{\mathbf{I}} \cdot \mathbf{V} \cdot \hat{\mathbf{I}} \quad (2.137)$$

$$= \frac{2}{3} \hbar\omega_Q \hat{\mathbf{I}} \cdot \mathbf{v} \cdot \hat{\mathbf{I}}, \quad (2.138)$$

where we have defined the reduced EFG tensor as $\mathbf{v} = \mathbf{V}/(eq)$. We see that the strength of the interaction is proportional to the quadrupolar splitting frequency. This Hamiltonian contains the generalized Cartesian scalar product $\hat{\mathbf{I}} \cdot \mathbf{v} \cdot \hat{\mathbf{I}}$. To facilitate the following discussion, this quantity is more conveniently written in terms of irreducible spherical tensors, which gives the following equivalent form of the Hamiltonian:

$$\hat{H}_{IQ} = \frac{2}{3} \hbar\omega_Q \sum_{m=-2}^{+2} (-1)^m v_{2m} \hat{I}_{2-m}. \quad (2.139)$$

We now proceed to calculate the resulting first- and second-order terms in Equation 2.132.

The first-order nuclear quadrupole interaction

The first-order quadrupolar interaction Hamiltonian $\overline{H}_{IQ}^{(1)}$ is calculated according to the protocol in section 2.6.1. The Hamiltonian has a simple form in which only the term in \hat{I}_{20} is retained from Equation 2.139:

$$\overline{H}_{IQ}^{(1)} = \frac{2}{3} \hbar\omega_Q v_{20} \hat{I}_{20} \quad (2.140)$$

$$= \frac{2}{3} \hbar\omega_Q \hat{I}_{20} \sum_{m=-2}^{+2} \tilde{v}_{2m} D_{m0}^{(2)}(\Omega_{QL}), \quad (2.141)$$

which we see is proportional to ω_Q . On the second line we have written v_{20} in terms of the irreducible spherical tensor components in the PAF \tilde{v}_{2m} , which are given by:

$$\tilde{v}_{20} = \sqrt{\frac{3}{2}}, \quad (2.142)$$

$$\tilde{v}_{2\pm 1} = 0, \quad (2.143)$$

$$\tilde{v}_{2\pm 2} = \frac{1}{2} \eta^Q. \quad (2.144)$$

Substituting these into Equation 2.141 gives the following explicit expression for $\overline{H}_{IQ}^{(1)}$:

$$\overline{H}_{IQ}^{(1)} = \frac{1}{2} \hbar \omega_Q \left[3 \cos^2(\beta_{QL}) - 1 + \eta^Q \sin^2(\beta_{QL}) \cos(2\alpha_{QL}) \right] \left[\hat{I}_z^2 - \frac{1}{3} I(I+1) \hat{1} \right]. \quad (2.145)$$

The corresponding frequency of transition from state $|IM_1\rangle$ to state $|IM_2\rangle$ is therefore:

$$\Omega_{IQ}^{(M_1 \rightarrow M_2)}(\alpha_{QL}, \beta_{QL}) = \frac{1}{2} \omega_Q \left[3 \cos^2(\beta_{QL}) - 1 + \eta^Q \sin^2(\beta_{QL}) \cos(2\alpha_{QL}) \right] \left[M_2^2 - M_1^2 \right]. \quad (2.146)$$

We see that, in contrast to the chemical shielding interaction, the transition frequency depends on the difference in the squares of the two magnetic quantum numbers. An important consequence of this is that any symmetric transition with $M_2 = -M_1$ has no contribution from the quadrupolar interaction. This point is explored in more detail in chapter 11.

The second-order nuclear quadrupole interaction

There are two second-order terms in the Hamiltonian in Equation 2.141 which are due to the quadrupolar interaction. The larger and more important of these is $\overline{H}_{I,Q \times Q}^{(2)}$, which is due solely to the nuclear quadrupole. It is calculated using the same protocol given for the second-order chemical shielding term as described in section 2.6.1. The Hamiltonian is given by the time-integral of the commutator $[\tilde{H}_{IQ}(t_2), \tilde{H}_{IQ}(t_1)]$ in the second-order average Hamiltonian. Evaluating this gives the following expression

$$\overline{H}_{I,Q \times Q}^{(2)} = -\frac{2\hbar\omega_Q^2}{45\omega_0} \left[2(4v_{2-1}v_{2+1} + v_{2-2}v_{2+2}) \left(5\hat{I}_z^3 - (3I(I+1) - 1)\hat{I}_z \right) + (v_{2-1}v_{2+1} - v_{2-2}v_{2+2}) (4I(I+1) - 3)\hat{I}_z, \right] \quad (2.147)$$

which has a magnitude that is proportional to ω_Q^2/ω_0 . This indicates that this second-order interaction decreases in size as we increase the external magnetic field B_0 .

The spatial properties of the interaction are elucidated by writing the products $v_{2-m}v_{2m}$ in terms of the following irreducible spherical tensor components $W_{L0}^{(Q,Q)}$ in the coupled representation.

$$W_{L0}^{(Q,Q)} = \sum_m \langle 22m - m | L0 \rangle v_{2m} v_{2-m}. \quad (2.148)$$

In this representation the Hamiltonian is

$$\begin{aligned}\overline{H}_{I,Q \times Q}^{(2)} = & \frac{4\hbar\omega_Q^2}{9\omega_0} W_{00}^{(Q,Q)} \left[\frac{3}{5\sqrt{5}} (5\hat{I}_z^3 - (3I(I+1) - 1)\hat{I}_z) + \frac{4I(I+1) - 3}{5\sqrt{5}} \hat{I}_z \right] \\ & + \frac{4\hbar\omega_Q^2}{9\omega_0} W_{20}^{(Q,Q)} \left[-\frac{3}{5} \sqrt{\frac{2}{7}} (5\hat{I}_z^3 - (3I(I+1) - 1)\hat{I}_z) + \frac{4I(I+1) - 3}{10\sqrt{14}} \hat{I}_z \right] \\ & + \frac{4\hbar\omega_Q^2}{9\omega_0} W_{40}^{(Q,Q)} \left[-\frac{51}{15} \sqrt{\frac{1}{70}} (5\hat{I}_z^3 - (3I(I+1) - 1)\hat{I}_z) - \frac{3}{10\sqrt{70}} (4I(I+1) - 3)\hat{I}_z \right].\end{aligned}\quad (2.149)$$

We see that the interaction contains a part that depends on the rank-zero tensor $W_{00}^{(Q,Q)}$, and is therefore spatially isotropic. The anisotropic parts are of ranks two and four. Finally we note that the transition frequencies depend on $M_2 - M_1$ and $M_2^3 - M_1^3$, and so symmetric transitions are affected by the quadrupolar interaction to second order.

The second-order quadrupole-SA cross term

The final second-order interaction Hamiltonian $\overline{H}_{I,Q \times C}^{(2)}$ is due to the combination of the quadrupolar and chemical shielding interactions. In the second-order average Hamiltonian treatment the Hamiltonian is given by the integral of $[\tilde{H}_{IQ}(t_2), \tilde{H}_{IC}(t_1)] + [\tilde{H}_{IC}(t_2), \tilde{H}_{IQ}(t_1)]$, which is the sum of the two cross terms between these two interactions [193]. The resulting expression for $\overline{H}_{I,Q \times C}^{(2)}$ is:

$$\overline{H}_{I,Q \times C}^{(2)} = \hbar\omega_Q [(\sigma_{1+1} + \sigma_{2+1})v_{2-1} - (\sigma_{1-1} - \sigma_{2-1})v_{2+1}] \left[\hat{I}_z^2 - \frac{1}{3}I(I+1)\hat{1} \right], \quad (2.150)$$

which we see is proportional to the product of the quadrupolar splitting frequency ω_Q and the components of the symmetric and antisymmetric anisotropic parts of the chemical shielding tensor σ_{2m} and σ_{1m} . As before we can deduce the spatial properties by writing the tensor products in terms of the coupled tensor components

$$W_{L0}^{(Cl,Q)}$$

$$W_{L0}^{(Cl,Q)} = \sum_m \langle l2m - m | L0 \rangle \sigma_{lm} v_{2-m}, \quad (2.151)$$

which gives

$$\overline{H}_{I,Q \times C}^{(2)} = \hbar\omega_Q \left[-\frac{2}{\sqrt{5}} W_{00}^{(C2,Q)} + \sqrt{2} W_{20}^{(C1,Q)} + \sqrt{\frac{2}{7}} W_{20}^{(C2,Q)} + 4\sqrt{\frac{2}{35}} W_{40}^{(C2,Q)} \right] \left[\hat{I}_z^2 - \frac{1}{3}I(I+1)\hat{1} \right]. \quad (2.152)$$

As for the other second-order terms, this contribution also has parts of spatial ranks zero, two, and four. We also note that, as for the first-order quadrupolar interaction, the transition frequencies are proportional to $M_2^2 - M_1^2$, and so this interaction does not affect symmetric transitions.

2.8 The hyperfine interaction

The coupling interaction between the nucleus and the unpaired electrons is of central importance when discussing the effect of the latter on the NMR of paramagnetic systems. This coupling is referred to as the hyperfine interaction as it results in a “hyperfine” splitting structure in the EPR resonance. As we will see the hyperfine coupling constant, which describes the dependence of the interaction on the spatial orientation, contains both an isotropic contact term, which is analogous to the J -coupling interaction between nuclei, and a symmetric anisotropic dipolar coupling term.

In deriving the Hamiltonian \hat{H}_{SI} describing the hyperfine interaction we can choose to view it either as the interaction of the nuclear magnetic moment $\hat{\mu}_I$ with a magnetic field due to the electron, or equivalently as the interaction of the electronic magnetic moment $\hat{\mu}_S$ with a magnetic field due to the nucleus. A detailed derivation can be found in Abragam and Bleaney [184], who show that \hat{H}_{SI} is equal to

$$\hat{H}_{\text{SI}} = -\frac{\mu_0}{4\pi} \left[(\hat{\mu}_S \cdot \nabla)(\hat{\mu}_I \cdot \nabla) - (\hat{\mu}_S \cdot \hat{\mu}_I) \nabla^2 \right] \frac{1}{r}, \quad (2.153)$$

where ∇ is the vector derivative operator del, which is given by

$$\nabla = \left(\frac{\partial}{\partial x}, \frac{\partial}{\partial y}, \frac{\partial}{\partial z} \right). \quad (2.154)$$

The coordinates (x, y, z) describe the position of a point relative to the nucleus, and $r = \sqrt{x^2 + y^2 + z^2}$ is the distance from the nucleus. As will become apparent shortly, it is convenient to separate the Hamiltonian into two parts as follows:

$$\hat{H}_{\text{SI}} = -\frac{\mu_0}{4\pi} \left[(\hat{\mu}_S \cdot \nabla)(\hat{\mu}_I \cdot \nabla) - \frac{1}{3} (\hat{\mu}_S \cdot \hat{\mu}_I) \nabla^2 \right] \frac{1}{r} + \frac{\mu_0}{4\pi} \left[\frac{2}{3} (\hat{\mu}_S \cdot \hat{\mu}_I) \nabla^2 \right] \frac{1}{r}. \quad (2.155)$$

The two terms in Equation 2.155 are the spin-dipolar and contact parts of the hyperfine interaction respec-

tively, which we now explore in detail.

2.8.1 Interaction with a single delocalised electron

We assume that that electron is spatially delocalized, and the nucleus is localised at the single point $\mathbf{r} = \mathbf{0}$. This description is appropriate when for example considering $3d$ electrons of first-row d -block transition-metal ions that are delocalized into ligand orbitals. The full magnetic interaction is calculated by multiplying \hat{H}_{SI} with the electron density $\rho(\mathbf{r})$, which is given by the square of the electron wavefunction $\psi(\mathbf{r})$, i.e. $\rho(\mathbf{r}) = |\psi(\mathbf{r})|^2$, and then integrating over all space. We consider two cases, firstly when the electron and nucleus are well separated, and secondly when the electron is within the immediate vicinity of the nucleus. In the first case we set $r \neq 0$, which for instance would be the case when the electron occupies an orbital other than an s -orbital. The second term in Equation 2.155 then integrates to zero, and the first term $\hat{H}_{\text{SI}}^{r \neq 0}$ becomes [184]

$$\hat{H}_{\text{SI}}^{r \neq 0} = -\frac{\mu_0}{4\pi} \int \frac{3(\hat{\boldsymbol{\mu}}_S \cdot \mathbf{r})(\hat{\boldsymbol{\mu}}_I \cdot \mathbf{r}) - (\hat{\boldsymbol{\mu}}_S \cdot \hat{\boldsymbol{\mu}}_I) r^2}{r^5} |\psi(\mathbf{r})|^2 d^3r \quad (2.156)$$

$$= -\frac{\mu_0}{4\pi} \int [3(\hat{\boldsymbol{\mu}}_S \cdot \mathbf{e})(\hat{\boldsymbol{\mu}}_I \cdot \mathbf{e}) - \hat{\boldsymbol{\mu}}_S \cdot \hat{\boldsymbol{\mu}}_I] \frac{|\psi(\mathbf{r})|^2}{r^3} d^3r, \quad (2.157)$$

where \mathbf{r} is the vector displacement of the electron with respect to the nucleus, \mathbf{e} is the corresponding unit vector, and $\psi(\mathbf{r})$ is the electron wavefunction. The square of the magnitude of the wavefunction, $|\psi(\mathbf{r})|^2$, gives the electron density at position \mathbf{r} . This interaction term is referred to as the *spin-dipolar interaction*.

The situation where the electron is in the immediate vicinity of the nucleus corresponds to setting $r = 0$. Physically we would encounter this situation when the electron resides in an s -orbital centred at the nucleus. It can be shown that, in this case, the dipolar coupling term of the hyperfine interaction is equal to zero, and we are then left with the second term of Equation 2.155 which integrates to give $\hat{H}_{\text{SI}}^{r=0}$:

$$\hat{H}_{\text{SI}}^{r=0} = -\frac{2}{3}\mu_0 (\hat{\boldsymbol{\mu}}_S \cdot \hat{\boldsymbol{\mu}}_I) |\psi(\mathbf{0})|^2. \quad (2.158)$$

This term, which is referred to as the *Fermi-contact interaction*, is purely isotropic and arises due to the delocalisation of the electron onto the nucleus [184], which is reflected by the dependence of the size of the interaction on $|\psi(\mathbf{0})|^2$, which is the electron density at the nucleus, where $\mathbf{r} = \mathbf{0}$. Summing $\hat{H}_{\text{SI}}^{r \neq 0}$ and $\hat{H}_{\text{SI}}^{r=0}$

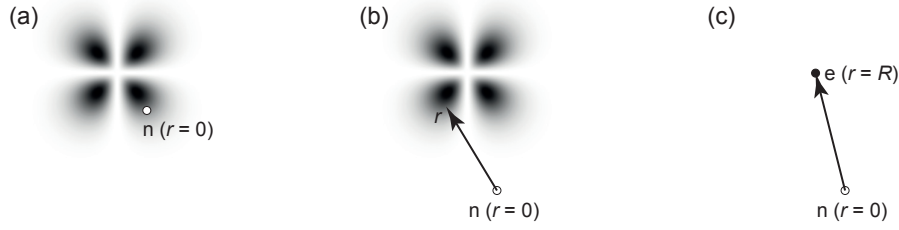


Figure 2.9: Illustration of the hyperfine interaction between a nucleus and unpaired electron. In (a) is shown the contact interaction. The nucleus n interacts with a delocalised electron, the electron density of which here takes the shape of a $3d$ -orbital centred on a different nucleus. The size of the interaction is proportional to the electron density located at the nuclear position $\mathbf{r} = \mathbf{0}$ (Equation 2.158). In (b) the same unpaired electron interacts with a more remote nuclear spin via the spin-dipolar interaction. The size of the interaction is given by the integral over all positions \mathbf{r} relative to the nucleus in Equation 2.157. When the electron is approximated as a point electronic dipolar moment \mathbf{e} in (c), the hyperfine interaction is given by Equation 2.162, and depends on the distance R between the nucleus and electron. Now if $R \neq 0$ the Fermi-contact interaction is zero, and the hyperfine interaction is purely spin-dipolar in nature.

yields the full hyperfine Hamiltonian,

$$\hat{H}_{\text{SI}} = -\frac{\mu_0}{4\pi} \left[\int \frac{3(\hat{\boldsymbol{\mu}}_S \cdot \mathbf{r})(\hat{\boldsymbol{\mu}}_I \cdot \mathbf{r}) - (\hat{\boldsymbol{\mu}}_S \cdot \hat{\boldsymbol{\mu}}_I) r^2}{r^5} |\psi(\mathbf{r})|^2 d^3r + \frac{8\pi}{3} (\hat{\boldsymbol{\mu}}_S \cdot \hat{\boldsymbol{\mu}}_I) |\psi(\mathbf{0})|^2 \right]. \quad (2.159)$$

The Fermi-contact and spin-dipolar interactions with a delocalised electron are illustrated in Figure 2.9 (a) and (b).

2.8.2 Interaction with a single localised electron

In cases where we can model the electron as being completely localised on the paramagnetic centre, we treat the electron as a point charge and point dipole. In this case we replace the electron density $|\psi(\mathbf{r})|^2$ in Equation 2.159 with the three-dimensional Dirac delta function $\delta(\mathbf{r} - \mathbf{R})$ [189], where \mathbf{R} is the position of the electron relative to the nucleus, and the integral simplifies to

$$\int \frac{3(\hat{\boldsymbol{\mu}}_S \cdot \mathbf{r})(\hat{\boldsymbol{\mu}}_I \cdot \mathbf{r}) - (\hat{\boldsymbol{\mu}}_S \cdot \hat{\boldsymbol{\mu}}_I) r^2}{r^5} |\psi(\mathbf{r})|^2 d^3r = \int \frac{3(\hat{\boldsymbol{\mu}}_S \cdot \mathbf{r})(\hat{\boldsymbol{\mu}}_I \cdot \mathbf{r}) - (\hat{\boldsymbol{\mu}}_S \cdot \hat{\boldsymbol{\mu}}_I) r^2}{r^5} \delta(\mathbf{r} - \mathbf{R}) d^3r \quad (2.160)$$

$$= \frac{3(\hat{\boldsymbol{\mu}}_S \cdot \mathbf{e})(\hat{\boldsymbol{\mu}}_I \cdot \mathbf{e}) - \hat{\boldsymbol{\mu}}_S \cdot \hat{\boldsymbol{\mu}}_I}{R^3} \quad (2.161)$$

where R is the distance of the electron from the nucleus. We note here that, formally, \mathbf{R} is the position of the *unpaired electron* relative to the nucleus of interest. However in situations where this nucleus of interest is different to the paramagnetic centre, \mathbf{R} is effectively the position of the *nucleus of the paramagnetic centre* relative to the nucleus of interest, i.e. the positions of the nucleus and electron of the paramagnetic centre are essentially indistinguishable. If the errors introduced by this approximation are non-negligible, then we are automatically *not* in the point-dipole regime, which is the situation described by Walder et al [199]. Assuming that the point-dipole approximation holds, the total hyperfine Hamiltonian is

$$\hat{H}_{\text{SI}} = -\frac{\mu_0}{4\pi} \left[\frac{3(\hat{\boldsymbol{\mu}}_S \cdot \mathbf{e})(\hat{\boldsymbol{\mu}}_I \cdot \mathbf{e}) - \hat{\boldsymbol{\mu}}_S \cdot \hat{\boldsymbol{\mu}}_I}{R^3} + \frac{8\pi}{3} (\hat{\boldsymbol{\mu}}_S \cdot \hat{\boldsymbol{\mu}}_I) \delta(\mathbf{R}) \right], \quad (2.162)$$

The first term is the well-known interaction between point dipoles [194], and the second term is the Fermi-contact interaction which is equal to zero unless the nucleus is actually located at the exact position of the electron, i.e. $\mathbf{R} = \mathbf{0}$. This is illustrated in Figure 2.9 (c).

In order to simplify the calculation of the hyperfine interaction it is frequently assumed that we can apply the point-dipole approximation to determine the spin-dipolar part, and need only use electron delocalization for the Fermi-contact part. The errors in the former approximation are not great at large distances from the paramagnetic centre, i.e. typically when $R > 4 \text{ \AA}$, but can lead to inaccuracies for nuclei that are closer. This comparison has been discussed in some detail by Autschbach et al [200]. The point-dipole approximation for the spin-dipolar interaction has been widely used for both paramagnetic proteins, and solid materials [11, 17, 44, 45, 65, 66, 101].

2.8.3 Interaction with a paramagnetic centre of multiple delocalised electrons

The expression for the hyperfine interaction Hamiltonian given above describes a hyperfine coupling to a single electron. For a system containing an ion with multiple unpaired electrons i with total electronic spin S , the Hamiltonian in Equation 2.159 is modified so that we sum over all the electrons [184]:

$$\hat{H}_{\text{SI}} = -\frac{\mu_0}{4\pi} \sum_i \left[\int \frac{3(\hat{\boldsymbol{\mu}}_{s,i} \cdot \mathbf{r})(\hat{\boldsymbol{\mu}}_I \cdot \mathbf{r}) - (\hat{\boldsymbol{\mu}}_{s,i} \cdot \hat{\boldsymbol{\mu}}_I) r^2}{r^5} |\psi_i(\mathbf{r})|^2 d^3 r + \frac{8\pi}{3} (\hat{\boldsymbol{\mu}}_{s,i} \cdot \hat{\boldsymbol{\mu}}_I) |\psi_i(\mathbf{0})|^2 \right], \quad (2.163)$$

where $\hat{\mu}_{s,i}$, and $\psi_i(\mathbf{r})$ are the magnetic moment, and wavefunction of electron i . We can simplify the Hamiltonian by writing the sum over the electrons i in terms of the average spin density per electron $\rho^{\alpha-\beta}(\mathbf{r})/(2S)$, where $\rho^{\alpha-\beta}(\mathbf{r})$ is the *total* spin-unpaired electron density at position \mathbf{r} , and $2S$ is the number of unpaired electrons. The Fermi-contact term can then be written as

$$-\frac{2\mu_0}{3} \sum_i (\hat{\mu}_{s,i} \cdot \hat{\mu}_I) |\psi_i(\mathbf{0})|^2 = -\frac{2\mu_0}{3} (\hat{\mu}_S \cdot \hat{\mu}_I) \frac{1}{2S} \rho^{\alpha-\beta}(\mathbf{0}), \quad (2.164)$$

where $\hat{\mu}_S = \sum_i \hat{\mu}_{s,i}$ is the magnetic moment operator for the total electron spin \hat{S} . Likewise the spin-dipolar term can be written as

$$\begin{aligned} & -\frac{\mu_0}{4\pi} \sum_i \int \frac{3(\hat{\mu}_S^{(i)} \cdot \mathbf{r})(\hat{\mu}_I \cdot \mathbf{r}) - (\hat{\mu}_S^{(i)} \cdot \hat{\mu}_I) r^2}{r^5} |\psi_i(\mathbf{r})|^2 d^3r \\ & = -\frac{\mu_0}{4\pi} \int \frac{3(\hat{\mu}_S \cdot \mathbf{r})(\hat{\mu}_I \cdot \mathbf{r}) - (\hat{\mu}_S \cdot \hat{\mu}_I) r^2}{r^5} \frac{\rho^{\alpha-\beta}(\mathbf{r})}{2S} d^3r. \end{aligned} \quad (2.165)$$

The total hyperfine Hamiltonian is therefore

$$\hat{H}_{SI} = -\frac{\mu_0}{8\pi S} \left[\int \frac{3(\hat{\mu}_S \cdot \mathbf{r})(\hat{\mu}_I \cdot \mathbf{r}) - (\hat{\mu}_S \cdot \hat{\mu}_I) r^2}{r^5} \rho^{\alpha-\beta}(\mathbf{r}) d^3r + \frac{8\pi}{3} (\hat{\mu}_S \cdot \hat{\mu}_I) \rho^{\alpha-\beta}(\mathbf{0}) \right]. \quad (2.166)$$

2.8.4 Interaction with a paramagnetic centre of multiple localised electrons

Finally we consider the case where all the electrons are localised at the same position \mathbf{R} , which we refer to as the position of the paramagnetic centre. The densities of each of the electrons i can now be replaced with the same Dirac delta function $|\psi_i(\mathbf{r})|^2 = \delta(\mathbf{r} - \mathbf{R})$, and we can write the hyperfine Hamiltonian in terms of the effective spin electronic magnetic moment $\hat{\mu}_S$ as follows:

$$\hat{H}_{SI} = -\frac{\mu_0}{4\pi} \sum_i \left[\frac{3(\hat{\mu}_{s,i} \cdot \mathbf{e})(\hat{\mu}_I \cdot \mathbf{e}) - \hat{\mu}_{s,i} \cdot \hat{\mu}_I}{R^3} + \frac{8\pi}{3} (\hat{\mu}_{s,i} \cdot \hat{\mu}_I) \delta(\mathbf{R}) \right] \quad (2.167)$$

$$= -\frac{\mu_0}{4\pi} \left[\frac{3(\hat{\mu}_S \cdot \mathbf{e})(\hat{\mu}_I \cdot \mathbf{e}) - \hat{\mu}_S \cdot \hat{\mu}_I}{R^3} + \frac{8\pi}{3} (\hat{\mu}_S \cdot \hat{\mu}_I) \delta(\mathbf{R}) \right], \quad (2.168)$$

which is the same as Equation 2.162. Note in particular that, for localised electrons, there is no scaling of the hyperfine Hamiltonian by the factor $1/(2S)$.

2.8.5 The hyperfine coupling constant

For all the situations we have described above, we can write the hyperfine Hamiltonian in terms of the spin operators. Substituting in the corresponding expressions for the nuclear and electronic magnetic moments, namely $\hat{\mu}_I = \hbar\gamma_I\hat{\mathbf{I}}$ and $\hat{\mu}_S = -\mu_B g_e \hat{\mathbf{S}}$, we obtain an expression of the form

$$\hat{H}_{SI} = \hat{\mathbf{S}} \cdot \mathbf{A} \cdot \hat{\mathbf{I}}, \quad (2.169)$$

where \mathbf{A} is the hyperfine coupling tensor, which we have seen can be divided into the isotropic Fermi-contact coupling constant A^{FC} and the traceless and symmetric spin-dipolar tensor \mathbf{A}^{SD} :

$$\mathbf{A} = A^{\text{FC}}\mathbf{1} + \mathbf{A}^{\text{SD}}. \quad (2.170)$$

If the electrons are delocalised onto the ligands the Fermi-contact coupling constant, and the Cartesian components of the spin-dipolar tensor are given by [184, 201]

$$A^{\text{FC}} = \frac{\mu_0 \mu_B g_e \hbar \gamma_I}{3S} \rho^{\alpha-\beta}(\mathbf{0}), \quad (2.171)$$

$$A_{ij}^{\text{SD}} = \frac{\mu_0 \mu_B g_e \hbar \gamma_I}{8\pi S} \int \frac{3r_i r_j - \delta_{ij} r^2}{r^5} \rho^{\alpha-\beta}(\mathbf{r}) d^3 r, \quad (2.172)$$

where i and j are equal to x , y , or z , e_i is the unit vector along axis i , and δ_{ij} is the Kronecker delta. The coupling constant describing the hyperfine interaction to a multi-electron paramagnetic centre has a complicated interpretation. The Fermi-contact coupling constant is proportional to the total unpaired electron spin density transferred to the nucleus, i.e. the sum of the contributions from the individual electrons. But since each unpaired electron resides in a different orbital with a different spatial distribution of electron density, the contribution to the hyperfine interaction from each electron is different. For example, imagine a diatomic system comprising a d -transition-metal centre whose d_{z^2} orbital is coordinated to an s -orbital of the atom containing the nucleus of interest. We would expect the contribution to the Fermi-contact term from the d_{z^2} orbital to be non-zero. However an electron in the d_{xy} orbital may not be delocalized at all into the s -orbital due to the different symmetry, and so would have a Fermi-contact contribution of zero. In order to make the Fermi-contact contributions from different metal ions in different systems comparable we divide the

coupling constant by the number of unpaired electrons, which is equal to $2S$ so as to give a ‘‘Fermi-contact coupling constant per electron’’, which is also known as the many-electron Fermi-contact coupling constant. The same considerations also apply to the spin-dipolar interaction.

If, on the other hand, the electrons can be treated as a point dipole with spin S , the hyperfine coupling tensor parameters are

$$A^{\text{FC}} = \frac{2\mu_0\mu_{\text{B}}g_e\hbar\gamma_I}{3}\delta(\mathbf{R}), \quad (2.173)$$

$$A_{ij}^{\text{SD}} = b_{SI} [3e_i e_j - \delta_{ij}], \quad (2.174)$$

where the point-dipole coupling constant b_{SI} is

$$b_{SI} = \frac{\mu_0\mu_{\text{B}}g_e\hbar\gamma_I}{4\pi R^3}. \quad (2.175)$$

Here the scaling by the number of electrons has already been implicitly included. Since the electrons are point dipoles, the different spatial variation of the individual orbitals is suppressed, and each electron makes exactly the same contribution to the interaction. Hence the factor of $2S$ is not present.

We can also write Equation 2.169 in terms of irreducible spherical tensors as follows

$$\hat{H}_{\text{SI}} = \sum_{l=0,2} \sum_{m=-l}^{+l} (-1)^m A_{lm} \hat{T}_{l-m}. \quad (2.176)$$

In the high-field limit, only the terms with $m = 0$ are retained and the Hamiltonian reduces to

$$\hat{H}_{\text{SI}} = A_{00}\hat{T}_{00} + A_{20}\hat{T}_{20}. \quad (2.177)$$

The spin tensors \hat{T}_{l0} can be written down after referring to Table 2.2, with one important difference. Because the energy corresponding to the difference between the electron and nuclear Larmor frequencies is several orders of magnitude greater than the hyperfine coupling constant, the scalar product $\hat{\mathbf{I}} \cdot \hat{\mathbf{S}}$ can be simplified as the flip-flop term $\hat{I}_x\hat{S}_x + \hat{I}_y\hat{S}_y$ is averaged to zero in the calculation of the first-order average Hamiltonian,

and only the longitudinal term $\hat{I}_z \hat{S}_z$ remains [1]. Therefore the spin tensors are

$$\hat{T}_{00} = -\sqrt{\frac{1}{3}} \hat{I}_z \hat{S}_z \quad (2.178)$$

$$\hat{T}_{20} = \sqrt{\frac{2}{3}} \hat{I}_z \hat{S}_z. \quad (2.179)$$

The spatial tensor components A_{l0} can be written down after referring to Table 2.3. Using this information we can write the spatial tensor components for delocalised electrons as

$$A_{00} = -\sqrt{3} A^{\text{FC}} \quad (2.180)$$

$$\tilde{A}_{20} = \sqrt{\frac{3}{2}} (\tilde{A}_{zz} - A^{\text{FC}}) \quad (2.181)$$

$$= \sqrt{\frac{3}{2}} \frac{\mu_0 \mu_B g_e \hbar \gamma_I}{8\pi S} \int \frac{3z_{\text{PAF}}^2 - r_{\text{PAF}}^2}{r_{\text{PAF}}^5} \rho^{\alpha-\beta}(\mathbf{r}_{\text{PAF}}) d^3 r_{\text{PAF}} \quad (2.182)$$

$$\tilde{A}_{2\pm 1} = 0 \quad (2.183)$$

$$\tilde{A}_{2\pm 2} = -\frac{1}{2} \eta^{\text{SD}} (\tilde{A}_{zz} - A^{\text{FC}}), \quad (2.184)$$

where η^{SD} is the asymmetry parameter, and $r_{i,\text{PAF}}$ is a position coordinate measured in the PAF of the spin-dipolar tensor. Note that the spin-dipolar interaction is not necessarily axially symmetric. For localised electrons, the spatial tensor components are:

$$A_{00} = -\sqrt{3} A^{\text{FC}} \quad (2.185)$$

$$\tilde{A}_{20} = \sqrt{\frac{3}{2}} (\tilde{A}_{zz} - A^{\text{FC}}) \quad (2.186)$$

$$= \sqrt{6} b_{SI} \quad (2.187)$$

$$\tilde{A}_{2\pm 1} = 0 \quad (2.188)$$

$$\tilde{A}_{2\pm 2} = 0, \quad (2.189)$$

where $\tilde{A}_{zz} - A^{\text{FC}} = 2b_{SI}$. The spin-dipolar interaction between two point magnetic dipoles is always axially symmetric, and so η^{SD} and $\tilde{A}_{2\pm 2}$ are therefore zero.

2.8.6 The hyperfine interaction in solid insulators

We now consider the form of the hyperfine interaction in solids. As discussed in section 2.3.2, insulating materials exhibit no charge conductivity, and so we can treat the unpaired electrons as being largely localized on the paramagnetic centres. In this case we can write the hyperfine interaction Hamiltonian as a sum of terms of the type given in section 2.8.5, to give

$$\hat{H}_{IS} = \sum_A \hat{\mathbf{S}}^{(A)} \cdot \mathbf{A}^{(A)} \cdot \hat{\mathbf{I}}. \quad (2.190)$$

Here $\hat{\mathbf{S}}^{(A)}$ and $\mathbf{A}^{(A)}$ are the electronic spin operator and the hyperfine coupling tensor due to the unpaired electrons on paramagnetic centre A .

2.8.7 The hyperfine interaction in solid metals

The hyperfine interaction Hamiltonian in metallic materials has a similar form to the Hamiltonian describing an isolated paramagnetic centre, but with some notable differences. Firstly we note that we cannot necessarily write the interaction in terms of a total electronic spin operator $\hat{\mathbf{S}}$. We therefore write the Hamiltonian as a sum over the N electrons:

$$\hat{H}_{IS} = \frac{\mu_0 \mu_B g_e \hbar \gamma_I}{4\pi} \hat{\mathbf{I}} \cdot \sum_l \left[\frac{3(\mathbf{r}_l \cdot \hat{\mathbf{s}}_l) \mathbf{r}_l - r_l^2 \hat{\mathbf{s}}_l}{r_l^5} + \frac{8\pi}{3} \delta(\mathbf{r}_l) \hat{\mathbf{s}}_l \right]. \quad (2.191)$$

Secondly, in the sum over the electrons l , only electrons in states close to the Fermi level contribute to the hyperfine coupling. The other electrons are spin paired, and so do not contribute. Equation 2.191 assumes that the electrons can be approximated as free electrons, with g -factor g_e .

We proceed as before and calculate the expectation value of \hat{H}_{IS} with respect to the electronic spatial degrees of freedom in a spatial state described by the many-electron wavefunction of Equation 2.26. The result is a sum of hyperfine interactions with the individual electronic spins:

$$\hat{H}_{IS} = \sum_l \hat{\mathbf{s}}_l \cdot \mathbf{a}_l \cdot \hat{\mathbf{I}}, \quad (2.192)$$

where \mathbf{a}_l is the hyperfine coupling tensor describing the interaction with electron l , which is given by

$$\mathbf{a}_l = \frac{\mu_0 \mu_B g_e \hbar \gamma_l}{4\pi} \int \psi(\mathbf{r}_1, \mathbf{r}_2, \dots, \mathbf{r}_N)^* \left[\frac{3\mathbf{r}_l \mathbf{r}_l - r_l^2 \hat{\mathbf{1}}}{r_l^5} + \frac{8\pi}{3} \delta(\mathbf{r}_l) \hat{\mathbf{1}} \right] \psi(\mathbf{r}_1, \mathbf{r}_2, \dots, \mathbf{r}_N) d^3 r_1 d^3 r_2 \dots d^3 r_N. \quad (2.193)$$

The NMR properties that result from this interaction are explored in section 7.12.

2.8.8 Finite nucleus effects

The treatment of the hyperfine interaction in this section has so far assumed that the nucleus can be accurately modelled as a point charge eZ , with a distribution of infinitesimal width given by $\rho(\mathbf{r}_I) = eZ\delta(\mathbf{r}_I)$, where \mathbf{r}_I is the nuclear position coordinate. Assuming this model, we obtain a hyperfine Hamiltonian of the form of Equation 2.159, from which follow all the remaining formulae up to the end of section 2.8.7. However it has been shown that finite nucleus effects, where the nuclear charge has a finite volume, can have a non-negligible effect on the hyperfine interaction, particularly for heavy nuclei [202–205]. A finite nucleus has two effects on the hyperfine interaction, namely the change in electronic structure due to the non-zero nuclear volume and the change to the relevant operators due to the spread of nuclear charge [204].

The effect of a finite nucleus is modelled by replacing the point nuclear charge with a charge distribution $\rho(\mathbf{r}_I)$ of finite width. This distribution can be modelled with any suitable function, but a radial Gaussian $G_\xi(\mathbf{r}_I)$ is commonly used [202–205]:

$$\rho(\mathbf{r}_I) = eZ G_\xi(\mathbf{r}_I), \quad (2.194)$$

$$G_\xi(\mathbf{r}_I) = \left(\frac{\xi}{\pi} \right)^{3/2} \exp(-\xi r_I^2), \quad (2.195)$$

where ξ is a parameter that is inversely proportional to the mean-square width of the distribution $\langle r_I^2 \rangle$:

$$\xi = \frac{3}{2 \langle r_I^2 \rangle}, \quad (2.196)$$

and the distribution is centred at $\mathbf{r}_I = \mathbf{0}$. The electron–nucleus potential $V_{SI}(\mathbf{r})$ is then given by

$$V_{SI}(\mathbf{r}) = -\frac{Ze}{r} P\left(1/2, \xi r^2\right), \quad (2.197)$$

where \mathbf{r} is the position of the electron relative to the centre of the nuclear charge distribution. The function $P(a, x)$ is defined as

$$P(a, x) = \frac{1}{\Gamma(a)} \int_0^x t^{a-1} \exp(-t) dt, \quad (2.198)$$

where $\Gamma(a)$ is the gamma function, and $a > 0$.

The hyperfine interaction Hamiltonian can now be modified to include the finite nucleus effect. If we consider the hyperfine interaction with a single unpaired electron, we simply modify Equation 2.159 to include the nuclear distribution. The modified hyperfine Hamiltonian is

$$\hat{H}_{\text{SI}} = -\frac{\mu_0}{4\pi} \left[\int P(5/2, \xi r^2) \frac{3(\hat{\boldsymbol{\mu}}_S \cdot \mathbf{r})(\hat{\boldsymbol{\mu}}_I \cdot \mathbf{r}) - (\hat{\boldsymbol{\mu}}_S \cdot \hat{\boldsymbol{\mu}}_I) r^2}{r^5} |\psi(\mathbf{r})|^2 d^3r + \frac{8\pi}{3} (\hat{\boldsymbol{\mu}}_S \cdot \hat{\boldsymbol{\mu}}_I) \int G_\xi(\mathbf{r}) |\psi(\mathbf{r})|^2 \right]. \quad (2.199)$$

The first term is due to the spin-dipolar interaction with a nucleus of finite charge distribution, and the second term is the corresponding Fermi-contact distribution. For the remainder of this review, we do not consider finite nucleus effects further. However we should remember that these effects become important for heavy elements [202–205].

2.9 Key concepts

- Nuclei and unpaired electrons possess magnetic moments, due to their spin, which define their molecular/atomic-level magnetic properties.
- The magnetization and magnetic susceptibility define the bulk magnetic properties of ensembles of nuclei and electrons.
- Solid materials with unpaired electrons can be characterized as insulators, semi-conductors, or metals according to their electronic structure.
- The molecular/atomic-level magnetic moments of nuclei and unpaired electrons couple with an external magnetic field, giving the Zeeman interaction, which is responsible for both the NMR and EPR spectra.
- The nuclear Zeeman resonance frequency depends on the local environment of the nucleus, with nuclei in different chemical sites having different resonance frequencies. This is the origin of the chemical shielding and chemical shift.

- The chemical shielding, in general, depends on the orientation of the chemical environment with respect to the external magnetic field. The orientationally-dependent part of the shielding is known as the CSA, and is described by a rank-two spherical tensor.
- The nuclear and electronic magnetic moments couple to each other resulting in the hyperfine interaction.
- The hyperfine interaction in isolated molecules, solid insulators, and metals is described by a hyperfine coupling constant, which comprises a ‘through-bond’ isotropic Fermi-contact term, and a ‘through-space’ anisotropic spin-dipolar term.
- For heavy nuclei, finite nuclear effects modify the hyperfine interaction. Here the nuclear charge distribution is modelled by a function of non-zero spatial width.

Chapter 3

The paramagnetic shift in electron spin-only systems

In this chapter we describe the origin of the paramagnetic shifts of nuclei that are coupled to the unpaired electrons of paramagnetic systems such as organic radicals or transition-metal ions. The discussion is initially limited to spin-only paramagnets, where the electrons occupy a non-degenerate orbital state, with the more complicated effects due to orbital angular momentum, spin-orbit coupling, and the crystal field being dealt with in the following chapters.

The first question that is answered is why the hyperfine interaction, which takes exactly the same form as a heteronuclear coupling interaction, causes a shift in the nuclear resonance frequency and *not* a splitting of the NMR resonance. The reason for this is that the unpaired electrons relax on a timescale that is several orders of magnitude shorter than the timescales of both nuclear relaxation and the NMR experiment. Values of electron relaxation times for a range of metal ions have been tabulated [15], and are generally between 10^{-14} and 10^{-8} s, which are considerably shorter than typical nuclear longitudinal relaxation times of between 1 ms and several minutes. As a result the nucleus in effect does not interact with an electronic magnetic moment, but rather with its average value. This interaction has the same form as a chemical shift. However we should note that whilst this model is sufficient to describe the NMR shift, it is not able to account for all the effects of the hyperfine interaction that are measurable by NMR. For example, in order to model the

nuclear relaxation enhancement, we must consider the full interaction between the nuclear and electronic dipole moments, which is discussed at length in chapters 8 and 9.

Three different, but essentially equivalent, explanations of why the paramagnetic shift occurs are proposed. Firstly we calculate the form of the NMR spectrum of a nucleus coupled to a free electron, and show that the effect of the fast electron relaxation is to average the two components of the resonance splitting to a single line that is shifted with respect to the nominal nuclear Larmor frequency. Secondly we show that we can also explain the shift as a result of the nucleus coupling to an average electronic magnetic moment that can be calculated from an average over the thermally-accessible electron energy levels. Thirdly we show that the thermal average of the electron magnetic moment is related to the bulk magnetic properties of the material via the magnetic susceptibility, and that we can therefore relate the paramagnetic shift to these bulk properties.

3.1 The origin of the paramagnetic shift

We begin by deriving the form of the spectrum of a heteronuclear spin system comprising two spins-1/2, which is already familiar to an NMR audience. Following this we will then substitute a single free electron for the second nucleus, and derive the corresponding paramagnetic shift.

3.1.1 Two-spin system comprising two spin-1/2 heteronuclei

We initially consider a spin system comprising two nuclear spins-1/2 I and S of different species that interact via an isotropic J -coupling. Note however that the argument that follows also applies to a dipolar coupling in a static single crystal, and can be extended in a straightforward manner to powder samples, and to include the effects of sample rotation. We also assume that the gyromagnetic ratios of I and S are positive and negative respectively, and that $|\omega_{0,S}| > |\omega_{0,I}| \gg |J|$, where $\omega_{0,S}$ and $\omega_{0,I}$ are the I -spin and S -spin Larmor frequencies respectively, and J is the heteronuclear J -coupling constant in rad s^{-1} , which is here taken to be positive. This choice allows us to change the S -spin into an electron later on, without having to change the signs in all of the derived expressions.

The high-field Hamiltonian is

$$\hat{H} = \hbar\omega_{0,I}\hat{I}_z + \hbar\omega_{0,S}\hat{S}_z + \hbar J\hat{I}_z\hat{S}_z, \quad (3.1)$$

where the first and second terms represent I -spin and S -spin Zeeman interactions respectively, and the third term is the heteronuclear J -coupling interaction. The eigenstates of \hat{H} are the functions $|IM_I, SM_S\rangle$, which depend on the four quantum numbers $I = 1/2$, $S = 1/2$, M_I , and M_S . Here we omit I and S , and use the labels α and β to represent the allowed values of both M_I and M_S . In addition it proves useful to emphasize the energy order of the four spin states, and so we also label them as $|1\rangle$, $|2\rangle$, $|3\rangle$, and $|4\rangle$ in order of increasing energy as follows

$$|1\rangle = |\alpha\beta\rangle, \quad (3.2)$$

$$|2\rangle = |\beta\beta\rangle, \quad (3.3)$$

$$|3\rangle = |\alpha\alpha\rangle, \quad (3.4)$$

$$|4\rangle = |\beta\alpha\rangle. \quad (3.5)$$

The corresponding energies E_n are

$$E_1 = \frac{1}{2}\hbar\omega_{0,I} - \frac{1}{2}\hbar\omega_{0,S} - \frac{1}{4}\hbar J \quad (3.6)$$

$$E_2 = -\frac{1}{2}\hbar\omega_{0,I} - \frac{1}{2}\hbar\omega_{0,S} + \frac{1}{4}\hbar J, \quad (3.7)$$

$$E_3 = \frac{1}{2}\hbar\omega_{0,I} + \frac{1}{2}\hbar\omega_{0,S} + \frac{1}{4}\hbar J, \quad (3.8)$$

$$E_4 = -\frac{1}{2}\hbar\omega_{0,I} + \frac{1}{2}\hbar\omega_{0,S} - \frac{1}{4}\hbar J. \quad (3.9)$$

Note that the order of the energies is correct as $\omega_{0,I} < 0$ and $\omega_{0,S} > 0$. A schematic of the energy levels is shown in Figure 3.1 (a).

We are interested in the transitions which give resonances in the NMR spectrum of the I -spin. These are the two single quantum transitions $|1\rangle \rightarrow |2\rangle$ and $|3\rangle \rightarrow |4\rangle$, which have the transition frequencies $\Delta\omega_{1\rightarrow 2}$ and

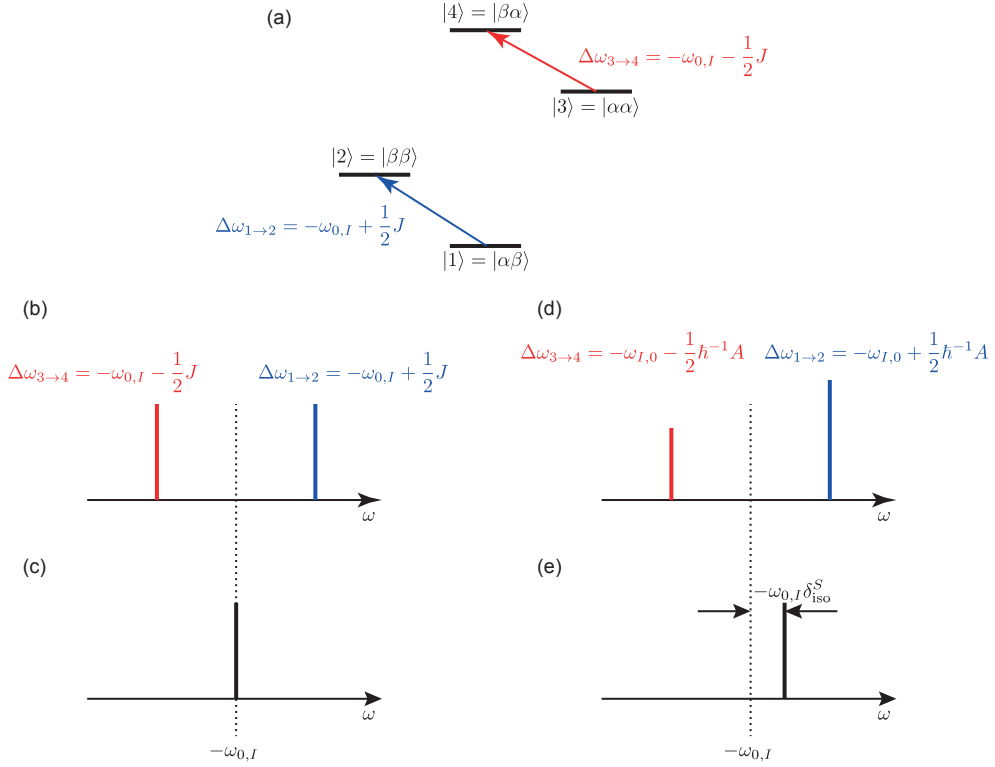


Figure 3.1: Illustration of the spin energy levels and NMR spectrum of a two-spin-1/2 system I - S , showing the differences between a system of two coupled nuclear spins-1/2 of different species, and a spin-1/2 coupled to an electron. In (a) is shown the array of four energy levels, 1-4, assuming that $|\omega_{0,S}| > |\omega_{0,I}| > |J|$, $\omega_{0,S} > 0$, $\omega_{0,I} < 0$, and $J > 0$. The two I -spin transitions are shown with a red and blue arrow, and are labelled with their frequencies $\Delta\omega_{1\rightarrow 2}$ and $\Delta\omega_{3\rightarrow 4}$. The corresponding schematic of the I -spin NMR spectrum is shown in (b) for the case where S is a second nuclear spin. The spectrum contains two components of a doublet with the same intensity, centred on $-\omega_{0,I}$, and separated by the coupling constant J . Decoupling of the S -spin, or other fast exchange of the two S -spin spin states leads to a singlet at $-\omega_{0,I}$ as shown in (c). The energy level diagram in (a) also applies to a nuclear spin I coupled to an electron S if we substitute J for A/\hbar . The corresponding nuclear I -spin spectrum is shown in (d), and exhibits the same features as the spectrum in (b) with the exception that the two components of the doublet now have different intensities because the larger energy separation between the pairs of I -spin energy levels in the two transitions leads, via the Boltzmann distribution, to different equilibrium spin state population differences. The rapid electronic relaxation of S ‘decouples’ the I spin spectrum to give a singlet which is positioned at the centre of mass of the two doublet components as shown in (e). The singlet is thus offset from $-\omega_{0,I}$ by an offset frequency $-\omega_{0,I}\delta_{\text{iso}}^S$, where δ_{iso}^S is the ‘paramagnetic shift’ due to the electron S .

$\Delta\omega_{3\rightarrow 4}$ given by:

$$\Delta\omega_{1\rightarrow 2} = \frac{E_2 - E_1}{\hbar} \quad (3.10)$$

$$= -\omega_{0,I} + \frac{1}{2}J, \quad (3.11)$$

$$\Delta\omega_{3\rightarrow 4} = \frac{E_4 - E_3}{\hbar} \quad (3.12)$$

$$= -\omega_{0,I} - \frac{1}{2}J. \quad (3.13)$$

The two resonances are split by the coupling constant J and centred on $-\omega_{0,I}$, and so can be interpreted as the two components of the I -spin doublet, with the component due to the $|1\rangle \rightarrow |2\rangle$ transition representing the I -spin single-quantum transition when the S -spin is in the $|\beta\rangle$ state, and the $|3\rangle \rightarrow |4\rangle$ transition occurring with the S -spin in the $|\alpha\rangle$ state.

The intensity of each peak is proportional to the population difference of the two states. For example the intensity $I_{n\rightarrow p}$ of the transition $|n\rangle \rightarrow |p\rangle$ varies as

$$I_{n\rightarrow p} \propto P_n - P_p. \quad (3.14)$$

The population of the state $|n\rangle$, P_n is given by the Boltzmann distribution,

$$P_n = \frac{\exp(-\beta E_n)}{Q}, \quad (3.15)$$

where $\beta = 1/kT$, k is the Boltzmann constant, T is the absolute temperature, and Q is the partition function

$$Q = \sum_n \exp(-\beta E_n). \quad (3.16)$$

Using these expressions we can write down the fraction $f_{n\rightarrow p}$ of the total spectral intensity that is contained

in the peak due to the transition $|n\rangle \rightarrow |p\rangle$. For the two I -spin transitions these fractional intensities are:

$$f_{1\rightarrow 2} = \frac{I_{1\rightarrow 2}}{I_{1\rightarrow 2} + I_{3\rightarrow 4}} \quad (3.17)$$

$$= \frac{P_1 - P_2}{P_1 - P_2 + P_3 - P_4}, \quad (3.18)$$

$$f_{3\rightarrow 4} = \frac{I_{3\rightarrow 4}}{I_{1\rightarrow 2} + I_{3\rightarrow 4}} \quad (3.19)$$

$$= \frac{P_3 - P_4}{P_1 - P_2 + P_3 - P_4}. \quad (3.20)$$

Note that, according to these definitions, $f_{1\rightarrow 2} + f_{3\rightarrow 4} = 1$.

We can simplify these expressions somewhat by noting that the thermal energy kT greatly exceeds the energy separation of the four energy levels, which allows us to expand the exponential in the expression for the population of the state $|n\rangle$ as a Taylor series in β , and to truncate it at the first-order term:

$$\exp(-\beta E_n) = 1 - \beta E_n + O(\beta^2). \quad (3.21)$$

Substituting this into the expressions in Equations 3.18 and 3.20 we obtain, to zeroth order in β ,

$$f_{1\rightarrow 2} = \frac{E_2 - E_1}{E_4 - E_3 + E_2 - E_1} + O(\beta) \quad (3.22)$$

$$= \frac{\Delta\omega_{1\rightarrow 2}}{\Delta\omega_{3\rightarrow 4} + \Delta\omega_{1\rightarrow 2}} + O(\beta), \quad (3.23)$$

$$f_{3\rightarrow 4} = \frac{E_4 - E_3}{E_4 - E_3 + E_2 - E_1} + O(\beta) \quad (3.24)$$

$$= \frac{\Delta\omega_{3\rightarrow 4}}{\Delta\omega_{3\rightarrow 4} + \Delta\omega_{1\rightarrow 2}} + O(\beta), \quad (3.25)$$

and hence

$$f_{1\rightarrow 2} = \frac{-\omega_{0,I} + \frac{1}{2}J}{-2\omega_{0,I}}, \quad (3.26)$$

$$f_{3\rightarrow 4} = \frac{-\omega_{0,I} - \frac{1}{2}J}{-2\omega_{0,I}}. \quad (3.27)$$

Remembering that $|J| \ll |\omega_{0,I}|$, we see that both transitions, and therefore both components of the doublet, have the same fractional intensity of $1/2$. A schematic of the corresponding I -spin spectrum is shown in

Figure 3.1 (b).

Now let us imagine that the spectrum is acquired whilst the $|\alpha\rangle$ and $|\beta\rangle$ spin states of the S -spin are rapidly interconverted. Such a situation may arise either because we are applying decoupling irradiation to S , or because S is relaxing on a timescale that is fast compared to the I -spin relaxation. Under these circumstances the two components of the I -spin doublet collapse to a singlet, the spectral position of which $\bar{\omega}$ is given by the average of the two spectral frequencies:

$$\bar{\omega} = f_{1\rightarrow 2}\Delta\omega_{1\rightarrow 2} + f_{3\rightarrow 4}\Delta\omega_{3\rightarrow 4} \quad (3.28)$$

$$= \frac{1}{2}\left(-\omega_{0,I} + \frac{1}{2}J\right) + \frac{1}{2}\left(-\omega_{0,I} - \frac{1}{2}J\right) \quad (3.29)$$

$$= -\omega_{0,I}, \quad (3.30)$$

i.e. the peak appears at minus the I -spin Larmor frequency, as shown in Figure 3.1 (c).

3.1.2 Two-spin system comprising one spin-1/2 nucleus and a free electron

A spin system comprising a single spin-1/2 nucleus I coupled to a free electron S can be treated in an analogous way. The high-field Hamiltonian is the same as in Equation 3.1, with the exception that we write the electron Zeeman interaction in terms of $\mu_B g_e$, and we replace the coupling $\hbar J$ with a hyperfine coupling constant A (which is in units of energy, rather than frequency):

$$\hat{H} = \hbar\omega_{0,I}\hat{I}_z + \mu_B g_e \hat{S}_z + A\hat{I}_z\hat{S}_z. \quad (3.31)$$

The eigenstates are the same as those in Equations 3.2–3.5, and have the corresponding energies:

$$E_1 = \frac{1}{2}\hbar\omega_{0,I} - \frac{1}{2}\mu_B g_e - \frac{1}{4}A, \quad (3.32)$$

$$E_2 = -\frac{1}{2}\hbar\omega_{0,I} - \frac{1}{2}\mu_B g_e + \frac{1}{4}A, \quad (3.33)$$

$$E_3 = \frac{1}{2}\hbar\omega_{0,I} + \frac{1}{2}\mu_B g_e + \frac{1}{4}A, \quad (3.34)$$

$$E_4 = -\frac{1}{2}\hbar\omega_{0,I} + \frac{1}{2}\mu_B g_e - \frac{1}{4}A. \quad (3.35)$$

The two nuclear-spin transitions have the following frequencies:

$$\Delta\omega_{1\rightarrow 2} = \frac{E_2 - E_1}{\hbar} \quad (3.36)$$

$$= -\omega_{0,I} + \frac{1}{2}\hbar^{-1}A, \quad (3.37)$$

$$\Delta\omega_{3\rightarrow 4} = \frac{E_4 - E_3}{\hbar} \quad (3.38)$$

$$= -\omega_{0,I} - \frac{1}{2}\hbar^{-1}A. \quad (3.39)$$

Here we encounter the key difference between the energy levels of the heteronuclear two-spin system, and the nucleus–electron two-spin system, which is that the electron Zeeman interaction is much larger than the nuclear Zeeman interaction. This is reflected in the values of the gyromagnetic ratios for ^1H and the free electron which are $2.675 \times 10^8 \text{ rad s}^{-1}$ and $-1.761 \times 10^{11} \text{ rad s}^{-1}$ respectively (ratio $|\gamma_S/\gamma_I| = 658$), and the Larmor frequencies of -500 MHz and $+329 \text{ GHz}$ at a magnetic field of 11.74 T . Therefore when we calculate the intensities of the spectral peaks using Equations 3.18 and 3.20 we have to bear in mind that the larger ratio of $\mu_B g_e/(kT)$ means we can no longer truncate the exponential factors in the Boltzmann distribution at first order in β , and must include terms of order β^2 :

$$\exp(-\beta E_n) = 1 - \beta E_n + \frac{1}{2}\beta^2 E_n^2 + \mathcal{O}(\beta^3). \quad (3.40)$$

If we again assume that the coupling constant has a negligible effect on the populations of the states the intensities of the two nuclear transitions are, to first order in β :

$$f_{1\rightarrow 2} = \frac{1}{2} + \frac{1}{4}\mu_B g_e B_0 \beta, \quad (3.41)$$

$$f_{3\rightarrow 4} = \frac{1}{2} - \frac{1}{4}\mu_B g_e B_0 \beta. \quad (3.42)$$

We see that the transition between the two lower states, $|1\rangle$ and $|2\rangle$, has a greater intensity than the transition between the two higher states, $|3\rangle$ and $|4\rangle$. The corresponding NMR spectrum is illustrated in Figure 3.1 (d). In a magnetic field of 11.74 T at a temperature of 298 K , the difference in peak intensities is approximately 0.03 , or 3% . At first sight this appears to be very small, but as we will see it is enough to exert a decisive effect on the NMR spectrum.

The rapid electron relaxation effectively “decouples” the NMR spectrum, resulting in a singlet appearing at a frequency $\bar{\omega}$ that is the weighted average of the two peaks. This frequency is

$$\bar{\omega} = f_{1 \rightarrow 2} \Delta\omega_{1 \rightarrow 2} + f_{3 \rightarrow 4} \Delta\omega_{3 \rightarrow 4} \quad (3.43)$$

$$= -\omega_{0,I} + \frac{\mu_B g_e A B_0}{4\hbar k T}. \quad (3.44)$$

The corresponding spectrum is shown in Figure 3.1 (e). We see immediately that the resonance is offset from $-\omega_{0,I}$ by an amount $\mu_B g_e A B_0 / (4\hbar k T)$ that is proportional to the magnetic field B_0 . It is therefore equivalent to an isotropic chemical shift which, from Equations 2.109 and 2.130, has a Hamiltonian $\hat{H} = \hbar\omega_{0,I}(1 + \delta_{\text{iso}}^S)$ from which we can calculate a transition frequency

$$\bar{\omega} = -\omega_{0,I} (1 + \delta_{\text{iso}}^S). \quad (3.45)$$

Comparing Equations 3.44 and 3.45 we deduce that the shift is equal to

$$\delta_{\text{iso}}^S = \frac{\mu_B g_e A}{4\hbar\gamma_I k T}. \quad (3.46)$$

We have identified this contribution as the paramagnetic shift, as it is due solely to the interaction between the nucleus and the unpaired electron. The paramagnetic shift scales as $A/(kT)$, which can be understood as follows. Increasing the temperature results in a smaller shift, simply because the higher-energy states become more populated relative to the lower-energy states, and the difference between the intensities of the two transitions is reduced. Eventually we approach the limit encountered in the case of the heteronuclear two-spin system, with the paramagnetic shift tending to zero. This inverse proportionality is a form of the Curie Law, which we will see again in the discussion of the magnetic susceptibility. On the other hand as we increase the hyperfine coupling constant the shift also increases as we are averaging over a larger separation of the peaks.

These observations all point to the idea that the hyperfine interaction has been scaled down by a temperature-dependent factor to give the paramagnetic shift. This is an idea we will return to later, and quantify more formally, when we discuss the role of the magnetic susceptibility.

3.2 The thermal average of the electron magnetic moment: the Brillouin function and the Curie spin

The ideas developed in the previous section act as a visual explanation of why we observe a paramagnetic shift in the presence of unpaired electrons. However this is not the most convenient way to calculate the shift, especially for more complex systems with multiple electrons and orbital angular momentum. A better method turns out to be to calculate the average electronic magnetic moment first, and then to couple that to the nucleus via the hyperfine interaction.

3.2.1 The Hamiltonian and the pseudo spin

The Hamiltonian we use in this section is

$$\hat{H} = \hbar\omega_{0,I}\hat{I}_z + \mu_B g_e B_0 \hat{S}_z + \hat{S} \cdot \mathbf{A} \cdot \hat{I}, \quad (3.47)$$

where the first term is the nuclear Zeeman interaction, which ignores the effects of the orbital contribution to the chemical shielding, the second term is the electron Zeeman interaction, and the third term is the hyperfine coupling.

For the electron Zeeman interaction we assume that the interaction is spatially isotropic, with a g -factor equal to g_e . However we no longer restrict the discussion to a single free electron, but to a *paramagnetic centre* containing N unpaired electrons with total spin S . Such a situation is appropriate, for instance, for describing spin-only transition-metal ions in a perfectly cubic ligand-field environment. Here we introduce the concept of *pseudo spin*, where we model the energy levels of the electrons as being due to a single effective spin \tilde{S} which has the same multiplicity $2\tilde{S} + 1$ as the true states [184]. For the first-row d -block transition metals the pseudo spin is the same as the true spin S , so we drop the tilde.

The form of the hyperfine interaction we use here does not make use of the high-field approximation. This allows us to treat coupling constants that are not small compared to the Zeeman interactions in the most general way possible. At this point we remind ourselves that the hyperfine coupling tensor is the sum of an isotropic Fermi-contact term, and a symmetric spin-dipolar tensor.

We saw in the previous section that the paramagnetic shift is due to electronic relaxation, which occurs on

a timescale that is orders of magnitude shorter than nuclear relaxation, so that during the observation of the nuclear-spin transitions the electronic spins are effectively sampling all the electronic energy levels according to their equilibrium configuration. This means that, in effect, the hyperfine interaction \hat{H}_{SI} does not really couple the nuclear magnetic moment to the electronic magnetic moment, but rather to the *average* of the electronic magnetic moment. Before continuing, we note that whilst this model is sufficient for understanding the paramagnetic shift, it does not give a correct explanation of nuclear relaxation in paramagnetic systems. This is because the random processes that cause nuclear relaxation occur on timescales that are several orders of magnitude shorter than those of nuclear relaxation itself, and so we must consider the full interaction between the nuclear and electronic dipole moments. This is discussed in more detail in chapters 8 and 9. For now we confine our discussion to the shift, and are therefore able to write the hyperfine Hamiltonian as

$$\hat{H}_{SI} = \langle \hat{\mathbf{S}} \rangle \cdot \mathbf{A} \cdot \hat{\mathbf{I}}, \quad (3.48)$$

where $\langle \hat{\mathbf{S}} \rangle$ is the expectation value of the electronic spin vector. This expectation value represents the time average of the electron spin, which we will assume to be equivalent to the average over the entire ensemble of paramagnetic centres. The latter is equal to the Boltzmann average of the components \hat{S}_i of the spin:

$$\langle \hat{S}_i \rangle = \frac{\sum_n \langle n | \hat{S}_i | n \rangle \exp(-\beta E_n)}{\sum_n \exp(-\beta E_n)}, \quad (3.49)$$

where the $|n\rangle$ and the E_n are the eigenstates and energies of the Hamiltonian in Equation 3.47. To proceed we simplify matters by noting that the dominant term in the Hamiltonian is the electronic Zeeman interaction, and that the other terms have a negligible effect on the electronic spin energy levels. Therefore we take the eigenstates and energies simply to be those of the Zeeman interaction, namely

$$|n\rangle = |S M_S\rangle, \quad E_n \equiv E(S, M_S) = \mu_B g_e B_0 M_S. \quad (3.50)$$

We note that the lowest-energy state is $|S - S\rangle$, which is consequence of the negative gyromagnetic ratio of the electron.

We see immediately that the transverse components of the expectation value of the spin are zero:

$$\langle \hat{S}_x \rangle = \langle \hat{S}_y \rangle = 0. \quad (3.51)$$

This is because these components are perpendicular to the applied field, and so there is no driving force for inducing a net magnetic moment in these directions. However there is such a driving force parallel to the field, resulting in the longitudinal component $\langle \hat{S}_z \rangle$ being non-zero:

$$\langle \hat{S}_z \rangle = \frac{\sum_{M_S=-S}^{+S} \langle S M_S | \hat{S}_z | S M_S \rangle \exp(-\beta E(S, M_S))}{\sum_{M_S=-S}^{+S} \exp(-\beta E(S, M_S))} \quad (3.52)$$

$$= \frac{\sum_{M_S=-S}^{+S} M_S \exp(-\beta \mu_B g_e B_0 M_S)}{\sum_{M_S=-S}^{+S} \exp(-\beta \mu_B g_e B_0 M_S)}. \quad (3.53)$$

Defining $x = -\beta \mu_B g_e B_0$ we can write Equation 3.53 as

$$\langle \hat{S}_z \rangle = \frac{\sum_{M_S=-S}^{+S} M_S \exp(M_S x)}{\sum_{M_S=-S}^{+S} \exp(M_S x)} \quad (3.54)$$

$$= \frac{d}{dx} \ln \left[\sum_{M_S=-S}^{+S} \exp(M_S x) \right], \quad (3.55)$$

where the move to the last line can be verified by calculating the derivative. The sum is a simple geometric progression, which can be written in the following closed form:

$$\sum_{M_S=-S}^{+S} \exp(M_S x) = \frac{\sinh \left[\left(S + \frac{1}{2} \right) x \right]}{\sinh \left[\frac{1}{2} x \right]}. \quad (3.56)$$

Calculating the derivative now gives, after some algebra:

$$\frac{d}{dx} \ln \left[\frac{\sinh \left[\left(S + \frac{1}{2} \right) x \right]}{\sinh \left[\frac{1}{2} x \right]} \right] = \left(S + \frac{1}{2} \right) \coth \left[\left(S + \frac{1}{2} \right) x \right] - \frac{1}{2} \coth \left[\frac{1}{2} x \right]. \quad (3.57)$$

The expectation value of the the z-component of the spin is now

$$\langle \hat{S}_z \rangle = -S B_S(y), \quad (3.58)$$

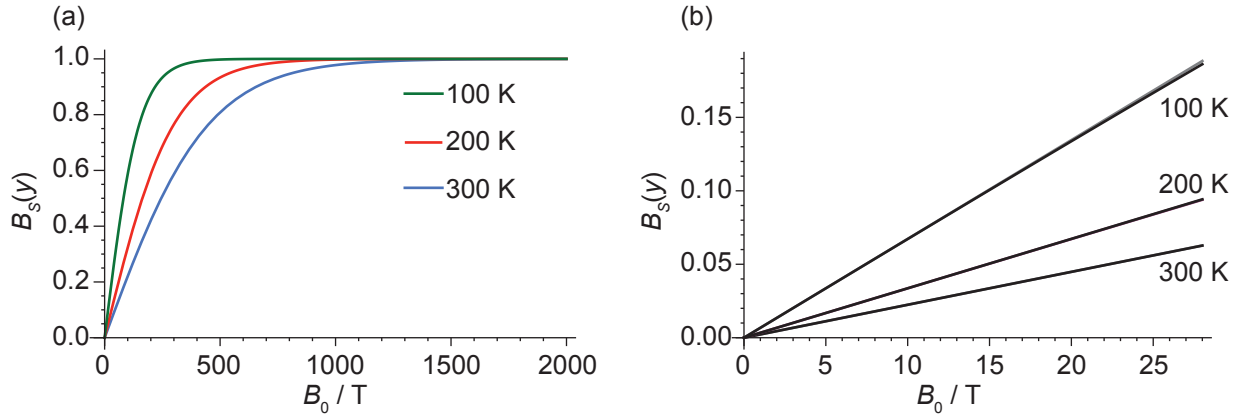


Figure 3.2: The Brillouin function in Equation 3.59 for an electronic spin $S = 1/2$ plotted as a function of the applied magnetic field for a range of experimentally-available temperatures. The plots in (a) show the Brillouin function $B_S(y)$ for values of the external field up to 2000 T for temperatures of 100, 200, and 300 K. Saturation is reached at values of B_0 between approximately 300 T (at 100 K) and 1500 T (300 K). Part (b) shows as expansion of the plots in (a) up to the commercially-available magnetic field of 28 T (black curves), along with the linear approximation of Equation 3.61 (grey curves). For each temperature the two curves are indistinguishable, except for the lowest temperature of 100 K where there is a small departure of $B_S(y)$ from linear behaviour.

where the Brillouin function $B_S(y)$ is defined as

$$B_S(y) = \frac{2S+1}{2S} \coth\left(\frac{2S+1}{2S}y\right) - \frac{1}{2S} \coth\left(\frac{y}{2S}\right), \quad (3.59)$$

and $y = \beta\mu_B g_e B_0 S = -Sx$.

Equation 3.58 is a general expression for the value of the expectation value of \hat{S}_z for *any* temperature and magnetic field. Representative curves are plotted in Figure 3.2 (a) for a range of magnetic fields and temperatures. However for typical values of the field and temperature in high-resolution NMR, including the current maximum available field of 28.18 T and the lowest readily-available temperature of 90 K, we are in the high-temperature limit $\mu_B g_e B_0 / kT \ll 1$, and the general form of the Brillouin function is not needed. We can therefore expand the coth function as a Laurent series [189],

$$\coth(z) = \frac{1}{z} + \frac{1}{3}z - \frac{1}{45}z^3 + \frac{2}{945}z^5 + \mathcal{O}(z^7), \quad (3.60)$$

and truncate at the lowest order in y to give the following approximation to the Brillouin function:

$$B_S(y) = \frac{S+1}{3S}y + \mathcal{O}(y^3). \quad (3.61)$$

The expectation value of \hat{S}_z is therefore

$$\langle \hat{S}_z \rangle = -\frac{\mu_B g_e S(S+1)B_0}{3kT}. \quad (3.62)$$

The $\langle \hat{S}_z \rangle$ above is referred to as the *Curie spin*, as it exhibits a Curie temperature dependence of $1/T$. The Brillouin function is an odd function in β , and so the next-lowest-order term in the expansion varies as $1/T^3$, i.e. there is no term in $1/T^2$ for an isotropic spin system. Comparisons of the full Brillouin function and the high-temperature approximation are shown in Figure 3.2 (b).

We see immediately that the Curie spin is negative, which we rationalise by noting that, at finite temperature, the states with the more negative values of M_S are more populated, as we see in Figure 3.3 (a). In addition we see that the magnitude of the Curie spin is proportional to the electron Zeeman energy $\mu_B g_e B_0$. If we increase this energy, for example by raising the magnetic field, the separation between the energy levels increases and the lower-energy states with negative M_S become more populated relative to the higher energy states, as seen in Figure 3.3 (b). A similar argument also explains the Curie temperature dependence, namely that a lower thermal energy kT increases the populations of the lower-energy states relative to the higher-energy states, as we see in Figure 3.3 (c). In both cases the magnitude of the Curie spin increases. The components of the expectation value of the electronic magnetic moment are proportional to those of the Curie spin, i.e. $\langle \hat{\mu}_i \rangle = -\mu_B g_e \langle \hat{S}_i \rangle$, and are given by the following expressions:

$$\langle \hat{\mu}_x \rangle = \langle \hat{\mu}_y \rangle = 0 \quad (3.63)$$

$$\langle \hat{\mu}_z \rangle = \frac{\mu_B^2 g_e^2 S(S+1)B_0}{3kT}. \quad (3.64)$$

We note that $\langle \hat{\mu}_z \rangle$ is proportional to the square of the magnitude of the total electronic magnetic moment $\mu_{\text{eff}} = \mu_B g_e \sqrt{S(S+1)}$.

Another regime of interest is the saturation regime, where either the field is sufficiently high or the temperature is sufficiently low that $\mu_B g_e B_0/kT \rightarrow \infty$. In this case both the coth function and $B_S(y)$ tend

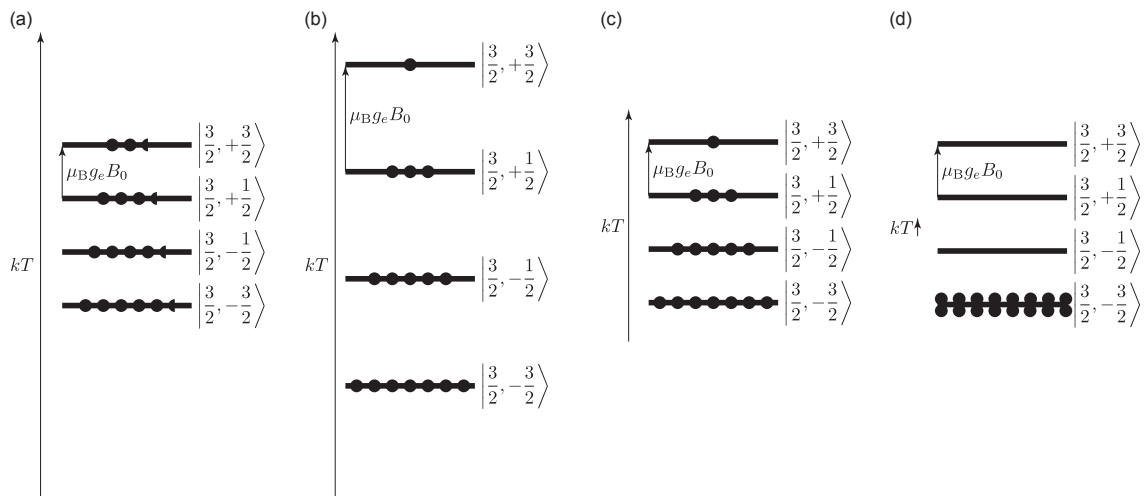


Figure 3.3: Illustration of the factors affecting the populations of the electronic spin states according to the Boltzmann distribution, and the resulting Curie spin. The population distribution of the electronic spin states $|S M_S\rangle$ is shown for an electronic spin $S = 3/2$ in (a). The states with more negative M_S lie lower in energy and are more populated relative to the higher-energy states, hence the Curie spin is negative. The populations of the lower-energy states can be increased relative to those of the higher-energy states either by increasing the size of the external magnetic field B_0 (b), or decreasing the temperature T (c). When the field is increased, or the temperature is lowered, sufficiently that $\mu_B g_e B_0 / kT \rightarrow \infty$ only the lowest-energy state with $M_S = -S$ is populated, and the electronic spins are saturated, as shown in (d).

to unity, and the expectation value of \hat{S}_z , $\langle \hat{S}_z \rangle_{\text{sat}}$, is

$$\langle \hat{S}_z \rangle_{\text{sat}} = -S. \quad (3.65)$$

At saturation only the lowest-energy state with $M_S = -S$ is populated, with all the paramagnetic centres having this same M_S . This situation is shown in Figure 3.3 (d).

Returning to the high-temperature regime we see that the Curie spin is linear in B_0 , so is the corresponding hyperfine interaction Hamiltonian $\langle \hat{S} \rangle \cdot \mathbf{A} \cdot \hat{\mathbf{I}}$. It has exactly the same form as the nuclear shielding interaction Hamiltonian in Equation 2.84, and we can equate the two to determine the corresponding paramagnetic shielding tensor:

$$\hbar\gamma_I \mathbf{B} \cdot \boldsymbol{\sigma}^S \cdot \hat{\mathbf{I}} = \langle \hat{S} \rangle \cdot \mathbf{A} \cdot \hat{\mathbf{I}}, \quad (3.66)$$

from which we obtain:

$$\hbar\gamma_I \mathbf{B} \cdot \boldsymbol{\sigma}^S = \langle \hat{S} \rangle \cdot \mathbf{A}. \quad (3.67)$$

Our calculation of the Curie spin assumes a magnetic field B_0 along z , and so the only components of the paramagnetic shielding we obtain are the σ_{zj} , where j is x , y , or z :

$$\sigma_{zj} = \frac{\langle \hat{S}_z \rangle A_{zj}}{\hbar\gamma_I B_0}. \quad (3.68)$$

We can repeat the calculation with the field along x or y , with a Zeeman interaction of $\mu_B g_e B_0 \hat{S}_x$ or $\mu_B g_e B_0 \hat{S}_y$ respectively, and obtain the corresponding x - and y -components of the Curie spin, which are the same as the z -component above, i.e.

$$\langle \hat{S}_x \rangle = \langle \hat{S}_y \rangle = \langle \hat{S}_z \rangle = -\frac{\mu_B g_e S(S+1)B_0}{3kT}. \quad (3.69)$$

Note that, for each calculation, the components of the Curie spin that are perpendicular to the applied field are zero, and so in order to obtain the full paramagnetic shielding tensor we must apply the field along each of the three axes in turn. This is because only three of the nine components of the shielding tensor dictate the response of the system to a field applied in a single direction. The full form of the shielding tensor is therefore

$$\boldsymbol{\sigma}^S = -\frac{\mu_B g_e S(S+1)}{3\hbar\gamma_I kT} \mathbf{A}. \quad (3.70)$$

The Curie spin is, of course, proportional to the thermal average of the magnetic moment of the total spin S , and multiplying the hyperfine coupling constant in Equations 2.171 and 2.172 by the Curie spin gives the total paramagnetic shift due to all the unpaired electrons.

Note that although the hyperfine tensor \mathbf{A} depends on the nuclear species, the ratio $\mathbf{A}/(\hbar\gamma_I)$, which appears in the expression for the paramagnetic shielding in Equation 3.70 does not, as it is independent of γ_I . This independence from the nuclear species is a general property of all chemical shielding tensors.

We can write the paramagnetic shielding tensor in terms of the irreducible spherical tensor components σ_{lm}^S , and apply the high-field approximation. We saw in section 2.6 that the only components that are significant at high field are σ_{00}^S and σ_{20}^S . Note that, although the high-field approximation may not be valid for the hyperfine interaction, it can be more safely applied to the paramagnetic shielding interaction as the size of the hyperfine coupling constant is scaled down by the Curie spin. The irreducible spherical tensor components are therefore

$$\sigma_{00}^S = -\frac{\mu_B g_e S(S+1)}{3\hbar\gamma_I kT} A_{00}, \quad (3.71)$$

$$\sigma_{20}^S = -\frac{\mu_B g_e S(S+1)}{3\hbar\gamma_I kT} A_{20}. \quad (3.72)$$

The orientation dependence of the rank-two part of σ is exactly the same as the orientation dependence of the rank-two part of \mathbf{A} , and both share the same PAF.

The isotropic part of the paramagnetic shielding tensor σ_{iso}^S is

$$\sigma_{\text{iso}}^S = -\sqrt{\frac{1}{3}} \sigma_{00}^S \quad (3.73)$$

$$= -\frac{\mu_B g_e S(S+1)}{3\hbar\gamma_I kT} \left(-\sqrt{\frac{1}{3}} A_{00} \right) \quad (3.74)$$

$$= -\frac{\mu_B g_e S(S+1)}{3\hbar\gamma_I kT} A^{\text{FC}}. \quad (3.75)$$

We see that the Fermi-contact interaction gives a paramagnetic shielding that is entirely isotropic. Substituting in the expression in Equation 2.171 we obtain

$$\sigma_{\text{iso}}^S = -\frac{\mu_0 \mu_B^2 g_e^2 (S+1)}{9kT} \rho^{\alpha-\beta}(\mathbf{0}). \quad (3.76)$$

By contrast we expect the spin-dipolar contribution to the paramagnetic shielding to be wholly anisotropic and symmetric, and therefore contribute only to the anisotropy and asymmetry of the interaction. If we compare the spherical components of the rank-two part of the shielding and hyperfine tensors in their common PAF:

$$\tilde{\sigma}_{20}^S = \sqrt{\frac{3}{2}}\Delta\sigma^S, \quad \tilde{A}_{20} = \sqrt{\frac{3}{2}}(\tilde{A}_{zz} - A^{\text{FC}}) = \sqrt{\frac{3}{2}}\frac{\mu_0\mu_B g_e \hbar \gamma_I}{8\pi S} \int \frac{3z_{\text{PAF}}^2 - r_{\text{PAF}}^2}{r_{\text{PAF}}^5} \rho^{\alpha-\beta}(\mathbf{r}_{\text{PAF}}) d^3 r_{\text{PAF}}, \quad (3.77)$$

$$\tilde{\sigma}_{2\pm 1}^S = 0, \quad \tilde{A}_{2\pm 1} = 0, \quad (3.78)$$

$$\tilde{\sigma}_{2\pm 2}^S = -\frac{1}{2}\eta^S \Delta\sigma^S, \quad \tilde{A}_{2\pm 2} = -\frac{1}{2}\eta^{\text{SD}}(\tilde{A}_{zz} - A^{\text{FC}}), \quad (3.79)$$

we can deduce that the shielding anisotropy $\Delta\sigma^S$ and asymmetry parameter η^S are:

$$\Delta\sigma^S = -\frac{\mu_0\mu_B^2 g_e^2 (S+1)}{24\pi kT} \int \frac{3z_{\text{PAF}}^2 - r_{\text{PAF}}^2}{r_{\text{PAF}}^5} \rho^{\alpha-\beta}(\mathbf{r}_{\text{PAF}}) d^3 r_{\text{PAF}}, \quad (3.80)$$

$$\eta^S = \eta^{\text{SD}}. \quad (3.81)$$

In terms of the shift convention, these expressions become

$$\delta_{\text{iso}}^S = \frac{\mu_0\mu_B^2 g_e^2 (S+1)}{9kT} \rho^{\alpha-\beta}(\mathbf{0}), \quad (3.82)$$

$$\Delta\delta^S = \frac{\mu_0\mu_B^2 g_e^2 (S+1)}{24\pi kT} \int \frac{3z_{\text{PAF}}^2 - r_{\text{PAF}}^2}{r_{\text{PAF}}^5} \rho^{\alpha-\beta}(\mathbf{r}_{\text{PAF}}) d^3 r_{\text{PAF}}, \quad (3.83)$$

$$\eta^S = \eta^{\text{SD}}. \quad (3.84)$$

The interaction of a nucleus with a single paramagnetic centre therefore results in an isotropic paramagnetic shift δ_{iso}^S due to the Fermi-contact interaction, usually referred to as the Fermi-contact shift and first described by McConnell and Chesnut [35], and a shielding anisotropy $\Delta\delta^S$ due to the spin-dipolar interaction, and hence referred to as the dipolar shift anisotropy.

Finally we note that if we set $S = 1/2$ in Equation 3.82 we obtain the same value for the isotropic shift in Equation 3.46 that we derived by averaging the position of the two components of the doublet in the NMR spectrum.

3.3 The magnetic susceptibility

As discussed in the previous section, the effect of applying a magnetic field to an electronic spin system is to lift the degeneracy of the manifold of states, giving the net magnetic moment in Equation 3.64 that is parallel to the direction of the applied field, and whose magnitude is proportional to the Curie spin. To complement the quantum mechanical treatment we have already seen, we can also determine the average effect of the magnetic field on the *bulk* material via the magnetic susceptibility χ , which is of interest as this property can be measured independently. Following the description by Bertini et al. [16], we describe the susceptibility and relate it to the paramagnetic shift tensor.

3.3.1 Magnetism of the bulk

The application of an external magnetic field H_0 to an ensemble of spins induces a bulk magnetization M (the total induced magnetic moment μ_{ind} per unit volume V), which is proportional to H_0 , as seen from Equation 2.10:

$$M = \chi_V H_0, \quad (3.85)$$

where the dimensionless constant of proportionality χ_V is the magnetic susceptibility per unit volume. As seen in section 2.2 we can, for a linear and paramagnetic material, relate the magnetic field H_0 to the induction B_0 via the expression

$$B_0 \approx \mu_0 H_0, \quad (3.86)$$

and so the magnetisation is given by [187]:

$$M = \frac{1}{\mu_0} \chi_V B_0. \quad (3.87)$$

In addition to χ_V there are other definitions of the susceptibility. For example the molar susceptibility χ_M (units $\text{m}^3 \text{mol}^{-1}$) relates the size of the induced magnetic moment per mole to the external field. The molar susceptibility is given by $\chi_M = V_M \chi_V$, where V_M is the volume that contains one mole of the paramagnetic system, and so

$$M V_M = \mu_{\text{ind}} \frac{V_M}{V} = \frac{1}{\mu_0} \chi_M B_0, \quad (3.88)$$

where we identify $\mu_{\text{ind}}V_M/V$ as the total induced magnetic moment per mole. For a large ensemble of spins, we can write this quantity as $\langle\mu\rangle N_A$, where $\langle\mu\rangle$ is the ensemble average of the induced magnetic moment, and N_A is Avogadro's number. This leads us to another definition of the susceptibility, which is the magnetic susceptibility per molecule $\chi = \chi_M/N_A$ (units m^3), which relates $\langle\mu\rangle$ to the external field as follows:

$$\langle\mu\rangle = \frac{1}{\mu_0} \chi B_0. \quad (3.89)$$

Throughout the rest of this review this definition is the one we utilise, and we refer to χ simply as the “magnetic susceptibility”. In a solid paramagnetic material containing a single species of metal ion, and in which there are no clear molecular units, χ is more properly identified as the magnetic susceptibility per metal ion.

Equation 3.89 gives the average magnetic moment per molecule induced by a magnetic field B_0 , which is in turn a result of the Zeeman interaction of the individual magnetic moments of the spins i , $\mu^{(i)} = -\mu_B g_e S_z^{(i)}$, where $S_z^{(i)}$ is the z -component of the spin i . We are therefore able to draw a parallel between the bulk susceptibility χ and the g -factor g_e , and identify the former as a ‘bulk representation’ of the latter. This correspondence will be presented more formally in the following section.

3.3.2 The susceptibility in terms of the molecular/atomic-level parameters

We can immediately relate the average induced magnetic moment $\langle\mu\rangle$ in Equation 3.89 to the expectation value of $\hat{\mu}_z$. We have already calculated this in the high-temperature limit, with the result shown in Equation 3.64, and reproduced below:

$$\langle\hat{\mu}_z\rangle = \frac{\mu_B^2 g_e^2 S(S+1)B_0}{3kT}. \quad (3.90)$$

Comparing this with Equation 3.89 gives us the expression for the magnetic susceptibility [16]:

$$\chi = \frac{\mu_0}{B_0} \langle\hat{\mu}_z\rangle \quad (3.91)$$

$$= \frac{\mu_0 \mu_B^2 g_e^2 S(S+1)}{3kT}. \quad (3.92)$$

The susceptibility has a Curie temperature dependence, and is proportional to the square of the magnitude of the electronic magnetic moment μ_{eff} .

3.3.3 Relating the paramagnetic shift to the magnetic susceptibility

We now derive the expression for the paramagnetic shift tensor in terms of the magnetic susceptibility. As before we begin with the Hamiltonian describing the hyperfine interaction, this time using the form in Equation 2.166 which is in terms of the electronic and nuclear magnetic moments. However, as before, we must remember that the nuclear magnetic moment couples to the expectation value of the electronic magnetic moment $\langle \hat{\mu}_S \rangle$, and so we must modify Equation 2.166 accordingly to give the paramagnetic shielding Hamiltonian \hat{H} :

$$\hat{H} = -\frac{\mu_0}{8\pi S} \left[\int \frac{3(\langle \hat{\mu}_S \rangle \cdot \mathbf{r})(\hat{\mu}_I \cdot \mathbf{r}) - (\langle \hat{\mu}_S \rangle \cdot \hat{\mu}_I)r^2}{r^5} \rho^{\alpha-\beta}(\mathbf{r}) d^3r + \frac{8\pi}{3} (\langle \hat{\mu}_S \rangle \cdot \hat{\mu}_I) \rho^{\alpha-\beta}(\mathbf{0}) \right], \quad (3.93)$$

where we have assumed that the electrons are delocalised. The above Hamiltonian can easily be modified for localised electrons as described previously. The expectation value of the electronic magnetic moment in terms of the susceptibility is the operator equivalent of Equation 3.89 which, for an arbitrary direction of the external magnetic field \mathbf{B}_0 is

$$\langle \hat{\mu}_S \rangle = \frac{1}{\mu_0} \chi \mathbf{B}_0. \quad (3.94)$$

Using this expression, and the expression for the nuclear magnetic moment in terms of the nuclear spin, $\hat{\mu}_I = \hbar\gamma_I \hat{I}$, gives the following Hamiltonian:

$$\hat{H} = -\frac{\hbar\gamma_I \chi}{8\pi S} \left[\int \frac{3(\mathbf{B}_0 \cdot \mathbf{r})(\hat{I} \cdot \mathbf{r}) - (\mathbf{B}_0 \cdot \hat{I})r^2}{r^5} \rho^{\alpha-\beta}(\mathbf{r}) d^3r + \frac{8\pi}{3} (\mathbf{B}_0 \cdot \hat{I}) \rho^{\alpha-\beta}(\mathbf{0}) \right]. \quad (3.95)$$

This Hamiltonian is linear in both the magnetic field and the nuclear spin, and so can be written in terms of a chemical shielding tensor σ^χ , with isotropic and anisotropic parts σ_{iso}^χ and $\sigma_{\text{aniso}}^\chi$ as follows:

$$\hat{H} = \hbar\gamma_I \mathbf{B}_0 \cdot \sigma^\chi \cdot \hat{I}, \quad (3.96)$$

$$= \hbar\gamma_I \mathbf{B}_0 \cdot (\sigma_{\text{iso}}^\chi \mathbf{1} + \sigma_{\text{aniso}}^\chi) \cdot \hat{I}. \quad (3.97)$$

Comparing Equation 3.95 with Equation 3.97 we identify the isotropic and anisotropic parts of the shielding tensor as

$$\sigma_{\text{iso}}^{\chi} = -\frac{\chi}{3S}\rho^{\alpha-\beta}(\mathbf{0}), \quad (3.98)$$

$$\sigma_{\text{aniso},ij}^{\chi} = -\frac{\chi}{8\pi S} \int \frac{3r_i r_j - r^2 \delta_{ij}}{r^5} \rho^{\alpha-\beta}(\mathbf{r}) d^3 r, \quad (3.99)$$

where we see that the former is due to the Fermi-contact interaction, and the latter is due to the spin-dipolar interaction. We note that this expression for the paramagnetic shielding is symmetric, as is the expression in terms of the Curie spin σ^S .

We can also write the shielding tensor as the product of the susceptibility and a reduced coupling tensor C :

$$\sigma^{\chi} = -\chi C, \quad (3.100)$$

where

$$C = \frac{1}{\mu_0 \mu_B g_e \hbar \gamma_I} \mathbf{A}. \quad (3.101)$$

This tensor C is the sum of an isotropic Fermi-contact part C^{FC} and anisotropic spin-dipolar part C^{SD} ,

$$C = C^{\text{FC}} \mathbf{1} + C^{\text{SD}}, \quad (3.102)$$

where:

$$C^{\text{FC}} = \frac{\rho^{\alpha-\beta}(\mathbf{0})}{3S} \quad (3.103)$$

$$C_{ij}^{\text{SD}} = \frac{1}{8\pi S} \int \frac{3r_i r_j - r^2 \delta_{ij}}{r^5} \rho^{\alpha-\beta}(\mathbf{r}) d^3 r. \quad (3.104)$$

This way of writing down the shielding tensor emphasises that it can be separated into two factors which describe different parts of the shielding interaction. The magnetic susceptibility is a bulk quantity that describes the unpaired electrons in that it quantifies the size of the average electronic magnetic moment per unit field, or equivalently the Curie spin per unit field, that we can expect from our paramagnetic centre at a certain temperature. It is important to draw the distinction that χ represents an average over the whole

system, whereas the paramagnetic shielding tensor describes local structural and electronic effects. Therefore the susceptibility description of the shielding may not capture more local phenomena, such as we may encounter in a heterogeneous solid material. The coupling tensor describes the relationship of the nucleus of interest with respect to the paramagnetic centre, with C^{FC} giving the unpaired spin density per electron that is delocalized onto the nucleus, and C^{SD} giving the geometrical position of the nucleus with respect to the paramagnetic centre. These are molecular/atomic-level properties that depend on the geometry and bonding in the paramagnetic material. Note that neither the susceptibility nor the reduced coupling tensor depends on the nuclear species, as is usual for shielding tensors, which are independent of γ_I .

Using this description we can write down the irreducible spherical tensor components of the paramagnetic shielding σ_{lm}^{χ} in terms of the corresponding components of the reduced hyperfine coupling tensor C_{lm} :

$$\sigma_{lm}^{\chi} = -\chi C_{lm}. \quad (3.105)$$

In the high-field regime, only the components σ_{00}^{χ} and σ_{20}^{χ} are retained. The isotropic part is proportional to C_{00} , which is given by:

$$C_{00} = -\frac{\rho^{\alpha-\beta}(\mathbf{0})}{\sqrt{3}S}. \quad (3.106)$$

The isotropic shielding $\sigma_{\text{iso}}^{\chi}$ is:

$$\sigma_{\text{iso}}^{\chi} = -\chi C^{\text{FC}} \quad (3.107)$$

$$= -\chi \frac{\rho^{\alpha-\beta}(\mathbf{0})}{3S} \quad (3.108)$$

$$= -\frac{\mu_0 \mu_{\text{B}}^2 g_e^2 (S+1)}{9kT} \rho^{\alpha-\beta}(\mathbf{0}), \quad (3.109)$$

which is exactly the same as the expression derived in Equation 3.76. The anisotropy parameters can be determined from σ_{20}^{χ} , which is proportional to C_{20} . In the PAF of the reduced coupling tensor, the spherical

components \tilde{C}_{2m} are

$$\tilde{C}_{20} = \sqrt{\frac{3}{2}} (\tilde{C}_{zz} - C_{\text{iso}}) \quad (3.110)$$

$$= \sqrt{\frac{3}{2}} \frac{1}{8\pi S} \int \frac{3z_{\text{PAF}}^2 - r_{\text{PAF}}^2}{r_{\text{PAF}}^5} \rho^{\alpha-\beta}(\mathbf{r}_{\text{PAF}}) d^3 r_{\text{PAF}}, \quad (3.111)$$

$$\tilde{C}_{2\pm 1} = 0, \quad (3.112)$$

$$\tilde{C}_{2\pm 2} = \frac{1}{2} (\tilde{C}_{xx} - \tilde{C}_{yy}) \quad (3.113)$$

$$= -\frac{1}{2} \eta^{\text{SD}} (\tilde{C}_{zz} - C_{\text{iso}}). \quad (3.114)$$

If the electrons are localised at the paramagnetic centre, we can write the unpaired electron density as $\rho^{\alpha-\beta}(\mathbf{r}) = 2S\delta(\mathbf{r} - \mathbf{R})$, where \mathbf{R} is the position of the electrons relative to the nucleus. The Cartesian components of the reduced hyperfine coupling tensor are then

$$C_{ij} = \frac{1}{4\pi} \left[\frac{3R_i R_j - R^2 \delta_{ij}}{R^5} + \frac{8\pi}{3} \delta(\mathbf{R}) \delta_{ij} \right], \quad (3.115)$$

and the spherical-tensor components in the PAF become

$$C_{00} = -\frac{2\delta(\mathbf{R})}{\sqrt{3}}, \quad (3.116)$$

$$\tilde{C}_{20} = \sqrt{\frac{3}{2}} \frac{1}{2\pi R^3}, \quad (3.117)$$

$$\tilde{C}_{2\pm 1} = 0, \quad (3.118)$$

$$\tilde{C}_{2\pm 2} = 0. \quad (3.119)$$

In the general case the spherical components of the shielding tensor are:

$$\tilde{\sigma}_{20}^{\chi} = -\sqrt{\frac{3}{2}} \frac{\chi}{8\pi S} \int \frac{3z_{\text{PAF}}^2 - r_{\text{PAF}}^2}{r_{\text{PAF}}^5} \rho^{\alpha-\beta}(\mathbf{r}_{\text{PAF}}) d^3 r_{\text{PAF}}, \quad (3.120)$$

$$\tilde{\sigma}_{2\pm 1}^{\chi} = 0, \quad (3.121)$$

$$\tilde{\sigma}_{2\pm 2}^{\chi} = \frac{\eta^{\text{SD}} \chi}{16\pi S} \int \frac{3z_{\text{PAF}}^2 - r_{\text{PAF}}^2}{r_{\text{PAF}}^5} \rho^{\alpha-\beta}(\mathbf{r}_{\text{PAF}}) d^3 r_{\text{PAF}}, \quad (3.122)$$

and hence the following shielding anisotropy $\Delta\sigma^\chi$ and asymmetry parameter η^χ have the forms:

$$\Delta\sigma^\chi = \sqrt{\frac{2}{3}}\sigma_{20}^\chi \quad (3.123)$$

$$= -\frac{\chi}{8\pi S} \int \frac{3z_{\text{PAF}}^2 - r_{\text{PAF}}^2}{r_{\text{PAF}}^5} \rho^{\alpha-\beta}(\mathbf{r}_{\text{PAF}}) d^3 r_{\text{PAF}} \quad (3.124)$$

$$= -\frac{\mu_0 \mu_{\text{B}}^2 g_e^2 (S+1)}{24\pi kT} \int \frac{3z_{\text{PAF}}^2 - r_{\text{PAF}}^2}{r_{\text{PAF}}^5} \rho^{\alpha-\beta}(\mathbf{r}_{\text{PAF}}) d^3 r_{\text{PAF}}, \quad (3.125)$$

$$\eta^\chi = \eta^{\text{SD}}. \quad (3.126)$$

We see that these are exactly the same expressions in Equations 3.80 and 3.81 that we derived using the Curie spin, thus demonstrating the equivalence of the two approaches.

Finally in terms of the chemical shift convention, the isotropic paramagnetic shift δ_{iso}^χ , paramagnetic SA $\Delta\delta^\chi$, and asymmetry parameter η^χ are

$$\delta_{\text{iso}}^\chi = \chi \frac{\rho^{\alpha-\beta}(\mathbf{0})}{3S} \quad (3.127)$$

$$= \frac{\mu_0 \mu_{\text{B}}^2 g_e^2 (S+1)}{9kT} \rho^{\alpha-\beta}(\mathbf{0}), \quad (3.128)$$

$$\Delta\delta^\chi = \frac{\chi}{8\pi S} \int \frac{3z_{\text{PAF}}^2 - r_{\text{PAF}}^2}{r_{\text{PAF}}^5} \rho^{\alpha-\beta}(\mathbf{r}_{\text{PAF}}) d^3 r_{\text{PAF}} \quad (3.129)$$

$$= \frac{\mu_0 \mu_{\text{B}}^2 g_e^2 (S+1)}{24\pi kT} \int \frac{3z_{\text{PAF}}^2 - r_{\text{PAF}}^2}{r_{\text{PAF}}^5} \rho^{\alpha-\beta}(\mathbf{r}_{\text{PAF}}) d^3 r_{\text{PAF}}, \quad (3.130)$$

$$\eta^\chi = \eta^{\text{SD}}. \quad (3.131)$$

3.4 The scaling factor

In the previous sections we commented that the paramagnetic shielding tensor, which has the form shown in Equation 3.70, is essentially proportional to the hyperfine tensor, with the proportionality constant equal to a factor that scales down the size of the interaction. So far we have avoided giving a precise description of the exact quantity that is scaled down, and what the scaling factor represents. A full discussion will be presented in this section, following the description of Kim et al [53], who use the idea of scaling the hyperfine interaction calculated from first principles to determine a paramagnetic shift.

The calculation is performed on a system in which all the effective electron spins are aligned parallel in a ferromagnetic configuration. Note that the ferromagnetic alignment is not necessarily the lowest-energy configuration, but reflects the system in the saturation regime at a temperature of 0 K that we have discussed previously. It turns out that this arrangement is convenient for performing the calculation. So far, we have not included any interactions between the paramagnetic centres, which we still assume to be independent of each other, and so there is no energetic driving force for preferential alignment of the electronic spins. The calculation provides the *total* unpaired-spin density $\rho^{\alpha-\beta}(\mathbf{r})$, whence is determined the total hyperfine tensor \mathcal{A} , which is the sum of Fermi-contact $\mathcal{A}^{\text{FC}}\mathbf{1}$ and spin-dipolar \mathcal{A}^{SD} parts as before. The hyperfine Hamiltonian takes the usual form:

$$\hat{H}_{SI} = \hat{\mathbf{S}} \cdot \mathcal{A} \cdot \hat{\mathbf{I}}, \quad (3.132)$$

in which the calculated Fermi-contact and spin-dipolar contributions are

$$\mathcal{A}^{\text{FC}} = \frac{2}{3}\mu_0\mu_B g_e \hbar \gamma_I \rho^{\alpha-\beta}(\mathbf{0}), \quad (3.133)$$

$$\mathcal{A}_{ij}^{\text{SD}} = \frac{\mu_0\mu_B g_e \hbar \gamma_I}{4\pi} \int \frac{3r_i r_j - r^2 \delta_{ij}}{r^5} \rho^{\alpha-\beta}(\mathbf{r}) d^3r. \quad (3.134)$$

We note that this definition of the hyperfine tensor, involving the full unpaired electron spin density, has *not* been normalised by dividing by the number of electrons. The spin-dipolar tensor is usually written in a form in which the total electronic wavefunction $|\psi(\mathbf{r})\rangle$ of the unpaired electrons is expressed as a superposition of basis functions, for example molecular orbitals, $|\epsilon\rangle$, as follows

$$|\psi(\mathbf{r})\rangle = \sum_{\epsilon} (c_{\epsilon}^{\alpha} |\epsilon\rangle + c_{\epsilon}^{\beta} |\epsilon\rangle), \quad (3.135)$$

where the c_{ϵ}^{α} and c_{ϵ}^{β} are coefficients relating to electrons of α and β spin in molecular orbital $|\epsilon\rangle$. The expansion can, in principle, include contributions from several unit cells. The resulting tensors are

$$\mathcal{A}^{\text{FC}} = \frac{2}{3}\mu_0\mu_B g_e \hbar \gamma_I \sum_{\epsilon\tau} P_{\epsilon\tau}^{\alpha-\beta} \langle \epsilon | \delta(\mathbf{r}) | \tau \rangle, \quad (3.136)$$

$$\mathcal{A}_{ij}^{\text{SD}} = \frac{\mu_0\mu_B g_e \hbar \gamma_I}{4\pi} \sum_{\epsilon\tau} P_{\epsilon\tau}^{\alpha-\beta} \left\langle \epsilon \left| \frac{3r_i r_j - r^2 \delta_{ij}}{r^5} \right| \tau \right\rangle, \quad (3.137)$$

where $P_{\epsilon\tau}^{\alpha-\beta} = \overline{c_\epsilon^\alpha} c_\tau^\alpha - \overline{c_\epsilon^\beta} c_\tau^\beta$ is the spin density matrix, and the overbar represents the complex conjugate.

The size of the hyperfine splitting expressed as a chemical shielding is proportional to the hyperfine coupling constant divided by the nuclear Zeeman energy:

$$-\frac{\mathcal{A}}{2\hbar\gamma_I B_0}, \quad (3.138)$$

where the factor of 1/2 is included because, in the high-field regime, the hyperfine interaction splits the nuclear resonance into two peaks which appear at frequencies located at $\pm\mathcal{A}_{zz}/2$ either side of the nuclear Larmor frequency. This chemical shielding is the value that would be observed when all the effective electron spins are aligned, which occurs at saturation. The expectation value of \hat{S}_z is, under these circumstances, given by Equation 3.65

$$\langle \hat{S}_z \rangle_{\text{sat}} = -S. \quad (3.139)$$

Experimentally we observe the system in the weaker paramagnetic regime, in which $\langle \hat{S}_z \rangle$ has been scaled down by the Brillouin function. Therefore in order to obtain the shielding tensor of the paramagnetic system, we must scale the expression in Equation 3.138 by

$$\frac{\langle \hat{S}_z \rangle_{\text{para}}}{\langle \hat{S}_z \rangle_{\text{sat}}} = B_S \left(\frac{\mu_B g_e B_0 S}{kT} \right) \quad (3.140)$$

$$\approx \frac{\mu_B g_e (S+1) B_0}{3kT}. \quad (3.141)$$

In terms of the susceptibility the scaling factor is

$$\frac{\langle \hat{S}_z \rangle_{\text{para}}}{\langle \hat{S}_z \rangle_{\text{sat}}} = \frac{\chi B_0}{\mu_0 \mu_B g_e S}. \quad (3.142)$$

The paramagnetic shielding tensor thus obtained is

$$\sigma^S = -\frac{\mathcal{A}}{2\hbar\gamma_I B_0} \frac{\langle \hat{S}_z \rangle_{\text{para}}}{\langle \hat{S}_z \rangle_{\text{sat}}} \quad (3.143)$$

$$= -\frac{\chi}{\mu_0 \mu_B g_e \hbar \gamma_I} \frac{\mathcal{A}}{2S} \quad (3.144)$$

$$= -\frac{\mu_B g_e S(S+1)}{3\hbar\gamma_I kT} \frac{\mathcal{A}}{2S}, \quad (3.145)$$

which, when we note that $A = \mathcal{A}/(2S)$, is the same expression as the one obtained in Equation 3.70.

3.5 Key concepts

- In a system of two coupled spin-1/2 nuclei I and S , the I -spin NMR spectrum contains a resonance that is centred on the I -spin Larmor frequency, and split into two peaks separated by the coupling constant.
- In a system of a nuclear spin-1/2 I coupled to an electron S , the NMR spectrum contains a single peak offset from the I -spin Larmor frequency by the “paramagnetic shift”.
- The paramagnetic shift is the result of the electron relaxation between its Zeeman spin states occurring on a timescale that is orders of magnitude faster than the corresponding nuclear dynamics.
- The paramagnetic shift can be calculated from the hyperfine coupling between the nucleus and the electronic pseudo-spin with a thermally averaged magnetic moment (the Curie spin).
- The Curie spin, and therefore the paramagnetic shift, both have a Curie temperature dependence of $1/(kT)$.
- We can also calculate the paramagnetic shift from the bulk magnetic susceptibility.
- The role of the magnetic susceptibility in determining the paramagnetic shift is to scale down the hyperfine coupling constant between the nuclear and electronic spins, from the saturation regime to the high-temperature paramagnetic regime.

Chapter 4

The paramagnetic shift due to *d*-block transition-metals with spin-orbit coupling

The EPR parameters in many *d*-block transition-metal systems are strongly influenced by the effects of spin-orbit (SO) coupling. In turn these changes to the EPR properties strongly influence the form of the paramagnetic shift and SA. The formalism presented in the previous chapter ignored the effects of SO coupling, and so is only valid when the metal ion behaves strictly as a spin-only ion. Whilst this formalism could be applied successfully to more complex systems where the paramagnetic shifts are dominated by non-SO effects, such as the Fermi-contact interaction [53], it is often inadequate for describing the shift when such non-SO effects are small [15]. Kurland and McGarvey were the first to derive a general equation for the isotropic shift that includes these additional effects, but this did not describe the effects leading to the SA [37]. More recently Moon and Patchkovskii proposed a formula for the entire shift tensor due to a paramagnetic centre with spin $S = 1/2$ in terms of the EPR parameters; this remains the benchmark for all theoretical work that has been proposed since [38]. Following this milestone Pennanen and Vaara extended the theory to describe the paramagnetic shifts at high temperature of first-row (*3d*) transition-metal ions with spin $S > 1/2$, which are subject to a SO coupling that is smaller than the ligand-field interaction [39]. More recently van

den Heuvel and Soncini proposed a different formalism which extends the theory to low temperatures, and larger SO coupling interactions [86, 88]. This generalised treatment gives the paramagnetic shift in terms of the effective spin EPR parameters for electronic spins greater than $S = 1/2$.

We begin this chapter by deriving the form of the EPR effective spin Hamiltonian, the parameters in which are used to calculate the paramagnetic shift. The discussion here will be limited to d -transition-metal ions with spin-orbit coupling that is weak compared to the ligand-field interaction, and which is described by the Russell–Saunders (LS) coupling scheme. We then outline an EPR theory of the paramagnetic shielding tensor and highlight the new features that are introduced as a result of SO coupling. Finally we show that the magnetic susceptibility of such systems becomes anisotropic [16], and we show how this tensor can be related to the paramagnetic shielding tensor.

4.1 The EPR effective spin Hamiltonian

4.1.1 Derivation

For a spin-only d -block transition-metal ion we have seen that the electronic magnetic moment is proportional to the effective spin, i.e. $\hat{\mu}_S = -\mu_B g_e \hat{S}$. Transition-metal ions with non-zero orbital angular momentum L , on the other hand, have an orbital contribution to the magnetic moment $\hat{\mu}_L = -\mu_B \hat{L}$, where \hat{L} is the operator representing the total orbital angular momentum, that is orientation-dependent. In the limit of LS coupling we can define the total angular momentum operator \hat{J} as the sum of \hat{L} and \hat{S} , i.e. $\hat{J} = \hat{L} + \hat{S}$, and the total magnetic moment operator \hat{m} as

$$\hat{m} = -\mu_B (\hat{L} + g_e \hat{S}). \quad (4.1)$$

We note that the vectors representing the total angular momentum and total magnetic moment, shown in Figure 4.1 (a) and (b) respectively, are not parallel because g_e is not equal to unity. The orbital angular momentum is quantized and represented by the quantum number L which takes integer values. Each level L comprises a manifold of $2L + 1$ states that are labelled by the orbital magnetic quantum number M_L which takes integer values from $-L$ to $+L$.

The Hamiltonian \hat{H} describing the electronic spin system of a d -block transition-metal ion in a ligand

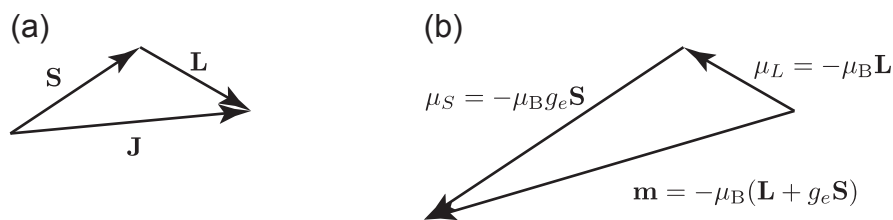


Figure 4.1: The angular momentum properties of a metal ion subject to Russell–Saunders spin-orbit coupling. The total angular momentum \mathbf{J} , which is the vector sum of the spin \mathbf{S} and orbital angular momentum \mathbf{L} , is shown in (a). The total magnetic moment \mathbf{m} , which is the sum of the spin and orbital magnetic moments μ_S and μ_L is shown in (b). We note that \mathbf{m} is not parallel to \mathbf{J} .

field is given by

$$\hat{H} = \hat{H}_{\text{LF}} + \hat{H}_1, \quad (4.2)$$

where \hat{H}_{LF} is the interaction of the ion with the ligand field, and \hat{H}_1 encompasses the other interactions. The ligand-field interaction is the largest contribution to \hat{H} , giving rise to a splitting in the energy levels of the order of 10^4 cm^{-1} . The smaller contribution \hat{H}_1 can be broken down into a sum of the following terms:

$$\hat{H}_1 = \hat{H}_{\text{SO}} + \hat{H}_{\text{SS}} + \hat{H}_{\text{HF}} + \hat{H}_{\text{Z}}. \quad (4.3)$$

The first term \hat{H}_{SO} is the Hamiltonian representing the SO coupling interaction which, for LS coupling and assuming Hund's rules are obeyed, is

$$\hat{H}_{\text{SO}} = \lambda \hat{\mathbf{L}} \cdot \hat{\mathbf{S}}, \quad (4.4)$$

$$\lambda = \pm \zeta / 2S. \quad (4.5)$$

The many-electron SO coupling parameter λ is given above in terms of the single-electron SO coupling parameter ζ , where for the free ion the + sign is required for a shell that is less than half filled, and the – sign for a shell that is more than half filled. Values of ζ have been tabulated by Abragam and Bleaney [184], and take values between 10^2 and 10^3 cm^{-1} . The SO coupling is therefore the largest interaction after the ligand-field splitting. The second term \hat{H}_{SS} is the spin-spin interaction which represents the magnetic

coupling between the individual electrons. In the LS coupling regime it is given by [184]

$$\hat{H}_{SS} = -\rho \left[(\hat{\mathbf{L}} \cdot \hat{\mathbf{S}})^2 + \frac{1}{2} (\hat{\mathbf{L}} \cdot \hat{\mathbf{S}}) - \frac{1}{3} L(L+1)S(S+1)\mathbf{1} \right], \quad (4.6)$$

where ρ is an energy coefficient that, for $3d$ metal ions, takes values up to 1 cm^{-1} . We can also write the spin-spin interaction Hamiltonian as

$$\hat{H}_{SS} = -\rho \sum_{ij} \left[\frac{1}{2} (\hat{L}_i \hat{L}_j + \hat{L}_j \hat{L}_i) - \frac{1}{3} L(L+1) \delta_{ij} \right] \hat{S}_i \hat{S}_j. \quad (4.7)$$

The third term \hat{H}_{HF} is the hyperfine interaction Hamiltonian which, for spin-only systems, was derived in section 2.8. For systems with non-zero orbital angular momentum \hat{H}_{HF} can be generalised to [184]

$$\hat{H}_{\text{HF}} = \mathcal{P} \left[\{ \xi L(L+1) - \kappa \} (\hat{\mathbf{S}} \cdot \hat{\mathbf{I}}) - \frac{3}{2} \xi \{ (\hat{\mathbf{L}} \cdot \hat{\mathbf{S}})(\hat{\mathbf{L}} \cdot \hat{\mathbf{I}}) + (\hat{\mathbf{L}} \cdot \hat{\mathbf{I}})(\hat{\mathbf{L}} \cdot \hat{\mathbf{S}}) \} + \hat{\mathbf{L}} \cdot \hat{\mathbf{I}} \right], \quad (4.8)$$

$$\mathcal{P} = \frac{\mu_0 \mu_B g_e \hbar \gamma_I}{4\pi} \left\langle \frac{1}{r^3} \right\rangle, \quad (4.9)$$

$$\xi = \frac{2l+1-4S}{S(2l-1)(2l+3)(2L-1)}, \quad (4.10)$$

where \mathcal{P} is the dipolar coupling constant, ξ is a coefficient that depends on the total spin and orbital quantum numbers S and L and the one-electron orbital quantum number l , and κ is a dimensionless number that accounts for the Fermi-contact term. Finally we have the electronic Zeeman interaction \hat{H}_Z which is the sum of the orbital Zeeman $\mu_B \mathbf{B}_0 \cdot \hat{\mathbf{L}}$ and spin Zeeman $\mu_B g_e \mathbf{B}_0 \cdot \hat{\mathbf{S}}$ terms:

$$\hat{H}_Z = \mu_B \mathbf{B}_0 \cdot (\hat{\mathbf{L}} + g_e \hat{\mathbf{S}}). \quad (4.11)$$

The Zeeman splitting varies with the applied magnetic field B_0 , with $\mu_B B_0$ taking a maximum value of 13 cm^{-1} at the maximum field of 28.18 T that is currently commercially available ($\mu_B g_e B_0 = 26 \text{ cm}^{-1}$). The typical ranges of the magnitudes of the ligand-field interaction and the additional four perturbation interactions are plotted in Figure 4.2. For now we neglect the nuclear Zeeman interaction and the orbital contribution to the chemical shielding as they are both much smaller than the interactions above.

Clearly the perturbation Hamiltonian depends on both the spin- and spatially-dependent orbital angular

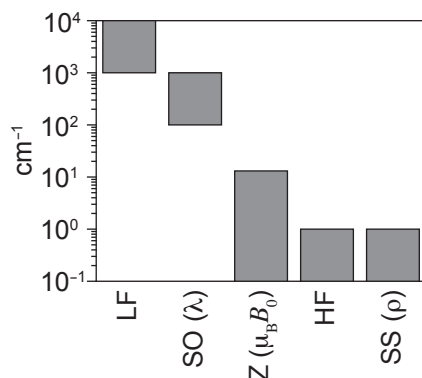


Figure 4.2: Typical ranges of the magnitudes of electronic-spin interactions that are relevant to the EPR properties of the metal ion. The largest interaction is the ligand field (LF). The four relevant perturbations are the spin-orbit (SO) coupling, electronic Zeeman (Z), hyperfine (HF), and the electronic spin-spin (SS) interactions.

momentum operators. It is our task to convert this to a Hamiltonian that contains only spin operators, and which can therefore be used in the interpretation of both EPR and paramagnetic NMR experiments. We do this by applying time-independent perturbation theory [206] to the eigenstates $|n\rangle$ of the ligand-field Hamiltonian, which have energies E_n , i.e.

$$\hat{H}_{LF}|n\rangle = E_n|n\rangle. \quad (4.12)$$

The $|n\rangle$ are orbital states, and so have no dependence on the spin.

We apply perturbation theory to the orbital ground state $|0\rangle$, which for ease of derivation we assume to be a singlet. Orbital ground states of larger degeneracy are more difficult to treat, and so we do not discuss them further. The consequence of assuming a singlet ground state is that the expectation values of the components of the orbital angular momentum operator \hat{L}_i in the ground state are zero:

$$\langle 0 | \hat{L}_i | 0 \rangle = 0. \quad (4.13)$$

The first-order perturbation Hamiltonian $\hat{H}_1^{(1)}$ is given by

$$\hat{H}_1^{(1)} = \langle 0 | \hat{H}_1 | 0 \rangle. \quad (4.14)$$

Inserting the expression for \hat{H}_1 in Equation 4.3 we obtain

$$\hat{H}_1^{(1)} = \langle 0 | \hat{H}_{SO} | 0 \rangle + \langle 0 | \hat{H}_{SS} | 0 \rangle + \langle 0 | \hat{H}_{HF} | 0 \rangle + \langle 0 | \hat{H}_Z | 0 \rangle \quad (4.15)$$

$$\begin{aligned} &= \lambda \sum_i \langle 0 | \hat{L}_i | 0 \rangle \hat{S}_i - \rho \sum_{ij} \left\langle 0 \left| \left[\frac{1}{2} (\hat{L}_i \hat{L}_j + \hat{L}_j \hat{L}_i) - \frac{1}{3} L(L+1) \delta_{ij} \right] \right| 0 \right\rangle \hat{S}_i \hat{S}_j \\ &+ \mathcal{P} \sum_{ij} \left[\langle 0 | \{ \xi L(L+1) - \kappa \} | 0 \rangle \delta_{ij} \hat{S}_i \hat{I}_j - \left\langle 0 \left| \frac{3}{2} \xi \{ \hat{L}_i \hat{L}_j + \hat{L}_j \hat{L}_i \} \right| 0 \right\rangle \hat{S}_i \hat{I}_j + \delta_{ij} \langle 0 | \hat{L}_i | 0 \rangle \hat{I}_j \right] \\ &+ \mu_B \sum_i B_{0,i} (\langle 0 | \hat{L}_i | 0 \rangle + \langle 0 | 0 \rangle g_e \hat{S}_i) \end{aligned} \quad (4.16)$$

$$= -\rho \sum_{ij} \hat{S}_i l_{ij} \hat{S}_j - \mathcal{P} \sum_{ij} \hat{S}_i (\kappa \delta_{ij} + 3\xi l_{ij}) \hat{I}_j + \mu_B g_e \sum_i B_{0,i} \hat{S}_i. \quad (4.17)$$

This is an example of an effective spin Hamiltonian, which comprises three terms. The first is referred to either as the zero-field splitting (ZFS) or the electric quadrupole interaction [207]. The latter name emphasises the fact that the Hamiltonian is formally equivalent to that of a nuclear quadrupole interaction $\hat{I} \cdot \mathbf{Q} \cdot \hat{I}$, where \mathbf{Q} is the tensor describing the orientation dependence of the quadrupolar coupling. To first order the ZFS is due to the spin-spin interaction, and has a spatial dependence given by the tensor l_{ij} whose components are given by

$$l_{ij} = \frac{1}{2} \langle 0 | \hat{L}_i \hat{L}_j + \hat{L}_j \hat{L}_i | 0 \rangle - \frac{1}{3} L(L+1) \delta_{ij}. \quad (4.18)$$

In common with the quadrupolar coupling interaction the ZFS tensor is symmetric, and is equal to zero for $S < 1$ or for an environment of perfectly cubic symmetry.

The second term is the hyperfine interaction comprising both the isotropic Fermi-contact $-\mathcal{P}\kappa$ and anisotropic spin-dipolar $-3\mathcal{P}\xi l_{ij}$ parts. The third term is the electron Zeeman interaction. The Hamiltonian in Equation 4.17 is often referred to as non-relativistic (NR) as it does not depend on the SO coupling [201]. In fact this Hamiltonian is *only* valid in the absence of SO coupling effects, for example for spin-only metal ions. When SO coupling is present we must continue the perturbation theory calculation to at least second order, remembering that as the SO interaction is the largest term in \hat{H}_1 , some of the second-order terms may be larger than the first order terms in the NR Hamiltonian.

The second-order perturbation Hamiltonian $\hat{H}_1^{(2)}$ is given by [206]

$$\hat{H}_1^{(2)} = - \sum_{n \neq 0} \frac{\langle 0 | \hat{H}_1 | n \rangle \langle n | \hat{H}_1 | 0 \rangle}{E_n - E_0} \quad (4.19)$$

$$= \langle 0 | \hat{H}_1 \hat{\Sigma} \hat{H}_1 | 0 \rangle, \quad (4.20)$$

where $\hat{\Sigma}$ is a sum of the projection operators of the excited orbital states $|n\rangle\langle n|$ where each term is weighted by the reciprocal of the difference in the energy of the state from the ground state E_0 :

$$\hat{\Sigma} = - \sum_{n \neq 0} \frac{|n\rangle\langle n|}{E_n - E_0}. \quad (4.21)$$

The expression in Equation 4.20 contains products between all the various terms in \hat{H}_1 , the largest of which is expected to be the self term involving \hat{H}_{SO} SO–SO, which is

$$\langle 0 | \hat{H}_{\text{SO}} \hat{\Sigma} \hat{H}_{\text{SO}} | 0 \rangle = \lambda^2 \sum_{ij} \langle 0 | \hat{L}_i \hat{\Sigma} \hat{L}_j | 0 \rangle \hat{S}_i \hat{S}_j \quad (4.22)$$

$$= -\lambda^2 \sum_{ij} \hat{S}_i \Lambda_{ij} \hat{S}_j. \quad (4.23)$$

where

$$\Lambda_{ij} = \sum_{n \neq 0} \frac{\langle 0 | \hat{L}_i | n \rangle \langle n | \hat{L}_j | 0 \rangle}{E_n - E_0}. \quad (4.24)$$

We see that this term varies as the square of the SO coupling energy coefficient λ^2 , and is bilinear in the components of \hat{S} , and so it contributes to the ZFS in the effective spin Hamiltonian. The spatial tensor Λ_{ij} is real and symmetric.

Whilst the SO–SO self term is the largest of the second-order contributions, we also expect there to be significant contributions from the cross terms between \hat{H}_{SO} and the other parts of \hat{H}_1 . These are the only remaining terms we consider here, and we ignore the smaller contributions such as the cross terms between the spin-spin and hyperfine interactions. The cross term between the spin-spin and SO interactions SS–SO is

given by

$$\begin{aligned} \langle 0 | \hat{H}_{\text{SO}} \hat{\Sigma} \hat{H}_{\text{SS}} + \hat{H}_{\text{SS}} \hat{\Sigma} \hat{H}_{\text{SO}} | 0 \rangle &= -\frac{1}{2} \lambda \rho \sum_{ijk} \langle 0 | \hat{L}_i \hat{\Sigma} (\hat{L}_j \hat{L}_k + \hat{L}_k \hat{L}_j) | 0 \rangle \hat{S}_i \hat{S}_j \hat{S}_k \\ &\quad - \frac{1}{2} \lambda \rho \sum_{ijk} \langle 0 | (\hat{L}_j \hat{L}_k + \hat{L}_k \hat{L}_j) \hat{\Sigma} \hat{L}_i | 0 \rangle \hat{S}_i \hat{S}_j \hat{S}_k \end{aligned} \quad (4.25)$$

$$= \lambda \rho \sum_{ij} \hat{S}_i (\Lambda'_{ij} + \Lambda'_{ji}) \hat{S}_j, \quad (4.26)$$

where the tensor Λ'_{ij} is given by

$$\Lambda'_{ij} = -\frac{i}{2} \sum_{kl} \varepsilon_{ikl} \sum_{n \neq 0} \frac{\langle 0 | \hat{L}_l | n \rangle \langle n | \hat{L}_j \hat{L}_k + \hat{L}_k \hat{L}_j | 0 \rangle}{E_n - E_0}, \quad (4.27)$$

and ε_{ijk} is the Levi–Civita tensor. Note that Λ'_{ij} is not necessarily symmetric. This term is again a contribution to the ZFS which is proportional to the product of the spin-spin and SO interaction energies, and so we expect it to be smaller than the SO–SO term. It is also spatially symmetric, even though Λ'_{ij} may not be. The cross term between the SO and hyperfine Hamiltonians SO–HF gives a contribution to the hyperfine part of the effective spin Hamiltonian:

$$\langle 0 | \hat{H}_{\text{SO}} \hat{\Sigma} \hat{H}_{\text{HF}} + \hat{H}_{\text{HF}} \hat{\Sigma} \hat{H}_{\text{SO}} | 0 \rangle = -2\lambda \mathcal{P} \sum_{ij} \hat{S}_i \Lambda_{ij} \hat{I}_j + 3\xi \lambda \mathcal{P} \sum_{ij} \hat{S}_i \Lambda'_{ij} \hat{I}_j, \quad (4.28)$$

where the first term is symmetric and the second, in general, is not. The final cross term we will consider is that between the SO and Zeeman Hamiltonians SO–Z, which gives us a contribution to the electronic Zeeman Hamiltonian:

$$\langle 0 | \hat{H}_{\text{SO}} \hat{\Sigma} \hat{H}_Z + \hat{H}_Z \hat{\Sigma} \hat{H}_{\text{SO}} | 0 \rangle = \mu_B \lambda \sum_{ij} B_{0,i} \langle 0 | \hat{L}_i \hat{\Sigma} \hat{L}_j + \hat{L}_j \hat{\Sigma} \hat{L}_i | 0 \rangle \hat{S}_j \quad (4.29)$$

$$= -2\mu_B \lambda \sum_{ij} B_{0,i} \Lambda_{ij} \hat{S}_j. \quad (4.30)$$

More specifically, this is the cross term between the SO and orbital Zeeman interactions, as the cross term with the spin Zeeman interaction is zero. We note that the tensor coupling the electronic spin to the magnetic field is now spatially anisotropic, and is proportional to $\mu_B \lambda$. All these second-order terms sum to give us an SO, or relativistic, contribution to the effective spin Hamiltonian.

We collect all of the above first- and second-order contributions to give the total EPR effective spin Hamiltonian \hat{H}_{EPR} :

$$\hat{H}_{\text{EPR}} = \mu_{\text{B}} \mathbf{B}_0 \cdot \mathbf{g} \cdot \hat{\mathbf{S}} + \hat{\mathbf{S}} \cdot \mathbf{A} \cdot \hat{\mathbf{I}} + \hat{\mathbf{S}} \cdot \mathbf{D} \cdot \hat{\mathbf{S}}, \quad (4.31)$$

which comprises three terms. The first term is the electronic Zeeman interaction describing the interaction of the magnetic moment of the electrons with the external magnetic field. We see that this interaction is now spatially anisotropic, and is described by a g -tensor \mathbf{g} which is given by:

$$g_{ij} = g_e \delta_{ij} - 2\lambda \Lambda_{ij}. \quad (4.32)$$

This is the sum of the free-electron g -factor and the g -shift term $-2\lambda \Lambda_{ij}$ which arises because of SO coupling. This g -shift plays the role of a “chemical shielding” for the electron as it modifies the reference resonance frequency that is due to g_e , in the same way that the chemical shielding of the nucleus gives a deviation of the nuclear resonance frequency from the Larmor frequency. We note that the g -shift contribution above is symmetric. However we must bear in mind that this is not a general feature and that, on including other cross terms and higher-order perturbations, the g -tensor is not necessarily symmetric [208, 209]. We can see that, from this form of the Zeeman interaction, we can write down an expression for the electronic magnetic moment $\hat{\mathbf{m}}$ in terms of the g -tensor:

$$\hat{\mathbf{m}} = -\mu_{\text{B}} \mathbf{g} \cdot \hat{\mathbf{S}}. \quad (4.33)$$

This expression is apparently different to that in Equation 4.1 which contains both the orbital and electronic contributions to $\hat{\mathbf{m}}$. The difference can be understood by noting that the expression in Equation 4.1 contains $\hat{\mathbf{L}}$, thus giving the magnetic moment an intrinsic spatial dependence. On calculating the effective spin Hamiltonian we remove the explicit dependence on $\hat{\mathbf{L}}$ and, by definition, retain only the spin operators. However the spatial dependence is retained and is encoded in the g -tensor anisotropy, the leading contribution to which is the cross term between the SO coupling and orbital Zeeman interaction Hamiltonians. As we will see, this definition of the electronic magnetic moment operator corresponds to that used by van den Heuvel and Soncini in their description of the EPR formalism of the paramagnetic shielding tensor [86, 88].

The second term is the hyperfine interaction from which we can write down a hyperfine coupling tensor

\mathbf{A} as follows:

$$A_{ij} = -\mathcal{P}(\kappa\delta_{ij} + 3\xi l_{ij} + 2\lambda\Lambda_{ij} - 3\xi\lambda\Lambda'_{ij}). \quad (4.34)$$

The first two terms of \mathbf{A} are due to the NR Fermi-contact and spin-dipolar interactions, and the second two terms are due to SO coupling. Both of the SO terms contribute to the anisotropy of \mathbf{A} , which is now not necessarily symmetric due to the presence of the last term which is proportional to Λ'_{ij} . The final interaction is the ZFS, which is mediated by a tensor \mathbf{D} , the Cartesian components of which are given by

$$D_{ij} = -\lambda^2\Lambda_{ij} - \rho l_{ij} + \lambda\rho(\Lambda'_{ij} + \Lambda'_{ji}). \quad (4.35)$$

This interaction is only non-zero for effective spins $S > 1/2$, in complete analogy with the nuclear quadrupole interaction which is only non-zero for $I > 1/2$. The first term $-\lambda^2\Lambda_{ij}$ is dominant for $3d$ metal ions due to the relative sizes of the SO and spin-spin splitting parameters λ and ρ . The ZFS tensor \mathbf{D} is always symmetric due to the symmetric form of the ZFS Hamiltonian. We also note that, whilst \mathbf{D} is not necessarily traceless, we can ignore the isotropic contribution as it shifts all the spin energy levels by the same amount in the same direction, and so does not affect the frequencies of the transitions between these levels. Henceforth we refer to the ZFS as a traceless and symmetric interaction.

4.1.2 The NMR and EPR tensors

If we now include the nuclear Zeeman and chemical shielding interactions the EPR Hamiltonian becomes

$$\hat{H}_{\text{EPR}} = -\hbar\gamma_I\mathbf{B}_0 \cdot (\mathbf{1} - \boldsymbol{\sigma}^{\text{orb}}) \cdot \hat{\mathbf{I}} + \mu_B\mathbf{B}_0 \cdot \mathbf{g} \cdot \hat{\mathbf{S}} + \hat{\mathbf{S}} \cdot \mathbf{A} \cdot \hat{\mathbf{I}} + \hat{\mathbf{S}} \cdot \mathbf{D} \cdot \hat{\mathbf{S}}. \quad (4.36)$$

As we have already discussed in section 2.6.1 it is common practice in NMR to employ high-field conditions, in which we retain only those terms in the Hamiltonian that commute with the unmodified Zeeman interaction, which in this case is $\hbar\omega_0\hat{I}_z + \mu_B g_e B_0 \hat{S}_z$. Such an approximation is only valid if the Zeeman interaction is several orders of magnitude larger than the other interactions. However this is not the case for \hat{H}_{EPR} as the dominant interaction may be the ZFS, and so the high-field approximation does not apply.

We can expand the EPR tensors as Taylor series in the fine structure constant α which takes the value

1/137.036 [201]. For instance the g -tensor can be written as the sum of the NR and SO terms

$$\mathbf{g} = \mathbf{g}_{\text{NR}} + \mathbf{g}_{\text{SO}}, \quad (4.37)$$

where the NR term \mathbf{g}_{NR} is of order $O(\alpha^0)$ and the SO term \mathbf{g}_{SO} is $O(\alpha^2)$. These two terms can further be written as [209]

$$\mathbf{g}_{\text{NR}} = g_e \mathbf{1}, \quad O(\alpha^0), \quad (4.38)$$

$$\mathbf{g}_{\text{SO}} = \Delta g_{\text{iso}} \mathbf{1} + \Delta \mathbf{g}, \quad O(\alpha^2). \quad (4.39)$$

Thus, as indicated by the previous perturbation theory calculation, the NR contribution is simply the isotropic free-electron g -factor, and the SO contribution can be separated into an isotropic part Δg_{iso} and a traceless anisotropic part $\Delta \mathbf{g}$ that is not necessarily symmetric.

In the same way we can expand the hyperfine coupling constant as a Taylor series in α [210]:

$$\mathbf{A} = \mathbf{A}_{\text{NR}} + \mathbf{A}_{\text{SO}}, \quad (4.40)$$

$$\mathbf{A}_{\text{NR}} = A^{\text{FC}} \mathbf{1} + \mathbf{A}^{\text{SD}}, \quad O(\alpha^2), \quad (4.41)$$

$$\mathbf{A}_{\text{SO}} = A^{\text{FC},2} \mathbf{1} + \mathbf{A}^{\text{SD},2} + \mathbf{A}^{\text{as}}, \quad O(\alpha^4). \quad (4.42)$$

The NR contribution is the sum of the isotropic Fermi-contact term and the symmetric and anisotropic spin-dipolar part that we have already encountered. The SO contribution contains an isotropic part $A^{\text{FC},2}$ that is also due to the delocalisation of unpaired electron density into the s orbital of the nucleus. It has also been referred to as a ‘pseudo-contact’ term [210], but since this leads to confusion with the established NMR term ‘pseudo-contact shift’ we will simply refer to it as a second-order Fermi-contact coupling constant. The SO hyperfine constant also comprises a symmetric and anisotropic component $\mathbf{A}^{\text{SD},2}$ which is labelled as a second-order spin-dipolar interaction, but is actually an interaction of shorter range than the NR spin-dipolar term. Nevertheless we include it with \mathbf{A}^{SD} as it is also a rank-two tensor. We note that this is similar to diamagnetic NMR where the anisotropic J -coupling is often absorbed into the larger dipolar coupling. Finally there is also an antisymmetric anisotropic contribution to the hyperfine tensor \mathbf{A}^{as} . Explicit expressions for

the SO coupling contribution to the hyperfine tensors are given in appendix B.

The ZFS tensor is given by [211]

$$\mathbf{D} = \mathbf{D}_{\text{NR}} + \mathbf{D}_{\text{SO}}, \quad (4.43)$$

where the NR part \mathbf{D}_{NR} is due to the electron spin-spin interaction, and is usually dominated by the SO term \mathbf{D}_{SO} . We recall that \mathbf{D} is symmetric and traceless, and is equal to zero either for electronic spins $S < 1$ or for transition metals in perfectly cubic environments.

We expect the NR terms of all three tensors to be the only contributions to spin-only $3d$ metal ions, with the SO terms only being observed in the presence of SO coupling. We recall that we have already encountered the NR contributions to both \mathbf{g} and \mathbf{A} in chapter 3 when we calculated the paramagnetic shift tensors in spin-only systems. That theoretical treatment ignored the NR spin-spin contribution to the ZFS, and so is only an approximation for $S > 1/2$.

We can write all the terms in the EPR Hamiltonian in terms of irreducible spherical tensor operators, according to Equation 2.67. The expressions for the spin-spin spherical tensors used in the hyperfine and ZFS interactions, and the spin-field tensor used in the electronic Zeeman interaction are given in Table 2.2. The spherical spatial tensors are given in Table 2.3, and can in turn be written in terms of the isotropic value, antisymmetric anisotropy, symmetric anisotropy, and asymmetry parameter. We return to this topic in chapter 5. For now we give the single example of the ZFS. The spatial tensor is symmetric and traceless, and so contains only rank two components. The Hamiltonian is therefore

$$\hat{\mathbf{S}} \cdot \mathbf{D} \cdot \hat{\mathbf{S}} = \sum_{m=-2}^{+2} (-1)^m D_{lm} \hat{T}_{l-m}(SS) \quad (4.44)$$

$$= \sum_{m=-2}^{+2} (-1)^m \hat{T}_{l-m}(SS) \sum_{m'=-2}^{m'} \tilde{D}_{lm'} D_{m'm}^{(2)}(\alpha_{\text{DL}}, \beta_{\text{DL}}, \gamma_{\text{DL}}), \quad (4.45)$$

where $(\alpha_{\text{DL}}, \beta_{\text{DL}}, \gamma_{\text{DL}})$ are the Euler angles that give the orientation of the ZFS PAF in the laboratory frame.

The spin operators $\hat{T}_{2m}(SS)$ are equivalent to the spin operators describing the nuclear quadrupole interaction:

$$\hat{T}_{20}(SS) = \sqrt{\frac{1}{6}} (3\hat{S}_z^2 - S(S+1)\hat{1}), \quad (4.46)$$

$$\hat{T}_{2\pm 1}(SS) = \mp \frac{1}{2} (\hat{S}_z \hat{S}_{\pm} + \hat{S}_{\pm} \hat{S}_z), \quad (4.47)$$

$$\hat{T}_{2\pm 2}(SS) = \frac{1}{2} \hat{S}_{\pm}^2. \quad (4.48)$$

The spatial irreducible spherical tensors \tilde{D}_{2m} in the PAF are given by

$$\tilde{D}_{20} = \sqrt{\frac{2}{3}}D, \quad (4.49)$$

$$\tilde{D}_{2\pm 1} = 0, \quad (4.50)$$

$$\tilde{D}_{2\pm 2} = E, \quad (4.51)$$

where D and E are the established symbols for the axial and rhombic anisotropies:

$$D = \tilde{D}_{zz} - \frac{1}{2}(\tilde{D}_{xx} + \tilde{D}_{yy}), \quad (4.52)$$

$$E = \frac{1}{2}(\tilde{D}_{xx} - \tilde{D}_{yy}). \quad (4.53)$$

Note that for the ZFS it is conventional to define the interaction in terms of D and E , rather than the anisotropy ΔD and asymmetry η .

4.2 The EPR formalism of the paramagnetic shielding

In chapter 3 we saw that the hyperfine interaction between the nucleus and unpaired electrons results in a “paramagnetic shift” of the nuclear resonance frequency, rather than a splitting, and that the shielding tensor depends on the electronic g -factor and hyperfine coupling tensor. We have a similar situation when the metal ion is subject to SO coupling, but the details of the theory are more complicated. In the following we relate the EPR tensor parameters to the paramagnetic shielding tensor.

4.2.1 General derivation of the paramagnetic shielding tensor

The description of the chemical shielding interaction in paramagnetic systems follows that of van den Heuvel and Soncini. Although the remainder of this chapter is concerned with $3d$ metal ions, it should be noted that the derivation of van den Heuvel and Soncini is more general, since there are no assumptions made about whether or not the theory is at the relativistic level, or about the SO coupling strength. Therefore the expression we derive here is one we will return to later in chapter 6 when considering more complex metal ions, such as lanthanides and actinides. There is a short review of this formalism by Autschbach, which

summarizes its theory and practice in quantum chemistry [212].

We equate the chemical shielding interaction to the terms in the effective temperature-dependent Hamiltonian that are linear in both the external magnetic field and the nuclear magnetic moment. This effective Hamiltonian is given by the single-particle Helmholtz free energy \bar{F} , to which we apply Rayleigh–Schrödinger perturbation theory to find the chemical shielding tensor, the components of which are [88]

$$\sigma_{ij} = \frac{1}{\hbar\gamma_I} \left(\frac{\partial^2 \bar{F}}{\partial B_{0,i} \partial \hat{I}_j} \right)_{\mathbf{B}_0=0, \hat{\mathbf{I}}=\hat{\mathbf{0}}} . \quad (4.54)$$

The electronic Hamiltonian $\hat{H}(\mathbf{B}_0, \hat{\mathbf{I}})$ is written as the sum of \hat{H}_0 , which describes the electrons in the absence of the external field and the nuclear magnetic moments, and a perturbative term $\hat{V}(\mathbf{B}_0, \hat{\mathbf{I}})$ which includes these latter effects:

$$\hat{H}(\mathbf{B}_0, \hat{\mathbf{I}}) = \hat{H}_0 + \hat{V}(\mathbf{B}_0, \hat{\mathbf{I}}). \quad (4.55)$$

The term \hat{H}_0 is the dominant part of the Hamiltonian and includes parts such as the Born–Oppenheimer Hamiltonian, the crystal-field interaction, and the ZFS interaction. The smaller term \hat{V} is written as the sum of three parts that are linear in either \mathbf{B}_0 , $\hat{\mathbf{I}}$, or both:

$$\hat{V} = \hat{H}_Z + \hat{H}_{\text{HF}} + \hat{H}_D, \quad (4.56)$$

$$\hat{H}_Z = -\mathbf{B}_0 \cdot \hat{\mathbf{m}}, \quad (4.57)$$

$$\hat{H}_{\text{HF}} = \hat{\mathcal{F}} \cdot \hat{\mathbf{I}}, \quad (4.58)$$

$$\hat{H}_D = \mathbf{B}_0 \cdot \mathcal{D} \cdot \hat{\mathbf{I}}. \quad (4.59)$$

The Hamiltonian \hat{H}_Z is the electronic Zeeman interaction between the electronic magnetic moment operator $\hat{\mathbf{m}} = -\mu_B(\hat{\mathbf{L}} + g_e\hat{\mathbf{S}})$ and the external field, \hat{H}_{HF} is the hyperfine interaction between the hyperfine field operator $\hat{\mathcal{F}}$ and the nuclear magnetic moment operator, and \hat{H}_D represents the diamagnetic nuclear-electron field coupling via the spatial tensor \mathcal{D} . There are additional terms of higher degree in \mathbf{B}_0 and $\hat{\mathbf{I}}$, but these do not contribute to the shielding tensor, and so are not considered here. It proves convenient to partition the Hamiltonian as follows

$$\hat{H} = \hat{H}_0 + \lambda\hat{H}_1 + \lambda^2\hat{H}_2, \quad (4.60)$$

where λ is a perturbation parameter that represents the combined order of \mathbf{B}_0 and $\hat{\mathbf{I}}$, and \hat{H}_1 and \hat{H}_2 are

$$\hat{H}_1 = \hat{H}_Z + \hat{H}_{\text{HF}}, \quad (4.61)$$

$$\hat{H}_2 = \hat{H}_{\text{D}}. \quad (4.62)$$

The Helmholtz free energy is given by Equation 2.18 as

$$\bar{F} = -\frac{1}{\beta} \ln Q, \quad (4.63)$$

where Q is the partition function. We write Q as the sum of the diagonal elements of the matrix representation of the density operator $\hat{\rho}$, that has been computed in the basis operators of the electronic spin:

$$Q = \text{Tr}_S(\hat{\rho}). \quad (4.64)$$

The notation Tr_S indicates that the sum is over the matrix elements of a *spin* operator, and not a sum of the diagonal elements of a *spatial* tensor. The equilibrium density operator is defined as

$$\hat{\rho} = \exp(-\beta\hat{H}). \quad (4.65)$$

We can expand both $\hat{\rho}$ and Q as Taylor series in λ :

$$\hat{\rho} = \hat{\rho}_0 + \lambda\hat{\rho}_1 + \lambda^2\hat{\rho}_2 + \mathcal{O}(\lambda^3), \quad (4.66)$$

$$Q = Q_0 + \lambda Q_1 + \lambda^2 Q_2 + \mathcal{O}(\lambda^3), \quad (4.67)$$

where $\hat{\rho}_0 = \exp(-\beta\hat{H}_0)$, $\hat{\rho}_n$ is the n th-order correction to $\hat{\rho}$, and $Q_n = \text{Tr}_S(\hat{\rho}_n)$ is the n th-order correction to

Q . We are now in a position to expand \bar{F} as a power series in λ :

$$\bar{F} = -\frac{1}{\beta} \ln [Q_0 + \lambda Q_1 + \lambda^2 Q_2 + \mathcal{O}(\lambda^3)] \quad (4.68)$$

$$= -\frac{1}{\beta} \ln Q_0 - \frac{1}{\beta} \ln \left[1 + \lambda \frac{Q_1}{Q_0} + \lambda^2 \frac{Q_2}{Q_0} + \mathcal{O}(\lambda^3) \right] \quad (4.69)$$

$$= \bar{F}_0 - \frac{\lambda}{\beta} \frac{Q_1}{Q_0} + \frac{\lambda^2}{\beta} \left[\frac{1}{2} \left(\frac{Q_1}{Q_0} \right)^2 - \frac{Q_2}{Q_0} \right] + \mathcal{O}(\lambda^3), \quad (4.70)$$

where $\bar{F}_0 = -\beta^{-1} \ln Q_0$ is the Helmholtz free energy in the absence of the external magnetic field and nuclear magnetic moment. The principle of time-reversal symmetry [190] states that the free energy must be time-even, and therefore an even function of the time-odd parameters \mathbf{B}_0 and $\hat{\mathbf{I}}$. Hence it must only contain even powers of λ , from which we deduce that Q_1 must be zero. The free energy is therefore

$$\bar{F} = \bar{F}_0 - \frac{\lambda^2}{\beta} \frac{Q_2}{Q_0} + \mathcal{O}(\lambda^4). \quad (4.71)$$

We now need an expression for the partition function Q_2 . We note that $\hat{\rho}$ satisfies a form of the Schrödinger equation:

$$\frac{\partial \hat{\rho}}{\partial \beta} = -\hat{H} \hat{\rho}. \quad (4.72)$$

On substituting Equations 4.60 and 4.66 for \hat{H} and $\hat{\rho}$ into the Schrödinger equation, and collecting terms of equal order in λ , we obtain the following differential equations for $\hat{\rho}_1$ and $\hat{\rho}_2$:

$$\frac{\partial \hat{\rho}_1}{\partial \beta} = -\hat{H}_0 \hat{\rho}_1 - \hat{H}_1 \hat{\rho}_0, \quad (4.73)$$

$$\frac{\partial \hat{\rho}_2}{\partial \beta} = -\hat{H}_0 \hat{\rho}_2 - \hat{H}_1 \hat{\rho}_1 - \hat{H}_2 \hat{\rho}_0. \quad (4.74)$$

The solutions to these equations can be found using standard techniques [189], which give:

$$\hat{\rho}_1 = - \int_0^\beta dw \exp((w - \beta) \hat{H}_0) \hat{H}_1 \exp(-w \hat{H}_0), \quad (4.75)$$

$$\begin{aligned} \hat{\rho}_2 = & - \int_0^\beta dw \exp((w - \beta) \hat{H}_0) \hat{H}_2 \exp(-w \hat{H}_0) \\ & + \int_0^\beta dw \int_0^w dw' \exp((w - \beta) \hat{H}_0) \hat{H}_1 \exp((w' - w) \hat{H}_0) \hat{H}_1 \exp(-w' \hat{H}_0). \end{aligned} \quad (4.76)$$

Alternatively one can substitute Equations 4.75 and 4.76 into Equations 4.73 and 4.74 to verify that the former are solutions of the latter. The partition function Q_2 is given by the trace of $\hat{\rho}_2$. Taking the trace of the first term gives

$$\begin{aligned}
\text{Tr}_S \left[- \int_0^\beta dw \exp((w - \beta) \hat{H}_0) \hat{H}_2 \exp(-w \hat{H}_0) \right] &= - \int_0^\beta dw \text{Tr}_S \left[\exp((w - \beta) \hat{H}_0) \hat{H}_2 \exp(-w \hat{H}_0) \right] \\
&= - \int_0^\beta dw \text{Tr}_S \left[\exp(-w \hat{H}_0) \exp((w - \beta) \hat{H}_0) \hat{H}_2 \right] \\
&= - \int_0^\beta dw \text{Tr}_S \left[\exp(-\beta \hat{H}_0) \hat{H}_2 \right] \\
&= -\beta \text{Tr}_S \left[\hat{\rho}_0 \hat{H}_2 \right], \tag{4.77}
\end{aligned}$$

where, to go to the third line, we have used the identity $\text{Tr}(\hat{A}\hat{B}\hat{C}) = \text{Tr}(\hat{C}\hat{A}\hat{B}) = \text{Tr}(\hat{B}\hat{C}\hat{A})$. The Boltzmann average $\langle \hat{U} \rangle_0$ of an operator \hat{U} over the energy levels of \hat{H}_0 is equal to

$$\langle \hat{U} \rangle_0 = \frac{\text{Tr}_S (\hat{\rho}_0 \hat{U})}{Q_0}, \tag{4.78}$$

and so Equation 4.77 can be written in its final form as

$$-\beta \langle \hat{H}_2 \rangle_0 Q_0, \tag{4.79}$$

i.e. this part of $\hat{\rho}_2$ is proportional to the thermal average of \hat{H}_2 over the energy levels of \hat{H}_0 .

The trace of the second term in Equation 4.76 is more complex to compute. We start by noting that

$$\begin{aligned}
&\text{Tr}_S \left[\int_0^\beta dw \int_0^w dw' \exp((w - \beta) \hat{H}_0) \hat{H}_1 \exp((w' - w) \hat{H}_0) \hat{H}_1 \exp(-w' \hat{H}_0) \right] \\
&= \int_0^\beta dw \int_0^w dw' \text{Tr}_S \left[\hat{\rho}_0 \exp((w - w') \hat{H}_0) \hat{H}_1 \exp(-(w - w') \hat{H}_0) \hat{H}_1 \right] \tag{4.80}
\end{aligned}$$

$$= \int_0^\beta du \int_0^u dv \text{Tr}_S \left[\hat{\rho}_0 \exp(v \hat{H}_0) \hat{H}_1 \exp(-v \hat{H}_0) \hat{H}_1 \right], \tag{4.81}$$

where to go to the last line we have performed a change in the dummy integration variables $u = w$ and $v = w - w'$. This integral is still rather tricky to evaluate in its present form, but fortunately it can be simplified after some straightforward algebra. Firstly we apply the change of variable $v' = v - \beta$ to the first

integral, which gives

$$\int_0^\beta du \int_{-\beta}^{u-\beta} dv' \text{Tr}_S [\hat{\rho}_0 \exp(-v' \hat{H}_0) \hat{H}_1 \exp(v' \hat{H}_0) \hat{H}_1], \quad (4.82)$$

followed by a second change of variable $v = -v'$, which yields

$$\int_0^\beta du \int_{\beta-u}^\beta dv \text{Tr}_S [\hat{\rho}_0 \exp(v \hat{H}_0) \hat{H}_1 \exp(-v \hat{H}_0) \hat{H}_1]. \quad (4.83)$$

Secondly we apply a similar change of variables to u in the second integral, namely $u' = u - \beta$ which gives

$$\int_{-\beta}^0 du' \int_{-u'}^\beta dv \text{Tr}_S [\hat{\rho}_0 \exp(v \hat{H}_0) \hat{H}_1 \exp(-v \hat{H}_0) \hat{H}_1], \quad (4.84)$$

followed by $u = -u'$ after which the double integral becomes

$$\int_0^\beta du \int_u^\beta dv \text{Tr}_S [\hat{\rho}_0 \exp(v \hat{H}_0) \hat{H}_1 \exp(-v \hat{H}_0) \hat{H}_1]. \quad (4.85)$$

The integrals in Equations 4.81 and 4.85 sum to give

$$\begin{aligned} & \int_0^\beta du \int_0^u dv \text{Tr}_S [\hat{\rho}_0 \exp(v \hat{H}_0) \hat{H}_1 \exp(-v \hat{H}_0) \hat{H}_1] + \int_0^\beta du \int_u^\beta dv \text{Tr}_S [\hat{\rho}_0 \exp(v \hat{H}_0) \hat{H}_1 \exp(-v \hat{H}_0) \hat{H}_1] \\ &= \int_0^\beta du \int_0^\beta dv \text{Tr}_S [\hat{\rho}_0 \exp(v \hat{H}_0) \hat{H}_1 \exp(-v \hat{H}_0) \hat{H}_1]. \end{aligned} \quad (4.86)$$

However the integrals on the first line are equal, and so we can finally write Equation 4.81 in a form that is more straightforward to evaluate:

$$\int_0^\beta du \int_0^u dv \text{Tr}_S [\hat{\rho}_0 \exp(v \hat{H}_0) \hat{H}_1 \exp(-v \hat{H}_0) \hat{H}_1] = \frac{1}{2} \int_0^\beta du \int_0^\beta dv \text{Tr}_S [\hat{\rho}_0 \exp(v \hat{H}_0) \hat{H}_1 \exp(-v \hat{H}_0) \hat{H}_1] \quad (4.87)$$

$$= \frac{\beta}{2} \int_0^\beta dv \text{Tr}_S [\hat{\rho}_0 \exp(v \hat{H}_0) \hat{H}_1 \exp(-v \hat{H}_0) \hat{H}_1] \quad (4.88)$$

$$= \frac{\beta}{2} \left\langle \int_0^\beta dw \exp(w \hat{H}_0) \hat{H}_1 \exp(-w \hat{H}_0) \hat{H}_1 \right\rangle_0, \quad (4.89)$$

i.e. it is proportional to the Boltzmann average of the integral of $\exp(w \hat{H}_0) \hat{H}_1 \exp(-w \hat{H}_0) \hat{H}_1$ over w . Com-

binning Equations 4.71, 4.79, and 4.89 we arrive at the final expression for the Helmholtz free energy

$$\bar{F} = \bar{F}_0 + \langle \hat{H}_2 \rangle_0 - \frac{1}{2} \left\langle \int_0^\beta dw \exp(w\hat{H}_0) \hat{H}_1 \exp(-w\hat{H}_0) \hat{H}_1 \right\rangle_0 + \dots, \quad (4.90)$$

where we have set $\lambda = 1$, as it has served its purpose as an expansion parameter and is no longer needed. Substituting in the expressions for \hat{H}_1 and \hat{H}_2 and performing the double differentiation gives us the expression for the chemical shielding:

$$\sigma_{ij} = \frac{1}{\hbar\gamma_I} \left(\frac{\partial^2 \bar{F}}{\partial B_{0,i} \partial \hat{I}_j} \right)_{B_0=0, \hat{I}=0} \quad (4.91)$$

$$\begin{aligned} &= \frac{1}{\hbar\gamma_I} \langle \mathcal{D}_{ij} \rangle_0 + \frac{1}{2\hbar\gamma_I} \left\langle \int_0^\beta dw \exp(w\hat{H}_0) \hat{m}_i \exp(-w\hat{H}_0) \hat{\mathcal{F}}_j \right\rangle_0 \\ &\quad + \frac{1}{2\hbar\gamma_I} \left\langle \int_0^\beta dw \exp(w\hat{H}_0) \hat{\mathcal{F}}_j \exp(-w\hat{H}_0) \hat{m}_i \right\rangle_0. \end{aligned} \quad (4.92)$$

The second integral can be rewritten as

$$\begin{aligned} &\frac{1}{2\hbar\gamma_I} \left\langle \int_0^\beta dw \exp(w\hat{H}_0) \hat{\mathcal{F}}_j \exp(-w\hat{H}_0) \hat{m}_i \right\rangle_0 \\ &= \frac{1}{2\hbar\gamma_I Q_0} \int_0^\beta dw \text{Tr}_S \left[\exp(-\beta\hat{H}_0) \exp(w\hat{H}_0) \hat{\mathcal{F}}_j \exp(-w\hat{H}_0) \hat{m}_i \right] \end{aligned} \quad (4.93)$$

$$= \frac{1}{2\hbar\gamma_I Q_0} \int_0^\beta dw \text{Tr}_S \left[\exp(-w\hat{H}_0) \hat{m}_i \exp(-\beta\hat{H}_0) \exp(w\hat{H}_0) \hat{\mathcal{F}}_j \right]. \quad (4.94)$$

Making a change of variable $u = \beta - w$ we obtain

$$\begin{aligned} &\frac{1}{2\hbar\gamma_I Q_0} \int_0^\beta du \text{Tr}_S \left[\exp(-\beta\hat{H}_0) \exp(u\hat{H}_0) \hat{m}_i \exp(-u\hat{H}_0) \hat{\mathcal{F}}_j \right] \\ &= \frac{1}{2\hbar\gamma_I} \left\langle \int_0^\beta du \exp(u\hat{H}_0) \hat{m}_i \exp(-u\hat{H}_0) \hat{\mathcal{F}}_j \right\rangle_0, \end{aligned} \quad (4.95)$$

which is equal to the first integral in Equation 4.92. The expression for the shielding tensor is therefore

$$\sigma_{ij} = \frac{1}{\hbar\gamma_I} \langle \mathcal{D}_{ij} \rangle_0 + \frac{1}{\hbar\gamma_I} \left\langle \int_0^\beta dw \exp(w\hat{H}_0) \hat{m}_i \exp(-w\hat{H}_0) \hat{\mathcal{F}}_j \right\rangle_0. \quad (4.96)$$

To evaluate the integral we need to write the Boltzmann averages in terms of the energy levels and states

of the Hamiltonian \hat{H}_0 . We will denote the eigenstates as $|nv\rangle$ where ν denotes the states with the same energy E_n , i.e.

$$\hat{H}_0 |nv\rangle = E_n |nv\rangle. \quad (4.97)$$

Using this we write Equation 4.96 as

$$\begin{aligned} \sigma_{ij} &= \frac{1}{\hbar\gamma_I Q_0} \sum_{nv} \exp(-\beta E_n) \langle nv | \mathcal{D}_{ij} | nv \rangle \\ &+ \frac{1}{\hbar\gamma_I Q_0} \sum_{nv, m\mu} \exp(-\beta E_n) \langle nv | \hat{m}_i | m\mu \rangle \langle m\mu | \hat{\mathcal{F}}_j | nv \rangle \int_0^\beta dw \exp(w(E_n - E_m)). \end{aligned} \quad (4.98)$$

This integral is now easy to evaluate, and we obtain as the final result for the chemical shielding tensor

$$\begin{aligned} \sigma_{ij} &= \frac{1}{\hbar\gamma_I} \left[\frac{1}{Q_0} \sum_n \exp(-\beta E_n) \sum_\nu \langle nv | \mathcal{D}_{ij} | nv \rangle \right. \\ &+ \frac{1}{Q_0} \sum_n \exp(-\beta E_n) \sum_{m \neq n} \sum_{\nu, \mu} \frac{\langle nv | \hat{m}_i | m\mu \rangle \langle m\mu | \hat{\mathcal{F}}_j | nv \rangle + \text{c.c.}}{E_m - E_n} \\ &\left. + \frac{\beta}{Q_0} \sum_n \exp(-\beta E_n) \sum_{\nu, \nu'} \langle nv | \hat{m}_i | \nu' \rangle \langle \nu' | \hat{\mathcal{F}}_j | nv \rangle \right], \end{aligned} \quad (4.99)$$

where c.c. is the complex conjugate of $\langle nv | \hat{m}_i | m\mu \rangle \langle m\mu | \hat{\mathcal{F}}_j | nv \rangle$.

This apparently complicated expression comprises three terms. The first two are the ‘diamagnetic’ σ_{ij}^{dia} and ‘paramagnetic’ $\sigma_{ij}^{\text{para}}$ contributions to the chemical shielding that Ramsey calculated for a non-degenerate, singlet ground state [191], and which van den Heuvel and Soncini generalised to an open-shell electronic configuration with thermally accessible electronic excited states [86, 88]:

$$\sigma_{ij}^{\text{dia}} = \frac{1}{\hbar\gamma_I Q_0} \sum_n \exp(-\beta E_n) \sum_\nu \langle nv | \mathcal{D}_{ij} | nv \rangle, \quad (4.100)$$

$$\sigma_{ij}^{\text{para}} = \frac{1}{\hbar\gamma_I Q_0} \sum_n \exp(-\beta E_n) \sum_{m \neq n} \sum_{\nu, \mu} \frac{\langle nv | \hat{m}_i | m\mu \rangle \langle m\mu | \hat{\mathcal{F}}_j | nv \rangle + \text{c.c.}}{E_m - E_n}. \quad (4.101)$$

We again note that Ramsey’s use of the term ‘paramagnetic’ is different to the one employed here. Pennanen and Vaara gathered the diamagnetic term and the spin-independent part of the paramagnetic term together into the ‘orbital’ component of their chemical shielding tensor σ_{ij}^{orb} . However we must bear in mind that, for open-

shell configurations exhibiting appreciable SO coupling, the ‘paramagnetic’ term includes the spin-dependent terms in both \hat{m} and $\hat{\mathcal{F}}$, and so σ^{para} is not a pure orbital term. The third term in Equation 4.99 exhibits a leading Curie temperature dependence of $1/(kT)$, which is familiar from our earlier discussions. One interesting feature of this term is that it receives a zero contribution from any levels n that are non-degenerate. Hence if we have an isolated non-degenerate ground state $n = 0$ we obtain

$$\sigma_{ij} = \frac{1}{\hbar\gamma_I} \langle 0 | \mathcal{D}_{ij} | 0 \rangle + \frac{1}{\hbar\gamma_I} \sum_{m \neq 0} \sum_{\mu} \frac{\langle 0 | \hat{m}_i | m\mu \rangle \langle m\mu | \hat{\mathcal{F}}_j | 0 \rangle + \text{c.c.}}{E_m - E_0}, \quad (4.102)$$

which is the Ramsey expression [191].

In our discussion of paramagnetic shifts, we retain both the Curie term and the spin-dependent part of the ‘paramagnetic’ term and combine both in our paramagnetic shielding σ_{ij}^S :

$$\begin{aligned} \sigma_{ij}^S &= \frac{2}{\hbar\gamma_I Q_0} \sum_n \exp(-\beta E_n) \sum_{m \neq n} \sum_{\nu, \mu} \frac{\langle n\nu | \hat{m}_i | m\mu \rangle \langle m\mu | \hat{\mathcal{F}}_j | n\nu \rangle}{E_m - E_n} \\ &+ \frac{\beta}{\hbar\gamma_I Q_0} \sum_n \exp(-\beta E_n) \sum_{\nu, \nu'} \langle n\nu | \hat{m}_i | n\nu' \rangle \langle n\nu' | \hat{\mathcal{F}}_j | n\nu \rangle. \end{aligned} \quad (4.103)$$

Note that $\langle n\nu | \hat{m}_i | m\mu \rangle \langle m\mu | \hat{\mathcal{F}}_j | n\nu \rangle$ in the first term is always real, and so we have removed the c.c. and replaced it with a factor of 2 in front of the sum. Henceforth we only consider σ_{ij}^S in our discussion.

4.2.2 The EPR formalism applied to d -block transition-metal systems

Equation 4.103 is a correct, if opaque, form of the paramagnetic shielding tensor. However for d -block transition-metal ions we can convert it to an intuitively more useful form by using the explicit EPR Hamiltonian in Equation 4.36, from which we can write down \hat{H}_0 and \hat{H}_1 as

$$\hat{H}_0 = \hat{S} \cdot D \cdot \hat{S}, \quad (4.104)$$

$$\hat{H}_1 = \mu_B \mathbf{B}_0 \cdot \mathbf{g} \cdot \hat{S} + \hat{S} \cdot \mathbf{A} \cdot \hat{I}, \quad (4.105)$$

where we see that the ZFS interaction is the Hamiltonian in the absence of the external field and nuclear magnetic moments. We can deduce the expressions for both the magnetic moment \hat{m}_i and the hyperfine field

$\hat{\mathcal{F}}_j$ operators to be

$$\hat{m}_i = -\mu_B \sum_k g_{ik} \hat{S}_k, \quad (4.106)$$

$$\hat{\mathcal{F}}_j = \sum_l \hat{S}_l A_{lj}. \quad (4.107)$$

Substituting these into the EPR expression for the paramagnetic shielding in Equation 4.103 we obtain

$$\begin{aligned} \sigma_{ij}^S = & -\frac{2\mu_B}{\hbar\gamma_I} \sum_{kl} g_{ik} A_{lj} \frac{1}{Q_0} \sum_n \exp(-\beta E_n) \sum_{m \neq n} \sum_{\nu, \mu} \frac{\langle n\nu | \hat{S}_k | m\mu \rangle \langle m\mu | \hat{S}_l | n\nu \rangle}{E_m - E_n} \\ & - \frac{\mu_B}{\hbar\gamma_I kT} \sum_{kl} g_{ik} A_{lj} \frac{1}{Q_0} \sum_n \exp(-\beta E_n) \sum_{\nu, \nu'} \langle n\nu | \hat{S}_k | n\nu' \rangle \langle n\nu' | \hat{S}_l | n\nu \rangle, \end{aligned} \quad (4.108)$$

where the $|n\nu\rangle$ and E_n are the eigenstates and eigenvalues of the ZFS interaction Hamiltonian. This is simplified to give

$$\sigma_{ij}^S = -\frac{\mu_B}{\hbar\gamma_I} \sum_{kl} g_{ik} Z_{kl} A_{lj}, \quad (4.109)$$

or alternatively

$$\boldsymbol{\sigma}^S = -\frac{\mu_B}{\hbar\gamma_I} \mathbf{g} \cdot \mathbf{Z} \cdot \mathbf{A}. \quad (4.110)$$

The tensor Z_{kl} contains all the information pertaining to the ZFS, and the form of the temperature dependence of the whole shielding tensor. It takes the form

$$Z_{kl} = \left\langle \int_0^\beta dw \exp(w\hat{H}_0) \hat{S}_k \exp(-w\hat{H}_0) \hat{S}_l \right\rangle_0 \quad (4.111)$$

$$= \frac{1}{Q_0} \text{Tr}_S \left\{ \exp(-\beta\hat{H}_0) \int_0^\beta dw \exp(w\hat{H}_0) \hat{S}_k \exp(-w\hat{H}_0) \hat{S}_l \right\} \quad (4.112)$$

$$\begin{aligned} &= \frac{2}{Q_0} \sum_n \exp(-\beta E_n) \sum_{m \neq n} \sum_{\nu, \mu} \frac{\langle n\nu | \hat{S}_k | m\mu \rangle \langle m\mu | \hat{S}_l | n\nu \rangle}{E_m - E_n} \\ &+ \frac{\beta}{Q_0} \sum_n \exp(-\beta E_n) \sum_{\nu, \nu'} \langle n\nu | \hat{S}_k | n\nu' \rangle \langle n\nu' | \hat{S}_l | n\nu \rangle. \end{aligned} \quad (4.113)$$

In the absence of a ZFS interaction $\mathbf{D} = \mathbf{0}$ and there is a single degenerate level $n = 0$ with energy $E_0 = 0$.

In this case the Equation 4.108 reduces to a simple expression with a Curie temperature dependence:

$$\sigma_{ij}^S = -\frac{\mu_B}{\hbar\gamma_I kT} \sum_{kl} g_{ik} A_{lj} \sum_{\nu, \nu'} \frac{\langle 0\nu | \hat{S}_k | 0\nu' \rangle \langle 0\nu' | \hat{S}_l | 0\nu \rangle}{2S + 1} \quad (4.114)$$

$$= -\frac{\mu_B}{\hbar\gamma_I kT} \sum_{kl} g_{ik} A_{lj} \frac{\text{Tr}_S (\hat{S}_k \hat{S}_l)}{2S + 1} \quad (4.115)$$

$$= -\frac{\mu_B}{\hbar\gamma_I kT} \sum_{kl} g_{ik} A_{lj} \frac{1}{3} S(S + 1) \delta_{kl} \quad (4.116)$$

$$= -\frac{\mu_B S(S + 1)}{3\hbar\gamma_I kT} \sum_k g_{ik} A_{kj}, \quad (4.117)$$

which can also be written

$$\boldsymbol{\sigma}^S = -\frac{\mu_B S(S + 1)}{3\hbar\gamma_I kT} \mathbf{g} \cdot \mathbf{A}. \quad (4.118)$$

In fact this is the same expression that was derived by Moon and Patchkovskii [38]. We note the following features. Firstly this expression is reminiscent of that for the spin-only ion in Equation 3.70, with the main difference that the g -factor g_e has been replaced by the full g -tensor \mathbf{g} . The tensors \mathbf{g} and \mathbf{A} couple together via conventional matrix multiplication. Secondly, as in Equation 3.70, the temperature dependence varies according to the $1/kT$ Curie law. We see in the next section that this is not the case when there is a non-zero ZFS.

4.2.3 The EPR formalism in different temperature limits

It is instructive to explore the form of the EPR expression for the paramagnetic shielding tensor in different temperature regimes. This has been investigated in some detail by Martin and Autschbach, who considered expansions of the EPR expression for the shielding tensor up to $1/(kT)^3$ for metal ions with the full range of spins appropriate for the d -block, which range from $1/2$ to $5/2$ [89, 90]. It is particularly informative to consider the case of high temperatures, where the expression is considerably simplified. The term ‘high temperature’ refers to the size of kT with respect to the ZFS parameters D and E , and is therefore quantified by the ratios $|D|/kT$ and $|E|/kT$, with smaller ratios indicating a better agreement with the high-temperature limit. We examine two related facets of this limit in order to illustrate the connection between the two formalisms. Firstly we note that the integral in Equation 4.112 is over values of w from 0 to β , which corresponds to temperatures from infinity down to the experimental temperature T . If we assume that this

range of temperatures is ‘high’, such that we can approximate the operators $\exp(\pm w\hat{H}_0)$ by the identity operator, then Z_{kl} reduces to the expression calculated by Pennanen and Vaara Z_{kl}^{PV} [39]:

$$Z_{kl} = \frac{1}{Q_0} \text{Tr}_S \left\{ \exp(-\beta\hat{H}_0) \int_0^\beta dw \exp(w\hat{H}_0) \hat{S}_k \exp(-w\hat{H}_0) \hat{S}_l \right\} \quad (4.119)$$

$$\approx \frac{1}{Q_0} \text{Tr}_S \left\{ \exp(-\beta\hat{H}_0) \int_0^\beta dw \hat{S}_k \hat{S}_l \right\} \quad (4.120)$$

$$= \beta \frac{\text{Tr}_S \left\{ \exp(-\beta\hat{H}_0) \hat{S}_k \hat{S}_l \right\}}{Q_0} \quad (4.121)$$

$$= Z_{kl}^{\text{PV}}. \quad (4.122)$$

The Pennanen–Vaara expression is therefore a high-temperature approximation of the EPR expression [40]. Note that we have not explicitly assumed that $\exp(-\beta\hat{H}_0)$ is also approximated by the identity; this approximation has only been applied to temperatures higher than T .

Even higher temperatures can be examined further by expanding both Z_{kl}^{PV} and Z_{kl} as Taylor series in β . The expansion of the former is straightforward:

$$Z_{kl}^{\text{PV}} = \beta \frac{\text{Tr}_S (\hat{S}_k \hat{S}_l)}{Q_0} - \beta^2 \frac{\text{Tr}_S (\hat{H}_0 \hat{S}_k \hat{S}_l)}{Q_0} + \frac{\beta^3}{2} \frac{\text{Tr}_S (\hat{H}_0^2 \hat{S}_k \hat{S}_l)}{Q_0} + \mathcal{O}(\beta^4). \quad (4.123)$$

The expansion of the EPR expression Z_{kl} requires more tedious algebra, which gives the following

$$\begin{aligned} Z_{kl} &= \frac{1}{Q_0} \text{Tr}_S \left\{ \left(\hat{1} - \beta\hat{H}_0 + \frac{1}{2}\beta^2\hat{H}_0^2 - \frac{1}{6}\beta^3\hat{H}_0^3 + \mathcal{O}(\beta^4) \right) \right. \\ &\quad \times \int_0^\beta dw \left(\hat{1} + w\hat{H}_0 + \frac{1}{2}w^2\hat{H}_0^2 + \mathcal{O}(w^3) \right) \hat{S}_k \left(\hat{1} - w\hat{H}_0 + \frac{1}{2}w^2\hat{H}_0^2 + \mathcal{O}(w^3) \right) \hat{S}_l \left. \right\} \end{aligned} \quad (4.124)$$

$$\begin{aligned} &= \frac{1}{Q_0} \text{Tr}_S \left\{ \left(\hat{1} - \beta\hat{H}_0 + \frac{1}{2}\beta^2\hat{H}_0^2 - \frac{1}{6}\beta^3\hat{H}_0^3 + \mathcal{O}(\beta^4) \right) \right. \\ &\quad \times \left(\beta\hat{S}_k \hat{S}_l + \frac{1}{2}\beta^2\hat{H}_0 \hat{S}_k \hat{S}_l - \frac{1}{2}\beta^2\hat{S}_k \hat{H}_0 \hat{S}_l + \frac{1}{6}\beta^3\hat{H}_0^2 \hat{S}_k \hat{S}_l - \frac{1}{3}\beta^3\hat{H}_0 \hat{S}_k \hat{H}_0 \hat{S}_l + \frac{1}{6}\beta^3\hat{S}_k \hat{H}_0^2 \hat{S}_l + \mathcal{O}(\beta^4) \right) \left. \right\} \end{aligned} \quad (4.125)$$

$$\begin{aligned} &= \beta \frac{\text{Tr}_S (\hat{S}_k \hat{S}_l)}{Q_0} + \beta^2 \left[\frac{\text{Tr}_S (\hat{H}_0 (\hat{S}_k \hat{S}_l - \hat{S}_k \hat{S}_l))}{2Q_0} - \frac{\text{Tr}_S (\hat{H}_0 \hat{S}_k \hat{S}_l)}{Q_0} \right] \\ &\quad + \beta^3 \left[\frac{\text{Tr}_S \left\{ \hat{H}_0^2 (\hat{S}_k \hat{S}_l + \hat{S}_k \hat{S}_l) + \hat{H}_0 \hat{S}_k \hat{H}_0 \hat{S}_l \right\}}{6Q_0} \right] + \mathcal{O}(\alpha^4). \end{aligned} \quad (4.126)$$

The first term of order β^2 is proportional to the trace of $\hat{H}_0 [\hat{S}_k, \hat{S}_l]$, which is equal to zero:

$$\text{Tr}_S \{ \hat{H}_0 [\hat{S}_k, \hat{S}_l] \} = \sum_{m,n,p} \sum_{\mu,\nu,\pi} \langle m\mu | \hat{H}_0 | n\nu \rangle [\langle n\nu | \hat{S}_k | p\pi \rangle \langle p\pi | \hat{S}_l | m\mu \rangle - \langle n\nu | \hat{S}_l | p\pi \rangle \langle p\pi | \hat{S}_k | m\mu \rangle] \quad (4.127)$$

$$= \sum_{n,p} \sum_{\nu,\pi} E_n [\langle n\nu | \hat{S}_k | p\pi \rangle \langle p\pi | \hat{S}_l | n\nu \rangle - \langle n\nu | \hat{S}_l | p\pi \rangle \langle p\pi | \hat{S}_k | n\nu \rangle] \quad (4.128)$$

$$= 0, \quad (4.129)$$

where to go to the last line we use the argument set out in appendix D. We therefore see that Z_{kl}^{PV} and Z_{kl} are identical out to and including the terms in $1/(kT)^2$, and differ only in the third-order terms and above. Both formalisms therefore give the same second-order expression:

$$Z_{kl} = \beta \frac{\text{Tr}_S (\hat{S}_k \hat{S}_l)}{Q_0} - \beta^2 \frac{\text{Tr}_S (\hat{H}_0 \hat{S}_k \hat{S}_l)}{Q_0} \quad (4.130)$$

$$= \frac{\beta}{3} S(S+1) \delta_{kl} - \frac{\beta^2}{30} S(S+1)(2S-1)(2S+3) D_{kl}, \quad (4.131)$$

where we have replaced \hat{H}_0 with the ZFS interaction Hamiltonian. The calculation is described in detail in appendix D. This form of Z_{kl} results in a high-temperature expression for the paramagnetic shielding tensor that was first derived by Bleaney [61]:

$$\sigma^S \approx -\frac{\mu_B S(S+1)}{3\hbar\gamma kT} \mathbf{g} \cdot \mathbf{A} + \frac{\mu_B S(S+1)(2S-1)(2S+3)}{30\hbar\gamma_l(kT)^2} \mathbf{g} \cdot \mathbf{D} \cdot \mathbf{A}. \quad (4.132)$$

The conclusion is that if kT is sufficiently large that the Boltzmann average over the ZFS energy levels can be well-approximated to $1/(kT)^2$ in the Taylor expansion, both formalisms give the same result.

An example of the temperature dependence of the paramagnetic shielding tensor

The deviation of both the Bleaney and Pennanen–Vaara theories from the EPR shielding formalism becomes important at low temperature, and for very large values of the ZFS. To investigate this we employ a discussion along the lines of van den Heuvel and Soncini [87], upon which we expand, and calculate the form of the shielding tensor due to a paramagnetic centre with spin $S = 1$. Initially we assume that the ZFS interaction

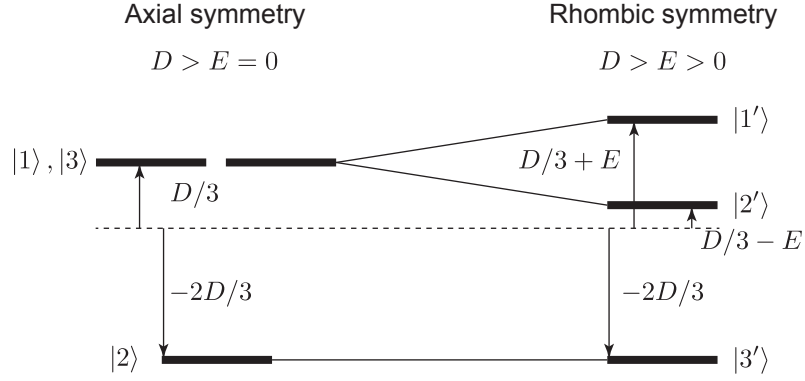


Figure 4.3: Energy levels of an electronic spin $S = 1$ subject to a ZFS. The levels are shown in coordination environments of axial and rhombic symmetry. The dotted line represents the barycentre at zero energy.

is axially symmetric and traceless. In the PAF of the ZFS the Hamiltonian \hat{H} is given by

$$\hat{H} = \tilde{D}_{20} \hat{T}_{20} \quad (4.133)$$

$$= D \left(\hat{S}_z^2 - \frac{1}{3} S(S+1) \hat{1} \right), \quad (4.134)$$

and has the following eigenstates and energies:

$$|1\rangle = |+1\rangle, \quad E_1 = \frac{1}{3}D, \quad (4.135)$$

$$|2\rangle = |0\rangle, \quad E_2 = -\frac{2}{3}D, \quad (4.136)$$

$$|3\rangle = |-1\rangle, \quad E_3 = \frac{1}{3}D, \quad (4.137)$$

where we see that states $|1\rangle$ and $|3\rangle$ are degenerate and form a doublet state, and $|2\rangle$ is a non-degenerate singlet state. The energy levels are shown in Figure 4.3 and the matrix representations of the spin operators \hat{S}_i are given in Table 4.1. It should be noted that these energy levels are of the same form as those that describe nuclear quadrupolar resonance (NQR) spectra of nuclei with spin $I = 1$.

We obtain the components of the tensor Z_{kl} by taking all possible products of the matrix elements of two

Symmetry	\hat{S}_x	\hat{S}_y	\hat{S}_z
Axial	$\begin{pmatrix} 0 & 1/\sqrt{2} & 0 \\ 1/\sqrt{2} & 0 & 1/\sqrt{2} \\ 0 & 1/\sqrt{2} & 0 \end{pmatrix}$	$\begin{pmatrix} 0 & -i/\sqrt{2} & 0 \\ i/\sqrt{2} & 0 & -i/\sqrt{2} \\ 0 & i/\sqrt{2} & 0 \end{pmatrix}$	$\begin{pmatrix} 1 & 0 & 0 \\ 0 & 0 & 0 \\ 0 & 0 & -1 \end{pmatrix}$
Rhombic	$\begin{pmatrix} 0 & 1 & 0 \\ 1 & 0 & 0 \\ 0 & 0 & 0 \end{pmatrix}$	$\begin{pmatrix} 0 & 0 & 0 \\ 0 & 0 & -i \\ 0 & i & 0 \end{pmatrix}$	$\begin{pmatrix} 0 & 0 & -1 \\ 0 & 0 & 0 \\ -1 & 0 & 0 \end{pmatrix}$

Table 4.1: Matrix representations of the spin operators \hat{S}_i in the basis of a spin $S = 1$ subject to a ZFS interaction of axial or rhombic symmetry.

spin operators. In the full EPR formalism we obtain the following diagonal components:

$$\tilde{Z}_{xx} = \tilde{Z}_{yy} = \frac{2}{D} \frac{e^{2\beta D/3} - e^{-\beta D/3}}{2e^{-\beta D/3} + e^{2\beta D/3}}, \quad (4.138)$$

$$\tilde{Z}_{zz} = 2\beta \frac{e^{-\beta D/3}}{2e^{-\beta D/3} + e^{2\beta D/3}}. \quad (4.139)$$

The off-diagonal elements are zero, as a result of our working in the PAF of the ZFS tensor. The implication is that the both the Z- and ZFS tensors share the same PAF. Furthermore we see that $\tilde{Z}_{xx} = \tilde{Z}_{yy}$, and so the Z-tensor is axially symmetric, like the ZFS. In the Pennanen–Vaara formalism we calculate $\tilde{Z}_{kl}^{\text{PV}}$ in a similar way to obtain the following diagonal elements:

$$\tilde{Z}_{xx}^{\text{PV}} = \tilde{Z}_{yy}^{\text{PV}} = \beta \frac{e^{-\beta D/3} + e^{2\beta D/3}}{2e^{-\beta D/3} + e^{2\beta D/3}}, \quad (4.140)$$

$$\tilde{Z}_{zz}^{\text{PV}} = 2\beta \frac{e^{-\beta D/3}}{2e^{-\beta D/3} + e^{2\beta D/3}}. \quad (4.141)$$

We can see immediately that the two formalisms give different results for the \tilde{Z}_{xx} and \tilde{Z}_{yy} , but the same value for \tilde{Z}_{zz} . However, as seen above, if we expand both $\tilde{Z}_{xx}^{\text{PV}}$ and \tilde{Z}_{xx} as Taylor series

$$\tilde{Z}_{xx}^{\text{PV}} = \frac{2}{3}\beta + \frac{1}{9}D\beta^2 + \frac{1}{54}D^2\beta^3 + O(\beta^4), \quad (4.142)$$

$$\tilde{Z}_{xx} = \frac{2}{3}\beta + \frac{1}{9}D\beta^2 - \frac{1}{27}D^2\beta^3 + O(\beta^4), \quad (4.143)$$

we see that the deviation only appears in the terms of order β^3 and higher. Finally we use the Taylor

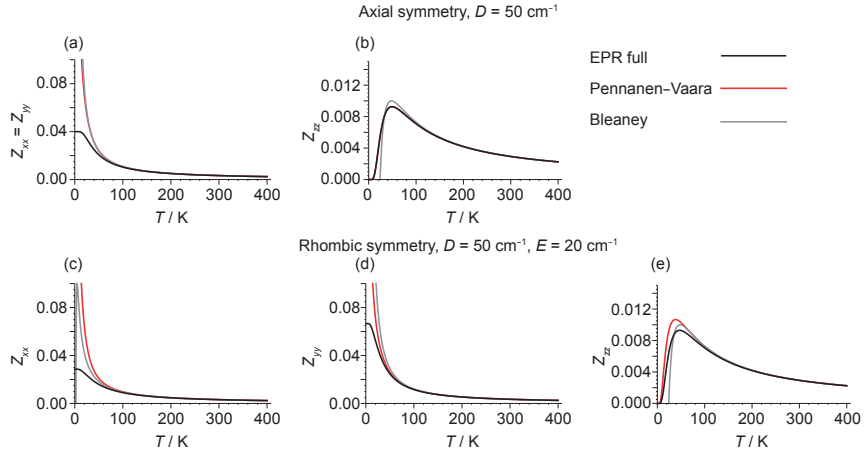


Figure 4.4: Comparison between the expressions of the paramagnetic chemical shielding Z -tensor as a function of temperature as derived using the EPR formalism of van den Heuvel and Soncini [86, 88], and the Pennanen–Vaara [39], and Bleaney [61] theories for a spin $S = 1$ subject to the ZFS interaction. In each plot the EPR curve is in black, the Pennanen–Vaara curve is in red, and the Bleaney curve is in grey. Shown in (a) and (b) are the $\tilde{Z}_{xx} / \tilde{Z}_{yy}$ and \tilde{Z}_{zz} curves due to an axially symmetric ZFS with $D = 50 \text{ cm}^{-1}$. In (b) the black and red curves are exactly coincident. The temperature variations of \tilde{Z}_{xx} , \tilde{Z}_{yy} , and \tilde{Z}_{zz} are shown in (c), (d), and (e) for a rhombic ZFS interaction with $D = 50 \text{ cm}^{-1}$ and $E = 20 \text{ cm}^{-1}$.

expansions to obtain the Bleaney expressions for the Z -tensor \tilde{Z}_{kl}^B , which are:

$$\tilde{Z}_{xx}^B = \tilde{Z}_{yy}^B = \frac{2}{3}\beta + \frac{1}{9}D\beta^2, \quad (4.144)$$

$$\tilde{Z}_{zz}^B = \frac{2}{3}\beta - \frac{2}{9}D\beta^2. \quad (4.145)$$

We need an idea of the size of the discrepancies between the three theories under standard conditions for high-resolution NMR. Figure 4.4 shows plots of the three diagonal components of the Z -tensor as a function of temperature in the EPR, Pennanen–Vaara, and Bleaney formalisms. Parts (a) and (b) compare the temperature variation of $\tilde{Z}_{xx,yy}$ and \tilde{Z}_{zz} respectively for each formalism from 0 K to 400 K for a large axial ZFS of $D = 50 \text{ cm}^{-1}$. The non-Curie behaviour of all four curves is immediately seen, and for the xx and yy components we see that the differences between the three curves are only apparent below approximately 100 K, with both the Pennanen–Vaara and Bleaney curves tending to infinity at 0 K, whilst the EPR curve shows better behaviour by tending to a constant, finite value of $2/D$. The EPR and Pennanen–Vaara curves of the zz component are coincident, as we have shown with the calculations above, and both tend to zero at

zero temperature. The Bleaney curve is not well-behaved at very low temperatures (here below 50 K), as it tends to minus infinity. Nevertheless the Bleaney curve matches extremely well with the others at higher temperatures.

The discrepancies between the curves appear at higher temperatures if the system possesses a larger ZFS. Interestingly we note that the Bleaney theory, although considerably simpler than the other two, performs remarkably well down to temperatures of 100 K, and in particular has very good agreement with the more complicated Pennanen–Vaara theory. However out of these three formulae we would expect the full EPR formula to be more likely to be correct at low temperatures simply because at very low temperature only the lowest-energy state $|2\rangle \equiv |0\rangle$ is populated, and so the shielding tensor should be temperature independent and not tend to infinity [87].

We can repeat the calculation for a ZFS of rhombic symmetry with Hamiltonian

$$\hat{H} = \tilde{D}_{20}\hat{T}_{20} + \tilde{D}_{2-2}\hat{T}_{2+2} + \tilde{D}_{2+2}\hat{T}_{2-2} \quad (4.146)$$

$$= D\left(\hat{S}_z^2 - \frac{1}{3}S(S+1)\hat{1}\right) + E\left(\hat{S}_x^2 - \hat{S}_y^2\right), \quad (4.147)$$

where we are once again working within the PAF of the ZFS tensor. The eigenstates and energies are:

$$|1'\rangle = \sqrt{\frac{1}{2}}(|+1\rangle + |-1\rangle), \quad E'_1 = \frac{1}{3}D + E, \quad (4.148)$$

$$|2'\rangle = |0\rangle, \quad E'_2 = -\frac{2}{3}D, \quad (4.149)$$

$$|3'\rangle = \sqrt{\frac{1}{2}}(-|+1\rangle + |-1\rangle), \quad E'_3 = \frac{1}{3}D - E. \quad (4.150)$$

The Hamiltonians $\hat{T}_{2\pm 2}$ are double-quantum operators, being proportional to \hat{S}_\pm^2 , and so mix together the states $|\pm 1\rangle$, which are no longer degenerate but are split by $2E$, and leave $|0\rangle$ unperturbed. The energy levels under rhombic symmetry are shown in Figure 4.3. We need the matrix elements of \hat{S}_i in the new basis, the representations within which are given in Table 4.1.

The EPR formula gives the following non-zero diagonal values of \tilde{Z}_{kl} :

$$\tilde{Z}_{xx} = \frac{2}{D+E} \frac{e^{2\beta D/3} - e^{-\beta(D/3+E)}}{e^{-\beta(D/3+E)} + e^{2\beta D/3} + e^{-\beta(D/3-E)}}, \quad (4.151)$$

$$\tilde{Z}_{yy} = \frac{2}{D-E} \frac{e^{2\beta D/3} - e^{-\beta(D/3-E)}}{e^{-\beta(D/3+E)} + e^{2\beta D/3} + e^{-\beta(D/3-E)}}, \quad (4.152)$$

$$\tilde{Z}_{zz} = \frac{1}{E} \frac{e^{-\beta(D/3-E)} - e^{-\beta(D/3+E)}}{e^{-\beta(D/3+E)} + e^{2\beta D/3} + e^{-\beta(D/3-E)}}. \quad (4.153)$$

We note that the Z -tensor is still diagonal, but no longer axially symmetric due to the introduction of the rhombic anisotropy E . The Pennanen–Vaara formula gives the following non-zero values of $\tilde{Z}_{kl}^{\text{PV}}$:

$$\tilde{Z}_{xx}^{\text{PV}} = \beta \frac{e^{-\beta(D/3+E)} + e^{2\beta D/3}}{e^{-\beta(D/3+E)} + e^{2\beta D/3} + e^{-\beta(D/3-E)}}, \quad (4.154)$$

$$\tilde{Z}_{yy}^{\text{PV}} = \beta \frac{e^{2\beta D/3} + e^{-\beta(D/3-E)}}{e^{-\beta(D/3+E)} + e^{2\beta D/3} + e^{-\beta(D/3-E)}}, \quad (4.155)$$

$$\tilde{Z}_{zz}^{\text{PV}} = \beta \frac{e^{-\beta(D/3+E)} + e^{-\beta(D/3-E)}}{e^{-\beta(D/3+E)} + e^{2\beta D/3} + e^{-\beta(D/3-E)}}. \quad (4.156)$$

We see that the expressions for the zz components are no longer the same, which is a result of the lifting of the axial symmetry. However the Taylor series of the expressions up to β^2 are once again identical, and are equal to the expressions obtained from the Bleaney theory:

$$\tilde{Z}_{xx}^{\text{B}} = \frac{2}{3}\beta + \frac{1}{9}(D-3E)\beta^2, \quad (4.157)$$

$$\tilde{Z}_{yy}^{\text{B}} = \frac{2}{3}\beta + \frac{1}{9}(D+3E)\beta^2, \quad (4.158)$$

$$\tilde{Z}_{zz}^{\text{B}} = \frac{2}{3}\beta - \frac{2}{9}D\beta^2. \quad (4.159)$$

All these expressions for \tilde{Z}_{xx} , \tilde{Z}_{yy} , and \tilde{Z}_{zz} are plotted in Figure 4.4 (c)–(e) for ZFS anisotropies of $D = 50 \text{ cm}^{-1}$ and $E = 20 \text{ cm}^{-1}$. Once again the discrepancies from the EPR curves are only apparent at low temperatures, here below 100 K for these specific values of D and E , with the EPR curves for $\tilde{Z}_{xx}^{\text{HS}}$ and $\tilde{Z}_{yy}^{\text{HS}}$ tending to constant values of $2/(D+E)$ and $2/(D-E)$ respectively at 0 K. It is once again striking how well the Bleaney theory performs at higher temperatures.

Therefore the conclusion is that the general EPR formalism, due to van den Heuvel and Soncini, presented in this chapter gives an exact description of the paramagnetic shielding tensor at all temperatures. However

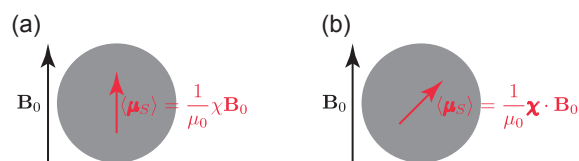


Figure 4.5: Illustration of the induced magnetic moment per paramagnetic ion due to magnetically isotropic and anisotropic materials. A magnetically isotropic material is shown in (a). The size of the induced magnetic moment per paramagnetic ion is proportional to the size of the external field, and does not vary with the field direction. However the induced magnetic moment always remains parallel to the field. In a magnetically anisotropic material, shown in (b), the induced magnetic moment per paramagnetic ion is in general not parallel to the external field, and changes in size and direction as the material is rotated within the field.

the simpler Pennanen–Vaara or Bleaney forms can be used if the temperature is sufficiently high that the shielding expression can be truncated at $1/(kT)^2$. In practice, this means that for first-row transition-metal ions for which D has a maximum of approximately 50 cm^{-1} at temperatures above 100 K we can safely use either the Pennanen–Vaara or Bleaney formula.

4.3 The magnetic susceptibility tensor

4.3.1 Magnetism of the bulk

We saw that for a linear material containing an ensemble of spin-only transition metal centres, an applied magnetic field induces a bulk magnetisation that is proportional in size and parallel in direction to the field, with the constant of proportionality equal to the volume magnetic susceptibility, as shown in Equation 3.87. In particular we noted that the magnetization is independent of the relative orientation of the field to the material. Such a bulk material is said to be magnetically isotropic. This situation is shown in Figure 4.5 (a). For spin systems subject to SO coupling we can apply the same reasoning to determine the induced magnetization, with one important difference. Because the magnetic moments of the paramagnetic centres are now spatially anisotropic, via either \hat{L} or g depending on how we choose to define the spin Hamiltonian, we also expect the induced magnetization vector M to vary as the direction of the applied field is changed. The bulk material is therefore anisotropic, and Equation 3.87 should be modified to account for this:

$$M = \frac{1}{\mu_0} \chi_V \cdot B_0. \quad (4.160)$$

The constant of proportionality is replaced by the volume magnetic susceptibility tensor χ_V , in which is encoded the anisotropic response of the material to the field. The effect of the anisotropic susceptibility tensor is that in general the magnetisation vector is no longer parallel to the field, as shown in Figure 4.5 (b). From here we can also generalise Equation 3.89 to give an expression for the average induced magnetic moment per paramagnetic centre $\langle \hat{\mu}_S \rangle$ of such spin systems:

$$\langle \hat{\mu}_S \rangle = \frac{1}{\mu_0} \chi \cdot \mathbf{B}_0, \quad (4.161)$$

where χ is the molecular magnetic susceptibility tensor.

To calculate the average energy E per paramagnetic centre that results from the interaction of the average moment with the field we recall Equation 2.13, which gives the infinitesimal change in internal energy of the whole sample due to a change in magnetic field at constant entropy and constant volume as $-VM \cdot d\mathbf{B}$. From this we express the infinitesimal change in the average energy per paramagnetic centre as

$$\frac{dE}{d\mathbf{B}_0} = -\langle \hat{\mu}_S \rangle \quad (4.162)$$

$$= -\frac{1}{\mu_0} \chi \cdot \mathbf{B}_0. \quad (4.163)$$

Integrating this expression we obtain

$$E = -\frac{1}{2\mu_0} \mathbf{B}_0 \cdot \chi \cdot \mathbf{B}_0, \quad (4.164)$$

from which we see that the χ tensor must be symmetric. It therefore just contains zeroth- and second-rank irreducible spherical tensor components χ_{00} and χ_{2m} . Writing the latter in the PAF these components are

$$\chi_{00} = -\sqrt{3}\chi_{\text{iso}}, \quad (4.165)$$

$$\tilde{\chi}_{20} = \sqrt{\frac{2}{3}}\Delta\chi_{\text{ax}}, \quad (4.166)$$

$$\tilde{\chi}_{2\pm 1} = 0, \quad (4.167)$$

$$\tilde{\chi}_{2\pm 2} = \frac{1}{2}\Delta\chi_{\text{rh}}, \quad (4.168)$$

where χ_{iso} is the isotropic susceptibility, and $\Delta\chi_{\text{ax}}$ and $\Delta\chi_{\text{rh}}$ are the axial and rhombic susceptibility anisotropies

which are defined as

$$\Delta\chi_{\text{ax}} = \tilde{\chi}_{zz} - \frac{1}{2}(\tilde{\chi}_{xx} + \tilde{\chi}_{yy}) \quad (4.169)$$

$$\Delta\chi_{\text{rh}} = \tilde{\chi}_{xx} - \tilde{\chi}_{yy}. \quad (4.170)$$

Note that in this convention we order the principal components of the tensor as $\tilde{\chi}_{zz} > \tilde{\chi}_{yy} > \tilde{\chi}_{xx}$.

4.3.2 The susceptibility tensor in terms of the molecular/atomic-level parameters according to the EPR formalism

The EPR formalism for the paramagnetic shielding tensor can be adapted to calculate the magnetic susceptibility tensor [88]. Here, following the computation of the Helmholtz free energy we look for terms that are bilinear in the external magnetic field, which is done by calculating the following derivative:

$$\chi_{ij} = -\mu_0 \left(\frac{\partial^2 \bar{F}}{\partial B_{0,i} \partial B_{0,j}} \right)_{\mathbf{B}_0=0}. \quad (4.171)$$

The paramagnetic susceptibility tensor can be written down from Equation 4.103 on substituting \hat{m}_j for $\hat{\mathcal{F}}_j$. The expression is

$$\begin{aligned} \chi_{ij} = & \frac{2\mu_0}{Q_0} \sum_n \exp(-\beta E_n) \sum_{m \neq n} \sum_{\nu, \mu} \frac{\langle n\nu | \hat{m}_i | m\mu \rangle \langle m\mu | \hat{m}_j | n\nu \rangle}{E_m - E_n} \\ & + \frac{\mu_0}{kT} \frac{1}{Q_0} \sum_n \exp(-\beta E_n) \sum_{\nu, \nu'} \langle n\nu | \hat{m}_i | n\nu' \rangle \langle n\nu' | \hat{m}_j | n\nu \rangle, \end{aligned} \quad (4.172)$$

which is a form of the van Vleck equation [213]. This is the general expression for the paramagnetic susceptibility tensor.

In the specific case of an ensemble of d -block transition-metal ions, we once again write the electronic magnetic moment operator as $\hat{m}_i = -\mu_B \sum_k g_{ik} \hat{S}_k$, and we obtain Equation 4.173:

$$\chi = \mu_0 \mu_B^2 \mathbf{g} \cdot \mathbf{Z} \cdot \mathbf{g}^T, \quad (4.173)$$

where the matrix \mathbf{Z} is the same as that encountered earlier in Equation 4.113. If the EPR expression for

\mathbf{Z} is used, this expression gives the susceptibility tensor at arbitrary temperature. The expression for the susceptibility tensor reduces to the Pennanen–Vaara expression if we use \mathbf{Z}^{PV} for \mathbf{Z} . In addition, as for the paramagnetic shielding tensor, we can also approximate χ to second order in $1/(kT)$. Once again the expression for \mathbf{Z} approximates to the same expression \mathbf{Z}^{B} regardless of which formalism we employ, and we obtain the Bleaney expression for χ :

$$\chi \approx \frac{\mu_0 \mu_{\text{B}}^2 S(S+1)}{3kT} \mathbf{g} \cdot \mathbf{g}^T - \frac{\mu_0 \mu_{\text{B}}^2 S(S+1)(2S-1)(2S+3)}{30(kT)^2} \mathbf{g} \cdot \mathbf{D} \cdot \mathbf{g}^T. \quad (4.174)$$

This describes the susceptibility tensor in the high-temperature limit, such that $|D|, |E| \ll kT$.

4.3.3 Relating the paramagnetic shift to the magnetic susceptibility tensor

We can now derive the connection between the paramagnetic shielding and the magnetic susceptibility tensors. We start by writing down the Hamiltonian describing the hyperfine interaction between the nuclear spin and the average electronic magnetic moment. The general widely-used expression is [214, 215]

$$\hat{H}_{SI} = -\mu_0 \langle \hat{\boldsymbol{\mu}}_S \rangle \cdot \mathbf{C} \cdot \hat{\boldsymbol{\mu}}_I, \quad (4.175)$$

where we write the reduced hyperfine coupling tensor in a completely general way as the sum of isotropic C^{con} , antisymmetric C^{as} , and traceless symmetric C^{dip} parts:

$$\mathbf{C} = C^{\text{con}} \mathbf{1} + C^{\text{as}} + C^{\text{dip}}. \quad (4.176)$$

We will see shortly that the isotropic and symmetric anisotropic parts C^{con} and C^{dip} are not strictly equal to the NR Fermi-contact and spin-dipolar parts C^{FC} and C^{SD} respectively. Nevertheless this approximation is frequently made, in which case the expressions for C^{con} and C^{dip} are the same as those for C^{FC} and C^{SD} given in Equations 3.103 and 3.104, and the corresponding irreducible spherical tensor components are those given in Equations 3.106 and 3.110–3.114. This equivalence (or lack thereof) is a subtle point that is discussed further in sections 4.4 and 4.5. The antisymmetric hyperfine term C^{as} is characterised by the antisymmetric anisotropy ζ^C , which is given by

$$\zeta^C = \sqrt{(C_{xy}^{\text{as}})^2 + (C_{yz}^{\text{as}})^2 + (C_{xz}^{\text{as}})^2}. \quad (4.177)$$

In the PAF of C^{as} , the three rank-one irreducible spherical tensor components are

$$\bar{C}_{10} = -i\sqrt{2}\zeta^C, \quad (4.178)$$

$$\bar{C}_{1\pm 1} = 0. \quad (4.179)$$

Substituting the expressions for the average electronic magnetic moment in Equation 4.161 and the nuclear magnetic moment operator into Equation 4.175, we obtain

$$\hat{H}_{SI} = -\mathbf{B}_0 \cdot \boldsymbol{\chi} \cdot \mathbf{C} \cdot \hat{\boldsymbol{\mu}}_I \quad (4.180)$$

$$= -\hbar\gamma_I \mathbf{B}_0 \cdot \boldsymbol{\chi} \cdot \mathbf{C} \cdot \hat{\mathbf{I}}. \quad (4.181)$$

This Hamiltonian represents an interaction that is linear in the components of both the magnetic field and the nuclear spin, i.e. a chemical shielding. We can therefore write the interaction in the form $\hbar\gamma_I \mathbf{B}_0 \cdot \boldsymbol{\sigma}^\chi \cdot \hat{\mathbf{I}}$, where the shielding due to the susceptibility tensor $\boldsymbol{\sigma}^\chi$ is

$$\boldsymbol{\sigma}^\chi = -\boldsymbol{\chi} \cdot \mathbf{C}. \quad (4.182)$$

This is the generalised form of Equation 3.100 which we derived for spin-only paramagnetic centres. Note that Equation 4.182 has been derived without making any specific assumptions about the form of the susceptibility tensor, other than it being field-independent. We now provide the last link in the connection between the EPR and susceptibility formalisms. We start from the Hamiltonian of the hyperfine interaction

$$\hat{H}_{SI} = -\mu_0 \hat{\boldsymbol{\mu}}_S \cdot \mathbf{C} \cdot \hat{\boldsymbol{\mu}}_I, \quad (4.183)$$

and we substitute in the expressions for the magnetic moment operators $\hat{\boldsymbol{\mu}}_I = \hbar\gamma_I \hat{\mathbf{I}}$ and $\hat{\boldsymbol{\mu}}_S = -\mu_B \mathbf{g} \cdot \hat{\mathbf{S}}$. This expression for the electronic magnetic moment encodes both the orbital and spin components of the magnetic moment. The hyperfine interaction Hamiltonian becomes

$$\hat{H}_{SI} = \mu_0 \mu_B \hbar\gamma_I \hat{\mathbf{S}} \cdot \mathbf{g}^T \cdot \mathbf{C} \cdot \hat{\mathbf{I}} \quad (4.184)$$

$$= \hat{\mathbf{S}} \cdot \mathbf{A} \cdot \hat{\mathbf{I}}, \quad (4.185)$$

where the hyperfine coupling constant is given by

$$\mathbf{A} = \mu_0 \mu_B \hbar \gamma_I \mathbf{g}^T \cdot \mathbf{C}. \quad (4.186)$$

We have written it as the matrix product of the transpose of the g -matrix and the reduced hyperfine coupling matrix $\mathbf{g}^T \cdot \mathbf{C}$. We note that writing the hyperfine tensor in this form means that the magnitude and sign of the interaction change as the spatially-anisotropic electronic magnetic moment changes orientation due to the presence of \mathbf{g}^T . This property is missing in the EPR expression for the hyperfine tensor, which is dominated by the NR terms A^{FC} and A^{SD} , which only contain information about the NR part of the electronic magnetic moment via g_e . We note that it is exactly this inclusion of the g -tensor in Equation 4.186, and in particular the anisotropic part of the g -tensor, which means that C^{con} and C^{dip} are not strictly equivalent to C^{FC} and C^{SD} . Rather, C^{con} contains contributions from both A^{FC} and A^{SD} . We also note that this discrepancy is not addressed by including the SO coupling terms from Equation 4.42 in the EPR expression. Firstly these terms usually have a negligible impact on the shift when compared to other SO coupling effects, such as the g -shift and ZFS. Secondly the second-order contribution to the hyperfine tensor $A^{\text{SD},2}$ is only referred to as a “dipolar coupling” as it is symmetric like the NR contribution A^{SD} , but does not have the same long-range dependence on distance. This is due to it being a cross term in the perturbation expansion of the effective-spin Hamiltonian, and therefore representing a shorter-range effect. Combining the expression in Equation 4.186 with the EPR formula for the paramagnetic shielding in Equation 4.109 gives

$$\sigma^S = -\frac{\mu_B}{\hbar \gamma_I} \mathbf{g} \cdot \mathbf{Z} \cdot \mathbf{A} \quad (4.187)$$

$$= -\mu_0 \mu_B^2 \mathbf{g} \cdot \mathbf{Z} \cdot \mathbf{g}^T \cdot \mathbf{C} \quad (4.188)$$

$$= -\chi \cdot \mathbf{C}. \quad (4.189)$$

Equations 4.182 and 4.189 are the same, thus establishing the self-consistency of the derived expressions. This provides the foundation for showing that the EPR and susceptibility expressions σ^S and σ^χ for the paramagnetic shielding tensor are indeed equivalent. A previous attempt at providing a similar argument was made by Benda et al., which covered a lot of ground on unifying the description of the PCS in both formalisms [216]. However there are still some subtleties that remain in the argument, which mainly originate from the

interpretation of the hyperfine tensors \mathbf{A} and \mathbf{C} . These points are addressed in the following sections on the scaling-factor model of Kim et al. (section 4.4) [53], and on the Kurland–McGarvey formalism (section 4.5) [37]. We begin by writing the susceptibility tensor as the sum of the isotropic χ^{iso} and anisotropic $\Delta\chi$ parts, i.e. $\chi = \chi^{\text{iso}}\mathbf{1} + \Delta\chi$, and the expression for σ^χ becomes

$$\sigma^\chi = -\chi^{\text{iso}}C^{\text{con}}\mathbf{1} - \Delta\chi C^{\text{con}} - \chi^{\text{iso}}C^{\text{ras}} - \Delta\chi \cdot C^{\text{ras}} - \chi^{\text{iso}}C^{\text{dip}} - \Delta\chi \cdot C^{\text{dip}}. \quad (4.190)$$

This establishes that σ^χ is the sum of different terms that originate from different parts of the hyperfine interaction, and contribute differently to the isotropic shift and SA. If the different contributions to the hyperfine tensor are interpreted correctly, the susceptibility expression for the paramagnetic shielding is exactly equivalent to the EPR formalism. However if we make the approximation $C^{\text{con}} = C^{\text{FC}}$ and $C^{\text{dip}} = C^{\text{SD}}$ differences do arise between the formalisms.

We examine these points in more detail in the next sections 4.4 and 4.5, and later in chapter 5.

4.4 The scaling factor revisited

It was shown in section 3.4 that the paramagnetic shielding tensor for spin-only transition-metal ions can be viewed as the ratio of the hyperfine coupling tensor to the nuclear Zeeman energy, given by $-\mathcal{A}/(2\hbar\gamma_I B_0)$, that is calculated in the saturation regime, and then scaled into the high-temperature paramagnetic regime by multiplication with a scaling factor that depends on both temperature, and the electronic magnetic moment. This scaling factor is proportional to the magnetic susceptibility, and so can be determined from measurements of the bulk magnetism. When we include the effects of SO coupling this picture becomes more complicated. We have seen that the magnetic susceptibility becomes a spatially-anisotropic tensor, and so we would expect the scaling factor to also be anisotropic. However if we restrict the discussion to an NR hyperfine tensor, and only account for the SO coupling effects in the electronic magnetic moment, we can apply a modified form of the scaling-factor idea of Kim et al. [53], which has been employed by Clément et al. to first-row d -block ions [30].

The idea is to scale down the same NR hyperfine $-\mathcal{A}/(2\hbar\gamma_I B_0)$, comprising the NR Fermi-contact and spin-dipolar parts, as shown in section 3.4, but with a scaling factor that includes SO coupling effects. This

scaling factor is the ratio of the paramagnetic electronic magnetic moment to the saturated magnetic moment. The electronic angular momentum properties are described in full in section 6.4.1. However for present purposes we simply note that the paramagnetic centre is described by a total angular momentum J , and has a magnetic moment operator given by $\hat{m} = -\mu_B g_J \hat{J}$, where g_J is the isotropic Born–Landé g -factor. We note here that we do not account for the spatial anisotropy of the g -tensor. Following the discussion in section 3.2, the z -component of the average electronic magnetic moment $\langle \hat{m}_z \rangle_{\text{para}}$ is given by

$$\langle \hat{m}_z \rangle_{\text{para}} = \mu_B g_J J B_J(y), \quad (4.191)$$

where $B_J(y)$ is a form of the Brillouin function that depends on the total angular momentum quantum number J :

$$B_J(y) = \frac{2J+1}{2J} \coth \left[\left(\frac{2J+1}{2J} \right) y \right] - \frac{1}{2J} \coth \left[\frac{y}{2J} \right], \quad (4.192)$$

and $y = \beta \mu_B g_J B_0 J$. In the high-temperature limit the Brillouin function is approximated by $B_J(y) \approx y(J+1)/(3J)$, and $\langle \hat{m}_z \rangle_{\text{para}}$ is given by

$$\langle \hat{m}_z \rangle_{\text{para}} = \frac{\mu_{\text{eff}}^2 B_0}{3kT}. \quad (4.193)$$

In Equation 4.193 we have defined the magnitude of the effective electronic magnetic moment as $\mu_{\text{eff}} = \mu_B g_J \sqrt{J(J+1)}$. However in practice we treat μ_{eff} as an empirical parameter that can be determined from measurements of the magnetic susceptibility, which is given by

$$\chi^{\text{iso}} = \frac{\mu_0 \mu_{\text{eff}}^2}{3kT}. \quad (4.194)$$

The treatment of μ_{eff} in this way avoids the need for any explicit calculation of the SO coupling effects. The average electronic magnetic moment in the saturation regime $\langle \hat{m}_z \rangle_{\text{sat}}$ is formally given by $\mu_B g_J J$. However, as we do not include SO coupling effects in the calculation of either the electronic magnetic moment or the hyperfine tensor, we instead use the NR expression derived in section 3.2, where $J \rightarrow S$ and $g_J \rightarrow g_e$:

$$\langle \hat{m}_z \rangle_{\text{sat}} = \mu_B g_e S. \quad (4.195)$$

The scaling factor is therefore

$$\frac{\langle \hat{m}_z \rangle_{\text{para}}}{\langle \hat{m}_z \rangle_{\text{sat}}} = \frac{\chi^{\text{iso}} B_0}{\mu_0 \mu_B g_e S} \quad (4.196)$$

$$= \frac{\mu_{\text{eff}}^2 B_0}{3 \mu_B g_e S kT}. \quad (4.197)$$

The expression in terms of the magnetic susceptibility is the same as for spin-only paramagnetic centres. However in the present case we note that the magnetic susceptibility here includes the SO coupling contributions to the electron magnetic moments, and does not have the same expression as in the spin-only case. Finally, in this formalism, the paramagnetic shielding tensor is

$$\sigma^S = -\frac{\langle \hat{m}_z \rangle_{\text{para}}}{\langle \hat{m}_z \rangle_{\text{sat}}} \frac{\mathcal{A}}{2\hbar\gamma_I B_0} \quad (4.198)$$

$$= -\frac{\chi^{\text{iso}}}{\mu_0 \mu_B g_e \hbar\gamma_I} \frac{\mathcal{A}}{2S} \quad (4.199)$$

$$= -\frac{\mu_{\text{eff}}^2}{3\mu_B g_e \hbar\gamma_I kT} \frac{\mathcal{A}}{2S} \quad (4.200)$$

$$= -\frac{\mu_{\text{eff}}^2}{3\mu_B g_e \hbar\gamma_I kT} \mathbf{A}, \quad (4.201)$$

where we have written $\mathbf{A} = \mathcal{A}/(2S)$ as the hyperfine tensor per electron. As mentioned earlier the effective electronic magnetic moment in Equation 4.201 can be treated as an empirical parameter which hides all the SO coupling effects, such as the g -shift. The hyperfine tensor \mathbf{A} is calculated in the NR regime, and so if we make the approximations $C^{\text{con}} = C^{\text{FC}}$ and $C^{\text{dip}} = C^{\text{SD}}$, the shielding tensor in this formalism is equivalent to the part $-\chi^{\text{iso}} C^{\text{con}} \mathbf{1} - \chi^{\text{iso}} C^{\text{dip}}$ in Equation 4.190. This model of the paramagnetic shielding tensor is therefore an approximation, as it neglects SO coupling effects in the hyperfine tensor and does not account for magnetic anisotropy, which gives rise to the PCS. Nevertheless it has been shown to be very effective for calculating the contact shifts of solid paramagnetic battery materials [30, 54–56].

4.4.1 The scaling tensor in the presence of magnetic susceptibility anisotropy

The scaling factor picture can be modified in a straightforward manner to also account for the effects of the susceptibility anisotropy due to both the g -anisotropy and ZFS. We note that when the susceptibility anisotropy is taken into account, rather than the scaling factor being a scalar quantity that is proportional to the

isotropic magnetic susceptibility, the scaling factor becomes a tensor with the same spatial properties as the susceptibility tensor. We can back-calculate the scaling factor from the shielding tensor in the susceptibility formalism in Equation 4.182. If we assume that the hyperfine tensor is still well approximated in the NR regime, Equation 4.186 gives is the following expression for the total hyperfine tensor:

$$\mathcal{A} = 2S\mu_0\mu_B g_e \hbar \gamma_I C. \quad (4.202)$$

Rearranging Equation 4.182 gives us

$$\sigma^x = -\frac{B_0\chi}{\mu_0\mu_B g_e S} \cdot \frac{\mathcal{A}}{2\hbar\gamma_I B_0}. \quad (4.203)$$

From here we can define the *scaling tensor* as

$$\frac{B_0}{\mu_0\mu_B g_e S} \chi. \quad (4.204)$$

The physical explanation for this expression comes from the fact that the electronic magnetic moments that contribute to the magnetic susceptibility tensor are orientation-dependent, and so the required scaling of the hyperfine interaction into the paramagnetic regime is also orientation-dependent. When we compare this expression for the shielding with Equation 4.190 we see that it contains the following terms: $-\chi^{\text{iso}}C^{\text{con}}\mathbf{1} - \Delta\chi C^{\text{con}} - \chi^{\text{iso}}C^{\text{dip}} - \Delta\chi \cdot C^{\text{dip}}$, i.e. all the cross terms between the isotropic and anisotropic parts of the susceptibility tensor and the contact and spin-dipolar parts of the hyperfine tensor, with only contributions from the antisymmetric hyperfine tensor missing. Therefore the model of the paramagnetic shielding in terms of a scaling tensor accounts for both the contact shift [53] and PCS [16].

4.5 The Kurland–McGarvey formalism

We complete our survey of the different formalisms for the paramagnetic shielding tensor by examining the classic general treatment by Kurland and McGarvey [37]. The expression for the PCS in the Kurland–McGarvey formalism exactly matches that in the susceptibility formalism introduced in Equation 4.190, namely $-\Delta\chi \cdot C^{\text{dip}}$, but there is a discrepancy in the expressions for the contact shielding, which in the

susceptibility and scaling-factor formalisms is given by $-\chi^{\text{iso}}C^{\text{con}}\mathbf{1}$. This reason for this discrepancy can be understood by noting that in the susceptibility formalism, we neglect the effect of the g -shift in the expression linking the two hyperfine interactions in the definition in Equation 4.186, and choose to write:

$$A^{\text{FC}} = \mu_0\mu_B g_e \hbar \gamma_I C^{\text{con}}, \quad (4.205)$$

$$A^{\text{SD}} = \mu_0\mu_B g_e \hbar \gamma_I C^{\text{dip}}. \quad (4.206)$$

This is the approach taken in the exposition of the scaling-factor models in section 4.4. However there may be cases in which the g -shift in Equation 4.186 cannot be neglected. The correct expression for C to use in the susceptibility formalism is given by inverting Equation 4.186 to give [200]:

$$C = \frac{1}{\mu_0\mu_B \hbar \gamma_I} [\mathbf{g}^T]^{-1} \cdot \mathbf{A}. \quad (4.207)$$

This, in turn, gives us the following expression for the paramagnetic shielding in the susceptibility formalism:

$$\sigma^{\chi} = -\frac{1}{\mu_0\mu_B \hbar \gamma_I} \chi \cdot [\mathbf{g}^T]^{-1} \cdot \mathbf{A}. \quad (4.208)$$

We now write the hyperfine tensor as the sum of the NR Fermi-contact and spin-dipolar parts, which results in a shielding tensor which is the sum of two terms:

$$\sigma^{\chi} = -\frac{A^{\text{FC}}}{\mu_0\mu_B \hbar \gamma_I} \chi \cdot [\mathbf{g}^T]^{-1} - \frac{1}{\mu_0\mu_B \hbar \gamma_I} \chi \cdot [\mathbf{g}^T]^{-1} \cdot A^{\text{SD}}. \quad (4.209)$$

The first term gives us the Fermi-contact shift and associated SA, whilst the second gives us the PCS and the SA due to the spin-dipolar interaction.

The isotropic contact shielding is given by

$$\sigma^{\text{FC}} = -\frac{A^{\text{FC}}}{3\mu_0\mu_B \hbar \gamma_I} \text{Tr} \left[\chi \cdot [\mathbf{g}^T]^{-1} \right] \quad (4.210)$$

The trace can, of course, be computed in any spatial reference frame. For convenience, we choose the common PAF of both the susceptibility and symmetric part of the g -tensor. Evaluating the trace then gives us

the Kurland–McGarvey expression for the contact shielding [37]:

$$\sigma^{\text{FC}} = -\frac{A^{\text{FC}}}{3\mu_0\mu_B\hbar\gamma_I} \left[\frac{\tilde{\chi}_{xx}}{\tilde{g}_{xx}} + \frac{\tilde{\chi}_{yy}}{\tilde{g}_{yy}} + \frac{\tilde{\chi}_{zz}}{\tilde{g}_{zz}} \right]. \quad (4.211)$$

On comparing this expression with that due to the scaling-factor model in Equation 4.199, we see that the two are only equal when the g -tensor is equal to the free-electron g -factor, which is one of the initial assumptions of the scaling-factor model [53]. The Kurland–McGarvey expression for the contact shielding in Equation 4.211 can therefore be regarded as a generalization of the contact shielding calculated using the scaling-factor approach in the susceptibility formalism. In commenting on the difference between the two expressions, we note that to use the Kurland–McGarvey expression we need to know the principal values of the susceptibility tensor, which cannot be independently measured for molecules in solution, or for solid powders, and may also be difficult to determine for single crystals, as discussed in chapter 7. The scaling-factor expression, on the other hand, only requires knowledge of the isotropic susceptibility, which can be readily obtained for all these samples. Therefore the scaling-factor model is almost always more convenient to use than the Kurland–McGarvey formula.

The pseudo-contact shielding is given by the expression

$$\sigma^{\text{PCS}} = -\frac{1}{3\mu_0\mu_B\hbar\gamma_I} \text{Tr} \left[\chi \cdot [\mathbf{g}^{\text{T}}]^{-1} \cdot \mathbf{A}^{\text{SD}} \right]. \quad (4.212)$$

If we write \mathbf{A}^{SD} in terms of \mathbf{C}^{SD} via Equation 3.102 we obtain

$$\sigma^{\text{PCS}} = -\frac{1}{3} \text{Tr} \left[\chi' \cdot \mathbf{C}^{\text{SD}} \right], \quad (4.213)$$

where $\chi' = \chi \cdot [\mathbf{g}^{\text{T}}]^{-1} g_e$ is the pseudo-susceptibility tensor defined by Benda et al. in their description of the PCS obtained following a first-principles calculation of χ via the g - and ZFS tensors [216]. As for the contact shielding, there is a discrepancy between this expression for the pseudo-contact shielding and that from the susceptibility formalism, $-\Delta\chi \cdot \mathbf{C}^{\text{dip}}$. The reason for this discrepancy can be traced back to the difference between the NR hyperfine spin-dipolar tensor \mathbf{C}^{SD} and the antisymmetric tensor in the presence of SO coupling \mathbf{C}^{dip} . The former is a ‘true’ dipolar coupling, and may be represented as a point-dipolar interaction where appropriate, whereas the latter is the second-rank component of \mathbf{C} that is proportional to

$[g^T]^{-1} \cdot \mathbf{A}$ and is not a pure spin-dipolar contribution, as there is a contribution from the g -anisotropy. Care is needed in differentiating between these two cases.

4.6 Key concepts

- The coupling between the electronic spin and orbital angular momentum changes the form of the EPR parameters, resulting in the Hamiltonian of Equation 4.36.
- The free-electron g -factor is modified so that it becomes a spatially anisotropic g -tensor.
- The hyperfine tensor gains additional contributions to the isotropic and symmetric parts, as well as an antisymmetric part.
- For electronic spins greater than $1/2$ there is also a zero-field splitting interaction.
- The SO-induced changes to the EPR parameters also change the form of the paramagnetic shielding tensor, as given in the EPR formalism (Equation 4.109).
- The SO coupling also introduces anisotropy to the bulk magnetic properties, with the magnetic susceptibility becoming a spatially anisotropic tensor (Equation 4.173).
- The paramagnetic shielding can also be calculated in terms of the susceptibility tensor, as in Equation 4.189.
- The paramagnetic shielding due to SO coupling can also be approximated by a scaling of the NR hyperfine tensor. The scaling factor contains an empirical effective electronic magnetic moment that can be calculated, or measured separately (Equation 4.201).
- The susceptibility formalism also provides the Kurland–McGarvey expressions for the contact and pseudo-contact shieldings (Equations 4.211 and 4.213). These expressions may be regarded as generalizations of those obtained from the scaling-factor formalism.

Chapter 5

The interpretation of the paramagnetic shielding tensor of *d*-block transition-metal ions

This chapter contains a full discussion of the various terms that arise from the expression for the paramagnetic shielding tensor presented in chapter 4, and how they may be interpreted in terms of the structural and electronic properties of the system under study. We explore the form of the shielding tensor in two different formalisms: the EPR formalism, in terms of the molecular/atomic-level EPR tensor parameters, and the susceptibility formalism, in terms of the bulk magnetic susceptibility tensor. In each formalism the shielding tensor is broken down into a number of contributions that can be grouped according to the different parts of the hyperfine interaction. There are three such groups of terms, corresponding to the isotropic contact interaction, the symmetric anisotropic spin-dipolar interaction, and the antisymmetric hyperfine interaction. We derive explicit formulae for all these contributions using both formalisms, and link both approaches together. It is particularly important to link the two formalisms, so that we can compare the forms of the paramagnetic shielding tensor we obtain from each, and to be able to judge whether the differences we observe are merely superficial, or due to the fundamental differences between the two pictures.

5.1 Correspondence between the EPR and susceptibility formalisms of the paramagnetic shielding tensor

The terms in both the EPR and susceptibility formalisms are listed in Table 5.1 and ordered into three groups: terms giving rise to the contact shift (con), the dipolar shift (dip), and the shift from the antisymmetric part of the hyperfine tensor (as). We recall that $A^{\text{SD},2}$ is not a long-range interaction term, unlike A^{SD} , and that the notation ‘SD,2’ is somewhat misleading. Nevertheless we include it with the other dipolar terms, since it is also a rank-two tensor and shares the same angular properties.

We see that the correspondence between the formalisms is not perfect, as for example in the lack of rank-one contact shielding terms in the susceptibility formalism. This reason for this discrepancy is that in the EPR formalism the magnetic anisotropy of the metal ion is accounted for by the local SO coupling effects which give rise to the g -anisotropy and ZFS, whereas in the susceptibility formalism the magnetic anisotropy is described wholly as a bulk effect in the magnetic susceptibility tensor. So for instance we see that the rank-one contact shielding tensor components are due to the antisymmetric part of the g -tensor in the EPR formalism. In the susceptibility formalism, on the other hand, the antisymmetric part of the g -tensor is ‘hidden’ in the susceptibility tensor, which itself is symmetric and so does not produce any rank-one terms in the contact shielding. For the spin-dipolar interaction the antisymmetric shielding terms are present, but we will see that these are due to the coupling of the symmetric susceptibility anisotropy tensor with the dipolar coupling tensor. However we do not dwell on this specific point, since the rank-one shielding terms are unobservable under high-field conditions. A second reason for any possible discrepancy is that the terms present in the EPR formalism form a series expansion in the fine structure constant α , with only terms of order up to and including α^4 being retained.

Throughout this chapter we assume that the chemical shielding interaction is in the high-field approximation. Even though this approximation may not be valid for the ZFS and electron Zeeman interactions in the EPR Hamiltonian, it can be applied more safely to the paramagnetic shielding interaction as the latter is obtained by scaling down the hyperfine tensor, as we have seen previously [53]. In the high-field

Type	Term	Order	σ^S		σ^X	
			With ZFS Expression ^a	Rank	Without ZFS Expression ^b	Rank
con	1	α^2	$g_e A^{FC} Z$	0, 2	$g_e A^{FC}$	0
	3	α^4	$g_e A^{FC,2} Z$	0, 2	$g_e A^{FC,2}$	0
	6	α^4	$\Delta g_{iso} A^{FC} Z$	0, 2	$\Delta g_{iso} A^{FC}$	0
	8	α^4	$A^{FC} \Delta g \cdot Z$	0, 1, 2	$A^{FC} \Delta g$	1, 2
dip	2	α^2	$g_e Z \cdot A^{SD}$	0, 1, 2	$g_e A^{SD}$	2
	4	α^4	$g_e Z \cdot A^{SD,2}$	0, 1, 2	$g_e A^{SD,2}$	2
	7	α^4	$\Delta g_{iso} Z \cdot A^{SD}$	0, 1, 2	$\Delta g_{iso} A^{SD}$	2
	9	α^4	$\Delta g \cdot Z \cdot A^{SD}$	0, 1, 2	$\Delta g \cdot A^{SD}$	0, 1, 2
as	5	α^4	$g_e Z \cdot A^{as}$	1, 2	$g_e A^{as}$	1
					$-\chi^{iso} C^{con}$	0
					$-\Delta \chi C^{con}$	2
					$-\chi^{iso} C^{dip}$	2
					$-\Delta \chi \cdot C^{dip}$	0, 1, 2
					$-\chi^{iso} C^{as}$	1
					$-\Delta \chi \cdot C^{as}$	1, 2

Table 5.1: Comparison of the terms contributing to the paramagnetic shielding tensor arising from the EPR formalism [86, 88] with those arising from the susceptibility formalism. The different terms are separated into groups arising from the contact interaction (con), spin-dipolar interaction (dip), and the antisymmetric hyperfine interaction (as). The spatial irreducible spherical tensor ranks have been included for situations in which the ZFS is both present and absent.

^aMultiply by $-\mu_B/(h\gamma I)$ to obtain full shielding expression

^bMultiply by $-\mu_B S(S+1)/(3h\gamma kT)$ to obtain full shielding expression

approximation the paramagnetic shielding in terms of irreducible spherical tensors is given by Equation 2.96:

$$\sigma^{(1)} = -\sqrt{\frac{1}{3}}\sigma_{00}^S + \sqrt{\frac{2}{3}}\sigma_{20}^S \quad (5.1)$$

$$= \sigma_{\text{iso}}^S + \sqrt{\frac{2}{3}} \sum_{m=-2}^{+2} \tilde{\sigma}_{2m}^S \exp(-im\alpha_{\text{PL}}) d_{m0}^2(\beta_{\text{PL}}), \quad (5.2)$$

from which we see that we are only able to observe the isotropic and symmetric parts of the shielding tensor. Hence we do not concern ourselves with the rank-one parts of the shielding tensor. In Cartesian tensor components the high-field paramagnetic shielding adopts the simple form

$$\sigma^{(1)} = \sigma_{zz}^S. \quad (5.3)$$

The same interaction can also be written in terms of the susceptibility expression for the paramagnetic shielding as follows:

$$\sigma^{(1)} = -\sqrt{\frac{1}{3}}\sigma_{00}^X + \sqrt{\frac{2}{3}}\sigma_{20}^X \quad (5.4)$$

$$= \sigma_{\text{iso}}^X + \sqrt{\frac{2}{3}} \sum_{m=-2}^{+2} \tilde{\sigma}_{2m}^X \exp(-im\alpha_{\text{PL}}) d_{m0}^2(\beta_{\text{PL}}), \quad (5.5)$$

$$= \sigma_{zz}^X. \quad (5.6)$$

We now proceed to analyse the terms in Table 5.1 in both formalisms, and examine in detail the contributions from the contact, spin-dipolar, and antisymmetric hyperfine interactions.

5.2 Summary of the relevant tensor parameters

The interpretation of the paramagnetic shielding tensor using either the susceptibility or EPR formalisms requires the definition of a number of spatial tensors.

The magnetic susceptibility tensor

The magnetic susceptibility tensor χ is symmetric, and can be decomposed into two components as follows:

$$\chi = \chi^{\text{iso}} \mathbf{1} + \Delta\chi, \quad (5.7)$$

where χ^{iso} is the isotropic part, and $\Delta\chi$ is the traceless and symmetric susceptibility anisotropy. The susceptibility anisotropy is parameterised according to one of two conventions. The first is in terms of the axial and rhombic anisotropies $\Delta\chi_{\text{ax}}$ and $\Delta\chi_{\text{rh}}$, which are defined in terms of the PAF components $\tilde{\chi}_{ii}$ as

$$\Delta\chi_{\text{ax}} = \tilde{\chi}_{zz} - \frac{1}{2}(\tilde{\chi}_{xx} + \tilde{\chi}_{yy}), \quad (5.8)$$

$$\Delta\chi_{\text{rh}} = \tilde{\chi}_{xx} - \tilde{\chi}_{yy}. \quad (5.9)$$

The PAF components are defined so that $\tilde{\chi}_{zz} \geq \tilde{\chi}_{yy} \geq \tilde{\chi}_{xx}$. Alternatively we can define the PAF components to satisfy $|\tilde{\chi}_{zz} - \chi^{\text{iso}}| \geq |\tilde{\chi}_{xx} - \chi^{\text{iso}}| \geq |\tilde{\chi}_{yy} - \chi^{\text{iso}}|$, and define the anisotropy $\Delta\chi$ and asymmetry parameter η^x as

$$\Delta\chi = \tilde{\chi}_{zz} - \chi^{\text{iso}}, \quad (5.10)$$

$$\eta^x = \frac{\tilde{\chi}_{yy} - \tilde{\chi}_{xx}}{\Delta\chi}. \quad (5.11)$$

The orientation of the PAF of $\Delta\chi$ is specified by the Euler angles $\Omega_{\text{XL}} = (\alpha_{\text{XL}}, \beta_{\text{XL}}, \gamma_{\text{XL}})$.

The susceptibility tensor is given in terms of the EPR parameters by the following expression

$$\chi = \mu_0 \mu_{\text{B}}^2 \mathbf{g} \cdot \mathbf{Z} \cdot \mathbf{g}^T. \quad (5.12)$$

The expressions for both the isotropic and anisotropic parts of the susceptibility contain the g -shift and ZFS tensors, which are both due to SO coupling.

The hyperfine coupling tensor

The hyperfine coupling tensor \mathbf{A} takes the following form

$$\mathbf{A} = (\mathbf{A}^{\text{FC}} + \mathbf{A}^{\text{FC},2}) \mathbf{1} + \mathbf{A}^{\text{as}} + (\mathbf{A}^{\text{SD}} + \mathbf{A}^{\text{SD},2}). \quad (5.13)$$

The isotropic part A^{iso} is due to the NR Fermi-contact and the SO second-order contact interactions:

$$A^{\text{iso}} = A^{\text{FC}} + A^{\text{FC},2}. \quad (5.14)$$

The antisymmetric part is due entirely to the SO-coupling term \mathbf{A}^{as} and is characterised by the antisymmetric anisotropy ζ^A which is given by

$$\zeta^A = \sqrt{(A_{xy}^{\text{as}})^2 + (A_{yz}^{\text{as}})^2 + (A_{xz}^{\text{as}})^2}. \quad (5.15)$$

The orientation of the PAF of \mathbf{A}^{as} is specified by the Euler angles $\Omega_{\text{AAL}} = (\alpha_{\text{AAL}}, \beta_{\text{AAL}}, \gamma_{\text{AAL}})$. The symmetric part is due to the NR and SO spin-dipolar terms \mathbf{A}^{SD} and $\mathbf{A}^{\text{SD},2}$. The symmetric anisotropy ΔA and asymmetry parameter η^A are therefore given by

$$\Delta A = \tilde{A}_{zz}^{\text{SD}} + \tilde{A}_{zz}^{\text{SD},2}, \quad (5.16)$$

$$\eta^A = \frac{\tilde{A}_{yy}^{\text{SD}} + \tilde{A}_{yy}^{\text{SD},2} - \tilde{A}_{xx}^{\text{SD}} - \tilde{A}_{xx}^{\text{SD},2}}{\Delta A}. \quad (5.17)$$

The tilde denotes that the matrix elements are evaluated in the PAF of the symmetric part of the *whole* hyperfine tensor, i.e. $\mathbf{A}^{\text{SD}} + \mathbf{A}^{\text{SD},2}$. The orientation of this PAF is specified by the Euler angles $\Omega_{\text{ASL}} = (\alpha_{\text{ASL}}, \beta_{\text{ASL}}, \gamma_{\text{ASL}})$. Note that in the point-dipole approximation, the interaction is given by the long-range NR term, and the anisotropy and asymmetry parameter are

$$\Delta A = 2b_{SI}, \quad (5.18)$$

$$\eta^A = 0, \quad (5.19)$$

where b_{SI} is the dipolar coupling constant.

In the susceptibility formalism we make use of the reduced hyperfine coupling tensor \mathbf{C} , which comprises an isotropic contact term C^{con} , antisymmetric term C^{as} , and a symmetric spin-dipolar term C^{dip} . The isotropic contact term is equal to

$$C^{\text{con}} = \frac{1}{3S} \rho^{\alpha-\beta}(\mathbf{0}), \quad (5.20)$$

i.e. it is proportional to the unpaired electron spin density at the nucleus $\rho^{\alpha-\beta}(\mathbf{0})$. The antisymmetric hyperfine

term C^{as} is characterised by the antisymmetric anisotropy ζ^C , which is given by

$$\zeta^C = \sqrt{(C_{xy}^{\text{as}})^2 + (C_{yz}^{\text{as}})^2 + (C_{xz}^{\text{as}})^2}. \quad (5.21)$$

The symmetric anisotropy ΔC and asymmetry parameter η^C are due to the spin-dipolar interaction and are given by

$$\Delta C = \tilde{C}_{zz}^{\text{dip}}, \quad (5.22)$$

$$\eta^C = \frac{\tilde{C}_{yy}^{\text{dip}} - \tilde{C}_{xx}^{\text{dip}}}{\Delta C}. \quad (5.23)$$

We will see that the corresponding expressions in the point-dipole approximation are of interest; these are derived from Equations 3.115–3.119 to give:

$$\Delta C = \frac{1}{2\pi R^3}, \quad (5.24)$$

$$\eta^C = 0. \quad (5.25)$$

The orientations of the PAFs of the antisymmetric and symmetric parts of C are specified by the Euler angles $\Omega_{\text{CAL}} = (\alpha_{\text{CAL}}, \beta_{\text{CAL}}, \gamma_{\text{CAL}})$ and $\Omega_{\text{CSL}} = (\alpha_{\text{CSL}}, \beta_{\text{CSL}}, \gamma_{\text{CSL}})$ respectively.

The g -tensor

The g -tensor has the following generic form:

$$\mathbf{g} = (g_e + \Delta g_{\text{iso}}) \mathbf{1} + \mathbf{\Delta g}, \quad (5.26)$$

where the isotropic free-electron g -factor g_e is the NR contribution. The effect of SO coupling manifests itself in the g -shift part of the tensor, which comprises an isotropic part Δg_{iso} and an anisotropic part $\mathbf{\Delta g}$ which, in general, contains both symmetric and antisymmetric contributions.

The isotropic g -tensor is simply

$$g^{\text{iso}} = g_e + \Delta g_{\text{iso}}. \quad (5.27)$$

The anisotropic g -tensor is defined by both the antisymmetric and symmetric anisotropy parameters. The antisymmetric g -anisotropy ζ^g is given by

$$\zeta^g = \frac{1}{2} \sqrt{(\Delta g_{xy} - \Delta g_{yx})^2 + (\Delta g_{yz} - \Delta g_{zy})^2 + (\Delta g_{xz} - \Delta g_{zx})^2}, \quad (5.28)$$

and the symmetric g -anisotropy Δg and asymmetry η^g are:

$$\Delta g = \tilde{\Delta} g_{zz}, \quad (5.29)$$

$$\eta^g = \frac{\tilde{\Delta} g_{yy} - \tilde{\Delta} g_{xx}}{\Delta g}, \quad (5.30)$$

where the $\tilde{\Delta} g_{ii}$ are the principal components of the symmetric part of $\Delta \mathbf{g}$ in its PAF. The orientations of the PAFs of the antisymmetric and symmetric parts of \mathbf{g} are specified by the Euler angles $\Omega_{\text{GAL}} = (\alpha_{\text{GAL}}, \beta_{\text{GAL}}, \gamma_{\text{GAL}})$ and $\Omega_{\text{GSL}} = (\alpha_{\text{GSL}}, \beta_{\text{GSL}}, \gamma_{\text{GSL}})$ respectively.

The zero-field splitting and Z tensors

The final interaction of interest for single transition-metal ions is the ZFS, which is characterised by a traceless and symmetric spatial tensor D . This tensor is described by the axial and rhombic anisotropy parameters D and E which are conventionally defined in terms of the principal values \tilde{D}_{ii} as follows:

$$D = \tilde{D}_{zz} - \frac{1}{2} (\tilde{D}_{xx} + \tilde{D}_{yy}), \quad (5.31)$$

$$E = \frac{1}{2} (\tilde{D}_{xx} - \tilde{D}_{yy}). \quad (5.32)$$

Note that the definition of the rhombic anisotropy E differs from the rhombic susceptibility $\Delta \chi_{\text{rh}}$ by a factor of 1/2 included in the former. Alternatively we can adopt an alternative convention and specify the ZFS anisotropy ΔD and asymmetry parameter η^D as follows:

$$\Delta D = \tilde{D}_{zz}, \quad (5.33)$$

$$\eta^D = \frac{\tilde{D}_{yy} - \tilde{D}_{xx}}{\Delta D}, \quad (5.34)$$

where we use the following convention for the ordering of the principal values: $|\tilde{D}_{zz}| \geq |\tilde{D}_{xx}| \geq |\tilde{D}_{yy}|$. The orientation of the PAF of D is specified by the Euler angles $\Omega_{DL} = (\alpha_{DL}, \beta_{DL}, \gamma_{DL})$.

The ZFS tensor does not usually enter the expression for the paramagnetic shielding directly, but rather does so within the tensor Z , which is an average of a product of electronic spin operators over the ZFS energy levels. The tensor can be written as the sum of an isotropic part Z^{iso} and a symmetric anisotropic part ΔZ :

$$Z = Z^{\text{iso}} \mathbf{1} + \Delta Z. \quad (5.35)$$

We recall that a general expression for Z is given by the van den Heuvel–Soncini theory in Equation 4.113, of which the Pennanen–Vaara theory (Equation 4.121) is a high-temperature approximation. As for the other symmetric anisotropic tensors, we can define the anisotropy ΔZ and asymmetry parameter η^Z according to

$$\Delta Z = \tilde{Z}_{zz} - Z^{\text{iso}}, \quad (5.36)$$

$$\eta^Z = \frac{\tilde{Z}_{yy} - \tilde{Z}_{xx}}{\Delta Z}, \quad (5.37)$$

where the \tilde{Z}_{ii} are the principal components of the whole Z tensor which have been ordered according to: $|\tilde{Z}_{zz} - Z^{\text{iso}}| \geq |\tilde{Z}_{xx} - Z^{\text{iso}}| \geq |\tilde{Z}_{yy} - Z^{\text{iso}}|$. The PAF of Z coincides with that of D , and therefore has an orientation specified by the Euler angles $\Omega_{ZL} = \Omega_{DL}$.

In general the expressions for Z^{iso} , ΔZ , and η^Z are complicated. However, as has been shown in the previous chapter, when we apply the high-temperature limit up to second order in $1/(kT)$, as shown in Equation 4.131, they simplify to the expressions derived by Bleaney [61]:

$$Z^{\text{iso}} \approx \frac{S(S+1)}{3kT}, \quad (5.38)$$

$$\Delta Z \approx -\frac{S(S+1)(2S-1)(2S+3)}{30(kT)^2} D. \quad (5.39)$$

In this high-temperature limit the first-order term is wholly isotropic, and the second-order term is wholly anisotropic. We subsequently see that, in this regime, the anisotropy and asymmetry of Z are proportional to

those of D :

$$\Delta Z = -\frac{S(S+1)(2S-1)(2S+3)}{30(kT)^2}\Delta D, \quad (5.40)$$

$$\eta^Z = \eta^D. \quad (5.41)$$

It is worth examining the temperature dependence of Z^{iso} , ΔZ , and η^Z more closely through an example. In section 4.2.3 we calculated the Z -matrix of an electronic spin $S = 1$ subject to a ZFS interaction with rhombic symmetry. The principal values of Z were given in Equations 4.151–4.153. They are reproduced below for convenience, having been reordered according to the Haebleren convention assuming $D = 5E/2 > 0$:

$$\tilde{Z}_{xx} = \frac{1}{E} \frac{e^{-\beta(D/3-E)} - e^{-\beta(D/3+E)}}{e^{-\beta(D/3+E)} + e^{2\beta D/3} + e^{-\beta(D/3-E)}}, \quad (5.42)$$

$$\tilde{Z}_{yy} = \frac{2}{D+E} \frac{e^{2\beta D/3} - e^{-\beta(D/3+E)}}{e^{-\beta(D/3+E)} + e^{2\beta D/3} + e^{-\beta(D/3-E)}}, \quad (5.43)$$

$$\tilde{Z}_{zz} = \frac{2}{D-E} \frac{e^{2\beta D/3} - e^{-\beta(D/3-E)}}{e^{-\beta(D/3+E)} + e^{2\beta D/3} + e^{-\beta(D/3-E)}}. \quad (5.44)$$

The previous example focussed on the case where the axial and rhombic anisotropies are $D = 50 \text{ cm}^{-1}$ and $E = 20 \text{ cm}^{-1}$ respectively, giving ordered principal values of D of $\tilde{D}_{xx} = 33.33 \text{ cm}^{-1}$, $\tilde{D}_{yy} = 3.33 \text{ cm}^{-1}$, and $\tilde{D}_{zz} = -36.67 \text{ cm}^{-1}$. Figure 5.1 shows plots of the isotropic value and anisotropy of Z as a function of temperature. Part (a) compares the isotropic values of Z calculated from Equations 5.42–5.44 with the high-temperature Bleaney expression in Equation 5.38. The comparison of the values of ΔZ calculated from Equations 5.42–5.44 with the high-temperature Bleaney expression in Equation 5.40 is shown in (b). Interestingly, we note that the asymmetry parameter η^Z is temperature-independent, and is always equal to the ZFS asymmetry parameter η^D , taking in this case the value $\eta^Z = 9/11$.

We note that, as seen previously in section 4.2.3, the curves calculated from the high-temperature approximation match the exact curves very well down to a temperature of 100 K. The general value of this high-temperature ‘cut-off’ threshold depends on the values of $D/(kT)$ and $E/(kT)$. We also see that the anisotropy of Z tends to zero at higher temperatures more quickly than the isotropic part, on account of the latter varying as $1/(kT)$, and the former being due to a second-order effect with a temperature dependence of $1/(kT)^2$.

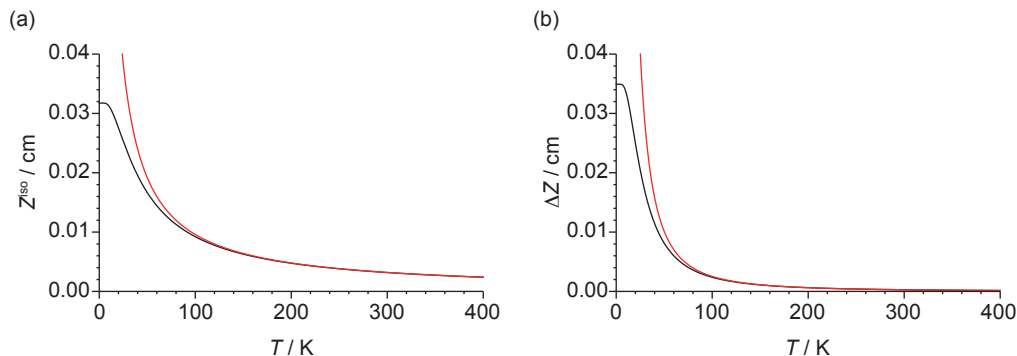


Figure 5.1: Example plots of the isotropic value Z^{iso} and anisotropy ΔZ of the \mathbf{Z} -tensor as a function of temperature. The isotropic part is plotted in (a), and the anisotropy is plotted in (b). The asymmetry parameter is temperature-independent. For both plots the curves in black are calculated from the general EPR expressions in Equations 5.42–5.44. The red curves are plotted from the high-temperature Bleaney expressions in Equations 5.38 and 5.40. The electronic spin is $S = 1$, and the ZFS parameters are $D = 50 \text{ cm}^{-1}$ and $E = 20 \text{ cm}^{-1}$, giving principal values of $\tilde{D}_{xx} = 33.33 \text{ cm}^{-1}$, $\tilde{D}_{yy} = 3.33 \text{ cm}^{-1}$, $\tilde{D}_{zz} = -36.67 \text{ cm}^{-1}$, and an anisotropy and asymmetry of $\Delta D = -36.67 \text{ cm}^{-1}$, and $\eta^D = 9/11$.

5.3 The paramagnetic shift in the susceptibility formalism

We now examine in detail the terms contributing to the paramagnetic shielding tensor according to the susceptibility formalism, as listed in Table 5.1. In this section we treat the susceptibility tensor as an empirical quantity that can be either measured experimentally or calculated using Equation 5.12. However we remember that χ^{iso} depends on both NR and SO coupling effects, and that $\Delta\chi$ is due entirely to SO coupling, and so the simple expressions obtained in this section actually hide a high level of complexity. At this stage we do not make the explicit link between the various terms and the EPR parameters, the discussion of which we defer until section 5.4. We separate the terms into three groups, which are (1) terms due to a contact interaction (contact shielding), (2) terms due to a spin-dipolar interaction (dipolar shielding), and (3) terms due to the antisymmetric hyperfine interaction (antisymmetric hyperfine shielding). Within each group we examine the isotropic and symmetric anisotropic contributions to the shielding tensor. Note that as the antisymmetric shielding is not observable under high-field conditions we neglect it.

5.3.1 The contact shift and shift anisotropy

The contact shielding contains two terms, namely $-\chi^{\text{iso}}C^{\text{con}}$ and $-C^{\text{con}}\Delta\chi$, which are of spherical-tensor ranks 0 and 2. They contribute to the isotropic shift and shift anisotropy respectively.

The contact shift

The isotropic contact shielding $\sigma_{\text{iso}}^{\text{con},\chi}$ is proportional to both the isotropic susceptibility and the contact coupling constant:

$$\sigma_{\text{iso}}^{\text{con},\chi} = -\chi^{\text{iso}}C^{\text{con}}. \quad (5.45)$$

The contact coupling constant is proportional to the unpaired electron density at the nucleus, and so $\sigma_{\text{iso}}^{\text{con},\chi}$ can be written as

$$\sigma_{\text{iso}}^{\text{con},\chi} = -\frac{\chi^{\text{iso}}}{3S}\rho^{\alpha-\beta}(\mathbf{0}). \quad (5.46)$$

Using the chemical shift convention we can also define the contact shift as $\delta_{\text{iso}}^{\text{con},\chi} = -\sigma_{\text{iso}}^{\text{con},\chi}$, which then has the form given by McConnell and Chesnut [35]

$$\delta_{\text{iso}}^{\text{con},\chi} = \chi^{\text{iso}}C^{\text{con}} \quad (5.47)$$

$$= \frac{\chi^{\text{iso}}}{3S}\rho^{\alpha-\beta}(\mathbf{0}). \quad (5.48)$$

There are three things to note about the contact shift. Firstly it is proportional to the isotropic magnetic susceptibility, indicating that paramagnetic metal ions that exhibit a stronger tendency for their electronic magnetic moments to align with the external magnetic field also give larger contact shifts. Secondly the contact shift is also proportional to the magnitude of the unpaired electron density that is present at the nuclear site. This indicates that larger shifts result from the more extensive overlap between the orbitals of the metal ion and the s -orbital of the nucleus via the orbitals of any bridging atoms. Finally the sign of the contact shift is the same as that of the unpaired electron density at the nucleus. Therefore the contact shift can be used as a tool to determine whether the unpaired electrons are delocalised onto the nucleus, giving a positive shift, or whether the unpaired electrons polarise a negative spin density at the nucleus, which gives a negative shift [217].

The contact shift anisotropy

The term $-C^{\text{con}} \Delta\chi$ gives rise to a purely anisotropic paramagnetic chemical shielding which is parameterised by the anisotropy $\Delta\sigma^{\text{con},\chi}$ and asymmetry parameter $\eta^{\text{con},\chi}$. The form of these anisotropy parameters is easily deduced by noting that this contribution to the shielding tensor has exactly the same symmetry as $\Delta\chi$, and therefore the same PAF. The value of $\Delta\sigma^{\text{con},\chi}$ is then simply proportional to $\Delta\chi$, and the $\eta^{\text{con},\chi}$ is exactly equal to η^χ :

$$\Delta\sigma^{\text{con},\chi} = -C^{\text{con}} \Delta\chi \quad (5.49)$$

$$= -\frac{\Delta\chi}{3S} \rho^{\alpha-\beta}(\mathbf{0}), \quad (5.50)$$

$$\eta^{\text{con},\chi} = \eta^\chi. \quad (5.51)$$

This form of the contact shielding anisotropy has obvious similarities to that of the isotropic contact shift. The size and sign of $\Delta\sigma^{\text{con},\chi}$ both depend on the size and sign of the unpaired electron density transferred to the nuclear site. However the anisotropy is proportional to $\Delta\chi$, rather than χ^{iso} , indicating that metals which exhibit a greater degree of spatial anisotropy in the tendency for their electronic magnetic moments to align with the external field also give larger contact shielding anisotropies. In addition the shape of the shielding tensor, as described by the ellipsoid in Figure 2.7, exactly matches the shape of the susceptibility tensor.

5.3.2 The spin-dipolar shift and shift anisotropy

The spin-dipolar shielding contribution to the paramagnetic chemical shielding tensor has two terms, namely $-\chi^{\text{iso}} C^{\text{dip}}$ and $-\Delta\chi \cdot C^{\text{dip}}$. The former has a simple form and is purely anisotropic with spherical-tensor rank 2. However the latter is more complicated as it couples together the two rank-two tensors $\Delta\chi$ and C^{dip} and therefore requires special consideration.

The secular part $\sigma^{(1)}$ of $-\Delta\chi \cdot C^{\text{dip}}$ is, in terms of the Cartesian tensor components:

$$\sigma^{(1)} = -\Delta\chi_{zx} C_{xz}^{\text{dip}} - \Delta\chi_{zy} C_{yz}^{\text{dip}} - \Delta\chi_{zz} C_{zz}^{\text{dip}}. \quad (5.52)$$

It proves convenient to rewrite this expression in terms of the irreducible spherical tensor components $\Delta\chi_{2m}$

and C_{2m}^{dip} :

$$\sigma^{(1)} = -\frac{2}{3}\Delta\chi_{20}C_{20}^{\text{dip}} + \frac{1}{2}\Delta\chi_{2-1}C_{2+1}^{\text{dip}} + \frac{1}{2}\Delta\chi_{2+1}C_{2-1}^{\text{dip}}. \quad (5.53)$$

The spatial dependence of $\sigma^{(1)}$ can now be deduced by writing the products $\Delta\chi_{2m}C_{2-m}^{\text{dip}}$ in terms of the coupled irreducible spherical tensor components $W_{L0}(22)$, which are defined as

$$W_{L0}(22) = \sum_{m=-2}^{+2} \langle 22m - m|L0 \rangle \Delta\chi_{2m}C_{2-m}^{\text{dip}}, \quad (5.54)$$

where the rank L can take values between 0 and 4 in integer steps. The inverse of Equation 5.54 is

$$\Delta\chi_{2m}C_{2-m}^{\text{dip}} = \sum_{L=0}^4 \langle 22m - m|L0 \rangle W_{L0}(22). \quad (5.55)$$

Substituting Equation 5.55 into Equation 5.53 we obtain the following expression for the secular shielding in terms of the coupled tensor components:

$$\sigma^{(1)} = \sum_{L=0}^4 a_L W_{L0}(22), \quad (5.56)$$

where the coefficients a_L are given by

$$a_L = -\frac{2}{3} \langle 2200|L0 \rangle + \frac{1}{2} \langle 22 - 1 + 1|L0 \rangle + \frac{1}{2} \langle 22 + 1 - 1|L0 \rangle \quad (5.57)$$

$$= -\frac{2}{3} \langle 2200|L0 \rangle + \frac{1}{2} (1 + (-1)^L) \langle 22 - 1 + 1|L0 \rangle. \quad (5.58)$$

The Clebsch–Gordan coefficients are easily evaluated to obtain

$$a_0 = -\frac{\sqrt{5}}{3}, \quad (5.59)$$

$$a_1 = 0, \quad (5.60)$$

$$a_2 = \frac{1}{3} \sqrt{\frac{7}{2}}, \quad (5.61)$$

$$a_3 = 0, \quad (5.62)$$

$$a_4 = 0. \quad (5.63)$$

The terms with odd L are zero due to the symmetry properties of the Clebsch–Gordan coefficients. Furthermore we see that there are no terms of rank $L = 4$. This is because the coupling of the two tensors is a standard matrix multiplication. The only terms that contribute to the secular shielding tensor are therefore of ranks 0 and 2, which correspond to the isotropic and symmetric anisotropic parts of the interaction. The shielding is therefore given by

$$\sigma^{(1)} = \frac{1}{3} \left(-\sqrt{5}W_{00}(22) + \sqrt{\frac{7}{2}}W_{20}(22) \right). \quad (5.64)$$

The $W_{00}(22)$ term is the only isotropic component of the shielding tensor that originates from the spin-dipolar interaction, and results in the so-called ‘pseudo-contact shift’ (PCS). The shift anisotropy term resulting from $W_{20}(22)$ is present in addition to the shift anisotropy due to the $-\chi^{\text{iso}}C^{\text{dip}}$ term. Both contributions are referred to as spin-dipolar anisotropy. The three contributions are now discussed.

The pseudo-contact shift

The sole isotropic term in the paramagnetic shielding is due to the $W_{00}(22)$ term in Equation 5.64. On comparing this expression with Equation 5.4 we see that the isotropic pseudo-contact shielding $\sigma_{\text{iso}}^{\text{pcs},\chi}$ is given by

$$\sigma_{\text{iso}}^{\text{pcs},\chi} = -\frac{\sqrt{5}}{3}W_{00}(22). \quad (5.65)$$

The isotropic tensor $W_{00}(22)$ is given in terms of $\Delta\chi_{2m}$ and C_{2m}^{dip} by Equation 5.54, which gives the following

$$\sigma_{\text{iso}}^{\text{pcs},\chi} = -\frac{\sqrt{5}}{3} \sum_{m=-2}^{+2} \langle 22m - m|00 \rangle \Delta\chi_{2m} C_{2-m}^{\text{dip}} \quad (5.66)$$

$$= -\frac{1}{3} \sum_{m=-2}^{+2} (-1)^m \Delta\chi_{2m} C_{2-m}^{\text{dip}}, \quad (5.67)$$

where to go to the second line we have used the identity $\langle 22m - m|00 \rangle = (-1)^m / \sqrt{5}$. The sum in Equation 5.67 is recognisable as the generalised scalar product of the tensors $\Delta\chi$ and C^{dip} written in the irreducible spherical tensor basis [190]. Further progress is made by writing $\Delta\chi_{2m}$ and C_{2-m}^{dip} in terms of their PAF values:

$$\sigma_{\text{iso}}^{\text{pcs},\chi} = -\frac{1}{3} \sum_{m'} \tilde{\Delta}\chi_{2m'} \sum_{m''} \tilde{C}_{2m''}^{\text{dip}} \sum_m (-1)^m D_{m'm}^{(2)}(\alpha_{\text{XL}}, \beta_{\text{XL}}, \gamma_{\text{XL}}) D_{m''-m}^{(2)}(\alpha_{\text{CS,L}}, \beta_{\text{CS,L}}, \gamma_{\text{CS,L}}). \quad (5.68)$$

The second Wigner rotation matrix element can be rewritten as

$$D_{m''-m}^{(2)}(\alpha_{\text{CS,L}}, \beta_{\text{CS,L}}, \gamma_{\text{CS,L}}) = (-1)^{m''-m} D_{m-m''}^{(2)}(-\gamma_{\text{CS,L}}, -\beta_{\text{CS,L}}, -\alpha_{\text{CS,L}}), \quad (5.69)$$

where $(-\gamma_{\text{CS,L}}, -\beta_{\text{CS,L}}, -\alpha_{\text{CS,L}})$ are the Euler angles representing the inverse rotation to $(\alpha_{\text{CS,L}}, \beta_{\text{CS,L}}, \gamma_{\text{CS,L}})$.

The pseudo-contact shielding then simplifies to

$$\begin{aligned} \sigma_{\text{iso}}^{\text{pcs},\chi} &= -\frac{1}{3} \sum_{m'} \tilde{\Delta}\chi_{2m'} \sum_{m''} \tilde{C}_{2m''}^{\text{dip}} \sum_m (-1)^{m''} D_{m''m}^{(2)}(\alpha_{\text{XL}}, \beta_{\text{XL}}, \gamma_{\text{XL}}) D_{m-m''}^{(2)}(-\gamma_{\text{CS,L}}, -\beta_{\text{CS,L}}, -\alpha_{\text{CS,L}}) \\ &= -\frac{1}{3} \sum_{m'} \tilde{\Delta}\chi_{2m'} \sum_{m''} \tilde{C}_{2m''}^{\text{dip}} \sum_m D_{m''m}^{(2)}(\alpha_{\text{XL}}, \beta_{\text{XL}}, \gamma_{\text{XL}}) D_{m-m''}^{(2)}(-\gamma_{\text{CS,L}}, -\beta_{\text{CS,L}}, -\alpha_{\text{CS,L}}) \end{aligned} \quad (5.70)$$

$$= -\frac{1}{3} \sum_{m'} \tilde{\Delta}\chi_{2m'} \sum_{m''} \tilde{C}_{2m''}^{\text{dip}} D_{m''-m''}^{(2)}(\alpha_{\text{X,CS}}, \beta_{\text{X,CS}}, \gamma_{\text{X,CS}}), \quad (5.71)$$

where $(\alpha_{\text{X,CS}}, \beta_{\text{X,CS}}, \gamma_{\text{X,CS}})$ are the Euler angles that specify the orientation of the PAF of the susceptibility tensor relative to the PAF of the spin-dipolar tensor. To go to the second line, we have used the fact that $\tilde{C}_{2\pm 1}^{\text{dip}} = 0$ and therefore m'' is always even, and to go to the last line we have used the following closure identity for the Wigner rotation matrix elements [190]:

$$\sum_{m''} D_{mm''}^{(l)}(\alpha_1, \beta_1, \gamma_1) D_{m''m'}^{(l)}(\alpha_2, \beta_2, \gamma_2) = D_{mm'}^{(l)}(\alpha, \beta, \gamma), \quad (5.72)$$

where (α, β, γ) represents the rotation resulting from applying $(\alpha_1, \beta_1, \gamma_1)$ followed by $(\alpha_2, \beta_2, \gamma_2)$. Now we can substitute the explicit expressions for the $\tilde{\Delta}\chi_{2m}$ and the C_{2m}^{dip} in terms of the relevant anisotropy and asymmetry parameters, which are given in Equations 5.22?5.25, to give the final form of the pseudo-contact shielding:

$$\begin{aligned} \sigma_{\text{iso}}^{\text{pcs},\chi} &= -\frac{1}{6} \Delta C \left[\Delta\chi_{\text{ax}} (3 \cos^2(\beta_{\text{X,CS}}) - 1) + \frac{3}{2} \Delta\chi_{\text{rh}} \sin^2(\beta_{\text{X,CS}}) \cos(2\alpha_{\text{X,CS}}) \right. \\ &\quad \left. - \eta^C \left\{ \Delta\chi_{\text{ax}} \sin^2(\beta_{\text{X,CS}}) \cos(2\gamma_{\text{X,CS}}) + \Delta\chi_{\text{rh}} \cos^4(\beta_{\text{X,CS}}/2) \cos(2(\alpha_{\text{X,CS}} + \gamma_{\text{X,CS}})) \right. \right. \\ &\quad \left. \left. + \Delta\chi_{\text{rh}} \sin^4(\beta_{\text{X,CS}}/2) \cos(2(\alpha_{\text{X,CS}} - \gamma_{\text{X,CS}})) \right\} \right]. \end{aligned} \quad (5.73)$$

Using the chemical shift convention we obtain the pseudo-contact shift $\delta_{\text{iso}}^{\text{pcs},\chi}$:

$$\delta_{\text{iso}}^{\text{pcs},\chi} = \frac{1}{6} \Delta C \left[\Delta\chi_{\text{ax}} \left(3 \cos^2(\beta_{\text{X,CS}}) - 1 \right) + \frac{3}{2} \Delta\chi_{\text{rh}} \sin^2(\beta_{\text{X,CS}}) \cos(2\alpha_{\text{X,CS}}) \right. \\ \left. - \eta^C \left\{ \Delta\chi_{\text{ax}} \sin^2(\beta_{\text{X,CS}}) \cos(2\gamma_{\text{X,CS}}) + \Delta\chi_{\text{rh}} \cos^4(\beta_{\text{X,CS}}/2) \cos(2(\alpha_{\text{X,CS}} + \gamma_{\text{X,CS}})) + \Delta\chi_{\text{rh}} \sin^4(\beta_{\text{X,CS}}/2) \cos(2(\alpha_{\text{X,CS}} - \gamma_{\text{X,CS}})) \right\} \right]. \quad (5.74)$$

The Euler angles $(\alpha_{\text{X,CS}}, \beta_{\text{X,CS}}, \gamma_{\text{X,CS}})$ depend only on the internal geometry of the system, and so are independent of crystallite orientation as required for an isotropic shift. We can also specify the orientation between the two PAFs in terms of the Euler angles $(\alpha_{\text{CS,X}}, \beta_{\text{CS,X}}, \gamma_{\text{CS,X}})$, which give the orientation of the PAF of the dipolar coupling tensor relative to the PAF of the susceptibility. In this case Equation 5.71 becomes

$$\sigma_{\text{iso}}^{\text{pcs},\chi} = -\frac{1}{3} \sum_{m'} \tilde{\Delta}\chi_{2m'} \sum_{m''} \tilde{C}_{2m''}^{\text{dip}} D_{m''-m'}^{(2)}(\alpha_{\text{CS,X}}, \beta_{\text{CS,X}}, \gamma_{\text{CS,X}}), \quad (5.75)$$

and the final expression for the PCS is

$$\delta_{\text{iso}}^{\text{pcs},\chi} = \frac{1}{6} \Delta C \left[\Delta\chi_{\text{ax}} \left(3 \cos^2(\beta_{\text{CS,X}}) - 1 \right) + \frac{3}{2} \Delta\chi_{\text{rh}} \sin^2(\beta_{\text{CS,X}}) \cos(2\gamma_{\text{CS,X}}) \right. \\ \left. - \eta^C \left\{ \Delta\chi_{\text{ax}} \sin^2(\beta_{\text{CS,X}}) \cos(2\alpha_{\text{CS,X}}) \right. \right. \\ \left. \left. + \Delta\chi_{\text{rh}} \cos^4(\beta_{\text{CS,X}}/2) \cos(2(\alpha_{\text{CS,X}} + \gamma_{\text{CS,X}})) + \Delta\chi_{\text{rh}} \sin^4(\beta_{\text{CS,X}}/2) \cos(2(\alpha_{\text{CS,X}} - \gamma_{\text{CS,X}})) \right\} \right]. \quad (5.76)$$

The PCS is a shift that originates from the through-space spin-dipolar interaction, and so has a form that is very different to that of the contact shift. Both depend on the interaction with the unpaired electron spin density, but whereas the contact shift results from the spin density at the nuclear site, the PCS is a longer-range effect that depends on the spatial position of the nucleus with respect to the paramagnetic ion. This form of the PCS emphasises that it depends only on the susceptibility anisotropy, through the axial and rhombic anisotropy parameters, and *not* on the isotropic susceptibility. Therefore the PCS only arises for metal ions with electronic configurations that are subject to SO coupling. At ion–nucleus separations that are sufficiently large, typically more than 4Å, we can employ the point-dipole approximation for the unpaired electrons. The PCS then takes on the well-known form that was first derived by McConnell and Robertson

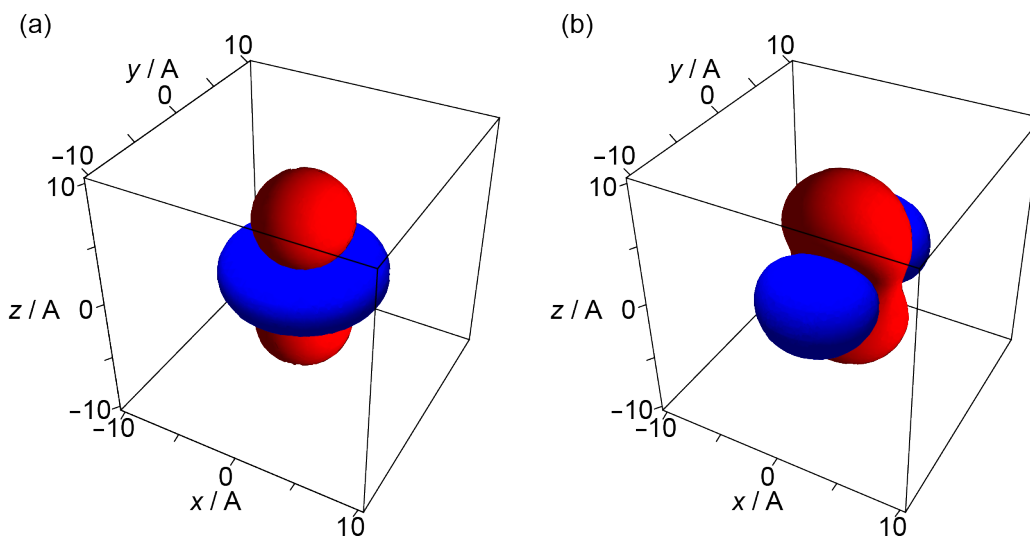


Figure 5.2: Representative surfaces plots of the PCS as a function of the position (x, y, z) of the NMR-active nucleus relative to an anisotropic paramagnetic centre. The PCS due to two examples of the magnetic susceptibility are shown with the susceptibility in (a) being axially symmetric, and that in (b) having a non-zero rhombic component. The susceptibility anisotropy parameters are: $\Delta\chi_{\text{ax}} = 10^{-32} \text{ m}^3$ in both cases, and $\Delta\chi_{\text{rh}} = 0$ for (a) and $\Delta\chi_{\text{rh}} = 0.9 \times 10^{-32} \text{ m}^3$ for (b). The surfaces show the position at which we see a positive PCS of 1 ppm (in red), and a negative PCS of -1 ppm (in blue).

[36]:

$$\delta_{\text{iso}}^{\text{PCS},\chi} = \frac{1}{12\pi R^3} \left[\Delta\chi_{\text{ax}} (3 \cos^2(\theta) - 1) + \frac{3}{2} \Delta\chi_{\text{rh}} \sin^2(\theta) \cos(2\phi) \right]. \quad (5.77)$$

The angles θ and ϕ are the polar and azimuthal angles that are defined through $\beta_{\text{X,CS}} = \theta$ and $\alpha_{\text{X,CS}} = \phi$, or equivalently $\beta_{\text{CS,X}} = \theta$ and $\gamma_{\text{CS,X}} = \phi$. Hence (θ, ϕ) can be interpreted either as the angles relating the PAF of the susceptibility tensor relative to the metal ion–nucleus vector, or vice versa. The point-dipole PCS therefore depends on five parameters: the spherical polar coordinates (R, θ, ϕ) of the nucleus relative to the PAF of the susceptibility tensor of the metal ion, and the axial and rhombic anisotropy parameters of the susceptibility. Two examples of the position-dependence of the PCS are shown in Figure 5.2, for an axially-symmetric susceptibility tensor (a), and a susceptibility tensor with a rhombic component (b). The former plot has the appearance of a $3d_{z^2}$ orbital, which is due to the polar-angle dependence of $(3 \cos^2 \theta - 1)$ in Equation 5.77. The inclusion of the rhombic term has the effect of splitting the ‘doughnut’ ring into two distinct lobes.

Equivalent expressions for the PCS in different coordinate systems can be formulated; an extensive list of

these has been provided by Bertini et al. for the point-dipole regime [16]. Here we give two expressions in Cartesian coordinates for the case where the point-dipole model applies. We write the PCS as

$$\delta_{\text{iso}}^{\text{pcs}} = \frac{1}{3} \text{Tr}(\Delta\chi \cdot C^{\text{dip}}). \quad (5.78)$$

Starting from Equation 3.104 we write the Cartesian components of C^{dip} as

$$C_{ij}^{\text{dip}} = \frac{3R_i R_j - R^2 \delta_{ij}}{4\pi R^5}. \quad (5.79)$$

Because the PCS is isotropic, we obtain the same result independent of which reference frame we use. Therefore for convenience we adopt the PAF of the susceptibility tensor, so that $\Delta\chi_{ij} = \tilde{\Delta}\chi_{ii}\delta_{ij}$. In this frame the Cartesian coordinates (x, y, z) give the position of the nucleus in the PAF of the susceptibility tensor. The PCS can now be evaluated easily:

$$\begin{aligned} \delta_{\text{iso}}^{\text{pcs}} &= \frac{1}{12\pi R^5} \text{Tr} \left[\begin{pmatrix} \tilde{\Delta}\chi_{xx} & 0 & 0 \\ 0 & \tilde{\Delta}\chi_{yy} & 0 \\ 0 & 0 & \tilde{\Delta}\chi_{zz} \end{pmatrix} \begin{pmatrix} 3x^2 - R^2 & 3xy & 3xz \\ 3xy & 3y^2 - R^2 & 3yz \\ 3xz & 3yz & 3z^2 - R^2 \end{pmatrix} \right] \\ &= \frac{1}{12\pi R^5} \left[\tilde{\Delta}\chi_{xx} (3x^2 - R^2) + \tilde{\Delta}\chi_{yy} (3y^2 - R^2) + \tilde{\Delta}\chi_{zz} (3z^2 - R^2) \right]. \end{aligned} \quad (5.80)$$

In terms of the axial and rhombic susceptibility anisotropy parameters Equation 5.80 becomes

$$\delta_{\text{iso}}^{\text{pcs}} = \frac{1}{12\pi R^5} \left[\Delta\chi_{\text{ax}} (2z^2 - x^2 - y^2) + \frac{3}{2} \Delta\chi_{\text{rh}} (x^2 - y^2) \right]. \quad (5.81)$$

This form of the PCS again emphasises that the shift depends only on the susceptibility anisotropy, and not on the isotropic susceptibility.

The spin-dipolar shift anisotropy

There are two contributions to the spin-dipolar shift anisotropy, namely the anisotropy shielding term $-\chi^{\text{iso}} C^{\text{dip}}$, and the anisotropic component of $-\Delta\chi \cdot C^{\text{dip}}$ as given in Equation 5.64. The symmetry of the former shielding tensor exactly matches the symmetry of the dipolar coupling tensor, and so they both share the same PAF, the

same anisotropy to within a multiplicative constant of proportionality, and the same asymmetry parameter. The shielding anisotropy $\Delta\sigma^{\text{dip},\chi,1}$ and asymmetry parameter $\eta^{\text{dip},\chi,1}$ are therefore

$$\Delta\sigma^{\text{dip},\chi,1} = -\chi^{\text{iso}}\Delta C, \quad (5.82)$$

$$\eta^{\text{dip},\chi,1} = \eta^C. \quad (5.83)$$

The former is proportional to the isotropic magnetic susceptibility. In the point-dipole approximation the anisotropy ΔC is equal to twice the reduced dipolar coupling constant $1/(4\pi R^3)$, and the asymmetry parameter η^C is zero. The anisotropic shielding parameters are therefore

$$\Delta\sigma^{\text{dip},\chi,1} = -\frac{\chi^{\text{iso}}}{2\pi R^3}, \quad (5.84)$$

$$\eta^{\text{dip},\chi,1} = 0. \quad (5.85)$$

We expect this contribution to the spin-dipolar shielding anisotropy to be the most dominant of the two.

The second shift anisotropy contribution from Equation 5.64 gives a rank-2 shielding $\sigma_{20}^{\text{dip},\chi,2}$ equal to

$$\sigma_{20}^{\text{dip},\chi,2} = \frac{1}{2} \sqrt{\frac{7}{3}} W_{20}(22). \quad (5.86)$$

The anisotropy $\Delta\sigma^{\text{dip},\chi,2}$ and asymmetry parameter $\eta^{\text{dip},\chi,2}$ of this contribution to the shielding match those of the coupled tensor $W_{20}(22)$, which we denote as $\Delta W(22)$ and $\eta^{W(22)}$ respectively:

$$\Delta\sigma^{\text{dip},\chi,2} = \frac{1}{3} \sqrt{\frac{7}{2}} \Delta W(22), \quad (5.87)$$

$$\eta^{\text{dip},\chi,2} = \eta^{W(22)}. \quad (5.88)$$

These parameters contain information on the anisotropic properties of both the susceptibility and dipolar coupling tensors.

5.3.3 The antisymmetric hyperfine shift anisotropy

The final contribution to consider is that due to the antisymmetric hyperfine interaction C^{as} . The only contribution to the shielding that is observable under high-field conditions is the symmetric anisotropic part of $-\Delta\chi \cdot C^{\text{as}}$, which contributes to the shift anisotropy. This term is calculated from the secular part of $-\Delta\chi \cdot C^{\text{as}}$, which is given by

$$\sigma^{(1)} = -\Delta\chi_{zx}C_{xz}^{\text{as}} - \Delta\chi_{zy}C_{yz}^{\text{as}}, \quad (5.89)$$

where we have acknowledged that C_{zz}^{as} is zero by definition. Applying the same treatment as for the coupled spin-dipolar contribution to the shielding, we rewrite Equation 5.89 in terms of the irreducible spherical tensor basis to obtain

$$\sigma^{(1)} = -\frac{1}{2}\Delta\chi_{2-1}C_{1+1}^{\text{as}} + \frac{1}{2}\Delta\chi_{2+1}C_{1-1}^{\text{as}}. \quad (5.90)$$

We can now express the tensor products $\Delta\chi_{2m}C_{1-m}^{\text{as}}$ in terms of the coupled tensor components $W_{L0}(21)$ which are defined through the relations

$$W_{L0}(21) = \sum_{m=-1}^{+1} \langle 21m - m|L0 \rangle \Delta\chi_{2m}C_{1-m}^{\text{as}}, \quad (5.91)$$

$$\Delta\chi_{2m}C_{1-m}^{\text{as}} = \sum_{L=1}^3 \langle 21m - m|L0 \rangle W_{L0}(21), \quad (5.92)$$

where the rank L runs from 1 to 3. In terms of the $W_{L0}(21)$ the secular shielding is

$$\sigma^{(1)} = \sum_{L=1}^3 b_L W_{L0}(21), \quad (5.93)$$

where the coefficients b_L are given by

$$b_L = -\frac{1}{2} \langle 21 - 1 + 1|L0 \rangle + \frac{1}{2} \langle 21 + 1 - 1|L0 \rangle \quad (5.94)$$

$$= -\frac{1}{2} (1 + (-1)^L) \langle 21 - 1 + 1|L0 \rangle. \quad (5.95)$$

Type	Term	σ^χ	δ_{iso}	$\Delta\sigma$	η	Present in magnetically isotropic transition-metal systems?
con	A	$-\chi^{\text{iso}} C^{\text{con}}$	$\chi^{\text{iso}} C^{\text{con}}$	0	—	yes
	B	$-\Delta\chi C^{\text{con}}$	0	$-\Delta\chi C^{\text{con}}$	η^χ	no
dip	C	$-\chi^{\text{iso}} C^{\text{dip}}$	0	$-\chi^{\text{iso}} \Delta C$	η^C	yes
	D	$-\Delta\chi \cdot C^{\text{dip}}$	$\delta_{\text{iso}}^{\text{pcs}}$	$\frac{1}{3} \sqrt{\frac{7}{2}} \Delta W(22)$	$\eta^{W(22)}$	no
as	E	$-\chi^{\text{iso}} C^{\text{as}}$	0	0	—	no
	F	$-\Delta\chi \cdot C^{\text{as}}$	0	$\sqrt{\frac{1}{2}} \Delta W(21)$	$\eta^{W(21)}$	no

Table 5.2: Summary of the various terms in the paramagnetic shielding tensor in the susceptibility formalism, and their respective contributions to the isotropic paramagnetic shift, shielding anisotropy, and asymmetry parameter.

We see immediately that the coefficients are zero if L is odd, and therefore the only contribution is from the rank-2 part $W_{20}(21)$:

$$b_1 = 0, \quad (5.96)$$

$$b_2 = \sqrt{\frac{1}{2}}, \quad (5.97)$$

$$b_3 = 0. \quad (5.98)$$

The secular shielding is therefore

$$\sigma^{(1)} = \sqrt{\frac{1}{2}} W_{20}(21). \quad (5.99)$$

The corresponding shielding anisotropy $\Delta\sigma^{\text{as},\chi}$ and asymmetry parameter $\eta^{\text{as},\chi}$ are given in terms of the corresponding anisotropy and asymmetry of $W_{20}(21)$, which we denote as $\Delta W(21)$ and $\eta^{W(21)}$ respectively:

$$\Delta\sigma^{\text{as},\chi} = \sqrt{\frac{1}{2}} \Delta W(21), \quad (5.100)$$

$$\eta^{\text{as},\chi} = \eta^{W(21)}. \quad (5.101)$$

5.3.4 Summary

The various terms in the susceptibility formalism of the paramagnetic shielding, and their contributions to the isotropic paramagnetic shift, shift anisotropy, and asymmetry are summarised in Table 5.2. The questions that now arise are what is the relative importance of these various terms, and can the interpretation of the observed shifts and shift anisotropies in the NMR spectrum be simplified by considering only a subset of

them.

Magnetically isotropic transition-metal ions

The first case to consider is that of transition metal ions with an isotropic magnetic susceptibility. This includes metal ions that are not subject to SO coupling, such as those with a half-full high-spin d -shell configuration, for example Mn^{2+} , and metal ions which may exhibit SO coupling effects, but in a perfectly cubic coordination environment. In this case the only contributions to the shielding tensor are terms A and C. Hence the isotropic paramagnetic shift is due entirely to the contact interaction, and the shift anisotropy is due entirely to the spin-dipolar interaction. In such systems the interpretation of the NMR spectrum is relatively straightforward, with the isotropic and anisotropic shifts providing information on the spin-transfer pathways from the unpaired electrons to the nucleus, and the spatial geometry of the system, respectively. One important observation is that the shift anisotropy has a distance dependence of $1/R^3$, and so is considerably longer range than the spin-transfer that gives the isotropic shift. Therefore nuclei that are outside the coordination environment of the metal ion, and hence exhibit no contact shift, are still expected to have a significant shift anisotropy due to the spin-dipolar interaction.

The effect of magnetic anisotropy

Metal ions that are subject to SO coupling effects, and in coordination environments of non-cubic symmetry, possess a susceptibility anisotropy which results in a more complicated form of the paramagnetic shielding tensor, as can be seen from Table 5.2. In such systems the isotropic paramagnetic shift is a combination of the contact (term A) and pseudo-contact (term D) interactions. These give complementary information on the through-bond and through-space interactions with the unpaired electrons. Whether one or the other is dominant is a complex issue, and depends on the precise nature of the system. In situations where the s -orbitals of the relevant nucleus receive appreciable transfer of electronic spin density due to, for example, favourable orbital overlap, the contact shift is likely to dominate the overall isotropic shift and the PCS can safely be neglected. However in situations where the orbital overlap is less favourable, or where the nucleus is outside the immediate coordination environment of the metal ion, the contact shift is small, and the PCS becomes more important. In structural studies of proteins with a paramagnetic centre, the PCS is observed for nuclei up to a range of approximately 50 \AA , at which distance the contact shift is zero. Because

of the long-range nature of the PCS, and its dependence on the position of the nucleus with respect to the susceptibility tensor of the metal ion, the PCS is an extremely useful tool here, as will be seen in chapters 12 and 13.

The form of the overall shielding anisotropy is more complicated, having four contributions that are due to the anisotropy of the hyperfine tensor, the susceptibility tensor, and the coupling of the two. The anisotropy due to term B is due to the susceptibility anisotropy and the contact interaction, and is therefore only expected to be important for nuclei that are within the coordination environment of a metal ion with large magnetic anisotropy. Terms C and D are longer-range effects, being due to the spin-dipolar interaction. Term C is proportional to the isotropic susceptibility whereas term D depends on the susceptibility anisotropy, and so the former is expected to be the more important contribution of the two, especially for metal ions with a small magnetic anisotropy. In addition both C and D contain the product of an NR term with a SO coupling term, and so both are expected to be larger than term F, which is formed by coupling together *two* tensors due entirely to SO coupling, namely $\Delta\chi$ and C^{as} .

5.4 The paramagnetic shift in terms of the molecular/atomic-level EPR parameters

We now begin the more complex task of interpreting the form of the paramagnetic shielding tensor in terms of the EPR tensor parameters, and elucidating more thoroughly the links between this formalism and the susceptibility formalism. This link can be summarised by the expression for the magnetic susceptibility tensor in Equation 5.12. If we expand this expression by using the full forms of \mathbf{g} and \mathbf{Z} we obtain

$$\chi = \mu_0 \mu_B^2 (g_e \mathbf{1} + \Delta g_{\text{iso}} \mathbf{1} + \Delta \mathbf{g}) \cdot (\mathbf{Z}^{\text{iso}} \mathbf{1} + \Delta \mathbf{Z}) \cdot (g_e \mathbf{1} + \Delta g_{\text{iso}} \mathbf{1} + \Delta \mathbf{g}^T). \quad (5.102)$$

We see that both the isotropic and anisotropic parts of χ contain contributions due to the SO coupling. In the absence of SO coupling however both \mathbf{Z} and the susceptibility are wholly isotropic, and χ reduces to the NR

form we have seen previously:

$$\chi^{\text{iso}} = \mu_0 \mu_B^2 g_e^2 Z^{\text{iso}} \quad (5.103)$$

$$= \frac{\mu_0 \mu_B^2 g_e^2 S(S+1)}{3kT}, \quad (5.104)$$

where we have used the NR expression for Z . We begin by re-examining the NR case, and then include the SO coupling terms. The contributions are separated into contact, spin-dipolar, and antisymmetric hyperfine terms in the same way as for the susceptibility formalism.

5.4.1 Magnetically isotropic transition-metal ions in the absence of spin-orbit coupling

In the absence of SO coupling the only terms in Table 5.1 that remain are the Fermi-contact term (1), and the NR spin-dipolar term (2). These give rise to the isotropic paramagnetic shift and shift anisotropy respectively. The expressions given in this section are the same as those presented in chapter 3.

The Fermi-contact shift

The isotropic Fermi-contact paramagnetic shielding $\sigma_{\text{iso}}^{\text{FC},S}$ is given by

$$\sigma_{\text{iso}}^{\text{FC},S} = -\frac{\mu_B g_e S(S+1)}{3\hbar\gamma_I kT} A^{\text{FC}}. \quad (5.105)$$

We can also define the corresponding Fermi-contact shift $\delta_{\text{iso}}^{\text{FC},S}$ as

$$\delta_{\text{iso}}^{\text{FC},S} = \frac{\mu_B g_e S(S+1)}{3\hbar\gamma_I kT} A^{\text{FC}}. \quad (5.106)$$

This expression is exactly equal to the corresponding contact shift in the susceptibility formalism $\delta_{\text{iso}}^{\text{con},\chi} = \chi^{\text{iso}} C^{\text{con}}$ when we note that both χ^{iso} and C^{con} take their respective NR forms:

$$\delta_{\text{iso}}^{\text{con},\chi} = \chi^{\text{iso}} C^{\text{con}} \quad (5.107)$$

$$= \left[\frac{\mu_0 \mu_{\text{B}}^2 g_e^2 S(S+1)}{3kT} \right] \left[\frac{\rho^{\alpha-\beta}(\mathbf{0})}{3S} \right] \quad (5.108)$$

$$= \left[\frac{\mu_{\text{B}} g_e S(S+1)}{3\hbar\gamma_I kT} \right] \left[\frac{1}{3S} \mu_0 \mu_{\text{B}} g_e \hbar\gamma_I \rho^{\alpha-\beta}(\mathbf{0}) \right] \quad (5.109)$$

$$= \frac{\mu_{\text{B}} g_e S(S+1)}{3\hbar\gamma_I kT} A^{\text{FC}}, \quad (5.110)$$

where to go to the third line we have multiplied the numerator and denominator by $\hbar\gamma_I$. The final expression is exactly the one given in Equation 5.106.

The spin-dipolar shift anisotropy

The shielding anisotropy due to the spin-dipolar term SD is parameterised in terms of the shielding anisotropy and asymmetry, which are given by:

$$\Delta\sigma^{\text{SD},S} = -\frac{\mu_{\text{B}} g_e S(S+1)}{3\hbar\gamma_I kT} \Delta A^{\text{SD}}, \quad (5.111)$$

$$\eta^{\text{SD},S} = \eta^{\text{SD}}, \quad (5.112)$$

where ΔA^{SD} and η^{SD} are the anisotropy and asymmetry parameter of the NR spin-dipolar interaction. The overall shielding tensor therefore has the same PAF and anisotropic properties as the NR spin-dipolar coupling tensor. By following the same line of reasoning as with the Fermi-contact shift in Equations 5.107–5.110, we can show that this value of $\Delta\sigma^{\text{SD},S}$ is exactly equivalent to the corresponding NR expression given by the susceptibility formalism $\Delta\sigma^{\text{dip},\chi,1} = -\chi^{\text{iso}} \Delta C$ when we note that $\Delta A^{\text{SD}} = \mu_0 \mu_{\text{B}} g_e \hbar\gamma_I \Delta C$.

5.4.2 The contact shift and shift anisotropy

We now examine the contact contribution to the shielding tensor in the presence of SO coupling. The relevant terms from Table 5.1 are (1), (3), (6), and (8). Terms (1), (6), and (8) are due to the NR Fermi-contact interaction with coupling constant A^{FC} , whilst term (3) originates from the SO contact term with coupling

constant $A^{\text{FC},2}$. The link can be made to the susceptibility formalism when we note that C^{con} contains contributions from both A^{FC} and $A^{\text{FC},2}$.

The contact shift

All four terms have an isotropic part, the sum of which gives the overall isotropic contact shielding $\sigma_{\text{iso}}^{\text{con},S}$:

$$\sigma_{\text{iso}}^{\text{con},S} = -\frac{\mu_{\text{B}}}{\hbar\gamma_{\text{I}}} Z^{\text{iso}} \left[g_e A^{\text{FC}} + g_e A^{\text{FC},2} + \Delta g_{\text{iso}} A^{\text{FC}} \right] - \frac{\mu_{\text{B}}}{3\hbar\gamma_{\text{I}}} \text{Tr} [\Delta \mathbf{g} \cdot \Delta \mathbf{Z}] A^{\text{FC}}. \quad (5.113)$$

The first three terms (1, 3, and 6) in Equation 5.113 depend on the isotropic part of the g -tensor, and the isotropic part of \mathbf{Z} . Therefore the leading temperature dependence of these terms matches that of Z^{iso} , which is first order in $1/(kT)$. On the other hand the final isotropic term (8) is formed from coupling together the anisotropic part of \mathbf{Z} and the anisotropic and symmetric part of \mathbf{g} . The temperature dependence of this term is that of $\Delta \mathbf{Z}$, which is $1/(kT)^2$, i.e. second order. This is also observed in the corresponding isotropic shielding in the susceptibility formalism where, in the presence of SO coupling, χ^{iso} contains contributions from $\Delta \mathbf{Z}$ and $\Delta \mathbf{g}$ in addition to Z^{iso} and $g_e + \Delta g_{\text{iso}}$. The overall isotropic contact shift is given by

$$\delta_{\text{iso}}^{\text{con},S} = \frac{\mu_{\text{B}}}{\hbar\gamma_{\text{I}}} Z^{\text{iso}} \left[g_e A^{\text{FC}} + g_e A^{\text{FC},2} + \Delta g_{\text{iso}} A^{\text{FC}} \right] + \frac{\mu_{\text{B}}}{3\hbar\gamma_{\text{I}}} \text{Tr} [\Delta \mathbf{g} \cdot \Delta \mathbf{Z}] A^{\text{FC}}. \quad (5.114)$$

This expression is completely general for transition-metal ions subject to SO coupling.

In the high-temperature limit we can approximate the contact shift to $1/(kT)^2$, which gives the Bleaney expression:

$$\begin{aligned} \delta_{\text{iso}}^{\text{con},S} &= \frac{\mu_{\text{B}} S(S+1)}{3\hbar\gamma_{\text{I}} kT} \left[g_e A^{\text{FC}} + g_e A^{\text{FC},2} + \Delta g_{\text{iso}} A^{\text{FC}} \right] \\ &\quad - \frac{\mu_{\text{B}} S(S+1)(2S-1)(2S+3)}{90\hbar\gamma_{\text{I}} (kT)^2} \text{Tr} [\Delta \mathbf{g} \cdot \mathbf{D}] A^{\text{FC}}. \end{aligned} \quad (5.115)$$

This form of the contact shift emphasises that both the isotropic g -factor, including the SO coupling contribution, and the SO coupling contribution to the Fermi-contact interaction appear to first order in $1/(kT)$. The g -anisotropy and ZFS, on the other hand, only appear to second order in $1/(kT)$. In the absence of the ZFS

the fourth term is zero and we are left with

$$\delta_{\text{iso}}^{\text{con},S} = \frac{\mu_B S(S+1)}{3\hbar\gamma_I kT} \left[g_e A^{\text{FC}} + g_e A^{\text{FC},2} + \Delta g_{\text{iso}} A^{\text{FC}} \right], \quad (5.116)$$

which is a simple modification of the NR expression that accounts for the SO-coupling-induced changes to both the isotropic g -factor and contact coupling interaction.

The contact shift anisotropy

The anisotropy associated with the contact shielding is represented by the symmetric anisotropic part of the contact shielding, which we denote $\sigma^{\text{con,sym},S}$. The full expression is

$$\begin{aligned} \sigma^{\text{con,sym},S} = & -\frac{\mu_B}{\hbar\gamma_I} \left[g_e A^{\text{FC}} + g_e A^{\text{FC},2} + \Delta g_{\text{iso}} A^{\text{FC}} \right] \Delta \mathbf{Z} \\ & -\frac{\mu_B}{\hbar\gamma_I} A^{\text{FC}} Z^{\text{iso}} \Delta \mathbf{g}^{\text{sym}} \\ & -\frac{\mu_B}{\hbar\gamma_I} A^{\text{FC}} \{ \Delta \mathbf{g} \cdot \Delta \mathbf{Z} \}^{\text{sym}}, \end{aligned} \quad (5.117)$$

where the notation \mathbf{A}^{sym} indicates the symmetric anisotropic part of \mathbf{A} , and $\{ \mathbf{A} \cdot \mathbf{B} \}^{\text{sym}}$ represents the symmetric anisotropic part of the matrix product of \mathbf{A} and \mathbf{B} . Hence $\Delta \mathbf{g}^{\text{sym}}$ and $\{ \Delta \mathbf{g} \cdot \Delta \mathbf{Z} \}^{\text{sym}}$ are the symmetric anisotropic parts of those tensors, which are given by

$$\Delta \mathbf{g}^{\text{sym}} = \frac{1}{2} (\Delta \mathbf{g} + \Delta \mathbf{g}^T), \quad (5.118)$$

$$\{ \Delta \mathbf{g} \cdot \Delta \mathbf{Z} \}^{\text{sym}} = \frac{1}{2} (\Delta \mathbf{g} \cdot \Delta \mathbf{Z} + \Delta \mathbf{Z} \cdot \Delta \mathbf{g}^T) - \frac{1}{3} \text{Tr}(\Delta \mathbf{g} \cdot \Delta \mathbf{Z}) \mathbf{1}. \quad (5.119)$$

All of these terms correspond to the single term in the susceptibility formalism $-\Delta \chi^{\text{con}}$. Thus the shielding anisotropy is the sum of three terms $\sigma^{\text{con,sym},A,S}$, $\sigma^{\text{con,sym},B,S}$, and $\sigma^{\text{con,sym},C,S}$, to each of which can be ascribed

an anisotropy $\Delta\sigma^{\text{con},X,S}$ and asymmetry parameter $\eta^{\text{con},X,S}$, $X = A, B, C$. These are given by:

$$\Delta\sigma^{\text{con},A,S} = -\frac{\mu_B}{\hbar\gamma_I} \left[g_e A^{\text{FC}} + g_e A^{\text{FC},2} + \Delta g_{\text{iso}} A^{\text{FC}} \right] \Delta Z, \quad (5.120)$$

$$\eta^{\text{con},A,S} = \eta^Z, \quad (5.121)$$

$$\Delta\sigma^{\text{con},B,S} = -\frac{\mu_B}{\hbar\gamma_I} A^{\text{FC}} Z^{\text{iso}} \Delta g, \quad (5.122)$$

$$\eta^{\text{con},B,S} = \eta^g, \quad (5.123)$$

$$\Delta\sigma^{\text{con},C,S} = -\frac{\mu_B}{\hbar\gamma_I} A^{\text{FC}} \Delta \{ \Delta \mathbf{g} \cdot \Delta \mathbf{Z} \}, \quad (5.124)$$

$$\eta^{\text{con},C,S} = \eta^{\{ \Delta \mathbf{g} \cdot \Delta \mathbf{Z} \}}, \quad (5.125)$$

where $\Delta \{ \Delta \mathbf{g} \cdot \Delta \mathbf{Z} \}$ and $\eta^{\{ \Delta \mathbf{g} \cdot \Delta \mathbf{Z} \}}$ are shorthand notation for the anisotropy and asymmetry parameter respectively of the matrix product $\{ \Delta \mathbf{g} \cdot \Delta \mathbf{Z} \}$. In general each term has its own PAF which does not necessarily coincide with the other two, and therefore the overall contact shift anisotropy and asymmetry parameter are not simple combinations of the contributions given above, but are rather calculated by diagonalising the total symmetric anisotropic contact shielding $\sigma^{\text{con},\text{sym},S}$. Nevertheless it is instructive to analyse the three terms separately to understand better the anisotropic properties of the contact shielding. Term A depends on the ZFS tensor, with the anisotropy and asymmetry parameter being proportional to ΔZ and η^Z respectively, and the PAF being coincident with that of the ZFS. Term B depends only on the anisotropic g -tensor, with an anisotropy proportional to Δg , an asymmetry parameter equal to η^g , and the same PAF as the symmetric g -tensor. Term C is more complicated, with an anisotropy, asymmetry parameter, and PAF that depend on the product of the anisotropic parts of \mathbf{Z} , and \mathbf{g} .

In the high-temperature limit the anisotropic contact shielding is given by

$$\begin{aligned} \sigma^{\text{con},\text{sym},S} = & \frac{\mu_B S(S+1)(2S-1)(2S+3)}{30\hbar\gamma_I(kT)^2} \left[g_e A^{\text{FC}} + g_e A^{\text{FC},2} + \Delta g_{\text{iso}} A^{\text{FC}} \right] \mathbf{D} \\ & - \frac{\mu_B S(S+1)}{3\hbar\gamma_I kT} A^{\text{FC}} \Delta \mathbf{g}^{\text{sym}} \\ & + \frac{\mu_B S(S+1)(2S-1)(2S+3)}{30\hbar\gamma_I(kT)^2} A^{\text{FC}} \{ \Delta \mathbf{g} \cdot \mathbf{D} \}^{\text{sym}}. \end{aligned} \quad (5.126)$$

The three contributions to the contact shielding anisotropy and asymmetry parameter are now

$$\Delta\sigma^{\text{con,A},S} = \frac{\mu_B S(S+1)(2S-1)(2S+3)}{30\hbar\gamma_I(kT)^2} \left[g_e A^{\text{FC}} + g_e A^{\text{FC},2} + \Delta g_{\text{iso}} A^{\text{FC}} \right] \Delta D, \quad (5.127)$$

$$\eta^{\text{con,A},S} = \eta^D, \quad (5.128)$$

$$\Delta\sigma^{\text{con,B},S} = -\frac{\mu_B S(S+1)}{3\hbar\gamma_I kT} A^{\text{FC}} \Delta g, \quad (5.129)$$

$$\eta^{\text{con,B},S} = \eta^g, \quad (5.130)$$

$$\Delta\sigma^{\text{con,C},S} = \frac{\mu_B S(S+1)(2S-1)(2S+3)}{30\hbar\gamma_I(kT)^2} A^{\text{FC}} \Delta \{ \Delta \mathbf{g} \cdot \mathbf{D} \}, \quad (5.131)$$

$$\eta^{\text{con,C},S} = \eta^{\{ \Delta \mathbf{g} \cdot \mathbf{D} \}}. \quad (5.132)$$

We see that the ZFS only contributes to second order in $1/(kT)$, whereas the g -anisotropy contributes to first order. Finally in the absence of the ZFS interaction we obtain the following simple expression for the contact shielding anisotropy:

$$\sigma^{\text{con,sym},S} = -\frac{\mu_B S(S+1)}{3\hbar\gamma_I kT} A^{\text{FC}} \Delta \mathbf{g}^{\text{sym}}. \quad (5.133)$$

Only term B is present, and so the total shielding anisotropy and asymmetry parameter are wholly given by the anisotropic properties of the symmetric part of the g -tensor:

$$\Delta\sigma^{\text{con,B},S} = -\frac{\mu_B S(S+1)}{3\hbar\gamma_I kT} A^{\text{FC}} \Delta g, \quad (5.134)$$

$$\eta^{\text{con,B},S} = \eta^g. \quad (5.135)$$

5.4.3 The spin-dipolar shift and shift anisotropy

The spin-dipolar contribution to the shielding tensor comprises four terms from Table 5.1, namely (2), (4), (7), and (9). Three of these terms (2, 7, and 9) are due to the NR spin-dipolar interaction with coupling tensor \mathbf{A}^{SD} , and the fourth term (4) is due to the SO coupling contribution $\mathbf{A}^{\text{SD},2}$. As for the contact shielding, the link to the susceptibility formalism can be made when we note that \mathbf{C}^{dip} includes both the NR and SO parts of the dipolar coupling tensor.

The pseudo-contact shift

In order to obtain an isotropic chemical shielding from the spin-dipolar interaction in the EPR formalism we need the terms that contain a matrix product of the spin-dipolar tensor with at least one other anisotropic and symmetric tensor. Writing down these terms and taking the trace we obtain the pseudo-contact shielding

$\sigma_{\text{iso}}^{\text{pcs},S}$:

$$\begin{aligned} \sigma_{\text{iso}}^{\text{pcs},S} = & -\frac{\mu_B}{3\hbar\gamma_I} \left[g_e \text{Tr}(\Delta \mathbf{Z} \cdot \mathbf{A}^{\text{SD}}) + g_e \text{Tr}(\Delta \mathbf{Z} \cdot \mathbf{A}^{\text{SD},2}) + \Delta g_{\text{iso}} \text{Tr}(\Delta \mathbf{Z} \cdot \mathbf{A}^{\text{SD}}) \right] \\ & - \frac{\mu_B}{3\hbar\gamma_I} \left[Z^{\text{iso}} \text{Tr}(\Delta \mathbf{g} \cdot \mathbf{A}^{\text{SD}}) + \text{Tr}(\Delta \mathbf{g} \cdot \Delta \mathbf{Z} \cdot \mathbf{A}^{\text{SD}}) \right]. \end{aligned} \quad (5.136)$$

From this we can write down the expression for the PCS $\delta_{\text{iso}}^{\text{pcs},S}$:

$$\begin{aligned} \delta_{\text{iso}}^{\text{pcs},S} = & \frac{\mu_B}{3\hbar\gamma_I} \left[g_e \text{Tr}(\Delta \mathbf{Z} \cdot \mathbf{A}^{\text{SD}}) + g_e \text{Tr}(\Delta \mathbf{Z} \cdot \mathbf{A}^{\text{SD},2}) + \Delta g_{\text{iso}} \text{Tr}(\Delta \mathbf{Z} \cdot \mathbf{A}^{\text{SD}}) \right] \\ & + \frac{\mu_B}{3\hbar\gamma_I} \left[Z^{\text{iso}} \text{Tr}(\Delta \mathbf{g} \cdot \mathbf{A}^{\text{SD}}) + \text{Tr}(\Delta \mathbf{g} \cdot \Delta \mathbf{Z} \cdot \mathbf{A}^{\text{SD}}) \right]. \end{aligned} \quad (5.137)$$

The first three terms (2, 4, and 7) of both Equations 5.136 and 5.137 contain the product of the symmetric part of the Z-tensor with a spin-dipolar coupling tensor, the fourth term (9) contains the product of the g -anisotropy tensor with the NR spin-dipolar coupling tensor, with only the symmetric part of $\Delta \mathbf{g}$ contributing to the PCS, and the fifth (also 9) contains the triple product $\Delta \mathbf{g} \cdot \Delta \mathbf{Z} \cdot \mathbf{A}^{\text{SD}}$. The term containing the SO spin-dipolar term is of shorter range than the other four, and so has a negligible contribution to $\sigma_{\text{iso}}^{\text{pcs},S}$ at longer distances from the metal. However it may be important at shorter distances. In analogy with the PCS in the susceptibility formalism we can deduce the following about this form of the PCS.

The first and third terms depend on the Euler angles $\Omega_{\text{A}^{\text{SD}}\text{D}}$ which specify the orientation of the PAF of the NR spin-dipolar tensor relative to the PAF of the ZFS tensor. The second term is similar, with the difference that the relevant Euler angles $\Omega_{\text{A}^{\text{SD},2}\text{D}}$ are those that now specify the orientation of the PAF of the SO coupling spin-dipolar tensor relative to the PAF of the ZFS tensor. Both terms have a leading temperature dependence of $1/(kT)^2$. The fourth term, which has a leading temperature dependence of $1/(kT)$, depends on the Euler angles $\Omega_{\text{A}^{\text{SD}}\text{GS}}$, which give the orientation of the PAF of the NR spin-dipolar tensor relative to the PAF of the symmetric part of the g -tensor. The fifth term is more complicated, and depends on the orientation of the NR spin-dipolar tensor PAF relative to the PAF of the symmetric part of the product $\Delta \mathbf{g} \cdot \Delta \mathbf{Z}$. It has a leading

temperature dependence of $1/(kT)^2$.

In the high-temperature limit we obtain the following PCS

$$\begin{aligned} \delta_{\text{iso}}^{\text{pcs},S} &= \frac{\mu_B S(S+1)}{9\hbar\gamma_I kT} \text{Tr}(\Delta\mathbf{g} \cdot \mathbf{A}^{\text{SD}}) \\ &\quad - \frac{\mu_B S(S+1)(2S-1)(2S+3)}{90\hbar\gamma_I (kT)^2} \left[g_e \text{Tr}(\mathbf{D} \cdot \mathbf{A}^{\text{SD}}) + g_e \text{Tr}(\mathbf{D} \cdot \mathbf{A}^{\text{SD},2}) + \Delta g_{\text{iso}} \text{Tr}(\mathbf{D} \cdot \mathbf{A}^{\text{SD}}) \right] \\ &\quad - \frac{\mu_B S(S+1)(2S-1)(2S+3)}{90\hbar\gamma_I (kT)^2} \text{Tr}(\Delta\mathbf{g} \cdot \mathbf{D} \cdot \mathbf{A}^{\text{SD}}). \end{aligned} \quad (5.138)$$

The g -anisotropy appears in terms with both a first- and second-order temperature dependence, whilst the ZFS only affects the PCS to second order. In the absence of the ZFS all the terms bar the first are zero, and we are left with a very simple form of the PCS

$$\delta_{\text{iso}}^{\text{pcs},S} = \frac{\mu_B S(S+1)}{9\hbar\gamma_I kT} \text{Tr}(\Delta\mathbf{g} \cdot \mathbf{A}^{\text{SD}}). \quad (5.139)$$

The PCS now depends only on the g -anisotropy, and the orientation of the PAF of the NR dipolar coupling tensor with respect to the PAF of the symmetric part of the g -tensor.

The question that now arises is how different are the two expressions for the PCS that are given in Equations 5.76 and 5.137? This point was explored in section 4.5. There it was shown that if we attempt to interpret the rank-two part of the reduced hyperfine tensor as a pure spin-dipolar interaction, we recover an expression for the PCS where the true susceptibility tensor is substituted by a modified (non-symmetric) tensor χ' . Therefore we recover an equation of the form of Equation 5.76, but containing the tensor components of the rank-two part of χ' . If this substitution is made, Equations 5.76 and 5.137 become exactly equivalent [216].

The spin-dipolar shift anisotropy

The anisotropic shielding $\sigma^{\text{dip,sym,S}}$ that arises from the spin-dipolar interaction is given by

$$\begin{aligned}
\sigma^{\text{dip,sym,S}} = & -\frac{\mu_{\text{B}}}{\hbar\gamma_{\text{I}}} Z^{\text{iso}} \left[g_e \mathbf{A}^{\text{SD}} + g_e \mathbf{A}^{\text{SD},2} + \Delta g_{\text{iso}} \mathbf{A}^{\text{SD}} \right] \\
& -\frac{\mu_{\text{B}}}{\hbar\gamma_{\text{I}}} Z^{\text{iso}} \left\{ \Delta \mathbf{g} \cdot \mathbf{A}^{\text{SD}} \right\}^{\text{sym}} \\
& -\frac{\mu_{\text{B}}}{\hbar\gamma_{\text{I}}} \left[g_e \left\{ \Delta \mathbf{Z} \cdot \mathbf{A}^{\text{SD}} \right\}^{\text{sym}} + g_e \left\{ \Delta \mathbf{Z} \cdot \mathbf{A}^{\text{SD},2} \right\}^{\text{sym}} + \Delta g_{\text{iso}} \left\{ \Delta \mathbf{Z} \cdot \mathbf{A}^{\text{SD}} \right\}^{\text{sym}} \right] \\
& -\frac{\mu_{\text{B}}}{\hbar\gamma_{\text{I}}} \left\{ \Delta \mathbf{g} \cdot \Delta \mathbf{Z} \cdot \mathbf{A}^{\text{SD}} \right\}^{\text{sym}} .
\end{aligned} \tag{5.140}$$

The term on the first line is an anisotropy that depends wholly on the NR and SO-coupling dipolar part of the hyperfine tensor, and corresponds to the term in the susceptibility formalism $-\chi^{\text{iso}} \mathbf{C}^{\text{dip}}$. The remaining terms contain one or both of the anisotropic part of the g -tensor and of the ZFS tensor, as part of $\Delta \mathbf{Z}$, and therefore correspond to the anisotropic symmetric part of $-\Delta \chi \cdot \mathbf{C}^{\text{dip}}$.

In the high-temperature approximation the expression for $\sigma^{\text{dip,sym,S}}$ becomes

$$\begin{aligned}
\sigma^{\text{dip,sym,S}} = & -\frac{\mu_{\text{B}} S(S+1)}{3\hbar\gamma_{\text{I}} kT} \left[g_e \mathbf{A}^{\text{SD}} + g_e \mathbf{A}^{\text{SD},2} + \Delta g_{\text{iso}} \mathbf{A}^{\text{SD}} \right] \\
& -\frac{\mu_{\text{B}} S(S+1)}{3\hbar\gamma_{\text{I}} kT} \left\{ \Delta \mathbf{g} \cdot \mathbf{A}^{\text{SD}} \right\}^{\text{sym}} \\
& +\frac{\mu_{\text{B}} S(S+1)(2S-1)(2S+3)}{30\hbar\gamma_{\text{I}} (kT)^2} \left[g_e \left\{ \mathbf{D} \cdot \mathbf{A}^{\text{SD}} \right\}^{\text{sym}} + g_e \left\{ \mathbf{D} \cdot \mathbf{A}^{\text{SD},2} \right\}^{\text{sym}} + \Delta g_{\text{iso}} \left\{ \mathbf{D} \cdot \mathbf{A}^{\text{SD}} \right\}^{\text{sym}} \right] \\
& +\frac{\mu_{\text{B}} S(S+1)(2S-1)(2S+3)}{30\hbar\gamma_{\text{I}} (kT)^2} \left\{ \Delta \mathbf{g} \cdot \mathbf{D} \cdot \mathbf{A}^{\text{SD}} \right\}^{\text{sym}} .
\end{aligned} \tag{5.141}$$

The terms on the first two lines, which depend only on the dipolar coupling tensors and g -anisotropy have a leading temperature dependence of $1/(kT)$. The other terms, which also depend on the ZFS tensor, have a leading temperature dependence of $1/(kT)^2$ as we have seen with the other contributions to the shielding tensor. In the absence of the ZFS interaction the anisotropic shielding is

$$\begin{aligned}
\sigma^{\text{dip,sym,S}} = & -\frac{\mu_{\text{B}} S(S+1)}{3\hbar\gamma_{\text{I}} kT} \left[g_e \mathbf{A}^{\text{SD}} + g_e \mathbf{A}^{\text{SD},2} + \Delta g_{\text{iso}} \mathbf{A}^{\text{SD}} \right] \\
& -\frac{\mu_{\text{B}} S(S+1)}{3\hbar\gamma_{\text{I}} kT} \left\{ \Delta \mathbf{g} \cdot \mathbf{A}^{\text{SD}} \right\}^{\text{sym}} ,
\end{aligned} \tag{5.142}$$

which contains contributions due to A^{SD} , $A^{\text{SD},2}$, Δg_{iso} , and Δg . In all these cases we note again that $A^{\text{SD},2}$ represents a shorter-range interaction than A^{SD} , and so is only important at shorter distances from the metal ion.

5.4.4 The antisymmetric hyperfine shift anisotropy

The final term to consider is the paramagnetic chemical shielding due to the antisymmetric hyperfine interaction, as given by term (5) in Table 5.1. This contribution corresponds to the susceptibility formalism contribution $-\Delta\chi \cdot C^{\text{as}}$. As in the susceptibility formalism the anisotropic hyperfine interaction does not contribute to the isotropic paramagnetic shift, but does contribute to the shielding anisotropy through the term

$$\sigma^{\text{as,sym},S} = -\frac{\mu_{\text{B}}}{\hbar\gamma_I} g_e \{\Delta\mathbf{Z} \cdot \mathbf{A}^{\text{as}}\}^{\text{sym}}. \quad (5.143)$$

The anisotropic properties therefore depend on those of the matrix product $\Delta\mathbf{Z} \cdot \mathbf{A}^{\text{as}}$. The g -anisotropy does not play a role here, but the dependence on $\Delta\mathbf{Z}$ indicates that the shielding anisotropy and asymmetry do depend on the ZFS. In the high-temperature limit Equation 5.143 becomes

$$\sigma^{\text{as,sym},S} = \frac{\mu_{\text{B}}S(S+1)(2S-1)(2S+3)}{30\hbar\gamma_I(kT)^2} g_e \{\mathbf{D} \cdot \mathbf{A}^{\text{as}}\}^{\text{sym}}. \quad (5.144)$$

The leading temperature dependence is therefore $1/(kT)^2$. In the absence of the ZFS this term disappears altogether.

5.4.5 Summary

As has been seen in this chapter, the form of the paramagnetic shielding tensor in terms of the EPR parameters is rather complex. Therefore to finish this discussion we outline the salient points, which are the roles that the various EPR parameters play in the forms of the isotropic shift and shift anisotropy, the temperature dependences of the various contributions, and which are the most important for different systems. This last point closely follows the corresponding discussion of the susceptibility formalism in section 5.3.4. The different terms are summarised in Table 5.3, where it is shown whether each term contributes to the shift and/or shift anisotropy, and also the leading temperature dependence of each contribution.

Type	Term	Shielding expression ^a	Leading temp dependence 1/kT Isotropic shift	Shift anisotropy	Leading temp dependence 1/(kT) ² Isotropic shift	Shift anisotropy
con	1a	$g_e Z^{\text{iso}} A^{\text{FC}}$	✓			
	3a	$g_e Z^{\text{iso}} A^{\text{FC},2}$	✓			
	6a	$\Delta g_{\text{iso}} Z^{\text{iso}} A^{\text{FC}}$	✓			
	8a	$Z^{\text{iso}} A^{\text{FC}} \Delta g$		✓		
	1b	$g_e A^{\text{FC}} \Delta Z$				✓
	3b	$g_e A^{\text{FC},2} \Delta Z$				✓
	6b	$\Delta g_{\text{iso}} A^{\text{FC}} \Delta Z$				✓
	8b	$A^{\text{FC}} \Delta g \cdot \Delta Z$			✓	✓
dip	2a	$g_e Z^{\text{iso}} A^{\text{SD}}$		✓		
	4a	$g_e Z^{\text{iso}} A^{\text{SD},2}$		✓		
	7a	$\Delta g_{\text{iso}} Z^{\text{iso}} A^{\text{SD}}$		✓		
	9a	$Z^{\text{iso}} \Delta g \cdot A^{\text{SD}}$		✓		
	2b	$g_e \Delta Z \cdot A^{\text{SD}}$	✓			✓
	4b	$g_e \Delta Z \cdot A^{\text{SD},2}$				✓
	7b	$\Delta g_{\text{iso}} \Delta Z \cdot A^{\text{SD}}$				✓
	9b	$\Delta g \cdot \Delta Z \cdot A^{\text{SD}}$			✓	✓
	as	5a	$g_e Z^{\text{iso}} A^{\text{RS}}$			
5b		$g_e \Delta Z \cdot A^{\text{RS}}$				✓

Table 5.3: Summary of the terms appearing in the EPR formalism of the paramagnetic shielding tensor, including the leading temperature dependence of the isotropic and anisotropic parts. A tick shows that the shielding contribution gives an isotropic shift or shift anisotropy of the indicated leading temperature dependence. The different terms are separated into groups arising from the contact interaction (con), spin-dipolar interaction (dip), and the antisymmetric hyperfine interaction (as). The term numbering 1, 2, ... corresponds to that in Table 5.1, with the appended letter a and b representing a term containing Z^{iso} and ΔZ respectively.

^aMultiply by $-\mu_{\text{B}}/(h\nu_I)$ to obtain full shielding expression

In the absence of spin-orbit coupling

As has been shown, the only terms to contribute to metal ions which do not exhibit SO coupling are (1a) and (2a), which contribute to the isotropic shift and shift anisotropy respectively. The shielding tensor therefore has a simple form, with a temperature dependence of $1/kT$. Such paramagnetic systems only show an isotropic paramagnetic shift if the nucleus is within the coordination environment of the metal ion and receives unpaired electron density within its s -orbital. Nuclei outside the coordination site therefore have zero isotropic paramagnetic shift. The shift anisotropy is longer range, as it depends on the spin-dipolar interaction, and so nuclei exhibit a shift anisotropy even when several 10s of Å from the metal ion.

The effect of spin-orbit coupling

The simple picture described above is complicated significantly when SO coupling is present, with the extra contributions to the hyperfine, g - and ZFS tensors adding several more terms to the paramagnetic shielding tensor. The ZFS tensor is responsible for a more complicated temperature dependence, through the tensor Z . In the high-temperature limit, such that Z can be truncated at second order in $1/(kT)^2$, the ZFS tensor only appears in the shielding, with a leading temperature dependence of $1/(kT)^2$. For metal ions where the ZFS is small its contribution to the shielding can be neglected, and the temperature dependence is simply $1/kT$. Under these circumstances the contact shift is given by the sum of terms (1a), (3a), and (6a) with the NR term (1a) dominating. In addition the PCS is due entirely to the coupling of the g -anisotropy to the NR dipolar coupling tensor in term (9a). The total shift anisotropy contains a contact contribution from the g -anisotropy, in term (8a), and four terms due to the spin-dipolar interaction (2a), (4a), (7a), and (9a). The dominant spin-dipolar term is expected to be the NR contribution (2a). The contact anisotropy is only significant if the nucleus is within the coordination environment of the metal ion, so that the Fermi-contact interaction is comparable to or greater than the spin-dipolar interaction.

For metal ions with a larger ZFS anisotropy, the terms in $1/(kT)^2$ become important. The isotropic contact shift now includes a contribution in $1/(kT)^2$, term (8b), and the contact shift anisotropy includes four extra terms (1b), (3b), (6b), and (8b). The ZFS contribution to the PCS comprises four terms (2b), (4b), (7b), and (9b), of which (2b) is expected to be the most important as it depends on the product of the NR free-electron g -factor g_e and the NR spin-dipolar coupling constant, whereas in the other terms either the g -tensor or hyperfine tensor is an SO coupling contribution. The relative importance of the ZFS contribution (2b) and

the g -anisotropy contribution (9a) depends on the relative sizes of the g - and ZFS anisotropies. There are also four additional contributions to the spin-dipolar anisotropy, which are terms (2b), (4b), (7b), and (9b). Finally there is one more contribution to the shift anisotropy (5b) which comes from the antisymmetric hyperfine interaction, which can usually be neglected.

As discussed in section 5.3.4 the isotropic shift is dominated by the contact shift (1a) when nucleus is in the coordination site of the metal ion, and the transfer of unpaired electronic spin density is large. In situations where the orbital overlap is poor and the spin transfer is relatively low, or where the nucleus is outside the coordination environment of the metal the PCS terms begin to dominate. For nuclei outside the coordination environment of the metal ion the dominant contribution to the shift anisotropy is the spin-dipolar term (2a). The contact anisotropy terms become more important for nuclei within the coordination environment.

5.5 Key concepts

- The paramagnetic shielding tensor can be expressed either in terms of the EPR parameters, or the bulk magnetic susceptibility tensor. The correspondence between the two formalisms is given in Table 5.1.
- In both formalisms we can separate the shift into contributions from the contact, spin-dipolar, and antisymmetric hyperfine interactions.
- The contact interaction gives an isotropic contact shift that is proportional to the isotropic susceptibility, and a shift anisotropy that is proportional to the susceptibility anisotropic. Both contributions are also proportional to the unpaired electron spin density at the nuclear site.
- The spin-dipolar interaction produces an isotropic pseudo-contact shift, that depends on the susceptibility anisotropy and the spatial position of the nucleus with respect to the PAF of the susceptibility tensor, and a shift anisotropy that is the product of the isotropic susceptibility and spin-dipolar coupling tensor.
- The terms in the EPR formalism of the paramagnetic shielding tensor are summarised in Table 5.3.

Chapter 6

The paramagnetic shift due metal ions with arbitrary spin-multiplicity and spin-orbit coupling strength: application to *d*-transition metals, lanthanides, and actinides

Chapters 4 and 5 provide a practicable formalism for the paramagnetic shielding tensor in terms of the g -, hyperfine, and ZFS tensors due to a d -block transition-metal ion. The initial part of the derivation gives an exact expression for the chemical shielding that is valid for an arbitrary electronic spin S , and makes no assumptions about the relative orientations of the tensors in the EPR Hamiltonian. Following the derivation of the general expression, a number of assumptions are applied in order to make further progress. These assumptions are that (i) the effective electronic spin S is equal to the real spin of the ion, (ii) the SO coupling is weak in comparison to the ligand-field interaction, (iii) the spin system can be described by the EPR Hamiltonian in Equation 4.36, and (iv) we need only consider contributions from the ground state spin

manifold, i.e. there are no thermally-accessible excited states. Assumption (iii) effectively means that the final expression is only exact for electronic spins up to $S = 1$ and is only an approximation for larger spins, and all three assumptions limit the theory to the application of d metal ions.

We now extend the description to paramagnetic ions with arbitrary SO coupling strength and arbitrary spin, such as the lanthanides and actinides. In systems with lanthanide ions the crystal-field interaction is much weaker than the SO coupling, whilst for actinides both interactions are large, and of comparable magnitude. In both cases the EPR Hamiltonian is more complex than the perturbation expression derived in chapter 4, and in particular higher-order terms in the EPR Hamiltonian need to be considered to provide a proper description.

We first describe the crystal-field interaction explicitly, and extend the concept of “effective electronic spin”. We then generalise the EPR Hamiltonian and use this to derive an expression for the paramagnetic shielding tensor and the magnetic susceptibility of a paramagnetic system of arbitrary SO coupling strength and spin. This is first applied to d -block transition-metal ions, and spin-only f -block ions with an f^7 electronic configuration which exhibit equivalent behaviour. Then we indicate how the EPR formalism may be applied to lanthanides and actinides generally, and we link the EPR formalism to the Bleaney theory of paramagnetic shifts due to lanthanides.

The Bleaney formalism assumes that the magnetic properties of the coordinated lanthanide ions can be approximated by those of the free ion, and that the crystal-field interaction is sufficiently small that all levels are equally thermally populated. Therefore this part of the discussion begins with a description of the electronic properties of the free lanthanide ions in terms of the total angular momentum \mathbf{J} , and the Landé g -factor g_J .

Finally we include a short discussion about the paramagnetic shieldings in paramagnetic actinide complexes.

6.1 The crystal-field interaction and the effective spin

In chapter 4 we introduced the concept of the crystal- or ligand-field, as the interaction between the metal ion and the ligands following the immersion of a free metal ion into a coordination complex. For the d -block transition-metal ions to which we have hitherto restricted the discussion the crystal-field interaction is

sufficiently large that (1) only the ground state is thermally populated at relevant experimental temperatures, and (2) it dominates the other interactions relevant to the EPR properties, such as the SO coupling. This results in an EPR Hamiltonian that is characterised by a spin quantum number that is equal to the true spin of the metal ion. This description is not valid for metal ions such as lanthanides and actinides where the larger SO coupling and greater complexity of the electronic structure result in a more complicated form of the shielding tensor. In lanthanides the contracted nature of the $4f$ -orbitals containing the unpaired electrons results in a weaker crystal-field interaction, which is now dominated by the SO coupling, whereas for actinides the $5f$ electrons participate directly in bonding to the ligand, and so the crystal-field and SO interactions are both large, and of comparable magnitude. In these cases we need to describe the crystal-field interaction explicitly.

6.1.1 The effective spin

For a free ion subject to SO coupling the electron configuration gives rise to a series of energy levels each of which is, in general, degenerate. Each level can be represented as an effective spin \tilde{S} whose multiplicity $2\tilde{S} + 1$ matches the degeneracy of the level. In general \tilde{S} is not equal to the true spin S . In addition the different levels will, in general, have different effective spins. If we immerse the free ion into a complex the effect of the crystal field is to separate the energies of the states of each level, thus reducing their degeneracy. This results in the formation of a number of sub-levels from each level, each of which has lower degeneracy compared to the original level. Each sub-level can therefore be represented by a new effective spin, again whose multiplicity matches the degeneracy of that sub-level.

In order to interpret the EPR and NMR data of paramagnetic systems with an arbitrary SO coupling strength we apply the following logic. Firstly the combination of the SO coupling and crystal-field interactions creates a ladder of (degenerate) energy sub-levels n , to each of which can be assigned an effective spin \tilde{S}_n , whose multiplicity matches the degeneracy of the corresponding sub-level. These energy levels are properties of the metal ion and the surrounding crystal-field environment and, of course, are independent of the external magnetic field and nuclear magnetic moments. Secondly we introduce the effects of the external magnetic field and nuclear magnetic moments as ‘external’ perturbations, which allows us to define an electronic Zeeman interaction, a hyperfine interaction, and a ZFS *for each level n* which are dependent on the effective spin \tilde{S}_n of that level. Since the corresponding EPR tensor parameters depend on the effective spin, rather than the true spin, they are different in the different sub-levels. This idea is explored further in

this chapter.

6.1.2 The crystal-field interaction

The crystal field can be modelled as the interaction of the unpaired electrons of the metal ion with a potential $V(\mathbf{r})$ due to the ligands of the coordination site. The potential is given by

$$V(\mathbf{r}) = -\frac{e}{4\pi\epsilon_0} \sum_l \frac{Z_l}{|\mathbf{R}_l - \mathbf{r}|}, \quad (6.1)$$

where ϵ_0 is the permittivity of free space, and the sum is over all the ligands l , each one of which is modelled as a point charge $-Z_l e$ at position \mathbf{R}_l [218]. We define the positions of the ligand charges with the spherical polar coordinates (a_l, θ_l, ϕ_l) , and place the unpaired electron at (r, θ, ϕ) . If we assume that the electron is closer to the paramagnetic centre than to the ligands, so that $a_l > r$, we can expand the factor $|\mathbf{R}_l - \mathbf{r}|^{-1}$ as a sum of products of spherical harmonic functions $Y_{kq}(\theta, \phi)$ to give

$$V(\mathbf{r}) = -\frac{e}{4\pi\epsilon_0} \sum_l \sum_{k=0}^{\infty} \sum_{q=-k}^{+k} \frac{4\pi}{2k+1} \frac{Z_l}{a_l^{k+1}} r^k Y_{kq}(\theta, \phi)^* Y_{kq}(\theta_l, \phi_l), \quad (6.2)$$

where k and q are the spherical harmonic rank and order. The crystal-field Hamiltonian $\hat{\mathcal{H}}_{\text{CF}}$ is given by the sum of the interactions of the unpaired electrons i with the potential:

$$\hat{\mathcal{H}}_{\text{CF}} = -e \sum_i V(\mathbf{r}_i) \quad (6.3)$$

$$= \frac{e^2}{4\pi\epsilon_0} \sum_i \sum_l \sum_{k=0}^{\infty} \sum_{q=-k}^{+k} \frac{4\pi}{2k+1} \frac{Z_l}{a_l^{k+1}} r_i^k Y_{kq}(\theta_i, \phi_i)^* Y_{kq}(\theta_l, \phi_l), \quad (6.4)$$

where $\mathbf{r}_i = (r_i, \theta_i, \phi_i)$ is the position of the i th electron.

It was shown by Stevens that this Hamiltonian can be transformed into a different form \hat{H}_{CF} by replacing each term in the sum over k and q with an *operator equivalent* [219]. The most convenient choice of operator basis comprises the irreducible spherical tensors operators \hat{O}_{kq} of rank k and order q , which represent either the orbital or total angular momentum according to the particular situation. These operator equivalents are formed by coupling together the tensor components \hat{O}_{1q} of rank 1 with those components $\hat{O}_{k-1,q}$ of rank $k-1$

using the expression

$$\hat{O}_{kq} = \sum_{q_1, q_2} \hat{O}_{k-1, q_1} \hat{O}_{1q_2} \langle k-1, 1, q_1, q_2 | kq \rangle. \quad (6.5)$$

The expressions for these irreducible spherical tensor operators have been tabulated extensively by Buckmaster et al [220]. This gives the following Hamiltonian:

$$\hat{H}_{\text{CF}} = \sum_k \sum_{q=-k}^{+k} (-1)^q B_{kq} \hat{O}_{k-q}, \quad (6.6)$$

where the B_{kq} are components of the crystal-field spatial tensor in the irreducible spherical tensor basis, which satisfy

$$B_{kq}^* = (-1)^q B_{k-q}. \quad (6.7)$$

Not all the components in Equation 6.6 are retained, and it can be shown that only those components of even rank, up to a maximum of $k = 6$, are non zero.[218]. In addition the rank-zero component has the effect of simply shifting all the energy levels by the same amount, resulting in no effect on the transition frequencies, and so is also dropped. Therefore the remaining spherical tensor components in the crystal-field Hamiltonian have ranks 2 and 4, for d -block transition-metal ions, and ranks 2, 4, and 6 for f -block transition-metal ions [218].

6.1.3 Crystal-field vs zero-field splitting

The crystal-field terms with $k = 2$ have the same mathematical form as the ZFS interaction, which we have already encountered in the discussion of the first-row transition metal ions. However great care must be taken in correctly interpreting the crystal-field and ZFS interaction Hamiltonians [221]. In summary the crystal-field interaction is a *physical property* of the metal ion and its coordination environment, and therefore depends on the orbital and total angular momenta of the system. This interaction lifts the degeneracy of the electron configuration in zero external magnetic field, and creates a number of distinct sub-levels. To each sub-level can be assigned an effective spin \tilde{S} , the multiplicity $2\tilde{S} + 1$ of which matches the degeneracy of the sub-level. Each sub-level is associated with a set of effective EPR Hamiltonians including the electronic Zeeman, hyperfine, and ZFS interactions, each of which acts only within the designated sub-space that is defined by \tilde{S} . Hence the effective spin Hamiltonians are properties of the *effective* spin only. One consequence

is that for a particular metal ion the tensor parameters change according to the sub-level under consideration [221]. We can see from this that the crystal-field and ZFS interactions are completely different, and should not be confused with each other.

6.2 The generalized EPR spin Hamiltonian and paramagnetic shielding tensor

At arbitrary SO coupling strength we can no longer treat the SO coupling interaction as a perturbation to the ligand, or crystal, field interaction, and in fact the former may be larger than the latter. Nevertheless we can still write down the EPR Hamiltonian within each sub-level n in terms of an *effective* electronic spin operator \hat{S} which represents the effective spin quantum number \tilde{S} which we have seen may or may not be equal to the true spin quantum number. The general Hamiltonian is equal to a sum of terms of the form $KB^r\tilde{S}^sI^t$, where B^r is a product of the components of the external magnetic field with degree r , and \tilde{S}^s and I^t respectively are products of s and t components of the electronic and nuclear spin operators respectively [222]. The size and spatial dependence of the interaction is given by K , which is a component of the relevant tensor. The EPR Hamiltonian in Equation 4.36 contains terms with $r = t = 1$ and $s = 0$ (the orbital chemical shielding interaction), $r = s = 1$ and $t = 0$ (the electronic Zeeman interaction), $s = t = 1$ and $r = 0$ (the hyperfine interaction), and finally $s = 2$ and $r = t = 0$ (the ZFS interaction). However these are not the only terms that are present in the Hamiltonian, as we could in principle include terms with larger values of r , s , and t . There are three conditions that we must impose on the form of the terms, the first being that $r + s + t$ must be even in order to ensure that the Hamiltonian is even with respect to time reversal [190], since the field and spin angular momenta are each time-odd. Secondly the maximum value that s can take is $2\tilde{S}$, i.e. twice the effective electronic spin, and the third condition is that the maximum value of t is $2I$ [222]. The electronic configurations of d -block transition metals result in a maximum possible spin of $S = 5/2$ and so, for systems containing these ions, we need only consider terms containing products of \hat{S} with $s \leq 5$. Likewise for f -block metal ions, the maximum spin is $S = 7/2$, and so the maximum value of s we need consider is 7.

The dominant terms in the nuclear chemical shielding interaction are linear in both the external field and nuclear spin with higher-order terms being negligible. We therefore ignore any terms with $r > 1$ and $t > 1$ as these will not give us the required chemical shielding tensor. Nevertheless we retain any terms with $s > 1$

as these can contribute important effects to the electronic Zeeman, hyperfine, and ZFS interactions. The term with $t = 2$ and $r = s = 0$ is due to the nuclear quadrupole interaction which is present for quadrupolar nuclei with spin $I > 1/2$ [198]. This is a very important interaction in the NMR of such nuclear spins, but since it does not directly impact on our discussion of paramagnetic shifts we do not consider it further. We can therefore write the generalized EPR Hamiltonian \hat{H}_{EPR} as

$$\hat{H}_{\text{EPR}} = -\hbar\gamma_I \mathbf{B}_0 \cdot (\mathbf{1} - \boldsymbol{\sigma}^{\text{orb}}) \cdot \hat{\mathbf{I}} + \hat{H}_Z + \hat{H}_{\text{HF}} + \hat{H}_{\text{ZFS}}, \quad (6.8)$$

where \hat{H}_Z , \hat{H}_{HF} , and \hat{H}_{ZFS} are the Hamiltonians representing the electronic Zeeman, hyperfine, and ZFS interactions as described below. Henceforth, in the interests of simplifying the notation, we denote the effective spin operator as \hat{S} rather than $\hat{\tilde{S}}$, i.e. we omit the tilde.

6.2.1 The electronic Zeeman interaction

We can write the general electronic Zeeman interaction Hamiltonian as

$$\hat{H}_Z = - \sum_i B_{0,i} \hat{m}_i, \quad (6.9)$$

where, in an electronic state with effective spin S , the general magnetic moment vector operator \hat{m}_i is [222]

$$\hat{m}_i = -\mu_B \sum_{k=0}^{2S} \sum_{q=-k}^{+k} (-1)^q \hat{S}_{k-q} \hat{g}_{kq,i}, \quad (6.10)$$

where the $g_{kq,i}$ are the components of a complex g -tensor of rank k and order q . The complex conjugate of $g_{kq,i}$ is

$$g_{kq,i}^* = (-1)^q g_{k-q,i}, \quad (6.11)$$

which ensures that \hat{H}_Z is Hermitian. We note that, because \hat{H}_Z is linear in $B_{0,i}$ the sum in Equation 6.10 only contains terms of odd rank k . Explicitly this means that the terms of ranks 1, 3, and 5 are relevant for d -block metal ions, whereas terms of ranks 1, 3, 5, and 7 are needed for f -block metal ions. We have already encountered the terms of rank one in chapter 4.

As an example, we consider the generalized Zeeman interaction of the Gd^{3+} , which has spin $S = 7/2$.

The relevant g -tensors are approximately isotropic as the $4f$ subshell is half filled, giving an electronic ground state with term ${}^8S_{7/2}$. We can therefore write the Zeeman Hamiltonian as [223]

$$\hat{H}_Z = \mu_B g B_0 \hat{S}_z + \mu_B g' B_0 \hat{S}_z^3 + \mu_B g'' B_0 \hat{S}_z^5 + \mu_B g''' B_0 \hat{S}_z^7, \quad (6.12)$$

where g , g' , g'' , and g''' are the g -factors associated with the Zeeman interactions of increasing order, consistent with measurements of the g -factors of Gd^{3+} defects within diamagnetic host crystalline lattices of different symmetries. Early measurements of the first-order factors g have been reviewed by Buckmaster and Shing, and are found to be slightly smaller than g_e , taking typical values of 1.985–1.992. The higher-order g -factors have also been examined separately by Marshall and Tilton [224], and Buckmaster et al [225]. Marshall and Tilton acquired EPR spectra of Gd^{3+} in ThO_2 , and measured an upper bound of g' of 2×10^{-7} , with the higher-order g -factors expected to have progressively smaller values [224]. Buckmaster et al. measured the g -factors of Gd^{3+} in $\text{La}(\text{C}_2\text{H}_3\text{SO}_4)_3 \cdot \text{H}_2\text{O}$, and found that g' has an upper bound of 2×10^{-6} [225]. This indicates that, although measurable, the higher-order Zeeman interactions in these systems are much weaker than the first-order Zeeman interaction, and consequently less important to the EPR/NMR properties.

6.2.2 The hyperfine interaction

The general hyperfine interaction can be written as a scalar product between the nuclear spin operator and the hyperfine field vector operator $\hat{\mathcal{F}}$.

$$\hat{H}_{\text{HF}} = \sum_i \hat{\mathcal{F}}_i \hat{I}_i, \quad (6.13)$$

The hyperfine field operator in an electronic state with effective spin S has a form that is similar to the magnetic moment vector operator in Equation 6.10 in that it is written in terms of the irreducible spherical tensor operators \hat{S}_{kq} [222]:

$$\hat{\mathcal{F}}_i = \sum_{k=0}^{2S} \sum_{q=-k}^{+k} (-1)^q \hat{S}_{k-q} A_{kq,i}. \quad (6.14)$$

The $A_{kq,i}$ are the components of a complex hyperfine tensor of rank k and order q which, like the $g_{kq,i}$ components, obey the following relation:

$$A_{kq,i}^* = (-1)^q A_{k-q,i}. \quad (6.15)$$

We note that, as for the electronic Zeeman interaction, the hyperfine field vector operator contains only terms of odd rank k to ensure the hermiticity of the hyperfine interaction Hamiltonian, i.e. $k = 1, 3,$ and 5 for d -block metal ions, and $k = 1, 3, 5,$ and 7 for f -block metal ions. We have already encountered the terms of rank one in chapter 4.

6.2.3 The ZFS interaction

The general ZFS interaction Hamiltonian is

$$\hat{H}_{\text{ZFS}} = \sum_{k=0}^{2S} \sum_{q=-k}^{+k} (-1)^q D_{kq} \hat{S}_{k-q}, \quad (6.16)$$

where the ZFS irreducible spherical spatial tensor components D_{kq} have rank k and order q , and satisfy the relation:

$$D_{kq}^* = (-1)^q D_{k-q}. \quad (6.17)$$

In contrast to the Zeeman and hyperfine interactions, the ZFS retains non-zero terms with even k , i.e. $k = 2,$ and 4 for d -block metal ions, and $k = 2, 4,$ and 6 for f -block metal ions. We have already encountered the terms of rank two in chapter 4. The principal values of the generalized ZFS tensor of rank k and order q are conventionally written in terms of the energy parameters $b_k^{|q|}$. In cubic systems we define the three principal axes to be along the three four-fold (proper or improper) rotation axes, whereas in tetragonal, hexagonal, and trigonal systems the principal z -axis is defined to be parallel to the highest-order rotation axis. In orthorhombic groups the principal axes are defined according to the two-fold rotation axes. Adopting these conventions we obtain the principal values of the ZFS tensors described by Buckmaster and Shing, which are tabulated in Table 6.1.

The rank-four ZFS parameters have been measured for Mn^{2+} and Fe^{3+} (both $S = 5/2$) [207], and the rank-four and rank-six parameters have been measured extensively for Gd^{3+} in diamagnetic host lattices of

Rank k	Order q	\tilde{D}_{kq} for different symmetries				
		cubic	tetragonal	hexagonal	trigonal	orthorhombic
2	0	0	$(\sqrt{2/3})b_2^0$	$(\sqrt{2/3})b_2^0$	$(\sqrt{2/3})b_2^0$	$(\sqrt{2/3})b_2^0$
	± 1	0	0	0	0	0
	± 2	0	0	0	0	$(1/3)b_2^2$
4	0	$(\sqrt{70/30})b_4^0$	$(\sqrt{70/30})b_4^0$	$(\sqrt{70/30})b_4^0$	$(\sqrt{70/30})b_4^0$	$(\sqrt{70/30})b_4^0$
	± 1	0	0	0	0	0
	± 2	0	0	0	0	$(\sqrt{7/60})b_4^2$
	± 3	0	0	0	$\pm(\sqrt{2/6})b_4^3$	0
	± 4	$(1/6)b_4^0$	$(1/30)b_4^4$	0	0	$(1/30)b_4^4$
6	0	$(\sqrt{231/315})b_6^0$	$(\sqrt{231/315})b_6^0$	$(\sqrt{231/315})b_6^0$	$(\sqrt{231/315})b_6^0$	$(\sqrt{231/315})b_6^0$
	± 1	0	0	0	0	0
	± 2	0	0	0	0	$((\sqrt{11/5})/315)b_6^2$
	± 3	0	0	0	$\pm((\sqrt{11/5})/18)b_6^3$	0
	± 4	$-((\sqrt{11/6})/15)b_6^0$	$((\sqrt{11/6})/315)b_6^4$	0	0	$((\sqrt{11/6})/315)b_6^4$
	± 5	0	0	0	0	0
	± 6	0	0	$(1/315)b_6^6$	$(1/315)b_6^6$	$(1/315)b_6^6$

Table 6.1: The principal values of the spatial parts of the generalized ZFS interaction up to rank six. The second-rank parameters are related to the axial and rhombic ZFS anisotropies by $b_2^0 = D$ and $b_2^2 = 3E$. The point groups corresponding to each symmetry class are: O_h , O , T_d , and T (cubic); C_4 , C_{4v} , C_{4h} , D_4 , D_{4h} , and D_{2d} (tetragonal); C_6 , C_{6v} , C_{6h} , C_{3h} , D_6 , D_{6h} , and D_{3h} (hexagonal); C_3 , S_6 , C_{3v} , D_3 , and D_{3d} (trigonal); C_{2v} , D_2 , and D_{2h} (orthorhombic). In the cubic groups the principal axes of the PAF are along the three four-fold rotation axes. In the tetragonal, hexagonal, and trigonal groups the PAF is defined so that the z -axis is aligned with the highest-order rotation axis. In the orthorhombic groups, the three principal axes coincide with the three two-fold rotation axes.

various symmetry groups [223]. The maximum values of the ZFS parameters for Gd^{3+} are generally found to be $b_2^0 \sim 1$ GHz, $b_4^0 \sim 100$ MHz, and $b_4^4 \sim 10$ MHz. In non-cubic systems the rank-two ZFS is generally expected to dominate the other ZFS terms. However in cubic systems with either a small or no rank-two ZFS, the higher-order ZFS interactions may become important.

6.2.4 The EPR formalism of the paramagnetic shielding tensor

The form of the generalized EPR Hamiltonian has a profound effect on the form of the paramagnetic shielding tensor, which is given by the EPR formula in Equation 4.103 and reproduced below for convenience:

$$\begin{aligned}
\sigma_{ij}^S = & \frac{2}{\hbar\gamma_I Q_0} \sum_n \exp(-\beta E_n) \sum_{m \neq n} \sum_{\nu, \mu} \frac{\langle n\nu | \hat{m}_i | m\mu \rangle \langle m\mu | \hat{\mathcal{F}}_j | n\nu \rangle}{E_m - E_n} \\
& + \frac{\beta}{\hbar\gamma_I Q_0} \sum_n \exp(-\beta E_n) \sum_{\nu, \nu'} \langle n\nu | \hat{m}_i | n\nu' \rangle \langle n\nu' | \hat{\mathcal{F}}_j | n\nu \rangle.
\end{aligned} \tag{6.18}$$

The EPR expression in Equation 6.18 is a completely general formula for the paramagnetic shielding tensor due to a paramagnetic centre of any spin multiplicity and SO coupling strength. As we mentioned in section 4.2.1, this formalism makes no assumptions about the level of theory, i.e. relativistic or not, the SO coupling strength, or the multiplicity of the electronic energy levels. Therefore this formalism has a much wider scope than the 3d metal ions we have so far discussed, and can be applied to more complex ions such as lanthanides and actinides. The general, and unspecified, forms of the electronic magnetic moment \hat{m} and hyperfine $\hat{\mathcal{F}}$ operators in Equation 6.18 are valid for situations where several energy levels of the crystal-field interaction are thermally populated. However this formula suffers from the disadvantage of being rather unwieldy. The remainder of this chapter is orientated towards examining the situations in which we may simplify the formalism.

Paramagnetic chemical shielding of a thermally-isolated degenerate ground state

Van den Heuvel proposed a simplification of Equation 6.18 that can be employed when only the ground state sub-manifold due to the crystal-field splitting is thermally occupied [88]. In practice this would occur when the energy separation between the ground sub-manifold $n = 0$ and the lowest-lying excited sub-manifold is much greater than kT . In this case Equation 6.18 can be simplified to give

$$\sigma_{ij}^{\tilde{S}} = \frac{\beta}{\hbar\gamma_I} \frac{1}{2\tilde{S} + 1} \sum_{\nu, \nu'} \langle 0\nu | \hat{m}_i^{(0)} | 0\nu' \rangle \langle 0\nu' | \hat{\mathcal{F}}_j^{(0)} | 0\nu \rangle \quad (6.19)$$

$$= \frac{\beta}{\hbar\gamma_I} \frac{1}{2\tilde{S} + 1} \text{Tr}_{\tilde{S}} [\hat{m}_i^{(0)} \hat{\mathcal{F}}_j^{(0)}] \quad (6.20)$$

$$= -\frac{\mu_B \beta}{\hbar\gamma_I} \frac{1}{2\tilde{S} + 1} \sum_{k, k'} \sum_{q, q'} (-1)^{q+q'} g_{kq, i}^{(0)} A_{k'q', j}^{(0)} \text{Tr}_{\tilde{S}} [\hat{S}_{k-q} \hat{S}_{k'-q'}], \quad (6.21)$$

where we have added a superscript (0) to the g - and hyperfine tensor parameters to reflect the fact that they are properties of the $n = 0$ sub-manifold. The trace can be further simplified following the discussion in appendix D to give

$$\sigma_{ij}^{\tilde{S}} = -\frac{\mu_B}{\hbar\gamma_I kT} \sum_{k=0}^{2\tilde{S}} \frac{\langle \tilde{S} || \hat{S}_k || \tilde{S} \rangle^2}{2k + 1} \sum_{q=-k}^{+k} (-1)^q g_{kq, i}^{(0)} A_{k-q, j}^{(0)}, \quad (6.22)$$

where only the terms with $k' = k$ and $q' = q$ remain. The $\langle S || \hat{S}_k || S' \rangle$ are the reduced matrix elements of the tensor \hat{S}_k [190] which, for tensors \hat{S}_k that are formed according to Equation 6.5 with $\hat{O}_{kq} = \hat{S}_{kq}$, can be

calculated from the formula of Buckmaster et al. [220]:

$$\langle S || \hat{S}_k || S' \rangle = \sqrt{\frac{k!k!(2S+k+1)!}{2^k(2k)!(2S-k)!(2S+1)}} \delta_{SS'}. \quad (6.23)$$

This paramagnetic shielding in this expression has a Curie temperature dependence, which is because the electronic spin system behaves analogously to the spin system with an anisotropic g -tensor and no ZFS discussed by Moon and Patchkovskii [38]. In fact we may regard Equation 6.22 as the generalization of the Moon–Patchkovskii Equation 4.118 resulting from considering the EPR interaction terms with ranks k greater than one. If we retain only those terms with $k = 1$, then Equation 6.22 reduces to Equation 4.118.

6.3 The paramagnetic shielding and magnetic susceptibility tensors due to a transition-metal ion with arbitrary spin multiplicity

In this section we return to the case of a d -block transition-metal ion in a thermally-isolated ground state $n = 0$ of the crystal-field splitting interaction Hamiltonian, in which the effective spin is the same as the formal true spin. The generalized EPR Hamiltonian in section 6.2 describes the electronic spin properties of this ground state, and dictates the form of the paramagnetic shielding tensor. We use the forms of the operators \hat{m} and $\hat{\mathcal{F}}$ that are given in terms of \hat{S}_{kq} , and set the energy levels of the Boltzmann averages so that they correspond to the eigenvalues of the generalized ZFS Hamiltonian. Note that this situation is different to that which resulted in Equation 6.22, since in that case it is also assumed that the electronic spin system is thermally isolated in the ZFS ground state in addition to the crystal field splitting ground state. In the present case the paramagnetic shielding tensor then takes the form:

$$\sigma_{ij}^S = -\frac{\mu_B}{\hbar\gamma_I} \sum_{k=0}^{2S} \sum_{k'=0}^{2S} \sum_{q=-k}^{+k} \sum_{q'=-k'}^{+k'} (-1)^{q+q'} g_{kq,i} Z_{kk'qq'} A_{k'q',j}, \quad (6.24)$$

where the dependence on both the temperature and the zero-field Hamiltonian is encoded in $Z_{kk'qq'}$, which is given by

$$\begin{aligned} Z_{kk'qq'} &= \frac{2}{Q_0} \sum_n \exp(-\beta E_n) \sum_{m \neq n} \sum_{\nu, \mu} \frac{\langle n\nu | \hat{S}_{k-q} | m\mu \rangle \langle m\mu | \hat{S}_{k'-q'} | n\nu \rangle}{E_m - E_n} \\ &+ \frac{\beta}{Q_0} \sum_n \exp(-\beta E_n) \sum_{\nu, \nu'} \langle n\nu | \hat{S}_{k-q} | n\nu' \rangle \langle n\nu' | \hat{S}_{k'-q'} | n\nu \rangle. \end{aligned} \quad (6.25)$$

To second order in $1/(kT)$ the paramagnetic shielding tensor is given by

$$\begin{aligned} \sigma_{ij}^S &= -\frac{\mu_B}{\hbar\gamma_I} \left[\frac{\beta}{2S+1} \sum_{kk'qq'} (-1)^{q+q'} g_{kq,i} A_{k'q',j} \text{Tr}_S \left(\hat{S}_{k-q} \hat{S}_{k'-q'} \right) \right. \\ &\left. - \frac{\beta^2}{2S+1} \sum_{kk'k''qq'q''} (-1)^{q+q'+q''} g_{kq,i} A_{k'q',j} D_{k''q''} \text{Tr}_S \left(\hat{S}_{k-q} \hat{S}_{k'-q'} \hat{S}_{k''-q''} \right) \right] + O(\beta^3). \end{aligned} \quad (6.26)$$

The details of the calculation are given in appendix D. This expression can be simplified by calculating the traces (also see Appendix D). The term that is first-order in $1/(kT)$, $\sigma_{ij}^{S,1}$, is then given by [88]:

$$\sigma_{ij}^{S,1} = -\frac{\mu_B}{\hbar\gamma_I kT} \sum_{k=0}^{2S} \frac{\langle S || \hat{S}_k || S \rangle^2}{2k+1} \sum_{q=-k}^{+k} (-1)^q g_{kq,i} A_{k-q,j}, \quad (6.27)$$

where we notice that the only contributing terms from the sum are those with $k = k'$ and $q = -q'$. This is an analogous expression to that in Equation 6.22. However we recall that here the electronic spin is not thermally isolated in the ground state of the ZFS. The second-order term $\sigma_{ij}^{S,2}$ is given by

$$\begin{aligned} \sigma_{ij}^{S,2} &= \frac{\mu_B}{\hbar\gamma_I (kT)^2} (-1)^{2S} (2S+1)^{1/2} \sum_{kk'k''} \langle S || \hat{S}_k || S \rangle \langle S || \hat{S}_{k'} || S \rangle \langle S || \hat{S}_{k''} || S \rangle \left\{ \begin{matrix} k' & k'' & k \\ S & S & S \end{matrix} \right\} \\ &\times \sum_{qq'q''} g_{kq,i} A_{k'q',j} D_{k''q''} \left(\begin{matrix} k' & k'' & k \\ -q' & -q'' & -q \end{matrix} \right), \end{aligned} \quad (6.28)$$

where the arrays contained in parentheses and braces are Wigner $3j$ and Wigner $6j$ symbols respectively.

It is important to note that the symmetry properties of the Wigner $3j$ and Wigner $6j$ symbols impose restrictions on both the ranks and orders of the irreducible spherical tensors that can contribute to the second-

order paramagnetic chemical shielding. Firstly the symmetry of the $6j$ symbol dictates that the triplets (k, S, S) , (k', S, S) , and (k'', S, S) must satisfy the triangle condition $k, k', k'' \leq 2S$. This is simply a reinforcement of the restriction on the ranks of the interaction tensors that we stated earlier. Secondly, both the $3j$ and $6j$ symbols require (k, k', k'') to also satisfy the triangle condition that any one of the three ranks must be less than or equal to the sum of the other two. This has important consequences for the shielding tensor to second order, as we will see later. Finally, from the $3j$ symbol, the sum of the three orders must be zero, $q + q' + q'' = 0$.

As we have also noted in chapter 4, the g -tensor is responsible for introducing a term into the paramagnetic shielding tensor with a leading temperature dependence of $1/(kT)$, and the ZFS gives a term with a leading temperature dependence of $1/(kT)^2$. This feature is also present in the Bleaney expression in Equation 4.132. However the present situation is more general, as we have explicitly considered the higher-order irreducible spherical tensor components of the EPR parameters. Hence Equations 6.27 and 6.28 are generalized forms of the Bleaney expression in Equation 4.132.

6.3.1 The Bleaney expression for d -block metal ions revisited

We now calculate the paramagnetic shielding tensor up to $O(1/(kT)^2)$ for a Hamiltonian comprising an electronic Zeeman term and a hyperfine term that are both linear in \hat{S} , and a ZFS term with terms of ranks 2, 4, and 6:

$$\hat{H} = \mu_B \mathbf{B}_0 \cdot \mathbf{g} \cdot \hat{S} + \hat{S} \cdot \mathbf{A} \cdot \hat{I} + \sum_{k=2,4,6} \sum_{q=-k}^{+k} (-1)^q D_{kq} \hat{S}_{k-q} \quad (6.29)$$

$$= \mu_B \sum_i B_{0,i} \sum_{q=-1}^{+1} (-1)^q \hat{S}_{1-q} g_{1q,i} + \sum_i \sum_{q=-1}^{+1} (-1)^q \hat{S}_{1-q} A_{1q,i} \hat{I}_i + \sum_{k=2,4,6} \sum_{q=-k}^{+k} (-1)^q D_{kq} \hat{S}_{k-q}. \quad (6.30)$$

In the ZFS term, we encounter the terms of rank 4 for transition metal ions with $S \geq 2$, and the rank-6 terms for the lanthanide ions [184]. Henceforth we concentrate on the transition-metal ions of the d block and those of the f block with an f^7 configuration, such as Gd^{3+} , with the aim being to reproduce the Bleaney expression in Equation 4.132. We can write down the first- and second-order parts of the shielding tensor

from Equations 6.27 and 6.28:

$$\sigma_{ij}^{S,1} = -\frac{\mu_B}{\hbar\gamma_I kT} \frac{\langle S \parallel \hat{S}_1 \parallel S \rangle^2}{3} \sum_{q=-1}^{+1} (-1)^q g_{1q,i} A_{1-q,j}, \quad (6.31)$$

$$\begin{aligned} \sigma_{ij}^{S,2} = & \frac{\mu_B}{\hbar\gamma_I(kT)^2} (-1)^{2S} (2S+1)^{1/2} \langle S \parallel \hat{S}_1 \parallel S \rangle^2 \sum_{k''=2,4,6} \langle S \parallel \hat{S}_{k''} \parallel S \rangle \begin{Bmatrix} 1 & k'' & 1 \\ S & S & S \end{Bmatrix} \\ & \times \sum_{qq'q''} g_{1q,i} A_{1q',j} D_{k''q''} \begin{Bmatrix} 1 & k'' & 1 \\ -q' & -q'' & -q \end{Bmatrix}. \end{aligned} \quad (6.32)$$

As we have come to expect, the first-order term is proportional to the product of the g - and hyperfine tensors, and is independent of the ZFS tensor. In the second-order term we have hitherto retained terms in the ZFS tensor of all possible ranks, but we can see that a simplification is possible. Since k , k' , and k'' must satisfy the triangle condition, the only ZFS tensor components that contribute to the second-order shielding tensor are of rank $k'' = 2$, as was previously noted by Bleaney [61], and McGarvey and Kurland [37].

We can now proceed with the calculation by writing down the analytical expressions of all the factors involved. The reduced matrix elements of the first- and second-rank spin tensors are given by Equation 6.23, and have the following explicit expressions:

$$\langle S \parallel \hat{S}_1 \parallel S \rangle = \sqrt{S(S+1)}, \quad (6.33)$$

$$\langle S \parallel \hat{S}_2 \parallel S \rangle = \sqrt{\frac{S(S+1)(2S-1)(2S+3)}{6}}. \quad (6.34)$$

The exact expression for the Wigner $6j$ symbol with $k'' = 2$ has been derived by Edmonds [226], and is

$$\begin{Bmatrix} 1 & 2 & 1 \\ S & S & S \end{Bmatrix} = \begin{cases} (-1)^{2S} \sqrt{\frac{(2S-1)(2S+3)}{30S(S+1)(2S+1)}}, & S \geq 1 \\ 0, & \text{otherwise.} \end{cases} \quad (6.35)$$

It can also be shown that the exact expression for the Wigner $3j$ symbol is [190]

$$\begin{Bmatrix} 1 & 2 & 1 \\ -q' & -q'' & -q \end{Bmatrix} = (-1)^{-q'-q} \sqrt{\frac{(1+q')!(2-q'')!(2+q'')!(1-q)!}{30(1-q')!((1+q'+q'')!)^2((1-q''-q)!)^2(1+q)!}}, \quad (6.36)$$

for $q + q' + q'' = 0$ and zero otherwise. Finally the components of the g - and hyperfine tensors $g_{1q,i}$ and $A_{1q,i}$ can be calculated from the Cartesian components. The g -tensor comprises three vectors \mathbf{g}_{1q} , one for each value of q , which are equal to:

$$\mathbf{g}_{1\pm 1} = \mp \sqrt{\frac{1}{2}} \begin{pmatrix} g_{xx} \pm ig_{xy} \\ g_{yx} \pm ig_{yy} \\ g_{zx} \pm ig_{zy} \end{pmatrix}, \quad \mathbf{g}_{10} = \begin{pmatrix} g_{xz} \\ g_{yz} \\ g_{zz} \end{pmatrix}. \quad (6.37)$$

Likewise the three vectors comprising the hyperfine tensor \mathbf{A}_{1q} are:

$$\mathbf{A}_{1\pm 1} = \mp \sqrt{\frac{1}{2}} \begin{pmatrix} A_{xx} \pm iA_{yx} \\ A_{xy} \pm iA_{yy} \\ A_{xz} \pm iA_{yz} \end{pmatrix}, \quad \mathbf{A}_{10} = \begin{pmatrix} A_{zx} \\ A_{zy} \\ A_{zz} \end{pmatrix}. \quad (6.38)$$

Combining all these expressions results in the final expression for the paramagnetic shielding tensor to second order in $1/(kT)$:

$$\sigma^S = -\frac{\mu_B S(S+1)}{3\hbar\gamma kT} \mathbf{g} \cdot \mathbf{A} + \frac{\mu_B S(S+1)(2S-1)(2S+3)}{30\hbar\gamma(kT)^2} \mathbf{g} \cdot \mathbf{D} \cdot \mathbf{A}, \quad (6.39)$$

where \mathbf{D} is the second-rank part of the ZFS interaction tensor. This expression is identical to that derived earlier in Equation 4.132, but is in fact more general. The former expression was calculated assuming that the zero-field Hamiltonian was described entirely by the second-rank ZFS tensor, whereas the present derivation has shown that the fourth- and sixth-rank parts do not contribute to the shielding tensor to second order in $1/(kT)$. However these higher-order components are present in the terms of third order and higher in $1/(kT)$ [37]. We recall that if the higher-order ZFS terms are zero or negligible, the shielding tensor has the form of Equation 4.109.

6.3.2 The EPR formalism of the magnetic susceptibility tensor

The EPR formalism can also be used to calculate the magnetic susceptibility tensor [88]. Following the discussion leading to the paramagnetic shielding tensor in Equation 6.24, and substituting the hyperfine field

operator for the electronic magnetic moment operator, we obtain a susceptibility tensor of a similar form:

$$\chi_{ij} = \mu_0 \mu_B^2 \sum_{k=0}^{2S} \sum_{k'=0}^{2S} \sum_{q=-k}^{+k} \sum_{q'=-k'}^{+k'} (-1)^{q+q'} g_{kq,i} Z_{kk'qq'} g_{k'q',j}. \quad (6.40)$$

We can write down the first- and second-order terms in $1/(kT)$ in the susceptibility tensor following the same procedure as for the paramagnetic shielding tensor. The first-order term $\chi_{ij}^{(1)}$ is

$$\chi_{ij}^{(1)} = \frac{\mu_0 \mu_B^2}{kT} \sum_{k=0}^{2S} \frac{\langle S \parallel \hat{S}_k \parallel S \rangle^2}{2k+1} \sum_{q=-k}^{+k} (-1)^q g_{kq,i} g_{k-q,j}, \quad (6.41)$$

and the second-order term $\chi_{ij}^{(2)}$ is

$$\begin{aligned} \chi_{ij}^{(2)} = & -\frac{\mu_0 \mu_B^2}{(kT)^2} (-1)^{2S} (2S+1)^{1/2} \sum_{kk'k''} \langle S \parallel \hat{S}_k \parallel S \rangle \langle S \parallel \hat{S}_{k'} \parallel S \rangle \langle S \parallel \hat{S}_{k''} \parallel S \rangle \begin{Bmatrix} k' & k'' & k \\ S & S & S \end{Bmatrix} \\ & \times \sum_{qq'q''} g_{kq,i} g_{k'q',j} D_{k''q''} \begin{pmatrix} k' & k'' & k \\ -q' & -q'' & -q \end{pmatrix}. \end{aligned} \quad (6.42)$$

We immediately notice the similarity between these expressions and the corresponding expressions for the shielding tensor in Equations 6.27 and 6.28.

If we further assume that the system can be described with the EPR Hamiltonian in Equation 6.30 we obtain Equation 4.174, which is reproduced below

$$\chi \approx \frac{\mu_0 \mu_B^2 S(S+1)}{3kT} \mathbf{g} \cdot \mathbf{g}^T - \frac{\mu_0 \mu_B^2 S(S+1)(2S-1)(2S+3)}{30(kT)^2} \mathbf{g} \cdot \mathbf{D} \cdot \mathbf{g}^T. \quad (6.43)$$

Once again, as noted by Bleaney [61] and Kurland and McGarvey [37], the only terms of the ZFS Hamiltonian that contribute to the susceptibility tensor to second order are those of spatial rank two. We recall at this point that higher-order ZFS terms do contribute to shielding terms of order higher than $1/(kT)^2$. However when the fourth- and sixth-rank ZFS terms are either zero or negligible we can write down a general form of the susceptibility tensor as follows

$$\chi = \mu_0 \mu_B^2 \mathbf{g} \cdot \mathbf{Z} \cdot \mathbf{g}^T, \quad (6.44)$$

which is the same expression as given in Equation 4.173.

6.4 Electronic properties of the lanthanide ions

We now turn our attention to the lanthanide ions, focussing on the formalism for the paramagnetic shielding and magnetic susceptibility tensors proposed by Bleaney [61]. This approach assumes that the coordinated lanthanides can be modelled as free metal ions with the crystal-field due to the ligands added as a perturbation. We therefore begin by summarizing the free-ion properties, and then introduce the crystal-field interaction.

6.4.1 The free lanthanide ions

The lanthanide ions are predominantly, but not exclusively, trivalent with the unpaired electrons residing in the $4f$ orbitals. Unlike the $3d$ shell of the first-row transition-metal ions, the $4f$ orbitals of the lanthanides are not valence orbitals and so participate in the metal-ligand coordination to a lesser extent. In addition the SO coupling strength of the lanthanides is much larger than for the $3d$ metal ions. This places the lanthanide ions in the ‘weak crystal-field limit’, where the SO coupling is much stronger than the crystal-field interaction, and so cannot be treated as a perturbation as in chapter 4. We therefore use the approach of Bleaney [61], which is to assume that the $4f$ orbitals are sufficiently radially contracted for the properties of the coordinated metal ions to be adequately described by the free ions, with the crystal-field interaction added as a perturbation.

The magnetic properties of the free lanthanides are described in terms of the total angular momentum J which, in the limit of LS coupling, is written as the sum of the total orbital L and spin S angular momenta of the electronic configuration, according to the LS coupling scheme:

$$J = L + S. \quad (6.45)$$

The total angular momentum is quantized, and labelled with the total angular momentum quantum number J which takes values according to the Clebsch–Gordan series, i.e. $L + S, L + S - 1, \dots, |L - S|$. The electronic levels corresponding to the configuration of the free ion can therefore be labelled by these three quantum numbers and are usually represented by term symbols $^{2S+1}L_J$. The ground level is given by Hund’s rules [206], and is generally the only level that is thermally occupied at room temperature and is therefore the only

Ion	Configuration	S	L	J	Term	ζ / cm^{-11}	$\lambda / \text{cm}^{-12}$
Ce ³⁺	f^1	1/2	3	5/2	$^2F_{5/2}$	640	640
Pr ³⁺	f^2	1	5	4	3H_4	750	375
Nd ³⁺	f^3	3/2	6	9/2	$^4I_{9/2}$	900	300
Pm ³⁺	f^4	2	6	4	5I_4	—	—
Sm ³⁺	f^5	5/2	5	5/2	$^6H_{5/2}$	1180	236
Eu ³⁺	f^6	3	3	0	7F_0	1360	227
Gd ³⁺	f^7	7/2	0	7/2	$^8S_{7/2}$	—	—
Tb ³⁺	f^8	3	3	6	7F_6	1620	-270
Dy ³⁺	f^9	5/2	5	15/2	$^6H_{15/2}$	1820	-364
Ho ³⁺	f^{10}	2	6	8	5I_8	2080	-520
Er ³⁺	f^{11}	3/2	6	15/2	$^4I_{15/2}$	2470	-823
Tm ³⁺	f^{12}	1	5	6	3H_6	2750	-1375
Yb ³⁺	f^{13}	1/2	3	7/2	$^2F_{7/2}$	2950	-2950

Table 6.2: List of the trivalent lanthanide ions, and the parameters defining the electronic ground states of the free ions assuming LS -coupling. The f -electron configurations are given, along with the total spin S , orbital L , and total J angular momenta. The ground state is given by Hund's rules, and is represented by the term symbol. The one-electron ζ and many-electron λ SO coupling parameters are also given, except for Pm³⁺, which is radioactive, and Gd³⁺, which has a half-filled $4f$ shell and therefore an SO interaction of zero.

state we need consider. The exceptions to this assertion are the ions with configurations $4f^5$ and $4f^6$, namely Sm³⁺ and Eu³⁺, where we also have to consider the lowest-lying excited states. The free-ion properties of the trivalent lanthanides Ln³⁺ with between 1 and 13 $4f$ electrons, and the one-electron and many-electron SO coupling constants ζ and λ [185], are given in Table 6.2.

Each electronic level $^{2S+1}L_J$ comprises $2J + 1$ electronic states that are labelled with the azimuthal quantum number M_J , which takes values from $+J$ to $-J$ in integer steps. In the absence of other interactions the states of a particular level are degenerate, and may therefore be described as corresponding to an effective spin $\tilde{S} = J$ whose multiplicity $2\tilde{S} + 1$ matches the true degeneracy. Clearly levels with different J therefore correspond to different effective spins.

The effective spin EPR Hamiltonian can therefore be written in terms of the operator for the total angular momentum \hat{J} . For the free ion the ZFS is zero by symmetry, and so we need only consider the electronic Zeeman interaction, and the hyperfine coupling between the unpaired electrons and the lanthanide nucleus. We have seen that the total magnetic moment μ_J is not parallel to the total angular momentum J , as illustrated in Figure 4.1. However, from the projection theorem outlined in Appendix A.1, the matrix elements of the operator $\hat{\mu}_J$ are proportional to those of \hat{J} , and so the component of the magnetic moment that appears in the Zeeman interaction Hamiltonian is that which commutes with \hat{J} , i.e. $-\mu_B g_J \hat{J}$, as shown in Figure 6.1.

¹Values taken from Weil and Bolton [185].

²Calculated using $\lambda = \pm\zeta/(2S)$ with the plus sign for f -shells that are less than half full, and the minus sign for shells that are more than half full. When the shell is exactly half full, the SO coupling is essentially zero.

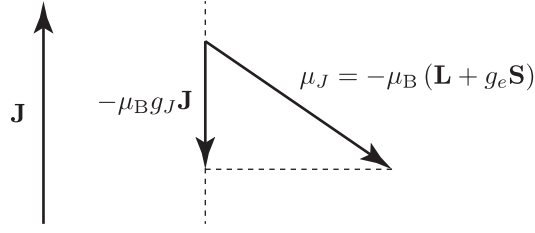


Figure 6.1: Illustration of the relationship between the total angular momentum \mathbf{J} and the total magnetic moment $\boldsymbol{\mu}_J$ under the Russell–Saunders coupling scheme. In general $\boldsymbol{\mu}_J$ is not parallel to \mathbf{J} . However the electronic Zeeman interaction depends only on the component of the magnetic moment that is parallel to \mathbf{J} , namely $-\mu_B g_J \mathbf{J}$.

The Zeeman interaction Hamiltonian $\hat{H}_Z = \mu_B \mathbf{B}_0 \cdot (\hat{\mathbf{L}} + g_e \hat{\mathbf{S}})$ can therefore be written in terms of $\hat{\mathbf{J}}$:

$$\hat{H}_Z = \mu_B g_J \mathbf{B}_0 \cdot \hat{\mathbf{J}}. \quad (6.46)$$

The number g_J is the isotropic Landé g -factor which is given by

$$g_J = \frac{g_S + g_L}{2} + (g_L - g_S) \frac{L(L+1) - S(S+1)}{2J(J+1)}, \quad (6.47)$$

where g_L and g_S are the orbital and electronic g -factors. Writing $g_L = 1$ and approximating g_S as 2 gives us the familiar expression

$$g_J = \frac{3}{2} + \frac{S(S+1) - L(L+1)}{2J(J+1)}. \quad (6.48)$$

This expression for g_J can be derived by calculating the projection of the total magnetic moment $\boldsymbol{\mu}_J$ onto the total angular momentum \mathbf{J} , as shown in appendix A.1. The Zeeman interaction lifts the degeneracy of the each level J and, for an external magnetic field along z , the Zeeman energy of each state is $M_J \mu_B g_J B_0$. One important property of the Landé g -factor is that it varies with J , and so we would expect a different g -factor, and therefore a different Zeeman splitting, for each level. This may appear trivial, but does in fact have important consequences for the EPR and NMR spectra of lanthanide compounds subject to a large crystal-field splitting of the electronic energy levels.

We can write the hyperfine coupling Hamiltonian \hat{H}_{HF} as

$$\hat{H}_{\text{HF}} = A_J \hat{\mathbf{J}} \cdot \hat{\mathbf{I}}, \quad (6.49)$$

where A_J is an isotropic contact hyperfine coupling constant. Here \hat{H}_{HF} describes the interaction between the unpaired $4f$ electrons and the lanthanide nuclear spin.

6.4.2 The crystal-field interaction

The crystal-field interaction Hamiltonian can be described by Equation 6.6, but in terms of the total angular momentum. The expression is here given explicitly:

$$\hat{H}_{\text{CF}} = \sum_{k=2,4,6} \sum_{q=-k}^{+k} (-1)^q B_{kq} \hat{J}_{k-q}, \quad (6.50)$$

where the \hat{J}_{kq} are irreducible spherical tensor operators of the total angular momentum of rank k and order q . In the absence of an external magnetic field and nuclear magnetic moments, this Hamiltonian has the effect of lifting the degeneracy of the manifold of states of level J , creating a set of sub-manifolds each with a multiplicity lower than $2J + 1$.

It is common to write the crystal-field splitting Hamiltonian \hat{H}_{CF} using the following alternative form, rather than in terms of the irreducible spherical tensor operators:

$$\hat{H}_{\text{CF}} = \sum_{k=2,4,6} \sum_{q=0}^{+k} A_k^q \langle r^k \rangle \langle J || k || J \rangle \hat{O}_k^q. \quad (6.51)$$

In Equation 6.51 the spin part of the interaction is represented by the Stevens operator equivalents \hat{O}_k^q of rank k , and an order q that takes values from 0 to $+k$ [219]. These operators should not be confused with the irreducible spherical tensor operators \hat{O}_{kq} introduced earlier. For example the operators \hat{O}_2^0 and \hat{O}_2^2 are given by

$$\hat{O}_2^0 = 3\hat{J}_z^2 - J(J+1)\hat{1}, \quad (6.52)$$

$$\hat{O}_2^2 = \frac{1}{2}(\hat{J}_+^2 + \hat{J}_-^2), \quad (6.53)$$

and the additional relevant expressions for $k \geq 2$ can be found in Abragam and Bleaney [184]. The spatial part of the interaction is represented by the A -energy coefficients A_k^q of rank k and order q . The reduced matrix elements $\langle J || k || J \rangle$ are numerical coefficients that depend only on J . It is common to use the notation α, β , and

γ for $k = 2, 4,$ and 6 so that, for example, $\langle J \parallel \alpha \parallel J \rangle \equiv \langle J \parallel 2 \parallel J \rangle$. However we do not use that convention here. The remaining factor $\langle r^k \rangle$ is the mean k th power of the electronic radius of the $4f$ orbitals. The principal values of the rank-two part of the B -tensor, \tilde{B}_{ii} , are related to A_2^0 and A_2^2 as follows [61]:

$$\tilde{B}_{xx} = \langle r^2 \rangle \langle J \parallel 2 \parallel J \rangle (A_2^2 - A_2^0), \quad (6.54)$$

$$\tilde{B}_{yy} = \langle r^2 \rangle \langle J \parallel 2 \parallel J \rangle (-A_2^2 - A_2^0), \quad (6.55)$$

$$\tilde{B}_{zz} = \langle r^2 \rangle \langle J \parallel 2 \parallel J \rangle 2A_2^0, \quad (6.56)$$

from which we can define the axial and rhombic anisotropies of B , ΔB_{ax} and ΔB_{rh} , as

$$\Delta B_{\text{ax}} = \langle r^2 \rangle \langle J \parallel 2 \parallel J \rangle 3A_2^0, \quad (6.57)$$

$$\Delta B_{\text{rh}} = \langle r^2 \rangle \langle J \parallel 2 \parallel J \rangle 2A_2^2. \quad (6.58)$$

These crystal-field splitting parameters can be calculated from first principles as demonstrated by, for example, Vonci et al [73].

Each sub-manifold can therefore be described by an effective spin \tilde{S} chosen so that the degeneracy is equal to $2\tilde{S} + 1$. We can now write down the EPR Hamiltonian of the lanthanide within a particular sub-manifold n as

$$\hat{H}^{(n)} = \mu_B \sum_i B_{0,i} \sum_{k=0}^{2\tilde{S}} \sum_{q=-k}^{+k} (-1)^q \hat{S}_{k-q} \hat{g}_{kq,i}^{(n)} + \sum_{k=0}^{2\tilde{S}} \sum_{q=-k}^{+k} (-1)^q \hat{S}_{k-q} \sum_i A_{kq,i}^{(n)} \hat{I}_i + \sum_{k=0}^{2\tilde{S}} \sum_{q=-k}^{+q} (-1)^q D_{kq}^{(n)} \hat{S}_{k-q}, \quad (6.59)$$

where the superscript (n) denotes the EPR tensor parameters in the n th sub-level. We note that the g -tensor in each sub-level is no longer isotropic due to the lowering of the symmetry of the metal environment, and that the hyperfine interaction can now refer to the coupling between the unpaired electrons and a nucleus in the ligand. These tensor parameters are actually different for the different sub-manifolds that are present as a result of the crystal field splitting [184]. To take an example, the four states of the $J = 3/2$ level of a free lanthanide ion will, when subjected to an axially-symmetric crystal-field of spatial rank two, split into two doubly-degenerate sub-manifolds, each corresponding to an effective spin $\tilde{S} = 1/2$. The PAF components of the rank-one g -tensor are $\tilde{g}_{zz} = 3g_J$ and $\tilde{g}_{xx} = \tilde{g}_{yy} = 0$ for one sub-manifold, and $\tilde{g}_{zz} = g_J$ and $\tilde{g}_{xx} = \tilde{g}_{yy} = 2g_J$

for the other. In practice this means that the effective g - and hyperfine tensors that we measure during an EPR experiment depend on the relative populations of the sub-manifolds at the given temperature.

6.5 The Bleaney theory of the paramagnetic shielding tensor due to lanthanide ions

Bleaney derived a form of the paramagnetic chemical shielding tensor for lanthanide ions using a method that is distinct from the EPR formalism [61]. He assumed that (i) only the ground-state J manifold is thermally occupied, and that (ii) the $2J + 1$ states are split by the crystal field by an overall amount that does not exceed kT . Condition (i) is a good assumption for the lanthanide ions, with the exception of those metal ions with either a $4f^5$ or $4f^6$ configuration. However Bleaney calculated corrections involving the excited states for these cases. Condition (ii) is reasonable for many lanthanide compounds. This latter assumption also allows us to make a simplification to the form of the electron Zeeman interaction. We have seen that the different sub-manifolds of the level J under the crystal-field splitting have g -tensors with different anisotropies, and whose PAFs have different orientations. Kurland and McGarvey pointed out that, when all the sub-manifolds have a substantial thermal population, the g -anisotropies from the different sub-manifolds cancel to a first approximation, and we are left with an overall g -tensor that is isotropic, and equal to the Landé factor g_J . We can therefore write down a Hamiltonian that comprises this Zeeman interaction, and terms for the hyperfine and crystal-field interactions as:

$$\hat{H}_J = \mu_B g_J B_0 \cdot \hat{\mathbf{J}} + \hat{\mathbf{J}} \cdot \mathbf{A} \cdot \hat{\mathbf{I}} + \sum_{k=2,4,6} \sum_{q=-k}^{+k} (-1)^q B_{kq} \hat{J}_{k-q}. \quad (6.60)$$

Note that, in contrast to the effective-spin Hamiltonians we have so far encountered, the Hamiltonian in Equation 6.60 is a property of the total angular momentum of the physical system, rather than of the effective spin of a particular sub-level. This is why there is a term for the crystal-field interaction, rather than a ZFS. We can use this Hamiltonian to derive an expression for the paramagnetic shielding tensor in terms of the total angular momentum. We begin by deriving the following electronic magnetic moment and hyperfine

field operators:

$$\hat{m}_i = -\mu_B \sum_{q=-1}^{+1} (-1)^q \hat{J}_{1-q} g_{1q,i}, \quad (6.61)$$

$$\hat{\mathcal{F}}_i = \sum_{q=-1}^{+1} (-1)^q \hat{J}_{1-q} A_{1q,i}, \quad (6.62)$$

where

$$\mathbf{g}_{1\pm 1} = \mp \sqrt{\frac{1}{2}} g_J \begin{pmatrix} 1 \\ \pm i \\ 0 \end{pmatrix}, \quad \mathbf{g}_{10} = g_J \begin{pmatrix} 0 \\ 0 \\ 1 \end{pmatrix}, \quad (6.63)$$

and

$$\mathbf{A}_{1\pm 1} = \mp \sqrt{\frac{1}{2}} \begin{pmatrix} A_{xx} \pm iA_{yx} \\ A_{xy} \pm iA_{yy} \\ A_{xz} \pm iA_{yz} \end{pmatrix}, \quad \mathbf{A}_{10} = \begin{pmatrix} A_{zx} \\ A_{zy} \\ A_{zz} \end{pmatrix}. \quad (6.64)$$

The hyperfine coupling constant can be written as $\mathbf{A} = A^{\text{con}} \mathbf{1} + \mathbf{A}^{\text{dip}}$, i.e. as the sum of an isotropic contact term and an anisotropic dipolar term.

We can now derive the Bleaney expression for the shielding tensor σ_{ij}^J by expanding the expression from the EPR formalism to second order in $1/(kT)$, which gives us (from Appendix D)

$$\begin{aligned} \sigma_{ij}^J = & -\frac{\mu_B}{\hbar\gamma_I} \left[\frac{\beta}{2J+1} \sum_{qq'} (-1)^{q+q'} g_{1q,i} A_{1q',j} \text{Tr}_J (\hat{J}_{1-q} \hat{J}_{1-q'}) \right. \\ & \left. - \frac{\beta^2}{2J+1} \sum_{k''q'q''} (-1)^{q+q'+q''} g_{1q,i} A_{1q',j} B_{k''q''} \text{Tr}_J (\hat{J}_{1-q} \hat{J}_{1-q'} \hat{J}_{k''-q''}) \right] + O(\beta^3), \end{aligned} \quad (6.65)$$

where we have replaced S with J , and Tr_J refers to a summation over the $2J+1$ states of the level J . As previously we can simplify the traces to obtain (see Appendix D) the first-order and second-order contributions

to the shift $\sigma_{ij}^{J,1}$ and $\sigma_{ij}^{J,2}$:

$$\sigma_{ij}^{J,1} = -\frac{\mu_B}{\hbar\gamma_I kT} \frac{\langle J \parallel \hat{J}_1 \parallel J \rangle^2}{3} \sum_{q=-1}^{+1} (-1)^q g_{1q,i} A_{1-q,j}, \quad (6.66)$$

$$\begin{aligned} \sigma_{ij}^{J,2} = & \frac{\mu_B}{\hbar\gamma_I (kT)^2} (-1)^{2J} (2J+1)^{1/2} \langle J \parallel \hat{J}_1 \parallel J \rangle^2 \sum_{k''=2,4,6} \langle J \parallel \hat{J}_{k''} \parallel J \rangle \left\{ \begin{matrix} 1 & k'' & 1 \\ J & J & J \end{matrix} \right\} \\ & \times \sum_{qq'q''} g_{1q,i} A_{1q',j} B_{k''q''} \left(\begin{matrix} 1 & k'' & 1 \\ -q' & -q'' & -q \end{matrix} \right). \end{aligned} \quad (6.67)$$

Substituting in the values for the spatial tensor parameters, and the $3j$ and $6j$ symbols, we obtain the Bleaney expression for the paramagnetic shielding tensor:

$$\boldsymbol{\sigma}^J \approx -\frac{\mu_B g_J J(J+1)}{3\hbar\gamma kT} \mathbf{A} + \frac{\mu_B g_J J(J+1)(2J-1)(2J+3)}{30\hbar\gamma (kT)^2} \mathbf{B} \cdot \mathbf{A}, \quad (6.68)$$

where we note that only the rank k'' terms in the crystal-field Hamiltonian contribute to the shielding tensor to second order.

6.5.1 The paramagnetic chemical shielding in terms of the magnetic susceptibility tensor

We can also use the EPR formula to derive the paramagnetic susceptibility tensor, in terms of J , of a system containing an ensemble of lanthanide ions. To second order in $1/(kT)^2$, the susceptibility tensor is

$$\chi \approx \frac{\mu_0 \mu_B^2 g_J^2 J(J+1)}{3kT} \mathbf{1} - \frac{\mu_0 \mu_B^2 g_J^2 J(J+1)(2J-1)(2J+3)}{30(kT)^2} \mathbf{B}. \quad (6.69)$$

This expression exhibits a complete separation of the isotropic and anisotropic contributions of the susceptibility according to their temperature dependence, which is a direct result of treating the g -tensor of the lanthanide ions as isotropic. The term that varies as $1/(kT)$ is purely isotropic whereas the $1/(kT)^2$ term is purely anisotropic, with an anisotropy that is proportional to, and with the same orientation as, that of the second-rank part of the spatial tensor of the crystal-field interaction Hamiltonian.

As for the first-row transition metals, we can write the hyperfine coupling constant in terms of the reduced

Type	Term	σ^J	σ^χ	Rank
Contact	1	$-\frac{\mu_B g_J J(J+1)}{3\hbar\gamma kT} A^{\text{con}}$	$-\chi^{(1)} C^{\text{con}}$	0
	2	$\frac{\mu_B g_J J(J+1)(2J-1)(2J+3)}{30\hbar\gamma(kT)^2} \mathbf{B} A^{\text{con}}$	$-\chi^{(2)} C^{\text{con}}$	2
Dipolar	3	$-\frac{\mu_B g_J J(J+1)}{3\hbar\gamma kT} \mathbf{A}^{\text{dip}}$	$-\chi^{(1)} C^{\text{dip}}$	2
	4	$\frac{\mu_B g_J J(J+1)(2J-1)(2J+3)}{30\hbar\gamma(kT)^2} \mathbf{B} \cdot \mathbf{A}^{\text{dip}}$	$-\chi^{(2)} \cdot C^{\text{dip}}$	0,1,2

Table 6.3: The terms present in the paramagnetic chemical shielding tensor due in a lanthanide system, expressed in terms of both the molecular/atomic-level parameters σ^J , and the bulk magnetic susceptibility tensor σ^χ .

coupling constant C as

$$\mathbf{A} = \mu_0 \mu_B g_J \hbar \gamma_I \mathbf{C}, \quad (6.70)$$

where C is the sum of an isotropic contact part C^{con} and an anisotropic dipolar part C^{dip} . The paramagnetic shielding tensor σ^χ in terms of the susceptibility tensor now takes on a form that we have seen before:

$$\sigma^\chi = -\chi \cdot C. \quad (6.71)$$

We are now in a position to write down all the terms in the expression for the shielding tensor that are formed from the cross-terms between the coupling constant and the susceptibility tensor. They are summarised in Table 6.3, where we have written the first- and second-order terms in the susceptibility as $\chi^{(1)}$ and $\chi^{(2)}$ respectively. The contact interaction produces two terms in the shielding tensor, both of which are due to the unpaired electron spin density that is present at the nucleus. Term 1 is purely isotropic, and exhibits a temperature dependence of $1/(kT)$ whilst term 2 is purely anisotropic, with a temperature dependence of $1/(kT)^2$ and anisotropy parameters that are proportional to those of the second-rank crystal-field splitting tensor. The two terms that are due to the dipolar interaction, 3 and 4, are a result of the long-range spin-dipolar interaction between the nucleus and metal ion. Term 3 is purely anisotropic, with tensor parameters that are proportional to those of the dipolar coupling tensor, and exhibits a temperature dependence of $1/(kT)$. Term 4 is more complex because it is given by the matrix product of the crystal-field splitting tensor with the dipolar coupling tensor, and so contains isotropic, antisymmetric, and symmetric anisotropic parts. Like term 3, it also has a $1/(kT)^2$ temperature dependence. The isotropic part of term 4 is a pseudo-contact term, as it is given by the product of the anisotropic part of the susceptibility tensor with the dipolar coupling tensor. Assuming that the $4f$ electrons can be modelled as point-dipole moments, the pseudo-contact shielding is

given by Equation 5.77 as

$$\sigma_{\text{iso}}^{\text{pcs}} = -\frac{1}{12\pi R^3} \left[\Delta\chi_{\text{ax}} (3 \cos^2 \theta - 1) + \frac{3}{2} \Delta\chi_{\text{rh}} \sin^2 \theta \cos 2\phi \right], \quad (6.72)$$

where θ and ϕ are the polar and azimuthal angles describing the orientation of the susceptibility tensor to the dipolar coupling tensor. In terms of the axial and rhombic crystal-field splitting tensor parameters ΔB_{ax} and ΔB_{rh} , the pseudo-contact shielding is equal to

$$\sigma_{\text{iso}}^{\text{pcs}} = \frac{\mu_0 \mu_{\text{B}}^2 g_J^2 J(J+1)(2J-1)(2J+3)}{360\pi(kT)^2 R^3} \left[\Delta B_{\text{ax}} (3 \cos^2 \theta - 1) + \frac{3}{2} \Delta B_{\text{rh}} \sin^2 \theta \cos 2\phi \right]. \quad (6.73)$$

This is the main result of Bleaney's theory.

Trends in the contact and pseudo-contact shielding, and shielding anisotropy

We are now in a position to decompose the terms in the paramagnetic shielding tensor in Equation 6.68 into products of two contributions, the first of which depends on the electronic properties of the free lanthanide ion, and the second of which depends on the coordination environment. For example the first term in Equation 6.68, which is proportional to the hyperfine tensor \mathbf{A} , can be decomposed as follows. The free-ion part that depends on the lanthanide ion being studied is a function of g_J and J , and is equal to

$$C_J^{\text{SA}} = g_J^2 J(J+1). \quad (6.74)$$

We recall that the hyperfine tensor is proportional to g_J , hence the above factor contains g_J^2 . The coordination environment is due to the unpaired electron density present in the s -orbital of the observed nuclear spin, and the distance of this nucleus from the lanthanide ion, both of which are contained within the hyperfine tensor. These factors dictate the size of both the Fermi-contact shift and the dominant part of the SA. Therefore the factor C_J^{SA} indicates the sign and magnitude of the dominant part of the SA. The form of the contact shielding is actually more complicated than predicted by the simple Bleaney theory, and requires special treatment, as first proposed by Golding and Halton [60]. This is discussed below.

The second term of Equation 6.69 gives rise to the PCS, and a secondary contribution to the SA. The

lanthanide ion-dependent part is

$$C_J^{\text{PCS}} = g_J^2 J(J+1)(2J-1)(2J+3) \langle J \| 2 \| J \rangle, \quad (6.75)$$

and the coordination-environment dependent part is due to the crystal-field splitting factors $\langle r^2 \rangle A_2^0$ and $\langle r^2 \rangle A_2^2$.

The form of the contact contribution to the isotropic shielding is more complicated than suggested by the Bleaney theory. The reason for this is that the contact interaction requires the through-bond transfer of the unpaired electronic spin density, and so we cannot separate the shielding into parts that depend solely on the properties of the free ion and coordination environment. One way of treating the contact shielding has been proposed by Golding and Halton [60]. The idea is to essentially treat the electronic configuration of the lanthanide as a free ion, but include a modification to account for the bonding to the ligands. This modification is the inclusion of an orbital reduction parameter γ that takes values close to unity. The factor C_J^{con} which gives the sign and magnitude of the contact shielding when the ion is in an SO coupling level J can be shown to be

$$C_J^{\text{con}} = \frac{(g_J - \gamma)g_J J(J+1)}{2 - \gamma} + \left(\frac{2kT}{\lambda} \right) \frac{(g_J - \gamma)(g_J - 2)}{2 - \gamma}. \quad (6.76)$$

The first term has a similar form to C_J^{SA} , with the inclusion of the γ factor. The second term accounts for the effect of SO coupling strength λ .

Numerical values of the ion-dependent contributions for both terms in the paramagnetic shielding are given in Table 6.4. These values depend only on the nature of the ion, and so can be used to compare the size of the expected shifts and SAs for a series of lanthanide ions in the same coordination site, assuming that both the coordination geometry and the factors $\langle r^2 \rangle A_2^q$ are unchanged. Note also that, whilst these numerical factors can be used to compare, for example, the expected pseudo-contact shifts for a series of ions, they cannot be used to compare the sizes of the contact shifts versus the pseudo-contact shifts as this comparison also requires knowledge of the Fermi-contact and spin-dipolar components of the hyperfine tensor. For instance we would expect both Ce^{3+} and Pm^{3+} to give relatively small SAs, with the relative factors being 6.4 and 7.2 respectively, whereas we would expect the corresponding values for Dy^{3+} and Ho^{3+} to be approximately 16

³Values taken from Abragam and Bleaney [184], and Bleaney [61].

⁴Values taken from Golding and Halton [60].

⁵Values taken from Bleaney [61].

Ion	Configuration	J	g_J	$\langle J 2 J \rangle^3$	C_J^{SA}	$C_J^{\text{con}4}$	$C_J^{\text{PCS}5}$
Ce ³⁺	f^1	5/2	6/7	-0.0571	6.4	-0.98	-11.8
Pr ³⁺	f^2	4	4/5	-0.0210	12.8	-2.9	-20.7
Nd ³⁺	f^3	9/2	8/11	-0.00643	13.1	-4.4	-8.08
Pm ³⁺	f^4	4	3/5	0.00771	7.2	—	4.28
Sm ³⁺	f^5	5/2	2/7	0.0413	0.7	0.3	0.943
Eu ³⁺	f^6	0	—	—	—	—	—
		1	3/2	-0.200	4.5	1.0	-4.5
		2	3/2	-0.0349	13.5	4.0	-9.9
Gd ³⁺	f^7	7/2	2	0	63.0	31.5	0
Tb ³⁺	f^8	6	3/2	-0.0101	94.5	31.9	-157.5
Dy ³⁺	f^9	15/2	4/3	-0.00635	113.3	28.6	-181
Ho ³⁺	f^{10}	8	5/4	-0.00222	112.5	22.6	-71.3
Er ³⁺	f^{11}	15/2	6/5	0.00254	91.8	15.4	58.8
Tm ³⁺	f^{12}	6	7/6	0.0101	57.2	8.2	95.3
Yb ³⁺	f^{13}	7/2	8/7	0.0317	20.6	2.6	39.2

Table 6.4: Parameters pertaining to the size of the contact [60] and pseudo-contact [61] shifts, and the SA of the different lanthanides. The contact shift is proportional to C_J^{con} , the pseudo-contact shift to C_J^{PCS} , and the SA is proportional to C_J^{SA} . The contact-shift terms are evaluated with $\gamma = 1$, and at 300 K.

times larger. We see a different trend for the sizes of the PCSs with Ce³⁺ and Pm³⁺ giving values that differ more in magnitude than their contact/SA contributions, and which are also of opposite sign. In addition we expect Gd³⁺ and Tb³⁺ to give the largest contact shifts, but Dy³⁺ to give the largest pseudo-contact shifts.

6.5.2 Contact shift contributions from excited states of different J

The theory presented above assumes that only the lowest-energy J level, with $J = J_0$, contributes to the electronic properties of the lanthanide, and therefore to the paramagnetic shift. If the $4f$ shell is less than half full the lowest excited state is $J_0 + 1$, whilst for $4f$ shells that are more than half full it is $J_0 - 1$. In general, in the free ion, the lowest-lying excited J levels are 2000 cm⁻¹ or more above the ground level, and we do not need to consider them. However there are two exceptions amongst the trivalent ions, which are Sm³⁺ ($4f^5$; ground term $^6H_{5/2}$), and Eu³⁺ ($4f^6$; ground term 7F_0). The lowest-lying excited level of Sm³⁺ is $J = 7/2$ which lies at 1000 cm⁻¹ above the ground level, and for Eu³⁺ it is $J = 1$ which lies at 400 cm⁻¹ above the ground level. In order to describe the paramagnetic chemical shielding due to these lanthanides we must account for these low-lying ground states, and must include them in the sum over states in the EPR formula in Equation 4.103. The states $|n\nu\rangle$ now contain information about the different J levels that result from SO coupling as well as the crystal-field splitting of each J level.

The effect of thermal population of the excited states on the total isotropic contact shielding parameter

Ion	Configuration	C^{con}
Ce ³⁺	f^1	-0.98
Pr ³⁺	f^2	-3.0
Nd ³⁺	f^3	-4.5
Pm ³⁺	f^4	-4.0
Sm ³⁺	f^5	0.063
Eu ³⁺	f^6	10.7
Gd ³⁺	f^7	31.5
Tb ³⁺	f^8	31.8
Dy ³⁺	f^9	28.5
Ho ³⁺	f^{10}	22.6
Er ³⁺	f^{11}	15.4
Tm ³⁺	f^{12}	8.2
Yb ³⁺	f^{13}	2.6

Table 6.5: The parameters C^{con} dictating the sign and size of the contact shift for the full series of trivalent lanthanide ions calculated by considering the excited SO coupling states; the values given here are taken from Golding and Halton [60]. $\gamma = 1$, and the temperature is 300 K.

C^{con} can be calculated from the following Boltzmann average over the excited J levels:

$$C^{\text{con}} = \frac{\sum_J C_J^{\text{con}} (2J + 1) \exp(-E_J/kT)}{\sum_J (2J + 1) \exp(-E_J/kT)}, \quad (6.77)$$

where the energies E_J are due to the SO coupling, and are given by

$$E_J = \frac{\lambda}{2} [J(J + 1) - L(L + 1) - S(S + 1)]. \quad (6.78)$$

The values at 300 K, taken from Golding and Halton, are tabulated in Table 6.5 [60]. If we compare the values of C^{con} with those calculated from the ground level only in Table 6.4 we see the the inclusion of thermal population of the excited levels has a negligible effect on the contact coupling, with the exception of Sm³⁺ and Eu³⁺. In the former case the excited states reduce the magnitude of the (already small) contact shielding by almost an order of magnitude. However the most substantial effect is seen for Eu³⁺, where the inclusion of the excited states increases the contact shielding from zero to the largest value seen in the series of lanthanides.

6.5.3 Pseudo-contact shift contributions from excited states of different J

The excited states also play an important role for the pseudo-contact shift in the Bleaney formalism. Here we examine the cases of Sm³⁺ and Eu³⁺, and also comment on Gd³⁺.

Ion	a	b	$kT/\Delta E$ at 300 K	$a(kT/\Delta E)$	$b(kT/\Delta E)^2$
Ce ³⁺	-0.555	-0.0833	0.09	-0.050	-0.00067
Pr ³⁺	-0.497	-0.0535	0.095	-0.047	-0.00048
Nd ³⁺	-0.673	-0.0678	0.105	-0.071	-0.00075
Pm ³⁺	-1.426	-0.178	0.125	-0.18	-0.0028
Sm ³⁺	-11.25	-3	0.20	-2.25	-0.12
Tb ³⁺	-0.287	+0.0139	0.10	-0.029	0.00014
Dy ³⁺	-0.185	+0.0081	0.07	-0.013	0.000040
Ho ³⁺	-0.142	+0.0062	0.05	-0.0071	0.000016
Er ³⁺	-0.127	+0.0061	0.03	-0.0038	0.0000055
Tm ³⁺	-0.133	+0.0081	0.025	-0.0033	0.0000051
Yb ³⁺	-0.181	+0.0188	0.02	-0.0036	0.0000075

Table 6.6: The values of the coefficients a and b , and the factor $kT/\Delta E$ at 300 K used in the correction factor for the pseudo-contact shift resulting from the mixing of excited states into the ground state. Values for the trivalent lanthanides (excluding Eu³⁺ and Gd³⁺) are taken from Bleaney [61].

The Sm³⁺ ion: $4f^5, {}^6H_{5/2}$

To calculate the correction to the PCS for all the trivalent lanthanide ions with the exception of Eu³⁺, we need only consider the effects of mixing the excited states into the ground state, which results in the PCS in Equation 6.73 being multiplied by the following correction factor [61]:

$$1 + a \left(\frac{kT}{\Delta E} \right) + b \left(\frac{kT}{\Delta E} \right)^2 + c \left(\frac{(kT)^2}{\Delta E \Delta E'} \right). \quad (6.79)$$

In Equation 6.79 a , b , and c are coefficients, ΔE is the energy of the lowest-lying excited state relative to the ground state, and $\Delta E'$ is the energy of the lowest-lying excited state resulting from different values of S and L to those of the ground state. The coefficients a and b and the ratio $kT/\Delta E$ have been calculated by Bleaney, and are reproduced in Table 6.6 [61]. These correction terms are negligible for all the ions apart from Sm³⁺, which has values $a(kT/\Delta E) = -2.25$, $b/(kT/\Delta E)^2 = -0.12$, and also $c(kT)^2/(\Delta E \Delta E') = +0.14$ at 300 K [61]. The overall multiplicative factor is then -1.23 , which results in a change in sign of the PCS predicted from the ground state only. The lowest-lying excited J level $J = 7/2$ is sufficiently high for its thermal population to be negligibly small, we need only consider the effects of mixing in of the excited states into the ground state.

The Eu³⁺ ion: $4f^6, {}^7F_0$

For the Eu³⁺ ion the situation is more complex. The ground level of $J = 0$ is diamagnetic, but the mixing of the excited states into the ground state gives rise to a temperature-independent paramagnetic shift. In addition

to the $J = 1$ excited level at 400 cm^{-1} above the ground level, we must also consider the second excited level $J = 2$ at 1200 cm^{-1} , and possibly the third $J = 3$. We may also see contributions to the paramagnetic shift from the thermal population of these same excited states, which gives temperature-dependent contributions to the PCS [61]. The energies quoted here are those in the free ion and so we must bear in mind that the excited levels may be lower-lying in a bound ion [184].

The Gd³⁺ ion: $4f^7, {}^8S_{7/2}$

The Gd³⁺ ion represents a special case amongst the trivalent lanthanides as it possesses a half-full $4f$ shell, and is therefore an S term. The SO coupling is effectively zero, and so the ion exhibits behaviour more akin to a first-row transition-metal ion with $S = 7/2$ than to the other lanthanides. One important property is that the reduced matrix element $\langle J || 2 || J \rangle$ is zero, and so the PCS is zero. The zero PCS is a property that Gd³⁺ shares with transition-metal ions with half-filled d shells, such as high-spin Mn²⁺ and Fe³⁺. It should also be noted that, because there is no SO coupling, there are no low-lying J -levels that mix with the ground level $J = 7/2$.

6.5.4 The shortcomings of the Bleaney theory

The Bleaney theory is currently the only theory of paramagnetic shifts due to lanthanides that has been applied with any regularity to the interpretation of the NMR data of systems containing rare earths [66, 68, 74]. However the theory has a number of shortcomings which mean that it is not generally applicable to all systems. Some of these have already been mentioned in this chapter, and these and other shortcomings have been enumerated in more detail by Funk et al [62]. There are two minor and two more important points to be addressed, which are detailed and expanded upon here.

Firstly Funk et al. point out that it is often assumed that the PAF of the second-rank crystal-field splitting tensor is invariant when comparing lanthanide ions in an isostructural series of materials. This assumption does not hold in general, as the differences in ion size and electronic properties can result in differences in the coordination geometry for different ions. However, contrary to the claim of Funk et al. this is not a deficiency in the Bleaney theory per se, but is rather a cautionary note that the differences in the PAF orientation must be accounted for when comparing the effects of different lanthanide ions in isostructural systems. For example Bertini et al. performed a study in which the full series of lanthanide ions, with the exceptions of Pm³⁺ and

Gd^{3+} , were incorporated into the C-terminal calcium binding site of the dicalcium protein calbindin D_{9k} [74]. The measured PCSs enabled the determination of the anisotropic components of the magnetic susceptibility tensor and the orientation of the PAF for each lanthanide. The axes of the largest anisotropy were found to vary by up to 20° across the series.

Secondly the simplest implementation of the Bleaney theory assumes a point-dipole model for the unpaired electron density in the $4f$ orbitals. The justification for this is that the f -orbitals are relatively contracted, and so the electron density is confined to a relatively small space. In the study of Bertini et al. the observed nuclei were separated from the lanthanide ion by more than 8 \AA , where the point-dipole model is a good approximation [74]. However the point-dipole approximation begins to break down when the nucleus is closer to the metal ion, and the spread of electron density must be taken into account. For first-row transition-metal ions the cutoff separation below which the point-dipole model begins to break down is approximately 4 \AA , but this value may be smaller for lanthanides due to the more contracted nature of the $4f$ orbitals relative to the $3d$ orbitals, where the electron density is delocalised to a greater extent onto the ligands. However the lifting of the point-dipole restriction is relatively straightforward and, whilst the Bleaney formula itself is no longer valid, the expressions given in section 5.3.2 are still applicable.

This brings us to the more serious deficiencies in the Bleaney theory. The third point is the central assumption that the crystal-field splitting parameters B_{lm} are much smaller in magnitude than kT . This is generally not true, as B_{20} can take values up to 1500 cm^{-1} in some cases [227], compared to $kT = 205 \text{ cm}^{-1}$ at 298 K. Since this assumption lies at the heart of the Bleaney theory, there is no easy fix to this problem. A related issue is that the Bleaney formula is calculated from a series expansion up to $1/(kT)^2$, to which the higher-rank crystal-field terms do not contribute. However since the crystal-field splittings may be comparable to or greater than kT the second-order term may not be sufficient to account for the paramagnetic shielding, and the higher-rank crystal-field terms may become important. The fourth shortcoming is that it is assumed that the SO coupling is adequately described by the Russell–Saunders coupling scheme, and that J is a good quantum number. However this may not be the case for the heavy lanthanide ions with larger SO coupling constants. Both of these points are not easily fixed in the Bleaney formalism, and a different approach is needed. In cases where the deficiencies in the Bleaney theory are too important to be neglected it will be necessary to adopt a more general EPR formalism, as summarised by the expression of the paramagnetic shielding tensor in Equation 6.18. Nevertheless it should be pointed out that the Bleaney

theory has been remarkably successful in driving the field of paramagnetic NMR of lanthanide ions forward.

6.6 The paramagnetic shielding due to actinides

A comparatively small number of paramagnetic NMR studies have been performed on systems containing actinide ions, including small molecules in solution [228–230] and solid oxides [13]. However only relatively recently have first-principles calculations of the paramagnetic shifts been performed [212].

6.6.1 Electronic structure of actinide ions

The magnetic properties of the actinide ions are defined by the $5f$ electrons. Whilst one might expect these properties to mirror those of the lanthanide ions, there are some important differences. Firstly, in contrast to the lanthanide ions, actinides exhibit a greater range of oxidation states. For example, uranium exhibits oxidation states up to its diamagnetic ($5f^0$) state of +6. Secondly the SO coupling is not the dominant interaction. Rather, both the crystal-field and SO interactions are large, and comparable in magnitude. In addition we expect there to be greater deviation from the Russell–Saunders coupling scheme than for lanthanide ions. Thirdly, the partially-occupied $5f$ orbitals are more directly involved in bonding interactions with the metal coordination site.

6.6.2 The EPR formalism for the paramagnetic shielding tensor

The paramagnetic shielding tensor due to an actinide ion is given by the general formula of van den Heuvel and Soncini in Equation 6.18. When the electronic energy levels are parameterized in terms of the EPR effective-spin parameters, we obtain separate shielding tensors for each of the electronic levels, each of which has the form of Equation 6.22 if we neglect the ZFS. Otherwise, if we include the ZFS we obtain a similar sum of terms, with each now having the form of Equation 6.24. We recall that each level has a distinct set of EPR parameters.

First-principles calculations of the paramagnetic shielding tensor have recently been carried out by Gendron et al. where they investigated the $5f^1$ complexes $\text{UO}_2(\text{CO}_3)_3^{5-}$ and $\text{NpO}_2(\text{CO}_3)_3^{4-}$, and the $5f^2$ complexes $\text{PuO}_2(\text{CO}_3)_3^{4-}$ and $(\text{C}_3\text{H}_5)_3\text{U}\text{CH}_3$ [91, 92]. Here they showed that the main contributions are due to the Fermi-contact and spin-dipolar interactions, giving the contact shift and PCS respectively, and a third term

known as the paramagnetic spin–orbital interaction (PSO), which is a coupling between the nuclear spin and the electron orbital angular momentum.

Research in this area is still relatively new, but progressing rapidly, and it is expected that both experiments and calculations in actinide complexes, in addition to solid systems, will become more widespread.

6.7 Key concepts

- In a free ion subject to spin-orbit coupling each electronic energy level can be represented as an effective spin \tilde{S} with multiplicity $2\tilde{S} + 1$ that matches the actual degeneracy of the level.
- The immersion of a metal ion in a complex results in a crystal- or ligand-field interaction which partially lifts the degeneracy of the electron energy levels creating a number of sub-levels to each of which is assigned an (different) effective spin \tilde{S} .
- Each sub-level is associated with a different set of EPR parameters.
- The EPR Hamiltonian in a level with effective spin \tilde{S} contains terms with powers of \hat{S} up to $2\tilde{S}$.
- Lanthanide ions form complexes with crystal-field interactions that are much weaker than the SO coupling.
- Actinide ions form complexes in which the crystal-field interactions and SO coupling are both large, and of comparable magnitude.
- The paramagnetic shielding tensor can also be parameterised in terms of the EPR parameters associated with all the thermally accessible crystal-field energy levels (Equation 6.24).
- The magnetic properties of the free lanthanide ions are characterised by the total angular momentum J .
- The crystal-field interaction of lanthanide complexes is much weaker than the SO coupling.
- The paramagnetic shielding tensor due to lanthanide ions is given by the general EPR expression in Equation 6.18.

- A simplified form of the paramagnetic shielding tensor is given by the Bleaney formula in Equation 6.68.
- The Bleaney theory is an approximate description of the shielding tensor, and assumes that the lanthanide can be treated as a free ion, subject to a crystal-field interaction that is sufficiently small so that all the energy levels are equally populated at the relevant temperature.
- The paramagnetic shielding tensor due to actinide ions can be calculated from the general expression of van den Heuvel and Soncini (Equation 6.18), which can, in turn, be expressed in terms of the EPR parameters of each electronic level, giving a sum of terms of the form of Equation 6.22 (neglecting ZFS) or Equation 6.24 (including ZFS).

Chapter 7

The paramagnetic shift in multi-metal-ion systems, and solid materials

Our discussion of the paramagnetic shift has so far only considered systems containing a single paramagnetic metal ion. This is sufficient for describing monometallic complexes in solution, but is obviously inadequate for molecular systems containing metal clusters, crystallised molecular complexes, and solid materials. In these systems we must account for the contributions to the paramagnetic shift from multiple metal ions, and the effects of magnetic exchange interactions between the unpaired electrons of different metal ions. In general these interactions can lead to either ferromagnetic or antiferromagnetic alignment of the paramagnetic centres at low temperature. In this review we are not interested in this regime per se, but rather in the high-temperature paramagnetic behaviour of these materials.

We begin by exploring how the exchange coupling interactions influence the form of the paramagnetic shielding tensor due to small clusters of metal ions. These principles can also be applied to solid materials containing an extended network of coupled metal ions. We also provide a simplified description of these solid materials using a mean-field expression of the magnetic properties, leading to the Curie–Weiss model of the magnetic susceptibility [187] and the paramagnetic shielding tensor. The discussion in this chapter focuses

exclusively on the first-row d -transition-metal ions.

7.1 The paramagnetic shift due to multiple non-interacting metal ions

Initially we consider the relatively simple case of the paramagnetic shift of a nucleus that is hyperfine-coupled to multiple non-interacting metal ions. The EPR Hamiltonian \hat{H}_{EPR} can then be written as a sum of Hamiltonians $\hat{H}_{\text{EPR}}^{(A)}$, each containing the interactions pertaining to an individual metal ion A :

$$\hat{H}_{\text{EPR}} = -\hbar\gamma_I \mathbf{B}_0 \cdot (\mathbf{1} - \boldsymbol{\sigma}^{\text{orb}}) \cdot \hat{\mathbf{I}} + \sum_A \hat{H}_{\text{EPR}}^{(A)}. \quad (7.1)$$

The individual Hamiltonians $\hat{H}_{\text{EPR}}^{(A)}$ are given by

$$\hat{H}_{\text{EPR}}^{(A)} = \mu_B \mathbf{B}_0 \cdot \mathbf{g}^{(A)} \cdot \hat{\mathbf{S}}^{(A)} + \hat{\mathbf{S}}^{(A)} \cdot \mathbf{A}^{(A)} \cdot \hat{\mathbf{I}} + \hat{\mathbf{S}}^{(A)} \cdot \mathbf{D}^{(A)} \cdot \hat{\mathbf{S}}^{(A)}, \quad (7.2)$$

where each symbol has its usual meaning, and the superscript (A) indicates that the relevant tensor or spin operator refers to the metal ion A .

In such a system the paramagnetic chemical shielding tensor is simply the sum of contributions from each metal ion, with the expression for each contribution being given by Equation 4.109:

$$\boldsymbol{\sigma}^S = -\frac{\mu_B}{\hbar\gamma_I} \sum_A \mathbf{g}^{(A)} \cdot \mathbf{Z}^{(A)} \cdot \mathbf{A}^{(A)}, \quad (7.3)$$

where the tensor $\mathbf{Z}^{(A)}$ contains both the temperature dependence of the shielding, and the information of the ZFS tensor of metal ion A . The EPR formalism gives the following expression for $Z_{kl}^{(A)}$:

$$\begin{aligned} Z_{kl}^{(A),\text{HS}} &= \frac{2}{Q_0^{(A)}} \sum_n \exp(-\beta E_n^{(A)}) \sum_{m \neq n} \sum_{\nu, \mu} \frac{\langle n\nu | \hat{S}_k^{(A)} | m\mu \rangle \langle m\mu | \hat{S}_l^{(A)} | n\nu \rangle}{E_m^{(A)} - E_n^{(A)}} \\ &+ \frac{\beta}{Q_0^{(A)}} \sum_n \exp(-\beta E_n^{(A)}) \sum_{\nu, \nu'} \langle n\nu | \hat{S}_k^{(A)} | n\nu' \rangle \langle n\nu' | \hat{S}_l^{(A)} | n\nu \rangle. \end{aligned} \quad (7.4)$$

We note here that the expression for the shielding tensor does not contain any ‘cross terms’ involving two or more metal ions. This is because there are no interactions between the metal ions, with the result that they are

independent. This observation is no longer true once we introduce the interactions between the spins, when the cross terms become extremely important.

7.2 The Heisenberg exchange Hamiltonian

In this section we describe the simplest coupling interaction between the unpaired electron clouds of two paramagnetic metal ions, referred to as the Heisenberg exchange interaction. The Hamiltonian \hat{H}_{ex} describing the interaction between two electronic spins $\mathbf{S}^{(1)}$ and $\mathbf{S}^{(2)}$ is given by [187]

$$\hat{H}_{\text{ex}} = -2\mathcal{J}^{(12)} \hat{\mathbf{S}}^{(1)} \cdot \hat{\mathbf{S}}^{(2)}, \quad (7.5)$$

where $\mathcal{J}^{(12)}$ is the spatially-isotropic Heisenberg exchange coupling constant, and the factor of two is present by convention. The exchange constant $\mathcal{J}^{(12)}$ is a signed quantity, with the sign having a profound effect on the behaviour of the spin system, as we will see shortly. This Hamiltonian bears an obvious resemblance to the Hamiltonian describing a homonuclear J -coupling interaction between two nuclei [194], and much of the theory of nuclear spin systems subject to J -couplings is applicable to exchange interactions and vice versa.

7.2.1 The exchange interaction between two electronic spins 1/2

Many of the important properties of the exchange interaction are illustrated by considering a metal dimer containing two electronic spins 1/2. An example of this in practice might be a system containing two Cu^{2+} ions, each of which has a $3d^9$ electronic configuration.

Each spin can be described using a basis comprising the functions $|\alpha\rangle$ and $|\beta\rangle$, which describe the spin states referred to as ‘spin up’ and ‘spin down’ respectively, and we write down the spin 1 and spin 2 bases as $\{|\alpha_1\rangle, |\beta_1\rangle\}$ and $\{|\alpha_2\rangle, |\beta_2\rangle\}$. However these bases are not sufficient for describing the interacting spin system, and we need to construct a new basis by taking the direct product of the two one-spin bases. The two-spin basis functions are therefore

$$\{|\alpha_1\rangle, |\beta_1\rangle\} \otimes \{|\alpha_2\rangle, |\beta_2\rangle\} = \{|\alpha_1\alpha_2\rangle, |\alpha_1\beta_2\rangle, |\beta_1\alpha_2\rangle, |\beta_1\beta_2\rangle\} \quad (7.6)$$

$$\equiv \{|\alpha\alpha\rangle, |\alpha\beta\rangle, |\beta\alpha\rangle, |\beta\beta\rangle\}. \quad (7.7)$$

The exchange Hamiltonian has four eigenfunctions, denoted $|S M_S\rangle$, which are linear combinations of the basis functions. The notation $|S M_S\rangle$ emphasises that each eigenstate represents the spin system as an object with total spin $\mathbf{S} = \mathbf{S}_1 + \mathbf{S}_2$, the spin quantum number S of which is given by a value of the Clebsch–Gordan series $S_1 + S_2, S_1 + S_2 - 1, \dots, |S_1 - S_2|$. The corresponding total magnetic quantum number M_S takes values from $+S$ to $-S$ in integer steps as usual. For $S_1 = S_2 = 1/2$ the allowed values of S are 1 and 0, and so we can separate the four eigenstates into the $S = 1$ triplet and the $S = 0$ singlet states. All the states with the same total spin quantum number S are degenerate, and have energy E_S . The energies and eigenstates are:

$$E_1 = -\mathcal{J}^{(12)}/2, \quad |1 + 1\rangle = |\alpha\alpha\rangle \quad (7.8)$$

$$|10\rangle = \sqrt{\frac{1}{2}} (|\alpha\beta\rangle + |\beta\alpha\rangle) \quad (7.9)$$

$$|1 - 1\rangle = |\beta\beta\rangle, \quad (7.10)$$

$$E_0 = +3\mathcal{J}^{(12)}/2, \quad |00\rangle = \sqrt{\frac{1}{2}} (|\alpha\beta\rangle - |\beta\alpha\rangle). \quad (7.11)$$

The three triplet states $|1M_S\rangle$ correspond to the two spins being aligned co-parallel, which is referred to as ferromagnetic alignment. By contrast the singlet state $|00\rangle$ is formed by summing the two spin angular momenta when they are aligned anti-parallel to each other, which represents antiferromagnetic alignment. The question as to which level is the ground level, and therefore the nature of the alignment at low temperature when only this level is occupied, depends on the sign of $\mathcal{J}^{(12)}$. If $\mathcal{J}^{(12)} > 0$, the triplet is lowest in energy, and therefore the spins are aligned ferromagnetically at low temperature. On the other hand if $\mathcal{J}^{(12)} < 0$ the low-temperature alignment is antiferromagnetic. The energy levels for the two cases are shown in Figure 7.1 (a) and (b). At high temperatures, such that all the states are substantially occupied, there is no strong preference for either ferro- or antiferromagnetic alignment of the two spins i.e. the thermal fluctuations disrupt the tendency for the spins to align, and the two spins begin to act as if they are independent and exhibit paramagnetic behaviour. The temperature at which we can expect to observe this ferro/antiferromagnetic-to-paramagnetic transition is a topic we will return to later.

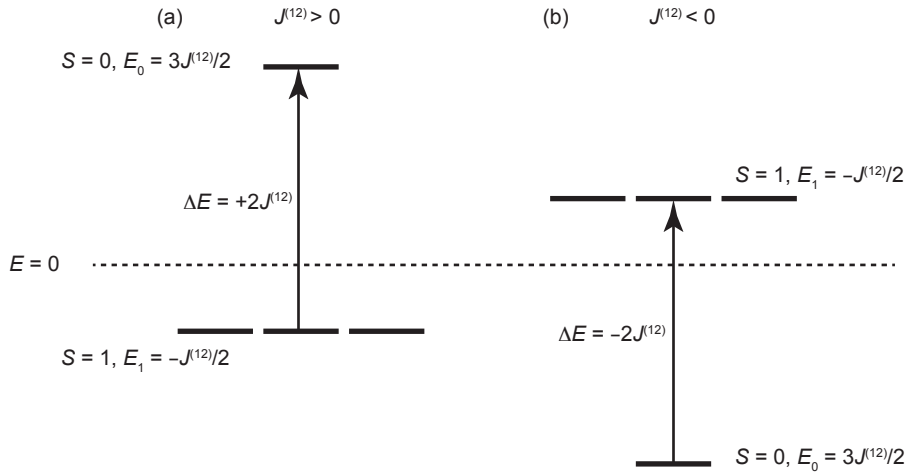


Figure 7.1: The energy levels resulting from the exchange coupling of two electronic spins $1/2$. The energy levels, energies, and effective spins are shown for (a) ferromagnetic coupling with a positive exchange coupling constant $J^{(12)}$, and (b) antiferromagnetic coupling with a negative exchange coupling constant $J^{(12)}$.

7.2.2 The exchange interaction between two arbitrary electronic spins

We now turn our attention to the exchange interaction between two arbitrary spins. The basis set of the two-spin system is formed by the direct product of the two one-spin bases $|S_1 M_1\rangle$ and $|S_2 M_2\rangle$, and comprises $(2S_1 + 1)(2S_2 + 1)$ functions $|S_1 S_2 M_1 M_2\rangle$. We can take linear combinations of the direct-product basis functions to give the eigenfunctions $|S_1 S_2 S M_S\rangle$ of the exchange Hamiltonian, which are characterised by S and M_S . The eigenfunctions are given by

$$|S_1 S_2 S M_S\rangle = \sum_{M_1, M_2} |S_1 S_2 M_1 M_2\rangle \langle S_1 S_2 M_1 M_2 | S M_S \rangle \quad (7.12)$$

$$= (-1)^{S_1 - S_2 + M_S} \sqrt{2S + 1} \sum_{M_1, M_2} |S_1 S_2 M_1 M_2\rangle \begin{pmatrix} S_1 & S_2 & S \\ M_1 & M_2 & -M_S \end{pmatrix}, \quad (7.13)$$

where $S = S_1 + S_2, S_1 + S_2 - 1, \dots, |S_1 - S_2|$, and $M_S = M_1 + M_2$.

We can calculate the corresponding energies by rewriting the exchange Hamiltonian in terms of the total

spin. First we note that $\hat{S}^2 = (\hat{S}_1 + \hat{S}_2)^2 = \hat{S}_1^2 + \hat{S}_2^2 + 2\hat{S}_1 \cdot \hat{S}_2$, and therefore

$$\hat{H}_{\text{ex}} = -2\mathcal{J}^{(12)} \hat{S}^{(1)} \cdot \hat{S}^{(2)} \quad (7.14)$$

$$= -\mathcal{J}^{(12)} [\hat{S}^2 - \hat{S}_1^2 - \hat{S}_2^2] \quad (7.15)$$

$$= -\mathcal{J}^{(12)} [S(S+1) - S_1(S_1+1) - S_2(S_2+1)] \hat{1}. \quad (7.16)$$

The exchange Hamiltonian therefore depends only on $\mathcal{J}^{(12)}$, S_1 , S_2 , and S , and splits the $(2S_1+1)(2S_2+1)$ states into a series of manifolds $|S_1 S_2 S M_S\rangle$, each of which is labelled with the total spin quantum number S and is $(2S+1)$ -fold degenerate. The energies $E(S, S_1, S_2)$ of the states within each manifold S are given by [47]

$$E(S, S_1, S_2) = -\mathcal{J}^{(12)} [S(S+1) - S_1(S_1+1) - S_2(S_2+1)]. \quad (7.17)$$

As with the case of the two coupled spins $1/2$ we see that a positive exchange coupling constant results in the states with the maximum S lying lowest in energy, and therefore favours ferromagnetic alignment at low temperature. In addition, a negative exchange coupling constant results in the lowest-energy manifold having the minimum value of S , which favours antiferromagnetic alignment at low temperature. Levels that are adjacent in energy have values of S that differ by one, e.g. S and $S-1$. The energy separation between such adjacent levels is given by an interval rule, and is equal to $2|\mathcal{J}^{(12)}|S_>$ where $S_>$ is the larger of the two values of S .

7.3 The paramagnetic shift due to a coupled electronic spin system

The exchange-coupled electronic spin system induces a paramagnetic contribution to the chemical shielding tensor in a similar way to a single transition-metal ion. On the application of an external magnetic field B_0 each individual electronic manifold $|S_1 S_2 S M_S\rangle$ is split by the Zeeman interaction. The resulting total energies $E(S, S_1, S_2, M_S)$ are

$$E(S, S_1, S_2, M_S) = E(S, S_1, S_2) + \mu_B g_e B_0 M_S \quad (7.18)$$

$$= -\mathcal{J}^{(12)} [S(S+1) - S_1(S_1+1) - S_2(S_2+1)] + \mu_B g_e B_0 M_S, \quad (7.19)$$

where we have ignored the spin-spin contribution to the ZFS tensor. Examples of the ladders of the spin energy levels are shown in Figure 7.2 for both ferro- and antiferromagnetic coupling and in the absence and presence of an external magnetic field B_0 . The example spin systems are two coupled electronic spins 1/2 in (a) and (b), a spin 1/2 coupled to a spin 1 in (c) and (d), and two coupled spins 1 in (e) and (f).

The average electronic magnetic moments are characterised both by the individual Curie spins $\langle \hat{S}_{iz} \rangle$, where $i = 1, 2$, and the total Curie spin $\langle \hat{S}_z \rangle$ of the coupled spin system. This latter quantity is the Boltzmann average over the states with energies $E(S, S_1, S_2, M_S)$:

$$\langle \hat{S}_z \rangle = \frac{\sum_{S=|S_1-S_2|}^{S_1+S_2} \sum_{M_S=-S}^{+S} M_S \exp(-E(S, S_1, S_2, M_S)/kT)}{\sum_{S=|S_1-S_2|}^{S_1+S_2} \sum_{M_S=-S}^{+S} \exp(-E(S, S_1, S_2, M_S)/kT)}, \quad (7.20)$$

where we have explicitly separated the sums over the Zeeman states in each manifold S from the sum over the manifolds themselves.

Initially we consider the case where only the ground manifold is occupied so that $|\mathcal{J}^{(12)}| \gg kT$, and the spin system behaves as a single electronic spin S . The Curie spin then takes exactly the same value as we calculated for a single metal ion in Equation 3.62:

$$\langle \hat{S}_z \rangle = \frac{\sum_{M_S=-S}^{+S} M_S \exp(-(E(S, S_1, S_2) + \mu_B g_e B_0 M_S)/kT)}{\sum_{M_S=-S}^{+S} \exp(-(E(S, S_1, S_2) + \mu_B g_e B_0 M_S)/kT)} \quad (7.21)$$

$$= \frac{\sum_{M_S=-S}^{+S} M_S \exp(-\mu_B g_e B_0 M_S/kT)}{\sum_{M_S=-S}^{+S} \exp(-\mu_B g_e B_0 M_S/kT)}, \quad (7.22)$$

The interpretation of this situation is that we have an ensemble of spin pairs with no interactions *between* the pairs, and so we can view the system as comprising an ensemble of paramagnetic ions with spin S . We employ the high-temperature approximation for the thermal populations of the Zeeman energy levels, and we obtain the familiar expression for the spin-only Curie spin:

$$\langle \hat{S}_z \rangle = -\frac{\mu_B g_e S(S+1)B_0}{3kT}. \quad (7.23)$$

The corresponding paramagnetic shielding tensor is

$$\sigma^S = -\frac{\mu_B g_e S(S+1)}{3\hbar\gamma_I kT} \mathbf{A}, \quad (7.24)$$

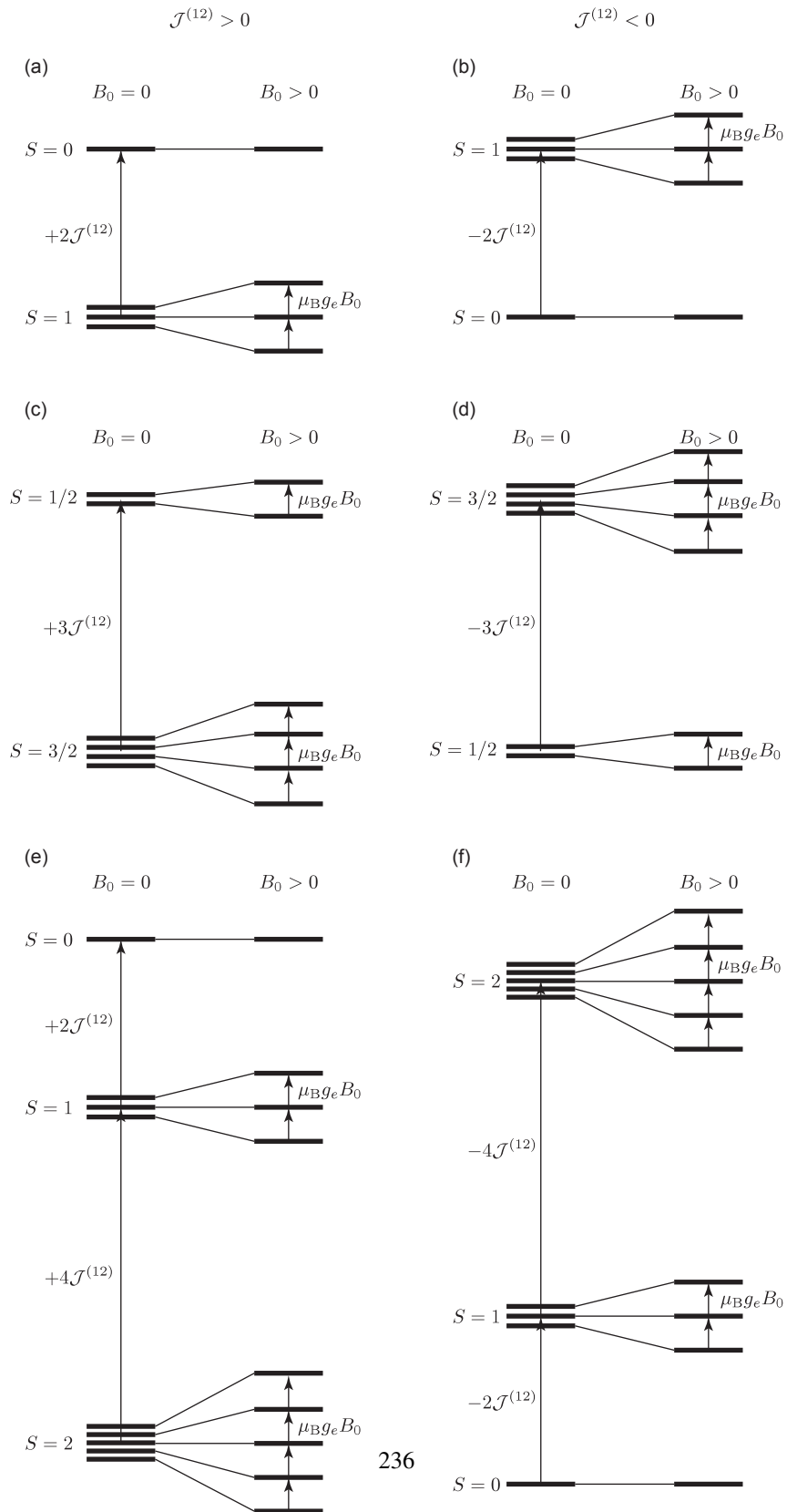


Figure 7.2: Energy levels due to the ferro- and antiferromagnetic exchange coupling between two electronic spins in the absence and presence of an external magnetic field. The energy levels are shown for (a)–(b) two coupled electronic spins 1/2, (c)–(d) a spin 1/2 coupled to a spin 1, and (e)–(f) two coupled spins 1. The energy levels due to ferromagnetic coupling are shown in (a), (c), and (e), and those due to antiferromagnetic coupling are shown in (b), (d), and (f).

where the hyperfine tensor is calculated from the total unpaired electron density of the combined spin system. Now let us consider the simplest example of a coupled spin system we introduced above, namely with $S_1 = S_2 = 1/2$. If $\mathcal{J}^{(12)}$ is positive and the spins are ferromagnetically aligned, the lowest-energy manifold is the triplet with $S = 1$, and both the EPR and NMR parameters we measure reflect those of a fictitious ion with that spin. If, on the other hand, $\mathcal{J}^{(12)}$ is negative it is the singlet $S = 0$ that is lowest in energy. The system is effectively diamagnetic and therefore exhibits no EPR signal. Therefore we observe no paramagnetic contribution to the shielding tensor of the nuclei. More generally we can extend the above discussion to include systems of more than two interacting spins. For instance this has been done by Bertini et al. who considered the case of a cluster containing four iron ions in an iron-sulphide protein [46].

Now we consider the other extreme situation where the thermal energy dominates the exchange coupling, i.e. $|\mathcal{J}^{(12)}| \ll kT$. The exponential factors in Equation 7.20 can now be expanded to first order in $\mathcal{J}^{(12)}/kT$, in addition to first order in $\mu_B g_e B_0 M_S / kT$:

$$\langle \hat{S}_z \rangle \approx \frac{\sum_{S=|S_1-S_2|}^{S_1+S_2} \sum_{M_S=-S}^{+S} M_S \left(1 - \frac{E(S, S_1, S_2)}{kT} - \frac{\mu_B g_e B_0 M_S}{kT}\right)}{\sum_{S=|S_1-S_2|}^{S_1+S_2} \sum_{M_S=-S}^{+S} \left(1 - \frac{E(S, S_1, S_2)}{kT} - \frac{\mu_B g_e B_0 M_S}{kT}\right)} \quad (7.25)$$

We now obtain a Curie spin that is simply the sum of the two independent Curie spins:

$$\langle \hat{S}_z \rangle = -\frac{\mu_B g_e [S_1(S_1 + 1) + S_2(S_2 + 1)] B_0}{3kT} \quad (7.26)$$

$$= \langle \hat{S}_{1z} \rangle + \langle \hat{S}_{2z} \rangle. \quad (7.27)$$

Since both electronic spins are independent, we can write the total paramagnetic shielding tensor as the sum of two independent contributions

$$\boldsymbol{\sigma}^S = -\frac{\mu_0 g_e S_1(S_1 + 1)}{3\hbar\gamma_I kT} \mathbf{A}^{(1)} - \frac{\mu_0 g_e S_2(S_2 + 1)}{3\hbar\gamma_I kT} \mathbf{A}^{(2)}, \quad (7.28)$$

where $\mathbf{A}^{(A)}$ is the hyperfine coupling tensor due to ion A . The two metal ions are now effectively non-interacting, and the system is reduced to the paramagnetic ensemble, which we have seen previously in section 7.1.

In each individual regime the paramagnetic shielding tensor has a Curie temperature dependence of

$1/(kT)$. However we should note that the dependence over the full range of temperatures is more complicated, since the expression for the shielding changes on moving from one regime to another via an intermediate regime where $|\mathcal{J}^{(12)}| \approx kT$ that we have not explicitly examined. This is an example of the exchange interactions introducing a deviation from the Curie behaviour.

7.4 The general exchange Hamiltonian for transition metal ions subject to spin-orbit coupling

The previous section described the behaviour of an electronic spin system and the corresponding paramagnetic chemical shielding tensor of two spin-only transition-metal ions that interact via an isotropic exchange interaction in both the low-temperature ordered and high-temperature paramagnetic regimes. The results above can easily be generalised to a finite cluster of metal ions. The case where the metal ions are subject to SO coupling is a little more complex, as there are several other terms that must be included in the exchange coupling Hamiltonian, which is where we turn our attention now.

The general spin Hamiltonian $\hat{\mathcal{H}}_0$ describing the exchange interactions between the transition-metal ions is

$$\hat{\mathcal{H}}_0 = \hat{\mathcal{H}}_0^{\text{NR}} + \hat{\mathcal{H}}_0^{\text{SO}}, \quad (7.29)$$

where $\hat{\mathcal{H}}_0^{\text{NR}}$ and $\hat{\mathcal{H}}_0^{\text{SO}}$ are the NR and SO contributions respectively. The NR contribution can be written as [231]

$$\hat{\mathcal{H}}_0^{\text{NR}} = -2 \sum_{A>B} \mathcal{J}^{(AB)} \hat{\mathbf{S}}^{(A)} \cdot \hat{\mathbf{S}}^{(B)} + \sum_{A>B} \hat{\mathbf{S}}^{(A)} \cdot \mathbf{D}^{(AB)} \cdot \hat{\mathbf{S}}^{(B)}, \quad (7.30)$$

where the sums are over pairs of coupled metal ions (A, B). The first term is the isotropic Heisenberg exchange Hamiltonian with isotropic exchange coupling constant $\mathcal{J}^{(AB)}$, and the second term is the anisotropic dipolar coupling interaction and $\mathbf{D}^{(AB)}$ is the symmetric dipolar coupling constant [232]. This latter interaction is weaker than the former, but can be important in establishing either long-range ferromagnetic or antiferromagnetic ordering in three dimensions. The presence of SO coupling adds two important terms that are

contained in $\hat{\mathcal{H}}_0^{\text{SO}}$, which is given by [231]

$$\hat{\mathcal{H}}_0^{\text{SO}} = \sum_A \hat{\mathbf{S}}^{(A)} \cdot \mathbf{D}^{(A)} \cdot \hat{\mathbf{S}}^{(A)} + \sum_{A>B} \mathbf{d}^{(AB)} \cdot (\hat{\mathbf{S}}^{(A)} \times \hat{\mathbf{S}}^{(B)}). \quad (7.31)$$

The first term represents the ZFS interactions of the ions, with which we are already familiar, and which are sometimes referred to as the single-ion anisotropy interactions [233]. The symmetric and traceless ZFS tensor for ion A is denoted $\mathbf{D}^{(A)}$. The second term is referred to as the Dzyaloshinskii–Moriya (DM) interaction [233–235]. The spatial dependence is encoded in the vector $\mathbf{d}^{(AB)}$, the three components of which can also be described by an antisymmetric (i.e. rank-one) tensor, and so this interaction is entirely anisotropic. The DM interaction depends on the vector product between $\hat{\mathbf{S}}^{(A)}$ and $\hat{\mathbf{S}}^{(B)}$, and is therefore zero if the two spins are exactly collinear, which we have seen is the preferred alignment for both ferro- and antiferromagnetic interactions. The effect of the DM term is therefore to perturb the spin orientations away from the perfect ferro- or antiferromagnetic collinear alignment, a process which is referred to as spin canting. We have neglected any SO contribution to the dipolar coupling interaction, which we absorb into the NR dipolar coupling term.

For convenience we recast the Hamiltonians in Equations 7.29, 7.30, and 7.31 into the following form

$$\hat{\mathcal{H}}_0 = \sum_A \sum_{q=-2}^{+2} (-1)^q D_{2q}^{(A)} \hat{\mathbf{S}}_{2-q}^{(A)} + \sum_{A>B} \sum_{k=0}^2 \sum_{q=-k}^{+k} (-1)^q J_{kq}^{(AB)} \hat{\mathbf{T}}_{k-q}^{(AB)}, \quad (7.32)$$

which is written in terms of irreducible spherical tensors. The first sum represents the rank-two ZFS interactions experienced by all the metal ions, the spatial and spin parts of which are given by the usual expressions. The second sum contains all the two-spin interaction terms, including the isotropic Heisenberg exchange, dipolar interaction, and DM parts. The spin tensor $\hat{\mathbf{T}}_{k-q}^{(AB)}$ is a direct tensor product of the rank-one spin operators:

$$\hat{\mathbf{T}}_{k-q}^{(AB)} = \sum_{q_1, q_2} \hat{\mathbf{S}}_{1q_1}^{(A)} \hat{\mathbf{S}}_{1q_2}^{(B)} \langle 11q_1q_2 | k - q \rangle \quad (7.33)$$

$$= (-1)^q \sqrt{2k+1} \sum_{q_1, q_2} \hat{\mathbf{S}}_{1q_1}^{(A)} \hat{\mathbf{S}}_{1q_2}^{(B)} \begin{pmatrix} 1 & 1 & k \\ q_1 & q_2 & q \end{pmatrix}, \quad (7.34)$$

and the components of the spatial tensor $J_{kq}^{(AB)}$ can be written down with reference to Table 2.3. The rank-zero part of the interaction is purely isotropic, and so represents the isotropic Heisenberg interaction. The spatial component $J_{00}^{(AB)}$ is therefore given by

$$J_{00}^{(AB)} = 2\sqrt{3}\mathcal{J}^{(AB)}. \quad (7.35)$$

The rank-one part is anisotropic and antisymmetric, and so represents the DM interaction. In terms of the Cartesian components of the DM interaction vector $\mathbf{d}^{(AB)}$ the irreducible spherical tensor components $J_{1q}^{(AB)}$ are:

$$J_{10}^{(AB)} = -i\sqrt{2}d_z^{(AB)}, \quad (7.36)$$

$$J_{1\pm 1}^{(AB)} = -(d_y^{(AB)} \pm id_x^{(AB)}). \quad (7.37)$$

Finally we have the rank-two components of the two-ion interaction, which are symmetric and therefore represent the ion-ion dipolar coupling interaction. In terms of the Cartesian tensor $\mathbf{D}^{(AB)}$ the irreducible spherical tensor components $J_{kq}^{(AB)}$ are given by:

$$J_{20}^{(AB)} = \sqrt{\frac{3}{2}}D_{zz}^{(AB)}, \quad (7.38)$$

$$J_{2\pm 1}^{(AB)} = \mp (D_{xz}^{(AB)} \pm iD_{yz}^{(AB)}), \quad (7.39)$$

$$J_{2\pm 2}^{(AB)} = \frac{1}{2}(D_{xx}^{(AB)} - D_{yy}^{(AB)} \pm 2iD_{xy}^{(AB)}). \quad (7.40)$$

From Equation 7.34 the irreducible spherical spin components satisfy the following identity when the ion labels A and B are swapped:

$$\hat{T}_{kq}^{(AB)} = (-1)^k \hat{T}_{kq}^{(BA)}. \quad (7.41)$$

Hence, in order for the Hamiltonian to remain invariant under such a label change, the irreducible spherical spatial components of the exchange coupling tensor must also satisfy

$$J_{kq}^{(AB)} = (-1)^k J_{kq}^{(BA)}. \quad (7.42)$$

This indicates that the isotropic coupling constant and dipolar-coupling tensor do not change sign when the

ions are coupled in the opposite order, whereas the DM tensor undergoes a sign change.

7.5 The paramagnetic shift due to a coupled electronic spin system subject to spin-orbit coupling

7.5.1 The EPR formalism

In this section we calculate the form of the paramagnetic chemical shielding tensor due to a cluster of coupled transition-metal ions. We firstly consider the case where the exchange coupling constants are sufficiently large that only the ground manifold is thermally populated, and secondly spend more time deriving the form of the shielding tensor in the high-temperature paramagnetic regime to second order in $1/(kT)^2$.

In the former case where only the ground manifold is thermally populated, we can describe the metal cluster as a single effective spin S , which possesses a single g -, hyperfine, and ZFS tensor. The EPR Hamiltonian is therefore of the form that we have already seen for a single metal ion in Equation 4.36, and we can immediately write down the paramagnetic chemical shielding tensor:

$$\sigma^S = -\frac{\mu_B}{\hbar\gamma_I} \mathbf{g} \cdot \mathbf{Z} \cdot \mathbf{A}. \quad (7.43)$$

This has the same form as the shielding due to a single transition-metal ion.

We have seen that in the high-temperature paramagnetic regime, so that kT dominates the exchange coupling constants, we can treat the metal ions as being independent. One important consequence of this is that we are able to assign to each ion its own g -, hyperfine, and ZFS interaction tensor. The exchange Hamiltonian $\hat{\mathcal{H}}_0$ introduced above can be included in the EPR Hamiltonian $\hat{\mathcal{H}}_{\text{EPR}}$ with the electronic Zeeman and hyperfine interaction Hamiltonians. We consider a system containing a single spin-1/2 nucleus I that is coupled to several paramagnetic centres. The following Hamiltonian represents the starting point for our calculation of the paramagnetic chemical shielding tensor:

$$\hat{\mathcal{H}}_{\text{EPR}} = \mu_B \sum_A \mathbf{B}_0 \cdot \mathbf{g}^{(A)} \cdot \hat{\mathbf{S}}^{(A)} + \sum_A \hat{\mathbf{S}}^{(A)} \cdot \mathbf{A}^{(A)} \cdot \hat{\mathbf{I}} + \hat{\mathcal{H}}_0 \quad (7.44)$$

$$= \mu_B \sum_A \mathbf{B}_0 \cdot \mathbf{g}^{(A)} \cdot \hat{\mathbf{S}}^{(A)} + \sum_A \hat{\mathbf{S}}^{(A)} \cdot \mathbf{A}^{(A)} \cdot \hat{\mathbf{I}} + \sum_A \hat{\mathbf{S}}^{(A)} \cdot \mathbf{D}^{(A)} \cdot \hat{\mathbf{S}}^{(A)} + \sum_{A>B} \hat{\mathbf{S}}^{(A)} \cdot \mathbf{J}^{(AB)} \cdot \hat{\mathbf{S}}^{(B)}. \quad (7.45)$$

The first and second terms represent the electronic Zeeman interactions of all the metal ions, and the hyperfine couplings between these ions and the single nucleus. As before these interactions are the origin of the electronic magnetic moment and hyperfine field operators \hat{m} and $\hat{\mathcal{F}}$, the cross terms between which give us the chemical shielding tensor according to the EPR formalism. The terms contained in $\hat{\mathcal{H}}_0$, namely the ZFS and two-spin exchange interactions, are independent of both the external magnetic field and the nuclear magnetic moment, so their eigenfunctions and energies are used to calculate the Boltzmann average in the expressions for the shielding tensor.

The details of the calculation of the paramagnetic shielding tensor are somewhat complicated, and are contained in appendix E, with only the results given here. We can write the paramagnetic shielding as the sum of three terms up to $O(\beta^2)$:

$$\sigma_{ij}^S = \sigma_{ij}^{S,1} + \sigma_{ij}^{S,2A} + \sigma_{ij}^{S,2B} + O(\beta^3). \quad (7.46)$$

The first term $\sigma_{ij}^{S,1}$ is of order $1/(kT)$, and there are two terms of order $1/(kT)^2$ which we have labelled $\sigma_{ij}^{S,2A}$ and $\sigma_{ij}^{S,2B}$.

The first term is calculated to be

$$\sigma_{ij}^{S,1} = -\frac{\mu_B}{3\hbar\gamma_I kT} \sum_A \langle S^{(A)} \| \hat{S}_1^{(A)} \| S^{(A)} \rangle^2 \sum_q (-1)^q g_{1q,i}^{(A)} A_{1-q,j}^{(A)}, \quad (7.47)$$

which is a sum of terms each of which has the same form as the expression we have already encountered in Equation 6.27. Substituting in the expression for the reduced matrix element and simplifying the sum over q as before, we obtain a familiar expression for the first-order shielding:

$$\sigma_{ij}^{S,1} = -\frac{\mu_B}{3\hbar\gamma_I kT} \sum_A S^{(A)} (S^{(A)} + 1) \mathbf{g}^{(A)} \cdot \mathbf{A}^{(A)}. \quad (7.48)$$

We note that this contribution depends only on the g - and hyperfine tensors of the individual spins and is independent of the ZFS, as before, and of the two-spin exchange tensors. Hence this term is a simple sum of contributions from each paramagnetic centre, as it contains no information on how the ions interact with each other.

The second term, which is of order $1/(kT)^2$, is also familiar to us, being a sum of expressions which have

the same form as Equation 6.28:

$$\begin{aligned} \sigma_{ij}^{S,2A} &= \frac{\mu_B}{\hbar\gamma_I(kT)^2} \sum_A (-1)^{2S^{(A)}} (2S^{(A)} + 1)^{1/2} \langle S^{(A)} \parallel \hat{S}_1^{(A)} \parallel S^{(A)} \rangle^2 \langle S^{(A)} \parallel \hat{S}_2^{(A)} \parallel S^{(A)} \rangle \\ &\times \left\{ \begin{array}{ccc} 1 & 2 & 1 \\ S^{(A)} & S^{(A)} & S^{(A)} \end{array} \right\} \sum_{qq'q''} (-1)^{q+q'+q''} g_{1q,i}^{(A)} A_{1q',j}^{(A)} D_{2q''}^{(A)} \begin{pmatrix} 1 & 2 & 1 \\ -q' & -q'' & -q \end{pmatrix}. \end{aligned} \quad (7.49)$$

This term can also be simplified using the same method as before to give

$$\sigma_{ij}^{S,2A} = \frac{\mu_B}{30\hbar\gamma_I(kT)^2} \sum_A S^{(A)} (S^{(A)} + 1) (2S^{(A)} - 1) (2S^{(A)} + 3) \mathbf{g}^{(A)} \cdot \mathbf{D}^{(A)} \cdot \mathbf{A}^{(A)}, \quad (7.50)$$

which depends on the ZFS tensors in addition to the g - and hyperfine tensors. Once again it is a simple sum of contributions from each paramagnetic ion, which is again a result of it containing no information about the couplings between the paramagnetic centres.

The third term, also of order $1/(kT)^2$ is given by

$$\begin{aligned} \sigma_{ij}^{S,2B} &= \frac{\mu_B}{9\hbar\gamma_I(kT)^2} \sum_{A,B \neq A} \langle S^{(A)} \parallel \hat{S}_1^{(A)} \parallel S^{(A)} \rangle^2 \langle S^{(B)} \parallel \hat{S}_1^{(B)} \parallel S^{(B)} \rangle^2 \\ &\times \sum_{k''q'q''} g_{1q,i}^{(A)} A_{1q',j}^{(B)} J_{k''q''}^{(AB)} \sqrt{2k'' + 1} \begin{pmatrix} 1 & 1 & k'' \\ q & q' & q'' \end{pmatrix}. \end{aligned} \quad (7.51)$$

This is an expression we have not encountered before, as it results from the exchange couplings between the paramagnetic centres. On simplifying we obtain the concise expression

$$\sigma_{ij}^{S,2B} = \frac{\mu_B}{9\hbar\gamma_I(kT)^2} \sum_{A,B \neq A} S^{(A)} (S^{(A)} + 1) S^{(B)} (S^{(B)} + 1) \mathbf{g}^{(A)} \cdot \mathbf{J}^{(AB)} \cdot \mathbf{A}^{(B)}, \quad (7.52)$$

which is now a sum of contributions from pairs of metal ions that have a non-zero coupling between them. Each contribution is a cross term containing the g -tensor of one metal ion and the hyperfine tensor of another. Note that if the exchange coupling constant between any two ions is zero, that pair of ions will not give a joint contribution to the overall paramagnetic shielding tensor. To summarise, the final expression for the

paramagnetic chemical shielding tensor is

$$\begin{aligned}
\sigma^S = & -\frac{\mu_B}{3\hbar\gamma_I kT} \sum_A S^{(A)} (S^{(A)} + 1) \mathbf{g}^{(A)} \cdot \mathbf{A}^{(A)} \\
& + \frac{\mu_B}{30\hbar\gamma_I (kT)^2} \sum_A S^{(A)} (S^{(A)} + 1) (2S^{(A)} - 1) (2S^{(A)} + 3) \mathbf{g}^{(A)} \cdot \mathbf{D}^{(A)} \cdot \mathbf{A}^{(A)} \\
& + \frac{\mu_B}{9\hbar\gamma_I (kT)^2} \sum_{A,B \neq A} S^{(A)} (S^{(A)} + 1) S^{(B)} (S^{(B)} + 1) \mathbf{g}^{(A)} \cdot \mathbf{J}^{(AB)} \cdot \mathbf{A}^{(B)}.
\end{aligned} \tag{7.53}$$

The third term adds both isotropic and anisotropic contributions to both the contact and pseudo-contact shifts.

In this high-temperature regime, we may also write the paramagnetic shielding tensor in terms of Z -tensors, as for non-interacting ions. In the present case, however, the expression is more complicated:

$$\sigma^S = -\frac{\mu_B}{\hbar\gamma_I} \sum_A \mathbf{g}^{(A)} \cdot \left[\mathbf{Z}^{(A)} \cdot \mathbf{A}^{(A)} + \sum_{B \neq A} \mathbf{Z}^{(AB)} \cdot \mathbf{A}^{(B)} \right]. \tag{7.54}$$

The tensor $\mathbf{Z}^{(A)}$ is the one-ion Z -tensor, and takes the form that we have seen before:

$$\mathbf{Z}^{(A)} = \frac{S^{(A)} (S^{(A)} + 1)}{3kT} \mathbf{1} - \frac{S^{(A)} (S^{(A)} + 1) (2S^{(A)} - 1) (2S^{(A)} + 3)}{30(kT)^2} \mathbf{D}^{(A)}, \tag{7.55}$$

which depends on the single-ion g - and ZFS tensors. The tensor $\mathbf{Z}^{(AB)}$ is the two-ion Z -tensor, which is given by

$$\mathbf{Z}^{(AB)} = -\frac{S^{(A)} (S^{(A)} + 1) S^{(B)} (S^{(B)} + 1)}{9(kT)^2} \mathbf{J}^{(AB)}, \tag{7.56}$$

and contains all the information about the exchange coupling tensors.

7.5.2 Example: two coupled electronic spins-1/2

We complete this section with the illustration of a practical example of the paramagnetic shielding tensor due to a cluster of coupled paramagnetic ions, with a particular emphasis on the temperature dependence of the shielding. The example we choose is that of electronic spins-1/2 A and B with different isotropic g -factors $g^{(A)}$ and $g^{(B)}$, which interact via an isotropic exchange interaction with coupling constant $\mathcal{J}^{(AB)}$. We focus on the paramagnetic shielding of a nuclear spin I which interacts with both paramagnetic centres via different Fermi-contact coupling constants $A^{\text{FC},(A)}$ and $A^{\text{FC},(B)}$. This choice of isotropic interaction parameters results

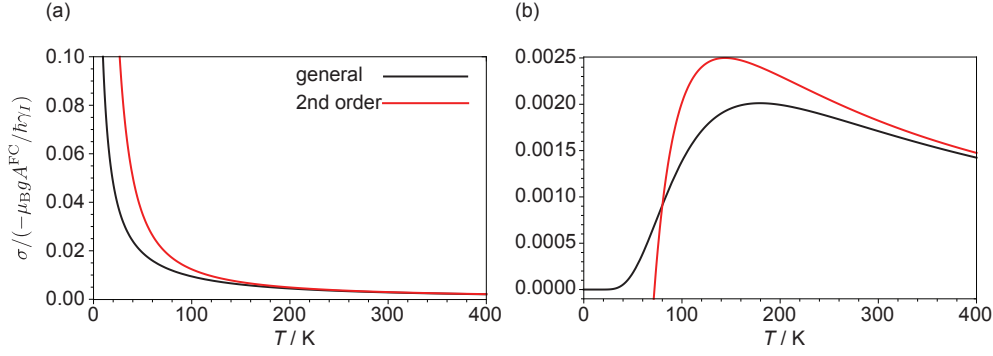


Figure 7.3: Plots of the temperature dependence of the isotropic paramagnetic shielding due to two coupled electronic spins-1/2. The plot in (a) is for a positive exchange coupling constant of $\mathcal{J}^{(AB)} = +100 \text{ cm}^{-1}$, and the plot in (b) corresponds to a negative exchange constant of $\mathcal{J}^{(AB)} = -100 \text{ cm}^{-1}$. In both cases the temperature curves calculated from both the general EPR expression and the high-temperature second-order approximation are included.

in a paramagnetic shielding that is also wholly isotropic. Since we are mainly interested in the temperature dependence of the shielding this choice is sufficient, but we note here that the extension to anisotropic spatial tensors is straightforward.

We begin by deriving the general paramagnetic shielding tensor from the EPR formula in Equation 4.103, where the energy levels E_n are the eigenvalues of the singlet and triplet states of the exchange Hamiltonian given in Equations 7.8–7.11, and the hyperfine and electronic magnetic moment operators are each the sum of the operators for each paramagnetic centre. The general shielding tensor is isotropic and is given by

$$\sigma_{\text{gen}}^S = \frac{\mu_B \Delta g \Delta A - \mu_B \exp(2\beta \mathcal{J}^{(AB)}) [\Delta g \Delta A + 2\beta \Sigma g \Sigma A \mathcal{J}^{(AB)}]}{4\hbar \gamma_I \mathcal{J}^{(AB)} [1 + 3 \exp(2\beta \mathcal{J}^{(AB)})]}, \quad (7.57)$$

where $\Delta g = g^{(A)} - g^{(B)}$, $\Delta A = A^{\text{FC},(A)} - A^{\text{FC},(B)}$, $\Sigma g = g^{(A)} + g^{(B)}$, and $\Sigma A = A^{\text{FC},(A)} + A^{\text{FC},(B)}$ are the sums and differences of the g -factors and Fermi-contact coupling constants. For comparison we can also calculate the shielding tensor to second-order in $\beta \sigma_{2\text{nd}}^S$ using the expressions in Equations 7.54–7.56 to give

$$\sigma_{2\text{nd}}^S = -\frac{\mu_B}{4\hbar \gamma_I kT} (g^{(A)} A^{\text{FC},(A)} + g^{(B)} A^{\text{FC},(B)}) - \frac{\mu_B \mathcal{J}^{(AB)}}{8\hbar \gamma_I (kT)^2} (g^{(A)} A^{\text{FC},(B)} + g^{(B)} A^{\text{FC},(A)}). \quad (7.58)$$

The general and second-order shielding tensors are plotted as a function of temperature in Figure 7.3 with both positive and negative exchange coupling constants. In both plots the expressions are simplified

by assuming that $g^{(A)} = g^{(B)} \equiv g$ and $A^{\text{FC},(A)} = A^{\text{FC},(B)} \equiv A^{\text{FC}}$. The temperature plot of the paramagnetic shielding for a positive exchange coupling constant of $\mathcal{J}^{(AB)} = +100 \text{ cm}^{-1}$ is shown in Figure 7.3 (a). Here ferromagnetic alignment at low temperature results in a triplet electronic spin ground state with $S = 1$. The shielding decreases as the temperature increases from 0 K, due to two factors. At temperatures below $\mathcal{J}^{(AB)}/k = 144 \text{ K}$ the decrease in the shielding is primarily due to the thermal population of the excited Zeeman energy levels of the triplet manifold, which reduces the Curie spin of this state; this temperature variation can therefore be modelled with a Curie law with $S = 1$. As the temperature increases above 144 K the diamagnetic singlet excited state with $S = 0$ begins to be substantially populated. At still higher temperatures where kT dominates the exchange coupling interaction the two spins-1/2 behave as independent independent spins, each with its own separate contribution to the shielding. The total shielding is then equal to the sum of the two independent contributions, as given by the first-order term in Equation 7.58, which follows a Curie temperature law.

In Figure 7.3 (b) is shown the corresponding temperature plot of the shielding with a negative exchange coupling of $\mathcal{J}^{(AB)} = -100 \text{ cm}^{-1}$. This interaction gives a diamagnetic singlet ground state with $S = 0$. The temperature dependence is markedly different from the ferromagnetic case as the shielding first increases with increasing temperature, before reaching a maximum at $|\mathcal{J}^{(AB)}|/k = 144 \text{ K}$ and then decreasing. Initially, at temperatures below 40 K, only the singlet state is thermally occupied, and so there is no contribution to the paramagnetic shielding tensor. The increase in the shielding above 40 K is due to the increasing thermal population of the triplet state. This trend persists up to 144 K, above which both the singlet and triplet states are substantially populated and the two spins-1/2 start to behave as independent Curie spins. The subsequent decrease in the shielding with increasing temperature is then due to each Curie spin following a Curie law.

One interesting aspect of these plots is that they suggest that NMR can be used to determine the exchange coupling constants of a cluster of coupled electronic spins by measuring the paramagnetic shielding tensors at multiple temperatures.

7.6 Ferromagnetic and antiferromagnetic interactions in solid insulators: the Curie–Weiss law

We now extend the previous discussion on magnetic exchange coupling interactions to solid insulator materials containing an ensemble of metal ions which possess unpaired electrons. The interactions between the unpaired electrons result in ferromagnetic or antiferromagnetic ordering of the bulk material, and we will see how this ordering affects the magnetic susceptibility and the paramagnetic shielding tensor of the nuclei. Whereas in isolated metal-ion clusters the electronic energy levels form a discrete ladder, the case of solid materials is considerably more complicated as the extremely large number of interactions results in a continuum of energy levels. This means that whilst for isolated clusters we are able to define EPR parameters, such as the g -tensor, which are properties of the entire coupled spin system with total spin S , it becomes much less clear how to define such parameters for an infinite lattice of coupled electronic spins. Therefore we use the simplest successful model for extended systems of coupled electronic spins, namely mean-field theory and the Weiss model, which we apply to spin-only transition-metal ions.

7.6.1 The Weiss model of ferromagnetism

We describe the material with the simplest Hamiltonian that can be used to describe magnetic ordering, which contains the electronic Zeeman and isotropic Heisenberg exchange terms:

$$\hat{H} = \mu_B g_e \sum_A \mathbf{B}_0 \cdot \hat{\mathbf{S}}^{(A)} - 2 \sum_{A>B} \mathcal{J}^{(AB)} \hat{\mathbf{S}}^{(A)} \cdot \hat{\mathbf{S}}^{(B)}, \quad (7.59)$$

where the sum is over the metal ions A and B . We assume that the ions are spin only, and therefore exhibit no SO coupling. As is the case for the two-spin system of section 7.2, the exchange coupling constants $\mathcal{J}^{(AB)}$ between the nearest neighbours are positive for ferromagnetic alignment, and negative for antiferromagnetic alignment.

In the Weiss model we approximate the above Hamiltonian with a *mean field* term which describes the interaction of spin A with a mean molecular field \mathbf{B}_{mf} that is due to the other spins. Furthermore we restrict our discussion to an ensemble of metal ions of the same type, and consider only nearest-neighbour

interactions. The molecular magnetic field experienced by ion A is given by

$$\mathbf{B}_{\text{mf}} = -\frac{2}{\mu_{\text{B}}g_e} \sum_{B \neq A} \mathcal{J}^{(AB)} \hat{\mathbf{S}}^{(B)}, \quad (7.60)$$

and is assumed to be the same for *all* the metal ions in the solid. The total effective mean-field Hamiltonian, which replaces Equation 7.59, is then

$$\hat{H} = \mu_{\text{B}}g_e \sum_A (\mathbf{B}_0 + \mathbf{B}_{\text{mf}}) \cdot \hat{\mathbf{S}}^{(A)}. \quad (7.61)$$

This expression has the form of the Hamiltonian of an ensemble of spin-only paramagnetic ions in a magnetic field $\mathbf{B}_0 + \mathbf{B}_{\text{mf}}$. The mean molecular field is responsible for the ordering of the system at low temperature, and so we assume that it is proportional to the bulk magnetization of the system:

$$\mathbf{B}_{\text{mf}} = \Lambda \mathbf{M}, \quad (7.62)$$

where Λ is the constant of proportionality that characterises the strength of the molecular field as a function of the magnetization. We find it useful to employ an alternative expression for the mean molecular field in terms of the Curie spin:

$$\mathbf{B}_{\text{mf}} = -\lambda \langle \hat{\mathbf{S}} \rangle, \quad (7.63)$$

where the minus sign is present because \mathbf{M} and $\langle \hat{\mathbf{S}} \rangle$ have opposite sign. Note that we have dropped the superscript (A) from the Curie spin, as a result of the assumption that all ions experience the same molecular field. With these conventions, both Λ and λ are positive for a ferromagnet.

The form of the Hamiltonian in Equation 7.61 implies that magnetic ordering of the electronic spins can be achieved with the mean molecular field, even in the absence of an external field. At low temperatures this leads to the formation of a spontaneous magnetization in a ferromagnet. As the temperature is raised, the higher-energy states become occupied, and the magnetic ordering is disrupted, with all order being destroyed above a transition temperature. At temperatures above the transition temperature, the material behaves as a paramagnet. This is the Weiss model of ferromagnetism.

In order to elucidate the magnetic behaviour of a ferromagnetic material, and to derive the expression for

the transition temperature above which we observe paramagnetic behaviour, we apply a modified form of the general expression for the Curie spin in Equation 3.58:

$$\frac{\langle \hat{S}_z \rangle}{\langle \hat{S}_z \rangle_{\text{sat}}} = B_S(y), \quad (7.64)$$

where the Brillouin function $B_S(y)$ is given in Equation 3.59. The quantity y has a similar expression to that in Equation 3.59, but we have added the term $-\lambda \langle \hat{S}_z \rangle$ to account for the mean molecular field:

$$y = \frac{\mu_B g_e S (B_0 - \lambda \langle \hat{S}_z \rangle)}{kT}. \quad (7.65)$$

Note that we assume that B_0 , the Curie spin, and therefore the mean molecular field are all along z . We obtain the conditions for spontaneous ferromagnetic alignment of the spins in the absence of an external field as follows. We set $B_0 = 0$, and rearrange Equation 7.65 in terms of $\langle \hat{S}_z \rangle / \langle \hat{S}_z \rangle_{\text{sat}}$ (where $\langle \hat{S}_z \rangle_{\text{sat}} = -S$). In combination with Equation 7.64 we now have two simultaneous equations that we must solve to obtain the alignment conditions:

$$\frac{\langle \hat{S}_z \rangle}{\langle \hat{S}_z \rangle_{\text{sat}}} = B_S(y), \quad (7.66)$$

$$\frac{\langle \hat{S}_z \rangle}{\langle \hat{S}_z \rangle_{\text{sat}}} = \frac{kTy}{\mu_B g_e S^2 \lambda}. \quad (7.67)$$

The second equation depends on the temperature, and so the solutions can be found by identifying the temperature, referred to as the *Curie temperature* T_C , below which we obtain solutions consistent with spontaneous ferromagnetism. The solutions are illustrated graphically in Figure 7.4 (a), which shows as a function of y a plot of both the Brillouin function, and the linear relation $\langle \hat{S}_z \rangle / \langle \hat{S}_z \rangle_{\text{sat}} = kTy / (\mu_B g_e S^2 \lambda)$, at three different temperatures. When the temperature is higher than T_C there is only one solution to the two simultaneous equations, $\langle \hat{S}_z \rangle / \langle \hat{S}_z \rangle_{\text{sat}} = y = 0$, indicating that there is no spontaneous magnetization in the absence of the external field. At temperatures below T_C we see that there are two solutions in addition to the one at $y = 0$. These two further solutions, with non-zero values of $\langle \hat{S}_z \rangle / \langle \hat{S}_z \rangle_{\text{sat}}$, with equal magnitudes and opposite signs, indicate the presence of a spontaneous magnetization, and therefore ferromagnetic behaviour.

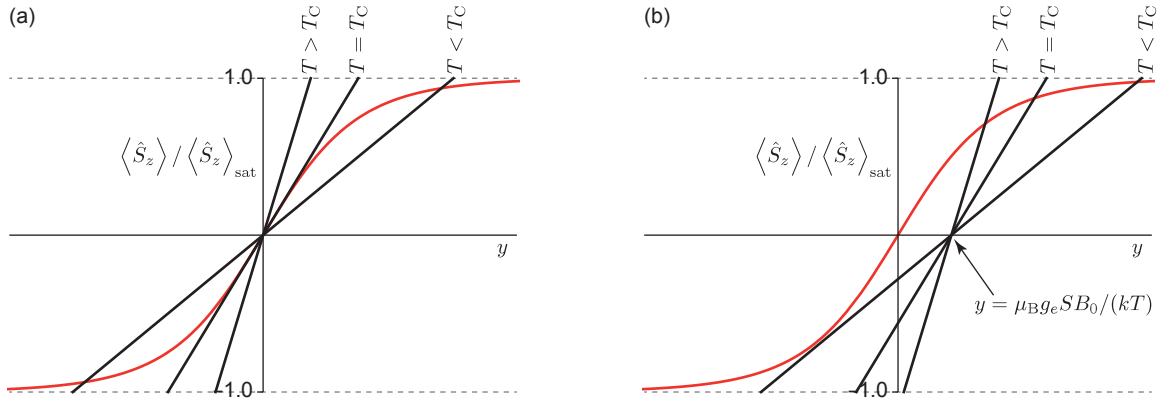


Figure 7.4: Plot illustrating the conditions for spontaneous ferromagnetism in the absence of an external field, and the effect of a subsequently applied field. In (a) are shown plots of Equations 7.66 (in red) and 7.67 (black), with the second equation plotted at three different temperatures. Simultaneous solutions are found at the points where the two curves intersect, and indicate the conditions under which the sample is spontaneously magnetised. These plots indicate that the sample must be below a certain critical temperature T_C for spontaneous ferromagnetism to occur. The graph in (b) shows plots of Equations 7.70 and 7.71, which illustrate the conditions for non-zero magnetisation in a ferromagnet in an externally applied magnetic field. The effect of the field is to magnetise the sample irrespective of the temperature.

The transition between the paramagnetic and ferromagnetic behaviour occurs at $T = T_C$, which is the temperature at which the gradient of the linear relation in Equation 7.67 is exactly equal to the gradient of the Brillouin function at $y = 0$. Equating the two gradients, we obtain an expression for the Curie temperature in terms of the mean-field parameter:

$$\frac{S + 1}{3S} = \frac{kT_C}{\mu_B g_e S^2 \lambda} \quad (7.68)$$

$$T_C = \frac{\mu_B g_e S(S + 1)\lambda}{3k}. \quad (7.69)$$

The application of an external magnetic field B_0 results in a non-zero magnetization at all temperatures. This can be deduced from Equations 7.64 and 7.65, by rearranging the latter as before, but this time retaining

a non-zero B_0 . The result is the following pair of simultaneous equations:

$$\frac{\langle \hat{S}_z \rangle}{\langle \hat{S}_z \rangle_{\text{sat}}} = B_S(y), \quad (7.70)$$

$$\frac{\langle \hat{S}_z \rangle}{\langle \hat{S}_z \rangle_{\text{sat}}} = -\frac{B_0}{\lambda S} + \frac{kTy}{\mu_B g_e S^2 \lambda}. \quad (7.71)$$

Equation 7.71 differs from Equation 7.67 by the additive factor $-B_0/(\lambda S)$. The effect of this factor is to shift the straight line parallel to the y -axis so that it crosses $\langle \hat{S}_z \rangle / \langle \hat{S}_z \rangle_{\text{sat}} = 0$ at $y = \mu_B g_e S B_0 / kT$, rather than $y = 0$, with the result that the line always intersects the Brillouin function at a non-zero value of the Curie spin for all temperatures. Hence, for all temperatures above and below the Curie temperature, there is a non-zero net magnetization, as shown in Figure 7.4 (b). The implication is that there is always an energetic advantage for the magnetic moments of a ferromagnet to line up with the external field. We return to this topic in section 7.6.3, when we discuss the magnetic susceptibility of magnetically ordered systems.

7.6.2 The Weiss model of antiferromagnetism

In the Weiss model of antiferromagnetism we apply the same basic assumptions as for ferromagnetism, namely that the ions are of the same species, that we only consider nearest-neighbour interactions, and that we can replace the terms in the exchange Hamiltonian with a mean molecular field term. However we have to modify the phenomenological form of the molecular field in Equation 7.63 in the following way. The negative exchange coupling constants result in the magnetic moments of the nearest-neighbour ions lying antiparallel to one another. Hence, from a conceptual point of view, we can divide the ions into two interpenetrating sub-lattices, where within each sub-lattice the magnetic moments at low temperature are aligned the same way. In one sub-lattice all the magnetic moments point ‘up’, and in the other they point ‘down’. In the simple cubic oxides MO, such as NiO and MnO, which adopt the rock-salt structure, all the nearest neighbours of a particular M^{2+} ion on *one* sub-lattice must belong entirely to the *other* sub-lattice. In addition the simplest implementation of mean-field theory assumes that the exchange interactions only occur between nearest neighbours, so that a particular spin interacts only with spins on the other sub-lattice. The result is that the mean molecular field on the former must be proportional to the magnetization of the latter. Whilst this represents a clear simplification of the physics of antiferromagnetism, it is nevertheless sufficient

to introduce most of the important features of the magnetic ordering. However we note that in real materials next-nearest-neighbour interactions are not negligible. This situation requires a modification of the model discussed here, which is presented in section 7.6.4.

Therefore, according to the Weiss model, the molecular fields on the ‘up’ and ‘down’ sub-lattices B_{mf}^+ and B_{mf}^- are given by

$$B_{\text{mf}}^+ = -\lambda \langle \hat{S} \rangle^- \quad (7.72)$$

$$B_{\text{mf}}^- = -\lambda \langle \hat{S} \rangle^+, \quad (7.73)$$

where $\langle \hat{S} \rangle^\pm$ are the Curie spins of the two sub-lattices, which we label + and –, and the mean-field constant λ is negative for antiferromagnetic ordering. The Curie spin of each sub-lattice, and therefore the conditions for spontaneous magnetization in each of the two sub-lattices can be found in a similar way as for the ferromagnetic systems in the previous section. In the absence of an external field, the $\langle \hat{S} \rangle^\pm$ are given by

$$\frac{\langle \hat{S}_z \rangle^\pm}{\langle \hat{S}_z \rangle_{\text{sat}}} = B_S(y^\pm), \quad (7.74)$$

where

$$y^\pm = -\frac{\mu_B g_e S \lambda \langle \hat{S}_z \rangle^\mp}{kT}, \quad (7.75)$$

and we have assumed that the Curie spins are aligned along $\pm z$. The two sub-lattices are equivalent, and differ only in the opposite directions of their spontaneous magnetization vectors. Therefore

$$\langle \hat{S}_z \rangle^+ = -\langle \hat{S}_z \rangle^- = \langle \hat{S}_z \rangle, \quad (7.76)$$

where $\langle \hat{S}_z \rangle$ is the magnitude of the Curie spin of each sub-lattice, which is now given by

$$\frac{\langle \hat{S}_z \rangle}{\langle \hat{S}_z \rangle_{\text{sat}}} = B_S(y), \quad (7.77)$$

$$y = \frac{\mu_B g_e S \lambda \langle \hat{S}_z \rangle}{kT}. \quad (7.78)$$

The situation is now exactly the same as for the ferromagnetic system in section 7.6.1. We rearrange Equation 7.78 to obtain a pair of simultaneous equations that can be solved in the same way:

$$\frac{\langle \hat{S}_z \rangle}{\langle \hat{S}_z \rangle_{\text{sat}}} = B_S(y), \quad (7.79)$$

$$\frac{\langle \hat{S}_z \rangle}{\langle \hat{S}_z \rangle_{\text{sat}}} = - \frac{kTy}{\mu_B g_e S^2 \lambda}. \quad (7.80)$$

These two equations can be solved using Figure 7.4, which shows that for temperatures below a certain transition temperature we obtain a spontaneous magnetization in each sub-lattice, which disappears above the transition temperature. This transition temperature is referred to as the *Néel temperature* T_N , and can be shown to have an expression in terms of the mean-field parameter that is similar to the Curie temperature:

$$T_N = - \frac{\mu_B g_e S(S+1)\lambda}{3k}. \quad (7.81)$$

We note that there is an additional sign compared to the expression for T_C . This is because for antiferromagnetic alignment λ is negative, and the minus sign ensures that T_N is positive.

At this point we also note that, although each sub-lattice exhibits spontaneous magnetization below T_N , the magnetization vectors of the two sub-lattices are equal in magnitude and opposite in direction. This means that the material as a whole has zero magnetization in the absence of an external magnetic field. This magnetic transition may also be accompanied by a change in structure. For example MnO undergoes a rhombohedral distortion from the high-temperature cubic structure on cooling below the Néel temperature.

7.6.3 The magnetic susceptibility

We have derived expressions for the Curie and Néel temperatures, below which a solid material shows ferromagnetic and antiferromagnetic behaviour respectively in the absence of an external magnetic field. Now we must move further and consider the effect of an external magnetic field when applied to these materials, as it is under these conditions we observe the NMR spectrum. At this point we assume that, under the experimental conditions, we are operating in a temperature regime where $T > T_C$ or $T > T_N$, and the material behaves as a paramagnet. Before we calculate the magnetic susceptibility we note that, so far, we have treated

the ferromagnetic and antiferromagnetic systems differently in order to acknowledge the differences between the two models. However, since we have now shown that both systems behave in the same way above their respective transition temperatures we can unify the descriptions. In doing so, we note that the expressions for T_C and T_N differ only in their signs. Therefore we can define a single parameter, called the Weiss constant Θ , which is given by

$$\Theta = \frac{\mu_B g_e S(S+1)\lambda}{3k}. \quad (7.82)$$

When we are referring to a ferromagnetic material the mean-field parameter λ is positive, and so Θ is positive and is equal to the Curie temperature, $\Theta = T_C$. On the other hand antiferromagnetic materials have negative λ , and so Θ is negative and given by $\Theta = -T_N$.

In the presence of an external magnetic field B_0 of the strength used in high-resolution NMR we can truncate the Brillouin function at the first-order term in y . For a ferromagnetic material we take the expressions for the Curie spin and the quantity y in Equations 7.64 and 7.65 and obtain:

$$\langle \hat{S}_z \rangle = -S B_S(y) \quad (7.83)$$

$$\approx -\frac{S+1}{3}y \quad (7.84)$$

$$= -\frac{\mu_B g_e S(S+1)}{3k} \left(\frac{B_0 - \lambda \langle \hat{S}_z \rangle}{T} \right) \quad (7.85)$$

$$= -\frac{\Theta}{\lambda} \left(\frac{B_0 - \lambda \langle \hat{S}_z \rangle}{T} \right). \quad (7.86)$$

For an antiferromagnetic material the treatment is similar with an additional step. We take the expressions for the Curie spins of the two sub-lattices in Equation 7.74 and the quantities y^\pm in Equation 7.78, and modify the latter to include B_0 . The effect of the external field is to make both Curie spins more negative, so that they are no longer equal and opposite. We average them to obtain the total Curie spin $\langle \hat{S}_z \rangle = (\langle \hat{S}_z \rangle^+ + \langle \hat{S}_z \rangle^-)/2$, for which we obtain the same expression as for the ferromagnetic case in Equation 7.86. Henceforth we can treat both cases using this same expression for the Curie spin, which rearranges to give

$$\langle \hat{S}_z \rangle = -\frac{\Theta B_0}{\lambda(T - \Theta)}. \quad (7.87)$$

The z component of the average electronic magnetic moment operator is then

$$\langle \hat{\mu}_z \rangle = -\mu_B g_e \langle \hat{S}_z \rangle \quad (7.88)$$

$$= \frac{\mu_B g_e \Theta B_0}{\lambda(T - \Theta)}. \quad (7.89)$$

Finally, substituting this last expression in Equation 3.89 gives the magnetic susceptibility

$$\chi = \frac{\mu_0 \mu_B^2 g_e^2 S(S+1)}{3k(T - \Theta)}. \quad (7.90)$$

This expression has the same form as the susceptibility of an ensemble of non-interacting paramagnetic spins, with the exception that the $1/T$ Curie temperature dependence has been replaced by a $1/(T - \Theta)$ dependence. The temperature dependence of the susceptibility in Equation 7.90 is an example of the Curie–Weiss law.

7.6.4 The Néel temperature and Weiss constant in antiferromagnetic materials

The mean-field theory of antiferromagnetism that we have presented so far indicates that the Néel temperature and the Weiss constant have the same value within a sign, i.e. $\Theta = -T_N$. However we should bear in mind that the two quantities are physically distinct, with the Néel temperature being the temperature below which we observe antiferromagnetic ordering, and the Weiss constant being a parameter that characterises the magnetic susceptibility in the paramagnetic regime. The two parameters are therefore measured in different temperature regimes, and may in fact take very different values for some antiferromagnetic materials. For example in materials such as MnO, FeO, and CoO the measured Weiss constants have greater magnitude than the Néel temperature, $|\Theta| > T_N$; in the case of MnO T_N and Θ are 116 K and -510 K respectively [187]. The discrepancy can be explained when we note that in the mean-field theory of section 7.6.2 it was assumed that exchange interactions occur only between nearest neighbouring spins on different sub-lattices, so that the mean field experienced by one sub-lattice is due entirely to the other sub-lattice. However this is generally not true, and we may have to account for next-nearest-neighbour interactions between spins on the same sub-lattice, which introduces an additional mean-field term.

We can write down the two mean fields experienced by the + and – sub-lattices, B_{mf}^+ and B_{mf}^- , as

$$B_{\text{mf}}^+ = \xi \langle \hat{S} \rangle^+ - \lambda \langle \hat{S} \rangle^- \quad (7.91)$$

$$B_{\text{mf}}^- = \xi \langle \hat{S} \rangle^- - \lambda \langle \hat{S} \rangle^+, \quad (7.92)$$

where the quantity ξ parameterises the strength of the mean field from the same sub-lattice. If we now repeat the derivation of the Néel temperature in section 7.6.2, we now obtain the following expression:

$$T_{\text{N}} = -\frac{\mu_{\text{B}} g_e S(S+1)(\lambda + \xi)}{3k}. \quad (7.93)$$

If the field parameter ξ is positive the Néel temperature is lower than predicted by the previous expression in equation 7.81. If we recalculate the magnetic susceptibility in the paramagnetic regime according to section 7.6.3, we obtain the Curie–Weiss expression in Equation 7.90, but with a different expression for the Weiss constant:

$$\Theta = \frac{\mu_{\text{B}} g_e S(S+1)(\lambda - \xi)}{3k}, \quad (7.94)$$

which for positive ξ has a lower value than predicted by Equation 7.82. Therefore this formulation of the mean-field theory predicts that $|\Theta| \geq T_{\text{N}}$, with the equality only being observed when $\xi = 0$.

We emphasize again that the Néel temperature and Weiss constant are distinct quantities that measure fundamentally different aspects of the bulk magnetic properties of the material. The former is measured from the experimental magnetic susceptibility data at temperatures in the vicinity of which we observe the onset of magnetic ordering. Therefore T_{N} is the temperature below which we see antiferromagnetic behaviour, and above which we are in the paramagnetic regime. On the other hand the Weiss constant parameterizes the magnetic susceptibility in the paramagnetic regime at temperatures above T_{N} , and so in principle is independent of the lower-temperature regime where we observe magnetic ordering. As we will see in section 7.7, the paramagnetic shielding tensor is also parameterized by the Weiss constant.

In materials such as the metal oxides where $|\Theta| \geq T_{\text{N}}$ the temperature at which we acquire NMR data may be larger than the Néel temperature, but lower than the magnitude of the Weiss constant, i.e. $T_{\text{N}} < T < |\Theta|$. For example this is the case for FeO where $T_{\text{N}} = 116$ K and $\Theta = -610$ K, and thus considerable residual (antiferromagnetic) interactions persist at typical operating temperatures of around 300 K [187]. In this case

the material is in the paramagnetic regime as we are above the Néel temperature and there is no magnetic ordering. A classic example where $T_N \ll |\Theta|$ occurs is in frustrated magnets. In the conceptually simplest example of these materials, the triangular lattice, three sublattices are coupled antiferromagnetically, and thus no simple ordering scheme exists. The extent of residual magnetic couplings at room temperature is determined by the strength of the antiferromagnetic couplings, but long range magnetic ordering may not occur until temperatures much below $|\Theta|$, if at all in the case of spin-glasses.

For completeness, we note that ferrimagnets are materials with two or more magnetic sublattices that are coupled antiferromagnetically (i.e., Θ is negative) but because the magnetic moments of the two sublattices are not equal, ferromagnetism is observed below T_N .

7.6.5 The magnetic susceptibility in terms of the isotropic exchange coupling

So far we have examined the magnetic properties of paramagnetic solid insulator materials by employing a phenomenological approach using mean-field theory. We now round off this section by linking this model to the explicit exchange interactions between the magnetic ions and deriving the expression linking the Weiss constant to the exchange coupling constants for transition-metal ions. We focus on the isotropic exchange interactions as these dominate the effects of anisotropic exchange in determining the magnetic properties of these materials.

We start by writing the total Hamiltonian \hat{H} in Equation 7.59 with the isotropic exchange interaction terms written with irreducible spherical tensors:

$$\hat{H} = \mu_B g_e \sum_A \mathbf{B}_0 \cdot \hat{\mathbf{S}}^{(A)} + \sum_{A,B \neq A} J_{00}^{(AB)}(11) \hat{T}_{00}^{(AB)}(11). \quad (7.95)$$

The second term describes all the exchange interactions, and comprises a sum of terms, each of which is the product of an electronic spin part $\hat{T}_{00}^{(AB)}(11)$ and a spatial part $J_{00}^{(AB)}(11)$. The former is the direct-product irreducible spherical tensor operator of two one-spin operators $\hat{S}_{1q_1}^{(A)}$ and $\hat{S}_{1q_2}^{(B)}$, and is written as

$$\hat{T}_{00}^{(AB)}(11) = -\sqrt{\frac{1}{3}} \hat{\mathbf{S}}^{(A)} \cdot \hat{\mathbf{S}}^{(B)}. \quad (7.96)$$

The rank-zero spatial tensor of the exchange interaction is written in terms of the isotropic exchange coupling

constant $-2\mathcal{J}^{(AB)}$ as follows

$$J_{00}^{(AB)}(11) = 2\sqrt{3}\mathcal{J}^{(AB)}, \quad (7.97)$$

where we have retained the factor of two as before. Note that we are restricting the discussion to the isotropic exchange interaction. A central assumption of mean-field theory is that each ion experiences exactly the same mean molecular magnetic field. The same assumption is made here, and is equivalent to assuming that all the ions are of the same species, and that the network of exchange interactions experienced by a particular ion A is the same for all the other ions in the lattice (or sub-lattice in the case of antiferromagnetic materials). Therefore the magnetic susceptibility tensor calculated for ion A , χ_{ij} , corresponds to the total susceptibility tensor per metal ion for the whole material.

The magnetic susceptibility tensor per ion can be calculated to second order in $1/(kT)$ from the EPR formalism. Following a similar calculation in appendix E, and after much algebraic manipulation, the expression is

$$\chi_{ij} = \mu_0\mu_B^2 \left[\frac{\beta}{\omega} \sum_B \sum_{qq'} (-1)^{q+q'} g_{1q,i}^{(A)} g_{1q',j}^{(B)} \text{Tr}_S \left(\hat{S}_{1-q}^{(A)} \hat{S}_{1-q'}^{(B)} \right) - \frac{\beta^2}{\omega} \sum_B \sum_{\Gamma>\Delta} \sum_{qq'} (-1)^{q+q'} g_{1q,i}^{(A)} g_{1q',j}^{(B)} J_{00}^{(\Gamma\Delta)}(11) \text{Tr}_S \left(\hat{S}_{1-q}^{(A)} \hat{S}_{1-q'}^{(B)} \hat{T}_{00}^{(\Gamma\Delta)}(11) \right) \right], \quad (7.98)$$

where we have only retained the Zeeman terms with a rank one spin operator, we have written the g -tensor components of ion A $g_{1q,i}^{(A)}$ in their most general form, and ω is the total number of electronic spin states. The trace Tr_S is a sum over all the states of the entire extended spin system. This expression can be simplified after the tedious task of computing the two traces, following the calculations presented in appendix E. The first-order term in the susceptibility $\chi_{ij}^{(1)}$ is given by:

$$\chi_{ij}^{(1)} = \frac{\mu_0\mu_B^2}{kT} \frac{1}{\omega} \sum_B \sum_{qq'} (-1)^{q+q'} g_{1q,i}^{(A)} g_{1q',j}^{(B)} \text{Tr}_S \left(\hat{S}_{1-q}^{(A)} \hat{S}_{1-q'}^{(B)} \right) \quad (7.99)$$

$$= \frac{\mu_0\mu_B^2}{3kT} \sum_B \sum_{qq'} (-1)^{q+q'} g_{1q,i}^{(A)} g_{1q',j}^{(B)} \langle S^{(A)} || \hat{S}_1^{(A)} || S^{(A)} \rangle^2 \delta_{q-q'} \delta_{AB} \quad (7.100)$$

$$= \frac{\mu_0\mu_B^2}{3kT} \sum_q (-1)^q g_{1q,i}^{(A)} g_{1-q,j}^{(A)} \langle S^{(A)} || \hat{S}_1^{(A)} || S^{(A)} \rangle^2, \quad (7.101)$$

where the reduced matrix element of $\hat{S}_1^{(A)}$ is evaluated in the basis functions of ion A . As a result of the

mean-field approximation, all the ions are of the same type and therefore have the same spin S , and all the reduced matrix elements are equal to $\sqrt{S(S+1)}$. The second-order susceptibility term $\chi_{ij}^{(2)}$ is more complicated, and is equal to

$$\chi_{ij}^{(2)} = -\frac{\mu_0\mu_B^2}{(kT)^2} \frac{1}{\omega} \sum_B \sum_{\Gamma>\Delta} \sum_{qq'} (-1)^{q+q'} g_{1q,i}^{(A)} g_{1q',j}^{(B)} J_{00}^{(\Gamma\Delta)}(11) \text{Tr}_S \left(\hat{S}_{1-q}^{(A)} \hat{S}_{1-q'}^{(B)} \hat{T}_{00}^{(\Gamma\Delta)}(11) \right) \quad (7.102)$$

$$= -\frac{\mu_0\mu_B^2}{9(kT)^2} \sum_{B\neq A} \sum_{\Gamma>\Delta} \sum_{qq'} g_{1q,i}^{(A)} g_{1q',j}^{(B)} J_{00}^{(\Gamma\Delta)}(11) \langle S^{(A)} \parallel \hat{S}_1^{(A)} \parallel S^{(A)} \rangle^2 \langle S^{(B)} \parallel \hat{S}_1^{(B)} \parallel S^{(B)} \rangle^2 \\ \times \begin{pmatrix} 1 & 1 & 0 \\ q & q' & 0 \end{pmatrix} \delta_{\Gamma A} \delta_{\Delta B} \quad (7.103)$$

$$= -\frac{\mu_0\mu_B^2}{9(kT)^2} \sum_{B\neq A} \sum_{qq'} g_{1q,i}^{(A)} g_{1q',j}^{(B)} J_{00}^{(AB)}(11) \langle S^{(A)} \parallel \hat{S}_1^{(A)} \parallel S^{(A)} \rangle^2 \langle S^{(B)} \parallel \hat{S}_1^{(B)} \parallel S^{(B)} \rangle^2 \\ \times \frac{(-1)^{1-q} \delta_{q-q'}}{\sqrt{3}} \quad (7.104)$$

$$= \frac{\mu_0\mu_B^2}{9\sqrt{3}(kT)^2} \langle S^{(A)} \parallel \hat{S}_1^{(A)} \parallel S^{(A)} \rangle^2 \sum_{B\neq A} \langle S^{(B)} \parallel \hat{S}_1^{(B)} \parallel S^{(B)} \rangle^2 J_{00}^{(AB)}(11) \sum_q (-1)^q g_{1q,i}^{(A)} g_{1-q,j}^{(B)}. \quad (7.105)$$

We now acknowledge that we are assuming that the transition-metal ions have a spin-only ground state, and write the g -factors for each ion $g_{1q,i}^{(A)}$ in terms of g_e :

$$\mathbf{g}_{1\pm 1}^{(A)} = \mp \sqrt{\frac{1}{2}} g_e \begin{pmatrix} 1 \\ \pm i \\ 0 \end{pmatrix}, \quad \mathbf{g}_{10}^{(A)} = g_e \begin{pmatrix} 0 \\ 0 \\ 1 \end{pmatrix}. \quad (7.106)$$

The sum of the product of g -factors that occurs in the expressions for both the first- and second-order susceptibility tensors then takes the simple form:

$$\sum_q (-1)^q g_{1q,i}^{(A)} g_{1-q,j}^{(B)} = g_e^2 \delta_{ij}. \quad (7.107)$$

We note that, as a consequence of both the Zeeman and exchange interactions being spatially isotropic, the

susceptibility χ is also isotropic. The final expression is

$$\chi = \chi^{(1)} + \chi^{(2)} \quad (7.108)$$

$$= \frac{\mu_0 \mu_B^2 g_e^2 S(S+1)}{3kT} + \frac{2\mu_0 \mu_B^2 g_e^2 S^2(S+1)^2}{9(kT)^2} \sum_{B \neq A} \mathcal{J}^{(AB)}. \quad (7.109)$$

The first-order term is independent of the exchange coupling constants, and is equal to the expression we derived previously for a system of non-interacting transition-metal ions. The exchange interactions only contribute to the susceptibility to second order, with this term being proportional to the sum of the exchange coupling constants describing the couplings to a particular ion [184]. For ferromagnetic ordering all the coupling constants are positive, and the second-order susceptibility is positive. On the other hand, if we assume that the nearest-neighbour exchange couplings are dominant, then antiferromagnetic ordering results in a sum of coupling constants that is negative, and the second-order susceptibility is also negative. If there are no exchange couplings this term is zero, as we have also seen previously for non-interacting metal ions.

Now we need to establish the connection between Equation 7.109 and the susceptibility from the mean-field model in Equation 7.90. The former is written as a Taylor series in $1/(kT)$, so to facilitate the comparison we also expand the latter as a Taylor series giving

$$\chi = \frac{\mu_0 \mu_B^2 g_e^2 S(S+1)}{3kT} + \frac{\mu_0 \mu_B^2 g_e^2 S(S+1)}{3kT^2} \Theta. \quad (7.110)$$

The first term in Equation 7.110 is equal to the susceptibility from an ensemble of non-interacting metal ions, as for Equation 7.109. The second term depends on the Weiss constant, which contains all the information about the exchange interactions, in the same way that only the second term of Equation 7.109 depends on the exchange coupling constants. If we equate the two we obtain an expression for the Weiss constant in terms of the sum of exchange coupling constants [184]:

$$\Theta = \frac{2S(S+1)}{3k} \sum_{\beta \neq \alpha} \mathcal{J}^{(AB)}. \quad (7.111)$$

Considering only the nearest-neighbour interactions, we can make a similar observation to before: ferromagnetic order is characterised by positive nearest-neighbour exchange constants, and therefore a positive Weiss constant, whilst antiferromagnetic ordering is characterised by negative exchange coupling constants, and

therefore a negative Weiss constant.

7.7 The paramagnetic shielding tensor in solid insulator materials

Equation 7.53 is a general expression for the paramagnetic shielding tensor in either a system containing a cluster of transition-metal ions, or a solid insulator, and includes the effects of anisotropic exchange, g -anisotropy, and the ZFS interaction. Many solid systems, such as battery materials, can be approximated by a simpler formula which neglects SO coupling, and in which the dependence on the isotropic exchange coupling constants is replaced by a Curie–Weiss temperature dependence [5, 53, 54]. The link between this model and Equation 7.53 is now examined in detail. As for the magnetic susceptibility the isotropic exchange interactions, rather than anisotropic exchange, dominate the form of the paramagnetic shielding tensor, and so we focus exclusively on the former interactions.

7.7.1 The Curie–Weiss expression for the paramagnetic shielding tensor

In the spin-only limit we replace the g -tensor with the free-electron g -factor, and remove both any SO coupling contributions to the ZFS tensor, and the DM part of the exchange coupling constants. In addition we will also ignore the NR parts of the ZFS and the anisotropic exchange interaction, which are due to dipolar couplings between the electrons and are expected to be small. The paramagnetic shielding tensor in a solid insulator containing only spin-only transition-metal ions of the same species is now given by a simplified form of Equation 7.53:

$$\sigma^S = -\frac{\mu_B g_e S(S+1)}{3\hbar\gamma_I kT} \sum_A \mathbf{A}^{(A)} - \frac{2\mu_B g_e S^2(S+1)^2}{9\hbar\gamma_I (kT)^2} \sum_A \sum_{B \neq A} \mathcal{J}^{(AB)} \mathbf{A}^{(B)}. \quad (7.112)$$

So far we have made no assumptions about the exchange coupling constants. However in order to make the link with the Curie–Weiss law we need to introduce a mean-field approximation. As we have already seen this equates to stating that the network of exchange couplings experienced by any one metal ion is the same as for all metal ions. This means that in the second term of Equation 7.112, the sum over the exchange coupling

constants is independent of one of the indices, and we can partition the double sum as follows:

$$\sum_A \sum_{B \neq A} \mathcal{J}^{(AB)} \mathbf{A}^{(B)} = \sum_{B \neq A} \mathcal{J}^{(AB)} \sum_{\Gamma} \mathbf{A}^{(\Gamma)}, \quad (7.113)$$

where we have labelled the index in the sum of the hyperfine coupling constants as Γ to emphasise the separation from the sum over B . We can also simplify the sum over the hyperfine coupling tensors further. We have already seen that for each metal ion the hyperfine coupling tensor $\mathbf{A}^{(A)}$ that we include in the expression for the paramagnetic shielding as derived from the EPR formalism represents the coupling per electron. This is because the different electrons reside in different orbitals, each of which may couple differently to the nuclear spin. However, at this point, it proves convenient to write the shielding tensor in terms of the total hyperfine coupling constant \mathcal{A} , due to *all* the electrons in *all* the metal ions that couple to the nucleus:

$$\mathcal{A} = 2S \sum_A \mathbf{A}^{(A)}. \quad (7.114)$$

With these two simplifications the paramagnetic shielding tensor is now

$$\sigma^S = -\frac{\mu_B g_e (S+1)}{6\hbar\gamma_I kT} \mathcal{A} - \frac{\mu_B g_e S(S+1)^2}{9\hbar\gamma_I (kT)^2} \sum_{B \neq A} \mathcal{J}^{(AB)} \mathcal{A}. \quad (7.115)$$

We can also write down a phenomenological form of the shielding tensor. We have seen that the magnetic susceptibility per metal ion of an ensemble of spin-only transition-metal ions, as given in Equation 7.90, has a Curie–Weiss temperature dependence, and since the shielding is proportional to the susceptibility, we expect the shielding tensor to have the form

$$\sigma^S = -\frac{\mu_B g_e S(S+1)}{3\hbar\gamma_I k(T-\Theta)} \sum_A \mathbf{A}^{(A)} \quad (7.116)$$

$$= -\frac{\mu_B g_e (S+1)}{6\hbar\gamma_I k(T-\Theta)} \mathcal{A}. \quad (7.117)$$

Expanding Equation 7.117 as a Taylor series in $1/(kT)$, and equating terms of order $1/(kT)^2$ as we did for the magnetic susceptibility, we obtain the same expression for the Weiss constant as we calculated in Equation 7.111. This establishes the Curie–Weiss temperature dependence of the paramagnetic shift at temperatures above $|\Theta|$ that is often assumed in the calculation and interpretation of the paramagnetic shifts of solid

insulating materials [53, 236].

7.7.2 The scaling factor

In section 3.4 we introduced the idea of Kim et al. [53] that the paramagnetic shielding tensor can be thought of as a quantity that is calculated with all the effective electronic spins aligned with ferromagnetic ordering, and then scaled down into the paramagnetic regime by a factor that accounts for the thermal occupation of the excited electronic spin states. The quantity that is averaged is

$$-\frac{\mathcal{A}}{2\hbar\gamma_I B_0}, \quad (7.118)$$

where \mathcal{A} is the total hyperfine coupling tensor calculated in the ferromagnetic regime from the electron density of *all* the unpaired electrons from *all* the paramagnetic centres coupled to the nucleus. This expression is the same as the one quoted in section 3.4 for non-interacting metal ions, and we again note that the ferromagnetic phase of the material in which the calculation of \mathcal{A} is performed need not necessarily represent the ground state.

The factor which scales this quantity to give the paramagnetic shielding tensor is the ratio of the Curie spins in the paramagnetic and saturated (i.e. spin-aligned) regimes. The saturated Curie spin $\langle \hat{S}_z \rangle_{\text{sat}}$ is simply $-S$, as before, and the paramagnetic Curie spin is given by Equation 7.87, and contains the Curie–Weiss temperature dependence. The scaling factor is therefore

$$\frac{\langle \hat{S}_z \rangle_{\text{para}}}{\langle \hat{S}_z \rangle_{\text{sat}}} = \frac{\Theta B_0}{S \lambda (T - \Theta)} \quad (7.119)$$

$$= \frac{\mu_B g_e (S + 1) B_0}{3k(T - \Theta)} \quad (7.120)$$

$$= \frac{\chi B_0}{\mu_0 \mu_B g_e S}, \quad (7.121)$$

and has been written in terms of both the local parameters, and the bulk magnetic susceptibility. To go to the second line we have used the expression for the Weiss constant in terms of the mean-field parameter λ as

given in Equation 7.82. The scaled paramagnetic shielding tensor is therefore

$$\sigma^S = -\frac{\mathcal{A}}{2\hbar\gamma_I B_0} \frac{\langle \hat{S}_z \rangle_{\text{para}}}{\langle \hat{S}_z \rangle_{\text{sat}}} \quad (7.122)$$

$$= -\frac{\chi}{2\mu_0\mu_B g_e \hbar\gamma_I S} \mathcal{A} \quad (7.123)$$

$$= -\frac{\mu_B g_e (S + 1)}{6\hbar\gamma_I k(T - \Theta)} \mathcal{A}. \quad (7.124)$$

These expressions open up two possibilities for calculating paramagnetic shifts in the solid state. In both cases the hyperfine coupling tensor can be calculated using either quantum chemistry or DFT methods [53, 210, 237]. The scaling factor can then be calculated either from (1) the experimental magnetic susceptibility or the experimental Weiss constant [53], which have been determined independently from the NMR measurement, or (2) the computed values of the exchange couplings from which a Weiss constant can be calculated.

If SO coupling effects need to be considered, we can employ an alternative form of the scaling factor, as shown in the absence of magnetic ordering in section 4.4. Here the scaling factor is given by the ratio of the paramagnetic and saturation electronic magnetic moments, in terms of an empirical effective magnetic moment μ_{eff} :

$$\frac{\langle \hat{m}_z \rangle_{\text{para}}}{\langle \hat{m}_z \rangle_{\text{sat}}} = \frac{\mu_{\text{eff}}^2 B_0}{3\mu_B g_e S k(T - \Theta)}. \quad (7.125)$$

The paramagnetic shielding tensor is then:

$$\sigma^S = -\frac{\mu_{\text{eff}}^2}{3\mu_B g_e \hbar\gamma_I k(T - \Theta)} \mathcal{A}. \quad (7.126)$$

This is the same as Equation 4.201, except with the inclusion of the Weiss constant. As discussed in section 4.4 this form of the shielding tensor is approximate, as it neglects SO coupling effects in the hyperfine tensor and does not account for magnetic anisotropy, which gives rise to the PCS. However it has been successfully used to calculate contact shifts due to first-row *d*-block ions for a range of solid battery electrode materials [30, 54–56].

7.7.3 A word of caution

In the light of the discussion in section 7.7.2, and the Curie–Weiss temperature dependence of the paramagnetic chemical shielding tensor, there is the very attractive prospect of determining the Weiss constant experimentally from the measured temperature dependence of either the isotropic shift or the SA. For example, at temperatures above $|\Theta|$, the isotropic paramagnetic shift δ_{iso}^S has the dependence

$$\delta_{\text{iso}}^S = \frac{\kappa}{T - \Theta}, \quad (7.127)$$

where the constant κ is equal to

$$\kappa = \frac{\mu_B g_e (S + 1)}{6\hbar\gamma_I k} \mathcal{A}^{\text{FC}}, \quad (7.128)$$

and \mathcal{A}^{FC} is the total Fermi-contact coupling constant. Equation 7.127 can be rearranged to give

$$\frac{1}{\delta_{\text{iso}}^S} = \frac{T}{\kappa} - \frac{\Theta}{\kappa}, \quad (7.129)$$

from which one would plot $1/\delta_{\text{iso}}^S$ versus T to obtain Θ from the y -intercept, and then relate this to the exchange coupling constants. However there are a number of problems with this approach. The first is that the temperature range over which NMR data can be acquired is generally limited either by the available hardware, or the nature of the material, which may undergo a structural phase transition above or below a certain temperature, or decompose. In such cases there will be a significant error introduced when extrapolating the line in Equation 7.129 back to $T = 0$ K to obtain the intercept, and in some cases the errors will be sufficiently large that even the sign of Θ cannot be obtained. This problem is exacerbated for large Weiss constants when we note that Equation 7.129 is only valid at temperatures above $|\Theta|$. In practice, this problem can be overcome by taking the susceptibility measured at the temperature of the NMR experiment and using this to calculate the scaling factor.

The second, and more fundamental, problem is that Equation 7.127 is only valid for spin-only transition-metal ions. For metal ions with SO coupling, the resulting g -anisotropy and ZFS splitting tensor combine to give a contribution that varies as $1/(kT)^2$ in addition to the contribution from the exchange couplings, as seen in Equation 7.53. The measured Weiss constant is then a function not only of the exchange coupling constants, but also of the g - and ZFS tensors, and the different contributions cannot be separated without

further experimental or computational data.

7.7.4 The magnetic susceptibility and paramagnetic shielding tensors in solid materials with more than one species of paramagnetic metal ion

The previous discussion in sections 7.6.3, and 7.7.1–7.7.3 focussed on solid materials with only one species of transition-metal ion, and neglected the effects of SO coupling. We lift the first assumption here, and delay the discussion of SO coupling effects to section 7.10.

The presence of only one species of transition-metal ion in the material allows us to relate the bulk magnetic properties, such as the magnetic susceptibility and Weiss constant, to the local paramagnetic shielding in a straightforward manner. This is because each metal ion has the same local magnetic properties, which are equal to the average of those of the ensemble. If the material contains more than one species of transition-metal ion this assertion is no longer true, as the average of the bulk properties fails to distinguish the differences between the ions. It therefore appears that we can no longer use the bulk magnetic properties to calculate the shielding tensor. However we show here that a simple modification of the discussion of the scaling factor does indeed allow us to do this with no significant difficulty.

The trick is to break the material up into interpenetrating sub-lattices, each one of which contains a single species of metal ion. For example a material containing two species of metal ion 1 and 2 can be separated into two sub-lattices, which contain exclusively ions of type 1 and type 2 respectively. We note that this treatment is analogous to that used in the Weiss model of antiferromagnetism, where the two sub-lattices contained metal ions with spin-up and spin-down electron spins. In the present case we can associate a magnetic susceptibility per ion $\chi^{(A)}$ with the sub-lattice with metal ions A . The sum of these sub-lattice susceptibilities gives the *total* magnetic susceptibility per ion χ :

$$\chi = \frac{1}{N} \sum_A \chi^{(A)}, \quad (7.130)$$

where N is the number of distinct species of metal ion in the material. Each metal ion species has electronic spin $S^{(A)}$, and can also be associated with its own Weiss constant $\Theta^{(A)}$, which describes the exchange interactions associated with ion A , which are assumed to be the same as for all ions of species A . In the spin-only

approximation this allows us to write $\chi^{(A)}$ as

$$\chi^{(A)} = \frac{\mu_0 \mu_B^2 g_e^2 S^{(A)} (S^{(A)} + 1)}{3k(T - \Theta^{(A)})}, \quad (7.131)$$

where the corresponding Weiss constant is

$$\Theta^{(A)} = \frac{2S^{(A)} (S^{(A)} + 1)}{3k} \sum_{B \neq A} \mathcal{J}^{(AB)}. \quad (7.132)$$

The exchange coupling constants in the expression for the Weiss constant of ion A in Equation 7.132 describe both the couplings within the sub-lattice A , and also between each ion A and the metal ions in the other sub-lattices.

The total paramagnetic shielding tensor of a particular nuclear spin σ^S can be written as the sum of the contributions $\sigma^{S,(A)}$ from the metal ions from all the sub-lattices:

$$\sigma^S = \sum_A \sigma^{S,(A)}. \quad (7.133)$$

In general each contribution $\sigma^{S,(A)}$ from a sub-lattice A contains the hyperfine interactions from all the ions in that sub-lattice. We now see that relating the bulk magnetic properties to the shielding tensor is actually straightforward. We simply scale the hyperfine tensors $\mathcal{A}^{(A)}$ from each sub-lattice separately according to either Equation 7.120 or 7.121, using the susceptibility and Weiss constants pertaining to the relevant sub-lattice. The sub-lattice contributions to the shielding tensor $\sigma^{S,(A)}$ are then given by:

$$\sigma^{S,(A)} = - \frac{\mathcal{A}^{(A)} \langle \hat{S}_z^{(A)} \rangle_{\text{para}}}{2\hbar\gamma_I B_0 \langle \hat{S}_z^{(A)} \rangle_{\text{sat}}} \quad (7.134)$$

$$= - \frac{\chi^{(A)}}{2\mu_0 \mu_B g_e \hbar \gamma_I S} \mathcal{A}^{(A)} \quad (7.135)$$

$$= - \frac{\mu_B g_e (S^{(A)} + 1)}{6\hbar\gamma_I k (T - \Theta^{(A)})} \mathcal{A}^{(A)}. \quad (7.136)$$

This process is of particular importance for studying mixed transition-metal ion materials, or materials containing metal ions of mixed valency.

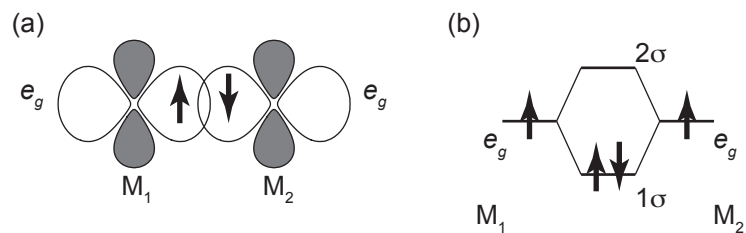


Figure 7.5: Illustration of the direct isotropic exchange interaction between two paramagnetic metal ions at low temperature. One example is given, which shows the exchange that results from σ -overlap between two e_g orbitals of metal ions M_1 and M_2 , each one of which contains an unpaired electron, as is shown in (a). The overlap between both atomic orbitals gives a bonding molecular orbital 1σ , and an anti-bonding molecular orbital 2σ , as shown in (b). It can be seen that the two electrons are paired in the 1σ orbital, leaving the 2σ vacant. The electron pairing results in an overall spin of $S = 0$, and hence antiferromagnetic alignment.

7.8 Types of isotropic exchange interaction

In the discussion of the magnetic exchange interactions and their effect on the susceptibility and paramagnetic shielding tensors we have hitherto avoided a detailed discussion of the physical nature of the interactions. We turn to this topic now.

7.8.1 Direct exchange

The first mechanism involves the direct interaction between unpaired electrons of neighbouring metal ions, and is known as direct exchange. The interaction is due to the overlap of the atomic orbitals of the two ions, an example of which is shown in Figure 7.5 (a). Here the two metal ions M_1 and M_2 each possess a half-occupied orbital of e_g symmetry, which overlap to form molecular orbitals of σ symmetry. The resulting alignment of the two unpaired electrons at low temperature, i.e. below the magnetic ordering temperature T_C or T_N , can be understood by employing the linear combination of atomic orbitals (LCAO) model. This is the foundation of the Goodenough–Kanamori rules, which allow the prediction of the sign of the exchange coupling constant [238–240]. In this case the LCAO model predicts the formation of two molecular orbitals, which are the 1σ bonding and 2σ anti-bonding orbitals. As shown in Figure 7.5 (b) the energy of the 1σ lies below that of the two e_g atomic orbitals, while the energy of the 2σ lies above. Therefore the two unpaired electrons both occupy the lower-energy 1σ orbital, with configuration $1\sigma^2$, and must do so with paired spins to satisfy the Pauli principle. This results in the $S = 0$ spin state having the lower energy, and the electrons are

aligned antiferromagnetically. We note that the $S = 1$ spin state can only be reached with the higher-energy electronic configuration of $1\sigma^1 2\sigma^1$, where occupancy of the anti-bonding orbital causes the bond to break.

Although the direct interaction is the most obvious exchange mechanism, it is not the most prevalent, due to the difficulty of obtaining sufficient overlap between the metal orbitals. For example direct exchange is unlikely to be effective between lanthanide ions, since the contracted nature of the $4f$ orbitals means that there is negligible overlap over typical atomic spacings. For d -transition metals the d -orbitals extend further from the nucleus, and so direct overlap is more common particularly for the less radially-contracted $3d$ ions on the left-hand side of the $3d$ series, and the larger $4d$ and $5d$ ions. However other exchange mechanisms are generally more important in determining the magnetic properties of d -transition-metal materials.

7.8.2 Superexchange

Many ionic solid materials, such as metal oxides, exhibit magnetic ordering at low temperatures even though there is no direct overlap between the metal-ion orbitals. In these cases the exchange interaction is indirect, and occurs via an intermediate bridging anion, such as O^{2-} . This mechanism, which is clearly longer range than direct exchange, is referred to as superexchange. The superexchange mechanism is dominated by the overlap of the two metal orbitals with the orbitals of the bridging anion, and may be ferro- or antiferromagnetic depending on the exact nature of the overlap. An example of each is shown in Figure 7.6. In Figure 7.6 (a) is shown the orbital overlap that occurs when the metal ions M_1 and M_2 and O^{2-} ion are arranged as M_1-O-M_2 with a bridging angle of 180° . The two half-filled metal e_g orbitals both overlap with the filled oxygen $2p_\sigma$ orbital to give three molecular orbitals of σ symmetry, labelled 1σ , 2σ , and 3σ , as shown in Figure 7.6 (b). The four electrons fill the 1σ and 2σ orbitals as two pairs, giving a configuration of $1\sigma^2 2\sigma^2$ with $S = 0$. This superexchange interaction is therefore antiferromagnetic.

A different result arises in the situation shown in Figure 7.6 (c) where the M_1-O-M_2 bridging angle is 90° . In this case an unfilled t_{2g} orbital of each metal ions overlaps with a different filled oxygen $2p_\pi$ orbital. Therefore the orbitals formed by M_1-O overlap are orthogonal to those formed by M_2-O overlap. The resulting molecular orbitals are shown in Figure 7.6 (d), and comprise a doubly-degenerate 1π bonding level, and a doubly-degenerate 2π anti-bonding level. The low-temperature electronic configuration of the six electrons is $1\pi^4 2\pi^2$, i.e. the two 1π orbitals are filled with two pairs of electrons, with the remaining two electrons in the 2π orbitals. The lowest-energy arrangement of these latter two electrons is that they

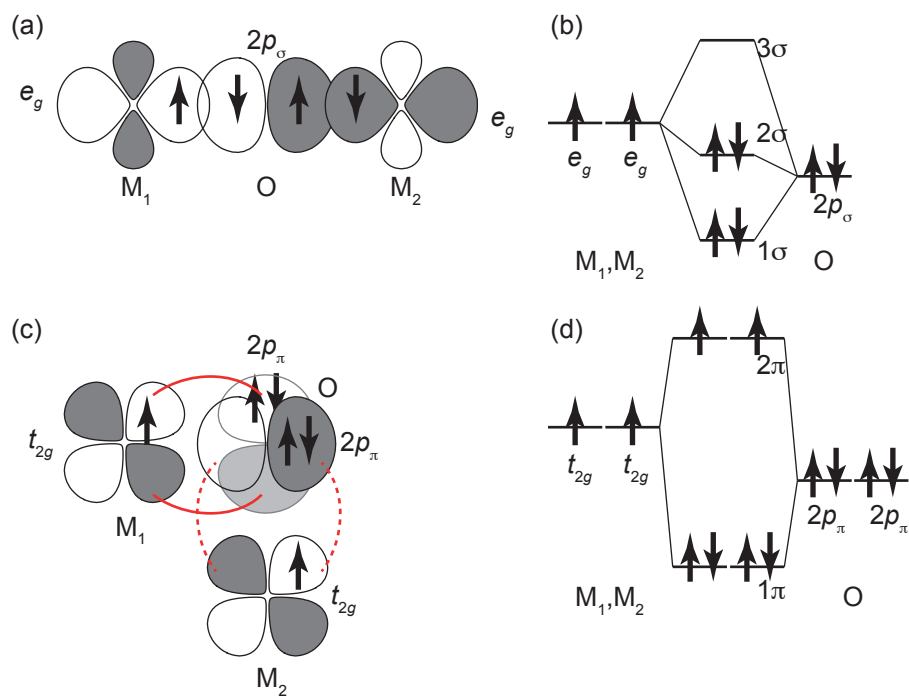


Figure 7.6: Illustration of the indirect isotropic superexchange interaction between two paramagnetic metal ions via a bridging anion at low temperature. Two examples are given which show the superexchange that results from the overlap between the atomic orbitals of two metal ions M_1 and M_2 , each one of which contains an unpaired electron, and the filled $2p$ orbitals of a bridging O^{2-} anion. In the first example, shown in (a) two metal e_g orbitals interact with one filled oxygen $2p_\sigma$ orbital with a 180° bridging angle to give molecular orbitals of σ symmetry. Three such orbitals are formed, labelled 1σ , 2σ , and 3σ , as shown in (b). The four electrons occupy the bonding 1σ and 2σ orbitals in pairs, leaving the anti-bonding 3σ orbital vacant. The total spin is $S = 0$, and hence the interaction is antiferromagnetic. A different example is shown in (c) and (d), in which the bridging angle is 90° , and involving two orthogonal atomic orbitals of the bridging oxygen. The t_{2g} orbitals of M_1 and M_2 each overlap with a different oxygen $2p_\pi$ orbital, resulting in two separate π interactions as shown in (c). The energy levels are shown in (d), from which can be seen that a pair of degenerate 1π bonding orbitals and a pair of degenerate 2π anti-bonding orbitals are formed. Four of the six electrons fill the two 1π as two pairs, with the remaining two occupying the 2π . According to Hund's first rule these latter two electrons occupy different 2π orbitals with parallel spins, thus giving ferromagnetic alignment with $S = 1$.

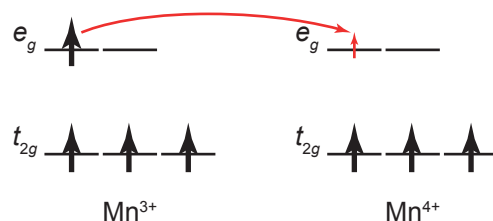


Figure 7.7: Illustration of the indirect isotropic double-exchange interaction between two paramagnetic metal ions of different valency. The two interacting ions are the Mn^{3+} and Mn^{4+} cations in octahedral coordination environments, and with electronic configurations of $t_{2g}^3 e_g^1$ and t_{2g}^3 respectively. The single e_g electron on the Mn^{3+} ion undergoes hopping to a vacant e_g orbital of Mn^{4+} as shown by the red arrow. This hopping occurs without a change in electron polarization, and so is energetically most favourable when the electrons of Mn^{3+} are spin-aligned so they are parallel to those of Mn^{4+} , according to Hund's first rule. The double-exchange interaction is therefore ferromagnetic.

occupy different 2π orbitals with parallel spins, according to Hund's first rule. The lowest-energy spin state is therefore $S = 1$ and the alignment is ferromagnetic. It is generally observed that the ferromagnetic superexchange interaction is weaker than antiferromagnetic superexchange. It is also worth noting that, in the second example in Figure 7.6 (c) and (d), direct overlap between the two metal t_{2g} orbitals may occur if the distance is sufficiently short, resulting in an antiferromagnetic direct exchange interaction in addition to the ferromagnetic superexchange interaction. This has been suggested to happen in Li_2MnO_3 , with direct exchange between the two Mn^{4+} ions proving to be the dominant interaction, resulting in antiferromagnetic alignment [241].

7.8.3 Double exchange

Some metal oxide materials contain metal ions which are present in more than one oxidation state and exhibit a ferromagnetic exchange interaction. This is due to the double exchange mechanism, which is illustrated in 7.7 for an interaction between Mn^{3+} and Mn^{4+} , which have free-ion electronic configurations of $3d^4$ and $3d^3$. In an octahedral ligand field the electronic configurations are $t_{2g}^3 e_g^1$ and t_{2g}^3 , and have effective spins of $S = 2$ and $S = 3/2$ due to Hund's first rule. In the double-exchange mechanism the e_g electron of the Mn^{3+} ion can hop into a vacant e_g orbital of the Mn^{4+} ion on a neighbouring site. This hopping electron does not undergo a change in spin polarization, and so this process is only energetically favourable if the polarization of this electron matches that of the t_{2g} electrons in the destination ion. This means that the Mn^{4+} t_{2g} electrons must

have the same polarization as the Mn^{3+} t_{2g} electrons, which in turn requires ferromagnetic alignment of the two metal ions.

Double exchange is also an important exchange mechanism in iron materials of mixed valency, i.e. containing Fe^{2+} ($3d^6$) and Fe^{3+} ($3d^5$).

7.8.4 Ruderman–Kittel–Kasuya–Yosida exchange

The final mechanism we consider here is Ruderman–Kittel–Kasuya–Yosida (RKKY) exchange, which is observed in metals. The interaction occurs between two localized effective electronic spins via the conduction electrons, hence it is an indirect exchange mechanism and may occur over long distances. It can be shown that the exchange constant varies with distance r as

$$\mathcal{J}^{(AB)} \propto \frac{\cos(2k_F r)}{r^3}, \quad (7.137)$$

i.e. the sign oscillates with distance, and so the interaction may be either ferro- or antiferromagnetic [187].

7.9 Predicting the Fermi-contact shift with the Goodenough–Kanamori rules

In solid-oxide materials the isotropic paramagnetic shift is usually dominated by electron transfer processes, and is therefore given by the Fermi-contact shift. Therefore we now examine the problem of interpreting and rationalizing the Fermi-contact shifts obtained in such materials. It turns out that we can use the Goodenough–Kanamori rules [238–240] to make simple predictions about the Fermi-contact shift which have proved to represent a practical and intuitive method with which to interpret the NMR spectra of, for example, a series of paramagnetic battery materials [5]. The concepts introduced in this section are therefore closely related to those for predicting the sign of the isotropic exchange coupling constants introduced in section 7.8.

The isotropic Fermi-contact shift can be determined from Equation 7.124 to be

$$\delta_{\text{iso}}^{\text{FC}} = \frac{\mu_B g_e (S + 1)}{6\hbar\gamma_I k(T - \Theta)} \mathcal{A}^{\text{FC}}, \quad (7.138)$$

where we have focussed on a single sub-lattice containing a single species of metal ion. However the ideas discussed here are easily generalized to materials containing more than one metal-ion species, and also to systems with no magnetic ordering, such as paramagnetic molecules in solution. The Fermi-contact shift is proportional to the Fermi-contact coupling constant, which is given by Equation 2.171 and reproduced below for convenience:

$$\mathcal{A}^{\text{FC}} = \frac{2\mu_0\mu_{\text{B}}g_e\hbar\gamma_I}{3}\rho^{\alpha-\beta}(\mathbf{0}). \quad (7.139)$$

Thus the Fermi-contact shift is proportional to, and has the same sign as, the unpaired electron density $\rho^{\alpha-\beta}(\mathbf{0})$ that is within the s -orbital of the nucleus. In general accurate values of $\rho^{\alpha-\beta}(\mathbf{0})$ require either quantum-chemical or DFT calculations. However it may be possible to determine and/or rationalise the sign of $\rho^{\alpha-\beta}(\mathbf{0})$, and hence the sign of the Fermi-contact shift, more simply by using the Goodenough–Kanamori rules [238–240]. The rules stem from the fact that, on the formation of a bonding interaction between two atoms, the atomic orbitals of compatible symmetry of the two atoms combine to form a molecule orbital, or ‘bond’. The electrons present in both atomic orbitals are now shared between the two atoms. In particular any unpaired electrons present on one atom become delocalised, or partially transferred, into the atomic orbitals of the second, and if the second orbital is an s -orbital this *delocalisation mechanism* results in a Fermi-contact shift. Alternatively the s -orbital may form a bond with an unoccupied metal orbital. If this metal orbital receives electron density as a result this density must be spin-aligned to any other unpaired electrons in other metal orbitals. This results in unpaired electron density with a well-defined polarization being transferred to the s -orbital. This *polarization mechanism* also results in a Fermi-contact shift. The essence of the Goodenough–Kanamori rules is that this electronic spin transfer occurs so that the total electronic spin angular momentum of the system is conserved.

An illustration of the use of the Goodenough–Kanamori rules to predict the sign of the Fermi-contact shift is given by three examples in Figure 7.8. Part (a) shows the simplest case, where a half-filled atomic orbital of a metal ion M overlaps with a vacant s -orbital on the atom X with the NMR-active nucleus. The single unpaired spin-up electron on M is shared between the two atoms with a certain proportion being delocalised into the vacant orbital of X. The transferred electron density must have the same spin polarisation as the original electron, and so is also spin up. The result is that the net spin density $\rho^{\alpha-\beta}(\mathbf{0})$ is positive, and hence the Fermi-contact shift is also positive. The second example, shown in (b), is the case where the half-filled

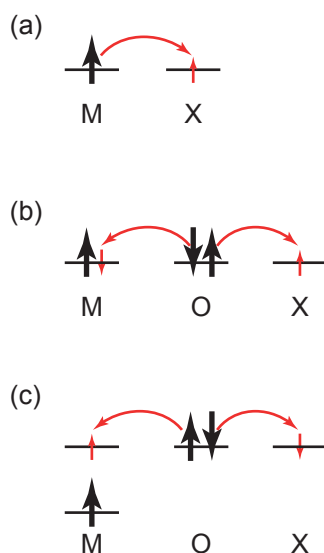


Figure 7.8: Schematic illustrating the transfer of unpaired-electron spin density between the orbitals of a transition-metal ion M and the vacant s -orbital of the NMR-active nucleus X, possibly via the filled orbital of a bridging atom O. The unpaired electrons formally present in each orbital are illustrated with black arrows. The transfer of polarisation is indicated with a curved red arrow, and the transferred spin is shown with a small red arrow. In (a) is shown the direct delocalisation of an unpaired electron on M to the vacant orbital on X. Both the unpaired electron and the transferred polarisation have the same ‘up’ polarisation, giving a positive spin density $\rho^{\alpha-\beta}(\mathbf{O})$ at X, and therefore a positive Fermi-contact shift. In (b) is shown the spin transfer that occurs when the M orbital, which contains a single spin-up electron, interacts with a vacant X-orbital via the filled orbital of the bridging atom O. There is transferred polarisation from the O-orbital of both the ‘up’ and ‘down’ electrons, with the latter being transferred to the M-orbital to satisfy the Pauli principle, and the former being transferred to X to give both a positive spin density and Fermi-contact shift. The situation in (c) is similar with the exception that the M-orbital that interacts with the filled O-orbital is unoccupied. The result is that the ‘up’ electron is transferred to the vacant M-orbital so as to satisfy Hund’s first rule and be spin-aligned with the unpaired electron in the lower-energy half-filled M-orbital. The ‘down’ electron is therefore transferred to X, giving a negative spin density at X, which results in a negative Fermi-contact shift. The situations in (a) and (b) are examples of unpaired-electron delocalization, and the situation in (c) is an example of unpaired-electron polarization.

M-orbital overlaps with the vacant s -orbital on X via a filled atomic orbital of a bridging atom, say oxygen O. In this case the delocalisation is a transfer of two electrons from the O atom, one to each of the other two atoms M and X. Since the unpaired electron already present on M is spin up, any additional electronic spin partially transferred from O must be of the opposite polarisation so as to satisfy the Pauli exclusion principle. The remaining spin-up electron on O is then partially transferred into the s -orbital of X, thus giving a net positive spin density at the nucleus and a positive Fermi-contact shift. In the final example (c) the M-orbital involved in the overlap with O and X is vacant, and the only electrons present in the molecular orbitals are the pair on O. The M-orbital that contains the spin-up unpaired electron, shown as having lower energy in (c), does not have compatible symmetry with either the O- or X-orbitals, and so does not participate directly in any covalent bonding. The unpaired electron density that is now transferred from O to the vacant M-orbital must have the same polarisation as the unpaired electron in the second M-orbital, i.e. spin-up, so as to satisfy the requirements of Hund's first rule, and therefore the electronic spin density transferred from O to X is spin down. This polarization mechanism results in a net negative spin density at the X nucleus, and therefore a negative Fermi-contact shift.

Figure 7.9 shows how the Goodenough–Kanamori rules are applied in practice using the solid lithium manganates as examples [5]. In these materials $M = \text{Mn}^{4+}$ has a $3d^3$ electronic configuration, which becomes t_{2g}^3 in octahedral coordination sites, i.e. the t_{2g} orbitals are each half filled, and the e_g are vacant. The O atom forms the bridge via the filled $2p$ orbitals, and X is the Li^+ ion which possesses a vacant $2s$ orbital into which is transferred the unpaired electron density. The metal–lithium interactions are formed by sets of $\text{Mn}^{4+}-\text{O}^{2-}-\text{Li}^+$ bonds, which are characterised by the angle subtended at the O atom. The signs of the Fermi-contact shifts can be rationalised easily in two special cases of bond geometry, namely when the bond angle is either 90° or 180° . Figure 7.9 (a) shows the overlap of the orbitals for a 90° bond angle. A half-filled t_{2g} orbital of Mn^{4+} is of the correct symmetry to overlap with one of the filled $2p_\pi$ orbitals of O to give a π -bond, which in turn overlaps with the vacant Li^+ $2s$ orbital. As discussed above and shown in Figure 7.8 (b), this form of overlap gives a positive Fermi-contact shift for both ^6Li and ^7Li . In addition, direct overlap between the t_{2g} and $2s$ orbitals is possible, which also results in a positive shift as shown in Figure 7.8 (a). In this bonding geometry the vacant e_g orbitals make no contribution as their symmetry properties result in there being no net overlap between them and the Li^+ $2s$, either directly or through any bridging O $2p$ orbital. By contrast a 180° bonding angle gives the overlap of orbitals shown in Figure 7.9 (b). In this case the $t_{2g}-2p_\pi$

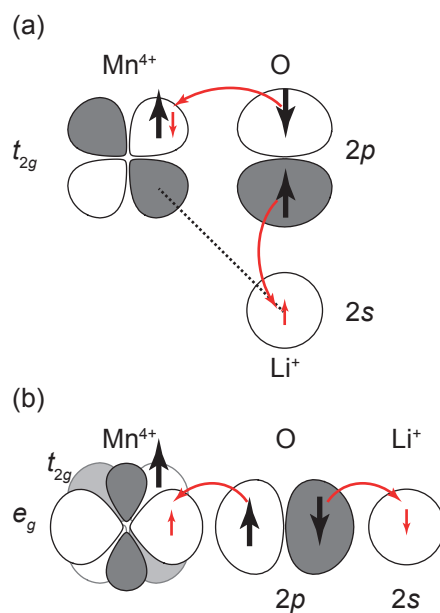


Figure 7.9: Illustration of the orbital overlap and electron spin transfer in an $\text{Mn}^{4+}\text{-O-Li}$ arrangement of ions in the solid lithium manganates, for 90° and 180° angles subtended at O [5]. The unpaired electrons formally present in each orbital are illustrated with black arrows. The transfer of polarisation is indicated with a curved red arrow, and the transferred spin is shown with a small red arrow. In (a) is shown the orbital overlap that occurs in a $\text{Mn}^{4+}\text{-O-Li}$ link with a 90° angle. Both direct overlap between the M t_{2g} and the Li^+ $2s$ orbitals, indicated by the dashed line, and overlap via the filled bridging O $2p$ orbitals are possible, both of which result in a positive Fermi-contact shift via electron delocalization as shown in Figure 7.8 (a) and (b). In (b) is shown the orbital overlap that occurs with a 180° bond angle, which results in a negative electronic spin density being transferred to the $2s$ via polarization, and hence a negative Fermi-contact shift as shown in Figure 7.8 (c).

π -bond has symmetry that is incompatible with that of the Li^+ $2s$ orbital, and so does not contribute directly. However the σ -overlap between a vacant e_g orbital and a filled O $2p_\sigma$ gives a σ -bond which does have a net overlap with the Li^+ $2s$. The electronic spin transferred to the e_g must be spin up, so as to be aligned with the unpaired electrons in the t_{2g} which, as shown in Figure 7.8 (c), results in both a negative electronic spin density transferred to the Li^+ $2s$, and a negative Fermi-contact shift for ^6Li and ^7Li .

7.10 The magnetic susceptibility and paramagnetic shielding tensors in solid materials due to metal ions with SO coupling

We now extend the Curie–Weiss description of the paramagnetic shielding tensor in solid insulator materials by including the effects of SO coupling. In particular we once again provide a link between the bulk magnetic properties, namely the magnetic susceptibility tensor and the Weiss constant, and the local paramagnetic shielding tensor. Whilst we include the effects of SO coupling on the g - and ZFS tensors, we continue to neglect the SO contributions to the exchange interactions, namely the DM interaction, as well as the NR dipolar coupling. The justification for this is that isotropic exchange is the most important contribution to the interactions between the metal ions.

In the following discussion we assume for simplicity that only one species of transition-metal ion is present. However we note that the extension to more than one species is easily made by using the sub-lattice model of section 7.7.4. The assumption of one species of metal ion is not as trivial a point as it first appears. The reason is that it restricts all the metal ions to have the same g - and ZFS tensors. Importantly this means that not only must, for example, the g -tensors have the same principal components, but they must also have PAFs with the same orientation. Even if the unit cell contains only one metal ion, the solid may not satisfy the single-species condition. For example consider the battery cathode material LiFePO_4 , the unit cell of which contains one Fe^{2+} site. However closer inspection reveals that there are actually four Fe^{2+} sites that are related to each other by rotational symmetry operations. This means that, whilst the four Fe^{2+} ions have the same principal values for the g - and ZFS tensors, their PAFs have different orientations which are related to each other by the same rotational symmetry operations. Therefore in order to describe this system we would require four separate sub-lattices.

The magnetic susceptibility tensor

Assuming only one species of transition-metal ion we can write down the magnetic susceptibility tensor per metal ion χ_{ij} to second order in $1/(kT)$ as an extension of Equation 7.98:

$$\begin{aligned} \chi_{ij} = & \mu_0 \mu_B^2 \left[\frac{\beta}{\omega} \sum_B \sum_{qq'} (-1)^{q+q'} g_{1q,i}^{(A)} g_{1q',j}^{(B)} \text{Tr}_S \left(\hat{S}_{1-q}^{(A)} \hat{S}_{1-q'}^{(B)} \right) \right. \\ & - \frac{\beta^2}{\omega} \sum_{B,\Gamma} \sum_{qq'q''} (-1)^{q+q'+q''} g_{1q,i}^{(A)} g_{1q',j}^{(B)} D_{2q''}^{(\Gamma)} \text{Tr}_S \left(\hat{S}_{1-q}^{(A)} \hat{S}_{1-q'}^{(B)} \hat{S}_{1-q''}^{(\Gamma)} \right) \\ & \left. - \frac{\beta^2}{\omega} \sum_B \sum_{\Gamma > \Delta} \sum_{qq'} (-1)^{q+q'} g_{1q,i}^{(A)} g_{1q',j}^{(B)} J_{00}^{(\Gamma\Delta)}(11) \text{Tr}_S \left(\hat{S}_{1-q}^{(A)} \hat{S}_{1-q'}^{(B)} \hat{T}_{00}^{(\Gamma\Delta)}(11) \right) \right], \end{aligned} \quad (7.140)$$

where we have included the second-order contribution from the ZFS tensor. As for Equation 7.98, and with reference to appendix E, we simplify the expressions for the traces to obtain:

$$\chi = \frac{\mu_0 \mu_B^2 S(S+1)}{3kT} \mathbf{g} \cdot \mathbf{g}^T - \frac{\mu_0 \mu_B^2 S(S+1)(2S-1)(2S+3)}{30(kT)^2} \mathbf{g} \cdot \mathbf{D} \cdot \mathbf{g}^T + \frac{2\mu_0 \mu_B^2 S^2(S+1)^2}{9(kT)^2} \mathbf{g} \cdot \mathbf{g}^T \sum_{B \neq A} \mathcal{J}^{(AB)}. \quad (7.141)$$

We have seen the first two terms before, which are simply the first- and second-order contributions that also occur in systems with no magnetic ordering, and which depend on the matrix products $\mathbf{g} \cdot \mathbf{g}^T$ and $\mathbf{g} \cdot \mathbf{D} \cdot \mathbf{g}^T$ respectively. The third term, which depends on the exchange coupling constants, is analogous to the second term in Equation 7.109, with the factor g_e^2 replaced with $\mathbf{g} \cdot \mathbf{g}^T$. Note that the form of this susceptibility tensor requires the metal ions to have the same g -tensor \mathbf{g} and ZFS tensor \mathbf{D} .

In order to link the susceptibility Equation 7.141 Weiss constant we require a phenomenological expression for χ that depends on Θ . For this we propose the following modified version of Equation 7.90, into which we have introduced the g - and ZFS tensors:

$$\chi = \frac{\mu_0 \mu_B^2 S(S+1)}{3k(T-\Theta)} \mathbf{g} \cdot \mathbf{g}^T - \frac{\mu_0 \mu_B^2 S(S+1)(2S-1)(2S+3)}{30k^2(T-\Theta)^2} \mathbf{g} \cdot \mathbf{D} \cdot \mathbf{g}^T. \quad (7.142)$$

In order to link this expression to Equation 7.141 we expand the former as a Taylor series in $1/(kT)$ to second order, which gives us

$$\chi \approx \frac{\mu_0 \mu_B^2 S(S+1)}{3kT} \mathbf{g} \cdot \mathbf{g}^T - \frac{\mu_0 \mu_B^2 S(S+1)(2S-1)(2S+3)}{30(kT)^2} \mathbf{g} \cdot \mathbf{D} \cdot \mathbf{g}^T + \frac{\mu_0 \mu_B^2 S(S+1)}{3kT^2} \mathbf{g} \cdot \mathbf{g}^T \Theta. \quad (7.143)$$

On comparing terms in this expression and Equation 7.141 with the same temperature dependence we obtain the same expression for the Weiss constant as calculated previously in Equation 7.111.

The paramagnetic shielding tensor

We now calculate the SO coupling expression for the paramagnetic shielding tensor, where we include the SO coupling contributions to the g -, ZFS, and hyperfine tensors, but only consider the isotropic exchange coupling constants. From the discussion in appendix E we obtain the following expression for the shielding tensor:

$$\begin{aligned} \sigma_{ij}^S = & -\frac{\mu_B}{\hbar\gamma_I} \left[\frac{\beta}{\omega} \sum_{A,B} \sum_{qq'} (-1)^{q+q'} g_{1q,i}^{(A)} A_{1q',j}^{(B)} \text{Tr}_S \left(\hat{S}_{1-q}^{(A)} \hat{S}_{1-q'}^{(B)} \right) \right. \\ & - \frac{\beta^2}{\omega} \sum_{A,B,\Gamma} \sum_{qq'q''} (-1)^{q+q'+q''} g_{1q,i}^{(A)} A_{1q',j}^{(B)} D_{2q''}^{(\Gamma)} \text{Tr}_S \left(\hat{S}_{1-q}^{(A)} \hat{S}_{1-q'}^{(B)} \hat{S}_{2-q''}^{(\Gamma)} \right) \\ & \left. - \frac{\beta^2}{\omega} \sum_{A,B} \sum_{\Gamma>\Delta} \sum_{qq'} (-1)^{q+q'} g_{1q,i}^{(A)} A_{1q',j}^{(B)} J_{00}^{(\Gamma\Delta)}(11) \text{Tr}_S \left(\hat{S}_{1-q}^{(A)} \hat{S}_{1-q'}^{(B)} \hat{T}_{00}^{(\Gamma\Delta)}(11) \right) \right] \quad (7.144) \end{aligned}$$

Following the calculation of the expressions for the traces we obtain the following expression:

$$\sigma^S = -\frac{\mu_B S(S+1)}{3\hbar\gamma_I kT} \mathbf{g} \cdot \sum_A \mathbf{A}^{(A)} + \frac{\mu_B S(S+1)(2S-1)(2S+3)}{30(kT)^2} \mathbf{g} \cdot \mathbf{D} \cdot \sum_A \mathbf{A}^{(A)} - \frac{2\mu_B g_e S^2(S+1)^2}{9\hbar\gamma_I (kT)^2} \mathbf{g} \cdot \sum_A \sum_{B \neq A} \mathcal{J}^{(AB)} \mathbf{A}^{(B)}, \quad (7.145)$$

where the first term is the first-order contribution that depends only on the g -tensor, the second term is a second-order contribution that depends on the g - and ZFS tensors, and the third term contains all the information about the exchange couplings. The first step in linking this expression with the Weiss constant is to write the many-electron hyperfine tensors $\mathbf{A}^{(A)}$ in terms of the total hyperfine tensors \mathcal{A} using Equations 7.113 and 7.114:

$$\sigma^S = -\frac{\mu_B S(S+1)}{6\hbar\gamma_I kT} \mathbf{g} \cdot \mathcal{A} + \frac{\mu_B S(S+1)(2S-1)(2S+3)}{60(kT)^2} \mathbf{g} \cdot \mathbf{D} \cdot \mathcal{A} - \frac{\mu_B S(S+1)^2}{9\hbar\gamma_I (kT)^2} \sum_{B \neq A} \mathcal{J}^{(AB)} \mathbf{g} \cdot \mathcal{A}. \quad (7.146)$$

The phenomenological expression for the paramagnetic shielding tensor is given by an expression that is analogous to the magnetic susceptibility tensor in Equation 7.142:

$$\sigma^S = -\frac{\mu_B(S+1)}{6\hbar\gamma_I k(T-\Theta)} \mathbf{g} \cdot \mathcal{A} + \frac{\mu_B(S+1)(2S-1)(2S+3)}{60k^2(T-\Theta)^2} \mathbf{g} \cdot \mathbf{D} \cdot \mathcal{A} \quad (7.147)$$

Expanding this as a Taylor series in $1/(kT)$ and comparing the second-order terms, we once again obtain the expression for the Weiss constant in Equation 7.111. Equation 7.147 is therefore a practical expression for the paramagnetic shielding tensor in a solid exhibiting magnetic ordering. If the solid contains more than one species of metal ion, we may repeat the analysis of section 7.7.4, and treat Equation 7.147 as the contribution to the shielding tensor from a single sub-lattice containing one species of metal ion. For the example of LiFePO_4 introduced above, this would require the specification of four sub-lattices, each corresponding to a Fe^{2+} ion with a different PAF orientation.

7.11 Exchange interactions between transition-metal ions and lanthanides

Throughout this chapter we have focussed exclusively on the exchange interactions between transition-metal ions, and the consequences for the paramagnetic shift. Before we leave this topic we very briefly note the additional effects that we may expect from an exchange interaction between a transition-metal ion and a lanthanide ion. For such a spin system it has been shown that the exchange Hamiltonian is given by the expressions in Equations 7.29, 7.30, and 7.31 to which have been added terms of higher degree in the electronic spin operators [231]. The most important of these is the biquadratic exchange, which takes the form [242]

$$\sum_{A>B} K^{(AB)} (\hat{\mathbf{S}}^{(A)} \cdot \hat{\mathbf{S}}^{(B)})^2, \quad (7.148)$$

where the sum is restricted to only include interactions between one transition-metal ion and one lanthanide ion, and $K^{(AB)}$ is the biquadratic exchange coupling constant. These terms can be included in the irreducible spherical tensor form of the Hamiltonian in Equation 7.32 by adding terms of spatial and spin ranks greater than two to give a new Hamiltonian of the form

$$\hat{\mathcal{H}}_0 = \sum_A \sum_{kq} (-1)^q D_{kq}^{(A)} \hat{S}_{k-q}^{(A)} + \sum_{A>B} \sum_{kq} (-1)^q J_{kq}^{(AB)}(k_1 k_2) \hat{T}_{k-q}^{(AB)}(k_1 k_2). \quad (7.149)$$

This Hamiltonian can be used in conjunction with the EPR formalism to derive a general form of the paramagnetic chemical shielding tensor, using the method in appendix E.

7.12 The paramagnetic shift in metals

We now turn to the final topic of this chapter, which is the paramagnetic shift in metals. This shift was first described by Townes and Knight, and is referred to as the Knight shift [243]. It is interesting to compare the form of the Knight shift in metals with the corresponding paramagnetic shifts in insulators. We will see that there are striking similarities, as well as important differences. The latter are due to the differences in the paramagnetism in the two materials. We have seen that in insulators, the unpaired electrons are largely localized to the paramagnetic centres, which act as effective electronic spins S . In the paramagnetic regime, above the ordering temperature, these effective spins act independently of each other which can result in large magnetic susceptibilities and induced magnetic moments. On the other hand, in metals at zero temperature the electrons occupy orbitals that are delocalized across the entire lattice with energies up to the Fermi energy. The electrons are paired, and so the material is diamagnetic. On increasing the temperature the orbitals just above the Fermi level are partially populated at the expense of those just below and the material exhibits paramagnetism. The key difference to insulators is that in metals only the electrons close to the Fermi level contribute to the paramagnetism, and these are delocalized across the entire lattice. The resulting magnetic susceptibilities are therefore much smaller than in insulators. We should note that the form of the Knight shift is also valid for the paramagnetic shifts of semiconductors [244]. We derive the form of the Knight shift here, following the protocols of Slichter [245] and Abragam [183].

7.12.1 The Knight shift

Like all paramagnetic shifts, the Knight shift of a nuclear spin is due to the hyperfine interaction with the unpaired electrons. For metals the correct form of the hyperfine interaction Hamiltonian is given in Equation 2.191. We note that, as for other paramagnetic systems, the electronic relaxation dynamics are several orders of magnitude faster than the nuclear spin dynamics. This means that, in effect, the nuclear spins actually interact with the average electronic magnetic moments. We account for this by modifying the hyperfine coupling Hamiltonian in Equation 2.191 by computing its expectation value with the wavefunction that is

the product of the spatial ground state of Equation 2.26, and a spin wavefunction which is the correctly symmetrized product of the one-electron functions $|m\rangle$. We make the assumption that the metal has cubic symmetry, and that therefore we only need to consider the contact interaction, and furthermore we do not consider SO coupling effects. The resulting Knight shift is therefore purely spatially isotropic, and takes the form of a Fermi-contact shift. The role of the spin-dipolar interaction and the susceptibility anisotropy would be to introduce an SA, which for metals is generally smaller than the isotropic shift [183].

Following these assertions and assumptions the Hamiltonian \hat{H} describing the nuclear spin interaction with the average electronic magnetic moments is given by the contact part of Equation 2.191 following the calculation of the expectation value in the many-electron space-spin wavefunction. Since $\delta(\mathbf{r}_l)$ and \hat{s}_l are one-electron space and spin operators and the one-electron wavefunctions are orthogonal, the only terms of the wavefunction in Equation 2.26 that contribute are those with no permutations of the electron labels. The Hamiltonian is therefore

$$\hat{H} = \frac{2}{3}\mu_0\mu_B g_e \hbar \gamma_I \sum_l \langle \phi_{\mathbf{k}_l}(\mathbf{r}_l) | \delta(\mathbf{r}_l) | \phi_{\mathbf{k}_l}(\mathbf{r}_l) \rangle \langle m_l | \hat{s}_l | m_l \rangle \cdot \hat{I}, \quad (7.150)$$

where we have placed the nucleus at the origin $\mathbf{r} = \mathbf{0}$. Whilst the sum is over all the electrons l in the metal, we note that only those electrons present in partially filled orbitals actually make a net contribution to both the hyperfine interaction and \hat{H} . As discussed before these electrons occupy states that lie close to the Fermi level. To simplify this Hamiltonian we replace the sum over l with a double sum over the wavevectors \mathbf{k} in the partially occupied band, as the other filled bands make no net contribution, and electronic spin states m . We also note that, as the external magnetic field is applied along z , the nuclear spin system is quantised along z and we retain only the component \hat{I}_z in the scalar product. The result is

$$\hat{H} = \frac{2}{3}\mu_0\mu_B g_e \hbar \gamma_I \hat{I}_z \sum_{\mathbf{k}, m} |\phi_{\mathbf{k}}(\mathbf{0})|^2 m f_m(\mathbf{k}) \quad (7.151)$$

$$= \frac{2}{3}\mu_0\mu_B g_e \hbar \gamma_I \hat{I}_z \sum_{\mathbf{k}, m} \frac{1}{V} |u_{\mathbf{k}}(\mathbf{0})|^2 m f_m(\mathbf{k}), \quad (7.152)$$

where we have included the Fermi–Dirac distribution function $f_m(\mathbf{k})$ for electrons in spin state m . This function provides the necessary weighting to the state populations as a result of the non-zero temperature, and replaces the Boltzmann distribution function used for insulators.

At this point we are able to make the connection between this interaction and the bulk magnetic properties of the metal. When an external magnetic field is applied to the metal, the electrons with wavevector \mathbf{k} are partially aligned with the field, and can be described by an average magnetic moment per electron $\langle \hat{\mu}_{\mathbf{k},z} \rangle$. This is given by

$$\langle \hat{\mu}_{\mathbf{k},z} \rangle = -\mu_B g_e \sum_m m f_m(\mathbf{k}) \quad (7.153)$$

$$= -\frac{1}{2} \mu_B g_e [f_\alpha(\mathbf{k}) - f_\beta(\mathbf{k})], \quad (7.154)$$

which is proportional to the difference in populations of electrons with different polarizations in the state \mathbf{k} . Written in terms of the average electronic magnetic moments the Hamiltonian becomes

$$\hat{H} = -\frac{2}{3} \mu_0 \hbar \gamma_I \hat{I}_z \sum_{\mathbf{k}} |\phi_{\mathbf{k}}(\mathbf{0})|^2 \langle \hat{\mu}_{\mathbf{k},z} \rangle. \quad (7.155)$$

This form of the expression emphasises that electrons far from the Fermi level, for which $f_\alpha(\mathbf{k}) \approx f_\beta(\mathbf{k})$, have zero net magnetic moment as indicated by Equation 7.154, and do not contribute. In complete analogy with paramagnetic molecules in solution, or paramagnetic insulators, the average electronic magnetic moment due to wavevector \mathbf{k} is proportional to B_0 :

$$\langle \hat{\mu}_{\mathbf{k},z} \rangle = \frac{1}{\mu_0} \chi_{\mathbf{k}} B_0, \quad (7.156)$$

where the $\chi_{\mathbf{k}}$ is the magnetic susceptibility per electron with wavevector \mathbf{k} . The sum of these susceptibilities divided by the volume of the system is the total magnetic susceptibility per unit volume, which for metals is called the Pauli susceptibility χ_P :

$$\chi_P = \frac{1}{V} \sum_{\mathbf{k}} \chi_{\mathbf{k}}. \quad (7.157)$$

In terms of the individual magnetic susceptibilities the Hamiltonian is

$$\hat{H} = -\frac{2}{3} \hbar \gamma_I B_0 \hat{I}_z \sum_{\mathbf{k}} |\phi_{\mathbf{k}}(\mathbf{0})|^2 \chi_{\mathbf{k}}. \quad (7.158)$$

This clearly has the form of a chemical shielding Hamiltonian:

$$\hat{H} = \hbar \gamma_I \sigma_{\text{iso}}^K B_0 \hat{I}_z, \quad (7.159)$$

with an isotropic shielding σ_{iso}^K . In the shift convention we write the Knight shift $K = -\sigma_{\text{iso}}^K$ as

$$K = \frac{2}{3} \sum_{\mathbf{k}} |\phi_{\mathbf{k}}(\mathbf{0})|^2 \chi_{\mathbf{k}}. \quad (7.160)$$

We can see that this form of the Knight shift is a sum of terms due to each electron, with each term proportional to the product of the density of that electron at the nucleus $|\phi_{\mathbf{k}}(\mathbf{0})|^2$, and its isotropic magnetic susceptibility $\chi_{\mathbf{k}}$. Therefore each term is equivalent in form to a Fermi-contact shift from one electron, but with two differences. Firstly the magnetic susceptibility per electron has a different form to that for independent electrons, as discussed in section 7.12.2. Secondly we note that the Knight shift is written as a sum over electronic spatial states that appear to be independent, whereas for a paramagnetic centre in an insulator we combine the electrons into a single effective spin with a total unpaired spin density. This appears to be a significant difference, but we now show that we can rewrite the expression for the Knight shift in terms of a single contribution that has a form closer to that of the Fermi-contact shift.

We can simplify the sum over \mathbf{k} by recalling that as the volume of the system becomes infinitely large, the spacing between the allowed values of \mathbf{k} decreases until the wavevector space becomes a continuum, and we can replace the sum with an integral over energy as in Equation 2.30:

$$\lim_{V \rightarrow \infty} \frac{1}{V} \sum_{\mathbf{k}} |\phi_{\mathbf{k}}(\mathbf{0})|^2 \chi_{\mathbf{k}} = \int \langle |\phi_{\mathbf{k}}(\mathbf{0})|^2 \rangle_{E_{\mathbf{k}}} \chi(E_{\mathbf{k}}) g(E_{\mathbf{k}}) dE_{\mathbf{k}}. \quad (7.161)$$

Here we have acknowledged that the magnetic susceptibilities $\chi_{\mathbf{k}}$ only depend on \mathbf{k} via the energies $E_{\mathbf{k}}$, and so the susceptibilities are written as $\chi(E_{\mathbf{k}})$. However the electron spin densities $|\phi_{\mathbf{k}}(\mathbf{0})|^2$ have a more complicated dependence on \mathbf{k} , and so must be averaged over all values of \mathbf{k} that have the same energy $E_{\mathbf{k}}$ before we compute the integral. We recall that the only electrons that contribute to the Knight shift are those that are close to, i.e. within a range kT of, the Fermi level. We also assume that the variation of the average of the spin density $\langle |\phi_{\mathbf{k}}(\mathbf{0})|^2 \rangle_{E_{\mathbf{k}}}$ over this range of energies is small, and so we can replace the average at energy $E_{\mathbf{k}}$ with the average over the Fermi energy. This allows us to bring the factor of $\langle |\phi_{\mathbf{k}}(\mathbf{0})|^2 \rangle_{E_{\mathbf{F}}}$ outside

the integral to give

$$\lim_{V \rightarrow \infty} \frac{1}{V} \sum_{\mathbf{k}} |\phi_{\mathbf{k}}(\mathbf{0})|^2 \chi_{\mathbf{k}} = \langle |\phi_{\mathbf{k}}(\mathbf{0})|^2 \rangle_{E_F} \int \chi(E_{\mathbf{k}}) g(E_{\mathbf{k}}) dE_{\mathbf{k}} \quad (7.162)$$

$$= \langle |\phi_{\mathbf{k}}(\mathbf{0})|^2 \rangle_{E_F} \chi_P, \quad (7.163)$$

where to go to the last line we have written the total Pauli susceptibility as the integral

$$\chi_P = \int \chi(E_{\mathbf{k}}) g(E_{\mathbf{k}}) dE_{\mathbf{k}}. \quad (7.164)$$

The Knight shift now takes the simple form

$$K = \frac{2}{3} \langle |\phi_{\mathbf{k}}(\mathbf{0})|^2 \rangle_{E_F} \chi_P V. \quad (7.165)$$

This expression is a contact shift proportional to the total susceptibility of the metal $\chi_P V$, and the average one-electron spin density at the Fermi level $\langle |\phi_{\mathbf{k}}(\mathbf{0})|^2 \rangle_{E_F}$. To further investigate the form of the Knight shift, we need an expression for the Pauli susceptibility.

7.12.2 The Pauli magnetic susceptibility

The origin of the paramagnetic magnetic moment in a metal induced by an external magnetic field B_0 can be understood from Figure 7.10. In the absence of the external field the electrons are divided into two bands with spin polarization α and β , referred to as the spin-up and spin-down bands respectively. Both bands have the same density of states at all energies, given by Equation 2.33, and both bands are equally populated as shown in Figure 7.10 (a). When we apply the magnetic field the electrons acquire an additional Zeeman energy term $\mu_B g_e B_0 m$, where m is the magnetic-quantum number for a single electron. Hence the spin-up band is shifted up in energy by $\mu_B g_e B_0 / 2$, and the spin-down band is shifted down by the same amount, as shown in Figure 7.10 (b). In order to maintain the lowest-energy electronic configuration, electrons move from the spin-up band to the spin-down band, resulting in a greater population of the latter and hence a net non-zero electronic magnetic moment. The expressions for the density of states for the two bands $g_{\alpha}(E)$ and $g_{\beta}(E)$ are modified

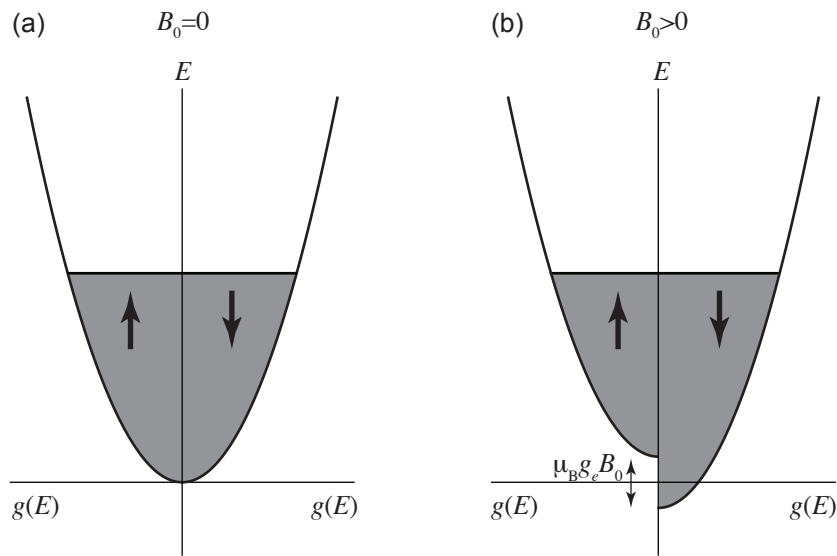


Figure 7.10: Illustration of the effect of an external magnetic field on the band structure of a metal. In the absence of the field the spin-up (α) and spin-down (β) electrons have the same band structure and are equally populated, as shown by the left- and right-hand density-of-states plots in (a). When the field is applied the spin-up band is shifted to higher energy by an amount $\mu_B g_e B_0/2$, and the spin-down band is shifted down by the same amount, as shown in (b). The populations of the levels change so as to maintain the same average Fermi level, with the result that electrons transfer from the spin-up band to the spin-down band.

from those in Equation 2.33 to account for the field, and are given by:

$$g_{\alpha}(E) = \frac{1}{2}g\left(E - \frac{1}{2}\mu_{\text{B}}g_e B_0\right), \quad (7.166)$$

$$g_{\beta}(E) = \frac{1}{2}g\left(E + \frac{1}{2}\mu_{\text{B}}g_e B_0\right). \quad (7.167)$$

The numbers of electrons per unit volume in the spin-up and spin-down bands n_{α} and n_{β} are then given by the integral expressions:

$$n_{\alpha} = \frac{1}{2} \int_0^{\infty} g\left(E - \frac{1}{2}\mu_{\text{B}}g_e B_0\right) f(E) dE, \quad (7.168)$$

$$n_{\beta} = \frac{1}{2} \int_0^{\infty} g\left(E + \frac{1}{2}\mu_{\text{B}}g_e B_0\right) f(E) dE. \quad (7.169)$$

We recall that the Zeeman energy is much smaller than the thermal energy $\mu_{\text{B}}g_e B_0 \ll kT$, and so we can expand the expressions for the density of states as Taylor series,

$$g\left(E \pm \frac{1}{2}\mu_{\text{B}}g_e B_0\right) = g(E) \pm \frac{1}{2}\mu_{\text{B}}g_e B_0 g'(E) + O\left(\left(\frac{1}{2}\mu_{\text{B}}g_e B_0\right)^2\right), \quad (7.170)$$

from which we can clearly see that the spin-down band has a greater population than the spin-up band.

The magnetization, i.e. the net magnetic moment per unit volume, is proportional to the difference in spin populations:

$$M = \frac{1}{2}\mu_{\text{B}}g_e (n_{\beta} - n_{\alpha}). \quad (7.171)$$

Expanding the density of states functions as Taylor series we obtain the following expression for M :

$$M = \frac{1}{4}\mu_{\text{B}}^2 g_e^2 B_0 \int_0^{\infty} g'(E) f(E) dE \quad (7.172)$$

$$= \frac{1}{4}\mu_{\text{B}}^2 g_e^2 B_0 \left\{ [g(E)f(E)]_0^{\infty} - \int_0^{\infty} g(E) f'(E) dE \right\} \quad (7.173)$$

$$= -\frac{1}{4}\mu_{\text{B}}^2 g_e^2 B_0 \int_0^{\infty} g(E) f'(E) dE, \quad (7.174)$$

where to go to the second line we have employed integration by parts, and to go to the last line we have removed the first term by noting that $g(0) = 0$ and $f(E) \rightarrow 0$ as $E \rightarrow \infty$. To proceed we need to evaluate the

derivative for the Fermi–Dirac distribution function with respect to energy. We recall that, at zero temperature, $f(E)$ is proportional to the Heaviside step function with the discontinuity at $E = E_F$, and that at higher temperatures the discontinuity is smoothed out. Nevertheless at practicable experimental temperatures the Fermi–Dirac function is still well-approximated by the Heaviside step function, and so we can write its derivative as [189]

$$f'(E) = -\delta(E - E_F). \quad (7.175)$$

Substituting this into Equation 7.174 we obtain the final expression for the magnetization:

$$M = \frac{1}{4}\mu_B^2 g_e^2 B_0 g(E_F). \quad (7.176)$$

The Pauli susceptibility per unit volume is therefore

$$\chi_P = \frac{\mu_0 M}{B_0} \quad (7.177)$$

$$= \frac{1}{4}\mu_0 \mu_B^2 g_e^2 g(E_F). \quad (7.178)$$

We see that the Pauli susceptibility is proportional to the density of states at the Fermi level. This is because the Zeeman interaction is very small, and so the unpaired electrons resulting from the application of the field are located in the vicinity of the Fermi level. A greater number of states in this range of energies, which is given by $g(E_F)$, results in a greater number of unpaired electrons, and hence a greater magnetization and susceptibility. It is notable that the Pauli susceptibility, in contrast to the Curie expression for isolated electrons, is temperature independent. This is because in this derivation we have assumed the zero-temperature form of the Fermi–Dirac function, and hence we have ignored the effects of thermal population. Nevertheless the inclusion of temperature results in only a small correction, because the electron populations follow the Fermi–Dirac distribution rather than the Boltzmann distribution.

7.12.3 Comparison between the paramagnetic shifts in metals and insulators

We are now in a position to compare the Knight shift of a metal with the Fermi-contact shift obtained from an insulator. In order to make a fair comparison we compare two solids with the same number of electrons in the same volume. In the case of the metal these N electrons occupy the delocalized orbitals with energies

determined by the density of states and populations by the Fermi–Dirac distribution, whilst in the insulator the N electrons are each localized to N paramagnetic centres of spin $S = 1/2$. The expression for the Knight shift is taken from Equation 7.165, and the Fermi-contact shift for the insulator is adapted from Equation 3.108. These expressions are reproduced here for convenience:

$$K = \frac{2}{3} \langle |\phi_{\mathbf{k}}(\mathbf{0})|^2 \rangle_{E_F} \chi_P V \quad (7.179)$$

$$\delta^{\text{FC}} = \frac{2}{3} \rho^{\alpha-\beta}(\mathbf{0}) \chi_V V \frac{N_A}{N}, \quad (7.180)$$

where N_A is the number of equivalent paramagnetic centres that contribute to the Fermi-contact shift of the insulator. We note that we have written the Fermi-contact shift in terms of the volume susceptibility, which is related to the susceptibility per paramagnetic centre by $\chi_V = \chi(N/V)$. The two expressions are similar except for the additional factor of N_A/N in the latter. This reflects the fundamental differences in the two cases between the small number of electrons that contribute to the shift. For the metal all N electrons are delocalized over the entire lattice, and hence they all contribute spin density to the s -orbital of the observed nucleus. The fact that only the fraction at the Fermi level make a *net* contribution is addressed by the Pauli susceptibility. However for the insulator the N electrons are localized at their paramagnetic centres and only a small number N_A , which are located in the bonding environment of the nucleus, actually contribute to the shift. The other electrons are not delocalized at all into the s -orbital.

In both cases the shift is proportional to the size of the average unpaired electron density per electron that is present in the s -orbital of the nucleus. For the metal this is given by $\langle |\phi_{\mathbf{k}}(\mathbf{0})|^2 \rangle_{E_F}$, which is the average of the one-electron spin density over the electrons located at the Fermi level. For the insulator the one-electron density in the expression for the Fermi-contact shift is $\rho^{\alpha-\beta}(\mathbf{0})$, and is due to the single electron on the paramagnetic ion. We have seen that $\rho^{\alpha-\beta}(\mathbf{0})$, and therefore the Fermi-contact shift, can either be positive or negative depending whether the electron transfer occurs via a delocalization or polarization mechanism. The same principles also apply to $\langle |\phi_{\mathbf{k}}(\mathbf{0})|^2 \rangle_{E_F}$, and so the Knight shift may also be positive or negative depending on the nature of the electron transfer. Furthermore if the effective spin of the paramagnetic centres is greater than $S = 1/2$, this electron density is divided by $2S$ to give the unpaired electron density per unpaired electron.

In order to compare the sizes of the two shifts we compare the two magnetic susceptibilities. For the

insulator we take the expression from Equation 3.92, set $S = 1/2$, and multiply by n to obtain the volume susceptibility χ_V . For the metal the comparison with the Pauli susceptibility χ_P is difficult unless we specify the form of the density of states. Therefore we apply the simplified free-electron model, for which the density of states at the Fermi level is given by Equation 2.48. The two volume susceptibilities are given below:

$$\chi_P = \frac{3\mu_0\mu_B^2 g_e^2 n}{8kT_F} \quad (7.181)$$

$$\chi_V = \frac{\mu_0\mu_B^2 g_e^2 n}{4kT}. \quad (7.182)$$

The two expressions appear to be remarkably similar, but with one crucial difference. The expression for the insulator has a Curie temperature difference, and therefore χ_V and the Fermi-contact shift increase with decreasing temperature. The Pauli susceptibility, however, is temperature independent. The temperature that does appear in the denominator of χ_P is the constant Fermi temperature T_F . For metals T_F generally takes values from 10^4 – 10^5 K, and so the Pauli susceptibility is between two and three orders of magnitude lower than the corresponding Curie susceptibility at all practicable temperatures. Therefore Fermi-contact shifts are generally much larger than Knight shifts.

7.13 Key concepts

- The paramagnetic shielding tensor due to multiple non-interacting metal ions is simply the sum of the individual independent contributions from each ion.
- Neighbouring metal ions often interact with each other via an exchange coupling, which gives either ferromagnetic or antiferromagnetic alignment of the effective spins.
- The exchange interaction comprises an isotropic exchange term, antisymmetric Dzyaloshinskii–Moriya term, and a symmetric dipolar term.
- In the high-temperature regime the paramagnetic shielding tensor due to clusters of interacting metal ions is modified by the exchange coupling, which gives an additional term in $1/(kT)^2$ (Equation 7.53).
- The magnetic properties of extended networks of interacting metal ions in solid insulator materials can be approximated by mean-field theory.

- The magnetic susceptibility (Equation 7.90) and paramagnetic shielding tensor (Equation 7.117) of solid insulator materials generally exhibit a Curie–Weiss temperature dependence.
- In systems either with large Weiss constants, or with magnetic ordering temperatures close to room temperature, it is not appropriate, even in the paramagnetic state, to use the spin-only values to estimate the magnetic susceptibility.
- Under certain circumstances the signs of both the isotropic exchange coupling constants and the Fermi-contact shift can be predicted using the Goodenough–Kanamori rules.
- The paramagnetic shift in a metal or semiconductor is referred to as the Knight shift (Equation 7.165), and depends on the Pauli susceptibility of the material (Equation 7.178).
- Both the Pauli susceptibility and Knight shift are 100–1000 smaller than their equivalents in solid insulators, and are temperature-independent.

Chapter 8

Relaxation in paramagnetic systems under fast-motional and high-field conditions

We now turn our attention to a feature of paramagnetic NMR that we have rather neglected up until now, but which is nevertheless extremely important, and that is the relaxation behaviour of paramagnetic systems. The relaxation rates of the nuclear spins contain contributions from effects that are present in both diamagnetic and paramagnetic systems, such as nuclear–nuclear dipolar couplings and the quadrupole interaction, and effects that are present only in paramagnetic systems, namely the hyperfine couplings to unpaired electrons. For many systems the paramagnetic effects dominate the relaxation properties, with very large contributions to the rate constants that are often referred to as *paramagnetic relaxation enhancements* (PREs). Here we provide a basic description of the PRE under the high-field conditions of high-resolution NMR, and the conditions of fast electron dynamics. A more complete treatment for arbitrary field and electron dynamics is deferred until chapter 9.

We begin with a brief account of the Redfield theory of relaxation, and then document the applications to the calculation of electron relaxation rates and the PRE of the nuclei. We discuss the main mechanisms responsible for electron relaxation in both complexes in solution, and solid insulators. The relaxation

properties of the unpaired electrons are directly responsible for the PRE. However electron relaxation is more complicated than nuclear relaxation as Redfield theory does not usually provide a valid description [95]. Therefore for the remainder of this chapter we model the effect of the electron relaxation on the PRE phenomenologically.

We then describe the PRE using semi-classical Redfield theory [246], which in this specific case is known as the Solomon–Bloembergen–Morgan theory. The treatment of relaxation given here is valid for systems with fast motional dynamics, such as those encountered in the rotational diffusion of small and large molecules in solution, and under high-field conditions, which are defined as those where the electronic Zeeman interaction dominates the ZFS interaction.

We derive the expressions for the contributions to the relaxation rate constants originating from the different parts of the hyperfine interaction, and in different motional regimes including small complexes in solution, large biomolecules in solution, and solid insulators with no rotational dynamics. The discussion in this chapter is limited to the non-relativistic description of the hyperfine interaction, and we ignore SO coupling effects on the PRE, although we acknowledge that SO coupling is important for electronic relaxation, via the ZFS and the g -anisotropy.

Further reading on the subject of relaxation in solution can be found in the contributions from Kowalewski and Mäler [95], Bertini et al [15, 247], and Kruk [248, 249]. The specific topic of paramagnetic relaxation in solution has recently been reviewed by Kowalewski and Kruk [250].

8.1 Overview of the models of electronic and nuclear relaxation

Both this chapter and the next present the different models of electronic and nuclear relaxation in paramagnetic systems, for different experimental conditions and within different approximations. Whilst this plethora of different models and approaches may initially seem confusing, they are in fact related to each other in a straightforward way, as shown by the two flow charts in Figures 8.1 and 8.2.

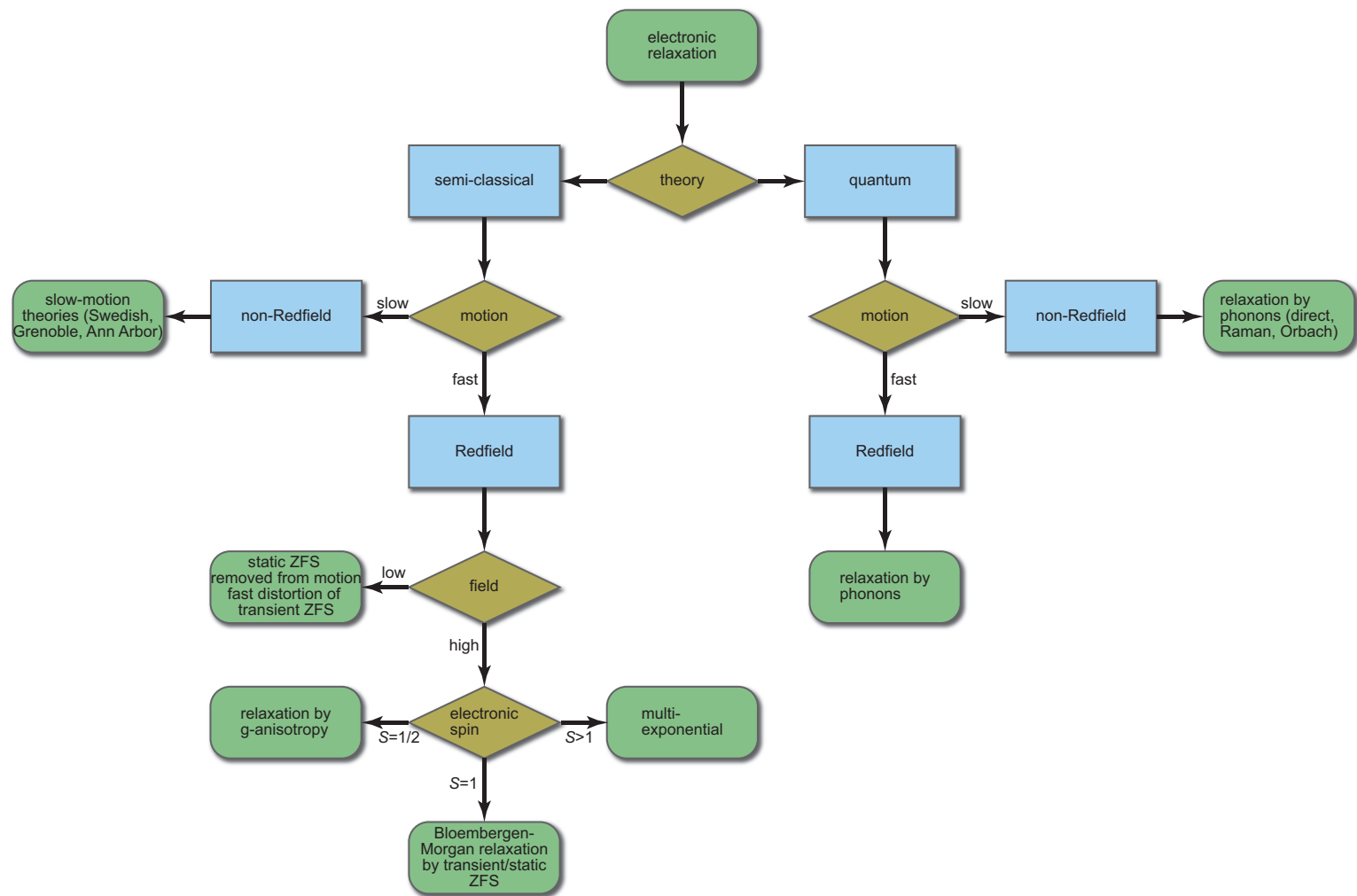


Figure 8.1: Flow chart showing the relationship between the different models describing electronic relaxation. The chart differentiates between the full-quantum and semi-classical treatment of the lattice, fast (Redfield) and slow (non-Redfield) motions and, within Redfield theory, between high and low field, and between different electronic spins. Definitions: fast motion $\Omega\tau_c \ll 1$, slow motion $\Omega\tau_c \gg 1$, high field $|D| \ll \mu_B g_e B_0$, low field $|D| \gg \mu_B g_e B_0$. Ω is the strength of the fluctuating spin interaction, τ_c is the correlation time, D is the axial ZFS anisotropy, B_0 is the applied magnetic field.

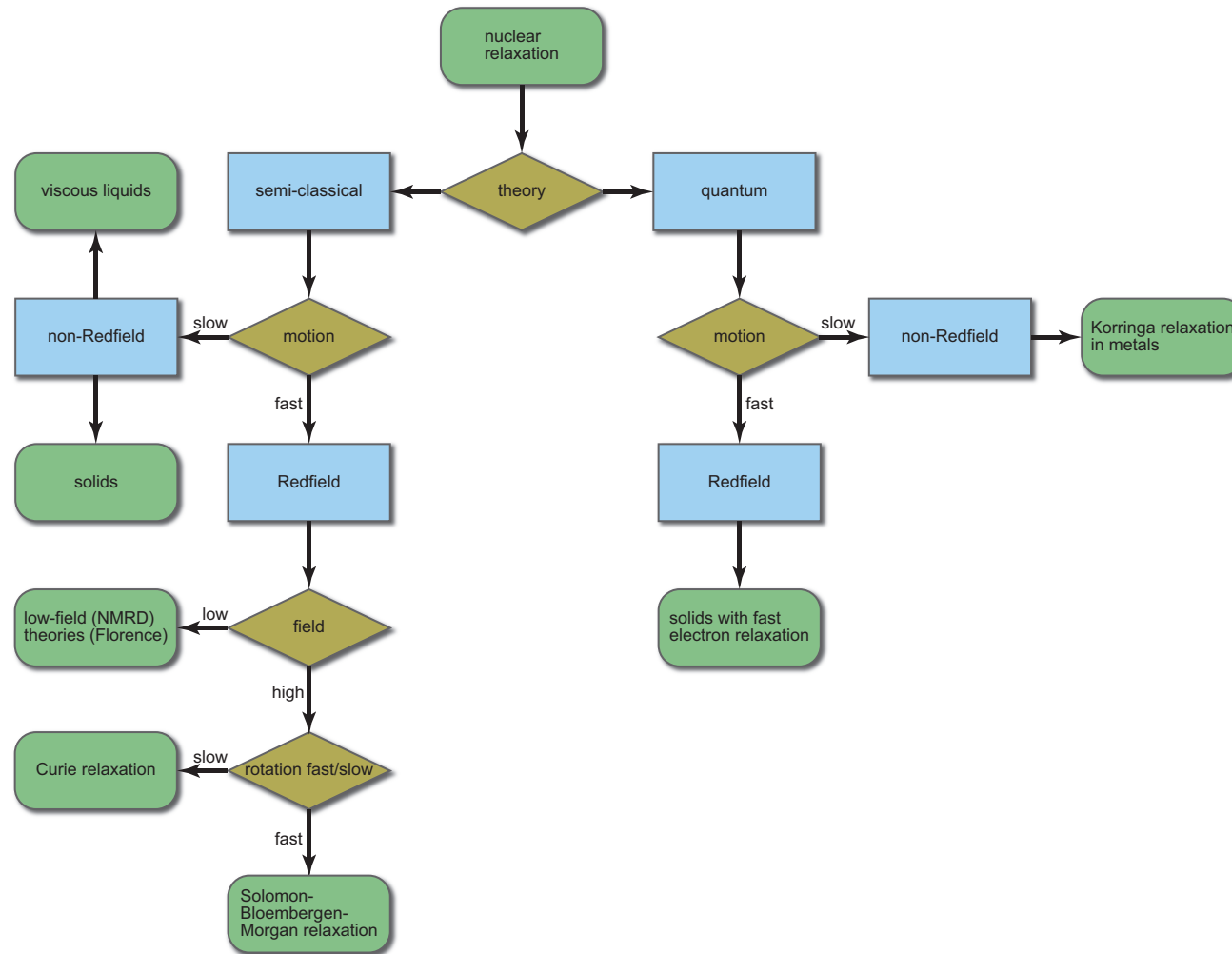


Figure 8.2: Flow chart showing the relationship between the different models describing nuclear relaxation in paramagnetic systems. The chart differentiates between the full-quantum and semi-classical treatment of the lattice, fast (Redfield) and slow (non-Redfield) motions and, within Redfield theory, between high and low field, and between fast and slow rotations. Definitions: fast motion $\Omega\tau_c \ll 1$, slow motion $\Omega\tau_c \gg 1$, high field $|\omega_Q| \ll |\omega_0|$, low field $|\omega_Q| \gg |\omega_0|$, fast rotation $\tau_r \ll T_{1e}, T_{2e}$, slow rotation $\tau_r \gg T_{1e}, T_{2e}$. Ω is the strength of the fluctuating spin interaction, τ_c is the correlation time, τ_r is the rotational correlation time, T_{1e} and T_{2e} are the electronic spin-lattice and spin-spin relaxation times, ω_Q is the quadrupolar splitting, ω_0 is the nuclear Larmor frequency.

Figure 8.1 shows how the models of electronic relaxation at different levels of theory (quantum vs semi-classical treatment of the lattice), timescales of motion (fast vs slow), size of the external magnetic field (high vs low), and the electronic spin ($S = 1/2$, $S = 1$, $S > 1$) are related to each other. Figure 8.2 presents the same relationship for nuclear relaxation, this time for different levels of theory (quantum vs semi-classical treatment of the lattice), timescales of motion (fast vs slow), size of the external magnetic field (high vs low), and timescale of rotation (fast vs slow). Full definitions of these terms are provided at later points in chapters 8 and 9.

These flow charts are intended to act as visual aids to help place the various relaxation models in their proper context. In particular, there are a number of cases in chapter 9 where a more advanced theory of relaxation is subjected to a set of assumptions that result in a description that is equivalent to one obtained with a simpler theory. Figures 8.1 and 8.2 will help to illuminate these cases more clearly.

The expressions for the relaxation rate constants derived in these two chapters were verified using SpinDynamica, which is a set of packages for spin dynamics calculations in Mathematica. Details about numerical implementations of relaxation calculations are given in Belorizky et al [251].

8.2 The Redfield theory of relaxation

In this section we summarize the main features of semi-classical Redfield theory, and establish the conventions and notation that we continue to use later. Readers interested in complete and accessible descriptions of Redfield theory are referred to the contributions by Redfield [246], Goldman [252, 253], and Kowalewski and Maler [95].

8.2.1 The equation of motion

We separate the system into two parts: the combined electronic–nuclear spin system, and the lattice which comprises everything else, such as the molecular framework. In the semi-classical formulation of Redfield theory we treat the combined electronic–nuclear spin system using quantum mechanics, and model the lattice classically. We therefore describe the time-evolution of the spin system with the Hamiltonian $\hat{H}(t)$, which is the sum of a dominant part \hat{H}_0 , containing coherent terms such as the Zeeman interactions, and a perturbation $\hat{H}_1(t)$ with a random time dependence and zero time-average, which describes incoherent effects such as

relaxation and chemical exchange:

$$\hat{H}(t) = \hat{H}_0 + \hat{H}_1(t). \quad (8.1)$$

The dominant part \hat{H}_0 essentially describes both the experimental conditions we impose upon the spin system, for example the size of the external magnetic field via the Zeeman interaction, or else the effects of radiofrequency (RF) irradiation during the pulse sequence, in addition to any coherent internal spin interactions. We therefore note that \hat{H}_0 may also be time-dependent if it includes, for example, terms describing a time-dependent radiofrequency (RF) irradiation, or the periodic modulation of spatially anisotropic interactions due to sample spinning. However when describing the spin-lattice and spin-spin relaxation of molecules in solution \hat{H}_0 generally contains only isotropic interactions. We also add RF terms when describing relaxation during extended spin-lock pulses or pulse sequences, which may be time-dependent. However, here we mainly consider the case of relaxation in solution with no RF irradiation where \hat{H}_0 is time-independent, as written here. However we should note that, since introducing RF irradiation or sample rotation changes the form of \hat{H}_0 , we expect these effects to also change the measured relaxation properties. The behaviour of the ensemble of spin systems in the sample under the action of $\hat{H}(t)$ is determined by calculating the time evolution of the density operator $\hat{\rho}(t)$ with the Liouville–von Neumann equation:

$$\frac{d\hat{\rho}(t)}{dt} = -\frac{i}{\hbar} [\hat{H}_0 + \hat{H}_1(t), \hat{\rho}(t)]. \quad (8.2)$$

The random time dependence of the part $[\hat{H}_1(t), \hat{\rho}(t)]$ makes the equation in this form insoluble. However we are able to proceed by factoring out the ‘motion’ of the density operator due to the static Hamiltonian \hat{H}_0 , which we do by transforming both $\hat{H}_1(t)$ and $\hat{\rho}(t)$ into the interaction representation of \hat{H}_0 . The reference frame of the interaction representation changes orientation so that it follows the time evolution due to \hat{H}_0 in the laboratory frame. Both the random Hamiltonian and density operator in the interaction representation of \hat{H}_0 can be calculated from their laboratory frame counterparts at any time t using the following expressions:

$$\hat{H}_1^T(t) = \exp(i\hat{H}_0t/\hbar) \hat{H}_1(t) \exp(-i\hat{H}_0t/\hbar), \quad (8.3)$$

$$\hat{\rho}^T(t) = \exp(i\hat{H}_0t/\hbar) \hat{\rho}(t) \exp(-i\hat{H}_0t/\hbar), \quad (8.4)$$

where the superscript T denotes an operator in the interaction representation.

The evolution of $\hat{\rho}^T(t)$ under the action of $\hat{H}_1^T(t)$ can be solved to second order in a perturbation expansion to give the Redfield master equation

$$\frac{d\hat{\rho}^T(t)}{dt} = -\frac{1}{\hbar^2} \int_0^\infty \overline{[\hat{H}_1^T(t), [\hat{H}_1^T(t-\tau), \hat{\rho}^T(t) - \hat{\rho}_0]]} d\tau, \quad (8.5)$$

where the overbar denotes an average over the spin systems in the ensemble, and $\hat{\rho}_0$ is the equilibrium density operator, which commutes with \hat{H}_0 and is therefore unchanged by the transformation into the interaction representation. Equation 8.5 depends on a series of approximations. Firstly we assume that the motions of the lattice are characterised by a correlation time τ_c which is sufficiently short that its product with the r.m.s. size Ω of the interaction represented by $\hat{H}_1(t)$, in frequency units, is much less than unity:

$$\Omega\tau_c \ll 1, \quad (8.6)$$

where $\hbar\Omega = |\hat{H}_1(t)|^{1/2}$. This is the motional narrowing regime, in which the fluctuations of the interactions in $\hat{H}_1(t)$ due to stochastic motion lead to a narrowing of the spectroscopic peak in comparison to the lineshape that would be obtained due to the spread of frequencies if the spin systems were static. Secondly, in order to be able to stop the perturbation expansion at second order, we assume that the time t during which we observe the system satisfies the inequalities

$$\tau_c \ll t \ll \frac{1}{\Omega}. \quad (8.7)$$

The upper-bound inequality, $t \ll \Omega^{-1}$, is potentially problematic as the inverse frequency Ω^{-1} is often much shorter than typical NMR observation times of between milliseconds and seconds. For example an interaction frequency of $\Omega/(2\pi) = 100$ kHz would give an inverse frequency of $1.6 \mu\text{s}$, which is much shorter than our NMR acquisition time! However this problem can be circumvented by noting that we can divide our observation time t into discrete chunks, each one of which satisfies Equation 8.7, and which we can safely assume is independent of the others due to the random nature of the perturbation. This leaves the lower-bound inequality of Equation 8.7, which amounts to the relaxation times always being longer than the correlation time.

The next step is to write the random perturbation Hamiltonian $\hat{H}_1(t)$ in terms of the irreducible spherical

tensor operators as follows:

$$\hat{H}_1(t) = \sum_{\Lambda} \sum_l \sum_{m=-l}^{+l} (-1)^m K_{lm}^{(\Lambda)}(t) \hat{T}_{l-m}^{(\Lambda)}(t) \quad (8.8)$$

$$= \sum_{\Lambda} \sum_l \sum_{m=-l}^{+l} (-1)^m K_{lm}^{(\Lambda)}(t) * \hat{T}_{l-m}^{(\Lambda)}(t)^\dagger. \quad (8.9)$$

We have written the total perturbation as a sum of terms from different interactions Λ , with each interaction having a distinct set of spatial tensors $K_{lm}^{(\Lambda)}(t)$ and spin tensors $\hat{T}_{l-m}^{(\Lambda)}(t)$. This form of the Hamiltonian separates the lattice variables and the spin variables into the spatial tensors and spin tensors respectively. We have included the time-dependence explicitly in both the $K_{lm}^{(\Lambda)}(t)$, and the $\hat{T}_{l-m}^{(\Lambda)}(t)$ to account for all the possible causes of the random fluctuations in $\hat{H}_1(t)$, a subject we return to in more detail later. In the following discussion we consider the effect of just a single interaction (which for nuclear relaxation we will later take to be the hyperfine interaction, and for electronic relaxation the ZFS) and so we drop both the sum over Λ and the superscript. We return to the case of the combined effects of more than one interaction on nuclear relaxation in section 8.8. We can write the spatial tensors in terms of their components in the PAF as follows

$$K_{lm}(t) = \sum_{\mu=-l}^{+l} D_{\mu m}^{(l)}(\alpha_l(t), \beta_l(t), \gamma_l(t)) \tilde{K}_{l\mu}(t), \quad (8.10)$$

where we have acknowledged that the random lattice fluctuations can result in a fluctuation of either the PAF components $\tilde{K}_{l\mu}(t)$, or the orientation of the PAF in the laboratory frame, due to changes in the Euler angles $(\alpha_l(t), \beta_l(t), \gamma_l(t))$. These Euler angles describe a pair of rotations, the first of which gives the orientation of the PAF in a frame fixed relative to the molecular geometry, and the second of which gives the orientation of this molecular frame in the laboratory frame. Each interaction clearly has a different set of Euler angles. However for a single interaction, each part of different rank may have also have a different set of Euler angles, since the PAFs may not be coincident. For example we generally expect the the rank-one and rank-two parts of the hyperfine tensor to have different PAFs. This is why we have written the Euler angles as having a dependence on l .

Before inserting the operator expression into the master equation, we first need to transform the spin tensors into the interaction representation of \hat{H}_0 . At this point we assume high-field conditions such that \hat{H}_0 is dominated by the electronic and nuclear Zeeman interactions, and that the electronic g -tensor is isotropic

and equal to g_e . Therefore the transformation into the interaction representation is a rotation about the z -axes of the I - and S -spin operators. We recall, from the rotation properties of irreducible spherical tensor operators, that rotations about z depend only on the order m of the operators \hat{T}_{lm} and not on the rank l , and that the effect of such a rotation is to impart a phase factor that depends only on m . Therefore $\hat{T}_{l-m}^T(t)$ is equal to

$$\hat{T}_{l-m}^T(t) = \exp(i\hat{H}_0 t/\hbar) \hat{T}_{l-m}(t) \exp(-i\hat{H}_0 t/\hbar) \quad (8.11)$$

$$= \sum_n \hat{T}_{l-m}^{(n)}(t) \exp(i\omega_{-m}^{(n)} t), \quad (8.12)$$

where we have split each spin tensor operator $\hat{T}_{l-m}(t)$ into a sum of operators $\hat{T}_{l-m}^{(n)}(t)$, labelled by a superscript (n) , each of which evolves at frequency $\omega_{-m}^{(n)}$ in the interaction representation. We note that the inclusion of this superscript is necessary when the two spins have different Larmor frequencies, as is the case for a system comprising a nuclear spin I coupled to an electronic spin S . The Hermitian conjugate of $\hat{T}_{l-m}^T(t)$ is simply given by

$$\hat{T}_{l-m}^T(t)^\dagger = \sum_n \hat{T}_{l-m}^{(n)}(t)^\dagger \exp(-i\omega_{-m}^{(n)} t). \quad (8.13)$$

Inserting the operator expression into the master equation in Equation 8.5, we now obtain the Redfield operator equation:

$$\begin{aligned} \frac{d\hat{\rho}^T(t)}{dt} = & -\frac{1}{\hbar^2} \sum_{l'} \sum_{mm'} \sum_{nn'} (-1)^{m+m'} \exp[i(\omega_{-m}^{(n)} - \omega_{-m'}^{(n')})t] \\ & \times \int_0^\infty \overline{[\hat{T}_{l-m}^{(n)}(t), [\hat{T}_{l'-m'}^{(n')}(t-\tau)^\dagger, \hat{\rho}^T(t) - \hat{\rho}_0]]} K_{lm}(t) K_{l'm'}(t-\tau)^* \exp(i\omega_{-m}^{(n)} \tau) d\tau. \end{aligned} \quad (8.14)$$

We have included the simultaneous ensemble average over all the spatial and spin-dependent parts of the expression, which is a formal requirement. However we can simplify things by assuming that the different stochastic processes are independent to each other, which enables us to perform the ensemble averages for

each process independently. This is the decomposition approximation, in which we can write:

$$\begin{aligned}
& \overline{\left[\hat{T}_{l-m}^{(n)}(t), \left[\hat{T}_{l'-m'}^{(n')}(t-\tau)^\dagger, \hat{\rho}^T(t) - \hat{\rho}_0 \right] \right]} K_{lm}(t) K_{l'm'}(t-\tau)^* \\
&= \overline{\left[\hat{T}_{l-m}^{(n)}(t), \left[\hat{T}_{l'-m'}^{(n')}(t-\tau)^\dagger, \hat{\rho}^T(t) - \hat{\rho}_0 \right] \right]} \times \sum_{\mu\mu'} \overline{D_{\mu m}^{(l)}(\alpha_l(t), \beta_l(t), \gamma_l(t)) D_{\mu' m'}^{(l')}(\alpha_{l'}(t-\tau), \beta_{l'}(t-\tau), \gamma_{l'}(t-\tau))^*} \\
& \times \overline{\tilde{K}_{\mu}(t) \tilde{K}_{\mu'}(t-\tau)^*}. \tag{8.15}
\end{aligned}$$

In situations where the two spins relax on timescales that differ by several orders of magnitude, the faster-relaxing spin acts as a source of a rapidly fluctuating magnetic field that influences the slower-relaxing spin via the coupling between them. This effect is accounted for by the ensemble average over the double commutator of spin operators. For example electronic relaxation occurs on a timescale, typically between 0.1 ps and 10 ns for metal ions, that is generally several orders of magnitude shorter than the timescale of nuclear relaxation, which is typically between 1 ms and several hours or longer. Therefore this factor describes the effect of the rapid electronic relaxation on the PRE of the nucleus. On the other hand, when describing electronic relaxation this part of the ensemble average can be dispensed with. The ensemble average over the product of Wigner matrix elements accounts for the fluctuations due to random spatial reorientation of the anisotropic interaction tensor, a process known as rotational diffusion. It only affects elements of tensor rank $l > 0$. The final factor is the ensemble average of the product of the PAF tensor components, and accounts for the instantaneous changes that may occur in these components either through distortion of the molecular geometry of the system, or chemical exchange of the nucleus or electron between different sites. We now examine these three mechanisms in detail.

8.2.2 Relaxation by spatial reorientation of the interaction tensor

We begin by examining the effect of the random rotational diffusion of the spatial tensor. Specifically we consider the case of paramagnetic molecules in solution that experience unrestricted isotropic tumbling. The local magnetic field experienced by the spin fluctuates in both size and direction as a result of the random time dependence. The ensemble average of the product of the spatial tensor components can be written in the

decomposition approximation as

$$\begin{aligned} \overline{K_{lm}(t)K_{l'm'}(t-\tau)^*} &= \sum_{\mu\mu'} \overline{D_{\mu m}^{(l)}(\alpha_l(t), \beta_l(t), \gamma_l(t)) D_{\mu' m'}^{(l')}(\alpha_{l'}(t-\tau), \beta_{l'}(t-\tau), \gamma_{l'}(t-\tau))^*} \\ &\quad \times \overline{\tilde{K}_{l\mu}(t)\tilde{K}_{l'\mu'}(t-\tau)^*}. \end{aligned} \quad (8.16)$$

Our first step is to assume that the random fluctuations that modulate the different interactions are uncorrelated. For the PRE, this means that the fluctuations of the Fermi-contact interaction are independent of those of the spin-dipolar interaction, and that both fluctuate independently of any other relevant interactions that cause relaxation. For electronic relaxation we assume that the fluctuations of the ZFS, Zeeman, and hyperfine interactions are all independent of each other. In practice the result is that we consider only those terms in the double-commutator where the two Hamiltonians are of the same interaction, e.g. both Fermi contact, or both spin dipolar, and neglect the cross-terms due to cross correlation between different interactions (to which we will return later). Hence we set $l = l'$.

The average product $\overline{K_{lm}(t)K_{l'm'}(t-\tau)^*}$ depends only on the *difference* τ between the times at which we evaluate each element in the product, and not on t itself. We can therefore simplify the average of the product of the Wigner rotation matrix elements as follows:

$$\begin{aligned} &\overline{D_{\mu m}^{(l)}(\alpha_l(t), \beta_l(t), \gamma_l(t)) D_{\mu' m'}^{(l)}(\alpha_l(t-\tau), \beta_l(t-\tau), \gamma_l(t-\tau))^*} \\ &= \left[\frac{1}{8\pi^2} \int_0^{2\pi} d\alpha_l \int_0^\pi \sin(\beta_l) d\beta_l \int_0^{2\pi} d\gamma_l D_{\mu m}^{(l)}(\alpha_l, \beta_l, \gamma_l) D_{\mu' m'}^{(l)*}(\alpha_l, \beta_l, \gamma_l) \right] g_l^R(\tau) \end{aligned} \quad (8.17)$$

$$= \frac{1}{2l+1} \delta_{mm'} \delta_{\mu\mu'} g_l^R(\tau), \quad (8.18)$$

where to go to the second line we have factored out the τ -dependence into a function $g_l^R(\tau)$ which is the reduced rotational correlation function describing the random reorientation of the spatial tensors, we have used the fact that, for isotropic tumbling, the average product of the Wigner matrix elements at $\tau = 0$ is given by the integral over *all the Euler angles*, and we have assumed that all orientations are equally probable at $\tau = 0$. To go to the last line we have used the well-known orthogonality relations of the Wigner elements [190].

We do not specify the form of the reduced correlation function at this point other than to say that, by

definition, $g_l^R(0) = 1$, and that at times longer than the associated correlation time $g_l^R(\tau)$ decays to zero. The reduced correlation function also, in principle, depends on the spatial rank l , which allows us to differentiate between second-rank interactions, which are affected by spatial reorientation, and zeroth-rank interactions which are invariant. The average product $\overline{K_{lm}(t)K_{l'm'}(t-\tau)^*}$ can now be written in the following simplified form:

$$\overline{K_{lm}(t)K_{l'm'}(t-\tau)^*} = \frac{1}{2l+1} \delta_{ll'} \delta_{mm'} g_l^R(\tau) \sum_{\mu} \overline{\tilde{K}_{l\mu}(t)\tilde{K}_{l\mu}(t-\tau)^*}. \quad (8.19)$$

The next step is to evaluate the sum over μ .

8.2.3 Relaxation by fast chemical exchange

The sizes of the tensor components in the PAF are modulated by fast chemical exchange, or distortions in the molecular geometry surrounding the site of the spin. A simple example is a nuclear spin, fixed in a chemical site, that is coupled to a second spin which undergoes rapid exchange. The size of the coupling interaction fluctuates in both sign and magnitude when the second spin is exchanged for another with a different magnetic quantum number m_S , and thus acts as a relaxation mechanism for the first spin. This mechanism is responsible for the time dependence and ensemble average contained in the sum over μ in Equation 8.19. The τ -dependence can be factored out of this sum to give

$$\sum_{\mu} \overline{\tilde{K}_{l\mu}(t)\tilde{K}_{l\mu}(t-\tau)^*} = \sum_{\mu} |\tilde{K}_{l\mu}|^2 g_l^M(\tau), \quad (8.20)$$

where $g_l^M(\tau)$ is the reduced exchange correlation function. In contrast to rotational diffusion this mechanism is also active for scalar interactions, as chemical exchange modulates the size of the interaction. If the interaction under consideration is indeed of rank zero, then the chemical exchange mechanism described here is an example of *scalar relaxation of the first kind* [183].

8.2.4 The spin-dependent part

The final source of relaxation we consider here is a rapidly-fluctuating local magnetic field experienced by one spin due to the rapid relaxation of a second spin to which the former is coupled. This situation is very important in paramagnetic systems, as the unpaired electrons relax on a timescale that is orders of magnitude

shorter than typical nuclear relaxation times. The rapidly-relaxing unpaired electrons induce a fluctuating local field at the nucleus via both the isotropic and anisotropic hyperfine interactions. We can therefore rewrite the ensemble average of the double commutator of spin operators as follows.

For computing electronic relaxation, we note that the relaxation of the nucleus has no effect on the relaxation of the electrons, and so we rewrite the double commutator by removing both the time dependence from $\hat{T}_{l-m}^{(n)}$, and the ensemble average to give:

$$\overline{\left[\hat{T}_{l-m}^{(n)}(t), \left[\hat{T}_{l-m}^{(n')}(t-\tau)^\dagger, \hat{\rho}^T(t) - \hat{\rho}_0 \right] \right]} = \left[\hat{T}_{l-m}^{(n)}, \left[\left(\hat{T}_{l-m}^{(n')} \right)^\dagger, \hat{\rho}^T(t) - \hat{\rho}_0 \right] \right]. \quad (8.21)$$

Electronic relaxation is discussed in section 8.4. The situation for nuclear relaxation is more complicated. Here both the τ -dependence and ensemble average are factored out into the reduced electronic relaxation correlation function $g_{l-mmn'}^S(\tau)$, and the double commutator is rewritten as

$$\overline{\left[\hat{T}_{l-m}^{(n)}(t), \left[\hat{T}_{l-m}^{(n')}(t-\tau)^\dagger, \hat{\rho}^T(t) - \hat{\rho}_0 \right] \right]} = \left[\hat{T}_{l-m}^{(n)}, \left[\left(\hat{T}_{l-m}^{(n')} \right)^\dagger, \hat{\rho}^T(t) - \hat{\rho}_0 \right] \right] g_{l-mmn'}^S(\tau). \quad (8.22)$$

We have acknowledged that $g_{l-mmn'}^S(\tau)$, in general, depends on the rank l , order $-m$, and the indices n and n' , as the associated electronic spin operators relax at different rates depending on whether they represent coherences (\hat{S}_\pm or equivalently $\hat{S}_{1\pm 1}$), or populations (\hat{S}_z or equivalently \hat{S}_{10}). This in turn affects the correlation function. As is the case for chemical exchange, electronic relaxation is able to induce nuclear relaxation via the isotropic hyperfine interaction as well as the anisotropic interaction. Relaxation via the isotropic part is referred to as *scalar relaxation of the second kind* [183].

8.2.5 The nuclear relaxation superoperator

Now that we have defined the reduced correlation functions above we can write the Redfield differential equation for the nuclear PRE from Equation 8.14 as

$$\frac{d\hat{\rho}^T(t)}{dt} = -\hat{\Gamma} \left(\hat{\rho}^T(t) - \hat{\rho}_0 \right), \quad (8.23)$$

where $\hat{\Gamma}$ is the relaxation superoperator which takes the form

$$\begin{aligned} \hat{\Gamma}\hat{O} &= \frac{1}{\hbar^2} \sum_{lmmn'} \frac{1}{2l+1} \exp[i(\omega_{-m}^{(n)} - \omega_{-m}^{(n')})t] \left[\hat{T}_{l-m}^{(n)}, \left[(\hat{T}_{l-m}^{(n')})^\dagger, \hat{O} \right] \right] \\ &\times \int_0^\infty g_l^M(\tau) g_l^R(\tau) g_{l-mn'}^S(\tau) \exp(i\omega_{-m}^{(n')}\tau) d\tau \sum_\mu |\tilde{K}_{l\mu}|^2. \end{aligned} \quad (8.24)$$

This expression emphasizes that the relaxation superoperator acts on an operator \hat{O} to produce a new operator $\hat{\Gamma}\hat{O}$. The integral over τ contains only the product of the reduced correlation functions as only these are functions of τ . The integral is complex, but is dominated by the real and even part which contributes to the relaxation rate. The smaller imaginary and odd part is responsible for a relaxation-induced shift in the resonance frequency [95], which is not considered further here. We therefore change the lower limit of integration from 0 to $-\infty$ and introduce a factor of 1/2.

Equation 8.24 contains a number of terms that oscillate during t at frequency $\omega_{-m}^{(n)} - \omega_{-m}^{(n')}$. The terms where this frequency is non-zero are non-secular and are expected to not contribute significantly to the relaxation rate if the oscillation is on a timescale that is much shorter than the relaxation times, as the net contribution averages to zero. We therefore choose to retain only the secular terms, for which $\omega_{-m}^{(n)} = \omega_{-m}^{(n')}$. For spin systems in which all the spins have widely separated Larmor frequencies, such as an effective electronic spin coupled to a single nucleus, the secular approximation is made by setting $n' = n$. The secular relaxation superoperator is therefore

$$\hat{\Gamma}\hat{O} = \frac{1}{2\hbar^2} \sum_{lmm} \frac{1}{2l+1} \left[\hat{T}_{l-m}^{(n)}, \left[(\hat{T}_{l-m}^{(n)})^\dagger, \hat{O} \right] \right] j_{l-mn}(-\omega_{-m}^{(n)}) \sum_\mu |\tilde{K}_{l\mu}|^2. \quad (8.25)$$

In Equation 8.25 we have defined the reduced spectral density $j_{l-mn}(\omega)$ as

$$j_{l-mn}(\omega) = \int_{-\infty}^\infty g_{l-mn}(\tau) \exp(-i\omega\tau) d\tau, \quad (8.26)$$

i.e. the Fourier transform of the overall reduced correlation function $g_m(\tau)$ which is the product of the three reduced correlation functions defined above:

$$g_{l-mn}(\tau) = g_l^M(\tau) g_l^R(\tau) g_{l-mn}^S(\tau). \quad (8.27)$$

We note that both $g_{l-mn}(\tau)$ and $j_{l-mn}(\omega)$ depend on l , m , and n for the reasons given above, and that we have dropped the dependence on n' following the application of the secular approximation.

8.3 The correlation function and spectral density

We are now in a position to calculate nuclear relaxation rates using the superoperator in Equation 8.25, which is the final result of the Redfield theory. Once we have decided on the mechanism, and the associated Hamiltonian, that we wish to study all that remains is to decide on the form of the reduced correlation function, which contains all the information about the dynamics, chemical exchange, and electronic relaxation properties. There are a number of correlation functions $g(\tau_c; \tau)$ that can be applied depending on the details of the dynamics of the system [95]. However we use the simplest, which is an exponential decay

$$g(\tau_c; \tau) = \exp(-|\tau|/\tau_c), \quad (8.28)$$

where τ_c is the correlation time. This form of the reduced correlation function can be rationalised for unrestricted rotational motion of the system by using the principles of rotational diffusion as described by Fick's law [95], and has been used to describe the relaxation due to overall tumbling of small- to large-sized molecules in an isotropic solution. We also assume that the correlation functions describing the effects of chemical exchange and electron relaxation have the form of an exponential decay, but with different correlation times.

The reduced spectral density $j(\tau_c; \omega)$ is the Fourier transform of $g(\tau_c; \tau)$:

$$j(\tau_c; \omega) = \int_{-\infty}^{\infty} g(\tau_c; \tau) \exp(-i\omega\tau) d\tau \quad (8.29)$$

$$= \frac{2\tau_c}{1 + \omega^2\tau_c^2}. \quad (8.30)$$

This is a Lorentzian function, examples of which are plotted as a function of the correlation time, and for particular frequencies, in Figure 8.3 (a). The spectral density, and hence its contribution to the relaxation rate, is at a maximum when $|\omega\tau_c| = 1$, where $j(\tau_c; \omega)$ takes the value $|1/\omega|$.

One regime of particular interest is the *extreme-narrowing limit* where the correlation time is sufficiently

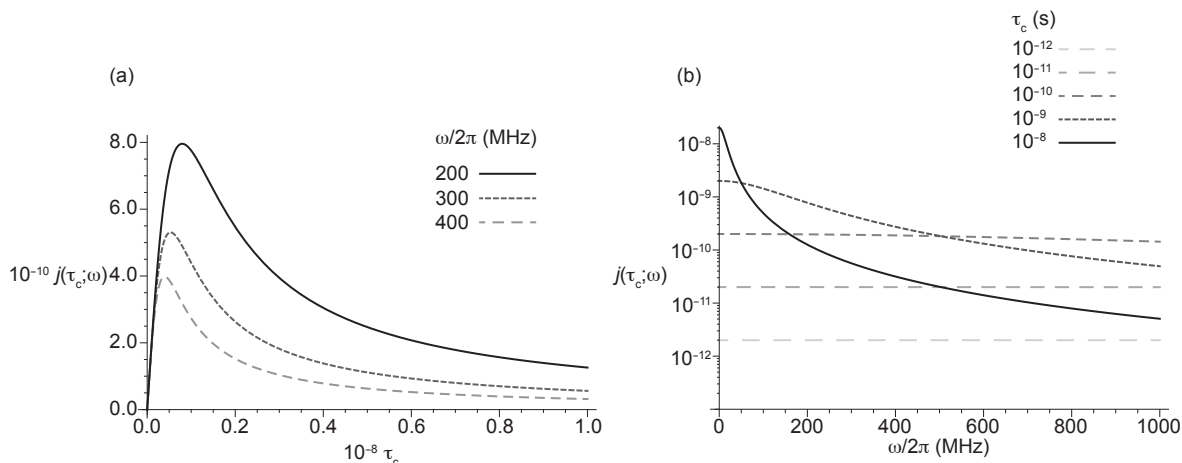


Figure 8.3: Plots of reduced spectral densities $j(\tau_c; \omega)$ as a function of (a) the correlation time τ_c , and (b) the frequency ω . The expression for the reduced spectral density is given by Equation 8.30. In (a) three plots are shown for the frequencies of 200, 300, and 400 MHz. In each case the maximum value of $j(\tau_c; \omega)$ occurs when $|\omega\tau_c| = 1$ and is equal to $|1/\omega|$. In (b) the plots are for the five values of τ_c of 10^{-12} , 10^{-11} , 10^{-10} , 10^{-9} , and 10^{-8} s.

short that $|\omega\tau_c| \ll 1$. This situation is encountered, for example, in the unrestricted tumbling of small molecules in solution. In this limit the spectral density is equal to

$$j(\tau_c; \omega) \approx 2\tau_c, \quad (8.31)$$

and is independent of the frequency ω . This is shown in Figure 8.3 (b), where the reduced spectral density is plotted against frequency for five particular correlation times. For correlation times up to 10 ps we are in the extreme-narrowing limit, and so we see no variation of the reduced spectral density with frequencies of up to 1 GHz, as expected.

Another regime of interest is the *spin-diffusion limit* in which the correlation time is sufficiently long so that $|\omega\tau_c| \gg 1$. In this limit the spectral density has the approximate expression

$$j(\tau_c; \omega) \approx \frac{2}{\omega^2\tau_c}, \quad (8.32)$$

which decreases to zero at longer correlation times and larger frequencies. This is shown in Figure 8.3 (b) for correlation times of 1 ns and above, where we see a decrease in the reduced spectral density with increasing

frequency.

8.3.1 A note on terminology for motional regimes

We have hitherto encountered three different regimes within which we have defined the timescale of dynamic processes as corresponding to either “fast” or “slow” dynamics. Before we continue further, it is worth taking the time to properly define what these terms actually mean. Of course, the terms “fast” and “slow” are only meaningful if they are quoted relative to something, usually the size of an interaction, or another timescale.

The first use of these terms we encountered was in the discussion on the validity of the Redfield theory. Here we defined the motional narrowing limit in Equation 8.6, where $\Omega\tau_c \ll 1$. This limit is also known as the *fast-motion limit*, where “fast” means that the correlation time must be much shorter than the inverse of the strength of the fluctuating interaction. If this condition is met, the Redfield theory is valid. The other regime $\Omega\tau_c \gg 1$ is known as the *slow-motion limit*, which is explored in more detail in chapter 9. The electronic spin interactions are usually much larger than nuclear spin interactions, and so the absolute timescales associated with “fast” and “slow” motions are different for electronic and nuclear relaxation, with the motional-narrowing limit usually violated at shorter correlation times for the former.

The second use of “fast” and “slow” pertains only to nuclear relaxation, as it refers to the timescale of the rotational diffusion processes that modulate the spin-dipolar hyperfine interaction compared to the electronic relaxation time constants. Here we define the *fast-rotation limit* as $\tau_r \ll T_{1e}, T_{2e}$, where rotational diffusion is faster than electronic relaxation, and the *slow-rotation limit* where $\tau_r \gg T_{1e}, T_{2e}$. Both cases correspond to situations where nuclear relaxation is described within the Redfield limit. This distinction is important as, under high-field conditions, it defines which description of nuclear relaxation is appropriate. We will see that, in the fast-rotation limit, the correct description is that in section 8.6, leading to the Solomon–Bloembergen–Morgan equations. In the slow-rotation limit, however, we need to employ the Curie mechanism in section 8.7.

The final classification of motional regimes is described earlier in this section, and refers to the size of the correlation time compared to the inverse of the frequency ω that appears in the spectral density. The *extreme-narrowing limit* is defined as $|\omega|\tau_c \ll 1$, where the correlation time is much shorter than the period of Larmor precession. By contrast, the *spin-diffusion limit* is defined for longer correlation times such that $|\omega|\tau_c \gg 1$. This distinction is important as it allows us to simplify the spectral densities in these regimes. We

note that the frequency ω describes the size of the dominant coherent term \hat{H}_0 in the total Hamiltonian, and so is much larger than the frequency describing the strength of the perturbing interaction $\hat{H}_1(t)$, i.e. $|\omega| \gg |\Omega|$. This implies that the extreme-narrowing limit always falls in the motional-narrowing regime, and that the spin-diffusion limit may do too.

8.4 Electronic relaxation

We now discuss electronic relaxation very briefly. One point that must be made very clear at the outset is that Redfield theory does not provide an adequate description of the relaxation of electrons in the majority of systems due to the larger magnitude of the interactions involved compared to nuclear relaxation, which means that the motional-narrowing condition in Equation 8.6 is violated at shorter correlation times [95]. Nevertheless there are some systems for which Redfield theory is applicable, such as highly-symmetric metal environments in which the anisotropic interactions are somewhat smaller. We therefore describe how Redfield theory may be applied in these cases.

The Hamiltonian $\hat{H}_1(t)$ that gives rise to electron relaxation may be written as

$$\hat{H}_1(t) = \mu_B \mathbf{B}_0 \cdot \mathbf{g}(t) \cdot \hat{\mathbf{S}} + \hat{\mathbf{S}} \cdot \mathbf{A}(t) \cdot \hat{\mathbf{I}} + \hat{\mathbf{S}} \cdot \mathbf{D}(t) \cdot \hat{\mathbf{S}}, \quad (8.33)$$

which we recognise as a standard EPR Hamiltonian in which the time dependence has been explicitly indicated in the g -tensor $\mathbf{g}(t)$, hyperfine tensor $\mathbf{A}(t)$, and ZFS tensor $\mathbf{D}(t)$. The time dependence is due to stochastic changes in the orientations of the tensors, in addition to changes in the sizes of the PAF components due to chemical exchange and other random processes. The dominant relaxation source for metal ions with $S = 1/2$ in high external fields is the g -tensor, with an important example being the Cu^{2+} ion. The majority of ions are of spin $S > 1/2$, and for these relaxation is predominantly due to the ZFS interaction, which is the case we focus on here. From Equation 8.25 the Redfield relaxation superoperator $\hat{\Gamma}_S$ is equal to

$$\hat{\Gamma}_S \hat{\mathcal{O}} = \frac{1}{10\hbar^2} \sum_{mn} \left[\hat{\mathcal{S}}_{2-m}^{(n)}, \left[\left(\hat{\mathcal{S}}_{2-m}^{(n)} \right)^\dagger, \hat{\mathcal{O}} \right] \right] j(-\omega_{-m}^{(n)}) \sum_{\mu} |\tilde{D}_{2\mu}|^2, \quad (8.34)$$

for which the relevant spin operators $\hat{\mathcal{S}}_{2m}^{(n)}$ and frequencies $\omega_m^{(n)}$ are given in Table 8.1. The spectral density function $j(\omega)$ is independent of m .

m	$\hat{S}_{2m}^{(n)}$ $n = 1$	$\omega_m^{(n)}$ $n = 1$
0	$\sqrt{\frac{1}{6}} (3\hat{S}_z^2 - S(S+1)) \hat{1}$	0
± 1	$\mp \frac{1}{2} (\hat{S}_z \hat{S}_\pm + \hat{S}_\pm \hat{S}_z)$	$\pm \omega_S$
± 2	$\frac{1}{2} \hat{S}_\pm^2$	$\pm 2\omega_S$

Table 8.1: The spin operators $\hat{S}_{2m}^{(n)}$ and frequencies $\omega_m^{(n)}$ for the ZFS interaction used in the calculation of the electron relaxation rates.

It was shown by Bloembergen and Morgan [98] that, for hydrated first-row transition-metal ions with $S = 1$ at high magnetic field, the Redfield master equation for longitudinal (spin–lattice) relaxation can be written in the following form:

$$\frac{dS_z(t)}{dt} = -\frac{1}{T_{1e}} (S_z(t) - S_{z,0}), \quad (8.35)$$

where $S_z(t)$ is the ensemble average of the expectation value of \hat{S}_z at time t (note the lack of the ‘hat’ in the former), $S_{z,0}$ is the corresponding equilibrium value, and T_{1e} is the electron longitudinal (spin–lattice) relaxation time constant. This equation can be solved to give a mono-exponential expression for $S_z(t)$:

$$S_z(t) = (S_z(0) - S_{z,0}) \exp(-t/T_{1e}) + S_{z,0}, \quad (8.36)$$

where T_{1e} is calculated from the expectation value of $\hat{\Gamma}_S$ in the state $|\hat{S}_z\rangle$ of Liouville space:

$$\frac{1}{T_{1e}} = \frac{(\hat{S}_z | \hat{\Gamma}_S | \hat{S}_z)}{(\hat{S}_z | \hat{S}_z)} \quad (8.37)$$

$$= \frac{\text{Tr}_S (\hat{S}_z \hat{\Gamma}_S \hat{S}_z)}{\text{Tr}_S (\hat{S}_z^2)}. \quad (8.38)$$

The notation $(\hat{S}_z | \hat{\Gamma}_S | \hat{S}_z)$ represents the inner product in Liouville space, which takes the explicit form $\text{Tr}_S (\hat{S}_z \hat{\Gamma}_S \hat{S}_z)$, where Tr_S refers to a trace taken over the states of the S -spin manifold.

The transverse (spin–spin) relaxation time constant T_{2e} of the electron can be calculated in a similar way. The ensemble average of the expectation value of the operators \hat{S}_\pm , which represent coherences, denoted $S_\pm(t)$, satisfy the following differential equations:

$$\frac{dS_\pm(t)}{dt} = -\frac{1}{T_{2e}} S_\pm(t), \quad (8.39)$$

which have solutions

$$S_{\pm}(t) = S_{\pm}(0) \exp(-t/T_{2e}). \quad (8.40)$$

The time constant T_{2e} is given by the following expectation value of $\hat{\Gamma}_S$:

$$\frac{1}{T_{2e}} = \frac{(\hat{S}_- | \hat{\Gamma}_S | \hat{S}_+)}{(\hat{S}_- | \hat{S}_+)} \quad (8.41)$$

$$= \frac{\text{Tr}_S (\hat{S}_- \hat{\Gamma}_S \hat{S}_+)}{\text{Tr}_S (\hat{S}_- \hat{S}_+)}. \quad (8.42)$$

As well as referring to the relaxation time constants T_{ie} , it is also common to refer to the relaxation rates R_{ie} which are simply the reciprocals of the former. Hence the electronic longitudinal and transverse rate constants are $R_{1e} = 1/T_{1e}$ and $R_{2e} = 1/T_{2e}$ respectively.

The relaxation by the ZFS interaction can be divided into two separate mechanisms. The first concerns metal ions in a cubic coordination environment, for which the ZFS tensor is zero by symmetry. However, random, time-dependent distortions of the coordination sphere can lead to instantaneous deviations from cubic symmetry, which in turn give rise to a *transient* ZFS. The second mechanism applies to metal ions in environments of symmetry lower than cubic for which there is a permanent, non-zero *static* ZFS tensor. These are considered in turn.

8.4.1 Relaxation due to the transient ZFS

The transient ZFS is characterised by quantity Δ_t^2 , which is the trace of the mean square of the interaction tensor

$$\Delta_t^2 = \bar{D}_{xx}^2 + \bar{D}_{yy}^2 + \bar{D}_{zz}^2 \quad (8.43)$$

$$= \frac{2}{3} D^2 + 2E^2, \quad (8.44)$$

where D and E are the axial and rhombic anisotropies of the transient ZFS. This expression is also equal to the sum of the square moduli of the PAF components in the expression for the Redfield superoperator

$$\sum_{\mu=-2}^{+2} |\tilde{D}_{2\mu}|^2 = \Delta_t^2. \quad (8.45)$$

The process by which the coordination shell is distorted is responsible for the modulation of the transient ZFS. We can model this process as a rapid reorientation of the PAF of the transient ZFS tensor relative to a frame fixed relative to the molecule, with the magnitudes of the anisotropies D and E remaining constant. This is the pseudo-rotation model proposed by Rubinstein et al [115]. This stochastic process is therefore characterised by a reduced correlation function $g_2(\tau)$ which is analogous to that which describes unrestricted rotational motion $g_2^R(\tau)$:

$$g_2(\tau) = g_2^R(\tau) \quad (8.46)$$

$$= \exp(-|\tau|/\tau_v), \quad (8.47)$$

where τ_v is the distortional, or pseudo-rotational, correlation time. The analogy between this stochastic distortion and the stochastic rotation of the system is the origin of the term ‘pseudo-rotation’. It has been shown that this model generates correlation times τ_v of the order of 1–10 ps [109, 123, 124], which are values consistent with efficient electronic relaxation: at 11.74 T the electronic Larmor frequency is 329 GHz, which corresponds to an optimum correlation time of $1/|\omega_S|$ of 0.5 ps.

Combining these expressions with the double commutators calculated from the operators in Table 8.1 we obtain the following expressions for T_{1e} and T_{2e} :

$$\frac{1}{T_{1e}} = \Delta_t^2 \left[\frac{1}{10} j^R(\omega_S) + \frac{2}{5} j^R(2\omega_S) \right] \quad (8.48)$$

$$= \frac{\Delta_t^2}{5} \left[\frac{\tau_v}{1 + \omega_S^2 \tau_v^2} + \frac{4\tau_v}{1 + 4\omega_S^2 \tau_v^2} \right], \quad (8.49)$$

$$\frac{1}{T_{2e}} = \Delta_t^2 \left[\frac{3}{20} j^R(0) + \frac{1}{4} j^R(\omega_S) + \frac{1}{10} j^R(2\omega_S) \right] \quad (8.50)$$

$$= \frac{\Delta_t^2}{10} \left[3\tau_v + \frac{5\tau_v}{1 + \omega_S^2 \tau_v^2} + \frac{2\tau_v}{1 + 4\omega_S^2 \tau_v^2} \right], \quad (8.51)$$

where $j^R(\omega)$ is the spectral density at frequency ω that describes the distortion process.

It must be remembered that Equations 8.48–8.51 are valid only for an electronic spin $S = 1$ in the motional-narrowing limit $\Delta_t \tau_v \ll 1$. For hydrated transition-metal complexes in solution τ_v is of the order of 10^{-12} s, and so we are within the motional-narrowing limit for values of Δ_t to up approximately 0.5 cm^{-1} .

We note that T_{1e} and T_{2e} are not necessarily the same, which is an observation of electron relaxation that holds in more general cases. In the present case the two time constants only take the same value when we are in the extreme-narrowing limit $|\omega_S \tau_v| \ll 1$, where the expressions for T_{1e} and T_{2e} reduce to:

$$\frac{1}{T_{1e}} = \frac{1}{T_{2e}} = \Delta_t^2 \tau_v. \quad (8.52)$$

In this regime both T_{1e} and T_{2e} are independent of field, and decrease with increasing τ_v , i.e. the relaxation rates increase as the timescale of distortion becomes longer.

8.4.2 Relaxation due to the static ZFS

The Redfield expressions for the relaxation time constants due to the static ZFS interaction are analogous to those calculated in Equations 8.48–8.51 for the transient ZFS, with two important differences. Firstly we replace Δ_t with the trace of the square of the permanent ZFS interaction tensor Δ_s , which has the form

$$\Delta_s^2 = \frac{2}{3}D^2 + 2E^2. \quad (8.53)$$

Secondly we ascribe the modulation of the static ZFS to actual random reorientation of the tensor, a process which is described by the correlation function $g_2^R(\tau)$, so that $g_2(\tau)$ is given by

$$g_2(\tau) = g_2^R(\tau) \quad (8.54)$$

$$= \exp(-|\tau|/\tau_R), \quad (8.55)$$

and τ_R is the corresponding dynamic correlation time. The time constants T_{1e} and T_{2e} are now

$$\frac{1}{T_{1e}} = \Delta_s^2 \left[\frac{1}{10} j^R(\omega_S) + \frac{2}{5} j^R(2\omega_S) \right] \quad (8.56)$$

$$= \frac{\Delta_s^2}{5} \left[\frac{\tau_R}{1 + \omega_S^2 \tau_R^2} + \frac{4\tau_R}{1 + 4\omega_S^2 \tau_R^2} \right], \quad (8.57)$$

$$\frac{1}{T_{2e}} = \Delta_s^2 \left[\frac{3}{20} j^R(0) + \frac{1}{4} j^R(\omega_S) + \frac{1}{10} j^R(2\omega_S) \right] \quad (8.58)$$

$$= \frac{\Delta_s^2}{10} \left[3\tau_R + \frac{5\tau_R}{1 + \omega_S^2 \tau_R^2} + \frac{2\tau_R}{1 + 4\omega_S^2 \tau_R^2} \right]. \quad (8.59)$$

Once again Equations 8.56–8.59 are only valid in the motional-narrowing limit. However this condition is much more difficult to fulfil than for the transient ZFS, as the dynamic correlation time is usually orders of magnitude longer than 10^{-12} s, and so the theory is only valid for metal ions such as Mn^{2+} , which has a symmetrical electron configuration of $3d^5$ and therefore a small ZFS.

8.4.3 Beyond the simple Redfield approximation

The theory of Bloembergen and Morgan for describing electron relaxation has two important shortcomings, which are that the resulting relaxation time constants are valid only for $S = 1$ and in the Redfield limit. The first limitation is important because, as shown by Rubinstein et al., electronic relaxation is multi-exponential for spins $S \geq 3/2$ even within the Redfield limit, provided we are not inside the extreme-narrowing regime [115]. In such cases the multi-exponential form of the relaxation curves must be accounted for when considering both electronic relaxation and the form of the correlation function when calculating the PRE. However, for the latter, we may be able to approximate the correlation function with a mono-exponential decay containing a correlation time τ_S that represents the best fit to the true multi-exponential electronic relaxation curve. The regime outside which Redfield theory does not apply is referred to as the slow-motion regime. An improved model of electronic relaxation for $S \geq 1$, comprising the effects of slow and fast motion, and higher-order ZFS effects has been proposed by Rast et al. and applied to Gd^{3+} complexes in solution [116]. Some of these features are discussed in more detail in chapter 9.

8.4.4 Other electronic relaxation mechanisms involving spin-orbit coupling

The preceding discussion has focussed both on the motional modulation of the anisotropic electronic spin interactions, such as the g -anisotropy and particularly the static ZFS, and the collisional distortion of the coordination geometry, leading to the transient ZFS. Both the ZFS and g -anisotropy are dominated by SO coupling effects, with the result that both interactions increase in size with the strength of SO coupling. Therefore we would expect both of the electronic relaxation mechanisms to become more efficient with increasing size of the SO interaction. This is borne out in the observation that, for first-row transition metal ions subject to a small SO coupling interaction, typical T_{1e} values are of the order 10^{-12} – 10^{-8} s, whilst lanthanide ions with significantly larger SO coupling experience shorter T_{1e} values of 10^{-14} – 10^{-12} s, the exception being Gd^{3+} which has a spatially non-degenerate electronic state.

In the solid state, where the system lattice experiences little, or possibly no, rotational motion, we need another mechanism to account for electronic relaxation. One mechanism that has been proposed is the transition between vibrational energy levels, often referred to as phonons. Phonons occur on timescales that are orders of magnitude shorter than rotational diffusion, and which are too short to contribute directly to nuclear relaxation in an efficient manner [254]. However they are more efficient at inducing electronic relaxation [119], where the relaxation rates are highest when the correlation time is of the order of $|1/\omega_S|$.

For metal ions with non-zero orbital angular momentum, there is an interaction between the orbital angular momentum and the lattice which is modulated by the phonons. This requires phonons with energies that match the transition energies between the electronic spin levels, and can occur via three principal mechanisms [15]. The first is the direct transition between electronic spin states of the ground electronic manifold [255], and occurs only when the phonon energy matches the electronic Zeeman energy, as shown in Figure 8.4 (a). It is the least important mechanism at high temperature, where the phonon energies are generally too large for the required electronic spin transition, and this process only becomes significant at temperatures of the order of 10 K. The second process is due to the Raman effect [255, 256], where two phonons simultaneously interact with the spin system, both of which are of energy that is too large for the spin transition. However their energy difference is equal to the spin transition energy, thus allowing the spin transition to take place. This is shown in Figure 8.4 (b). The final mechanism is due to the Orbach process where the electronic spin has low-lying excited states [256]. This process allows the coupling of the electronic spin to a higher-energy phonon, which causes a transition from an electronic state in the ground manifold to

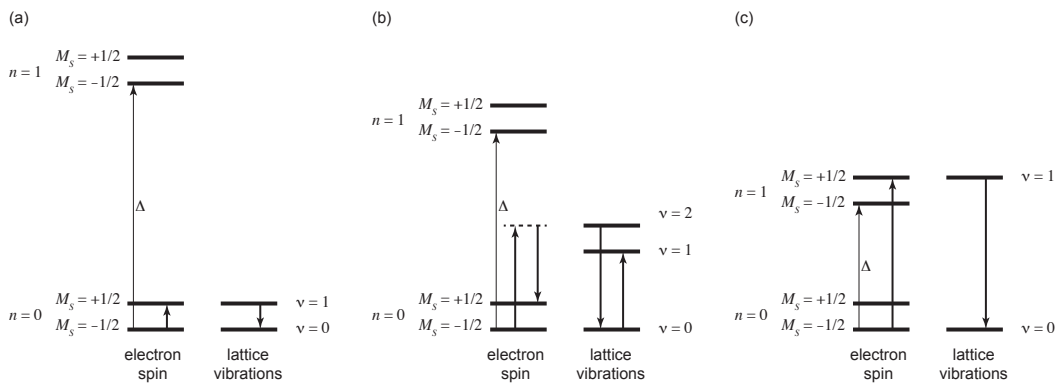


Figure 8.4: The mechanisms of electronic spin transitions induced by energy exchange between the spin and the lattice vibrational states. The direct process is illustrated in (a) in which the transition from the lower energy spin state to a higher spin state in the ground electronic manifold $n = 0$ occurs with absorption of energy that is emitted from an excited lattice vibrational state $\nu = 1$ to a lower state, here the ground state $\nu = 0$. The separation of this phonon must equal the electronic spin transition energy. The Raman process is shown in (b). Here two lattice phonons simultaneously interact with the electronic spin. The difference in the energies of these phonons is exactly equal to the energy required for the electronic spin transition. In (c) is illustrated the Orbach process. The excited electronic manifold $n = 1$ is relatively low-lying, so that the transition energy between the lattice states $\nu = 0$ and $\nu = 1$ is equal to the separation between the spin state $M_S = -1/2$ in the ground manifold $n = 0$, and the spin state $M_S = +1/2$ in the low-lying excited manifold $n = 1$. The latter transition is therefore caused by interaction with the corresponding lattice phonon. The energy parameter Δ is the separation between the ground $n = 0$ and first-excited $n = 1$ spin manifolds, and the lattice vibrational states are labelled with the vibrational quantum number ν .

a state in a higher-energy manifold, as shown in Figure 8.4 (c). This is usually the fastest mechanism for electronic transitions in the high-temperature limit.

8.5 Nuclear relaxation

Having outlined some of the difficulties associated with electronic relaxation, we now move onto the main topic of this chapter, which is the Redfield description of the PRE. The source of the PRE is the hyperfine interaction with the unpaired electrons, and so we can write down the incoherent time-dependent Hamiltonian $\hat{H}_1(t)$ as

$$\hat{H}_1(t) = \hat{S}(t) \cdot \mathbf{A}(t) \cdot \hat{I}, \quad (8.60)$$

where we have acknowledged that the time dependence is due to both modulation of the hyperfine coupling tensor $\mathbf{A}(t)$ and the variation of the electronic spin operator $\hat{S}(t)$ due to electronic relaxation. The spin operators \hat{T}_{l-m} used to describe the interaction are formed by the direct product of the I -spin and S -spin operators and are given by

$$\hat{T}_{l-m} = \sum_{q_1, q_2} \langle 11q_1q_2 | l-m \rangle \hat{I}_{1q_1} \hat{S}_{1q_2}, \quad (8.61)$$

where each term is only non-zero if $q_1 + q_2 = -m$. The expression for the Redfield relaxation superoperator partitions these basis operators into operators $\hat{T}_{l-m}^{(n)}$ that are labelled with an index n , and which evolve under different frequencies on transformation into the interaction representation of \hat{H}_0 . In terms of the direct product notation, for each order m the index n refers to a unique pair of one-spin orders q_1 and q_2 , i.e. $n \equiv n(q_1, q_2)$, and so we are able to write $\hat{T}_{l-m}^{(n)}$ as

$$\hat{T}_{l-m}^{(n)} = \langle 11q_1q_2 | l-m \rangle \hat{I}_{1q_1} \hat{S}_{1q_2}. \quad (8.62)$$

The Hermitian conjugate of $\hat{T}_{l-m}^{(n)}$ is given by

$$\left(\hat{T}_{l-m}^{(n)} \right)^\dagger = \langle 11q_1q_2 | l-m \rangle \hat{I}_{1q_1}^\dagger \hat{S}_{1q_2}^\dagger \quad (8.63)$$

$$= (-1)^m \langle 11q_1q_2 | l-m \rangle \hat{I}_{1-q_1} \hat{S}_{1-q_2}. \quad (8.64)$$

m	$\hat{T}_{2m}^{(n)}$			$\omega_m^{(n)}$			τ_S		
	$n=1$	$n=2$	$n=3$	$n=1$	$n=2$	$n=3$	$n=1$	$n=2$	$n=3$
0	$\sqrt{\frac{2}{3}}\hat{I}_z\hat{S}_z$	$-\frac{1}{2}\sqrt{\frac{1}{6}}\hat{I}_+\hat{S}_-$	$-\frac{1}{2}\sqrt{\frac{1}{6}}\hat{I}_-\hat{S}_+$	0	$\omega_I - \omega_S$	$-\omega_I + \omega_S$	T_{1e}	T_{2e}	T_{2e}
± 1	$\mp\frac{1}{2}\hat{I}_\pm\hat{S}_z$	$\mp\frac{1}{2}\hat{I}_z\hat{S}_\pm$	—	$\pm\omega_I$	$\pm\omega_S$	—	T_{1e}	T_{2e}	—
± 2	$\frac{1}{2}\hat{I}_\pm\hat{S}_\pm$	—	—	$\pm(\omega_I + \omega_S)$	—	—	T_{2e}	—	—

Table 8.2: The spin operators $\hat{T}_{2m}^{(n)}$, frequencies $\omega_m^{(n)}$, and electron correlation times τ_S for the spin-dipolar interaction used in the calculation of the PRE.

m	$\hat{T}_{00}^{(n)}$			$\omega_0^{(n)}$			τ_S		
	$n=1$	$n=2$	$n=3$	$n=1$	$n=2$	$n=3$	$n=1$	$n=2$	$n=3$
0	$-\sqrt{\frac{1}{3}}\hat{I}_z\hat{S}_z$	$-\frac{1}{2}\sqrt{\frac{1}{3}}\hat{I}_+\hat{S}_-$	$-\frac{1}{2}\sqrt{\frac{1}{3}}\hat{I}_-\hat{S}_+$	0	$\omega_I - \omega_S$	$-\omega_I + \omega_S$	T_{1e}	T_{2e}	T_{2e}

Table 8.3: The spin operators $\hat{T}_{00}^{(n)}$, frequencies $\omega_0^{(n)}$, and electron correlation times τ_S for the Fermi-contact interaction used in the calculation of the PRE.

We consider only the non-relativistic spin-dipolar and Fermi-contact interactions, the operators $\hat{T}_{lm}^{(n)}$ corresponding to which are given in Tables 8.2 and 8.3. Also given are the characteristic evolution frequencies in the interaction representation, and the electron correlation times used in the electron correlation functions.

Using Equations 8.62 and 8.63 we can write the double commutator in the Redfield superoperator as

$$\overline{\left[\hat{T}_{l-m}^{(n)}(t), \left[\hat{T}_{l-m}^{(n)}(t-\tau)^\dagger, \hat{\rho}^T(t) - \hat{\rho}_0\right]\right]} = (-1)^m \langle 11q_1q_2|l-m\rangle^2 \overline{\left[\hat{I}_{1q_1}\hat{S}_{1q_2}(t), \left[\hat{I}_{1-q_1}\hat{S}_{1-q_2}(t-\tau), \hat{\rho}^T(t) - \hat{\rho}_0\right]\right]} \quad (8.65)$$

$$= (-1)^m \langle 11q_1q_2|l-m\rangle^2 \left\{ \hat{I}_{1q_1} \left[\hat{I}_{1-q_1}, \hat{\rho}^T(t) - \hat{\rho}_0 \right] \overline{\left[\hat{S}_{1q_2}(t), \hat{S}_{1-q_2}(t-\tau)\right]} \right. \\ \left. + \left[\hat{I}_{1q_1}, \left[\hat{I}_{1-q_1}, \hat{\rho}^T(t) - \hat{\rho}_0 \right] \right] \overline{\left[\hat{S}_{1-q_2}(t-\tau)\hat{S}_{1q_2}(t)\right]} \right\}, \quad (8.66)$$

where to go to the last line we have used the fact that the rapid electronic relaxation means that only the electronic spin operators are time-dependent on the timescale we are interested in, and so the ensemble average is only over these operators. As before, we can factor out the τ -dependence and rewrite the ensemble

averages of the products of the electronic spin operators as

$$\overline{\hat{S}_{1\pm 1}(t)\hat{S}_{1\mp 1}(t-\tau)} = \overline{\hat{S}_{1\pm 1}(t-\tau)\hat{S}_{1\mp 1}(t)} = \hat{S}_{1\pm 1}\hat{S}_{1\mp 1}g_{\pm 1}^S(\tau) \quad (8.67)$$

$$= -\frac{1}{2}\hat{S}_{\pm}\hat{S}_{\mp}g_{\pm 1}^S(\tau), \quad (8.68)$$

$$\overline{\hat{S}_{10}(t)\hat{S}_{10}(t-\tau)} = \hat{S}_{10}^2g_0^S(\tau) \quad (8.69)$$

$$= \hat{S}_z^2g_0^S(\tau). \quad (8.70)$$

Here we have used the fact that operators representing electronic coherences such as $\hat{S}_{1\pm 1}$, or equivalently \hat{S}_{\pm} , relax according to the electronic transverse relaxation time constant, and that this is represented by a reduced electronic correlation function $g_{\pm 1}^S(\tau)$. Likewise the longitudinal electronic spin operator \hat{S}_{10} , or equivalently \hat{S}_z , relaxes according to the electronic longitudinal relaxation time constant, and we represent this by a reduced electronic correlation function $g_0^S(\tau)$. The double commutator is therefore

$$\begin{aligned} \overline{\left[\hat{T}_{l-m}^{(n)}(t), \left[\hat{T}_{l-m}^{(n)}(t-\tau)^\dagger, \hat{\rho}^T(t) - \hat{\rho}_0\right]\right]} &= (-1)^m \langle 11q_1q_2 | l-m \rangle^2 \left\{ \hat{I}_{1q_1} \left[\hat{I}_{1-q_1}, \hat{\rho}^T(t) - \hat{\rho}_0 \right] \left[\hat{S}_{1q_2}, \hat{S}_{1-q_2} \right] \right. \\ &\quad \left. + \left[\hat{I}_{1q_1}, \left[\hat{I}_{1-q_1}, \hat{\rho}^T(t) - \hat{\rho}_0 \right] \right] \hat{S}_{1-q_2} \hat{S}_{1q_2} \right\} g_{q_2}^S(\tau), \end{aligned} \quad (8.71)$$

where we have labelled the reduced electronic correlation function with the index q_2 which indicates the order of the rank-one S -spin spherical tensor operator.

The overall reduced correlation function $g_{lq_2}(\tau)$, which combines all the sources of fluctuating fields experienced by the nucleus, is labelled by two indices l and q , and is given by the product of three correlation functions:

$$g_{lq}(\tau) = g^M(\tau)g_l^R(\tau)g_q^S(\tau). \quad (8.72)$$

The first function $g^M(\tau)$ in the product is the reduced correlation function that encodes the effects of chemical exchange, and takes the simple exponential form:

$$g^M(\tau) = \exp(-|\tau|/\tau_M), \quad (8.73)$$

where τ_M is the chemical exchange correlation time. The second factor $g_l^R(\tau)$ is the reduced dynamic, or rotational, correlation function. It depends on the spatial rank of the interaction tensor l and takes the

following form:

$$g_l^R(\tau) = \begin{cases} \exp(-|\tau|/\tau_R), & l = 2, \\ 1, & l = 0. \end{cases} \quad (8.74)$$

For spatial ranks $l = 2$ the correlation function is a simple exponential decay with rotational correlation time τ_R . By contrast spatially isotropic interactions with $l = 0$ are invariant to rotational diffusion, and so the corresponding correlation function is simply unity. The third factor in the overall reduced correlation function $g_q^S(\tau)$ is due to electronic relaxation. The index q takes values of 0 or ± 1 in order to distinguish between the longitudinal and transverse relaxation of the unpaired electrons respectively, with the correlation functions being given by:

$$g_0^S(\tau) = \exp(-|\tau|/T_{1e}), \quad (8.75)$$

$$g_{\pm 1}^S(\tau) = \exp(-|\tau|/T_{2e}). \quad (8.76)$$

We see that $g_0^S(\tau)$ decays according to T_{1e} , and $g_{\pm 1}^S(\tau)$ decays according to T_{2e} .

The overall reduced correlation function $g_{lq}(\tau)$, and therefore the spectral density $j_{lq}(\omega)$, takes two distinct forms depending on whether the interaction in question is spatially isotropic or not. For spatially isotropic interactions, these are

$$g_{0q}(\tau) = \exp(-|\tau|/\tau_{E,q}), \quad (8.77)$$

$$j_{0q}(\omega) = \frac{2\tau_{E,q}}{1 + \omega^2\tau_{E,q}^2}, \quad (8.78)$$

where the effective correlation times $\tau_{E,q}$ are equal to

$$\tau_{E,q}^{-1} = \tau_M^{-1} + T_{qe}^{-1}, \quad q = 1, 2 \quad (8.79)$$

and the index q distinguishes between electronic longitudinal and electronic transverse relaxation. We note that both the chemical exchange and electronic relaxation time constants contribute to $\tau_{E,q}$, but that the rotational correlation time does not. By contrast interactions that are spatially anisotropic with spatial rank

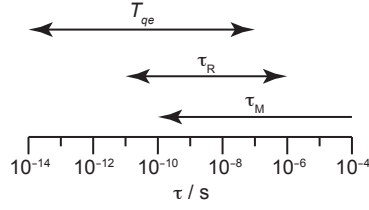


Figure 8.5: Typical timescales of the electronic relaxation times T_{qe} ($q = 1, 2$), the rotational correlation time τ_R , and the chemical exchange correlation time τ_M . Note that τ_M can extend to longer values than are shown on the scale, which are not considered here.

$l = 2$ have the following reduced correlation time and reduced spectral density:

$$g_{2q}(\tau) = \exp(-|\tau|/\tau_{c,q}), \quad (8.80)$$

$$j_{2q}(\omega) = \frac{2\tau_{c,q}}{1 + \omega^2\tau_{c,q}^2}. \quad (8.81)$$

The correlation times $\tau_{c,q}$ are still labelled by q , but now also contain contributions from τ_R as the interaction tensors are modulated by rotations of the system:

$$\tau_{c,q}^{-1} = \tau_M^{-1} + \tau_R^{-1} + T_{qe}^{-1}, \quad q = 1, 2. \quad (8.82)$$

Typical ranges of the correlation times T_{qe} , τ_R , and τ_M are shown in Figure 8.5. There is significant overlap of the timescales of the three processes, especially when we have both fast rotational diffusion and chemical exchange, but the mean values of the ranges can be ordered as $T_{qe} < \tau_R < \tau_M$ [15].

The nuclear longitudinal relaxation time constant T_1 is given by the following expectation value of the relaxation superoperator in Liouville space:

$$\frac{1}{T_1} = \frac{(\hat{I}_z | \hat{\Gamma} | \hat{I}_z)}{(\hat{I}_z | \hat{I}_z)} \quad (8.83)$$

$$= \frac{\text{Tr}_{IS}(\hat{I}_z \hat{\Gamma} \hat{I}_z)}{\text{Tr}_I(\hat{I}_z^2) \text{Tr}_S(\hat{I}_S)} \quad (8.84)$$

$$= \frac{\text{Tr}_{IS}(\hat{I}_z \hat{\Gamma} \hat{I}_z)}{\text{Tr}_I(\hat{I}_z^2) (2S + 1)}, \quad (8.85)$$

where Tr_I and Tr_S indicate traces taken over the manifold of states of the I -spin and S -spin respectively, and Tr_{IS} is a trace taken over the entire direct-product manifold of states of the combined I - S spin system. On moving from Equation 8.83 to Equation 8.84 we see that the trace of the S -spin identity operator $\hat{1}_S$ appears in the denominator. This is because the inner products appearing in the former equation are defined as sums over the direct-product manifold of states of the combined spin system. However when the operator in the inner product is a simple direct product of an I -spin operator with an S -spin operator, the trace of the product is equal to the product of the traces of the two individual operators over the two separate manifolds of I -spin and S -spin states. Since here \hat{I}_z^2 implies $\hat{I}_z^2 \otimes \hat{1}_S$, the S -spin trace is over the identity, and is equal to $\text{Tr}_S(\hat{1}_S) = 2S + 1$. Similarly the nuclear transverse relaxation time constant T_2 is given by

$$\frac{1}{T_2} = \frac{(\hat{I}_- | \hat{\Gamma} | \hat{I}_+)}{(\hat{I}_- | \hat{I}_+)} \quad (8.86)$$

$$= \frac{\text{Tr}_{IS}(\hat{I}_- \hat{\Gamma} \hat{I}_+)}{\text{Tr}_I(\hat{I}_- \hat{I}_+) (2S + 1)}. \quad (8.87)$$

As for electronic relaxation we can also define rate constants for longitudinal and transverse nuclear relaxation, which are equal to $R_1 = 1/T_1$ and $R_2 = 1/T_2$ respectively.

The traces in the numerators of Equations 8.85 and 8.87 are calculated from the trace of the operator in Equation 8.71, which is given by

$$\text{Tr}_{IS} \left\{ \overline{[\hat{T}_{l-m}^{(n)}(t), [\hat{T}_{l-m}^{(n)}(t-\tau)^\dagger, \hat{I}_a]]} \right\} = (-1)^m \langle 11q_1q_2 | l - m \rangle^2 \text{Tr}_I \left\{ [\hat{I}_{1q_1}, [\hat{I}_{1-q_1}, \hat{I}_a]] \right\} \text{Tr}_S \left\{ \hat{S}_{1-q_2} \hat{S}_{1q_2} \right\} g_{q_2}^S(\tau), \quad (8.88)$$

where $a = z$ or \pm . We have used the fact that $\text{Tr}_S[\hat{S}_{1q_2}, \hat{S}_{1-q_2}]$ is always zero for any value of q_2 . We can therefore proceed with the calculation by using the following expressions for the traces of the products of the S -spin operators:

$$\text{Tr}_S \left\{ \hat{S}_{10}^2 \right\} / (2S + 1) = S(S + 1)/3, \quad (8.89)$$

$$\text{Tr}_S \left\{ \hat{S}_{1\pm 1} \hat{S}_{1\mp 1} \right\} / (2S + 1) = -S(S + 1)/3. \quad (8.90)$$

We now examine some specific models for the PRE.

8.6 The Solomon–Bloembergen–Morgan theory of paramagnetic nuclear relaxation

The simplest and most commonly-used model for the PRE is Solomon–Bloembergen–Morgan theory. It is a non-relativistic theory, meaning that the parts of the hyperfine tensor we use in the calculation of the relaxation time constants are limited to the first-order Fermi-contact and spin-dipolar parts. In calculating the Solomon–Bloembergen–Morgan equations for T_1 and T_2 we consider the two parts of the hyperfine tensor separately, firstly focusing on the spin-dipolar part for both localised and delocalised electrons, and then on the Fermi-contact part.

8.6.1 Relaxation due to the spin-dipolar interaction with delocalized electrons

For a metal ion possessing unpaired electrons that are spatially delocalised we must calculate the sum of the squares of the PAF tensor components using the expressions in Equation 2.172. Thus the tensor can be expressed in terms of the principal component $\tilde{A}_{zz}^{\text{SD}}$, which contains an integral over all space of the electron density, and an asymmetry parameter η^{SD} that is, in general, non-zero. The sum of the squares of the tensor parameters in the PAF is therefore

$$\sum_{\mu=-2}^{+2} |\tilde{A}_{2\mu}^{\text{SD}}|^2 = \frac{1}{2} \left(3 + (\eta^{\text{SD}})^2 \right) (\tilde{A}_{zz}^{\text{SD}})^2. \quad (8.91)$$

Evaluating the expression for the Redfield relaxation superoperator, and substituting it into Equation 8.85 gives us the expression for T_1 :

$$\frac{1}{T_1} = S(S+1) \left(3 + (\eta^{\text{SD}})^2 \right) \left(\frac{\tilde{A}_{zz}^{\text{SD}}}{\hbar} \right)^2 \left[\frac{1}{60} j_{21}(\omega_I) + \frac{1}{30} j_{22}(\omega_S + \omega_I) + \frac{1}{180} j_{22}(\omega_S - \omega_I) \right] \quad (8.92)$$

$$= \frac{S(S+1) \left(3 + (\eta^{\text{SD}})^2 \right)}{90} \left(\frac{\tilde{A}_{zz}^{\text{SD}}}{\hbar} \right)^2 \left[\frac{3\tau_{c,1}}{1 + \omega_I^2 \tau_{c,1}^2} + \frac{6\tau_{c,2}}{1 + (\omega_S + \omega_I)^2 \tau_{c,2}^2} + \frac{\tau_{c,2}}{1 + (\omega_S - \omega_I)^2 \tau_{c,2}^2} \right], \quad (8.93)$$

where, to go to the second line, we have substituted in the explicit expressions for the reduced spectral densities. In addition we can calculate the PRE contribution to T_2 , which is

$$\frac{1}{T_2} = S(S+1) \left(3 + (\eta^{\text{SD}})^2\right) \left(\frac{\tilde{A}_{zz}^{\text{SD}}}{\hbar}\right)^2 \left[\frac{1}{90} j_{21}(0) + \frac{1}{60} j_{22}(\omega_S) + \frac{1}{120} j_{21}(\omega_I) + \frac{1}{60} j_{22}(\omega_S + \omega_I) + \frac{1}{360} j_{22}(\omega_S - \omega_I) \right] \quad (8.94)$$

$$= \frac{S(S+1) \left(3 + (\eta^{\text{SD}})^2\right)}{180} \left(\frac{\tilde{A}_{zz}^{\text{SD}}}{\hbar}\right)^2 \left[4\tau_{c,1} + \frac{6\tau_{c,2}}{1 + \omega_S^2 \tau_{c,2}^2} + \frac{3\tau_{c,1}}{1 + \omega_I^2 \tau_{c,1}^2} + \frac{6\tau_{c,2}}{1 + (\omega_S + \omega_I)^2 \tau_{c,2}^2} + \frac{\tau_{c,2}}{1 + (\omega_S - \omega_I)^2 \tau_{c,2}^2} \right]. \quad (8.95)$$

8.6.2 Relaxation due to the spin-dipolar interaction with localised electrons (the Solomon mechanism)

When the nucleus is sufficiently far from the paramagnetic centre, typically at distances of more than 4 Å, we can safely approximate the unpaired electrons as being localised at the paramagnetic ion, and therefore treat them as point dipole moments of spin S . The dipolar coupling interaction then simplifies to the interaction between an electronic point dipole and a nuclear point dipole, allowing us to write the spin-dipolar tensor parameters as

$$\tilde{A}_{zz}^{\text{SD}} = 2b_{SI}, \quad (8.96)$$

$$\eta^{\text{SD}} = 0, \quad (8.97)$$

where b_{SI} is the dipolar coupling constant for the interaction between the two point dipoles, which is given by Equation 2.175. The T_1 and T_2 time constants are then calculated by substituting these values into Equations 8.93 and 8.95. This results in the familiar expression for T_1

$$\frac{1}{T_1} = S(S+1) \left(\frac{b_{SI}}{\hbar}\right)^2 \left[\frac{1}{5} j_{21}(\omega_I) + \frac{2}{5} j_{22}(\omega_S + \omega_I) + \frac{1}{15} j_{22}(\omega_S - \omega_I) \right] \quad (8.98)$$

$$= \frac{2}{15} S(S+1) \left(\frac{b_{SI}}{\hbar}\right)^2 \left[\frac{3\tau_{c,1}}{1 + \omega_I^2 \tau_{c,1}^2} + \frac{6\tau_{c,2}}{1 + (\omega_S + \omega_I)^2 \tau_{c,2}^2} + \frac{\tau_{c,2}}{1 + (\omega_S - \omega_I)^2 \tau_{c,2}^2} \right], \quad (8.99)$$

and for T_2 :

$$\begin{aligned} \frac{1}{T_2} &= S(S+1) \left(\frac{b_{SI}}{\hbar} \right)^2 \left[\frac{2}{15} j_{21}(0) + \frac{1}{5} j_{22}(\omega_S) + \frac{1}{10} j_{21}(\omega_I) + \frac{1}{5} j_{22}(\omega_S + \omega_I) + \frac{1}{30} j_{22}(\omega_S - \omega_I) \right] \quad (8.100) \\ &= \frac{1}{15} S(S+1) \left(\frac{b_{SI}}{\hbar} \right)^2 \left[4\tau_{c,1} + \frac{6\tau_{c,2}}{1 + \omega_S^2 \tau_{c,2}^2} + \frac{3\tau_{c,1}}{1 + \omega_I^2 \tau_{c,1}^2} + \frac{6\tau_{c,2}}{1 + (\omega_S + \omega_I)^2 \tau_{c,2}^2} + \frac{\tau_{c,2}}{1 + (\omega_S - \omega_I)^2 \tau_{c,2}^2} \right]. \quad (8.101) \end{aligned}$$

These expressions were first calculated by Solomon, and so relaxation by the point-dipole part of the hyperfine interaction is sometimes referred to as the Solomon mechanism [96]. It is of interest to note that, once we have set $S = 1/2$ and replaced all the correlation times with the same time τ_c , these expressions are identical to those for the relaxation time constants due to the stochastic fluctuation of the dipolar coupling tensor between two nuclei in a diamagnetic molecule in solution experiencing unrestricted rotation [95, 183, 252, 257, 258].

8.6.3 Relaxation due to the Fermi-contact interaction (the Bloembergen mechanism)

The second mechanism for paramagnetic nuclear relaxation in the Solomon–Bloembergen–Morgan theory is via the isotropic Fermi-contact interaction, as first described by Bloembergen [97]. As we have seen the fluctuating local field at the nucleus can be induced by chemical exchange and electronic relaxation, so the Bloembergen mechanism comprises scalar relaxation of both the first and second kinds [183].

The calculation of the contributions to T_1 and T_2 proceeds as follows. The sum of the square modulus of the PAF tensor components reduces to a single term, which is

$$|A_{00}^{\text{FC}}|^2 = 3(A^{\text{FC}})^2, \quad (8.102)$$

where A^{FC} is the Fermi-contact coupling constant in Equation 2.171. The double commutators can now be computed in the same way as for the Solomon mechanism, which gives the following simple expression for

T_1 :

$$\frac{1}{T_1} = \frac{1}{3}S(S+1)\left(\frac{A^{\text{FC}}}{\hbar}\right)^2 j_{02}(\omega_S - \omega_I) \quad (8.103)$$

$$= \frac{2}{3}S(S+1)\left(\frac{A^{\text{FC}}}{\hbar}\right)^2 \frac{\tau_{E,2}}{1 + (\omega_S - \omega_I)^2 \tau_{E,2}^2}, \quad (8.104)$$

and likewise the following expression for T_2 :

$$\frac{1}{T_2} = \frac{1}{6}S(S+1)\left(\frac{A^{\text{FC}}}{\hbar}\right)^2 [j_{01}(0) + j_{02}(\omega_S - \omega_I)] \quad (8.105)$$

$$= \frac{1}{3}S(S+1)\left(\frac{A^{\text{FC}}}{\hbar}\right)^2 \left[\tau_{E,1} + \frac{\tau_{E,2}}{1 + (\omega_S - \omega_I)^2 \tau_{E,2}^2} \right]. \quad (8.106)$$

8.6.4 The Solomon–Bloembergen–Morgan equations

The final step in the Solomon–Bloembergen–Morgan theory is to note that the contributions from the relaxation rate constants R_i from the different mechanisms are additive, which is the result of neglecting cross-correlation between the Fermi-contact and spin-dipolar interactions. Hence we can write down the overall Solomon–Bloembergen–Morgan equation for T_1 by summing the Solomon and Bloembergen contributions, which gives [95]

$$\begin{aligned} \frac{1}{T_1} = & \frac{2}{3}S(S+1)\left(\frac{A^{\text{FC}}}{\hbar}\right)^2 \frac{\tau_{E,2}}{1 + (\omega_S - \omega_I)^2 \tau_{E,2}^2} \\ & + \frac{2}{15}S(S+1)\left(\frac{b_{SI}}{\hbar}\right)^2 \left[\frac{3\tau_{c,1}}{1 + \omega_I^2 \tau_{c,1}^2} + \frac{6\tau_{c,2}}{1 + (\omega_S + \omega_I)^2 \tau_{c,2}^2} + \frac{\tau_{c,2}}{1 + (\omega_S - \omega_I)^2 \tau_{c,2}^2} \right]. \end{aligned} \quad (8.107)$$

Similarly the corresponding expression for T_2 is [95]

$$\begin{aligned} \frac{1}{T_2} = & \frac{1}{3}S(S+1)\left(\frac{A^{\text{FC}}}{\hbar}\right)^2 \left[\tau_{E,1} + \frac{\tau_{E,2}}{1 + (\omega_S - \omega_I)^2 \tau_{E,2}^2} \right] \\ & + \frac{1}{15}S(S+1)\left(\frac{b_{SI}}{\hbar}\right)^2 \left[4\tau_{c,1} + \frac{6\tau_{c,2}}{1 + \omega_S^2 \tau_{c,2}^2} + \frac{3\tau_{c,1}}{1 + \omega_I^2 \tau_{c,1}^2} + \frac{6\tau_{c,2}}{1 + (\omega_S + \omega_I)^2 \tau_{c,2}^2} + \frac{\tau_{c,2}}{1 + (\omega_S - \omega_I)^2 \tau_{c,2}^2} \right]. \end{aligned} \quad (8.108)$$

These equations provide a description of the PRE in systems experiencing rapid rotational diffusion such that τ_R is not much longer than the electronic relaxation times T_{1e} and T_{2e} . The theory therefore applies to small complexes in solution. In situations where the dynamics are slowed so that $\tau_R, \tau_M \gg T_{1e}, T_{2e}$, the correlation times $\tau_{c,q}$ and $\tau_{E,q}$ are approximately equal to T_{qe} , so the relaxation properties of the nucleus are dominated by the electron relaxation and are essentially independent of any molecular dynamics. However this is not observed experimentally for systems undergoing sluggish rotational dynamics, such as large biomolecules in solution, a subject we return to in section 8.7. A special case of slow dynamics occurs in rigid solids, where τ_R essentially becomes infinite. This represents a violation of the Redfield theory as the observation time is no longer much greater than τ_R , and so care needs to be taken when writing down the relaxation rate constants under such conditions. This is the subject of section 8.9.

8.6.5 Shortcomings of the Solomon–Bloembergen–Morgan theory

The Solomon–Bloembergen–Morgan model presented here is the simplest possible theory of the PRE and so, inevitably, contains a number of approximations that may not be valid in all situations. The use of the point-dipole model for the unpaired electrons is questionable for distances from the paramagnetic centre of less than 4 Å [259], and deviations have been reported even for distances beyond 10 Å [260]. However, as we have seen, this simplification can be addressed relatively simply by using a more complex form of the spin-dipolar coupling tensor [261].

Additional approximations that have been made are that the reduced correlation functions are all assumed to have the form of a simple exponential decay. For the rotational correlation function, this is only true for small- to medium-sized molecules in solution. However for larger molecules, such as proteins, more sophisticated dynamic correlation functions are needed that account for simultaneous restricted rotation and internal motions, such as are used in the Lipari–Szarbo model [262]. A related problem is the assumption of mono-exponential electronic relaxation, which we have seen is generally not valid even in the Redfield limit if $S > 1$. Multi-exponential electronic relaxation, and the resulting effect on the PRE, has been treated by Westlund in the Redfield limit, and under conditions of high field so that the Zeeman interactions dominate \hat{H}_0 [263]. The resulting model is referred to as the generalised Solomon–Bloembergen–Morgan theory.

A more serious problem concerns the approximation that the processes of chemical exchange, rotational diffusion, and electronic relaxation are uncorrelated, which allows us to write the overall correlation function

as the product of three separate functions, each of which corresponds to one of these processes. This assumption probably holds when the three processes occur on very different timescales, but this is often not the case and this deficiency is not easy to repair. Nevertheless work has been performed in this area by Bertini et al. [108] and Kruk et al [109].

8.7 Curie-spin relaxation

The Solomon–Bloembergen–Morgan theory does not provide a correct description of large paramagnetic molecules with sluggish rotational diffusion where electron relaxation is the fastest stochastic process described by the correlation function. The reason for this is that we have ignored the effect of the differences in the populations of the electronic spin energy levels due to the relatively large electronic magnetic moment. It is this which is responsible for the measurable Curie spin in Equation 3.62. It was shown by Gueron [99], and Vega and Fiat [100] that in situations where electronic relaxation occurs on a much shorter timescale than the rotational processes, the primary role of the former is to generate a thermal average of the electronic spin, equal to the Curie spin, and the role of the latter is to cause a random spatial fluctuation in the hyperfine interaction to the Curie spin on a longer timescale. Given that the Curie spin is proportional to B_0 we would expect the relaxation effects due to the Curie spin to become more important at high field.

For an ensemble of spin-only transition-metal ions, the Curie spin is parallel to the external magnetic field, conventionally the z -direction. We must therefore modify the expression for the longitudinal electronic spin operator $\hat{S}_{10}(t)$, which we write as the sum of a time-independent Curie-spin term, and a fluctuating remainder $\hat{s}_{10}(t)$ with zero time average:

$$\hat{S}_{10}(t) = \langle \hat{S}_{10} \rangle \hat{1}_S + \hat{s}_{10}(t). \quad (8.109)$$

This expression indicates that the electronic spin operator $\hat{S}_{10}(t)$ fluctuates about its average value of $\langle \hat{S}_{10} \rangle \hat{1}_S$. This decomposition changes the expression of the ensemble average $\overline{\hat{S}_{10}(t)\hat{S}_{10}(t-\tau)}$ compared to that used

in the Solomon–Bloembergen–Morgan theory. The new expression is

$$\overline{\hat{S}_{10}(t)\hat{S}_{10}(t-\tau)} = \langle \hat{S}_{10} \rangle^2 \hat{I}_S + \overline{\hat{s}_{10}(t)\langle \hat{S}_{10} \rangle} + \langle \hat{S}_{10} \rangle \overline{\hat{s}_{10}(t-\tau)} + \overline{\hat{s}_{10}(t)\hat{s}_{10}(t-\tau)} \quad (8.110)$$

$$= \langle \hat{S}_{10} \rangle^2 \hat{I}_S + \overline{\hat{s}_{10}(t)\hat{s}_{10}(t-\tau)} \quad (8.111)$$

$$= \langle \hat{S}_{10} \rangle^2 \hat{I}_S + \left[\hat{S}_{10}^2 - \langle \hat{S}_{10} \rangle^2 \hat{I}_S \right] g_0^S(\tau), \quad (8.112)$$

where to go to the second line we have used the fact that $\overline{\hat{s}_{10}(t)} = 0$, and to go to the last line we have interpreted \hat{S}_{10}^2 as the difference between the squares of \hat{S}_{10} and the Curie term $\langle \hat{S}_{10} \rangle \hat{I}_S$. We see that the expression comprises two terms. The first is the Curie term $\langle \hat{S}_{10} \rangle^2 \hat{I}_S$ which, as the absence of any τ -dependence suggests, is independent of the electronic relaxation processes. This is because the effects of electronic relaxation have already been accounted for in the calculation of the Curie spin. The second term is a remainder that is affected by longitudinal electronic relaxation through the electronic correlation function $g_0^S(\tau)$. This part is similar to that in the corresponding Solomon–Bloembergen–Morgan expression, with the difference that it is reduced in size by $\langle \hat{S}_{10} \rangle^2 \hat{I}_S$.

The operators representing the coherences $\hat{S}_{1\pm 1}(t)$ are unchanged, as the transverse components of the Curie spin are zero. Therefore the ensemble average $\overline{\hat{S}_{1\pm 1}(t)\hat{S}_{1\mp 1}(t-\tau)}$ has the same expression as in the Solomon–Bloembergen–Morgan theory:

$$\overline{\hat{S}_{1\pm 1}(t)\hat{S}_{1\mp 1}(t-\tau)} = \overline{\hat{S}_{1\pm 1}(t-\tau)\hat{S}_{1\mp 1}(t)} = \hat{S}_{1\pm 1}\hat{S}_{1\mp 1}g_{\pm 1}^S(\tau) \quad (8.113)$$

$$= -\frac{1}{2}\hat{S}_{\pm}\hat{S}_{\mp}g_{\pm 1}^S(\tau). \quad (8.114)$$

We now have two new interactions to include in our calculation of the relaxation time constants in addition to those considered in the Solomon–Bloembergen–Morgan theory, the Fermi-contact and spin-dipolar interactions between the nuclear spin and the Curie spin. We therefore need two additional reduced correlation functions to describe the stochastic time dependence of these interactions, and two corresponding reduced spectral densities which we label $g_l^C(\tau)$ and $f_l^C(\omega)$, with $l = 0, 2$, respectively. The Fermi-contact interaction

to the Curie spin has the following reduced correlation function and spectral density with $l = 0$:

$$g_0^C(\tau) = \exp(-|\tau|/\tau_M), \quad (8.115)$$

$$j_0^C(\omega) = \frac{2\tau_M}{1 + \omega^2\tau_M^2}. \quad (8.116)$$

The interaction is spatially isotropic, and so the overall correlation time is simply the chemical exchange correlation time τ_M . The relaxation mechanism is therefore an example of scalar relaxation of the first kind. For the spin-dipolar interaction the reduced correlation function and spectral density, with $l = 2$, are given by

$$g_2^C(\tau) = \exp(-|\tau|/\tau_D), \quad (8.117)$$

$$j_2^C(\omega) = \frac{2\tau_D}{1 + \omega^2\tau_D^2}. \quad (8.118)$$

The interaction is spatially anisotropic, and so the correlation time τ_D is now a combination of the correlation times for the chemical exchange and the rotational diffusion of the system:

$$\tau_D^{-1} = \tau_M^{-1} + \tau_R^{-1}. \quad (8.119)$$

We recall that these interactions are not modulated by electronic relaxation, as this is already accounted for in the calculation of the Curie spin.

8.7.1 Relaxation due to the spin-dipolar interaction with delocalized electrons

We can now derive the expressions for the Curie relaxation time constants via the spin-dipolar interaction with a source of delocalized electrons. The calculation can be summarised as follows. We take the Solomon–Bloembergen–Morgan equation, and replace any term that depends on T_{1e} with two similar terms. The first term is a Curie term that is weighted by S_C^2 (where S_C denotes the Curie spin $\langle \hat{S}_{10} \rangle$) and in which $\tau_{c,1}$ is replaced with τ_D , and the second is weighted by $S(S + 1)/3 - S_C^2$ and otherwise unchanged. In addition, any

terms that depend on T_{2e} are unchanged. The new expression for T_1 is:

$$\begin{aligned} \frac{1}{T_1} &= \left(3 + (\eta^{\text{SD}})^2\right) \left(\frac{\tilde{A}_{zz}^{\text{SD}}}{\hbar}\right)^2 \left[S_C^2 \frac{1}{20} j_2^{\text{C}}(\omega_I) + \left(\frac{1}{3} S(S+1) - S_C^2\right) \frac{1}{20} j_{21}(\omega_I) \right. \\ &\quad \left. + S(S+1) \left(\frac{1}{30} j_{22}(\omega_S + \omega_I) + \frac{1}{180} j_{22}(\omega_S - \omega_I) \right) \right] \end{aligned} \quad (8.120)$$

$$\begin{aligned} &= \frac{1}{90} \left(3 + (\eta^{\text{SD}})^2\right) \left(\frac{\tilde{A}_{zz}^{\text{SD}}}{\hbar}\right)^2 \left[S_C^2 \frac{9\tau_{\text{D}}}{1 + \omega_I^2 \tau_{\text{D}}^2} + \left(\frac{1}{3} S(S+1) - S_C^2\right) \frac{9\tau_{\text{c},1}}{1 + \omega_I^2 \tau_{\text{c},1}^2} \right. \\ &\quad \left. + S(S+1) \left(\frac{6\tau_{\text{c},2}}{1 + (\omega_S + \omega_I)^2 \tau_{\text{c},2}^2} + \frac{\tau_{\text{c},2}}{1 + (\omega_S - \omega_I)^2 \tau_{\text{c},2}^2} \right) \right]. \end{aligned} \quad (8.121)$$

We can write this expression as the sum of two separate terms

$$T_1^{-1} = (T_1^{\text{C}})^{-1} + (T_1^{\text{SBM}})^{-1}, \quad (8.122)$$

where we define T_1^{C} as the Curie contribution and T_1^{SBM} as a modified Solomon–Bloembergen–Morgan contribution to the overall T_1 :

$$\frac{1}{T_1^{\text{C}}} = \left(3 + (\eta^{\text{SD}})^2\right) \left(\frac{\tilde{A}_{zz}^{\text{SD}}}{\hbar}\right)^2 \left[S_C^2 \frac{1}{20} j_2^{\text{C}}(\omega_I) \right], \quad (8.123)$$

$$\begin{aligned} \frac{1}{T_1^{\text{SBM}}} &= \left(3 + (\eta^{\text{SD}})^2\right) \left(\frac{\tilde{A}_{zz}^{\text{SD}}}{\hbar}\right)^2 \left[\left(\frac{1}{3} S(S+1) - S_C^2\right) \frac{1}{20} j_{21}(\omega_I) \right. \\ &\quad \left. + S(S+1) \left(\frac{1}{30} j_{22}(\omega_S + \omega_I) + \frac{1}{180} j_{22}(\omega_S - \omega_I) \right) \right]. \end{aligned} \quad (8.124)$$

In exactly the same way we can write down an overall expression for the T_2 time constant, which is

$$\begin{aligned} \frac{1}{T_2} &= \left(3 + (\eta^{\text{SD}})^2\right) \left(\frac{\tilde{A}_{zz}^{\text{SD}}}{\hbar}\right)^2 \left[S_C^2 \left(\frac{1}{30} j_2^{\text{C}}(0) + \frac{1}{40} j_2^{\text{C}}(\omega_I) \right) + \left(\frac{1}{3} S(S+1) - S_C^2\right) \left(\frac{1}{30} j_{21}(0) + \frac{1}{40} j_{21}(\omega_I) \right) \right. \\ &\quad \left. + S(S+1) \left(\frac{1}{60} j_{22}(\omega_S) + \frac{1}{60} j_{22}(\omega_S + \omega_I) + \frac{1}{360} j_{22}(\omega_S - \omega_I) \right) \right] \end{aligned} \quad (8.125)$$

$$\begin{aligned} &= \frac{1}{180} \left(3 + (\eta^{\text{SD}})^2\right) \left(\frac{\tilde{A}_{zz}^{\text{SD}}}{\hbar}\right)^2 \left[S_C^2 \left(12\tau_{\text{D}} + \frac{9\tau_{\text{D}}}{1 + \omega_I^2 \tau_{\text{D}}^2} \right) + \left(\frac{1}{3} S(S+1) - S_C^2\right) \left(12\tau_{\text{c},1} + \frac{9\tau_{\text{c},1}}{1 + \omega_I^2 \tau_{\text{c},1}^2} \right) \right. \\ &\quad \left. + S(S+1) \left(\frac{6\tau_{\text{c},2}}{1 + \omega_S^2 \tau_{\text{c},2}^2} + \frac{6\tau_{\text{c},2}}{1 + (\omega_S + \omega_I)^2 \tau_{\text{c},2}^2} + \frac{\tau_{\text{c},2}}{1 + (\omega_S - \omega_I)^2 \tau_{\text{c},2}^2} \right) \right]. \end{aligned} \quad (8.126)$$

This expression can also be decomposed into the constituent Curie T_2^{C} and modified Solomon–Bloembergen–

Morgan T_2^{SBM} parts

$$T_2^{-1} = (T_2^{\text{C}})^{-1} + (T_2^{\text{SBM}})^{-1}, \quad (8.127)$$

where

$$\frac{1}{T_2^{\text{C}}} = \left(3 + (\eta^{\text{SD}})^2\right) \left(\frac{\tilde{A}_{zz}^{\text{SD}}}{\hbar}\right)^2 \left[S_{\text{C}}^2 \left(\frac{1}{30} j_2^{\text{C}}(0) + \frac{1}{40} j_2^{\text{C}}(\omega_I) \right) \right], \quad (8.128)$$

$$\begin{aligned} \frac{1}{T_2^{\text{SBM}}} = & \left(3 + (\eta^{\text{SD}})^2\right) \left(\frac{\tilde{A}_{zz}^{\text{SD}}}{\hbar}\right)^2 \left[\left(\frac{1}{3} S(S+1) - S_{\text{C}}^2 \right) \left(\frac{1}{30} j_{21}(0) + \frac{1}{40} j_{21}(\omega_I) \right) \right. \\ & \left. + S(S+1) \left(\frac{1}{60} j_{22}(\omega_S) + \frac{1}{60} j_{22}(\omega_S + \omega_I) + \frac{1}{360} j_{22}(\omega_S - \omega_I) \right) \right]. \end{aligned} \quad (8.129)$$

We note that both Curie terms depend only on spectral densities of the form $j_2^{\text{C}}(\omega)$, and the correlation time τ_{D} .

8.7.2 Relaxation due to the spin-dipolar interaction with localised electrons

If we can approximate the unpaired electron density at the paramagnetic centre as a localised electronic spin S , we can use the point-dipole form of the spin-dipolar interaction and set $\tilde{A}_{zz}^{\text{SD}} = 2b_{\text{SI}}$ and $\eta^{\text{SD}} = 0$. The T_1 time constant is now

$$\frac{1}{T_1} = \left(\frac{b_{\text{SI}}}{\hbar}\right)^2 \left[S_{\text{C}}^2 \frac{3}{5} j_2^{\text{C}}(\omega_I) + \left(\frac{1}{3} S(S+1) - S_{\text{C}}^2 \right) \frac{3}{5} j_{21}(\omega_I) + S(S+1) \left(\frac{2}{5} j_{22}(\omega_S + \omega_I) + \frac{1}{15} j_{22}(\omega_S - \omega_I) \right) \right] \quad (8.130)$$

$$\begin{aligned} = & \frac{2}{15} \left(\frac{b_{\text{SI}}}{\hbar}\right)^2 \left[S_{\text{C}}^2 \frac{9\tau_{\text{D}}}{1 + \omega_I^2 \tau_{\text{D}}^2} + \left(\frac{1}{3} S(S+1) - S_{\text{C}}^2 \right) \frac{9\tau_{\text{c},1}}{1 + \omega_I^2 \tau_{\text{c},1}^2} \right. \\ & \left. + S(S+1) \left(\frac{6\tau_{\text{c},2}}{1 + (\omega_S + \omega_I)^2 \tau_{\text{c},2}^2} + \frac{\tau_{\text{c},2}}{1 + (\omega_S - \omega_I)^2 \tau_{\text{c},2}^2} \right) \right], \end{aligned} \quad (8.131)$$

and T_2 becomes

$$\begin{aligned} \frac{1}{T_2} &= \left(\frac{b_{SI}}{\hbar}\right)^2 \left[S_C^2 \left(\frac{2}{5} j_2^C(0) + \frac{3}{10} j_2^C(\omega_I) \right) + \left(\frac{1}{3} S(S+1) - S_C^2 \right) \left(\frac{2}{5} j_{21}(0) + \frac{3}{10} j_{21}(\omega_I) \right) \right. \\ &\quad \left. + S(S+1) \left(\frac{1}{5} j_{22}(\omega_S) + \frac{1}{5} j_{22}(\omega_S + \omega_I) + \frac{1}{30} j_{22}(\omega_S - \omega_I) \right) \right] \end{aligned} \quad (8.132)$$

$$\begin{aligned} &= \frac{1}{15} \left(\frac{b_{SI}}{\hbar}\right)^2 \left[S_C^2 \left(12\tau_D + \frac{9\tau_D}{1 + \omega_I^2 \tau_D^2} \right) + \left(\frac{1}{3} S(S+1) - S_C^2 \right) \left(12\tau_{c,1} + \frac{9\tau_{c,1}}{1 + \omega_I^2 \tau_{c,1}^2} \right) \right. \\ &\quad \left. + S(S+1) \left(\frac{6\tau_{c,2}}{1 + \omega_S^2 \tau_{c,2}^2} + \frac{6\tau_{c,2}}{1 + (\omega_S + \omega_I)^2 \tau_{c,2}^2} + \frac{\tau_{c,2}}{1 + (\omega_S - \omega_I)^2 \tau_{c,2}^2} \right) \right]. \end{aligned} \quad (8.133)$$

The Curie contributions to both time constants now have the simple forms

$$\frac{1}{T_1^C} = \left(\frac{b_{SI}}{\hbar}\right)^2 S_C^2 \frac{3}{5} j_2^C(\omega_I), \quad (8.134)$$

$$\frac{1}{T_2^C} = \left(\frac{b_{SI}}{\hbar}\right)^2 S_C^2 \left(\frac{2}{5} j_2^C(0) + \frac{3}{10} j_2^C(\omega_I) \right). \quad (8.135)$$

8.7.3 Relaxation due to the Fermi-contact interaction

Finally we consider the effect of the Curie spin on the Fermi-contact relaxation mechanism. Since the Fermi-contact term is spatially isotropic, we expect that any Curie contribution to the relaxation rates is due to modulation only by chemical exchange, and so only contains terms that depend on the reduced spectral density $j_0^C(0)$. As before we take each term in the Solomon–Bloembergen–Morgan expression and replace any term that depends on T_{1e} with a Curie term and a modified Solomon–Bloembergen–Morgan term, and leave unchanged any terms that depend on T_{2e} . The Fermi-contact contribution to the nuclear T_1 depends only on T_{2e} , and so is unchanged by the effect of the Curie spin:

$$\frac{1}{T_1} = \frac{1}{3} S(S+1) \left(\frac{A^{FC}}{\hbar}\right)^2 j_{02}(\omega_S - \omega_I) \quad (8.136)$$

$$= \frac{2}{3} S(S+1) \left(\frac{A^{FC}}{\hbar}\right)^2 \frac{\tau_{E,2}}{1 + (\omega_S - \omega_I)^2 \tau_{E,2}^2}. \quad (8.137)$$

By contrast the expression for T_2 acquires a Curie term with reduced spectral density $j_0^C(0)$:

$$\frac{1}{T_2} = \left(\frac{A^{\text{FC}}}{\hbar}\right)^2 \left[\frac{1}{2} S_C^2 j_0^C(0) + \frac{1}{2} \left(\frac{1}{3} S(S+1) - S_C^2 \right) j_{01}(0) + \frac{1}{6} S(S+1) j_{02}(\omega_S - \omega_I) \right] \quad (8.138)$$

$$= \frac{1}{3} S(S+1) \left(\frac{A^{\text{FC}}}{\hbar}\right)^2 \left[3S_C^2 \tau_M + 3 \left(\frac{1}{3} S(S+1) - S_C^2 \right) \tau_{E,1} + \frac{\tau_{E,2}}{1 + (\omega_S - \omega_I)^2 \tau_{E,2}^2} \right]. \quad (8.139)$$

As before we can write each total rate constant as the sum of a Curie term and a modified Solomon–Bloembergen–Morgan term. The former are given by

$$\frac{1}{T_1^C} = 0, \quad (8.140)$$

$$\frac{1}{T_2^C} = \left(\frac{A^{\text{FC}}}{\hbar}\right)^2 \frac{1}{2} S_C^2 j_0^C(0). \quad (8.141)$$

Again we note that the Curie relaxation only affects the transverse PRE.

8.7.4 Comparison of the Curie terms with the relaxation rate constants due to stochastic fluctuation of the paramagnetic chemical shielding interaction

Having introduced the relaxation rate constants resulting from the Curie interaction, we now explore how we may interpret these contributions. Following the introduction of the Curie spin in section 3.2, we showed how the parameters of the induced paramagnetic shielding could be related to the Curie spin. As a reminder we reproduce the relevant expressions for the isotropic shielding, shielding anisotropy, and asymmetry parameter below:

$$\sigma_{\text{iso}}^S = \frac{S_C A^{\text{FC}}}{\hbar \gamma_I B_0}, \quad (8.142)$$

$$\Delta \sigma^S = \frac{S_C \tilde{A}_{zz}^{\text{SD}}}{\hbar \gamma_I B_0}, \quad (8.143)$$

$$\eta^S = \eta^{\text{SD}}. \quad (8.144)$$

l	m	$\hat{T}_{lm}^{(n)}$ $n = 1$	$\omega_m^{(n)}$ $n = 1$
0	0	$-\sqrt{\frac{1}{3}}B_0\hat{I}_z$	0
2	0	$\sqrt{\frac{2}{3}}B_0\hat{I}_z$	0
	± 1	$\mp \frac{1}{2}B_0\hat{I}_{\pm}$	$\pm\omega_I$
	± 2	0	$\pm 2\omega_I$

Table 8.4: The spin operators $\hat{T}_{lm}^{(n)}$, and frequencies $\omega_m^{(n)}$ for the chemical shielding interaction used in the calculation of the PRE.

If the electrons are localised at the paramagnetic centre, the anisotropy and asymmetry become

$$\Delta\sigma^S = \frac{2S_C b_S I}{\hbar\gamma_I B_0}, \quad (8.145)$$

$$\eta^S = 0. \quad (8.146)$$

Since the Curie spin induces a shielding tensor at the nucleus via the hyperfine interaction, we can interpret the Curie relaxation mechanism as resulting from the stochastic modulation of this shielding tensor due to fast chemical exchange, and rotational diffusion. The random Hamiltonian that we use is

$$\hat{H}_1(t) = \hbar\gamma_I B_0 \cdot \sigma^S(t) \cdot \hat{I}, \quad (8.147)$$

where the time dependence is encoded entirely in the shielding tensor through changes in the orientation of the PAF, with the associated correlation time τ_R , and changes in the PAF components themselves, with the associated correlation time τ_M . We consider relaxation due both to the isotropic parts of the shielding, which depend on the Fermi-contact coupling constant, and to the anisotropic part, which depends on the spin-dipolar coupling parameters. The relevant irreducible spherical tensor operators are given in Table 8.4, and the sums of the squares of the PAF parameters are:

$$\sum_{\mu} |\tilde{K}_{l\mu}|^2 = \begin{cases} 3\hbar^2\gamma_I^2\sigma_{\text{iso}}^2, & l = 0 \\ \frac{1}{2}\hbar^2\gamma_I^2\Delta\sigma^2(3 + \eta^2), & l = 2 \end{cases}. \quad (8.148)$$

Incorporating these expressions into the Redfield superoperator in Equation 8.25, and computing the expectation values of the longitudinal and coherence I -spin operators, gives us the following expressions for the

Curie longitudinal and transverse relaxation time constants:

$$\frac{1}{T_1^C} = \frac{1}{20} \omega_I^2 \Delta\sigma^2 (3 + \eta^2) j_2^C(\omega_I) \quad (8.149)$$

$$= \frac{1}{10} \omega_I^2 \Delta\sigma^2 (3 + \eta^2) \frac{\tau_D}{1 + \omega_I^2 \tau_D^2}, \quad (8.150)$$

$$\frac{1}{T_2^C} = \frac{1}{2} \omega_I^2 \sigma_{\text{iso}}^2 j_0^C(0) + \omega_I^2 \Delta\sigma^2 (3 + \eta^2) \left[\frac{1}{30} j_2^C(0) + \frac{1}{40} j_2^C(\omega_I) \right] \quad (8.151)$$

$$= \omega_I^2 \sigma_{\text{iso}}^2 \tau_M + \omega_I^2 \Delta\sigma^2 (3 + \eta^2) \left[\frac{1}{15} \tau_D + \frac{1}{20} \frac{\tau_D}{1 + \omega_I^2 \tau_D^2} \right]. \quad (8.152)$$

It is easily verified that these expressions are the same as those calculated previously by substituting in the expressions for the shielding tensor parameters in Equations 8.142–8.146. In particular we note that the isotropic shielding interaction contributes only to T_2^C , and not to T_1^C , as it does not correspond to a transition between nuclear energy levels, as shown by the dependence on $j_0^C(0)$. In addition this term only contributes in the presence of fast chemical exchange. The anisotropic shielding contributes both to T_1^C and T_2^C relaxation due to modulation by both fast chemical exchange and rotational diffusion.

8.7.5 The importance of the Curie term

Following the discussion of Curie relaxation, the obvious practical question is under what circumstances does the Curie contribution become an important contribution to the overall PRE? We recall that under the typical conditions of high-resolution NMR, namely high magnetic field and high temperature, we can approximate the expression of the Curie spin in the high-temperature limit, with the result that $|S_C| \ll 1$. Therefore we might expect the contribution to the PRE to be insignificant since it is proportional to S_C^2 , whereas the corresponding factors in the modified Solomon–Bloembergen–Morgan contribution are $S(S+1)/3 - S_C^2$ and $S(S+1)$. For example, an ensemble of electronic spins $S = 1$ immersed in a magnetic field of 11.74 T at a temperature of 298 K induces a Curie spin of -0.035 , and the corresponding Curie term is weighted by $S_C^2 = 0.001$.

Nevertheless the Curie term can become the dominant factor in T_2 relaxation under conditions of fast electronic relaxation and long rotational correlation times, so that $T_{1e}, T_{2e} \ll \tau_R$, as is observed for proteins in solution. Additionally we can expect the Curie term to become more important at high field, since $S_C^2 \propto B_0^2$, in complete analogy to the increase in the importance of CSA-induced relaxation at high field in diamagnetic

systems. This is illustrated in Figure 8.6, which shows the Curie and modified Solomon–Bloembergen–Morgan contributions to the spin-dipolar R_1 and R_2 rates of a ^1H nucleus plotted as functions of τ_R , for two different electronic relaxation times (T_{1e} is assumed to be equal to T_{2e}) of 0.1 and 1.0 ps, using the parameters for the Curie spin given in the previous paragraph, and assuming there is no chemical exchange. For electronic relaxation times of 1.0 ps, the longitudinal relaxation rate is dominated by the Solomon–Bloembergen–Morgan contribution, as shown in (a). The Curie term varies according to the spectral density $j_2^C(\omega_I)$, which reaches a maximum value at $\tau_R = 0.3$ ns. By contrast the Solomon–Bloembergen–Morgan contribution is independent of τ_R in the slow-rotation limit as the overall correlation time is dominated by the rapid electron relaxation, i.e. $\tau_{c,q} \approx T_{qe}$. The transverse relaxation rate, shown in (b), shows very different behaviour with the Curie contribution becoming larger than the Solomon–Bloembergen–Morgan contribution when τ_R is longer than approximately 1 ns. At longer τ_R , the Curie term dominates completely due to the dependence $j_2^C(0)$, which is larger than $j_{21}(0)$ as $\tau_R \gg \tau_{c,q} \approx T_{qe}$. If we reduce the electronic relaxation times to 0.1 ps, the Solomon–Bloembergen–Morgan contributions to both the longitudinal and transverse relaxation rates, shown in (c) and (d), are reduced, with the result that the Curie term is a larger contribution still to the overall relaxation rates. We note here that for large paramagnetic systems with slow rotational dynamics, the transverse relaxation rate is completely dominated by Curie relaxation, whereas the longitudinal relaxation rate is dominated by Solomon–Bloembergen–Morgan relaxation. For systems with rotational dynamics that are intermediate between those of small molecules in solution and large systems, with correlation times of approximately 1 ns, both the Curie and Solomon–Bloembergen–Morgan mechanisms are important for both longitudinal and transverse relaxation.

8.8 Cross-correlation between the paramagnetic and diamagnetic relaxation mechanisms in solution

We now turn our attention to an interesting feature of relaxation in paramagnetic systems that is observed in large biomolecules, which is the interference between the relaxation mechanisms resulting in the PRE and the relaxation mechanisms due to non-paramagnetic interactions. So far we have assumed that the random modulations of different interactions that act as local fields for relaxation vary independently of each other, so that the relaxation rates are purely additive. However in some cases the fluctuations are not independent,

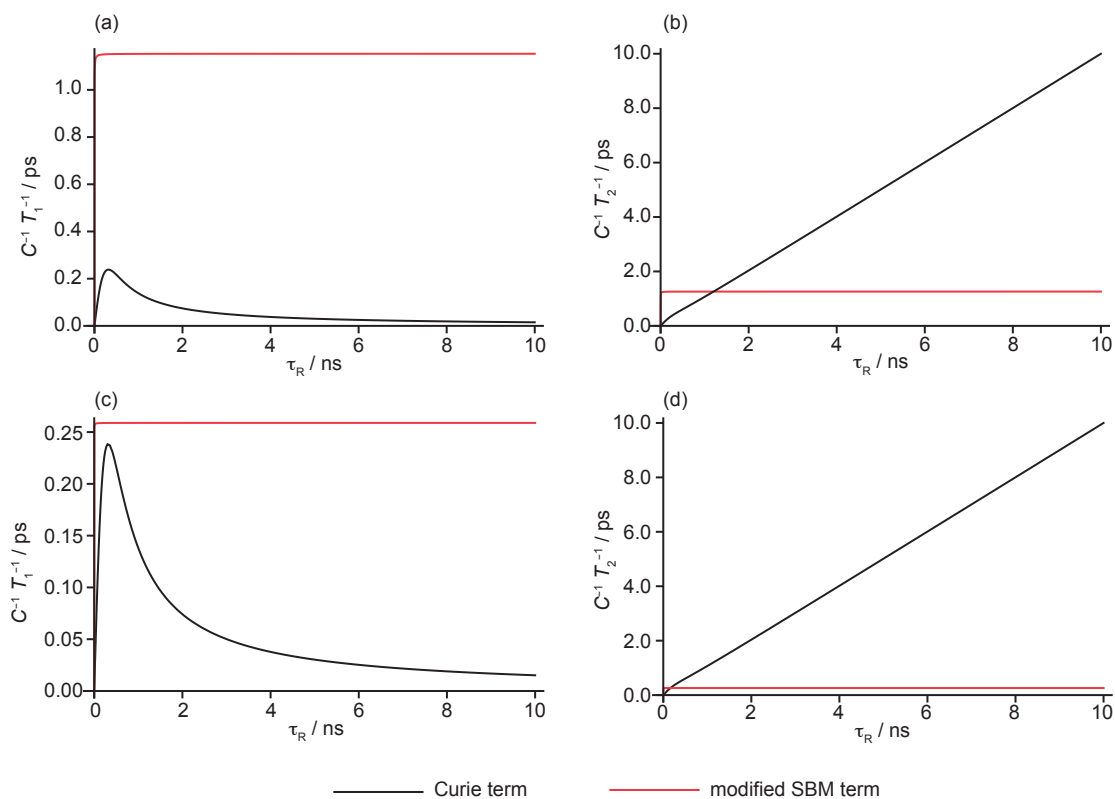


Figure 8.6: Comparison of the size of the Curie and Solomon–Bloembergen–Morgan terms in the spin-dipolar relaxation rate constants under the influence of slow rotational diffusion. The plots in (a) and (b) show the longitudinal and transverse rate constants T_1^{-1} and T_2^{-1} as a function of τ_R , which takes relatively long values of up to 10 ns, and constant electron relaxation time constants $T_{1e} = T_{2e} = 1$ ps. The corresponding plots in (c) and (d) show the longitudinal and transverse rate constants T_1^{-1} and T_2^{-1} as a function of τ_R with shorter electronic relaxation time constants of $T_{1e} = T_{2e} = 0.1$ ps. The relaxation curves correspond to a ^1H nucleus coupled to an electronic spin $S = 1$ at 11.74 T. The Curie spin is calculated at 298 K, and takes the value $S_C = -3.5 \times 10^{-2}$. The constant $C = (3 + (\eta^{\text{SD}})^2) (\tilde{A}_{zz}^{\text{SD}}/\hbar)^2/12$, or $(b_{SI}/\hbar)^2$.

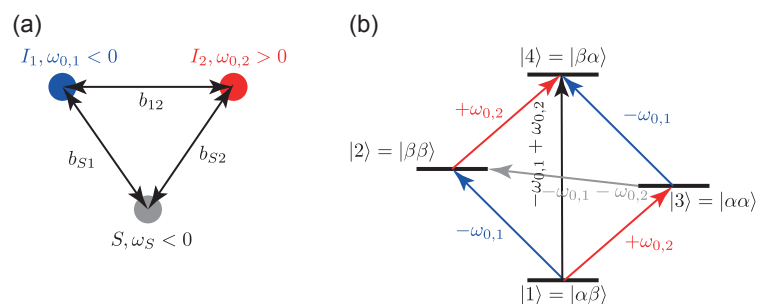


Figure 8.7: Illustration of a combined nuclear–electronic spin system in which we observe cross-correlated relaxation between the nuclear–nuclear dipolar coupling and Curie mechanisms. The spin system is shown in (a). The Larmor frequencies of the two nuclear spins I_1 and I_2 , denoted $\omega_{0,1}$ and $\omega_{0,2}$ are assumed to be positive and negative respectively, so that the system represents a ^1H – ^{15}N spin system in a protein. The dipolar coupling between the two nuclei is b_{12} . The electronic spin S has Larmor frequency ω_S and interacts with the two nuclei via point-dipolar-coupling interactions with constants b_{S1} and b_{S2} . The nuclear energy levels and transition frequencies are shown in (b).

but are strongly correlated. One example that is commonly encountered is that of the dynamic processes in a protein that cause fluctuations in both the ^{15}N CSA and ^1H – ^{15}N dipolar coupling interactions. Here it is clear that the same source of fluctuations causes random modulations of both the interactions, which are then obviously not mutually independent. This phenomenon is referred to as cross-correlated relaxation (CCR), and results in an additional relaxation rate constant that is added to the others.

Here we investigate the effect of cross correlation observed in a spin system comprising two spin-1/2 nuclei I_1 and I_2 , coupled together by a dipolar coupling interaction with constant b_{12} , both of which experience a spin-dipolar interaction with an electronic spin S with constants b_{S1} and b_{S2} . The spin system and nuclear-spin energy levels are illustrated in Figure 8.7 (a) and (b). In this spin system we have defined the Larmor frequency of I_1 , $\omega_{0,1}$, to be negative and the Larmor frequency of I_2 , $\omega_{0,2}$, to be positive. Therefore we may interpret Figure 8.7 as representing the spins in an H–N amide group in a paramagnetic protein, with $I_1 = ^1\text{H}$ and $I_2 = ^{15}\text{N}$. To simplify the discussion we neglect chemical exchange, and assume that the only sources of the stochastic fluctuations are unrestricted rotational diffusion and electronic relaxation.

8.8.1 Nuclear–nuclear dipolar-coupling relaxation and cross-correlation with the Curie mechanism

We proceed to calculate the full form of the relaxation superoperator corresponding to the spin system in Figure 8.7 (a). The Hamiltonian $\hat{H}_1(t)$ that contains all the time-dependent random interactions is given by

$$\hat{H}_1(t) = \hat{H}_C^{(1)}(t) + \hat{H}_C^{(2)}(t) + \hat{H}_{\text{SBM}}^{(S1)}(t) + \hat{H}_{\text{SBM}}^{(S2)}(t) + \hat{H}_{\text{DD}}^{(12)}(t). \quad (8.153)$$

The first two terms $\hat{H}_C^{(1)}(t)$ and $\hat{H}_C^{(2)}(t)$ represent the interactions of nuclear spins I_1 and I_2 with the Curie spin of the paramagnetic centre. As discussed in section 8.7.4, both interactions can be represented by the corresponding SA subject to rotational diffusion, and so they also include the orbital contributions to the SA that are present in diamagnetic systems. The spin operators are $\hat{T}_{C1,2m}$ and $\hat{T}_{C2,2m}$, which take the expressions in Table 8.4. Both of these terms are responsible for the Curie PREs, and the CSA-contributions to relaxation in diamagnetic systems. The third and fourth terms in the Hamiltonian are $\hat{H}_{\text{SBM}}^{(S1)}(t)$ and $\hat{H}_{\text{SBM}}^{(S2)}(t)$, which represent the time-dependent spin-dipolar interactions between I_1 and S , and I_2 and S respectively that are modulated by rotational diffusion and electronic relaxation. The spin operators are given in Table 8.2. Both terms are responsible for the modified Solomon contribution to the PREs. The final term in the Hamiltonian is $\hat{H}_{\text{DD}}^{(12)}(t)$, which represents the nuclear–nuclear dipolar coupling interaction that is modulated by rotational diffusion. The spin operators $\hat{T}_{\text{DD},2m}^{(n)}$ are given in Table 8.2 with the substitutions $I \rightarrow I_1$ and $S \rightarrow I_2$.

We can now write the total relaxation superoperator $\hat{\Gamma}$ as a sum of terms:

$$\hat{\Gamma} = \hat{\Gamma}_{\text{PRE}}^{(1)} + \hat{\Gamma}_{\text{PRE}}^{(2)} + \hat{\Gamma}_{\text{DD}}^{(12)} + \hat{\Gamma}_{\text{CCR}}^{(1)} + \hat{\Gamma}_{\text{CCR}}^{(2)}. \quad (8.154)$$

The terms $\hat{\Gamma}_{\text{PRE}}^{(1)}$ and $\hat{\Gamma}_{\text{PRE}}^{(2)}$ are responsible for the total PRE experienced by spins I_1 and I_2 due to both the Solomon and Curie relaxation mechanisms. Both superoperators and the corresponding relaxation rates as the same as calculated previously. The relaxation contribution from the nuclear–nuclear dipolar interaction is due to the term $\hat{\Gamma}_{\text{DD}}^{(12)}$, which takes the expression

$$\hat{\Gamma}_{\text{DD}}^{(12)} \hat{\mathcal{O}} = \frac{3b_{12}^2}{5\hbar^2} \sum_{mn} \left[\hat{T}_{\text{DD},2-m}^{(n)} \left[\left(\hat{T}_{\text{DD},2-m}^{(n)} \right)^\dagger, \hat{\mathcal{O}} \right] \right] j^{\text{R}}(-\omega_{-m}^{(n)}). \quad (8.155)$$

The spectral density function $j^R(\omega) = 2\tau_R / (1 + \omega^2\tau_R^2)$ represents unrestricted rotational diffusion. Finally the relaxation contributions due to CCR for I_1 and I_2 are represented by the superoperator terms $\hat{\Gamma}_{\text{CCR}}^{(1)}$ and $\hat{\Gamma}_{\text{CCR}}^{(2)}$. We only consider the cross correlation between the Curie and nuclear–nuclear dipolar interactions. Assuming the SAs of both nuclear spins are axially symmetric (which is the case for a single point-spin-dipolar hyperfine interaction), with anisotropies $\Delta\sigma_2^S$ and $\Delta\sigma_1^S$ respectively, the two CCR superoperators have the expressions:

$$\hat{\Gamma}_{\text{CCR}}^{(1)} \hat{\mathcal{O}} = \frac{3\gamma_1 b_{12} \Delta\sigma_1^S}{10\hbar} d_{00}^{(2)}(\vartheta_1) \sum_m \left\{ \left[\hat{T}_{\text{DD},2-m}^{(0)}, \left[(\hat{T}_{\text{C1},2-m})^\dagger, \hat{\mathcal{O}} \right] \right] + \left[\hat{T}_{\text{C1},2-m}, \left[(\hat{T}_{\text{DD},2-m}^{(0)})^\dagger, \hat{\mathcal{O}} \right] \right] \right\} j^R(-\omega_{-m}^{(0)}), \quad (8.156)$$

$$\hat{\Gamma}_{\text{CCR}}^{(2)} \hat{\mathcal{O}} = \frac{3\gamma_2 b_{12} \Delta\sigma_2^S}{10\hbar} d_{00}^{(2)}(\vartheta_2) \sum_m \left\{ \left[\hat{T}_{\text{DD},2-m}^{(0)}, \left[(\hat{T}_{\text{C2},2-m})^\dagger, \hat{\mathcal{O}} \right] \right] + \left[\hat{T}_{\text{C2},2-m}, \left[(\hat{T}_{\text{DD},2-m}^{(0)})^\dagger, \hat{\mathcal{O}} \right] \right] \right\} j^R(-\omega_{-m}^{(0)}), \quad (8.157)$$

where γ_1 and γ_2 are the two nuclear gyromagnetic ratios. The angle ϑ_1 is the angle between the PAF of the SA tensor of I_1 and the I_1 – I_2 internuclear vector; and likewise for ϑ_2 .

Using these expressions we compute the relaxation rates for both longitudinal and transverse relaxation in turn.

8.8.2 Longitudinal relaxation

The Solomon equations

When we apply the total relaxation superoperator in Equation 8.154 to the total nuclear-spin density operator, we obtain a set of differential equations that link the relaxation behaviour of the expectation values of the operators that represent the total I_1 longitudinal magnetization \hat{I}_{1z} , the total I_2 longitudinal magnetization \hat{I}_{2z} , and the longitudinal two-spin order $2\hat{I}_{1z}\hat{I}_{2z}$. These equations are referred to as the Solomon equations for two nuclear spins, and are given by

$$\frac{dI_{1z}}{dt} = -R_1^{(1)} (I_{1z} - I_{1z}^{(0)}) - \sigma_{12} (I_{2z} - I_{2z}^{(0)}) - \Delta_1^{(1)} 2I_{1z}I_{2z}, \quad (8.158)$$

$$\frac{dI_{2z}}{dt} = -\sigma_{12} (I_{1z} - I_{1z}^{(0)}) - R_1^{(2)} (I_{2z} - I_{2z}^{(0)}) - \Delta_1^{(2)} 2I_{1z}I_{2z}, \quad (8.159)$$

$$\frac{d2I_{1z}I_{2z}}{dt} = -\Delta_1^{(1)} (I_{1z} - I_{1z}^{(0)}) - \Delta_1^{(2)} (I_{2z} - I_{2z}^{(0)}) - R_1^{(1,2)} 2I_{1z}I_{2z}, \quad (8.160)$$

where I_{1z} and I_{2z} are the expectation values of \hat{I}_{1z} and \hat{I}_{2z} , $I_{1z}^{(0)}$ and $I_{2z}^{(0)}$ are the corresponding expectation values at equilibrium, and $2I_{1z}I_{2z}$ is the expectation value of $2\hat{I}_{1z}\hat{I}_{2z}$ (which has an equilibrium value of zero). The rate constants $R_1^{(1)}$, $R_1^{(2)}$, and $R_1^{(1,2)}$ are the self-relaxation rate constants for I_{1z} , I_{2z} , and $2I_{1z}I_{2z}$ and describe their return to their equilibrium values. The cross-relaxation rate constant σ_{12} describes the process by which \hat{I}_{1z} and \hat{I}_{2z} are interconverted, and is responsible for the nuclear Overhauser effect which is used to establish the close spatial proximity of nuclei in molecules. The last two cross-relaxation rate constants $\Delta_1^{(1)}$ and $\Delta_1^{(2)}$ describe the interconversion between \hat{I}_{1z} and $2I_{1z}I_{2z}$, and \hat{I}_{2z} and $2I_{1z}I_{2z}$ respectively.

Longitudinal self-relaxation

The three longitudinal self-relaxation rate constants are given by:

$$R_1^{(1)} = R_1^{\text{PRE},(1)} + \underbrace{\left(\frac{b_{12}}{\hbar}\right)^2 \left[\frac{3}{20}j^{\text{R}}(\omega_{0,1}) + \frac{3}{10}j^{\text{R}}(\omega_{0,1} + \omega_{0,2}) + \frac{1}{20}j^{\text{R}}(\omega_{0,1} - \omega_{0,2}) \right]}_{R_1^{\text{DD},(1)}}, \quad (8.161)$$

$$R_1^{(2)} = R_1^{\text{PRE},(2)} + \underbrace{\left(\frac{b_{12}}{\hbar}\right)^2 \left[\frac{3}{20}j^{\text{R}}(\omega_{0,2}) + \frac{3}{10}j^{\text{R}}(\omega_{0,1} + \omega_{0,2}) + \frac{1}{20}j^{\text{R}}(\omega_{0,1} - \omega_{0,2}) \right]}_{R_1^{\text{DD},(2)}}, \quad (8.162)$$

$$R_1^{(1,2)} = \underbrace{R_1^{\text{PRE},(1)} + R_1^{\text{PRE},(2)}}_{R_1^{\text{PRE},(1,2)}} + \underbrace{\left(\frac{b_{12}}{\hbar}\right)^2 \left[\frac{3}{20}j^{\text{R}}(\omega_{0,1}) + \frac{3}{20}j^{\text{R}}(\omega_{0,2}) \right]}_{R_1^{\text{DD},(1,2)}}. \quad (8.163)$$

Each rate constant is the sum of a PRE term and a contribution from the nuclear–nuclear dipolar coupling relaxation mechanism. For example the self-relaxation rate constant for spin I_1 is the sum of the longitudinal PRE $R_1^{\text{PRE},(1)}$, which is given by Equation 8.131, and the longitudinal nuclear–nuclear dipolar coupling rate constant $R_1^{\text{DD},(1)}$. The corresponding expression for spin I_2 takes a similar expression. The rate constant for the longitudinal two-spin order is the sum of a PRE term $R_1^{\text{PRE},(1,2)}$, which is the sum of the two one-spin longitudinal PREs $R_1^{\text{PRE},(1)}$ and $R_1^{\text{PRE},(2)}$, and a longitudinal nuclear–nuclear dipolar coupling rate constant $R_1^{\text{DD},(1,2)}$. We note that the three rate constants do not have a term due to the CCR.

Longitudinal cross-relaxation

The cross-relaxation rate constant σ_{12} is given by the expression

$$\sigma_{12} = \left(\frac{b_{12}}{\hbar}\right)^2 \left[\frac{3}{10} j^{\text{R}}(\omega_{0,1} + \omega_{0,2}) - \frac{1}{20} j^{\text{R}}(\omega_{0,1} - \omega_{0,2}) \right]. \quad (8.164)$$

This rate constant is due only to the nuclear–nuclear dipolar coupling interaction, as this is the only term in the Hamiltonian that connects the two nuclear spins. Therefore we expect no paramagnetic relaxation contribution to the conventional NOE. However the situation is different for cross relaxation between each longitudinal magnetization term and the longitudinal two-spin order term. Here the two cross-relaxation rate constants $\Delta_1^{(1)}$ and $\Delta_1^{(2)}$ are only non-zero because of the CCR between the nuclear–nuclear dipolar coupling and the Curie mechanism. They are given by

$$\Delta_1^{(1)} = \frac{3}{10} \left(\frac{b_{12}}{\hbar}\right) \gamma_1 B_0 \Delta \sigma_1^S d_{00}^{(2)}(\vartheta_1) j^{\text{R}}(\omega_{0,1}), \quad (8.165)$$

$$\Delta_1^{(2)} = \frac{3}{10} \left(\frac{b_{12}}{\hbar}\right) \gamma_2 B_0 \Delta \sigma_2^S d_{00}^{(2)}(\vartheta_2) j^{\text{R}}(\omega_{0,2}). \quad (8.166)$$

This is also observed for cross correlation between a dipolar coupling and a CSA in diamagnetic systems [254]. In the absence of CCR both relaxation rate constants are zero. Hence the detection of polarization transfer, such as $\hat{I}_{1z} \rightarrow 2\hat{I}_{1z}\hat{I}_{2z}$, may indicate the presence of CCR.

8.8.3 Transverse relaxation

The Solomon equations

We now examine transverse relaxation processes that affect coherences. The observable single-quantum coherences for a spin system comprising two nuclei have a more complicated form than for a simple one-spin system. For a system of two nuclear spins-1/2 there are four such coherences, which are indicated on energy levels in Figure 8.7 (b). Two of the coherences involve a spin-state flip of spin I_1 , with the second spin I_2 in an unchanged spin state of either α or β . These two coherences form a doublet, and are represented by the product operators $\hat{I}_{1+}\hat{I}_{2\alpha}$ and $\hat{I}_{1+}\hat{I}_{2\beta}$, where \hat{I}_{i+} is the raising operator for spin I_i , and $\hat{I}_{i\alpha}$ and $\hat{I}_{i\beta}$ are the two projection operators for spin I_i in the two spin states. Likewise there are two coherences representing a spin flip of I_2 , which are represented by the product operators $\hat{I}_{1\alpha}\hat{I}_{2+}$ and $\hat{I}_{1\beta}\hat{I}_{2+}$.

The two spin- I_1 coherences $\hat{I}_{1+}\hat{I}_{2\alpha}$ and $\hat{I}_{1+}\hat{I}_{2\beta}$ may have different phases. Therefore we may represent their superposition as a combination of an in-phase coherence operator \hat{I}_{1+} , in which both $\hat{I}_{1+}\hat{I}_{2\alpha}$ and $\hat{I}_{1+}\hat{I}_{2\beta}$ have the same phase, and an anti-phase coherence operator $2\hat{I}_{1+}\hat{I}_{2z}$, in which both $\hat{I}_{1+}\hat{I}_{2\alpha}$ and $\hat{I}_{1+}\hat{I}_{2\beta}$ have phases that differ by π . Likewise we can also define the in-phase \hat{I}_{2+} and anti-phase $2\hat{I}_{1z}\hat{I}_{2+}$ coherence operators for I_2 . The four operators are given by:

$$\hat{I}_{1+} = \hat{I}_{1+}\hat{I}_{2\alpha} + \hat{I}_{1+}\hat{I}_{2\beta}, \quad (8.167)$$

$$2\hat{I}_{1+}\hat{I}_{2z} = \hat{I}_{1+}\hat{I}_{2\alpha} - \hat{I}_{1+}\hat{I}_{2\beta}, \quad (8.168)$$

$$\hat{I}_{2+} = \hat{I}_{1\alpha}\hat{I}_{2+} + \hat{I}_{1\beta}\hat{I}_{2+}, \quad (8.169)$$

$$2\hat{I}_{1z}\hat{I}_{2+} = \hat{I}_{1\alpha}\hat{I}_{2+} - \hat{I}_{1\beta}\hat{I}_{2+}. \quad (8.170)$$

The relaxation behaviour of the magnetization terms representing the in-phase and anti-phase coherence of spin I_1 is described by a pair of connected differential equations that are given by

$$\frac{dI_{1+}}{dt} = -R_2^{(1)}I_{1+} - \Delta_2^{(1)}2I_{1+}I_{2z}, \quad (8.171)$$

$$\frac{d2I_{1+}I_{2z}}{dt} = -\Delta_2^{(1)}I_{1+} - R_2^{(1,2)}2I_{1+}I_{2z}. \quad (8.172)$$

The in-phase and anti-phase magnetization terms both relax according to the transverse self-relaxation rate constants $R_2^{(1)}$ and $R_2^{(1,2)}$, and cross relax with rate constant $\Delta_2^{(1)}$. Likewise the in-phase and anti-phase magnetization terms of spin I_2 are connected by the following pair of differential equations:

$$\frac{dI_{2+}}{dt} = -R_2^{(2)}I_{2+} - \Delta_2^{(2)}2I_{1z}I_{2+}, \quad (8.173)$$

$$\frac{d2I_{1z}I_{2+}}{dt} = -\Delta_2^{(2)}I_{2+} - R_2^{(2,1)}2I_{1z}I_{2+}. \quad (8.174)$$

The in-phase and anti-phase self-relaxation rate constants are $R_2^{(2)}$ and $R_2^{(2,1)}$, and the cross-relaxation rate constant is $\Delta_2^{(2)}$.

Transverse self-relaxation

The four self-relaxation rate constants are given by:

$$R_2^{(1)} = R_2^{\text{PRE},(1)} + \underbrace{\left(\frac{b_{12}}{\hbar}\right)^2 \left[\frac{1}{10}j^{\text{R}}(0) + \frac{3}{20}j^{\text{R}}(\omega_{0,2}) + \frac{3}{40}j^{\text{R}}(\omega_{0,1}) + \frac{3}{20}j^{\text{R}}(\omega_{0,1} + \omega_{0,2}) + \frac{1}{40}j^{\text{R}}(\omega_{0,1} - \omega_{0,2}) \right]}_{R_2^{\text{DD},(1)}}, \quad (8.175)$$

$$R_2^{(2)} = R_2^{\text{PRE},(2)} + \underbrace{\left(\frac{b_{12}}{\hbar}\right)^2 \left[\frac{1}{10}j^{\text{R}}(0) + \frac{3}{20}j^{\text{R}}(\omega_{0,1}) + \frac{3}{40}j^{\text{R}}(\omega_{0,2}) + \frac{3}{20}j^{\text{R}}(\omega_{0,1} + \omega_{0,2}) + \frac{1}{40}j^{\text{R}}(\omega_{0,1} - \omega_{0,2}) \right]}_{R_2^{\text{DD},(2)}}, \quad (8.176)$$

$$R_2^{(1,2)} = \underbrace{R_2^{\text{PRE},(1)} + R_1^{\text{PRE},(2)}}_{R_2^{\text{PRE},(1,2)}} + \underbrace{\left(\frac{b_{12}}{\hbar}\right)^2 \left[\frac{1}{10}j^{\text{R}}(0) + \frac{3}{40}j^{\text{R}}(\omega_{0,1}) + \frac{3}{20}j^{\text{R}}(\omega_{0,1} + \omega_{0,2}) + \frac{1}{40}j^{\text{R}}(\omega_{0,1} - \omega_{0,2}) \right]}_{R_2^{\text{DD},(1,2)}}, \quad (8.177)$$

$$R_2^{(2,1)} = \underbrace{R_1^{\text{PRE},(1)} + R_2^{\text{PRE},(2)}}_{R_2^{\text{PRE},(2,1)}} + \underbrace{\left(\frac{b_{12}}{\hbar}\right)^2 \left[\frac{1}{10}j^{\text{R}}(0) + \frac{3}{40}j^{\text{R}}(\omega_{0,2}) + \frac{3}{20}j^{\text{R}}(\omega_{0,1} + \omega_{0,2}) + \frac{1}{40}j^{\text{R}}(\omega_{0,1} - \omega_{0,2}) \right]}_{R_2^{\text{DD},(2,1)}}. \quad (8.178)$$

The two rate constants for in-phase relaxation $R_2^{(i)}$ are each the sum of a transverse PRE term, given by Equation 8.133, and a diamagnetic term due to the nuclear–nuclear dipolar coupling $R_2^{\text{DD},(i)}$. The two anti-phase self-relaxation rate constants are more complicated. For example the PRE contribution to the rate constant for $2I_1+I_2z$, $R_2^{(1,2)}$, is the sum of the one-spin PRE terms for transverse relaxation of I_1 $R_2^{\text{PRE},(1)}$ and longitudinal relaxation of I_2 $R_1^{\text{PRE},(2)}$. The remaining contribution $R_2^{\text{DD},(1,2)}$ is due to the nuclear–nuclear dipolar coupling. We note that none of the self-relaxation rate constants has a contribution from CCR. However this is not the full story; the relaxation rate constants above give only the *average* relaxation rate of the two coherences represented by each in-phase or anti-phase operator. As we will see each component of the doublet relaxes at a different rate.

Relaxation-induced coherence transfer

The cross-relaxation between the in-phase and anti-phase coherence terms is very interesting. The two cross-relaxation rate constants are only non-zero in the presence of CCR between the nuclear–nuclear dipolar

coupling and Curie relaxation mechanisms. They are given by:

$$\Delta_2^{(1)} = \left(\frac{b_{12}}{\hbar}\right) \gamma_1 B_0 \Delta \sigma_1^S d_{00}^{(2)}(\vartheta_1) \left[\frac{1}{5} j^R(0) + \frac{3}{20} j^R(\omega_{0,1}) \right], \quad (8.179)$$

$$\Delta_2^{(2)} = \left(\frac{b_{12}}{\hbar}\right) \gamma_2 B_0 \Delta \sigma_2^S d_{00}^{(2)}(\vartheta_2) \left[\frac{1}{5} j^R(0) + \frac{3}{20} j^R(\omega_{0,2}) \right]. \quad (8.180)$$

This is intriguing because it implies that during a delay an in-phase coherence on I_1 can evolve into an anti-phase coherence, also on I_1 , via a relaxation-induced transformation of the form $\hat{I}_{1+} \rightarrow 2\hat{I}_{1+}\hat{I}_{2z}$. A subsequent pulse or combination of pulses can then transform this anti-phase term into an anti-phase term on the second spin I_2 . This is an example of relaxation-allowed coherence transfer [264].

In solution NMR in the absence of CCR the only way in which such a coherence transfer can occur is if the isotropic J -coupling J_{12} between the two spins is non-zero. In this case the transformation from the in-phase to anti-phase coherences is

$$\hat{I}_{1+} \rightarrow \hat{I}_{1+} \cos(\pi J_{12}t) - i2\hat{I}_{1+}\hat{I}_{2z} \sin(\pi J_{12}t). \quad (8.181)$$

The anti-phase term can then be transferred to a coherence on I_2 . Therefore in the absence of CCR, as for small molecules, the observation of such a coherence transfer indicates that the two spins are coupled by a J -coupling interaction. This is used extensively in correlation spectroscopy to identify the bonding networks within molecules. However for large macromolecules in solution which exhibit measurable CCR we may observe relaxation-induced coherence transfer, which complicates the interpretation of the spectrum. This is particularly important to bear in mind for homonuclear correlation spectroscopy (COSY) of paramagnetic proteins [265].

Differential line broadening due to cross-correlation between the nuclear–nuclear dipolar and Curie relaxation mechanisms

The self-relaxation rate constants given in Equations 8.175–8.178 are the average rate constants for the in- and anti-phase coherences of the two spins. However, as we have already pointed out, this does not provide a complete picture of the transverse self-relaxation of the system, for which we need to consider the relaxation properties of the expectation values $I_{1+}I_{2\alpha}$, $I_{1+}I_{2\beta}$, $I_{1\alpha}I_{2+}$, and $I_{1\beta}I_{2+}$ which represent the four individual

coherences. In large paramagnetic macromolecules experiencing slow rotational diffusion, CCR between the nuclear–nuclear dipolar coupling and Curie mechanisms results in different transverse relaxation rates for the two coherences $I_{1+I_{2\alpha}}$ and $I_{1+I_{2\beta}}$, and therefore different linewidths in the spectrum. We calculate this effect here in the spin-diffusion limit where $|\omega_I\tau_R| \gg 1$, where we can approximate the spectral density functions as $j^R(0) = 2\tau_R$, and $j^R(\omega_{0,1}) \approx j^R(\omega_{0,2}) \approx j^R(\omega_{0,1} + \omega_{0,2}) \approx j^R(\omega_{0,1} - \omega_{0,2}) \approx 0$. Under this condition the two expectation values $I_{1+I_{2\alpha}}$ and $I_{1+I_{2\beta}}$ relax independently with different self-relaxation rate constants $R_2^{(1,\alpha)}$ and $R_2^{(1,\beta)}$ that are given by:

$$R_2^{(1,\alpha)} = \underbrace{\frac{1}{10} \left(\frac{b_{12}}{\hbar}\right)^2 j^R(0)}_{\text{DD}} + \underbrace{\frac{1}{10} (\gamma_1 B_0 \Delta\sigma_1^S)^2 j^R(0)}_{\text{Curie}} + \underbrace{\frac{1}{5} \left(\frac{b_{12}}{\hbar}\right) (\gamma_1 B_0 \Delta\sigma_1^S) d_{00}^{(2)}(\vartheta_1) j^R(0)}_{\text{CCR}}, \quad (8.182)$$

$$R_2^{(1,\beta)} = \underbrace{\frac{1}{10} \left(\frac{b_{12}}{\hbar}\right)^2 j^R(0)}_{\text{DD}} + \underbrace{\frac{1}{10} (\gamma_1 B_0 \Delta\sigma_1^S)^2 j^R(0)}_{\text{Curie}} - \underbrace{\frac{1}{5} \left(\frac{b_{12}}{\hbar}\right) (\gamma_1 B_0 \Delta\sigma_1^S) d_{00}^{(2)}(\vartheta_1) j^R(0)}_{\text{CCR}}. \quad (8.183)$$

Both rate constants have the same contribution from the dipolar (DD) and Curie relaxation mechanisms, and the difference arises only from the different sign of the CCR contribution. The conclusion is that the effect of CCR is to reduce the relaxation rate of one coherence in the doublet, and to increase the relaxation rate of the second. Which rate is increased and which is reduced depends on the overall sign of the CCR contribution, which depends in turn on the signs of b_{12} , γ_1 , Δ_1^S , and $d_{00}^{(2)}(\vartheta_1)$. This effect is also utilized for large proteins in solution in a method called Transverse Relaxation-Optimized Spectroscopy (TROSY), where the CCR between the diamagnetic CSA and DD relaxation mechanisms is used to maximise the resolution at high magnetic fields [266].

If, as predicted by the relaxation differential equations, the decay due to transverse relaxation is exponential, the linewidths of the two peaks (defined as the full-width at half-maximum) are equal to $2R_2^{(1,\alpha)}$ and $2R_2^{(1,\beta)}$. This means that the CCR manifests itself in the spectrum by the two components of the doublet having different linewidths, with one peak being narrowed and the other broadened. Figure 8.8 illustrates the form of the in-phase and anti-phase doublets that are obtained with and without CCR for different values of the J -coupling constant. The average linewidth is set to 100 Hz, with the CCR contribution equal to ± 50 Hz. Spectra with values of J_{12} ranging from 200 Hz down to 0 Hz are depicted. In the absence of CCR both components of the doublet have the same linewidth. In the absence of CCR the effect of reducing J_{12} on the in-phase doublet is to reduce the separation between the two components of the doublet, until the splitting is

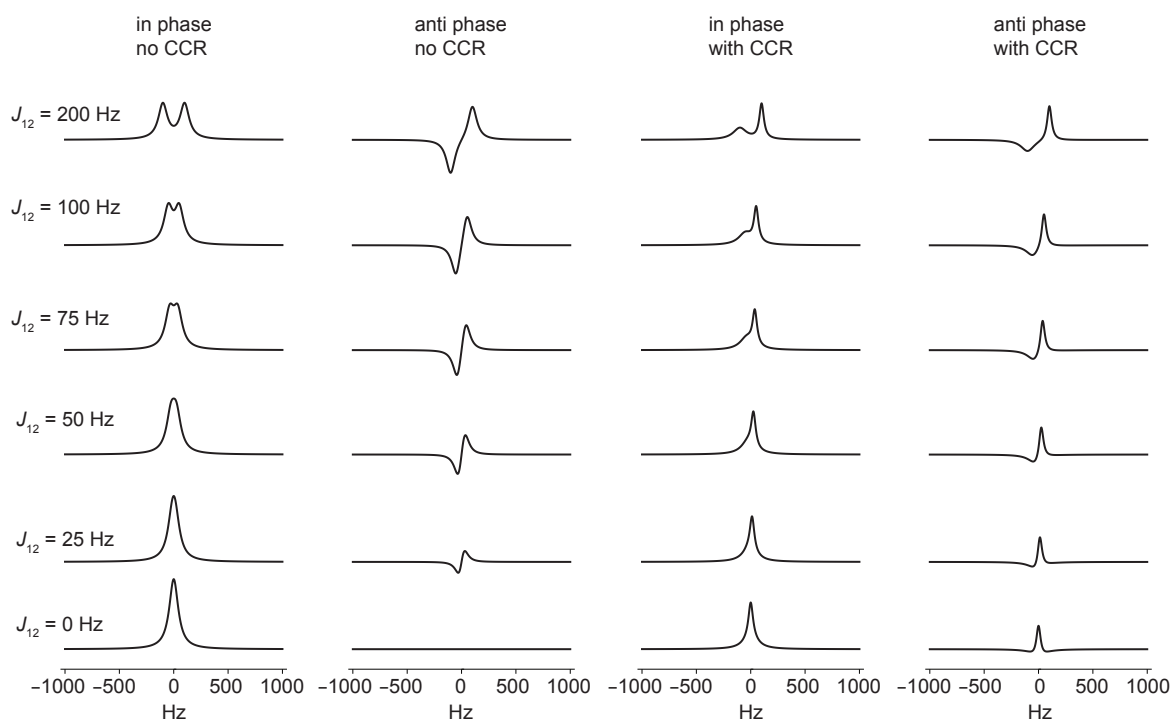


Figure 8.8: Simulated in-phase and anti-phase doublets with and without cross-correlation between the dipolar-coupling and Curie relaxation mechanisms for different J -coupling constants. In the absence of CCR the linewidth of both components is 100 Hz. The CCR contribution to the two components is 50 Hz, with the high-frequency line being narrowed and the low-frequency line broadened. The coupling constants J_{12} are as indicated.

no longer resolved. Finally, at $J_{12} = 0$, the two components are at the same frequency and we see a singlet. For the anti-phase doublet, reducing J_{12} causes increased cancellation between the intensities of the peaks as their separation is reduced. At zero coupling the intensities cancel exactly resulting in no spectrum. Thus, in the absence of CCR effects, anti-phase coherences can only be generated and observed if the two spins interact via a non-zero J -coupling.

However if we introduce the CCR effect the result is different. The two components of the doublet have different linewidths with one being narrowed (here the high-frequency component) and the other broadened. This superposition of different linewidths is still seen with zero J -coupling as it results from the incoherent effect of the dipolar coupling between the spins and of their paramagnetic SAs. The most notable effect at zero J -coupling is seen in the anti-phase doublet in which the intensities do not cancel due to the different linewidths; the result is that this anti-phase doublet can still be observed, in complete contrast to the situation without CCR. Hence in the presence of CCR it is possible both to generate anti-phase coherences via cross-relaxation-allowed coherence transfer, and to observe the resulting anti-phase doublet [264]. As noted earlier this means that the interpretation of NMR spectra that correlate between pairs of spins via the J -coupling need to be interpreted with care, since cross-relaxation-allowed coherence transfer results in correlations even with zero J -coupling [265].

8.9 Paramagnetic relaxation enhancements in non-dynamic solid insulators

We now turn to a different motional regime to those considered so far, in which chemical exchange and random reorientation of the interaction tensor, on a timescale that is conducive to efficient relaxation, are completely absent. This situation is regularly encountered in rigid solids, including materials and crystalline phases of small molecules in a rigid lattice with no flexible parts, so there is neither overall tumbling nor internal motional dynamics on the relevant timescale. The only motions that are present are due to vibrations, which are not an efficient source of nuclear relaxation, and so such diamagnetic systems often exhibit very long T_1 relaxation times, of the order of minutes or hours. On the other hand, paramagnetic systems still exhibit short relaxation times as the vibrational motion still causes efficient electronic relaxation [119], and the relaxing electrons act to relax the nuclei.

When deciding on the model to use for the PRE in these systems, it is tempting to use the Curie model of Gueron [99], and Vega and Fiat [100], and extend τ_R and τ_M to infinity. However this is *not* valid as the extension of the correlation times in this way would cause a violation of one of the basic assumptions of Redfield theory, which is that the observation time must be longer than the correlation times. We therefore begin instead from the Solomon–Bloembergen–Morgan model and ignore chemical exchange and stochastic reorientation from the beginning, so that the overall correlation times are simply equal to the electronic longitudinal and transverse relaxation time constants:

$$\tau_{E,q} = \tau_{c,q} = T_{qe}, \quad q = 1, 2. \quad (8.184)$$

We then take the Solomon–Bloembergen–Morgan equations and make the substitution of the correlation times directly, resulting in the following nuclear T_1 relaxation time constant

$$\begin{aligned} \frac{1}{T_1} = & \frac{2}{3}S(S+1) \left(\frac{A^{\text{FC}}}{\hbar} \right)^2 \frac{T_{2e}}{1 + (\omega_S - \omega_I)^2 T_{2e}^2} \\ & + \frac{2}{15}S(S+1) \left(\frac{b_{SI}}{\hbar} \right)^2 \left[\frac{3T_{1e}}{1 + \omega_I^2 T_{1e}^2} + \frac{6T_{2e}}{1 + (\omega_S + \omega_I)^2 T_{2e}^2} + \frac{T_{2e}}{1 + (\omega_S - \omega_I)^2 T_{2e}^2} \right], \end{aligned} \quad (8.185)$$

and the following nuclear T_2 relaxation time constant

$$\begin{aligned} \frac{1}{T_2} = & \frac{1}{3}S(S+1) \left(\frac{A^{\text{FC}}}{\hbar} \right)^2 \left[T_{1e} + \frac{T_{2e}}{1 + (\omega_S - \omega_I)^2 T_{2e}^2} \right] \\ & + \frac{1}{15}S(S+1) \left(\frac{b_{SI}}{\hbar} \right)^2 \left[4T_{1e} + \frac{6T_{2e}}{1 + \omega_S^2 T_{2e}^2} + \frac{3T_{1e}}{1 + \omega_I^2 T_{1e}^2} + \frac{6T_{2e}}{1 + (\omega_S + \omega_I)^2 T_{2e}^2} + \frac{T_{2e}}{1 + (\omega_S - \omega_I)^2 T_{2e}^2} \right]. \end{aligned} \quad (8.186)$$

These expressions assume a point-dipole model for the electrons. However the correction for delocalisation effects is relatively straightforward, as we have seen.

Figure 8.9 shows a general comparison of the Solomon and Bloembergen longitudinal and transverse relaxation rates for a ^1H nucleus in a field of 11.74 T, for a range of electronic relaxation times, with the assumption that $T_{1e} = T_{2e} \equiv \tau_S$. In (a) and (b) are shown the Solomon and Bloembergen contributions to the longitudinal relaxation rates plotted against τ_S . We see that the Solomon contribution is always the larger of the two, and completely dominates for all electronic relaxation times, apart from the shortest below

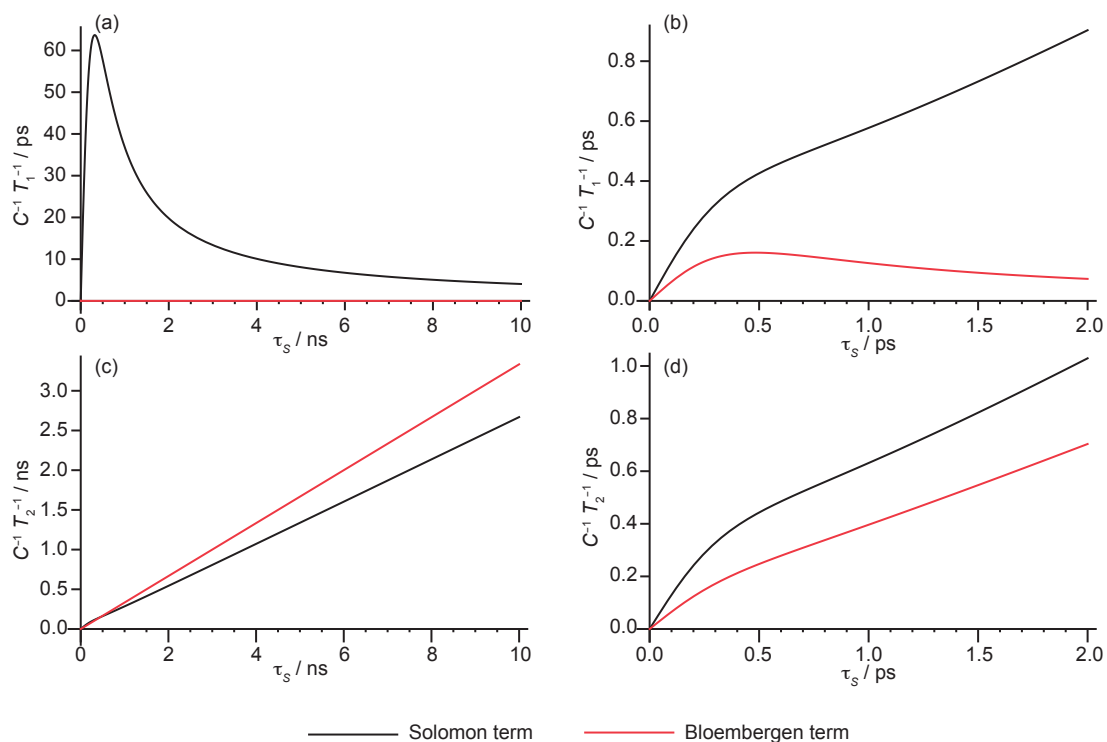


Figure 8.9: Comparison of the sizes of the longitudinal and transverse relaxation rates due to the Solomon and Bloembergen mechanisms in a non-dynamic solid as a function of the electron relaxation time. It is assumed that $T_{1e} = T_{2e} \equiv \tau_S$. The variation of the longitudinal rates is shown in (a), and the transverse rates in (c), both up to a τ_S of 10 ns. In (b) and (d) are shown expansions of the plots in (a) and (c), up to a τ_S of 2 ps. The nuclear spins are ^1H in an external field of 11.74 T. The constant $C = S(S + 1)(3 + (\eta^{\text{SD}})^2)(\tilde{A}_{zz}^{\text{SD}}/\hbar)^2/12$, i.e. $S(S + 1)(b_{SI}/\hbar)^2$ for the Solomon mechanism, and $S(S + 1)(A^{\text{FC}}/\hbar)^2$ for the Bloembergen mechanism.

approximately 1.0 ps where the Bloembergen contribution is still smaller, but nevertheless significant. Both the Solomon and overall relaxation rate are dominated by the reduced spectral density $j_{21}(\omega_I)$ which, for an external field of 11.74 T, reaches a maximum at $T_{1e} = 0.32$ ns. Shorter electronic relaxation times, such as those of the order of 0.1–1.0 ps that are observed for lanthanides, therefore lead to longer values of T_1 . We see a different variation for the transverse relaxation rates in (c) and (d). Here the Solomon and Bloembergen terms are comparable, and are dominated by the reduced spectral densities $j_{21}(0)$ and $j_{01}(0)$ respectively, both of which depend on T_{1e} . Both contributions to the relaxation rate therefore simply increase with T_{1e} .

The trends shown in Figure 8.9 indicate a general property of the relaxation properties of paramagnetic systems, which is that, in the absence of dynamic or motional effects, the enhancements in both R_1 and R_2 are dominated by electronic longitudinal relaxation via the time constant T_{1e} . Slower electronic longitudinal relaxation rapidly increases the rate of the transverse PRE, and rapidly increases the longitudinal PRE to a maximum at $T_{1e} = 1/|\omega_I|$, after which it slowly drops off.

8.10 Paramagnetic relaxation enhancements due to lanthanide ions

We now round off this chapter with a very brief review of the expressions for the relaxation rate constants that could be applied to lanthanide systems. As we saw in chapter 6, the EPR interaction and paramagnetic shift tensors due to lanthanide ions can be extremely complicated, as a result of the need to consider the effects of strong SO coupling and the low-lying excited states due to the crystal-field interaction and higher-energy SO coupling levels. However we also saw that we can simplify matters by assuming that kT is sufficiently large that the crystal-field energy levels are all significantly populated, and treating the lanthanide ions as free metal ions [61]. To a reasonable approximation, we can then take the expressions for the relaxation rate constants derived earlier, and replace S with J , and g_e with g_J to obtain the correct expressions.

In the Solomon–Bloembergen–Morgan relaxation model, we take the Fermi-contact coupling constant A^{FC} and spin-dipolar coupling constant to be:

$$A^{\text{FC}} = \frac{\mu_0 \mu_B g_J \hbar \gamma_I}{3S} \rho^{\alpha-\beta}(\mathbf{0}), \quad (8.187)$$

$$b_{JI} = \frac{\mu_0 \mu_B g_J \hbar \gamma_I}{4\pi R^3}. \quad (8.188)$$

Then replacing S with J we obtain the following expression for T_1 :

$$\begin{aligned} \frac{1}{T_1} = & \frac{2}{3} J(J+1) \left(\frac{A^{\text{FC}}}{\hbar} \right)^2 \frac{\tau_{\text{E},2}}{1 + (\omega_S - \omega_I)^2 \tau_{\text{E},2}^2} \\ & + \frac{2}{15} J(J+1) \left(\frac{b_{\text{II}}}{\hbar} \right)^2 \left[\frac{3\tau_{\text{c},1}}{1 + \omega_I^2 \tau_{\text{c},1}^2} + \frac{6\tau_{\text{c},2}}{1 + (\omega_S + \omega_I)^2 \tau_{\text{c},2}^2} + \frac{\tau_{\text{c},2}}{1 + (\omega_S - \omega_I)^2 \tau_{\text{c},2}^2} \right]. \end{aligned} \quad (8.189)$$

Likewise the T_2 time constant is

$$\begin{aligned} \frac{1}{T_2} = & \frac{1}{3} J(J+1) \left(\frac{A^{\text{FC}}}{\hbar} \right)^2 \left[\tau_{\text{E},1} + \frac{\tau_{\text{E},2}}{1 + (\omega_S - \omega_I)^2 \tau_{\text{E},2}^2} \right] \\ & + \frac{1}{15} J(J+1) \left(\frac{b_{\text{SI}}}{\hbar} \right)^2 \left[4\tau_{\text{c},1} + \frac{6\tau_{\text{c},2}}{1 + \omega_S^2 \tau_{\text{c},2}^2} + \frac{3\tau_{\text{c},1}}{1 + \omega_I^2 \tau_{\text{c},1}^2} + \frac{6\tau_{\text{c},2}}{1 + (\omega_S + \omega_I)^2 \tau_{\text{c},2}^2} + \frac{\tau_{\text{c},2}}{1 + (\omega_S - \omega_I)^2 \tau_{\text{c},2}^2} \right]. \end{aligned} \quad (8.190)$$

For relaxation due to slow molecular motions we can use the Curie model, in which the ‘‘Curie spin’’ is now defined as the thermal average of the z component of the total angular momentum operator \hat{J}_z :

$$J_{\text{C}} \equiv \langle \hat{J}_z \rangle \quad (8.191)$$

$$= - \frac{\mu_{\text{B}} g_J J(J+1) B_0}{3kT}. \quad (8.192)$$

The expressions for the total T_1 and T_2 relaxation time constants including both the Fermi-contact and spin-dipolar contributions, are

$$\begin{aligned} \frac{1}{T_1} = & \frac{2}{3} J(J+1) \left(\frac{A^{\text{FC}}}{\hbar} \right)^2 \frac{\tau_{\text{E},2}}{1 + (\omega_S - \omega_I)^2 \tau_{\text{E},2}^2} + \frac{2}{15} \left(\frac{b_{\text{II}}}{\hbar} \right)^2 \left[J_{\text{C}}^2 \frac{9\tau_{\text{D}}}{1 + \omega_I^2 \tau_{\text{D}}^2} + \left(\frac{1}{3} J(J+1) - J_{\text{C}}^2 \right) \frac{9\tau_{\text{c},1}}{1 + \omega_I^2 \tau_{\text{c},1}^2} \right. \\ & \left. + J(J+1) \left(\frac{6\tau_{\text{c},2}}{1 + (\omega_S + \omega_I)^2 \tau_{\text{c},2}^2} + \frac{\tau_{\text{c},2}}{1 + (\omega_S - \omega_I)^2 \tau_{\text{c},2}^2} \right) \right], \end{aligned} \quad (8.193)$$

and

$$\begin{aligned}
\frac{1}{T_2} = & \frac{1}{3}J(J+1)\left(\frac{A^{\text{FC}}}{\hbar}\right)^2\left[3J_C^2\tau_M + 3\left(\frac{1}{3}J(J+1) - J_C^2\right)\tau_{E,1} + \frac{\tau_{E,2}}{1 + (\omega_S - \omega_I)^2\tau_{E,2}^2}\right] \\
& + \frac{1}{15}\left(\frac{b_{II}}{\hbar}\right)^2\left[J_C^2\left(12\tau_D + \frac{9\tau_D}{1 + \omega_I^2\tau_D^2}\right) + \left(\frac{1}{3}J(J+1) - J_C^2\right)\left(12\tau_{c,1} + \frac{9\tau_{c,1}}{1 + \omega_I^2\tau_{c,1}^2}\right)\right. \\
& \left. + J(J+1)\left(\frac{6\tau_{c,2}}{1 + \omega_S^2\tau_{c,2}^2} + \frac{6\tau_{c,2}}{1 + (\omega_S + \omega_I)^2\tau_{c,2}^2} + \frac{\tau_{c,2}}{1 + (\omega_S - \omega_I)^2\tau_{c,2}^2}\right)\right]. \quad (8.194)
\end{aligned}$$

For lanthanide ions the Fermi-contact coupling interaction is relatively small compared to the spin-dipolar interaction, due to the contracted nature of the $4f$ orbitals and the corresponding reduced electronic-spin transfer. Therefore we expect the Solomon mechanism to dominate the Bloembergen mechanism in the overall relaxation behaviour. Furthermore electronic relaxation for lanthanide ions is considerably faster than for $3d$ ions, as we see in the following section, and so for typical ranges of rotational and chemical-exchange correlation times we are able to approximate the overall correlation times as $\tau_{c,q} \approx \tau_{E,q} \approx T_{qe}$, with the result that electronic relaxation is the stochastic process that dominates the PRE.

8.11 Relaxation properties of specific paramagnetic metal ions

Following the examination of the theory of the PRE we now quantify the PREs of different paramagnetic metal ions in different motional regimes, and due to the Solomon, Bloembergen, and Curie mechanisms. To compare the PREs due to different metal ions on a particular nucleus in a particular system requires a quantification of the values of T_{1e} and T_{2e} of that particular metal ion in that particular system. Electronic relaxation times have been measured extensively for complexes and metalloproteins in solution and glasses, and these values have been used to estimate the PREs of nuclei in similar complexes by Bertini et al [15]. Table 8.5 gives the ranges of electronic relaxation times for a selection of first-, second-, and third-row d -block transition-metal ions, and also the calculated longitudinal PREs R_1 and R_2 , and Table 8.6 gives the equivalent values for the lanthanide ions. The tables include calculations for a ^1H nucleus in a small complex in solution with a rotational correlation time of $\tau_R = 10^{-10}$ s, and a large biomolecule in solution with $\tau_R = 10^{-8}$ s assuming spin-dipolar Solomon and Curie mechanisms respectively at 298 K and a nucleus-ion separation of 5 Å, and at a ^1H Larmor frequency of -800 MHz. Also included are calculations for the Bloembergen

mechanism for a one-electron Fermi-contact coupling constant of 4.47 MHz.

The nuclear relaxation of molecules in solution is very well understood [95, 246, 252, 253], and the predominant difficulty in calculating PREs is the incorporation of the details relating to the electronic relaxation processes [95]. On the other hand, in solids both nuclear and electronic relaxation are poorly understood by comparison. Tables 8.5 and 8.6 also include estimates of the PREs obtained in solid materials assuming that the range of electronic relaxation times matches that in solution.

8.11.1 The *d*-block transition-metal ions

The electronic relaxation times in Table 8.5 have been grouped together into a generic electronic correlation time τ_S . There is a very wide range of such times, which lie between 10^{-8} and 10^{-13} s. The electronic relaxation of *d*-block transition-metal ions is due to the stochastic modulation of both the permanent anisotropic EPR tensors, and any transient changes in their values due to distortions of the coordination sphere. Of the EPR tensors the ZFS provides the dominant effect, followed by the *g*-anisotropy. Both are due to SO coupling effects, and their sizes depend on the size of the many-electron SO coupling parameter λ . Therefore there is a general trend for a larger SO coupling energy to result in faster electronic relaxation.

High-spin metal ions with half-full *d*-shells essentially have zero SO coupling energy, and therefore the ZFS and *g*-anisotropy are very small. This is the reason for the relatively long τ_S of 10^{-8} s for Mn^{2+} . Transition-metal ions of other configurations relax more quickly due to the presence of SO coupling. However ions with $S = 1/2$ have no ZFS, and so the electronic relaxation is due principally to the *g*-anisotropy. The result is that the relaxation for such ions may also be comparatively slow, as can be seen for VO^{2+} and Cu^{2+} , which have τ_S values between 10^{-8} and 10^{-9} s.

The expression for the longitudinal PRE R_1 is dominated by the spectral density $j(\omega_I)$, which is a maximum when $\tau_c = 1/|\omega_I|$ which, for the examples given here, is 2.0×10^{-10} s. Therefore for electronic relaxation times below this value, increasing T_{1e} and T_{2e} increases R_1 , whereas increasing T_{1e} and T_{2e} above 2.0×10^{-10} s has the effect of reducing R_1 . The transverse PRE R_2 is dominated by the spectral density $j(0)$ at longer correlation times, which increases linearly with the correlation time. By contrast, in the extreme-narrowing limit, such that $\tau_c \ll 1/|\omega_I|$, the Solomon longitudinal and transverse PREs are equal.

This explains why the overall longitudinal PRE is dominated by the Solomon mechanism, rather than the Bloembergen mechanism, as only the former depends on the spectral density $j(\omega_I)$, and the latter depends

Ion	Configuration	S	τ_S / s^a	Bloembergen relaxation rates / s^{-1}	Dipolar relaxation rates / s^{-1}	Small molecules ($\tau_R = 10^{-10}$ s)	Large molecules ($\tau_R = 10^{-8}$ s)	References
				R_1^b R_2^c	R_1^d R_2^e	R_1^f R_2^g	R_1^h R_2^i	
Ti ³⁺	3d ¹	1/2	10 ⁻¹⁰ -10 ⁻¹¹	0.4-4	47-378	43-223	47-375	[267, 268]
VO ²⁺	3d ¹	1/2	10 ⁻⁸	0.004	19	376	501	[269-271]
V ³⁺	3d ²	1	10 ⁻¹¹	2	126	115	134	[272, 273]
V ²⁺	3d ³	3/2	10 ⁻⁹	0.02	902	1782	2327	[274]
Cr ³⁺	3d ³	3/2	5 × 10 ⁻⁹ -5 × 10 ⁻¹⁰	0.004-0.04	187-1620	1680-1869	2156-2483	[115, 275, 276]
Cr ²⁺	3d ⁴	2	10 ⁻¹¹ -10 ⁻¹²	2-16	45-379	45-345	46-375	[277]
Mn ³⁺	3d ⁴	2	10 ⁻¹⁰ -10 ⁻¹¹	0.2-2	379-3026	345-1783	375-2967	[272, 276, 278]
Mn ²⁺	3d ⁵	5/2	10 ⁻⁸	0.002	219	4387	5842	[115, 279]
Fe ³⁺ HS	3d ⁵	5/2	10 ⁻⁹ -10 ⁻¹¹	0.02-2	553-2106	503-4158	587-5429	[8366-41,657]
Fe ³⁺ LS	3d ⁵	1/2	10 ⁻¹¹ -10 ⁻¹³	4-36	1-47	1-43	2-47	[282, 283]
Fe ²⁺ HS	3d ⁶ , 5-6 coord.	2	10 ⁻¹² -10 ⁻¹³	16-18	12-45	12-45	13-46	[284, 285]
Co ²⁺ HS	3d ⁷ , 5-6 coord.	3/2	5 × 10 ⁻¹² -10 ⁻¹³	2	379	345	402	[286]
Co ²⁺ LS	3d ⁷ , 4 coord.	3/2	10 ⁻¹¹	2	7-119	7-114	8-119	[287, 288]
Ni ²⁺	3d ⁸ , 5-6 coord.	1	10 ⁻¹⁰	0.04-0.4	237	215	252	[289]
	3d ⁸ , 4 coord.	1	10 ⁻¹²	0.2	1009	594	718	—
Cu ²⁺	3d ⁹	1/2	5 × 10 ⁻⁹ -10 ⁻⁹	0.007-0.04	37-180	356-374	456-497	[290]
Ru ³⁺	4d ⁵	1/2	10 ⁻¹¹ -10 ⁻¹²	4-33	6-47	6-43	6-50	[291, 292]
Re ³⁺	5d ⁴	1	10 ⁻¹² -10 ⁻¹³	22-24	4-15	4-15	4-17	[294]

Table 8.5: Summary of the relaxation properties of, and PREs due to, a selection of transition-metal ions. For each ion is given the range of T_{1e} and T_{2e} electronic relaxation times, taken from Bertini, Luchinat, and Parigi [15] and the additional references indicated, and grouped together as a relaxation time τ_S . The corresponding range of PRE rates R_1 and R_2 for a ¹H experiencing a hyperfine coupling to the unpaired electrons are also given for the Bloembergen mechanism, and the dipolar-interaction mechanism in the fast- ($\tau_R = 10^{-10}$ s) and slow-rotation ($\tau_R = 10^{-8}$ s) limits. The equations used are indicated with J used in lieu of S . The Bloembergen relaxation rates are calculated assuming a one-electron Fermi-contact coupling constant of 4.47 MHz. The dipolar relaxation rates are calculated assuming the point-dipole model with a separation between nucleus and paramagnetic centre of 5 Å. In all cases it is assumed there is no chemical exchange. The magnetic field is 18.78 T, and the temperature used in the Curie-spin is 298K. HS refers to ‘high-spin’ and LS to ‘low-spin’.

^aQuoted as a range of values for T_{1e} and T_{2e} .

^bEquation 8.104.

^cEquation 8.106.

^dEquation 8.185.

^eEquation 8.186.

^fEquation 8.99.

^gEquation 8.101.

^hEquation 8.131.

ⁱEquation 8.133.

only on $j(\omega_S \pm \omega_I)$, which is much smaller in these motional regimes. The Bloembergen mechanism, however, makes a more important contribution to the transverse PRE due to the dependence on $j(0)$. Transition-metal ions with electronic relaxation times in the range 10^{-11} – 10^{-13} s, such as low-spin Fe^{3+} , high-spin 5- and 6-coordinate Co^{2+} , Ru^{3+} , and Re^{3+} , have Solomon relaxation rates for rigid solids and small complexes that are approximately equal. On the other hand metal ions with slowly relaxing electrons, with time constants in the range 10^{-8} – 10^{-9} s such as Mn^{2+} and Cu^{2+} , exhibit transverse Solomon PREs that are significantly larger than their longitudinal counterparts. In the slow-rotation regime, such that Curie-spin relaxation becomes important, we see that the most significant effects are seen on the transverse PREs, which increase substantially due to the increasing τ_R .

Superimposed upon the dependence on the electronic relaxation times is the observation that metal ions with higher spins S give larger PREs due to the dependence on $S(S + 1)$.

8.11.2 The lanthanide ions

For molecules in solution the electronic relaxation times T_{1e} and T_{2e} of the lanthanide ions generally take values from 0.01 to 0.1 ps, and so are shorter than those of the first-row transition-metal ions. This is due to the larger SO coupling of the former. The smaller electronic relaxation times of the lanthanides tend to result in lower PREs, particularly for transverse relaxation, than for the $3d$ metal ions. Table 8.6 summarises the range of electronic relaxation times, grouped together as ‘electronic correlation times’ τ_S , and the resulting calculated PREs. For the non-dynamic solid and small molecule $T_1 \approx T_2$, and so the relaxation properties are in the extreme-narrowing limit. We leave this regime as τ_R increases, as for large biomolecules dominated by slow rotational diffusion. These systems are then subject to Curie relaxation, and the the transverse relaxation rates are several orders of magnitude larger than the longitudinal rates.

The Gd^{3+} ion: $4f^7, {}^8S_{7/2}$

An important exception to the general relaxation behaviour of the trivalent lanthanides is Gd^{3+} , which possesses a half-full $4f$ shell and therefore effectively has an SO coupling interaction of zero. The Gd^{3+} ion exhibits electronic relaxation times of the order of 1 to 10 ns, which are up to six orders of magnitude greater than for the other lanthanides. These longer electronic correlations result in larger PREs for all relaxation mechanisms with the exception of longitudinal relaxation due to the Bloembergen mechanism,

Ion	Configuration	J	τ_S / s^a	Bloembergen relaxation rates / s^{-1}	Dipolar relaxation rates / s^{-1}	Small molecules ($\tau_R = 10^{-10}$ s)	Large molecules ($\tau_R = 10^{-8}$ s)	References	
				R_1^b	R_2^c	R_1^f	R_1^h		
Ce ³⁺	f^1	5/2	4×10^{-13} – 10^{-13}	76–123	80–230	3–7	3–7	263–267	—
Pt ³⁺	f^2	4	3×10^{-13} – 6×10^{-14}	24–63	25–95	4–13	4–13	1033–1043	[295, 296]
Nd ³⁺	f^3	9/2	8×10^{-13} – 2×10^{-13}	19–27	32–86	11–21	11–21	1088–1100	[295]
Sm ³⁺	f^5	5/2	2×10^{-13} – 5×10^{-14}	0.2–0.5	0.2–0.6	0.2–0.6	0.2–0.5	3–4	[295, 296]
Eu ²⁺	f^7	7/2	5×10^{-14} – 10^{-14}	2–8	2–8	3–16	18–29	24,948–24,960	[295]
Gd ³⁺	f^7	7/2	10^{-8} – 10^{-9}	0.002–0.02	84,479–844,793	393–3782	770–3986	84,825–343,744	[297–302]
Tb ³⁺	f^8	6	8×10^{-13} – 2×10^{-13}	34–48	58–155	78–153	103–176	56,200–56,287	[295]
Dy ³⁺	f^9	15/2	10^{-12} – 4×10^{-13}	50–86	162–323	132–212	167–244	80,856–80,951	[295, 296]
Ho ³⁺	f^{10}	8	8×10^{-13} – 2×10^{-13}	92–128	157–416	93–182	130–215	79,632–79,733	[295, 296]
Er ³⁺	f^{11}	15/2	8×10^{-13} – 3×10^{-13}	134–202	302–603	94–150	116–170	53,056–53,121	[295, 296]
Tm ³⁺	f^{12}	6	2×10^{-12} – 5×10^{-13}	84–251	595–1920	73–190	80–194	20,614–20,750	[295]
Yb ³⁺	f^{13}	7/2	5×10^{-13} – 2×10^{-13}	361–376	458–856	17–26	17–26	2676–2687	[295, 296, 299, 300]

Table 8.6: Summary of the relaxation properties of, and PREs due to, the lanthanide ions. For each ion is given the range of T_{1e} and T_{2e} electronic relaxation times, taken from Bertini, Luchinat, and Parigi [15] and the additional references indicated, and grouped together as a relaxation time τ_S . The corresponding range of PRE rates R_1 and R_2 for a ^1H experiencing a hyperfine coupling to the unpaired electrons are also given for the Bloembergen mechanism, and the dipolar-interaction mechanism in the fast- ($\tau_R = 10^{-10}$ s) and slow-rotation ($\tau_R = 10^{-8}$ s) limits. The equations used are indicated with J used in lieu of S . The Bloembergen relaxation rates are calculated assuming a one-electron Fermi-contact coupling constant of 2.23 MHz. The dipolar relaxation rates are calculated assuming the point-dipole model with a separation between nucleus and paramagnetic centre of 5 Å. In all cases it is assumed there is no chemical exchange. The magnetic field is 18.78 T, and the temperature used in the Curie-spin is 298K.

^aQuoted as a range of values for T_{1e} and T_{2e} .

^bEquation 8.104.

^cEquation 8.106.

^dEquation 8.185.

^eEquation 8.186.

^fEquation 8.99.

^gEquation 8.101.

^hEquation 8.131.

ⁱEquation 8.133.

which is negligible compared to the other lanthanides. In particular the larger τ_S values have the effect of increasing the rate of transverse relaxation, which is now dominated by the term proportional to τ_S , in all cases so that it is orders of magnitude faster than for the other ions. The large relaxation effects result in Gd^{3+} complexes exerting long-range PREs, which make these systems good contrast agents for MRI [127, 129]. However it is difficult to study the paramagnetic NMR effects *within* these complexes as the large short-range PRE tends to render the nuclei unobservable.

8.12 Key concepts

- Under conditions of fast stochastic dynamics, such that the timescale of motion is much shorter than the reciprocal of the relevant interaction, electronic and nuclear relaxation can be described using Redfield theory.
- Redfield theory is usually valid for nuclear relaxation in solution, and in solids containing rapidly fluctuating electrons.
- Redfield theory does not usually provide a good description of electronic relaxation, and is only valid in highly-symmetric complexes.
- The principal mechanisms of electronic relaxation are modulation of the transient and/or static zero-field splitting, and phonons.
- Under high-field and fast-motional conditions, nuclear relaxation is described by the Solomon–Bloembergen–Morgan equations.
- The principal mechanisms of nuclear relaxation are the spin-dipolar hyperfine interaction (the Solomon mechanism), and the Fermi-contact interaction (Bloembergen mechanism).
- In systems where the rotational dynamics are slow compared to the rates of electronic relaxation the nuclear transverse relaxation is dominated by the Curie mechanism.
- In paramagnetic biomolecules with slow rotational diffusion in solution there is cross correlation between the nuclear–nuclear dipolar coupling to a second nuclear spin and paramagnetic SA, which

results in the two components of the doublet having different linewidths. Relaxation-allowed coherence transfer can therefore occur between the two nuclei even in the absence of a J -coupling between them.

- In solids with no rotational dynamics, Curie relaxation is absent.
- Metal ions with $S = 1/2$ and half-full d^5 configurations have relatively long electronic relaxation times due to the absence of the ZFS.
- Electronic relaxation times tend to decrease down a triad due to the increasing spin-orbit coupling.
- The paramagnetic relaxation enhancement due to lanthanide ions is typically smaller than that for first-row d -block transition-metal ions, due to the faster electronic relaxation.

Chapter 9

Relaxation in paramagnetic systems under general conditions

In chapter 8 a treatment of nuclear relaxation was presented, valid for (1) high-field conditions, (2) fast motional dynamics, (3) a non-relativistic description of the electron spin, and (4) incorporating a phenomenological description of the electronic relaxation. In this chapter we expand on the previous description, by adopting a full quantum-mechanical treatment of the relaxation processes. This enables us to derive expressions for the PRE where the electronic relaxation is outside the Redfield limit, and including relativistic effects such as SO coupling. The electronic relaxation is therefore treated properly, and the resulting expressions for the PRE are valid at all fields.

We begin by deriving a general expression for the PRE under general conditions, employing a version of Redfield theory in which we treat both the spin system and lattice using quantum mechanics. Whilst this expression is correct and general, it resembles a ‘black box’ in that it is not always obvious how to use it to obtain usable expressions that are easily understood. We therefore illustrate the scope of the formalism by deriving the expressions for the PRE in a number of special cases, including low external field, fast rotational motion in solution, and including the effects of vibrations on electronic relaxation. In all cases the treatments are valid for arbitrary electronic spin S . Finally we examine the case of relaxation in metallic solids.

Further reading on the general theory of paramagnetic relaxation can be found in the reviews of Kowalewski

et al. [93, 94].

9.1 Introduction to the slow-motion theory of relaxation

9.1.1 The different approaches for slow relaxation dynamics

In the description of the PRE in chapter 8 we modelled the problem as a quantum mechanical spin system, comprising both the nuclear and electronic spins, coupled to a lattice that is treated classically, and which comprises the remaining parts of the system such as the molecular framework. The random time variation of the classical degrees of freedom of the lattice is the cause of the relaxation of the spin system. This time dependence is included in the Hamiltonian describing the spin–lattice coupling $\hat{H}_1(t)$, which is characterised by a strength parameter which is ω_{IL} in angular units. The validity of the entire semi-classical Redfield description is restricted to the motional-narrowing, or Redfield, limit which we quoted as $|\omega_{IL}| \tau_c \ll 1$, where τ_c is the correlation time we defined earlier. If the spin–lattice coupling strength is sufficiently large, or else the correlation time is sufficiently long so that the Redfield limit is violated, we must formulate the problem in another way. This problem is frequently encountered when the spin system contains electronic spins, as they are frequently subject to very large anisotropic interactions, such as the ZFS. In fact the electron–lattice coupling parameters are typically so large that we find ourselves in the *slow-motion limit* $|\omega_{IL}| \tau_c \gg 1$.

Three practical approaches to resolving this problem can be found in the literature. The first is the *Swedish slow-motion theory*, which introduces the concept of a nuclear spin interacting with a *composite lattice*, comprising both the quantized electronic degrees of freedom, and the classical degrees of freedom due to rotational diffusion, distortions, chemical exchange, etc. [93, 102, 105, 106]. The second approach is the *Grenoble method*, which models the rotational diffusion and collision dynamics using a large number of random configurations of the spin system, with each given a random trajectory of the relevant parameters describing the fluctuations of the spin-dipolar coupling vector, and static and transient ZFS parameters [110, 111]. The third approach is the *Ann Arbor method*, in which the electronic dynamics are treated using electronic wavefunctions rather than in Liouville space [112–114]. Although these three methods represent, at first sight, very different formulations of electronic relaxation and the PRE, it has been shown by Belorizky et al. that they predict very similar results under certain conditions, implying that the underlying physics is the same in each case [251].

Figure 9.1 shows comparisons of the NMRD PREs simulated using the Swedish slow-motion, Grenoble, and Ann Arbor models for two different metal ions, and two different rotational correlation times [251]. In all cases the simulations were performed under the following conditions:

- Two values of the electronic spin quantum number were chosen, $S = 7/2$ corresponding to Gd^{3+} , and $S = 1$ corresponding to high-spin Ni^{2+} . The nucleus was ^1H ;
- The ZFS Hamiltonian comprises both a static and transient part, which were chosen to be axially symmetric, with magnitudes given by Δ_s and Δ_t respectively. These interactions were the sources of electronic relaxation;
- The source of the nuclear relaxation was the spin-dipolar interaction. The PAF of this interaction did not coincide with that of the static ZFS, but they were assumed to be separated from each other by the polar angle θ , which was assumed fixed;
- Both the spin-dipolar and ZFS interactions were modulated by rotational diffusion with correlation times τ_r ;
- The transient ZFS was modulated by distortions of the metal coordination geometry due to solvent collisions with correlation time τ_v .

The simulations for $S = 7/2$ were performed with static and transient ZFS parameters of $\Delta_s = 0.01 \text{ cm}^{-1}$ and $\Delta_t = 0.05 \text{ cm}^{-1}$, a spin-dipolar coupling constant of 16.7 MHz, and θ angles of 0° and 90° . These ZFS parameters are typical values for Gd^{3+} , and the coupling constant corresponds to a dipolar interaction with ^1H at a distance of 310 pm from the metal ion. The distortional correlation time was $\tau_v = 5 \text{ ps}$. The ^1H PRE profiles are shown in Figure 9.1 (a) and (b) for rotational correlation times of $\tau_r = 100 \text{ ps}$ and $1 \mu\text{s}$ respectively. In both cases modulation of the transient ZFS is within the Redfield approximation. However the rotational modulation of the ZFS and spin-dipolar interaction only satisfy the Redfield condition for the shorter rotational correlation time in (a). We also see that all three slow-motion theories predict essentially the same behaviour, being indistinguishable above fields of 0.1 T, and with only a small deviation of the Ann Arbor method from the others at lower fields.

The simulations for $S = 1$ were performed for larger static and transient ZFS parameters of $\Delta_s = 1 \text{ cm}^{-1}$ and $\Delta_t = 10 \text{ cm}^{-1}$, typical for high-spin Ni^{2+} , with all other parameters the same as for $S = 7/2$. The results,

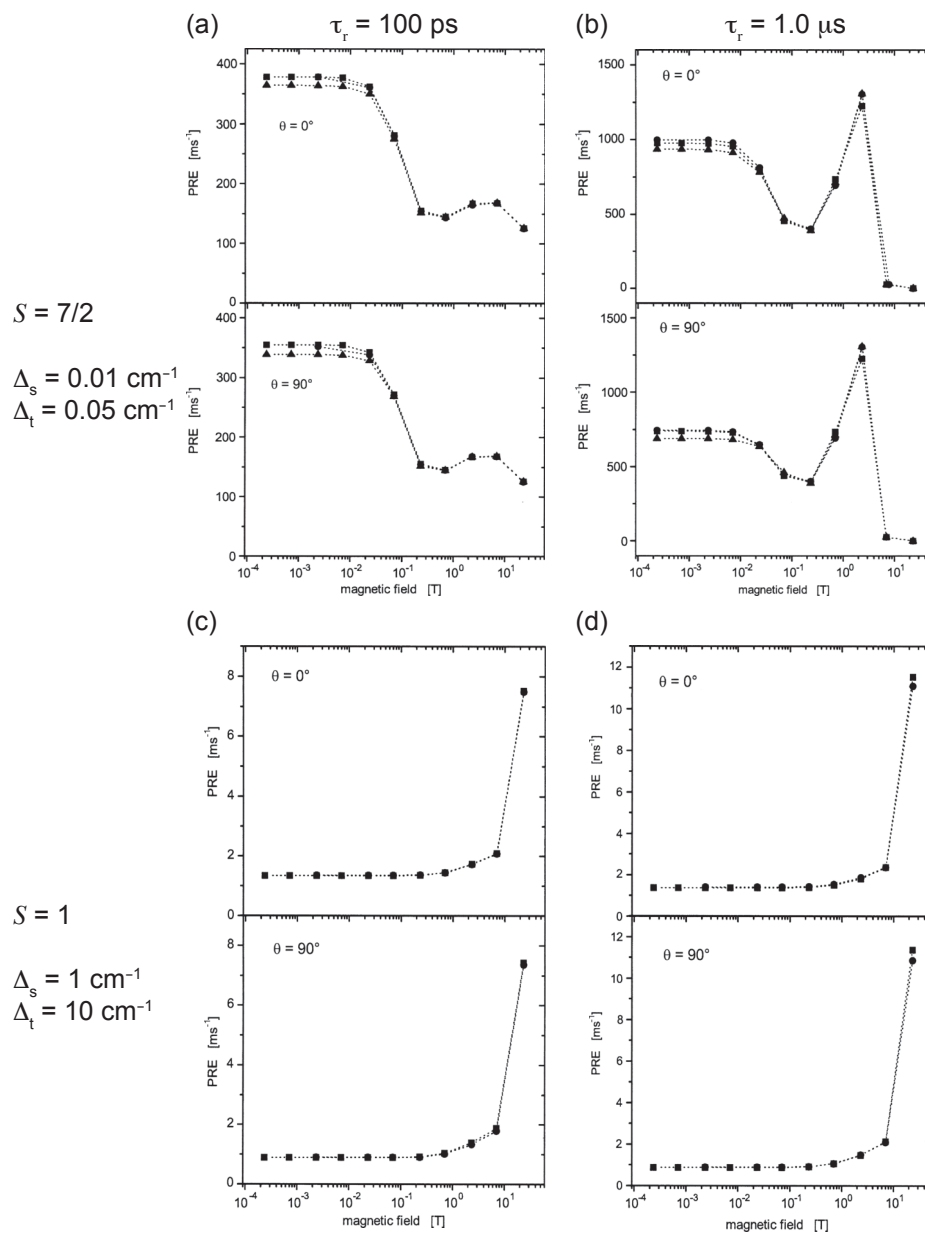


Figure 9.1: Simulated proton PRE NMRD profiles, calculated using the three slow-motion models for two different metal ions. The profiles in (a) and (b) are calculated for an electronic spin quantum number $S = 7/2$, and rotational correlation times of (a) $\tau_r = 100 \text{ ps}$ and (b) $1 \mu\text{s}$. The static and transient ZFS parameters are $\Delta_s = 0.01 \text{ cm}^{-1}$ and $\Delta_t = 0.05 \text{ cm}^{-1}$. The profiles in (c) and (d) are calculated for $S = 1$, rotational correlation times of (c) $\tau_r = 100 \text{ ps}$ and (d) $1 \mu\text{s}$, and static and transient ZFS parameters of $\Delta_s = 1 \text{ cm}^{-1}$ and $\Delta_t = 10 \text{ cm}^{-1}$. Note that no Ann Arbor data are shown for (c) and (d) as the results diverge. In all cases the spin-dipolar coupling constant is $b_{SI} = 16.7 \text{ MHz}$, and the distortional correlation time is $\tau_v = 5 \text{ ps}$. ▲ the Ann Arbor method; ● the Swedish slow-motion method; ■ the Grenoble method. Adapted from [251], with the permission of AIP Publishing.

for the rotational correlation times of $\tau_r = 100$ ps and 1μ s, are shown in Figure 9.1 (c) and (d). Here the static and transient ZFS dynamics are outside the Redfield limit in both cases, and the spin-dipolar interaction dynamics are only within the Redfield limit for the shorter rotational correlation time in (c). This proved to be a difficult problem that was beyond the Ann Arbor method, for which the results deviated considerably (data not shown) [251]. However it is striking that both the Swedish slow-motion and Grenoble methods predict the same behaviour at all fields.

In the light of the similarities between the Swedish and Grenoble approaches, we choose a single method when describing the formalism of electronic and nuclear relaxation in paramagnetic systems, namely the Swedish slow-motion theory.

9.1.2 The Swedish slow-motion theory

We often encounter the situation where the interactions between the nuclei and their surroundings are sufficiently weak to satisfy the Redfield condition, and so can be treated using Redfield theory, even when the interactions between the electrons and their surroundings are not. This situation has been treated separately by Hwang et al. [304, 305], and a number of groups in Sweden [102–104, 107]. The idea is to sidestep the problem of the strong coupling between the electrons and their surroundings by treating the electrons as *part of the lattice*. Therefore the lattice is now a composite comprising both the classical degrees of freedom, such as the rotational dynamics, and the quantised degrees of freedom of the electronic interactions. The spin system now comprises only the nuclear spin, the coupling of which to the lattice can be treated properly using Redfield theory.

Clearly this description can only be realised by treating the lattice as a quantum object, requiring the full quantum formulation of the Redfield theory [93, 183, 253], which we give in the following section using the stochastic Liouville formalism. In addition to catering for the slow-motion dynamics of the unpaired electrons, the stochastic Liouville formalism also has the advantage of being able to treat the electronic relaxation of spins $S > 1$ properly, rather than phenomenologically as in the Solomon–Bloembergen–Morgan theory. The Solomon–Bloembergen–Morgan theory also assumes that the only electronic interaction is the spatially isotropic Zeeman interaction, meaning that the resulting equations are only valid at external magnetic fields that are sufficiently high that the ZFS can be neglected. This restriction is lifted in the stochastic Liouville formalism and all relevant electronic spin interactions, including SO coupling effects

such as the g -anisotropy and the ZFS, are included.

9.2 The stochastic Liouville formalism

We now introduce the stochastic Liouville formalism, and derive the form of the relaxation superoperator.

9.2.1 The Hamiltonian and Liouvillian

The Hamiltonian \hat{H} describing the entire system, including the nuclear spin system and the composite lattice comprising both the classical degrees of freedom of motion and the quantized electronic degrees of freedom, is

$$\hat{H} = \hat{H}_I + \hat{H}_L + \hat{H}_{IL}. \quad (9.1)$$

The Hamiltonian is divided into three parts describing the nuclear spin system (\hat{H}_I), the lattice (\hat{H}_L), and the coupling between the two (\hat{H}_{IL}). Note that, unlike in the semi-classical formulation of the Redfield theory, all the terms are time-independent. In the Liouville formalism the total Hamiltonian is associated with a total Liouvillian $\hat{\mathcal{L}}$. The Liouvillian is a commutation superoperator which is defined so that it acts on an operator \hat{O} to produce a new operator according to the following transformation [257]:

$$\hat{\mathcal{L}}\hat{O} = [\hat{H}, \hat{O}]. \quad (9.2)$$

The total Liouvillian is the sum of the three Liouvillians describing the spin system $\hat{\mathcal{L}}_I$, lattice $\hat{\mathcal{L}}_L$, and spin–lattice coupling $\hat{\mathcal{L}}_{IL}$:

$$\hat{\mathcal{L}} = \hat{\mathcal{L}}_I + \hat{\mathcal{L}}_L + \hat{\mathcal{L}}_{IL}. \quad (9.3)$$

Each Liouvillian is defined by a relation analogous to that in Equation 9.2.

The nuclear spin system

The Hamiltonian and Liouvillian describing the nuclear spin system contain in principle all the terms associated with the nuclear spin interactions, such as the Zeeman interaction, chemical and paramagnetic shielding, nuclear quadrupolar interaction, and dipolar and J -couplings. As in chapter 8 we restrict the discussion to a

single nuclear spin 1/2 and neglect the effects of the chemical shielding. Therefore the spin Hamiltonian is simply the nuclear Zeeman interaction

$$\hat{H}_I = \hbar\omega_I \hat{I}_z, \quad (9.4)$$

as before.

The spin–lattice coupling

In this formulation of the Redfield theory, the spin–lattice coupling Hamiltonian is simply the hyperfine coupling Hamiltonian. However there is an important difference in the exact form of the Hamiltonian in this formalism compared to the semi-classical Redfield theory. Before, we wrote down the (spin–lattice) hyperfine interaction Hamiltonian in the irreducible spherical tensor basis as

$$\hat{H}_{IL} = \sum_{l=0}^2 \sum_{m=-l}^{+l} (-1)^m A_{lm} \hat{T}_{l-m}, \quad (9.5)$$

where the operators \hat{T}_{lm} contain both nuclear and electronic spin operators. This form is appropriate in the semi-classical Redfield formalism as we have separated the nuclear–electronic spin system (in \hat{T}_{lm}) from the classical degrees of freedom of the lattice (in A_{lm}). However this form is not appropriate in the present formalism as the electronic spins are now part of the lattice. We therefore rewrite Equation 9.5 as follows:

$$\hat{H}_{IL} = \sum_{l=0}^2 \sum_{m=-l}^{+l} (-1)^m A_{lm} \sum_{m'=-1}^{+1} \langle 11, -m', -m + m' | l - m \rangle \hat{I}_{1-m'} \hat{S}_{1,-m+m'} \quad (9.6)$$

$$= \sum_{m'=-1}^{+1} \hat{I}_{1-m'} \sum_{l=0}^2 \sum_{m=-l}^{+l} (-1)^m \langle 11, -m', -m + m' | l - m \rangle \hat{S}_{1,-m+m'} A_{lm}. \quad (9.7)$$

The nuclear spin properties are now contained in the rank-one operators \hat{I}_{1m} , and the composite lattice properties are encoded in the products $\hat{S}_{1,-m+m'} A_{lm}$. To complete the formulation of the hyperfine interaction Hamiltonian we define the rank-one lattice operators \hat{L}_{1m} as

$$\hat{L}_{1m} = \sum_{l=0}^2 \sum_{m'=-l}^{+l} (-1)^{m+m'} \langle 11, -m, -m' + m | l - m' \rangle \hat{S}_{1,-m'+m} A_{lm'}, \quad (9.8)$$

and write the hyperfine interaction Hamiltonian as the scalar contraction of \hat{I}_{1m} and \hat{L}_{1m} :

$$\hat{H}_{IL} = \sum_{m=-1}^{+1} (-1)^m \hat{I}_{1-m} \hat{L}_{1m}. \quad (9.9)$$

For completeness we simplify the expression for the lattice operator in Equation 9.8 by introducing the index $q = m - m'$ to give

$$\hat{L}_{1m} = \sum_{l=0}^2 \sum_{q=-1}^{+1} (-1)^q \langle 11, -m, q | l, q - m \rangle \hat{S}_{1q} A_{lm-q} \quad (9.10)$$

$$= (-1)^m \sum_{l=0}^2 (-1)^l \sqrt{2l+1} \sum_{q=-1}^{+1} \begin{pmatrix} l & 1 & 1 \\ m-q & q & -m \end{pmatrix} \hat{S}_{1q} A_{lm-q}. \quad (9.11)$$

In the following discussion on the expressions for the PRE rate constants it proves convenient to write the lattice operator \hat{L}_{1m} as a sum of contributions of different ranks l :

$$\hat{L}_{1m} = (-1)^m \sum_{l=0}^2 \hat{L}_{1m}^{(l)}, \quad (9.12)$$

where the term $\hat{L}_{1m}^{(l)}$ is given by

$$\hat{L}_{1m}^{(l)} = (-1)^l \sqrt{2l+1} \sum_{q=-1}^{+1} \begin{pmatrix} l & 1 & 1 \\ m-q & q & -m \end{pmatrix} \hat{S}_{1q} A_{lm-q}. \quad (9.13)$$

Hence $\hat{L}_{1m}^{(0)}$ describes the contact contributions to the spin-lattice coupling, $\hat{L}_{1m}^{(1)}$ gives the contribution due to antisymmetric part of the hyperfine interaction, and $\hat{L}_{1m}^{(2)}$ describes the spin-dipolar contribution.

The lattice

The electronic-spin part of the lattice is described by a Hamiltonian \hat{H}_S which comprises the electronic Zeeman interaction \hat{H}_Z , the static ZFS $\hat{H}_{ZFS,S}$, and the transient ZFS $\hat{H}_{ZFS,T}$:

$$\hat{H}_S = \hat{H}_Z + \hat{H}_{ZFS,S} + \hat{H}_{ZFS,T}. \quad (9.14)$$

With each contribution and with the sum is associated a Liouvillian. The total electronic spin Liouvillian $\hat{\mathcal{L}}_S$ is the sum of the electronic Zeeman $\hat{\mathcal{L}}_Z$, static ZFS $\hat{\mathcal{L}}_{ZFS,S}$, and transient ZFS $\hat{\mathcal{L}}_{ZFS,T}$ Liouvillians:

$$\hat{\mathcal{L}}_S = \hat{\mathcal{L}}_Z + \hat{\mathcal{L}}_{ZFS,S} + \hat{\mathcal{L}}_{ZFS,T}. \quad (9.15)$$

As discussed in chapter 8 the static part of the ZFS is the time average of the ZFS interaction during the rapid distortions of the coordination geometry due to vibrations and collisions, and the transient ZFS is the deviation from the average.

The total lattice Liouvillian is obtained by adding the electronic spin Liouvillian to other Liouvillians that describe the stochastic motion within the relevant degrees of freedom, which for example include stochastic rotational diffusion, stochastic distortions, stochastic translational motion, chemical exchange, and vibrations. The total lattice Liouvillian is therefore written as

$$\hat{\mathcal{L}}_L = \hat{\mathcal{L}}_S + \hat{\mathcal{L}}_R + \hat{\mathcal{L}}_D + \hat{\mathcal{L}}_T + \hat{\mathcal{L}}_M + \hat{\mathcal{L}}_V. \quad (9.16)$$

The stochastic rotational diffusion Liouvillian is $\hat{\mathcal{L}}_R = -i\hat{\Gamma}_R$, where $\hat{\Gamma}_R$ is the stationary Markov operator that describes the conditional probability distributions of orientations via the differential equation

$$\frac{d}{dt}P(\Omega|\Omega_0) = -\hat{\Gamma}_R P(\Omega|\Omega_0), \quad (9.17)$$

where $P(\Omega|\Omega_0)$ is the probability that at time t the orientation is given by the Euler angles Ω if the orientation was Ω_0 at $t = 0$. The Liouvillian $\hat{\mathcal{L}}_D$ describing the stochastic distortions of the lattice geometry due to collisions can similarly be written in terms of the stationary Markov operator $\hat{\Gamma}_D$ as $\hat{\mathcal{L}}_D = -i\hat{\Gamma}_D$. The stochastic translational motion is described by $\hat{\mathcal{L}}_T$, and chemical exchange is represented by $\hat{\mathcal{L}}_M$. The quantum vibrational motion of the lattice is represented by the Liouvillian $\hat{\mathcal{L}}_V$.

9.2.2 The density operator

The quantum states of the system $|N\rangle$ are written as the direct product of the nuclear spin states $|IM_I\rangle$ with the lattice states $|L\rangle$:

$$|N\rangle = |IM_I\rangle \otimes |L\rangle. \quad (9.18)$$

In addition the entire system is described by a density operator $\hat{X}(t)$, which is the direct product of the density operators that represent the nuclear spin system $\hat{\rho}(t)$ and the lattice $\hat{P}(t)$:

$$\hat{X}(t) = \hat{\rho}(t) \otimes \hat{P}(t). \quad (9.19)$$

The lattice is a much larger entity than the spin system, and so we can assume that it remains in thermal equilibrium at a temperature T_L that is unchanged by exchanges of energy with the spin system. The lattice density operator is therefore time-independent and equal to the equilibrium lattice density operator \hat{P}_0 ,

$$\hat{P}_0 = \frac{\exp(-\beta_L \hat{H}_L)}{\text{Tr}_L [\exp(-\beta_L \hat{H}_L)]}, \quad (9.20)$$

where Tr_L is the trace taken over all the lattice states $|L\rangle$, and $\beta_L = 1/(kT_L)$. From the definition in Equation 9.20, it is easy to see that the trace of \hat{P}_0 over the lattice states is unity:

$$\text{Tr}_L (\hat{P}_0) = 1. \quad (9.21)$$

Combining this property with Equation 9.19 we see that

$$\text{Tr}_L (\hat{X}(t)) = \hat{\rho}(t) \text{Tr}_L (\hat{P}_0) \quad (9.22)$$

$$= \hat{\rho}(t), \quad (9.23)$$

i.e. that the nuclear spin density operator is equal to the total density operator after taking the trace over the lattice states. This property is important in the derivation of the nuclear spin relaxation superoperator in the following section.

9.3 Derivation of the stochastic Liouville equation

In this section we derive the equation of motion for nuclear relaxation, the form of the relaxation superoperator, and the longitudinal and transverse relaxation rate constants using the stochastic Liouville formalism.

9.3.1 The relaxation superoperator

The starting point is the Redfield master equation for the evolution of the density operator of the combined nuclear spin system and lattice, which takes a similar form to the corresponding expression in the semi-classical Redfield theory in Equation 8.5:

$$\frac{d\hat{X}^T(t)}{dt} = -\frac{1}{\hbar^2} \int_0^\infty [\hat{H}_{IL}^T(t), [\hat{H}_{IL}^T(t-\tau), \hat{X}^T(t)]] d\tau. \quad (9.24)$$

As for the semi-classical theory described in the previous chapter, the application of Equation 9.24 is subject to two key approximations concerning the strength of the coupling between the spin system and the lattice, and the correlation time. Firstly the strength of the coupling must be sufficiently small compared to the inverse of the correlation time that it satisfies the motional-narrowing condition in Equation 8.6, which is adapted here:

$$|\omega_{IL}| \tau_c \ll 1. \quad (9.25)$$

Secondly, in order to truncate the perturbation expansion to second order and extend the upper time limit in the integral to infinity, we assume that the spin system is only observed at times satisfying the inequalities in Equation 8.7:

$$\tau_c \ll t \ll \left| \frac{1}{\omega_{IL}} \right|. \quad (9.26)$$

Equations 8.5 and 9.24 are therefore subject to the same set of approximations in Redfield theory. However there are two key differences between them. Firstly Equation 9.24 is not averaged over an ensemble of systems. We will see that this average is replaced by the sum over all lattice states in the full quantum-mechanical treatment of the lattice. Secondly the double commutator in Equation 9.24 contains the density operator $\hat{X}^T(t)$ rather than the difference between $\hat{X}^T(t)$ and the equilibrium density operator \hat{X}_0 . The inclusion of the equilibrium density operator in the semi-classical master equation (8.5) was phenomenological, and was required because otherwise the semi-classical theory would predict that $\hat{\rho}(t) \rightarrow 0$ rather than $\hat{\rho}_0$ as $t \rightarrow \infty$, i.e. it predicts a steady state corresponding to an infinite temperature. This anomaly arises because of the failure to treat the lattice ‘properly’ as a quantum object. However, as the lattice is modelled as a quantum object here, this phenomenological correction is not needed. The superscript ‘T’ of the spin–lattice coupling Hamiltonian and density operator indicates that these operators are in the interaction representation of the

spin and lattice Hamiltonians, which is defined as

$$\hat{H}_{IL}^T(t) = \exp\left[i\left(\hat{H}_I + \hat{H}_L\right)t/\hbar\right] \hat{H}_{IL} \exp\left[-i\left(\hat{H}_I + \hat{H}_L\right)t/\hbar\right], \quad (9.27)$$

$$\hat{X}^T(t) = \exp\left[i\left(\hat{H}_I + \hat{H}_L\right)t/\hbar\right] \hat{X}(t) \exp\left[-i\left(\hat{H}_I + \hat{H}_L\right)t/\hbar\right], \quad (9.28)$$

using the conventional notation of operator transformations. In terms of the corresponding Liouvillians the transformations have the form

$$\hat{H}_{IL}^T(t) = \exp\left[i\left(\hat{\mathcal{L}}_I + \hat{\mathcal{L}}_L\right)t/\hbar\right] \hat{H}_{IL}, \quad (9.29)$$

$$\hat{X}^T(t) = \exp\left[i\left(\hat{\mathcal{L}}_I + \hat{\mathcal{L}}_L\right)t/\hbar\right] \hat{X}(t). \quad (9.30)$$

We are interested in the relaxation behaviour of the nuclear spin system, rather than the combined spin system and lattice, and so we require an equation of motion of the nuclear-spin-system density operator $\hat{\rho}(t)$. This is derived from Equation 9.24 by taking the trace over all lattice states, and using Equation 9.23 to obtain:

$$\frac{d\hat{\rho}^T(t)}{dt} = \frac{d}{dt} \text{Tr}_L(\hat{X}^T(t)) \quad (9.31)$$

$$= -\frac{1}{\hbar^2} \int_0^\infty \text{Tr}_L\left\{\left[\hat{H}_{IL}^T(t), \left[\hat{H}_{IL}^T(t-\tau), \hat{\rho}^T(t)\hat{P}_0\right]\right]\right\} d\tau, \quad (9.32)$$

where, for reasons of compactness, we have omitted the direct product symbol in the product $\hat{\rho}^T(t)\hat{P}_0$ both here and in the subsequent equations. Equation 9.32 is valid for any coupling interaction between the nuclear spin system and lattice. However we are interested in the particular case of a hyperfine interaction as described by the Hamiltonian in Equation 9.9. When transformed into the interaction representation this Hamiltonian has the form

$$\hat{H}_{IL}^T(t) = \sum_{m=-1}^{+1} (-1)^m \hat{I}_{1-m}^T(t) \hat{L}_{1m}^T(t) \quad (9.33)$$

$$= \sum_{m=-1}^{+1} (-1)^m \left[\exp\left(i\hat{\mathcal{L}}_I t/\hbar\right) \hat{I}_{1-m} \right] \left[\exp\left(i\hat{\mathcal{L}}_L t/\hbar\right) \hat{L}_{1m} \right], \quad (9.34)$$

where $\hat{I}_{1-m}^T(t)$ and $\hat{L}_{1m}^T(t)$ are the forms of the nuclear-spin and lattice operators in the spin and lattice

m	\hat{I}_{1m}	ω_m
0	\hat{I}_z	0
± 1	$\mp \sqrt{\frac{1}{2}} \hat{I}_{\pm}$	$\pm \omega_I$

Table 9.1: The rank-one nuclear-spin operators \hat{I}_{1m} , and frequencies ω_m used for the calculation of the PRE in the stochastic Liouville formalism.

interaction representations, which are defined respectively by the Liouvillians $\hat{\mathcal{L}}_I$ and $\hat{\mathcal{L}}_L$. The form of the lattice operators in the lattice interaction representation depends on which terms we include in the lattice Liouvillian, which we do not specify at this stage. By contrast the nuclear-spin Liouvillian simply contains the nuclear Zeeman interaction, and so the spin-operators $\hat{I}_{1-m}^T(t)$ and their adjoints have a very simple form:

$$\hat{I}_{1-m}^T(t) = \hat{I}_{1-m} \exp(i\omega_{-m}t), \quad (9.35)$$

$$\hat{I}_{1-m}^T(t)^\dagger = \hat{I}_{1-m}^\dagger \exp(-i\omega_{-m}t). \quad (9.36)$$

The rank-one operators \hat{I}_{1m} and their characteristic frequencies ω_m are specified in Table 9.1.

On substituting the hyperfine Hamiltonian into Equation 9.32 we obtain

$$\begin{aligned} \frac{d\hat{\rho}^T(t)}{dt} = & -\frac{1}{\hbar^2} \sum_{m,m'} (-1)^{m+m'} \exp[i(\omega_{-m'} - \omega_{-m})t] \\ & \times \int_0^\infty \text{Tr}_L \left\{ \left[\hat{I}_{1-m'} \hat{\mathcal{L}}_{1m'}^T(t), \left[\hat{I}_{1-m}^\dagger \hat{\mathcal{L}}_{1m}^T(t-\tau)^\dagger, \hat{\rho}^T(t) \hat{P}_0 \right] \right] \right\} \exp(i\omega_{-m}\tau) d\tau. \end{aligned} \quad (9.37)$$

The double commutator is simplified by using the identity

$$[\hat{A}\hat{B}, \hat{C}\hat{D}] = \hat{A}\hat{C}[\hat{B}, \hat{D}] + \hat{A}[\hat{B}, \hat{C}]\hat{D} + \hat{C}[\hat{A}, \hat{D}]\hat{B} + [\hat{A}, \hat{C}]\hat{D}\hat{B}. \quad (9.38)$$

Noting that all nuclear-spin operators commute with all lattice operators, and that the trace of a commutator is zero, we obtain, after some effort, the following expression for the trace of the double commutator:

$$\begin{aligned} \text{Tr}_L \left\{ \left[\hat{I}_{1-m'} \hat{\mathcal{L}}_{1m'}^T(t), \left[\hat{I}_{1-m}^\dagger \hat{\mathcal{L}}_{1m}^T(t-\tau)^\dagger, \hat{\rho}^T(t) \hat{P}_0 \right] \right] \right\} = & \left[\hat{I}_{1-m'}, \hat{I}_{1-m}^\dagger \hat{\rho}^T(t) \right] \text{Tr}_L \left\{ \left[\hat{\mathcal{L}}_{1m}^T(t-\tau)^\dagger, \hat{P}_0 \right] \hat{\mathcal{L}}_{1m'}^T(t) \right\} \\ & + \left[\hat{I}_{1-m'}, \left[\hat{I}_{1-m}^\dagger, \hat{\rho}^T(t) \right] \right] \text{Tr}_L \left\{ \hat{P}_0 \hat{\mathcal{L}}_{1m}^T(t-\tau)^\dagger \hat{\mathcal{L}}_{1m'}^T(t) \right\}. \end{aligned} \quad (9.39)$$

The equation of motion of the nuclear-spin density operator is now

$$\begin{aligned} \frac{d\hat{\rho}^T(t)}{dt} = & -\frac{1}{\hbar^2} \sum_{m,m'} (-1)^{m+m'} \exp [i(\omega_{-m'} - \omega_{-m})t] \\ & \times \int_0^\infty \left[[\hat{I}_{1-m'}, [\hat{I}_{1-m}^\dagger, \hat{\rho}^T(t)]] \text{Tr}_L \{ \hat{P}_0 \hat{L}_{1m}^T(t-\tau)^\dagger \hat{L}_{1m'}^T(t) \} - [\hat{I}_{1-m'}, \hat{I}_{1-m}^\dagger \hat{\rho}^T(t)] \text{Tr}_L \{ [\hat{P}_0, \hat{L}_{1m}^T(t-\tau)^\dagger] \hat{L}_{1m'}^T(t) \} \right] \\ & \times \exp(i\omega_{-m}\tau) d\tau. \end{aligned} \quad (9.40)$$

Although at first sight this equation has a rather complicated form, the second term in the integrand can be simplified (see Appendix F) to give [253]

$$[\hat{I}_{1-m'}, \hat{I}_{1-m}^\dagger \hat{\rho}^T(t)] \text{Tr}_L \{ [\hat{P}_0, \hat{L}_{1m}^T(t-\tau)^\dagger] \hat{L}_{1m'}^T(t) \} = [\hat{I}_{1-m'}, [\hat{I}_{1-m}^\dagger, \hat{\rho}_0]] \text{Tr}_L \{ \hat{P}_0 \hat{L}_{1m}^T(t-\tau)^\dagger \hat{L}_{1m'}^T(t) \}, \quad (9.41)$$

from which the equation of motion can now be written as

$$\begin{aligned} \frac{d\hat{\rho}^T(t)}{dt} = & -\frac{1}{\hbar^2} \sum_{m,m'} (-1)^{m+m'} \exp [i(\omega_{-m'} - \omega_{-m})t] [\hat{I}_{1-m'}, [\hat{I}_{1-m}^\dagger, \hat{\rho}^T(t) - \hat{\rho}_0]] \\ & \times \int_0^\infty \text{Tr}_L \{ \hat{P}_0 \hat{L}_{1m}^T(t-\tau)^\dagger \hat{L}_{1m'}^T(t) \} \exp(i\omega_{-m}\tau) d\tau. \end{aligned} \quad (9.42)$$

The equilibrium nuclear-spin density operator is present in the double commutator as a direct consequence of the fact that we are now treating the lattice as a quantum-mechanical object. It is no longer a phenomenological correction, as it is in the semi-classical theory.

In the equation of motion 9.42 we see that the individual terms have been factored into a part that depends only on the nuclear spin, and a factor that depends only on the composite lattice. We associate the latter with the correlation function and spectral density. Hence we define the correlation function $G_{mm'}(\tau)$ as

$$\begin{aligned} G_{mm'}(\tau) = & \text{Tr}_L \left[\hat{P}_0 \hat{L}_{1m}^T(t-\tau)^\dagger \hat{L}_{1m'}^T(t) \right] \\ = & \text{Tr}_L \left[\hat{P}_0 \exp(i\hat{H}_L(t-\tau)) \hat{L}_{1m}^\dagger \exp(-i\hat{H}_L(t-\tau)) \exp(i\hat{H}_L t) \hat{L}_{1m'} \exp(-i\hat{H}_L t) \right] \\ = & \text{Tr}_L \left[\hat{L}_{1m}^\dagger \exp(-i\hat{H}_L(t-\tau)) \exp(i\hat{H}_L t) \hat{L}_{1m'} \exp(-i\hat{H}_L t) \exp(i\hat{H}_L(t-\tau)) \hat{P}_0 \right] \\ = & \text{Tr}_L \left[\hat{L}_{1m}^\dagger \exp(i\hat{H}_L \tau) \hat{L}_{1m'} \exp(-i\hat{H}_L \tau) \hat{P}_0 \right] \\ = & \text{Tr}_L \left[\hat{L}_{1m}^\dagger \left\{ \exp(i\hat{\mathcal{L}}_L \tau) \hat{L}_{1m'} \right\} \hat{P}_0 \right], \end{aligned} \quad (9.43)$$

where, to go to the third line, we have noted that \hat{P}_0 commutes with \hat{H}_L by definition, and that the trace of a product of operators is invariant to a cyclic permutation of those operators. We see that in this definition of the correlation function, the ensemble average in the semi-classical theory has been replaced by the trace over the lattice functions. We now define the spectral density at frequency ω , $K_{mm'}(\omega)$, as the Fourier–Laplace transform of the correlation function:

$$K_{mm'}(\omega) = \int_0^{\infty} G_{mm'}(\tau) \exp(-i\omega\tau) d\tau. \quad (9.44)$$

Substituting these expressions into Equation 9.42 we obtain

$$\frac{d\hat{\rho}^T(t)}{dt} = -\frac{1}{\hbar^2} \sum_{m,m'} (-1)^{m+m'} \exp[i(\omega_{-m'} - \omega_{-m})t] \left[\hat{I}_{1-m'}, \left[\hat{I}_{1-m}^\dagger, \hat{\rho}^T(t) - \hat{\rho}_0 \right] \right] \text{Re}(K_{mm'}(-\omega_{-m})). \quad (9.45)$$

Note that the imaginary part of the spectral density has a negligible effect on the relaxation behaviour of the nuclear spins, and so we retain only the real part [95]. In the semi-classical Redfield theory we implemented the same assumption by extending the lower limit of the Fourier transform from 0 to $-\infty$.

The final part of the derivation concerns the oscillating phase factor $\exp[i(\omega_{-m'} - \omega_{-m})t]$ that is present in each of the terms of the double sum. The frequency difference $\omega_{-m'} - \omega_{-m}$ takes values that are equal to 0, $\pm\omega_I$, or $\pm 2\omega_I$ depending on the indices m and m' . As noted in the derivation of the semi-classical Redfield equation of motion, the terms associated with a non-zero frequency difference oscillate too rapidly (on the order of the nuclear Larmor frequency) to contribute to the relaxation process, which occurs on a much longer timescale. Therefore the only terms that contribute significantly to the relaxation behaviour of the nuclear spins are the secular terms with $m' = m$. Following the retention of only the secular terms the equation of motion simplifies to

$$\frac{d\hat{\rho}^T(t)}{dt} = -\frac{1}{\hbar^2} \sum_m \left[\hat{I}_{1-m}, \left[\hat{I}_{1-m}^\dagger, \hat{\rho}^T(t) - \hat{\rho}_0 \right] \right] \text{Re}(K_{mm}(-\omega_{-m})). \quad (9.46)$$

We can now write this equation in terms of the relaxation superoperator $\hat{\Gamma}$ as

$$\frac{d\hat{\rho}^T(t)}{dt} = -\hat{\Gamma}(\hat{\rho}^T(t) - \hat{\rho}_0), \quad (9.47)$$

$$\hat{\Gamma} \cdot = \frac{1}{\hbar^2} \sum_m \left[\hat{I}_{1-m} \cdot \left[\hat{I}_{1-m}^\dagger, \cdot \right] \right] \text{Re}(K_{mm}(-\omega_{-m})). \quad (9.48)$$

As we have seen in chapter 8 it is the relaxation superoperator that is the key to calculating and understanding the relaxation properties of the spin system.

9.3.2 The longitudinal and transverse relaxation times

The longitudinal and transverse nuclear relaxation times due to the PRE can be calculated from the relaxation superoperator using expressions that are analogous to those in Equations 8.83 and 8.86. The expression for T_1 is

$$\frac{1}{T_1} = \frac{\left(\hat{I}_z \left| \hat{\Gamma} \right| \hat{I}_z \right)}{\left(\hat{I}_z \hat{I}_z \right)} \quad (9.49)$$

$$= \frac{\text{Tr}_I \left(\hat{I}_z \hat{\Gamma} \hat{I}_z \right)}{\text{Tr}_I \left(\hat{I}_z^2 \right)}. \quad (9.50)$$

This bears a clear resemblance to Equation 8.83, with the important difference that the trace is now taken only over the nuclear spin states, rather than over the nuclear and the electronic spin states. We recall that the latter are now accounted for in the trace over the lattice states in the expression for the time-correlation function. The corresponding expression for T_2 is

$$\frac{1}{T_2} = \frac{\left(\hat{I}_- \left| \hat{\Gamma} \right| \hat{I}_+ \right)}{\left(\hat{I}_- \hat{I}_+ \right)} \quad (9.51)$$

$$= \frac{\text{Tr}_I \left(\hat{I}_- \hat{\Gamma} \hat{I}_+ \right)}{\text{Tr}_I \left(\hat{I}_- \hat{I}_+ \right)}. \quad (9.52)$$

Applying the relaxation superoperator in Equation 9.48 we obtain the following expressions for T_1 and T_2 in terms of the spectral densities:

$$\frac{1}{T_1} = \frac{1}{\hbar^2} \text{Re} (K_{-1-1}(-\omega_I) + K_{11}(\omega_I)), \quad (9.53)$$

$$\frac{1}{T_2} = \frac{1}{\hbar^2} \text{Re} (K_{00}(0) + K_{-1-1}(-\omega_I)). \quad (9.54)$$

It is shown in appendix F that, to a very good approximation, we can write

$$\text{Re} (K_{-1-1}(-\omega_I)) = \text{Re} (K_{11}(\omega_I)), \quad (9.55)$$

from which we obtain the following simplified expressions for the relaxation time constants:

$$\frac{1}{T_1} = \frac{2}{\hbar^2} \text{Re} (K_{11}(\omega_I)), \quad (9.56)$$

$$\frac{1}{T_2} = \frac{1}{\hbar^2} \text{Re} (K_{00}(0) + K_{11}(\omega_I)). \quad (9.57)$$

The expressions in Equations 9.56 and 9.57 are completely general, and also somewhat deceptively simple. However we must remember that there is considerable complexity hidden in the form of the time-correlation function and spectral density, in Equations 9.43 and 9.44 respectively. We can gain some insight into the PRE expressions by writing the lattice operators as sums of terms of different ranks l , as in Equation 9.12. From Equation 9.43, the time-correlation functions then have the form

$$G_{mm}(\tau) = \sum_{l,l'} G_{mm}^{(l,l')}(\tau), \quad (9.58)$$

where the $G_{mm}^{(l,l')}(\tau)$ are equal to

$$G_{mm}^{(l,l')}(\tau) = \text{Tr}_L \left[\left(\hat{L}_{1m}^{(l)} \right)^\dagger \left\{ \exp \left(i \hat{L}_L \tau \right) \hat{L}_{1m}^{(l')} \right\} \hat{P}_0 \right]. \quad (9.59)$$

The Fourier–Laplace transform is linear, and so the spectral density can also be written as a sum of terms that

depend on the double index ll' :

$$K_{mm}(\omega) = \sum_{l,l'} K_{mm}^{(ll')}(\omega), \quad (9.60)$$

$$K_{mm}^{(ll')}(\omega) = \int_0^\infty G_{mm}^{(ll')}(\tau) \exp(-i\omega\tau) d\tau, \quad (9.61)$$

where we have used Equation 9.44. It can be shown (cf. appendix F) that the spectral densities $K_{mm}^{(ll')}(\omega)$ satisfy the following relation

$$\text{Re} \left(K_{-m-m}^{(l'l)}(-\omega_m) \right) \approx \text{Re} \left(K_{mm}^{(ll')}(-\omega_{-m}) \right). \quad (9.62)$$

The expressions for T_1 and T_2 can now be written as a sum of terms, as follows:

$$\frac{1}{T_1} = \frac{2}{\hbar^2} \sum_{l,l'} \text{Re} \left(K_{11}^{(ll')}(\omega_l) \right), \quad (9.63)$$

$$\frac{1}{T_2} = \frac{1}{\hbar^2} \sum_{l,l'} \text{Re} \left(K_{00}^{(ll')}(0) + K_{11}^{(ll')}(\omega_l) \right). \quad (9.64)$$

In both expressions the ‘self’ terms with $l = l' = 0$ are those in which both lattice operators that appear in the expression for the spectral density depend on the rank-zero component of the hyperfine tensor, and therefore depend only on the contact interaction terms. They therefore correspond to the part of the PRE that is a generalisation of the Bloembergen mechanism discussed chapter 8. The self terms with $l = l' = 2$ depend only on the spin-dipolar terms, and therefore represent a generalisation of the part of the PRE that is due to the Solomon mechanism. Both of these contributions are present in their NR forms in the Solomon–Bloembergen–Morgan theory. There are additional contributions, not seen in the Solomon–Bloembergen–Morgan formalism, that arise from terms with $l = 0$ and $l' = 2$, and $l = 2$ and $l' = 0$, which represent cross-correlations between the contact and spin-dipolar interactions [93]. There are also self- and cross-correlation terms involving the antisymmetric hyperfine terms, but these are usually neglected.

9.3.3 Summary of the formalism

We have outlined the stochastic Liouville formalism of nuclear relaxation in a paramagnetic system. Unlike the previous treatment in chapter 8, the present formalism has the advantage that it can be applied under conditions of arbitrary external magnetic field, slow motional dynamics, incorporating relevant SO coupling

effects describing the electronic spin, and treating electronic relaxation explicitly rather than phenomenologically. However, unlike the Solomon–Bloembergen–Morgan and Curie formalisms, the stochastic Liouville treatment has a disadvantage in that it is something of a ‘black box’ and does not permit easy interpretation of the forms of the relaxation time constants without detailed calculations. The expressions for T_1 and T_2 in Equations 9.56 and 9.57 are deceptive in their apparent simplicity, with the spectral density hiding a considerable amount of complexity.

Following a discussion of electronic relaxation in the Redfield limit in section 9.4, we devote the remainder of this chapter to reestablishing some of the insight lost in the increased complexity of the relaxation model by examining some very specific applications of the theory. Firstly we revisit the Solomon–Bloembergen–Morgan theory and establish the connection between it and the present formalism in section 9.5. Then we examine the PRE properties of low-symmetry complexes with $S \geq 1$ in solution at low field in section 9.6 [138, 139], complexes with $S \geq 1$ in solution under fast-rotational dynamics [306] in section 9.7, and the effects of vibrations on the PRE in solution [119] in section 9.8. This final section includes a perspective for calculating the PRE in solids [307, 308].

9.4 Electronic relaxation in the Redfield limit

We have seen that in many cases electronic relaxation cannot be described by the Redfield theory, especially when the coupling of the electronic spin to the rest of the lattice is large, and the timescale of modulation is sufficiently long. This is why, when describing nuclear relaxation, we include the electronic spin in the composite lattice, so that the effects of electronic relaxation can still be accounted for whilst treating the coupling of the nuclear spin to the composite lattice in the Redfield limit. However there are cases when the electronic relaxation processes *are* within the Redfield limit, and under such circumstances we may want to describe this relaxation explicitly. This is also done with the stochastic Liouville formalism, as we now outline.

9.4.1 The spin system, lattice, and spin–lattice coupling

As for nuclear relaxation we can write the Hamiltonian \hat{H} as a sum of terms due to the spin system \hat{H}_S , the lattice \hat{H}_F , and the coupling between them \hat{H}_{SF} :

$$\hat{H} = \hat{H}_S + \hat{H}_F + \hat{H}_{SF}. \quad (9.65)$$

The way in which we partition the various interactions between the spin system, lattice, and spin–lattice coupling is a rather delicate matter, and depends on the dynamics of the system we are studying. For example under conditions of fast rotational diffusion, the rotational motion modulates the spatially anisotropic interactions, such as the static ZFS and anisotropic Zeeman interactions. The electronic spin system Liouvillian $\hat{\mathcal{L}}_S^{\text{fast}}$ then contains the unmodulated isotropic Zeeman interaction $\hat{\mathcal{L}}_{Z,\text{iso}}$:

$$\hat{\mathcal{L}}_S^{\text{fast}} = \hat{\mathcal{L}}_{Z,\text{iso}}. \quad (9.66)$$

The spin-lattice coupling Liouvillian $\hat{\mathcal{L}}_{SF}^{\text{fast}}$ then contains the rotationally-modulated static ZFS $\hat{\mathcal{L}}_{ZFS,S}$ and anisotropic Zeeman $\hat{\mathcal{L}}_{Z,\text{aniso}}$ interactions, as well as the transient ZFS $\hat{\mathcal{L}}_{ZFS,T}$, which is modulated by distortions of the metal-ion coordination site:

$$\hat{\mathcal{L}}_{SF}^{\text{fast}} = \hat{\mathcal{L}}_{Z,\text{aniso}} + \hat{\mathcal{L}}_{ZFS,S} + \hat{\mathcal{L}}_{ZFS,T}. \quad (9.67)$$

The lattice Liouvillian $\hat{\mathcal{L}}_F^{\text{fast}}$ contains the terms that lead to modulation of the spin–lattice coupling interactions due to rotational diffusion $\hat{\mathcal{L}}_R$, distortions due to solvent collisions $\hat{\mathcal{L}}_D$, and vibrational motions $\hat{\mathcal{L}}_V^{(0)} - i\hat{\Gamma}_V$:

$$\hat{\mathcal{L}}_F^{\text{fast}} = \hat{\mathcal{L}}_R + \hat{\mathcal{L}}_D + \hat{\mathcal{L}}_V^{(0)} - i\hat{\Gamma}_V. \quad (9.68)$$

The rotational diffusion term is responsible for motional modulation of the static ZFS and g -anisotropy, whilst the collisions and vibrations modulate the transient ZFS.

In the other limit of slow rotational diffusion, the rotational motion is unable to completely average out the static ZFS and anisotropic Zeeman interactions. These interactions are effectively stationary, and are therefore removed from the spin–lattice coupling Liouvillian and included in the electronic spin Liouvillian

$\hat{\mathcal{L}}_S^{\text{slow}}$, which is given by

$$\hat{\mathcal{L}}_S^{\text{slow}} = \hat{\mathcal{L}}_Z + \hat{\mathcal{L}}_{\text{ZFS},S}, \quad (9.69)$$

where $\hat{\mathcal{L}}_Z$ is the sum of the isotropic and anisotropic Zeeman interactions. The modulation of the transient ZFS by collisions and vibrations still occurs on a sufficiently fast timescale, and so the spin–lattice coupling Liouvillian $\hat{\mathcal{L}}_{SF}^{\text{slow}}$ still contains this interaction:

$$\hat{\mathcal{L}}_{SF}^{\text{slow}} = \hat{\mathcal{L}}_{\text{ZFS},T}. \quad (9.70)$$

Finally the lattice Liouvillian $\hat{\mathcal{L}}_F^{\text{slow}}$ is given by the fast-motional expression, but with the rotational diffusion term removed:

$$\hat{\mathcal{L}}_F^{\text{slow}} = \hat{\mathcal{L}}_D + \hat{\mathcal{L}}_V^{(0)} - i\hat{\Gamma}_V. \quad (9.71)$$

We now discuss the form of the spin–lattice coupling Hamiltonian, which for $S \geq 1$ always contains the transient ZFS, and may also contain the anisotropic Zeeman, and static ZFS interactions. However we can usually neglect the Zeeman term and consider only the ZFS terms, which dominate the electronic relaxation properties. The Hamiltonians of both the static and transient ZFS contributions have the same operator form, namely

$$\hat{H}_{SF} = \sum_{m=-2}^{+2} (-1)^m \hat{F}_{2m} \hat{S}_{2-m}, \quad (9.72)$$

where \hat{F}_{2m} are the lattice operators that describe the size and spatial properties of the interaction. If we consider only classical (non-quantized) degrees of freedom of the lattice, such as rotational diffusion of the static ZFS or distortional motion of the transient ZFS in the pseudo-rotation model, the lattice operators \hat{F}_{2m} can be replaced by functions describing the spatial variation. As before we transform this Hamiltonian into the interaction representation of the spin system and the lattice to give the new operator $\hat{H}_{SF}^T(t)$:

$$\hat{H}_{SF}^T(t) = \exp\left(i\hat{\mathcal{L}}_S t\right) \exp\left(i\hat{\mathcal{L}}_F t\right) \hat{H}_{SF} \quad (9.73)$$

$$= \sum_{m=-2}^{+2} (-1)^m \hat{F}_{2m}^T(t) \hat{S}_{2-m}^T(t). \quad (9.74)$$

The interaction-representation spin- and lattice operators $\hat{S}_{2m}^T(t)$ and $\hat{F}_{2m}^T(t)$ are given by

$$\hat{S}_{2m}^T(t) = \exp\left(i\hat{\mathcal{L}}_S t\right)\hat{S}_{2m}, \quad (9.75)$$

$$\hat{F}_{2m}^T(t) = \exp\left(i\hat{\mathcal{L}}_F t\right)\hat{F}_{2m}. \quad (9.76)$$

As we have seen before it is usual to write the spin operator \hat{S}_{2m} as the sum of terms $\hat{S}_{2m}^{(n)}$, each of which evolves at a characteristic frequency $\omega_m^{(n)}$ under the action of the electronic spin Liouvillian:

$$\exp\left(i\hat{\mathcal{L}}_S t\right)\hat{S}_{2m} = \sum_n \hat{S}_{2m}^{(n)} \exp\left(i\omega_m^{(n)} t\right). \quad (9.77)$$

The exact form of this partitioning, and indeed whether it needs to be done at all, depends on the form of $\hat{\mathcal{L}}_S$, and whether or not, in the slow-motion limit, it includes the static ZFS.

9.4.2 The electronic spin relaxation superoperator

In the Redfield limit we can describe the relaxation of the electronic density operator $\hat{\rho}_S(t)$ with the following equation of motion:

$$\frac{d\hat{\rho}_S^T(t)}{dt} = -\frac{1}{\hbar^2} \sum_{m,m'} \sum_{n,n'} (-1)^{m+m'} \exp\left[i\left(\omega_{-m'}^{(n')} - \omega_{-m}^{(n)}\right)t\right] \left[\tilde{S}_{2-m'}^{(n')}, \left[\left(\tilde{S}_{2-m}^{(n)}\right)^\dagger, \hat{\rho}_S^T(t) - \hat{\rho}_{S,0}\right]\right] J_{mm'}\left(-\omega_{-m}^{(n)}\right). \quad (9.78)$$

where $\hat{\rho}_S^T(t)$ is the electronic density operator in the interaction representation and $\hat{\rho}_{S,0}$ is the equilibrium electronic density operator. As for nuclear relaxation the electronic relaxation behaviour is defined by a time-correlation function, which we denote $\langle \hat{F}_{2m}(0)^\dagger \hat{F}_{2m'}(-\tau) \rangle$, and which is given by

$$\langle \hat{F}_{2m}(0)^\dagger \hat{F}_{2m'}(-\tau) \rangle = \text{Tr}_F \left[\hat{L}_{2m}^\dagger \left\{ \exp\left(i\hat{\mathcal{L}}_F \tau\right) \hat{L}_{2m'} \right\} \hat{P}_0 \right]. \quad (9.79)$$

The trace is taken over the lattice states, and \hat{P}_0 is the equilibrium lattice density operator. The spectral density functions $J_{mm'}(\omega)$ in Equation 9.78 are then defined as the real part of the Fourier–Laplace transform

of the time-correlation functions:

$$J_{mm'}(\omega) = \text{Re} \left[\int_0^{\infty} \langle \hat{F}_{2m}(0)^\dagger \hat{F}_{2m'}(-\tau) \rangle \exp(-i\omega\tau) d\tau \right]. \quad (9.80)$$

If we remove the oscillating non-secular terms with $m \neq m'$ and $n \neq n'$ from the equation of motion, we obtain the following expression

$$\frac{d\hat{\rho}_S^T(t)}{dt} = -\hat{\Gamma}_e (\hat{\rho}_S^T(t) - \hat{\rho}_{S,0}), \quad (9.81)$$

where $\hat{\Gamma}_e$ is the electronic relaxation superoperator, which is given by

$$\hat{\Gamma}_e \hat{O} = \frac{1}{\hbar^2} \sum_m \sum_n \left[\tilde{S}_{2-m}^{(n)}, \left[(\tilde{S}_{2-m}^{(n)})^\dagger, \hat{O} \right] \right] J_{mm}(-\omega_{-m}^{(n)}). \quad (9.82)$$

However we note that the secular approximation must be applied with care. As we will see, non-secular terms can sometimes make an important contribution to the relaxation properties of the electronic spin.

9.5 The Solomon–Bloembergen–Morgan theory revisited

In this section we briefly revisit the Solomon–Bloembergen–Morgan theory originally examined in section 8.6 using the semi-classical Redfield theory. We will once again obtain the Solomon–Bloembergen–Morgan equations, showing that the theory of relaxation derived using the stochastic Liouville formalism is exactly equivalent to the semi-classical theory when subject to the same set of restrictions, namely high-field conditions, and a classical description of chemical exchange and rotational diffusion.

9.5.1 The lattice

The lattice comprises the quantised electronic states, the classical rotational degrees of freedom, and the degrees of freedom associated with chemical exchange. The corresponding Liouvillian must account for all these parts of the lattice, and is therefore written as follows:

$$\hat{\mathcal{L}}_L = \hat{\mathcal{L}}_Z + \hat{\mathcal{L}}_e + \hat{\mathcal{L}}_R + \hat{\mathcal{L}}_M. \quad (9.83)$$

The Liouvillian superoperators $\hat{\mathcal{L}}_R$ and $\hat{\mathcal{L}}_M$ account for the stochastic rotational diffusion and exchange processes. The former superoperator changes the spatial orientation of the system by acting on the classical Wigner rotation matrix elements as follows:

$$D_{mm'}^{(l)}(\Omega_{\text{PL}}(t)) = \exp\left(-i\hat{\mathcal{L}}_R t\right) D_{mm'}^{(l)}(\Omega_{\text{PL}}(0)), \quad (9.84)$$

i.e. the orientation of the PAF is changed from $\Omega_{\text{PL}}(0)$ at time $t = 0$, to $\Omega_{\text{PL}}(t)$ at time t .

Chemical exchange has the effect of shuttling the nuclear spin between different sites in which the hyperfine interaction tensor components are different. This can be described by the action of $\hat{\mathcal{L}}_M$ on the PAF components of the hyperfine tensor $\tilde{A}_{\mu}(t)$ as follows:

$$\tilde{A}_{\mu}(t) = \exp\left(-i\hat{\mathcal{L}}_M t\right) \tilde{A}_{\mu}(0). \quad (9.85)$$

Once again we have assumed that the chemical exchange and rotational diffusion processes occur on sufficiently different timescales to be independent of each other.

As we have seen previously with the Solomon–Bloembergen–Morgan theory the only coherent electronic interaction that we consider is the electronic Zeeman interaction, with Liouvillian $\hat{\mathcal{L}}_Z$. The electronic Zeeman Liouvillian transforms the electronic spin operators \hat{S}_{1q} as follows:

$$\exp\left(-i\hat{\mathcal{L}}_Z t\right) \hat{S}_{1q} = \hat{S}_{1q} \exp(-iq\omega_S t), \quad (9.86)$$

i.e. the operator evolves at frequency $-q\omega_S$. We also need a mechanism for electronic relaxation, which is accounted for here by $\hat{\mathcal{L}}_e = -i\hat{\Gamma}_e$, where $\hat{\Gamma}_e$ is the electronic relaxation superoperator. We recall that in the Solomon–Bloembergen–Morgan theory the relaxation processes are not accounted for explicitly, but are modelled phenomenologically by the effective electronic longitudinal and transverse relaxation times T_{1e} and T_{2e} . The transformations are:

$$\exp\left(-i\hat{\mathcal{L}}_e t\right) \hat{S}_{10} = \hat{S}_{10} \exp(-\tau/T_{1e}), \quad (9.87)$$

$$\exp\left(-i\hat{\mathcal{L}}_e t\right) \hat{S}_{1\pm 1} = \hat{S}_{1\pm 1} \exp(-\tau/T_{2e}), \quad (9.88)$$

where $\hat{\mathcal{L}}_e = -i\hat{\Gamma}_e$ is the Liouvillian that describes electronic relaxation via the Markov superoperator $\hat{\Gamma}_e$.

9.5.2 The spectral densities

The nuclear relaxation times are calculated from Equations 9.63 and 9.64. The Solomon–Bloembergen–Morgan theory ignores the effects of cross-correlation between the hyperfine coupling interactions of different spatial ranks, and only considers the NR Fermi-contact and spin-dipolar contributions. Hence the relaxation times have the following simplified expressions

$$\frac{1}{T_1} = \frac{2}{\hbar^2} \text{Re} \left(K_{11}^{\text{FC}}(\omega_I) + K_{11}^{\text{SD}}(\omega_I) \right), \quad (9.89)$$

$$\frac{1}{T_2} = \frac{1}{\hbar^2} \text{Re} \left(K_{00}^{\text{FC}}(0) + K_{11}^{\text{FC}}(\omega_I) + K_{00}^{\text{SD}}(0) + K_{11}^{\text{SD}}(\omega_I) \right), \quad (9.90)$$

where we have replaced the superscripts (00) and (22) with ‘FC’ and ‘SD’ respectively. Hence the spectral densities $K_{mm}^{\text{FC}}(\omega)$ contribute to the Bloembergen mechanism, and the spectral densities $K_{mm}^{\text{SD}}(\omega)$ contribute to the Solomon mechanism.

To proceed we write down the form of the time-correlation function $G_{mm}^{(l)}(\tau)$ by combining Equation 9.13 for the lattice operator of spatial rank l with Equation 9.59, and write the components of the hyperfine tensor in the PAF of the spin-dipolar interaction tensor. The result is

$$\begin{aligned} G_{mm}^{(l)}(\tau) = & (2l+1) \sum_{q,q'=-1}^{+1} \begin{pmatrix} l & 1 & 1 \\ m-q & q & -m \end{pmatrix} \begin{pmatrix} l & 1 & 1 \\ m-q' & q' & -m \end{pmatrix} \\ & \times \sum_{\mu,\mu'=-l}^{+l} \text{Tr}_L \left[\tilde{A}_{l\mu}(0)^* D_{\mu,m-q}^{(l)}(\Omega_{\text{PL}}(0))^* \hat{S}_{1q}^\dagger \left\{ \exp\left(i\hat{\mathcal{L}}_L\tau\right) \tilde{A}_{l\mu'}(0) D_{\mu',m-q'}^{(l)}(\Omega_{\text{PL}}(0)) \hat{S}_{1q'} \right\} \hat{P}_0 \right]. \quad (9.91) \end{aligned}$$

We factorize the trace into three parts, comprising the product of the PAF hyperfine tensor components, an

orientational part comprising the Wigner rotation matrix elements, and a trace over the electronic spin states:

$$\begin{aligned}
G_{mm}^{(l)}(\tau) &= (2l+1) \sum_{q,q'=-l}^{+l} \begin{pmatrix} l & 1 & 1 \\ m-q & q & -m \end{pmatrix} \begin{pmatrix} l & 1 & 1 \\ m-q' & q' & -m \end{pmatrix} \\
&\times \sum_{\mu,\mu'=-l}^{+l} \left\langle \tilde{A}_{l\mu}(0)^* \left\{ \exp\left(i\hat{\mathcal{L}}_M\tau\right) \tilde{A}_{l\mu'}(0) \right\} \right\rangle \left\langle D_{\mu,m-q}^{(l)}(\Omega_{\text{PL}}(0))^* \left\{ \exp\left(i\hat{\mathcal{L}}_R\tau\right) D_{\mu',m-q'}^{(l)}(\Omega_{\text{PL}}(0)) \right\} \right\rangle \\
&\times \text{Tr}_S \left[\hat{S}_{1q}^\dagger \left\{ \exp\left(i\left(\hat{\mathcal{L}}_Z + \hat{\mathcal{L}}_e\right)\tau\right) \hat{S}_{1q'} \right\} \hat{P}_{0,S} \right] \tag{9.92}
\end{aligned}$$

$$\begin{aligned}
&= (2l+1) \sum_{q,q'=-l}^{+l} \begin{pmatrix} l & 1 & 1 \\ m-q & q & -m \end{pmatrix} \begin{pmatrix} l & 1 & 1 \\ m-q' & q' & -m \end{pmatrix} \\
&\times \sum_{\mu,\mu'=-l}^{+l} \left\langle \tilde{A}_{l\mu}(0)^* \tilde{A}_{l\mu'}(-\tau) \right\rangle \left\langle D_{\mu,m-q}^{(l)}(\Omega_{\text{PL}}(0))^* D_{\mu',m-q'}^{(l)}(\Omega_{\text{PL}}(-\tau)) \right\rangle \\
&\times \text{Tr}_S \left[\hat{S}_{1q}^\dagger \left\{ \exp\left(i\left(\hat{\mathcal{L}}_Z + \hat{\mathcal{L}}_e\right)\tau\right) \hat{S}_{1q'} \right\} \hat{P}_{0,S} \right], \tag{9.93}
\end{aligned}$$

where $\hat{P}_{0,S}$ is the equilibrium density operator of the electronic spin. Equation 9.93 now contains three independent correlation functions. The rotational correlation function, which correlates the Wigner rotation matrix elements, can be written as an integral over all Euler angles Ω_{PL} as follows:

$$\left\langle D_{\mu,m-q}^{(l)}(\Omega_{\text{PL}}(0))^* D_{\mu',m-q'}^{(l)}(\Omega_{\text{PL}}(-\tau)) \right\rangle = \left[\frac{1}{8\pi^2} \int_{\Omega} D_{\mu,m-q}^{(l)}(\Omega_{\text{PL}})^* D_{\mu',m-q'}^{(l)}(\Omega_{\text{PL}}) d\Omega_{\text{PL}} \right] g_l^{\text{R}}(\tau) \tag{9.94}$$

$$= \frac{1}{2l+1} \delta_{\mu\mu'} \delta_{qq'} g_l^{\text{R}}(\tau), \tag{9.95}$$

where $g_l^{\text{R}}(\tau)$ is the reduced rotational correlation function used in the Solomon–Bloembergen theory, as defined in chapter 8, and we have assumed isotropic tumbling. The chemical exchange correlation function can be simplified by setting $\mu = \mu'$:

$$\left\langle \tilde{A}_{l\mu}(0)^* \tilde{A}_{l\mu}(-\tau) \right\rangle = |\tilde{A}_{l\mu}|^2 g^{\text{M}}(\tau), \tag{9.96}$$

where $g^{\text{M}}(\tau)$ is the chemical exchange reduced correlation function. We note that we have encountered both of these results before, in chapter 8. The remaining correlation function is the electronic correlation function, which has the form of the trace of a product of electronic spin operators over the spin states. In the

high-temperature limit the equilibrium density operator can be approximated by $\hat{P}_{0,S} = \hat{1}_S / (2S + 1)$, with only a small deviation of order β_L . This allows us to simplify the electronic correlation function as follows

$$\text{Tr}_S \left[\hat{S}_{1q}^\dagger \left\{ \exp \left(i \left(\hat{\mathcal{L}}_Z + \hat{\mathcal{L}}_e \right) \tau \right) \hat{S}_{1q} \right\} \hat{P}_{0,S} \right] = \frac{1}{2S + 1} \text{Tr}_S \left[\hat{S}_{1q}^\dagger \hat{S}_{1q} \right] \exp(iq\omega_S \tau) g_q^S(\tau), \quad (9.97)$$

where we have set $q = q'$ as required by the form of the rotational correlation function, and $g_q^S(\tau)$ is the reduced electronic correlation function we defined in chapter 8. The trace can be simplified to give

$$\frac{1}{2S + 1} \text{Tr}_S \left[\hat{S}_{1q}^\dagger \hat{S}_{1q} \right] = \frac{1}{2S + 1} (-1)^q \text{Tr}_S \left[\hat{S}_{1-q} \hat{S}_{1q} \right] \quad (9.98)$$

$$= \frac{1}{2S + 1} (-1)^{2q} \frac{2S + 1}{3} \langle S \| \hat{S}_1 \| S \rangle^2 \quad (9.99)$$

$$= \frac{1}{3} S(S + 1). \quad (9.100)$$

Combining Equations 9.93–9.100 we obtain the final expression for the time-correlation function:

$$G_{mm}^{(ll)}(\tau) = \frac{1}{3} S(S + 1) \left[\sum_{\mu} |\tilde{A}_{l\mu}|^2 \right] \sum_q \left(\begin{array}{ccc} l & 1 & 1 \\ m - q & q & -m \end{array} \right)^2 \exp(iq\omega_S \tau) g_{lq}(\tau), \quad (9.101)$$

where $g_{lq}(\tau)$ is the total correlation function. Taking the Fourier–Laplace transform of the correlation function finally gives us the spectral density

$$K_{mm}^{(ll)}(\omega) = \frac{1}{6} S(S + 1) \left[\sum_{\mu} |\tilde{A}_{l\mu}|^2 \right] \sum_q \left(\begin{array}{ccc} l & 1 & 1 \\ m - q & q & -m \end{array} \right)^2 j_{l,|q|+1}(\omega - q\omega_S), \quad (9.102)$$

where $j_{lq}(\omega)$ is the total reduced spectral density in the Solomon–Bloembergen–Morgan theory.

9.5.3 The Solomon–Morgan–Bloembergen equations

The Solomon mechanism

Focussing on the spin-dipolar part of the hyperfine interaction we remember that

$$\sum_{\mu=-2}^{+2} |\tilde{A}_{2\mu}|^2 = \frac{1}{2} \left(3 + (\eta^{\text{SD}})^2 \right) (\tilde{A}_{zz}^{\text{SD}})^2, \quad (9.103)$$

and obtain the following expression for the spectral density:

$$K_{mm}^{\text{SD}}(\omega) = \frac{1}{12}S(S+1)\left(3 + (\eta^{\text{SD}})^2\right)\left(\tilde{A}_{zz}^{\text{SD}}\right)^2 \sum_{q=-1}^{+1} \begin{pmatrix} 2 & 1 & 1 \\ m-q & q & -m \end{pmatrix}^2 j_{2,|q|+1}(\omega - q\omega_S). \quad (9.104)$$

The important spectral densities for calculating the relaxation times are $K_{11}^{\text{SD}}(\omega_I)$ and $K_{00}^{\text{SD}}(0)$, which are calculated to be:

$$K_{11}^{\text{SD}}(\omega_I) = \frac{1}{2}S(S+1)\left(3 + (\eta^{\text{SD}})^2\right)\left(\tilde{A}_{zz}^{\text{SD}}\right)^2 \left[\frac{1}{60}j_{21}(\omega_I) + \frac{1}{30}j_{22}(\omega_S + \omega_I) + \frac{1}{180}j_{22}(\omega_S - \omega_I) \right],$$

$$K_{00}^{\text{SD}}(0) = S(S+1)\left(3 + (\eta^{\text{SD}})^2\right)\left(\tilde{A}_{zz}^{\text{SD}}\right)^2 \left[\frac{1}{90}j_{21}(0) + \frac{1}{60}j_{22}(\omega_S) \right].$$

When the unpaired electronic spin behaves as a point dipole moment, $\tilde{A}_{zz}^{\text{SD}} = 2b_{SI}$, $\eta^{\text{SD}} = 0$, and the spectral densities become:

$$K_{11}^{\text{SD}}(\omega_I) = \frac{1}{2}S(S+1)b_{SI}^2 \left[\frac{1}{5}j_{21}(\omega_I) + \frac{2}{5}j_{22}(\omega_S + \omega_I) + \frac{1}{15}j_{22}(\omega_S - \omega_I) \right],$$

$$K_{00}^{\text{SD}}(0) = S(S+1)b_{SI}^2 \left[\frac{2}{15}j_{21}(0) + \frac{1}{5}j_{22}(\omega_S) \right].$$

The Bloembergen mechanism

We now turn our attention to the Bloembergen mechanism, where the PRE is due to the Fermi-contact interaction. Noting that

$$|A_{00}|^2 = 3(A^{\text{FC}})^2, \quad (9.105)$$

we obtain the following spectral density function:

$$K_{mm}^{\text{FC}}(\omega) = \frac{1}{2}S(S+1)(A^{\text{FC}})^2 \sum_{q=-1}^{+1} \begin{pmatrix} 0 & 1 & 1 \\ m-q & q & -m \end{pmatrix}^2 j_{0,|q|+1}(\omega - q\omega_S). \quad (9.106)$$

The two spectral density functions that determine the PRE $K_{11}^{\text{FC}}(\omega_I)$ and $K_{00}^{\text{FC}}(0)$ are therefore:

$$K_{11}^{\text{FC}}(\omega_I) = \frac{1}{2}S(S+1)(A^{\text{FC}})^2 \begin{pmatrix} 0 & 1 & 1 \\ 0 & 1 & -1 \end{pmatrix}^2 j_{02}(\omega_S - \omega_I) \quad (9.107)$$

$$= \frac{1}{6}S(S+1)(A^{\text{FC}})^2 j_{02}(\omega_S - \omega_I), \quad (9.108)$$

$$K_{00}^{\text{FC}}(0) = \frac{1}{2}S(S+1)(A^{\text{FC}})^2 \begin{pmatrix} 0 & 1 & 1 \\ 0 & 0 & 0 \end{pmatrix}^2 j_{01}(0) \quad (9.109)$$

$$= \frac{1}{6}S(S+1)(A^{\text{FC}})^2 j_{01}(0). \quad (9.110)$$

The PRE

On substituting the expressions for the spectral densities into Equations 9.89 and 9.90 we obtain the Solomon–Bloembergen–Morgan equations for the PRE. The expression for T_1 is

$$\frac{1}{T_1} = \frac{2}{3}S(S+1) \left(\frac{A^{\text{FC}}}{\hbar} \right)^2 \frac{\tau_{E,2}}{1 + (\omega_S - \omega_I)^2 \tau_{E,2}^2} + \frac{2}{15}S(S+1) \left(\frac{b_{SI}}{\hbar} \right)^2 \left[\frac{3\tau_{c,1}}{1 + \omega_I^2 \tau_{c,1}^2} + \frac{6\tau_{c,2}}{1 + (\omega_S + \omega_I)^2 \tau_{c,2}^2} + \frac{\tau_{c,2}}{1 + (\omega_S - \omega_I)^2 \tau_{c,2}^2} \right], \quad (9.111)$$

and the corresponding expression for T_2 is

$$\frac{1}{T_2} = \frac{1}{3}S(S+1) \left(\frac{A^{\text{FC}}}{\hbar} \right)^2 \left[\tau_{E,1} + \frac{\tau_{E,2}}{1 + (\omega_S - \omega_I)^2 \tau_{E,2}^2} \right] + \frac{1}{15}S(S+1) \left(\frac{b_{SI}}{\hbar} \right)^2 \left[4\tau_{c,1} + \frac{6\tau_{c,2}}{1 + \omega_S^2 \tau_{c,2}^2} + \frac{3\tau_{c,1}}{1 + \omega_I^2 \tau_{c,1}^2} + \frac{6\tau_{c,2}}{1 + (\omega_S + \omega_I)^2 \tau_{c,2}^2} + \frac{\tau_{c,2}}{1 + (\omega_S - \omega_I)^2 \tau_{c,2}^2} \right], \quad (9.112)$$

where we have used the explicit Lorentzian expressions for the reduced spectral densities. We note that these are exactly the same expressions given in Equations 8.107 and 8.108 in chapter 8.

9.6 Low-field theory of the PRE in low-symmetry complexes in solution

9.6.1 Introduction

The Solomon–Bloembergen–Morgan equations describe the PRE under high-field conditions, where the Zeeman interaction is the dominant electronic spin interaction. However the theory is not applicable under conditions of low magnetic field where the ZFS dominates the electronic energy level structure. This low-field limit is of interest when studying the field-dependent behaviour of relaxation rates in NMR dispersion (NMRD) experiments, for which it is important to have corresponding expressions for the PRE [95]. Here we summarise the low-field theory of the PRE in paramagnetic complexes in solution as described by Westlund [137], Bertini et al. [108], and Nilsson and Kowalewski [138, 139], derive the PRE due to an electronic spin $S = 1$ subject to an axially symmetric static ZFS, and highlight the differences from the high-field Solomon–Bloembergen–Morgan approach. Finally we summarize the work done in deriving expressions for an $S = 1$ subject to a rhombic static ZFS, and electronic spins $S = 2, 5/2, 3,$ and $7/2$.

The low-field theory is subject to the following assumptions:

1. We are in the limit of low magnetic field, which we define as the regime where the axial ZFS anisotropy D is much greater than the electronic Zeeman splitting, $|D| \gg \mu_B g_e B_0$.
2. The electronic relaxation can be described in the Redfield limit, which requires that the electronic relaxation processes occur on a sufficiently fast timescale.
3. The dynamics which cause nuclear relaxation are much slower than the electronic spin dynamics, so that we can apply the decomposition approximation. Hence this is also an example of a slow-motion theory, where $|\omega_{IL}| \tau_c \gg 1$.
4. The relevant electronic spin interactions, namely the static ZFS and Zeeman interactions, are not fully averaged by molecular reorientation, and so do not contribute to electronic relaxation. This is a consequence of assumption 3.
5. For $S > 3/2$, quartic and higher-order ZFS terms are neglected.

6. The spin-dipolar hyperfine interaction and static ZFS tensor share a common PAF.

As in the previous section we now define the lattice and the corresponding Liouvillian, and derive the spectral densities for an arbitrary electronic spin S . We then restrict the discussion to $S = 1$ and derive the electronic relaxation rates, and incorporate these into the calculation and discussion of the PRE.

9.6.2 The lattice

The paramagnetic complex is assumed to be of low symmetry, so that the electronic spin is subject to a static ZFS in addition to the Zeeman interaction. The combined lattice is a composite of the electronic and rotational degrees of freedom, and is represented by a Liouvillian that is given by the sum of the electronic and rotational diffusion Liouvillians:

$$\hat{\mathcal{L}}_L = \hat{\mathcal{L}}_S + \hat{\mathcal{L}}_R, \quad (9.113)$$

where

$$\hat{\mathcal{L}}_S = \hat{\mathcal{L}}_{\text{ZFS},S} + \hat{\mathcal{L}}_Z + \hat{\mathcal{L}}_e. \quad (9.114)$$

The electronic Zeeman Liouvillian can be neglected at low magnetic fields such that $|D| \gg \mu_B g_e B_0$, as outlined in assumption 1 above. The superoperator $\hat{\mathcal{L}}_e$ describes the electronic relaxation due to the transient ZFS, which can be modelled by the pseudo-rotation model of Rubinstein et al [115]. The overall lattice equilibrium density operator \hat{P}_0 is the direct product of the equilibrium density operators of the electron spin $\hat{P}_{0,S}$ and rotational degrees of freedom $\hat{P}_{0,L}$:

$$\hat{P}_0 = \hat{P}_{0,S} \otimes \hat{P}_{0,L}. \quad (9.115)$$

As in the Solomon–Bloembergen–Morgan theory, the electronic equilibrium density operator in the high-temperature limit is simply $\hat{1}_S/(2S + 1)$.

9.6.3 The spectral densities

As we have seen before the PRE is due to the hyperfine interaction, which couples the nuclear spin to the unpaired electrons in the lattice. Here we consider only the spin-dipolar interaction, which is represented by

the following Hamiltonian \hat{H}^{SD} and lattice operator \hat{L}_{1m}^{SD} :

$$\hat{H}^{\text{SD}} = \sum_{m=-2}^{+2} (-1)^m \hat{I}_{1-m} \hat{L}_{1m}^{\text{SD}}, \quad (9.116)$$

$$\hat{L}_{1m}^{\text{SD}} = (-1)^m \sqrt{30} b_{SI} \sum_{q=-1}^{+1} \begin{pmatrix} 2 & 1 & 1 \\ m-q & q & -m \end{pmatrix} \hat{S}_{1q} D_{0,m-q}^{(2)}(\Omega_{\text{PL}}), \quad (9.117)$$

where Ω_{PL} is the set of Euler angles that gives the orientation of the common PAF of the spin-dipolar and static ZFS tensors in the laboratory frame, and we have assumed that the electronic spin can be modelled as a point dipole moment. The spectral density functions $K_{mm}^{\text{SD}}(\omega)$ are therefore given by

$$\begin{aligned} K_{mm}^{\text{SD}}(\omega) = & 30 b_{SI}^2 \sum_{q,q'} \begin{pmatrix} 2 & 1 & 1 \\ m-q & q & -m \end{pmatrix} \begin{pmatrix} 2 & 1 & 1 \\ m-q' & q' & -m \end{pmatrix} \\ & \times \int_0^\infty \text{Tr}_L \left[\hat{S}_{1q}^\dagger D_{0,m-q}^{(2)}(\Omega_{\text{PL}}(0))^* \left\{ \exp(i\hat{\mathcal{L}}_L \tau) \hat{S}_{1q'} D_{0,m-q'}^{(2)}(\Omega_{\text{PL}}(0)) \right\} \hat{P}_0 \right] \\ & \times \exp(-i\omega\tau) d\tau. \end{aligned} \quad (9.118)$$

The expression in Equation 9.118 is identical to that used in the slow-motion theory. However to proceed into the low-field regime we need further steps. Firstly, because the electron spin dynamics are dominated by the static ZFS, we need to express the electronic spin operators \hat{S}_{1q} in terms of the spin operators in the PAF \tilde{S}_{1q} , through the following relation:

$$\hat{S}_{1q} = \sum_p \tilde{S}_{1p} D_{pq}^{(1)}(\Omega_{\text{PL}}). \quad (9.119)$$

Secondly we apply the following contraction law for the products of Wigner rotation matrix elements [190]:

$$D_{0,m-q}^{(2)}(\Omega_{\text{PL}}) D_{pq}^{(1)}(\Omega_{\text{PL}}) = \sum_{C=1}^3 (2C+1) \begin{pmatrix} 2 & 1 & C \\ 0 & p & -p \end{pmatrix} \begin{pmatrix} 2 & 1 & C \\ m-q & q & -m \end{pmatrix} D_{-p,-m}^{(C)}(\Omega_{\text{PL}})^*. \quad (9.120)$$

Applying Equations 9.119 and 9.120 to Equation 9.118 we obtain

$$\begin{aligned}
K_{mm}^{\text{SD}}(\omega) = & 30b_{SI}^2 \sum_{q,q'} \sum_{p,n} (-1)^{p+n} \begin{pmatrix} 2 & 1 & 1 \\ m-q & q & -m \end{pmatrix}^2 \begin{pmatrix} 2 & 1 & 1 \\ m-q' & q' & -m \end{pmatrix}^2 \\
& \times 9 \begin{pmatrix} 2 & 1 & 1 \\ 0 & p & -p \end{pmatrix} \begin{pmatrix} 2 & 1 & 1 \\ 0 & n & -n \end{pmatrix} \\
& \times \int_0^\infty \text{Tr}_L \left[\tilde{S}_{1n}^\dagger D_{nm}^{(1)}(\Omega_{\text{PL}}(0))^* \left\{ \exp(i\hat{\mathcal{L}}_L \tau) \tilde{S}_{1p} D_{pm}^{(1)}(\Omega_{\text{PL}}(0)) \right\} \hat{P}_0 \right] \\
& \times \exp(-i\omega\tau) d\tau, \tag{9.121}
\end{aligned}$$

where we have retained only those contacted Wigner rotation matrix elements with rank $C = 1$ [138].

We now invoke assumption 3, and apply the decomposition approximation to separate the rotational diffusion dynamics from the electronic spin dynamics. The lattice trace is therefore given by

$$\begin{aligned}
& \text{Tr}_L \left[\tilde{S}_{1n}^\dagger D_{nm}^{(1)}(\Omega_{\text{PL}}(0))^* \left\{ \exp(i\hat{\mathcal{L}}_L \tau) \tilde{S}_{1p} D_{pm}^{(1)}(\Omega_{\text{PL}}(0)) \right\} \hat{P}_0 \right] \\
= & \left\langle D_{nm}^{(1)}(\Omega_{\text{PL}}(0))^* D_{pm}^{(1)}(\Omega_{\text{PL}}(-\tau)) \right\rangle \text{Tr}_S \left[\tilde{S}_{1n}^\dagger \left\{ \exp(i\hat{\mathcal{L}}_S \tau) \tilde{S}_{1p} \right\} \hat{P}_{0,S} \right]. \tag{9.122}
\end{aligned}$$

As the molecule is tumbling isotropically the spatially-dependent factor simplifies to

$$\left\langle D_{nm}^{(1)}(\Omega_{\text{PL}}(0))^* D_{pm}^{(1)}(\Omega_{\text{PL}}(-\tau)) \right\rangle = \frac{1}{3} \delta_{pn} \exp(-\tau/(3\tau_R)). \tag{9.123}$$

The rotational correlation time τ_R above corresponds to a rank-two tensor. However since we are describing the reorientational motion of a rank-one tensor, we require a factor of 1/3 in the exponent. We now simply the spectral density to

$$\begin{aligned}
K_{mm}^{\text{SD}}(\omega) = & 90b_{SI}^2 \left[\sum_q \begin{pmatrix} 2 & 1 & 1 \\ m-q & q & -m \end{pmatrix}^2 \sum_{q'} \begin{pmatrix} 2 & 1 & 1 \\ m-q' & q' & -m \end{pmatrix}^2 \right] \sum_p \begin{pmatrix} 2 & 1 & 1 \\ 0 & p & -p \end{pmatrix}^2 \\
& \times \frac{1}{2S+1} \int_0^\infty \text{Tr}_S \left[\tilde{S}_{1p}^\dagger \left\{ \exp(i\hat{\mathcal{L}}_S \tau) \tilde{S}_{1p} \right\} \right] \exp[-(i\omega + 1/(3\tau_R))\tau] d\tau. \tag{9.124}
\end{aligned}$$

The Wigner 3j symbols can be written in terms of their numerical values [190]:

$$\sum_q \begin{pmatrix} 2 & 1 & 1 \\ m-q & q & -m \end{pmatrix}^2 = \frac{1}{3}, \quad (9.125)$$

$$\begin{pmatrix} 2 & 1 & 1 \\ 0 & p & -p \end{pmatrix}^2 = \begin{cases} \frac{1}{30}, & p = \pm 1, \\ \frac{2}{15}, & p = 0, \end{cases} \quad (9.126)$$

to give the final expression for the spectral density:

$$K_{mm}^{\text{SD}}(\omega) = \frac{b_{SI}^2 S(S+1)}{9} \left[s_{-1-1}^{\text{SD}}(\omega) + 4s_{00}^{\text{SD}}(\omega) + s_{11}^{\text{SD}}(\omega) \right], \quad (9.127)$$

which we note is independent of m . The functions $s_{pp}^{\text{SD}}(\omega)$ are the electronic spin spectral density functions defined in the common PAF, which are defined as

$$s_{pp}^{\text{SD}}(\omega) = \frac{3}{S(S+1)(2S+1)} \int_0^\infty \text{Tr}_S \left[\tilde{S}_{1p}^\dagger \left\{ \exp(i\hat{\mathcal{L}}_S \tau) \tilde{S}_{1p} \right\} \right] \exp[-(i\omega + 1/(3\tau_R))\tau] d\tau. \quad (9.128)$$

The functions $s_{pp}^{\text{SD}}(\omega)$ contain all the information pertaining to the electron spin dynamics. In particular $s_{00}^{\text{SD}}(\omega)$ describes the spin dynamics of longitudinal relaxation, and $s_{\pm 1 \pm 1}^{\text{SD}}(\omega)$ describes transverse relaxation in the common PAF of the spin-dipolar and ZFS tensors.

The nuclear relaxation rates can now be written down in terms of the $s_{pp}^{\text{SD}}(\omega)$ as follows. The longitudinal PRE is given by

$$\frac{1}{T_1} = \frac{2b_{SI}^2 S(S+1)}{9\hbar^2} \text{Re} \left[s_{-1-1}^{\text{SD}}(\omega_I) + 4s_{00}^{\text{SD}}(\omega_I) + s_{11}^{\text{SD}}(\omega_I) \right], \quad (9.129)$$

and the transverse PRE is

$$\frac{1}{T_2} = \frac{b_{SI}^2 S(S+1)}{9\hbar^2} \text{Re} \left[s_{-1-1}^{\text{SD}}(0) + 4s_{00}^{\text{SD}}(0) + s_{11}^{\text{SD}}(0) + s_{-1-1}^{\text{SD}}(\omega_I) + 4s_{00}^{\text{SD}}(\omega_I) + s_{11}^{\text{SD}}(\omega_I) \right]. \quad (9.130)$$

So far these expressions are general for any electronic spin S , subject to a static ZFS of any symmetry, under the assumptions 1–6 above. We have not yet specified explicitly the form of the electronic relaxation, which is our next step.

9.6.4 Electronic relaxation

The relaxation of the unpaired electronic spin is due to the transient ZFS interaction, the Hamiltonian of which is written in the PAF of the static ZFS as

$$\hat{H}_{\text{ZFS,T}} = \sum_{m=-2}^{+2} (-1)^m F_{2m} \tilde{\mathcal{S}}_{2-m}, \quad (9.131)$$

where F_{2m} are the spatial functions in the irreducible spherical tensor basis. The electronic relaxation superoperator is $\hat{\mathcal{L}}_{\text{del}} = -i\hat{\Gamma}_{\text{ZFS,T}}$, where $\hat{\Gamma}_{\text{ZFS,T}}$ is the superoperator representing the stochastic modulation of the transient ZFS. This modulation is described by the pseudo-rotation model of Rubinstein et al, which assumes that the transient ZFS has a constant amplitude and a direction that changes with time according to a rotational diffusion equation [115]. Therefore, as we have seen before, the transient ZFS is described by two parameters: the magnitude Δ_t and correlation time τ_v . As before the magnitude is defined as follows:

$$\Delta_t^2 = \sum_{m=-2}^{+2} |\tilde{F}_{2m}|^2 \quad (9.132)$$

$$= \frac{2}{3} D_t^2 + 2E_t^2, \quad (9.133)$$

where the \tilde{F}_{2m} are the transient ZFS spatial functions in their (time-dependent) PAF, and D_t and E_t are the axial and rhombic anisotropies that are assumed to be constant in the pseudo-rotation model.

We assume that the electronic relaxation is in the Redfield limit (assumption 2), and so can be described by the equation of motion in Equation 9.78:

$$\frac{d\hat{\rho}_S^T(t)}{dt} = -\frac{1}{\hbar^2} \sum_{m,m'} \sum_{n,n'} (-1)^{m+m'} \exp[i(\omega_{-m'}^{(n')} - \omega_{-m}^{(n)})t] \left[\tilde{\mathcal{S}}_{2-m'}^{(n')}, \left[(\tilde{\mathcal{S}}_{2-m}^{(n)})^\dagger, \hat{\rho}_S^T(t) - \hat{\rho}_{S,0} \right] \right] J_{mm'}(-\omega_{-m}^{(n)}). \quad (9.134)$$

The relaxation rates are defined in terms of the spectral density functions $J_{mm'}(\omega)$, which are given in terms of the correlation functions $\langle F_{2m}(0)^* F_{2m'}(-\tau) \rangle$ by Equation 9.80:

$$J_{mm'}(\omega) = \text{Re} \left[\int_0^\infty \langle F_{2m}(0)^* F_{2m'}(-\tau) \rangle \exp(-i\omega\tau) d\tau \right]. \quad (9.135)$$

In the pseudo-rotation model the correlation functions $\langle F_{2m}(0)^* F_{2m'}(-\tau) \rangle$ are

$$\langle F_{2m}(0)^* F_{2m'}(-\tau) \rangle = \sum_{\mu, \mu'} \tilde{F}_{2\mu}^* \tilde{F}_{2\mu'} \langle D_{\mu m}^{(2)}(\Omega_{\text{FP}}(0))^* D_{\mu' m'}^{(2)}(\Omega_{\text{FP}}(-\tau)) \rangle \quad (9.136)$$

$$= \sum_{\mu, \mu'} \tilde{F}_{2\mu}^* \tilde{F}_{2\mu'} \frac{1}{5} \delta_{\mu\mu'} \delta_{mm'} \exp(-\tau/\tau_v) \quad (9.137)$$

$$= \frac{1}{5} \delta_{mm'} \exp(-\tau/\tau_v) \sum_{\mu} |\tilde{F}_{2\mu}|^2 \quad (9.138)$$

$$= \frac{1}{5} \delta_{mm'} \Delta_t^2 \exp(-\tau/\tau_v), \quad (9.139)$$

where $\Omega_{\text{FP}}(t)$ are the time-dependent Euler angles that describe the constantly-changing orientation of the PAF of the transient ZFS in the PAF of the static ZFS. The spectral density functions are therefore

$$J_{mm'}(\omega) = \frac{\Delta_t^2}{5} \frac{\tau_v}{1 + \omega^2 \tau_v^2} \delta_{mm'}, \quad (9.140)$$

which we note are non-zero only for $m = m'$. The equation of motion now simplifies to

$$\frac{d\hat{\rho}_S^T(t)}{dt} = -\frac{1}{\hbar^2} \sum_m \sum_{n, n'} \exp[i(\omega_{-m}^{(n')} - \omega_{-m}^{(n)})t] \left[\tilde{S}_{2-m}^{(n')}, \left[\left(\tilde{S}_{2-m}^{(n)} \right)^\dagger, \hat{\rho}_S^T(t) - \hat{\rho}_{S,0} \right] \right] J_{mm}(-\omega_{-m}^{(n)}). \quad (9.141)$$

If we remove the non-secular terms with $n \neq n'$ from the equation of motion, we obtain the following expression:

$$\frac{d\hat{\rho}_S^T(t)}{dt} = -\frac{1}{\hbar^2} \sum_m \sum_n \left[\tilde{S}_{2-m}^{(n)}, \left[\left(\tilde{S}_{2-m}^{(n)} \right)^\dagger, \hat{\rho}_S^T(t) - \hat{\rho}_{S,0} \right] \right] J_{mm}(-\omega_{-m}^{(n)}). \quad (9.142)$$

As in section 9.4.2, we note that non-secular terms can sometimes make an important contribution.

Electronic relaxation of $S = 1$ in an axially-symmetric environment

We now illustrate the theory of electronic relaxation in low-field conditions with the calculation of the relaxation time constants of the simplest spin system that is subject to a ZFS interaction, namely an electronic spin $S = 1$ in an axially-symmetric complex. This case was originally treated by Bertini et al [108]. We can neglect the electronic Zeeman interaction for integer spin at low field, and so the coherent part of $\hat{\mathcal{L}}_S$ is simply the static ZFS interaction. The *static* ZFS is axially symmetric with an anisotropy D and an associated frequency of transition $\omega_D = D/(2\pi)$, whilst the *transient* ZFS possesses both an axial and rhombic anisotropy

m	$\hat{S}_{2m}^{(n)}$		$\omega_m^{(n)}$	
	$n = 1$	$n = 2$	$n = 1$	$n = 2$
0	$\sqrt{\frac{1}{6}} (\hat{S}_z^2 - S(S+1)\hat{1}_S)$	—	0	—
± 1	$\mp \frac{1}{2} \hat{S}_z \hat{S}_\pm$	$\mp \frac{1}{2} \hat{S}_\pm \hat{S}_z$	ω_D	$-\omega_D$
± 2	$\frac{1}{2} \hat{S}_\pm^2$	—	0	—

Table 9.2: The spin operators $\hat{S}_{2m}^{(n)}$ and associated frequencies $\omega_m^{(n)}$ of an electronic spin $S = 1$ subject to an axially symmetric static ZFS interaction.

D_t and E_t , as the *instantaneous* distortion of the coordination environment need not necessarily be axial. The electronic relaxation superoperator is

$$\hat{\Gamma}_{\text{ZFS}, T} = \frac{1}{\hbar^2} \sum_m \sum_{n, n'} \left[\hat{S}_{2-m}^{(n')}, \left[\left(\hat{S}_{2-m}^{(n)} \right)^\dagger, \cdot \right] \right] J_{|m|}(-\omega_{-m}^{(n)}), \quad (9.143)$$

where we have retained the sum over both n and n' . The operators $\hat{S}_{2m}^{(n)}$ of the transient ZFS and their characteristic frequencies $\omega_m^{(n)}$ due to evolution under the static ZFS are given in Table 9.2. We also write the spectral density functions as $J_{|m|}(\omega) \equiv J_{+m+m}(\omega) = J_{-m-m}(\omega)$, where we take $+m$ as positive, as they are independent of the sign of m .

The longitudinal relaxation of the spin is described by two time constants $T_{1e}^{(10)}$ and $T_{1e}^{(20)}$, which describe the relaxation of the expectation values of the operators \hat{S}_{10} and \hat{S}_{20} respectively. They are determined from the following expressions:

$$\frac{1}{T_{1e}^{(10)}} = \frac{\left(\hat{S}_{10} \left| \hat{\Gamma}_{\text{ZFS}, T} \right| \hat{S}_{10} \right)}{\left(\hat{S}_{10} \left| \hat{S}_{10} \right. \right)}, \quad (9.144)$$

$$\frac{1}{T_{1e}^{(20)}} = \frac{\left(\hat{S}_{20} \left| \hat{\Gamma}_{\text{ZFS}, T} \right| \hat{S}_{10} \right)}{\left(\hat{S}_{20} \left| \hat{S}_{20} \right. \right)}. \quad (9.145)$$

Explicit calculations give the following time constants:

$$\frac{1}{T_{1e}^{(10)}} = J_1(\omega_D) + 4J_2(0), \quad (9.146)$$

$$\frac{1}{T_{1e}^{(20)}} = 3J_1(\omega_D). \quad (9.147)$$

We see that the two spectral densities present in these expressions are $J_1(\omega_D)$ and $J_2(0)$. The reason why

these spectral densities are evaluated at these frequencies is readily understood by reference to Figure 4.3. The former spectral density function refers to a transition between either the states $|1-1\rangle \rightarrow |10\rangle$ or $|1+1\rangle \rightarrow |10\rangle$, both of which occur with transition frequency ω_D at zero field. Hence $J_1(\omega)$ is evaluated at frequency ω_D . The latter spectral density refers to a transition between the states $|1-1\rangle \rightarrow |1+1\rangle$, which occurs at zero frequency due to the degeneracy at zero field. Hence $J_2(\omega)$ is evaluated at zero frequency.

The transverse relaxation is described by three time constants $T_{2e}^{(1\pm 1)}$, $T_{2e}^{(2\pm 1)}$, and $T_{2e}^{(2\pm 2)}$, which refer to the relaxation of the operators $\hat{S}_{1\pm 1}$, $\hat{S}_{2\pm 1}$, and $\hat{S}_{2\pm 2}$ respectively. They are calculated from:

$$\frac{1}{T_{2e}^{(1+1)}} = \frac{\left(\hat{S}_{1+1}^\dagger \left| \hat{I}_{\text{ZFS,T}} \right| \hat{S}_{1+1} \right)}{\left(\hat{S}_{1+1}^\dagger \left| \hat{S}_{1+1} \right. \right)}, \quad (9.148)$$

$$\frac{1}{T_{2e}^{(2+1)}} = \frac{\left(\hat{S}_{2+1}^\dagger \left| \hat{I}_{\text{ZFS,T}} \right| \hat{S}_{2+1} \right)}{\left(\hat{S}_{2+1}^\dagger \left| \hat{S}_{2+1} \right. \right)}, \quad (9.149)$$

$$\frac{1}{T_{2e}^{(2+2)}} = \frac{\left(\hat{S}_{2+2}^\dagger \left| \hat{I}_{\text{ZFS,T}} \right| \hat{S}_{2+2} \right)}{\left(\hat{S}_{2+2}^\dagger \left| \hat{S}_{2+2} \right. \right)}, \quad (9.150)$$

which, in turn, give the expressions:

$$\frac{1}{T_{2e}^{(1\pm 1)}} = \frac{3}{2}J_0(0) + \frac{5}{2}J_1(\omega_D) + J_2(0), \quad (9.151)$$

$$\frac{1}{T_{2e}^{(2\pm 1)}} = \frac{3}{2}J_0(0) + \frac{1}{2}J_1(\omega_D) + J_2(0), \quad (9.152)$$

$$\frac{1}{T_{2e}^{(2\pm 2)}} = J_1(\omega_D) + 2J_2(0). \quad (9.153)$$

We will see that the important electronic relaxation processes that determine the PRE at low field are those that contribute to $T_{1e}^{(10)}$ and $T_{2e}^{(1+1)}$.

9.6.5 Nuclear relaxation

Nuclear relaxation due to $S = 1$ in an axially-symmetric environment

We now derive the closed expressions for the longitudinal and transverse relaxation times constants for the PRE due to an electronic spin $S = 1$ in an axially-symmetric coordination environment, as treated by Bertini

et al [108]. In order to calculate the forms of the PRE time constants we must evaluate the electronic spectral density functions in Equation 9.128 for the electronic spin system in question. We begin by determining the transformation of the electronic Liouvillian $\hat{\mathcal{L}}_S$ on the rank-one electronic spin operators. For the $S = 1$ spin at low field, the Liouvillian is given by $\hat{\mathcal{L}}_S = \hat{\mathcal{L}}_{\text{ZFS},S} - i\hat{\Gamma}_{\text{ZFS},T}$. The coherent static ZFS Liouvillian transforms the rank-one spin operators as follows:

$$\exp\left(-i\hat{\mathcal{L}}_{\text{ZFS},S}t\right)\tilde{\mathcal{S}}_{10} = \tilde{\mathcal{S}}_{10}, \quad (9.154)$$

$$\exp\left(-i\hat{\mathcal{L}}_{\text{ZFS},S}t\right)\tilde{\mathcal{S}}_{1\pm 1} = \cos(\omega_D t)\tilde{\mathcal{S}}_{1\pm 1} \mp i\sqrt{2}\sin(\omega_D t)\tilde{\mathcal{S}}_{2\pm 1}, \quad (9.155)$$

where we are in the PAF of the static ZFS. The incoherent transient ZFS Liouvillian causes the expectation values of the rank-one operators to decay in a mono-exponential fashion according to their longitudinal or transverse relaxation time constants:

$$\exp\left(-\hat{\Gamma}_{\text{ZFS},T}t\right)\tilde{\mathcal{S}}_{10} = \tilde{\mathcal{S}}_{10} \exp\left(-t/T_{1e}^{(10)}\right), \quad (9.156)$$

$$\exp\left(-\hat{\Gamma}_{\text{ZFS},T}t\right)\tilde{\mathcal{S}}_{1\pm 1} = \tilde{\mathcal{S}}_{1\pm 1} \exp\left(-t/T_{2e}^{(1+1)}\right). \quad (9.157)$$

The traces in Equation 9.128 therefore evaluate to

$$\text{Tr}_S \left[\tilde{\mathcal{S}}_{10}^\dagger \left\{ \exp\left(i\hat{\mathcal{L}}_S \tau\right) \tilde{\mathcal{S}}_{10} \right\} \right] = \frac{1}{3}S(S+1)(2S+1) \exp\left(-\tau/T_{1e}^{(10)}\right) \quad (9.158)$$

$$= 2 \exp\left(-\tau/T_{1e}^{(10)}\right), \quad (9.159)$$

$$\text{Tr}_S \left[\tilde{\mathcal{S}}_{1\pm 1}^\dagger \left\{ \exp\left(i\hat{\mathcal{L}}_S \tau\right) \tilde{\mathcal{S}}_{1\pm 1} \right\} \right] = \frac{1}{3}S(S+1)(2S+1) \cos(\omega_D \tau) \exp\left(-\tau/T_{2e}^{(1+1)}\right) \quad (9.160)$$

$$= 2 \cos(\omega_D \tau) \exp\left(-\tau/T_{2e}^{(1+1)}\right). \quad (9.161)$$

Following Fourier transformation we obtain the following expressions for the electronic spectral density functions:

$$\text{Re} \left[s_{00}^{\text{SD}}(\omega) \right] = \frac{\tau_{c,1}}{1 + \omega^2 \tau_{c,1}^2}, \quad (9.162)$$

$$\text{Re} \left[s_{\pm 1\pm 1}^{\text{SD}}(\omega) \right] = \frac{1}{2} \left[\frac{\tau_{c,2}}{1 + (\omega + \omega_D)^2 \tau_{c,2}^2} + \frac{\tau_{c,2}}{1 + (\omega - \omega_D)^2 \tau_{c,2}^2} \right], \quad (9.163)$$

where $\tau_{c,1}$ and $\tau_{c,2}$ are correlation times that depend upon the electronic longitudinal and transverse relaxation times respectively, and the rotational correlation time:

$$\tau_{c,1}^{-1} = \left(T_{1e}^{(10)}\right)^{-1} + \frac{1}{3}\tau_{\text{R}}^{-1}, \quad (9.164)$$

$$\tau_{c,2}^{-1} = \left(T_{2e}^{(1+1)}\right)^{-1} + \frac{1}{3}\tau_{\text{R}}^{-1}. \quad (9.165)$$

The expressions for T_1 and T_2 are given by Equations 9.129 and 9.130, and have the following forms:

$$\frac{1}{T_1} = \frac{4b_{SI}^2}{9\hbar^2} \left[\frac{4\tau_{c,1}}{1 + \omega_I^2\tau_{c,1}^2} + \frac{\tau_{c,2}}{1 + (\omega_I + \omega_D)^2\tau_{c,2}^2} + \frac{\tau_{c,2}}{1 + (\omega_I - \omega_D)^2\tau_{c,2}^2} \right], \quad (9.166)$$

$$\frac{1}{T_2} = \frac{2b_{SI}^2}{9\hbar^2} \left[4\tau_{c,1} + \frac{2\tau_{c,2}}{1 + \omega_D^2\tau_{c,2}^2} + \frac{4\tau_{c,1}}{1 + \omega_I^2\tau_{c,1}^2} + \frac{\tau_{c,2}}{1 + (\omega_I + \omega_D)^2\tau_{c,2}^2} + \frac{\tau_{c,2}}{1 + (\omega_I - \omega_D)^2\tau_{c,2}^2} \right]. \quad (9.167)$$

In the limit of low field, large static ZFS, and slow motional dynamics such that $|\omega_D\tau_{c,2}| \gg 1$, the relaxation rates are dominated by the terms that do not contain the ZFS frequency:

$$\frac{1}{T_1} = \frac{16b_{SI}^2}{9\hbar^2} \frac{\tau_{c,1}}{1 + \omega_I^2\tau_{c,1}^2}, \quad (9.168)$$

$$\frac{1}{T_2} = \frac{8b_{SI}^2}{9\hbar^2} \left[\tau_{c,1} + \frac{\tau_{c,1}}{1 + \omega_I^2\tau_{c,1}^2} \right]. \quad (9.169)$$

Hence for both relaxation processes the characteristics of the PRE are dominated by the terms that contain the correlation time $\tau_{c,1}$, which in the slow-motion limit is dominated by the electronic longitudinal relaxation properties.

Nuclear relaxation due to higher electronic spins

The expressions for the PRE in the low-field, slow-motion limit have also been derived for systems of higher electronic spin, and in environments of lower symmetry. Westlund derived the PRE expression for T_1 due to an electronic $S = 1$ in a rhombic environment [137]. The expression is clearly more complicated than for the axial case, as it depends on both the static axial and rhombic ZFS anisotropies, as well as three electronic relaxation times rather than two. Corresponding expressions have also been derived by Nilsson et al. for $S = 3/2$ in both axial and rhombic environments, and $S = 2$, $S = 5/2$, $S = 3$, and $S = 7/2$

in axially-symmetric environments [138, 139]. For low-field expressions of the PRE for arbitrary electronic spin, we use the general expressions in Equations 9.129 and 9.130.

9.7 The PRE under fast-rotation conditions in solution

9.7.1 Introduction

When the rotational motion of the paramagnetic complex is rapid, the application of the decomposition approximation to the rotational and electronic spin dynamics is not as straightforward as it is under slow-motion conditions. One significant difference the fast-motion regime has from the slow-motion regime is that the rapid motion modulates both the static ZFS and the spin-dipolar hyperfine interactions, with the former acting as a source of electronic relaxation, and the latter resulting in nuclear relaxation. This situation was investigated by Kruk and Kowalewski, under conditions of high and low external field [306].

This situation is of considerable interest for studying the relaxation properties of contrast agents in aqueous solution in MRI [127, 129]. A specific class of systems that we focus on here is paramagnetic complexes in solution, where the bound ligands are taken from the solvent, an example of which being the aqueous hexaaquairon(II) complex $[\text{Fe}(\text{H}_2\text{O})_6]^{2+}$. It is assumed that the solvent molecules are in chemical exchange between the bound (ligand) and unbound (bulk) sites. Under these circumstances we can identify two separate contributions to the PRE, known as the inner-sphere and outer-sphere contributions. In the inner-sphere mechanism the solvent molecules experience a substantial PRE when bound to the metal ion in the complex. The measured contribution to the nuclear relaxation rate depends upon this PRE, and upon the rate of exchange between the bound and unbound sites. The second, and less important, outer-sphere mechanism is the PRE experienced by solvent molecules that never enter into the complex with the metal ion. It depends on the translational diffusion of the solvent molecules through the bulk.

The fast rotational theory of the PRE describes both of these mechanisms. The main assumptions are:

1. The unperturbed electronic Hamiltonian is the Zeeman interaction at high field, and the static ZFS interaction at low field.
2. The fast motion results in orientational averaging of the static ZFS interaction, so that it acts as a source of electronic relaxation in addition to the transient ZFS.

3. The electronic relaxation is in the Redfield limit.
4. The spin-dipolar hyperfine and static ZFS interactions share the same PAF.
5. For outer-sphere relaxation the translational and rotational diffusion and electronic spin relaxation are all uncorrelated with each other.

Note that the second assumption is the opposite to that made in the slow-motion theory.

9.7.2 A simple model of inner- and outer-sphere relaxation

Before we examine the inner- and outer-sphere mechanisms in the stochastic Liouville formalism we summarise a simple theory for the PRE due to a complex in solution, proposed by Luz and Meiboom [120]. The overall longitudinal PRE $1/T_1$ is written as the sum of the inner-sphere and outer-sphere contributions. These contributions have a complicated form, which are characterised by the longitudinal inner- and outer-sphere PREs $1/T_{1,IS}$ and $1/T_{1,OS}$. However, as we will see, the inner-sphere contribution is not simply equal to $1/T_{1,IS}$.

The model of Luz and Meiboom deals specifically with inner-sphere relaxation in which the solvent molecules are in exchange between the bound (B) and unbound (U) sites. These two sites have lifetimes of τ_B and τ_U respectively, and are associated with different longitudinal relaxation times $T_{1,B}$ and $T_{1,U}$. The central assumption is that the paramagnetic species is dilute, so that the number of bound molecules n_B is much lower than the number of unbound molecules n_U . Hence the ratio of bound to unbound molecules f , which is defined as

$$f = \frac{n_B}{n_U} = \frac{\tau_B}{\tau_U}, \quad (9.170)$$

is much less than unity, i.e. $f \ll 1$.

The nuclear spins of solvent molecules in both sites give bulk magnetization vectors. As we are, at present, only considering longitudinal relaxation, we focus on the z -components of the magnetization vectors of the spins in their bound and unbound states $M_{z,B}(t)$ and $M_{z,U}(t)$. Following the assumption of the dilute nature of the paramagnetic species these magnetization components satisfy $|M_{z,B}(t)| \ll |M_{z,U}(t)|$ at all times. The equilibrium values of the magnetization vector components, $M_{z,B}^{(0)}$ and $M_{z,U}^{(0)}$, are related to the ratio f via $f = M_{z,B}^{(0)}/M_{z,U}^{(0)}$. The longitudinal relaxation behaviour of the magnetizations in the two sites is governed

by a pair of simultaneous differential equations [257]:

$$\frac{dM_{z,B}(t)}{dt} = -\frac{1}{T_{1,IS}} \left(M_{z,B}(t) - M_{z,B}^{(0)} \right) - \frac{1}{\tau_B} M_{z,B}(t) + \frac{1}{\tau_U} M_{z,U}(t), \quad (9.171)$$

$$\frac{dM_{z,U}(t)}{dt} = -\frac{1}{T_{1,U}} \left(M_{z,U}(t) - M_{z,U}^{(0)} \right) - \frac{1}{\tau_U} M_{z,U}(t) + \frac{1}{\tau_B} M_{z,B}(t), \quad (9.172)$$

where we have noted that the longitudinal relaxation time in the bound state $T_{1,B}$ is simply the inner-sphere relaxation time $T_{1,IS}$. We should note that the treatment of chemical exchange in this model is different to that in the Solomon–Bloembergen–Morgan theory of the PRE. In the Solomon–Bloembergen–Morgan theory the rate of chemical exchange is assumed to be sufficiently fast that it falls into the Redfield limit where it can be treated as a relaxation process, and the exchange lifetime used as a correlation time. However in the present situation the exchange need not be fast, and we note that Equations 9.171 and 9.172 are also valid in the limits of slow and intermediate exchange, which are outside the Redfield regime.

Since the fraction of bound solvent molecules f is small, we can approximate $dM_{z,B}(t)/dt \approx 0$, and simplify Equation 9.171 to give an expression for the z -magnetization of the nuclear spins in the bound molecules in terms of the z -magnetization from the spins in the unbound molecules:

$$M_{z,B}(t) = f \left(\frac{\tau_B M_{z,U}^{(0)} + T_{1,IS} M_{z,U}(t)}{\tau_B + T_{1,IS}} \right). \quad (9.173)$$

By substituting this into Equation 9.172 and simplifying we obtain an expression for the relaxation behaviour of the nuclear spins in the unbound molecules:

$$\frac{dM_{z,U}(t)}{dt} = -\left(\frac{1}{T_{1,U}} + \frac{f}{\tau_B + T_{1,IS}} \right) (M_{z,U}(t) - M_{z,U}^{(0)}). \quad (9.174)$$

This expression is of the form

$$\frac{dM_{z,U}(t)}{dt} = -\frac{1}{T_{1,eff}} \left(M_{z,U}(t) - M_{z,U}^{(0)} \right), \quad (9.175)$$

where $T_{1,eff}$ is an effective longitudinal relaxation time constant which is given by

$$\frac{1}{T_{1,eff}} = \frac{1}{T_{1,U}} + \frac{f}{\tau_B + T_{1,IS}}. \quad (9.176)$$

In the NMR experiment the observed signal is dominated by the nuclear spins in the unbound solvent molecules, as $|M_{z,B}(t)| \ll |M_{z,U}(t)|$, and so Equation 9.176 is the longitudinal relaxation time constant that is actually measured. The second term in Equation 9.176 is the enhancement of the relaxation rate, $1/T_{1,U}$, that would otherwise be observed in the absence of the paramagnetic species and so we associate it with the inner-sphere PRE:

$$\frac{1}{T_1} = \frac{f}{\tau_B + T_{1,IS}}, \quad (9.177)$$

which we see is related to the longitudinal nuclear relaxation time constant $T_{1,IS}$, the lifetime τ_B associated with the bound site, and the fraction f of bound molecules.

The outer-sphere relaxation contribution to the overall PRE is included by simply adding the term $1/T_{1,OS}$ to Equation 9.177:

$$\frac{1}{T_1} = \frac{f}{\tau_B + T_{1,IS}} + \frac{1}{T_{1,OS}}. \quad (9.178)$$

A description of outer-sphere relaxation is more difficult, as it requires a description of the stochastic variation of the distance between the nucleus and paramagnetic centre. We can also derive an analogous expression for the inner- and outer-sphere transverse PREs. The following sections are concerned with the calculation of the expressions for the inner- and outer-sphere relaxation time constants $T_{q,IS}$ and $T_{q,OS}$ that are used in Equation 9.178, using the stochastic Liouville formalism.

9.7.3 Inner-sphere relaxation at high field

In formulating the inner-sphere PREs $1/T_{1,IS}$ and $1/T_{2,IS}$ we model the ligand as being bound to the metal ion so that the distance between the nuclear spin and paramagnetic centre is fixed. The PRE is then calculated using the expression for the spectral density $K_{mm}^{SD}(\omega)$:

$$\begin{aligned} K_{mm}^{SD}(\omega) = & 30b_{SI}^2 \sum_{q,q'} \begin{pmatrix} 2 & 1 & 1 \\ m-q & q & -m \end{pmatrix} \begin{pmatrix} 2 & 1 & 1 \\ m-q' & q' & -m \end{pmatrix} \\ & \times \int_0^\infty \text{Tr}_L \left[\hat{S}_{1q}^\dagger D_{0,m-q}^{(2)}(\Omega_{PL}(0))^* \left\{ \exp\left(i\hat{\mathcal{L}}_L\tau\right) \hat{S}_{1q'} D_{0,m-q'}^{(2)}(\Omega_{PL}(0)) \right\} \hat{P}_0 \right] \\ & \times \exp(-i\omega\tau) d\tau. \end{aligned} \quad (9.179)$$

The relevant degrees of freedom in the lattice are those pertaining to the electronic spin, the rotational diffusion, and the distortion of the complex geometry via collisions. The Liouvillian is therefore given by:

$$\hat{\mathcal{L}}_L = \hat{\mathcal{L}}_S + \hat{\mathcal{L}}_R + \hat{\mathcal{L}}_D, \quad (9.180)$$

where the electronic spin Liouvillian comprises terms for the electronic Zeeman interaction and the static and transient ZFS interactions:

$$\hat{\mathcal{L}}_S = \hat{\mathcal{L}}_Z + \hat{\mathcal{L}}_{\text{ZFS,S}} + \hat{\mathcal{L}}_{\text{ZFS,T}}. \quad (9.181)$$

The equilibrium lattice density operator is given by the direct product of the electronic spin and rotational diffusion density operators: $\hat{P}_0 = \hat{P}_{0,S} \otimes \hat{P}_{0,R}$.

In the high-field limit the electronic Zeeman interaction dominates the electronic energy levels, and the static and transient ZFS interactions cause electronic relaxation via their stochastic time dependence, the former by rapid rotational diffusion and the latter by collisional distortions. The spin-dipolar hyperfine tensor is also modulated by the rotational diffusion. We can reformulate Equation 9.179 as follows:

$$\begin{aligned} K_{mm}^{\text{SD}}(\omega) = & 30b_{SI}^2 \sum_{q,q'} \begin{pmatrix} 2 & 1 & 1 \\ m-q & q & -m \end{pmatrix} \begin{pmatrix} 2 & 1 & 1 \\ m-q' & q' & -m \end{pmatrix} \\ & \times \int_0^\infty \text{Tr}_R \left[D_{0,m-q}^{(2)}(\Omega_{\text{PL}}(0))^* \text{Tr}_S \left[\hat{S}_{1q}^\dagger \left\{ \exp \left(i \left(\hat{\mathcal{L}}_S + \hat{\mathcal{L}}_D \right) \tau \right) \hat{S}_{1q'} \right\} \right] D_{0,m-q'}^{(2)}(\Omega_{\text{PL}}(-\tau)) \hat{P}_0 \right] \\ & \times \exp(-i\omega\tau) d\tau, \end{aligned} \quad (9.182)$$

where we have assumed that the static ZFS and spin-dipolar interactions have the same PAF, and so are both modulated according to the same time-dependent set of Euler angles $\Omega_{\text{PL}}(t)$. If we further assume that the rotational motion is so rapid that the electronic spins experience only the average effect of the reorientation we can factorize the part of the correlation function containing the electronic spin degrees of freedom from

the part containing the rotational diffusion, as we have done before:

$$\begin{aligned}
K_{mm}^{\text{SD}}(\omega) &= 30b_{SI}^2 \sum_{q,q'} \begin{pmatrix} 2 & 1 & 1 \\ m-q & q & -m \end{pmatrix} \begin{pmatrix} 2 & 1 & 1 \\ m-q' & q' & -m \end{pmatrix} \\
&\times \int_0^\infty \langle D_{0,m-q}^{(2)}(\Omega_{\text{PL}}(0))^* D_{0,m-q'}^{(2)}(\Omega_{\text{PL}}(-\tau)) \rangle \text{Tr}_S \left[\hat{S}_{1q}^\dagger \left\{ \exp\left(i\left(\hat{\mathcal{L}}_Z - i\hat{\Gamma}_e\right)\tau\right) \hat{S}_{1q'} \right\} \hat{P}_{0,S} \right] \\
&\times \exp(-i\omega\tau) d\tau \tag{9.183}
\end{aligned}$$

$$\begin{aligned}
&= 6b_{SI}^2 \sum_q \begin{pmatrix} 2 & 1 & 1 \\ m-q & q & -m \end{pmatrix}^2 \int_0^\infty \text{Tr}_S \left[\hat{S}_{1q}^\dagger \left\{ \exp\left(i\left(\hat{\mathcal{L}}_Z - i\hat{\Gamma}_e\right)\tau\right) \hat{S}_{1q} \right\} \hat{P}_{0,S} \right] \\
&\times \exp[-(i\omega + 1/\tau_R)\tau] d\tau, \tag{9.184}
\end{aligned}$$

where the electronic relaxation Liouvillian $\hat{\Gamma}_e$ is the sum of two terms corresponding to electronic relaxation under the static ZFS $\hat{\Gamma}_{\text{ZFS,S}}$ and transient ZFS $\hat{\Gamma}_{\text{ZFS,T}}$, i.e. $\hat{\Gamma}_e = \hat{\Gamma}_{\text{ZFS,S}} + \hat{\Gamma}_{\text{ZFS,T}}$.

We define the electronic spectral density in the laboratory frame as

$$s_{pp}^{\text{SD}}(\omega) = \frac{3}{S(S+1)(2S+1)} \int_0^\infty \text{Tr}_S \left[\hat{S}_{1p}^\dagger \left\{ \exp\left(i\left(\hat{\mathcal{L}}_Z - i\hat{\Gamma}_e\right)\tau\right) \hat{S}_{1p} \right\} \right] \exp[-(i\omega + 1/\tau_R)\tau] d\tau, \tag{9.185}$$

which is the high-field equivalent of Equation 9.128, but with the factor of 1/3 removed from the exponent as the correlation time now describes the effect of rotational diffusion on rank-two spatial tensors. We note the following differences: in the present expression the spin operators are expressed in the laboratory frame, rather than the PAF of the static ZFS tensor, and the static ZFS interaction appears as a relaxation superoperator. The spectral densities that are used to calculate the PREs are therefore given by:

$$K_{11}^{\text{SD}}(\omega_I) = \frac{1}{15} b_{SI}^2 S(S+1) \left(s_{11}^{\text{SD}}(\omega_I) + 3s_{00}^{\text{SD}}(\omega_I) + 6s_{-1-1}^{\text{SD}}(\omega_I) \right), \tag{9.186}$$

$$K_{00}^{\text{SD}}(0) = \frac{1}{15} b_{SI}^2 S(S+1) \left(3s_{11}^{\text{SD}}(0) + 4s_{00}^{\text{SD}}(0) + 3s_{-1-1}^{\text{SD}}(0) \right). \tag{9.187}$$

The resulting expressions for the longitudinal and transverse inner-sphere relaxation time constants are

therefore:

$$\frac{1}{T_{1,IS}} = \frac{2b_{SI}^2}{15\hbar^2} S(S+1) \text{Re} \left(s_{11}^{\text{SD}}(\omega_I) + 3s_{00}^{\text{SD}}(\omega_I) + 6s_{-1-1}^{\text{SD}}(\omega_I) \right), \quad (9.188)$$

$$\frac{1}{T_{2,IS}} = \frac{b_{SI}^2}{15\hbar^2} S(S+1) \text{Re} \left(3s_{11}^{\text{SD}}(0) + 4s_{00}^{\text{SD}}(0) + 3s_{-1-1}^{\text{SD}}(0) + s_{11}^{\text{SD}}(\omega_I) + 3s_{00}^{\text{SD}}(\omega_I) + 6s_{-1-1}^{\text{SD}}(\omega_I) \right). \quad (9.189)$$

These are the time constants that are used in the expressions of the form of Equation 9.177 to describe the overall inner-sphere PRE at high field. These expressions are valid for arbitrary electronic spin, and for electronic relaxation outside the Redfield limit. Further simplification requires both the selection of a particular electronic spin, and the assumption that the electronic relaxation processes are within the Redfield limit. If we assume the latter, the electronic relaxation rates are defined by spectral densities of the form already computed in Equation 9.140. The spectral densities due to relaxation under reorientational motion of the static ZFS tensor $J_{mm'}^S(\omega)$ and collisional modulation of the transient ZFS tensor $J_{mm'}^T(\omega)$ are therefore given by

$$J_{mm'}^S(\omega) = \frac{\Delta_s^2}{5} \frac{\tau_R}{1 + \omega^2 \tau_R^2} \delta_{mm'}, \quad (9.190)$$

$$J_{mm'}^T(\omega) = \frac{\Delta_t^2}{5} \frac{\tau_v}{1 + \omega^2 \tau_v^2} \delta_{mm'}, \quad (9.191)$$

where $\Delta_s^2 = 2D^2/3 + 2E^2$ is the strength of the static ZFS interaction. We now explore the special case of the inner-sphere PREs due to an electronic spin $S = 1$.

Inner-sphere relaxation for electronic $S = 1$ at high field

In the case of a paramagnetic centre with electronic spin $S = 1$, the electronic spectral densities in Equation 9.185 are characterised by the longitudinal and transverse electronic time constants $T_{1e}^{(10)}$ and $T_{2e}^{(1\pm 1)}$. When combined with the rotational correlation time we obtain the following overall correlation times $\tau_{c,1}$ and $\tau_{c,2}$:

$$\frac{1}{\tau_{c,1}} = \frac{1}{T_{1e}^{(10)}} + \frac{1}{\tau_R}, \quad (9.192)$$

$$\frac{1}{\tau_{c,2}} = \frac{1}{T_{2e}^{(1\pm 1)}} + \frac{1}{\tau_R}. \quad (9.193)$$

We recall that these correlation times are those encountered in the Solomon–Bloembergen–Morgan theory, but without the contribution from chemical exchange, which is included separately in the expression for the inner-sphere PRE in Equation 9.177.

The real parts of the electronic spectral densities are given by

$$\operatorname{Re} \left[s_{\pm 1 \pm 1}^{\text{SD}}(\omega) \right] = \frac{\tau_{c,2}}{1 + (\omega \mp \omega_S)^2 \tau_{c,2}^2}, \quad (9.194)$$

$$\operatorname{Re} \left[s_{00}^{\text{SD}}(\omega) \right] = \frac{\tau_{c,1}}{1 + \omega^2 \tau_{c,1}^2}. \quad (9.195)$$

Inserting these into Equations 9.188 and 9.189 we obtain the same Solomon contributions to the longitudinal and transverse relaxation rate constants that are calculated from the Solomon–Bloembergen–Morgan theory:

$$\frac{1}{T_1} = \frac{2}{15} S(S+1) \left(\frac{b_{SI}}{\hbar} \right)^2 \left[\frac{3\tau_{c,1}}{1 + \omega_I^2 \tau_{c,1}^2} + \frac{6\tau_{c,2}}{1 + (\omega_S + \omega_I)^2 \tau_{c,2}^2} + \frac{\tau_{c,2}}{1 + (\omega_S - \omega_I)^2 \tau_{c,2}^2} \right], \quad (9.196)$$

$$\frac{1}{T_2} = \frac{1}{15} S(S+1) \left(\frac{b_{SI}}{\hbar} \right)^2 \left[4\tau_{c,1} + \frac{6\tau_{c,2}}{1 + \omega_S^2 \tau_{c,2}^2} + \frac{3\tau_{c,1}}{1 + \omega_I^2 \tau_{c,1}^2} + \frac{6\tau_{c,2}}{1 + (\omega_S + \omega_I)^2 \tau_{c,2}^2} + \frac{\tau_{c,2}}{1 + (\omega_S - \omega_I)^2 \tau_{c,2}^2} \right]. \quad (9.197)$$

Here the electronic relaxation has been calculated explicitly, rather than included phenomenologically in the Solomon–Bloembergen–Morgan theory, and so these expressions are more rigorous. However we should note that they are only exact for a paramagnetic centre with electronic spin $S = 1$, and are not valid for higher electronic spins where the electronic relaxation requires more than two time constants for a proper description. In this case we either use Equations 9.188 and 9.189 directly, or else resort to the Solomon–Bloembergen–Morgan theory with a phenomenological description of the electronic relaxation via effective longitudinal and transverse relaxation time constants.

9.7.4 Outer-sphere relaxation at high field

The outer-sphere PRE is due to stochastic modulation of the spin-dipolar hyperfine tensor by translational diffusion. As for the inner-sphere case electronic relaxation is still due to rotational modulation of the static ZFS and distortional modulation of the transient ZFS. The total lattice Liouvillian is therefore the same as for

the inner-sphere case, with the addition of the stochastic translational-motion Liouvillian $\hat{\mathcal{L}}_T$:

$$\hat{\mathcal{L}}_L = \hat{\mathcal{L}}_S + \hat{\mathcal{L}}_R + \hat{\mathcal{L}}_D + \hat{\mathcal{L}}_T. \quad (9.198)$$

We also extend the lattice density operator to include the translational degrees of freedom, which are represented by the equilibrium density operator $\hat{P}_{0,T}$. The overall equilibrium lattice density operator is now the direct product of the equilibrium density operators for the electronic, rotational, and translational subsystems:

$$\hat{P}_0 = \hat{P}_{0,S} \otimes \hat{P}_{0,R} \otimes \hat{P}_{0,T}.$$

The outer-sphere longitudinal and transverse PREs $1/T_{1,OS}$ and $1/T_{2,OS}$ are given by

$$\frac{1}{T_{1,OS}} = \frac{2}{\hbar^2} \text{Re} \left(K_{11}^{OS}(\omega_I) \right), \quad (9.199)$$

$$\frac{1}{T_{2,OS}} = \frac{1}{\hbar^2} \text{Re} \left(K_{00}^{OS}(0) + K_{11}^{OS}(\omega_I) \right), \quad (9.200)$$

where the outer-sphere spectral density function $K_{mm}^{OS}(\omega)$ is:

$$\begin{aligned} K_{mm}^{OS}(\omega) = & 30c_{SI}^2 \sum_{q,q'} \begin{pmatrix} 2 & 1 & 1 \\ m-q & q & -m \end{pmatrix} \begin{pmatrix} 2 & 1 & 1 \\ m-q' & q' & -m \end{pmatrix} \\ & \times \int_0^\infty \text{Tr}_L \left[\hat{S}_{1q}^\dagger \frac{D_{0,m-q}^{(2)}(\Omega_{OL}(0))^*}{r(0)^3} \left\{ \exp(i\hat{\mathcal{L}}_L\tau) \hat{S}_{1q'} \frac{D_{0,m-q'}^{(2)}(\Omega_{OL}(0))}{r(0)^3} \right\} \hat{P}_0 \right] \\ & \times \exp(-i\omega\tau) d\tau, \end{aligned} \quad (9.201)$$

where $c_{SI} = \mu_0\mu_B g_{iso} \hbar \gamma_I / (4\pi)$ is a constant describing the strength of the spin-dipolar coupling. There are two differences between this function and the corresponding inner-sphere spectral density in Equation 9.179. Firstly the distance between the nuclear and electronic spins $r(t)$ is allowed to vary stochastically in the outer-sphere case. We recall that we treat r as constant in the inner-sphere case. Secondly the angular dependence of the outer-sphere dipolar coupling vector is encoded in the Euler angles Ω_{OL} , which give the orientation of the dipolar coupling PAF in the laboratory frame. We note that this PAF does not necessarily coincide with the common PAF of the inner-sphere spin-dipolar hyperfine interaction and static ZFS tensors. We assume that the translational motion is statistically uncorrelated with the electronic spin dynamics, and that the solvent molecules in the outer sphere move independently of the complex. Hence the translational

motion is also uncorrelated with the rotational motion of the complex. Thus we can factor the trace in Equation 9.201 into a part containing only the translational degrees of freedom, and a part pertaining only to the electronic spin:

$$\begin{aligned}
K_{mm}^{\text{OS}}(\omega) = & 30c_{SI}^2 \sum_{q,q'} \begin{pmatrix} 2 & 1 & 1 \\ m-q & q & -m \end{pmatrix} \begin{pmatrix} 2 & 1 & 1 \\ m-q' & q' & -m \end{pmatrix} \\
& \times \int_0^\infty \left\langle \frac{D_{0,m-q}^{(2)}(\Omega_{\text{OL}}(0))^* D_{0,m-q'}^{(2)}(\Omega_{\text{OL}}(-\tau))}{r(0)^3 r(-\tau)^3} \right\rangle \\
& \times \text{Tr}_S \left[\hat{S}_{1q}^\dagger \left\{ \exp \left(i \left(\hat{\mathcal{L}}_Z - i\hat{\Gamma}_e \right) \tau \right) \hat{S}_{1q'} \right\} \hat{P}_{0,S} \right] \\
& \times \exp(-i\omega\tau) d\tau.
\end{aligned} \tag{9.202}$$

A description of the correlation function for translational diffusion is provided by Kruk et al [121, 122]. The translational diffusion in the presence of intermolecular interactions is described by the Smoluchowski equation. Formally this equation gives the time variation of the probability $P(\mathbf{r}(t)|\mathbf{r}(0))$ of locating a molecule at position $\mathbf{r}(t)$ at time t , given that it started at position $\mathbf{r}(0)$ at time $t = 0$:

$$\frac{\partial P(\mathbf{r}(t)|\mathbf{r}(0))}{\partial t} = D_{12} \nabla \cdot \left[\nabla P(\mathbf{r}(t)|\mathbf{r}(0)) + P(\mathbf{r}(t)|\mathbf{r}(0)) \nabla \left(\frac{U(\mathbf{r}(t))}{kT} \right) \right]. \tag{9.203}$$

This equation considers two molecules, namely the metal-ion complex and the solvent molecule in the outer sphere, with translational diffusion coefficients D_1 and D_2 , and is parameterised by $D_{12} = D_1 + D_2$, which is the relative translational diffusion coefficient of the two molecules. The mutual interaction energy is denoted $U(\mathbf{r}(t))$, and is assumed to depend only on the distance $r(t)$ between the complex and outer-sphere solvent molecule, i.e. $U(\mathbf{r}(t)) = U(r(t))$. The potential can then be calculated from a radial distribution function $g_{\text{rdf}}(r)$ according to

$$\ln [g_{\text{rdf}}(r)] = -\frac{U(r)}{kT}. \tag{9.204}$$

The translational time-correlation function can then be shown to be equal to

$$\left\langle \frac{D_{mk}^{(2)}(\Omega_{\text{OL}}(0))^* D_{m'k'}^{(2)}(\Omega_{\text{OL}}(-\tau))}{r(0)^3 r(-\tau)^3} \right\rangle = \frac{4\pi}{5} N_S g^{\text{T}}(\tau) \delta_{mm'} \delta_{kk'}, \tag{9.205}$$

where N_S is the density of the electronic spins, and $g^T(\tau)$ is the reduced translational correlation function that is given by

$$g^T(\tau) = \int d\mathbf{r}(-\tau) \int d\mathbf{r}(0) \left\langle \frac{D_{mk}^{(2)}(\Omega_{OL}(0))^*}{r(0)^3} \frac{D_{m'k'}^{(2)}(\Omega_{OL}(-\tau))}{r(-\tau)^3} \right\rangle P(\mathbf{r}(-\tau)|\mathbf{r}(0)) g_{\text{rdf}}(r(0)). \quad (9.206)$$

With this form of the translational correlation function the outer-sphere spectral density function in Equation 9.202 takes the form:

$$K_{mm}^{\text{OS}}(\omega) = 24\pi N_S c_{SI}^2 \sum_q \left(\begin{array}{ccc} 2 & 1 & 1 \\ m-q & q & -m \end{array} \right)^2 \times \frac{1}{2S+1} \int_0^\infty \text{Tr}_S \left[\hat{S}_{1q}^\dagger \left\{ \exp\left(i\left(\hat{\mathcal{L}}_Z - i\hat{\Gamma}_e\right)\tau\right) \hat{S}_{1q} \right\} \right] g^T(\tau) \exp(-i\omega\tau) d\tau. \quad (9.207)$$

We see that the outer-sphere PREs are proportional to the density of paramagnetic centres, as expected. This expression can be written more simply by defining the outer-sphere electronic spectral density functions $s_{qq}^{\text{OS}}(\omega)$ as

$$s_{qq}^{\text{OS}}(\omega) = \frac{3}{S(S+1)(2S+1)} \int_0^\infty \text{Tr}_S \left[\hat{S}_{1q}^\dagger \left\{ \exp\left(i\left(\hat{\mathcal{L}}_Z - i\hat{\Gamma}_e\right)\tau\right) \hat{S}_{1q} \right\} \right] g^T(\tau) \exp(-i\omega\tau) d\tau. \quad (9.208)$$

This has the same form as the expression for inner-sphere relaxation in Equation 9.185, with the difference that the factor containing the rotational correlation time has been replaced with the translational-motion correlation function. Combining Equations 9.207 and 9.208 gives us the following expressions for the longitudinal and transverse PREs for outer-sphere relaxation at high field:

$$\frac{1}{T_{1,\text{OS}}} = \frac{8\pi N_S c_{SI}^2 S(S+1)}{15\hbar^2} \text{Re} \left(s_{+1+1}^{\text{OS}}(\omega_I) + 3s_{00}^{\text{OS}}(\omega_I) + 6s_{-1-1}^{\text{OS}}(\omega_I) \right), \quad (9.209)$$

$$\frac{1}{T_{2,\text{OS}}} = \frac{4\pi N_S c_{SI}^2 S(S+1)}{15\hbar^2} \text{Re} \left(3s_{+1+1}^{\text{OS}}(0) + 4s_{00}^{\text{OS}}(0) + 3s_{-1-1}^{\text{OS}}(0) + s_{+1+1}^{\text{OS}}(\omega_I) + 3s_{00}^{\text{OS}}(\omega_I) + 6s_{-1-1}^{\text{OS}}(\omega_I) \right), \quad (9.210)$$

which are valid for arbitrary electronic spin. Further simplification, say for a particular spin S , requires a closed expression for the translational correlation function.

9.7.5 Inner- and outer-sphere relaxation at low field

Under conditions of low field the static ZFS interaction dominates the electronic Zeeman interaction, and the latter can be neglected. The electronic relaxation is caused by the distortional modulation of the transient ZFS, independently of the rate of rotation, and both the electronic relaxation properties and the inner-sphere relaxation rates behave according to the low-field model of Nilsson and Kowalewski, and as already described in section 9.6 [138, 139].

The corresponding low-field outer-sphere relaxation behaviour is slightly different, and needs special consideration. The effects have been described by Kruk et al [121, 122]. We start from the outer-sphere spectral density in Equation 9.201:

$$\begin{aligned}
 K_{mm}^{\text{OS}}(\omega) = & 30c_{SI}^2 \sum_{q,q'} \begin{pmatrix} 2 & 1 & 1 \\ m-q & q & -m \end{pmatrix} \begin{pmatrix} 2 & 1 & 1 \\ m-q' & q' & -m \end{pmatrix} \\
 & \times \int_0^\infty \text{Tr}_L \left[\hat{S}_{1q}^\dagger \frac{D_{0,m-q}^{(2)}(\Omega_{\text{OL}}(0))^*}{r(0)^3} \left\{ \exp\left(i\hat{\mathcal{L}}_L\tau\right) \hat{S}_{1q'} \frac{D_{0,m-q'}^{(2)}(\Omega_{\text{OL}}(0))}{r(0)^3} \right\} \hat{P}_0 \right] \\
 & \times \exp(-i\omega\tau) d\tau,
 \end{aligned} \tag{9.211}$$

where the lattice Liouvillian is now given by

$$\hat{\mathcal{L}}_L = \hat{\mathcal{L}}_S + \hat{\mathcal{L}}_R + \hat{\mathcal{L}}_T, \tag{9.212}$$

$$\hat{\mathcal{L}}_S = \hat{\mathcal{L}}_{\text{ZFS,S}} + \hat{\mathcal{L}}_Z - i\hat{\Gamma}_{\text{ZFS,T}}. \tag{9.213}$$

Following the derivation of the slow-motion theory spectral density in section 9.6, we recall that in the low-field limit the electronic spin is quantized in the PAF of the static ZFS interaction, and so we write the electronic spin operators in that PAF using the relation in Equation 9.119. This gives the following general

expression for the spectral density function:

$$\begin{aligned}
K_{mm}^{\text{OS}}(\omega) = & 30c_{SI}^2 \sum_{q,q'} \begin{pmatrix} 2 & 1 & 1 \\ m-q & q & -m \end{pmatrix} \begin{pmatrix} 2 & 1 & 1 \\ m-q' & q' & -m \end{pmatrix} \\
& \times \sum_{p,p'} \int_0^\infty \text{Tr}_L \left[\tilde{S}_{1p}^\dagger D_{pq}^{(1)}(\Omega_{\text{PL}}(0))^* \frac{D_{0,m-q}^{(2)}(\Omega_{\text{OL}}(0))^*}{r(0)^3} \right. \\
& \times \left. \left\{ \exp(i\hat{\mathcal{L}}_L \tau) \tilde{S}_{1p'} D_{p'q'}^{(1)}(\Omega_{\text{PL}}(0)) \frac{D_{0,m-q'}^{(2)}(\Omega_{\text{OL}}(0))}{r(0)^3} \right\} \hat{P}_0 \right] \\
& \times \exp(-i\omega\tau) d\tau. \tag{9.214}
\end{aligned}$$

This function is simplified by applying the following three assumptions:

1. The translational and rotational motion are completely uncorrelated. Therefore the Euler angles Ω_{PL} are independent to the angles Ω_{OL} .
2. The rotational diffusion occurs on a sufficiently slow timescale compared to the electronic dynamics that the two are uncorrelated.
3. The electronic dynamics are uncorrelated with the translational motion.

We can now factorize the translational, rotational, and electronic parts of the spectral density to obtain:

$$\begin{aligned}
K_{mm}^{\text{OS}}(\omega) = & 30c_{SI}^2 \sum_{q,q'} \begin{pmatrix} 2 & 1 & 1 \\ m-q & q & -m \end{pmatrix} \begin{pmatrix} 2 & 1 & 1 \\ m-q' & q' & -m \end{pmatrix} \\
& \times \sum_{p,p'} \int_0^\infty \langle D_{pq}^{(1)}(\Omega_{\text{PL}}(0))^* D_{p'q'}^{(1)}(\Omega_{\text{PL}}(-\tau)) \rangle \\
& \times \left\langle \frac{D_{0,m-q}^{(2)}(\Omega_{\text{OL}}(0))^*}{r(0)^3} \frac{D_{0,m-q'}^{(2)}(\Omega_{\text{OL}}(-\tau))}{r(-\tau)^3} \right\rangle \\
& \times \text{Tr}_S \left[\tilde{S}_{1p}^\dagger \left\{ \exp(i\hat{\mathcal{L}}_S \tau) \tilde{S}_{1p'} \right\} \hat{P}_{0,S} \right] \exp(-i\omega\tau) d\tau. \tag{9.215}
\end{aligned}$$

The two factors in angular brackets can be simplified as before, to give us the final expression for the spectral density:

$$K_{mm}^{\text{OS}}(\omega) = \frac{8\pi}{9} N_S c_{SI}^2 S(S+1) \left(s_{11}^{\text{OS}}(\omega) + s_{00}^{\text{OS}}(\omega) + s_{-1-1}^{\text{OS}}(\omega) \right), \tag{9.216}$$

where the $s_{pp}^{\text{OS}}(\omega)$ are electronic spectral density functions, which have the form

$$s_{pp}^{\text{OS}}(\omega) = \frac{3}{S(S+1)(2S+1)} \int_0^\infty \text{Tr}_S \left[\tilde{S}_{1p}^\dagger \left\{ \exp(i\hat{\mathcal{L}}_S \tau) \tilde{S}_{1p} \right\} \right] g^T(\tau) \exp[-(i\omega + 1/(3\tau_R))\tau] d\tau. \quad (9.217)$$

These spectral density functions have a similar form to those used to calculate the inner-sphere relaxation spectral density at low field, but with the difference that the outer-sphere function contains information about the translational dynamics through the reduced spectral density $g^T(\tau)$. The resulting low-field outer-sphere PREs are:

$$\frac{1}{T_{1,\text{OS}}} = \frac{16\pi N_S c_{SI}^2 S(S+1)}{9\hbar^2} \text{Re} \left(s_{+1+1}^{\text{OS}}(\omega_I) + s_{00}^{\text{OS}}(\omega_I) + s_{-1-1}^{\text{OS}}(\omega_I) \right), \quad (9.218)$$

$$\frac{1}{T_{2,\text{OS}}} = \frac{8\pi N_S c_{SI}^2 S(S+1)}{9\hbar^2} \text{Re} \left(s_{+1+1}^{\text{OS}}(0) + s_{00}^{\text{OS}}(0) + s_{-1-1}^{\text{OS}}(0) + s_{+1+1}^{\text{OS}}(\omega_I) + s_{00}^{\text{OS}}(\omega_I) + s_{-1-1}^{\text{OS}}(\omega_I) \right). \quad (9.219)$$

As for the high-field case, further simplification requires a closed-form expression for the translational correlation function.

9.8 The effect of vibrational motion on the PRE

9.8.1 Introduction

We now turn our attention to the role of vibrational motions (phonons) on the PRE, and expand on the discussion in section 8.4.4. Vibrational motions occur on a timescale of the order of 100 fs, which is too short to influence nuclear relaxation directly [183]. This is because the correlation time where the contribution of the spectral density to the relaxation rate is a maximum is $\tau_c = |1/\omega_I|$, which for a nuclear Larmor frequency of 500 MHz, corresponding to a ^1H at 11.74 T, is 0.3 ns. However phonons do have a more substantial effect on electronic relaxation, as the magnitude of the electronic Larmor frequency is 658 times higher than that of ^1H [309]. For example an unpaired electron at 11.74 T experiences optimum relaxation with a correlation time of 500 fs. This mechanism for electronic relaxation provides an alternative to the modulation of the transient ZFS due to solvent collisions. The pseudo-rotation model of the latter process, where the transient ZFS is assumed to have constant amplitude and a PAF that changes direction with time, is clearly an over-simplified description of the distortion of the coordination environment, and can only be applied to molecular systems

in solution. The inclusion of phonons removes many of these restrictions, and results in a theory of electronic relaxation, and therefore the PRE, that can be extended to solid systems.

In this section we follow Kruk et al. [119] and explore the effects of phonons on the PRE, to reveal a hierarchy of events: the relaxation of the vibrational degrees of freedom leads to electronic-spin relaxation, which in turn leads to nuclear-spin relaxation. We begin by treating the vibrational motion of the lattice using quantum mechanics, assuming that it lies within the Redfield limit. The effect of this motion on the transient ZFS is then highlighted, leading to a description of the electronic relaxation behaviour, which we also assume can be described by the Redfield theory. We assume that the paramagnetic centre is located in an environment with a vibrationally-averaged geometry that is cubic, so we may ignore the static ZFS interaction. We then calculate the electronic relaxation times for the specific case of a spin $S = 1$ in high field. Finally we derive the expressions for the PRE, and show that for $S = 1$ at high field we recover the Solomon–Bloembergen–Morgan equations.

9.8.2 The vibrational subsystem

We begin by considering a paramagnetic molecule in solution. In this case the vibrational motion can be modelled using a Hamiltonian \hat{H} that comprises three terms [117]:

$$\hat{H} = \hat{H}_V + \hat{H}_B + \hat{H}_{VB}. \quad (9.220)$$

The first term \hat{H}_V describes the vibrational motion of the isolated molecule. The second term \hat{H}_B describes the liquid bath (lattice), to which the molecule is coupled via the third term \hat{H}_{VB} . We note that the form of \hat{H} is reminiscent of the Hamiltonian in the stochastic Liouville formalism used to describe a combined spin system and lattice.

An isolated molecule comprising N atoms possesses $3N - 6$ normal modes of vibration if non-linear, or $3N - 5$ if linear. For a particular normal mode i the displacement of the atoms during the vibration is described by the normal coordinate operator \hat{q}_i , which is a particular mass-weighted linear combination of the atomic displacements. The motion for each mode can be approximated by a simple harmonic oscillator that vibrates

at frequency $\omega_{V,i}$. The Hamiltonian \hat{H}_V is a sum of terms $\hat{H}_{V,i}$, each one of which represents a single mode:

$$\hat{H}_V = \sum_i \hat{H}_{V,i}, \quad (9.221)$$

where each $\hat{H}_{V,i}$ is given by

$$\hat{H}_{V,i} = -\frac{\hbar^2}{2} \frac{\partial^2}{\partial \hat{q}_i^2} + \frac{1}{2} \omega_{V,i}^2 \hat{q}_i^2. \quad (9.222)$$

We note that the normal modes are mutually orthogonal, and therefore independent of each other. For brevity we define a normal-coordinate vector $\hat{\mathbf{q}}$ of all the normal coordinates. Note that we have defined the system so that the equilibrium displacement of the molecule corresponds to $\hat{\mathbf{q}} = \hat{\mathbf{0}}$. The vibrational state of the molecule is described by a wavefunction $|n_1 n_2 \dots\rangle$, where n_i is the vibrational quantum number for normal mode i , which takes values $n_i = 0, 1, 2, \dots$. The total energy of the system $E_{n_1 n_2 \dots}$ is the sum of individual terms E_{n_i} for each mode:

$$E_{n_1 n_2 \dots} = \sum_i E_{n_i}, \quad (9.223)$$

$$E_{n_i} = \left(n_i + \frac{1}{2}\right) \hbar \omega_{V,i}. \quad (9.224)$$

The vibrational Liouvillian $\hat{\mathcal{L}}_V^{(0)}$ corresponds to \hat{H}_V , and therefore represents the coherent vibrational motion of all normal modes. The vibrational frequencies generally take values of the order 100–1000 cm^{-1} , and so the populations of the energy levels do not conform to the high-temperature approximation. Therefore the equilibrium population $p_{n_1 n_2 \dots}^{(0)}$ of each state $|n_1 n_2 \dots\rangle$ is given by the full Boltzmann distribution:

$$p_{n_1 n_2 \dots}^{(0)} = \frac{\exp(-\beta_L E_{n_1 n_2 \dots})}{Z_V}, \quad (9.225)$$

where Z_V is the partition function:

$$Z_V = \text{Tr}_V \left[\exp(-\beta_L \hat{H}_V) \right] \quad (9.226)$$

$$= \sum_{n_1, n_2, \dots} \exp(-\beta_L E_{n_1 n_2 \dots}), \quad (9.227)$$

and the trace is taken over all the vibrational states.

The Hamiltonian describing the bath \hat{H}_B need not be stated explicitly. However the coupling of the normal modes of vibration to the bath is of particular interest. The corresponding Hamiltonian is equal to the intermolecular potential $V(\hat{q}_1, \hat{q}_2, \dots)$ with which the normal modes interact. We expand the potential as a Taylor series in the q_i to give the expression for \hat{H}_{VB} :

$$\hat{H}_{VB} = \sum_i \left(\frac{\partial V}{\partial \hat{q}_i} \right)_{\hat{q}=\hat{0}} \hat{q}_i + \frac{1}{2} \sum_{i,j} \left(\frac{\partial^2 V}{\partial \hat{q}_i \partial \hat{q}_j} \right)_{\hat{q}=\hat{0}} \hat{q}_i \hat{q}_j + \dots, \quad (9.228)$$

where we have defined the potential in the equilibrium molecular geometry $V(\hat{0}, \hat{0}, \dots)$ to be zero. The relaxation of the vibrational subsystem is due to fluctuations in \hat{H}_{VB} . For example the first term in Equation 9.228 contains the intermolecular forces $F_i = \partial V / \partial q_i$, and so fluctuations in this first term are due to the time modulation of these forces, which can be shown to occur on a sub-picosecond timescale [117, 118]. These fluctuations occur on a timescale that is much shorter than the timescale of vibrational relaxation, and so we are in the Redfield limit. The relaxation is governed by the relaxation superoperator $\hat{\Gamma}_V$, and is characterized by two time constants associated with each normal mode, $T_{1V,i}$ and $T_{2V,i}$, with the former giving the lifetime of a vibrational state, and the latter governing the width of the transition observed in the vibrational spectrum.

We determine the time evolution of the vibrational density operator for the entire system $\hat{\rho}_V(t)$ via the Liouville–von Neumann equation

$$\frac{d\hat{\rho}_V(t)}{dt} = -\left(i\hat{\mathcal{L}}_V^{(0)} + \hat{\Gamma}_V \right) \hat{\rho}_V(t), \quad (9.229)$$

where we have included the effects of coherent vibrational motion via $\hat{\mathcal{L}}_V^{(0)}$, and vibrational relaxation via $\hat{\Gamma}_V$. We now focus on a simplified system possessing a single normal mode of vibration with normal coordinate q , vibrational frequency ω_V , and longitudinal and transverse relaxation times T_{1V} and T_{2V} . Further we assume that only the ground state $|0\rangle$ and first excited state $|1\rangle$, with energies E_0 and E_1 , need be considered, as these are the only states with non-negligible equilibrium populations $p_0^{(0)}$ and $p_1^{(0)}$. In Liouville space this system is described by a set of four basis operators $\hat{\rho}_{V,mm} \equiv |m\rangle\langle n|$. As with NMR the operators with $m = n$ correspond to the population of state $|n\rangle$, and those with $m \neq n$ correspond to a coherence between states $|m\rangle$ and $|n\rangle$.

Writing the Liouville–von Neumann equation (9.229) explicitly for the matrix elements $\rho_{V,mm}$ we obtain

$$\frac{d}{dt} \begin{pmatrix} \rho_{V,00}(t) \\ \rho_{V,11}(t) \\ \rho_{V,10}(t) \\ \rho_{V,01}(t) \end{pmatrix} = \begin{pmatrix} -T_{1V}^{-1} \exp(-\beta_L E_1) / Z_V & T_{1V}^{-1} \exp(-\beta_L E_0) / Z_V & 0 & 0 \\ T_{1V}^{-1} \exp(-\beta_L E_1) / Z_V & -T_{1V}^{-1} \exp(-\beta_L E_0) / Z_V & 0 & 0 \\ 0 & 0 & -i\omega_V - T_{2V}^{-1} & 0 \\ 0 & 0 & 0 & i\omega_V - T_{2V}^{-1} \end{pmatrix} \begin{pmatrix} \rho_{V,00}(t) \\ \rho_{V,11}(t) \\ \rho_{V,10}(t) \\ \rho_{V,01}(t) \end{pmatrix}. \quad (9.230)$$

The block-diagonal form of the Liouville supermatrix allows us to solve the equation separately for the populations, and each of the coherences. The matrix elements of the two population operators are coupled by two simultaneous differential equations, which have the following solutions:

$$\rho_{V,00}(t) = [p_1^{(0)} \rho_{V,00}(0) - p_0^{(0)} \rho_{V,11}(0)] \exp(-|t|/T_{1V}) + p_0^{(0)}, \quad (9.231)$$

$$\rho_{V,11}(t) = [-p_1^{(0)} \rho_{V,00}(0) + p_0^{(0)} \rho_{V,11}(0)] \exp(-|t|/T_{1V}) + p_1^{(0)}. \quad (9.232)$$

We see that at infinite time both population operators relax according to the time constant T_{1V} , and tend to their equilibrium expressions of $p_n^{(0)}$. The matrix elements of the two coherence operators evolve independently of each other according to

$$\rho_{V,10}(t) = \rho_{V,10}(0) \exp(-i\omega_V t) \exp(-|t|/T_{2V}), \quad (9.233)$$

$$\rho_{V,01}(t) = \rho_{V,01}(0) \exp(+i\omega_V t) \exp(-|t|/T_{2V}). \quad (9.234)$$

The coherence operators precess at frequency $\pm\omega_V$, and decay to zero with the time constant T_{2V} .

9.8.3 Electronic relaxation

The electronic spin is coupled to the lattice of quantum vibrations through the ZFS interaction. We now derive the form of the electronic relaxation rates by considering the resulting fluctuations in the transient ZFS. The evolution of the electronic spin is governed by the following Liouville–von Neumann equation

$$\frac{d\hat{\rho}_S(t)}{dt} = -\left(i\hat{\mathcal{L}}_Z + \hat{\Gamma}_e\right)\hat{\rho}_S(t), \quad (9.235)$$

where the coherent evolution is due to the electronic Zeeman interaction (we recall that the static ZFS is zero), and the relaxation is governed by the relaxation superoperator $\hat{\Gamma}_e$ in Equation 9.82. This relaxation is due to the modulation of the transient ZFS by the phonons, and so we can write $\hat{\Gamma}_e$ in terms of the transient ZFS and relaxation Liouvillians as

$$-i\hat{\Gamma}_e = \hat{\mathcal{L}}_{\text{ZFS,T}} + \hat{\mathcal{L}}_V^{(0)} - i\hat{\Gamma}_V. \quad (9.236)$$

The transient ZFS Hamiltonian is

$$\hat{H}_{\text{ZFS,T}} = \sum_{m=-2}^{+2} (-1)^m \hat{F}_{2m} \hat{S}_{2-m}, \quad (9.237)$$

where we have written the spatial tensors \hat{F}_{2m} explicitly as operators to acknowledge that they depend on the normal coordinate operators \hat{q} . As before we write \hat{F}_{2m} in terms of the corresponding tensors \tilde{F}_{2m} in the PAF of the interaction:

$$\hat{F}_{2m} = \sum_{m'=-2}^{+2} \tilde{F}_{2m'} D_{m'm}^{(2)}(\Omega_{\text{FL}}). \quad (9.238)$$

The PAF tensor components $\tilde{F}_{2m'}$ are functions of the normal coordinates, and so fluctuate with time during the vibrations. We can therefore define a set of functions $h_{2m'}(\hat{q})$, which depend on \hat{q} , and write the operators explicitly as

$$\hat{F}_{2m} = \sum_{m'=-2}^{+2} h_{m'}(\hat{q}). \quad (9.239)$$

We assume that the transient ZFS is independent of rotational motion, and so the form of \hat{F}_{2m} does not depend on m . For small displacements of the atomic positions from their equilibrium positions we can expand $h_{m'}(\hat{q})$ as a Taylor series in the normal coordinates as follows:

$$h_{m'}(\hat{q}) = h_{m'}(\hat{\mathbf{0}}) + \sum_i \left(\frac{\partial h_{m'}}{\partial \hat{q}_i} \right)_{\hat{q}=\hat{\mathbf{0}}} \hat{q}_i + \frac{1}{2} \sum_{i,j} \left(\frac{\partial^2 h_{m'}}{\partial \hat{q}_i \partial \hat{q}_j} \right)_{\hat{q}=\hat{\mathbf{0}}} \hat{q}_i \hat{q}_j + \dots \quad (9.240)$$

The zeroth order term $h_{m'}(\hat{\mathbf{0}})$ gives the magnitude and direction of the ZFS after motional averaging due to the vibrations, and therefore corresponds to the static ZFS. As already stated we treat this term as zero. The higher-order terms in the Taylor expansion correspond to the transient ZFS.

The electronic relaxation rates depend on the following spectral density function $J(\omega)$:

$$J(\omega) = \text{Re} \left[\int_0^{\infty} \langle \hat{F}_{2m}(0)^\dagger \hat{F}_{2m}(-\tau) \rangle \exp(-i\omega\tau) d\tau \right], \quad (9.241)$$

which, in turn, depends on the following the time-correlation function:

$$\langle \hat{F}_{2m}(0)^\dagger \hat{F}_{2m}(-\tau) \rangle = \text{Tr}_V \left[\hat{L}_{2m}^\dagger \left\{ \exp \left(i \left(\hat{\mathcal{L}}_V^{(0)} - i\hat{\Gamma}_V \right) \tau \right) \hat{L}_{2m} \right\} \hat{P}_{V,0} \right], \quad (9.242)$$

where the trace is taken over all vibrational states, and $\hat{P}_{V,0}$ is the equilibrium lattice density operator for the vibrational subsystem. We note that, since \hat{F}_{2m} do not depend on the index m , neither does the spectral density nor the correlation function. Because there is no coupling between the normal modes we are able to write the total spectral density as the sum of terms $J_i(\omega)$ due to each normal mode:

$$J(\omega) = \sum_i J_i(\omega). \quad (9.243)$$

To facilitate the discussion we therefore restrict ourselves again to considering a system with a single normal mode. The final result can then be easily generalised to several normal modes. From Equation 9.240 we write the transient ZFS spatial tensor operators \hat{F}_{2m} as Taylor series in \hat{q} , truncating at second order to give

$$\hat{F}_{2m} = A\hat{q} + B\hat{q}^2, \quad (9.244)$$

where the constants A and B are given by

$$A = \sum_{m'=-2}^{+2} \left(\frac{\partial h_{m'}}{\partial \hat{q}_i} \right)_{\hat{q}=\hat{0}}, \quad (9.245)$$

$$B = \frac{1}{2} \sum_{m'=-2}^{+2} \left(\frac{\partial^2 h_{m'}}{\partial \hat{q}_i \partial \hat{q}_j} \right)_{\hat{q}=\hat{0}}. \quad (9.246)$$

We can now write the correlation function in terms of the normal coordinate as follows:

$$\langle \hat{F}_{2m}(0)^\dagger \hat{F}_{2m}(-\tau) \rangle = A^2 \langle \hat{q}(0)^\dagger \hat{q}(-\tau) \rangle + B^2 \langle \hat{q}^2(0)^\dagger \hat{q}^2(-\tau) \rangle + AB \langle \hat{q}(0)^\dagger \hat{q}^2(-\tau) \rangle + BA \langle \hat{q}^2(0)^\dagger \hat{q}(-\tau) \rangle. \quad (9.247)$$

The terms in angular brackets denote correlation functions of powers of the normal coordinate operators,

which have the following general expressions:

$$\langle \hat{q}^x(0)^\dagger \hat{q}^y(-\tau) \rangle = \text{Tr}_V \left[\hat{q}^x(0)^\dagger \left\{ \exp \left(i \left(\hat{\mathcal{L}}_V^{(0)} - i \hat{\Gamma}_V \right) \tau \right) \hat{q}^y(0) \right\} \hat{P}_{V,0} \right] \quad (9.248)$$

$$= \frac{1}{Z_V} \text{Tr}_V \left[\hat{q}^x(0)^\dagger \hat{q}^y(-\tau) \exp \left(-\beta_L \hat{H}_V \right) \right] \quad (9.249)$$

$$= \sum_{m,n} \frac{\exp(-\beta_L E_m)}{Z_V} \langle m | \hat{q}^x(0)^\dagger | n \rangle \langle n | \hat{q}^y(-\tau) | m \rangle. \quad (9.250)$$

We therefore compute the correlation function by evaluating all the terms in Equation 9.247 in turn. Once again we consider only the states $n = 0$ and $n = 1$.

We begin by evaluating the first term in A^2 in Equation 9.247, which corresponds to the first-order coupling between the electronic spin and the vibrational lattice. To facilitate the calculation we write the normal coordinate operator as a linear combination of the vibrational basis operators $\hat{\rho}_{V,mn}$:

$$\hat{q} = \sum_{m,n} \langle m | \hat{q} | n \rangle \hat{\rho}_{V,mn}, \quad (9.251)$$

The matrix elements $\langle m | \hat{q} | n \rangle$ can be shown to be given by [206]

$$\langle m | \hat{q} | n \rangle = \left(\frac{\hbar}{2\mu\omega_V} \right)^{1/2} \left[(n+1)^{1/2} \delta_{m,n+1} + (n)^{1/2} \delta_{m,n-1} \right], \quad (9.252)$$

where μ is the reduced mass associated with the normal mode. Restricting ourselves to the two lowest-lying states we obtain the following expression for \hat{q} :

$$\hat{q} = \left(\frac{\hbar}{2\mu\omega_V} \right)^{1/2} [\hat{\rho}_{V,10} + \hat{\rho}_{V,01}], \quad (9.253)$$

which we see depends only on the two coherence operators. The time dependence of \hat{q} is determined by using the expressions for the time dependence of the vibrational coherence operators $\hat{\rho}_{V,10}(t)$ and $\hat{\rho}_{V,01}(t)$ which we have previously computed in Equations 9.233 and 9.234. The resulting expression for $\hat{q}(t)$ is therefore

$$\begin{aligned} \hat{q}(t) &= \left(\frac{\hbar}{2\mu\omega_V} \right)^{1/2} [\hat{\rho}_{V,10}(0) \exp(-i\omega_V t) + \hat{\rho}_{V,01}(0) \exp(i\omega_V t)] \exp(-|t|/T_{2V}) \\ &= \left(\frac{\hbar}{2\mu\omega_V} \right)^{1/2} [|1\rangle\langle 0| \exp(-i\omega_V t) + |0\rangle\langle 1| \exp(i\omega_V t)] \exp(-|t|/T_{2V}). \end{aligned}$$

Combining this expression and Equation 9.250 gives us the correlation function $\langle \hat{q}(0)^\dagger \hat{q}(-\tau) \rangle$, which is:

$$\langle \hat{q}(0)^\dagger \hat{q}(-\tau) \rangle = \frac{\hbar}{2\mu\omega_V} \left[p_0^{(0)} \exp(i\omega_V\tau) + p_1^{(0)} \exp(-i\omega_V\tau) \right] \exp(-\tau/T_{2V}). \quad (9.254)$$

The corresponding contribution to the spectral density $J^{(1)}(\omega)$ is given by the Fourier–Laplace transform, and is equal to

$$J^{(1)}(\omega) = \frac{A^2\hbar}{2\mu\omega_V} \left[p_0^{(0)} \frac{T_{2V}}{1 + (\omega - \omega_V)^2 T_{2V}^2} + p_1^{(0)} \frac{T_{2V}}{1 + (\omega + \omega_V)^2 T_{2V}^2} \right]. \quad (9.255)$$

We see that the first-order contribution contains spectral-density components at frequencies $\omega - \omega_V$ and $\omega + \omega_V$, and contains a correlation time that is equal to the transverse relaxation time constant T_{2V} of the vibrational subsystem.

The second term (in B^2) in Equation 9.247 represents a second-order coupling between the electronic spin and the vibrational lattice. Repeating the analysis for the first-order term, we begin by writing the operator \hat{q}^2 in terms of the basis operators $\hat{\rho}_{V,mm}$:

$$\hat{q}^2 = \sum_{m,n} \langle m | \hat{q}^2 | n \rangle \hat{\rho}_{V,mm}, \quad (9.256)$$

where the matrix elements $\langle m | \hat{q}^2 | n \rangle$ are [206]

$$\langle m | \hat{q}^2 | n \rangle = \frac{\hbar}{2\mu\omega_V} \left[((n+1)(n+2))^{1/2} \delta_{m,n+2} + (2n+1)\delta_{mm} + (n(n-1))^{1/2} \delta_{m,n-2} \right], \quad (9.257)$$

Considering only the states $n = 0$ and $n = 1$ we obtain:

$$\hat{q}^2 = \frac{\hbar}{2\mu\omega_V} [\hat{\rho}_{V,00} + 3\hat{\rho}_{V,11}]. \quad (9.258)$$

In contrast to the expression for \hat{q} , which depends only on the coherence operators, \hat{q}^2 depends only on the population operators. The time dependence of the population operators in Equations 9.231 and 9.232 gives us the following time-dependent expression for $\hat{q}^2(t)$:

$$\hat{q}^2(t) = \frac{\hbar}{\mu\omega_V} \left[p_0^{(0)} |1\rangle\langle 1| - p_1^{(0)} |0\rangle\langle 0| \right] \exp(-|t|/T_{1V}) + \frac{\hbar}{2\mu\omega_V} \left[p_0^{(0)} + 3p_1^{(0)} \right] \hat{1}_V. \quad (9.259)$$

The first term in Equation 9.259 is time dependence due to the longitudinal relaxation of the vibrational lattice, whereas the second represents its equilibrium configuration. In determining the electronic relaxation properties we are interested in the deviation of the vibrational lattice from its equilibrium configuration, and so we remove this second term and replace Equation 9.259 with the following:

$$\hat{q}^2(t) = \frac{\hbar}{\mu\omega_V} \left[p_0^{(0)} |1\rangle\langle 1| - p_1^{(0)} |0\rangle\langle 0| \right] \exp(-|t|/T_{1V}). \quad (9.260)$$

The correlation function is therefore evaluated to be

$$\langle \hat{q}^2(0)^\dagger \hat{q}^2(-\tau) \rangle = \left(\frac{\hbar}{\mu\omega_V} \right)^2 \left[p_0^{(0)} (p_1^{(0)})^2 + (p_0^{(0)})^2 p_1^{(0)} \right] \exp(-\tau/T_{1V}) \quad (9.261)$$

$$= \left(\frac{\hbar}{\mu\omega_V} \right)^2 \frac{\exp(-\beta_L \hbar \omega_V)}{(1 + \exp(-\beta_L \hbar \omega_V))^2} \exp(-\tau/T_{1V}). \quad (9.262)$$

The resulting second-order contribution from this normal mode to the spectral density $J^{(2)}(\omega)$ is

$$J^{(2)}(\omega) = B^2 \left(\frac{\hbar}{\mu\omega_V} \right)^2 \frac{\exp(-\beta_L \hbar \omega_V)}{(1 + \exp(-\beta_L \hbar \omega_V))^2} \frac{T_{1V}}{1 + \omega^2 T_{1V}^2}. \quad (9.263)$$

We see that this contribution to the spectral density does not depend on the vibrational frequency, and is characterised by a correlation time equal to the longitudinal vibrational relaxation time constant T_{1V} . This is because the operator \hat{q}^2 depends on the population operators, and not on the coherence operators, of the vibrational subsystem.

The remaining terms in Equation 9.247 do not contribute to the spectral density, as the mixed-order correlation functions are zero:

$$\langle \hat{q}(0)^\dagger \hat{q}^2(-\tau) \rangle = \langle \hat{q}^2(0)^\dagger \hat{q}(-\tau) \rangle = 0. \quad (9.264)$$

Therefore the total spectral density $J(\omega)$ for this single normal mode, up to second order, is

$$J(\omega) = J^{(1)}(\omega) + J^{(2)}(\omega) \quad (9.265)$$

$$= \frac{A^2 \hbar}{2\mu\omega_V} \left[p_0^{(0)} \frac{T_{2V}}{1 + (\omega - \omega_V)^2 T_{2V}^2} + p_1^{(0)} \frac{T_{2V}}{1 + (\omega + \omega_V)^2 T_{2V}^2} \right] + B^2 \left(\frac{\hbar}{\mu\omega_V} \right)^2 \frac{\exp(-\beta_L \hbar \omega_V)}{(1 + \exp(-\beta_L \hbar \omega_V))^2} \frac{T_{1V}}{1 + \omega^2 T_{1V}^2}. \quad (9.266)$$

In a system with more than one normal mode, we simply sum the individual contributions to the spectral density to obtain the total spectral density, as in Equation 9.243. The resulting spectral density is then

$$J(\omega) = \sum_i \left[\frac{A_i^2 \hbar}{2\mu_i \omega_{V,i}} \left\{ p_{0,i}^{(0)} \frac{T_{2V,i}}{1 + (\omega - \omega_{V,i})^2 T_{2V,i}^2} + p_{1,i}^{(0)} \frac{T_{2V,i}}{1 + (\omega + \omega_{V,i})^2 T_{2V,i}^2} \right\} + B_i^2 \left(\frac{\hbar}{\mu_i \omega_{V,i}} \right)^2 \frac{\exp(-\beta_L \hbar \omega_{V,i})}{(1 + \exp(-\beta_L \hbar \omega_{V,i}))^2} \frac{T_{1V,i}}{1 + \omega^2 T_{1V,i}^2} \right], \quad (9.267)$$

where we have added a subscript i to the parameters that are different for different normal modes. These results are general for an arbitrary electronic spin. We now examine the special case of $S = 1$.

Electronic relaxation of a spin $S = 1$

As already discussed the electronic relaxation properties of a paramagnetic centre with $S = 1$ are characterised by a relaxation time constant for each spin basis operator. The relaxation processes of the two basis operators \hat{S}_{10} and \hat{S}_{20} are described by the two time constants $T_{1e}^{(10)}$ and $T_{1e}^{(20)}$, whilst the operators $\hat{S}_{1\pm 1}$, $\hat{S}_{2\pm 1}$, and $\hat{S}_{2\pm 2}$ relax according to the transverse time constants $T_{2e}^{(1\pm 1)}$, $T_{2e}^{(2\pm 1)}$, and $T_{2e}^{(2\pm 2)}$. The time constants are calculated from the electronic relaxation superoperator $\hat{\Gamma}_e$ in Equation 9.82, and in the current formalism are given by

$$\frac{1}{T_{1e}^{(10)}} = J(\omega_S) + 4J(2\omega_S), \quad (9.268)$$

$$\frac{1}{T_{1e}^{(20)}} = 3J(\omega_S), \quad (9.269)$$

$$\frac{1}{T_{2e}^{(1\pm 1)}} = \frac{3}{2}J(0) + \frac{5}{2}J(\omega_S) + J(2\omega_S), \quad (9.270)$$

$$\frac{1}{T_{2e}^{(2\pm 1)}} = \frac{3}{2}J(0) + \frac{1}{2}J(\omega_S) + J(2\omega_S), \quad (9.271)$$

$$\frac{1}{T_{2e}^{(2\pm 2)}} = J(\omega_S) + J(2\omega_S). \quad (9.272)$$

We recall that we have neglected the static ZFS throughout this section, and only the electronic Zeeman interaction is considered.

9.8.4 The PRE

The electronic relaxation behaviour derived in the preceding section can be included in the spectral density functions describing the nuclear-spin relaxation. We can then use the following familiar equations to derive expressions for the longitudinal and transverse PREs:

$$\frac{1}{T_1} = \frac{2}{\hbar^2} \operatorname{Re} \left(K_{11}^{\text{FC}}(\omega_I) + K_{11}^{\text{SD}}(\omega_I) \right), \quad (9.273)$$

$$\frac{1}{T_2} = \frac{1}{\hbar^2} \operatorname{Re} \left(K_{00}^{\text{FC}}(0) + K_{11}^{\text{FC}}(\omega_I) + K_{00}^{\text{SD}}(0) + K_{11}^{\text{SD}}(\omega_I) \right). \quad (9.274)$$

These expressions can be evaluated in any motional regime, and at any field, as discussed in this chapter. As stressed at the beginning of this section the main role of the vibrational motions is to influence the electronic relaxation. Once this has been characterised the electronic relaxation properties are used in the common expression for the PRE.

The high-field PRE due to an electronic spin $S = 1$

A final example of a calculation of nuclear-spin relaxation concerns the PRE due to an electronic spin $S = 1$ at high field, and in the absence of a static ZFS interaction. The relevant electronic relaxation time constants are given in Equations 9.268 and 9.270. If we include them in the expressions for the PRE, we simply recover the Solomon–Bloembergen–Morgan equations:

$$\begin{aligned} \frac{1}{T_1} = & \frac{2}{3} S(S+1) \left(\frac{A^{\text{FC}}}{\hbar} \right)^2 \frac{\tau_{\text{E},2}}{1 + (\omega_S - \omega_I)^2 \tau_{\text{E},2}^2} \\ & + \frac{2}{15} S(S+1) \left(\frac{b_{\text{SI}}}{\hbar} \right)^2 \left[\frac{3\tau_{\text{c},1}}{1 + \omega_I^2 \tau_{\text{c},1}^2} + \frac{6\tau_{\text{c},2}}{1 + (\omega_S + \omega_I)^2 \tau_{\text{c},2}^2} + \frac{\tau_{\text{c},2}}{1 + (\omega_S - \omega_I)^2 \tau_{\text{c},2}^2} \right], \end{aligned} \quad (9.275)$$

$$\begin{aligned} \frac{1}{T_2} = & \frac{1}{3} S(S+1) \left(\frac{A^{\text{FC}}}{\hbar} \right)^2 \left[\tau_{\text{E},1} + \frac{\tau_{\text{E},2}}{1 + (\omega_S - \omega_I)^2 \tau_{\text{E},2}^2} \right] \\ & + \frac{1}{15} S(S+1) \left(\frac{b_{\text{SI}}}{\hbar} \right)^2 \left[4\tau_{\text{c},1} + \frac{6\tau_{\text{c},2}}{1 + \omega_S^2 \tau_{\text{c},2}^2} + \frac{3\tau_{\text{c},1}}{1 + \omega_I^2 \tau_{\text{c},1}^2} + \frac{6\tau_{\text{c},2}}{1 + (\omega_S + \omega_I)^2 \tau_{\text{c},2}^2} + \frac{\tau_{\text{c},2}}{1 + (\omega_S - \omega_I)^2 \tau_{\text{c},2}^2} \right]. \end{aligned} \quad (9.276)$$

As we discussed in chapter 8, these expressions are also relevant for solid-state paramagnetic systems.

9.9 Longitudinal relaxation in metallic solids

9.9.1 Introduction

The final topic that we review in our discussion of relaxation in paramagnetic systems is nuclear spin relaxation in solid metals. The primary interest here is to compare the result with the expressions for the PRE in solid insulators that have been derived in previous sections. Here we restrict the discussion to high-field conditions, so that we can compare the PRE calculated for a metal with the Solomon–Bloembergen–Morgan expression for a solid insulator in Equations 8.185 and 8.186.

As for the other cases discussed in this chapter, understanding the PRE in metallic systems requires us to treat the lattice as a quantum mechanical object, because the degrees of freedom include the energy levels associated with the electronic bands in addition to the electronic spins. However in contrast to the other cases of relaxation that we have discussed we do not employ Redfield theory. Instead we restrict the discussion to longitudinal relaxation, which we describe as being due to energy exchange between the nuclear spin system and the lattice, via transitions between the nuclear spin states accompanied by simultaneous transitions between the electronic states. The longitudinal relaxation rates were first described in this way by Korringa [310], whose treatment was later expanded upon by Abragam [183] and Slichter [245]. However this description is wholly inadequate for describing transverse relaxation, for which we would require a Redfield treatment [95, 252].

We proceed according to the following assumptions:

1. We are in the high-field regime, so that the nuclear-spin dynamics are dominated by the nuclear Zeeman interaction.
2. The temperature is sufficiently high that the nuclear-spin-state populations are described by the high-temperature approximation to the Boltzmann distribution.
3. We expect the only significant contributions to the PRE to be due to conduction electrons near the Fermi energy. It is assumed that the corresponding wavefunctions have substantial *s*-character, so that the hyperfine interaction is dominated by the Fermi-contact part.
4. The stochastic process that causes nuclear relaxation is the motion of the conduction electrons. The correlation time is given by the average duration over which the electron remains localized on a given

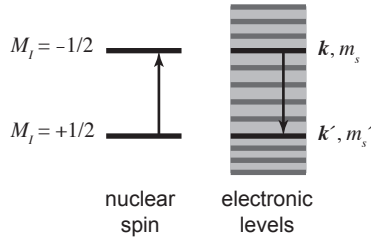


Figure 9.2: Illustration of the nuclear relaxation process for a nuclear spin coupled to an electronic lattice. Here the nuclear-spin absorption transition is accompanied by an emission transition in the lattice, so that energy is exchanged between the two parts of the system.

atom.

9.9.2 Longitudinal relaxation due to transitions between energy levels

As we have pointed out above, the longitudinal relaxation rate of a system can be calculated by considering the transitions between the energy levels of the system that are induced by stochastic processes. In order to conserve energy, any transition between the nuclear spin states must be accompanied by a transition of equal energy and in the opposite direction between the lattice states. This is illustrated in Figure 9.2, which shows an absorptive transition for a nuclear spin $1/2$ from the state $|+1/2\rangle$ to $|-1/2\rangle$ occurring simultaneously with an emissive transition in the lattice from state $|k, m_s\rangle$ to $|k', m'_s\rangle$. We are interested in the return to equilibrium of the populations of the nuclear spin states $|n\rangle$, as this corresponds to longitudinal relaxation. We can explain the relaxation process as arising from the rates of change of the state populations p_n , which are given by:

$$\frac{dp_n}{dt} = \sum_m (p_m W_{mn} - p_n W_{nm}). \quad (9.277)$$

The positive term $p_m W_{mn}$ in Equation 9.277 describes the increase in p_n due to a transition *from* state $|m\rangle$, whereas the negative term $-p_n W_{nm}$ describes a reduction in p_n due to a transition *to* state $|m\rangle$. The transition coefficient W_{mn} is the number of transitions from $|m\rangle$ to $|n\rangle$ that occur per unit time. At equilibrium the populations have their equilibrium values $p_n^{(0)}$, and their rate of change is zero. Therefore from Equation 9.277, we are able to deduce the following relationship between W_{mn} and W_{nm} :

$$p_m^{(0)} W_{mn} = p_n^{(0)} W_{nm}. \quad (9.278)$$

The longitudinal relaxation rate governing this return to equilibrium depends on the transition coefficients and the energies of the states. It can be shown that the expression is

$$\frac{1}{T_1} = \frac{1}{2} \frac{\sum_{m,n} W_{mn} (E_m - E_n)^2}{\sum_n E_n^2}. \quad (9.279)$$

If we only consider the effects of the conduction electrons near the Fermi surface, Equation 9.279 corresponds to the longitudinal PRE. We now require expressions for the transition coefficients.

9.9.3 The longitudinal PRE of nuclei in a metal

We first consider transitions of the combined spin system from the initial occupied state $|M_I \mathbf{k} m_s\rangle$ to the final unoccupied state $|M_I' \mathbf{k}' m_s'\rangle$. The corresponding transition coefficients $W_{M_I \mathbf{k} m_s, M_I' \mathbf{k}' m_s'}$ are given by the Fermi golden rule:

$$W_{M_I \mathbf{k} m_s, M_I' \mathbf{k}' m_s'} = \frac{2\pi}{\hbar} \left| \langle M_I' \mathbf{k}' m_s' | \hat{H}_{IL} | M_I \mathbf{k} m_s \rangle \right|^2 \delta(E_{M_I} + E_{\mathbf{k} m_s} - E_{M_I'} - E_{\mathbf{k}' m_s'}), \quad (9.280)$$

where E_{M_I} is the energy of nuclear spin state $|M_I\rangle$, and $E_{\mathbf{k} m_s}$ is the energy of the lattice state $|\mathbf{k} m_s\rangle$, and the Hamiltonian \hat{H}_{IL} describes the coupling between the nuclear spin system and the lattice, which here is due to the Fermi-contact interaction. We see that, due to the Dirac delta function, the rate of transition is non-zero only if the total energy is conserved, i.e. $E_{M_I} + E_{\mathbf{k} m_s} = E_{M_I'} + E_{\mathbf{k}' m_s'}$. These transition coefficients refer to transitions from the nuclear spin state $|M_I\rangle$ to $|M_I'\rangle$ that are accompanied by a transition between particular lattice states. However the same nuclear spin transitions can also occur simultaneously with other lattice transitions. We are therefore interested in the overall transition coefficient $W_{M_I, M_I'}$ that describes the number of nuclear-spin transitions per unit time that occur, irrespective of the lattice-state transitions involved. This is computed by summing the $W_{M_I \mathbf{k} m_s, M_I' \mathbf{k}' m_s'}$ both over all occupied initial lattice states $|\mathbf{k} m_s\rangle$, and over all unoccupied final lattice states $|\mathbf{k}' m_s'\rangle$:

$$W_{M_I, M_I'} = \sum_{\mathbf{k} m_s \text{ occ.}} \sum_{\mathbf{k}' m_s' \text{ unocc.}} W_{M_I \mathbf{k} m_s, M_I' \mathbf{k}' m_s'} \quad (9.281)$$

$$= \sum_{\mathbf{k} m_s, \mathbf{k}' m_s'} W_{M_I \mathbf{k} m_s, M_I' \mathbf{k}' m_s'} f_{m_s}(\mathbf{k}) [1 - f_{m_s'}(\mathbf{k}')]. \quad (9.282)$$

The Fermi–Dirac function $f_{m_s}(\mathbf{k})$ can be interpreted as the probability that the state $|\mathbf{k}m_s\rangle$ is occupied, and so $[1 - f_{m_s}(\mathbf{k}')] is the corresponding probability that $|\mathbf{k}'m'_s\rangle$ is unoccupied. Therefore the inclusion of the factor $f_{m_s}(\mathbf{k})[1 - f_{m_s}(\mathbf{k}')] in the second line allows us to remove the restriction of only summing over occupied or unoccupied states.$$

The coupling between the nuclear spin system and the lattice is described by the Fermi-contact interaction Hamiltonian from Equation 2.191. Here we consider the coupling to a single electron, which gives us the following Hamiltonian \hat{H}_{I_s} :

$$\hat{H}_{I_s} = \frac{2}{3}\mu_0\mu_B g_e \hbar \gamma_I \delta(\mathbf{r}) \hat{\mathbf{I}} \cdot \hat{\mathbf{s}}, \quad (9.283)$$

where the nucleus is at $\mathbf{r} = \mathbf{0}$. The first step in the calculation of the transition coefficients is to evaluate the matrix element of \hat{H}_{I_s} in Equation 9.280 using the combined states $|M_I \mathbf{k} m_s\rangle = |M_I\rangle |\phi_{\mathbf{k}}(\mathbf{r})\rangle |m_s\rangle$:

$$\langle M_I \mathbf{k} m_s | \hat{H}_{I_s} | M_I' \mathbf{k}' m'_s \rangle = \frac{2}{3}\mu_0\mu_B g_e \hbar \gamma_I \phi_{\mathbf{k}}(\mathbf{0})^* \phi_{\mathbf{k}'}(\mathbf{0}) \langle M_I | \hat{\mathbf{I}} | M_I' \rangle \cdot \langle m_s | \hat{\mathbf{s}} | m'_s \rangle. \quad (9.284)$$

Inserting this into the expression for the transition coefficient in the combined spin–lattice system, we obtain

$$W_{M_I \mathbf{k} m_s, M_I' \mathbf{k}' m'_s} = \frac{2\pi}{\hbar} \frac{4}{9} \mu_0^2 \mu_B^2 g_e^2 \hbar^2 \gamma_I^2 |\phi_{\mathbf{k}}(\mathbf{0})|^2 |\phi_{\mathbf{k}'}(\mathbf{0})|^2 \delta(E_{M_I} + E_{\mathbf{k}m_s} - E_{M_I'} - E_{\mathbf{k}'m'_s}) \\ \times \sum_{i,j} \langle M_I | \hat{I}_i | M_I' \rangle \langle M_I' | \hat{I}_j | M_I \rangle \langle m_s | \hat{s}_i | m'_s \rangle \langle m'_s | \hat{s}_j | m_s \rangle. \quad (9.285)$$

We see that the rate of the transition is proportional to the electronic spin density at the nucleus in both the initial and final states.

We obtain the total transition coefficient for each pair of nuclear spin states by combining Equations 9.282 and 9.285. Recalling that the sums over \mathbf{k} and \mathbf{k}' can be replaced by integrals according to Equation 2.30, we

obtain the double integral:

$$\begin{aligned}
W_{M_I, M_I'} &= V^2 \sum_{m_s, m_s'} \iint \langle W_{M_I \mathbf{k} m_s, M_I' \mathbf{k}' m_s'} \rangle_{E_{\mathbf{k}}, E_{\mathbf{k}'}} f_{m_s}(E_{\mathbf{k}}) [1 - f_{m_s'}(E_{\mathbf{k}'})] g_{m_s}(E_{\mathbf{k}}) g_{m_s'}(E_{\mathbf{k}'}) dE_{\mathbf{k}} dE_{\mathbf{k}'} \quad (9.286) \\
&= \frac{2\pi}{\hbar} \frac{4}{9} \mu_0^2 \mu_B^2 g_e^2 \hbar^2 \gamma_I^2 V^2 \sum_{i,j} \langle M_I | \hat{I}_i | M_I' \rangle \langle M_I' | \hat{I}_j | M_I \rangle \sum_{m_s, m_s'} \langle m_s | \hat{s}_i | m_s' \rangle \langle m_s' | \hat{s}_j | m_s \rangle \\
&\quad \times \iint \langle |\phi_{\mathbf{k}}(\mathbf{0})|^2 \rangle_{E_{\mathbf{k}}} \langle |\phi_{\mathbf{k}'}(\mathbf{0})|^2 \rangle_{E_{\mathbf{k}'}} f_{m_s}(E_{\mathbf{k}}) [1 - f_{m_s'}(E_{\mathbf{k}'})] g_{m_s}(E_{\mathbf{k}}) g_{m_s'}(E_{\mathbf{k}'}) \\
&\quad \times \delta(E_{M_I} + E_{\mathbf{k} m_s} - E_{M_I'} - E_{\mathbf{k}' m_s'}) dE_{\mathbf{k}} dE_{\mathbf{k}'}, \quad (9.287)
\end{aligned}$$

where we have used the density of states for electrons in a particular spin state $g_{m_s}(E_{\mathbf{k}})$, and V is the volume of the metal. The first integral over the energy $E_{\mathbf{k}'}$ is easy to compute due to the Dirac delta function. The result is

$$\begin{aligned}
W_{M_I, M_I'} &= \frac{2\pi}{\hbar} \frac{4}{9} \mu_0^2 \mu_B^2 g_e^2 \hbar^2 \gamma_I^2 V^2 \sum_{i,j} \langle M_I | \hat{I}_i | M_I' \rangle \langle M_I' | \hat{I}_j | M_I \rangle \sum_{m_s, m_s'} \langle m_s | \hat{s}_i | m_s' \rangle \langle m_s' | \hat{s}_j | m_s \rangle \\
&\quad \times \int \langle |\phi_{\mathbf{k}}(\mathbf{0})|^2 \rangle_{E_{\mathbf{k}}} \langle |\phi_{\mathbf{k}'}(\mathbf{0})|^2 \rangle_{E_{\mathbf{k}'}} f(E_{\mathbf{k} m_s}) [1 - f(E_{\mathbf{k}' m_s'})] g_{m_s}(E_{\mathbf{k}}) g_{m_s'}(E_{\mathbf{k}'}) dE_{\mathbf{k}}, \quad (9.288)
\end{aligned}$$

where we have replaced $f_{m_s}(E_{\mathbf{k}})$ with $f(E_{\mathbf{k} m_s})$, and $E_{\mathbf{k}'}$ is equal to

$$E_{\mathbf{k}'} = E_{\mathbf{k}} + E_{m_s} - E_{m_s'} + E_{M_I} - E_{M_I'}. \quad (9.289)$$

To make further progress we now make some simplifications. In the expression relating the energies of the two k -states in Equation 9.289, we neglect the electronic and nuclear transition energies $E_{m_s'} - E_{m_s}$ and $E_{M_I'} - E_{M_I}$, and set $E_{\mathbf{k}'} = E_{\mathbf{k}} \equiv E$. This statement amounts to saying that $W_{mn} = W_{nm}$, which we recall results in zero nuclear polarization, which is unphysical. However we are able to neglect the difference between W_{mn} and W_{nm} here as this effect has already been included in Equation 9.278 [245]. Therefore a better interpretation of this statement is that it amounts to assuming low nuclear polarization. Hence this theory of relaxation implicitly contains a high-temperature approximation. This further allows us to replace the density of states for a particular spin state $g_{m_s}(E)$ with $g(E)/2$, where $g(E)$ is the total density of states.

This gives us

$$W_{M_I, M'_I} = \frac{2\pi}{\hbar} \frac{1}{9} \mu_0^2 \mu_B^2 g_e^2 \hbar^2 \gamma_I^2 V^2 \sum_{i,j} \langle M_I | \hat{I}_i | M'_I \rangle \langle M'_I | \hat{I}_j | M_I \rangle \sum_{m_s, m'_s} \langle m_s | \hat{S}_i | m'_s \rangle \langle m'_s | \hat{S}_j | m_s \rangle \times \int_0^\infty \langle |\phi_{\mathbf{k}}(\mathbf{0})|^2 \rangle_E^2 f(E) [1 - f(E)] g(E)^2 dE. \quad (9.290)$$

The integral is evaluated by noting that the factor containing the Fermi–Dirac functions $f(E) [1 - f(E)]$ is proportional to a Dirac delta function:

$$f(E) [1 - f(E)] = -kT f'(E) \quad (9.291)$$

$$= kT \delta(E - E_F), \quad (9.292)$$

from which we obtain

$$\int_0^\infty \langle |\phi_{\mathbf{k}}(\mathbf{0})|^2 \rangle_E^2 f(E) [1 - f(E)] g(E)^2 dE = \langle |\phi_{\mathbf{k}}(\mathbf{0})|^2 \rangle_{E_F}^2 g(E_F)^2 kT. \quad (9.293)$$

We see that the integral is proportional to the square of the one-electron spin density $\langle |\phi_{\mathbf{k}}(\mathbf{0})|^2 \rangle_{E_F}$ at the Fermi level that is present at the nucleus, the square of the density of states at the Fermi level, and the temperature.

The sum over the product of the electronic spin matrix elements is simply

$$\sum_{m_s, m'_s} \langle m_s | \hat{S}_i | m'_s \rangle \langle m'_s | \hat{S}_j | m_s \rangle = \text{Tr}_s (\hat{S}_i \hat{S}_j) \quad (9.294)$$

$$= \frac{1}{2} \delta_{ij}. \quad (9.295)$$

The final expression for the transition coefficients is therefore:

$$W_{M_I, M'_I} = \frac{\pi}{9} \mu_0^2 \mu_B^2 g_e^2 \hbar^2 \gamma_I^2 V^2 \langle |\phi_{\mathbf{k}}(\mathbf{0})|^2 \rangle_{E_F}^2 g(E_F)^2 kT \sum_i \langle M_I | \hat{I}_i | M'_I \rangle \langle M'_I | \hat{I}_i | M_I \rangle. \quad (9.296)$$

The transition coefficient is proportional to the square of the average single-electron spin density at the Fermi level $\langle |\phi_{\mathbf{k}}(\mathbf{0})|^2 \rangle_{E_F}$, and to the square of the density of states at the Fermi level $g(E_F)$. This means that the rate of nuclear-spin transitions is dominated by the conduction electrons at the Fermi level. As the temperature

increases the number of electrons that are promoted into excited states increases. Since these electrons are all in the vicinity of the Fermi level this means that we can expect the rate of nuclear transitions mediated by the Fermi-contact interaction with these electrons to also increase. This is observed by the proportionality of W_{M_I, M'_I} to T .

It now remains to compute the longitudinal PRE, which is done by inserting Equation 9.296 into Equation 9.279 to obtain

$$\frac{1}{T_1} = \frac{\pi}{18} \mu_0^2 \mu_B^2 g_e^2 \hbar \gamma_I^2 V^2 \langle |\phi_{\mathbf{k}}(\mathbf{0})|^2 \rangle_{E_F} g(E_F)^2 kT \frac{\sum_i \sum_{M_I, M'_I} \langle M_I | \hat{I}_i | M'_I \rangle \langle M'_I | \hat{I}_i | M_I \rangle (E_{M_I} - E_{M'_I})^2}{\sum_{M_I} E_{M_I}^2} \quad (9.297)$$

$$= - \frac{\pi}{18} \mu_0^2 \mu_B^2 g_e^2 \hbar \gamma_I^2 V^2 \langle |\phi_{\mathbf{k}}(\mathbf{0})|^2 \rangle_{E_F} g(E_F)^2 kT \frac{\sum_i \text{Tr}_I \left([\hat{H}_{IZ}, \hat{I}_i]^2 \right)}{\text{Tr}_I \left(\hat{H}_{IZ}^2 \right)}, \quad (9.298)$$

where to go to the second line we have invoked the high-field approximation and assumed that the nuclear spin Hamiltonian is dominated by the Zeeman Hamiltonian $\hat{H}_{IZ} = -\hbar \gamma_I B_0 \hat{I}_z$. The numerator and denominator of the quotient are evaluated to be

$$\sum_i \text{Tr}_I \left([\hat{H}_{IZ}, \hat{I}_i]^2 \right) = -\hbar^2 \gamma_I^2 B_0^2 \text{Tr}_I \left(\hat{I}_x^2 + \hat{I}_y^2 \right), \quad (9.299)$$

$$\text{Tr}_I \left(\hat{H}_{IZ}^2 \right) = \hbar^2 \gamma_I^2 B_0^2 \text{Tr}_I \left(\hat{I}_z^2 \right), \quad (9.300)$$

and since the following identity applies for all nuclear spins I :

$$\text{Tr}_I \left(\hat{I}_x^2 \right) = \text{Tr}_I \left(\hat{I}_y^2 \right) = \text{Tr}_I \left(\hat{I}_z^2 \right), \quad (9.301)$$

we calculate the quotient to be -2 . The final expression for the longitudinal PRE is therefore

$$\frac{1}{T_1} = \frac{\pi}{9} \mu_0^2 \mu_B^2 g_e^2 \hbar \gamma_I^2 V^2 \langle |\phi_{\mathbf{k}}(\mathbf{0})|^2 \rangle_{E_F} g(E_F)^2 kT. \quad (9.302)$$

As we have already commented for the transition coefficient W_{M_I, M'_I} , we see that the PRE increases with the square of the total electron spin density at the nucleus $\langle |\phi_{\mathbf{k}}(\mathbf{0})|^2 \rangle_{E_F} g(E_F)$, which is dominated by the electrons close in energy to the Fermi level, and with the temperature.

9.9.4 The Korringa relation

There is an important relationship between the longitudinal PRE in Equation 9.302 and the Knight shift in Equation 7.165, which is known as the Korringa relation [183, 245, 310]. Specifically the two expressions can be combined to give a quantity $T_1 K^2$ that is equal to

$$T_1 K^2 = \left(\frac{\chi_P}{g(E_F)} \right)^2 \frac{4}{\pi k T} \frac{1}{\mu_0^2 \mu_B^2 g_e^2 \hbar \gamma_I^2}. \quad (9.303)$$

We see that this quantity depends only on the magnetic susceptibility, the density of states at the Fermi level, and the temperature. In the special case of non-interacting electrons the magnetic susceptibility is given by the Pauli expression in Equation 7.178, and the Korringa relation becomes [310]:

$$T_1 K^2 = \frac{\hbar}{4\pi k T} \left(\frac{\gamma_S}{\gamma_I} \right)^2, \quad (9.304)$$

where $T_1 K^2$ depends only on the temperature, and the ratio of the electronic and nuclear gyromagnetic ratios. In principle it should be possible to use the Korringa relation to calculate T_1 relaxation times from Knight shifts. However care should be taken in the application of the Korringa relation, since it has been shown that, for simple metals, the experimental T_1 values are greater than the values predicted. This is because of the neglect of effects such as electron–electron interactions, and other relaxation mechanisms.

9.9.5 Comparison of the longitudinal PRE in solid insulators and metals

An initial comparison of the longitudinal PRE in a metal in Equation 9.302 with the corresponding expression for a solid insulator from the Solomon–Bloembergen–Morgan theory in Equation 8.185 appears to indicate that there is little similarity between the two expressions. The most obvious difference is that in a metal the dominant source of relaxation is a Bloembergen-type mechanism due to the Fermi-contact interaction, whereas we have shown that in an insulator the Bloembergen contribution is negligible compared to the Solomon contribution. However on closer examination there is greater similarity than one would expect.

Here we compare the longitudinal PRE in a metal to the Bloembergen expression in a solid insulator. In order to facilitate the discussion we take the expression for the metal in Equation 9.302, and assume the free-electron model. The density of states at the Fermi level then takes the simple expression $g(E_F) =$

$3N/(2VE_F)$, where N is the number of electrons, and we obtain:

$$\frac{1}{T_1^{\text{metal}}} = \frac{\pi}{4} (\mu_0 \mu_B g_e \gamma_I)^2 \left(N \langle |\phi_{\mathbf{k}}(\mathbf{0})|^2 \rangle_{E_F} \right)^2 \left(\frac{\hbar}{E_F} \right) \left(\frac{kT}{E_F} \right). \quad (9.305)$$

We can rationalize this expression as follows. The factor $N \langle |\phi_{\mathbf{k}}(\mathbf{0})|^2 \rangle_{E_F}$ is the total electronic density at the nucleus due to the N electrons, which is computed from the average one-electron density due to the electrons at the Fermi surface. The factor \hbar/E_F can be interpreted as follows. The fluctuation local field exerted by the electronic spin on the nucleus has a correlation time which is the average duration for which the conduction electron remains localized at the nucleus. The order of magnitude of this correlation time is \hbar/E_F [183]. For typical values of the Fermi energy in simple metals $\hbar/E_F \ll |\omega_S - \omega_I|$, indicating that we are in the extreme narrowing limit. Finally the factor kT/E_F gives the fraction of electrons that participate in the relaxation process at finite temperature, with the remainder having no overall contribution due to the spin pairing.

For a solid insulator the longitudinal PRE due to the Bloembergen mechanism is give in Equation 8.185. If we assume that the paramagnetic centre has a single unpaired electron, so that $S = 1/2$, and also assume that we are in the extreme-narrowing limit we obtain the following expression:

$$\frac{1}{T_1^{\text{insul.}}} = \frac{2}{9} (\mu_0 \mu_B g_e \gamma_I)^2 \rho^{\alpha-\beta}(\mathbf{0})^2 T_{2e}. \quad (9.306)$$

This expression bears some similarity to Equation 9.305. The electron-spin density at the nucleus is now given by $\rho^{\alpha-\beta}(\mathbf{0})$ which, unlike in the metal, is a contribution from a single unpaired electron. This reflects the fact that in an insulator the Fermi-contact interaction is short-range, as the electrons are largely localised in the metal coordination site, rather than delocalised throughout the material as in a metal. In addition the PRE is proportional to the electron T_{2e} , which plays the role of the correlation time. However we should note that T_{2e} has a very different interpretation to the correlation time in the metal, as in the insulator the electrons are largely localised, and the electronic relaxation is largely due to the vibrational motions.

9.10 Key concepts

- A general treatment of electronic and nuclear relaxation can be made using the stochastic Liouville–von Neumann equation.

- The resulting expressions for nuclear relaxation include the effects of electronic relaxation for spins $S > 1$ that is outside the Redfield limit, spin-orbit coupling effects on the electronic spin (g -anisotropy, and static ZFS), and low-field conditions.
- Under high-field conditions and for $S = 1$ we recover the Solomon–Bloembergen–Morgan equations (Equations 9.111 and 9.112). For higher electronic spins we recover the Solomon–Bloembergen–Morgan equations assuming a phenomenological treatment of electronic relaxation.
- Under conditions of low field and slow motions the PREs are given by Equations 9.129 and 9.130 for arbitrary electronic spin, and Equations 9.166 and 9.167 for $S = 1$.
- Metal ions in solution that coordinate to the solvent molecules have a complicated relaxation process that can be separated into inner- and outer-sphere mechanisms (Equation 9.178). The expressions for the inner-sphere relaxation rates at high field determined by Redfield theory are given in Equations 9.188 and 9.189. For inner-sphere relaxation at high field the expressions for $S = 1$ reduce to the Solomon–Bloembergen–Morgan equations. The expressions for the outer-sphere relaxation rates are given in Equations 9.209 and 9.210 at high field, and Equations 9.218 and 9.219 at low field.
- Vibrational motions are an important source of electronic relaxation both in solution and in solid insulators. The PRE expressions at high field are the Solomon–Bloembergen–Morgan equations.
- In a metal the PRE is mainly due to the Fermi-contact interaction with the delocalised electrons, and so shares some similarities with the Bloembergen mechanism in solid insulators. The longitudinal PRE is given in Equation 9.302.

Chapter 10

Inhomogeneous broadening due to the bulk paramagnetic susceptibility

The description of the paramagnetic shielding tensor has so far focussed on the *local* effects of the paramagnetic metal centres on the observed nuclear spin. However in certain cases we must also consider the *bulk* magnetic properties of the system, which can affect the measured values of the shift and the inhomogeneous linewidth in the spectrum. Such effects can be present in solution, single crystals, and solid powders. The important points to consider are the shape of the crystal containing the nucleus in solid samples, any neighbouring crystallites, and the shape of the sample container. These bulk properties are collectively known as bulk magnetic susceptibility (BMS) effects as they depend on the susceptibility tensor of the entire sample. The BMS has been shown to influence both the measured paramagnetic shift and shift anisotropy, and the line shape and linewidth [153, 154]. The treatment of the BMS effects in this chapter is based on the theory of classical electrodynamics, on which further information can be found in standard textbooks such as the one by Jackson [186]. Here we focus on paramagnetic solids, considering first single crystals, and then microcrystalline powders.

10.1 The BMS shift in a single crystal

10.1.1 The demagnetising field in a single crystal

In section 2.2 we introduced the concept that a magnetic field can be described either in terms of the H -field $\mathbf{H}(\mathbf{r})$ or the B -field $\mathbf{B}(\mathbf{r})$, which are related by Equation 2.9, which is repeated below for convenience:

$$\mathbf{B}(\mathbf{r}) = \mu_0(\mathbf{H}(\mathbf{r}) + \mathbf{M}(\mathbf{r})), \quad (10.1)$$

where we have explicitly written in the dependence on position of both fields and the magnetization. The H -field $\mathbf{H}(\mathbf{r})$ is equal to the sum of the applied H -field \mathbf{H}_0 and a demagnetising H -field $\mathbf{H}_D(\mathbf{r})$, which is produced by the combined effect of all the magnetic moments in the solid crystal. The magnetic B -field $\mathbf{B}(\mathbf{r})$ is therefore given by

$$\mathbf{B}(\mathbf{r}) = \mu_0(\mathbf{H}_0 + \mathbf{H}_D(\mathbf{r}) + \mathbf{M}(\mathbf{r})) \quad (10.2)$$

$$= \mathbf{B}_0 + \mathbf{B}_D(\mathbf{r}), \quad (10.3)$$

where $\mathbf{B}_0 = \mu_0\mathbf{H}_0$ is the applied B -field, and $\mathbf{B}_D(\mathbf{r}) = \mu_0(\mathbf{H}_D(\mathbf{r}) + \mathbf{M}(\mathbf{r}))$ is the demagnetising B -field. So far this description is valid for any magnetic solid. Restricting the discussion to paramagnetic solids, the bulk magnetization *inside* the crystallite M_c is due to the applied field \mathbf{H}_0 , and can be written as

$$\mathbf{M}_c = \chi_V \cdot \mathbf{H}_0, \quad (10.4)$$

where χ_V is the bulk magnetic susceptibility tensor per unit volume, which in general is anisotropic. By contrast the magnetization outside the crystallite $\mathbf{M}(\mathbf{r})$ is zero.

For an object of micrometre dimensions or larger, the demagnetising fields can be calculated from classical magnetostatics, where we model the crystallite as a uniformly-magnetized object occupying a spatial volume V that is bounded by a surface S . The demagnetising H -field $\mathbf{H}_D(\mathbf{r})$ is then given by the vector gradient of a scalar potential $\Phi_D(\mathbf{r})$ [186]

$$\mathbf{H}_D(\mathbf{r}) = -\nabla\Phi_D(\mathbf{r}), \quad (10.5)$$

where we have acknowledged that both the field and scalar potential vary with position \mathbf{r} , the origin of which is the centre of mass of the crystallite. Note that the nucleus can be located either inside this crystallite, or outside in a second crystallite. The scalar potential is given by the following integral expression:

$$\Phi_D(\mathbf{r}) = -\frac{1}{4\pi} \iiint_V \frac{\nabla' \cdot \mathbf{M}(\mathbf{r}')}{|\mathbf{r} - \mathbf{r}'|} dV' + \frac{1}{4\pi} \iint_S \frac{\mathbf{n}' \cdot \mathbf{M}(\mathbf{r}')}{|\mathbf{r} - \mathbf{r}'|} da', \quad (10.6)$$

where \mathbf{r}' is the vector giving the position of the paramagnetic centre, \mathbf{r} is the position of the nucleus, \mathbf{n}' is the unit vector normal to the surface pointing outwards, and da' is an infinitesimal area located on the surface S . The first integral is over the volume of the crystallite, and the second integral is taken over the bounding surface of the crystallite. Both integrals are evaluated with respect to the primed coordinates. In the paramagnetic regime we assume that within the crystallite $\mathbf{M}(\mathbf{r}) = \mathbf{M}_c$ and is uniform throughout V , and hence both $\nabla' \cdot \mathbf{M}(\mathbf{r}')$ and the volume integral are equal to zero, which leaves us with

$$\Phi_D(\mathbf{r}) = \frac{1}{4\pi} \iint_S \frac{\mathbf{n}' \cdot \mathbf{M}_c}{|\mathbf{r} - \mathbf{r}'|} da'. \quad (10.7)$$

From Equations 10.4, 10.5, and 10.7 the magnetic field \mathbf{H}_D takes the following form [151]:

$$\mathbf{H}_D(\mathbf{r}) = -\mathbf{N}(\mathbf{r}) \cdot \chi_V \cdot \mathbf{H}_0, \quad (10.8)$$

where $\mathbf{N}(\mathbf{r})$ is the demagnetising tensor, which has the following components $N_{ij}(\mathbf{r})$:

$$N_{ij}(\mathbf{r}) = \frac{1}{4\pi} \frac{\partial}{\partial r_i} \iint_S \frac{n'_j}{|\mathbf{r} - \mathbf{r}'|} da' \quad (10.9)$$

$$= -\frac{1}{4\pi} \iint_S \frac{r_i - r'_i}{|\mathbf{r} - \mathbf{r}'|^3} n'_j da'. \quad (10.10)$$

The demagnetising H -field is therefore a matrix product of three parts, each of which is due to a different physical property of either the system or the experimental conditions. The demagnetising field has a magnitude proportional to \mathbf{H}_0 , but with a reduced size, and has a different direction due to the demagnetising and volume susceptibility tensors. The latter tensor χ_V encodes the influence of the (generally anisotropic) magnetic moments of the paramagnetic ions in the crystallite, in the same way as the single-ion susceptibility influences the local paramagnetic shielding tensor as shown in section 4, via the g - and ZFS tensors. The

demagnetising tensor $\mathbf{N}(\mathbf{r})$ contains all the information about the shape of the crystallite via the surface integral. We therefore expect it to be anisotropic for crystallites that deviate from spherical symmetry. This is also the only contribution to $\mathbf{H}_D(\mathbf{r})$ that is position dependent. The trace of the demagnetising tensor can be calculated to be

$$\text{Tr}(\mathbf{N}(\mathbf{r})) = -\frac{1}{4\pi} \iint_S \frac{(\mathbf{r} - \mathbf{r}') \cdot \mathbf{n}'}{|\mathbf{r} - \mathbf{r}'|^3} d\alpha' \quad (10.11)$$

$$= -\frac{1}{4\pi} \iiint_V \nabla' \cdot \left\{ \frac{(\mathbf{r} - \mathbf{r}')}{|\mathbf{r} - \mathbf{r}'|^3} \right\} dV' \quad (10.12)$$

$$= \iiint_V \delta(\mathbf{r}' - \mathbf{r}) dV' \quad (10.13)$$

$$= \begin{cases} 1, & \text{if } \mathbf{r} \text{ is inside the crystallite,} \\ 0, & \text{if } \mathbf{r} \text{ is outside the crystallite,} \end{cases} \quad (10.14)$$

where to go to the second line we have used the divergence theorem for the integrals of vector fields [189]. Figure 10.1 gives three examples of demagnetising tensors for crystals of different shapes that can be used for calculating the *internal* demagnetising field. We see that for each tensor the trace is equal to unity. In all three examples the form of $\mathbf{N}(\mathbf{r})$ matches the symmetry of the crystal shape. With the axis system shown this results in all three matrices being diagonal, and so these axes give the PAF of the tensor. If instead we take an axis system that is fixed to the laboratory frame of reference the tensor $\mathbf{N}(\mathbf{r})$ is of course not diagonal. We note that in any direction i where the crystal dimension extend to infinity there is no bounding surface, and so $N_{ii} = 0$.

Once we have calculated $\mathbf{H}_D(\mathbf{r})$ we can calculate the demagnetising B -field from

$$\mathbf{B}_D(\mathbf{r}) = \mu_0(\mathbf{H}_D + \mathbf{M}(\mathbf{r})) \quad (10.15)$$

$$= -\mu_0 \mathbf{N}(\mathbf{r}) \cdot \chi_V \cdot \mathbf{H}_0 + \mu_0 \mathbf{M}(\mathbf{r}) \quad (10.16)$$

$$= -\mathbf{N}(\mathbf{r}) \cdot \chi_V \cdot \mathbf{B}_0 + \mu_0 \mathbf{M}(\mathbf{r}), \quad (10.17)$$

where $\mathbf{M}(\mathbf{r})$ is equal to $\chi_V \cdot \mathbf{H}_0 = \chi_V \cdot \mathbf{B}_0 / \mu_0$ inside the crystallite, and zero outside the crystallite.

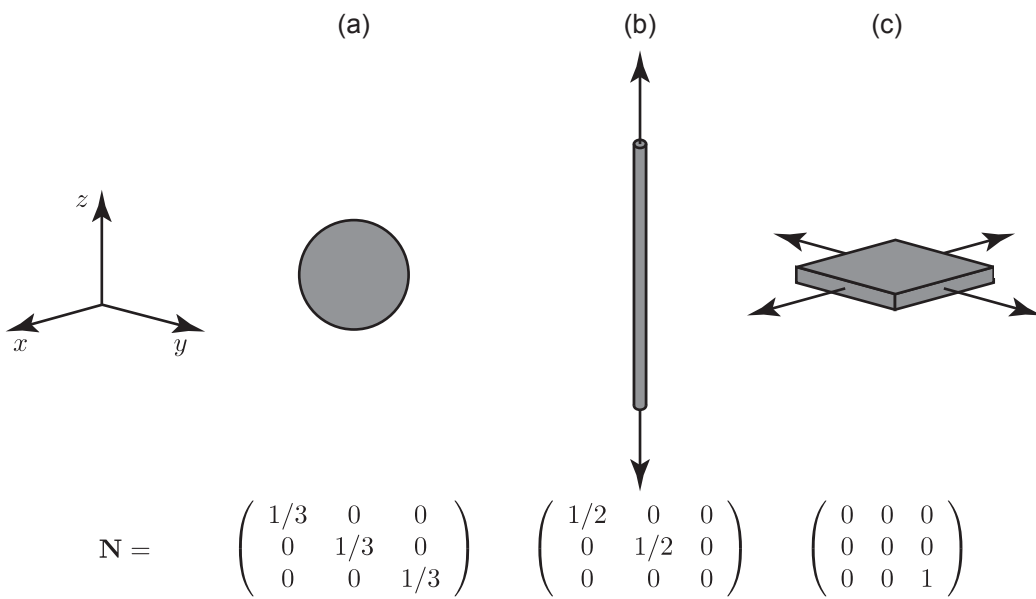


Figure 10.1: The demagnetising tensors of three uniformly-magnetized crystals of different three-dimensional shapes that give the demagnetising field at any point *within* each crystal. The crystal shapes are (a) a sphere, (b) an infinitely-long cylindrical rod, and (c) a plane extending to infinity in two dimensions. The arrows in (b) and (c) indicate the directions in which the crystals extend to infinity. The axis system is shown to the left.

Alternatively we can calculate $B_D(\mathbf{r})$ directly from the vector potential $A_D(\mathbf{r})$ from the relation

$$B_D(\mathbf{r}) = \nabla \times A_D(\mathbf{r}), \quad (10.18)$$

where the vector potential is given by

$$A_D(\mathbf{r}) = \frac{\mu_0}{4\pi} \iiint_V \frac{\nabla' \times M(\mathbf{r}')}{|\mathbf{r} - \mathbf{r}'|} dV' + \frac{\mu_0}{4\pi} \iint_S \frac{M(\mathbf{r}') \times \mathbf{n}'}{|\mathbf{r} - \mathbf{r}'|} da'. \quad (10.19)$$

If we, once again, assume that $M(\mathbf{r})$ is independent of position within the crystallite the volume integral is equal to zero and the vector potential reduces to

$$A_D(\mathbf{r}) = \frac{\mu_0}{4\pi} \iint_S \frac{M_c \times \mathbf{n}'}{|\mathbf{r} - \mathbf{r}'|} da'. \quad (10.20)$$

The calculation of $B_D(\mathbf{r})$ directly from the vector potential gives the same result as the calculation starting from the scalar potential via $H_D(\mathbf{r})$. The former method was used by Kubo et al [151], whereas the latter is the approach of Dickinson et al [152].

The demagnetising B -field can be thought of as inducing a chemical shielding at the nuclear spin. This BMS chemical shielding σ^{BMS} can be calculated by equating the two forms of the nuclear Zeeman interaction:

$$-\hbar\gamma_I B(\mathbf{r}) \cdot \hat{I} = -\hbar\gamma_I B_0 \cdot (\mathbf{1} - \sigma^{\text{BMS}}(\mathbf{r})) \cdot \hat{I} \quad (10.21)$$

$$[B_0 + B_D(\mathbf{r})] \cdot \mathbf{1} = B_0 \cdot (\mathbf{1} - \sigma^{\text{BMS}}(\mathbf{r})), \quad (10.22)$$

which gives

$$B_D(\mathbf{r}) \cdot \mathbf{1} = -B_0 \cdot \sigma^{\text{BMS}}(\mathbf{r}). \quad (10.23)$$

The final expression for the BMS shielding tensor is therefore

$$\sigma^{\text{BMS}}(\mathbf{r}) = \begin{cases} \chi_V \cdot (N(\mathbf{r})^T - \mathbf{1}), & \text{inside the crystallite,} \\ \chi_V \cdot N(\mathbf{r})^T, & \text{outside the crystallite.} \end{cases} \quad (10.24)$$

Both the isotropic and anisotropic parts of the BMS shielding tensor depend on the nature of the paramagnetic

centres via the bulk susceptibility tensor, and the crystallite shape via the demagnetizing tensor.

10.1.2 The BMS shift of a spherical crystallite

We now consider the simple case of a spherical crystallite with radius a_c . The scalar potential is given by Equation 10.7 following a conversion to spherical polar coordinates $\mathbf{r} \rightarrow (r, \theta, \phi)$ and $\mathbf{r}' \rightarrow (r', \theta', \phi')$:

$$\Phi_D(\mathbf{r}) = \frac{a_c^2}{4\pi} \int_0^{2\pi} d\phi' \int_0^\pi d\theta' \sin \theta' \frac{M_{c,x} \sin \theta' \cos \phi' + M_{c,y} \sin \theta' \sin \phi' + M_{c,z} \cos \theta'}{|\mathbf{r} - \mathbf{r}'|}. \quad (10.25)$$

The integrals can be computed by using the following identity for $|\mathbf{r} - \mathbf{r}'|^{-1}$ [186]:

$$\frac{1}{|\mathbf{r} - \mathbf{r}'|} = 4\pi \sum_{l=0}^{\infty} \sum_{m=-l}^{+l} \frac{1}{2l+1} \frac{r_{<}^l}{r_{>}^{l+1}} Y_{lm}(\theta', \phi')^* Y_{lm}(\theta, \phi), \quad (10.26)$$

where the $Y_{lm}(\theta, \phi)$ are spherical harmonic functions of rank l and order m . The distance $r_{<}$ is equal to the smaller of r and r' , and likewise $r_{>}$ to the larger of the two. Of the terms in Equation 10.26, only those with $l = 1$ give a non-zero contribution to the integral, and so the scalar potential has the simple expression

$$\Phi_D(\mathbf{r}) = \frac{1}{3} a_c^2 \left(\frac{r_{<}}{r_{>}^2} \right) \left(\frac{\mathbf{M}_c \cdot \mathbf{r}}{r} \right). \quad (10.27)$$

If the observed nuclear spin is located inside the crystallite the scalar potential becomes $\Phi_D^{\text{in}}(\mathbf{r})$, which is

$$\Phi_D^{\text{in}}(\mathbf{r}) = \frac{1}{3} \mathbf{M}_c \cdot \mathbf{r}, \quad (10.28)$$

and the corresponding demagnetising H -field \mathbf{H}_D^{in} is

$$\mathbf{H}_D^{\text{in}} = -\frac{1}{3} \mathbf{M}_c \quad (10.29)$$

$$= -\frac{1}{3} \chi_V \cdot \mathbf{H}_0. \quad (10.30)$$

Comparing this with Equation 10.8 we see that the demagnetising tensor $\mathbf{N}(\mathbf{r})$ is equal to

$$\mathbf{N}(\mathbf{r}) = \frac{1}{3} \mathbf{1}, \quad (10.31)$$

which is isotropic, as expected for a spherical crystallite. The BMS shielding of the nucleus inside the crystallite is now easily calculated from Equation 10.24, giving

$$\sigma^{\text{BMS}} = -\frac{2}{3}\chi_V, \quad \text{inside the crystallite.} \quad (10.32)$$

If the observed nuclear spin is outside the crystallite in question the scalar potential $\Phi_{\text{D}}^{\text{out}}(\mathbf{r})$ is:

$$\Phi_{\text{D}}^{\text{out}}(\mathbf{r}) = a_c^3 \frac{\mathbf{M}_c \cdot \mathbf{r}}{3r^3} \quad (10.33)$$

$$= V_c \frac{\mathbf{M}_c \cdot \mathbf{r}}{4\pi r^3} \quad (10.34)$$

$$= \frac{\mathbf{m}_c \cdot \mathbf{r}}{4\pi r^3}, \quad (10.35)$$

where $V_c = 4\pi a_c^3/3$ is the volume of the crystallite, and $\mathbf{m}_c = V_c \mathbf{M}_c$ is its total magnetic moment. The demagnetising field $\mathbf{H}_{\text{D}}^{\text{out}}$ evaluates to

$$\mathbf{H}_{\text{D}}^{\text{out}} = \frac{1}{4\pi} \left[\frac{3\mathbf{r}(\mathbf{m}_c \cdot \mathbf{r})}{r^5} - \frac{\mathbf{m}_c}{r^3} \right], \quad (10.36)$$

which we immediately recognise as the field exerted by a point dipole moment \mathbf{m}_c at position \mathbf{r} . We therefore obtain the result that a nucleus outside the crystallite experiences a dipolar coupling interaction with the crystallite, and that the crystallite can be modelled as a point dipole with a magnetic moment equal to the bulk value \mathbf{m}_c . The demagnetising tensor has the components

$$N_{ij}(\mathbf{r}) = -V_c C_{ij}^{\text{dip}}(\mathbf{r}), \quad (10.37)$$

where C^{dip} is the reduced point-dipolar coupling tensor:

$$C_{ij}^{\text{dip}}(\mathbf{r}) = \frac{3r_i r_j - r^2 \delta_{ij}}{4\pi r^5}. \quad (10.38)$$

Equation 10.24 gives the corresponding BMS shielding tensor:

$$\sigma^{\text{BMS}}(\mathbf{r}) = -V_c \chi_V \cdot C^{\text{dip}}(\mathbf{r}), \quad \text{outside the crystallite,} \quad (10.39)$$

Location	Type	Term	σ^{BMS}	
			Expression	Rank
inside	IBMS	1	$-\frac{2}{3}\chi_V^{\text{iso}}$	0
	ABMS	2	$-\frac{2}{3}\chi_V^{\text{an}}$	2
outside	IBMS	3	$-V_c\chi_V^{\text{iso}}\mathbf{C}^{\text{dip}}(\mathbf{r})$	2
	ABMS	4	$-V_c\chi_V^{\text{an}}\cdot\mathbf{C}^{\text{dip}}(\mathbf{r})$	0, 1, 2

Table 10.1: Terms contributing to the BMS paramagnetic shielding tensor of a nucleus due to a single spherical crystallite. The individual contributions 1–4 are separated according to whether they act on a nucleus that is either inside or outside the crystallite in question, and whether they are due to the isotropic (IBMS) or anisotropic (ABMS) part of the volume susceptibility tensor of the crystallite.

which is an analogous expression to that obtained for the spin-dipolar contribution to the local paramagnetic shielding tensor in terms of the single-paramagnetic-centre susceptibility tensor in Equation 4.182.

10.1.3 The IBMS and ABMS contributions to the paramagnetic shielding tensor

The contributions to the BMS shielding tensor of a nucleus both inside and outside a given crystallite can be separated into two groups: those due to the isotropic volume susceptibility of the crystallite, and those due to the volume susceptibility anisotropy. The former contributions give rise to isotropic bulk magnetic susceptibility (IBMS) effects, whilst the latter are responsible for the anisotropic bulk magnetic susceptibility (ABMS) effects. Four terms can be clearly distinguished, which are listed in Table 10.1 for a spherical crystallite, along with their irreducible spherical tensor ranks.

If the observed nucleus is within the crystallite in question, the two contributions to the BMS shielding tensor are 1 and 2. Term 1 is the IBMS contribution, with a size that is proportional to the isotropic volume susceptibility χ_V^{iso} and simply changes the isotropic shift. Term 2, on the other hand, is the ABMS contribution which is purely anisotropic, with anisotropy parameters that are proportional to those of the anisotropic volume susceptibility χ_V^{an} . These IBMS and ABMS shielding parameters are

$$\sigma_{\text{iso}}^{\text{IBMS},1} = -\frac{2}{3}\chi_V^{\text{iso}}, \quad (10.40)$$

$$\Delta\sigma^{\text{ABMS},2} = -\frac{2}{3}\Delta\chi_V, \quad (10.41)$$

$$\eta^{\text{ABMS},2} = \eta^{\chi_V}, \quad (10.42)$$

where $\sigma_{\text{iso}}^{\text{IBMS},1}$, $\Delta\sigma^{\text{ABMS},2}$, and $\eta^{\text{ABMS},1}$ are the isotropic shielding, SA, and asymmetry parameter of the BMS shielding tensor, and χ_V^{iso} , $\Delta\chi_V$, and η^{χ_V} are the isotropic part, anisotropy, and asymmetry parameter of the

volume susceptibility. Both the IBMS and ABMS contributions depend only on the volume susceptibility, and so are independent of both the size of the crystallite, and the position of the nucleus within the crystallite. Terms 1 and 2 are the “bulk equivalents” of the local shielding terms in the susceptibility formalism, given in Table 5.1, that are the contact shift $-\chi^{\text{iso}}C^{\text{con}}$ and SA $-\Delta\chi C^{\text{con}}$.

For a nuclear spin outside the crystallite, the IBMS and ABMS contributions to the shielding tensor are terms 3 and 4, both of which depend on the dipolar coupling between the nucleus and the whole crystallite. Term 3 is purely anisotropic, with anisotropic shielding parameters that depend solely on the dipolar coupling tensor. The resulting anisotropy $\Delta\sigma^{\text{IBMS},3}$ and asymmetry $\eta^{\text{IBMS},3}$ are

$$\Delta\sigma^{\text{IBMS},3} = -\frac{V_c}{2\pi r^3}\chi_V^{\text{iso}}, \quad (10.43)$$

$$\eta^{\text{IBMS},3} = 0. \quad (10.44)$$

The ABMS term 4 is a matrix product between the anisotropic part of the volume susceptibility tensor and the dipolar coupling tensor, and so contains parts of irreducible spherical tensor ranks 0 (isotropic), 1 (anisotropic and antisymmetric), and 2 (anisotropic and symmetric). The isotropic part $\sigma_{\text{iso}}^{\text{ABMS},4}$ has the form of a PCS:

$$\sigma_{\text{iso}}^{\text{ABMS},4} = -\frac{V_c}{12\pi r^3} \left[\Delta\chi_{V,\text{ax}} (3 \cos^2(\theta) - 1) + \frac{3}{2} \Delta\chi_{V,\text{rh}} \sin^2(\theta) \cos(2\phi) \right], \quad (10.45)$$

where $\Delta\chi_{V,\text{ax}}$ and $\Delta\chi_{V,\text{rh}}$ are the axial and rhombic anisotropies of the volume susceptibility tensor, and θ and ϕ are the spherical polar angles which give the orientation of χ_V^{an} with respect to the vector r connecting the nucleus to the centre of the crystallite. In contrast to the situation where the nucleus is inside the crystallite, the BMS shielding tensor contributions of a nucleus outside the crystallite are proportional to the volume V_c . This is because the dipolar coupling constant is proportional to the bulk magnetic moment of the crystallite, which is itself proportional to its volume. Therefore, doubling the volume of the crystallite has the effect of doubling both the isotropic and anisotropic parts of the BMS shielding tensor. In addition the tensor parameters all vary with the distance between the nucleus and the centre of the crystallite as $1/r^3$. Terms 3 and 4 are the “bulk equivalents” of the local terms $-\chi^{\text{iso}}C^{\text{dip}}$ and $-\Delta\chi \cdot C^{\text{dip}}$ in Table 5.1, which are the spin-dipolar parts of the local paramagnetic shielding tensor.

If the crystallite is non-spherical the expressions in Table 10.1 no longer apply, and we must use Equation

10.24 in its most general form. In this case terms 1 and 2 both contain mixtures of parts of ranks 0, 1, and 2 as N has an anisotropic component. Term 3 still has no isotropic part as $\text{Tr}(N(\mathbf{r})) = 0$ outside the crystallite. Analytical and numerical calculations of the demagnetising fields have been made for a range of geometries, both in the fields of NMR in chemistry and MRI of living organisms. Notable examples of geometries that have been considered include cylinders [311, 312], parallelepipeds [313], triangular surfaces [314], and cones, ellipsoids, paraboloids, and hyperboloids [152].

If the nucleus is outside a non-spherical crystallite, the resulting demagnetising tensor no longer has the form of a simple dipolar coupling interaction to a point dipole \mathbf{m}_c . Nevertheless we can still interpret $N(\mathbf{r})$ as the spatial part of a coupling interaction that approximately resembles a point-dipolar coupling interaction for approximately spherical crystallites. If the nuclear spin is sufficiently far from the crystallite so that $r \gg r'$, we can approximate the interaction as a point-dipolar coupling. This can be seen by writing the scalar potential as

$$\Phi_D(\mathbf{r}) = \frac{1}{4\pi} \iiint_S \frac{\mathbf{n}' \cdot \mathbf{M}_c}{|\mathbf{r} - \mathbf{r}'|} d\mathbf{a}' \quad (10.46)$$

$$= \frac{1}{4\pi} \iiint_V \nabla' \cdot \left\{ \frac{\mathbf{M}_c}{|\mathbf{r} - \mathbf{r}'|} \right\} dV' \quad (10.47)$$

$$= \frac{1}{4\pi} \iiint_V \mathbf{M}_c \cdot \left\{ \frac{\mathbf{r} - \mathbf{r}'}{|\mathbf{r} - \mathbf{r}'|^3} \right\} dV', \quad (10.48)$$

where to the go the second line we have used the divergence theorem [189]. This result is so far general for a nuclear spin in any location. However if we now assume that $r \gg r'$, we can simplify the expression for the scalar potential as follows

$$\Phi_D(\mathbf{r}) = \frac{\mathbf{M}_c \cdot \mathbf{r}}{4\pi r^3} \iiint_V dV' \quad (10.49)$$

$$= \frac{\mathbf{M}_c \cdot \mathbf{r}}{4\pi r^3} V_c \quad (10.50)$$

$$= \frac{\mathbf{m}_c \cdot \mathbf{r}}{4\pi r^3}, \quad (10.51)$$

which gives the expression for the scalar potential of a point-dipolar coupling interaction in Equation 10.35 [186]. The demagnetising tensor is therefore the dipolar coupling tensor in Equation 10.37.

10.2 The BMS shift in a polycrystalline powder

10.2.1 The IBMS and ABMS contributions to the paramagnetic shielding

The treatment of the BMS effects of a single crystallite can now be extended to the case of polycrystalline solids, which represents a far larger number of studies in solid-state NMR. This case was originally considered by both VanderHart and Earl [147], and Alla and Lippmaa [148], for both diamagnetic and paramagnetic samples. The model we use is that of Kubo et al [151], which is itself a modification of the model of Schwerk et al [150], and is shown in Figure 10.2. As shown in Figure 10.2 (a) we assume that the observed nucleus I is inside crystallite c_0 , and possesses a local paramagnetic shielding tensor σ^S which is a sum of contributions from the nearby paramagnetic centres $S^{(A)}$. The form of this tensor is the subject of chapters 3–7. The nuclear spin is at the centre of an Ewald sphere [186], with dimensions that are much smaller than those of the crystallite, within which the sum of contributions from the paramagnetic centres A converges. It is then assumed that the remainder of the crystallite is a uniformly-magnetised continuum which contributes a BMS shielding tensor σ_0^{BMS} to the total shielding of I , which can be calculated using the methods described both in this section and in section 10.1. The sample itself contains a number of crystallites c_k that are assumed to occupy the sites of a close-packed lattice with occupancy p_k , which either takes between 0 or 1 if the site is unoccupied or occupied respectively. Each crystallite contributes a term σ_k^{BMS} to the total BMS shielding tensor of I . Once again it is assumed that the sum of these contributions converges with an Ewald sphere with dimensions that are smaller than those of the sample container (Figure 10.2 (b)). The remainder of the sample is assumed to be uniformly magnetised, as shown in Figure 10.2 (c).

The total paramagnetic shielding tensor σ of the nuclear spin I is equal to the sum of the local σ^S and BMS σ^{BMS} contributions:

$$\sigma = \sigma^S + \sigma^{\text{BMS}}, \quad (10.52)$$

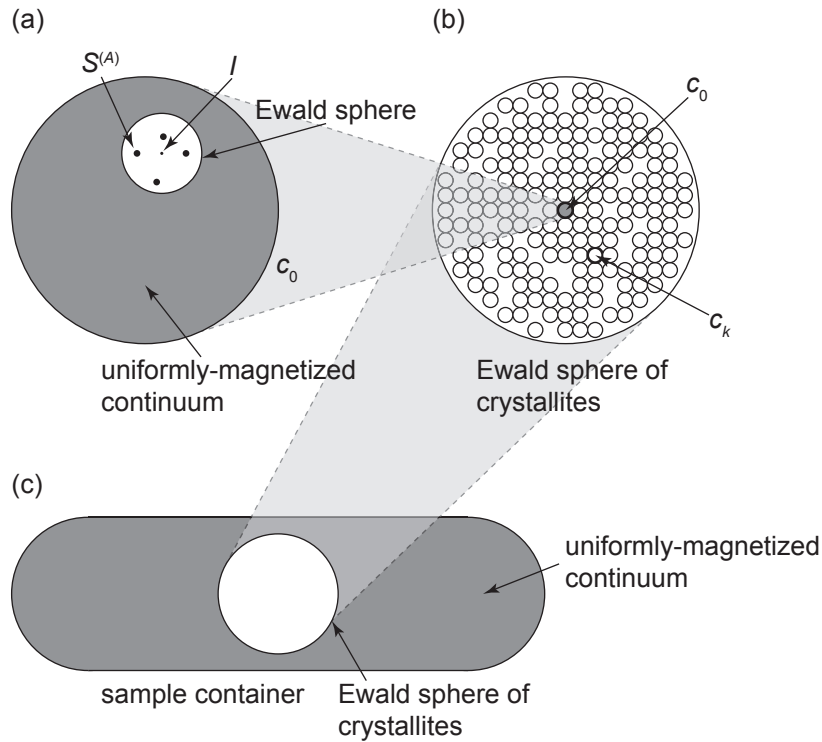


Figure 10.2: Illustration of the model of a polycrystalline sample. In (a) is shown a single crystallite c_0 that contains the nucleus I of interest. The nucleus experiences a local paramagnetic shielding σ^S that is due to the nearby paramagnetic metal ions $S^{(A)}$. The Ewald sphere is a sphere centred on the nucleus with a radius that is much smaller than the dimensions of the crystallite within which the sum of contributions to σ^S converges. The remainder of the crystallite is modelled as a uniformly-magnetized continuum (shown in grey) which contributes to the BMS shielding tensor σ_0^{BMS} of I . In (b) is shown a set of closely-packed crystallites c_k , with $k \neq 0$, within a Ewald sphere, each of which contributes a BMS shielding tensor σ_k^{BMS} . We assume that the distribution of the orientations of the bulk magnetic susceptibility tensors is random. This Ewald sphere is part of the entire sample which is held in a container as shown in (c). The remainder of the sample is assumed to be uniformly magnetised.

where σ^{BMS} is given by

$$\begin{aligned}\sigma^{\text{BMS}} = & \chi_V^{(0)} \cdot \left(\mathbf{N}^{(0)} (\mathbf{r} - \mathbf{r}^{(0)})^T - \frac{1}{3} \mathbf{1} \right) \\ & + \sum_{k \neq 0} p_k \chi_V^{(k)} \cdot \mathbf{N}^{(k)} (\mathbf{r} - \mathbf{r}^{(k)})^T \\ & + \chi_V^{(\text{R})} \cdot \left(\mathbf{N}^{(\text{R})} (\mathbf{r} - \mathbf{r}^{(\text{R})})^T - \frac{1}{3} \mathbf{1} \right),\end{aligned}\tag{10.53}$$

where $\chi_V^{(k)}$ and $\mathbf{r}^{(k)}$ are the volume susceptibility and the position of the centre of mass of crystallite k . The terms in Equation 10.53 can be summarised as follows. The first term is due to the uniformly-magnetized region of the crystallite c_0 , and the second is a sum of all the shielding contributions from the other crystallites c_k . The third term is due to the uniformly-magnetized region of the sample container, the centre of mass of which is located at position $\mathbf{r}^{(\text{R})}$, and which has a bulk volume susceptibility $\chi_V^{(\text{R})}$, and produces a demagnetising tensor $\mathbf{N}^{(\text{R})} (\mathbf{r} - \mathbf{r}^{(\text{R})})$. It is important to note that in calculating both the first and third terms in Equation 10.53 we have subtracted the contributions from the respective Ewald spheres. The two Ewald spheres would contribute the shielding tensors $-2\chi_V^{(0)}/3$ and $-2\chi_V^{(\text{R})}/3$ to the first and third terms respectively. Subtracting these contributions from each respective term prevents the double counting of the parts of the sample included in the Ewald spheres. In the case of the first term, the contribution from the Ewald sphere in Figure 10.2 (a) is already included in σ^{S} , whereas for the third term the contribution is already included in σ^{S} and the first two terms of the BMS shielding tensor.

The BMS contribution can be written as the sum of the IBMS and ABMS parts σ^{IBMS} and σ^{ABMS} :

$$\sigma^{\text{BMS}} = \sigma^{\text{IBMS}} + \sigma^{\text{ABMS}}, \quad (10.54)$$

$$\begin{aligned} \sigma^{\text{IBMS}} = & \chi_V^{(0),\text{iso}} \left(\mathbf{N}^{(0)} (\mathbf{r} - \mathbf{r}^{(0)})^T - \frac{1}{3} \mathbf{1} \right) \\ & + \sum_{k \neq 0} p_k \chi_V^{(k),\text{iso}} \mathbf{N}^{(k)} (\mathbf{r} - \mathbf{r}^{(k)})^T \\ & + \chi_V^{(\text{R}),\text{iso}} \left(\mathbf{N}^{(\text{R})} (\mathbf{r} - \mathbf{r}^{(\text{R})})^T - \frac{1}{3} \mathbf{1} \right), \end{aligned} \quad (10.55)$$

$$\begin{aligned} \sigma^{\text{ABMS}} = & \chi_V^{(0),\text{an}} \cdot \left(\mathbf{N}^{(0)} (\mathbf{r} - \mathbf{r}^{(0)})^T - \frac{1}{3} \mathbf{1} \right) \\ & + \sum_{k \neq 0} p_k \chi_V^{(k),\text{an}} \cdot \mathbf{N}^{(k)} (\mathbf{r} - \mathbf{r}^{(k)})^T \\ & + \chi_V^{(\text{R}),\text{an}} \cdot \left(\mathbf{N}^{(\text{R})} (\mathbf{r} - \mathbf{r}^{(\text{R})})^T - \frac{1}{3} \mathbf{1} \right), \end{aligned} \quad (10.56)$$

where $\chi_V^{(k),\text{iso}}$ and $\chi_V^{(k),\text{an}}$ are the isotropic and anisotropic parts of the volume susceptibility tensor of the k th crystallite, and $\chi_V^{(\text{R}),\text{iso}}$ and $\chi_V^{(\text{R}),\text{an}}$ are the isotropic and anisotropic parts of the volume susceptibility tensor of the uniformly-magnetised continuum part of the sample.

If all the crystallites and the sample container are perfectly spherical, the first and third terms drop out of Equation 10.53, and we are left with the sum over the dipolar coupling tensors of the neighbouring crystallites. The IBMS and ABMS parts of the BMS shielding tensor are then

$$\sigma^{\text{IBMS}} = - \sum_{k \neq 0} p_k V_c^{(k)} \chi_V^{(k),\text{iso}} \mathbf{C}^{\text{dip}} (\mathbf{r} - \mathbf{r}^{(k)}) \quad (10.57)$$

$$= - \frac{1}{4\pi} \sum_{k \neq 0} p_k V_c^{(k)} \chi_V^{(k),\text{iso}} \left[\frac{3 (\mathbf{r} - \mathbf{r}^{(k)}) (\mathbf{r} - \mathbf{r}^{(k)}) - |\mathbf{r} - \mathbf{r}^{(k)}|^2 \mathbf{1}}{|\mathbf{r} - \mathbf{r}^{(k)}|^5} \right], \quad (10.58)$$

$$\sigma^{\text{ABMS}} = - \sum_{k \neq 0} p_k V_c^{(k)} \chi_V^{(k),\text{an}} \cdot \mathbf{C}^{\text{dip}} (\mathbf{r} - \mathbf{r}^{(k)}) \quad (10.59)$$

$$= - \frac{1}{4\pi} \sum_{k \neq 0} p_k V_c^{(k)} \chi_V^{(k),\text{an}} \cdot \left[\frac{3 (\mathbf{r} - \mathbf{r}^{(k)}) (\mathbf{r} - \mathbf{r}^{(k)}) - |\mathbf{r} - \mathbf{r}^{(k)}|^2 \mathbf{1}}{|\mathbf{r} - \mathbf{r}^{(k)}|^5} \right], \quad (10.60)$$

where $V_c^{(k)}$ is the volume of the k th crystallite. We see that, in this case, the IBMS shielding is purely anisotropic and symmetric, and has the spatial properties of the total dipolar coupling field experienced by the nucleus, whereas the ABMS shielding tensor has components of irreducible spherical tensor ranks 0, 1,

and 2.

10.2.2 BMS inhomogeneous broadening

It was shown in section 2.6 that the chemical shielding tensor depends on the two Euler angles describing the orientation of the PAF in the laboratory frame, α_{PL} and β_{PL} . As we will see in the following section 11, in a static powder where crystallites of all orientations are present, this leads to a broadening of the NMR resonance with the width of the line proportional to the SA. Whilst this description is complete as far as the local shielding tensor σ^S is concerned, the BMS contribution is more complicated and requires more careful consideration. It was shown by both VanderHart and Earl [147], and Alla and Lippmaa [148], that the presence of BMS effects, particularly the ABMS, leads to a broader distribution of shifts, and is therefore an additional source of inhomogeneous broadening.

In the high-field approximation the chemical shielding σ of a nuclear spin in a particular crystallite q can be written in terms of the irreducible spherical tensor components σ_{00} and σ_{20} as

$$\sigma(q, \alpha_{\text{PL}}, \beta_{\text{PL}}) = -\sqrt{\frac{1}{3}}\sigma_{00}(q) + \sqrt{\frac{2}{3}}\sigma_{20}(q, \alpha_{\text{PL}}, \beta_{\text{PL}}), \quad (10.61)$$

where we have explicitly written the dependence of the terms on q and the Euler angles α_{PL} and β_{PL} . We emphasise that q labels all the crystallites with the same orientation, as defined by $(\alpha_{\text{PL}}, \beta_{\text{PL}})$. In order to calculate the spectrum of the whole powder, we first average over the crystallites q with the same orientation, and then perform the average over the Euler angles.

For the local shielding this first averaging step is easy as σ^S depends only on the Euler angles $(\alpha_{\text{PS,L}}, \beta_{\text{PS,L}})$:

$$\sigma^S(\alpha_{\text{PS,L}}, \beta_{\text{PS,L}}) = -\sqrt{\frac{1}{3}}\sigma_{00}^S + \sqrt{\frac{2}{3}}\sigma_{20}^S(\alpha_{\text{PS,L}}, \beta_{\text{PS,L}}), \quad (10.62)$$

where $(\alpha_{\text{PS,L}}, \beta_{\text{PS,L}})$ are the Euler angles giving the orientation of the PAF 'PS' of σ_{20}^S in the laboratory frame 'L'. We therefore see that the subset of crystallites q with the same orientation have exactly the same shielding tensor, and so an average over this subset will result in a sharp resonance in the NMR spectrum.

The IBMS and ABMS contributions both depend on q and the Euler angles giving the orientations of their

respective PAFs:

$$\sigma^{\text{IBMS}}(q, \alpha_{\text{PI,L}}, \beta_{\text{PI,L}}) = \sqrt{\frac{2}{3}} \sigma_{20}^{\text{IBMS}}(q, \alpha_{\text{PI,L}}, \beta_{\text{PI,L}}), \quad (10.63)$$

$$\sigma^{\text{ABMS}}(q, \alpha_{\text{PA,L}}, \beta_{\text{PA,L}}) = -\sqrt{\frac{1}{3}} \sigma_{00}^{\text{ABMS}}(q) + \sqrt{\frac{2}{3}} \sigma_{20}^{\text{ABMS}}(q, \alpha_{\text{PA,L}}, \beta_{\text{PA,L}}), \quad (10.64)$$

where ‘PI’ and ‘PA’ refer to the PAFs of the anisotropic parts of the IBMS and ABMS shielding tensors respectively and we have used the fact that, from Equation 10.58, the isotropic part of the IBMS shielding tensor is zero. If we average over the crystallites q with the same orientation q we obtain a very different result than for the local shielding tensor. This is because, from Equations 10.58 and 10.60, both the IBMS and ABMS shielding tensors of a particular crystallite depend on the configurations of the surrounding crystallites k , via p_k , their sizes, via $V_c^{(k)}$, and the orientations of their volume susceptibility tensors. As each crystallite is orientated independently of the others, this means that averaging over q results in a distribution of anisotropic shifts from the IBMS of the surrounding crystallites, and a distribution of both isotropic and anisotropic shifts from their ABMSes. Both effects are a source of inhomogeneous broadening in the NMR spectrum, and are often collectively referred to as BMS broadening.

10.3 Key concepts

- A sample (solution or single crystal) containing an ensemble of paramagnetic ions generates a demagnetising field that adds to the local paramagnetic magnetic fields. The demagnetising field can be described in terms of a bulk magnetic volume susceptibility tensor.
- The bulk magnetic susceptibility tensor leads to a BMS contribution to the shielding tensor (Equation 10.24).
- In a spherical crystal the bulk isotropic susceptibility changes the isotropic shift, and the bulk susceptibility anisotropy changes the shift anisotropy (Table 10.1).
- In a non-spherical crystal the bulk susceptibility anisotropy also affects the isotropic shift.
- In a powder sample the demagnetising fields of the surrounding crystallites result in bulk isotropic and anisotropic contributions to the paramagnetic shielding (Equations 10.58 and 10.60).

- The bulk susceptibility anisotropies of the surrounding crystallites result in inhomogeneous broadening of the resonance (the anisotropic bulk magnetic susceptibility broadening).

Chapter 11

The NMR spectrum for non-interacting spins

Up until now we have examined in some detail the theoretical aspects of the paramagnetic shielding interactions, the PRE, and bulk susceptibility effects. Now we focus on the impact these effects have on the NMR spectrum. We begin by summarising the quantum mechanical description of the nuclear-spin interactions, with a focus on the chemical shielding and quadrupolar interactions up to second order, and how we can use this description to calculate the resulting NMR spectrum for systems in solution, and static and spinning powders. Then we examine the specific forms of the conventional one-dimensional NMR spectra for spin $I = 1/2$ nuclei subject to a paramagnetic shielding interaction, and quadrupolar nuclei subject to both paramagnetic shielding and first- and second-order quadrupolar interactions.

11.1 The quantum mechanics of NMR

11.1.1 The Hamiltonian, propagator, and density operator

In NMR a sequence of pulses and delays is referred to as a pulse sequence. The effects of the sequence on the spin system are described by a Hamiltonian $\hat{H}(t)$ that is in general time-dependent, and comprises all the relevant interactions of the spin system and the effects of the radiofrequency (RF) pulses. This Hamiltonian

is written as the sum of a term $\hat{H}_0(t)$ that describes the spin interactions, and a term $\hat{H}_1(t)$ that describes the RF pulses:

$$\hat{H}(t) = \hat{H}_0(t) + \hat{H}_1(t). \quad (11.1)$$

The former term is time-dependent when the sample is rotated, for example under magic-angle spinning (MAS), and is time-independent otherwise. The latter term is time-dependent because the RF field amplitudes and phases vary throughout the sequence. This time dependence can either be piecewise, where the sequence can be broken down into sections within each of which the pulse amplitudes and phases are constant, or continuous, where the amplitudes and phases vary throughout the sequence.

The response of the nuclear spin system to the pulse sequence is described by the time evolution of the density operator $\hat{\rho}(t)$ during the sequence. The coherent time evolution of $\hat{\rho}(t)$ is governed by the Liouville–von Neumann equation:

$$\frac{d\hat{\rho}(t)}{dt} = -\frac{i}{\hbar} [\hat{H}(t), \hat{\rho}(t)]. \quad (11.2)$$

Note that here we neglect the effects of incoherent processes such as relaxation. To include them in Equation 11.2 we need to add an additional term, which for relaxation process is described in chapters 8 and 9. The solution to the Liouville–von Neumann equation in Equation 11.2 has the general form

$$\hat{\rho}(t) = \hat{U}(t, 0)\hat{\rho}(0)\hat{U}(t, 0)^{-1}, \quad (11.3)$$

where $\hat{U}(t, 0)$ is the propagator corresponding to $\hat{H}(t)$. In general the expression for the Hamiltonian at an arbitrary time point t_1 , $\hat{H}(t_1)$, does not commute with the Hamiltonian evaluated at a second arbitrary time point t_2 , $\hat{H}(t_2)$. In this case the propagator describing the evolution between t_1 and t_2 has the general form

$$\hat{U}(t_2, t_1) = \hat{T} \exp\left(-\frac{i}{\hbar} \int_{t_1}^{t_2} dt \hat{H}(t)\right), \quad (11.4)$$

where \hat{T} is the Dyson time-ordering operator, which ensures that the events described by the Hamiltonian occur in the proper order. Whilst this form of the propagator is general it is not analytically useful, and further analysis of the sequence generally requires other methods such as average Hamiltonian theory [192] or Floquet theory [315–318]. However in certain special cases the propagator does reduce to a simpler and more useful form.

In the first case, if the Hamiltonian evaluated at an arbitrary time always commutes with the Hamiltonian at a second arbitrary time, the propagator is:

$$\hat{U}(t_2, t_1) = \exp\left(-\frac{i}{\hbar} \int_{t_1}^{t_2} dt \hat{H}(t)\right). \quad (11.5)$$

This situation is encountered in solid-state MAS NMR when the spin interactions contain only single-spin operators of rank λ and order zero $\hat{I}_{\lambda 0}$, such as the nuclear interactions discussed in chapter 2, during a period of free precession where there are no pulses, so that $\hat{H}_1(t)$ is zero.

In the second case the Hamiltonian \hat{H} is time-independent, and the propagator reduces to the simple form

$$\hat{U}(t_2, t_1) = \exp\left(-\frac{i}{\hbar} \hat{H}(t_2 - t_1)\right). \quad (11.6)$$

For example this situation is encountered in solution NMR, and the solid-state NMR of static systems, during periods of free precession. In NMR sequences where the time dependence due to the pulses is piecewise, the propagator describing the evolution during the whole sequence can be written as the product of propagators of the form of Equation 11.7. For instance consider a sequence comprising two consecutive sections, which are labelled \mathcal{S}_{12} and \mathcal{S}_{23} respectively. Section \mathcal{S}_{12} starts at time $t = t_1$ and ends at t_2 and is described by the Hamiltonian \hat{H}_{12} , and the second section \mathcal{S}_{23} described by \hat{H}_{23} commences at t_2 and continues until time t_3 . The overall propagator describing the evolution of the spin system between times t_1 and t_3 is given by

$$\hat{U}(t_3, t_1) = \hat{U}(t_3, t_2)\hat{U}(t_2, t_1) = \exp\left(-\frac{i}{\hbar} \hat{H}_{23}(t_3 - t_2)\right) \exp\left(-\frac{i}{\hbar} \hat{H}_{12}(t_2 - t_1)\right). \quad (11.7)$$

The equilibrium density operator $\hat{\rho}_0$ represents the state of the system in the absence of RF irradiation, and where there is no dynamic change due to the interactions of the spins with either the external magnetic field or each other. We therefore see that, from Equation 11.2, $\hat{\rho}_0$ must commute with the system Hamiltonian $\hat{H}_0(t)$. We have seen that the nuclear-spin interactions are dominated by the Zeeman interaction, and so the

general expression for $\hat{\rho}_0$ is

$$\hat{\rho}_0 = \frac{\exp(-\beta\hat{H}_Z)}{\text{Tr}_I[\exp(-\beta\hat{H}_Z)]} \quad (11.8)$$

$$= \frac{\exp(\beta\hbar\gamma_I B_0 \hat{I}_z)}{\text{Tr}_I[\exp(\beta\hbar\gamma_I B_0 \hat{I}_z)]}. \quad (11.9)$$

In the high-temperature limit we expand the exponentials to first-order in a Taylor series, and obtain the following expression for $\hat{\rho}_0$:

$$\hat{\rho}_0 \approx \frac{\hat{1} - \beta\hbar\gamma_I B_0 \hat{I}_z}{2I + 1}. \quad (11.10)$$

The first term in $\hat{1}$ commutes with all Hamiltonians, does not produce any observable signal, and so we can ignore it. The second is proportional to \hat{I}_z and has a magnitude $\hbar\gamma_I B_0 / ((2I + 1)kT)$. The maximum amplitude of the observable signal following excitation is equal to this factor, and so we see that we obtain higher sensitivity for nuclei with larger gyromagnetic ratios, and under conditions of larger applied magnetic fields and lower temperatures. In practice, when analysing pulse sequences, we usually ignore this factor and write $\hat{\rho}_0 = \hat{I}_z$.

11.1.2 Radiofrequency pulses and sequences

A general RF pulse of duration τ_p with a time-dependent RF field amplitude $\omega_1(t)$ and phase $\phi_1(t)$ applied to a nuclear spin I has the following Hamiltonian:

$$\hat{H}_1(t) = \omega_1(t) \hat{R}_z(\phi_1(t)) \hat{I}_x \hat{R}_z(\phi_1(t))^{-1} \quad (11.11)$$

$$= \omega_1(t) [\cos(\phi_1(t)) \hat{I}_x + \sin(\phi_1(t)) \hat{I}_y], \quad (11.12)$$

where $\hat{R}_a(\phi) = \exp(-i\phi\hat{I}_a)$ is the unitary operator that represents a rotation of the spin operator in spin space through an angle ϕ about an axis a . The propagator representing the Hamiltonian $\hat{H}_1(t)$ at arbitrary time takes the general form in Equation 11.4. Neglecting the spin interactions in $\hat{H}_0(t)$ and considering only the effect of $\hat{H}_1(t)$ during the pulse, the net evolution can be represented as an overall rotation through a net angle ξ about a net axis with orientation relative to z specified by the spherical polar angles (θ, ϕ) . The propagator

that describes this net transformation due to the sequence \hat{U}_{seq} then has the form

$$\hat{U}_{\text{seq}} = \hat{R}_z(\phi)\hat{R}_y(\theta)\hat{R}_z(\xi)\hat{R}_y(\theta)^{-1}\hat{R}_z(\phi)^{-1}. \quad (11.13)$$

In the case where both the amplitude ω_1 and phase ϕ_1 are constant during the pulse, the net pulse propagator is

$$\hat{U}_{\text{seq}} = \hat{R}_z(\phi_1)\hat{R}_z(\xi_1)\hat{R}_z(\phi_1)^{-1}, \quad (11.14)$$

where $\xi_1 = \omega_1\tau_p$ is the flip angle of the pulse.

11.1.3 The spin interactions

We recall that the internal spin interactions are treated as perturbations to the nuclear Zeeman interaction, that the Zeeman Hamiltonian is removed from $\hat{H}_0(t)$, and that the remaining system Hamiltonians are calculated using the secular approximation [183]. The particular spin interactions with which we concern ourselves in this chapter are the secular chemical shift and quadrupolar interactions to second order. Hence all the terms in $\hat{H}_0(t)$ commute with each other at all times t_1 and t_2 , i.e. $[\hat{H}_0(t_2), \hat{H}_0(t_1)] = 0$. The total Hamiltonian is written as a sum of terms each of which is the product of a spatial tensor $K_{\lambda,0}^{(\Lambda)}(t)$ of space rank l , and a spin tensor operator $\hat{I}_{\lambda 0}^{(\Lambda)}$ of spin rank λ :

$$\hat{H}_0(t) = \sum_{\Lambda, l, \lambda} K_{\lambda,0}^{(\Lambda)}(t) \hat{I}_{\lambda 0}^{(\Lambda)}, \quad (11.15)$$

where Λ labels the distinct interactions. We note that the space tensor components $K_{\lambda,0}^{(\Lambda)}(t)$ are generally time-dependent if sample rotation is employed, and are time-independent otherwise. We also point out that for some interactions different spatial tensors of the same space rank may couple to spin tensors of different spin ranks. For example in the case of the second-order quadrupolar interaction there are two spatial tensors of space rank zero, one of which couples to the rank-one spin tensor and the other of which couples to the rank-three spin tensor. These two spatial tensors are different, and so we also indicate a dependence of $K_{\lambda,0}^{(\Lambda)}(t)$ on λ via the subscript. Likewise there are two spatial tensors of ranks two that couple the spin tensors of ranks one and three, and also two rank-four spatial tensors. To facilitate the calculation of the frequencies of evolution under $\hat{H}_0(t)$ we rewrite the Hamiltonian in terms of the frequency components $\Omega_{\lambda,0}^{(\Lambda)}(t)$ and reduced

spin tensor operators $\hat{I}_{\lambda 0}^{(\Lambda)}$ as follows:

$$\hat{H}_0(t) = \hbar \sum_{\Lambda, I, \lambda} \Omega_{\lambda, I 0}^{(\Lambda)}(t) \hat{I}_{\lambda 0}^{(\Lambda)}. \quad (11.16)$$

The reduced tensor operators are given in terms of the $\hat{I}_{\lambda 0}^{(\Lambda)}$ by

$$\hat{I}_{\lambda 0}^{(\Lambda)} = N_{\lambda 0}^{(\Lambda)} \hat{I}_{\lambda 0}^{(\Lambda)}, \quad (11.17)$$

where $N_{\lambda 0}^{(\Lambda)}$ are normalizing factors that are equal to

$$N_{00}^{(\Lambda)} = 1, \quad N_{10}^{(\Lambda)} = 1, \quad N_{20}^{(\Lambda)} = \sqrt{\frac{2}{3}}, \quad N_{30}^{(\Lambda)} = \frac{\sqrt{10}}{3}. \quad (11.18)$$

The operators therefore have the expressions

$$t_{00} = \hat{I}, \quad (11.19)$$

$$t_{10} = \hat{I}_z, \quad (11.20)$$

$$t_{20} = \hat{I}_z^2 - \frac{1}{3} I(I+1) \hat{I}, \quad (11.21)$$

$$t_{30} = \frac{1}{3} [5 \hat{I}_z^3 - (3I(I+1) - 1) \hat{I}_z]. \quad (11.22)$$

The frequency components are related to the spatial tensor components via

$$K_{\lambda, I 0}^{(\Lambda)}(t) = \hbar N_{\lambda 0}^{(\Lambda)} \Omega_{\lambda, I 0}^{(\Lambda)}(t). \quad (11.23)$$

For the one-spin interactions that we have so far considered the frequencies of the components with different spatial and spin ranks are given in Table 11.1.

The overall propagator $\hat{U}_0(t_2, t_1)$ that describes the time evolution of the density operator under these interactions, in the absence of RF irradiation, is

$$\hat{U}_0(t_2, t_1) = \exp\left(-\frac{i}{\hbar} \int_{t_1}^{t_2} dt \hat{H}_0(t)\right). \quad (11.24)$$

Interaction Λ	λ	$I = 0$	$\Omega_{\lambda, I, 0}^{(\Lambda)}$ $I = 2$	$I = 4$
1st-order quadrupolar	2	—	$\sqrt{\frac{2}{3}}\omega_Q v_{20}$	—
1st-order chemical shielding	1	$-\omega_0 \sigma_{\text{iso}}$	$-\sqrt{\frac{2}{3}}\omega_0 \sigma_{20}$	—
2nd-order quad-quad	1	$4\omega_Q^2 [4(I+1) - 3] w_{00}^{(Q,Q)} / (45\sqrt{5}\omega_0)$	$2\omega_Q^2 [4(I+1) - 3] w_{20}^{(Q,Q)} / (45\sqrt{14}\omega_0)$	$-2\omega_Q^2 [4(I+1) - 3] w_{40}^{(Q,Q)} / (15\sqrt{70}\omega_0)$
	3	$4\omega_Q^2 w_{00}^{(Q,Q)} / (5\sqrt{5}\omega_0)$	$-4\sqrt{2}\omega_Q^2 w_{20}^{(Q,Q)} / (5\sqrt{7}\omega_0)$	$-51\omega_Q^2 w_{40}^{(Q,Q)} / (20\sqrt{70}\omega_0)$
2nd-order quad-shield	2	$-2\omega_Q \omega_{00}^{(C2,Q)} / \sqrt{5}$	$\omega_Q \left[\sqrt{2} w_{20}^{(C1,Q)} + \sqrt{27} w_{20}^{(C2,Q)} \right]$	$4\sqrt{2/35}\omega_Q w_{40}^{(C2,Q)}$
2nd-order shield-shield	1	$\omega_0 \left[\sqrt{1/12} w_{00}^{(C1,C1)} + \sqrt{1/20} w_{00}^{(C2,C2)} \right]$	$\omega_0 \left[\sqrt{1/24} w_{20}^{(C1,C1)} - \sqrt{1/56} w_{20}^{(C2,C2)} \right]$	$-\omega_0 \sqrt{2/35} w_{40}^{(C2,C2)}$

Table 11.1: The frequency components $\Omega_{\lambda, I, 0}^{(\Lambda)}$ occurring in the Hamiltonian for certain nuclear spin interactions Λ arising from the different combinations of space ranks I and spin ranks λ .

Remembering the commutation properties of all the terms of $\hat{H}_0(t)$, we can write $\hat{U}_0(t_2, t_1)$ as

$$\hat{U}_0(t_2, t_1) = \prod_{\Lambda, l, \lambda} \exp\left(-i\Phi_{\lambda, l, 0}^{(\Lambda)}(t_2, t_1)\hat{I}_{\lambda, l, 0}^{(\Lambda)}\right), \quad (11.25)$$

where the phase factor $\Phi_{\lambda, l, 0}^{(\Lambda)}(t_2, t_1)$ is the integral of the frequency $\Omega_{\lambda, l, 0}^{(\Lambda)}(t)$ between times t_1 and t_2 :

$$\Phi_{\lambda, l, 0}^{(\Lambda)}(t_2, t_1) = \int_{t_1}^{t_2} dt \Omega_{\lambda, l, 0}^{(\Lambda)}(t). \quad (11.26)$$

We note that in this case the order of multiplication of the terms in Equation 11.25 does not matter as all the Hamiltonian terms commute with each other.

11.1.4 Basis operators

The nuclear spin wavefunction of a single nuclear spin I is conveniently written as a linear combination of $2I + 1$ basis operators. These basis operators are usually taken to be the eigenfunctions of the Zeeman Hamiltonian $|IM\rangle$, which are orthonormal:

$$\langle IM_1 | IM_2 \rangle = \delta_{M_1, M_2}. \quad (11.27)$$

In addition the description of the nuclear spin dynamics is facilitated by writing the density operator as a superposition of basis operators $\{\hat{B}_i\}$, of which there are $(2I + 1)^2$ and which are chosen to be orthogonal according to

$$(\hat{B}_i | \hat{B}_j) = \text{Tr}_I (\hat{B}_i^\dagger \hat{B}_j) \quad (11.28)$$

$$= N\delta_{ij}, \quad (11.29)$$

where N is a normalization factor.

Of course there is a choice of several bases. One common basis is the set of irreducible spherical tensor operators $\{\hat{I}_{\lambda\mu}\}$ of ranks λ from 0 to $2I$, and orders μ from $-\lambda$ to $+\lambda$, in integer steps [190]. These operators have been used extensively in this review for both nuclear and electronic spins. However for the subsequent discussion we adopt the single-element basis operators, which are denoted $\{|IM_1\rangle\langle IM_2|\}$. These operators

are so-called because in the Zeeman function basis each operator represents a single element of the density matrix. The single-element basis operators can be grouped as follows. There are $2I + 1$ operators for which $M_1 = M_2$, and which represent the populations of the corresponding states. We refer to these as population operators and denote them $\hat{I}_p^{(M)}$:

$$\hat{I}_p^{(M)} = |IM\rangle\langle IM|. \quad (11.30)$$

The remaining $2I(2I + 1)$ operators each represent a coherence between two different states. Half of these have $M_1 < M_2$, and are referred to as lowering operators $\hat{I}_-^{(M_2, M_1)}$. They are given by

$$\hat{I}_-^{(M_2, M_1)} = |IM_1\rangle\langle IM_2|. \quad (11.31)$$

The remaining coherence operators have $M_1 > M_2$ and are referred to as raising operators $\hat{I}_+^{(M_1, M_2)}$:

$$\hat{I}_+^{(M_1, M_2)} = |IM_1\rangle\langle IM_2|. \quad (11.32)$$

These basis operators can be used to write down expressions for other operators. For example the Cartesian operators $\{\hat{I}, \hat{I}_z, \hat{I}_-, \hat{I}_+\}$ are given by:

$$\hat{I} = \sum_{M=-I}^{+I} \hat{I}_p^{(M)}, \quad (11.33)$$

$$\hat{I}_z = \sum_{M=-I}^{+I} M \hat{I}_p^{(M)}, \quad (11.34)$$

$$\hat{I}_- = \sum_{M=-I+1}^{+I} \sqrt{I(I+1) - M(M-1)} \hat{I}_-^{(M, M-1)}, \quad (11.35)$$

$$\hat{I}_+ = \sum_{M=-I}^{+I-1} \sqrt{I(I+1) - M(M+1)} \hat{I}_+^{(M+1, M)}. \quad (11.36)$$

We see that both \hat{I} and \hat{I}_z are written in terms of the $2I + 1$ population operators. The identity operator represents the total population of all the spin states, and remains invariant as required. The operator \hat{I}_z represents the differences in populations of the spin states. The operator \hat{I}_- is written in terms of the $2I$ coherence operators $\hat{I}_-^{(M, M-1)}$ with $M_1 - M_2 = -1$, and so represents nuclear spin magnetization in the transverse plane. Likewise \hat{I}_+ is written in terms of the $2I$ coherence operators $\hat{I}_+^{(M+1, M)}$ with $M_1 - M_2 = +1$.

11.1.5 NMR frequencies and spin order

In order to make use of the advantages afforded by decomposing the density operator into a sum of basis operators, we need to determine how each basis operator evolves under the Hamiltonian $\hat{H}_0(t)$ that describes the internal spin interactions. We do this by calculating the evolution over time of a single basis operator $\hat{\rho}(0) = |IM_i\rangle\langle IM_j|$ subject to a single term in the Hamiltonian with a particular space-rank and spin-rank. The propagator is given by a single factor from Equation 11.25. Applying this to $\hat{\rho}(0)$ and allowing the system to evolve we obtain the density operator $\hat{\rho}(t)$ at time t :

$$\hat{\rho}(t) = \exp\left(-i\Phi_{\lambda,0}^{(\Lambda)}(t,0)\hat{t}_{\lambda 0}\right)\hat{\rho}(0)\exp\left(+i\Phi_{\lambda,0}^{(\Lambda)}(t,0)\hat{t}_{\lambda 0}\right), \quad (11.37)$$

where we have dropped the superscript (Λ) from the reduced spherical tensor spin operator $\hat{t}_{\lambda 0}$ as these operators are the same for all one-spin interactions. The spin states $|IM_i\rangle$ are also eigenstates of the operators $\hat{t}_{\lambda 0}$, and so we can determine $\hat{\rho}(t)$ in a straightforward manner:

$$\hat{\rho}(t) = \exp\left(-i\Phi_{\lambda,0}^{(\Lambda)}(t,0)\hat{t}_{\lambda 0}\right)|IM_i\rangle\langle IM_j|\exp\left(+i\Phi_{\lambda,0}^{(\Lambda)}(t,0)\hat{t}_{\lambda 0}\right) \quad (11.38)$$

$$= \exp\left(-i\Xi_{\lambda,M_iM_j}\Phi_{\lambda,0}^{(\Lambda)}(t,0)\right)|IM_i\rangle\langle IM_j|. \quad (11.39)$$

We see that the basis operator simply acquires a phase $-\Xi_{\lambda,M_iM_j}\Phi_{\lambda,0}^{(\Lambda)}(t,0)$ that is proportional to the intrinsic phase $\Phi_{\lambda,0}^{(\Lambda)}(t,0)$ of the interaction, multiplied by a factor Ξ_{λ,M_iM_j} that is given by

$$\Xi_{\lambda,M_iM_j} = \langle IM_i|\hat{t}_{\lambda 0}|IM_i\rangle - \langle IM_j|\hat{t}_{\lambda 0}|IM_j\rangle. \quad (11.40)$$

The factor Ξ_{λ,M_iM_j} is the spin-order of rank λ that defines the single-element basis operator $|IM_i\rangle\langle IM_j|$ [319]. The spin orders of ranks 0, 1, 2, and 3 are given the symbols $s_{M_iM_j}$, $p_{M_iM_j}$, $d_{M_iM_j}$, and $f_{M_iM_j}$ in analogy with

the hydrogen-like atomic orbitals in electronic structure theory [319]. They take the forms:

$$s_{M_i M_j} = \Xi_{0, M_i M_j} \quad (11.41)$$

$$= 0, \quad (11.42)$$

$$p_{M_i M_j} = \Xi_{1, M_i M_j} \quad (11.43)$$

$$= M_i - M_j, \quad (11.44)$$

$$d_{M_i M_j} = \Xi_{2, M_i M_j} \quad (11.45)$$

$$= M_i^2 - M_j^2, \quad (11.46)$$

$$f_{M_i M_j} = \Xi_{3, M_i M_j} \quad (11.47)$$

$$= \frac{1}{3} \left[5(M_i^3 - M_j^3) - (3I(I+1) - 1)(M_i - M_j) \right]. \quad (11.48)$$

The s -order $s_{M_i M_j}$ is associated with the identity operator and does not affect the evolution of the density operator, so we do not consider it further. The p -order $p_{M_i M_j}$ is also known as coherence order, which is an important concept in signal selection in multiple-pulse NMR experiments [320]. The rank-two spin order $d_{M_i M_j}$ is known as either d -order or satellite order [321]. Finally the rank-three order $f_{M_i M_j}$ is referred to as f -order. If for a particular interaction the Hamiltonian term of a particular space rank l is associated with more than one spin rank λ , we can use the spin-order defined in Equation 11.40 to define a total frequency $\Omega_{10, M_i M_j}^{(\Lambda)}(t)$ that depends only on l :

$$\Omega_{10, M_i M_j}^{(\Lambda)}(t) = - \sum_{\lambda} \Xi_{\lambda, M_i M_j} \Omega_{\lambda, 10}^{(\Lambda)}(t). \quad (11.49)$$

For the interactions considered here this only applies to the second-order quadrupolar interaction, where the terms of spatial ranks 0, 2, and 4 are each associated with two spin ranks 1 and 3. For this interaction we can write the frequencies in Equation 11.49 for the three space ranks $l = 0, 2, \text{ and } 4$ in terms of the c -order

parameters c_{l,M_iM_j} , which are given by:

$$c_{0,M_iM_j} = \frac{9}{5}f_{M_iM_j} + \frac{4I(I+1)-3}{5}p_{M_iM_j}, \quad (11.50)$$

$$c_{2,M_iM_j} = -\frac{18}{5}f_{M_iM_j} + \frac{4I(I+1)-3}{10}p_{M_iM_j}, \quad (11.51)$$

$$c_{4,M_iM_j} = -\frac{51}{5}f_{M_iM_j} - \frac{3[4I(I+1)-3]}{10}p_{M_iM_j}. \quad (11.52)$$

For all the one-spin interactions in Table 11.1, the frequencies defined in Equation 11.49 are given in Table 11.2. Using these definitions we can write down the evolution of the density operator term $|IM_i\rangle\langle IM_j|$ under the action of a Hamiltonian term corresponding to a particular interaction Λ and space rank l summed over the relevant spin ranks λ . The result is:

$$\hat{\rho}(t) = \exp\left(i\Phi_{l0,M_iM_j}^{(\Lambda)}(t, 0)\right)|IM_i\rangle\langle IM_j|, \quad (11.53)$$

$$\Phi_{l0,M_iM_j}^{(\Lambda)}(t_2, t_1) = \int_{t_1}^{t_2} dt \Omega_{l0,M_iM_j}^{(\Lambda)}(t). \quad (11.54)$$

The accrued phase factor $\Phi_{l0,M_iM_j}^{(\Lambda)}(t, 0)$ is simply the time integral of the frequency component.

During signal detection in the NMR experiment we acquire the two transverse components of the bulk nuclear magnetization, M_x and M_y , simultaneously using quadrature detection, and combine them into a single quadrature quantity $M_+ = M_x + iM_y$. The magnetization components M_x and M_y are proportional to the expectation values of \hat{I}_x and \hat{I}_y . Hence the quantity M_+ is proportional to the expectation value of \hat{I}_+ , and so the signal $s(t)$ is given by

$$s(t) = \frac{\text{Tr}_I(\hat{I}_+\hat{\rho}(t))}{\text{Tr}_I(\hat{I}_+\hat{I}_-)}. \quad (11.55)$$

The only term of the density operator that contributes to the trace in the numerator is \hat{I}_- , which we see from Equation 11.35 represents the sum of the basis operators of coherence (p -) order -1 . Each operator $\hat{I}_-^{(M,M-1)}$ contributing to \hat{I}_- evolves under a characteristic frequency to accrue a phase $\Phi_{l0,M-1,M}^{(\Lambda)}(t, 0)$, which gives the following expression for $\hat{\rho}(t)$:

$$\sum_{M=-I+1}^{+I} \hat{I}_-^{(M,M-1)} \sqrt{I(I+1)-M(M-1)} \exp\left(i\Phi_{l0,M-1,M}^{(\Lambda)}(t, 0)\right). \quad (11.56)$$

Interaction Λ	λ	$\Omega_{0,M_i,M_j}^{(\Lambda)}$		
		$l = 0$	$l = 2$	$l = 4$
1st-order quadrupolar	2	—	$-d_{M_i,M_j} \sqrt{\frac{2}{3}} \omega_Q \nu_{20}$	—
1st-order chemical shielding	1	$P_{M_i,M_j} \omega_0 \sigma_{\text{iso}}$	$P_{M_i,M_j} \sqrt{\frac{2}{3}} \omega_0 \sigma_{20}$	—
2nd-order quad–quad	1	$c_{0,M_i,M_j} 4\omega_Q^2 \omega_0 \sigma_{\text{iso}}^{(C1,C1)} / (9\sqrt{5}\omega_0)$	$c_{2,M_i,M_j} 4\omega_Q^2 \omega_0 \sigma_{20}^{(C1,C1)} / (9\sqrt{14}\omega_0)$	$c_{4,M_i,M_j} 4\omega_Q^2 \omega_0 \sigma_{40}^{(C1,C1)} / (9\sqrt{70}\omega_0)$
2nd-order quad–shield	2	$d_{M_i,M_j} 2\omega_Q \omega_0 \nu_{00}^{(C1,C1)} / \sqrt{5}$	$-d_{M_i,M_j} \omega_Q \left[\sqrt{2} \nu_{20}^{(C1,C1)} + \sqrt{2/7} \nu_{20}^{(C2,C2)} \right]$	$-d_{M_i,M_j} 4\sqrt{2/35} \omega_Q \nu_{40}^{(C2,C2)}$
2nd-order shield–shield	1	$-P_{M_i,M_j} \omega_0 \left[\sqrt{1/12} \nu_{00}^{(C1,C1)} + \sqrt{1/20} \nu_{00}^{(C2,C2)} \right]$	$-P_{M_i,M_j} \omega_0 \left[\sqrt{1/24} \nu_{20}^{(C1,C1)} - \sqrt{1/2} \nu_{20}^{(C1,C2)} - \sqrt{1/56} \nu_{20}^{(C2,C2)} \right]$	$P_{M_i,M_j} \omega_0 \sqrt{2/35} \nu_{40}^{(C2,C2)}$

Table 11.2: The frequency components $\Omega_{0,M_i,M_j}^{(\Lambda)}$ from different nuclear spin interactions Λ for different space ranks l , given in terms of the spin orders Ξ_{λ,M_i,M_j} .

Following summation over all relevant interactions Λ , we obtain the following signal in the time domain,:

$$s(t) = \frac{3}{2I(I+1)(2I+1)} \sum_{M=-I+1}^{+I} [I(I+1) - M(M-1)] \prod_{\Lambda} \exp(i\Phi_{I0,M-1,M}^{(\Lambda)}(t, 0)). \quad (11.57)$$

We see that a nuclear spin I has $2I$ observable signal components, which in general evolve with different frequencies to give $2I$ distinct peaks in the NMR spectrum.

11.1.6 Solution NMR

In the absence of sample rotation the frequency components $\Omega_{I0,M_iM_j}^{(\Lambda)}$ are time-independent, and are related to the PAF components of the irreducible spherical spatial tensor in its PAF $\tilde{K}_{\lambda,lm'}^{(\Lambda)}$ by the expression

$$\Omega_{I0,M_iM_j}^{(\Lambda)} = - \sum_{\lambda} \frac{\Xi_{\lambda,M_iM_j}}{\hbar N_{\lambda 0}^{(\Lambda)}} \sum_{mm'} \tilde{K}_{\lambda,lm'}^{(\Lambda)} D_{m'm}^{(l)}(\Omega_{\Lambda C}) D_{m0}^{(l)}(\Omega_{CL}). \quad (11.58)$$

The Euler angles $\Omega_{\Lambda C}$ describe the orientation of the PAF Λ in a frame of reference that is fixed relative to the molecular geometry in molecular systems, or the crystal geometry for solid crystals C. The $\Omega_{\Lambda C}$ are a fixed property of the system under study. The Euler angles Ω_{CL} give the orientation of the crystal/molecular-fixed reference frame relative to the laboratory reference frame L, and so depend on the orientation of that particular crystal or molecule in the sample container. We see that for static systems at high field the frequency depends only on two of the Euler angles, α_{CL} and β_{CL} , of the latter set.

In an isotropic solution of molecules, there are no restrictions on the orientations that the molecules, and therefore the PAFs of the interaction tensors, are able to take. Furthermore the molecules are tumbling rapidly in comparison to the Larmor frequency, so that each molecule samples all possible orientations, resulting in the overall frequency component being given simply by the orientational average over the Euler angles $(\alpha_{CL}, \beta_{CL}, \gamma_{CL})$. The orientational dependence is contained wholly within the Wigner rotation matrix elements $D_{m0}^{(l)}(\alpha_{CL}, \beta_{CL}, \gamma_{CL})$, and so the relevant integral is

$$\frac{1}{8\pi^2} \int_0^{2\pi} d\alpha_{PL} \int_0^{\pi} d\beta_{CL} \sin(\beta_{CL}) \int_0^{2\pi} d\gamma_{CL} D_{m0}^{(l)}(\alpha_{CL}, \beta_{CL}, \gamma_{CL}) = \delta_{l0} \delta_{m0}, \quad (11.59)$$

which we have simplified using the orthogonality relations of $D_{mm'}^{(l)}(\alpha_{CL}, \beta_{CL}, \gamma_{CL})$. We see that the only terms that survive the orientational averaging are those of rank $l = 0$, which are, by definition, the isotropic

terms. Each term in the density operator therefore evolves under a total isotropic frequency $\Omega_{\text{iso},M_iM_j}$, which is given by sum of the isotropic first-order shift frequency $\Omega_{00,M_iM_j}^{(C)}$, the second-order isotropic quadrupolar frequency $\Omega_{00,M_iM_j}^{(Q,Q)}$, the second-order isotropic frequency due to the cross-term between the quadrupolar and shift interactions $\Omega_{00,M_iM_j}^{(Q,C)}$, and the second-order isotropic shift frequency $\Omega_{00,M_iM_j}^{(C,C)}$:

$$\Omega_{\text{iso},M_iM_j} = \Omega_{00,M_iM_j}^{(C)} + \Omega_{00,M_iM_j}^{(Q,Q)} + \Omega_{00,M_iM_j}^{(Q,C)} + \Omega_{00,M_iM_j}^{(C,C)}. \quad (11.60)$$

Therefore the total phase acquired during signal acquisition is simply $\Omega_{\text{iso},M_iM_j}t$:

$$\Omega_{\text{iso},M_iM_j}t = \left[\Omega_{00,M_iM_j}^{(C)} + \Omega_{00,M_iM_j}^{(Q,Q)} + \Omega_{00,M_iM_j}^{(Q,C)} + \Omega_{00,M_iM_j}^{(C,C)} \right] t. \quad (11.61)$$

11.1.7 Solid-state NMR of static powders

In a solid sample with no tumbling the frequency components $\Omega_{I0,M_iM_j}^{(\Lambda)}$ are given by Equation 11.58, with all spatial ranks contributing. In a single crystal the evolution frequency depends on the crystal orientation through the pair of Euler angles $(\alpha_{\text{CL}}, \beta_{\text{CL}})$. The corresponding time-domain signal is $s(\alpha_{\text{CL}}, \beta_{\text{CL}}; t)$ given by

$$s(\alpha_{\text{CL}}, \beta_{\text{CL}}; t) = \frac{3}{2I(I+1)(2I+1)} \sum_{M=-I+1}^{+I} [I(I+1) - M(M-1)] \prod_{\Lambda} \exp(i\Omega_{I0,M-1,M}^{(\Lambda)}(\alpha_{\text{CL}}, \beta_{\text{CL}})t), \quad (11.62)$$

which gives a spectrum containing $2I$ distinct lines. The spectral positions of all these lines are, in general, orientation-dependent, varying with the crystal orientation.

If we have an ensemble of such crystallites with random orientations, such as in a solid powder, the total signal $s(t)$ is the average over all orientations $(\alpha_{\text{CL}}, \beta_{\text{CL}})$ of the individual signals $s(\alpha_{\text{CL}}, \beta_{\text{CL}}; t)$. For a large ensemble of crystallites this average is given by the double integral

$$s(t) = \frac{1}{4\pi} \int_0^{2\pi} d\alpha_{\text{CL}} \int_0^{\pi} d\beta_{\text{CL}} \sin(\beta_{\text{CL}}) s(\alpha_{\text{CL}}, \beta_{\text{CL}}; t). \quad (11.63)$$

The resulting NMR spectrum therefore contains a continuum of spectral intensity the width and shape of which is defined by the anisotropies ΔK and asymmetry parameters η^K of the interactions. Hence the anisotropic interactions result in resonance broadening, with the centre of mass of the resonance located at the isotropic frequency.

11.1.8 Solid-state NMR of spinning powders

In a spinning solid sample the Euler angles that specify the orientation of the crystal in the laboratory frame are time-dependent [322]. To recognise this we define the orientation of the PAF in the laboratory frame via three frame transformations, each of which is associated with its own set of Euler angles. As for static samples we first specify the orientation of the PAF Λ in the crystal-fixed frame C with the Euler angles $\Omega_{\Lambda C}$, which are fixed according to the geometry of the system. Secondly we specify the orientation of the crystal frame in a rotor-fixed frame R with Euler angles Ω_{CR} . This second set of angles changes as we change the orientation of the crystal in the sample container, and so are the angles we average over in a powder. Finally the orientation of the rotor frame relative to the laboratory frame L is defined by a set of time-dependent Euler angles $\Omega_{RL}(t)$. If the spinning axis of the rotor is inclined at a fixed angle β_{RL} relative to the external magnetic field, and the rotor spins at frequency ω_r from an initial angular position $\alpha_{RL}(0)$, this set of Euler angles is $\Omega_{RL}(t) = (\alpha_{RL}(0) + \omega_r t, \beta_{RL}, 0)$. We can now rewrite the frequencies $\Omega_{c,l_0,M_i M_j}^{(\Lambda)}(\gamma_{CR}; t)$ as Fourier series [323]

$$\Omega_{c,l_0,M_i M_j}^{(\Lambda)}(\gamma_{CR}; t) = \sum_{m=-l}^{+l} \omega_{c,lm,M_i M_j}^{(\Lambda)}(\gamma_{CR}) \exp(-im\omega_r t), \quad (11.64)$$

where the coefficients $\omega_{c,lm,M_i M_j}^{(\Lambda)}(\gamma_{CR})$ are frequencies that are given by the following expression:

$$\omega_{c,lm,M_i M_j}^{(\Lambda)}(\gamma_{CR}) = -\exp(-im\alpha_{RL}(0)) d_{m0}^{(l)}(\beta_{RL}) \sum_{\lambda} \frac{\Xi_{\lambda,M_i M_j}}{\hbar N_{\lambda 0}^{(\Lambda)}} \sum_{m''m'} \tilde{K}_{lm''}^{(\Lambda)} D_{m''m'}^{(l)}(\Omega_{\Lambda C}) D_{m'm}^{(l)}(\Omega_{CR}). \quad (11.65)$$

The frequency is periodic over the rotor period $\tau_r = 2\pi/\omega_r$. Note that, although the expression in Equation 11.64 is a sum of complex plane waves, the frequencies are in fact real. This is because the coefficients in Equation 11.65 satisfy $\omega_{c,l-m,M_i M_j}^{(\Lambda)}(\gamma_{CR}) = \omega_{c,lm,M_i M_j}^{(\Lambda)}(\gamma_{CR})^*$, and so the terms in the sum with $m \neq 0$ form conjugate pairs, and the remaining term with $m = 0$ is real. At this point it is useful to introduce the concept of a carousel c, which is a subset of crystallites that during the sample rotation occupy the same orientations but at different times. As shown by Levitt a single carousel contains crystallites with the same Euler angles α_{CR} and β_{CR} , but different γ_{CR} [324]. Therefore the dependence of the frequencies and phases on α_{CR} and β_{CR} is indicated with a subscript c, while the dependence on γ_{CR} is given explicitly. From Equation 11.65 the

γ_{CR} -dependence has the simple form:

$$\omega_{c,lm,M_iM_j}^{(\Lambda)}(\gamma_{\text{CR}}) = \omega_{c,lm,M_iM_j}^{(\Lambda)}(0) \exp(-im\gamma_{\text{CR}}). \quad (11.66)$$

In Equation 11.64 we see that a frequency component of spatial rank l comprises $2l + 1$ components m that oscillate at frequencies $-m\omega_r$. This proves to be important when calculating the signal from a powder sample. We see that the component with $m = 0$ is time-independent, and corresponds to a constant frequency. In particular we note that the time-independent coefficient with $m = 0$ is also independent of γ_{CR} .

The phase $\Phi_{c,l0,M_iM_j}^{(\Lambda)}(\gamma_{\text{CR}}; t_2, t_1)$ accrued during evolution under the Hamiltonian is calculated from the time integral of the frequency in Equation 11.64:

$$\Phi_{c,l0,M_iM_j}^{(\Lambda)}(\gamma_{\text{CR}}; t_2, t_1) = \omega_{c,l0,M_iM_j}^{(\Lambda)}(t_2 - t_1) + \sum_{m \neq 0} \frac{\omega_{c,lm,M_iM_j}^{(\Lambda)}(\gamma_{\text{CR}})}{-im\omega_r} [\exp(-im\omega_r t_2) - \exp(-im\omega_r t_1)]. \quad (11.67)$$

The phase is the sum of a part due to the time-independent frequency, and another part due to the time-dependent and periodic frequency. The complex exponential phase factor due to the latter is both periodic and cyclic, and so can be written as a complex Fourier series. The combined phase factor is then $\exp\left(i\Phi_{c,l0,M_iM_j}^{(\Lambda)}(\gamma_{\text{CR}}; t, 0)\right)$:

$$\exp\left(i\Phi_{c,l0,M_iM_j}^{(\Lambda)}(\gamma_{\text{CR}}; t, 0)\right) = \exp\left(i\omega_{c,\lambda,l0,M_iM_j}^{(\Lambda)} t\right) \sum_{\mu=-\infty}^{+\infty} A_{c,l0,M_iM_j}^{(\Lambda),(\mu)}(\gamma_{\text{CR}}) \exp\left[i\phi_{c,l0,M_iM_j}^{(\Lambda),(\mu)}(\gamma_{\text{CR}})\right] \exp[i\mu\omega_r t]. \quad (11.68)$$

The complex coefficients of the Fourier series have magnitudes $A_{c,l0,M_iM_j}^{(\Lambda),(\mu)}(\gamma_{\text{CR}})$ and phases $\phi_{c,l0,M_iM_j}^{(\Lambda),(\mu)}$. The evolution under the periodic part of the Hamiltonian therefore results in a spectral resonance that is split into a manifold of spinning sidebands. The μ th-order sideband appears at frequency $\omega_{c,\lambda,l0}^{(\Lambda)} + \mu\omega_r$, with an intensity $A_{c,l0,M_iM_j}^{(\Lambda),(\mu)}(\gamma_{\text{CR}})$ and a phase $\phi_{c,l0,M_iM_j}^{(\Lambda),(\mu)}(\gamma_{\text{CR}})$ that are given by

$$A_{c,l0,M_iM_j}^{(\Lambda),(\mu)}(\gamma_{\text{CR}}) \exp\left[i\phi_{c,l0,M_iM_j}^{(\Lambda),(\mu)}(\gamma_{\text{CR}})\right] = \frac{1}{\tau_r} \int_0^{\tau_r} \exp\left[i \sum_{m \neq 0} \frac{\omega_{c,lm,M_iM_j}^{(\Lambda)}(\gamma_{\text{CR}})}{-im\omega_r} [\exp(-im\omega_r t) - 1]\right] \exp[-i\mu\omega_r t] dt. \quad (11.69)$$

We can elucidate an important symmetry property relating to the dependence on γ_{CR} of the sideband intensities and phases, which was first described by Levitt [324]. Due to the γ_{CR} -dependence of the coefficients

given in Equation 11.66 we deduce that the frequency component at time t of a crystallite with angle γ_{CR} is equal to the frequency of a different crystallite with $\gamma_{\text{CR}} = 0$ evaluated at time $t + \gamma_{\text{CR}}/\omega_{\text{r}}$:

$$\Omega_{c,l_0,M_i,M_j}^{(\Lambda)}(\gamma_{\text{CR}}; t) = \Omega_{c,l_0,M_i,M_j}^{(\Lambda)}(0; t + \gamma_{\text{CR}}/\omega_{\text{r}}). \quad (11.70)$$

From this we can derive the following symmetry relation pertaining to the accrued phase:

$$\Phi_{c,l_0,M_i,M_j}^{(\Lambda)}(\gamma_{\text{CR}}; t, 0) = \Phi_{c,l_0,M_i,M_j}^{(\Lambda)}(0; t + \gamma_{\text{CR}}/\omega_{\text{r}}, 0) - \Phi_{c,l_0,M_i,M_j}^{(\Lambda)}(0; \gamma_{\text{CR}}/\omega_{\text{r}}, 0). \quad (11.71)$$

Substituting this into Equation 11.68 we obtain

$$\begin{aligned} & \exp\left(i\omega_{c,l_0,M_i,M_j}^{(\Lambda)} t\right) \sum_{\mu=-\infty}^{+\infty} A_{c,l_0,M_i,M_j}^{(\Lambda),(\mu)}(\gamma_{\text{CR}}) \exp\left[i\phi_{c,l_0,M_i,M_j}^{(\Lambda),(\mu)}(\gamma_{\text{CR}})\right] \exp[i\mu\omega_{\text{r}}t] \\ = & \exp\left(i\omega_{c,l_0,M_i,M_j}^{(\Lambda)} t\right) \sum_{\mu=-\infty}^{+\infty} A_{c,l_0,M_i,M_j}^{(\Lambda),(\mu)}(0) \exp\left[i\phi_{c,l_0,M_i,M_j}^{(\Lambda),(\mu)}(0)\right] \exp[i\mu(\omega_{\text{r}}t + \gamma_{\text{CR}})] \exp\left[-i \sum_{m \neq 0} \frac{\omega_{c,lm,M_i,M_j}^{(\Lambda)}(0)}{-im\omega_{\text{r}}} [\exp(-im\gamma_{\text{CR}}) - 1]\right], \end{aligned} \quad (11.72)$$

from which we see that the sideband intensities are independent of γ_{CR} , and the sideband phases have the following well-defined γ_{CR} dependence:

$$A_{c,l_0,M_i,M_j}^{(\Lambda),(\mu)}(\gamma_{\text{CR}}) = A_{c,l_0,M_i,M_j}^{(\Lambda),(\mu)}(0) \equiv A_{c,l_0,M_i,M_j}^{(\Lambda),(\mu)}, \quad (11.73)$$

$$\phi_{c,l_0,M_i,M_j}^{(\Lambda),(\mu)}(\gamma_{\text{CR}}) = \phi_{c,l_0,M_i,M_j}^{(\Lambda),(\mu)}(0) + \mu\gamma_{\text{CR}} - \sum_{m \neq 0} \frac{\omega_{c,lm,M_i,M_j}^{(\Lambda)}(0)}{-im\omega_{\text{r}}} [\exp(-im\gamma_{\text{CR}}) - 1]. \quad (11.74)$$

Henceforth we denote the sideband intensity as $A_{c,l_0,M_i,M_j}^{(\Lambda),(\mu)}$.

The signal component due to evolution under the Hamiltonian of a particular interaction for a single crystal is

$$s_c^{(\Lambda)}(\gamma_{\text{CR}}; t) = \frac{3}{2I(I+1)(2I+1)} \sum_{M=-I+1}^{+I} [I(I+1) - M(M-1)] \exp\left(i\Phi_{c,l_0,M-1,M}^{(\Lambda)}(\gamma_{\text{CR}}; t, 0)\right). \quad (11.75)$$

The signal due to the whole powder is conveniently calculated in two steps. Firstly we average the signal

$s_c^{(\Lambda)}(\gamma_{\text{CR}}; t)$ over all the γ_{CR} angles to obtain the signal $\bar{s}_c^{(\Lambda)}(t)$ from carousel c:

$$\bar{s}_c^{(\Lambda)}(t) = \frac{1}{2\pi} \int_0^{2\pi} d\gamma_{\text{CR}} s_c^{(\Lambda)}(\gamma_{\text{CR}}; t), \quad (11.76)$$

and secondly we average $\bar{s}_c^{(\Lambda)}$ over the remaining Euler angles α_{CR} and β_{CR} to obtain the signal from the whole powder $s^{(\Lambda)}(t)$:

$$s^{(\Lambda)}(t) = \frac{1}{4\pi} \int_0^{2\pi} d\alpha_{\text{CR}} \int_0^\pi d\beta_{\text{CR}} \sin(\beta_{\text{CR}}) \bar{s}_c^{(\Lambda)}(t). \quad (11.77)$$

For the first step we start from Equation 11.72 and expand the final phase factor as a Fourier series:

$$\begin{aligned} s_c^{(\Lambda)}(\gamma_{\text{CR}}; t) = & \frac{3}{2I(I+1)(2I+1)} \sum_{M=-I+1}^{+I} [I(I+1) - M(M-1)] \\ & \times \exp(i\omega_{c,\lambda,0,M-1,M}^{(\Lambda)} t) \sum_{\mu, \mu'=-\infty}^{+\infty} A_{c,0,M-1,M}^{(\Lambda),(\mu)} A_{c,0,M-1,M}^{(\Lambda),(\mu')} \exp[i(\phi_{c,0,M-1,M}^{(\Lambda),(\mu)}(0) - \phi_{c,0,M-1,M}^{(\Lambda),(\mu')}(0))] \exp[i\gamma_{\text{CR}}(\mu - \mu')] \exp[i\mu\omega_r t]. \end{aligned} \quad (11.78)$$

Following integration over the angle γ_{CR} the only terms that remain are those with $\mu = \mu'$, which gives the following time-domain signal for the carousel:

$$\bar{s}_c^{(\Lambda)}(t) = \frac{3}{2I(I+1)(2I+1)} \sum_{M=-I+1}^{+I} [I(I+1) - M(M-1)] \exp(i\omega_{c,\lambda,0,M-1,M}^{(\Lambda)} t) \sum_{\mu=-\infty}^{+\infty} [A_{c,0,M-1,M}^{(\Lambda),(\mu)}]^2 \exp[i\mu\omega_r t]. \quad (11.79)$$

All the sidebands have zero phase, and each has an intensity that is equal to the square of the corresponding single-crystal sideband intensity. Finally the signal from the whole powder is given by

$$s^{(\Lambda)}(t) = \frac{3}{2I(I+1)(2I+1)} \sum_{M=-I+1}^{+I} [I(I+1) - M(M-1)] \sum_{\mu=-\infty}^{+\infty} I_{\mu,M-1,M}(t) \exp[i\mu\omega_r t], \quad (11.80)$$

where the time-dependent sideband functions are given by

$$I_{\mu,M-1,M}(t) = \frac{1}{4\pi} \int_0^{2\pi} d\alpha_{\text{CR}} \int_0^\pi d\beta_{\text{CR}} \sin(\beta_{\text{CR}}) \exp(i\omega_{c,\lambda,0,M-1,M}^{(\Lambda)} t) [A_{c,0,M-1,M}^{(\Lambda),(\mu)}]^2. \quad (11.81)$$

The overall effect on the powder spectrum of the sample rotation is two-fold. Firstly the broad resonance due to the anisotropic interaction observed under static conditions is split into a manifold of spinning side-

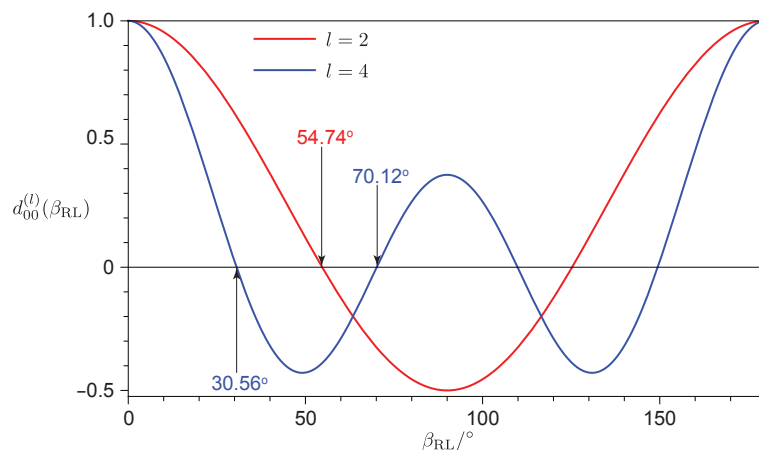


Figure 11.1: Plot of the reduced Wigner rotation matrix elements $d_{00}^{(2)}(\beta_{RL})$ and $d_{00}^{(4)}(\beta_{RL})$ as a function of the rotor angle β_{RL} . The angles at which the broadening due to the rank-two and rank-four anisotropic interactions is completely removed by spinning are indicated by arrows.

bands. Secondly the linewidth of each spinning sideband is given by the range of the static frequencies $\omega_{c,l,0}^{(\Lambda)}$ that we obtain following powder averaging. From Equation 11.65 we see that these frequency components are proportional to the reduced Wigner matrix elements $d_{00}^{(l)}(\beta_{RL})$. For frequencies with $l = 0$ this factor is $d_{00}^{(0)}(\beta_{RL}) = 1$, indicating that these frequencies are unaffected by the sample rotation. This is exactly as expected as these frequencies are due to spatially isotropic interactions that are, by definition, independent of crystallite orientation. These frequencies always appear in the NMR spectrum, but do not cause any orientation-dependent broadening of the resonance. For anisotropic frequencies of rank $l = 2$ the scaling factor is:

$$d_{00}^{(2)}(\beta_{RL}) = (3 \cos^2(\beta_{RL}) - 1) / 2. \quad (11.82)$$

This factor, plotted as a function of β_{RL} in Figure 11.1, is zero if we set the angle of the rotor axis β_{RL} to the magic angle, which is given by $\tan^{-1}(\sqrt{2}) = 54.74^\circ$ [322, 325]. Hence magic-angle spinning (MAS) completely removes the broadening of the spinning-sidebands from rank-two interactions.

Interactions of spatial rank $l = 4$ have static frequencies that are scaled down by

$$d_{00}^{(4)}(\beta_{RL}) = (35 \cos^4(\beta_{RL}) - 30 \cos^2(\beta_{RL}) + 3) / 8. \quad (11.83)$$

This factor is also plotted as a function of rotor angle in Figure 11.1. Spinning at the magic angle does not completely remove these frequency components, which are instead scaled down by a factor of $-7/18$. Hence the broadening due to this spread of frequencies is decreased by the same factor. The matrix element $d_{00}^{(4)}(\beta_{\text{RL}})$ does have two angles at which it is zero, namely 30.56° and 70.12° , and inclining the rotor axis at either of these two angles has the result of completely removing the broadening due to rank-four interactions. However spinning at either of these two angles does not suppress the broadening due to the rank-two interactions, which are then scaled down by factors of 0.61 and -0.33 respectively.

11.2 The shift and shift anisotropy in paramagnetic NMR

11.2.1 The chemical shielding frequencies

The Hamiltonian describing the chemical shielding interaction, truncated to first order in the secular approximation, is given by Equation 2.94 and reproduced here for convenience:

$$\hat{H} = -\hbar\omega_0 \left(-\sqrt{\frac{1}{3}}\sigma_{00} + \sqrt{\frac{2}{3}}\sigma_{20} \right) \hat{I}_z. \quad (11.84)$$

The terms in parentheses combine to give the chemical shielding, the irreducible spherical tensor components of which transform under a spatial rotation according to

$$\sigma_{lm} = \sum_{m'=-l}^{+l} \tilde{\sigma}_{lm'} D_{m'm}^{(l)}(\alpha_{\text{PL}}, \beta_{\text{PL}}, \gamma_{\text{PL}}). \quad (11.85)$$

The tensor is given in its most general form, without reference to the various contributions that are specific to the metal ion under consideration, or to the chemical environment. This enables us to highlight the features of the spectrum that are common to all paramagnetic systems. We do not consider the second-order shielding interaction, as it is predicted to be negligible compared to the other second-order interactions we have discussed.

From Table 11.2 we can write down the isotropic and anisotropic frequencies, $\Omega_{\text{iso},M_iM_j}$ and $\Omega_{\text{SA},M_iM_j}$,

under which a coherence represented by the basis operator $|IM_i\rangle\langle IM_j|$ evolves, as:

$$\Omega_{\text{iso},M_iM_j} = -p_{M_iM_j}\omega_0\sigma_{\text{iso}}, \quad (11.86)$$

$$\Omega_{\text{SA},M_iM_j} = -p_{M_iM_j}\sqrt{\frac{2}{3}}\omega_0\sigma_{20}. \quad (11.87)$$

For any nuclear spin I all the observable coherences have the same coherence order $p_{M_iM_j} = -I$, and so all $2I$ components in Equation 11.57 evolve at the same isotropic and anisotropic frequencies, which we denote Ω_{iso} and Ω_{SA} . If the chemical shielding is the only interaction present this means that the $2I$ components appear at the same position in the NMR spectrum, and so only a single distinct resonance is observed. This section therefore provides a complete description of the paramagnetic effects both for nuclear spins-1/2, and for quadrupolar nuclei in cubic environments for which $C_Q = 0$. To complete the picture for quadrupolar nuclei in non-cubic environments we also need to consider the quadrupolar interaction.

11.2.2 Solution NMR

We first consider a paramagnetic complex in an isotropic solution. The general features of solution NMR have been reviewed many times and can be found, for example, in the textbooks by Ernst et al [257], Levitt [1], and Keeler [254].

In solution we have seen that only the isotropic interactions remain during molecular tumbling. Therefore the only shielding contribution is the isotropic frequency $\Omega_{\text{iso}} = -\omega_0\sigma_{\text{iso}}$, which contains the local contributions due to the hyperfine coupling to the paramagnetic centres, including contact and pseudo-contact terms.

The lineshape and linewidth in the spectrum originate from two different sources: incoherent homogeneous, and inhomogeneous¹. The former is due to the stochastic fluctuation of the local field experienced by the nucleus, which gives rise to relaxation as discussed in chapters 8 and 9, whereas the latter is due to the distribution of Larmor frequencies over the sample volume. In the absence of inhomogeneous broadening the

¹Here we note that our usage of the terms 'homogeneous' and 'inhomogeneous' differs from the usage by Maricq and Waugh [322]. We use the terms to refer to the sources of line broadening in the spectrum, whilst Maricq and Waugh use the same terms to refer to the commutation properties of the Hamiltonians of spin interactions. Nevertheless, we note that there is a correspondence between the conventions. For instance the shift interaction is term inhomogeneous by Maricq and Waugh, and a distribution of shifts leads to inhomogeneous broadening according to the convention used here; homonuclear dipolar coupling interactions are homogeneous interactions, and lead to coherent homogeneous broadening in the spectrum of solids. The only contribution to spectral broadening not considered by Maricq and Waugh is due to relaxation, which is homogeneous.

time-domain signal, referred to as the free-induction decay (FID), $s(t)$ due to a single resonance is

$$s(t) = s_e^{\text{hom}}(t) \exp(i\Omega_{\text{iso}}t), \quad (11.88)$$

where $s_e^{\text{hom}}(t)$ is the envelope function describing the signal decay due to relaxation. The spectrum $S(\omega)$ is the Fourier transform of $s(t)$, which is given by

$$S(\omega) = \int_0^{\infty} dt s(t) \exp(-i\omega t). \quad (11.89)$$

As we saw in chapters 8 and 9, for a single spin $I = 1/2$ nucleus in the Redfield relaxation limit we can model the relaxation envelope function as a mono-exponential decay with a time constant T_2 , giving the following FID:

$$s(t) = \exp(i\Omega_{\text{iso}}t) \exp(-t/T_2). \quad (11.90)$$

For quadrupolar nuclei with $I > 1$ the decay is in general multi-exponential. However we still model it here using a mono-exponential decay function that is parameterized by an effective T_2 . For small paramagnetic complexes in solution, the T_2 relaxation time constant is given by the Solomon–Bloembergen–Morgan expression in Equation 8.108. The T_2 time constants of large biomolecules, on the other hand, are dominated by Curie relaxation processes, and T_2 is given by Equation 8.152. The Fourier transform of this function gives a spectrum with the Lorentzian lineshape:

$$S(\omega) = L_A(T_2; \omega - \Omega_{\text{iso}}) + iL_D(T_2; \omega - \Omega_{\text{iso}}). \quad (11.91)$$

The real and imaginary parts of the spectrum are the absorption-mode and dispersion-mode Lorentzian functions $L_A(T; \omega)$ and $L_D(T; \omega)$, which are given by

$$L_A(T; \omega) = \frac{T}{1 + \omega^2 T^2}, \quad (11.92)$$

$$L_D(T; \omega) = -\frac{\omega T^2}{1 + \omega^2 T^2}. \quad (11.93)$$

In high-resolution NMR we examine only the real part of the spectrum with the absorption-mode lineshape.

The spectrum therefore contains a single, sharp peak at position Ω_{iso} and with a linewidth (defined as the full-width at half-maximum, FWHM) of $2/T_2$ rad s⁻¹. An example is shown in Figure 11.2 (a).

In many cases the inhomogeneous broadening cannot be neglected, with notable contributions from the inhomogeneity of the applied magnetic field B_0 due to instrumental limitations, and a BMS contribution due to the non-spherical shape of the sample container, as discussed in section 10.2. The effect of the container shape, usually cylindrical, on the spectral resolution has been studied at length [312, 326, 327]. In the presence of inhomogeneity of the local magnetic field, the offset frequency becomes a function of position \mathbf{r} , and so can be written as $\Omega(\mathbf{r})$. We define it in terms of the position-dependent deviation $\Delta\Omega(\mathbf{r})$ from the nominal offset Ω_{iso} :

$$\Omega(\mathbf{r}) = \Omega_{\text{iso}} + \Delta\Omega(\mathbf{r}). \quad (11.94)$$

The FID is then given by averaging over all positions to give

$$s(t) = s_e^{\text{inhom}}(t) [\exp(i\Omega_{\text{iso}}t) \exp(-t/T_2)], \quad (11.95)$$

which is the product of the inhomogeneous envelope function $s_e^{\text{inhom}}(t)$, and, in brackets, the FID in the absence of inhomogeneous effects. The envelope function depends on the function $f(\mathbf{r})$ that describes the distribution of $\Delta\Omega(\mathbf{r})$ and, assuming the ideal case of constant signal per unit volume inside the active volume and zero signal outside, is given by an integral over the sample volume V :

$$s_e^{\text{inhom}}(t) = \frac{1}{V} \iiint_V d^3r f(\mathbf{r}) \exp(i\Delta\Omega(\mathbf{r})t). \quad (11.96)$$

The inhomogeneous spectral lineshape $S_e^{\text{inhom}}(\omega)$ is defined as the Fourier transform of $s_e^{\text{inhom}}(t)$:

$$S_e^{\text{inhom}}(\omega) = \int_0^\infty dt s_e^{\text{inhom}}(t) \exp(-i\omega t). \quad (11.97)$$

The FID in Equation 11.95 is the product of two functions, and so the resulting spectrum $S(\omega)$ is simply the convolution of the inhomogeneous linewidth function $S_e^{\text{inhom}}(\omega)$ and the Lorentzian in Equation 11.91:

$$S(\omega) = 2\pi [L_A(T_2; \omega - \Omega_{\text{iso}}) + iL_D(T_2; \omega - \Omega_{\text{iso}})] * S_e^{\text{inhom}}(\omega), \quad (11.98)$$

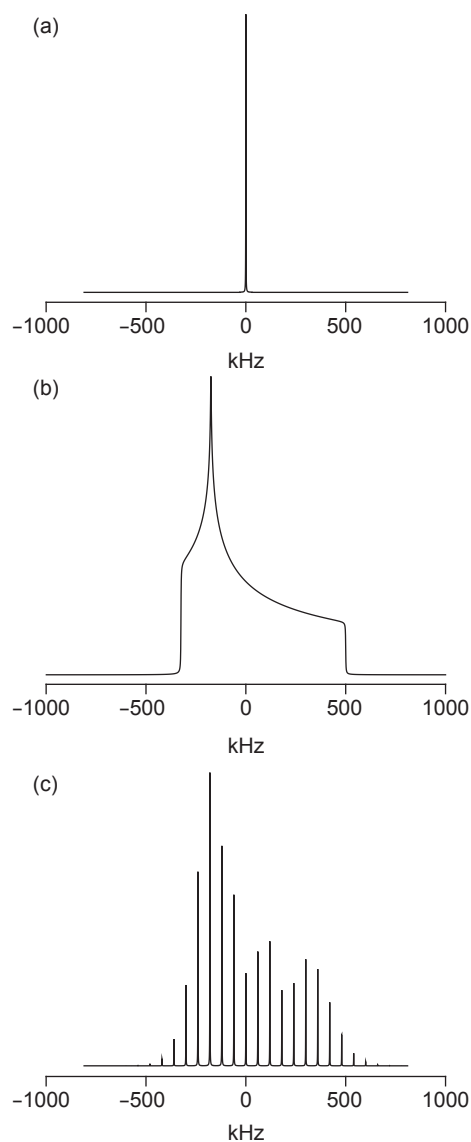


Figure 11.2: Simulated spectra of paramagnetic systems subject to a shielding interaction, and in the absence of inhomogeneous broadening. This picture is complete for spins-1/2, and quadrupolar nuclei in cubic environments where $C_Q = 0$. The high-resolution, isotropic solution spectrum is shown in (a), showing a single peak at the isotropic offset. A powder sample in the solid-state gives the classic CSA powder pattern in (b), which splits into a series of spinning sidebands under MAS, as shown in (c). The chemical shielding parameters are $-\omega_0 \Delta\sigma^S / 2\pi = 500$ kHz, and $\eta^S = 0.3$, and the frequency is measured relative to the isotropic offset Ω_{iso} . The MAS spectrum was simulated at 60 kHz MAS.

where the convolution of two functions is indicated by the *, and is defined as

$$(f * g)(\omega) = \int_{-\infty}^{+\infty} f(x)g(\omega - x)dx. \quad (11.99)$$

The overall spectral lineshape is therefore a mixture of the Lorentzian from the homogeneous decay, and the inhomogeneous lineshape. It is common to assume that the inhomogeneous lineshape is a Gaussian, or Lorentzian. In the latter case we can define an overall rate of signal decay which is mono-exponential, and characterised by a time constant T_2^* , which is equal to

$$\frac{1}{T_2^*} = \frac{1}{T_2} + \frac{1}{T_2^\dagger}, \quad (11.100)$$

where T_2^\dagger is the time constant associated with the mono-exponential inhomogeneous decay.

11.2.3 Solid-state NMR of static powders

The case of static powder solids is more complex than isotropic solutions, as we must now explicitly consider the effect of the anisotropic shielding terms on the form of the spectrum. The Hamiltonian in the absence of BMS effects was derived in section 2.6. For a crystallite q in which the PAF of the shielding tensor has an orientation relative to the crystal frame given by the Euler angles $(\alpha_{PC}, \beta_{PC}, \gamma_{PC})$, the Hamiltonian is given by Equation 2.109 [194]:

$$\hat{H} = \hbar (\Omega_{\text{iso}} + \Omega_{\text{SA}}(\Omega_{\text{PC}}, \Omega_{\text{CL}})) \hat{I}_z, \quad (11.101)$$

where we have written the isotropic offset $\Omega_{\text{iso}} = -\omega_0\sigma_{\text{iso}}$ as before, and $\Omega_{\text{SA}}(\Omega_{\text{PC}}, \Omega_{\text{CL}})$ is the anisotropic contribution to the offset of crystallite q , and is given in terms of the anisotropic shielding $\sigma_{\text{SA}}(\Omega_{\text{PC}}, \Omega_{\text{CL}})$:

$$\Omega_{\text{SA}}(\Omega_{\text{PC}}, \Omega_{\text{CL}}) = -\omega_0\sigma_{\text{SA}}(\Omega_{\text{PC}}, \Omega_{\text{CL}}), \quad (11.102)$$

$$\sigma_{\text{SA}}(\Omega_{\text{PC}}, \Omega_{\text{CL}}) = \frac{1}{2}\Delta\sigma \left\{ 3 \cos^2(\beta_{\text{PL}}) - 1 - \eta \cos(2\alpha_{\text{PL}}) \sin^2(\beta_{\text{PL}}) \right\}. \quad (11.103)$$

We have written $\sigma_{\text{SA}}(\Omega_{\text{PC}}, \Omega_{\text{CL}})$ in terms of the Euler angles $(\alpha_{\text{PL}}, \beta_{\text{PL}})$ that describe the overall rotation from the PAF to the laboratory frame via the crystal frame. Note that $\sigma_{\text{SA}}(\Omega_{\text{PC}}, \Omega_{\text{CL}})$, and therefore $\Omega_{\text{SA}}(\Omega_{\text{PC}}, \Omega_{\text{CL}})$, depends on neither γ_{PL} nor γ_{CL} . The homogeneous decay of the corresponding coherence during acquisition

now depends on *two* processes: incoherent homogeneous, and coherent homogeneous. The former process is due to transverse relaxation, characterised by the time constant T_2 as described in chapters 8 and 9, and the latter is a non-random dephasing due to the extended network of dipolar couplings in each crystallite [194]. The coherent homogeneous decay is commonly assumed to be mono-exponential and characterised by a time constant T_2^{coh} . The time constant that describes the overall homogeneous decay is T_2' , and is calculated from the following expression:

$$\frac{1}{T_2'} = \frac{1}{T_2} + \frac{1}{T_2^{\text{coh}}}. \quad (11.104)$$

The FID of the single crystallite following excitation $s(\Omega_{\text{PC}}, \Omega_{\text{CL}}; t)$ also depends on the same Euler angles, and has a form that is similar to the FID of an isotropic solution, with the difference that the offset includes the anisotropic term, and the decay time constant is T_2' and not T_2 :

$$s(\Omega_{\text{PC}}, \Omega_{\text{CL}}; t) = \exp(i\Omega_{\text{iso}}t) \exp(i\Omega_{\text{SA}}(\Omega_{\text{PC}}, \Omega_{\text{CL}})t) \exp(-t/T_2'). \quad (11.105)$$

The Fourier transform yields the spectrum, which contains a Lorentzian peak $S(\Omega_{\text{PC}}, \Omega_{\text{CL}}; \omega)$ at position $\Omega_{\text{iso}} + \Omega_{\text{SA}}(\Omega_{\text{PC}}, \Omega_{\text{CL}})$, with a linewidth equal to $2/T_2'$ rad s⁻¹. The real part of the spectrum is

$$S(\Omega_{\text{PC}}, \Omega_{\text{CL}}; \omega) = L_A(T_2'; \omega - \Omega_{\text{iso}} - \Omega_{\text{SA}}(\Omega_{\text{PC}}, \Omega_{\text{CL}})). \quad (11.106)$$

In order to obtain the form of the spectrum of the complete powder we must average the single-crystallite spectrum $S(\Omega_{\text{PC}}, \Omega_{\text{CL}}; \omega)$ over all possible orientations, giving

$$S(\omega) = \frac{1}{4\pi} \int_0^{2\pi} d\alpha_{\text{CL}} \int_0^\pi \sin(\beta_{\text{CL}}) d\beta_{\text{CL}} [L_A(T_2'; \omega - \Omega_{\text{iso}} - \Omega_{\text{SA}}(\Omega_{\text{PC}}, \Omega_{\text{CL}})) + iL_D(T_2'; \omega - \Omega_{\text{iso}} - \Omega_{\text{SA}}(\Omega_{\text{PC}}, \Omega_{\text{CL}}))]. \quad (11.107)$$

The powder spectrum has a width that is proportional to the SA $|\omega_0 \Delta\sigma^S|$, as shown by the example in Figure 11.2 (b). We note that neither the FID nor the spectrum of the powder depends on the Euler angles Ω_{PC} . This is a result of all crystallite orientations being represented in the spectrum, so that the information about the absolute orientation of the PAF in the crystal frame is lost. One consequence of this is the well-known observation that one cannot extract the absolute values of Ω_{PC} from the spectrum of a powder sample.

Hitherto we have neglected the inhomogeneous broadening we would expect from the BMS effects. We

have shown that these effects can be partitioned into IBMS and ABMS contributions. The former gives a purely anisotropic offset $\Omega_{SA}^{IBMS}(\Omega_{PI,C}(q), \Omega_{CL}, q)$, whilst the latter gives both isotropic and anisotropic contributions $\Omega_{iso}^{ABMS}(q)$ and $\Omega_{SA}^{ABMS}(\Omega_{PA,C}(q), \Omega_{CL}, q)$. They are given in terms of the corresponding chemical shieldings:

$$\Omega_{SA}^{IBMS}(\Omega_{PI,C}(q), \Omega_{CL}, q) = -\omega_0 \sigma_{SA}^{IBMS}(\Omega_{PI,C}(q), \Omega_{CL}, q), \quad (11.108)$$

$$\Omega_{iso}^{ABMS}(q) = -\omega_0 \sigma_{iso}^{ABMS}(q), \quad (11.109)$$

$$\Omega_{SA}^{ABMS}(\Omega_{PA,C}(q), \Omega_{CL}, q) = -\omega_0 \sigma_S^{ABMS}(\Omega_{PA,C}(q), \Omega_{CL}, q), \quad (11.110)$$

where $\Omega_{PI,C}$ and $\Omega_{PA,C}$ give the orientations of the IBMS and ABMS PAFs in the crystal reference frame. Here we have defined a parameter q which describes the variation of the isotropic shift, SA, asymmetry, and Euler angles giving the orientation of the BMS tensor in the crystal frame. If we assume that the crystallites are spherical, and make the somewhat unrealistic assumption that they are held in a spherical sample container, the BMS shielding contribution to a particular crystallite depends only on the dipolar coupling interaction with the *neighbouring* crystallites, and has no part from the internal bulk susceptibility. Hence the BMS shielding of the crystallite under consideration depends only on the configuration of the surrounding crystallites, which is defined by q .

In order to calculate the spectrum from the complete sample, we average over all the crystallites in two steps: firstly for all crystallites with the same configuration parameter q we average over the Euler angles Ω_{CL} ; secondly we average over the configurations q . If we define the total BMS frequency $\Delta\Omega(\Omega_{PI,C}(q), \Omega_{PA,C}(q), \Omega_{CL}, q)$ as

$$\Delta\Omega(\Omega_{PI,C}(q), \Omega_{PA,C}(q), \Omega_{CL}, q) = \Omega_{SA}^{IBMS}(\Omega_{PI,C}(q), \Omega_{CL}, q) + \Omega_{iso}^{ABMS}(q) + \Omega_{SA}^{ABMS}(\Omega_{PA,C}(q), \Omega_{CL}, q), \quad (11.111)$$

we can write the FID $s(q, \Omega_{CL}; t)$ from a particular crystallite orientation with a particular BMS configuration as

$$s(q, \Omega_{CL}; t) = \exp(i\Omega_{iso}t) \exp(i\Omega_{SA}(\Omega_{PI,C}, \Omega_{CL})t) \exp(i\Delta\Omega(\Omega_{PI,C}(q), \Omega_{PA,C}(q), \Omega_{CL}, q)t) \exp(-t/T_2'). \quad (11.112)$$

The signal from the whole powder is then

$$S(\omega) = \frac{1}{4\pi} \int_0^{2\pi} d\alpha_{\text{CL}} \int_0^\pi \sin(\beta_{\text{CL}}) d\beta_{\text{CL}} \frac{1}{N_q} \int dq f(q) s(q, \Omega_{\text{CL}}; t), \quad (11.113)$$

where $f(q)$ is a function describing the distribution of configurations, and N_q is a normalization factor.

The integral over the configurations q only affects the phase factor $\exp(i\Delta\Omega(\Omega_{\text{PL,C}}(q), \Omega_{\text{PA,C}}(q), \Omega_{\text{CL}}, q)t) \exp(-t/T_2')$. At this point, to simplify the discussion, we make the simplifying assumption that the integral over q is independent of the crystallite orientation Ω_{CL} , which is equivalent to stating that the inhomogeneous broadening depends only on the surrounding crystallites. This assumption is justified if the sum over the configurations contains a complete average over the orientation of the PAFs in the crystal frame, i.e. an average over all values of $\Omega_{\text{PL,C}}(q)$ and $\Omega_{\text{PA,C}}(q)$. If this is the case the integral over q is independent of the Euler angles Ω_{CL} , in the same way that the integral over Ω_{CL} in the absence of inhomogeneous broadening is independent of Ω_{PC} . We can then define a BMS decay envelope function $s_e^{\text{BMS}}(t)$ that describes the coherent decay due to the inhomogeneous broadening. This envelope function has a similar form to that for the isotropic solution:

$$s_e^{\text{BMS}}(t) = \frac{1}{N_q} \int dq f(q) \exp(i\Delta\Omega(\Omega_{\text{PL,C}}(q), \Omega_{\text{PA,C}}(q), \Omega_{\text{CL}}, q)t). \quad (11.114)$$

The Fourier transform of the envelope function $S_e^{\text{BMS}}(\omega)$ is defined in the same way as in Equation 11.97.

The FID from the sample is

$$s(t) = s_e^{\text{BMS}}(t) \frac{1}{4\pi} \int_0^{2\pi} d\alpha_{\text{CL}} \int_0^\pi \sin(\beta_{\text{CL}}) d\beta_{\text{CL}} \exp(i\Omega_{\text{iso}}t) \exp(i\Omega_{\text{SA}}(\Omega_{\text{PC}}, \Omega_{\text{CL}})t) \exp(-t/T_2'), \quad (11.115)$$

which is the product of the FID in the absence of the BMS, and the BMS envelope function. The overall spectrum $S(\omega)$ is then the convolution of $S_e^{\text{BMS}}(\omega)$ with the expression in Equation 11.107:

$$S(\omega) = 2\pi \left[\frac{1}{4\pi} \int_0^{2\pi} d\alpha_{\text{CL}} \times \int_0^\pi \sin(\beta_{\text{CL}}) d\beta_{\text{CL}} [L_A(T_2'; \omega - \Omega_{\text{iso}} - \Omega_{\text{SA}}(\Omega_{\text{PC}}, \Omega_{\text{CL}})) + iL_D(T_2'; \omega - \Omega_{\text{iso}} - \Omega_{\text{SA}}(\Omega_{\text{PC}}, \Omega_{\text{CL}}))] \right] * S_e^{\text{BMS}}(\omega), \quad (11.116)$$

The BMS lineshape has a complicated form which is non-trivial to model since it ultimately requires a

description of how particles of different sizes and shapes are packed in a compressed powder [150, 328]. It may, however, be approximated as a Gaussian, for which case an example of the resulting overall spectrum is shown in Figure 11.3 (a). It can be seen that the inhomogeneous broadening smears out the distinctive spectral features of the classic SA powder pattern. Some notable experimental examples of this lineshape in static solid-state NMR spectra include the battery samples presented by Kim et al [53].

11.2.4 Solid-state NMR of spinning powders

Under MAS conditions the anisotropic frequency is time-dependent, periodic, and cyclic over the rotor period τ_r . Therefore, as we have seen, the single-crystal FID $s_c(\gamma_{\text{CR}}; t)$ is split into a series of sideband contributions:

$$s_c(\gamma_{\text{CR}}; t) = \exp(i\Omega_{\text{iso}}t) \exp(i\Phi_c^{\text{SA}}(\gamma_{\text{CR}}; t, 0)) \exp(-t/T_2') \quad (11.117)$$

$$= \exp(i\Omega_{\text{iso}}t) \exp(-t/T_2') \sum_{m=-\infty}^{+\infty} A_c^{(m)} \exp(i(\phi_c^{(m)}(\gamma_{\text{CR}}) + m\omega_r t)). \quad (11.118)$$

We note that T_2' depends on the MAS frequency, since faster spinning has the effect of weakening the extended dipolar coupling network, thus reducing the rate of coherent dephasing. The single-crystal sideband amplitudes and phases are denoted $A_c^{(m)}$ and $\phi_c^{(m)}(\gamma_{\text{CR}})$. Following Fourier transformation we obtain the spinning sideband manifold in the spectrum:

$$S_c(\gamma_{\text{CR}}; \omega) = \sum_{m=-\infty}^{+\infty} A_c^{(m)} \exp(i(\phi_c^{(m)}(\gamma_{\text{CR}}))) [L_A(T_2'; \omega - \Omega_{\text{iso}} - m\omega_r) + iL_D(T_2'; \omega - \Omega_{\text{iso}} - m\omega_r)]. \quad (11.119)$$

The orientation dependence is contained wholly within the sideband amplitudes $A_c^{(m)}$ and phases $\phi_c^{(m)}(\gamma_{\text{CR}})$. The former depend only on α_{RL} and β_{RL} , whereas the latter depend on all three angles. The spectrum of the whole powder is therefore obtained by averaging the complex sideband coefficients over all orientations. The resulting spectrum is

$$S(\omega) = \sum_{m=-\infty}^{+\infty} I^{(m)} [L_A(T_2'; \omega - \Omega_{\text{iso}} - m\omega_r) + iL_D(T_2'; \omega - \Omega_{\text{iso}} - m\omega_r)], \quad (11.120)$$

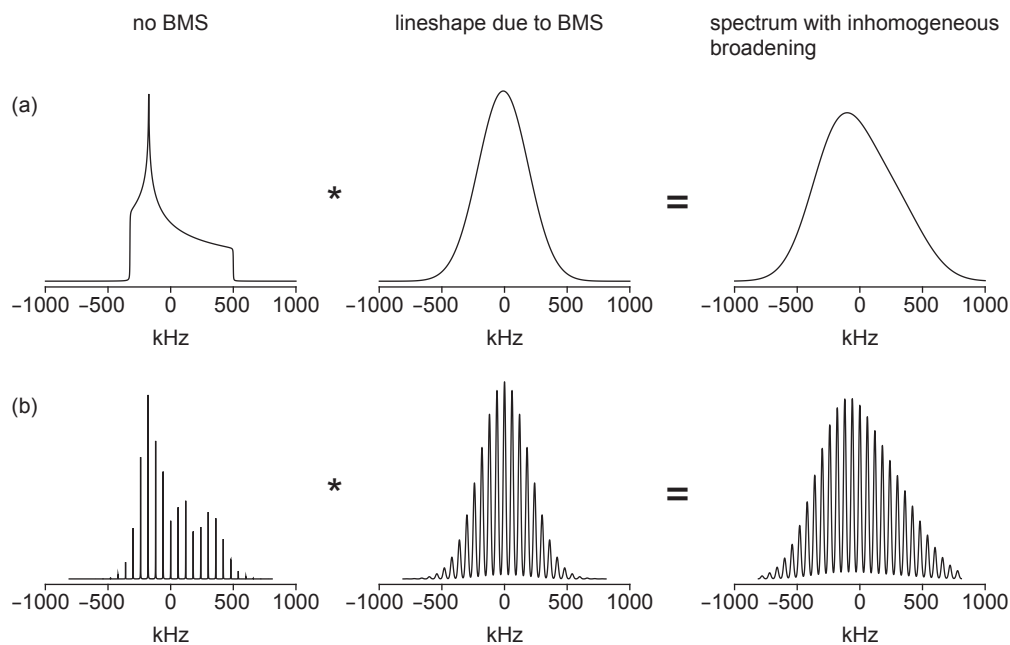


Figure 11.3: The effect of the inhomogeneous BMS broadening on static and MAS NMR spectra of a paramagnetic powder. The static spectra are shown in (a), and the MAS spectra are shown in (b). In both cases we partition the spectrum into two parts. The first is the spectrum in the absence of BMS effects, which exhibits either the classic CSA powder pattern, or the spinning-sideband manifold. The second shows the spectral lineshape due solely to BMS effects which, for the static case can be assumed to be Gaussian, and for the MAS case to be a manifold of spinning sidebands, each with a Gaussian lineshape. In both cases the final spectrum is given by the convolution of these two parts. The chemical shielding parameters are $-\omega_0\Delta\sigma^S/2\pi = 500$ kHz, and $\eta^S = 0.3$, and the frequency is measured relative to the isotropic offset Ω_{iso} . The MAS spectrum was simulated at 60 kHz MAS. For the static case the Gaussian function has a mean of 0 kHz and a standard deviation of 200 kHz. For the MAS case each individual sideband is a Gaussian function with a standard deviation of 10 kHz, and the intensities of the Gaussians in the manifold are weighted by a Gaussian function with a standard deviation of 200 kHz.

where the m th-order sideband intensity $I^{(m)}$ is equal to

$$I^{(m)} = \frac{1}{4\pi} \int_0^{2\pi} d\alpha_{\text{CR}} \int_0^\pi \sin(\beta_{\text{CR}}) d\beta_{\text{CR}} [A_c^{(m)}]^2. \quad (11.121)$$

An example of the spectrum obtained by MAS is shown in Figure 11.2 (c), which has been simulated using the same SA parameters as the spectrum of the static powder in Figure 11.2 (b).

The effect of the IBMS and ABMS on the inhomogeneous broadening can be considered in a similar way as for the static powder, but with the inclusion of the MAS. The isotropic ABMS shift frequency is labelled $\Omega_{\text{iso}}^{\text{ABMS}}(q)$, and we group together the IBMS and ABMS contributions to the SA to give the total BMS anisotropic frequency $\Omega_c^{\text{BMS,SA}}(q, \gamma_{\text{CR}}; t)$. During evolution under MAS the observable coherences accrue a periodic phase $\Phi_c^{\text{BMS,SA}}(q, \gamma_{\text{CR}}; t, 0)$ due to the evolution of the BMS SA. We compute the complete FID by averaging over the Euler angles γ_{CR} all the contributions from crystallites with the same q , and then averaging over q . As for the static case, we assume that the average of the BMS phase factors over q results in a BMS time-domain envelope function that is the same for all crystallite orientations Ω_{CR} . This function is then given by

$$\begin{aligned} s_e^{\text{BMS}}(t) &= \frac{1}{N_q} \int dq f(q) \exp(i\Omega_{\text{iso}}^{\text{ABMS}}(q)t) \exp(i\Phi_c^{\text{BMS,SA}}(q, \gamma_{\text{CR}}; t, 0)) \\ &= \frac{1}{N_q} \int dq f(q) \exp(i\Omega_{\text{iso}}^{\text{ABMS}}(q)t) \\ &\quad \times \sum_{m=-\infty}^{+\infty} B_c^{(m)}(q) \exp(i(\xi_c^{(m)}(q, \gamma_{\text{CR}}) + m\omega_r t)), \end{aligned} \quad (11.122)$$

where we have expanded the periodic phase factor due to the BMS SA as a Fourier series with sideband intensities $B_c^{(m)}(q)$ and phases $\xi_c^{(m)}(q, \gamma_{\text{CR}})$. We are able to write $s_e^{\text{BMS}}(t)$ in the following form:

$$s_e^{\text{BMS}}(t) = \sum_{m=-\infty}^{+\infty} s_e^{(m)}(t) \exp(im\omega_r t), \quad (11.123)$$

where

$$s_e^{(m)}(t) = \frac{1}{N_q} \int dq f(q) \exp(i\Omega_{\text{iso}}^{\text{ABMS}}(q)t) B_c^{(m)}(q) \exp(i(\xi_c^{(m)}(q, \gamma_{\text{CR}}))) \quad (11.124)$$

are sideband functions that decay with time. The envelope function is therefore a spinning-sideband manifold,

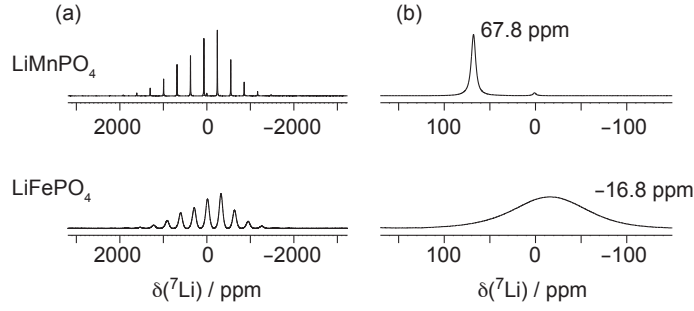


Figure 11.4: Solid-state ${}^7\text{Li}$ MAS NMR spectra of the cathode materials LiTMPO_4 , TM = Mn, Fe. For both spectra the full spinning-sideband manifold is shown in (a), and an expansion of the centreband is shown in (b). The MAS frequency is 60 kHz.

in which each sideband experiences an inhomogeneous decay. The intensities $B_c^{(m)}(q)$ only affect the overall magnitudes of the $s_e^{(m)}(t)$, whereas $\Omega_{\text{iso}}^{\text{ABMS}}(q)$ changes the overall rate of inhomogeneous decay. Therefore all the sidebands exhibit the same inhomogeneous broadening. The Fourier transform of $s_e^{\text{BMS}}(t)$ gives the function $S_e^{\text{BMS}}(\omega)$ which specifies the inhomogeneous broadening that we observe in the spinning-sideband manifold of the spectrum. This function has the form

$$S_e^{\text{BMS}}(\omega) = 4\pi^2 \sum_{m=-\infty}^{+\infty} S_e^{(m)}(\omega) * \delta(\omega - m\omega_r). \quad (11.125)$$

The delta functions $\delta(\omega - m\omega_r)$ in Equation 11.125 are the Fourier transforms of the complex exponentials $\exp(im\omega_r t)$, and the lineshape functions $S_e^{(m)}(\omega)$ are the Fourier transforms of the decay functions $s_e^{(m)}(t)$. The spectral inhomogeneous broadening function $S_e^{\text{BMS}}(\omega)$ therefore comprises a series of spinning sidebands whose effect is to broaden the spinning sidebands in the final spectrum, which is the convolution of Equations 11.120 and 11.125, as shown in Figure 11.3 (b) for Gaussian broadening. In addition to the ABMS broadening of the individual sidebands, we also see a perturbation of the sideband intensities from the ‘nominal’ intensities we would expect from a simple SA. The distribution of intensities shows a Gaussian distribution superimposed upon the nominal pattern.

The predicted form of the spinning-sideband manifold in the presence of BMS effects is illustrated with the solid-state ${}^7\text{Li}$ MAS NMR spectra of LiMnPO_4 and LiFePO_4 shown in Figure 11.4 [30]. Both transition metals are in the +2 oxidation state and occupy distorted octahedral sites as part of a TMO_6 unit, where TM refers to the transition metal, and have high-spin electronic configurations. The metal ion Mn^{2+} has

the octahedral electronic configuration $t_{2g}^3 e_g^2$ corresponding to a ground term ${}^6A_{1g}$ in the standard notation of group theory. For this system the SO-coupling effects can be neglected, and the metal ion behaves as a spin-only paramagnetic centre with an isotropic g -tensor that is close to the free-electron value, and a small ZFS. The susceptibility is approximately isotropic, and so the ABMS is negligible. The metal ion Fe^{2+} , on the other hand, has an electron configuration of $t_{2g}^4 e_g^2$, giving an orbitally-degenerate ground term of ${}^5T_{2g}$. The EPR parameters are therefore influenced by SO coupling, giving an anisotropic g -tensor and non-zero ZFS as a result of the distortion from cubic symmetry. Both the susceptibility anisotropy and ABMS are therefore non-zero. As can be seen from the full spectra in Figure 11.4 (a), both spinning-sideband manifolds show a Gaussian distribution of sideband intensities superimposed on the nominal pattern, which can be ascribed to the influence of the IBMS in both cases. The manifold of LiFePO_4 is also expected to be distorted by the ABMS, though we expect this effect to be smaller. In addition if we examine the centrebands of both manifolds, we see that the linewidth of 90 ppm for LiFePO_4 is considerably larger than that for LiMnPO_4 , despite the former sample giving a longer T_2' value for ${}^7\text{Li}$. The larger linewidth for LiFePO_4 can be ascribed to the ABMS inhomogeneous line broadening that is absent in the spectrum of LiMnPO_4 .

11.3 Paramagnetic NMR of integer-spin quadrupolar nuclei

We now examine the form of the NMR spectrum of an integer-spin quadrupolar nucleus subject to a first-order quadrupolar interaction. We focus on the simplest case of nuclei with nuclear spin $I = 1$. The first-order quadrupolar interaction is wholly anisotropic, and so does not influence the observed resonance frequencies in solution. We therefore consider the spectra of solid-state powders under both static and MAS conditions.

11.3.1 Static solid powders

We derived the Hamiltonian for the first-order quadrupolar interaction in chapter 2, with the result given in Equation 2.145. The Hamiltonian is characterised by a frequency of interaction $\Omega_Q(\Omega_{QC}, \Omega_{CL})$, which is given in terms of the quadrupolar splitting frequency ω_Q , asymmetry parameter η^Q , the Euler angles specifying the orientation of the PAF in the crystal frame Ω_{QC} , and the orientation of the crystal frame in the laboratory

frame Ω_{CL} :

$$\Omega_Q(\Omega_{QC}, \Omega_{CL}) = \sqrt{\frac{2}{3}} \omega_Q \nu_{20} \quad (11.126)$$

$$= \frac{1}{2} \omega_Q [3 \cos^2(\beta_{QL}) - 1 + \eta^Q \sin^2(\beta_{QL}) \cos(2\alpha_{QL})]. \quad (11.127)$$

There are two observable coherences, represented by the operators $|10\rangle\langle 1+1|$ and $|1-1\rangle\langle 10|$, which result in two distinct resonances in the spectrum. The two frequencies $\Omega_{Q,M_i M_j}(\Omega_{QC}, \Omega_{CL})$ are given by the expression in Table 11.2 in terms of the satellite order d by

$$\Omega_{Q,M_i M_j}(\Omega_{QC}, \Omega_{CL}) = -d_{M_i M_j} \Omega_Q(\Omega_{QC}, \Omega_{CL}). \quad (11.128)$$

The two coherences have d -values of -1 and $+1$ respectively, and so the two resonance frequencies are:

$$\Omega_{Q,M_i M_j}(\Omega_{QC}, \Omega_{CL}) = \begin{cases} +\Omega_Q(\Omega_{QC}, \Omega_{CL}), & |10\rangle\langle 1+1|, \\ -\Omega_Q(\Omega_{QC}, \Omega_{CL}), & |1-1\rangle\langle 10|. \end{cases} \quad (11.129)$$

The resulting FID for a single crystallite is calculated from Equation 11.62, and is given by

$$s(\Omega_{QC}, \Omega_{CL}; t) = \frac{1}{2} [\exp [+i\Omega_Q(\Omega_{QC}, \Omega_{CL})t] + \exp [-i\Omega_Q(\Omega_{QC}, \Omega_{CL})t]] \quad (11.130)$$

$$= \cos [\Omega_Q(\Omega_{QC}, \Omega_{CL})t]. \quad (11.131)$$

The resulting spectrum contains two peaks at frequencies $\pm\Omega_Q(\Omega_{QC}, \Omega_{CL})$ and is symmetrical about the reference frequency, which here is zero. Following the calculation of the powder average over the Euler angles Ω_{CL} , the two resonances broaden to give the same characteristic lineshapes as for the SA interaction in Figure 11.2 (b), with one lineshape related to the other by a reflection about the reference frequency. The resulting symmetrical spectrum is shown in Figure 11.5 (a), and exhibits a shape known as a Pake pattern [194].

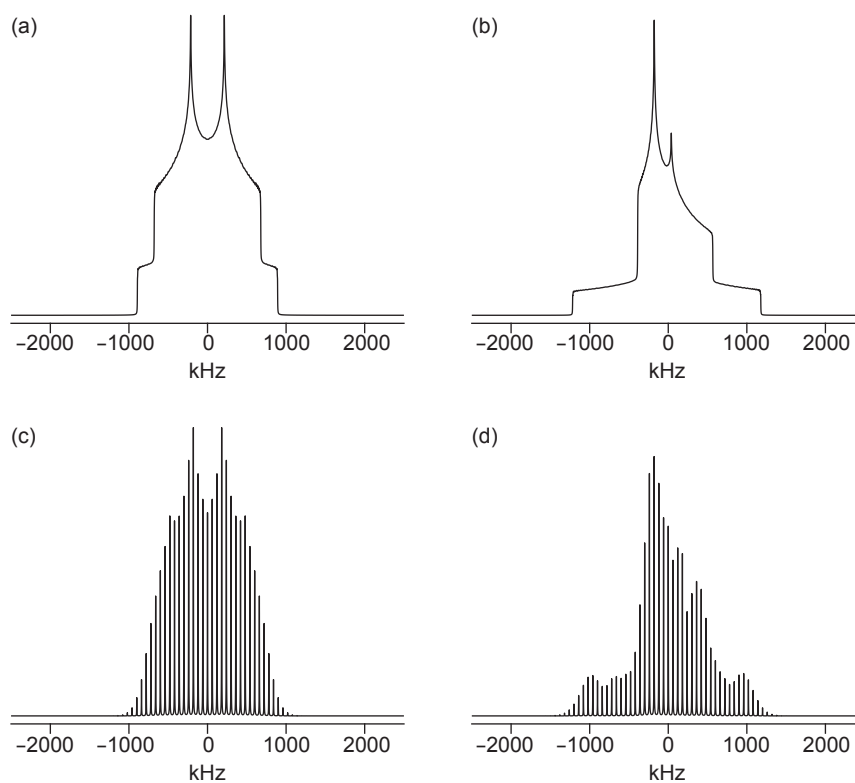


Figure 11.5: Simulated powder spectra of a spin $I = 1$ nucleus subject to a first-order quadrupolar and shielding interaction. The spectrum of a static powder with the first-order quadrupolar interaction only is shown in (a). Inclusion of the shift anisotropy under static conditions gives the more complicated spectrum in (b). Under MAS each resonance splits into a manifold of spinning sidebands, as shown in (c) and (d). The spectrum in (c) was simulated with the same first-order quadrupolar coupling parameters as (a) and in the absence of the shift anisotropy. Inclusion of the shift anisotropy gives the MAS spectrum in (d). The quadrupolar interaction parameters are $C_Q = 1.19$ MHz (corresponding to $\omega_Q/2\pi = 892.5$ kHz), $\eta^Q = 0.52$, and $\Omega_{QC} = (0^\circ, 0^\circ, 0^\circ)$. The chemical shielding parameters are $-\omega_0\Delta\sigma^S/2\pi = 500$ kHz, $\eta^S = 0.3$, and $\Omega_{PC} = (0^\circ, 90^\circ, 0^\circ)$. The frequency is measured relative to the isotropic offset Ω_{iso} . The MAS spectrum was simulated at 60 kHz MAS.

11.3.2 Solid powders under MAS

Under MAS conditions the quadrupolar frequency, now denoted $\Omega_c^Q(\gamma_{CR}; t)$, is time dependent and periodic. Therefore the two components of the FID each split into a spinning-sideband manifold, with the two manifolds related to each other by complex conjugation.

$$s_c(\gamma_{CR}; t) = \frac{1}{2} \left[\exp \left[+i\Phi_c^Q(\gamma_{CR}; t, 0) \right] + \exp \left[-i\Phi_c^Q(\gamma_{CR}; t, 0) \right] \right] \quad (11.132)$$

$$= \frac{1}{2} \sum_{m=-\infty}^{+\infty} \left[E_c^{(m)} \exp \left(i(\epsilon_c^{(m)}(\gamma_{CR}) + m\omega_r t) \right) + E_c^{(m)} \exp \left(-i(\epsilon_c^{(m)}(\gamma_{CR}) + m\omega_r t) \right) \right] \quad (11.133)$$

$$= \sum_{m=-\infty}^{+\infty} E_c^{(m)} \cos \left(i(\epsilon_c^{(m)}(\gamma_{CR}) + m\omega_r t) \right), \quad (11.134)$$

where $\Phi_c^Q(\gamma_{CR}; t, 0)$ is the periodic phase accrued by evolution of the frequency $\Omega_c^Q(\gamma_{CR}; t)$. The intensity and phase of the m th order sideband of the $|10\rangle\langle 1+1|$ coherence are $E_c^{(m)}/2$ and $\epsilon_c^{(m)}(\gamma_{CR})$ respectively, whereas for the $|1-1\rangle\langle 10|$ coherence they are $E_c^{(-m)}/2$ and $-\epsilon_c^{(-m)}(\gamma_{CR})$. Therefore the m th-order sideband of the sum of the two manifolds has a total complex intensity of $\left[E_c^{(m)} \exp \left(i\epsilon_c^{(m)}(\gamma_{CR}) \right) + E_c^{(-m)} \exp \left(-i\epsilon_c^{(-m)}(\gamma_{CR}) \right) \right] / 2$, which is equal to the complex intensity of the $-m$ th-order following complex conjugation. This results in a spectrum that is symmetrical about the reference frequency. This symmetry is also preserved in the powder average, as shown by the MAS spectrum in Figure 11.5 (c).

11.3.3 First-order quadrupolar and paramagnetic shift anisotropy interactions

In paramagnetic systems the NMR spectrum contains information about the paramagnetic shift and SA, as described in section 11.2, in addition to the first-order quadrupolar interaction. An example is given in Figure 11.5, in which the spectra in (a) and (c) are modified by including an SA interaction. The spectrum of the static powder is shown in Figure 11.5 (b), and the corresponding spectrum under MAS is in Figure 11.5 (d). Both spectra contain information about the size of the quadrupolar interaction, via ω_Q and η^Q , and the size of the SA, via $\Delta\sigma^S$ and η^S , and information about the relative orientation of one PAF relative to the other. Extracting all the available information can be a difficult task due to the complexity of the spectrum, which is exacerbated by the presence of substantial inhomogeneous broadening and multiple nuclear sites.

11.4 Paramagnetic NMR of half-integer-spin quadrupolar nuclei

We now examine the form of the NMR spectrum of a half-integer-spin quadrupolar nucleus subject to a first-order quadrupolar interaction, using the simplest case of $I = 3/2$ as an example. The principal difference between half-integer spins and integer spins is that the observable coherences of the former can be divided into a central transition (CT), which does not evolve under the first-order quadrupolar interaction, and a series of satellite transitions (STs) which do. For quadrupolar nuclei in symmetric environments with no CSA/SA, the resulting spectra are dominated by a narrow peak due to the CT, with the STs resulting in broader features that may be difficult to observe. However for nuclei with broad CT resonances, due either to a particularly large quadrupolar interaction or an SA, the STs cannot be neglected and must be considered for a proper interpretation of the spectra. In contrast to the previous section we also consider the effect of the second-order quadrupolar interaction, and the second-order cross term between the quadrupolar and SA interactions. Unlike the first-order interaction, the second-order interaction does affect the evolution of the CT coherence, and leads to broadening of the corresponding peak.

11.4.1 First-order quadrupolar interaction

Static solid powders

The frequencies of evolution under the first-order quadrupolar interaction are given by the expression in Equation 11.128 in terms of the satellite order d . For a spin $I = 3/2$ there are two observable ST coherences $|\frac{3}{2} + \frac{1}{2}\rangle\langle\frac{3}{2} + \frac{3}{2}|$ and $|\frac{3}{2} - \frac{3}{2}\rangle\langle\frac{3}{2} - \frac{1}{2}|$, which have d values of -2 and $+2$ respectively and so evolve under the first-order interaction with distinct frequencies. By contrast the CT coherence $|\frac{3}{2} - \frac{1}{2}\rangle\langle\frac{3}{2} + \frac{1}{2}|$ has $d = 0$, and so does not evolve. There are therefore three individual resonances in the FID, which evolve at the following frequencies:

$$\Omega_{Q,M_i,M_j}(\Omega_{QC}, \Omega_{CL}) = \begin{cases} +2\Omega_Q(\Omega_{QC}, \Omega_{CL}), & |\frac{3}{2} + \frac{1}{2}\rangle\langle\frac{3}{2} + \frac{3}{2}|, \\ 0, & |\frac{3}{2} - \frac{1}{2}\rangle\langle\frac{3}{2} + \frac{1}{2}|, \\ -2\Omega_Q(\Omega_{QC}, \Omega_{CL}), & |\frac{3}{2} - \frac{3}{2}\rangle\langle\frac{3}{2} - \frac{1}{2}|. \end{cases} \quad (11.135)$$

The single-crystal FID is calculated from Equation 11.62, and has the expression

$$s(\Omega_{\text{QC}}, \Omega_{\text{CL}}; t) = \frac{1}{10} [3 \exp [+2i\Omega_{\text{Q}}(\Omega_{\text{QC}}, \Omega_{\text{CL}})t] + 4 + 3 \exp [-2i\Omega_{\text{Q}}(\Omega_{\text{QC}}, \Omega_{\text{CL}})t]] \quad (11.136)$$

$$= \frac{1}{5} [3 \cos [2\Omega_{\text{Q}}(\Omega_{\text{QC}}, \Omega_{\text{CL}})t] + 2]. \quad (11.137)$$

An example of a spectrum of a powder sample is shown in Figure 11.6 (a). The spectrum is dominated by a sharp peak due to the CT, which is at zero frequency. The two STs give considerably broader resonances of lower intensity. A vertical expansion of the spectrum, shown in Figure 11.6 (c), reveals the form of the two ST resonances which, like the spectrum of the spin $I = 1$ nucleus in Figure 11.5 (a), combine to give a Pake pattern [194].

Solid powders under MAS

Under MAS the quadrupolar frequency $\Omega_{\text{c}}^{\text{Q}}(\gamma_{\text{CR}}; t)$ is time-dependent and periodic. As the spin system evolves the two ST coherences evolve at frequencies $\pm 2\Omega_{\text{c}}^{\text{Q}}(\gamma_{\text{CR}}; t)$, and accrue periodic phases of $\pm 2\Phi_{\text{c}}^{\text{Q}}(\gamma_{\text{CR}}; t, 0)$, whereas the CT coherence does not evolve. The result is that the FID contains a time-independent contribution from the CT, and two periodic contributions from the STs that each split into spinning-sideband manifolds:

$$s_{\text{c}}(\gamma_{\text{CR}}; t) = \frac{3}{10} [\exp [+2i\Phi_{\text{c}}^{\text{Q}}(\gamma_{\text{CR}}; t, 0)] + \exp [-2i\Phi_{\text{c}}^{\text{Q}}(\gamma_{\text{CR}}; t, 0)]] + \frac{2}{5} \quad (11.138)$$

$$= \frac{3}{10} \sum_{m=-\infty}^{+\infty} [F_{\text{c}}^{(m)} \exp (i(\theta_{\text{c}}^{(m)}(\gamma_{\text{CR}}) + m\omega_{\text{r}}t)) + F_{\text{c}}^{(m)} \exp (-i(\theta_{\text{c}}^{(m)}(\gamma_{\text{CR}}) + m\omega_{\text{r}}t))] + \frac{2}{5} \quad (11.139)$$

$$= \frac{3}{5} \sum_{m=-\infty}^{+\infty} F_{\text{c}}^{(m)} \cos (i(\theta_{\text{c}}^{(m)}(\gamma_{\text{CR}}) + m\omega_{\text{r}}t)) + \frac{2}{5}, \quad (11.140)$$

where $F_{\text{c}}^{(m)}$ and $\theta_{\text{c}}^{(m)}(\gamma_{\text{CR}})$ are the intensity and phase of the m th-order sideband in the manifold of the $|\frac{3}{2} + \frac{1}{2}\rangle \langle \frac{3}{2} + \frac{1}{2}|$ ST. As for the spin $I = 1$ MAS spectrum, the spinning-sideband manifold of the second ST is related to the first by a reflection about the reference frequency. The resulting MAS spectrum of the powder contains a single sharp peak due to the CT and a symmetrical and broad spinning-sideband manifold due to the two STs, whose centrebands are coincident with each other and with the CT peak, as shown in Figure 11.6 (e).

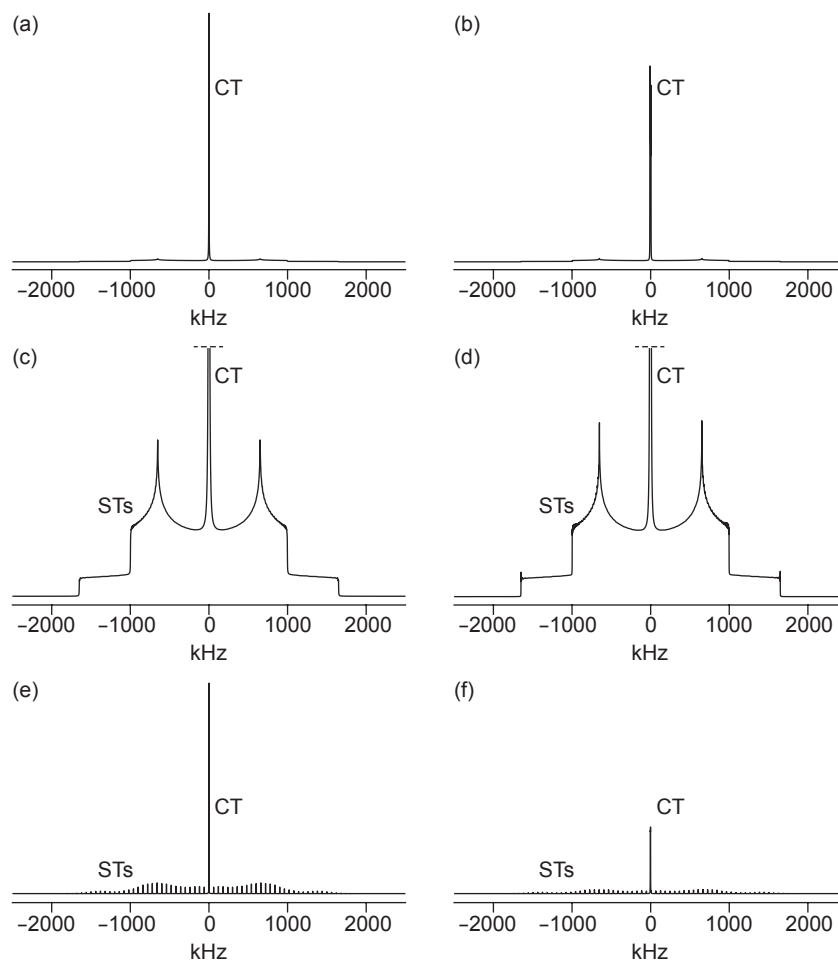


Figure 11.6: Simulated powder spectra of a spin $I = 3/2$ nucleus subject to a first- and second-order quadrupolar interaction. The spectrum of a static powder with the first-order quadrupolar interaction only is shown in (a). In (b) is shown the same spectrum calculated with the second-order quadrupolar interaction. The spectra in (c) and (d) are vertical expansions of (a) and (b) in order to highlight the broad ST resonances. Under MAS the ST resonances split into spinning-sideband manifolds, giving the spectra in (e) and (f). The spectrum in (e) was simulated with the first-order quadrupolar interaction only, whereas (f) includes the second-order interaction. The quadrupolar interaction parameters are $C_Q = 3.3$ MHz (corresponding to $\omega_Q/2\pi = 825$ kHz), $\eta^Q = 0.21$, and $\Omega_{QC} = (0^\circ, 0^\circ, 0^\circ)$. The nuclear Larmor frequency is $\omega_0/2\pi = -105.9$ MHz, giving $\omega_Q^2/(2\pi\omega_0) = -6.4$ kHz. The MAS spectrum was simulated at 60 kHz MAS.

11.4.2 Second-order quadrupolar interaction

We now turn our attention to the second-order quadrupolar interaction, the Hamiltonian of which is given in Equation 2.149. The frequency components, in Table 11.2, comprise an isotropic term, a rank-two term, and a rank-four term, that are proportional to the spin-order parameters c_{0,M_iM_j} , c_{2,M_iM_j} , and c_{4,M_iM_j} respectively. For all three contributions to the frequency both STs have the same value of c_i , which is different to that of the CT. Hence the value of c_0 is -6 for both STs and $+3$ for the CT, c_2 takes values of $+6$ and -12 for the STs and CT, and c_4 is equal to $+24$ and -27 for the STs and CT. The resulting frequencies of evolution for the three transitions are therefore:

$$\frac{4\omega_Q^2}{9\omega_0} \left[-\frac{6w_{00}^{(Q,Q)}}{\sqrt{5}} + \frac{6w_{20}^{(Q,Q)}}{\sqrt{14}} + \frac{24w_{40}^{(Q,Q)}}{\sqrt{70}} \right], \quad \left| \frac{3}{2} + \frac{1}{2} \right| \left\langle \frac{3}{2} + \frac{3}{2} \right\rangle, \quad (11.141)$$

$$\frac{4\omega_Q^2}{9\omega_0} \left[\frac{3w_{00}^{(Q,Q)}}{\sqrt{5}} - \frac{12w_{20}^{(Q,Q)}}{\sqrt{14}} - \frac{27w_{40}^{(Q,Q)}}{\sqrt{70}} \right], \quad \left| \frac{3}{2} - \frac{1}{2} \right| \left\langle \frac{3}{2} + \frac{1}{2} \right\rangle, \quad (11.142)$$

$$\frac{4\omega_Q^2}{9\omega_0} \left[-\frac{6w_{00}^{(Q,Q)}}{\sqrt{5}} + \frac{6w_{20}^{(Q,Q)}}{\sqrt{14}} + \frac{24w_{40}^{(Q,Q)}}{\sqrt{70}} \right], \quad \left| \frac{3}{2} - \frac{3}{2} \right| \left\langle \frac{3}{2} - \frac{1}{2} \right\rangle. \quad (11.143)$$

The effect of these second-order contributions is shown in the spectra in Figure 11.6, with the spectra calculated to first-order also shown for comparison. The full spectrum of the static powder in Figure 11.6 (b), the vertical expansion highlighting the STs in (d), and the MAS spectrum in (f) show a negligible change in the form of the ST resonances, since the broadening due to the first-order quadrupolar is much larger than the second-order broadening. In fact the only change that is immediately apparent is the reduction in the intensity of the CT peak, which is due to the broadening from the rank-four frequency component. Since the CT is unaffected by the first-order interaction, this second-order rank-four term is the only source of broadening in the CT peak due to the quadrupolar interaction, and so is non-negligible.

The CT peak is highlighted more clearly in the spectra of Figure 11.7, which are expansions of those shown in Figure 11.6. The spectra in Figure 11.7 (a) and (c) are calculated under static conditions and MAS respectively assuming the first-order quadrupolar interaction only. In the spectrum of the static powder in (a) the sharp peak of the CT is superimposed on the broad ST resonances, which here cannot be seen. Under MAS the sharp CT peak also contains a small contribution from the centrebands of the two ST spinning-sideband manifolds, as shown in (c). We recall that, to first order, the centrebands of the two STs are resonant both with each other and the CT, here at zero frequency. The introduction of the second-order interaction has

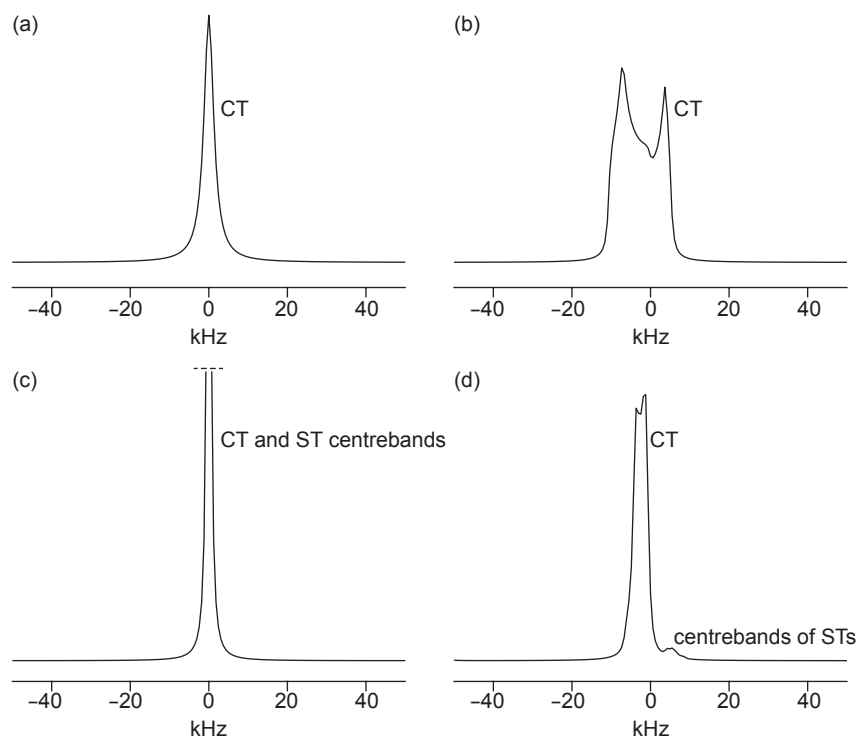


Figure 11.7: Expansions of the simulated powder spectra of a spin $I = 3/2$ nucleus shown in Figure 11.6 to highlight the CT. The spin is subject to a first- and second-order quadrupolar interaction. The CT resonance of a static powder with the first-order quadrupolar interaction only is shown in (a). In (b) is shown the same CT resonance calculated with the second-order quadrupolar interaction. The spectra in (c) and (d) were simulated under MAS. The spectrum in (c) was simulated with the first-order quadrupolar interaction only, whereas (d) includes the second-order interaction. The quadrupolar interaction parameters are $C_Q = 3.3$ MHz (corresponding to $\omega_Q/2\pi = 825$ kHz), $\eta^Q = 0.21$, and $\Omega_{QC} = (0^\circ, 0^\circ, 0^\circ)$. The frequency is measured relative to the isotropic offset Ω_{iso} . The nuclear Larmor frequency is $\omega_0/2\pi = -105.9$ MHz, giving $\omega_Q^2/(2\pi\omega_0) = -6.4$ kHz. The MAS spectrum was simulated at 60 kHz MAS.

two noticeable effects on the spectrum of the static powder, in Figure 11.7 (b). Firstly we see that the CT resonance is broadened due to the combination of the rank-two and rank-four frequency components. Secondly the centre of mass of the resonance is shifted from zero frequency due to the second-order isotropic frequency. Under MAS the broadening of the CT is reduced but not eliminated, as shown by the spectrum in Figure 11.7 (d). This is because, whilst the rank-two broadening is indeed removed the rank-four broadening is only scaled by a factor of $-7/18$. We note that this negative factor also results in a reversal of the lineshape relative to the frequency axis. Magic-angle spinning also reveals an additional feature of the second-order interactions. Because the CT and STs have different values of c_0 the former no longer appears at the same isotropic frequency as the latter. The opposite signs of the two c_0 values results in the CT and ST centrebands being shifted in opposite directions. Clearly care must be taken to recognize the ST centrebands and not to confuse them with additional nuclear sites.

11.4.3 Second-order quadrupolar and paramagnetic shift anisotropy interactions

In paramagnetic systems, NMR spectra are also affected by the SA interaction. Under static conditions the SA leads to an additional broadening of the spectrum, as shown in Figure 11.8 (a). The CT and ST resonances are both broadened by the rank-two SA, which leads to a complicated lineshape. As for the spin $I = 1$ case this spectrum also depends on the relative orientation of the SA tensor relative to the EFG tensor. Under MAS the broad lineshape splits into a manifold of spinning sidebands, as shown in Figure 11.8 (b). Like the static spectrum, the sideband manifold is very complicated and difficult to interpret, as it contains contributions principally from the first-order quadrupolar and SA interactions for the STs, and the SA for the CT. An expansion of the region containing the centrebands, Figure 11.8 (c), shows that the sidebands are broadened by the rank-four frequency components.

Finally we briefly mention the second-order cross term between the quadrupolar and SA interactions, the Hamiltonian of which is given in Equation 2.152. The frequency components, given in Table 11.2, comprise an isotropic, a rank-two, and a rank-four term, all of which are proportional to the satellite order $d_{M_i M_j}$. The

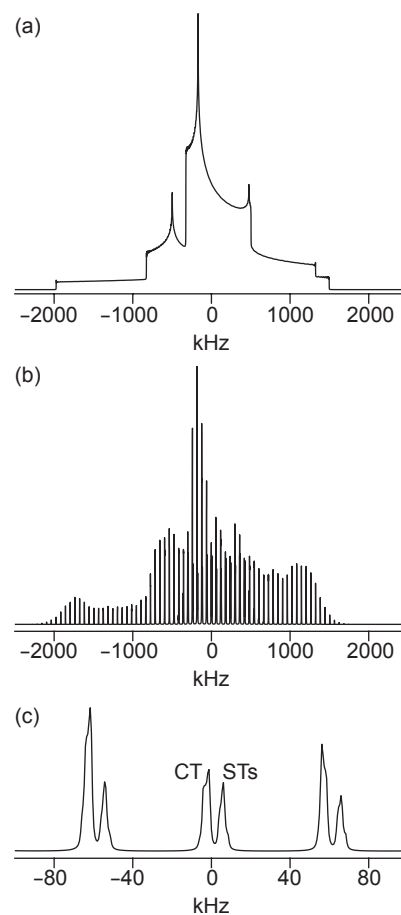


Figure 11.8: Simulated powder spectra of a spin $I = 3/2$ nucleus subject to a second-order quadrupolar interaction and a shift anisotropy. The spectrum of the static powder is shown in (a), which under MAS splits into the spinning-sideband manifold in (b). The spectrum in (c) is an expansion of (b) showing the centreband and the first-order sidebands of both the CT and ST resonances. The quadrupolar interaction parameters are $C_Q = 3.3$ MHz (corresponding to $\omega_Q/2\pi = 825$ kHz), $\eta^Q = 0.21$, and $\Omega_{QC} = (0^\circ, 0^\circ, 0^\circ)$. The chemical shielding parameters are $-\omega_0\Delta\sigma^S/2\pi = 500$ kHz, $\eta^S = 0.3$, and $\Omega_{PC} = (0^\circ, 90^\circ, 0^\circ)$. The frequency is measured relative to the isotropic offset Ω_{iso} . The nuclear Larmor frequency is $\omega_0/2\pi = -105.9$ MHz, giving $\omega_Q^2/(2\pi\omega_0) = -6.4$ kHz. The MAS spectrum was simulated at 60 kHz MAS.

evolution frequencies of the three transitions are therefore:

$$-2\omega_Q \left[\frac{2}{\sqrt{5}} w_{00}^{(C2,Q)} - \left(\sqrt{2} w_{20}^{(C1,Q)} + \sqrt{\frac{2}{7}} w_{20}^{(C2,Q)} \right) - 4 \sqrt{\frac{2}{35}} w_{40}^{(C2,Q)} \right], \quad \left| \frac{3}{2} + \frac{1}{2} \right| \left\langle \frac{3}{2} + \frac{3}{2} \right\rangle, \quad (11.144)$$

$$0, \quad \left| \frac{3}{2} - \frac{1}{2} \right| \left\langle \frac{3}{2} + \frac{1}{2} \right\rangle, \quad (11.145)$$

$$+2\omega_Q \left[\frac{2}{\sqrt{5}} w_{00}^{(C2,Q)} - \left(\sqrt{2} w_{20}^{(C1,Q)} + \sqrt{\frac{2}{7}} w_{20}^{(C2,Q)} \right) - 4 \sqrt{\frac{2}{35}} w_{40}^{(C2,Q)} \right], \quad \left| \frac{3}{2} - \frac{3}{2} \right| \left\langle \frac{3}{2} - \frac{1}{2} \right\rangle. \quad (11.146)$$

We see that the CT is unaffected by this cross term, and so experiences no additional broadening or resonance shift, whereas the two ST coherences evolve with frequencies of opposite sign. One consequence of this is that the centrebands of the two STs no longer appear at the same isotropic frequency. Hence the centreband region of the MAS spectrum now contains three distinct peaks instead of two, one for each transition.

11.5 Key concepts

- A paramagnetic solution results in an NMR spectrum where the shift is dominated by the isotropic paramagnetic shift, and the linewidth is given by a combination of the paramagnetic relaxation enhancement, and the inhomogeneous broadening due to the non-spherical shape of the sample container.
- A static paramagnetic powder results in an NMR spectrum where the shift is dominated by the isotropic paramagnetic shift, and the lineshape and linewidth are due to the shift anisotropy and bulk magnetic susceptibility broadening.
- A spinning paramagnetic powder produces a spinning-sideband manifold with an isotropic frequency given by the isotropic paramagnetic shift. The pattern of sideband intensities is due to both the shift anisotropy and the bulk magnetic susceptibility. The linewidth of each spinning sideband is due to a combination of the anisotropic bulk magnetic susceptibility broadening, paramagnetic relaxation enhancement, and the extended network of dipolar couplings between nuclei.
- Quadrupolar nuclei in paramagnetic systems have additional interactions due to the first- and second-order quadrupolar interactions.
- For integer-spin quadrupolar nuclei the quadrupolar interaction is an additional source of resonance

broadening under static conditions, and gives rise to a spinning-sideband manifold under MAS.

- For half-integer-spin quadrupolar nuclei the central transition is broadened by the second-order quadrupolar interaction in both static and spinning powders. The satellite transitions are broadened by the first-order quadrupolar interaction under static conditions, and give rise to an extensive spinning-sideband manifold under MAS. The isotropic peak of the satellite manifold is shifted relative to the isotropic peak of the manifold of the central transition by the second-order quadrupolar interaction, and so care must be taken not to confuse the former with an additional nuclear site.

Chapter 12

A survey of NMR methods for paramagnetic systems

In this chapter we survey the experimental NMR methods that have either been used on, or are applicable to, paramagnetic systems. There are many NMR pulse sequences that have been designed for diamagnetic systems, including small- to medium-sized molecules in solution [254], large biomolecules in solution [329], solid materials [2, 330], and biosolids [331]. However many of these methods cannot be easily applied to equivalent paramagnetic systems due to the large shifts, SAs, and short relaxation times. The methods we survey can be divided into two groups: the relatively small proportion of those which were designed for diamagnetic systems but can be applied to paramagnetic systems with little or no modification, and those which are designed specifically for paramagnetic systems in order to evaluate quantitatively paramagnetic effects. In addition we provide some general guidance on how to acquire NMR spectra of paramagnetic species.

We divide the survey into two parts. Firstly we discuss methods for solution NMR. Many of the topics covered here have already been discussed by Bertini et al [15, 332, 333], and so we keep the discussion brief. Secondly we discuss solid-state NMR methods. The development and application of solid-state NMR methods for paramagnetic materials and biomolecules is a field that has seen considerable progress in recent years, and so we devote more space to it here.

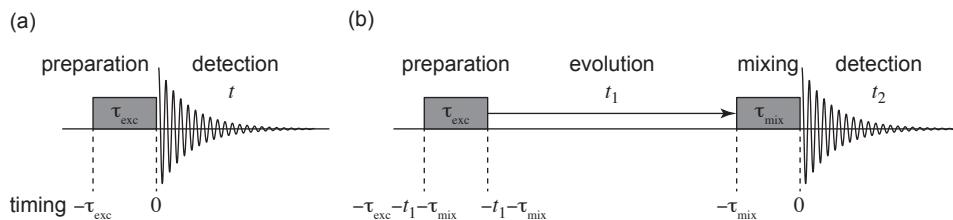


Figure 12.1: General schemes for one- and two-dimensional NMR pulse sequences. The general one-dimensional scheme is shown in (a), and the two-dimensional scheme is in (b).

We also add that this survey is not intended to be the final word on paramagnetic NMR methodology. There are still many potential improvements in RF probe technology and experimental schemes to be made in order to be able to study ever more demanding systems.

12.1 NMR pulse sequences

One- and two-dimensional NMR pulse sequences follow the general scheme in Figure 12.1. The general one-dimensional scheme in Figure 12.1 (a) comprises a preparation period, which contains an excitation sequence of duration τ_{exc} . This sequence is either a single RF pulse or a combination of pulses, and generates observable coherences of order $p = -1$. The coherences are then observed in the detection period of time t . The resulting FID is then subjected to Fourier transformation to produce the spectrum.

The general two-dimensional sequence, shown in Figure 12.1 (b), is more complex. Here the preparation period generates coherences which may or may not be directly observable. These coherences evolve during the evolution period, which comprises a time variable t_1 that is incremented stepwise. This is followed by a mixing period, during which magnetization is transferred from one nuclear species to another via a coupling interaction. The mixing period generates observable coherences of order $p = -1$, which are observed during the detection period t_2 . The acquisition strategy is as follows. Firstly we set $t_1 = 0$ and acquire a spectrum during t_2 in real time. We then increment t_1 by an amount Δt_1 and repeat the experiment to acquire a second FID in t_2 . This process is repeated until we have extended the evolution time t_1 to the desired value. The data are stored as data points sampled at discrete values of t_1 and t_2 , resulting in a two-dimensional FID $s(t_1, t_2)$ which is stored as an array, as shown in Figure 12.2 (a). This FID is subjected to a two-dimensional Fourier transform to give a two-dimensional spectrum $S(\omega_1, \omega_2)$, which is a function of the indirect frequency ω_1 and

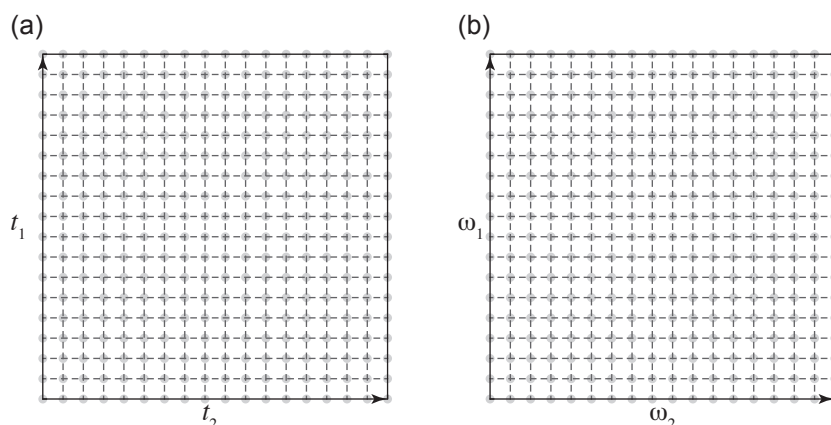


Figure 12.2: Array representation of the FID and spectrum from a two-dimensional experiment. The FID is shown in (a), and the spectrum is in (b).

the direct frequency ω_2 :

$$S(\omega_1, \omega_2) = \int_0^{\infty} dt_1 \int_0^{\infty} dt_2 s(t_1, t_2) \exp(-i\omega_1 t_1) \exp(-i\omega_2 t_2). \quad (12.1)$$

This is also presented as an array (Figure 12.2 (b)).

12.2 Solution NMR methods for paramagnetic systems

12.2.1 The general strategy

There are two principal observations associated with obtaining an NMR spectrum of a paramagnetic compound in solution. Firstly the large isotropic shifts result in a spectrum with a spectral dispersion that is considerably larger than that for diamagnetic molecules. This means that it is harder to excite the full spectral range efficiently with the RF powers that are typically available for solution NMR probes. Since the range of frequencies that are excited by a pulse, known as the bandwidth, is generally proportional to the RF field amplitude ω_1 , we expect pulse sequences containing only short, high-power RF pulses to be more applicable than sequences with longer periods of low-power irradiation, such as spin lock pulses and periods of decoupling. High-power spin-lock periods and decoupling sequences are not advisable as they may damage both the probe and the sample.

The second observation we encounter is that the relaxation times are typically very short due to the large PREs. On the one hand, the short T_1 and T_2 time constants result in a considerable loss of signal during an experiment, which severely limits the length of the pulse sequence that we can successfully employ. In addition the short T_2 gives very broad peaks in the spectrum. This is particularly problematic for large molecules such as proteins, where there is an appreciable Curie contribution to transverse relaxation. Both effects lead to low sensitivity, and some peaks may be missing altogether. On the other hand the short T_1 can be a useful property, as the dominant factor that determines the total length of the experiment is the recycle delay, which is the time between the individual scans we allow for the spin system to relax back to equilibrium, which is set to between $3T_1$ and $5T_1$ for a quantitative spectrum. The short T_1 values allow us to reduce the recycle delay, so that we can acquire more scans in a certain experiment time. This partly offsets the reduction in sensitivity resulting from broad peaks and signal losses during the sequence.

Spectral editing using relaxation time differences

When acquiring NMR spectra of paramagnetic molecules in solution one difficulty that may arise is that the broad, low-intensity signals from the paramagnetic species are difficult to observe as they are dominated by sharper, more intense signals from diamagnetic species, for example the solvent. This is frequently the case for paramagnetic proteins, where the solvent peak(s) dominate the spectrum. Fortunately solvent peaks can be suppressed easily by exploiting the fact that their longitudinal relaxation time constants are significantly longer than those for paramagnetic species. We denote the solvent and paramagnetic-species T_1 times T_1^{long} and T_1^{short} respectively. If we set the recycle delay so that it is equal to $5T_1^{\text{short}}$, but shorter than T_1^{long} , and acquire several scans, the signals components from the paramagnetic species are fully-relaxed at the start of each new scan, whereas the solvent signals are not. The former signals are acquired with maximum intensity, reflecting the size of their equilibrium longitudinal magnetization, whereas the latter are almost completely saturated. The resulting spectrum then contains far more of the signals from the paramagnetic species, with the longer-relaxing solvent signals being largely suppressed. This is a simple example of spectral editing, where the signal components with longer T_1 values are selectively suppressed to allow the observation of the signals with shorter T_1 time constants. The saturation is usually not perfect, and so improved techniques are required.

A more effective T_1 -spectral-editing technique is based on the Water Eliminated Fourier Transform

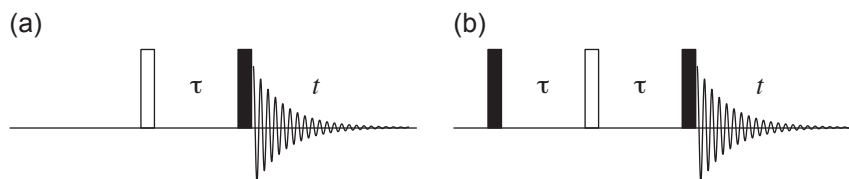


Figure 12.3: Pulse sequences for the selective suppression of signals from nuclear species with long T_1 . The basic sequence for the WEFT and super WEFT experiments is shown in (a), and (b) shows the MODEFT sequence. The filled and unfilled rectangles indicate pulses with nominal flip angles of 90° and 180° respectively, and phase x .

(WEFT) pulse sequence, which is shown in Figure 12.3 (a) [334]. The sequence is the simple inversion–recovery sequence, which can be used to measure T_1 . The z -magnetization vectors from all the signal components are inverted by the 180° pulse, and then relax during the subsequent recovery delay τ . For WEFT the delay τ is set to $T_1^{\text{long}} \ln 2$, at which time the z -magnetization due to the solvent passes through zero. If however T_1^{short} is sufficiently short the z -magnetization of the paramagnetic species is fully relaxed. The second pulse of 90° flip angle then excites coherences the magnitudes of which are proportional to the recovered z -magnetization, with the result that the spectrum contains only the rapidly-relaxing signal components from the paramagnetic species.

The WEFT experiment has been improved by employing the same sequence, but using different values of the recovery delay τ [335]. It has been shown that if the recycle delay is shortened so that the solvent peaks are saturated, but is also sufficiently long to enable full relaxation of the paramagnetic signals, then one can find a value of the delay τ at which the solvent signals have zero intensity after several scans. This experiment has been applied to paramagnetic proteins in solution in order to separate signals from the protein experiencing a moderate PRE from those that relax with a larger PRE. As an example, 200 MHz ^1H super WEFT NMR spectra of a heme-containing cytochrome *c* mutant Ala80cyt c are shown in Figure 12.4 [333, 336]. The super WEFT spectrum obtained with both τ and the recycle delay set to 250 ms, spectrum (a), shows several signals with paramagnetic shifts that take them outside the normal diamagnetic region, and which exhibit T_1 times of approximately 100 ms. However these signals obscure the peaks from the axially-coordinated histidine, which have shorter T_1 times, of the order of a few ms. These more rapidly-relaxing signals can be observed in the spectrum of Figure 12.4 (b), which was acquired by setting the τ and the recycle delays to 20 ms and 33 ms respectively.

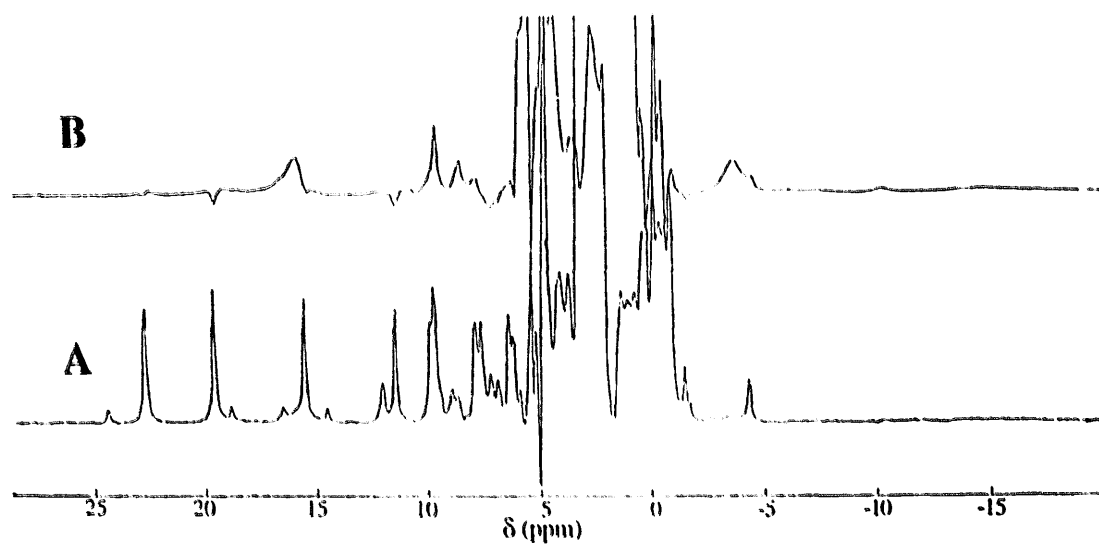


Figure 12.4: ^1H NMR spectra of the cyanide adduct of a cytochrome c mutant Ala80cytc acquired using the super WEFT pulse sequence. In (a) is shown the spectrum acquired with $\tau = 250$ ms and a recycle delay of 250 ms. The spectrum in (b) was acquired with $\tau = 20$ ms and a recycle delay of 33 ms, and clearly shows the two signals of the axially-coordinated histidine at 16.1 and -3.4 ppm [336]. Reproduced from [333], with permission from Elsevier.

Figure 12.3 (b) shows an alternative pulse sequence for suppressing the solvent signals, which is referred to as MODified Driven Equilibrium Fourier Transform (MODEFT) [337]. Here the delay τ is chosen to be short compared to T_1^{long} , and long compared to T_1^{short} . If these conditions are met, the solvent signals experience no significant relaxation during the spin echo, and the combined effect of the two 90° and 180° pulses is to rotate the equilibrium solvent magnetization by 360° so that it returns to its equilibrium position and the solvent signals are not excited. However the paramagnetic signals experience significant relaxation during the spin echo, at the end of which the magnetization has returned to equilibrium. The final pulse then acts as a simple excitation pulse, and we observe the paramagnetic signals. Typically super WEFT performs better than MODEFT when a single signal is to be suppressed, but MODEFT has comparable, or better, results when more than one slowly-relaxing signal needs to be suppressed [333].

12.2.2 Small molecules

There is an extensive suite of pulse sequences available for small molecules in solution, a comprehensive survey and explanation of which can be found in Keeler [254]. Here we provide a brief overview of sequences that have been employed in paramagnetic NMR.

Homonuclear through-bond correlations

One very important class of experiments is that of homonuclear through-bond correlation experiments. Correlations are observed between nuclear spins that are coupled to each other via a through-bond J -coupling interaction. The strength of this interaction is quantified by the J -coupling constant J , which typically has a magnitude of of 0–20 Hz for ^1H – ^1H interactions, and 0–100 Hz for ^{13}C – ^{13}C couplings. In the experiments described here the observation of a correlation requires that the indirect evolution time t_1 be sufficiently long to allow measurable evolution of the J -coupling. The desired signal varies as $\sin(\pi J t_1)$ and so the evolution time required for maximum cross-peak signal is of the order $1/(2J)$ [254], which for ^1H – ^1H correlation experiments means that t_1 must extend to times of the order of 25 ms. Clearly this may present a problem for systems with large transverse PREs.

Figure 12.5 shows three pulse sequences that have been successfully used [332]. The simplest experiment, shown in Figure 12.5 (a) is the CORrelation SpectroscopY (COSY) sequence, which has a mixing period comprising a single 90° pulse. There are only two pulses in the sequence, which is an advantage in that this

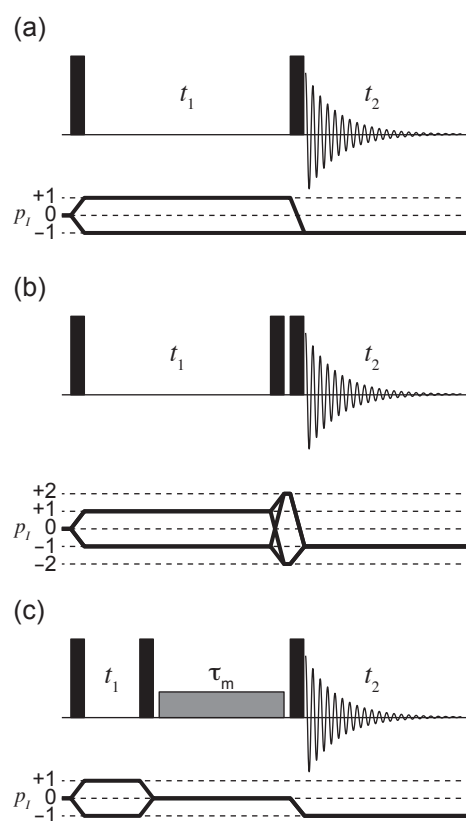


Figure 12.5: Pulse sequences and coherence-transfer pathways for two-dimensional homonuclear correlation experiments. The basic COSY sequence is shown in (a), the DQF-COSY sequence is shown in (b), and (c) shows the TOCSY sequence. The filled rectangles indicate pulses with a nominal flip angle of 90° and phase x . In the TOCSY experiment the grey rectangle represents continuous irradiation during an isotropic mixing sequence such as DIPSI-2.

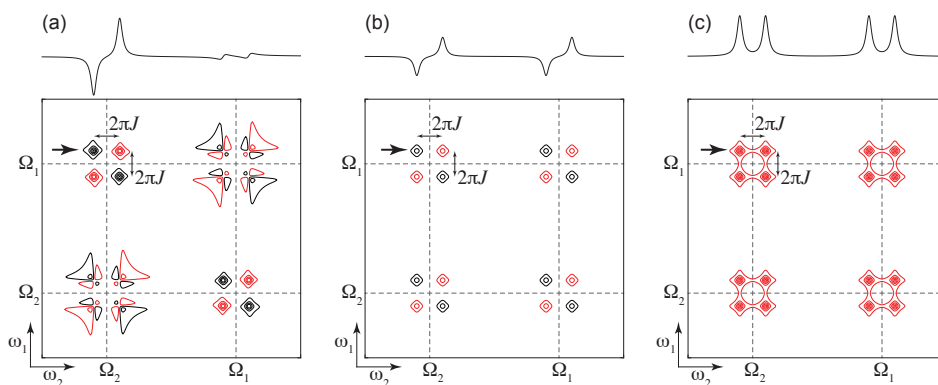


Figure 12.6: Examples of homonuclear through-bond correlation spectra of a two-spin system. The basic COSY spectrum shown in (a), the DQF-COSY spectrum is shown in (b), and in (c) is the TOCSY spectrum. The chemical shift offset frequencies of the two spins are Ω_1 and Ω_2 , and the coupling between them, in Hz, is J . The one-dimensional traces shown above each two-dimensional spectrum are taken parallel to the ω_2 -axis at $\omega_1 = \Omega_1 + \pi J$, as indicated by the arrow. Positive contours are coloured red, and negative contours are black.

minimizes the potential for problems with non-ideal excitation to occur. A simulated example of a spectrum is shown in Figure 12.6 (a). The spectrum contains both diagonal-peak multiplets, and cross-peak multiplets that indicate the presence of homonuclear correlations. Each diagonal-peak multiplet appears as an in-phase array, meaning that all the individual peaks have the same phase. By contrast the cross peaks are anti-phase in each dimension, so that the two components have intensities of opposite sign. The resulting multiplet appears as an anti-phase square array in the two-dimensional spectrum. This form of the spectrum has a disadvantage when the linewidth is comparable to or larger than the J -coupling, as the components of the cross-peak multiplet cancel to an extent, resulting in a low-intensity multiplet, whereas the diagonal peaks reinforce. Therefore it is often observed in rapidly-relaxing systems that COSY spectra exhibit very intense diagonal-peak multiplets that dominate the cross-peak multiplets. Furthermore the diagonal peaks are out of phase with the cross peaks by 90° in both dimensions. Hence if the cross peaks are phased to double absorption (i.e. absorption mode in both dimensions), as is conventionally done, the diagonal peaks are in double dispersion, and therefore have lineshapes with broad bases that can mask the presence of nearby cross-peaks.

The Double-Quantum-Filtered COSY (DQF-COSY) experiment (Figure 12.5 (b)) is an improvement over the basic COSY sequence. The mixing period comprises a double-quantum filter of two 90° pulses between

which only double-quantum coherences (with $p = \pm 2$) are retained. The main advantage over basic COSY is that the diagonal- and cross-peak multiplets have the same phase, and both appear as anti-phase square arrays so that there is a more equal balance of intensities. This is seen in the simulated spectrum in Figure 12.6 (b). In addition the double-quantum filter ensures that any nuclear spins that are not J -coupled do not contribute to the spectrum, and so there are no intense singlet resonances. The only disadvantage of the DQF-COSY experiment is that the double-quantum filter reduces the sensitivity relative to conventional COSY by a factor of two.

The ^1H - ^1H COSY spectrum of (2-NCH₃-21-CH₃CTPP)-NiCl in CDCl₃ is shown in Figure 12.7 [338]. Here the Ni²⁺ ion coordinates to a porphyrin ring 2-NCH₃-21-CH₃CTPPH, the structure of which is also shown, with the result that the ^1H nuclei experience appreciable paramagnetic shifts. Despite the larger dispersion of 60 ppm the COSY experiment yields a substantial number of ^1H - ^1H through-bond correlations. This is in part because the transverse PREs, which cause losses in sensitivity during the COSY pulse sequence, due to Ni²⁺ are relatively modest compared to other $3d$ metal ions, as seen from Table 8.5. Hence complexes of these other ions may be less suitable for ^1H - ^1H COSY.

It should be noted that, in order to maximize the signal-to-noise ratio of the cross peaks in the two-dimensional COSY spectrum, it is important to tailor the time-domain weighting functions to the expected T_2 time constants [257]. For a two-spin system the time modulation of the cross-peak multiplet between spins 1 and 2 in the FID has the form $\sin(\Omega_1 t_1) \sin(\pi J t_1) \exp(i\Omega_2 t_2) \sin(\pi J t_2) \exp(-t_1/T_2^{(1)}) \exp(-t_2/T_2^{(2)})$, where $T_2^{(i)}$ is the transverse relaxation time constant for spin i . When relaxation is negligible the signal maximum in the FID is at $t_1 = t_2 = 1/(2J)$, and so we require a weighting function with a maximum at this point. However for paramagnetic systems where $JT_2 \ll 1$ we require a weighting function with maxima at approximately $t_1 = t_2 = T_2$. Typically we then acquire data points in the t_1 dimension only out to a maximum time of $2T_2$.

The TOtal Correlation Spectroscopy (TOCSY) sequence is shown in Figure 12.5 (c). The mixing period is a z -filter, comprising two pulses between which coherences are suppressed and only longitudinal terms are retained, that contains a period of isotropic mixing. The latter, which is a period of continuous low-power RF irradiation with duration τ_m , which is referred to as the mixing time, is responsible for correlating signals. Transfer from one nuclear spin to another occurs due to the J -coupling, which for maximum signal requires τ_m to be of the order of $1/(2J)$. This mixing may result in low sensitivity due to (1) the length of the mixing time giving large relaxation losses, and (2) inefficient transfer due to the low RF field amplitude of

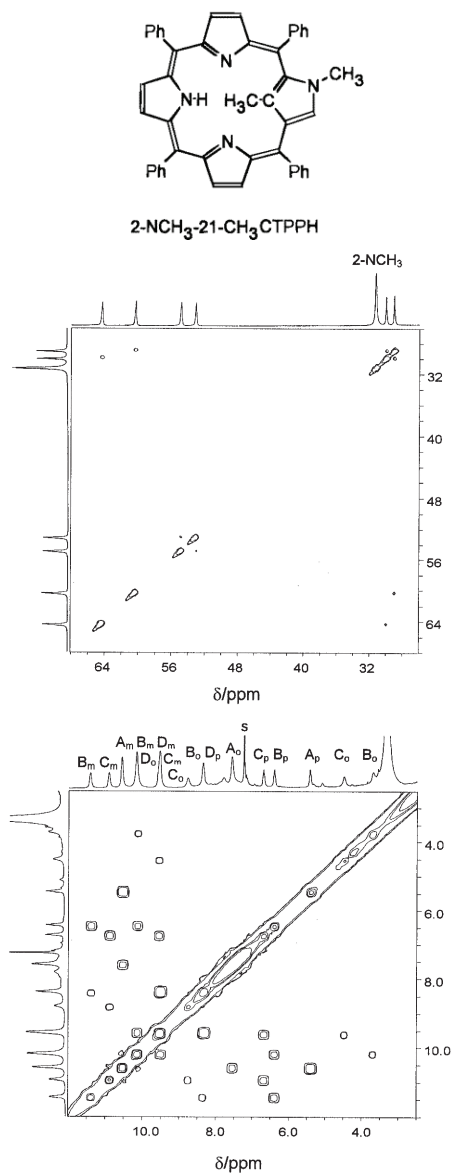


Figure 12.7: Experimental two-dimensional ^1H - ^1H COSY spectrum of (2-NCH₃-21-CH₃CTPP)-NiCl in CDCl₃. The upper spectrum shows the high chemical shift range of the pyrrole protons, and the lower spectrum shows the meso-phenyl region with lower shifts. The structure of the porphyrin ring 2-NCH₃-21-CH₃CTPPH is shown above the spectra. Adapted with permission from [338]. Copyright (1996) American Chemical Society.

the irradiation being insufficient to cover the spectral range of the paramagnetic shifts. The former problem is mitigated by compromising on the length of the mixing time, and ensuring that it is no longer than T_2 . However the form of the spectrum has a distinct advantage over COSY and DQF-COSY as *all* the multiplets are in phase. This means the cross-peak multiplets due to J -couplings that are comparable to the linewidth have a larger intensity, and so are easier to observe. An example of the simulated spectrum is shown in Figure 12.6 (c). One additional difference between TOCSY and the other experiments is that, for sufficiently long mixing times, we observe 'relay' cross peaks between spins that are not directly coupled to each other, provided that both are within the same continuously-coupled network of spins. For example consider a linear spin system A–M–X, in which A is coupled to M and M is coupled to X, but A and X are not coupled to each other. Both COSY and DQF-COSY give cross-peak multiplets between A and M, and M and X, only. However TOCSY also gives a cross-peak multiplet between A and X, due to a relayed transfer from A to M, and then from M to X (and vice versa). This allows TOCSY to be used to identify isolated spin systems within a molecule.

An example of a ^1H – ^1H TOCSY spectrum is shown in Figure 12.8 (b) [339]. The system is the medium-sized lanthanide-ion complex $\text{YbH}(\text{oep})(\text{tpp})$, the structure of which is shown in (a). Here the isotropic shift dispersion is relatively modest, as the ^1H shifts are dominated by a small PCS, and the Yb^{3+} induces a comparatively modest PRE. For this reason the isotropic mixing sequence is able to induce a transfer with sufficient efficiency across the spectrum in order to observe a number of cross-peaks.

Homonuclear through-space correlations

A second type of homonuclear correlation experiment that is very important for structure determination involves through-space magnetization transfers between nuclear spins via the dipolar coupling. In solution the dipolar couplings are averaged to zero by molecular tumbling of the molecules. However the stochastic fluctuations of the internuclear vectors result in a cross-relaxation mechanism in which magnetization is transferred from one nuclear spin to the other. This transfer mechanism, referred to as the nuclear Overhauser effect (NOE), is useful for determining both the conformations adopted by flexible molecules, and relative stereochemistry.

There are two pulse sequences that are commonly used. This first is the Nuclear Overhauser Effect Spectroscopy (NOESY) sequence, which is shown in Figure 12.9. The sequence has the same form as

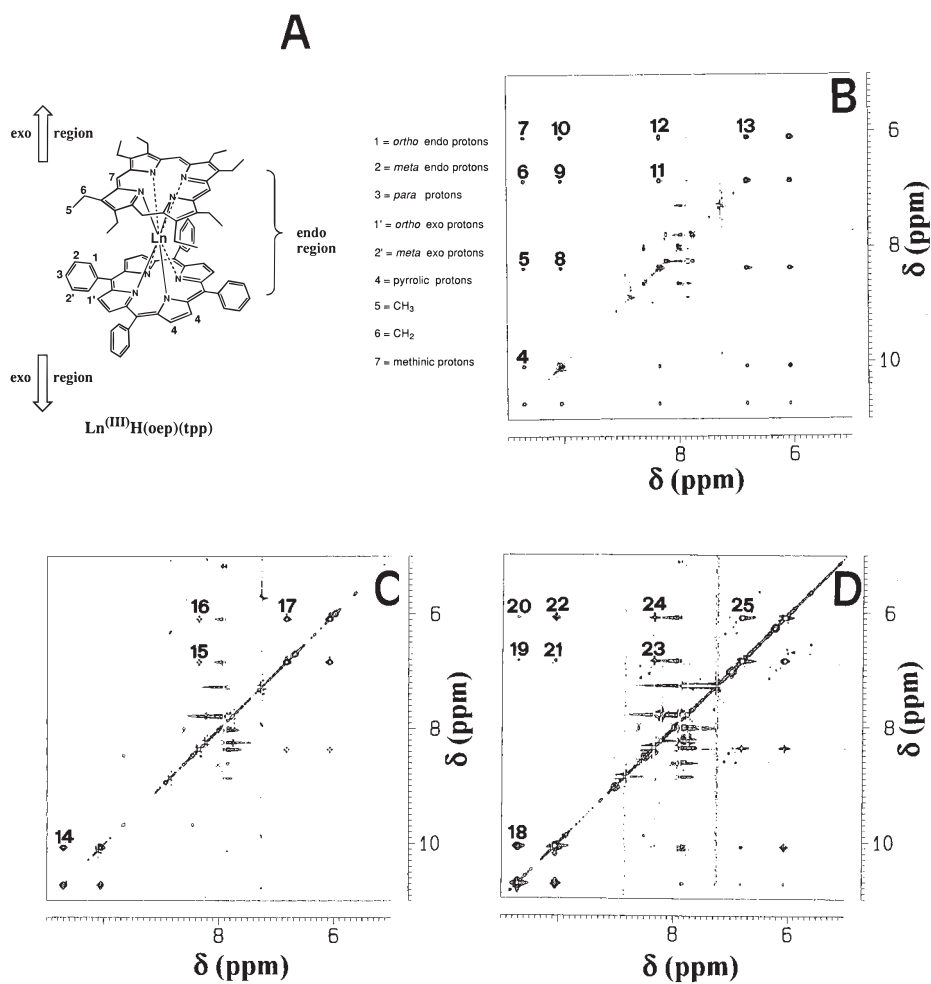


Figure 12.8: Experimental two-dimensional ^1H - ^1H homonuclear correlation spectra of $\text{YbH}(\text{oep})(\text{tpp})$ complex acquired in solution at 11.74 T and 298 K. The structure of the complex is shown in (A) with $\text{Ln}^{3+} = \text{Yb}^{3+}$. The spectra shown are (B) a TOCSY spectrum with an isotropic mixing time of 40 ms, (C) a NOESY spectrum with a mixing time of 40 ms, and (D) a ROESY spectrum with a spin-lock time of 20 ms. Adapted with permission from [339]. Copyright (1996) American Chemical Society.

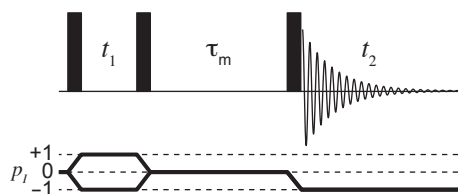


Figure 12.9: Pulse sequence and coherence-transfer pathway for the two-dimensional NOESY and EXSY experiments. The filled rectangles indicate pulses with a nominal flip angle of 90° and phase x .

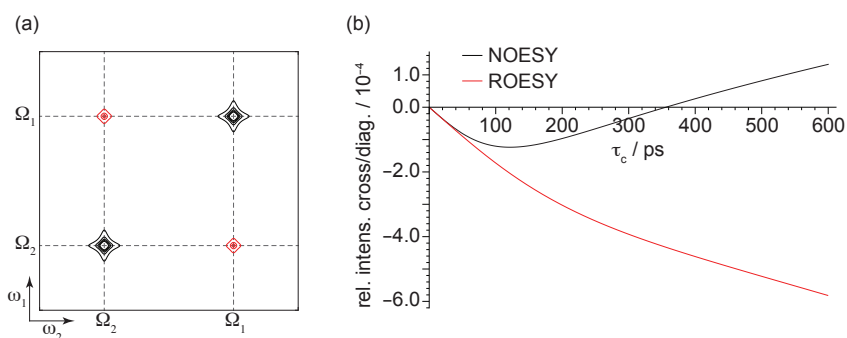


Figure 12.10: Example of a homonuclear through-space correlation spectrum of a two-spin system in a small molecule acquired using either the NOESY or ROESY pulse sequence. The two-dimensional spectrum is shown in (a). The chemical shift offset frequencies of the two spins are Ω_1 and Ω_2 . Positive contours are coloured red, and negative contours are black. The plot in (b) shows the variation of the intensity of the cross peak divided by the intensity of the diagonal peak as a function of correlation time for both two-dimensional NOESY and ROESY. The plot in (b) was calculated for two ^1H nuclei separated by 5 \AA , in a magnetic field of 11.74 T . The NOE/ROE mixing time is 100 ms . Here the correlation time at which the NOE enhancement is zero is 360 ps .

the TOCSY sequence, but without the isotropic mixing element; instead the mixing sequence is a simple z -filter of duration τ_m . The transfer of z -magnetization from one spin to another occurs during τ_m , which for diamagnetic systems is usually between 100 ms and 1 s . For paramagnetic systems, on the other hand, one should set τ_m so that it does not exceed T_1 . The two-dimensional spectrum contains both diagonal and cross peaks, both with the absorption lineshape. One interesting feature of the NOESY experiment is that the relative signs of the cross and diagonal peaks changes with the correlation time τ_c . For small molecules with rotational correlation times, of the order of 10^{-10} s , the cross peaks are of opposite sign to the diagonal peaks. Hence if we process the spectrum so that the diagonal peaks are of negative intensity, the cross-peaks are positive. A NOESY spectrum simulated for such a small molecule is shown in Figure 12.10 (a). On the other

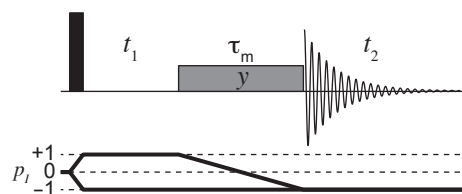


Figure 12.11: Pulse sequence and coherence-transfer pathway for the two-dimensional ROESY experiment. The filled rectangles indicate pulses with a nominal flip angle of 90° and phase x , and the grey rectangle is a spin-lock pulse of duration τ_m and phase y .

hand, large biomolecules with longer correlation times, of the order of 10^{-8} s, the sign of the cross-peaks is inverted so that it is the same as that of the diagonal peaks. This is shown in the plot of the ratio of the cross-peak and diagonal peak as a function of correlation time for a two-spin system in Figure 12.10 (b). It can be seen that there is an intermediate correlation time at which the rate of cross relaxation is zero; the precise value depends on the Larmor frequencies of the nuclei, and therefore the magnetic field, but is generally of the order of 5×10^{-10} s. This is disadvantageous if the molecule under study happens to have such a correlation time, as no cross peaks are observed.

The second experiment avoids this problem. The pulse sequence of this Rotating frame Overhauser Effect Spectroscopy (ROESY) experiment is shown in Figure 12.11. Here the mixing period comprises a spin lock of the single-quantum coherences, during which cross-relaxation takes place. The spin lock is often applied off resonance to avoid transfer via the TOCSY mechanism. The advantage of ROESY over NOESY is that the cross and diagonal peaks are always of opposite sign for any correlation time, as shown by the plot of the ratio of the intensities of the cross peak and diagonal peak in Figure 12.10 (b), and so the spectrum has the same form as that in Figure 12.10 (a). The disadvantage of ROESY is that it is necessary to spin lock for times of the order of 100 ms, and so only low RF field amplitudes can be used. This may be problematic for paramagnetic molecules with large spectral dispersion.

A comparison between the NOESY and ROESY spectra of the lanthanide complex $\text{YbH}(\text{oep})(\text{tpp})$ is shown in Figure 12.8 (c) and (d) [339]. For this system it can be seen that there are a number of cross peaks observed in the ROESY spectrum (19–22) that are not seen by NOESY. As for the TOCSY spectrum applied to this complex, we note that the modest shift dispersion and PRE induced by Yb^{3+} ensure that the spin-lock transfer in the ROESY sequence is relatively efficient.

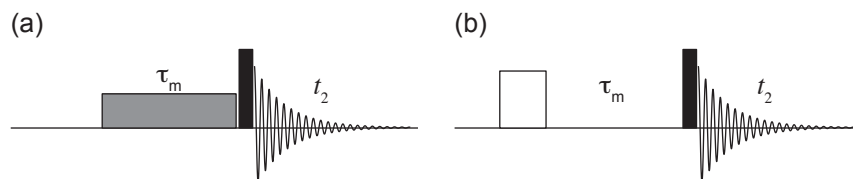


Figure 12.12: Pulse sequences for the (a) one-dimensional steady-state, and (b) one-dimensional selective-inversion-transfer NOESY experiments. The filled rectangles indicate pulses with a nominal flip angle of 90° , and unfilled rectangles indicate pulses with a nominal flip angle of 180° . The grey rectangle indicates a saturation pulse-sequence element.

The through-space NOE transfer can also be achieved using one-dimensional techniques, such as the steady-state and selective-inversion NOE pulse sequences shown in Figure 12.12 (a) and (b). In the steady-state experiment the longitudinal magnetization of one spin is perturbed from its equilibrium value by selective saturation for a time of the order of 1–100 ms. During the irradiation the magnetization is transferred via cross relaxation. A final 90° pulse then excites the resonances, which are observed during acquisition. The NOE transfer leads to an enhancement or diminution of the resonance intensities of the spins that are close in space to the irradiated spin. This enhancement can be seen more easily by subtracting from the steady-state spectrum a reference one-dimensional spectrum in which the amplitude of the irradiation field is set to zero or, more commonly, the irradiation frequency is set well outside the spectrum of interest. Furthermore it is found experimentally that it is preferable not to fully saturate the signal of interest, but rather to irradiate with just sufficient power to reduce the intensity to 60% of its initial value [340, 341]. The full set of NOE transfers can be obtained by repeating the experiment, irradiating each spin in turn. The inversion-transfer experiment follows a similar principle. Here one spin is perturbed from equilibrium by a selective 180° inversion pulse. The NOE transfer happens during the subsequent mixing time τ_m , and the spectrum is excited by the final 90° pulse. Once again the signal changes caused by the NOE are observed following subtraction of a reference spectrum.

Figure 12.13 shows a series of difference spectra acquired for $\text{YbH}(\text{oep})(\text{tpp})$ using the steady-state NOE sequence [339]. In the difference spectra the positive peaks from nuclei experiencing an NOE transfer are of low intensity, but can still be easily identified even when they are close to the more intense negative peak of the irradiated nuclear spin. The selective steady-state method has also been used to provide an unequivocal assignment of the resonances in the small paramagnetic molecule YbDOTMA in solution, which is an

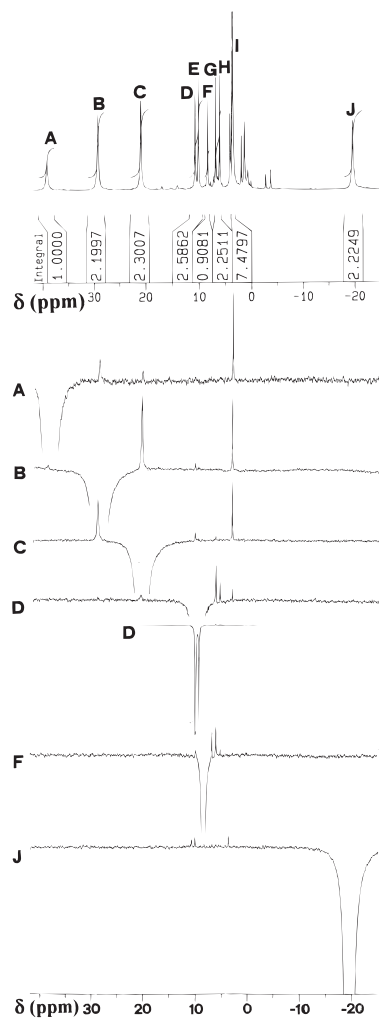


Figure 12.13: One-dimensional NOE difference spectra of the YbH(oep)(tpp) complex acquired at 11.74 T and 298 K. The upper trace is the reference spectrum, labelled with the integrals of selected regions. The six spectra (A)–(D), (F), and (J) are the NOE difference spectra acquired following saturation of the corresponding ¹H indicated in the reference spectrum. In all cases the irradiated ¹H gives a negative peak in the difference spectrum, and the ¹H nuclei experiencing an NOE transfer give positive peaks. The structure of YbH(oep)(tpp) is given in Figure 12.8 (a). Reproduced with permission from [339]. Copyright (1996) American Chemical Society.

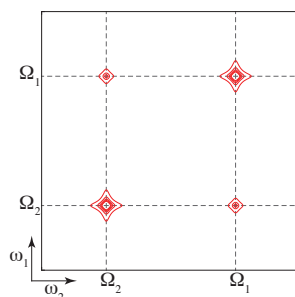


Figure 12.14: Example of a homonuclear EXSY spectrum of a two-spin system in which the two nuclear spins are in slow exchange. The chemical shift offset frequencies of the two spins are Ω_1 and Ω_2 . Positive contours are coloured red.

analogue of the MRI contrast agent GdDOTA[342]. This assignment was used to elucidate the conformation adopted in solution.

Homonuclear exchange correlations

The final homonuclear correlation experiment we consider is EXchange SpectroscopY (EXSY). This method correlates between nuclear species that are in slow chemical exchange, which is defined as being when the rate of exchange is small compared to the differences in chemical shifts expressed in frequency units. The pulse sequences are the same as for the NOESY and ROESY experiments in Figures 12.9 and 12.11. In both cases the transfer of magnetization between nuclear spins occurs during the mixing periods τ_m , and result in similar spectra. We note that when we are in the fast exchange limit, such that the rate of exchange is large compared to the difference in chemical shifts, the two distinct peaks in the spectrum collapse into a single resonance the linewidth of which depends in part on the exchange lifetime τ_M . Figure 12.14 gives an example of a simulated spectrum that would be observed for slow exchange between two sites with offset frequencies Ω_1 and Ω_2 .

Two-dimensional ^1H EXSY has been used to study the slow-exchange dynamics of the two isomeric forms of molecules derived from the MRI contrast agent GdDOTA. Expansions of the ^1H EXSY spectra of YbDOTA $^-$ acquired at two temperatures are shown in Figure 12.15 [295]. The spectrum acquired at 25°C in Figure 12.15 (a) shows several cross peaks between resonances of the two isomeric forms of the molecule. When the temperature is lowered to 0°C in Figure 12.15 (b), the rate of exchange is reduced and fewer cross peaks are observed at the same mixing time. An analogous study has been made of the molecule YbDOTMA

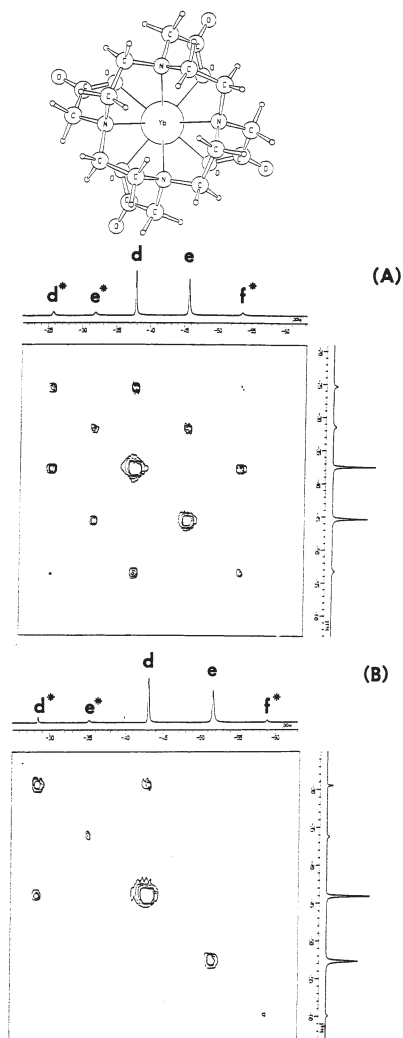


Figure 12.15: Expanded region of the two-dimensional ^1H EXSY spectrum of YbDOTA^- acquired at two temperatures. The structure of YbDOTA^- is given above the spectra. The spectrum acquired at 25°C is shown in (a), and the spectrum at 0°C is shown in (b). The ^1H Larmor frequency is -400 MHz, and the mixing time is 5 ms. Adapted with permission from [295]. Copyright (1992) American Chemical Society.

in solution [342].

Heteronuclear through-bond correlations

A central experiment in any spectral assignment strategy is correlation between different types of nuclear spin. For the NMR of small organic molecules the most acquired correlations are between ^1H and a heteronucleus X, which may for example be ^{13}C or ^{15}N at natural abundance. When choosing a pulse sequence we have a choice over which nucleus to excite at the beginning of the sequence, and which to observe. If the excited nuclear spin has gyromagnetic ratio γ_{exc} and longitudinal relaxation time constant T_1^{exc} , and the observed nucleus has gyromagnetic ratio γ_{obs} , it can be shown that the overall sensitivity is approximately proportional to [257]

$$\gamma_{\text{exc}}\gamma_{\text{obs}}^{3/2} \left[1 - \exp\left(-T/T_1^{\text{exc}}\right) \right], \quad (12.2)$$

where T is the recycle delay. Equation 12.2 represents an optimistic expectation for the achievable sensitivity, and in practice must be multiplied by factors that account for the efficiency of the coherence transfer(s) in the sequence, the quality factor of the probe for the observed nucleus, and the inverse linewidth of the observed nucleus. For diamagnetic molecules there is a sensitivity advantage to both exciting and detecting ^1H (via two transfers), as it has firstly both the larger gyromagnetic ratio, and secondly generally lower T_1 values which allow us to shorten the recycle delay. For paramagnetic molecules the advantage is less clear as the shorter ^1H T_2 time constants lead both to a loss in the efficiency of the coherence transfers, which is exacerbated by the use of a second transfer back to ^1H , and to broader ^1H lines. Nevertheless it is generally observed that for small paramagnetic molecules ^1H excitation and detection is preferable, whereas for large paramagnetic biomolecules with significant Curie broadening better sensitivity can be obtained by detecting the narrower heteronucleus resonances.

One experiment that has been successfully applied to paramagnetic molecules is the Heteronuclear Multiple-Quantum Correlation (HMQC) sequence for one-bond correlations shown in Figure 12.16 (a). The ^1H spin is excited by the first pulse, and then evolves under the heteronuclear J -coupling during the delay τ_1 . The coherence is transferred to X by the first X pulse, which generates multiple-quantum coherences between the two spins of total coherence orders -2 , 0 , and $+2$. The chemical shift of X then evolves during t_1 , before the second X pulse regenerates the ^1H single-quantum coherence and the J -coupling evolves during the second

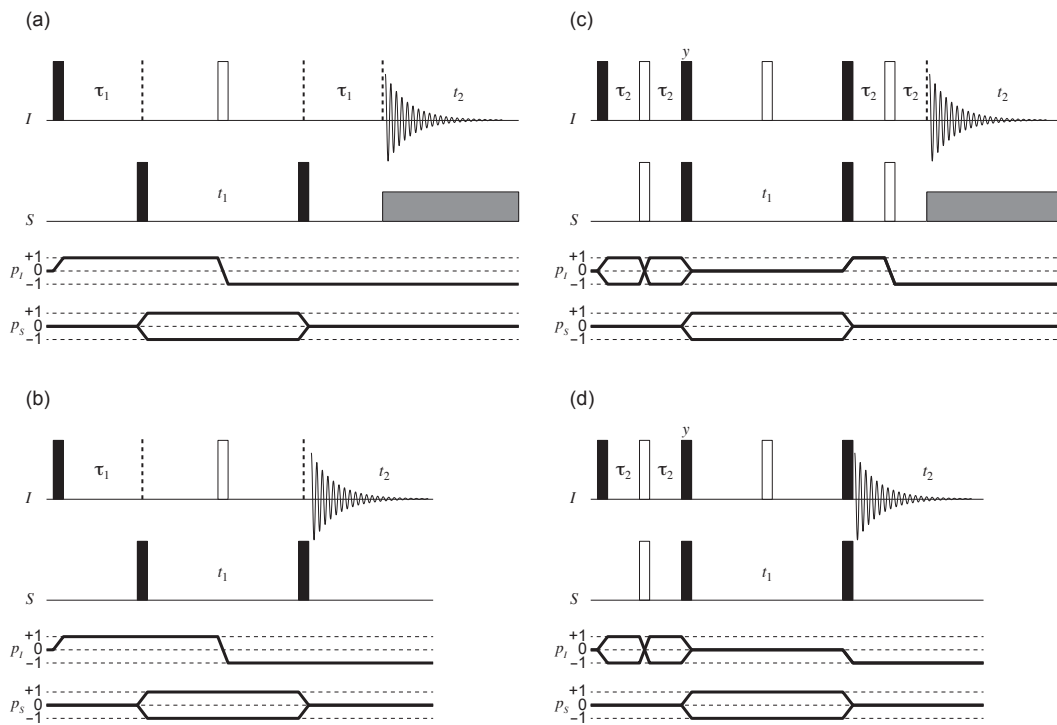


Figure 12.16: Pulse sequences and coherence-transfer pathways for the two-dimensional HMQC and HSQC experiments. The basic HMQC sequence is shown in (a), in which we detect the in-phase doublet during acquisition. Heteronuclear decoupling may be employed in order to observe a singlet. Alternatively we can observe the anti-phase doublet using the sequence in (b). The delays τ_1 have an optimum value of $1/(2J_{IS})$ in the absence of relaxation. The basic HSQC sequence is shown in (c), in which we observe either the in-phase doublet or, using heteronuclear decoupling, a singlet. We can also observe the anti-phase doublet directly using the HSQC sequence in (d). The delays τ_2 have an optimum value of $1/(4J_{IS})$. The filled rectangles indicate pulses with a nominal flip angle of 90° , and unfilled rectangles indicate pulses with a nominal flip angle of 180° . The grey rectangle represents broadband heteronuclear decoupling. All pulses have phase x .

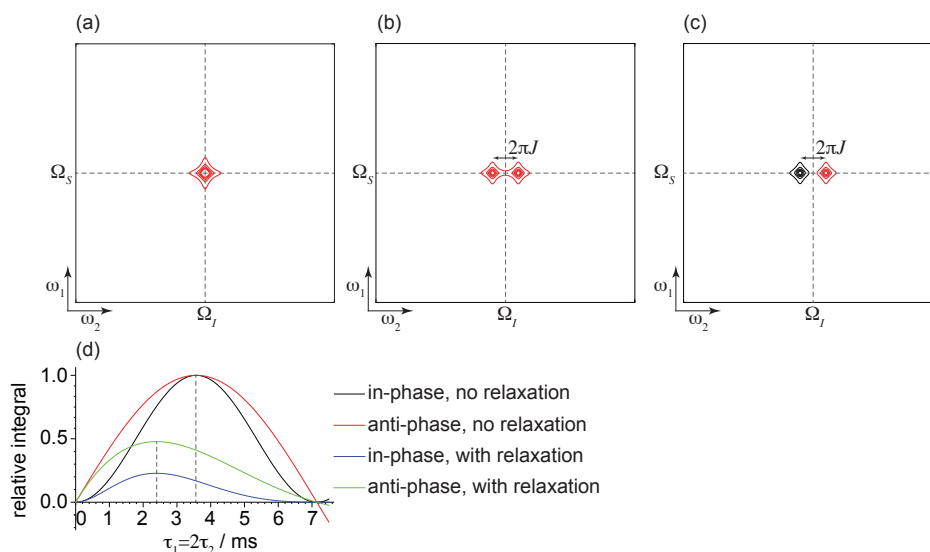


Figure 12.17: Examples of heteronuclear correlation spectra of a two-spin heteronuclear spin system I – S acquired using either the HMQC or HSQC experiment. The chemical shift offset frequencies of the two spins are Ω_I and Ω_S , and the heteronuclear J -coupling constant is J . In (a) is shown the spectrum obtained with heteronuclear S -spin decoupling during acquisition. In the absence of decoupling we obtain a doublet with an in-phase splitting in ω_2 , as shown in (b). Alternatively we can acquire immediately after the final 90° pulse(s), and obtain a spectrum with an anti-phase doublet, as shown in (c). Positive contours are coloured red, and negative contours are black. In (d) are shown the peak intensities obtained with and without transverse relaxation for the HMQC (as a function of τ_1) and HSQC (as a function of τ_2) pulse sequences that generate the in-phase and anti-phase doublets. These curves were generated with $J = 140$ Hz and $T_2 = 4$ ms.

delay τ_1 . Finally ^1H is detected during t_2 . If heteronuclear decoupling is applied to X during detection the spectrum contains a single peak, as shown by the simulated spectrum in Figure 12.17 (a). For paramagnetic systems heteronuclear decoupling may be ineffective, or deleterious to the quality of the spectrum. In this case the decoupling pulses can be omitted during acquisition, resulting in a spectrum containing a doublet with an in-phase splitting in the direct dimension, as shown in Figure 12.17 (b).

The advantage of this experiment is its simplicity: there are only four pulses in the sequence, which reduces the effects of imperfections when applied to paramagnetic systems. The two most significant sources of error are the 180° pulse on ^1H , and the heteronuclear decoupling during acquisition. The first problem arises because the bandwidths of 180° pulses are generally lower than those of 90° pulses. However if the conventional pulse proves to have insufficient bandwidth to excite the whole ^1H spectrum it can be replaced by more broadband composite 180° pulses, such as the broadband inversion pulses (BIPs) of Smith et al

[343]. The second problem is due to the large spectral dispersion of paramagnetic systems, which may make decoupling inefficient. However if this is the case the decoupling can simply be omitted.

The peak intensity is proportional to $\sin^2(\pi J_{IS} \tau_1)$, where J_{IS} is the one-bond heteronuclear J -coupling constant, and so the optimum value for τ_1 is $1/(2J_{IS})$. For one-bond correlations between ^1H and ^{13}C the coupling constant is typically 140 Hz, resulting in an optimum τ_1 of 3.6 ms, as shown in Figure 12.17 (d). However for short T_2 it is usually found that the optimum delay is shorter, as shown in Figure 12.17 (d) where a T_2 of 4 ms reduces the optimum value of τ_1 to 2.4 ms. The maximum peak intensity is reduced to 0.22 of the value expected with no relaxation. Such losses are expected for paramagnetic systems, but may be unacceptable when sensitivity is at a premium. In these cases we can simply omit the second delay τ_1 to mitigate this sensitivity loss, which gives the pulse sequence in Figure 12.16 (b). The resonance now appears as an anti-phase doublet, as shown in Figure 12.17 (c), with an intensity proportional to $\sin(\pi J_{IS} \tau_1)$ with no relaxation. However when we account for relaxation with the same T_2 of 4 ms, we see in Figure 12.17 (d) that the optimum τ_1 is again reduced to 2.4 ms, but that the intensity of the peak is reduced only to 0.48. Thus the omission of the second delay τ_1 can result in double the sensitivity compared to the first sequence.

A second heteronuclear correlation experiment that is widely used is the Heteronuclear Single-Quantum Correlation (HSQC). The basic pulse sequence, which contains more pulses than the HMQC sequence, is shown in Figure 12.16 (c). This experiment correlates the anti-phase single-quantum coherences of the S -spin in t_1 against the in-phase single-quantum coherence of the I -spin in t_2 . The anti-phase coherences are generated and reconverted by a pair of heteronuclear spin-echo sequences, with half-echo delays τ_1 . The form of the spectra in the presence and absence of heteronuclear decoupling during acquisition is, as shown in Figure 12.17 (a) and (b), the same as for the corresponding HMQC spectra. The intensity of the resonance is proportional to $\sin^2(2\pi J_{IS} \tau_2)$, which is a maximum when τ_2 is set to $1/(4J_{IS})$, if we neglect relaxation effects. For a coupling constant of 140 Hz, the optimum τ_2 is 1.8 ms. As for the HMQC experiment, the reconversion of the I -spin coherences from anti-phase to in-phase immediately prior to acquisition in the HSQC experiment can be omitted for systems with short T_2 times. The arguments for the improved sensitivity resulting from the omission of the second spin echo are the same as for the HMQC experiment given above, and so the plots in Figure 12.17 (d) also apply to the HSQC sequences with $\tau_1 = 2\tau_2$. This resulting HSQC pulse sequence is shown in Figure 12.16 (d), and produces a spectrum with an anti-phase splitting as shown in Figure 12.17 (c).

When any of these HMQC or HSQC sequences are applied to proteins in aqueous solution, it is very important to suppress the water signal. This can be done, for example, by incorporating pulse-sequence elements based on experiments like WEFT. This has been done recently by Ciofi-Baffoni et al. who incorporated water suppression in an HSQC sequence to give the IR-HSQC-AP experiment [344].

12.3 Solution NMR of paramagnetic proteins

The study of the structure and dynamics both of paramagnetic metalloproteins [345] in solution, and proteins carrying a paramagnetic tag [346], has seen substantial progress over the years. As for small molecules the paramagnetic ion in the protein is a rich source of structural information that can be exploited, but also presents spectroscopic challenges. Many of these challenges are the same as for small molecules. However there is an additional problem that we meet when studying paramagnetic proteins, which is that the transverse PREs are augmented by substantial Curie relaxation, which leads to very severe line broadening. These features are briefly discussed here, beginning with drawing a parallel with diamagnetic proteins.

12.3.1 General strategy for resonance assignment and structural restraints

When used to describe a protein the term ‘structure’ has a more complex meaning than for a small molecule. This is because a protein is a macromolecule, and exhibits structural features on four different levels. All proteins are formed from a sequence of amino acids, of which there are twenty with the basic structure $\text{H}_2\text{N}^+\text{CHR}\text{CO}_2\text{H}$, via a series of peptide bonds. Each amino acid comprises a carboxylic acid group, and an amine and sidechain R joined to the α carbon. The precise sequence of amino acids that forms the protein, and example of which is shown in Figure 12.18 (b), is referred to as the primary structure. The primary structure comprises two parts, referred to as the backbone and the sidechains. The former comprises a repeating sequence of the directly-bonded atoms of an amide nitrogen (N), which is joined to an α carbon (CA), which is joined to a carbonyl carbon (CO, or C'). To this basis sequence we also add the amide proton (H^{N}), α proton (H^{CA}), and the β carbon (CB), to give an extended backbone. The sidechains (SC) comprise the R groups of the amino acids.

The amino acid sequence can then form local structural conformations, such as α -helices or β -sheets; an example of the latter is shown in Figure 12.18 (b). These structural features are due to cooperative hydrogen

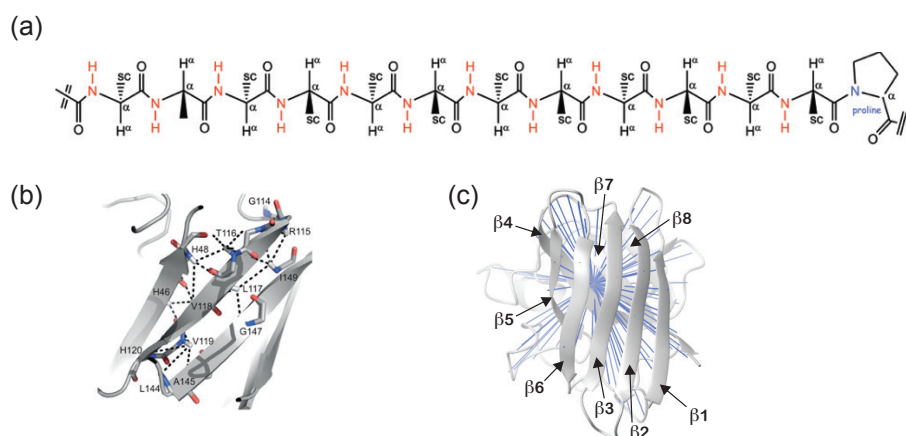


Figure 12.18: Illustration of the structure of a protein. The primary structure, comprising the sequence of amino acids, is shown in (a). The first step in the NMR structural analysis of the protein is to perform a sequential assignment of the nuclear spins along the backbone (HN, CO, CA, CB), and of the nuclear spins in the sidechains (SC). Following this the three-dimensional secondary and tertiary structures are determined by measuring distance restraints. This may involve measuring distances between ^1H nuclei in the backbone or sidechains via dipolar-based methods (b), or measuring the PCS induced by a paramagnetic centre (c).

bonds, and are referred to as secondary structure. The tertiary structure is the overall three-dimensional shape that the protein adopts when it folds, as shown in Figure 12.18 (c). Finally, individual protein units can aggregate to form larger assemblies, the quaternary structure.

Frequently a strategy for obtaining structural information about the protein comprises two parts. Firstly we need to obtain a complete assignment of the nuclear resonances along the protein backbone and sidechains. For the backbone this requires a so-called sequential assignment in which the connectivities of the N, CO, CA, CB, H^{N} , H^{CA} , and possibly H^{CB} are established using three- and higher-dimensional triple-resonance experiments that correlate the ^1H , ^{13}C , and ^{15}N nuclear spins. These experiments combine heteronuclear one-bond coherence transfers, using schemes based on either the HSQC or HMQC experiments and homonuclear ^1H - ^1H and ^{13}C - ^{13}C transfers either following spin-echo pulse sequence elements, or using TOCSY. There are experimental schemes that accomplish one-bond coherence transfers between spins within each amino acid, and other schemes that perform transfers across the CO-N bonds in order to establish connectivities between the resonances of one amino acid and those of the neighbouring residue. These experimental schemes are well-established, and generally follow the pattern that ^1H is both excited and directly detected in order to maximize sensitivity as in the HSQC experiment [347]. In addition similar techniques are used for the

sequential assignment of the amino acid sidechains [347].

Secondly, having obtained the assignment of the full set of resonances, we employ experimental schemes to establish which nuclear spins have a close spatial proximity. These distance restraints are then used in a restrained molecular dynamics simulation to determine how the protein folds in the tertiary structure. Typically we employ three- and higher-dimensional triple-resonance experiments which contain a NOESY through-space transfer block in order to measure H^N-H^N , H^N-H^{CA} , and $H^{CA}-H^{CA}$ distance restraints between the backbone protons, restraints between protons on the backbone and those on the sidechains, and restraints between sidechain protons [347].

In paramagnetic proteins we have the additional advantage that the paramagnetic effects can be used to measure the positions of the nuclear spins relative to the metal ion. These so-called paramagnetic restraints can then be combined with the other distance restraints described above. However we also encounter problems that arise from the large shifts and PREs that are experienced by nuclei close to the metal ion. These mean that nuclear spins close to the metal centre are harder to observe using conventional experimental schemes which use practicable RF fields and contain several coherence-transfer steps with an overall duration of several milliseconds. The result is that the protein contains a so-called blind sphere centred on the metal ion, within which we do not observe the nuclear spins using conventional experimental pulse sequences. This is illustrated in Figure 12.19, which also includes the other regions into which we can divide the protein, depending upon the effect of the paramagnetic centre. The size of the blind sphere depends on the nature of the metal ion, and in particular the size of the PRE. For example metal ions which induce large PREs, such as Mn^{2+} , Cu^{2+} , and Gd^{3+} , have larger blind spheres than metal ions associated with substantially lower induced PREs, such as the other trivalent lanthanide ions. If we employ both the excitation and detection of protons the typical radius of the blind sphere is in the range 8–10 Å for a 10 kDa protein, and becomes larger for increasing molecular mass. One key reason for the presence of the blind sphere is that the nuclear spins close to the metal ion experience a large SA which, in combination with the slow rotational diffusion of the protein, results in severe line broadening due to transverse Curie relaxation. However we can reduce the size of the sphere by employing protonless NMR methods, in which the strategies for both assignment and distance restraints are based only on ^{13}C and ^{15}N , which are of lower gyromagnetic ratio and therefore experience a lower PRE [345, 348–351]. Here we trade sensitivity for increased resolution. In such cases the blind sphere radius may be reduced to approximately 5.5 Å.

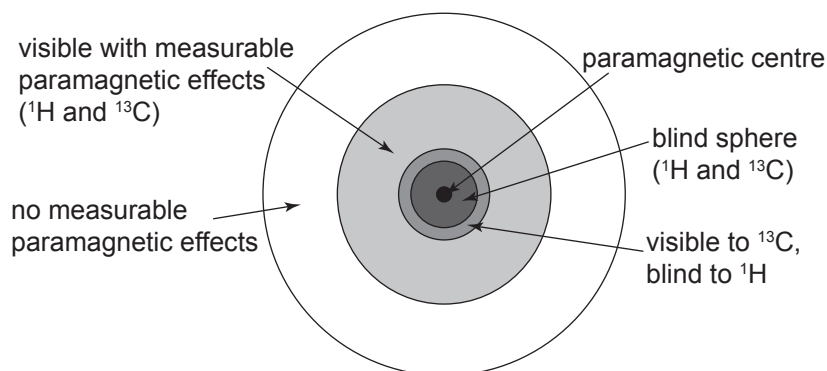


Figure 12.19: Schematic highlighting the different regions of a metalloprotein containing a paramagnetic metal ion that behave differently in the NMR experiment. There is a so-called ‘blind sphere’ centred on the metal ion, of typical radius 8–10 Å, where the nuclear spins cannot be observed using conventional NMR pulse sequences. The size of this sphere for any given protein is reduced if we employ protonless NMR methods and observe ^{13}C instead. Beyond the blind sphere there is a region where the nuclear spins can be observed using conventional methods, and which exhibit long-range paramagnetic effects, such as PCS and PRE, that are measurable. Beyond this region the nuclear spins are sufficiently far from the paramagnetic centre for the paramagnetic shifts and relaxation effects to be unmeasurable.

At distances from the metal centre beyond the blind sphere there is a region in which the nuclear spins are observable by conventional (or adapted) NMR experiments and exhibit measurable paramagnetic effects, such as the PCS and PRE, as shown in Figure 12.19. It is in this region that paramagnetic restraints can be used to refine the tertiary structure of the protein. Finally in very large proteins there is a further region at longer distances from the metal ion in which there are no paramagnetic shifts or relaxation effects. However we may see broadening from the BMS due to a non-spherical sample. Here standard NMR experiments can be used exactly as for diamagnetic proteins.

12.3.2 Paramagnetic NMR methods

Inside the blind sphere

Despite being referred to as the ‘blind sphere’ it is actually possible to observe and assign the nuclear spins within this region if we use pulse sequences that are optimized for large shifts and large PREs. Residue-specific assignments of the protons can be performed using simple NMR pulse sequences such as the one-dimensional steady-state NOE experiment [352], and two-dimensional COSY and NOESY[353, 354]. If necessary, additional sequences can be employed to aid the assignment, such as ^1H TOCSY and ^1H – ^{13}C

HMQC [46].

Great care must be taken in interpreting the COSY spectra of paramagnetic biomolecules with slow rotational diffusion. It has been shown by Bertini et al. that in addition to the expected cross peaks that indicate J -coupling, cross peaks may also appear due to relaxation-induced coherence transfer even in the absence of a J -coupling [265]. This is due to cross-correlation between the relaxation mechanism involving the dipolar coupling of the two spins in question with the Curie relaxation mechanism of one of the spins. As discussed in section 8.8.3, the presence of the cross-peak multiplet is due to cross-relaxation between the in-phase and anti-phase coherences of the spin that is induced by cross-correlated relaxation (CCR). In addition the CCR results in the two components of the doublet having different linewidths in the two dimensions, and so for zero J -coupling we do not obtain the perfect cancellation that we would see without CCR. The result is that with CCR, even in the limit of zero J -coupling, we can both generate an anti-phase coherence which is transferred to the second spin by the mixing period, and observe an anti-phase doublet in the cross-peak multiplet. However the COSY experiment remains an extremely useful assignment aid in the blind sphere of paramagnetic proteins [355].

Outside the blind sphere

Nuclear species outside the so-called blind sphere can be observed by employing the standard NMR experiments for diamagnetic proteins. For example two-dimensional ^1H - ^{15}N HSQC spectroscopy has been performed on the 30 kDa complex between the N-terminal domain of the ϵ subunit and the θ subunit of Escherichia coli DNA polymerase III both in the absence and presence of a paramagnetic metal ion [356]. In order to reduce sensitivity losses due to transverse Curie relaxation, the sequence in Figure 12.16 (d) was used in which the anti-phase splitting is detected in the direct ^1H dimension in the absence of ^{15}N decoupling.

Since ^1H has a larger gyromagnetic ratio than either ^{13}C or ^{15}N , both initial excitation and detection of ^1H are used in conventional sequences is used to maximize the sensitivity, according to Equation 12.2 [347]. However the larger gyromagnetic ratio also leads to a larger Curie transverse PRE in paramagnetic proteins, which leads to a reduction in sensitivity due to the increased line broadening observed in the ^1H dimension, and coherence decay during transfer steps that involve ^1H . For nuclei that are close to the metal ion the relaxation losses incurred may negate any increase in sensitivity from the initial excitation and detection of ^1H . In these cases it has been shown that protonless NMR experiments, in which the initial excitation and

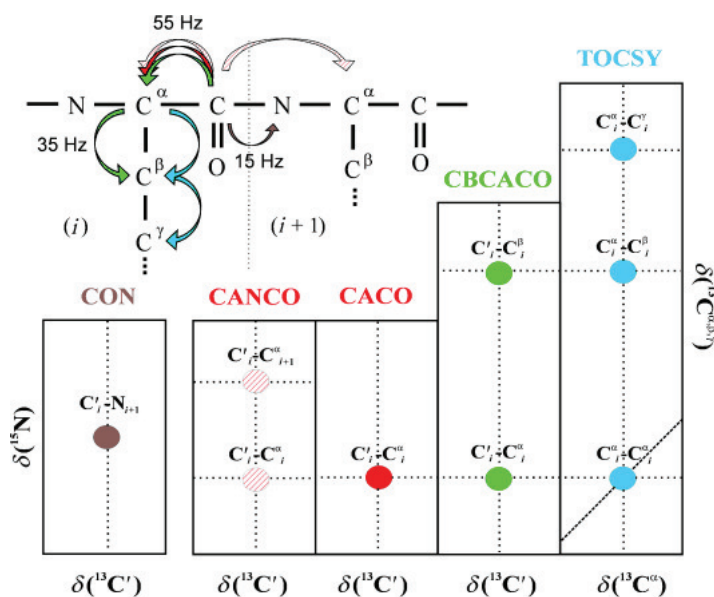


Figure 12.20: Illustration of the sequential assignment procedure using $^{13}\text{C}/^{15}\text{N}$ experiments. The relevant one-bond J -coupling constants are given. Reproduced with permission [345]. Copyright John Wiley and Sons.

observation are both on ^{13}C lead to better sensitivity closer to the metal centre, and allow us to detect nuclei closer to the paramagnetic ion, reducing the radius of the blind sphere from 8–10 Å to 4–5 Å [345, 348–351, 357–361]. For example single-resonance ^{13}C COSY, ^{13}C multiple-quantum experiments between CO and CA (COCAMQ), and ^{13}C NOESY have been shown to be useful for the detection of signals in $\text{Cu}^{2+}/\text{Zn}^{2+}$ superoxide dismutase (SOD), allowing detection as close as 4 Å to the Cu^{2+} ion [348], and in Tb^{3+} -substituted human oncomodulin (OM), where the use of protonless methods reduces the radius of the blind sphere from 16 Å to 8 Å [357].

A sequential assignment of the backbone and sidechain resonances can be achieved using a combination of the $^{13}\text{C}/^{15}\text{N}$ experiments CON, CANCO, CACO, CBCACO, and ^{13}C TOCSY [345, 349]. The assignment procedure is illustrated in Figure 12.20. We begin with the CACO experiment, which correlates between the CO and CA nuclei of the same amino acid residue. The CO is correlated to the CB via the CBCACO experiment, and the CA is correlated with the other carbons of the sidechain via the TOCSY. We then connect the sequence of amino acid residues together by measuring correlations between CO and N via the CON experiment, and the CA and CO via the CANCO experiment.

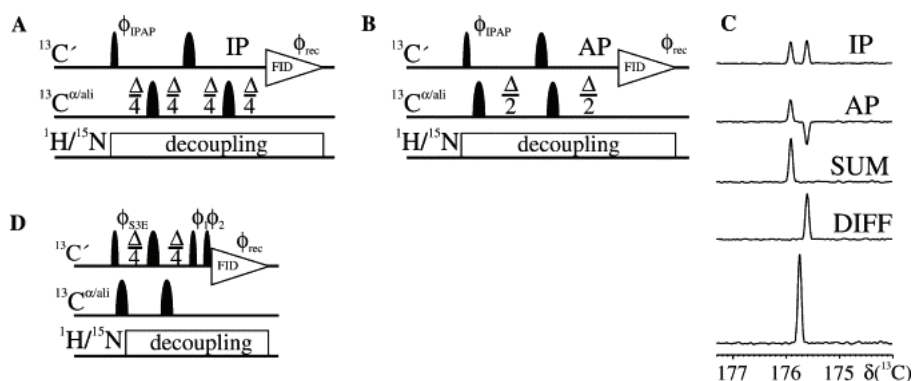


Figure 12.21: The IPAP and S³E pulse sequences for direct detection of CO with removal of the splitting due to the CO–CA *J*-coupling. The IPAP sequences are shown in (a) and (b). The sequence in (a) acquires the in-phase (IP) spectrum, and the anti-phase (AP) spectrum is acquired by (b). As shown in (c) the sum and difference of the two spectra give different components of the doublet. A frequency shift of each component to the position of the CO shift followed by a second summation gives the final decoupled spectrum. The same result can be achieved with the S³E experiment in (d), but with a shorter sequence. The delay Δ is set to $1/(2J_{\text{COCA}})$. Narrow and broad shapes indicate CO- or CA-selective 90° and 180° pulses respectively. The phases are: (a) $\phi_{\text{IPAP}} = x, -x$, and $\phi_{\text{rec}} = x, -x$; (b) $\phi_{\text{IPAP}} = -y, y$, and $\phi_{\text{rec}} = x, -x$; (d) $\phi_{\text{S}^3\text{E}}(1) = \pi/4, \pi/4$, $\phi_1(1) = x, y$, $\phi_2(1) = x, y$, $\phi_{\text{rec}}(1) = x, -x$, and $\phi_{\text{S}^3\text{E}}(2) = \pi/4, 5\pi/4$, $\phi_1(1) = x, y$, $\phi_2(1) = -x, -y$, $\phi_{\text{rec}}(1) = x, -x$, where (1) and (2) are the two experiments required to separate the in-phase and anti-phase spectra. Reproduced from [361], with permission from Elsevier.

In the resulting spectra a significant limitation in the available ¹³C resolution is the one-bond homonuclear *J*-coupling between the CO and CA, and the CA and CB carbons. Therefore it is of advantage to decouple these interactions, to obtain narrower resonances. Whilst in general homonuclear *J*-decoupling is very difficult, we are assisted in the present case by the uniformity of CO–CA and CA–CB *J*-coupling constants, which take values of 55 Hz and 35 Hz respectively. This uniformity allows us to apply methods such as the In-Phase Anti-Phase (IPAP) and Selective-Spin-State Excitation (S³E) methods shown in Figure 12.21 [361]. In the IPAP method two sequences are employed (Figure 12.21 (a) and (b)) which acquire two spectra of the CO resonances, in which the splitting due to the CO–CA coupling is in-phase (IP) and anti-phase (AP) respectively. This is achieved by allowing the CO coherence to evolve during selective spin-echoes in which the total echo delay is $\Delta = 1/(2J_{\text{COCA}}) = 9.1$ ms. As shown in Figure 12.21 (c), the sum of the IP and AP spectra yields a spectrum in which only one component of the doublet is present, and the difference yields the other component. Finally a frequency shift of the components in the two spectra so that they lie at the CO shift followed by summation results in a CO spectrum that is homonuclear *J*_{COCA}-decoupled. The S³E

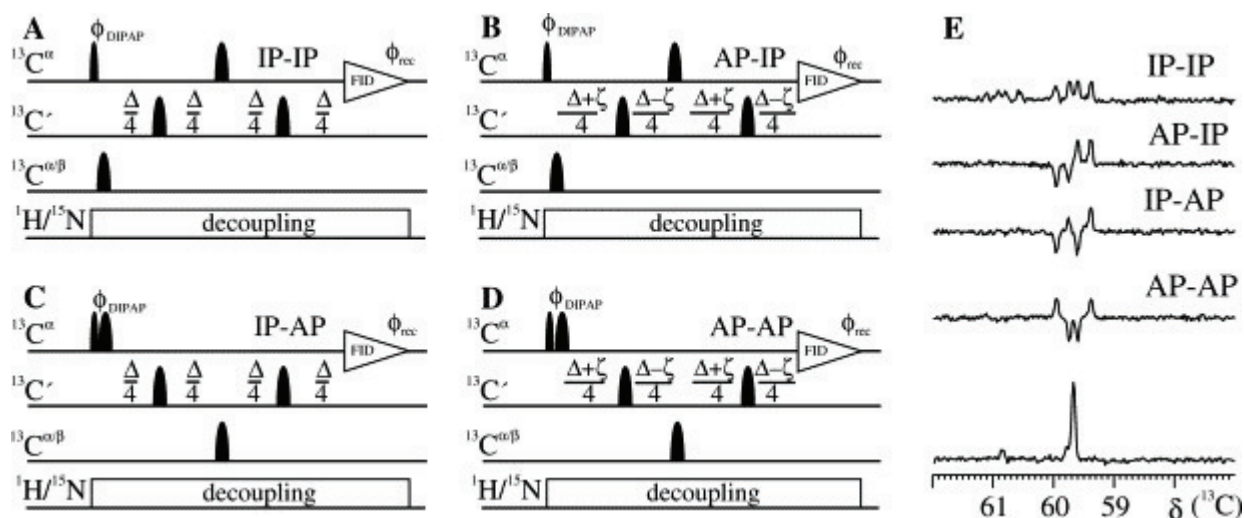


Figure 12.22: The DIPAP pulse sequences for direct detection of CA with removal of the two splittings due to the CO–CA and CA–CB J -couplings. The four sequences acquire spectra that are (a) in-phase with respect to both couplings (IP-IP), (b) anti-phase with respect to the CO–CA coupling only (AP-IP), (c) anti-phase with respect to the CA–CB coupling only (IP-AP), and (d) anti-phase with respect to both couplings (AP-AP). In (e) are shown the four spectra acquired from a single amino acid, plus the decoupled spectrum obtained from a suitable combination of the four spectra. The delays Δ and ξ are set to $1/(2J_{CACB})$ and $1/(2J_{COCA})$ respectively. Narrow and broad shapes indicate CO- or CA-selective 90° and 180° pulses respectively. The phases are: $\phi_{\text{DIPAP}}(\text{A}) = y, -y$, $\phi_{\text{DIPAP}}(\text{B}) = x, -x$, $\phi_{\text{DIPAP}}(\text{C}) = -y, y$, $\phi_{\text{DIPAP}}(\text{D}) = x, -x$, and $\phi_{\text{rec}} = x, -x$. Reproduced from [361], with permission from Elsevier.

method achieves the same result, but using the sequence in Figure 12.21 (d). Here two spectra are acquired following evolution during two selective spin-echo sequences with total echo delays of $\Delta/2 = 1/(4J_{\text{COCA}}) = 4.5$ ms. These are combined as for the IPAP method to give the decoupled CO spectrum. It is worth noting that the S^3E method has the advantage of using the shorter pulse sequences, and so incurs lower losses due to transverse Curie relaxation. Both methods can be incorporated into any more sophisticated correlation experiment in which the CO dimension is directly acquired.

Both the IPAP and S^3E methods can also be implemented for direct observation of the CA resonances in order to remove the splitting due to the CO–CA coupling. The resulting spectra will, of course, still contain the splitting due to the other large J -coupling between CA and CB. However this latter splitting can be removed too by employing the Double IPAP (DIPAP) method shown in Figure 12.22 [361]. Here we acquire four spectra using the pulse sequences in Figure 12.22 (a)–(d), in which the the CA resonance is (a) in-phase with respect to both couplings (IP-IP), (b) anti-phase with respect to the CO–CA coupling only

Experiment	Correlations	Reference
2D		
CACO-IPAP/S ³ E	CA _i -CO _i	[351, 358]
CBCACO-IPAP/S ³ E	CB _i -CO _i , CA _i -CO _i	[349, 351]
CCCO-IPAP/S ³ E	C(B,G,D,E) _i -CO _i , CA _i -CO _i	[351]
CON-IPAP	N _i -CO _{i-1}	[351, 362]
CANCO-IPAP	CA _i -CO _{i-1} , CA _{i-1} -CO _{i-1}	[359, 360]
CBCANCO-IPAP	CA _i -CO _{i-1} , CA _{i-1} -CO _{i-1} , CB _i -CO _{i-1} , CB _{i-1} -CO _{i-1}	[351]
3D		
CBCACO-IPAP/S ³ E	CB _i -CA _i -CO _i , CA _i -CA _i -CO _i	[349]
CCCO-IPAP/S ³ E	C(B,G,D,E) _i -CA _i -CO _i , CA _i -CA _i -CO _i	[351]
CANCO-IPAP	CA _i -N _i -CO _{i-1} , CA _{i-1} -N _i -CO _{i-1}	[359, 360]
CBCANCO-IPAP	CA _{i-1} -N _i -CO _{i-1} , CB _{i-1} -N _i -CO _{i-1}	[351]
CCCON-IPAP	CA _{i-1} -N _i -CO _{i-1} , C(B,G,D,E) _{i-1} -N _i -CO _{i-1}	[351]
CBCANCO-IPAP	CA _i -N _i -CO _{i-1} , CA _{i-1} -N _i -CO _{i-1} , CB _i -N _i -CO _{i-1} , CB _{i-1} -N _i -CO _{i-1}	[351]

Table 12.1: Two- and three-dimensional protonless NMR experiments available for obtaining sequential assignments of the C and N spins [361]. For each experiment the observed correlations are given, where the subscript refers to the residue number in the sequence.

(AP-IP), (c) anti-phase with respect to the CA-CB coupling only (IP-AP), and (d) anti-phase with respect to both couplings (AP-AP) as shown in Figure 12.22 (e). These four spectra are then summed and subtracted to give four new spectra, each one of which contains a single component of the doublet of doublets. Following a frequency shift and sum, we obtain the homonuclear-decoupled CA spectrum. As for the simple IPAP and S³E methods, the DIPAP method can be incorporated into any pulse sequence which detects the CA spins directly. The disadvantage of the DIPAP method compared to the simple IP method is that the selective spin echoes have a longer total echo time Δ , which is required for the complete conversion of the CA-CB in-phase coherence to an anti-phase coherence. Hence $\Delta = 1/(2J_{CACB}) = 14.3$ ms, which reflects the shorter CA-CB coupling constant compared to the CO-CA coupling constant.

A large number of two- and three-dimensional protonless NMR experiments has been proposed for the sequential assignment of the backbone and sidechains of paramagnetic proteins, incorporating the IPAP or S³E methods where appropriate. These are listed in Table 12.1 [361] Once the assignment has been obtained we can acquire structural restraints with the ¹³C NOESY experiment, and combine these with a set of paramagnetic structural restraints as described in section 12.3.3.

12.3.3 Paramagnetic structural restraints

The NMR methods described in the previous section for observing the nuclei outside the blind sphere are used to obtain structural restraints describing the position of either the nucleus or a nucleus-nucleus bond

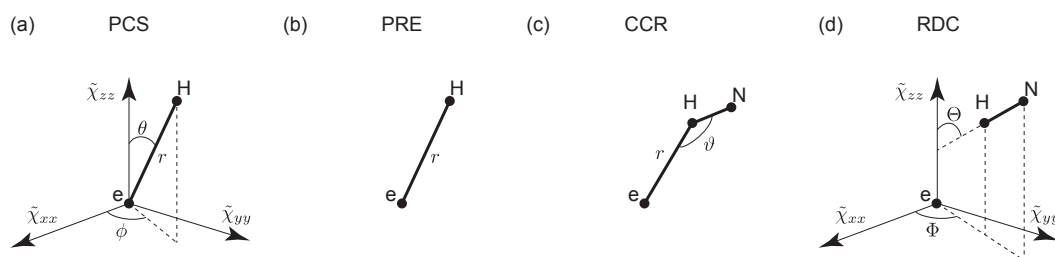


Figure 12.23: Illustration of the information available from the different paramagnetic restraints in a paramagnetic protein, applied to the N–H amide bond. The pseudo-contact shift (PCS) of the ^1H can be used to determine the position of the H with respect to the magnetic susceptibility tensor of the unpaired electrons, via the distance between the nucleus and paramagnetic centre r , and the angles (θ , ϕ) that define the orientation of the electronic–nuclear vector with respect to the PAF of the susceptibility tensor (a). The ^1H paramagnetic relaxation enhancement (PRE) is used to determine the distance r of the H from the paramagnetic centre (b). Both the cross-correlated relaxation (CCR) and residual dipolar coupling (RDC) provide structural restraints for the H–N bond. The CCR broadening of ^1H provides both the distance r between the paramagnetic centre and H, and the angle ϑ between the electronic–H vector and the H–N bond vector (c). The RDC depends on the angles (Θ , Φ) that describe the orientation of the N–H bond and the PAF of the magnetic susceptibility tensor.

with respect to the paramagnetic centre. These restraints can then be used in combination with conventional restraints, such as those obtained from NOESY, to obtain the three-dimensional protein structure. Here we describe four such restraints, namely the PCS, PRE, cross-correlated relaxation (CCR) between the Curie and diamagnetic dipolar mechanisms, and the residual dipolar coupling (RDC). The distance and orientation information that can be obtained from these four restraints is illustrated in Figure 12.23 [356]. In addition we comment on the measurement of contact shifts inside the so-called blind sphere, and their use as structural restraints for nuclei located in the metal binding site.

Intrinsic paramagnetic centres and paramagnetic tagging

When discussing paramagnetic structural restraints in protein NMR, we divide proteins into two groups. The first group comprises metalloproteins with one or more metal binding sites [345]. This includes proteins where the bound metal ion is paramagnetic or else becomes paramagnetic during the relevant metabolic process, such as in superoxide dismutase (SOD) where the copper ion changes between the Cu^+ and Cu^{2+} oxidation states. However we also include proteins that bind diamagnetic ions, such as Ca^{2+} or Zn^{2+} , which can be substituted with paramagnetic ions for the purpose of introducing paramagnetic effects into the NMR spectrum.

The second group contains all other types of protein that do not have an intrinsic metal binding site, but for which it would be desirable to introduce a paramagnetic species into the structure in order to measure the resulting paramagnetic effects to give more information on the structure and dynamics. The paramagnetic centre is introduced in the form of a tag, which is a molecular fragment that is attached to part of the protein [346]. There is a wide variety of different tags, each with different paramagnetic shift and PRE properties and which are optimized for the measurement of different paramagnetic restraints. A selection of organic-radical and metal-binding tags is summarized in Figure 12.24 [346]. The simplest tags are nitroxide labels (Figure 12.24 (1)–(3)), which have an unpaired electron in the NO group, and which can be easily attached to a cysteine amino acid residue that is exposed on the surface of the protein. The NO radical exhibits relatively slow electronic relaxation, and so is particularly useful for inducing large PREs in the region immediately surrounding the tag. The other tags are molecular fragments that bind metal ions. For instance peptides that are used to mimic a metal-binding site can be attached to either terminus of the protein. Other examples include tags based on ethylenediamine tetraacetic acid (EDTA) ((Figure 12.24 (4)–(6)), caged lanthanide-binding tags ((Figure 12.24 (7)–(9)), and tags based on dipicolinic acid ((Figure 12.24 (10)–(12)), which can be used to introduce metal ions onto specific surface-exposed amino acid residues. Such tags can bind to either 3*d*-transition-metal ions or lanthanide ions, depending on the particular paramagnetic restraint we wish to measure. The metal ions Mn²⁺, Cu²⁺, and Gd³⁺ can be used to induce large PREs, whereas Co²⁺ and non-Gd³⁺ lanthanide ions induce large PCS and RDC effects [346].

The diamagnetic reference

When performing measurements on a paramagnetic system, we should note that the paramagnetic contributions cannot be measured in isolation. Rather the quantity we measure contains contributions both from the diamagnetic (orbital) and paramagnetic effects. Therefore when obtaining paramagnetic restraints we need to perform two sets of measurements, one on a diamagnetic reference protein and the other on the paramagnetic protein. If the two proteins have the same structure, and the same diamagnetic electronic properties, the difference between a quantity measured on one and that measured on the other is equal to the paramagnetic contribution. For a paramagnetic metalloprotein with a Co²⁺-binding site, a suitable diamagnetic reference would be the same protein with the metal ion substituted with the diamagnetic Zn²⁺ ion. The question whether the two systems really do have the same structure and diamagnetic electronic properties is rather a

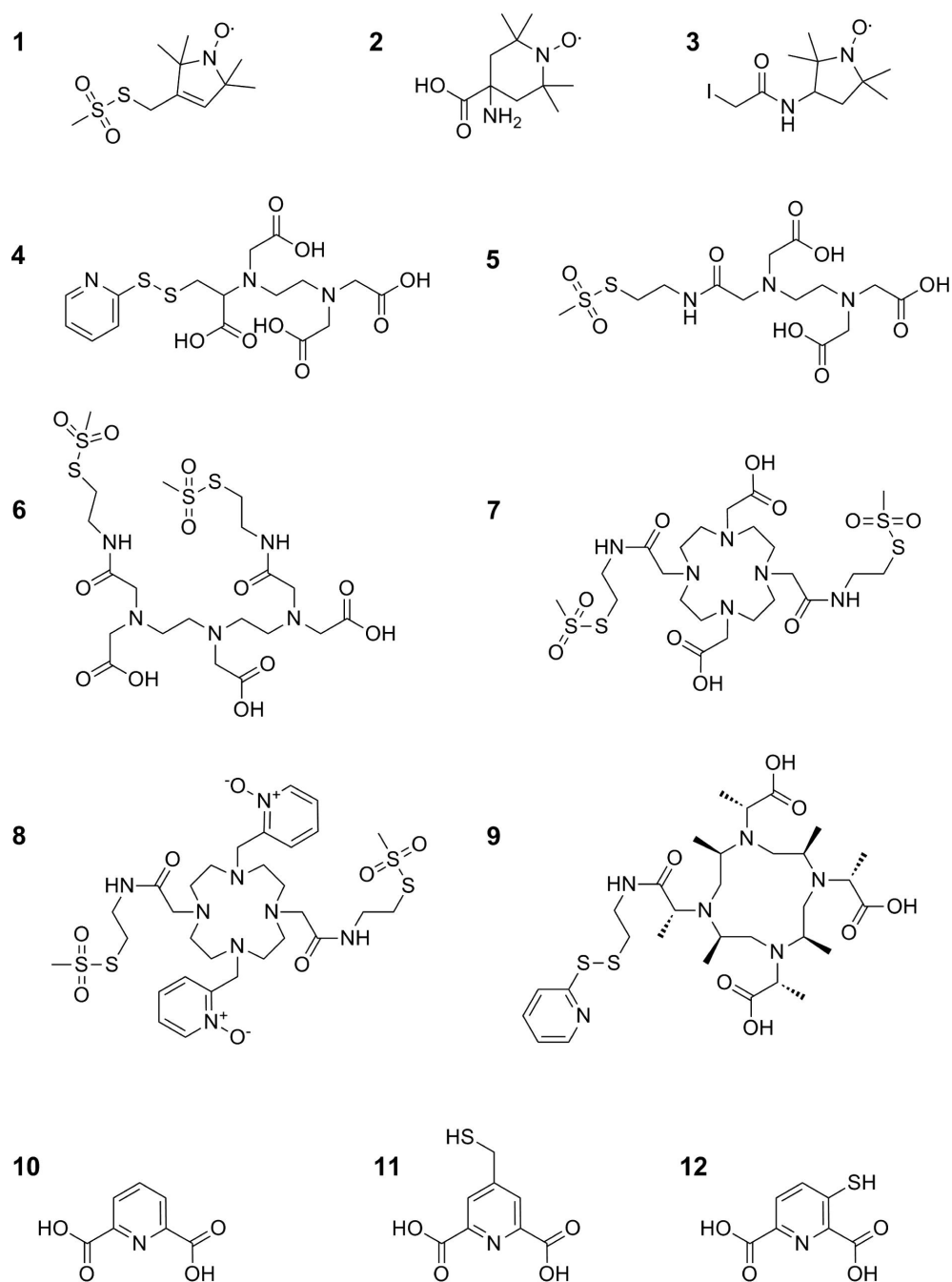


Figure 12.24: Structures of molecular fragments used as paramagnetic tags. Fragments (1)–(3) are nitroxide radicals, (4)–(6) are metal-binding tags based on EDTA, (7)–(9) are caged lanthanide-binding tags, and (10)–(12) are metal-binding tags based on dipicolinic acid. Reproduced from [346], with permission from Elsevier.

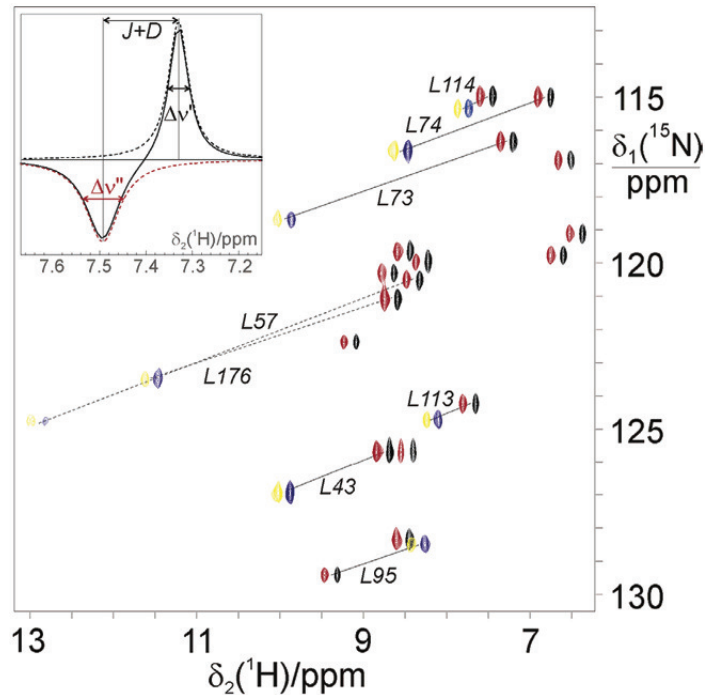


Figure 12.25: The ^1H - ^{15}N HSQC spectrum of the 30 kDa complex between the N-terminal domain of the ϵ subunit and the θ subunit of *Escherichia coli* DNA polymerase III in the absence and presence of a paramagnetic metal ion. The spectrum contains the anti-phase doublets of the two proteins, one binding paramagnetic Dy^{3+} (yellow and blue peaks) and the other with no metal ion (red and blue peaks). Straight dotted lines connect each paramagnetic resonance with the diamagnetic equivalent. Also shown is the one-dimensional trace in the ^1H dimension taken at $\delta_1 = 115$ ppm and $\delta_2 = 7.4$ ppm. The PCS is given by the overall change in chemical shift of the resonance, the transverse PRE is given by the overall line broadening, the CCR effects are measured from the difference in linewidth of the two components of the anti-phase doublet, and the RDC is calculated from the change in the splitting across the doublet. Reproduced with permission from [356]. Copyright (2004) American Chemical Society.

delicate one. However we can assume that any local structural distortions resulting from the change of metal ion are limited to within a few Å of the ion, and so are not measurable on the spins we observe outside the blind sphere, tens of Å from the metal ion. For short-range effects such as the contact shifts, however, the distortions of the metal binding site are more problematic, and the use of a diamagnetic reference may not be appropriate.

The measurement of paramagnetic restraints is illustrated with ^1H - ^{15}N HSQC spectra of the 30 kDa complex between the N-terminal domain of the ϵ subunit and the θ subunit of *Escherichia coli* DNA polymerase III in the absence and presence of a paramagnetic metal ion, shown in Figure 12.25 [356].

Pseudo-contact shifts

The paramagnetic shifts of nuclei outside the blind sphere can be ascribed entirely to the PCS, which in the point-dipole approximation is given by Equation 5.77, reproduced below for convenience:

$$\delta_{\text{PCS}} = \frac{1}{12\pi r^3} \left[\Delta\chi_{\text{ax}} (3 \cos^2(\theta) - 1) + \frac{3}{2} \Delta\chi_{\text{rh}} \sin^2(\theta) \cos(2\phi) \right]. \quad (12.3)$$

The PCS is calculated from the difference in chemical shift between corresponding resonances in the paramagnetic and diamagnetic proteins, as shown in Figure 12.25. The PCS can be used to back-calculate the distance r of the nucleus (here H) from the metal ion, and the angles (θ, ϕ) that fix the orientation of the ion–nucleus vector relative to the PAF of the magnetic susceptibility tensor $\Delta\chi$, as shown in Figure 12.23 (a) [16, 42]. Clearly a PCS is only observed for metal ions that have an anisotropic susceptibility tensor.

Contact shifts

For amino-acid residues close to the metal ion the shifts may also have an appreciable contribution from the contact interaction. The contact shifts have a sign and size that depend on the orbital occupancy of the metal ion, and the overlap between these metal orbitals and the s -orbitals of the observed nuclear spin, via any intermediate orbitals of bridging atoms. Therefore measurement of the contact shifts should provide important information regarding the geometry and unpaired electronic-spin transfer within the metal binding site [363]. However the measurement and interpretation of the contact shifts presents some difficulties. Firstly the distortion of the metal-binding site on substituting the paramagnetic metal ion with a diamagnetic analogue is expected to be significant enough that the orbital shifts also change, and so we cannot simply subtract one shift from another. Secondly these nuclei are also expected to have a significant PCS, which cannot be separated from the contact shift. Thirdly, even with reliable experimental contact shifts, their use as structural restraints is not straightforward without the use of first-principles quantum-chemistry or DFT calculations. For these reasons, contact shifts are currently not as widely used as PCS. However they have been used extensively for certain types of system, such as iron–sulphur proteins [354, 363–366], heme proteins [367–370], and blue copper proteins [371–373].

Paramagnetic relaxation enhancements

The PRE of a nuclear spin is calculated from the difference in measured relaxation rate constants between paramagnetic and diamagnetic systems. As shown in chapter 8 for both the Solomon–Bloembergen–Morgan and Curie mechanisms, the PRE has a simple variation with the distance of the nucleus from the metal ion of $1/r^6$; it can therefore be used to back-calculate this distance, as shown in Figure 12.23 (b) [99, 100]. The paramagnetic contribution to the linewidth λ_{PRE} is dominated by the transverse Curie PRE and, from Equation 8.128, is given by

$$\lambda_{\text{PRE}} = \frac{k}{r^6} \left[4\tau_{\text{R}} + \frac{3\tau_{\text{R}}}{1 + \omega_I^2\tau_{\text{R}}^2} \right], \quad (12.4)$$

in the absence of chemical exchange, and where k is a constant. This PRE can be measured either from the decay during a spin-echo sequence or, as shown in Figure 12.25, from the difference in linewidth between the paramagnetic and diamagnetic systems.

Cross-correlated relaxation

As shown in chapter 8 the effect of the CCR between the Curie and nuclear–nuclear dipolar coupling relaxation mechanisms on the H–N amide relaxation properties is to give a doublet in the ^1H dimension in which the two components have different linewidths. The difference between the two linewidths is given by

$$\Delta\lambda_{\text{CCR}} = \kappa \frac{3 \cos^2(\vartheta) - 1}{r^3} \left[4\tau_{\text{R}} + \frac{3\tau_{\text{R}}}{1 + \omega_I^2\tau_{\text{R}}^2} \right], \quad (12.5)$$

where ϑ is the angle between the N–H vector and the vector connecting the paramagnetic centre to the observed nucleus, the latter being of length r , and κ is a constant. This dependence on r and ϑ is shown in Figure 12.23 (c). The CCR restraint is determined from the difference in linewidth between the two doublet components as shown in Figure 12.25 [374–377].

Residual dipolar couplings

For a protein in isotropic solution, unrestricted rotational diffusion has the effect of completely averaging out anisotropic NMR interactions such as nuclear–nuclear dipolar couplings. Therefore the splitting in the resonances in the ^1H – ^{15}N HSQC spectrum is equal to the one-bond ^1H – ^{15}N J -coupling J_{IS} . The same is true

of a paramagnetic protein in which the magnetic susceptibility of the metal ion is isotropic. However for a paramagnetic protein with a susceptibility anisotropy, there is an energetic preference for the susceptibility tensor to orientate so that the axis of the PAF with the largest susceptibility component is parallel to the external field. Hence the rotational diffusion is no longer unrestricted, and the nuclear–nuclear dipolar couplings are averaged to a value that is non-zero, and referred to as the RDC. Therefore the splitting in the HSQC resonance is given by $J_{IS} + D_{\text{RDC}}$, where the RDC D_{RDC} is given by

$$D_{\text{RDC}} = K \left[\Delta\chi_{\text{ax}} (3 \cos^2(\Theta) - 1) + \frac{3}{2} \Delta\chi_{\text{rh}} \sin^2(\Theta) \cos(2\Phi) \right]. \quad (12.6)$$

This is illustrated in Figure 12.25. The RDC depends on the angles (Θ, Φ) which specify the orientation of the N–H bond relative to the PAF of the susceptibility tensor, as shown in Figure 12.23 (d), and so can be used to back-calculate these restraints [16, 378, 379]. In practice the RDCs are measured from the differences in the splittings measured in paramagnetic and diamagnetic systems.

12.3.4 Solvent PREs for measuring protein–solvent interactions

In addition to refining the three-dimensional protein structure it has been shown that paramagnetic restraints can be used to study the interactions between protein residues and solvent molecules. A key restraint used in these studies is the solvent PRE [380–383]. Here the solvent is doped with a paramagnetic molecule, which enhances the relaxation rates of any nuclei in residues that are exposed to the solvent via the spin-dipolar interaction. Therefore this solvent PRE can be used to distinguish between residues that are located on the solvent-exposed surface of the protein, and those that are located in the protein core and are not in contact with the solvent. In order for this technique to be effective it is crucial that we use a paramagnetic centre that induces a relatively large PRE. For this reason the popular choices of paramagnetic centres for measuring solvent PREs are those with slow electronic relaxation such as Gd^{3+} complexes similar to those used as MRI contrast agents, nitroxyl radicals, or molecular oxygen.

12.4 Measuring chemical exchange in solution NMR and MRI

In this section we briefly review the role of paramagnetic systems in the measurement of chemical exchange, and the observation of species with low concentrations in both solution NMR of small molecules and biomolecules, and in MRI. The specific methods we discuss are Chemical Exchange dependent Saturation Transfer (CEST) [384], and application of CEST with paramagnetic shift reagents (PARACEST) [385–387].

12.4.1 Chemical exchange dependent saturation transfer (CEST)

The CEST and PARACEST experiments are generally used to observe the NMR signals of dilute concentrations of a solute species in aqueous solution, where the former has exchangeable protons that are in slow chemical exchange with the water molecules of the latter [388]. We recall that slow chemical exchange is defined as when the exchange rate constants k describing the process are smaller than the difference in resonance frequencies of the signals of the two environments $\Delta\Omega$, i.e. $k \leq |\Delta\Omega|$. The peak of the protons in the solute environment may be of too low intensity to be observable in a conventional NMR spectrum. However we are able to detect the presence of this environment by performing a saturation–transfer experiment in which we irradiate the solute peak with a low-power presaturation pulse of RF field amplitude $\omega_1 \leq |\Delta\Omega|$, which causes a transfer of saturation via chemical exchange with the solvent proton sites. Therefore we observe the presence of the solute indirectly by direct detection of the solvent, resulting in an effective sensitivity enhancement of the solute signals. In addition CEST also enables us to measure the rate constants of the chemical exchange process, which are a probe of the pH of the system, and to perform imaging experiments on dilute species [388].

The CEST experiment can be described easily using the Bloch–McConnell equations:

$$\frac{dM_B(t)}{dt} = \gamma_I M_B(t) \times B(t) - R_B [M_B(t) - M_{0,B}] - k_{BU} M_B(t) + k_{UB} M_U(t), \quad (12.7)$$

$$\frac{dM_U(t)}{dt} = \gamma_I M_U(t) \times B(t) - R_U [M_U(t) - M_{0,U}] - k_{UB} M_U(t) + k_{BU} M_B(t). \quad (12.8)$$

Here we assume two-site exchange between the ‘bound’ protons in the solute (B) and the ‘unbound’ protons in the solvent (U). The magnetization vectors from each environment are denoted $M_B(t)$ and $M_U(t)$ respectively, and the equilibrium magnetization vectors are $M_{0,B}$ and $M_{0,U}$. The longitudinal and transverse

relaxation of each environment is governed by the relaxation supermatrices \mathbf{R}_B and \mathbf{R}_U , and the chemical exchange processes $B \rightarrow U$ and $U \rightarrow B$ are described by the exchange supermatrices k_{BU} and k_{UB} . The magnetic field, incorporating both the static B_0 field and that due to the RF pulse, is $\mathbf{B}(t)$. We focus on the z -magnetization components from the two environments, as it is these that give the observable signal components following the selective saturation and excitation. The relevant parts of the Bloch–McConnell equations are:

$$\frac{dM_{z,B}(t)}{dt} = \omega_1 M_{y,B} - \frac{1}{T_{1,B}} [M_{z,B}(t) - M_{0,B}] - k_{BU} M_{z,B}(t) + k_{UB} M_{z,U}(t), \quad (12.9)$$

$$\frac{dM_{z,U}(t)}{dt} = \omega_1 M_{y,U} - \frac{1}{T_{1,U}} [M_{z,U}(t) - M_{0,U}] - k_{UB} M_{z,U}(t) + k_{BU} M_{z,B}(t), \quad (12.10)$$

where $M_{i,B}(t)$ and $M_{i,U}(t)$ are the i -components of the magnetization vectors for the solute and solvent protons, $M_{0,B}$ and $M_{0,U}$ are the equilibrium values of the z -components, $T_{1,B}$ and $T_{1,U}$ are the two longitudinal relaxation time constants, and k_{BU} and k_{UB} are the exchange rate constants for the two processes $B \rightarrow U$ and $U \rightarrow B$. We assume that $|M_{z,B}(t)| \ll |M_{z,U}(t)|$ so that we can only observe the peak due to the solvent.

To simplify the description of CEST we focus on three limiting cases. Firstly we take the situation where the low-power presaturation is far off resonance for both the solvent and solute protons. In this case the Bloch–McConnell equations show that neither $M_{z,B}$ nor $M_{z,U}$ is perturbed from its equilibrium value, and the excitation following the presaturation gives the conventional spectrum. Secondly if the carrier is resonant with the solvent peak and we achieve complete saturation $M_{z,U}$ is zero at the end of the spin lock, and we observe no solvent signal in the corresponding spectrum. The final case is the most interesting, and is when the carrier frequency is resonant with the solute peak. Here we saturate the solute magnetization so that $M_{z,B} = 0$. The solvent magnetization reaches a time-independent steady-state $M_{z,U}^{SS}$, the expression for which is calculated from Equation 12.10:

$$M_{z,U}^{SS} = \frac{1}{1 + T_{1,U} k_{UB}} M_{0,U}. \quad (12.11)$$

From this expression we see immediately that the steady-state solvent magnetization is of the same sign as the equilibrium magnetization, but has a reduced magnitude. In the resulting spectrum we still observe the solvent peak, but with a reduced intensity compared to the conventional spectrum. This reduction in intensity of the solvent peak is easier to detect than the solute peak in the conventional spectrum, and so CEST is able

to detect the solute indirectly with an effective sensitivity enhancement [388]. This description is simplified for perfect saturation and ignores imperfect saturation and near-off-resonance effects of the presaturation. However these can be accounted for as described by Zhou and van Zijl [388].

In practice we apply CEST by performing a series of saturation–excitation experiments with different carrier frequencies, and acquiring the spectrum of the solvent peak for each. When the carrier is resonant with the solute peak we observe a decrease in the solvent resonance, and are therefore able to identify the chemical shift of the solute resonance. Further the complete solvent intensity profile as a function of carrier frequency can be fitted to the Bloch–McConnell equations to extract the chemical exchange rate constants.

12.4.2 Paramagnetic shift reagents in chemical exchange dependent saturation transfer (PARACEST)

To be able to perform a CEST experiment we need to be able to selectively irradiate the exchangeable proton of the solute, which also requires the exchange to be slow or intermediate, i.e. $k \leq |\Delta\Omega|$. For diamagnetic systems the proton chemical shift of the solute is typically within 6 ppm of the bulk water, and so CEST is limited to the study of exchange rate constants of up to the order of 1 kHz. However we can employ paramagnetic solute systems, such as chelated lanthanide ions, to study faster exchange processes. In these systems the bound protons experience paramagnetic shifts which increase the chemical shift difference from the bulk water, and so increase the upper bound of the exchange rate constant we are able to study by orders of magnitude. This application of CEST is referred to as PARACEST [385–387].

The first examples of PARACEST were demonstrated for lanthanide complexes by Zhang and Sherry [385, 386]. They studied the lanthanide complexes Ln–DOTA–4AmCE, with Ln = Pr, Nd, Eu, and Yb, which bind water molecules via a slow exchange process. Two PARACEST profiles for Eu–DOTA–4AmCE and Nd–DOTA–4AmCE are shown in Figure 12.26 (a) and (b) [388]. In both cases the intensity of the bulk water signal (assigned a shift of 0 ppm) was monitored as a function of the frequency of the presaturation pulse. For both profiles the observed features can be explained with reference to the simple saturation model described in section 12.4.1. In the case of Eu–DOTA–4AmCE in Figure 12.26 (a), we observe no reduction in the intensity of the bulk water signal when the presaturation is far off-resonance from both the bulk and bound water signals, for example at ± 80 ppm. When the presaturation frequency is at 0 ppm we completely saturate the magnetization due to bulk water with the result that the peak is completely suppressed. The

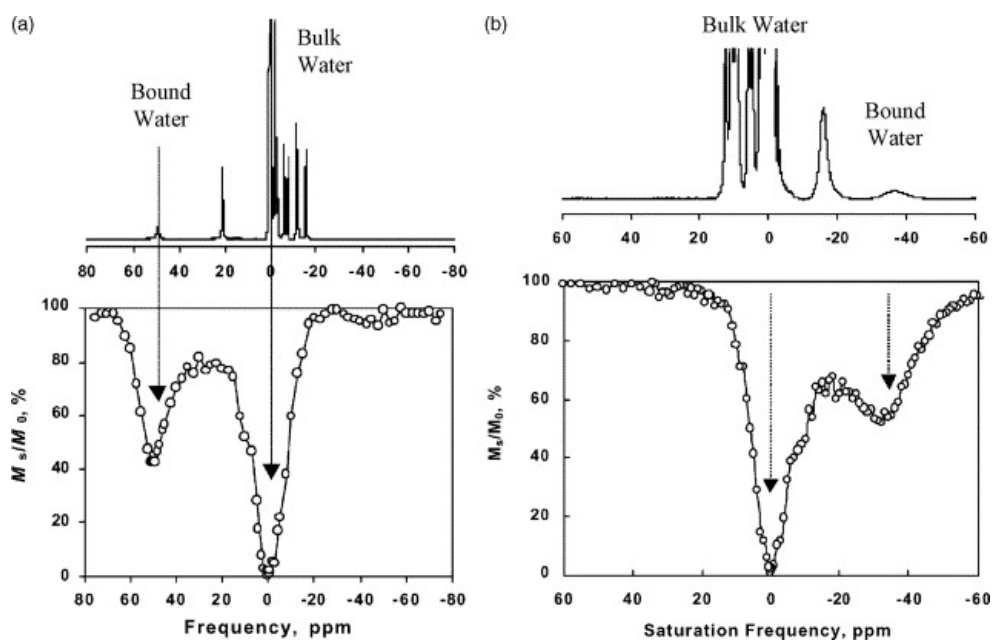


Figure 12.26: PARCEST data acquired from aqueous solutions of two lanthanide complexes Ln-DOTA-4AmCE with a concentration of 63 mM, pH of 7, and at room temperature. The PARCEST profiles were obtained at 4.7 T with a 1.0 s presaturation pulse, and the two ^1H spectra at the top were acquired at 11.74 T in order to be able to identify the signal from the bound water. The two lanthanide ions are (a) Eu^{3+} and (b) Nd^{3+} . In both cases the signal due to the bulk solvent water is assigned a shift of 0 ppm, and the bound water signals appear at 50 ppm and -32 ppm for Eu-DOTA-4AmCE and Nd-DOTA-4AmCE respectively. On irradiation of the bound water signals the bulk water signal is reduced in intensity by 57% and 48% respectively [385, 386]. Reproduced from [388], with permission from Elsevier.

feature that is of particular interest is the reduction in the intensity of the bulk water peak that is observed when the presaturation frequency is set to 57 ppm, which corresponds to the chemical shift of the bound water molecule. The saturation of the magnetization of this bound water molecule caused a transfer in the polarization to the bulk water signal resulting in a reduction of 57%. Furthermore the width of this dip in the PARACEST profile was used to estimate the exchange lifetime of the bound water, which was found to be 380 μ s [385, 386]. Similar features were observed in the PARACEST profile of Nd–DOTA–4AmCE in Figure 12.26 (b). Here the reduction in the bulk water peak was observed with a carrier frequency of –32 ppm, and the broader dip indicated a faster exchange process with a lifetime of 80 μ s [385, 386].

In vivo, the form of the PARACEST profiles is sensitive to a number of physiological conditions, such as pH and temperature. This has been exploited in a number of studies, and lanthanide complexes have been used to measure pH [387], detect the presence of particular metabolites [389], perform imaging within cells [390], and measure temperature [391].

12.5 Solid-state NMR methods for paramagnetic systems

12.5.1 The general strategy

When applying NMR methods to paramagnetic materials in the solid state we are faced with a task which has many similarities to, but also many differences from, the analysis of paramagnetic molecules in solution.

Some features of a paramagnetic NMR spectrum do not change between the two cases. Notably, a nucleus next to a paramagnetic centre displays identical isotropic paramagnetic shifts, contact or pseudo-contact in origin, independently of whether the NMR analysis is performed in solution or in the solid state. Therefore in both cases the spectroscopist may be confronted with the acquisition of signals with very large chemical shift dispersions, and with the interpretation of peak positions significantly different from conventional diamagnetic chemical shifts. This is a situation that already falls within the expertise of a solid-state NMR spectroscopist, as the community already has considerable experience in working with broad resonances in diamagnetic samples, due to the CSA and quadrupolar interactions.

The Solomon–Blombergen–Morgan relaxation mechanisms operate in the solid state in an analogous way to solution, and accelerate nuclear relaxation. As experienced in solution NMR, the resulting PREs may lead to a reduction in sensitivity due to signal loss during the pulse sequence, but at the same time have the effect

of allowing rapid acquisition of a large number of scans by reducing the recycle delay.

However a first main difference comes from the Curie broadening, which is the limiting factor in the study of large paramagnetic molecules by solution NMR. In solids, whilst there may still be a contribution to Curie relaxation from slow internal motions of the system, the overall rate of Curie relaxation, and the corresponding contribution to the linewidth, is generally lower than in solution. This is of particular importance for the study of systems containing paramagnetic centres for which the correlation times for the electronic fluctuations are short ($< 10^{-11}$ s). In solids, these centres (typically Co^{II} , Fe^{II} , Ln^{III}) significantly enhance the longitudinal relaxation of the surrounding spins, but have a negligible effect both on their observed linewidths and their coherence lifetimes, and so do not significantly reduce the efficiency of magnetization transfers.

A number of other phenomena affect a paramagnetic NMR spectrum specifically in the solid state. In addition to the features of paramagnetic systems in solution, we now also need to account for large anisotropic interactions, such as the paramagnetic shift anisotropy and quadrupolar interactions. These lead to broader spectra than are generally observed in solution NMR, which can lead to further difficulties in obtaining broadband excitation. This spectral broadening therefore also leads to a reduction in sensitivity. The strength of the SAs in particular is very large in solid materials that contain a dense array of paramagnetic ions, as the paramagnetic contributions add up.

Another important difference in solids is the presence of BMS effects, which lead to large inhomogeneous broadening in both static and MAS spectra. In solid materials containing paramagnetic ions with rapid electronic relaxation, it is generally found that it is this effect, and not the transverse PRE, that gives the largest contribution to the linewidth, and hence is the factor that limits resolution.

The sizes of the shift and SA, and the inhomogeneous broadening, scale with the external magnetic field, and so a low magnetic field (200 MHz or lower) results in a spectrum with lower dispersion that is easier to excite with practicable RF field amplitudes. However, this has the primary disadvantage that the overall sensitivity is reduced. A workaround can be adopted for nuclei with more than one NMR-active isotope, for example $^1/2\text{H}$ and $^6/7\text{Li}$. As the shift and SA scale with the gyromagnetic ratio, studying the isotope with the lower γ_I produces a narrower spectrum, which is easier to excite. However, as in the case of reducing the magnetic field, nuclei with lower γ_I also have lower intrinsic sensitivity. In addition the second-order quadrupolar interaction scales inversely with the external field, and so a low field increases the resonance broadening associated with this interaction in the spectra of quadrupolar nuclei such as ^{23}Na .

All of these observations suggest that the development of pulse sequences incorporating broadband excitation that can excite a wide range of shifts and SAs at high field would be advantageous. In recent years there has been growing interest in studying solids with increasingly strong paramagnetic effects, such as battery materials with a large density of paramagnetic ions in the lattice [53]. This has provided strong motivation for developing broadband NMR sequences specifically optimized for paramagnetic materials, as described in section 12.5.7 [56]. These methods provide a solution to studying nuclei with high gyromagnetic ratios and large SAs at high field. They include the development of tailored RF pulse schemes, and their combination into more sophisticated sequences, for example to resolve individual local environments [7, 30], or otherwise to separate the spectral features of a local environment due to different spin interactions [199, 392, 393]. In the presence of multiple nuclear local environments, each experiencing multiple interactions, these tools help to resolve complicated spectra with multiple overlapping features, and to extract the required interaction parameters with site-specific resolution.

Another difference between the NMR of solids and solutions is the presence of large homonuclear and heteronuclear dipolar couplings in the former, which are generally difficult to decouple.

It was recognized early on by Clayton et al. that heteronuclear ^1H decoupling is ineffective for increasing the resolution in the NMR spectra of paramagnetic complexes, due to the difficulty in efficiently irradiating the very broad resonances [22]. In addition, the use of high-power decoupling requires that the recycle delay is set to a minimum of five times the total decoupling time to prevent damage to the probe. This requirement often extends the recycle delay to longer than is required for complete longitudinal relaxation, which for paramagnetic systems means that the short T_1 is not being exploited. This idea was taken further by Ishii et al. who suggested that, because decoupling is at best ineffective and at worse has a deleterious effect on the spectrum, it is better not to decouple and to rely instead on fast MAS to average out the dipolar couplings [6, 25].

Increasing the MAS frequency also has an additional beneficial effect on resolution and sensitivity, as the signal in the spinning-sideband manifolds is concentrated in fewer sidebands that are more widely separated in the spectrum. Furthermore, the recycle delay now only reflects the short T_1 of the system, and not any requirements due to the decoupling, and so scans can be acquired more rapidly. An example of the benefits of fast spinning, rapid pulsing, and no decoupling are shown by the ^1H and ^{13}C MAS spectra of a paramagnetic organometallic complex in Figure 12.27 [7]. The ^1H spectra acquired at 11 kHz and 33 kHz in (a) and (b)

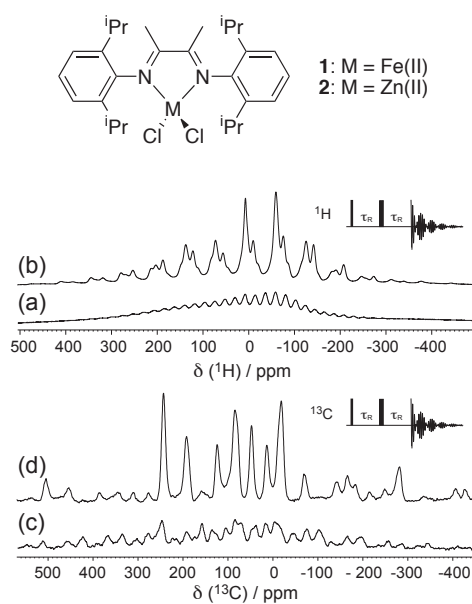


Figure 12.27: MAS NMR spectra of the compound **1** acquired at 11.74 T. The ¹H spectra acquired at 11 kHz and 33 kHz MAS are shown in (a) and (b). The corresponding ¹³C spectra acquired without decoupling at 11 kHz and 33 kHz MAS are shown in (c) and (d). All experiments were acquired using the spin-echo pulse sequence shown, with an echo delay of 90 μ s. Adapted with permission from [7]. Copyright (2006) American Chemical Society.

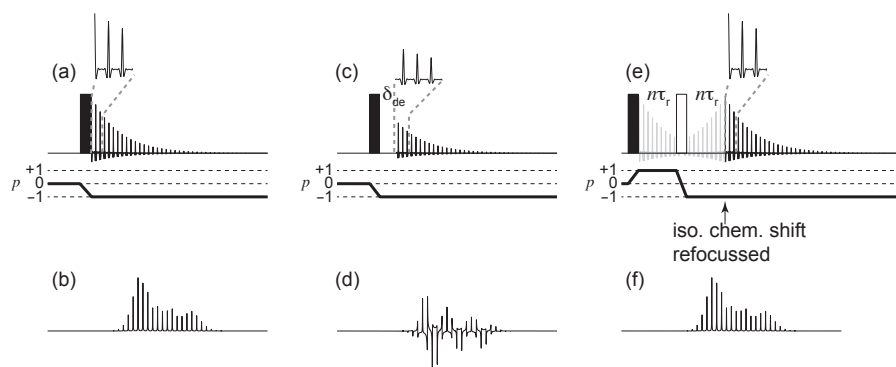


Figure 12.28: Pulse sequences and coherence-transfer pathways, and the simulated MAS NMR spectra due to an SA, for the one-pulse and spin-echo experiments. The pulse sequence for the one-pulse experiment is shown in (a). If the FID is collected immediately after an ideal pulse the spinning-sideband manifold of the MAS spectrum (b) has uniform phase. However in reality there is a short dead time δ_{de} between excitation and acquisition, as seen in the sequence in (c), which results in the loss of the first points of the FID, and a phase-distorted spectrum (d). The phase distortion is removed by employing the spin-echo sequence (e) [20], in which the isotropic and anisotropic shifts are refocused at the start of acquisition, resulting in a spectrum of uniform phase (f). Unless otherwise indicated filled rectangles indicate pulses with a nominal flip angle of 90° and unfilled rectangles indicate pulses with a nominal flip angle of 180° , and all pulses have phase x .

show that there is a clear improvement in both resolution and sensitivity on increasing the MAS frequency. The improvement is even more marked for ^{13}C . The spectacular enhancement experienced in sensitivity and resolution as compared to slower rates is nowadays amplified by the continuous development of new probes capable of faster MAS, allowing efficient detection of previously unobservable nuclei in highly paramagnetic substances.

12.5.2 One-dimensional NMR

One-pulse and spin-echo spectroscopy

The simplest pulse sequence for obtaining a one-dimensional MAS spectrum is the one-pulse sequence shown in Figure 12.28 (a). The sequence comprises a single pulse which generates $p = -1$ coherences that are observed during acquisition. In order to obtain maximum sensitivity the pulse flip angle should be set to a nominal value of 90° . However under circumstances where the pulse is of too low an RF field amplitude to ensure broadband excitation, a shorter pulse of the same amplitude can deliver a more uniform excitation response as there is less time for substantial deviations from ideal behaviour. The resulting sensitivity is lower,

but this can be offset when we note the partial excitation means that the system is closer to its equilibrium configuration than after a 90° pulse, and so a shorter recycle delay can be used. In the ideal case this excitation pulse gives a spectrum with a uniformly-excited spinning-sideband manifold, as shown in Figure 12.28 (b).

However we encounter a problem imposed by instrumental limitations, which means that this ideal performance is not observed in practice. In practice the acquisition period does not immediately follow excitation, since (1) the pulse has a non-zero duration, and (2) we require a delay of a few μs , known as the dead time δ_{de} , to switch from excitation mode to observation mode. Both effects lead to significant phase dispersion across the spectrum. As shown in the sequence in Figure 12.28 (c), the inclusion of the dead time means that we miss the initial points of the FID, and therefore do not acquire the initial evolution of both the isotropic shift and SA. This is more problematic for the larger spectral widths needed for paramagnetic systems, as the sampling rate of the FID is inversely proportional to the spectral width. The quality of the spectrum, shown in Figure 12.28 (d), is severely degraded by the resulting large frequency-dependent phase errors.

A solution to this problem is to employ the rotor-synchronised spin-echo pulse sequence shown in Figure 12.28 (e) [20]. Here the 90° excitation pulse is followed by two delays each of which is of the same duration $n\tau_r$, equal to an integer number of rotor periods n , that sandwich a 180° pulse, and we absorb the dead time into the second delay. The coherence-transfer pathway shown is the sole pathway available for ideal pulses, but in practice phase cycling of the 180° pulse phase is employed to eliminate unwanted pathways that arise from non-ideal behaviour such as insufficient bandwidth [320]. The sequence has the property that it refocuses the evolution of both the isotropic chemical shift and time-dependent SA at the start of acquisition. The refocussing process can be explained as follows. During a delay τ the sum of the frequencies due to both the isotropic and anisotropic shifts is proportional to the coherence order, and is given by $-p\Omega_{\text{iso}} - p\Omega_{\text{c}}^{\text{SA}}(\tau)$. During the first delay $n\tau_r$ the time-dependent SA self-refocusses due to the periodicity under MAS, and the total acquired phase is $-\Omega_{\text{iso}}(n\tau_r - 0) - \Phi_{\text{c}}^{\text{SA}}(n\tau_r, 0) = -\Omega_{\text{iso}}n\tau_r$. In the same way we can calculate the phase acquired following the 180° pulse as $\Omega_{\text{iso}}(2n\tau_r - n\tau_r) + \Phi_{\text{c}}^{\text{SA}}(2n\tau_r, n\tau_r) = \Omega_{\text{iso}}n\tau_r$. The two phases accrued before and after the 180° pulse then sum to zero. This refocussing means that at the start of acquisition we have effectively put the spin system into the same state as we would obtain from ideal one-pulse excitation, and we obtain the same spectrum without phase errors, as shown in Figure 12.28 (f). If the 180° pulse is sufficiently broadband, the only difference between the two sequences is the signal loss from dephasing

during the spin echo. This dephasing is due to relaxation and coherent homogeneous processes, but not to inhomogeneous decay as the chemical shift distribution of the latter is refocussed by the echo.

Experimental examples of spectra obtained from the one-pulse and spin-echo pulse sequences are shown in Figure 12.29 [34]. The system is the battery cathode material $\text{LiFe}_{0.5}\text{Mn}_{0.5}\text{PO}_4$, which has two species of paramagnetic transition-metal ions Fe^{2+} and Mn^{2+} in a 1:1 ratio. The ^7Li one-pulse and spin-echo spectra are shown in Figures 12.29 (a) and (b). The former clearly shows a frequency-dependent phase error across the spectrum, due to evolution of the SA during the dead time, which is removed in the latter. The range of isotropic shifts of the multiple Li sites is comparatively small at 90 ppm, which is approximately equal to the inhomogeneous broadening of the individual sidebands. The ^{31}P spectrum, by contrast, displays overlapping spinning-sideband manifolds from 32 distinct local environments with a range of isotropic shifts of 4000 ppm [30]. The one-pulse spectrum in Figure 12.29 (c) also has a frequency-dependent phase error, and a very poor signal-to-noise ratio that is worse than for ^7Li . This is due to the larger range of isotropic shifts which leads to a greater degree of differential evolution during the dead time. The spin-echo spectrum in Figure 12.29 (d) has improved phase properties and sensitivity, despite the T_2' decay during the echo, but also shows a smaller excitation bandwidth. This is because the range of isotropic frequencies over which we obtain quantitative inversion (the inversion bandwidth) with a 180° pulse is lower than the corresponding isotropic frequency range over which we obtain quantitative excitation (the excitation bandwidth) with a 90° pulse. This can be seen from the simulated 90° pulse excitation and 180° pulse inversion profiles shown in Figures 12.29 (e) and (f). Nevertheless the spin-echo sequence is an indispensable experiment in solid-state paramagnetic NMR. In addition to one-dimensional spectroscopy, the spin-echo pulse sequence can be appended to any of the more complex sequences presented here, such as those used for two-dimensional correlations, in order to obtain uniform phase in the direct dimension.

We make a final comment about the application of these pulse sequences to quadrupolar nuclei, considering half-integer and integer spins separately. In the solid state the NMR spectrum of an half-integer nuclear spin is dominated by the sharp and intense resonance due to the CT, with the ST resonances broadened to the point where they are sometimes difficult to detect. Hence in practice the spectrum is sometimes obtained by applying excitation pulses that are of low power, so that $\omega_1 \ll \omega_Q$, and are therefore selective for the CT. In this case the excitation Hamiltonian due to an excitation pulse phase x applied to a spin experiencing a

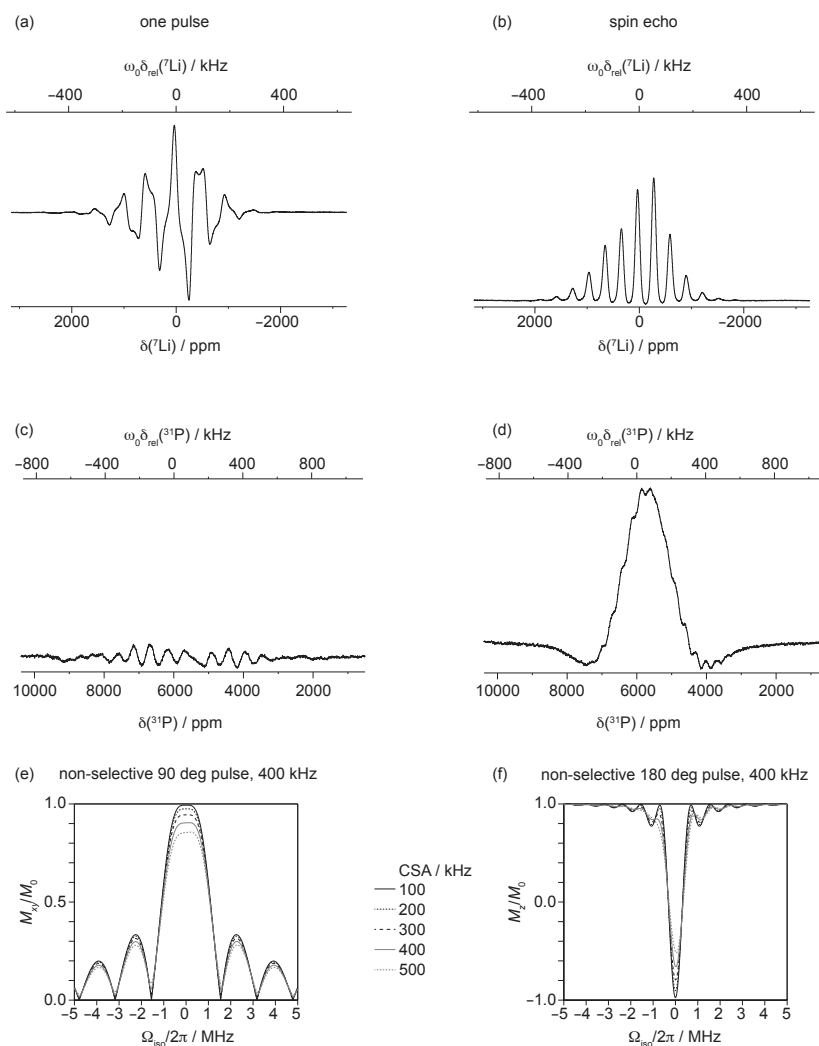


Figure 12.29: Experimental one-pulse and spin-echo spectra of the cathode material $\text{LiFe}_{0.5}\text{Mn}_{0.5}\text{PO}_4$ at 11.74 T and 60 kHz MAS. The one-pulse ($0.55 \mu\text{s}$ at 455 kHz RF field amplitude) ${}^7\text{Li}$ spectrum with 8192 scans is shown in (a), and exhibits poor phase properties. Using a spin-echo pulse sequence gives the spectrum in (b) with uniform phase. The reduced excitation bandwidth of the spin echo presents no problems because the isotropic chemical shifts of the different sites lie within a range of 60 kHz. The one-pulse ($0.60 \mu\text{s}$ at 417 kHz RF field amplitude) ${}^{31}\text{P}$ spectrum with 32768 scans has very poor sensitivity and phase, as shown in (c). Use of the spin echo gives some improvement in the phase across the spectrum, and a much better signal-to-noise ratio, but at the expense of excitation bandwidth, as the isotropic shifts cover a range of 800 kHz. The spectra in (a)–(d) have been plotted against both chemical shift and frequency scales. For the latter the frequency is calculated as $\omega_0\delta_{\text{rel}}$, where δ_{rel} is the chemical shift measured relative to 0 ppm for ${}^7\text{Li}$ and 6000 ppm for ${}^{31}\text{P}$. In (e) and (f) are shown simulations of the excitation profile of a 400 kHz 90° pulse, and the inversion profile of a 400 kHz 180° pulse at 60 kHz MAS, for a range of CSAs. Reproduced from [34], with permission from Elsevier.

first-order quadrupolar interaction can be approximated as

$$\overline{H}_Q^{(1)} + \omega_1 \hat{I}_x \approx \overline{H}_Q^{(1)} + \omega_1(I + 1/2) \hat{I}_x^{(+1/2, -1/2)}. \quad (12.12)$$

where $\hat{I}_x^{(+1/2, -1/2)} = (\hat{I}_+^{(+1/2, -1/2)} + \hat{I}_-^{(+1/2, -1/2)})/2$. We see that the effective RF field amplitude is $\omega_1(I + 1/2)$, i.e. it has been scaled up by the spin-dependent factor $(I + 1/2)$ [330]. Therefore we only apply the pulse for a time that is shorter by a factor $(I + 1/2)$ than the nominal pulse length. In paramagnetic systems we often need to apply higher-power pulses to fully excite the CT resonance, which is broadened by a large SA interaction. For nuclear species with small quadrupolar interactions, such as ^7Li , this means that the RF field amplitude is comparable to or greater than ω_Q , so that no scaling of the pulse length is required. However nuclear species with larger ω_Q frequencies, such as ^{23}Na and ^{27}Al , often still require a scaling of the pulse length. For example this means that the spin-echo sequence applied to ^{23}Na with $I = 3/2$ is $45^\circ - \tau_r - 90^\circ - \tau_r$, where the flip angles are the nominal values calibrated in the absence of the quadrupolar interaction.

For integer-spin nuclei such as ^2H and ^6Li , all the observable transitions are affected by the quadrupolar interaction to first order. In powder samples we generally excite all the observable transitions, and so do not scale the pulse length.

Frequency stepping

A simple method to overcome the bandwidth problem and obtain a quantitative, broadband one-dimensional spectrum is to set the transmitter offset to different values, with a step size that is equal to or smaller than the RF field amplitude, and to acquire a of sub-spectrum for each offset. The sub-spectra are then summed to give the final spectrum. The concept is illustrated for MAS NMR in Figure 12.30, which shows a spectrum in (a) obtained by summing the sub-spectra shown in (b) [394]. This method has usually been applied to static solids, for both quadrupolar nuclei and paramagnetic systems with large interactions, and has been referred to as spin-echo mapping [53, 396–402], Variable-Offset Cumulative Spectroscopy (VOCS) [403–405], and frequency stepping [406–411]. The accurate reconstruction of the spectrum is a delicate matter, particularly under MAS where the number of published examples is smaller [395, 412]. However a recent theoretical treatment of frequency stepping under MAS has shown that the spinning-sideband manifolds can be properly reproduced by careful summation of the sub-spectra [394]. Accordingly the number of experimental exam-

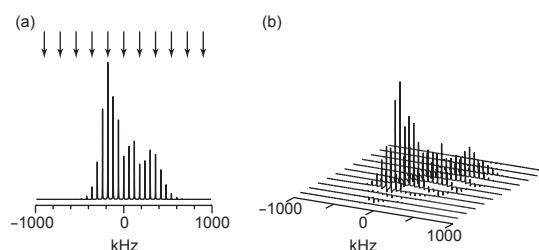


Figure 12.30: Illustration of the frequency-stepping method for obtaining a wide-line MAS NMR spectrum [394, 395]. The complete spectrum is shown in (a) with the frequencies to which the transmitter is tuned in turn indicated by arrows. The individual sub-spectra, shown in (b), are summed to recover the spectrum in (a). Adapted from [394], with the permission of AIP Publishing.

ples in material science is currently increasing [56, 57, 413]. An example of frequency stepping applied to a particularly challenging material is the solid-state ^{17}O MAS NMR spectrum of $\text{La}_2\text{NiO}_{4+\delta}$ [413], shown in Figure 12.31. The crystal structure in Figure 12.31 (a) shows three distinct ^{17}O sites which, with an additional resonance due to a LaAlO_3 impurity phase, give at least four resonances with isotropic shifts over a range of 8000 ppm as shown in the sum-spectrum in (b). There is additional broadening due to the SA interactions, which broaden the spectrum over 20000 ppm. The sum-spectrum was acquired with the spin-echo pulse sequence $30^\circ - \tau_r - 60^\circ - \tau_r$, where the nominal pulse lengths are reduced by a factor of three in the CT-selective regime. An expansion of the spectrum between 2000 and -1000 ppm is shown in Figure 12.31 (c).

Traditionally the acquisition of frequency-stepped solid-state NMR spectra has necessitated a manual retuning of the probe for each new sub-spectrum, making the whole process rather cumbersome. However Pecher et al. have recently developed an external automatic tuning and matching (eATM) robot, applicable to both static and MAS experiments, which allows the whole acquisition to be automated [414]. This has resulted in an increase in the efficiency of acquisition of frequency-stepped NMR spectra, for example outside normal working hours without regular user input.

Homonuclear signal enhancement of spin-1/2 nuclei: CPMG

One important limitation on the sensitivity that can be obtained in the one-dimensional spectrum of paramagnetic systems is the rapid decay of the FID due to both relaxation and inhomogeneous effects. For paramagnetic solids it is generally found that for metal ions with SO coupling the inhomogeneous broadening of each sideband is an order of magnitude greater than the linewidth due to relaxation, and so represents the

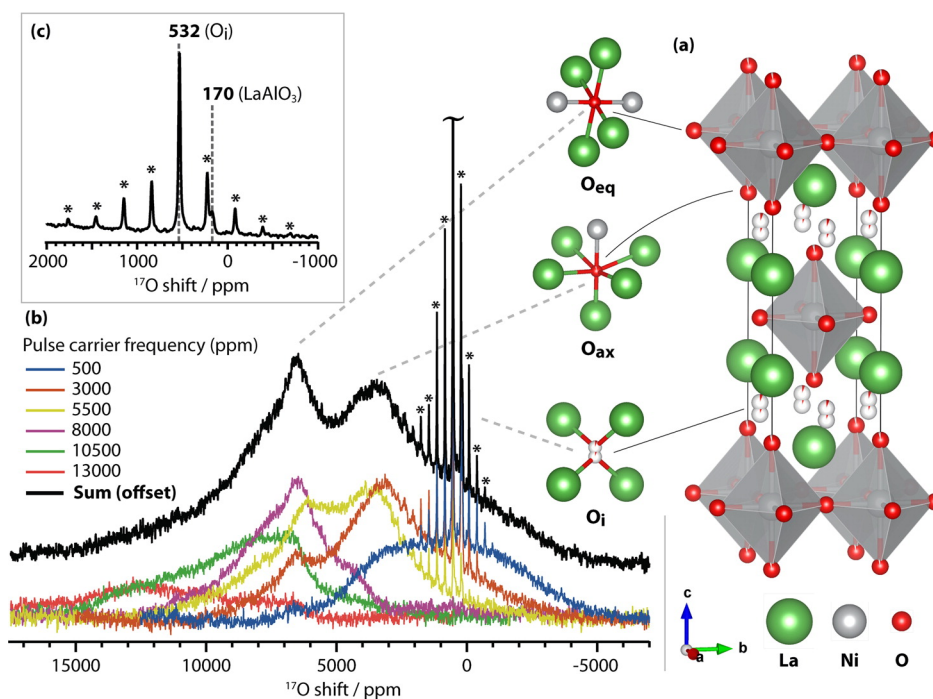


Figure 12.31: Solid-state ^{17}O MAS NMR spectrum of $\text{La}_2\text{NiO}_{4+\delta}$ acquired using frequency stepping, with assignments [413]. The crystal structure of $\text{La}_2\text{NiO}_{4.17}$ is shown in (a), with the oxygen sites in axial O_{ax} , equatorial O_{eq} , and interstitial O_{i} positions. The individual sub-spectra were acquired at the indicated transmitter offsets and summed to give the sum spectrum in (b). Each sub-spectrum was acquired with the rotor-synchronized spin-echo pulse sequence $30^\circ-\tau_r-60^\circ-\tau_r$, where the pulse lengths were scaled down by $I + 1/2 = 3$. An expansion of the spectral region between 2000 and -1000 ppm is shown in (c), showing the assignments to the LaAlO_3 impurity phase, and interstitial O_{i} in $\text{La}_2\text{NiO}_{4+\delta}$. The spectra were acquired at 7.05 T and 12.5 kHz MAS, with 120000 scans per sub-spectrum and a recycle delay of 0.5 s. Spinning sidebands are indicated with asterisks. Reproduced with permission from [413]. Copyright (2016) American Chemical Society.

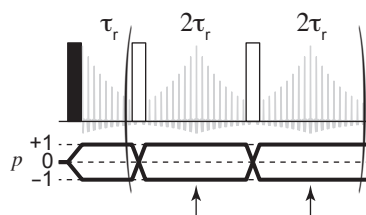


Figure 12.32: Pulse sequence and coherence-transfer pathway for the one-dimensional CPMG experiment [415, 416]. The time points at which the isotropic shift is refocused are indicated with arrows. Unless otherwise indicated, filled rectangles indicate pulses with a nominal flip angle of 90° and unfilled rectangles indicate pulses with a nominal flip angle of 180° , and all pulses have phase x .

larger sensitivity limitation. However greater sensitivity can be obtained by refocussing the inhomogeneous decay during the FID by applying the Carr–Purcell–Meiboom–Gill sequence in Figure 12.32 [415, 416]. Here the acquisition period comprises a series of concatenated spin-echoes with delays equal to the rotor period, during which the points of the FID are acquired. Both the isotropic shift and inhomogeneous decay are refocussed at the end of each echo, as indicated by the arrows on the coherence-transfer pathway in Figure 12.32, and so the decay envelope of the FID is given by the longer homogeneous decay time constant T_2' , resulting in greater sensitivity.

Heteronuclear signal enhancement of spin-1/2 nuclei: CP and TEDOR

One important method used in solid-state MAS NMR to enhance the signal from nuclei with a low gyromagnetic ratio is to transfer coherence from nuclear spins with a higher gyromagnetic ratio. For instance this idea is commonly employed for organic microcrystalline solids in order to enhance the low-natural-abundance ^{13}C signal by transferring coherences from the large bath of highly-abundant ^1H nuclei. For diamagnetic systems the most commonly-used pulse sequence is the Cross-Polarization (CP) experiment, which is shown in Figure 12.33 [18, 417]. The enhancement experiment is run here as a one-dimensional version of this sequence, where t_1 is set to zero. The coherence-transfer step comprises a pair of spin-lock pulses that are applied to the two channels simultaneously for a contact time τ_{con} (typically 1 ms), and with RF-field amplitudes $\omega_{1,I}$ and $\omega_{1,S}$ that satisfy either a zero-quantum Hartmann–Hahn condition $|\omega_{1,I} - \omega_{1,S}| = n\omega_r$ ($n = 1, 2$) [18], or a double-quantum condition $\omega_{1,I} + \omega_{1,S} = n\omega_r$ ($n = 1, 2$). It is generally found that applying a ramp to the ^1H spin lock improves the Hartmann–Hahn transfer, as this compensates for mismatching due to RF

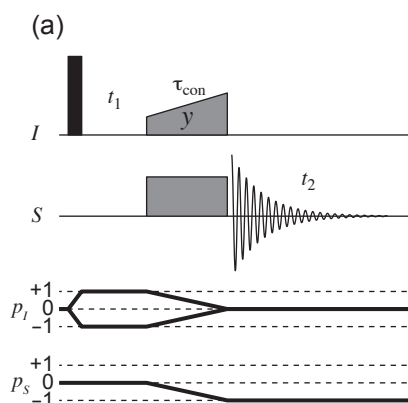


Figure 12.33: Pulse sequences and coherence-transfer pathway of the CP-HETCOR experiment with direct detection [18, 417]. The filled rectangle indicates a pulse with a nominal flip angle of 90° with phase x . The two shaded rectangles indicate the spin-lock pulses applied during cross polarization. The spin-lock pulses are applied simultaneously for a contact time τ_{con} during which the nominal I -spin and S -spin RF field amplitudes are set to a Hartmann–Hahn matching condition: $|\omega_{1,I} - \omega_{1,S}| = n\omega_r$, or $\omega_{1,I} + \omega_{1,S} = n\omega_r$, where $n = 1, 2$.

inhomogeneity and offset effects [417]. For paramagnetic systems the efficiency of the CP transfer is reduced considerably compared to diamagnetic systems, as shown by the comparison of the direct ^{13}C MAS and ^1H - ^{13}C CP spectra of a paramagnetic organometallic solid in Figure 12.34 (a) and (b) [7]. The comparison shows that the optimum CP experiment can actually be less sensitive than the direct-excitation experiment! The reasons for this are (1) the difficulty of efficiently spin-locking a resonance with a large SA under MAS with practicable RF field amplitudes, and (2) signal losses due to relaxation during the spin-lock pulses. The latter problem results in short optimum contact times, here $500 \mu\text{s}$, but even then the former problem still results in poor transfer.

An improvement in the heteronuclear coherence transfer can be used by employing the Transferred-Echo DOuble-Resonance (TEDOR) sequence [418], as first demonstrated by Kervern et al [7]. The basic pulse sequence is shown in Figure 12.35 (a), with t_1 set to zero. Here the I -spin in-phase coherences excited by the first pulse evolve during the I -spin-echo. During each half of the echo a series of recoupling 180° inversion pulses is applied to the S -spin, resulting in the recoupling of the heteronuclear dipolar coupling and the generation of anti-phase coherences. The coherence is then transferred to the S -spin by the pair of 90° pulses, after which the observable in-phase coherences on S are regenerated by the second recoupling sequence. The S -spin FID is then observed following a z -filter. The advantage of TEDOR over CP is that

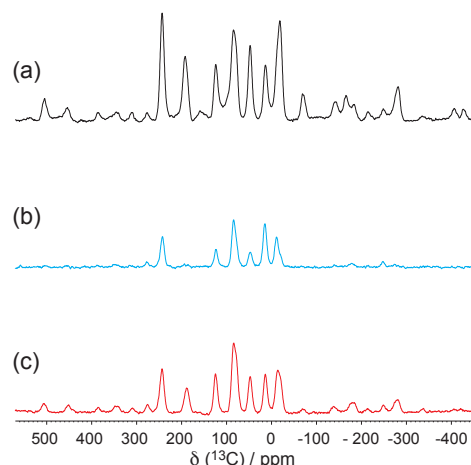


Figure 12.34: Comparison between the direct-excitation ^{13}C MAS spectrum, ^1H - ^{13}C CP spectrum, and ^1H - ^{13}C TEDOR spectrum of the compound **1**, the structure of which is shown in Figure 12.27 [7]. The direct-excitation ^{13}C spectrum acquired at 33 kHz MAS is shown in (a). The CP spectrum in (b) was acquired with a contact time of 500 μs , and the TEDOR spectrum in (c) was obtained with a recoupling time of 60 μs . Adapted with permission from [7]. Copyright (2006) American Chemical Society.

it uses only short, high-power pulses, which allows the use of higher RF field amplitudes, and avoids the need to spin-lock the large anisotropic resonances. This leads to a more efficient transfer, as shown by the ^1H - ^{13}C TEDOR spectrum in Figure 12.34 (c) which was acquired with a short recoupling time of 60 μs . We should note that although TEDOR is more efficient than CP, it still does not give a signal enhancement compared to the direct excitation spectrum, which is due to the short relaxation times leading to a reduction in the coherence intensities during the recoupling sequence. However the strength of this method is that it enables the efficient acquisition of two-dimensional heteronuclear correlation spectra, as described in section 12.5.5.

Signal enhancement of half-integer-spin quadrupolar nuclei: RAPT

We have seen in section 11.4 that quadrupolar nuclei of half-integer spin give NMR spectra with ST resonances that are broadened to the point of being undetectable, and relatively sharp CT resonances. For this reason solid-state NMR of quadrupolar nuclei usually employs low-power RF excitation pulses of amplitudes $\omega_1 \ll |\omega_Q|$ that are selective for the CT [198]. In paramagnetic systems however the CT resonance is broadened by the large SA, which gives a broad spinning-sideband manifold, and therefore requires a

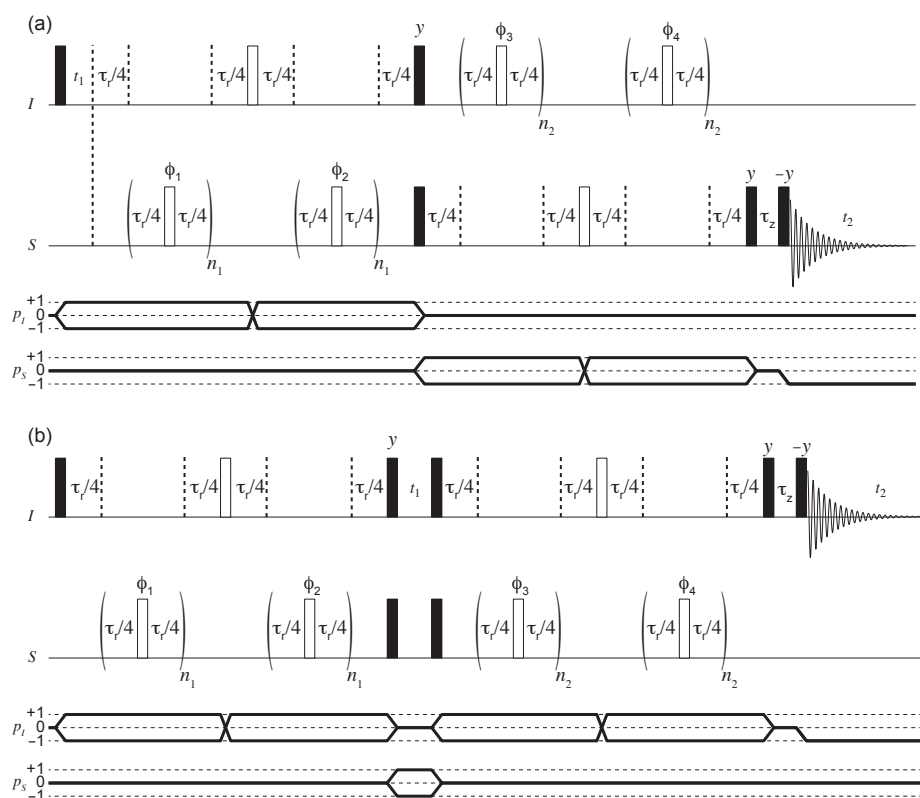


Figure 12.35: Pulse sequences and coherence-transfer pathways for the TEDOR experiments with direct- and indirect-detection. The pulse sequence for direct detection of the heteronucleus is shown in (a) [418]. The sequence in (b) is designed for indirect (proton) detection. The numbers of repetitions of the inversion pulses n_1 and n_2 must be odd in order to ensure refocussing of the SA of the active spin. For $n_0 = n_2 = 0$, these sequences are referred to as the DINEPT [26] and DHSQC respectively [27]. Unless otherwise indicated, filled rectangles indicate pulses with a nominal flip angle of 90° and unfilled rectangles indicate pulses with a nominal flip angle of 180° . All pulses have phase x , with the exception of the 180° TEDOR recoupling pulses inside the loops, which have phases ϕ_i that vary independently according to the XY-8 supercycle $xyxyxyx$ [419].

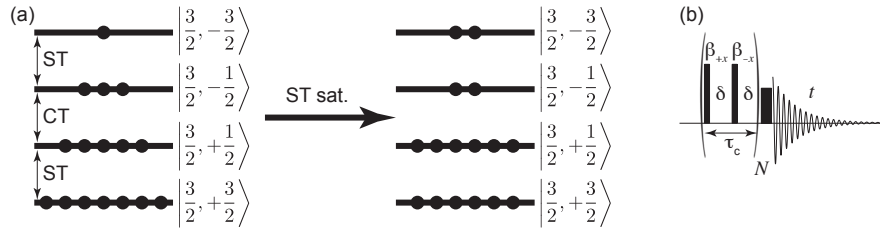


Figure 12.36: Illustration of the RAPT sequence for enhancing the signal from the CT of a half-integer-spin quadrupolar nucleus [420]. The effect of ST saturation is illustrated on the nuclear-spin energy level diagrams for a spin $I = 3/2$ in (a). Saturation of the two STs leads to the simultaneous removal of the ST polarization, and enhancement of the CT polarization. The RAPT pulse sequence is shown in (b). The saturation period comprises a pair of pulses with flip angle β and alternating phases $+x$ and $-x$ with total length τ_c , that is repeated N times. The final pulse is a CT-selective, low-power pulse calibrated to deliver a 90° rotation to the CT polarization.

higher-power pulse for excitation [55]. Practicable RF field amplitudes of the order of 100 kHz still result in a pulse that is CT selective for quadrupolar nuclei such as ^{23}Na , where a typical C_Q value of 3 MHz results in a quadrupolar splitting frequency of 750 kHz. One consequence of this is that the polarization that is excited, given by the population difference of the two states connected by the CT, is lower than the maximum available if we consider all the states, as shown in Figure 12.36 (a) for a spin $I = 3/2$. This results in a spectrum with a lower signal-to-noise ratio than is theoretically feasible.

In order to quantify the intensity of the CT that is available we can write the equilibrium density operator \hat{I}_z as a linear combination of the z -spin operators involving the pairs of states $|IM\rangle$ and $|I-M\rangle$, which we write as $\hat{I}_z^{(M,-M)} = (\hat{I}_p^{(M)} - \hat{I}_p^{(-M)})/2$. Hence the available polarization for the CT is represented by $\hat{I}_z^{(1/2,-1/2)}$. Using these operators \hat{I}_z is given by

$$\hat{I}_z = \sum_{M=1/2}^I 2M \hat{I}_z^{(M,-M)}. \quad (12.13)$$

Therefore we see the pair of levels giving the MQ transition has a polarization that is greater than that of the CT by a factor of $2M$. In principle we can increase the polarization of the CT by saturating all the STs so that their net polarization is reduced to zero, as shown for the spin $I = 3/2$ in Figure 12.36 (a). This has the effect of transforming the equilibrium density operator into a non-equilibrium population operator in which all the terms have the same polarization $I + 1/2$:

$$\sum_{M=1/2}^I (I + 1/2) \hat{I}_z^{(M,-M)}. \quad (12.14)$$

Hence the polarization of the CT has increased from 1 to $I + 1/2$, which results in a sensitivity enhancement of the CT resonance by a factor of $I + 1/2$, i.e. a factor of 2 for $I = 3/2$.

Enhancement of the CT polarization can be achieved in practice by using the Rotor-Assisted Population Transfer (RAPT) pulse sequence shown in Figure 12.36 (b) [420]. The CT-selective excitation pulse is preceded by the saturation sequence which comprises N pairs of RF pulses of flip-angle β and with alternating phases of $+x$ and $-x$ separated by short delays δ . Each unit of $\beta_{+x}-\delta-\beta_{-x}-\delta$ has a total length of τ_c . The effect of this sequence is to apply a net rotation to the ST magnetization terms, leaving the CT magnetization along z , whilst increasing its magnitude. The excitation of this enhanced CT polarization is achieved with a CT-selective pulse [421]. It has been shown by Prasad et al. that the optimum value of the cycle time τ_c is the inverse of the quadrupolar splitting frequency $2\pi/\omega_Q$, and is independent of η^Q [422]. This provides a simple method to allow the C_Q parameter to be estimated, where we acquire a series of RAPT spectra with varying τ_c to obtain the value corresponding to the maximum enhancement. This is of particular interest for paramagnetic systems, where the presence of the SA and inhomogeneous broadening in addition to the broadening from the quadrupolar interaction means that it is essentially impossible to measure the quadrupolar interaction parameters from a single one-dimensional spectrum.

The application of RAPT to paramagnetic Mg-ion battery materials is particularly striking. The only stable isotope of Mg that is NMR active is ^{25}Mg , which is of spin $I = 5/2$ and suffers from very low sensitivity due to both a low gyromagnetic ratio, and a low natural abundance of 10%. Figure 12.37 shows the experimental application of RAPT to the material Mg_6MnO_8 [58]. In (a) is shown the enhancement obtained as a function of the RAPT repetition frequency $\nu = 1/\tau_c$. A maximum enhancement of 1.6 is obtained for repetition rates 250–270 kHz. This is half of the theoretical maximum of $I + 1/2 = 3$, but nevertheless represents a very useful tool for increasing the sensitivity of the NMR experiment. Furthermore this maximum in the profile at the optimum repetition frequency $\nu_{\text{opt}} = 3C_Q/40$ gives an estimate of the C_Q value of between 3.3 and 3.6 MHz, which is in remarkably good agreement with the range of values of 3.64–3.69 MHz predicted from DFT [58]. The optimum spectrum showing the spinning-sideband manifold of the CT is shown in Figure 12.37 (b).

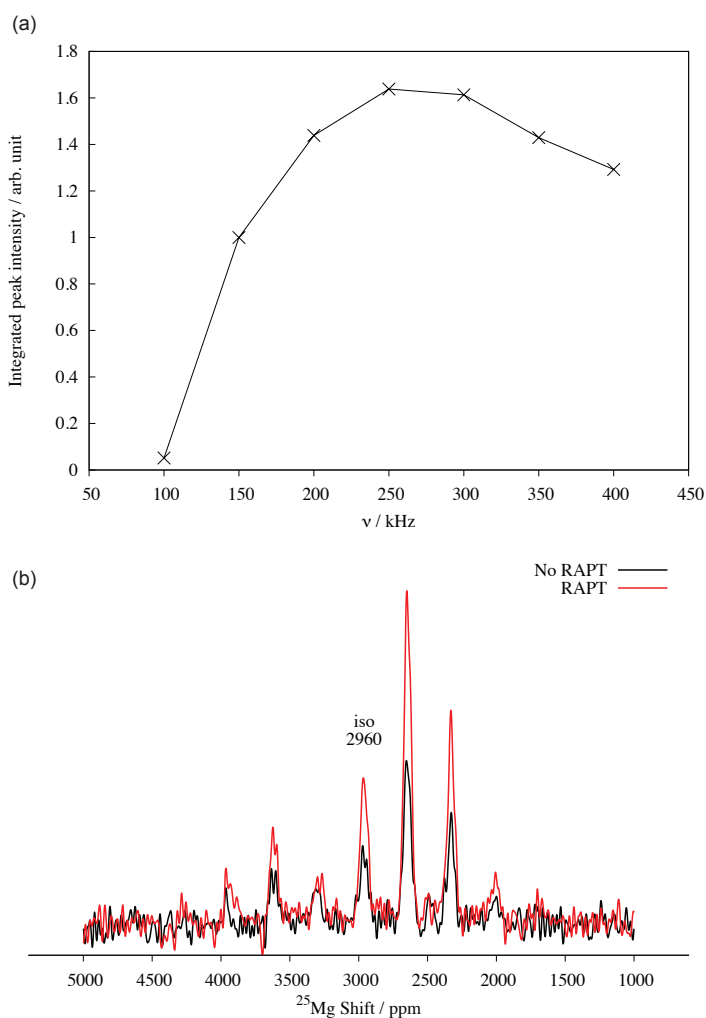


Figure 12.37: Illustration of the application of RAPT to the ^{25}Mg NMR of the battery material Mg_6MnO_8 . The enhancement profile showing the RAPT enhancement as a function of repetition frequency ν is shown in (a). The optimum enhancement is obtained with values of ν between 250 and 270 kHz, corresponding to an estimated C_Q of 3.3–3.6 MHz. A spectrum acquired separately with a repetition rate of 270 kHz is shown in (b), and exhibits an enhancement of 1.6. Reproduced by permission of the PCCP Owner Societies [58].

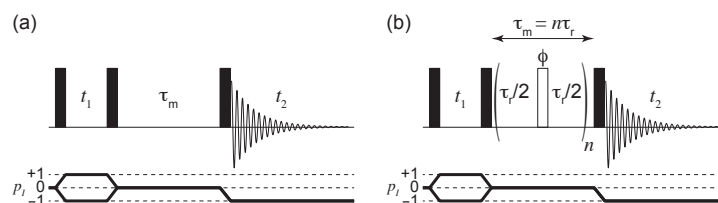


Figure 12.38: Pulse sequences and coherence-transfer pathways for the spin-diffusion and RFDR homonuclear correlation experiments. The basic spin-diffusion pulse sequence is shown in (a). Modification of this sequence to include RFDR homonuclear recoupling during the z -filter gives the sequence in (b) [424]. Unless otherwise indicated filled rectangles indicate pulses with a nominal flip angle of 90° and unfilled rectangles indicate pulses with a nominal flip angle of 180° . All 90° pulses have phase x . The phases ϕ of the 180° RFDR pulses vary according to the XY-8 supercycle $xyxyxyx$ [419].

12.5.3 Homonuclear through-space correlations

One important mechanism for homonuclear correlation spectroscopy in solids is spin diffusion, in which we transfer longitudinal magnetization from one spin to another via the homonuclear dipolar coupling [423]. This mechanism is particularly effective for ^1H nuclei, where it is referred to as proton spin diffusion (PSD), as the large gyromagnetic ratio gives large dipolar coupling constants, and therefore relatively rapid transfer. This mechanism bears a superficial resemblance to the NOE transfer in solution, but there is a fundamental difference. In solution the coherent dipolar coupling is averaged to zero by isotropic molecular tumbling, and so the NOE transfer occurs entirely through the stochastic modulation of the dipolar interaction. It is therefore a relaxation process. On the other hand the spin-diffusion mechanism in solids is due to the coherent dipolar coupling interaction, which is not averaged as there is no isotropic molecular tumbling. It can therefore occur in systems with no rotational dynamics. The basic pulse sequence is the same as used for NOESY in solution (Figure 12.9 (a)), and is shown in Figure 12.38 (a). This sequence has been shown to be efficient for ^1H - ^1H transfer in systems experiencing moderate PREs and at moderate MAS (20–30 kHz), where typical mixing times are of the order of $100\ \mu\text{s}$ [27]. The rate of transfer due to spin diffusion is reduced with increasing MAS frequency, and under fast MAS conditions ($> 40\ \text{kHz}$) may require mixing times of 100 ms. For paramagnetic systems this causes a severe reduction in sensitivity due to the rapid longitudinal relaxation that also occurs during the mixing period.

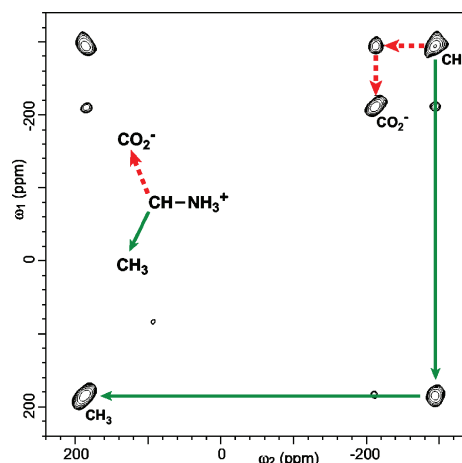


Figure 12.39: Experimental two-dimensional ^{13}C - ^{13}C dipolar correlation spectrum acquired with ^{13}C - and ^{15}N -labelled $\text{Cu}(\text{DL-Ala})_2$ with RFDR mixing at 40 kHz MAS. The two-dimensional correlation sequence was preceded by a ^1H - ^{13}C dipolar transfer with the DINEPT sequence [26]. The RFDR mixing period comprised a train of $4\ \mu\text{s}$ 180° pulses (125 kHz) and was of total duration 1.6 ms. Reproduced from [425], with the permission of AIP Publishing.

However the rate of transfer can be increased by employing a homonuclear dipolar recoupling sequence during the mixing time. One suitable sequence is the Radio-Frequency Driven Recoupling (RFDR) scheme, which comprises a chain of elements $\tau_r/2$ — 180° — $\tau_r/2$ comprising a high-power 180° pulse, giving the sequence in Figure 12.38 (b) [424]. As for the previous sequences discussed, the suitability for paramagnetic systems is due to the use of short, high-power pulses to obtain the best possible inversion bandwidth. An experimental example of a homonuclear ^{13}C - ^{13}C RFDR correlation spectrum of ^{13}C - and ^{15}N -labelled $\text{Cu}(\text{DL-Ala})_2$ acquired at 40 kHz MAS is shown in Figure 12.39 [425]. The spectrum shows the correlations between the three ^{13}C nuclei within each alanine molecule, due to both the short-range (one-bond) transfers between CA and CO and CA and CB, and to the longer-range transfer between CO and CB. The use of RFDR is crucial to obtaining any transfer as the fast MAS completely suppresses any direct spin diffusion between the ^{13}C nuclei on the timescale of longitudinal relaxation.

In order to ensure pure-phase lineshapes in the two-dimensional spectra, it is recommended that the t_1 increment is set to an integer multiple of the rotor period, so that there is no net evolution of the SA and only the isotropic shifts appear in the ω_1 dimension. The spectrum therefore has the form given in Figure 12.14, with the exception that the resonance is split into a spinning-sideband manifold in ω_2 . In cases where the

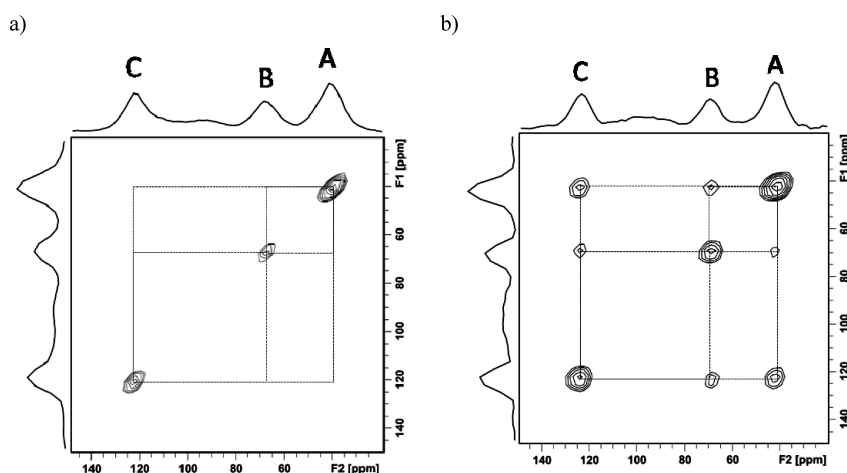


Figure 12.40: Experimental two-dimensional ${}^6\text{Li}$ EXSY spectra acquired with monoclinic $\text{Li}_3\text{Fe}_2(\text{PO}_4)_3$ at 25 kHz MAS. The one-dimensional spectrum contains three distinct resonances for the three Li sites A, B, and C. The spectrum in (a) was acquired with a mixing time of 0.5 ms, and shows no cross peaks. The spectrum in (b) was recorded with a longer mixing time of 3.0 ms, and exhibits cross peaks due to exchange between all three sites. The temperature is 311 K. Reproduced with permission from [427]. Copyright (2010) American Chemical Society.

dispersion of isotropic shifts is larger than the spinning frequency, it is necessary to employ a t_1 increment that is shorter than the rotor period. In this case we also obtain spinning sidebands in the ω_1 dimension, and no longer have pure-phase lineshapes [426]. This problem may be removed by refocussing the evolution of the SA during t_1 using the methods described in section 12.5.6 to obtain an ω_1 dimension free from spinning sidebands.

12.5.4 Homonuclear exchange correlations

Correlations between nuclear sites experiencing slow chemical exchange can be obtained using the same two-dimensional EXSY sequence as for solution NMR in Figure 12.9 (a), and with the same requirement that the mixing time take a maximum value of the order of T_1 . One interesting application of EXSY in paramagnetic solids has been the study of lithium exchange dynamics in lithium-ion-conducting materials [427, 428]. An example is the two-dimensional ${}^6\text{Li}$ EXSY spectra acquired on monoclinic $\text{Li}_3\text{Fe}_2(\text{PO}_4)_3$ at moderate MAS of 25 kHz shown in Figure 12.40. The conventional one-dimensional spectrum contains three resonances A, B, and C corresponding to the three distinct Li sites in the material. The ${}^7\text{Li}$ spins have

comparatively short T_1 times of 1.1 ms, and so ${}^6\text{Li}$ was used to measure the exchange as the lower γ_I gives smaller PREs, thus allowing the use of longer mixing times. Spectra acquired using two mixing times are shown. A short mixing time of 0.5 ms gives the spectrum in Figure 12.40 (a) with no cross peaks. However increasing the mixing time to 3.0 ms gives correlations between all three sites, as shown in Figure 12.40 (b), indicating that there is exchange amongst all the sites.

12.5.5 Heteronuclear through-space correlations

The two-dimensional heteronuclear correlation experiments that have been most successfully employed for paramagnetic systems are based on the TEDOR [7] (Figure 12.35 (a)), Dipolar Insensitive Nucleus Enhanced by Polarization Transfer (DINEPT) [26], and Dipolar Heteronuclear Single-Quantum Correlation (DHSQC) [27] experiments. As we have already seen for one-dimensional spectroscopy, these sequences give superior sensitivity compared to the CP-based HETeronuclear CORrelation (HETCOR) experiment in Figure 12.33.

As for heteronuclear correlation spectroscopy in solution, there is a choice to whether we observe the ${}^1\text{H}$ spin or heteronuclear spin in these experiments. In solid-state NMR there is a preference for direct detection of the heteronucleus as the observation of the narrower peaks usually offsets any penalty in sensitivity from the lower gyromagnetic ratio. Figure 12.35 (a) shows the TEDOR sequence that would be used for direct detection. When the loop counters n_1 and n_2 are both set to 1 we obtain a sequence that is closely related to the DINEPT experiment of Wickramasinghe and Ishii [26]. An example of a two-dimensional ${}^1\text{H}$ - ${}^{13}\text{C}$ TEDOR spectrum acquired for a paramagnetic organometallic complex is shown in Figure 12.41 (a) [7]. A short recoupling time of $60\ \mu\text{s}$ was used to selectively transfer the coherences over a distance scale corresponding to a single H-C bond. The spectrum allows the unambiguous assignment of the corresponding resonances. We also note that the resonances are broadened along a ridge that is inclined relative to both axes. This is due to the inhomogeneous broadening which is a consequence of the ABMS effects discussed in chapter 10. Because the broadening is a distribution of chemical shifts it leads to an elongation of the resonance in the two-dimensional spectrum that is inclined relative to the ω_1 axis with a gradient of $\Delta\omega_2/\Delta\omega_1 = |\gamma_S/\gamma_I|$, which is here equal to $1/4$ [257]. We are able to recover the intrinsically higher resolution in the absence of the ABMS broadening by shearing the two-dimensional spectrum parallel to ω_2 to give a new frequency axis $\omega'_2 = \omega_2 + \kappa\omega_1$, where κ is a shear ratio equal to $-|\gamma_S/\gamma_I|$, and then projecting onto ω'_2 . The spectra are shown in Figure 12.41 (b).

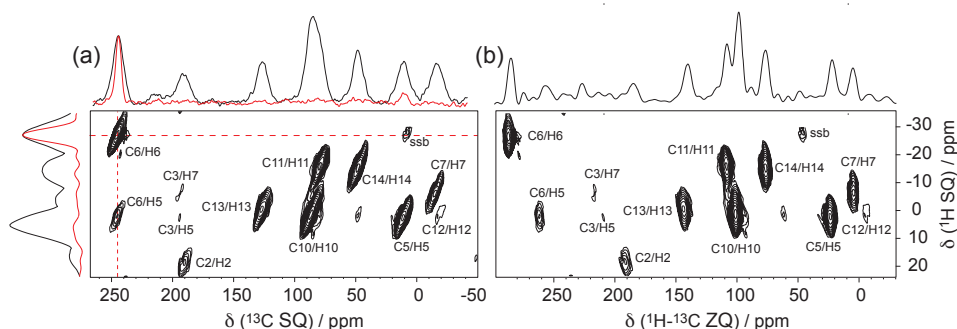


Figure 12.41: Experimental two-dimensional ^1H - ^{13}C TEDOR spectra acquired with compound **1** of Figure 12.27 using the pulse sequence in Figure 12.35 (a). The MAS frequency is 30 kHz, the loop counters were both set to 1, and the z -filter was omitted. The recoupling time of $60\ \mu\text{s}$ is selective for short-range transfers over the distance scale of a single H-C bond. The spectrum in (a) shows the region of the spectrum with the isotropic peaks. The black one-dimensional spectra along the ^1H and ^{13}C dimensions represent projections of the two-dimensional spectrum onto those axes, and the red traces are cross-sections extracted at the frequencies indicated by the dashed lines. The lines are broadened into ridges by inhomogeneous broadening. Applying a shearing transformation to the spectrum (see text for details) gives the spectrum in (b) where the horizontal dimension represents the high-resolution zero-quantum (ZQ) dimension. Reproduced with permission from [7]. Copyright (2006) American Chemical Society.

With the use of faster MAS it becomes possible to observe the ^1H spectrum directly. This allows us to employ a version of the TEDOR sequence with indirect detection, as shown in Figure 12.35 (b), which benefits from the higher sensitivity of observing the nucleus with the larger γ_I . This sequence is related to the DHSQC experiment used by Swamy et al. by setting $n_1 = n_2 = 0$ [27]. A comparison of the directly and indirectly-detected ^1H - ^{13}C correlation spectra of a paramagnetic Cu(II) complex is shown in Figure 12.42 [27]. The DINEPT spectrum acquired at 30 kHz MAS and a recoupling time of $33.33\ \mu\text{s}$ is shown in (a). The corresponding DHSQC spectrum is shown in (b). In both cases the combination of fast MAS and short recoupling times enabled the acquisition of spectra with good sensitivity and resolution.

12.5.6 Separation of shift and shift anisotropy interactions

The experimental methods presented in the previous sections are designed to measure correlations between the isotropic shifts of different nuclear sites. However in paramagnetic solids there are other interactions which lead to spectral broadening and a loss of resolution, but are also useful sources of structural information where they can be measured. One such interaction is the SA, which we have seen appears in the MAS NMR

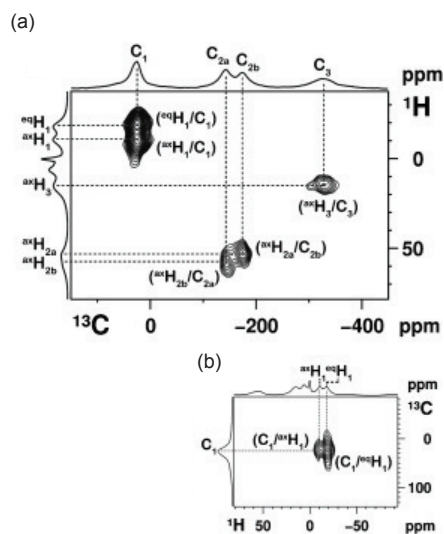


Figure 12.42: Two-dimensional ^1H - ^{13}C correlation spectra of a paramagnetic Cu(II)-cyclam complex at 30 kHz MAS. The DINEPT spectrum is shown in (a), and the DHSQC spectrum is shown in (b). The recoupling times for the generation of anti-phase coherences and reconversion back to in-phase coherences were both $33.33 \mu\text{s}$. Adapted with permission from [27]. Copyright John Wiley and Sons.

spectrum as a spinning-sideband manifold. In solid materials in which a particular nucleus is present in more than one site, the NMR spectrum contains multiple spinning-sideband manifolds that, in general, overlap. It is therefore a matter of great interest to use an experiment that can separate the SA from the isotropic shifts, so that both can be measured.

There are two widely-used two-dimensional experiments that remove the overlap between the spinning-sideband manifolds, that are referred to as the Phase-Adjusted Spinning Sidebands (PASS) experiment [429], and the Magic-Angle Turning (MAT) experiment [430]. They both have the same basic pulse sequence, which comprises a 90° excitation pulse followed by a sequence of n 180° refocussing pulses that occupy a recoupling delay $T = N\tau_r$, where N is an integer. This recoupling period forms the evolution period of the two-dimensional experiment, and is followed by direct acquisition. An example pulse sequence with five 180° pulses is shown in Figure 12.43 (a). We define the timings in the pulse sequence so that acquisition begins at $t = 0$, which means that the time point immediately following the excitation pulse is $t = -T$. The timing of the q th pulse is defined as $-T + \tau_q$. Hence the total phase accrued during the evolution period

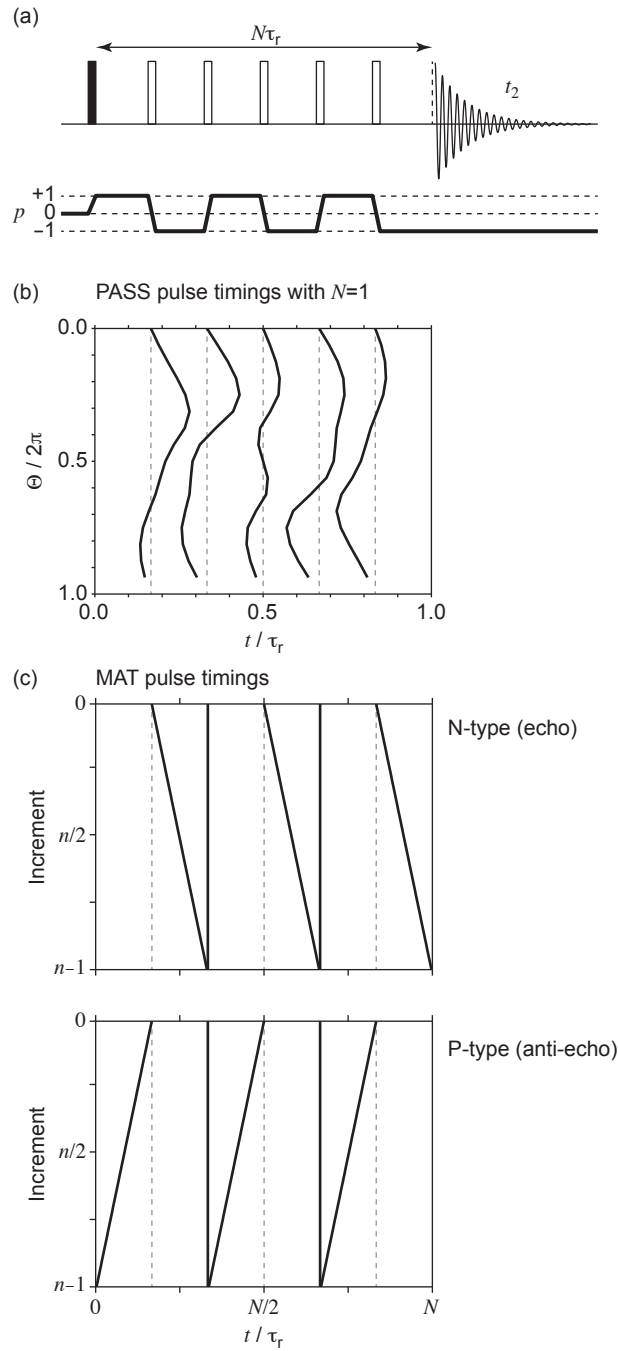


Figure 12.43: Pulse sequence, coherence-transfer pathway, and pulse timings of the two-dimensional PASS and MAT experiments for separating the isotropic shift and SA. The pulse sequence is shown in (a). To obtain a PASS spectrum the timings for the 180° refocussing pulses shown in (b) are used [429]. The timings in (c) are used for a MAT experiment, for which both N - and P -type datasets are required [430]. Unless otherwise indicated, filled rectangles indicate pulses with a nominal flip angle of 90° and unfilled rectangles indicate pulses with a nominal flip angle of 180° , and all pulses have phase x .

$\Phi_c(\gamma; 0, -T)$ is given by the sum of the phases due to the isotropic and anisotropic shifts, and is given by:

$$\Phi_c(\gamma; 0, -T) = \Omega_{\text{iso}} \tau_{\text{seq}} + \Phi_c^{\text{SA}}(\gamma; 0, -T + \tau_n) - (-1)^n \sum_{q=1}^n (-1)^q \Phi_c^{\text{SA}}(\gamma; -T + \tau_q, -T + \tau_{q-1}), \quad (12.15)$$

where we define $\tau_0 = 0$, and the effective evolution time of the isotropic shift τ_{seq} is

$$\tau_{\text{seq}} = T - 2 \sum_{q=1}^n (-1)^{n+q} \tau_q. \quad (12.16)$$

Whilst in conventional two-dimensional spectroscopy we map the evolution during the indirect dimension by incrementing the evolution time, we do not do so in the PASS and MAT experiments. Instead the total length of the evolution period is kept constant at T , and we map out the evolution of the isotropic shift or SA by varying the timings τ_q of the n refocusing pulses. In order to quantify the extent of evolution we define a ‘‘pseudo- t_1 ’’ variable Θ , which is known as the pitch. If we have N_{inc} increments the pitch for the j th increment ($j = 1, 2, \dots, N_{\text{inc}}$) is $\Theta = 2N\pi(j-1)/N_{\text{inc}}$. We now make a decision as to whether we wish to refocus the isotropic shift or SA during the evolution period. In the former case we obtain the PASS experiment, and in the latter we obtain MAT.

PASS

In the PASS experiment we refocus the isotropic shift in all the increments, and allow the SA to evolve progressively. Therefore the phase acquired during the evolution block in Equation 12.15 becomes

$$\Phi_c(\gamma; 0, -T) = \Phi_c^{\text{SA}}(\gamma; 0, \Theta/\omega_r), \quad (12.17)$$

and the effective evolution time of the isotropic shift is zero for all increments:

$$\tau_{\text{seq}} = 0. \quad (12.18)$$

If we define the pulse timings in terms of angles $\theta_q = \omega_r \tau_q$ and the total length of the evolution block via an angle $\theta_T = \omega_r T$, we obtain a set of five simultaneous equations that must be solved for each value of the pitch

in order to obtain the required pulse timings. Four equations pertain to the evolution of the SA, and are:

$$2 \sum_{q=1}^n (-1)^q \exp(-im\theta_q) + 1 - (-1)^n \exp(-im(\Theta + \theta_T)) = 0, \quad m = \pm 1, \pm 2, \quad (12.19)$$

whilst the fifth is the requirement that the isotropic shift is refocussed for all increments:

$$\theta_T - 2 \sum_{q=1}^n (-1)^{n+q} \theta_q = 0. \quad (12.20)$$

If we employ a sequence with $n = 5$ 180° pulses these simultaneous equations can be solved to give unambiguous timings for each increment. The solutions are non-trivial, but can be obtained by numerical solution of the five equations [429]. An example of the pulse timings is plotted in Figure 12.43 (b) for a recoupling block with a length of one rotor period.

When implementing the PASS experiment we set the number of increments N_{inc} to a power of two that is larger than the expected number of sidebands in the broadest manifold. A simulated PASS spectrum is shown in Figure 12.44 (b). We see that the two spinning-sideband manifolds that overlap in the one-dimensional spectrum are aligned parallel to the main diagonal $\omega_1 = \omega_2$ in the two-dimensional spectrum, and are separated. The isotropic shifts can be obtained by extracting a one-dimensional trace at $\omega_1 = 0$, which contains the centrebands. We note here that both the homogeneous and inhomogeneous linewidth in the indirect dimension are exactly zero. This is because firstly the evolution block has a constant length, and so there is no differential T'_2 dephasing as we increment the pitch; the T'_2 dephasing therefore only reduces the overall intensity of the spectrum. Secondly the refocussing of the isotropic shift in the indirect dimension also has the effect of refocussing the inhomogeneous decay. Therefore both sources of line broadening only lead to broadening in ω_2 .

MAT

The second strategy for separating the spinning-sideband manifolds is to allow the isotropic shift to evolve progressively during the evolution block, and to refocus the SA for all increments, which results in the MAT experiment [430]. In this case the pitch is used to define the increase of τ_{seq} from zero to a maximum value

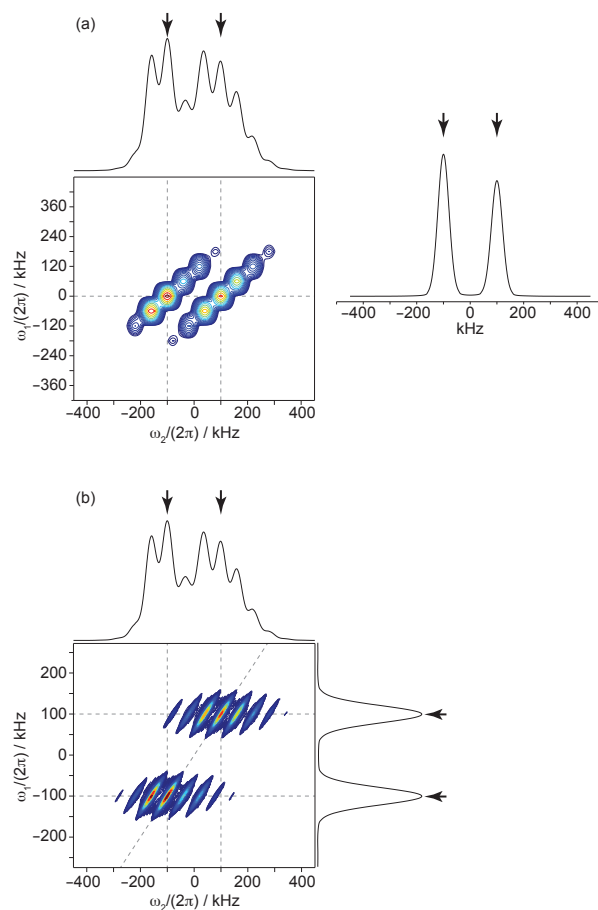


Figure 12.44: Simulated spectra illustrating the two two-dimensional spectroscopic methods for separating overlapping spinning-sideband manifolds. The conventional one-dimensional spectrum contains two overlapping spinning-sideband manifolds, both with Gaussian inhomogeneous broadening of the isotropic shifts. The PASS spectrum, in which the isotropic shift is refocussed in ω_1 , is shown in (a). The sidebands of the two manifolds are aligned parallel to the $\omega_1 = \omega_2$ main diagonal, and centred at $\omega_1 = 0$. The isotropic resonances, indicated by arrows, are now clearly separated in the one-dimensional trace to the right taken parallel to ω_2 through the centrebands. The inhomogeneous broadening is also parallel to ω_2 . The MAT spectrum is shown in (b). Here the two spinning-sideband manifolds are parallel to ω_2 , and centred at the isotropic frequencies in ω_1 . The isotropic projection onto the ω_1 axis containing only the isotropic resonances is shown to the right. The inhomogeneous broadening is parallel to the $\omega_1 = \omega_2$ main diagonal.

via

$$\tau_{\text{seq}} = \pm \frac{\Theta}{\omega_r}, \quad (12.21)$$

where the + sign refers to the P-type spectrum, and the – sign to the N-type spectrum. The total phase acquired during the evolution block is then

$$\Phi_c(\gamma; 0, -T) = \pm \Omega_{\text{iso}} \frac{\Theta}{\omega_r}. \quad (12.22)$$

As for PASS these restrictions give us five simultaneous equations that need to be solved to obtain the correct pulse timings. The first refers to the evolution of the isotropic shift:

$$\theta_T - 2 \sum_{q=1}^n (-1)^{n+q} \theta_q = \pm \Theta, \quad (12.23)$$

and the remaining four to the refocussing of the SA:

$$2 \sum_{q=1}^n (-1)^q \exp(-im\theta_q) + 1 - (-1)^n \exp(-im\theta_T) = 0, \quad m = \pm 1, \pm 2. \quad (12.24)$$

The solution to these five equations is simpler than for PASS. We again employ $n = 5$ 180° pulses, but with timings that are now given by [430]:

$$\tau_q = \frac{N\tau_r}{6} \left[q \pm \left(\frac{1 - (-1)^q}{2N_{\text{inc}}} \right) (j - 1) \right], \quad (12.25)$$

where the number of rotor periods N can take any integer value that is *not* an integer multiple of 3. These solutions are plotted graphically in Figure 12.43 (c) for the N-type and P-type experiments.

The MAT spectrum simulated with the same parameters as for the PASS spectrum discussed above is shown in Figure 12.44 (c). Here the spinning-sideband manifolds are parallel to the ω_2 dimension, and the ω_1 dimension contains the isotropic spectrum that can be obtained by a projection onto this axis. We also note that the inhomogeneous broadening is parallel to $\omega_1 = \omega_2$, in contrast to PASS, since now the isotropic shift evolves during the evolution block.

An example of MAT performed at slow MAS (0.5–1.5 kHz) is given in Figure 12.45 [431]. Figure 12.45 (a) shows the two-dimensional ^{13}C MAT spectrum of the system $[(\text{C}_2\text{H}_5)_4\text{N}]_2[\text{Fe}_4\text{S}_4(\text{S}^{13}\text{CH}_2\text{C}_6\text{H}_5)_4]$,

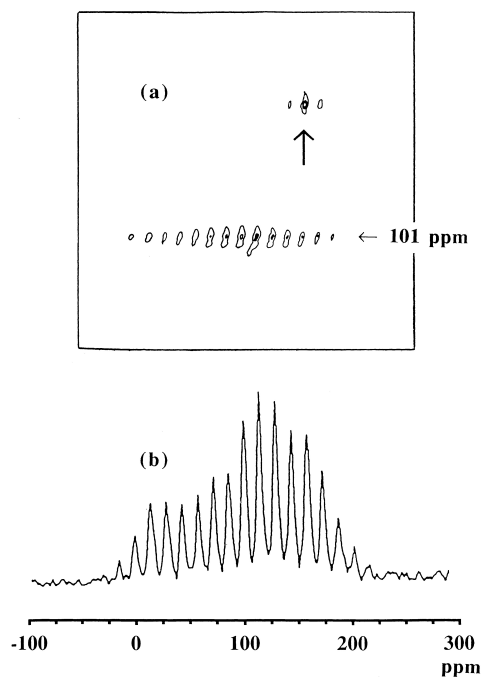


Figure 12.45: Two-dimensional ^{13}C MAT spectrum at room temperature of $[(\text{C}_2\text{H}_5)_4\text{N}]_2[\text{Fe}_4\text{S}_4(\text{S}^{13}\text{CH}_2\text{C}_6\text{H}_5)_4]$. The two-dimensional spectrum is shown in (a) The resonance marked by the vertical arrow is due to the strongest sharp line at 0 ppm from the natural abundance ^{13}C spins in the terminal methyl groups of the counterions. In (b) is shown the one-dimensional trace taken from the horizontal slice at 101 ppm. Reproduced with permission from [431]. Copyright (2000) American Chemical Society.

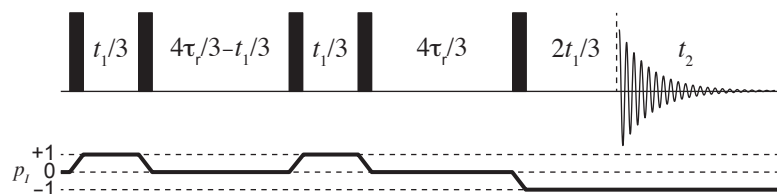


Figure 12.46: Pulse sequence and coherence-transfer pathway of the two-dimensional MAT-PASS experiment for separating the isotropic shift and SA [432]. The experiment comprises N_{inc} increments, where N_{inc} is a power of 2. The evolution time t_1 is incremented from an initial value of τ_r to a final value of $2\tau_r$ in steps of $\delta t_1 = \tau_r/N_{\text{inc}}$. The length of the sequence between the first pulse and start of acquisition therefore increases from $11\tau_r/3$ to $14\tau_r/3$. Filled rectangles indicate pulses with a nominal flip angle of 90° , and all pulses have phase x .

in which a single C atom has been ^{13}C labelled. The correlation reveals a broad spinning-sideband manifold with an isotropic shift of 101 ppm, which is shown in Figure 12.45 (b).

MATPASS

The PASS and MAT methods are both potentially very powerful for obtaining interpretable NMR data that would otherwise be of too low resolution to be usable. However both experiments have a weakness, which is that they employ a train of 180° pulses, which we have seen have a comparatively low bandwidth. One solution to this is to instead use more broadband pulse schemes, as described in section 12.5.7. A second solution, proposed by Hung et al., replaces all of the 180° pulses by 90° pulses which have a greater bandwidth [432]. The resulting MAT-PASS pulse sequence is shown in Figure 12.46. The sequence also reintroduces the real t_1 evolution variable, which takes values from τ_r to $2\tau_r$ in steps of $\delta t_1 = \tau_r/N_{\text{inc}}$. The spectrum has the same form as the conventional PASS spectrum in Figure 12.44 (c). However the overall improvement in the bandwidth comes at the cost of reduced sensitivity. Whereas the coherence-transfer pathway in the conventional PASS/MAT sequence is the only one produced under ideal conditions, in the MAS-PASS sequence the coherence-transfer pathway shown is only one of the four possible pathways that are generated by the pulses. Hence the overall sensitivity is reduced by a factor of four compared to conventional PASS; one reduction by two is due to the transfer $p = +1 \rightarrow 0 \rightarrow +1$ by the combination of the second and third pulses, the second factor of two is due to the transfer $p = +1 \rightarrow 0 \rightarrow -1$ by the combination of the fourth and fifth pulses. A second disadvantage is that the evolution block does not have a fixed duration, and but increases by one rotor period from $11\tau_r/3$ to $14\tau_r/3$. For materials with large PREs this leads to a measurable

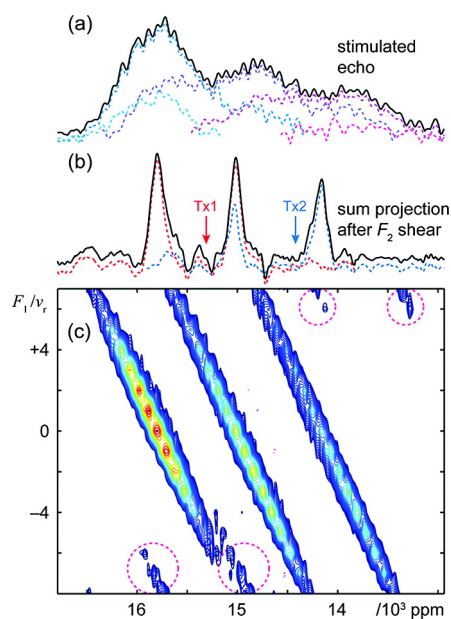


Figure 12.47: The ^{31}P MATPASS spectrum of $\text{Li}_3\text{Fe}_2(\text{PO}_4)_3$ acquired at 19.6 T and 30 kHz MAS. The one-dimensional spectrum shown in (a) comprises three overlapping resonances, which are completely separated in the two-dimensional MATPASS spectrum in (b). The isotropic spectrum that is shown was obtained following a shear (described in section 12.5.8) and projection. The MATPASS spectrum was acquired using the frequency-stepping scheme with two sub-spectra with the carrier positions denoted by Tx1 and Tx2 [394]. Reproduced with permission from [432]. Copyright (2012) American Chemical Society.

difference in coherence dephasing for different increments, and hence a coherent linewidth in the indirect dimension, and therefore an imperfect separation of the spinning-sideband manifolds [429].

Nevertheless the sequence has been used successfully in separating the spinning-sideband manifolds of multiple sites in paramagnetic battery materials. An example of such an application is the application of MATPASS to the ^{31}P MAS NMR of $\text{Li}_3\text{Fe}_2(\text{PO}_4)_3$, as shown in Figure 12.47 [432]. The one-dimensional spectrum in Figure 12.47 (a) comprises overlapping resonances from three distinct local environments. These three environments are fully separated in the two-dimensional MATPASS spectrum shown in Figure 12.47 (b). Whilst this pulse sequence does have a greater bandwidth than conventional PASS or MAT, it should be noted that here the MATPASS spectrum had to be acquired as two sub-spectra, using the frequency-stepping method [394]. This issue of broadband NMR is addressed in the following section 12.5.7. A second compelling example of MAT-PASS is its use in monitoring the change in the multiple ^7Li sites in the Na-ion cathode material $\text{P2-Na}_{0.8}[\text{Li}_{0.12}\text{Ni}_{0.22}\text{Mn}_{0.66}]\text{O}_2$ during the first electrochemical cycle [55]. Figure 12.48

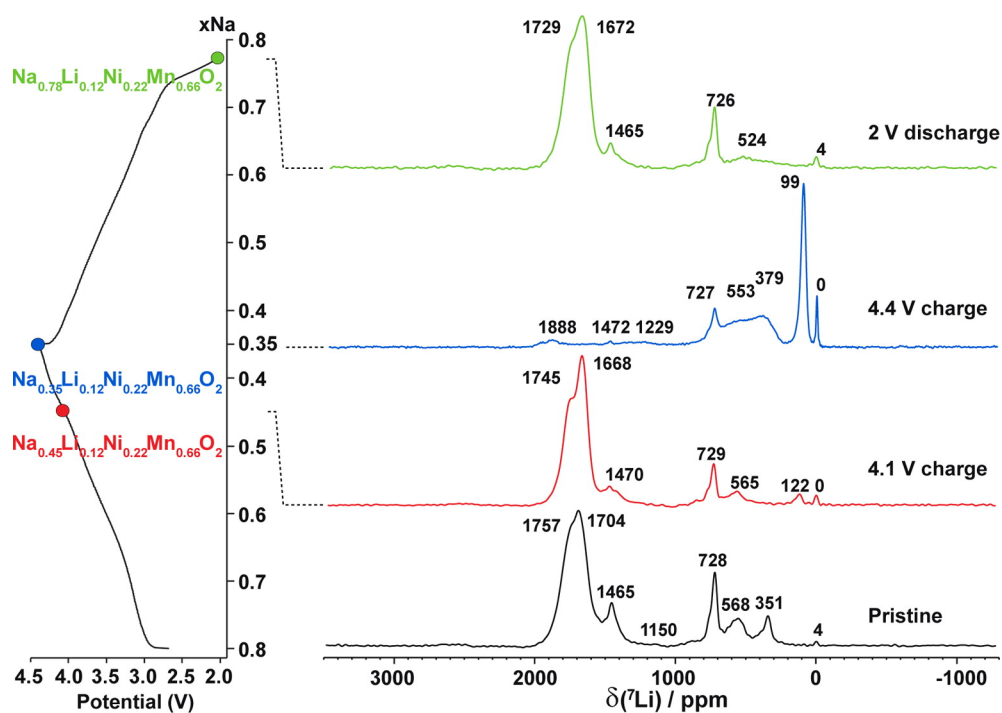


Figure 12.48: Isotropic slices extracted from the ^7Li MATPASS spectra of as-synthesized $\text{P2-Na}_{0.8}[\text{Li}_{0.12}\text{Ni}_{0.22}\text{Mn}_{0.66}]\text{O}_2$ and three different states of charge along the first electrochemical cycle. The spectra were acquired at a magnetic field strength of 4.70 T and at 60 kHz MAS. Reproduced with permission from [55]. Copyright (2014) American Chemical Society.

shows both the electrochemical cycle and the isotropic slices taken from MAT-PASS spectra recorded at four different stages of the electrochemical cycle.

12.5.7 Broadband NMR methods for spin-1/2 nuclei

Adiabatic pulse schemes

The methods for solid-state paramagnetic NMR have hitherto focussed on the pulse sequences that can be used to obtain the desired information about the system under study, such as the isotropic shifts, heteronuclear correlations etc. However the discussion has focussed only on the sequence and, with the exception of the section on frequency stepping, not on how may we achieve a broadband spectrum in the case where the width of the spectrum is substantially larger than the practicable RF field amplitude. When this is the case, conventional pulses are not suitable for excitation and alternative schemes are needed. The frequency-

pulse scheme	$\omega_1(t)$	$\phi_p(t)$	$\omega_{\text{rf}}(t)$
hyperbolic secant [434]	$\omega_1^{\text{max}} \text{sech}(\beta(2t/\tau_p - 1))$	$-\frac{\Delta\omega\tau_p}{4\beta} \left[\ln(\text{sech}(\beta(2t/\tau_p - 1))) \right]$	$\frac{\Delta\omega}{2} \tanh(\beta(2t/\tau_p - 1))$
tanh/tan [435]	$\omega_1^{\text{max}} \tanh\left(\frac{2\xi t}{\tau_p}\right), \quad 0 \leq t \leq \tau_p/2$ $\omega_1^{\text{max}} \tanh\left(2\xi\left(1 - \frac{t}{\tau_p}\right)\right), \quad \tau_p/2 < t \leq \tau_p$	$-\frac{\Delta\omega\tau_p}{4\kappa \tan \kappa} \ln(\cos(\kappa(1 - 2t/\tau_p)))$	$-\frac{1}{2}\Delta\omega \cot(\kappa) \tan(\kappa(1 - 2t/\tau_p))$
WURST [436]	$\omega_1^{\text{max}} \left(1 - \left \sin\left(\pi\left(\frac{t}{\tau_p} - \frac{1}{2}\right)\right)\right ^n\right)$	$\frac{\Delta\omega}{2} \left(\frac{t^2}{\tau_p} - t + \frac{\tau_p}{4}\right)$	$\frac{\Delta\omega}{2} \left(\frac{2t}{\tau_p} - 1\right)$

Table 12.2: Amplitude $\omega_1(t)$, phase $\phi_p(t)$, and frequency sweep $\omega_{\text{rf}}(t)$ profiles for a selection of swept-frequency adiabatic pulses. For each scheme the transmitter offset is swept through a range of frequencies $\Delta\omega$ during the pulse length of τ_p with a maximum RF field amplitude of ω_1^{max} . For the hyperbolic secant pulse β is a dimensionless parameter given by $\beta = \text{sech}^{-1}(f)$, where f is the fraction of ω_1^{max} at which the beginning and end of the amplitude profile are truncated. Typically this truncation factor is set to 1%, and so $\beta = \text{sech}^{-1}(0.01) = 5.2983$. For the tanh/tan pulse ξ and κ are dimensionless parameters which take values $\xi = 10$ and $\kappa = \tan^{-1}(20)$. For the WURST pulse n is a factor controlling the rate at which the amplitude profile is smoothed from zero to ω_1^{max} at the start and end of the pulse; typically $n = 20$.

stepping scheme that has already been discussed has proved useful for obtaining one-dimensional spectra, but is not a universal solution to the problem of broadband NMR as (1) there is a substantial increase in the experiment time required to acquire all the sub-spectra, and (2) this increase limits the practical application to one-dimensional spectroscopy. There is a requirement for pulse schemes that can acquire a broadband spectrum in a single experiment, and which can be easily incorporated into the more sophisticated multi-dimensional experimental pulse sequences that we have presented here.

One broadband pulse scheme that has been used widely in both solution NMR and MRI is the swept-frequency adiabatic pulse [433]. The important defining feature of all adiabatic pulses is that they are designed to have a transmitter offset which sweeps through the spectrum, rather than being fixed at a predefined frequency. The pulse is defined by a pulse length τ_p , a time-dependent RF field amplitude $\omega_1(t)$ and a time-dependent phase $\phi_p(t)$ that are both symmetric about the mid-point of the pulse. The RF field amplitude is designed so that it increases smoothly from zero at the start of the pulse to a maximum value of ω_1^{max} , and then decreases back to zero at the end of the pulse. The time-dependent phase is designed so that it induces a time-dependent sweep of the transmitter offset, $\omega_{\text{rf}}(t) = d\phi_p(t)/dt$, which sweeps through a range of frequencies $\Delta\omega$, and that is approximately linear at $t = \tau_p/2$. Many such pulse schemes have been designed, including the hyperbolic secant [434], tanh/tan [435], and WURST [436] pulses. The expressions for the RF field amplitude, phase, and induced transmitter offset are given in Table 12.2. These amplitude, phase, and frequency profiles are plotted in Figure 12.49. The profiles for the tanh/tan pulse are shown in Figure 12.49 (a)–(c), for the WURST pulse in Figure 12.49 (d)–(f), and the hyperbolic secant pulse in Figure 12.49 (g)–(i).

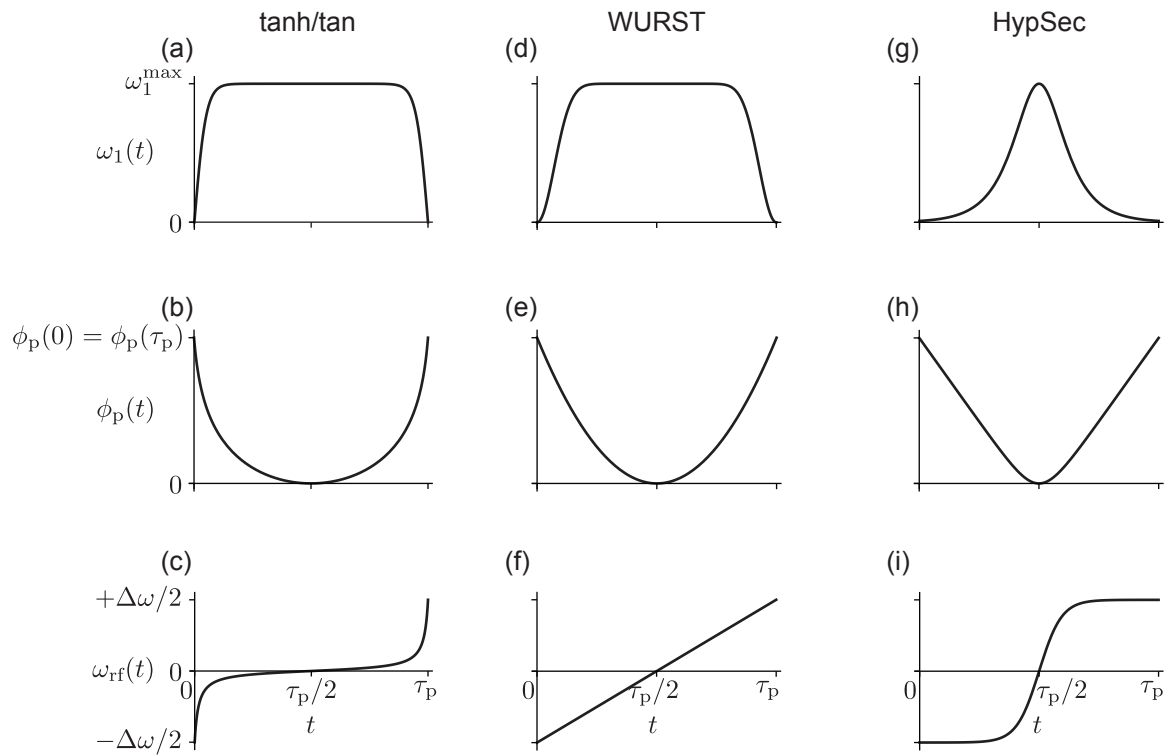


Figure 12.49: The amplitude, phase, and frequency-sweep profiles of three widely-used adiabatic pulse schemes. The amplitude, phase, and frequency-sweep profile for the tanh/tan pulse scheme are shown in (a), (b), and (c) [435]. This class of pulse is suitable for the broadband SHAP. The plots in (d), (e), and (f) show the amplitude, phase, and frequency-sweep profiles for WURST, which is used as a low-power S³AP [436]. Finally (g), (h), and (i) show the amplitude, phase, and frequency-sweep profiles for the hyperbolic secant, which can also be used as an S³AP [434].

The theory by which these pulses achieve inversion of a spin has been described in detail for isotropic systems in solution [433, 437], and for solids under MAS [34], and so we give only the salient points here. The rotating-frame Hamiltonian $\hat{H}(t)$ describing an adiabatic pulse applied to a spin with a time-dependent shift frequency $\Omega(t)$ due to, for example, an SA under MAS, is given by

$$\hat{H}(t) = \Omega(t)\hat{I}_z + \omega_1(t)\hat{R}_z(\phi_p(t))\hat{I}_x\hat{R}_z(\phi_p(t))^{-1}. \quad (12.26)$$

We can also define this Hamiltonian in the frequency-modulated frame, where the phase modulation of the pulse is converted into the modulation of the transmitter offset to give $\hat{H}_0(t)$:

$$\hat{H}_0(t) = \hat{R}_z(\phi_p(t))^{-1}\hat{H}(t)\hat{R}_z(\phi_p(t)) - \frac{d\phi_p(t)}{dt}\hat{I}_z \quad (12.27)$$

$$= (\Omega(t) - \omega_{\text{rf}}(t))\hat{I}_z + \omega_1(t)\hat{I}_x. \quad (12.28)$$

We can now define effective field of magnitude $\omega_{\text{eff}}^{(0)}(t)$ and angle of tilt from z $\theta^{(0)}(t)$, which are given by

$$\left[\omega_{\text{eff}}^{(0)}(t)\right]^2 = (\Omega(t) - \omega_{\text{rf}}(t))^2 + \omega_1(t)^2, \quad (12.29)$$

$$\tan\left[\theta^{(0)}(t)\right] = \frac{\omega_1(t)}{\Omega(t) - \omega_{\text{rf}}(t)}, \quad (12.30)$$

and rewrite $\hat{H}_0(t)$ as

$$\hat{H}_0(t) = \omega_{\text{eff}}^{(0)}(t)\hat{R}_y\left(\theta^{(0)}(t)\right)\hat{I}_z\hat{R}_y\left(\theta^{(0)}(t)\right)^{-1}. \quad (12.31)$$

For the schemes shown in Table 12.2 and Figure 12.49 we see that the effective field is aligned along $+z$ at the beginning of the pulse. During the pulse, the RF field amplitude increases to its maximum value, the transmitter offset increases from a negative value to a positive value, and the effective field is rotated about the y -axis from $+z$ to $-z$, and is therefore inverted.

If we are describing population inversion of a nuclear spin with initial density operator \hat{I}_z , the magnetization at the start of the pulse is aligned parallel to the effective field, and so is spin-locked to it. If the effective field inverts sufficiently slowly, the magnetization remains spin-locked throughout the pulse, and so is also inverted. If on the other hand we are describing refocusing of coherences, as occurs during a spin echo, the initial magnetization is orthogonal to the effective field at the start of the pulse. Here it is the plane

in which the magnetization evolves during the pulse that is tilted as the effective field inverts, and which leads to refocussing.

The question is, what do we mean by “if the effective field inverts sufficiently slowly”? This question can be answered by transforming the frame of reference of the adiabatic pulse from the frequency-modulated frame to the first adiabatic frame as follows, to give the Hamiltonian $\hat{H}_1(t)$ [433]:

$$\hat{H}_1(t) = \hat{R}_y(\theta^{(0)}(t))^{-1} \hat{H}_0(t) \hat{R}_y(\theta^{(0)}(t)) - \frac{d\theta^{(0)}(t)}{dt} \hat{I}_y \quad (12.32)$$

$$= \omega_{\text{eff}}^{(0)}(t) \hat{I}_z - \dot{\theta}^{(0)}(t) \hat{I}_y, \quad (12.33)$$

in which the effective field is now along +z, and we have introduced the transverse field $\dot{\theta}^{(0)}(t)$ along -y to account for the motion of the first adiabatic frame relative to the frequency-modulated frame. To achieve perfect inversion or refocussing we require the total field in the first adiabatic frame to remain along z throughout the pulse, which is achieved if $|\omega_{\text{eff}}^{(0)}(t)| \gg |\dot{\theta}^{(0)}(t)|$ throughout the pulse. This is quantified via the quality factor $Q^{(1)}$, which is defined by

$$\frac{1}{Q^{(1)}} = \max \left| \frac{\dot{\theta}^{(0)}(t)}{\omega_{\text{eff}}^{(0)}(t)} \right| \quad (12.34)$$

$$= \max \left| \frac{\dot{\omega}_1(t) [\Omega(t) - \omega_{\text{rf}}(t)] - \omega_1(t) [\dot{\Omega}(t) - \dot{\omega}_{\text{rf}}(t)]}{\omega_{\text{eff}}^{(0)}(t)^3} \right|. \quad (12.35)$$

For good inversion or refocussing behaviour we require $Q^{(1)} \gg 1$; this is the so-called adiabatic condition.

In an isotropic solution, where the shift offset is time-independent and equal to zero, and for typical values of the sweep width $\Delta\omega$ and RF field amplitude, the adiabatic condition is weakest at $t = \tau_p/2$ where the transmitter is resonant with the spin. Here $\omega_1(\tau_p/2) = \omega_1^{\text{max}}$, $\omega_{\text{rf}}(\tau_p/2) = 0$, $\omega_{\text{eff}}^{(0)}(\tau_p/2) = \omega_1^{\text{max}}$, and the adiabatic condition simplifies to $[\omega_1^{\text{max}}]^2 \gg |\omega_{\text{rf}}(\tau_p/2)|$. Therefore it can be seen that if a particular pulse is not adiabatic, it can be made so simply by raising the RF field amplitude.

For solid samples under MAS the application of adiabatic pulses is generally very difficult since the modulation of the SA leads to rapid oscillations in both the size and tilt angle of the effective field, and hence a weakening of the adiabatic condition. This is particularly problematic for paramagnetic species where the combination of large SAs and fast spinning results in quality factors that are typically much lower than unity

for typical pulse schemes. Therefore special measures need to be taken in order for adiabatic pulses to work properly [34]. Two such methods have been developed, which are referred to as short high-power adiabatic pulses (SHAPs) [28], and single-sideband-selective adiabatic pulses (S³APs) [31–33].

Short, high-power adiabatic pulses (SHAPs)

The first, and currently most successful, adiabatic pulse scheme for paramagnetic systems is the short high-power adiabatic pulse (SHAP) [28]. These pulses are designed with a large sweep width to give a large bandwidth, and a short duration to minimize signal losses due to the PRE. In order to compensate for the weakening of adiabaticity due to the modulation of the SA during MAS, we also use an RF field amplitude that is significantly larger than would be needed for isotropic spin systems. The SHAP represents a “brute force” solution to obtaining an adiabatic response for a system with a large SA under MAS. The class of pulse that is used to satisfy these requirements is the tanh/tan, which is used in MRI to obtain a large bandwidth [435]. The expressions for the amplitude, phase, and frequency-sweep profiles are given in Table 12.2. When designing a pulse suitable for paramagnetic MAS NMR the following optimization protocol should be followed:

1. The dimensionless parameters ξ and κ are set to $\xi = 10$ and $\kappa = \tan^{-1}(20)$, and are not varied.
2. The sweep width $\Delta\omega$ is set so that it is greater than the expected width of the spectrum. Typically we choose 5 MHz as an initial value, and may increase this if necessary.
3. The pulse length τ_p is chosen to be as short as possible, whilst still maintaining the adiabatic condition; typical values are 50–100 μs . For inversion and the spin-echo experiment it is not necessary for the pulse length to be an integer number of rotor periods. However this restriction does apply to more complex experiments such as MAT.
4. Once the pulse has been created the RF field amplitude is optimized. This is done either by optimizing the spectral intensity in a spin-echo experiment, or the inversion performance, by increasing the RF power.

In addition to broadband inversion, SHAPs can also be incorporated into a spin-echo experiment using the pulse sequence in Figure 12.50 (a). This sequence, referred to as the double-SHAP-spin-echo experiment, comprises two echoes the separation between the starting points of which is an integer number of rotor

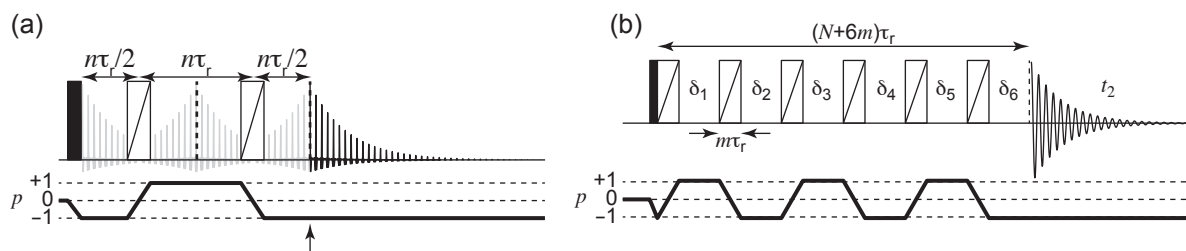


Figure 12.50: Broadband pulse sequences employing adiabatic refocussing pulses, and coherence-transfer pathways, for the double adiabatic spin-echo and aMAT experiments. The double adiabatic spin-echo sequence is shown in (a) with the coherence-transfer pathway [28]. The arrow indicates the time point at which the isotropic shift is refocussed. The SHAP need not be an integer multiple of the rotor period in length. The aMAT sequence is shown in (b) [30]. Here the length of the SHAP is an integer multiple m of the rotor period. Filled rectangles indicate pulses with a nominal flip angle of 90° , and unfilled rectangles with a diagonal stroke indicate SHAPs. All pulses have phase x .

periods. The reason why two echoes are required is that the first SHAP imparts a frequency-dependent phase error to the coherences which leads to a dephasing of the signal in the powder. However the second SHAP refocusses this phase error, leading to a complete refocussing of both the shift and SA at the end of the second echo. This refocussing property of the double echo is referred to as the excitation-sculpting principle [34, 438–440].

The inversion and refocussing performance are illustrated experimentally on the cathode material $\text{LiFe}_{0.5}\text{Mn}_{0.5}\text{PO}_4$ at 11.74 T and 60 kHz MAS in Figure 12.51 [34]. A comparison between the ^7Li conventional spin-echo and double-SHAP-echo experiments is given in Figure 12.51 (a) and (c). The two spectra appear to be identical, which is due to the small range of isotropic shifts of 90 ppm, and the relatively long relaxation times of approximately 1 ms [30]. However the ^{31}P double-SHAP-echo in Figure 12.51 (d) shows a significant improvement in the broadband excitation bandwidth compared to the conventional spin-echo spectrum in Figure 12.51 (b). This is due to the 32 distinct local ^{31}P environments having an isotropic shift dispersion of 4000 ppm (800 kHz at 11.74 T) which is too large for the practicable RF field amplitude of 417 kHz [30]. This improvement in bandwidth comes at the expense of reduced sensitivity due to the larger PRE losses during the two SHAPs which have a combined length of 100 μs , which is comparable to the range of ^{31}P T_2' times of 130–330 μs .

The inversion performance is also given for both ^7Li and ^{31}P with varying RF field amplitude in Figure 12.51 (e) and (f). For ^7Li we obtain complete inversion of the spectrum for a range of MAS frequencies

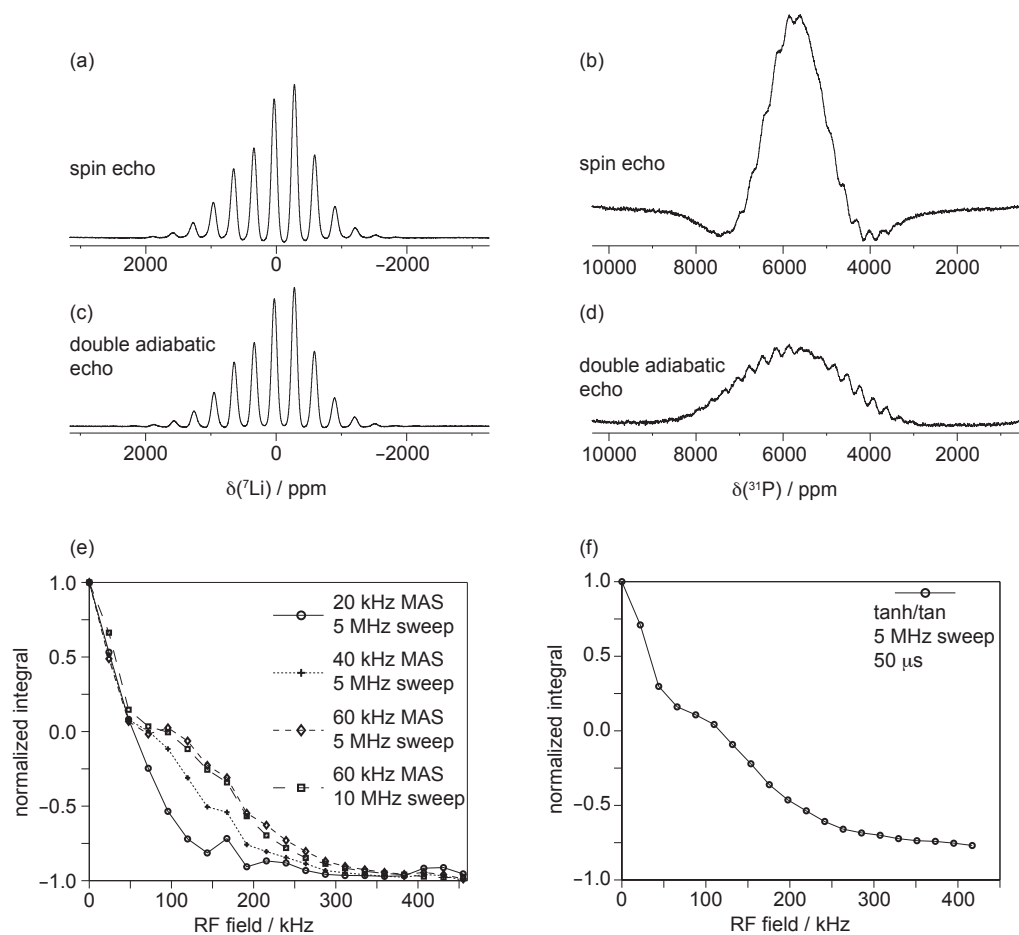


Figure 12.51: Experimental examples of the improved inversion and refocussing properties of SHAPs when applied to paramagnetic materials compared to conventional pulses. In (a) and (b) are shown the conventional ^7Li and ^{31}P rotor-synchronized spin-echo spectra of the cathode material $\text{LiFe}_{0.5}\text{Mn}_{0.5}\text{PO}_4$ at 11.74 T and 60 kHz MAS. The RF field amplitudes are 455 kHz for ^7Li and 417 kHz for ^{31}P . The ^7Li and ^{31}P double-SHAP-echo spectra are shown in (c) and (d) at 60 kHz MAS, with the latter showing increased bandwidth. The SHAP is a \tanh/\tan pulse sweeping through 5 MHz in 50 μs at RF field amplitudes of 455 kHz for ^7Li and 417 kHz for ^{31}P . Panel (e) shows the integrated intensity of the ^7Li spectrum following SHAP inversion at different RF field amplitudes and MAS frequencies. The integrated intensity of the ^{31}P spectrum following SHAP inversion at different RF field amplitudes is shown in (f). Reproduced from [34], with permission from Elsevier.

and sweep widths with RF field amplitudes above 350 kHz. We note that higher RF field amplitudes are required at higher MAS rates, as the faster modulation of the SA leads to a greater weakening of the adiabatic condition. For ^{31}P we obtain 75% inversion at an RF field amplitude of 400 kHz. In this case higher RF fields may only give a moderate increase in performance as there are intensity losses due to the short T_1 and T_2' times.

One advantage of SHAPs is that they are easily incorporated into more sophisticated experimental pulse schemes to give a more broadband spectrum. Figure 12.52 illustrates the use of a tanh/tan SHAP in the CPMG experiment at 66 kHz MAS. The system is the lanthanide-binding organometallic complex $\text{Tb}[\text{C}_5\text{H}_3\text{N}(\text{COO})_2\text{Na}]_3$, which gives a broad ^1H spectrum with a large SA, and has substantial inhomogeneous broadening of the sidebands due to the ABMS [29]. The ^1H spectra acquired using the double-SHAP-echo experiment at 20, 33, and 66 kHz MAS are shown in Figure 12.52 (a)–(c). Here we again see the benefit of applying fast MAS to a system with a very large SA. We see that the sidebands are broadened considerably, with baseline resolution only being obtained at 66 kHz MAS. Incorporating the SHAPs into the CPMG sequence gives the SHAP-CPMG experiment in Figure 12.52 (d), which was used to acquire the FID in Figure 12.52 (e). This FID exhibits a relatively slow decay corresponding to a T_2' of 1.68 ms. This indicates that the losses due to T_2' to be expected in longer pulse sequences are not as severe as from the large inhomogeneous line broadening in the conventional spectra would suggest. The SHAP-CPMG spectra are shown in Figure 12.52 (f) and (g). They have a higher sensitivity than the double-SHAP-echo spectra, and a homogeneous linewidth of 190 kHz.

A second striking application of SHAPs to paramagnetic NMR is in the two-dimensional MAT experiment used to separate overlapping spinning-sideband manifolds. The resulting adiabatic magic-angle turning (aMAT) sequence is shown in Figure 12.50 (b). Here a sixth pulse $q = 0$ is inserted immediately after the first excitation pulse in order to complete the refocussing of the phase errors from the other SHAPS, and remains fixed in this position for all increments. The other five SHAPs are inserted with timings that are the same as those in the conventional MAT sequence. Figure 12.53 shows the experimental ^{31}P aMAT spectrum acquired on $\text{LiFe}_{0.5}\text{Mn}_{0.5}\text{PO}_4$ at 11.74 T and 60 kHz MAS [30]. The 32 local ^{31}P environments each have a broad spinning-sideband manifold with isotropic shifts covering a range of 4000 ppm. These resonances overlap in the one-dimensional spectrum, as illustrated in Figure 12.51 (d), but have been partially separated into eight distinct groups of resonances in the aMAT spectrum, thus allowing the assignment and interpretation [30].

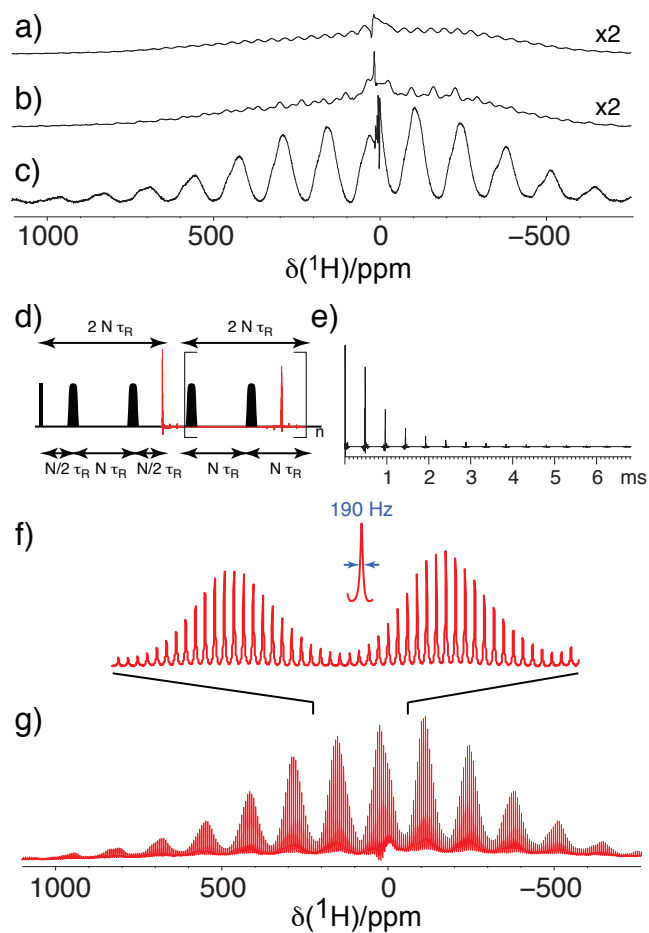


Figure 12.52: ^1H MAS spectra of the organometallic compound $\text{Tb}[\text{C}_5\text{H}_3\text{N}(\text{COO})_2\text{Na}]_3$ acquired using double-SHAP-spin-echo and SHAP-CPMG pulse sequences [29]. The double-SHAP-spin-echo spectra acquired at MAS frequencies of 20, 33, and 66 kHz are shown in (a), (b), and (c). Panel (d) shows the SHAP-CPMG pulse sequence that was used to acquire the FID at 66 kHz MAS in (e). The corresponding spectra are shown in (f) and (g). Reproduced with permission from [29]. Copyright (2007) American Chemical Society.

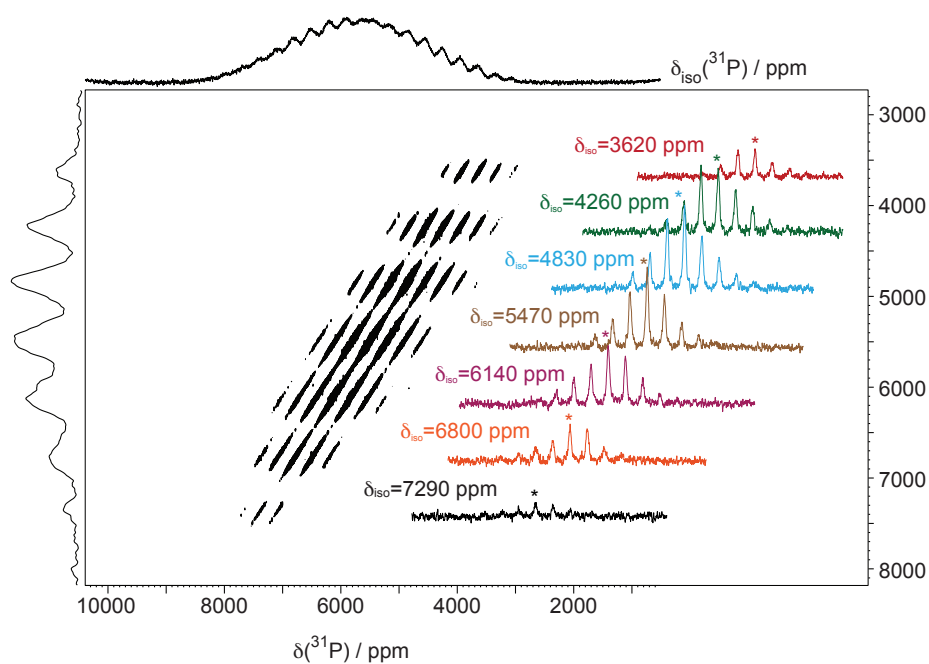


Figure 12.53: The two-dimensional ^{31}P aMAT spectrum of the cathode material $\text{LiFe}_{0.5}\text{Mn}_{0.5}\text{PO}_4$ acquired at 11.74 T and 60 kHz MAS. The SHAP is a tanh/tan pulse sweeping through 5 MHz in $50 \mu\text{s}$ at an RF field amplitude of 417 kHz. The length of the MAT recoupling period is 7 rotor periods, excluding the pulse lengths.

The SHAP is both effective and versatile, and has been successfully applied to a range of paramagnetic systems [10, 29, 30, 55, 56, 59, 71, 441–444]. However the main weakness in the SHAP scheme is that the RF field amplitude required increases with faster MAS rates. Therefore it may not be possible to obtain complete inversion at very fast MAS, such as 100 kHz, especially for nuclei of low gyromagnetic ratio where the RF field amplitude is limited. This issue is addressed by the second adiabatic pulse scheme

Single-sideband-selective adiabatic pulses (S³APs)

The second adiabatic pulse scheme is the single-sideband-selective adiabatic pulse S³AP, which employs a lower-power pulse in which the transmitter frequency is swept through a single sideband [31]. The basic method had been previously used to invert the broad spinning-sideband manifolds of ST resonances of quadrupolar nuclei in diamagnetic systems, where it was shown that both the hyperbolic secant and WURST pulse schemes are suitable for single-sideband irradiation [445–448]. The theory of broadband inversion by single-sideband adiabatic was then developed by employing a formalism from Caravatti et al. [449], and combining this with a Floquet-theory description of the resulting effective Hamiltonian [315–318] to provide a complete description of the S³AP [31, 32].

The basic idea behind a S³AP is that the bandwidth of the pulse is limited so that it affects only the irradiated sideband. The resonance of the SA is modulated by the MAS, and so shifts in and out of the effective pulse bandwidth during the course of the pulse, with the result that the spin is only resonant for a fraction of the total irradiation time. An alternative view is that the pulse is resonant for the whole of the irradiation time, and it is the RF field amplitude that is scaled down. If the pulse irradiates the m th-order sideband the effective Hamiltonian $\hat{H}_{\text{eff}}^{(1)}(t)$ for a single crystallite is [31]:

$$\hat{H}_{\text{eff}}^{(1)}(t) = \omega_1(t)A_c^{(m)}\hat{R}_z(\phi_p - \phi_c^{(m)}(\gamma_{\text{PR}}))\hat{I}_x\hat{R}_z(\phi_p - \phi_c^{(m)}(\gamma_{\text{PR}}))^{-1}, \quad (12.36)$$

which corresponds to a pulse with an effective RF field amplitude $\omega_1(t)A_c^{(m)}$ that is scaled down by the sideband intensity, and an effective phase $\phi_p - \phi_c^{(m)}(\gamma_{\text{PR}})$ that is offset by minus the sideband phase. This Hamiltonian describes the part of the spin dynamics that gives rise to adiabatic inversion and refocussing, provided the RF field amplitude is sufficiently high to offset the weakening of the condition by the scaling down of the effective RF field amplitude by $A_c^{(m)}$. There is also a contribution to the spin dynamics from

the rapidly-oscillating SA which is not included in this effective Hamiltonian. However this oscillation is averaged out over the course of the a rotor period, and has no overall effect [31].

The advantage of the S³AP over the SHAP is that the typical RF field amplitudes are equal to or lower than the spinning frequency, and so broadband inversion can be achieved using much lower power. This is shown by the simulations in Figure 12.54 [34], where the inversion performance of a spin subject to an SA of 200 kHz with a WURST-20 S³AP of duration 1 ms is compared at 20, 40, 60, 80, and 100 kHz MAS. The extent of inversion is plotted against both the RF field amplitude and carrier frequency in Figure 12.54 (a). We see that the performance of the S³AP increases with MAS frequency, as a greater proportion of the sideband intensity is then concentrated in the centreband $m = 0$, and the weakening of the adiabatic condition is reduced. Additionally the one-dimensional plots of inversion as a function of carrier frequency in Figure 12.54 (b) indicate that a larger spinning frequency allows the use of a larger sweep width without irradiating the neighbouring sidebands, thus increasing the bandwidth of isotropic shifts over which we invert. Finally the use of faster MAS also increases the range of RF field amplitudes (up to the MAS frequency) over which we obtain complete inversion, as shown by the one-dimensional RF field profiles in Figure 12.54 (c). The disadvantage of the S³AP is that the pulses are longer by at least an order of magnitude, and so significant signal losses due to the short relaxation times are expected.

The general recommendations for implementing an S³AP are:

1. Select either the hyperbolic-secant or WURST waveform. For the hyperbolic secant set the amplitude truncation factor to 1%, and therefore $\beta = \text{sech}^{-1}(0.01) = 5.2983$. For the WURST set $n = 20$. For both waveforms set the sweep width to the MAS frequency.
2. Set the pulse length between 0.5 and 5 ms. Longer pulse lengths result in greater relaxation losses during the pulse, but an adiabatic condition that is more easily satisfied.
3. Optimize the peak RF field amplitude from 0 kHz to the spinning frequency.

Figure 12.55 shows two experimental examples of S³AP inversion at slow and fast MAS. The spectra in Figure 12.55 (a)–(c) show the ⁷⁷Se NMR spectra of the diamagnetic compound **1** at 11 kHz MAS. The conventional ¹H–⁷⁷Se CP spectrum in (a) was inverted both with a high-power conventional 180° pulse (b) and with a low-power (10 kHz), 5 ms WURST-20 S³AP tuned to the centreband (c). Here the S³AP gives complete inversion, which matches the theoretical prediction from the simulated inversion profiles as a

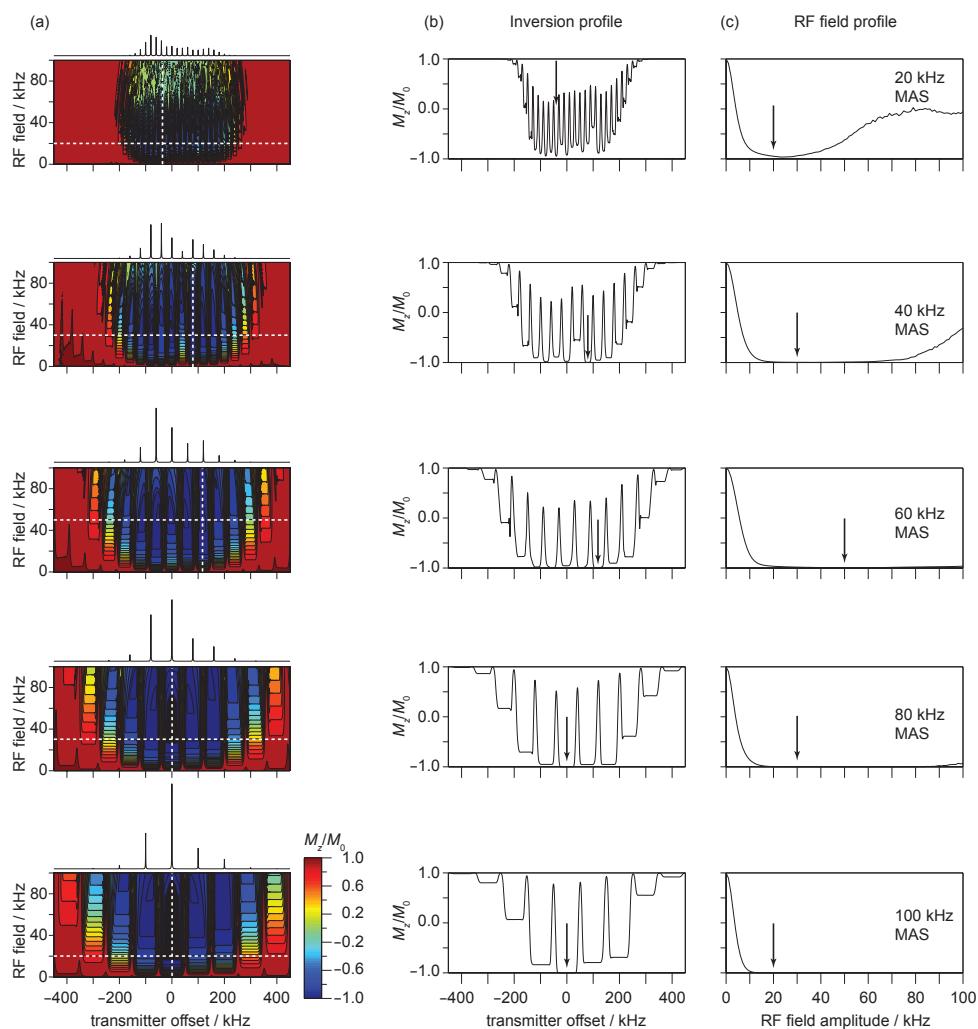


Figure 12.54: Simulated inversion performance of S^3 APs under MAS. In (a) are shown contour plots of the inversion of the powder sample as a function of RF field amplitude and carrier frequency at MAS frequencies of 20, 40, 60, 80, and 100 kHz. In each case, the S^3 AP is a WURST-20 pulse of length 1 ms with a sweep width equal to the spinning frequency. The best inversion occurs when the transmitter is resonant with one of the sidebands and the RF field amplitude is sufficiently high to satisfy the adiabatic condition for all crystallites. In (b) are shown horizontal cross sections through the contour plots, taken at the positions shown by the horizontal white dashed lines. The plots show the inversion as a function of transmitter offset. The RF amplitude profiles in (c) are cross sections taken at the positions of the vertical white dashed lines in the contour plots. The arrows in the plots in (b) and (c) indicate the transmitter offset and lowest RF field amplitude at which the best inversion performance is obtained for each MAS frequency. Each pair of optimum values is also indicated by the intersection of the two white dashed lines in each contour plot in (a). The optimum values of (sideband order, RF field amplitude) for the five MAS frequencies are: $(-2, 20 \text{ kHz})$ at 20 kHz MAS, $(+2, 30 \text{ kHz})$ at 40 kHz MAS, $(+2, 50 \text{ kHz})$ at 60 kHz MAS, $(0, 30 \text{ kHz})$ at 80 kHz MAS, and $(0, 20 \text{ kHz})$ at 100 kHz MAS. The shift tensor parameters are: isotropic shift 0 kHz, SA +200 kHz, and asymmetry parameter 0.3. Reproduced from [34], with permission from Elsevier.

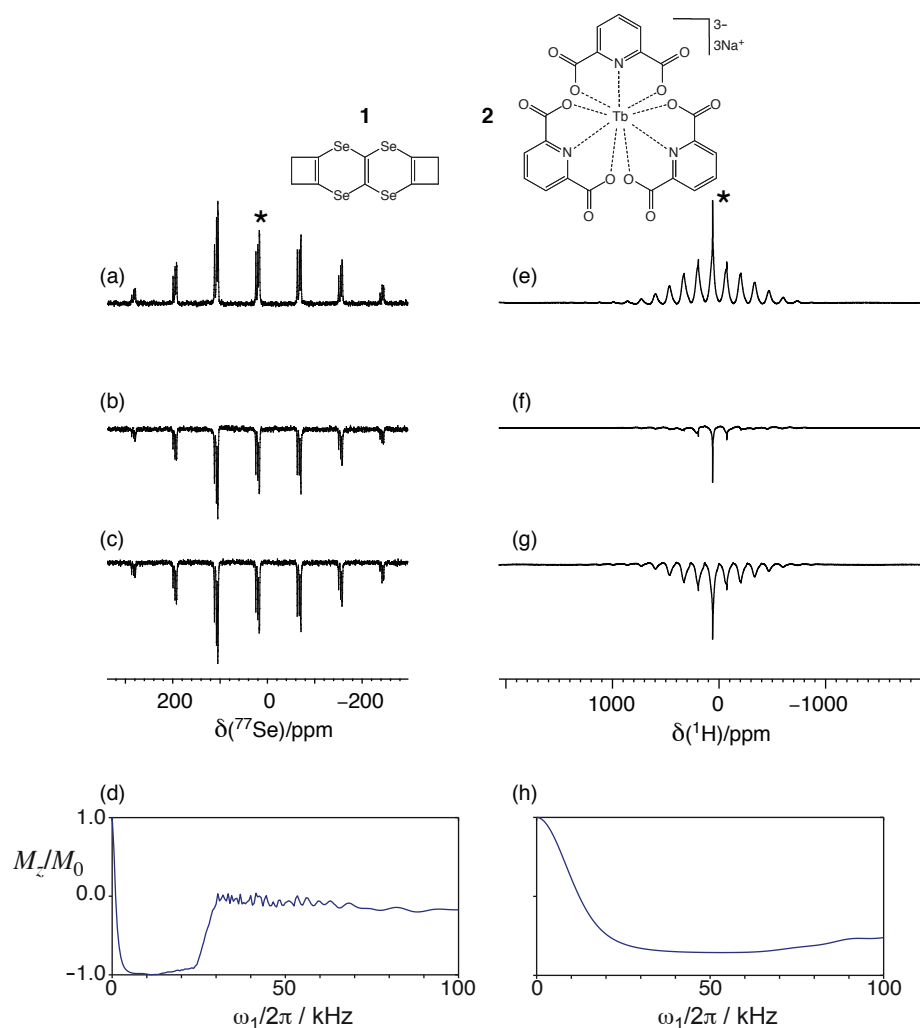


Figure 12.55: The ^{77}Se and ^1H NMR spectra of compounds **1** and **2** at 11.74 T, and 11 and 60 kHz MAS respectively, and the inversion performance with an S^3AP [31]. The conventional spectra are shown in (a) and (e). The spectra obtained following inversion with a 69 kHz and 200 kHz hard pulse, respectively, are shown in (b) and (f). Spectra obtained following inversion by irradiation of the centreband with an S^3AP are shown in (c) and (g). The inversion of the spectrum of **1** was achieved with a WURST-20 S^3AP with a sweep width of 10 kHz, duration of 5 ms, and peak RF field amplitude of 10 kHz. The inversion of **2** was achieved with a hyperbolic secant S^3AP with a sweep width of 70 kHz, duration of 495 μs , and peak RF field amplitude of 60 kHz. Simulations showing the expected degree of inversion vs RF power are shown in (d) and (h). The ^{77}Se spectra of **1** were obtained with ^1H - ^{77}Se CP followed by a z -filter during which the inversion pulse was applied. The ^1H spectra of **2** were obtained with a double-SHAP-echo sequence, using a \tanh/\tan SHAP of sweep width 5 MHz, length 60 μs , and peak RF field amplitude 60 kHz. The centrebands are marked with an asterisk. Reproduced from [31], with the permission of AIP Publishing.

function of RF field amplitude in Figure 12.55 (d). The second example is the paramagnetic compound **2** at 60 kHz MAS which presents a more exacting test. The one-dimensional ^1H double-SHAP-echo spectrum is shown in Figure 12.55 (e). Inversion with a conventional pulse at the high RF field amplitude yields a poor performance as shown in Figure 12.55 (f). A hyperbolic secant S^3AP applied to the centreband of length 495 μs and RF field amplitude 60 kHz performs considerably better, delivering 75% inversion, as shown in Figure 12.55 (g). The simulated inversion performance as a function of RF field amplitude is shown in Figure 12.55 (h), which includes the effects of T_1 relaxation and T_2' dephasing. The imperfect inversion performance is attributable mainly to relaxation losses. This method is expected to be more widely used with the advent of faster MAS, where shorter S^3AP s with larger isotropic bandwidths can be used.

12.5.8 Separation of shift-anisotropy and quadrupolar interactions

In this section we present experimental schemes that are designed to separate the contributions to the spectral lineshape from the paramagnetic SA and quadrupolar interactions. The motivation for developing experiments of this type is that quadrupolar nuclei in paramagnetic systems have complicated spectra, as seen in Figure 11.5 for $I = 1$ and Figure 11.8 for $I = 3/2$, from which the information about the two interactions cannot easily be extracted. Nevertheless the tensor parameters are useful indicators of the structural and electronic properties. We present the current state-of-the-art schemes that are applicable to integer and half-integer spins. We recall that there is a fundamental difference between the two types of quadrupolar nucleus, with half-integer spins having a CT but not the integer spins. Therefore the two types of spin can have different symmetry pathways, and so needs different, specifically-tailored, pulse sequences. We therefore treat integer and half-integer spins differently. For the former we review two experimental methods for static conditions [199, 392], and for the latter we present a technique for a powder spinning at 70.12° to the field [393]. Before exploring these methods in detail we first introduce the idea of a two-dimensional echo, which is a concept used to understand the time points in a pulse sequence where a particular interaction is refocussed, and then discuss shearing and scaling transformations, which are processing operations used to convert a two-dimensional FID into a spectrum where different interactions are separated along different principal frequency axes.

Two-dimensional echoes

The experimental schemes presented here are based on two-dimensional pulse sequences in which the evolutions due to the shift/SA and quadrupolar interactions are refocussed at different points in the sequence. Therefore the two interactions give rise to resonance broadening along different dimensions in the two-dimensional spectrum, thus leading to their separation. We begin by illustrating the concept of a general Ξ -echo in two-dimensional spectroscopy, where Ξ is the spin-order parameter that defines the frequency of evolution of the interaction in question, and how the corresponding tensor parameters can be extracted. The discussion here is limited to frequency components of interactions that are time-independent, such as isotropic interactions, all interactions in static solids, or the residual components of anisotropic interactions that remain time-independent under MAS such as the residual rank-four second-order quadrupolar interaction which broadens the resonance.

The two-dimensional experiments presented here are designed so that different coherences $|M_1\rangle\langle M_2|$ and $|M_3\rangle\langle M_4|$ evolve during t_1 and t_2 . Under a particular interaction Λ , the two coherences evolve at different frequencies $\Omega_{10,M_1M_2}^{(\Lambda)}$ and $\Omega_{10,M_3M_4}^{(\Lambda)}$ in t_1 and t_2 , and so the total phase acquired in the FID $\Phi_{10}^{(\Lambda)}(t_1, t_2)$ is given by

$$\Phi_{10}^{(\Lambda)}(t_1, t_2) = \Omega_{10,M_1M_2}^{(\Lambda)} t_1 + \Omega_{10,M_3M_4}^{(\Lambda)} t_2. \quad (12.37)$$

We are already familiar with the concept of refocussing in a spin-echo experiment, where the total phase accrued due to evolution of the chemical shift is equal to zero at the end of an echo. We can generalize this concept and define an echo in a two-dimensional FID to be the time points at which $\Phi_{10}^{(\Lambda)}(t_1, t_2) = 0$ [319]. The two evolution frequencies $\Omega_{10,M_1M_2}^{(\Lambda)}$ and $\Omega_{10,M_3M_4}^{(\Lambda)}$ differ only in their spin-order parameters, which we here refer to as a_1 and a_2 . Therefore the refocussing condition can be expressed succinctly as [319]

$$a_1 t_1 + a_2 t_2 = 0. \quad (12.38)$$

Therefore the refocussing of the interaction Λ occurs at all time points that lie on a straight line in (t_1, t_2) that is inclined at a gradient of $-a_1/a_2$ from the t_1 -axis and passes through the origin, as shown in Figure 12.56 (a). This line is referred as an echo ridge. In principle we can perform a skew projection of the two-dimensional FID onto this line to obtain a one-dimensional FID in which there is no evolution of this interaction Λ , and

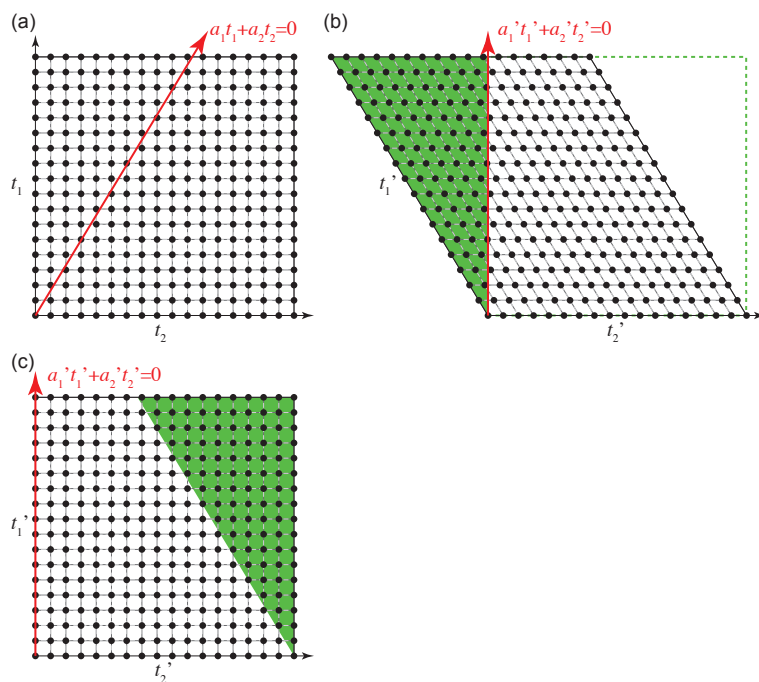


Figure 12.56: Illustration of echo formation in, and shear of, a two-dimensional FID. A two-dimensional FID $s(t_1, t_2)$ is shown in (a), sampled on a Cartesian grid $(t_{1,2})$. The red arrow indicates the formation of an echo of a particular interaction with spin-order a_1 and a_2 in t_1 and t_2 . After an active shear, where the time domain data rather than the coordinate axes are transformed, parallel to t_2 with shear ratio $\kappa_2 = a_1/a_2$ we obtain the FID $s(t_1', t_2')$ in (b), in which the Cartesian grid of sample points is distorted into a parallelogram. The green area has been sheared out of the original sampling grid. In (c) the shear has been calculated from the inverse Fourier transform of $\exp(+i\omega_2 \kappa_2 t_1) S(t_1, \omega_2)$. Here the Cartesian grid is preserved, and the green area is folded back into the original acquisition window.

which can be Fourier transformed to give a one-dimensional spectrum in which the spectral features due to this interaction are not present. Hence we have separated the interaction Λ from any others that may be present, therefore leading to a simpler spectrum. However skew projections are difficult to perform in practice, and we prefer instead to shear the FID so that the echo ridge is transformed to lie along either the t_1 - or t_2 -axis [319].

Shearing and scaling transformations

A shear transformation is characterized by both a “direction” and “size”. The former is defined by the axis along which the transformation takes place, and the latter by the shear ratio κ . We have two obvious choices of axis, namely the two principal axes t_1 and t_2 . If we perform an active shear parallel to t_2 , as shown in Figure 12.56 (b), we transform the rectangular sampling grid of the FID into a parallelogram. The time points of the sheared spectrum are measured relative to a new coordinate system (t'_1, t'_2) which is calculated from the old coordinate system (t_1, t_2) by

$$\mathbf{t}' = \mathcal{T}_{\kappa_2} \mathbf{t}. \quad (12.39)$$

The matrix \mathcal{T}_{κ_2} defines the mapping due to the shear, and is given by

$$\mathcal{T}_{\kappa_2} = \begin{pmatrix} 1 & 0 \\ \kappa_2 & 1 \end{pmatrix}, \quad (12.40)$$

where κ_2 is the shear ratio for the shear parallel to t_2 . The explicit expressions relating (t'_1, t'_2) to (t_1, t_2) are

$$\begin{pmatrix} t'_1 \\ t'_2 \end{pmatrix} = \begin{pmatrix} 1 & 0 \\ \kappa_2 & 1 \end{pmatrix} \begin{pmatrix} t_1 \\ t_2 \end{pmatrix} = \begin{pmatrix} t_1 \\ t_2 + \kappa_2 t_1 \end{pmatrix}. \quad (12.41)$$

The result of the shear is to shift the orientation of the echo ridge so that it lies closer to the new t'_1 axis. If we set the shear ratio to

$$\kappa_2 = \frac{a_1}{a_2}, \quad (12.42)$$

then we can see that after the shear the echo ridge is parallel to t'_1 , as shown in Figure 12.56 (b). The extraction of the slice of the two-dimensional FID along this axis yields a one-dimensional FID in which there is no

evolution of the interaction at any time point, and the resulting spectrum contains no spectral features due to this interaction. However before extracting the slice we should note that the apparent evolution frequencies of the other interactions along t'_1 are not necessarily equal to the nominal frequencies we would expect from a conventional one-dimensional spectrum. In general these remaining frequencies are scaled up or down by some factor. Therefore in order to recover the correct frequencies we need to scale the t'_1 times by some scaling factor ζ'_1 . The coordinate transformation matrix is $\mathcal{T}_{\zeta'_1}$, and is given by

$$\mathcal{T}_{\zeta'_1} = \begin{pmatrix} \zeta'_1 & 0 \\ 0 & 1 \end{pmatrix}. \quad (12.43)$$

Hence the total transformation comprises a shear parallel to t_2 with a ratio κ_2 , followed by a scaling of the new t'_1 axis by a factor ζ'_1 . The coordinate system resulting from both transformations is then related to the old system by

$$\mathbf{t}' = \mathcal{T}_{\zeta'_1} \mathcal{T}_{\kappa_2} \mathbf{t} \quad (12.44)$$

$$= \begin{pmatrix} \zeta'_1 & 0 \\ \kappa_2 & 1 \end{pmatrix} \begin{pmatrix} t_1 \\ t_2 \end{pmatrix} = \begin{pmatrix} \zeta'_1 t_1 \\ t_2 + \kappa_2 t_1 \end{pmatrix}. \quad (12.45)$$

The illustration of the shear in Figure 12.56 (b) is as a simple translation of the rows parallel to t_2 by a distance that is defined by the shear ratio. Whilst this is conceptually the simplest way to implement a shear, it is also inconvenient in practice since the Cartesian grid of sampling points in Figure 12.56 (a) is distorted into a parallelogram, and part of the FID (in green) is transformed outside the original sampling window. A more convenient method for performing the shear is to first compute the Fourier transform of the FID with respect to t_2 to give the mixed time–frequency domain function $S(t_1, \omega_2)$:

$$S(t_1, \omega_2) = \int_0^\infty s(t_1, t_2) \exp(-i\omega_2 t_2) dt_2. \quad (12.46)$$

We then multiply each point in this domain by a complex phase factor $\exp(+i\omega_2 \kappa_2 t_1)$. The result can be shown to be equal to the Fourier transform of the sheared FID $s(t_1, t_2 + \kappa_2 t_1)$ [189]:

$$s(t_1, t_2 + \kappa_2 t_1) \leftrightarrow \exp(+i\omega_2 \kappa_2 t_1) S(t_1, \omega_2). \quad (12.47)$$

Hence the inverse Fourier transform of $\exp(+i\omega_2\kappa_2t_1)S(t_1, \omega_2)$ with respect to ω_2 yields the sheared FID, which is shown in Figure 12.56 (c). This method has the advantage over the simple translation that now the Cartesian grid of sampling points is preserved, and the green region of points which was sheared outside the grid in Figure 12.56 (b) is folded back inside to the rectangular sampling space in Figure 12.56 (c).

Finally we can calculate the evolution frequencies of an arbitrary interaction following the combined shear and scale. The original evolution frequencies during t_1 and t_2 , which are Ω_1 and Ω_2 , are transformed into Ω'_1 and Ω'_2 in the new coordinate system. These frequencies are calculated from:

$$\begin{pmatrix} \Omega'_1 & \Omega'_2 \end{pmatrix} \begin{pmatrix} t'_1 \\ t'_2 \end{pmatrix} = \begin{pmatrix} \Omega_1 & \Omega_2 \end{pmatrix} \begin{pmatrix} t_1 \\ t_2 \end{pmatrix} \quad (12.48)$$

$$\begin{pmatrix} \Omega'_1 & \Omega'_2 \end{pmatrix} \begin{pmatrix} \zeta'_1 & 0 \\ \kappa_2 & 1 \end{pmatrix} \begin{pmatrix} t_1 \\ t_2 \end{pmatrix} = \begin{pmatrix} \Omega_1 & \Omega_2 \end{pmatrix} \begin{pmatrix} t_1 \\ t_2 \end{pmatrix}, \quad (12.49)$$

and are given by the following expressions:

$$\begin{pmatrix} \Omega'_1 & \Omega'_2 \end{pmatrix} = \begin{pmatrix} \Omega_1 & \Omega_2 \end{pmatrix} \begin{pmatrix} \zeta'_1 & 0 \\ \kappa_2 & 1 \end{pmatrix}^{-1} \quad (12.50)$$

$$= \begin{pmatrix} \frac{\Omega_1 - \kappa_2 \Omega_2}{\zeta'_1} & \Omega_2 \end{pmatrix}. \quad (12.51)$$

We note that the two evolution frequencies Ω'_1 and Ω'_2 are associated with new effective spin-order parameters a'_1 and a'_2 in the new coordinate system.

Alternatively we can shear the FID parallel to t_1 to map the echo ridge onto the new t'_2 axis and scale then scale t'_2 . The coordinate transformation is

$$\mathbf{t}' = \mathcal{T}_{\zeta'_2} \mathcal{T}_{\kappa_1} \mathbf{t}, \quad (12.52)$$

where \mathcal{T}_{κ_1} is the shear matrix characterised by the shear ratio κ_1 , and $\mathcal{T}_{\zeta'_2}$ represents the subsequent scaling of t'_2 by the factor ζ'_2 :

$$\mathcal{T}_{\zeta'_2} = \begin{pmatrix} 1 & 0 \\ 0 & \zeta'_2 \end{pmatrix}, \quad \mathcal{T}_{\kappa_1} = \begin{pmatrix} 1 & \kappa_1 \\ 0 & 1 \end{pmatrix}. \quad (12.53)$$

The explicit expressions for the new time coordinates are:

$$\mathbf{t}' = \begin{pmatrix} 1 & \kappa_1 \\ 0 & \zeta_2' \end{pmatrix} \begin{pmatrix} t_1 \\ t_2 \end{pmatrix} = \begin{pmatrix} t_1 + \kappa_1 t_2 \\ \zeta_2' t_2 \end{pmatrix}. \quad (12.54)$$

In order to map the echo ridge onto t_2' we require the shear ratio to be equal to

$$\kappa_1 = \frac{a_2}{a_1}. \quad (12.55)$$

In analogy with the shear parallel to t_2 it is more convenient in practice to implement the shear parallel to t_1 by first computing the mixed frequency–time domain $S(\omega_1, t_2)$ by Fourier transformation with respect to t_1 and then multiplying each point by the phase factor $\exp(+i\omega_1 \kappa_1 t_2)$. The inverse Fourier transform of the result is then the sheared FID $s(t_1 + \kappa_1 t_2, t_2)$:

$$s(t_1 + \kappa_1 t_2, t_2) \leftrightarrow \exp(+i\omega_1 \kappa_1 t_2) S(\omega_1, t_2). \quad (12.56)$$

Finally we can calculate the evolution frequencies relative to the transformed coordinate system to be:

$$\begin{pmatrix} \Omega_1' & \Omega_2' \end{pmatrix} = \begin{pmatrix} \Omega_1 & \Omega_2 \end{pmatrix} \begin{pmatrix} 1 & \kappa_1 \\ 0 & \zeta_2' \end{pmatrix}^{-1} \quad (12.57)$$

$$= \begin{pmatrix} \Omega_1 & \frac{\Omega_2 - \kappa_1 \Omega_1}{\zeta_2'} \end{pmatrix}. \quad (12.58)$$

Here the slice of the sheared FID along t_2' is a one-dimensional FID in which the interaction Λ does not evolve. The Fourier transform of this slice is therefore a one-dimensional spectrum with no spectral features due to this interaction.

We now use these shearing methods in combination with state-of-the-art pulse sequences to obtain two-dimensional separation of the paramagnetic SA and quadrupolar interactions for both integer-spin [199, 392], and half-integer-spin nuclei [393].

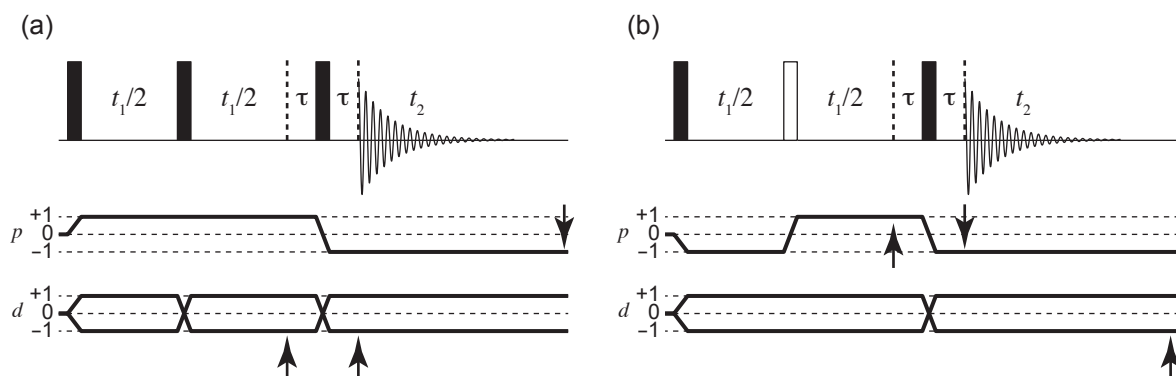


Figure 12.57: Pulse sequences and symmetry-transfer pathways for correlating the paramagnetic shift anisotropy and quadrupolar lineshapes for spin $I = 1$ nuclei. Also shown are the transfer pathways for the coherence order p and satellite order d . The sequence in (a) is for the shifting p -echo experiment of Antonijevic and Wimperis in which the first-order quadrupolar interaction is refocussed at the end of t_1 [392]. The sequence for the shifting d -echo sequence of Walder et al. is shown in (b) [199]. Here the SA is refocussed at the end of t_1 . The time points at which the shift and shift anisotropy, and the quadrupolar interaction are refocussed are indicated on the relevant symmetry pathways with arrows. Filled rectangles indicate pulses with a nominal flip angle of 90° and unfilled rectangles indicate pulses with a nominal flip angle of 180° . All pulses have phase x .

Integer-spin quadrupolar nuclei

Two related experimental methods have been developed for separating the spectral broadening from the SA and first-order quadrupolar interactions of nuclear spins $I = 1$ in static solids. Under static conditions we can in principle measure the effects on the spectrum of two different interactions: the isotropic shift and SA both evolve in the same way with frequencies that are proportional to the coherence order p , and the first-order quadrupolar interaction evolves with a frequency that is proportional to the satellite order d .

The first pulse sequence that was developed to separate these two interactions is the shifting p -echo experiment of Antonijevic and Wimperis, and is shown in Figure 12.57 (a) [392]. The p - and d -symmetry pathways are also shown. The former is explicitly selected unambiguously by phase cycling [320], whereas the latter is only selected implicitly. This means that the d -symmetry pathways shown are those that correspond to the p -symmetry pathway that is explicitly selected. The sequence contains a solid echo during the evolution period $t_1/2-90^\circ-t_1/2$ in which the pulse does not change the sign of p , but does change the sign of d . This means that the shift and SA evolve uninterrupted throughout t_1 , whereas the quadrupolar interaction is refocussed at the end of t_1 . Prior to acquisition there is a second solid echo which refocusses the evolution of

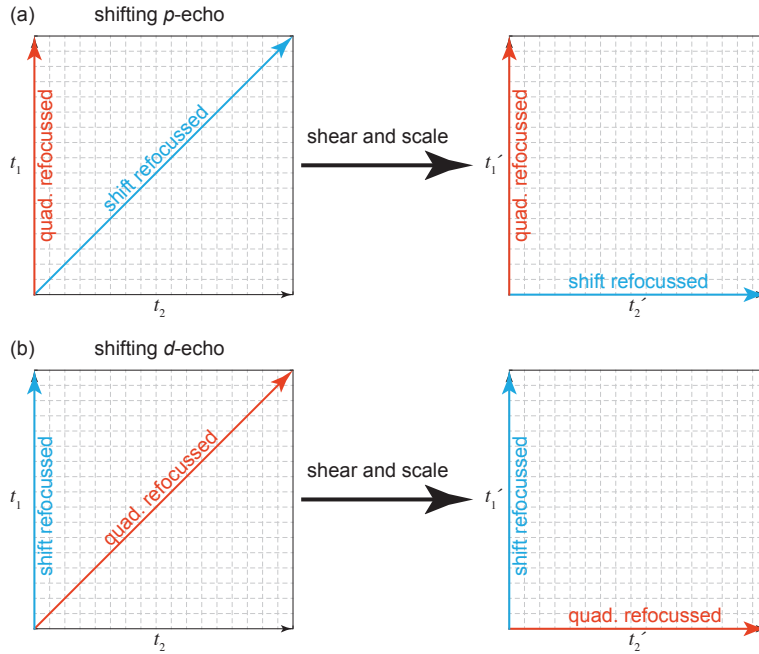


Figure 12.58: Illustration of the single shear parallel to t_1 with ratio $\kappa_1 = -1$ required for the separation of the paramagnetic shift and shift anisotropy from the first-order quadrupolar interaction in (a) the shifting p -echo of Antonijevic and Wimperis [392], and (b) the shifting d -echo sequence of Walder et al. [199].

both interactions during the two delays τ , and leads to the formation of a p -echo during acquisition. Therefore there are two echoes formed during the pulse sequence: the p -echo is formed at points where $t_1 = t_2$, and the d -echo is formed at $t_2 = 0$. This is shown in the representation of the two-dimensional FID in Figure 12.58 (a). The quadrupolar interaction echo ridge is therefore aligned along the t_1 -axis, whereas the shift/SA ridge echo is along $t_1 = t_2$. In order to complete the separation of the evolution of the two interactions in the FID we map the shift/SA echo ridge onto t_2' by applying a shear parallel to t_1 with shear ratio $\kappa_1 = -1$. We then obtain the correct signs of the frequencies in t_1' by applying a scaling along this axis with factor $\zeta_1' = -1$. The resulting FID is shown in Figure 12.58 (a), with the quadrupolar and shift/SA ridge echoes along t_1' and t_2' respectively. A two-dimensional Fourier transform therefore yields a spectrum in which the quadrupolar broadening is present only in the ω_2' dimension, and the shift/SA appears only in the ω_1' dimension.

There is room for improvement in this experiment as the coherence-order selection in each solid echo only retains half the total signal components, and so the sequence gives a maximum sensitivity that is one quarter of that theoretically attainable in the one-dimensional experiment. Secondly the selection of the symmetry

pathways as shown, when the RF field amplitude is not much larger than both the SA and quadrupolar frequencies, results in a spike appearing at zero frequency in the quadrupolar frequency dimension.

An improvement to the shifting *p*-echo experiment was proposed by Walder et al. who developed the shifting *d*-echo pulse sequence shown in Figure 12.57 (b) [199]. Here the solid echo during the evolution period is replaced with a spin echo, with the result that the *p*- and *d*-symmetry pathways are altered so that it is the *p*-echo that is now formed at $t_2 = 0$ and the *d*-echo that is formed at $t_1 = t_2$. The two-dimensional FID is shown in Figure 12.58 (b). As for the shifting *p*-echo experiment, complete separation of the two interactions is achieved using the same shearing and scaling transformations, with the result that the quadrupolar frequency is present only in the ω'_1 dimension, and the shift/SA appears only in the ω'_2 dimension.

The use of the spin echo is advantageous for two reasons: firstly the zero-frequency spike in the quadrupolar dimension is eliminated, and secondly the spin echo does not suffer from the reduction in signal intensity of the solid echo, with the result that the shifting *d*-echo experiment has double the sensitivity of the shifting *p*-echo experiment. The disadvantage of the shifting *d*-echo sequence is the lower bandwidth of the 180° pulse compared to the 90° pulse.

Simulated two-dimensional spectra generated using these methods are shown in Figure 12.59, showing the effect that the relative orientation between the PAFs of the two tensors (α, β, γ) has on the two-dimensional spectrum [199]. It should be noted that for all the spectra the projections onto the quadrupolar and shift/SA frequency axes give the same spectra. An experimental example is given in Figure 12.60, which show the ²H shifting *p*-echo and shifting *d*-echo spectra of solid CuCl₂ · 2D₂O in (ia) and (iia) respectively. In both cases a clean separation of the shift/SA and quadrupolar spectra is achieved, with the shifting *d*-echo spectrum in Figure 12.60 (iia) giving the superior result, with suppression of the zero-frequency spike and a signal-to-noise ratio that is higher by a factor of two. In both cases it is possible to extract unambiguous shift/SA and quadrupolar tensor parameters, which would be difficult to do from the one-dimensional spectrum only. The simulated spectra from the best-fit tensor parameters are shown in Figure 12.60 (ib) and (iib) respectively, with the best-fit residuals shown in Figure 12.60 (ic) and (iic).

This experiment is extremely useful for extracting the tensor parameters in paramagnetic systems containing a single $I = 1$ nuclear site. However for more complex materials there are potential difficulties. Firstly the presence of inhomogeneous broadening due to BMS effects distorts the spectrum in the shift/SA dimension, so that it may not be easily interpretable. However it should be noted that this broadening does not appear

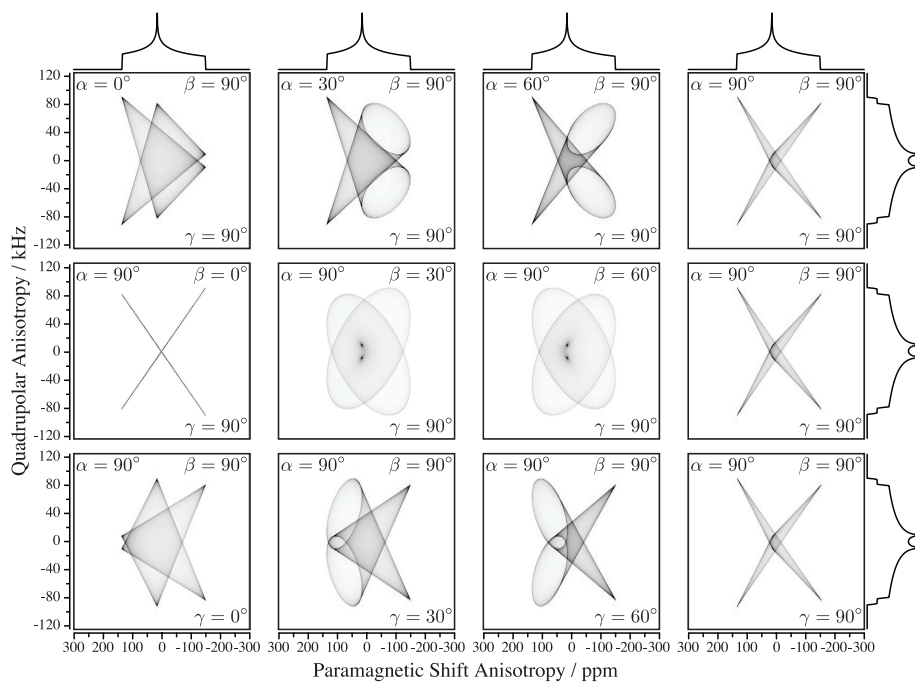


Figure 12.59: Simulated spectra of the shifting *p*-echo and shifting *d*-echo experiments, illustrating the effect of changing the relative orientation of the PAFs of the paramagnetic shielding and quadrupolar interaction tensors for an $I = 1$ nucleus. The Euler angles (α, β, γ) define the coordinate transformation from the PAF of the quadrupolar interaction tensor to the PAF of the paramagnetic shielding tensor. Other simulation parameters include $\omega_0/2\pi = 61.496022$ MHz, $C_Q = 120$ kHz, $\eta^Q = 0.8$, $\Delta\sigma^S = 150$ ppm, and $\eta^S = 0.8$. Note that the projection onto each axis remains unchanged as the relative orientation changes. Reproduced from [199], with the permission of AIP Publishing.

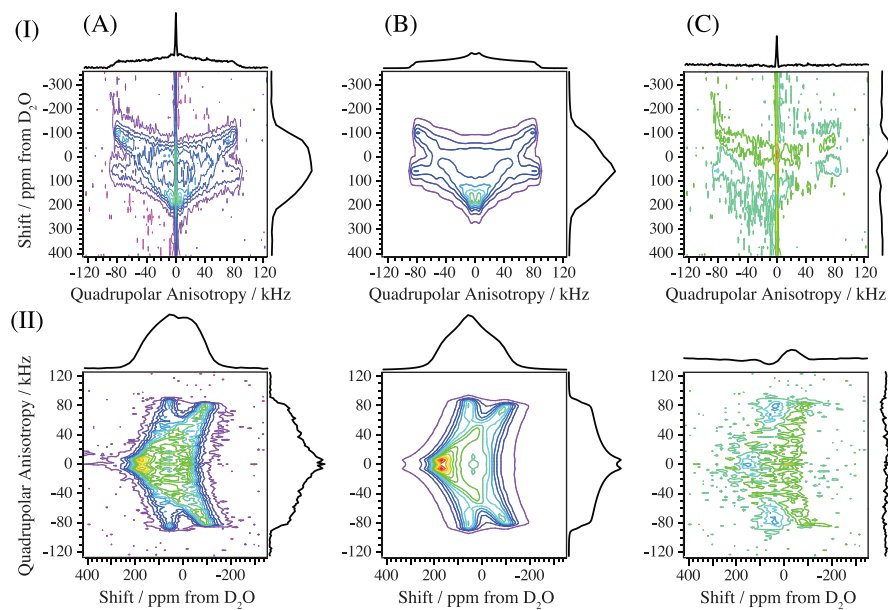


Figure 12.60: Experimental ^2H spectra acquired using the shifting p -echo and shifting d -echo experiments on polycrystalline $\text{CuCl}_2 \cdot 2\text{D}_2\text{O}$. The experimental shifting p -echo spectrum and best-fit simulated spectrum are shown in (ia) and (ib), with the best-fit residuals in (ic). Note that the experimental spectrum contains a sharp spike at zero frequency in the quadrupolar dimension. The experimental shifting d -echo spectrum and best-fit simulated spectrum are also shown in (iia) and (iib), with the best-fit residuals in (iic). Here there is no zero-frequency spike, and the experimental shifting d -echo spectrum has a signal-to-noise ratio that is larger by a factor of two. Reproduced from [199], with the permission of AIP Publishing.

in the quadrupolar dimension, which remains clean, and so we have the intriguing possibility of being able to extract quadrupolar coupling parameters even when there is severe BMS broadening. A second difficulty is that in materials with multiple sites there is expected to be considerable overlap in the two-dimensional spectrum and in both projections. If the number of sites is not already known this may lead to uninterpretable spectra. Nevertheless this method is extremely powerful, and is expected both to be widely used, and to inspire other methods for separating two or more large anisotropic interactions.

Half-integer-spin quadrupolar nuclei

A related method for separating the shift/SA interaction from the quadrupolar interaction for half-integer-spin nuclei, known as the COrelation of Anisotropies Separated Through Echo Refocusing (COASTER) experiment, has been presented by Ash et al [393]. It was initially designed for separating the CSA from the second-order quadrupolar broadening in diamagnetic materials, and is included in this survey as it represents an elegant method that is potentially applicable to paramagnetic species, even though there are as yet no paramagnetic examples. The COASTER pulse sequence is shown in Figure 12.61. It is a simple sequence that comprises two pulses, and is designed to correlate a symmetrical multiple-quantum coherence $|IM\rangle\langle I-M|$, such as the triple-quantum coherence $p = +3$, in t_1 with the CT coherence $|I-1/2\rangle\langle I+1/2|$ with $p = -1$ in t_2 . The experiment is carried out on a spinning powder, but with the rotor aligned at 70.12° to the field, rather than at the magic angle. This choice of angle ensures that the rank-four second-order quadrupolar broadening is completely removed by the sample rotation. If we assume that the increments in both t_1 and t_2 are rotor-synchronised, so that the sidebands are folded onto the centreband, the remaining interactions that evolve are those that are time-independent. They include the isotropic shift and residual SA remaining due to spinning off the magic angle, both of which evolve at frequencies proportional to p , the rank-zero second-order quadrupolar shift, the frequency of which is proportional to c_0 , and the rank-two second-order quadrupolar anisotropy the frequency of which is proportional to c_2 . We can define a symmetry pathway for all three symmetry-order parameters, which are also shown in Figure 12.61 for $I = 3/2$ (a) and $I = 5/2$ (b). Each of these interactions is refocussed along a distinct echo ridge. For the shift and SA this echo ridge is

$$p_1 t_1 + p_2 t_2 = 0, \quad (12.59)$$

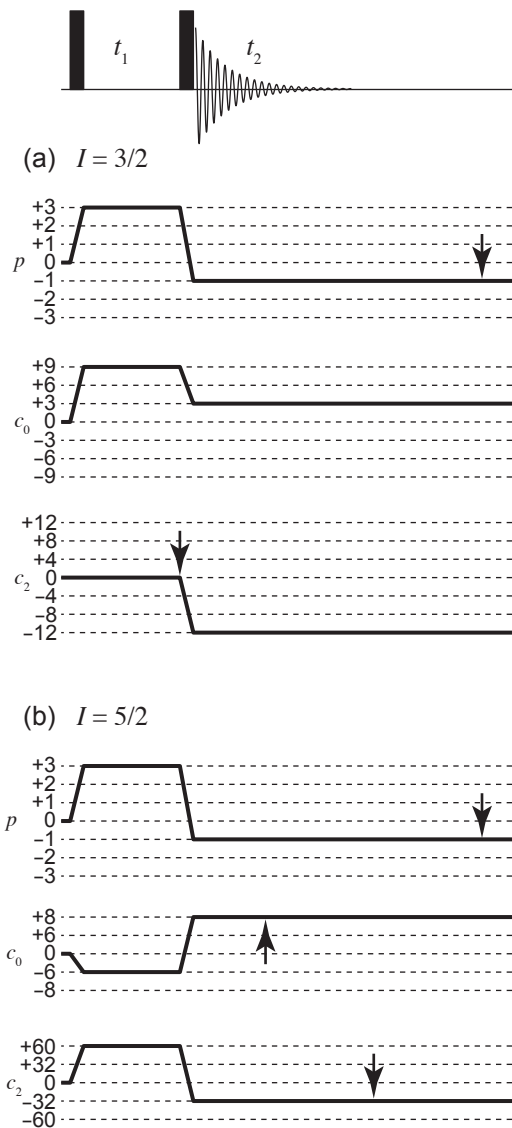


Figure 12.61: Pulse sequences and symmetry-transfer pathways for the COASTER experiment, which correlates the paramagnetic shift anisotropy and quadrupolar lineshape for half-integer-spin quadrupolar nuclei [393]. In this sequence we correlate a signal due to a symmetry multiple-quantum coherence in t_1 (in this case the $p = +3$ coherence) against the observable ($p = -1$) CT coherence in t_2 . The sets of symmetry pathways in (a) and (b) show the p -, c_0 -, and c_2 -order during experiments for $I = 3/2$ and $5/2$ respectively. The arrows on the symmetry pathways indicate the time points at which the relevant interactions are refocussed. Both pulses have phase x .

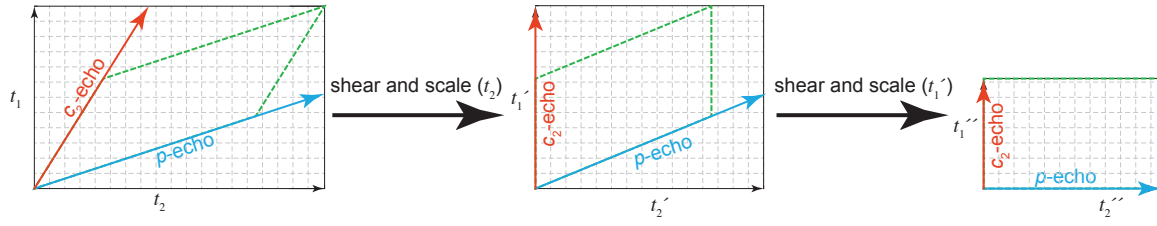


Figure 12.62: Illustration of the double shear and scaling transformations applied to a two-dimensional FID acquired using the COASTER experiment. The first shear is parallel to t_2 and maps the c_2 -echo of the rank-two second-order quadrupolar interaction onto the t_1' axis. The second shear is parallel to t_1' and maps the p -echo of the rank-two SA interaction onto the t_2'' axis.

where for all spins $p_1 = +3$ for the triple-quantum experiment and $p_2 = -1$. For the rank-zero and rank-two quadrupolar interactions the echo ridges are:

$$c_{0,1}t_1 + c_{0,2}t_2 = 0, \quad (12.60)$$

$$c_{2,1}t_1 + c_{2,2}t_2 = 0. \quad (12.61)$$

We note that both of these echo ridges are different for different spins and, for the coherence-transfer pathway in Figure 12.61 (a) there is no c_0 echo. Both the residual SA and rank-two second-order quadrupolar interaction are manifested as spectral broadening and therefore require separation in the two-dimensional experiment. By contrast the rank-zero second-order quadrupolar interaction does not broaden the spectrum and only shifts the resonances, and so we do not consider it further.

A schematic of the FID showing both the p and c_2 echo ridges is shown in Figure 12.62. Here we have two echo ridges which require mapping onto the two principal time axes, which we achieve with two combined shear and scale transformations. Firstly we apply a shear parallel to the t_2 axis to give a new coordinate system (t_1', t_2') , followed by a scaling of the t_1' axis. If we set the shear and scaling parameters to

$$\kappa_2 = \frac{c_{2,1}}{c_{2,2}}, \quad \zeta_1' = 1 + |\kappa_2|, \quad (12.62)$$

the result is the FID shown in Figure 12.62 in which the c_2 -echo is now along the t_1' axis. The result of this

I	$c_2^{(1)}$	$c_2^{(1)}$	κ_2	ζ_1'	$p^{(2)}/p^{(2)'} $	$p^{(1)}$	$p^{(1)'}$	κ_1'	ζ_2''
3/2	0	-12	0	1	-1	3	3	-1/3	4/3
5/2	60	-32	-15/8	23/8	-1	3	9/23	-23/9	32/9
7/2	144	-60	-12/5	17/5	-1	3	3/17	-17/3	20/3
9/2	252	-96	-21/8	29/8	-1	3	3/29	-29/3	32/3

Table 12.3: The shear ratios and scaling factors κ_2 and ζ_1' , and κ_1' and ζ_2'' required for the COASTER experiment that correlates the $p_1 = +3$ coherence $|I + 3/2\rangle \langle I - 3/2|$ with the observable CT coherence with $p_2 = -1, |I - 1/2\rangle \langle I + 1/2|$, for different nuclear spins I .

first transformation is to change the p echo ridge so that it is aligned in the (t_1', t_2') coordinate system so that

$$p_1' t_1' + p_2' t_2' = 0, \quad (12.63)$$

where p_1' and p_2' are given by

$$p_1' = \frac{p_1 - \kappa_2 p_2}{\zeta_1'}, \quad p_2' = p_2. \quad (12.64)$$

We now need a second shear parallel to t_1' , giving a new coordinate system (t_1'', t_2'') , to map the p -echo onto the t_2'' axis followed by a scaling of this axis. The shearing and scaling parameters are:

$$\kappa_1' = \frac{p_2'}{p_1'}, \quad \zeta_2'' = 1 + |\kappa_1'|. \quad (12.65)$$

The final FID, shown in Figure 12.62, exhibits a c_2 echo along t_2'' and a p -echo along t_1'' . The resulting two-dimensional spectrum in which the shift/SA and second-order quadrupolar interactions appear in the ω_1'' and ω_2'' dimensions respectively. The shearing ratios and scaling parameters required for the triple-quantum COASTER experiment are given for nuclear spins $I = 3/2$ to $9/2$ in Table 12.3.

Simulated examples of sheared COASTER spectra are given in Figures 12.63 and 12.64 [319]. Figure 12.63 shows the effect on the two-dimensional lineshape of varying both the SA and quadrupolar asymmetry parameters, whilst Figure 12.64 shows the effect of varying the relative orientation of the two tensors (α, β, γ) and keeping other parameters constant. We see that the two one-dimensional projections can be used to obtain $\Delta\sigma^S$, η^S , C_Q , and η^Q and that the relative orientation of the two PAFs can be obtained from the two-dimensional lineshape.

An experimental COASTER spectrum is shown in Figure 12.65 along with a simulation taken from the best-fit tensor parameters [393]. The spectrum is of the ^{59}Co resonance in low-spin (diamagnetic)

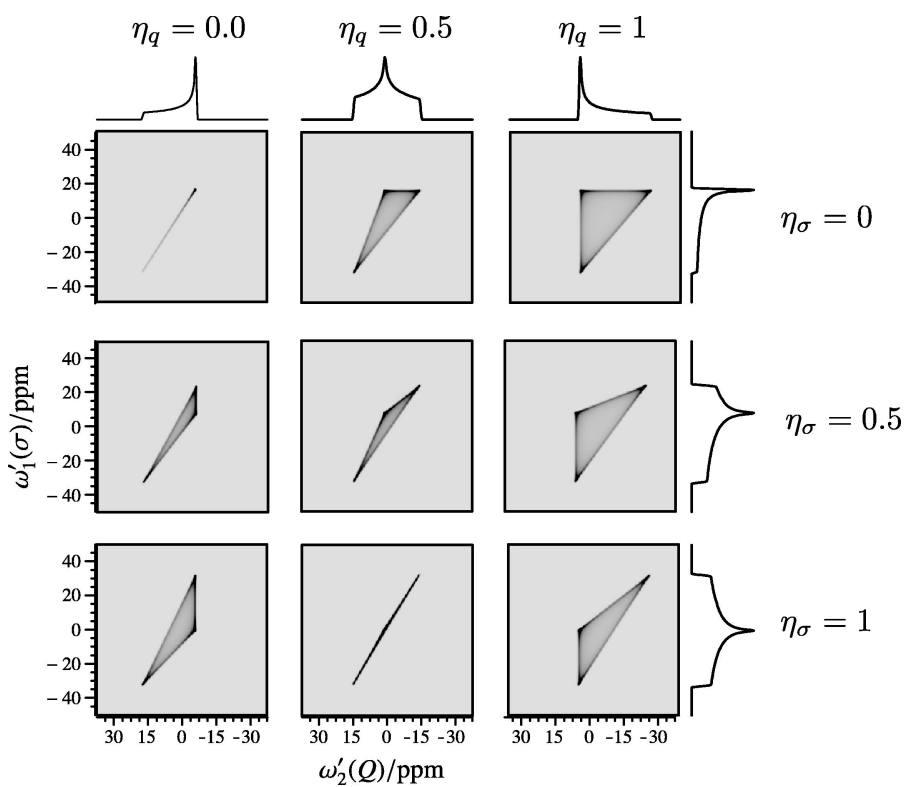


Figure 12.63: Comparison of simulated two-dimensional COASTER spectra showing the effect of changing the quadrupolar interaction and chemical shielding asymmetry parameters in the case where the two tensors have the same PAF. Other simulation parameters included $I = 3/2$, $\omega_0/2\pi = 100$ MHz, $C_Q = 3$ MHz, $\sigma_{\text{iso}} = 0$ ppm, and $\Delta\sigma^S = 33$ ppm. The one-dimensional projections onto the quadrupolar anisotropy axis $\omega'_2(Q)$ are the same for each η^Q value. Similarly the one-dimensional projections onto the shielding anisotropy axis $\omega'_1(\sigma)$ are the same for each η^S value. Reproduced from [319], with permission from Elsevier.

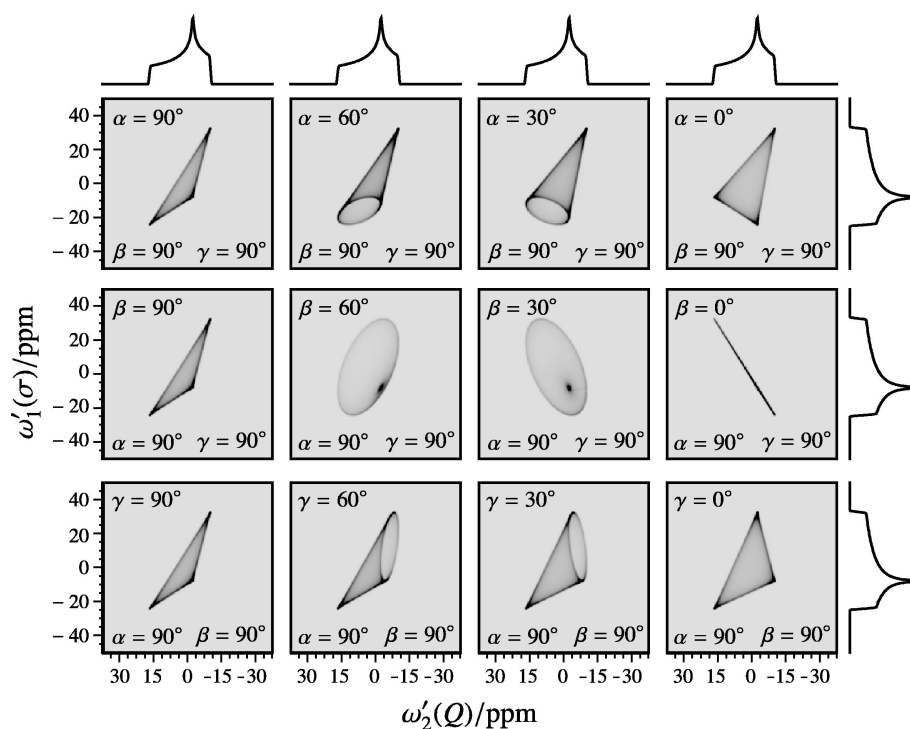


Figure 12.64: Comparison of simulated COASTER spectra showing the effect of the relative orientation of the quadrupolar and shift anisotropy tensors on the two-dimensional spectrum. Other simulation parameters included $I = 3/2$, $\omega_0/2\pi = 100$ MHz, $C_Q = 3$ MHz, $\eta^Q = 0.25$, $\sigma_{\text{iso}} = 0$ ppm, $\Delta\sigma^S = 33$ ppm, and $\eta^S = 0.5$. Note that the projection onto each axis remains unchanged as the relative orientation of the quadrupolar coupling and chemical shift tensors changes. Reproduced from [319], with permission from Elsevier.

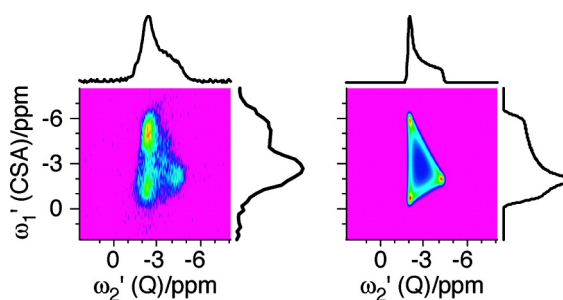


Figure 12.65: Sheared ^{59}Co COASTER spectrum of $\text{K}_3[\text{Co}(\text{CN})_6]$ at 9.4 T (left), with a simulation (right) using the parameters $C_Q = 6.2$ MHz, $\delta_{\text{iso}} = 14$ ppm, $\eta^Q = 1.0$, $\Delta\sigma = -62$ ppm, $\eta = 0.25$, and Euler angles describing the relative orientation of the two tensors $\alpha = 90^\circ$ and $\beta = \gamma = 0^\circ$. Reproduced with permission from [393]. Copyright (2008) American Chemical Society.

$\text{K}_3[\text{Co}(\text{CN})_6]$, and is indispensable for obtaining unambiguous tensor parameters.

The main disadvantages of COASTER are the same as for the shifting *p*- and *d*-echo experiments. Whilst high-quality spectra can be obtained for single-site materials, more complex systems containing multiple sites will be more difficult to interpret. In addition the use of sample spinning at 70.12° means that this experiment cannot be easily implemented with commercial MAS probes. Nevertheless we expect this method to be of interest to paramagnetic solid-state NMR.

12.6 Solid-state NMR of paramagnetic proteins

The solid-state NMR of proteins has experienced significant advances in recent years, having moved from a position where very few previously-unknown structures had been solved, to the point where systems of significant complexity and interest to the field of biology are being studied. The driving force behind these advances has been twofold. Firstly developments in fast-spinning probe technology, allowing up to 100 kHz MAS and beyond, have improved the spectral resolution and allowed the second advance, which is the development and application of more sophisticated pulse sequences for obtaining the sequential assignment and distance restraints. One crucial aspect of these advances is the employment of ^1H -detection, which improves sensitivity and allows us to obtain unambiguous distance restraints. Here we focus on the application to paramagnetic proteins, highlighting experimental schemes that have either been already applied, or otherwise have significant potential.

12.6.1 General strategy

In solid-state NMR of proteins the extensive network of large ^1H - ^1H dipolar couplings results in very short ^1H coherence lifetimes T_2' at moderate MAS rates. The peaks in the ^1H spectrum are therefore very broad, and any coherence-transfer blocks involving ^1H are often very inefficient, with the result that direct ^1H -detection is not used routinely. Therefore ^{13}C detection is normally used, as part of pulse sequences that correlate resonances of N^{H} , CO, CA, and CB. In addition to the large coherence broadening, the solid-state spectra also exhibit substantial inhomogeneous broadening due to structural disorder and, in the case of paramagnetic proteins, the ABMS. The result is that, even employing ^{13}C detection, small proteins give broader lines than in solution. However one advantage of solid-state NMR for large, paramagnetic proteins is that in the solid

state there is no overall slow rotational diffusion, with rotational dynamics due only to the internal motions of the protein, and so the Curie broadening is substantially reduced for large systems compared to solution. This indicates that solid-state NMR can potentially be used to study large systems which in solution would have peaks broadened beyond detection due to the slow rotational diffusion.

As in solution NMR, the solid protein can be divided into regions in which the nuclear spins exhibit different effects due to the paramagnetic centre, as shown in Figure 12.19. As in solution there is a blind sphere centred on the metal ion, in which the nuclear spins cannot be observed using conventional experimental methods. Beyond the blind sphere is a region which can be observed using these methods, and in which the nuclear spins are subject to measurable long-range paramagnetic effects, such as the PCS and PRE. The outermost region was characterized in solution NMR as showing no measurable paramagnetic effects. However in the solid state this description is not completely accurate. This is because the extended network of ^1H - ^1H dipolar couplings allows polarization to be transferred from one nuclear spin in this region, to another nuclear spin closer to the metal ion, and vice versa. For example one consequence of spin diffusion is that the measured T_1 relaxation times of a particular spin are the average of the T_1 values of the spins from which polarization has been transferred. This is not because the true relaxation times have changed, but rather the polarization spends only a fraction of the total time on any particular spin, due to rapid spin diffusion. Hence the nuclear spins in this outermost region are expected to exhibit T_1 times that are shorter than their true values, due to the exchange of polarization with nuclear spins that are closer to the metal ion, and exhibit a measurable PRE. Hence the two outermost regions in Figure 12.19 can be more accurately labelled as follows when discussing solid proteins. The inner of the two can be labelled as ‘visible with measurable *direct* paramagnetic effects’, as the nuclear spins exhibit a direct long-range interaction with the paramagnetic centre. The outermost region can then be labelled as ‘no measurable *direct* paramagnetic effects, but shows *indirect* paramagnetic effects due to spin diffusion’. As discussed, one such indirect paramagnetic effect would be a relayed longitudinal PRE. The precise distances from the metal ion that define the boundaries between these different regions depend upon the nuclear species that are excited and observed, for example ^1H or ^{13}C , whether the proton concentration is diluted by deuteration, the MAS frequency, and the types of experiments that are used, for example utilizing scalar- or dipolar-based coherence transfers.

If we employ fast MAS (in the 60 kHz regime and above) and proton dilution by deuteration we weaken the coherent effect of the dipolar coupling network, which has the effect of slowing spin diffusion sufficiently

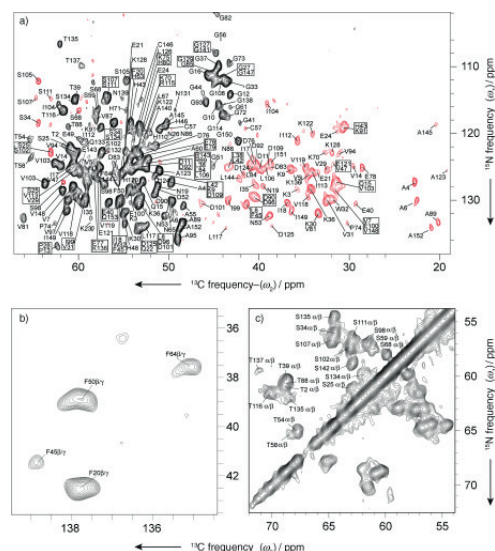


Figure 12.66: Two-dimensional ^{13}C -detected solid-state NMR spectra of the paramagnetic metalloprotein $[\text{U-}^{13}\text{C}, ^{15}\text{N}]\text{-Cu}^{2+}\text{-Zn}^{2+}$ SOD. The assigned NCACB double-quantum spectrum is shown in (a). The black contours correspond to positive cross peaks indicating one-bond $^{15}\text{N}\text{-}^{13}\text{C}$ correlations, and red contours indicate negative cross peaks due to two-bond $^{15}\text{N}\text{-}^{13}\text{C}$ correlations. Extracts from the $^{13}\text{C}\text{-}^{13}\text{C}$ PDS correlation spectrum are shown in (b) and (c). The MAS frequency is 15 kHz. Reproduced with permission from [450]. Copyright John Wiley and Sons.

to suppress this relayed transfer. Under such conditions we approach the situation in solution NMR, and Figure 12.19 resumes its original interpretation.

12.6.2 ^{13}C -detection

Historically the solid-state NMR of proteins has been performed under moderate MAS of 20 kHz and employing ^{13}C -detection. The experimental schemes used include two-dimensional correlation experiments to establish the connectivity between the N^{H} and the CO, CA, or CB resonances along the backbone, and spin-diffusion to measure $^{13}\text{C}\text{-}^{13}\text{C}$ distance restraints between C resonances on the backbone and sidechains. These methods have been used on paramagnetic proteins for the assignment [450] and the measurement of paramagnetic restraints [44]. They mainly concern two enzymes in microcrystalline form, human superoxide dismutase (SOD) and the catalytic domain of matrix-metalloproteinase-12 (MMP-12), two proteins with high-affinity binding sites for divalent paramagnetic cations such as Cu^{2+} (SOD) or Co^{2+} (MMP and SOD). Example spectra are shown in Figure 12.66 [450] for a paramagnetic metalloprotein $[\text{U-}^{13}\text{C}, ^{15}\text{N}]\text{-Cu}^{2+}\text{-Zn}^{2+}$

superoxide dismutase (SOD). The NCACB and ^{13}C - ^{13}C through-space correlation spectra acquired using proton-driven spin diffusion (PDS) are shown in Figure 12.66 (a), and Figure 12.66 (b)–(c) respectively. Here resonances as close to the paramagnetic Cu^{2+} ion as 5 Å are observed. An additional notable example is the study of the reactive state of a copper-binding misfolded amyloid β ($A\beta$) fibril [451]. Proton relaxation data lead to the conclusion that the $\text{Cu}^{2+/+}$ ions are bound to histidine amino acid residues, and act as reaction centres for the redox reaction with ascorbate and oxygen to produce H_2O_2 . This cycle was followed by measuring ^1H T_1 data to monitor the interconversion between the Cu^{2+} and Cu^+ oxidation states.

In addition to studying metalloproteins, paramagnetic effects have been used to accelerate acquisition of NMR spectra of low concentrations of diamagnetic proteins following doping with a paramagnetic agent [452]. For diamagnetic proteins the total experiment time required to obtain a spectrum is limited by the relatively long recycle delays of 1–4 s required for complete longitudinal relaxation. This so-called T_1 barrier often means that data cannot be acquired on low concentrations of protein in a practicable time. To address this problem Wickramasinghe et al. proposed a method in which the protein sample is prepared so that it is doped with a paramagnetic complex which enhances the relaxation rates of the ^1H nuclei, resulting in a shorter recycle delay, and thus allowing accelerated acquisition even for nanomolar concentrations of protein [452]. The protein sample studied was a fibrillized and uniformly ^{13}C - and ^{15}N -labeled $A\beta$ peptide of 87 nM concentration, which had been doped with a 200 mM concentration of Cu^{2+} -binding EDTA. The PRE was transmitted directly to the surface-exposed ^1H of the protein, and then transferred throughout the protein via ^1H spin diffusion. This enabled the acquisition of a ^{13}C - ^{13}C correlation spectrum in a time of 2.7 h with a recycle delay of 55 ms.

The combined use of faster spinning (initially between 40 and 60 kHz) and lower-power decoupling reduces the coherent broadening, leading to both longer coherence lifetimes T_2' , and reduced linewidths in the spectrum [9]. The lengthening of the coherence lifetimes is a particularly important advantage as it increases the efficiency of coherence transfer blocks, and thus allows the use of longer and more sophisticated pulses sequences for sequential assignment [453]. Experiments were developed employing ^{13}C -detection and fast MAS at 60 kHz for sequential assignment of the backbone resonances, in analogy to the protonless experiments employed in solution [361]. These experiments, which are listed in listed in Table 12.4, were designed to correlate the amide N resonance to either the CO and CA resonances in either the same or preceding amino acid residue in a two-dimensional spectrum. In all cases the S^3E block was used in the

Experiment	Correlations	Reference
2D		
(H)NCA-S ³ E	N _{<i>i</i>} -CA _{<i>i</i>}	[454]
(H)N(CA)CO-S ³ E	N _{<i>i</i>} -CO _{<i>i</i>}	[455]
(H)NCO-S ³ E	N _{<i>i+1</i>} -CO _{<i>i</i>}	[454]
(H)N(CO)CA-S ³ E	N _{<i>i+1</i>} -CA _{<i>i</i>}	[455]

Table 12.4: Two-dimensional ¹³C-detected experiments for establishing the sequential assignment of the protein backbone. The sequence of spins indicates the order, from left to right, in which the coherences are transferred. Heteronuclear transfers are performed using CP, and homonuclear ¹³C-¹³C are performed via the *J*-coupling. An atomic label in parentheses indicates that the coherence is transferred to the corresponding spin, but does not evolve during the evolution period or acquisition. An atomic label without parentheses indicates that the chemical shift of that nuclear spin evolves during either the evolution period or acquisition. For each experiment the correlations observed given, where the subscript refers to the residue number in the sequence.

direct ¹³C dimension in order to decouple the CO-CA one-bond *J*-coupling.

The (H)NCA-S³E pulse sequence works as follows [454]. We begin with excitation of all the ¹H nuclei, and then transfer the coherence to the amide N via CP. The N chemical shifts are then encoded during the evolution period, forming the indirect dimension of the FID and spectrum. Following this there is a second CP transfer from N to the closest CA nucleus (corresponding to the directly-bonded CA), after which we detect the CA directly with S³E. The (H)NCO-S³E sequence works in the same way, and correlates the directly-bonded N and CO resonances [454]. The remaining two sequences (H)N(CA)CO-S³E and (H)N(CO)CA-S³E are more complicated, as they both include a *J*-based coherence-transfer block to transfer unambiguously between the directly-bonded CO and CA resonances of the same amino acid residue [455]. Here, following the CP transfer from N to CO/CA, the *J*-based sequence transfers the coherence to the other carbon immediately prior to acquisition. The assigned (H)N(CO)CA-S³E spectrum of [U-²H,¹³C,¹⁵N]-Cu²⁺-Zn²⁺ SOD is shown in Figure 12.67 (a) [455]. In this sample of SOD the protons were uniformly deuterated, and the exchangeable amide deuterons were 100% back-exchanged for protons in H₂O. In this ¹³C-detected experiment resonances up to 8 Å in proximity to the Cu²⁺ ion are observed. This is an improvement on the corresponding three-dimensional ¹H-detected experiment (H)CA(CO)NH, the NC plane of which is superimposed upon the (H)N(CO)CA-S³E spectrum in Figure 12.67 (a), and which has peaks within 11 Å of the Cu²⁺ ion missing.

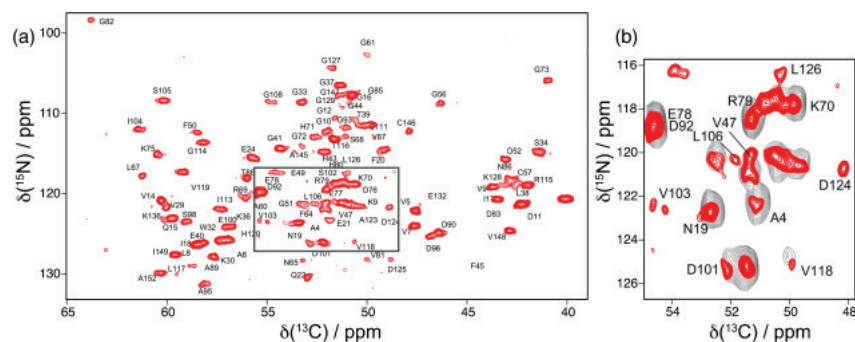


Figure 12.67: Two-dimensional solid-state NMR spectra at 60 kHz MAS of the paramagnetic metalloprotein [U-²H,¹³C,¹⁵N]-Cu²⁺-Zn²⁺ SOD. The (H)N(CO)CA-S³E spectrum is shown in (a). The expansion shown is reproduced in (b) (red contours) superimposed upon the NC projection of the three-dimensional (H)CA(CO)NH spectrum (grey contours). Reproduced with permission from [455]. Copyright John Wiley and Sons.

12.6.3 ¹H-detection

More recently, with the availability of faster-spinning probes, ¹³C-detection in solid-state protein NMR has been superseded by ¹H-detection. The advantages of the latter include increased sensitivity, and the ability now to measure dipolar-based distance restraints between protons.

In order to obtain useful resolution in the ¹H-dimension of spectra, initial strategies employed the complete deuteration of the amino acid residues in order to weaken the dipolar coupling network, followed by either complete [456, 457] or partial reprotonation at the exchangeable amide sites [458–460]. The choice of the level of reprotonation is a compromise between sensitivity and resolution: higher reprotonation levels give greater sensitivity, but also reintroduce more ¹H–¹H dipolar couplings that lead to shorter coherence lifetimes and lower resolution. At moderate MAS frequencies of 10–20 kHz, 10%–30% reprotonation is typically used.

At faster MAS frequencies of 60 kHz, the spinning is able to suppress the coherent decay and broadening sufficiently to allow us to use 100% amide reprotonation in a deuterated background [461]. The sensitivity is increased due both to the higher concentration of amide protons, and to the longer coherence lifetimes due to fast spinning and perdeuteration, which allow *J*-based ¹³C–¹³C transfer to be used in combination with heteronuclear coherence transfers. This allows the application of pulse sequences for sequential backbone assignment, such as the two-dimensional (H)NH sequence [461], and the three-dimensional (H)CONH,

Experiment	Correlations	Reference
2D		
(H)NH	$N_i-H_i^N$	[461, 463]
(H)CH	$CA_i-H_i^{CA}$, C-H sidechains	[464]
3D		
(H)NCAH	$N_i-CA_i-H_i^{CA}$	[464]
(H)CANH	$CA_i-N_i-H_i^N$	[461, 463]
(H)CO(CA)NH	$CO_i-N_i-H_i^N$	[461, 463]
(H)(CA)CB(CA)NH	$CB_i-N_i-H_i^N$	[462, 463]
(H)CO(N)CAH	$CO_i-CA_{i+1}-H_{i+1}^{CA}$	[464]
(H)CA(CO)NH	$CA_i-N_{i+1}-H_{i+1}^N$	[461]
(H)(CO)CA(CO)NH	$CA_i-N_{i+1}-H_{i+1}^N$	[462, 463]
(H)CONH	$CO_i-N_{i+1}-H_{i+1}^N$	[461, 463]
(H)(CA)CB(CA)(CO)NH	$CB_i-N_{i+1}-H_{i+1}^N$	[463]
(H)N(CA)(CO)NH	$N_i-N_{i+1}-H_{i+1}^N$	[464]
(H)N(CO)(CA)NH	$N_{i+1}-N_i-H_i^N$	[464]
(H)CCH TOCSY	sidechains	[464]

Table 12.5: Two- and three-dimensional ^1H -detected experiments for establishing the sequential assignment of the protein backbone and sidechains. The sequence of spins indicates the order, from left to right, in which the coherences are transferred. Heteronuclear transfers are performed using CP, and homonuclear ^{13}C - ^{13}C transfers are performed via the J -coupling. An atomic label in parentheses indicates that the coherence is transferred to the corresponding spin, but does not evolve during an evolution period or acquisition. An atomic label without parentheses indicates that the chemical shift of that nuclear spin evolves during either an evolution period or acquisition. For each experiment the correlations observed are given, where the subscript refers to the residue number in the sequence.

(H)CANH, (H)CO(CA)NH, (H)CA(CO)NH [461], (H)(CO)CA(CO)NH, (H)(CA)CB(CA)NH [462], and (H)(CA)CB(CA)(CO)NH [463] sequences. Furthermore, the increased amide concentration gives increased sensitivity in the measurement of ^1H - ^1H distance restraints using three-dimensional sequences such as the (H)NHH RFDR experiment [461].

Whilst this method provides us with a complete backbone assignment and with information about the protein fold, it does not give us an unambiguous and high-precision structure as we have used neither the CA protons nor the sidechains to provide distance restraints. In order to detect these resonances we need to use fully-protonated proteins with a more extensive dipolar-coupling network. Recently the advent of very-fast spinning probes capable of 100 kHz MAS has enabled high-resolution ^1H -detected spectra with sufficiently long coherence lifetimes to be acquired on such fully-protonated systems [464]. This in turn has led to the suite of experiments for backbone and sidechain assignment being greatly expanded with the complete set of experiments given in Table 12.5. In turn the assignment of the CA and sidechain protons allows us to interpret the distance restraints measured between these protons, using the set of experiments in Table 12.6. It is anticipated that 100 kHz MAS and ^1H -detection will provide invaluable tools for the study of paramagnetic

Experiment	Contacts	Reference
3D		
H(H)NH RFDR	$H^N-H^N, H^{CA}-H^N$	[464]
H(H)CH RFDR	$H^{CA}-H^{CA}$, sidechains	[464]
H(H)CH aromatic RFDR	sidechains	[464]
(H)NHH RFDR	H^H-H^H, H^N-H^{CA}	[461]
(H)CHH RFDR	$H^{CA}-H^{CA}$, sidechains	[464]

Table 12.6: Three-dimensional ^1H -detected experiments for measuring dipolar-coupling-based distance restraints between protons on the protein backbone and sidechains. The sequence of spins indicates the order, from left to right, in which the coherences are transferred. Heteronuclear transfers are performed using CP, and homonuclear $^1\text{H}-^1\text{H}$ through-space transfers are performed using the RFDR pulse sequence. An atomic label in parentheses indicates that the coherence is transferred to the corresponding spin, but does not evolve during an evolution period or acquisition. An atomic label without parentheses indicates that the chemical shift of that nuclear spin evolves during either an evolution period or acquisition. For each experiment the correlations observed are given, where the subscript refers to the residue number in the sequence.

proteins in the solid state.

12.6.4 Paramagnetic restraints

In complete analogy with solution NMR, paramagnetic restraints have also been used in solid-state NMR to give information on the position of an observed nucleus with respect to the paramagnetic centre. Pseudo-contact shifts have been measured, using ^{13}C -detection and MAS frequencies between 8 and 12 kHz, for the protein matrix metalloproteinase (MMP) [44]. The ^{13}C PCS values were determined by comparing the Co^{2+} -substituted protein CoMMP with the diamagnetic Zn^{2+} -substituted protein ZnMMP. Here dilution of the paramagnetic protein into a diamagnetic sample, or vice versa, prior to crystallization was needed to suppress the intermolecular or intramolecular PCSs respectively from the total contributions. While intramolecular PCSs allowed the refinement of the three-dimensional structure in combination with spin-diffusion and chemical shift data, the intermolecular PCSs allowed the determination of the relative orientations of neighbouring molecules in the crystals. Longitudinal amide N PREs have also been used as structural restraints for the B1 immunoglobulin-binding domain of protein G (GB1) by utilizing six cysteine-EDTA- Cu^{2+} mutants [101]. The relaxation rates were measured using ^{13}C -detected S^3E experiments at 40 kHz MAS.

Measurements of both PREs and PCSs have been performed on SOD using perdeuteration and 100% back-exchange of the amide protons, fast MAS at 60 kHz, and ^1H -detection. This experimental setup allows the rapid measurement of hundreds of site-specific paramagnetic effects, as discussed in section 13.8. Relaxation rates were measured on the Cu-Zn^{2+} -SOD protein with the Cu ion in both the diamagnetic +1 and

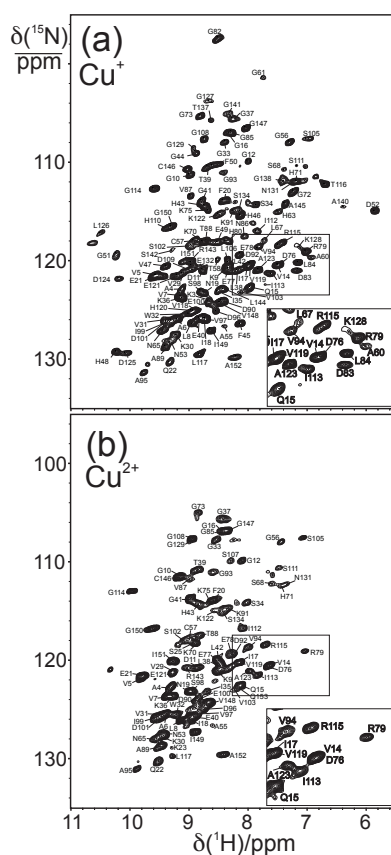


Figure 12.68: Solid-state (H)NH spectra of SOD acquired at 60 kHz MAS. The spectrum in (a) is of the diamagnetic reference protein $\text{Cu}^+-\text{Zn}^{2+}$ -SOD, and in (b) is shown the corresponding spectrum of the paramagnetic form Cu^{2+} - Zn^{2+} -SOD.

paramagnetic +2 oxidation states [11]. The two assigned two-dimensional (H)NH spectra are shown in Figure 12.68 (a) and (b) respectively. For both proteins, amide ^{15}N T_1 and $T_{1\rho}$ relaxation times and ^{13}CO T_1 and $T_{1\rho}$ relaxation times were measured. The PCS values for $^1\text{H}^{\text{N}}$, amide ^{15}N , ^{13}CO , and ^{13}CA were measured by comparing the shifts obtained in the three-dimensional (H)CONH and (H)CANH spectra of the diamagnetic reference (Zn^{2+} -SOD) with a paramagnetic protein Co^{2+} -SOD. The two (H)NH spectra exhibiting a PCS are shown in Figure 12.69. Both sets of structural restraints were used in combination with RFDR distance restraints obtained between the amide protons to provide structural refinement.

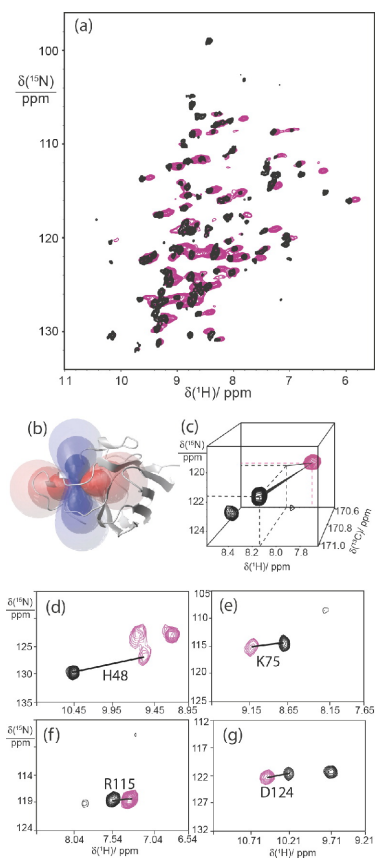


Figure 12.69: Measurement of the PCS values of the protein SOD at 60 kHz MAS. The two-dimensional (H)NH spectra of Co $^{2+}$ -SOD (magenta) and Zn $^{2+}$ -SOD (black) are superimposed in (a). The magnetic susceptibility tensor of Co $^{2+}$ in SOD is represented in (b) as a set of PCS isosurfaces with positive (blue) and negative (red) values of ± 1 , ± 0.25 , and ± 0.1 ppm. The spectrum in (c) is taken from the three-dimensional (H)CONH spectrum and exhibits a PCS in the ^1H , ^{15}N , and ^{13}C dimensions. The spectra in (d)–(g) are taken from the NH planes in the (H)CONH spectrum, and show the shift of the peak due to a PCS in both the ^1H and ^{15}N dimensions. Reproduced with permission from [45]. Copyright (2012) American Chemical Society.

12.7 Key concepts

- Small paramagnetic molecules in solution can be studied using homonuclear through-bond correlation experiments COSY, DQF-COSY, TOCSY, through-space correlation experiments such as 1D saturation-transfer NOE and 2D NOESY, and the heteronuclear correlation experiments HSQC and HMQC. Exchange processes can be measured using EXSY.
- Conventional ^1H -detected methods for paramagnetic proteins in solution can be used to observe nuclei far ($>5\text{--}8 \text{ \AA}$) from the paramagnetic centre. Nuclei closer to the paramagnetic centre cannot generally be observed with these methods, and so are in the so-called blind sphere.
- The use of protonless ^{13}C experiments enables observation closer to the metal, and can reduce the radius of the blind sphere to 5 \AA in some cases.
- For proteins in solution, PCS, PRE, CCR, and RDC measurements can be used for structural restraints.
- Solid-state NMR of paramagnetic materials is best performed using very fast MAS, short recycle delays, and no ^1H -decoupling even in ^1H -containing systems. Cross polarization is rarely useful for obtaining a sensitivity enhancement or establishing heteronuclear correlations.
- Low external magnetic fields, or the use of nuclei with low gyromagnetic ratios give smaller paramagnetic shifts and shift anisotropies, but inevitably result in sensitivity losses. In particular, if isotopic enrichment to improve sensitivity (e.g., with ^6Li) is possible, this is a useful and simple strategy for spectral simplification.
- Care should be used in interpreting a spectrum acquired with a spin-echo sequence, as the band width excited with a 180° pulse is much narrower than that excited with a shorter (less than or equal to 90°) pulse.
- Frequency-stepping experiments or shaped RF pulses may be required to excite the full spectrum.
- Solid-state homonuclear correlation spectra can be acquired using RFDR and EXSY. Heteronuclear correlations can be acquired using TEDOR sequences. Quadrupolar nuclei can be studied using signal-enhancement methods such as RAPT, and two-dimensional techniques to separate the quadrupolar and

SA interactions such as shifting d/p -echo experiments (for $I = 1$) and COASTER (for half-integer spins).

- Solid-state NMR of proteins can be performed using both ^{13}C and ^1H -detected experiments.
- For proteins in the solid state, PCS and PRE measurements can be used for structural restraints.

Chapter 13

Case studies in paramagnetic NMR

13.1 Introduction

The presentation of the theory of paramagnetic NMR in the first part of this review aimed to do two things. Firstly we attempted a completely general description of the paramagnetic properties that affect the NMR spectrum and its interpretation. The result was a full, if sometimes complicated, formulation. Secondly we adapted the resulting formulations to different situations such as different types of metal ion, molecules in solution vs solid state materials, etc., showing how the general treatment may be simplified or modified to provide a more accessible explanation of the features in the NMR spectrum for different systems. In this chapter we now see how these theoretical ideas are translated into practice by presenting some specific case studies in paramagnetic NMR from the literature. The examples comprise studies of small molecules in solution, solid materials such as battery cathodes, metalloproteins both in solution and the solid state, lanthanide-containing systems with interesting luminescent properties, actinide-containing systems, and multi-domain polymers used in pharmaceutical controlled-release formulations. In addition the case studies present the different paramagnetic effects arising from different types of paramagnetic centres, including isolated $3d$ transition-metal ions, coupled clusters of such metal ions, lanthanide ions, actinide ions, and organic radicals.

We attempt to answer questions such as the following: When should we use the EPR and susceptibility formalisms for the paramagnetic shift? In which situations do we need to consider relativistic effects, and which particular relativistic effects are important? What is the relative importance of the contact and pseudo-

contact shifts, under what circumstances do we only need to consider one of these contributions, and how do we use them to obtain information on the structure and/or electronic properties? What is the impact of the paramagnetic relaxation enhancement, how does the consequent broadening compare with bulk susceptibility contributions, and how may these effects be used to obtain structural information? How do all these different effects vary with the metal ion or organic radical, and the type of system? This chapter is not intended to be a comprehensive review of the literature. Rather, the examples presented have been chosen to highlight how these specific paramagnetic effects vary depending on the nature of the paramagnetic centre and the system as a whole.

The following sections in this chapter are organized to separate the case studies according to the nature of the paramagnetic centre. Sections 13.2–13.8 describe systems containing *3d* metal ions, sections 13.9–13.11 lanthanide-containing systems, sections 13.12 and 13.13 recent work on actinide systems, and section 13.14 the paramagnetic effects due to organic radicals, such as those used for DNP.

Section 13.2 summarizes the experimental and theoretical work performed in the EPR-formalism calculation of the paramagnetic shifts of **metallocene complexes** [39, 41]. Here the shifts are dominated by the Fermi-contact contribution, and it is shown how the magnitude and size of the shift vary considerably with the electronic configuration of the *3d* metal ions. This work provided a validation of the EPR formalism for the paramagnetic shift of *3d*-block metal ions, and the contact shifts provided an experimental probe of the electronic structure.

In section 13.3 we examine the theoretical study of **cobalt pyrazolylborates in solution** [465]. In contrast to the metallocenes it is shown here that the larger SO coupling effects of the Co^{2+} ion induce large SO coupling contributions to the total paramagnetic shift, including contact and pseudo-contact shifts due to the ZFS. The calculated shifts were used to correct an error in the original assignment of the experimental NMR spectra, demonstrating the importance of such computations.

In section 13.4 the focus changes to solid materials, with the specific case of layered **LiMO_2 Li-ion cathode materials** [48, 54]. Here the *3d* metal ions induce large shifts at the Li sites that are dominated by the contact interaction, and which vary with the metal ion and coordination geometry of the M–O–Li bonding. It is highlighted how the pathway contribution model can be used to rationalize the shifts in terms of the delocalization and polarization spin-transfer mechanisms. We also see how the combined NMR/DFT study of these materials was used to investigate dynamic distortions in the local structure of the metal binding

site due to the dynamic Jahn–Teller effect.

The next section 13.5 presents a study on a different class of solid materials, the **Prussian blue analogues** [4, 8]. These examples provide a particularly elegant illustration of the polarization mechanism of spin transfer using the observation of contact shifts.

The final case study involving *3d* metal ions in solid materials is presented in section 13.6, and focusses on **Li-ion cathode materials based on LiFePO₄** [30, 54, 466]. Here it is shown how the different metal ions induce very different paramagnetic effects in the NMR spectrum, such as variations in the contact shifts, relaxation enhancements, and inhomogeneous broadening. As in section 13.4 it is shown how the total shifts can be decomposed into distinct pathway contributions which reveal the nature of the spin-transfer mechanism over each bonding pathway. It is also shown how the pathway model can be used to rationalize the NMR spectra for LiMPO₄ materials with mixed metal compositions [30]. By simulating the spectra of these materials and assigning all of the multiple and overlapping resonances, it was shown that these materials form a random distribution of transition metal ions in the metal sites. Finally we describe the first application of the EPR formalism to a solid material, focusing on the pure-composition materials LiMPO₄.

The next two sections describe case studies of proteins that bind *3d* metal ions. Section 13.7 describes a solution NMR study of a **ferredoxin protein comprising Fe₄S₄ clusters** [363]. We focus on the contact shifts of the amino-acid residues that bind directly to the cluster. In particular we examine how the exchange interactions between the metal ions affects the temperature dependence of the shifts, and how the geometry of the bonding between the observed nucleus and the cluster influences the signs and sizes of the contact shifts. In particular the temperature dependence was used to gain insight into the electronic structure of the Fe₄S₄ cluster.

The second biological example is the use of long-range paramagnetic distance restraints for determining the structure of a metalloprotein in the solid state, as described in section 13.8 [45, 461]. Here pseudo-contact shifts and paramagnetic relaxation enhancements are used to refine the three-dimensional structure of **superoxide dismutase (SOD)**.

The next three studies concern the paramagnetic shifts in systems containing lanthanide ions. Section 13.9 presents a case study of the shifts in solid **lanthanide stannates** [64, 68]. It is shown that they are dominated by contact shifts, and that the lanthanide-dependent trends are described well by the Golding–Halton theory. This study therefore provided evidence for a covalent interaction between the *5d* orbitals of the lanthanide

ion and the coordinated ligands.

Section 13.10 presents the study of a lanthanide complex with interesting luminescent applications in **bio-imaging** [467]. The system forms a **supramolecular complex with the guanidinium cation in solution**. The shifts of the cation have a paramagnetic contribution that is due to the pseudo-contact shift, and which is accurately described by the Bleaney theory.

Section 13.11 presents a detailed study of the effects of different lanthanide ions when incorporated into a metal-binding site of the protein **calbindin D_{9k}** [74]. The measured pseudo-contact shifts due to 11 out of 13 of the paramagnetic lanthanides are used to calculate the susceptibility anisotropy parameters, which are shown to agree well with the Bleaney theory. The use of the Bleaney theory then allows the crystal-field splitting parameters to be extracted.

The next two sections concern recent contributions to the use of paramagnetic NMR spectroscopy to study actinide systems. Section 13.12 presents computational work on rationalizing the shifts obtained in three **actinyl tris-carbonate complexes** in solution. The calculations are a sophisticated application of relativistic quantum chemistry to NMR and EPR parameters [91, 92].

Section 13.13 describes an experimental study of five **actinide oxides** by ¹⁷O MAS solid-state NMR [13]. This work demonstrated the first acquisition of high-resolution MAS NMR for these highly radioactive materials, and opened the door to obtaining a better understanding of the behaviour of actinides in solid-state chemistry and materials science. In particular it was used to measure and rationalize trends in the actinide electronic magnetic moments.

Finally we present a recent contribution which describes and applies a new method for measuring domain sizes in materials comprising multiple components, such as **pharmaceutical controlled-release formulations**, in section 13.14 [468]. Here selective doping of the material with a solution of an organic biradical induces a paramagnetic relaxation enhancement which, when combined with spin diffusion, can be used to measure domain sizes on the nm– μ m length scale. This work provided a direct measurement of the domain sizes in these materials, of direct relevance to the pharmaceutical industry.

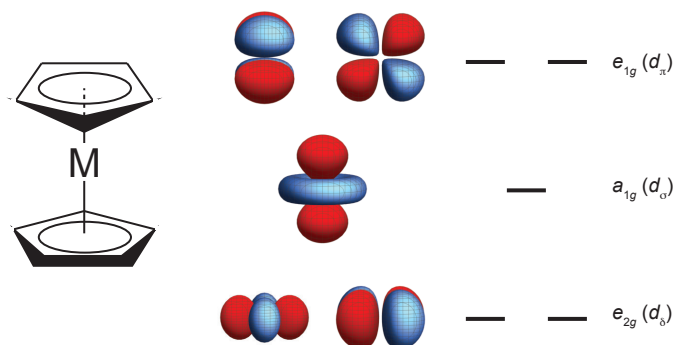


Figure 13.1: The structure and d -orbital splitting of the $3d$ metallocene complexes. The nominal forms of the $3d$ orbitals are also shown. Two sets of symmetry labels are given for each orbital set, corresponding to both the point group of the staggered conformation (D_{5d} : a_{1g} , e_{1g} , and e_{2g}), and the symmetry of the orbitals relative to the five-fold rotation axis (d_σ , d_π , and d_δ).

13.2 Transition-metal metallocenes $M(C_5H_5)_2$

13.2.1 Background

Transition-metal metallocene complexes are classic examples of molecular magnetic materials. They adopt the sandwich structure shown in Figure 13.1 in which one divalent d -block metal ion bonds to two cyclopentadienyl anions ($C_5H_5^-$, or Cp^-) via an η^5 covalent interaction with the conjugated π -orbitals. The nominal forms of the $3d$ orbitals are also shown, along with their energy splitting as predicted from ligand-field theory. More details about the molecular orbitals, including energy level diagrams calculated from hybrid-functional DFT, are given by Xu et al [469]. Discussions about the metallocenes usually consider the two Cp^- ligands to adopt either an eclipsed conformation (point group D_{5h}), or to be staggered (D_{5d}). Energy calculations of the two conformations indicate that the eclipsed forms are the energetically more stable for ferrocene, nickelocene, and vanadocene [470]. However the energy differences between the two conformers are very small, being 3.0, 0.4, and 0.7 kJ mol^{-1} for ferrocene, nickelocene, and vanadocene respectively, and at room temperature, where kT corresponds to 2400 kJ mol^{-1} , the Cp^- ligands rotate freely. Thus, it makes little difference which conformation we examine, and so here we consider the staggered conformation.

Here we compare the experimental ^{13}C and ^1H shifts of the family of metallocene complexes Cp_2V , Cp_2Cr , Cp_2Mn , Cp_2Fe , Cp_2Co , and Cp_2Ni , and show that they can be used, in combination with hybrid

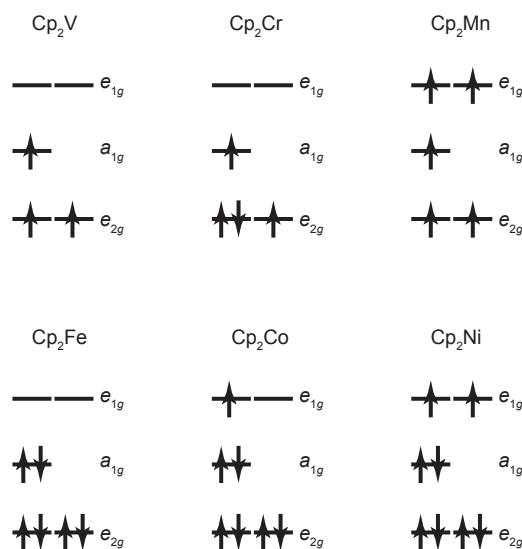


Figure 13.2: The d -orbital splitting and electronic configurations of the metallocene compounds Cp_2M in D_{5d} symmetry. The corresponding electronic terms are ${}^4A_{2g}$ (V), ${}^3E_{2g}$ (Cr), ${}^6A_{1g}$ (Mn), ${}^1A_{1g}$ (Fe), ${}^2E_{1g}$ (Co), and ${}^3A_{2g}$ (Ni).

DFT calculations, as an experimental probe of the electronic structure. The electronic configurations of the d -orbitals in the six metallocene complexes are shown in Figure 13.2. These diagrams are helpful aids for counting the number of unpaired electrons. However, when a system contains unpaired electrons, it is not correct to assume that the energies of the up- and down-spin (α and β) electrons are the same, as implied by these diagrams. We see that Cp_2Fe has a low-spin d^6 configuration, which gives a closed-shell diamagnetic compound. Hence the shifts in this molecule are due entirely to the orbital (i.e. chemical shift) contribution. However the other five compounds are all paramagnetic, and the orbital angular momentum is quenched to first order as the electronic states are either singly or doubly degenerate (i.e. are A or E states). The Mn^{2+} has a half-filled d -shell, and behaves as a spin-only ion, but for the other compounds we expect second-order SO coupling effects to be present due to the mixing of the electronic excited states with the ground state. Furthermore, due to the axial symmetry of the complex, the hyperfine, g -, and ZFS tensors are axially symmetric, i.e. the asymmetry parameters of the hyperfine and g -tensors, η^A and η^g , and the rhombic ZFS parameter E are all zero.

The rationalization of the metallocene shifts has a long history in the literature, beginning with the work of McConnell and Holm who offered two different explanations for the observed proton shifts in nickelocene.

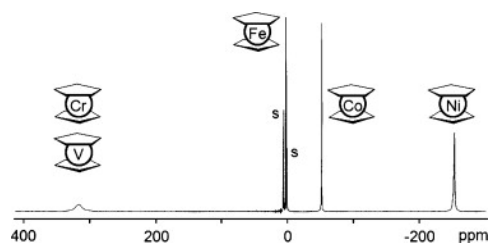


Figure 13.3: Solution ^1H spectrum of a mixture of Cp_2V , Cp_2Cr , Cp_2Fe , Cp_2Co , and Cp_2Ni in toluene- d_8 at 305 K. The peaks labelled S are due to the residual protonated solvent. Reproduced from [41], with permission from Elsevier.

They initially suggested that α electronic spin density is transferred from the Ni d -orbitals into the ligand π orbitals [471], and later reversed this argument to propose a mechanism where β spin density (i.e., spin density of the opposite sign) is instead transferred from the ligand to the partially-occupied d -orbitals [472]. This proposal has since been corroborated with the aid of hybrid DFT calculations [473].

13.2.2 Paramagnetic shifts

There have been numerous NMR studies of metallocene complexes over the years, both in solution [474–479] and in the solid state [3, 480–482]. A ^1H spectrum of a solution of a mixture of the five metallocene compounds Cp_2V , Cp_2Cr , Cp_2Fe , Cp_2Co , and Cp_2Ni is shown in Figure 13.3 [41]. The variation of the chemical shift with the metal ion, 600 ppm, is very large compared to the standard 10 ppm range of diamagnetic ^1H shifts. The only compound with a shift that falls into this standard region is the diamagnetic Cp_2Fe , which exhibits both a small shift and narrow line. The large value of the shifts from the other compounds, which has recently been discussed by Kaupp and Köhler [41], is due to unpaired electron density that is transferred between the metal ion and the Cp^- ligands. The ^{13}C and ^1H orbital shifts are both approximately constant across the series of compounds, with the result that the trend in the total chemical shift matches that of the Fermi-contact shift. One striking feature that is immediately apparent is that in the compounds Cp_2V and Cp_2Cr , the unpaired electrons of which occupy the e_{2g} and a_{1g} orbitals, both give large positive paramagnetic shifts, whereas Cp_2Co and Cp_2Ni , the unpaired electrons of which reside in the e_{1g} orbitals, both give large negative shifts.

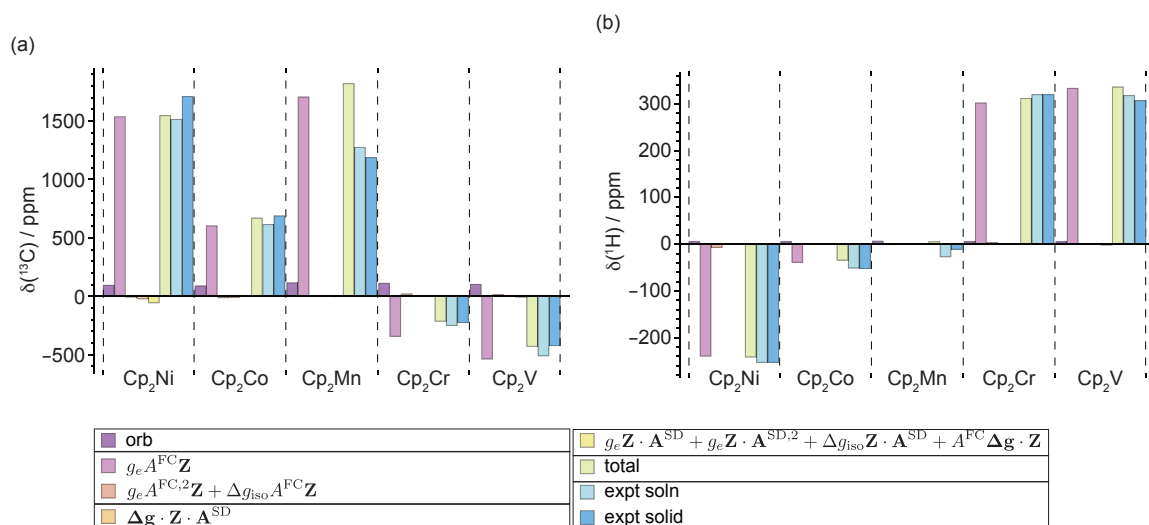


Figure 13.4: Breakdown of the contributions to the total ^{13}C and ^1H chemical shifts of selected metallocenes determined by first-principles calculations (with PBE0), and comparison with the experimental shifts, at 298 K. The ^{13}C shift contributions are shown in (a), and the ^1H shifts are shown in (b). The calculated shift contributions for Cp_2V , Cp_2Cr , Cp_2Mn , and Cp_2Ni are taken from Refs. [39] and [41], and the calculated shifts for Cp_2Co are taken from Refs. [483] and [41]. The experimental ^{13}C chemical shifts in solution are taken from Ref. [475] (Ni), [477] (Co), [476] (Mn), [474] (Cr), and [479] (V). The experimental ^1H chemical shifts in solution are taken from Refs. [474] (Ni), [477] (Co), and [478] (Mn, Cr, V). All solid-state chemical shifts are taken from Ref. [481], with the exception of the ^{13}C shift for Cr which is taken from Ref. [483].

The isotropic paramagnetic shift is calculated from Equation 4.109 to be

$$\delta_{\text{iso}}^{\text{S}} = \frac{\mu_{\text{B}}}{3\hbar\gamma_{\text{I}}} \text{Tr}[\mathbf{g} \cdot \mathbf{Z} \cdot \mathbf{A}], \quad (13.1)$$

where the cross-terms between the different components of \mathbf{g} , \mathbf{Z} , and \mathbf{A} are given in Table 5.1. In total there are nine contributions to the total shift, of which four are a contact shift and four a pseudo-contact (dipolar) shift, with the remaining term being the orbital shift. The values of the different terms have been calculated [39, 483], and tabulated by Kaupp and Köhler [41], and the results are presented here in Figure 13.4. The terms are grouped together as follows. Firstly the orbital shift is separated from the other terms, in order to isolate the effect of the unpaired electrons. Secondly three of the contact-shift terms are separated into two groups, corresponding to the NR Fermi-contact shift proportional to $g_e A^{\text{FC}} \mathbf{Z}$, and an SO contribution $g_e A^{\text{FC},2} \mathbf{Z} + \Delta g_{\text{iso}} A^{\text{FC}} \mathbf{Z}$, where A^{FC} is given by Equation 2.171, which are non-zero even in the absence of the ZFS. Thirdly there is a single term in the PCS which is non-zero in the absence of a ZFS: $\Delta \mathbf{g} \cdot \mathbf{Z} \cdot \mathbf{A}^{\text{SD}}$,

Compound	g-tensor			Ref.	ZFS tensor	
	g_{\parallel}	g_{\perp}			D / cm^{-1}	Ref.
Cp ₂ Ni	2.00	2.06 ± 0.10, 2.11 ± 0.03		[484, 485]	25.6–33.6	[484–486]
Cp ₂ Co	2.012	1.981–1.994		[487]	—	—
Cp ₂ Mn	1.99–2.01	1.99–2.01		[488]	0.25–0.50	[489]
Cp ₂ Cr	2.012	1.988		[490]	–15.1	[491]
Cp ₂ V	2.002, 2.002 ± 0.001	1.99, 1.990 ± 0.002		[492, 493]	0.83–2.7	[492–494]

Table 13.1: Experimental principal values of the g - and ZFS tensors for selected metallocene complexes.

where A^{SD} is given by Equation 2.172. Finally the remaining four terms are grouped together. In general whilst all the paramagnetic terms change in size with the introduction of the ZFS, the defining feature of the last group is that all the terms in it are only non-zero if the ZFS is also non-zero. The shift contributions were all computed using calculated values for the ZFS anisotropy D and g -shift tensor, and it is these values that are presented in Figure 13.4 [39, 483]. However there are two exceptions. The calculated values of the ZFS anisotropy for both Ni and Cr, 104.4 and -2.0 cm^{-1} , were shown to be far from the experimental values of 30 and -15.1 cm^{-1} , being severely over- and underestimated respectively. For this reason the corresponding ZFS contributions to the paramagnetic shift for both ^{13}C and ^1H were recalculated accordingly [41]. Whilst the presentation of these ‘mixed results’ appears to be inconsistent, we should remind ourselves that the ZFS contributions to the shift, which are only non-zero if we include the ZFS, are generally affected to a proportionately greater extent than the other contributions in the high-temperature limit $|D| < kT$ (kT is approximately 200 cm^{-1} at the temperatures under consideration). Therefore we gain a better picture of the relative importance of the different contributions if we adjust the ZFS contributions accordingly.

Inspection of Figure 13.4 immediately shows that the only significant contributions to both the ^{13}C and ^1H chemical shifts are the orbital and NR Fermi-contact terms, with the latter being dominant, i.e. the effect of the SO coupling, via the g -shift, ZFS, and hyperfine tensor, is negligible. This is also reflected in the comparatively small values observed experimentally for the g -shift and ZFS tensor parameters, which are given in Table 13.1. The g -shift and ZFS tensor parameters are particularly small for Cp₂Mn, due to the d -shell being half filled resulting in the quenching of the SO coupling to second-order. The largest ZFS contribution is for Cp₂Ni, as the Ni²⁺ ion has the largest D value, and the smallest is for Cp₂Co, where the electronic spin $S = 1/2$ results in the complete absence of the ZFS interaction.

Compound	$\delta_{\text{FC}}(^{13}\text{C}) / \text{ppm}$	$\rho^{(\alpha-\beta)}(^{13}\text{C}) / 10^{-3} \text{a.u.}$	$\delta_{\text{FC}}(^1\text{H}) / \text{ppm}$	$\rho^{(\alpha-\beta)}(^1\text{H}) / 10^{-3} \text{a.u.}$
Cp ₂ Ni	1537.1	9.73	-239.7	-1.52
Cp ₂ Co	602.9	5.09	-38.9	-0.33
Cp ₂ Mn	1706.1	6.17	-0.8	0.00
Cp ₂ Cr	-342.9	-2.17	302.1	1.91
Cp ₂ V	-537.2	-2.72	333.4	1.69

Table 13.2: Calculated Fermi-contact shifts and transferred electronic spin densities for ¹³C and ¹H in selected metallocenes [41].

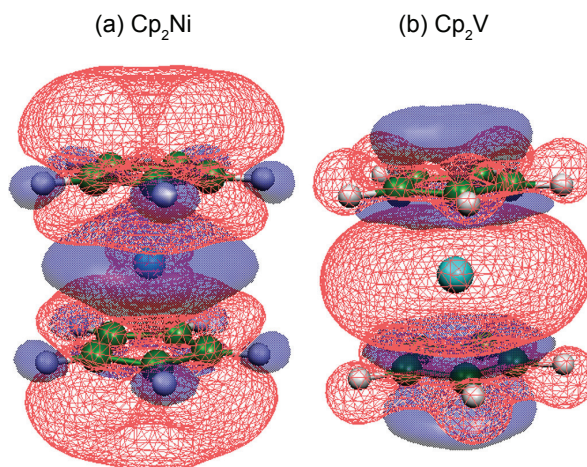


Figure 13.5: The unpaired electronic spin density in (a) Cp₂Ni and (b) Cp₂V. Red and blue isosurfaces indicate positive and negative spin density respectively, and are evaluated at $\pm 10^{-4}$ a.u. Adapted from [483], with the permission of AIP Publishing.

13.2.3 Interpretation

We have seen that the Fermi-contact coupling constant is proportional to the unpaired electronic spin density in the *s*-orbital of the nucleus $N \rho^{(\alpha-\beta)}(N)$, and so the Fermi-contact shift has a size that is also proportional to $\rho^{(\alpha-\beta)}(N)$ and has the same sign. This is seen in Table 13.2, where the Fermi-contact shifts and the associated electronic spin densities are given. Visual representations of the electronic spin density are also shown for Cp₂Ni and Cp₂V in Figure 13.5 (a) and (b) respectively [483]. Here we can see immediately that for both complexes the spin densities at the ¹³C and ¹H nuclei have opposite sign. This effect is reproduced for all the paramagnetic metallocene complexes, and results in the signs of the ¹H Fermi-contact coupling constants (and shifts) having opposite signs to the ¹³C coupling constants (and shifts). This change in sign is due to spin polarization of the C–H σ bond by the unpaired electron density in the π orbital [495].

We now focus on rationalizing the ^{13}C Fermi-contact shifts, concentrating on the two particular cases of Cp_2Ni and Cp_2V . The ^{13}C Fermi-contact shift of Cp_2Ni is large and positive, whereas the corresponding shift for Cp_2V has smaller magnitude and is negative. The corresponding opposite sign in the ^{13}C spin densities, which is clearly seen in Figure 13.5 [483], can be explained by decomposing total Fermi-contact coupling constants into contributions from the individual molecular orbitals, to determine which of the two spin-transfer mechanisms proposed by McConnell is correct [473]. This analysis also explains why Cp_2V has a smaller shift than Cp_2Ni , despite having more unpaired electrons.

In Cp_2Ni the two e_{2g} orbitals (of d_δ symmetry) and the single a_{1g} orbital (of d_σ symmetry) are fully occupied, and each of the two e_{1g} orbitals (of d_π symmetry) has a single unpaired electron, as shown in Figure 13.2. Aquino et al. showed that the two d_π orbitals do indeed donate α electron spin density into unoccupied orbitals of the Cp^- ligands according to McConnell's first mechanism, resulting in a positive spin density at ^{13}C and a positive Fermi-contact shift [473]. However this mechanism only accounts for approximately 15% of the total ^{13}C Fermi-contact shift, and so is not the dominant effect. The more important contribution is the donation of β spin density from the occupied ligand π orbitals into the d_π of the Ni^{2+} , according to McConnell's second mechanism. The corresponding reduction in β spin density in the ligand π system leaves an excess of α spin density, which in turn polarizes the σ orbitals, giving a positive ^{13}C Fermi-contact shift. This second effect accounts for the remaining 85% of this shift.

There is an alternative description of the electron transfer due to McConnell's second mechanism in terms of the difference between the molecular orbitals (MOs) containing the α and β electron spins. Although this description gives us a superficially different explanation of the process, the underlying chemistry is the same. The important idea is that the MOs containing the α and β electrons are not the same, and have different energies. As we have already remarked, this is a feature of the electronic structure that is missing from the simplified d -orbital splitting diagrams shown in Figure 13.2. Of particular relevance to metallocenes, the metal d -orbitals lie close in energy to the π -orbitals of the Cp^- ligands. For Cp_2Ni , the lower energy, bonding, and occupied (formally ligand-based) β e_{1g} MOs lie close in energy to the α d -orbitals (formally the Ni d -orbital-dominated MOs). The coefficient of the occupied e_{1g} d_π^α orbital (containing the α electron) in the e_{1g} MO wavefunction is different to that of the d_π^β orbital, and it is this inequality that results in the difference in α and β electronic spin densities on both Ni^{2+} and the ligand. A similar explanation is invoked to explain the polarization mechanism involving O $2p$ orbitals in section 13.4.2.

The case of Cp_2V is much more complex. Here, as seen in Figure 13.2, the V^{2+} ion formally has three unpaired $3d$ -electrons, one each in the two e_{2g} (d_δ) orbitals and single a_{1g} (d_σ) orbital. Aquino et al. showed that the contribution from the two d_δ orbitals to the Fermi-contact coupling constant is very small, with a magnitude of 7% of the total [473]. In order to properly understand the negative shift, we need to include a number of contributions. Firstly there is some transfer of α electron spin from the V^{2+} d_σ into the ligand σ orbitals, according to McConnell's first mechanism, giving a positive Fermi-contact coupling constant and shift. Secondly donation of β spin density from the ligand to the metal d_σ results in excess α spin density in the σ valence orbitals at the ^{13}C , which in turn polarizes the ^{13}C $1s$ orbitals with β spin density. This gives a large negative contribution to the Fermi-contact shift. Thirdly there are further negative contributions from non-nearest-neighbour σ orbitals and polarization of the π orbitals [473]. The overall Fermi-contact shift is a sum of these contributions, and turns out to be negative overall. We can also rationalize the smaller magnitude of the shift relative to that of Cp_2Ni . In Cp_2V only one unpaired electron (the d_σ) contributes to the Fermi-contact interaction, and there is significant cancellation of the different contributions, in Cp_2Ni there are two unpaired electrons (the d_π) and the two main contributions to the shift reinforce each other.

13.2.4 The delocalization error

The final point that we make here concerns a practical point in the calculation of the Fermi-contact shift. Accurate values of the Fermi-contact shift can only be obtained if we calculate the transfer of the electronic spin density correctly, i.e. if we treat the delocalization of the electrons properly. Failure to do so results in a so-called *delocalization error*.

In practice calculations of the paramagnetic shift employ some formulation of DFT to describe the spin densities. The spin densities can vary strongly with the choice of exchange–correlation functional, potentially leading to a large range of Fermi-contact shifts! The resulting delocalization errors are well known, and have been observed in a range of systems including metallocenes [496], acetylacetonato complexes [496, 497], and solid Li-ion battery materials [30, 53, 56–59, 498, 499].

In particular the calculation of the spin density donated from the ligand to the metal, such as that observed in metallocene complexes, is particularly sensitive to delocalization errors [500]. The general trend is that this electron transfer is underestimated when calculated using pure Hartree–Fock methods, which result in electrons that are too strongly localized, and is overestimated when calculated with non-hybrid functionals,

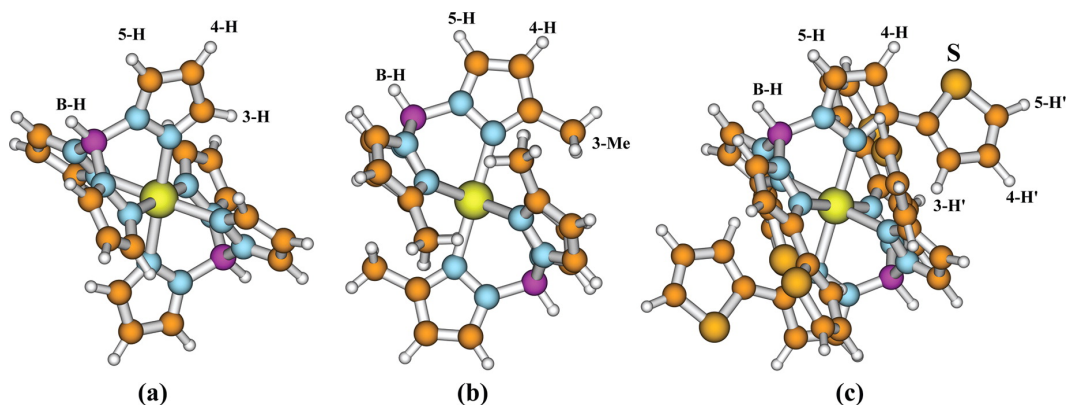


Figure 13.6: Structures of the high-spin Co^{2+} pyrazolylborate complexes. The three complexes are referred to as (a) system 1, (b) system 2, and (c) system 3. For each complex the chemically distinct ^1H environments are labelled. Reproduced with permission from [465]. Copyright (2015) American Chemical Society.

which result in electrons that are too extensively delocalized. The use of hybrid functionals results in a situation that is between these two extremes, and their use is therefore very important in DFT calculations of Fermi-contact shifts, as described in section 13.4.

13.3 Co(II) pyrazolylborate complexes in solution

13.3.1 Background

The paramagnetic NMR properties of the metallocene complexes in the previous section are dominated by non-relativistic effects, with the isotropic shift being dominated by the Fermi-contact interaction. However this is not a general observation for all small molecular complexes. We illustrate this point here by presenting a combined experimental and theoretical study of three Co^{2+} complexes, the structures of which are shown in Figure 13.6. These three molecules are referred to as systems 1 (a), 2 (b), and 3 (c). The ^1H shifts of these complexes have been measured in solution by Długopolska et al. [501], and more recently calculated by Rouf et al. [465].

The Co^{2+} ion is in a slightly-distorted octahedral coordination environment, and has a high-spin electronic configuration which can be approximated by the orbital splitting diagram shown in Figure 13.7. The electronic ground state therefore has spin $S = 3/2$, and can be labelled using the term $^4T_{1g}$. In this

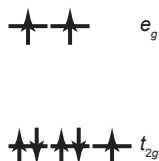


Figure 13.7: Splitting and occupancy of the Co^{2+} d -orbitals in an octahedral coordination site.

distorted coordination environment the Co^{2+} is expected to have larger SO coupling effects than seen in the metallocenes, which in turn lead to greater SO coupling contributions to the paramagnetic shifts.

13.3.2 The EPR tensor parameters

Rouf et al. calculated the total hyperfine tensor using DFT, and the g - and ZFS tensors using the ab initio CASSCF and NEVPT2 methods [465]. Both the g -shift and ZFS tensor parameters are larger than for the metallocenes, with system 1 giving a total isotropic g -value of 2.119, and ZFS anisotropies of $D = -112.3 \text{ cm}^{-1}$ and $E = -15.7 \text{ cm}^{-1}$. In particular the large D value is expected to give a substantial contribution to both the contact and pseudo-contact shift.

13.3.3 Paramagnetic shifts

The paramagnetic shift is given by Equation 13.1, with the components listed in Table 5.1. The total calculated shifts of the three systems are compared with the experimental values in Figure 13.8, along with the breakdown of the former into the different components. There is a large degree of variation between the systems, and for the individual ^1H sites within each complex, but there are some general trends that we can establish. Firstly there are generally only three significant contributions to each paramagnetic shift, which are the contact-shift term $g_e A^{\text{FC}} \mathbf{Z}$, and the two PCS contributions $g_e \mathbf{Z} \cdot \mathbf{A}^{\text{SD}}$ and $\Delta \mathbf{g} \cdot \mathbf{Z} \cdot \mathbf{A}^{\text{SD}}$. The two PCS terms are particularly significant in gauging the contribution of the SO coupling, as both are only non-zero if we account for the ZFS or, for $\Delta \mathbf{g} \cdot \mathbf{Z} \cdot \mathbf{A}^{\text{SD}}$, g -anisotropy. The relatively large values of the ZFS parameters can therefore be attributed to the significant PCS.

The variation of the shifts immediately illustrates the difficulties of assigning NMR spectra of paramagnetic molecules without using calculations. If we examine the contact shifts for system 1 in more detail (Figure 13.8 (a)), we see that the the values for 3-H, 4-H, and 5-H are similar, falling in the range 30–40

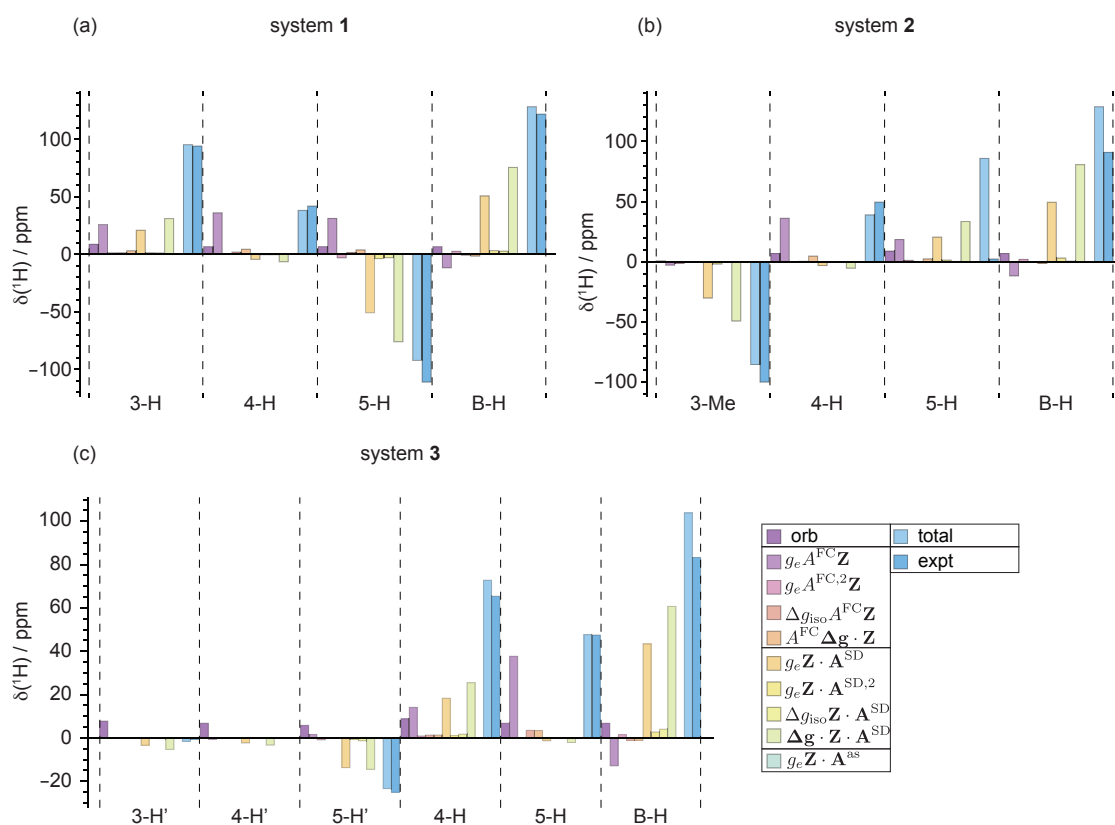


Figure 13.8: Breakdown of the contributions to the total ^1H chemical shifts of the three Co(II) pyrazolylborate complexes determined by first-principles calculations, and the comparison with the experimental shifts. The shifts for system 1 are shown in (a), system 2 in (b), and system 3 in (c). The calculated and experimental shifts are taken from Ref. [501] and [465].

ppm. This cannot be intuitively explained simply by reference to the structure in Figure 13.6 (a), as 3-H is nominally three bonds from the Co^{2+} ion, whereas 4-H and 5-H are both four bonds away. This observation emphasizes that the size of the unpaired electron transfer depends on more complicated factors than the number of bonds involved, but also on the coordination geometry, as all these factors influence the overlap between the relevant orbitals. The overall shifts cannot be assigned correctly by considering only the contact shift, as the two PCS contributions are significant. This is particularly important for 5-H in system 1, as the negative PCS is larger in magnitude than the positive contact shift, resulting in an overall shift that is negative.

System 2 is a modification of system 1 where the 3-H has been replaced by a methyl group, which is labelled 3-Me. If we compare the chemical shifts obtained from system 2, in Figure 13.8 (b), with those in system 1 we see some interesting similarities and differences. The total shift, and associated contributions, for 4-H and B-H have similar values in the two systems, although the experimental shift of the latter is significantly less positive in system 2. These observations indicate that 4-H and B-H have similar chemical environments in the two complexes, and that the two protons occupy similar spatial positions with respect to the Co^{2+} ion. However we see significant differences for 5-H in the two complexes. In system 2, there is a comparatively poor agreement between experiment and calculation, but the significant reduction in the magnitude of the experimental shift compared to system 1 indicates that the two environments are significantly different. According to the calculations this is because the PCS is now positive, rather than negative, indicating that the spatial geometry of the ring containing 5-H is different.

System 3 is a significantly larger complex in which the 3-Me is replaced by a $-\text{C}_4\text{H}_3\text{S}$ ring. The three protons 3-H', 4-H', and 4-H' all have smaller shifts than the other protons, which is due to the greater distance and bond separation of the former from the metal ion. Nevertheless we see that both the contact shift and PCS are still significant, which in the case of the former indicates that the spin transfer still persists over more than five bonds. The significant PCS is due to the long-range nature of the dipolar coupling.

13.4 Layered transition-metal oxides LiMO_2

13.4.1 Background

Paramagnetic materials are of particular interest in the field of energy storage as, for example, they form key constituents of Li-ion battery electrodes. The electrochemical properties of a battery are driven by the redox

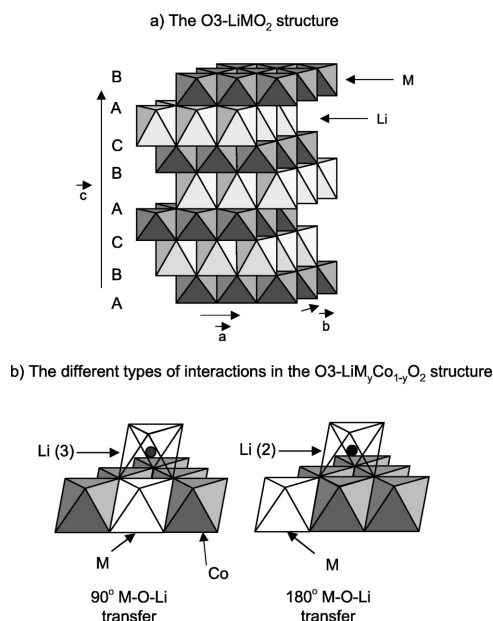


Figure 13.9: Structure of the O3-LiMO₂ materials. The alternating LiO₆ and MO₆ layers are shown in (a). In (b) are shown the two Li sites Li(2) and Li(3) in the dilute materials LiM_yCo_{1-y}O₂ that exhibit large contact shifts. Reproduced with permission from [48]. Copyright (2003) by the American Physical Society.

processes of the metal ions in the electrodes, and so understanding the changes to the local structure of metal ion and the electron-spin transfer to the surrounding atoms is key to gaining insight into the mechanisms of charge and discharge, and how these processes both function and fail. Many of these materials are either paramagnetic in their pristine phases, or become paramagnetic on electrochemical cycling, and so paramagnetic solid-state NMR is an indispensable method for studying them.

Layered lithium transition-metal oxide materials of the form LiMO₂ are a promising class of cathode materials. The diamagnetic material LiCoO₂, which was first used as a cathode by Goodenough et al. [502], has been used since 1991 in commercial Li-ion batteries by Sony. Considerable effort has been invested in using other metal ions in these materials which have lower toxicity and are cheaper than the Co³⁺ ion, or that improve electrochemical properties such as the capacity. These materials adopt a layered O3 (ordered rock salt) structure comprising alternating layers of edge-sharing LiO₆ and MO₆ octahedra, as shown in Figure 13.9 (a) [48]. Here we present the influence of three species of metal ion on the ⁷Li chemical shifts, namely Cr³⁺, Co³⁺, and Ni³⁺, as initially described by Carlier et al. [48] and later elaborated on by Middlemiss et

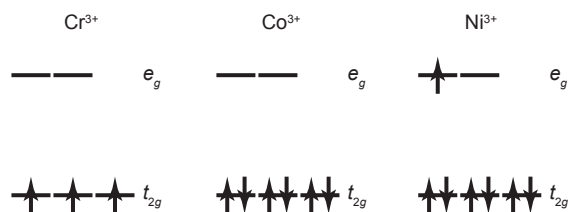


Figure 13.10: The d -orbital splitting and occupancy of the Cr^{3+} , Co^{3+} , and Ni^{3+} metal ions in the octahedral coordination sites of $\text{LiM}_y\text{Co}_{1-y}\text{O}_2$.

al. [54]. The electronic configurations of these three metal ions in an octahedral environment are given in Figure 13.10. The Cr^{3+} ion has a paramagnetic term ${}^4A_{2g}$ corresponding to a quenched singly-degenerate orbital state with spin $S = 3/2$, and the Co^{3+} ion has a low-spin diamagnetic configuration of ${}^1A_{1g}$. In both cases the non-degenerate spatial configurations result in no significant distortions from the nominal octahedral symmetry. The Ni^{3+} ion, on the other hand, has a doubly-degenerate spatial term of ${}^2E_{2g}$, which we expect to result in a Jahn–Teller distortion parallel to the C_4 rotation axis of the metal site. It will be seen that the ${}^7\text{Li}$ solid-state NMR combined with hybrid DFT calculations can be used to detect such a distortion.

13.4.2 Spin-transfer pathways in $\text{LiM}_y\text{Co}_{1-y}\text{O}_2$

In the oxide materials with a single transition-metal species the total paramagnetic shift is dominated by the contact interaction with the six nearest-neighbour (nn) metal ions via a 90° M–O–Li electron transfer, and the six next-nearest-neighbour (nnn) metal ions via 180° M–O–Li electron transfers, the bonding geometries of which are shown in Figure 13.9 (b). Carlier et al. [48] and Middlemiss et al. [54] investigated these individual pathways by DFT calculations on the mixed-metal species $\text{LiCr}_{1/8}\text{Co}_{7/8}\text{O}_2$ and $\text{LiNi}_{1/8}\text{Co}_{7/8}\text{O}_2$, in which the concentration of the metal ion is diluted. This dilution enables us to obtain experimental shifts from each of these individual isolated pathways, which can then be compared to the calculated values. We can then rationalize these individual contributions directly according to the Goodenough–Kanamori rules. For both materials the ${}^7\text{Li}$ solid-state NMR spectrum contains three peaks with distinct shifts, which are given in Table 13.3. Both mixed materials have a shift at 0 ppm which can be assigned by comparison with the diamagnetic LiCoO_2 as being due to the Li(1) site for which all the nn and nnn metal ions are Co^{3+} . Each mixed material also has two additional shifts, one positive and one negative, which are due to the Li(2) and

Material	Shift / ppm	Sign of calculated spin density	Assignment	Ref.
LiCr _{0.10} Co _{0.90} O ₂	35	+	Li(3)	[503]
	0		Li(1)	
	-70	-	Li(2)	
LiCoO ₂	0		All	[504]
LiNi _{0.30} Co _{0.70} O ₂	110	+	Li(2)	[505]
	0		Li(1)	
	-15	-	Li(3)	

Table 13.3: Experimental ⁷Li chemical shifts observed in three LiM_yCo_{1-y}O₂ layered oxides, with assignments.

Li(3) sites illustrated in Figure 13.9 (b). Density-functional theory calculations were helpful in confirming the assignments of these shifts.

The dominant contributions to the chemical shifts in these materials is the contact shift. The important contributions in the EPR formalism are expected to be those that are proportional to the NR Fermi-contact coupling constant, namely $g_e A^{\text{FC}} \mathbf{Z}$, $\Delta g_{\text{iso}} A^{\text{FC}} \mathbf{Z}$, and $A^{\text{FC}} \Delta \mathbf{g} \cdot \mathbf{Z}$ with the term due to $A^{\text{FC},2}$ being negligible. However it is more convenient to express the contact shift δ^{con} in terms of the susceptibility formalism in Equation 7.126,

$$\delta^{\text{con}} = \frac{\chi}{\mu_0 \mu_B g_e \hbar \gamma_I} \left(\frac{\mathcal{A}^{\text{FC}}}{2S} \right), \quad (13.2)$$

where $A^{\text{FC}} = \mathcal{A}^{\text{FC}} / (2S)$, and the SO coupling effects giving rise to the g -shift and ZFS, as well as the exchange interactions, are contained in the isotropic magnetic susceptibility χ . Assuming a Curie–Weiss temperature expression for the susceptibility we obtain

$$\delta^{\text{con}} = \frac{\mu_{\text{eff}}^2}{3\mu_B g_e \hbar \gamma_I k(T - \Theta)} \left(\frac{\mathcal{A}^{\text{FC}}}{2S} \right). \quad (13.3)$$

Hence the size of the contact shift is proportional to the size of the unpaired electronic spin density transferred to the Li 2s orbital, and both quantities have the same sign. When more than one metal ion i transfers spin density to the nucleus N via a pathway P_i , the total spin density $\rho^{(\alpha-\beta)}(N)$ is the sum of the individual contributions $\rho_{P_i}^{(\alpha-\beta)}(N)$ [54]:

$$\rho^{(\alpha-\beta)}(N) = \sum_i \rho_{P_i}^{(\alpha-\beta)}(N), \quad (13.4)$$

which in turn means that the total contact shift can be written as the sum of the individual pathway contribu-

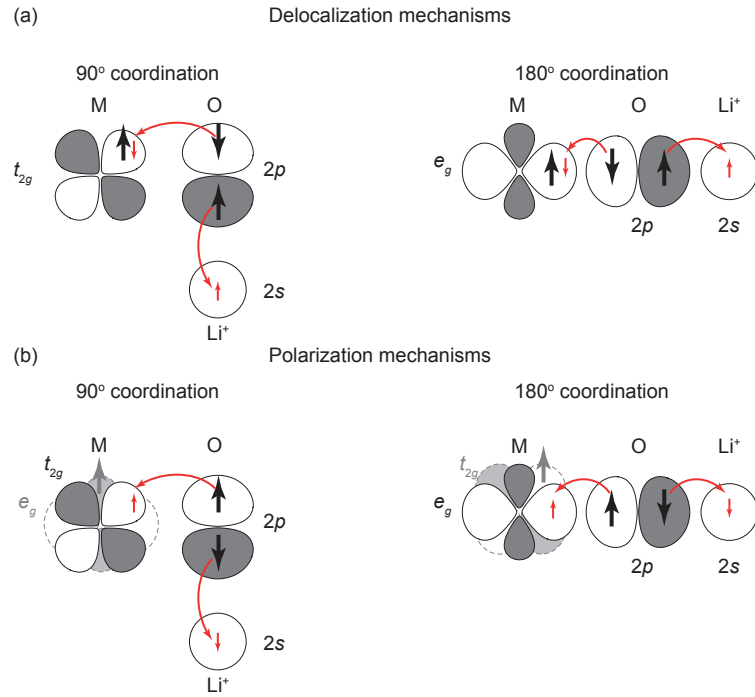


Figure 13.11: The different M–O–Li spin-transfer mechanisms in $\text{LiM}_y\text{Co}_{1-y}\text{O}_2$. The delocalization mechanisms for 90° and 180° are shown in (a), and the corresponding polarization mechanisms are shown in (b).

tions $\delta_{P_i}^{\text{con}}$ as follows:

$$\delta^{\text{con}} = \sum_i \delta_{P_i}^{\text{con}}, \tag{13.5}$$

where each contribution is given by an expression such as in Equation 13.2 or 13.3.

In section 7.9 we saw that the sign of the transferred electronic spin density, and therefore the sign of the contact shift, can be deduced from the Goodenough–Kanamori rules for 90° and 180° M–O–Li bonding geometries. Here we must distinguish between electron delocalization and polarization transfer mechanisms. In the former the metal 3d-orbital containing the unpaired electron overlaps with the Li 2s via an O 2p-orbital, resulting in a positive electron density at Li, whereas in the latter the metal 3d and Li 2s overlap with different orthogonal O 2p-orbitals, which results in a polarization of negative electron density at Li. These two mechanisms are illustrated in Figure 13.11 for both 90° and 180° M–O–Li bonding geometries. The two delocalization mechanisms shown in Figure 13.11 (a) occur for the 90° geometry when the unpaired electron

is in the metal t_{2g} , and the 180° geometry when the unpaired electron is in the metal e_g . The two polarization mechanisms shown in Figure 13.11 (b) are operative for the 90° geometry when the unpaired electron is in the metal e_g , and the 180° geometry when the unpaired electron is in the metal t_{2g} .

In the case of $\text{LiCr}_{1/8}\text{Co}_{7/8}\text{O}_2$ the unpaired electrons reside only in the t_{2g} orbitals, which indicates that the 90° Cr–O–Li results in spin delocalization, and the 180° Cr–O–Li in spin polarization. The delocalization and polarization mechanisms can be readily interpreted by using simple MO theory [5]. The delocalization mechanism for the Cr^{3+} ion results from the anti-bonding MO formed from the half-occupied t_{2g} d -orbital and the nearby (overlapping) O $2p$ -orbital, which results in a direct transfer of spin density to the $2p$ -orbital, and thus into the adjacent Li $2s$ orbital. The polarization mechanism results from a bonding MO involving the overlap of the empty e_g orbital with the relevant (overlapping) filled O $2p$ -orbital. The spin density in this case results from the different coefficients of the atomic orbitals in the α and β MOs, with an increased contribution of the coefficient of the e_g orbital to the α MO being driven by the exchange interaction, which serves to lower the overall energy of the system. Hence the spin density transferred to the two lithium sites Li(2) and Li(3) is negative and positive respectively. This is indeed the case as shown by the electron spin density map calculated by Carlier et al. in Figure 13.12 (a) [48]. The exact orbitals involved for each transfer are shown in Figure 13.13. Hence the shifts of 35 ppm and -70 ppm can be assigned to Li(3) and Li(2) respectively, as shown in Table 13.3.

In $\text{LiNi}_{1/8}\text{Co}_{7/8}\text{O}_2$ the unpaired electron resides in the e_g orbital, and so we expect the spin-transfer mechanisms to be different. For the 90° bonding geometry the half-filled e_g polarizes the t_{2g} orbitals, resulting in negative spin density on the Li $2s$ as shown in Figure 13.11 (b), which now gives a negative contact shift for Li(3). For the 180° bonding geometry the situation is more complicated, as there are two competing transfer mechanisms. Firstly the half-filled e_g delocalizes positive spin density into the Li $2s$, as shown in Figure 13.11 (a). However this same e_g orbital also polarizes the *other* unfilled e_g orbital, resulting in an additional transfer of negative spin density to Li, as shown in Figure 13.11 (b). The overall spin density is due to the combination of these two transfers. It turns out that the electron delocalization is the dominant process, giving a positive spin transfer and therefore a positive contact shift for Li(2), as shown by the spin-density map in Figure 13.12 (b) [48]. The relevant orbital interactions are summarized in Figure 13.13.

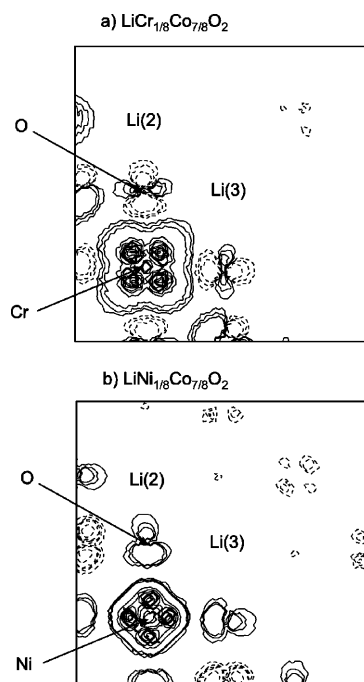


Figure 13.12: Calculated spin-density transfer map in a M–O–Li plane in the $\text{LiM}_y\text{Co}_{1-y}\text{O}_2$ materials, for Cr^{3+} (a) and Ni^{3+} (b). The DFT calculations were performed using the generalized gradient approximation (GGA) in the Vienna ab initio Simulation Package (VASP). Positive and negative contours are shown with solid and dashed lines respectively. Reproduced with permission from [48]. Copyright (2003) by the American Physical Society.

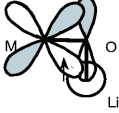
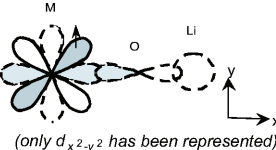
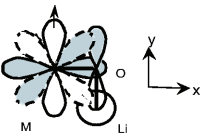
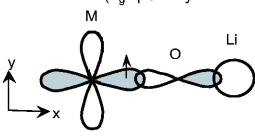
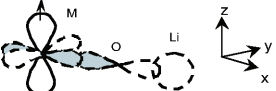
M in $\text{LiM}_{1/8}\text{Co}_{7/8}\text{O}_2$	involved spin orbital	M-O-Li angle	M-O-Li transfer	resulting sign on Li
Cr^{3+} (t_{2g}^3)	t_{2g}	90°	delocalization (t_{2g} - p_π -s hybridization) 	positive
	t_{2g}	180°	polarization of the e_g - p_σ -s orbitals  (only $d_{x^2-y^2}$ has been represented)	negative
Ni^{3+} ($t_{2g}^6 e_g^1$)	e_g	90°	polarization of the t_{2g} - p_π -s orbitals  (only $d_{x^2-y^2}$ and d_{xy} are shown)	negative
		180°	delocalization (e_g^* - $p\sigma$ -s hybridization)  (only $d_{x^2-y^2}$ is shown)	positive
	e_g	180°	polarization of the e_g - p_σ -s orbitals  (only the polarization of $d_{x^2-y^2}$ - p_σ -s by the d_{z^2} unpaired electron is shown)	negative

Figure 13.13: Illustration of the orbitals involved in the spin-transfer mechanisms in the $\text{LiM}_y\text{Co}_{1-y}\text{O}_2$ for the specific cases of Cr^{3+} and Ni^{3+} . Reproduced with permission from [48]. Copyright (2003) by the American Physical Society.

Material	M–O bond lengths / Å		$\mu_{\text{eff}}/\mu_{\text{B}}$	Θ / K
	Short (S)	Long (L)		
$\text{LiCr}_{1/8}\text{Co}_{7/8}\text{O}_2$	1.96	1.97	3.87	0
$\text{LiNi}_{1/8}\text{Co}_{7/8}\text{O}_2$	1.89	2.02	1.73	0

Table 13.4: The M–O bond lengths obtained from the Hyb20 DFT calculations, and magnetic parameters for $\text{LiM}_y\text{Co}_{1-y}\text{O}_2$ with $\text{M}=\text{Cr}^{3+}$ and Ni^{3+} , and $y = 1/8$. The effective magnetic moments were calculated from the spin-only values, and it was assumed that the Weiss constants are zero.

13.4.3 ^7Li contact shifts in $\text{LiM}_y\text{Co}_{1-y}\text{O}_2$

The spin-density calculations of Carlier et al. established the link between the electronic spin transfer and the NMR shifts observed in the spectrum, via the contact interaction. However they did not obtain the actual values of the interaction, and nor was the effect of the expected Jahn–Teller distortion of the metal coordination sites accounted for. Both of these issues were addressed in a DFT study by Middlemiss et al [54]. The first principles solid-state DFT calculations were performed using the CRYSTAL09 linear combination of atomic orbitals code, with two hybrid exchange correlation functionals. Firstly the B3LYP functional incorporating 20% Hartree–Fock exchange (Hyb20) was employed, as this is known to perform well in the calculation of the electronic structure and band gaps of a range of materials, particularly those with transition-metal ions. Secondly a related functional with 35% Hartree–Fock exchange (Hyb35) was used as this gives values of magnetic coupling constants that are in good agreement with experiment. In particular the Hyb20 and Hyb35 calculations provide a range of values of the contact shift that are in good agreement with the experimental values.

The Hyb20 structural optimization of the two mixed transition-metal oxides confirms the presence of a Jahn–Teller elongation along one of the pseudo- C_4 rotation axes, resulting in two long (L) M–O bonds and four short (S) M–O bonds, the values of which are given in Table 13.4. No Jahn–Teller distortion is expected for $\text{LiCr}_{1/8}\text{Co}_{7/8}\text{O}_2$ due to the non-degenerate orbital ground state of the octahedral configuration, as shown by the negligible difference in calculated bond lengths, whereas there is a substantial distortion for $\text{LiNi}_{1/8}\text{Co}_{7/8}\text{O}_2$. One effect of these distortions is to lift the chemical equivalence of the Li sites, so that instead of the three sites expected from the octahedral environment we obtain five, which are shown in Figure 13.14 [54]. The Li(1) site with only Co^{3+} in the nn and nnn remains distinct, and is now labelled Li(b). The Li(2) with the 180° M–O–Li bonding geometry is now split into two distinct sites Li(c) and Li(d) in the ratio 1:2, which are defined by a long (L) and short (S) M–O bond respectively. Finally the Li(3) site with the

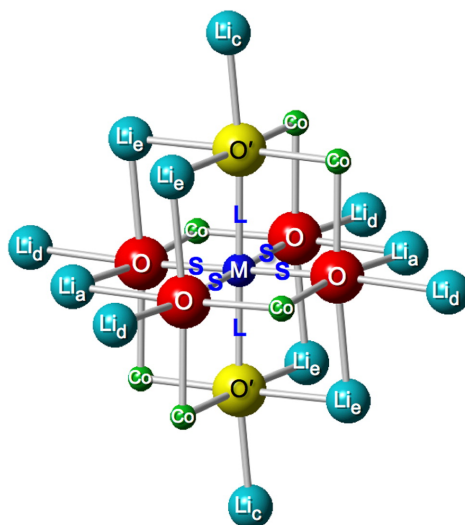


Figure 13.14: Local coordination environment for the Cr^{3+} and Ni^{3+} metal ion in the $\text{LiM}_{1/8}\text{Co}_{7/8}\text{O}_2$ structure subject to a Jahn–Teller distortion. Shown are the four short (S) and two long (L) M–O bonds to the equatorial and axial oxygens O and O', and four of the five Li sites. The Li(b) site with no M nn or nnn interactions is not shown. Reproduced with permission from [54]. Copyright (2013) American Chemical Society.

90° M–O–Li bonding geometry is split into two distinct sites Li(a) and Li(e). Site Li(a) is defined by a spin transfer via two short M–O and O–Li bonds (SS) bonds, whereas for Li(e) the transfer is via two long and two short (SL) bonds.

The contact shifts were obtained from the Fermi-contact coupling constant from Equation 13.2 using the values of μ_{eff} and Θ in 13.4. The two effective magnetic moments correspond to electronic configurations with quenched orbital angular momenta and $S = 3/2$ and $S = 1/2$ respectively. It was assumed that there are no measurable exchange interactions between the dilute paramagnetic metal ions, giving Weiss constants of zero. The results of the calculations of the contact shifts using the Hyb20 and Hyb35 functionals are given in Table 13.5 [54]. The results for $\text{LiCr}_{1/8}\text{Co}_{7/8}\text{O}_2$ are in agreement with the prior calculations of Carlier et al., namely that the 90° M–O–Li sites correspond to the positive shift, and the 180° M–O–Li sites to the negative shift. Examining the calculated values in more detail we see that the small Jahn–Teller elongation gives a negligible difference between the shifts of the two Li(3) sites, Li(a) and Li(e), with both functionals, and also a negligible difference between the shifts of the two Li(2) sites Li(c) and Li(d). In addition the small shift for Li(b) confirms the prior assertion that M–Li spin transfer beyond next-nearest neighbour is negligible.

Pathways		LiCr _{1/8} Co _{7/8} O ₂			LiNi _{1/8} Co _{7/8} O ₂		
Li Site	Bond lengths	Hyb20 / ppm	Hyb35 / ppm	Expt / ppm	Hyb20 / ppm	Hyb35 / ppm	Expt / ppm
90° nn pathways							
a	SS	46.0	29.8		4.2	10.0	
e	SL	44.3	26.6		-23.1	-21.6	
	axial average	44.9	27.7	35	-14.0	-11.1	-15
180° nnn pathways							
d	S	-81.2	-79.4		34.4	21.2	
c	L	-87.4	-84.7		314.8	259.2	
	axial average	-83.3	-81.2	-70	127.9	100.6	110
No nn or nnn pathways							
b	—	1.5	-0.4	0	-2.2	-2.0	0

Table 13.5: Computed ⁷Li contact shifts for the different sites in LiCr_{1/8}Co_{7/8}O₂ and LiNi_{1/8}Co_{7/8}O₂ using Hyb20 and Hyb35 functionals. Axial average values (assuming fast dynamic Jahn–Teller distortion) of the 90° nn shifts equal to $(\delta^{\text{con}}(a) + 2\delta^{\text{con}}(e)) / 3$, and of the 180° nn shifts equal to $(\delta^{\text{con}}(c) + 2\delta^{\text{con}}(d)) / 3$. Values taken from Ref. [54].

As expected, the Jahn–Teller distortion in LiNi_{1/8}Co_{7/8}O₂ results in a greater shift difference between Li(a) and Li(e), and also between Li(c) and Li(d). This highlights the sensitivity of the contact shift to such structural distortions. Therefore, if the distortion is static, as assumed in the calculations, we would expect to see five distinct resonances in the NMR spectrum instead of three. In particular we would be able to distinguish between the two shifts for Li(c) and Li(d). However the observation of only three distinct shift indicates that the Jahn–Teller distortion is not static, but rather dynamic in nature. If we assume rapid dynamics this process can be accounted for simply by averaging the shifts of the Li(a) and Li(e) sites to give a single axial average, and equivalently for Li(c) and Li(d). The values obtained for both LiCr_{1/8}Co_{7/8}O₂ and LiNi_{1/8}Co_{7/8}O₂ are in excellent agreement with experiment.

The results of the combined NMR and DFT approach of Middlemiss et al. present a compelling body of evidence for the observation of a dynamic Jahn–Teller distortion in the Ni³⁺-containing materials, and highlight the power of paramagnetic NMR to distinguish between static and dynamic structural distortions [54].

13.5 Prussian blue analogue materials A_nM'_x[M(CN)₆]_y · zH₂O

13.5.1 Background

Prussian blue analogues (PBAs) constitute one of the most important families of inorganic polymer materials. The original Prussian blue, ferric ferrocyanide Fe₄[Fe(CN)₆]₃ · zH₂O, is a synthetic dye that was discovered

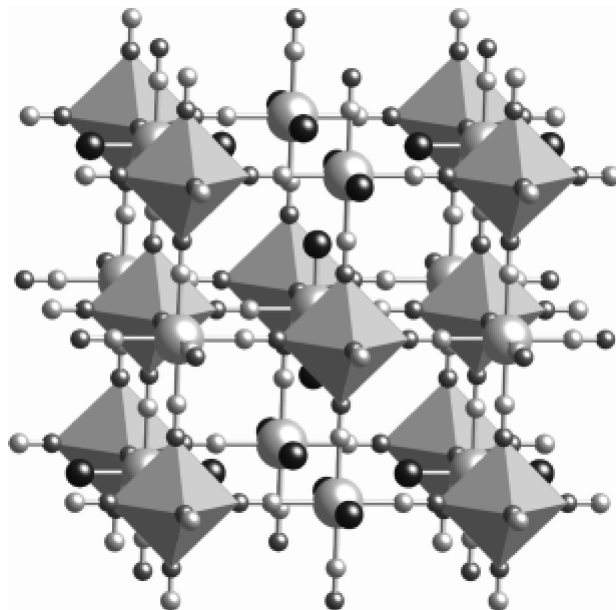


Figure 13.15: The ideal cubic structure for a PBA $A_nM'_x[M(CN)_6]_y \cdot zH_2O$. The grey octahedra indicate the $M(CN)_6$ units; large light grey spheres are A/M' metal ions; small black spheres are structural H_2O molecules; small dark grey spheres are C atoms; and small light grey spheres are N atoms. The interstitial H_2O is omitted. Reproduced with permission from [8]. Copyright John Wiley and Sons.

by the Berlin dye maker Diesbach in 1703 [506]. More recently a large variety of PBAs have attracted interest in diverse fields such as hydrogen gas storage [507], biosensors [508], waste recovery [509], molecular sieves [510], and battery electrode materials [511].

The formula for a general PBA is $A_nM'_x[M(CN)_6]_y \cdot zH_2O$, where A an alkali metal cation, and M and M' are six-coordinate octahedral transition-metal cations. The structure, shown in Figure 13.15, is a cubic lattice comprising alternating $M(CN)_6$ octahedra and A/M' metal ions, which are linked by the CN^- ligands [8]. Only a certain proportion of the $M(CN)_6$ sites are occupied (as low as 60%), with each resulting vacancy being filled with z' 'structural' H_2O molecules that coordinate to the nearest z' M' metal ions, and additional 'crystallization' interstitial H_2O molecules. This results in PBAs readily absorbing water from the air.

The bonding interactions in PBAs can be understood as follows. Firstly each metal ion M coordinates to six CN^- anions in an octahedral complex. The molecular orbital energy diagram of a CN^- ligand is shown in Figure 13.16. The highest-occupied molecular orbital (HOMO) is the 3σ , which is mainly formed from the C $2p_\sigma$ orbital. The electron pair is therefore aligned along the C–N axis pointing away from N. The

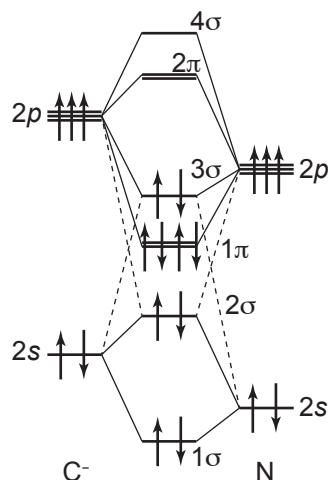


Figure 13.16: Molecular orbital energy diagram for the CN^- ligand in PBAs.

six 3σ orbitals of the six ligands interact with the e_g set of metal $3d$ -orbitals. Since the electrons in each 3σ are predominantly located on C, this results in the formation of six M–C σ -bonds. If we only consider these σ -bonds the t_{2g} set of metal $3d$ -orbitals remains non-bonding. However the six 2π lowest unoccupied molecular orbitals (LUMOs) of the six ligands do have symmetry that is compatible with an interaction with the t_{2g} . These anti-bonding orbitals are mainly formed from the C $2p_\pi$. The interaction stabilizes the t_{2g} containing the d -electrons relative to the e_g , resulting in an increase in the ligand energy splitting parameter Δ_{oct} , and thus a low-spin electronic configuration. A simplified molecular orbital diagram for $\text{Fe}(\text{CN})_6^{3-}$ that accounts for the important interactions is shown in Figure 13.17, in which $1t_{2g}$ HOMO and $2e_g$ LUMO are highlighted [512]. When incorporated into the cubic lattice of the PBA the $\text{M}(\text{CN})_6$ octahedra alternate with the A/M' metal ions, so that the latter interact with the N atoms of the CN^- ligands.

The magnetic exchange interactions between the paramagnetic centres result in magnetic ordering at low temperatures, which may persist up to room temperature. For example the PBA $\text{V}[\text{Cr}(\text{CN})_6]_{0.86} \cdot 2.8\text{H}_2\text{O}$ exhibits magnetic ordering with a Curie temperature of 315 K [513]. However many other PBAs are in the high-temperature paramagnetic regime at room temperature, many of which have been studied extensively with solid-state NMR by Köhler et al [4, 8, 217, 514, 515]. Here we present a case study comprising two particular examples, namely the materials $\text{Cs}_2\text{K}[\text{Fe}(\text{CN})_6]$ [4], and $\text{Cd}_3[\text{Fe}_x\text{Co}_{1-x}(\text{CN})_6]_2 \cdot 15\text{H}_2\text{O}$ [8], in which the Fe^{3+} and Co^{3+} ions are low-spin, with $S = 1/2$ and $S = 0$ respectively.

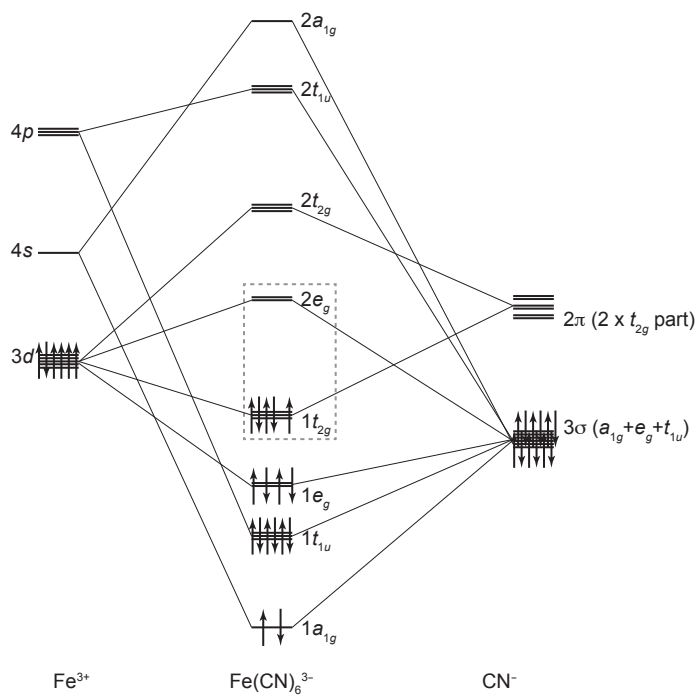


Figure 13.17: Simplified molecular orbital energy diagram for the $\text{Fe}(\text{CN})_6^{3-}$ octahedral unit in PBAs, showing the most important contributions to the σ - and π -bonds between the Fe^{3+} ion and CN^- ligands. The $1t_{2g}$ and $2e_g$ orbitals that are predominantly due to the metal $3d$ are highlighted by the dashed box.

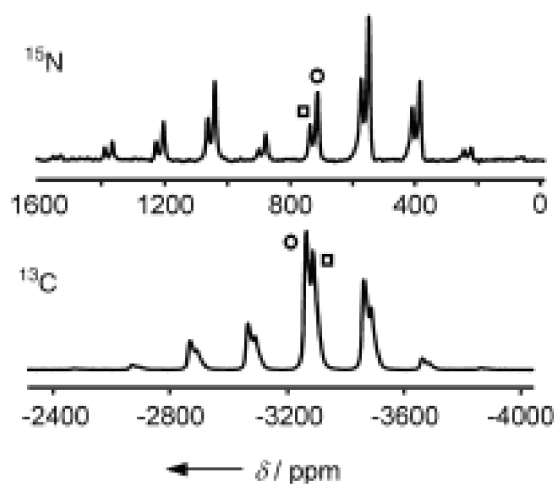


Figure 13.18: ^{15}N and ^{13}C solid-state MAS NMR spectra of $\text{Cs}_2\text{K}[\text{Fe}(\text{CN})_6]$ at 326.4 K. The ^{15}N and ^{13}C spectra were acquired at 5 and 15 kHz MAS respectively. The centrebands of the resonances due to axial and equatorial CN^- ligands are indicated with a \square and \circ respectively. Adapted with permission from [4]. Copyright John Wiley and Sons.

13.5.2 Solid-state NMR spectra

The ^{13}C and ^{15}N solid-state MAS NMR spectra of $\text{Cs}_2\text{K}[\text{Fe}^{\text{III}}(\text{CN})_6]$ acquired at 326.4 K are shown in Figure 13.18 [4]. In the ^{13}C spectrum, acquired at 15 kHz MAS, we can resolve two spinning-sideband manifolds with negative isotropic chemical shifts of -3269 and -3295 ppm which are ascribed to CN^- ligands in the axial and equatorial positions. The orbital contributions to these shifts are assumed to be equal to those of the diamagnetic analogue $\text{Cs}_2\text{K}[\text{Co}(\text{CN})_6]$. Following subtraction of the orbital shifts, we obtain paramagnetic shifts of -3134 and -3160 ppm for the axial and equatorial positions. As for the transition-metal oxide materials of the previous section, these paramagnetic contributions are dominated by the contact shift, which indicates that the Fe^{3+} ion transfers a negative spin density to C. The spinning-sideband manifolds are mainly due to the NR spin-dipolar interaction. A fit of the sideband intensities yields anisotropy parameters of 603 and 628 ppm for the axial and equatorial C.

The ^{15}N spectra were acquired at 5 kHz MAS, and also exhibit two spinning-sideband manifolds due to axial and equatorial N with chemical shifts of 727 and 704 ppm respectively. Following adjustment by subtracting the orbital shifts we obtain positive paramagnetic shifts of 810 and 783 ppm respectively, which are also dominated by the contact contribution, and indicate that the spin density transferred to both N $2s$

orbitals is positive. The shift anisotropy values, again dominated by the NR spin-dipolar interaction, are 1073 and 1023 ppm for axial and equatorial N.

To aid in the interpretation of the NMR shifts observed for ^{13}C and ^{15}N it would also be instructive to be able to monitor the transfer of unpaired electronic spin density to the metal ions in the A/M' positions. However neither Cs nor K has favourable nuclear spin properties for NMR, and so a different PBA analogue with a different metal ion in this position is needed. Flambard et al. studied a series of PBAs $\text{Cd}^{\text{II}}[\text{Fe}_x^{\text{III}}\text{Co}_{1-x}^{\text{III}}(\text{CN})_6]_2 \cdot 15\text{H}_2\text{O}$, with $x = 0, 0.25, 0.5, 0.75,$ and 1 , using ^{113}Cd solid-state MAS NMR [8]. The ^{113}Cd nucleus has spin $I = 1/2$, sufficient sensitivity, and a diamagnetic shift range of 500 to -125 ppm, and so the authors were able to determine the spin-transfer mechanism to this metal position for the first time.

From the stoichiometry of these PBAs it can be seen that only two thirds of the $\text{M}(\text{CN})_6$ sites are occupied, leaving one third vacancies (vac), each of which contains six 'structural' water molecules coordinated to the nearest Cd^{2+} metal ion, and a variable quantity of 'crystallization' water. The unit cell formula is therefore $[\text{Cd}_4^{\text{II}}\{\text{M}^{\text{III}}(\text{CN})_6\}_{8/3}(\text{vac})_{4/3}] \cdot x\text{H}_2\text{O}$ with $x = 12-20$, and the coordination of the Cd^{2+} metal ion can be described as $\text{Cd}^{\text{II}}(\text{NCM})_{6-a}(\text{OH}_2\text{vac})_a$. One important question that can be answered by solid-state NMR is whether the vacancies are ordered in the lattice, with limits on the values of a , or distributed randomly, with a taking all possible values from 0 to 6.

The solid-state ^{113}Cd NMR spectrum acquired at 15 kHz MAS and 310 K of the diamagnetic material $\text{Cd}_3^{\text{II}}[\text{Co}^{\text{III}}(\text{CN})_6]_2 \cdot 15\text{H}_2\text{O}$ (with $x = 0$) is shown in Figure 13.19 position 1 [8]. Two peaks are observed in the paramagnetic region at 63 and 81 ppm, which can be ascribed to the cis and trans isomers of the Cd sites $\text{Cd}^{\text{II}}(\text{NCCo})_4(\text{OH}_2\text{vac})_2$, suggesting some ordering of the vacancies. By contrast the all-Fe material $\text{Cd}_3^{\text{II}}[\text{Fe}^{\text{III}}(\text{CN})_6]_2 \cdot 15\text{H}_2\text{O}$ (with $x = 1$) gives a ^{113}Cd spectrum with four distinct sites, as shown in Figure 13.19 position 5. All four peaks are shifted to large negative values centred on -1300 ppm, which immediately suggests a contact interaction due to a transfer of negative electronic spin density along Fe-C-N-Cd to the Cd s -orbital, i.e. of the same sign as for C and opposite to N. The two most intense peaks at -1275 and -1327 can be attributed to the cis and trans isomers of $\text{Cd}^{\text{II}}(\text{NCFe})_4(\text{OH}_2\text{vac})_2$, with each shift being the sum of four pathway contributions Fe-C-N-Cd. Taking the average of the two contact shifts (i.e. the average deviation from the diamagnetic shifts from the all-Co compound) allows us to compute an average contribution from each pathway of -343 ppm. Immediately this allows us to assign the two lower-intensity peaks at -1000 ppm and -1537 ppm to the $\text{Cd}^{\text{II}}(\text{NCFe})_3(\text{OH}_2\text{vac})_3$ and $\text{Cd}^{\text{II}}(\text{NCFe})_5(\text{OH}_2\text{vac})$ sites, where

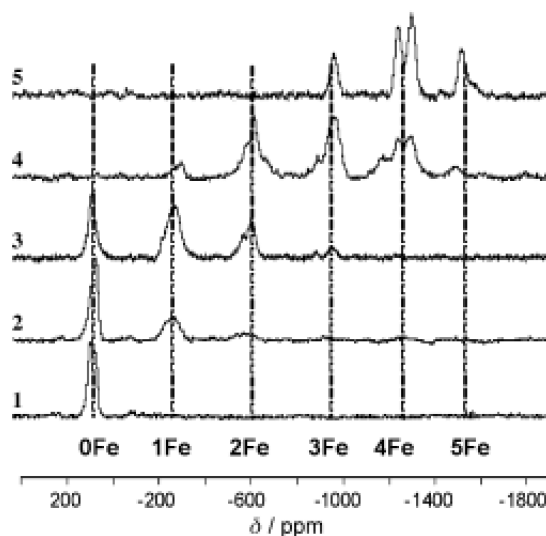


Figure 13.19: ^{113}Cd solid-state MAS NMR spectra of $\text{Cd}_3[\text{Fe}_x\text{Co}_{1-x}(\text{CN})_6]_2 \cdot 15\text{H}_2\text{O}$ acquired at 310 K and 15 kHz MAS. The Fe^{3+} contents are $x = (1) 0, (2) 0.25, (3) 0.5, (4) 0.75, \text{ and } (5) 1$. Dashed lines indicate the shifts at which ^{113}Cd experiences a contact shift pathway contribution from 0, 1, 2, 3, 4, and 5 Fe^{3+} ions. Reproduced with permission from [8]. Copyright John Wiley and Sons.

the Cd^{2+} ion is connected to Fe^{3+} by three and five pathways respectively. We note that there is no peak at -1880 ppm, which would be due to $\text{Cd}^{\text{II}}(\text{NCFe})_6$, again indicating that the vacancies are not randomly distributed.

The pathway contribution model of the contact shifts is further supported by the ^{113}Cd spectra of $\text{Cd}_3[\text{Fe}_x\text{Co}_{1-x}(\text{CN})_6]_2 \cdot 15\text{H}_2\text{O}$ with $x = 0.25, 0.5, \text{ and } 0.75$, which are shown in Figure 13.19 positions 2–4. A total of six distinct Cd environments is observed, in which the shifts are equally spaced by 300–350 ppm, which correspond to Cd sites coordinating to between zero and five Fe^{3+} ions via similar pathways. The sites can be written explicitly as $\text{Cd}(\text{para})_{6-a}(\text{dia})_a$, with para corresponding to NCFe and dia to either OH_2vac or NCCo . Within each resonance multiple peaks can be resolved, which correspond to different cis/trans or mer/fac isomers of the different $\text{Cd}(\text{para})_{6-a}(\text{dia})_a$ sites. Once again the non-observation of the Cd site with $a = 6$ indicates that the vacancies are partially ordered in the lattice [8].

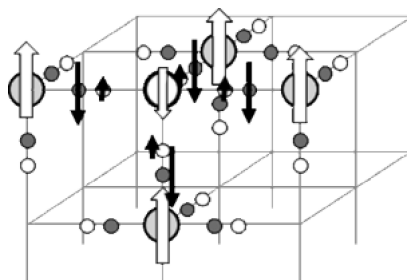


Figure 13.20: Diagram indicating the sign of the transferred electronic spin density in $\text{Cd}_3[\text{Fe}(\text{CN})_6]_2 \cdot 15\text{H}_2\text{O}$. The atoms are denoted as follows: Cd, large white circle; Fe, large light grey circle; N, small white circle; C small dark grey circle. The arrows represent both the magnitude of the transferred density, via their length, and the sign, with up indicating positive spin, and down indicating negative spin. Reproduced with permission from [8]. Copyright John Wiley and Sons.

13.5.3 Interpretation of the contact shifts

The NMR data can be used to elucidate a mechanism for the unpaired electronic spin transfer from the Fe^{3+} ion throughout the lattice to the s -orbitals of the other atoms. The measured chemical shifts are dominated by the contact shift, and are negative for both ^{13}C and ^{113}Cd , and positive for ^{15}N . This can be explained by the polarization mechanism as follows. Firstly the unpaired electron in the $\text{Fe}^{3+} t_{2g}$ orbital is delocalized into an anti-bonding π orbital of the CN^- ligand. However this π -orbital has a node along the C–N axis, and is therefore of incompatible symmetry for overlap with the C $2s$. Therefore this unpaired electron polarizes the e_g orbital of the Fe^{3+} with a positive density. The result is negative electron density polarized in the C $2s$, and a negative ^{13}C contact shift. This negative density then polarizes the N $2s$ orbital with electron density of the opposite sign, i.e. positive, leading to a positive ^{15}N contact shift. Finally the s -orbital of the Cd is polarized by the N $2s$, resulting in negative electron density and a negative contact shift. This ‘relay’ of the polarization effect through the lattice is shown in Figure 13.20. We expect the electron transfer to become weaker as we move further from the Fe^{3+} ion, which is why the ^{13}C contact shifts have a greater magnitude than the ^{15}N contact shifts (-3100 vs 800 ppm). For Cd that receives electron density along a single pathway the magnitude of the transfer is smaller still, giving a relatively small contact shift of -343 ppm. However for Cd sites with multiple transfer pathways, the individual transferred densities and pathway contributions are additive giving relatively large negative shifts up to -1900 ppm.

On a final point we note that the spin-polarization transfer has the effect of aligning the electronic spins of

the Fe^{3+} ions, and so we might expect the materials $\text{Cd}_3[\text{Fe}_x\text{Co}_{1-x}(\text{CN})_6]_2 \cdot 15\text{H}_2\text{O}$ to exhibit ferromagnetic ordering at low temperature. However magnetic susceptibility measurements indicate that there is no such effect, suggesting that the polarization mechanism is inefficient at ordering metal ions that are separated by six bonds [8].

13.6 Olivine-type lithium transition-metal phosphate cathode materials LiMPO_4

13.6.1 Background

The olivine class of materials LiMPO_4 with $M = \text{Mn}^{2+}$, Fe^{2+} , Co^{2+} , and Ni^{2+} has attracted a lot of interest in recent years as providing potential candidates for cathode materials in Li-ion batteries [516]. The pure-Fe phase, which is used commercially, has a $\text{Fe}^{2+}/\text{Fe}^{3+}$ couple of 3.4 V vs Li^+/Li . However this is not high enough for many applications, and so higher-voltage materials, such as with $M = \text{Mn}^{2+}$ and Co^{2+} for which the corresponding redox couples are of 4.1 V and 4.8 V vs Li^+/Li respectively, have been extensively studied. Whilst these metal ions have been exploited both in pure Mn and Co phases, the mixed phases $\text{LiFe}_x\text{M}_{1-x}\text{PO}_4$, where M is in a solid solution with Fe, tend to have better electrochemical performance, which in part is attributed to the local and long-range distortions of the lithiated and partially delithiated phases caused by cation substitution. Understanding these local structural effects is therefore key to understanding the electrochemistry.

The olivine structure of LiMPO_4 is shown in Figure 13.21. The material has $Pbnm$ symmetry, and comprises edge- and corner-sharing MO_6 octahedra and PO_4 tetrahedra. There are three crystallographically distinct O positions O_1 , O_2 , and O_3 that have occurrences in the ratio 1:1:2. The Li ions occupy the octahedral LiO_6 sites in the [010] channels, along which they have greater mobility compared to other directions. On delithiation the Li ions are removed from the channels, with the connectivity of the other structural units remaining largely unaltered. This accounts for the favourable electrochemical performance of the material. In the lithiated phases LiMPO_4 the octahedral transition metal sites are slightly distorted, but the splitting of the d -orbitals is nevertheless accurately described by the idealized splitting in the O_h point group. As shown in Figure 13.22 the four metal ions Mn^{2+} , Fe^{2+} , Co^{2+} , and Ni^{2+} all have a high-spin electronic configuration.

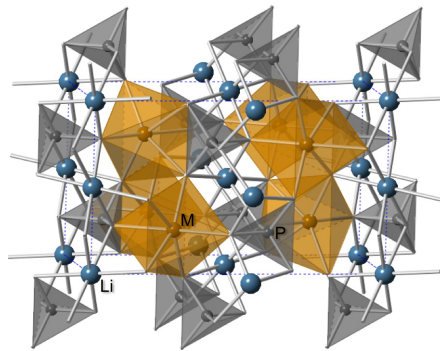


Figure 13.21: Crystal structure of the olivine LiMPO_4 materials showing the MO_6 (yellow) and PO_4 (grey) polyhedra, and the Li sites (blue). The $[010]$ channels with high Li mobility are vertical. Reproduced with permission from [54]. Copyright (2013) American Chemical Society.

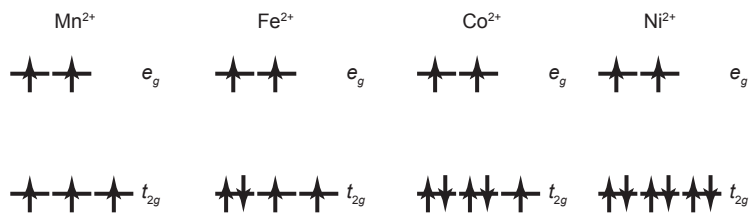


Figure 13.22: The idealized d -orbital splitting and electronic configurations of Mn^{2+} , Fe^{2+} , Co^{2+} , and Ni^{2+} in LiMPO_4 . The corresponding electronic states are denoted by the terms ${}^6A_{1g}$, ${}^5T_{2g}$, ${}^4T_{1g}$, and ${}^3A_{2g}$.

Material	$\mu_{\text{eff}}/\mu_{\text{B}}$	Θ / K
LiMnPO ₄	5.4	-58
LiFePO ₄	5.3	-72.5 ± 0.2
LiCoPO ₄	4.578	-77
LiNiPO ₄	3.1	-60

Table 13.6: The magnetic parameters defining the magnetic susceptibility and contact shifts of LiMPO₄. Data taken from Refs. [466, 517, 518].

In order to understand the effect of the local structure of the metal ions on the NMR properties in the mixed phases, it is necessary to fully understand the pure phases. We therefore present the combined NMR/DFT case studies of Middlemiss et al. [54], and Pigliapochi et al. to describe the form of the shifts and SAs in these materials in both the ⁷Li and ³¹P NMR spectra. In the former study we employ the scaling-factor model, and describe the shift and SA in terms of the Fermi-contact and spin-dipolar hyperfine interactions, using the values for the effective magnetic moment and Weiss constant in Table 13.6. The total shift is the sum of multiple pathways from more than one metal ion, and so in order to isolate the different pathway contributions a spin-flip approach was employed, as is described in detail in the next section. In the latter study the EPR formalism is used to investigate the explicit effect of the *g*-shift tensor on the shift and SA. Additionally we present some trends for the longitudinal relaxation times T_1 , coherence lifetimes T_2' and total sideband linewidths in order to show the different effects the different metal ions have on these quantities. Finally the single-phase results can be exploited to investigate the multi-phase materials [30].

13.6.2 ^{6/7}Li NMR shifts and relaxation properties

The ⁷Li NMR spectra of the full series of pure-phase LiMPO₄ acquired by Tucker et al. are shown in Figure 13.23 [466]. The spectra were recorded at an external field corresponding to a ⁷Li Larmor frequency of -38.9 MHz and under 10 kHz MAS. An initial inspection indicates that the isotropic chemical shifts for the four materials fall in the range 70 ppm to -100 ppm. Whilst this is outside the standard diamagnetic range we will see that the isotropic shifts are comparatively smaller than those measured in similar systems with a dense network of paramagnetic metal ions. The shift anisotropy $\Delta\delta^{\text{S}}$ is given in the scaling-factor formalism by an expression analogous to the isotropic shift in Equation 13.3, which is proportional to the total spin-dipolar

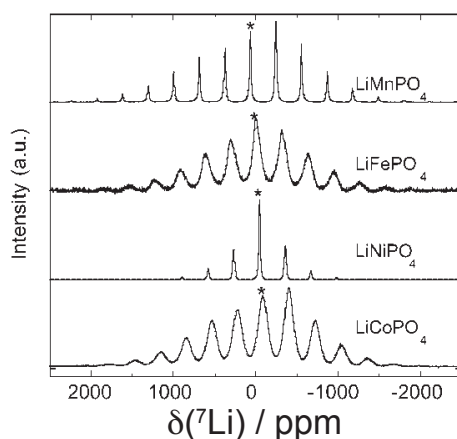


Figure 13.23: The ${}^7\text{Li}$ MAS NMR spectra of LiMPO_4 with $\text{M} = \text{Mn}^{2+}$, Fe^{2+} , Co^{2+} , and Ni^{2+} . The centrebands are marked with an *. The Larmor frequency is -38.9 MHz, and the MAS frequency is 10 kHz. Adapted with permission from [466]. Copyright (2002) American Chemical Society.

anisotropy $\Delta\mathcal{A}^{\text{SD}}$, and the asymmetry parameter η^{S} is equal to that of the spin-dipolar interaction

$$\Delta\delta^{\text{S}} = \frac{\mu_{\text{eff}}^2}{3\mu_{\text{B}}g_e\hbar\gamma_I k(T - \Theta)} \left(\frac{\Delta\mathcal{A}^{\text{SD}}}{2S} \right), \quad (13.6)$$

$$\eta^{\text{S}} = \eta^{\text{SD}}. \quad (13.7)$$

We expect this to be the dominant contribution to the spinning-sideband intensities, with an additional contribution to the apparent anisotropy due to the BMS effects and in particular the IBMS. The envelope of the sideband intensities in Figure 13.23 indicates that the effective anisotropies for LiMnPO_4 , LiFePO_4 , and LiCoPO_4 have similar magnitudes, which are significantly larger than for LiNiPO_4 . Furthermore the ‘slant’ of the intensities around the centreband indicates that the asymmetry parameters for all the systems have similar values, and that the SAs have the same sign. Finally we note that the individual spinning sidebands have considerably larger linewidths for LiFePO_4 and LiCoPO_4 than for LiMnPO_4 and LiNiPO_4 . This is ascribed to the larger ABMS broadening due to the magnetic anisotropy of the Fe^{2+} and Co^{2+} metal ions which have electronic ground states ${}^5T_{2g}$, ${}^4T_{1g}$ respectively, compared to Mn^{2+} and Ni^{2+} (${}^6A_{1g}$, and ${}^3A_{2g}$) in which the orbital angular momentum is quenched to first order. This is discussed in more detail later in this section.

Contact shifts

We can try to rationalize the form of the paramagnetic shifts using DFT calculations. Middlemiss et al. computed the total ${}^6/{}^7\text{Li}$ Fermi-contact shifts for LiMnPO_4 , LiFePO_4 , and LiCoPO_4 using the CRYSTAL09 code [54]. The total electronic spin density at the Li site $\rho_{\text{sat}}^{(\alpha-\beta)}(\text{Li})$ was computed in the fictitious ferromagnetic, or saturated, state in which all the effective electronic spins on the metal ions are aligned, giving the total Fermi-contact coupling constant \mathcal{A}^{FC} . This result was then scaled in to the paramagnetic regime using Equation 13.3, and the magnetism parameters in Table 13.6 used to give the total shift δ^{con} . In addition the individual pathway contributions were also calculated using the spin-flip approach. Here, in order to calculate the contribution from a metal ion i along pathway P_i we flip the electronic spin of one metal ion within the supercell used in the calculations, and repeat the calculation to give a new electronic spin density $\rho_{\text{flip},P_i}^{(\alpha-\beta)}(\text{Li})$, and hence a new contact shift $\delta_{\text{flip},P_i}^{\text{con}}(\text{Li})$. The difference between the initial density $\rho_{\text{sat}}^{(\alpha-\beta)}(\text{Li})$ and the new density gives the contribution to the electronic spin density from metal ion i along pathway P_i , i.e. $\rho_{P_i}^{(\alpha-\beta)}(\text{Li}) = (\rho_{\text{sat}}^{(\alpha-\beta)}(\text{Li}) - \rho_{\text{flip},P_i}^{(\alpha-\beta)}(\text{Li})) / 2$. This spin-flip approach is then repeated for all the metal ions within the cell. Since the same scaling factor parameters are applied to all the metal ions, the pathway contribution to the contact shift can be calculated from the difference in the corresponding shifts:

$$\delta_{P_i}^{\text{con}}(\text{Li}) = (\delta^{\text{con}}(\text{Li}) - \delta_{\text{flip},P_i}^{\text{con}}(\text{Li})) / 2$$

In practice, the periodic boundary conditions used in the DFT calculation mean that a spin-flip applied to a particular metal ion is also applied to all the other metal ions at symmetry-related positions outside the supercell. Therefore in order to isolated a single pathway with each spin flip, it is necessary to use a supercell that is significantly larger than the basic unit cell.

Figure 13.24 shows the local Li environment with the short-range pathways identified by Middlemiss et al [54]. For Li there are six pathways in total that fall into three crystallographically distinct pairs for LiMnPO_4 and LiFePO_4 that are labelled P_1 , P_2 , and P_3 . For LiCoPO_4 the situation is more complex, since there is a spontaneous lowering of the symmetry of the supercell which is characterized by the O_3 sites splitting into two sub-groups $\text{O}_{3\text{H}}$ and $\text{O}_{3\text{L}}$ which have higher and lower transferred spin densities than the average. This structure is stabilized relative to the more symmetric space group by 8 kJmol^{-1} . This results in the equivalence being lifted within pairs of pathways, resulting in six distinct pathways in total. The lower symmetry also results in the Li sites no longer being equivalent, but rather splitting into two distinct sub-sites with distinct total contact shifts. However there is no conclusive evidence of two distinct sites in the ${}^7\text{Li}$ NMR

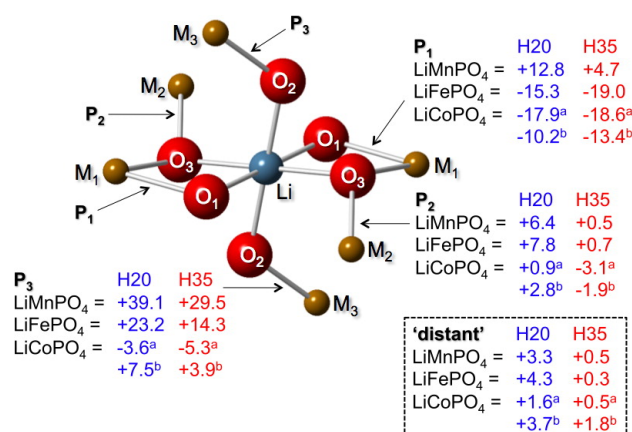


Figure 13.24: The Fermi-contact pathways and contributions for $^{6/7}\text{Li}$ in LiMPO_4 . For Co^{2+} the values marked *a* correspond to Li neighbouring $\text{O}_{3\text{H}}$, and those marked *b* are Li neighbouring $\text{O}_{3\text{L}}$. Reproduced with permission from [54]. Copyright (2013) American Chemical Society.

Material	$^{6/7}\text{Li}$ shifts Hyb20 / ppm			$^{6/7}\text{Li}$ shifts Hyb35 / ppm			Expt / ppm
	Direct	$\sum_i P_i$ total	$\sum_i P_i$ short-range only	Direct	$\sum_i P_i$ total	$\sum_i P_i$ short-range only	
LiMnPO ₄	116.6	123.3	116.6	73.0	70.3	69.3	57, 68
LiFePO ₄	38.4	40.1	31.5	-0.2	-7.4	-8.1	-8, -15
LiCoPO ₄	7.6	7.7	0.3	-19.1	-19.2	-22.8	-86, -92
	-39.7	-38.0	-41.2	-52.7	-52.8	-53.9	

Table 13.7: Comparison of the experimental chemical shifts and calculated contact shifts of $^{6/7}\text{Li}$ in LiMPO_4 . See text for details. The calculated shifts are from Ref. [54], and the experimental shifts are from Refs. [466, 519].

spectrum, suggesting that the lower-symmetry structure does not persist at the temperatures at which the data were acquired. In addition there are several longer-range (distant) pathways that are not shown. The different pathway contributions calculated from the Hyb20 and Hyb35 functionals are also given in Figure 13.24.

The individual short-range pathway contributions are all small, with values between -20 ppm and $+40$ ppm depending on the pathway and functional used. Therefore it is necessary to include the more distant contributions in order to reproduce the total contact shift. We should also bear in mind that, given the small contact shifts, the PCS may now represent a larger relative contribution to the total paramagnetic shift. This is discussed later in the context of the EPR formalism.

The results for the contact shift are summarised in Table 13.7. The shifts calculated directly ('Direct') are compared to the sums of the pathway contributions including and excluding the longer-range pathway contributions. Whilst the general agreement is good, there are discrepancies between the calculated shifts and

the experimental values, in some cases with the errors being of approximately the same order of magnitude as the shifts themselves. This may be due to the basis set not being adequate in this case, or to the neglect of the PCS.

Linewidths and PREs

The variation of the sideband linewidth, coherence lifetimes, and longitudinal relaxation times is also worth discussing in detail. It is apparent that there is an increase in linewidth on replacing Mn^{2+} with either Fe^{2+} or Co^{2+} , the source of which it is instructive to elucidate. Figure 13.25 (a) shows both the ${}^7\text{Li}$ T_1 and T_2' time constants for LiMnPO_4 and LiFePO_4 acquired at a different field of 11.74 T at 60 kHz MAS. Both time constants are longer for the latter material than for the former. The PREs of the longitudinal and transverse relaxation rates can each be modelled as a sum of contributions from the different metal ions, each of which is given by the Solomon–Bloembergen–Morgan equations in 8.185 and 8.186. The trend can be explained by a combination of the reduction of S from $5/2$ to 2 on going from Mn^{2+} to Fe^{2+} , and possible changes in the electronic relaxation times T_{1e} and T_{2e} . The values of T_{1e} and T_{2e} are both unknown, but it is likely that the interactions between the electronic spins of the network of metal ions have the effect of accelerating electronic relaxation so that it is faster than in complexes in solution that contain a single metal ion. If the T_{1e} and T_{2e} are sufficiently short for the nuclear relaxation to be in the extreme-narrowing limit, this means that longer electronic relaxation times result in larger PREs. Generally we expect the half-filled d -shell of Mn^{2+} to have longer T_{1e} and T_{2e} times than the T -term of the Fe^{2+} ion, due to the SO coupling strength in the latter, which would explain why the PREs in LiMnPO_4 are longer. Strictly speaking the coherence lifetimes also depend on the coherent dephasing, but we would also expect a lower transverse PRE to give a longer T_2' .

The total sideband linewidth can be decomposed into a homogeneous part, equal to $2/T_2'$ rad s^{-1} , and an inhomogeneous part which is equal to the difference between the total and homogeneous parts. The sideband linewidths in the ${}^7\text{Li}$ spectrum are shown in Figure 13.25 (b), and clearly indicate that the increase on going from LiMnPO_4 to LiFePO_4 is due entirely to an increase in the inhomogeneous part, and occurs in spite of an accompanying decrease in the homogeneous linewidth. In fact for LiMnPO_4 the total linewidth is almost entirely homogeneous and due to transverse relaxation and a residual coherent dephasing. The absence of any significant inhomogeneous broadening is due to the Mn^{2+} ions having no bulk susceptibility anisotropy. On the other hand, for LiFePO_4 the line broadening is due almost entirely to the inhomogeneous contribution

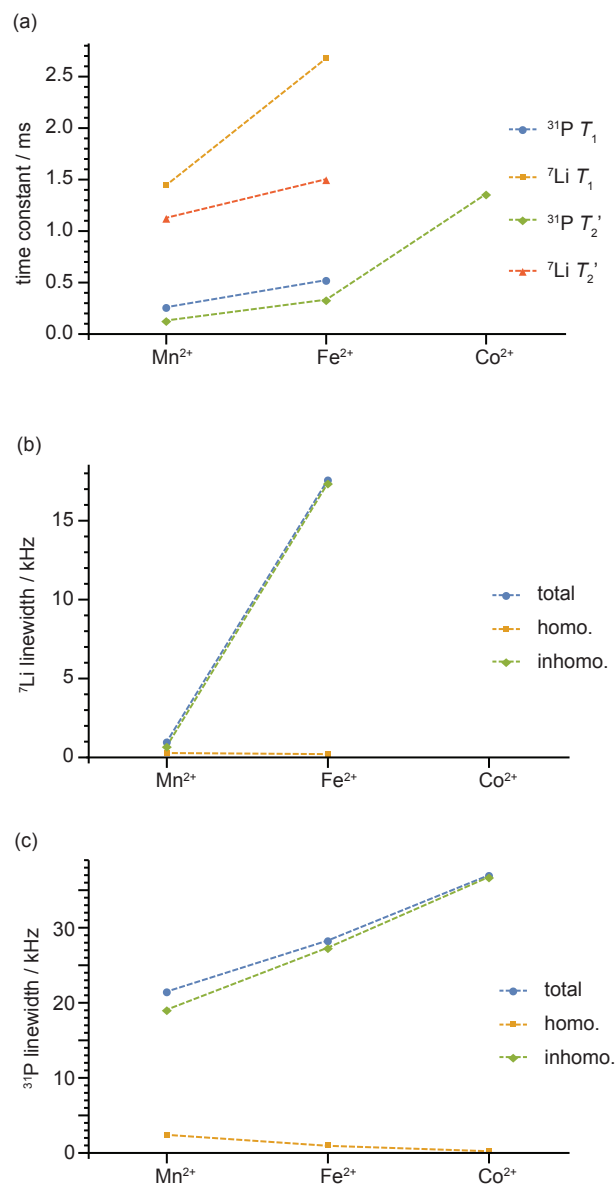


Figure 13.25: Longitudinal relaxation time constants, coherence lifetimes, and linewidths in the ^{7}Li and ^{31}P NMR spectra of LiMPO_4 acquired at 11.74 T and 60 kHz MAS. The ^{7}Li and ^{31}P T_1 and T_2' time constants are shown in (a). In (b) and (c) are plotted the contributions to the total sideband linewidth in the ^{7}Li and ^{31}P spectra respectively. The total linewidth was measured from the average FWHM of the sidebands. The homogeneous linewidth was computed from the coherence lifetime, and is equal to $2/T_2'$ rad s^{-1} . The inhomogeneous linewidth is estimated as the difference between the total and homogeneous linewidths.

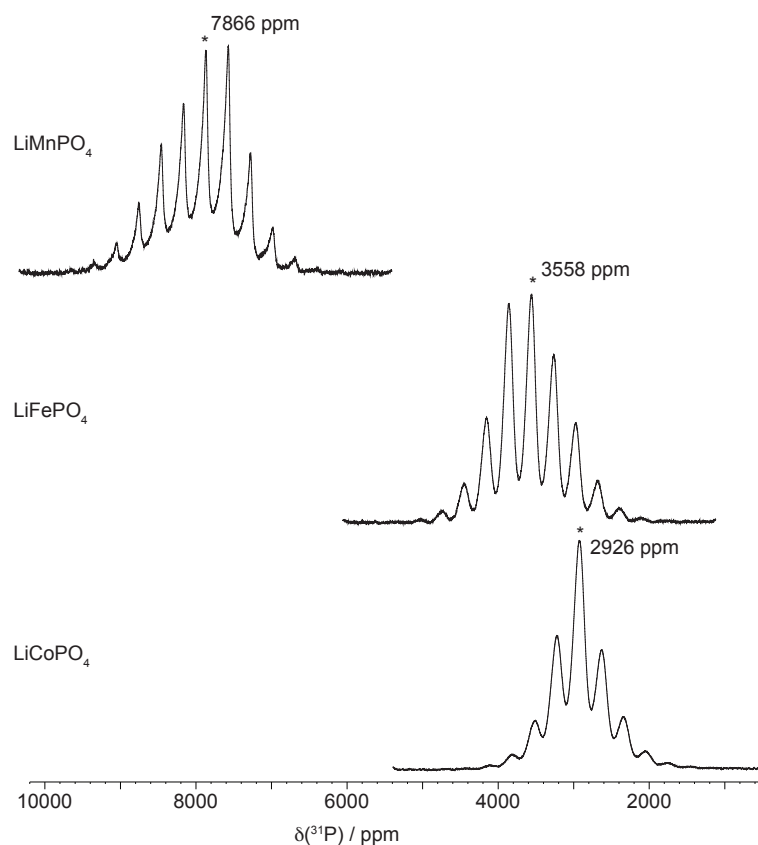


Figure 13.26: The ^{31}P MAS NMR spectra of LiMPO_4 with $\text{M} = \text{Mn}^{2+}$, Fe^{2+} , and Co^{2+} . The centrebands are marked with an *. The magnetic field is 11.74 T, and the MAS frequency is 60 kHz.

due to the ABMS of the magnetically anisotropic Fe^{2+} ion.

13.6.3 ^{31}P NMR shifts and relaxation properties

The ^{31}P NMR spectra of LiMnPO_4 , LiFePO_4 , and LiCoPO_4 acquired in a field of 11.74 T at 60 kHz MAS are shown in Figure 13.26. An initial inspection shows a decrease in the isotropic shift on going from Mn^{2+} to Fe^{2+} , and again from Fe^{2+} to Co^{2+} , from 7866 ppm to 3558 ppm to 2926 ppm. This is accompanied by a decrease in the width of the spinning-sideband manifold, indicating a reduction in the SA. Interestingly the change in the slant of the sidebands around the centreband for LiFePO_4 and LiCoPO_4 compared to LiMnPO_4 indicate a change in the sign of the anisotropy. This feature is discussed later in the context of the EPR formalism. Finally we observe an increase in the sideband linewidth, which we can again ascribe to a larger

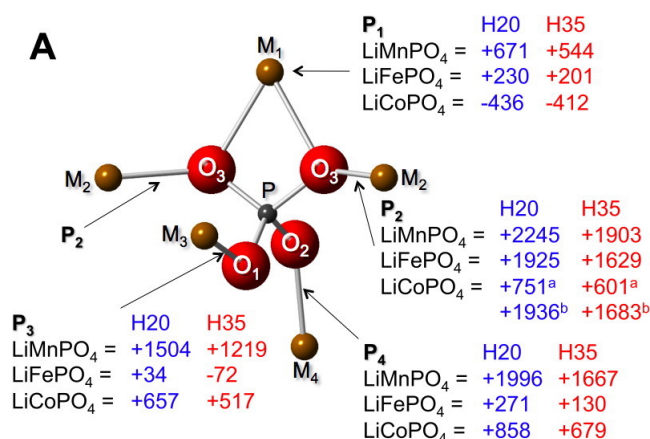


Figure 13.27: The Fermi-contact pathways and contributions for ^{31}P in LiMPO_4 . For Co^{2+} the P_2 values marked *a* correspond to P interacting via $\text{O}_{3\text{H}}$, and those marked *b* are P interacting via $\text{O}_{3\text{L}}$. Adapted with permission from [54]. Copyright (2013) American Chemical Society.

ABMS effect on going across the series.

Contact shifts

Compared to the $^{6/7}\text{Li}$ shifts, it is noticeable that the ^{31}P shifts are significantly larger, indicating a stronger orbital overlap along the M–O–P pathways than for the M–O–Li pathways, and therefore a larger Fermi-contact interaction. The calculation of the total contact shifts, and the individual pathways, proceeds using the same method as for the $^{6/7}\text{Li}$ shifts. There are five short-range pathways in total, which are shown in Figure 13.27. For LiMnPO_4 to LiFePO_4 two of the pathways, denoted P_2 , are equivalent and give the same contribution to the shift. However for LiCoPO_4 the lower symmetry which lifts the equivalency of the two O_3 sites, as described for $^{6/7}\text{Li}$, also lifts the equivalence of the two P_2 pathways, with one transfer going via an $\text{O}_{3\text{H}}$ and the other via an $\text{O}_{3\text{L}}$. However the P sites remain equivalent, and therefore still give a single distinct total contact shift, and in any case it should be reiterated that there is no evidence for the lower-symmetry structure persisting at higher temperatures. The values of the different pathway contributions are also given in Figure 13.27. They have a larger magnitude than the short-range M–O–Li pathway contributions, up to 2000 ppm, with the result that longer-range pathways can be neglected. For each pathway the M–O–P coordination angles are approximately 120° , with the exception of P_1 where the angle is 94° , and so it is difficult to rationalize the sign of the electron-spin transfer. All the contributions are positive indicating

Material	³¹ P shifts Hyb20 / ppm			³¹ P shifts Hyb35 / ppm			Expt / ppm
	Direct	$\sum_i P_i$ total	$\sum_i P_i$ short-range only	Direct	$\sum_i P_i$ total	$\sum_i P_i$ short-range only	
LiMnPO ₄	8650	8704	8661	7250	7225	7235	7296
LiFePO ₄	4361	4385	4385	3500	3451	3517	3352
LiCoPO ₄	3720	3755	3766	3054	3063	3069	2756

Table 13.8: Comparison of the experimental chemical shifts and calculated contact shifts of ³¹P in LiMPO₄. See text for details. The calculated shifts are from Ref. [54], and the experimental shifts are from Ref. [519].

a dominance of the delocalization spin-transfer mechanism, with the exception of P_3 for LiFePO₄ which is small, and changes sign depending on the amount of Hartree–Fock exchange used, and P_1 for LiCoPO₄ which is strongly negative indicating polarization. Generally it is likely that both delocalization and polarization mechanisms are active.

The total calculated and experimental contact shifts are summarised in Table 13.8. We see that since the contact interaction is larger, the agreement between experiment and theory is better for ³¹P than for ^{6/7}Li. This may be partly because the PCS is now insignificant. Furthermore, if we compare the results of the directly calculated contact shift with the sum of the pathways we see that the longer-range pathway contributions are negligible, and the shifts are dominated by the five nearest-neighbour interactions.

Linewidths and PREs

The ³¹P longitudinal relaxation time constants T_1 and coherence lifetimes T_2' for LiMnPO₄, LiFePO₄, and LiCoPO₄ acquired at 11.74 T and 60 kHz MAS are plotted in Figure 13.25 (a). Generally speaking the time constants are shorter than the corresponding values for ⁷Li, but exhibit the same trend, increasing from LiMnPO₄ to LiFePO₄; the values for LiCoPO₄ are longer still. The reason for this trend is the same as for ⁷Li, a combination of the reduction in S from 5/2 to 2 to 3/2, and a possible reduction in the electronic relaxation times on going from Mn²⁺ to Fe²⁺ to Co²⁺.

The trend in the linewidths shown in Figure 13.25 (c) is analogous to that for ⁷Li. The major difference is that the linewidths for all three materials are now dominated by the inhomogeneous contribution, which increases across the series, dominating over an accompanying decrease in the homogeneous linewidths. For LiFePO₄ and LiCoPO₄ the inhomogeneous line broadening can be attributed to the ABMS effect, whilst for LiMnPO₄ it is due to a temperature gradient across the spinning sample [30].

13.6.4 Shifts and shift anisotropies in the EPR formalism

The previous discussion of the paramagnetic shift employs the susceptibility (i.e. scaling factor) formalism, which is the conventional approach for solid materials such as LiMPO_4 and LiMO_2 . However it should also be possible to describe the shift in terms of the EPR formalism, which is an approach that has recently been adopted by Pigliapochi et al [498], and Mondal et al [499, 520]. Here the EPR tensors for each distinct metal ion A are calculated, with each giving a contribution to the paramagnetic shielding tensor in Equation 7.147. For solid-state systems, there are currently no reported SO hyperfine tensor calculations, and until the very recent contribution from Mondal and Kaupp [520], there were no similar schemes for calculating the ZFS tensor. The work by Pigliapochi et al. therefore restricted the SO coupling calculation to the g -tensor. The total shift tensor s in the EPR formalism is then

$$\delta^S = \frac{\mu_B S(S+1)}{3\hbar\gamma_I k(T - \Theta)} \sum_{A,i} g^{(A)} \cdot \left(\frac{\mathcal{A}^{(A,i)}}{2S} \right), \quad (13.8)$$

where the sum is taken both over the distinct metal ions A in the supercell, and over the supercells i .

In LiMPO_4 there is one crystallographically distinct M^{2+} ion per unit cell. However this does not mean that the sum over A comprises a single term. Whilst the M^{2+} ions are indeed symmetry-related, and have the same principal g -tensor components, there are actually four metal ions that are distinguished by having different PAF orientations relative to the crystal frame of reference. This means that the four g -tensors have the same principal components, and PAFs that are related to each other by the symmetry operations describing the $Pnma$ space group. This has profound consequences for calculating the effect of the g -anisotropy on the shift tensor, which are described below.

In the absence of the ZFS tensor there is a total of six terms in the EPR formalism that contribute to either the isotropic shift, SA , or both. The isotropic shift comprises two contact terms, $g_e A^{\text{FC}}$ and $\Delta g_{\text{iso}} A^{\text{FC}}$, and a single pseudo-contact term, $\Delta \mathbf{g} \cdot \mathbf{A}^{\text{SD}}$. The two contact terms have a direct correspondence with the susceptibility formalism, since the total isotropic g -tensor $g_e + \Delta g_{\text{iso}}$ is hidden inside the effective magnetic moment μ_{eff} which is used in the factor that scales the Fermi-contact coupling constant. The A^{FC} constant can be calculated in the same way as previously described, either directly or using the pathway-decomposition approach. The PCS term $\Delta \mathbf{g} \cdot \mathbf{A}^{\text{SD}}$ is a new contribution that is not accounted for in the scaling-factor formalism, and the calculation of this term requires more care. The PCS contribution for each metal ion A is

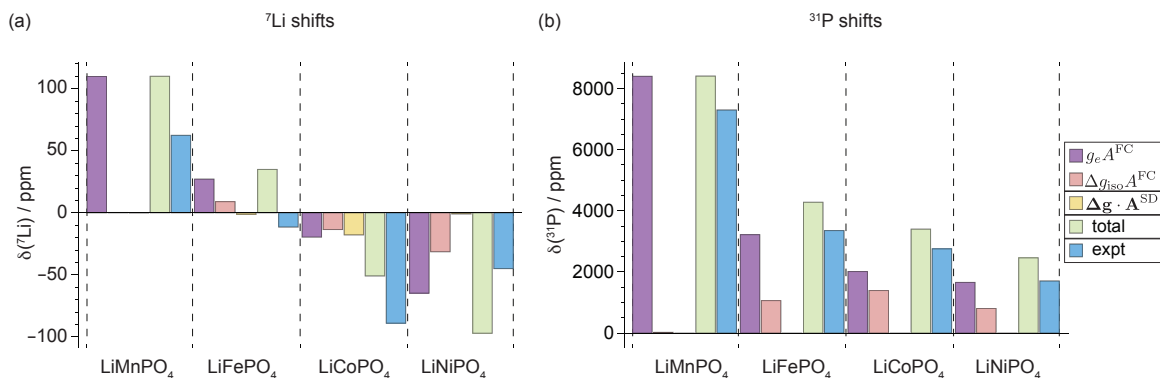


Figure 13.28: Breakdown of the contributions to the total ${}^7\text{Li}$ and ${}^{31}\text{P}$ chemical shifts in the EPR formalism for the series of olivine phosphate materials LiMnPO_4 , LiFePO_4 , LiCoPO_4 , and LiNiPO_4 determined by DFT calculations, and the comparison with the experimental shifts. The ${}^7\text{Li}$ shifts are shown in (a), and the ${}^{31}\text{P}$ shifts are shown in (b).

a matrix product of the site-specific g -tensor $g^{(A)}$ and the total hyperfine tensor due to the metals A from all the supercells, $\sum_i \mathcal{A}^{(A,i)}/(2S)$. This latter quantity can be calculated using a spin-flip approach in an analogous way to obtaining the pathway contributions to the Fermi-contact coupling constant. The supercell is selected so that it contains one each of the distinct metal ions A , the spins of which are aligned so that they are parallel. The resulting electron spin density is then used to calculate the total hyperfine spin-dipolar tensor. Following this each metal ion is spin-flipped in turn, and the new hyperfine coupling tensor calculated. If the supercell contains only one metal ion of each distinct type, then the periodic boundary conditions ensure that the flipping of A causes the same flipping of *all* the spins A in *all* the supercells. Therefore the difference between the two electron spin densities gives us the total though-space ‘pathway’ contribution from A , $\sum_i \mathcal{A}^{(A,i)}/(2S)$.

The calculated ${}^7\text{Li}$ and ${}^{31}\text{P}$ paramagnetic shift contributions for the full series of LiMPO_4 materials are shown in Figure 13.28 [498]. The ${}^7\text{Li}$ shifts in Figure 13.28 (a) indicate that, of the terms calculated, the two contact shifts are generally dominant, with the exception of LiCoPO_4 where there is an appreciable PCS. Regarding the contact terms, for LiMnPO_4 only the NR Fermi-contact shift $g_e A^{FC}$ contributes, due to the zero SO coupling strength in the half-filled d -shell. For the other systems the SO contribution to the contact shift $\Delta g_{iso} A^{FC}$ is important due to the significant isotropic g -shift of 0.17–0.35. The differences between the calculated and experimental shifts in Figure 13.28 (a) may be partly due to the neglect of the ZFS, and so it would be of considerable interest to include this contribution.

The dominance of the contact shift for Mn^{2+} and Fe^{2+} indicates that the scaling-factor formalism described in the previous section should give an accurate description of the shift, as is indeed shown in Table 13.7. Furthermore for Co^{2+} the neglect of the PCS is one factor that explains the significant deviation of the calculated and experimental shifts in Table 13.7. It has been recently shown by Mondal and Kaupp that the ZFS interaction also introduces a substantial contribution to the PCS [520].

The ^{31}P shifts in Figure 13.28 (b) are easier to rationalize. In all cases the PCS is negligible, and the total shift is dominated entirely by contact contributions. Once again only the term $g_e A^{\text{FC}}$ is important for Mn^{2+} , with the SO part becoming more important across the series. The overall agreement between theory and experiment is better, with the calculated shifts tending to slightly overestimate the experimental values.

We now turn to a feature of paramagnetic solid-state NMR that is all too often neglected in these studies, which is the measurement and interpretation of the shift anisotropy. Part of the reason for the neglect of the SA is the difficulty in measuring accurate values, since the intensity distributions of the spinning-sideband manifolds are perturbed by BMS effects. Nevertheless it is still possible to obtain a reasonable estimate of the SA $\Delta\Delta^{\text{S}}$ from a fit of the sideband manifolds, and it proves instructive to compare these values to calculation. The experimental and fitted ^7Li and ^{31}P spinning-sideband manifolds of LiMnPO_4 and LiFePO_4 , acquired at 11.74 T and 60 kHz MAS, are shown in Figure 13.29 [498]. There are some deviations between the experimental and fitted sideband intensities, due to the neglect of BMS effects in the latter, but the quality of the fit is sufficient to extract a good estimate of the anisotropy. The comparison between the fitted values and the calculations is shown in Figure 13.30 for ^7Li (a) and ^{31}P (b). The agreement is remarkably good, given the difficulty of obtaining good experimental values. One noteworthy point is that the calculations manage to reproduce the change in sign of the ^{31}P SA in LiFePO_4 relative to the other SAs.

The breakdown of the total calculated SAs into the individual terms is also given in Figure 13.30. There are four contributions to the SA, comprising one contact term $A^{\text{FC}} \Delta\mathbf{g}$ and three spin-dipolar terms $g_e A^{\text{SD}}$, $\Delta g_{\text{iso}} A^{\text{SD}}$, and $\Delta\mathbf{g} \cdot A^{\text{SD}}$. For the material LiMnPO_4 only the NR dipolar term $g_e A^{\text{SD}}$ contributes to both the ^7Li and ^{31}P SA. For LiFePO_4 there are significant contributions from the other dipolar terms $\Delta g_{\text{iso}} A^{\text{SD}}$ and $\Delta\mathbf{g} \cdot A^{\text{SD}}$. However the most interesting feature is the large contact SA $A^{\text{FC}} \Delta\mathbf{g}$ contribution to the ^{31}P SA of LiFePO_4 , since it is this term that results in the negative overall SA. The importance of this term stems from the fact that the total Fermi-contact interaction with ^{31}P is large compared to ^7Li . This result demonstrates that it is not only the isotropic shift that provides information on the bonding environment of the metal ion

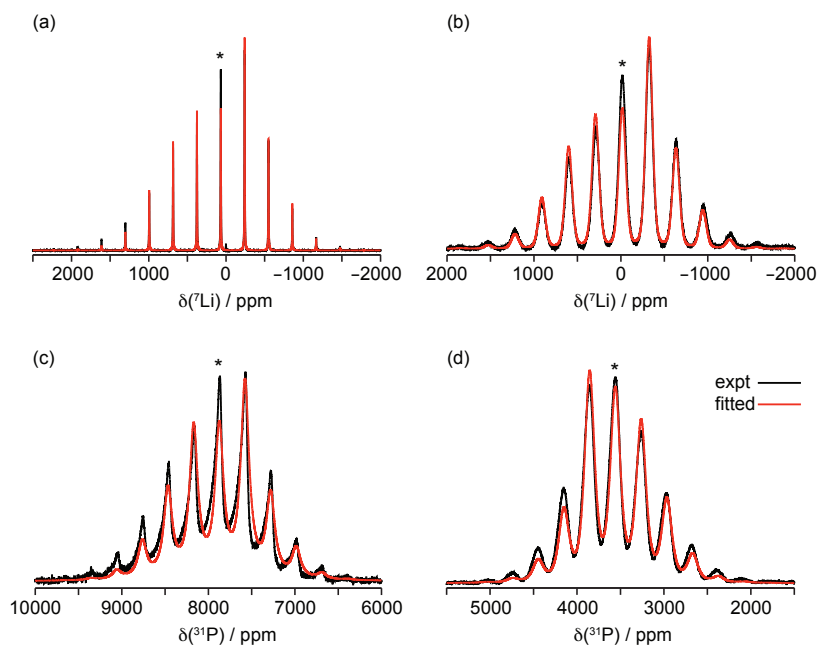


Figure 13.29: Comparison of the experimental and fitted spinning-sideband manifolds of the ${}^7\text{Li}$ (a) and ${}^{31}\text{P}$ MAS NMR spectra of LiMnPO_4 and LiFePO_4 . The ${}^7\text{Li}$ (a) and ${}^{31}\text{P}$ spectra of LiMnPO_4 are shown in (a) and (c), and the corresponding spectra of LiFePO_4 are shown in (b) and (d). The field is 11.74 T, and the spectra were acquired at 60 kHz MAS. The centreband is marked with an *. Adapted with permission from [498]. Copyright (2017) by American Physical Society.

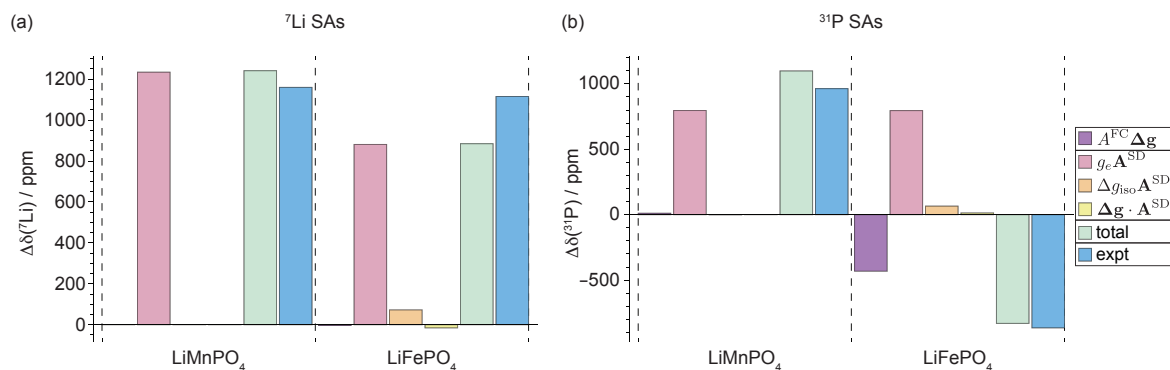


Figure 13.30: Breakdown of the contributions to the total ${}^7\text{Li}$ and ${}^{31}\text{P}$ shift anisotropies in the EPR formalism for the olivine phosphate materials LiMnPO_4 and LiFePO_4 determined by DFT calculations, and the comparison with the experimental SAs. The ${}^7\text{Li}$ SAs are shown in (a), and the ${}^{31}\text{P}$ SAs are shown in (b). The experimental SAs were taken from the fitted spectra in 13.29 (a)–(d).

and the nucleus, but also the SA. The measurement and interpretation of the SA in these systems points the way forward to the use of the SA as a structural restraint in the NMR of paramagnetic materials.

13.6.5 Experiments and calculations on $\text{LiFe}_x\text{Mn}_{1-x}\text{PO}_4$

The final topic in this case study is the use of paramagnetic solid-state MAS NMR and DFT calculations in the investigation of the mixed-metal-ion olivine phosphates $\text{LiFe}_x\text{Mn}_{1-x}\text{PO}_4$ with $x = 0.25, 0.5,$ and 0.75 . These materials have the same basic structure as shown in Figure 13.21, and the same local Li and P environments as in Figures 13.24 and 13.27. However the metal-ion sites are occupied by a solid-solution of the metal ions Mn^{2+} and Fe^{2+} . One consequence of this is that there are now multiple local P environments, as the chemical environment of these sites is dominated by the short-range contact interactions between the five metal ions. Hence there are $2^5 = 32$ P sites in the material, the populations of which are given by the probability of a random distribution of Mn^{2+} and Fe^{2+} resulting in the corresponding occupancies of the five metal sites.

The NMR spectra of $\text{LiFe}_x\text{Mn}_{1-x}\text{PO}_4$ with $x = 0, 0.25, 0.5, 0.75,$ and 1 were acquired at 11.74 T and 60 kHz MAS [30] using the double-adiabatic spin-echo pulse sequence in Figure 12.50 (a) [34], and are shown in Figure 13.31 (a). The spectra of the three mixed phases are very complicated, as each is a superposition of 32 spinning-sideband manifolds with different isotropic shifts. As such it is impossible to obtain any detailed information from these spectra, and we can simply note that at lower values of x the overall spectral intensity is biased towards the all-Mn shift of 7866 ppm due to the higher statistical probability of more metal sites being occupied by Mn^{2+} than Fe^{2+} . Similarly at higher Fe^{2+} content the spectral intensity is biased more towards the all-Fe shift of 3558 ppm.

The lack of resolution between the different resonances is due in large part to the overlap between the different spinning-sideband manifolds. This overlap was removed using the aMAT experiment in Figure 12.50 (b), giving a set of two-dimensional correlation spectra such as that for $\text{LiFe}_{0.5}\text{Mn}_{0.5}\text{PO}_4$ shown in Figure 12.53. The complete set of isotropic projection spectra is shown in Figure 13.31 (b). The beauty of this experiment is that it enabled the resolution of eight distinct groups of isotropic resonances, in which are located the resonances of the 32 local environments.

The total contact shifts for each site can be calculated from the pre-existing pathway contributions given in Figure 13.27, which saves effort otherwise required to calculate the shifts for each extended structure. The calculated shifts were compared with the values obtained from a fit of the three spectra of the mixed phases

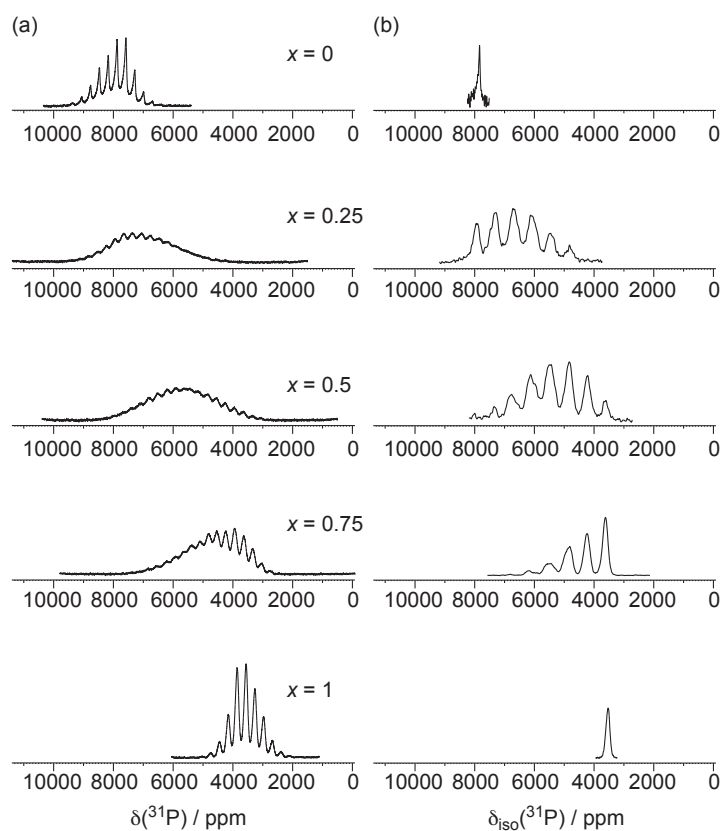


Figure 13.31: ^{31}P NMR spectra of the five $\text{LiFe}_x\text{Mn}_{1-x}\text{PO}_4$ materials ($x = 0, 0.25, 0.5, 0.75, 1$), all of which occur in the olivine-type structure. The one-dimensional spectra containing overlapping sideband patterns are shown in (a), and the projections of the aMAT spectrum containing just the isotropic shifts are shown in (b). Adapted with permission from [30]. Copyright (2012) American Chemical Society.

using the same pathway-contribution model in order to obtain a full assignment, as shown in Figure 13.32. The full set of 32 sites is given in (a), and the experimental and fitted spectra are compared in (b) labelled with the assignments [30]. In this investigation, pathway contributions for the two metal ions were also calculated for different coordination geometries in order to model the effects of structural disorder due to the substitution of one metal ion for another.

To summarize, this study concerns one of the most complex paramagnetic materials that has been investigated with solid-state NMR to date, and provides a notable benchmark for future NMR studies of paramagnetic systems. It was successfully repeated on the mixed-phase $\text{LiCo}_{1-x}\text{Fe}_x\text{PO}_4$ materials [56], and the aMAT experiment has also been applied to other battery materials including $\text{P2-Na}_x[\text{Li}_y\text{Ni}_z\text{Mn}_{1-y-z}]\text{O}_2$ with $(0 < x, y, z < 1)$ [55].

13.7 Contact shifts in ferredoxins due to coupled Fe_4S_4 clusters

13.7.1 Background

Ferredoxins are proteins containing iron–sulphur cores that mediate electron transfers in metabolic processes [521]. The key constituent of a ferredoxin is a Fe_xS_y unit, which can either donate or accept electrons causing a change in the oxidation state of the Fe ions, and catalysing biological redox reactions. We therefore present an example of a solution paramagnetic NMR study here as it forms a link to the previous discussion of battery materials.

The particular example we present is that of Bertini et al [363], which includes the assignment and interpretation of the ^1H and ^{13}C contact shifts in the cysteine residues of ferredoxin from *Clostridium acidii urici*, which catalyzes the reduction of CO_2 to formate [522]. This and similar studies, are notable as they are interesting examples of the application of solution NMR to observe nuclear spins from residues that directly coordinate to the metal ion. Ferredoxin from *Clostridium acidii urici*, the structure of which is shown in Figure 13.33 (a), contains two Fe_4S_4 cores, each one of which can either exist in an oxidized state $[\text{Fe}_4\text{S}_4]^{2+}$ or reduced state $[\text{Fe}_4\text{S}_4]^+$. In the oxidized state each cluster formally contains two Fe^{3+} ions and two Fe^{2+} , and has a diamagnetic electronic spin ground state of $S = 0$ indicating some antiferromagnetic alignment of the spins. However some temperature-dependent paramagnetism arises from the population of the excited electronic spin states. The reduced-state cluster contains one Fe^{3+} ion and three Fe^{2+} , and has an electronic

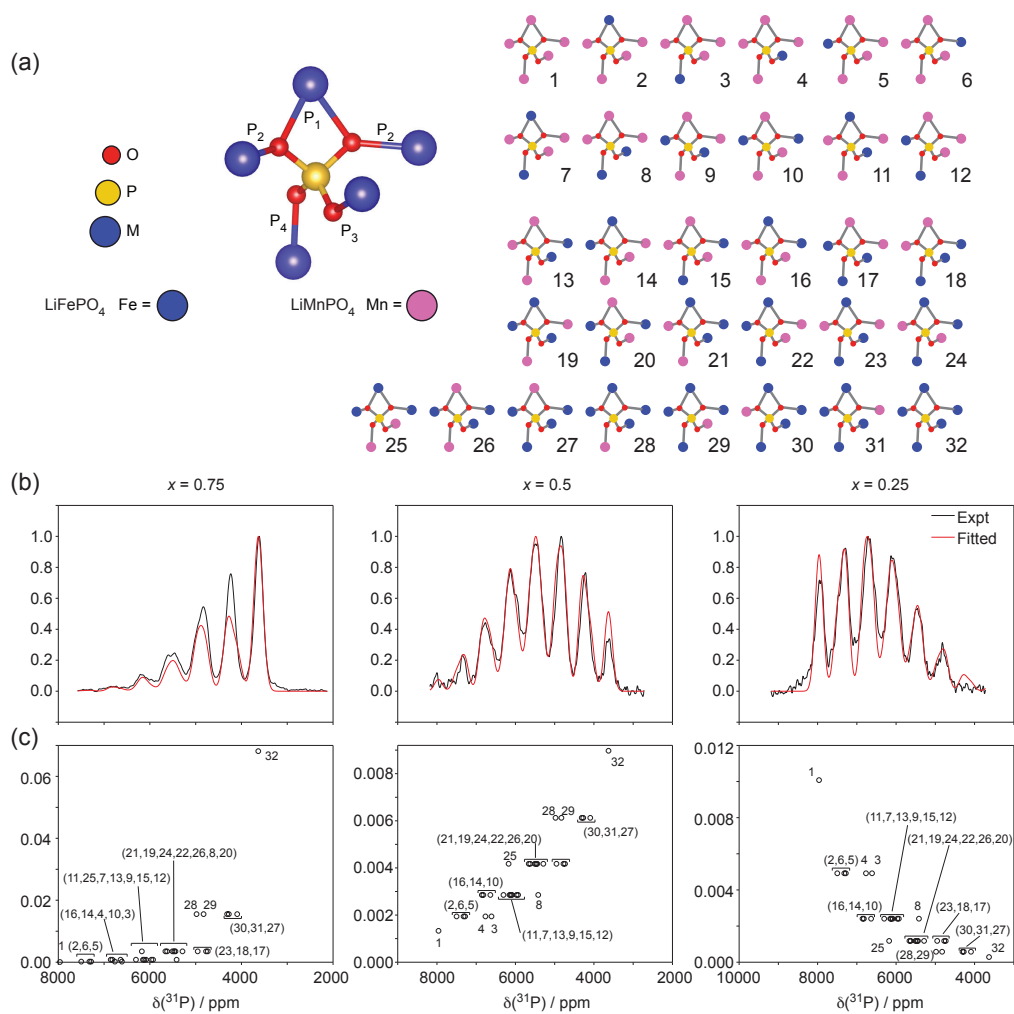


Figure 13.32: Results of the fitting of the isotropic projections of the aMAT spectra. Pathway contributions of the Mn^{2+} and Fe^{2+} ions to the total contact shift were varied to fit the isotropic projections of the experimental ^{31}P NMR spectra. The M–O–P pathway labels are shown in (a) together with the 32 possible configurations in the mixed $\text{Mn}^{2+}/\text{Fe}^{2+}$ phases. The comparison of the experimental and fitted isotropic spectra is shown in (b) for the $x = 0.75, 0.5$, and 0.25 phases. The contact shifts and relative intensities of the 32 peaks occurring in each spectrum are shown in the absence of line shape effects in (c), with labelling as in (a). The intensities shown in (c) take into account both the stoichiometry-dependent probability of the configuration and the T_2' dephasing effects. Adapted with permission from [30]. Copyright (2012) American Chemical Society.

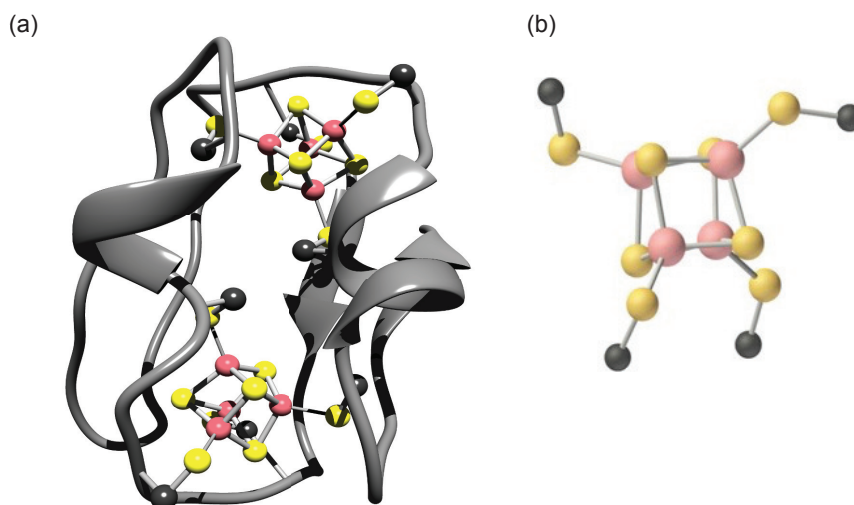


Figure 13.33: Structure of a ferredoxin and the Fe_4S_4 cluster. The protein is shown in (a), and the Fe_4S_4 cluster is shown in (b). The cluster is coordinated to four cysteine residues, with each Fe ion in the bonding to a S atom of a cysteine sidechain. The Fe ions are coloured pink, the S atoms are yellow, and the CB atoms are coloured black.

spin ground state of $S = 1/2$. Each Fe_4S_4 cluster binds to four cysteine amino acid residues, with each Fe ion forming a bond to the S of the $-\text{CBH}_2-\text{SH}$ sidechain, as shown in Figure 13.33 (b). The bonding between the cluster and the cysteine residue can therefore be represented as $\text{Fe}-\text{S}-\text{CB}(\text{HB}_1, \text{HB}_2)-\text{CA}(\text{HA}_1)-$. The nuclear spins of the cysteine sidechain and backbone are therefore expected to experience large paramagnetic shifts with a large contact contribution. In addition the exchange coupling constants within the cluster are of the same order of magnitude as kT at room temperature, and so we expect a non-Curie temperature dependence of the paramagnetic shifts of the type shown in section 7.5.2 [46].

Bertini et al. investigated both the oxidized form of the protein, with both clusters in the state $[\text{Fe}_4\text{S}_4]^{2+}$, and a partially reduced form [363]. Partial reduction gives the complex mixture of species shown in Figure 13.34, which are in exchange. There are two partially-reduced species, in which one cluster is oxidized and the other reduced, which are in fast exchange on the NMR timescale. Both species are also in slow exchange with both the fully-oxidized and fully-reduced species.

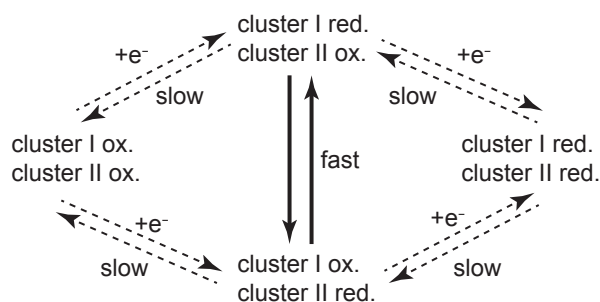


Figure 13.34: Representation of the equilibrium between the oxidation states of the two Fe_4S_4 clusters in a ferredoxin following the addition of a reducing agent to the fully-oxidized protein. The two intermediate-reduced species are in fast exchange with each other, and in slow exchange with both the fully-oxidized and fully-reduced species. Fast-exchange processes are indicated by thick solid arrows, and slow-exchange processes are indicated by thin dashed arrows.

13.7.2 NMR spectroscopy and assignment

Figure 13.35 (a) shows the one-pulse ^1H solution NMR spectrum of ferredoxin from *C. acidi urici* taken from Bertini et al [363]. Eight resonances are resolved above 10 ppm (labelled A–H). These signals exhibited short relaxation times and temperature-dependent shifts, and so were ascribed to ^1H s of the coordinated cysteine residues. These signals were assigned using COSY and NOESY, which identified A–H as the CB protons HB1 or HB2, and established correlations to the other geminal HB nuclei A'–H'. In addition correlations to the CA protons HA were also observed in the NOESY spectrum. These were assigned using a structural model of the related ferredoxin from *Clostridium pasteurianum* [363]. This resulted in the identification of eight groups of two HB and one HA protons, each corresponding to a single cysteine residue. However this was insufficient to assign each cysteine to a particular cluster, and so further experiments were performed on a partially-reduced sample of ferredoxin from *C. acidi urici*.

Figure 13.35 (b) shows the ^1H spectrum of the partially-reduced ferredoxin. We note that the resonances are broader than for the oxidized sample, which is due to the ground spin state of the cluster no longer being diamagnetic, but paramagnetic with $S = 1/2$. The cross-peaks between these broad signals in the COSY and NOESY spectra were expected to be weak, and so the assignment was performed using EXSY to identify correlations between the slowly-exchanging oxidized and intermediate species. Comparison of the spectra in Figure 13.35 (a) and (b) and subtraction results in two further spectra of the fully-reduced species (c), and the two intermediate species (d). The full set of chemical shifts for the oxidized, intermediate, and reduced

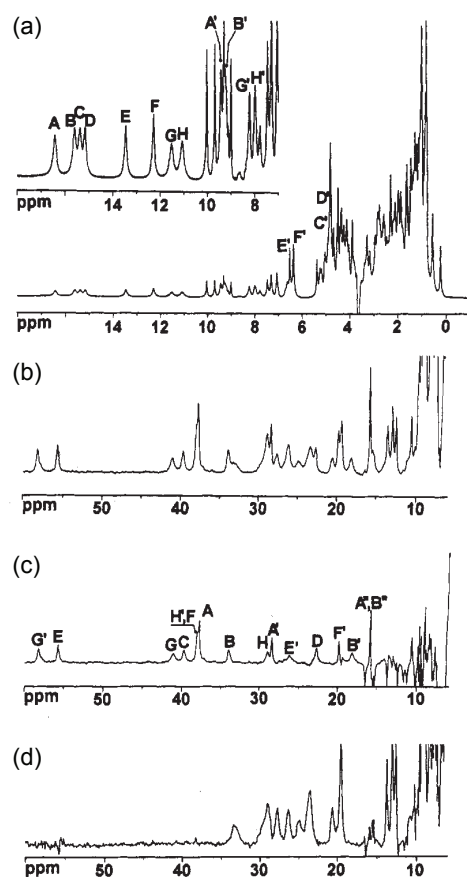


Figure 13.35: The ^1H NMR spectra acquired at 600 MHz and 298 K of the ferredoxin from *C. acidu urici*. The spectrum of the fully-oxidized species is shown in (a). Following partial reduction the spectrum in (b) was obtained. The spectra in (c) and (d) are of the fully-reduced species, and the two intermediate reduced species respectively. Spectrum (d) was obtained by acquiring a spectrum of a 90%/10% oxidized/partially-reduced species and subtracting from it spectrum (a). Spectrum (c) was obtained by subtracting (d) from the spectrum of a sample containing both partially- and fully-reduced ferredoxin. The reported assignment is given in Table 13.9. Adapted with permission from [363]. Copyright (1994) American Chemical Society.

Residue	Cluster I		Residue	Cluster II	
	Atom	Assignment		Atom	Assignment
Cys11	HB ₁	B'	Cys40	HB ₁	A'
	HB ₂	B		HB ₂	A
	HA	B''		HA	A''
Cys14	HB ₁	D	Cys43	HB ₁	C
	HB ₂	D'		HB ₂	C'
	HA	D''		HA	C''
Cys47	HB ₁	E'	Cys18	HB ₁	F'
	HB ₂	E		HB ₂	F
	HA	E''		HA	F''
Cys8	HB ₁	G	Cys37	HB ₁	H
	HB ₂	G'		HB ₂	H'
	HA	G''		HA	H''

Table 13.9: Assignment of the ¹H NMR spectrum in Figure 13.35 (a) of the oxidized ferredoxin from *C. acidurici*.

ferredoxin species allowed the assignment of each set of cysteine ¹H signals to either cluster I or II, i.e. the eight groups of signals could now be assigned to specific clusters.

The final step in the assignment process was to identify the residue number of each of the eight cysteines by establishing correlations to other residues in the amino acid sequence. This was achieved using a combination of NOESY and TOCSY on the fully-oxidized ferredoxin species. The full sequence-specific assignment of HB₁, HB₂, and HA is given in Table 13.9.

Following the complete ¹H assignment, a ¹H-¹³C HMQC spectrum was acquired to identify the ¹³CA and ¹³CB resonances in each cluster, which was the first time this had been achieved at natural abundance [363]. From the HMQC spectrum all eight ¹³CB resonances and six out of eight ¹³CA resonances were assigned.

13.7.3 Temperature dependence of the contact shifts

Having obtained the assignment of the cysteine resonances, the paramagnetic shifts were extracted in order to gain insight into both the electronic structure of the Fe₄S₄ cluster, and the mechanism of unpaired spin-transfer from the Fe to the nuclear spins. As discussed in section 12.3.3 it is necessary to have a complete assignment of a diamagnetic analogue of the paramagnetic system of interest in order to subtract the orbital chemical shifts, and that this strategy relies on the orbital contributions to the shifts not changing significantly on substitution of the paramagnetic ion for the diamagnetic one. In the present case the reference system was a zinc-finger protein, where the orbital shifts were taken to be the chemical shifts of the nuclei in the cysteine residues bound to Zn [363].

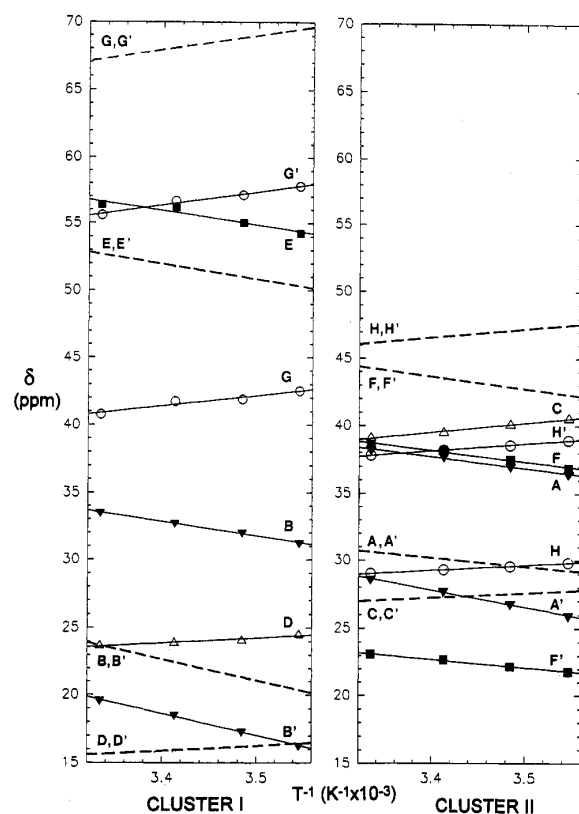


Figure 13.36: The experimental temperature dependence of the chemical shifts of the cysteine ^1HB signals of fully-reduced ferredoxin from *C. acidithiobacillus*. The data were obtained from EXSY spectra acquired at temperatures between 282 K and 300 K. The dashed lines give the estimated values of the angle-independent shifts for each CBH_2 pair. Reproduced with permission from [363]. Copyright (1994) American Chemical Society.

The temperature dependence of the paramagnetic shifts due to a coupled cluster of paramagnetic ions may be diagnostic of the spin state of the whole cluster and give estimates of the exchange coupling constant, as shown in section 7.5.2. With this aim in mind the chemical shifts of the CB protons in the fully-reduced protein were obtained from the EXSY spectrum over a range of temperatures between 282 and 300 K. The results are shown in Figure 13.36 [363]. Although the temperature range is too narrow to obtain a curve that is sufficient for a detailed analysis, it does show that for each cluster two pairs of CB protons have chemical shifts that increase with temperature, and two pairs that with shifts that decrease with temperature. This behaviour has been referred to as anti-Curie and Curie respectively. However we avoid the use of

such terminology here as it oversimplifies the true temperature dependence, which we have seen may be considerably more complicated.

Regarding the interpretation of the temperature dependence, it should be noted that the available temperature range is insufficient to obtain a detailed picture of the electronic structure of the Fe₄S₄ cluster. Nevertheless the temperature dependence does offer some insight, and indicate that the Fe ions are at least pairwise inequivalent [363]. The fact that half of the CB proton shifts increase with temperature indicates the presence of at least one antiferromagnetic coupling, so that the increase in temperature leads to a larger thermal population of a spin state with a larger spin S and hence a greater magnetic moment.

13.7.4 Angular dependence of the contact shifts

The CB nuclei are separated from the coordinating Fe by two bonds, the CA and HB by three bonds, and the HA by four bonds. We expect the shifts of these nuclear spins to be dominated by the Fermi-contact interaction, which we have seen depends on the bonding geometry relative to the metal ion. Hence we can obtain information on the spin-transfer mechanism from the dependence of the paramagnetic shift on the geometry of the cysteine relative to the Fe₄S₄ cluster. Here we focus on the contact shifts of the HB and CA spins which, due to the three-bond separation, have a geometry relative to the Fe that can be described by reference to Figure 13.37 (a). Here the geometry is specified by a dihedral angle θ which describes the angular separation between the planes defined by the Fe–S–CB linkage and the S–CB–HB linkage. If the unpaired electron density from the Fe resides mainly in the Fe–S σ bond the contact shift $\delta_{\text{con}}^{\sigma}$ can be shown to obey a Karplus relation of the form:

$$\delta_{\text{con}}^{\sigma} = a' \cos^2(\theta) + b' \cos(\theta) + c', \quad (13.9)$$

where a' , b' , and c' are coefficients [525]. Equation 13.9 follows from the fact that the overlap of the Fe–S σ bond with the HB s -orbital is at a maximum when Fe–S and CB–HB bonds are either co- or anti-parallel, corresponding to $\theta = 0$ and π , and a minimum when they are orthogonal with $\theta = \pi/2$. The magnitude of the contact shift varies accordingly. On the other hand, if the unpaired electron density is mainly located in a F–S

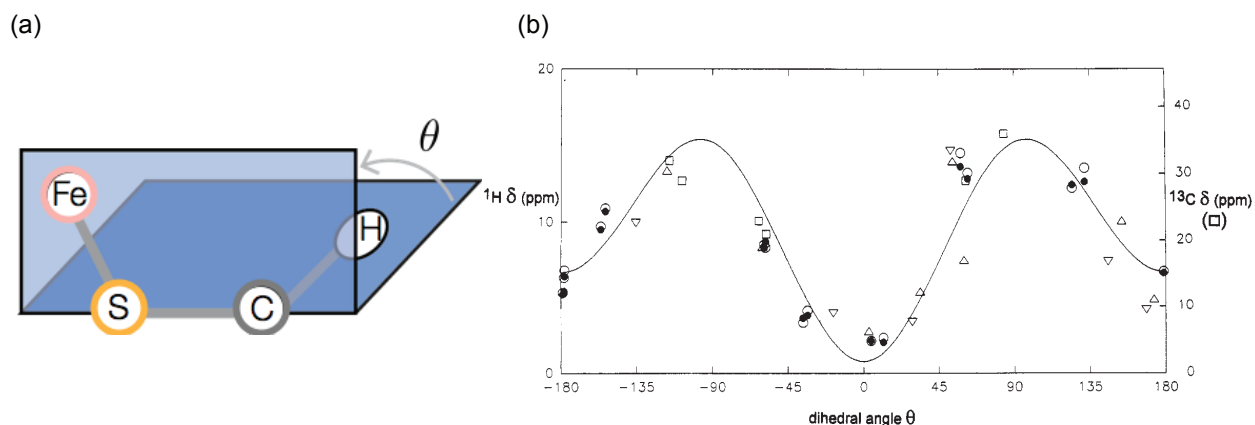


Figure 13.37: Plots of the contact shifts of the nuclei three bonds away from a Fe ion against the dihedral angle θ . In (a) is shown the dihedral angle θ between the two planes defined by the Fe–S–CB atoms on the one hand, and the S–CB–HB atoms on the other. The HB contact shift depends strongly on θ via a Karplus relation. There is also an analogous dependence for the CA contact shift on the dihedral angle between the planes containing the Fe–S–CB and S–CB–CA. The plot in (b) shows the ^1H contact shifts from the CBH_2 protons (left-hand axis) from the following proteins: oxidized ferredoxin from *C. acidi urici* (●) [363]; oxidized ferredoxin from *C. pasteurianum* (○) [353]; reduced HiPIP from *C. vinosum* (Δ) [523]; and reduced HiPIP II from *E. halophila* (▽) [524]. Here the dihedral angle is between the two planes defined by Fe–S–CB and S–CB–HB. The ^{13}C contact shifts in oxidized ferredoxin from *C. acidi urici* (right-hand axis) are also plotted (□). Here the dihedral angle is between the planes defined by Fe–S–CB and S–CB–CA. The curve is the best fit of Equation 13.11 to the ^1H shifts from oxidized ferredoxin from *C. acidi urici* (●) with $a = 11.5$, $b = -2.9$, and $c = 3.7$ ppm. Adapted with permission from [363]. Copyright (1994) American Chemical Society.

π bond a different Karplus relation is needed to give the contact shift $\delta_{\text{con}}^{\pi}$:

$$\delta_{\text{con}}^{\pi} = a'' \sin^2(\theta) + c'', \quad (13.10)$$

where a'' and c'' are different coefficients [526, 527]. Here the maximum overlap between the orbital containing the electron density and the HB s -orbital occurs when the Fe–S and CB–HB bonds are orthogonal. In the general case both transfer mechanisms may contribute to the overall contact shift δ_{con} , which is then a sum of Equations 13.9 and 13.10:

$$\delta_{\text{con}} = a \sin^2(\theta) + b \cos(\theta) + c, \quad (13.11)$$

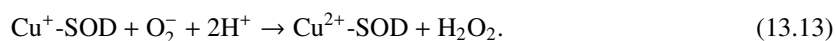
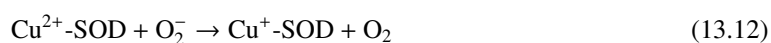
where $a = a'' - a'$, $b = b'$, and $c = a' + c' + c''$. The relative magnitudes of a and b indicate whether the dominant electron transfer is via the π or σ bonds. The same considerations also apply to the CA contact shift, with the difference that the dihedral angle is defined between the Fe–S–CB and S–CB–CA planes.

The Karplus hypothesis was tested by plotting the contact shifts against the observed dihedral angle for a range of systems, including the ^1HB and ^{13}CA shifts of oxidized ferredoxin from *C. acidi urici* in the present case study [363], and the ^1HB contact shifts from oxidized *C. pasteurianum* ferredoxin [353], reduced *C. vinosum* high-potential protein (HiPIP) [523], and reduced *E. halophila* HiPIP II [524]. The plot is reproduced in Figure 13.37 (b). The data generally follow the trend in Equation 13.11. We firstly notice that all the contact shifts are positive, which indicates that the electron delocalization mechanism dominates the contact interaction. When fitted to the HB shifts from *C. acidi urici* ferredoxin, we obtain the following parameters for the Karplus relation: $a = 11.5$, $b = -2.9$, and $c = 3.7$ ppm. Both the positive value of a and the observation that $|a| > |b|$ indicate that the electron transfer mechanism is dominated by delocalization from the Fe–S π bond.

13.8 Paramagnetic distance restraints in the metalloprotein superoxide dismutase (SOD)

13.8.1 Background

We now change to a paramagnetic NMR study of a different protein sample, with a case study that illustrates the use of long-range paramagnetic structural restraints to determine the structure of a protein in the solid state. The chosen study is that by Knight et al. on the metalloenzyme superoxide dismutase (SOD) [11, 45, 461]. Superoxide dismutase is a dimer comprising 2×153 amino-acid residues, each unit of which binds to two metal ions M_1^{m+} and M_2^{n+} [528, 529]. The enzyme has the physiological function of oxidizing the superoxide anion O_2^- , which is produced as a by-product of metabolic processes and can cause cell damage if not regulated. The form of the protein which binds one Cu and one Zn ion, (Cu^{n+}, Zn^{2+}) -SOD, catalyses the removal of superoxide via the following two reactions:



We see that the Cu ion is essential to the process, as the reactions are driven by the redox between the paramagnetic Cu^{2+} and diamagnetic Cu^+ oxidation states.

One advantageous aspect of SOD for the application of paramagnetic restraints is that different metal ions can be incorporated into the binding sites depending on which restraints we wish to measure, as shown in Figure 13.38 [530]. For example the (Cu^{n+}, Zn^{2+}) -SOD form was used to measure PREs as the long electronic relaxation times of 2.5 ns in the Cu^{2+} ion in the paramagnetic form resulted in large induced nuclear relaxation rates [11]. A section of the (H)NH spectrum is shown in Figure 13.38 (a) [530]. Here the diamagnetic reference protein was the reduced form (Cu^+, Zn^{2+}) -SOD. However the Cu^{2+} ion has a small magnetic anisotropy, as defined by the axial and rhombic susceptibility anisotropies, and so gives only small PCSs as seen in the (H)NH spectrum of Figure 13.38 (a) [530]. For this reason PCS values were measured on (Co^{2+}, E) -SOD, where E indicates that the second binding site is empty, as the larger magnetic anisotropy of the Co^{2+} ion gives larger PCSs that are more easily measurable, as shown by the (H)NH spectrum of this protein in Figure 13.38 (b) [530] [45]. The electronic relaxation times of the Co^{2+} ion are shorter than

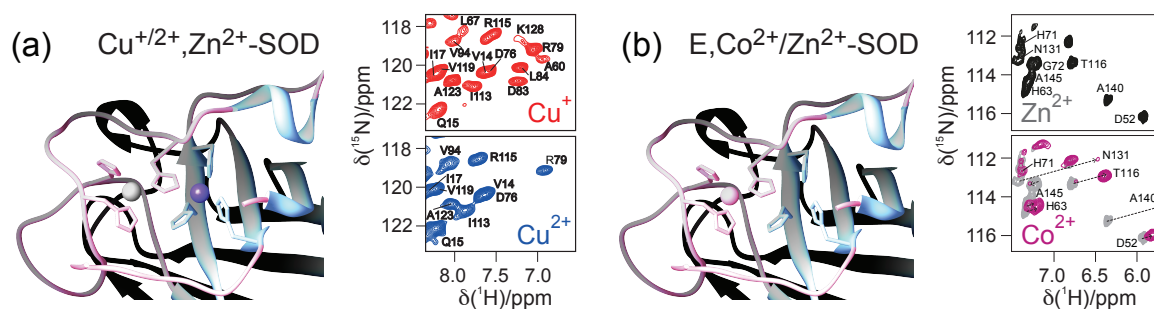


Figure 13.38: Two-dimensional (H)NH solid-state MAS NMR spectra of two forms of SOD. The spectra of paramagnetic ($\text{Cu}^{2+}, \text{Zn}^{2+}$)-SOD and its diamagnetic reference ($\text{Cu}^+, \text{Zn}^{2+}$)-SOD, which are shown in (a), were used to measure PREs due to the Cu^{2+} ion. In (b) are shown the spectra of paramagnetic (Co^{2+}, E)-SOD and its diamagnetic reference (Zn^{2+}, E)-SOD, with the former showing PCSs in both frequency dimensions. Reproduced with permission from [530]. Copyright (2013) American Chemical Society.

for Cu^{2+} , taking typical values of 1–10 ps. The coherence lifetimes are therefore longer, which allowed for more sensitive acquisition of PCS values closer to the metal ion. In this case the diamagnetic reference was (Zn^{2+}, E)-SOD.

In this study all the NMR data for the assignment, measurement of PCSs and PREs, and the ^1H – ^1H distance restraints were acquired under 60 kHz MAS on a sample that was perdeuterated with the exchangeable amide protons 100% back-exchanged. Triple-resonance proton-detected three-dimensional HCN experiments were acquired using a subset of the pulse sequences summarized in Tables 12.5 and 12.6.

13.8.2 Resonance assignment and structure calculation using non-paramagnetic ^1H – ^1H distance restraints

The sequential assignment of the backbone amide ^{15}N , $^1\text{H}^{\text{N}}$, ^{13}CO , and ^{13}CA was performed using the two-dimensional (H)NH sequence and the three-dimensional (H)CANH, (H)CONH, (H)CA(CO)NH, and (H)CO(CA)NH pulse sequences. For the diamagnetic reference protein (Zn^{2+}, E)-SOD all these resonances were assigned for 145 out of a total of 147 non-proline amino acid residues [461]. The assignment of the two Cu-bound proteins was performed using the same set of experiments, from which 136 amide resonances were assigned for ($\text{Cu}^+, \text{Zn}^{2+}$)-SOD, and 116 for ($\text{Cu}^{2+}, \text{Zn}^{2+}$)-SOD respectively.

Paramagnetic distance restraints alone are insufficient to generate a three-dimensional structure of a

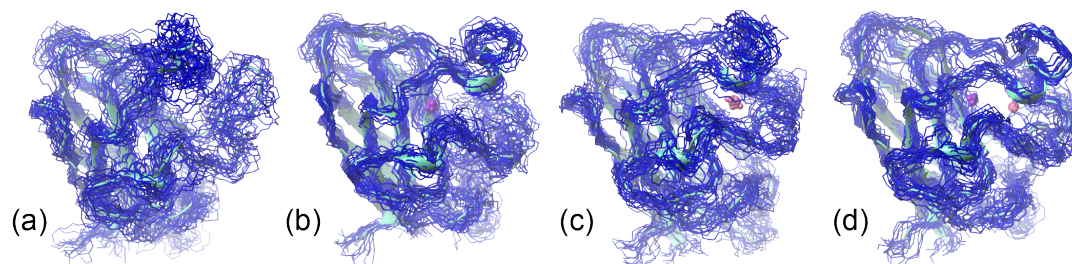


Figure 13.39: Structure bundles of SOD calculated from solid-state NMR data using different types of restraint. The bundle in (a) were calculated with no paramagnetic restraints, and has an rmsd of 3.1 Å. The structures in (b) were calculated using PREs, using an initial trial magnetic susceptibility tensor fitted from the mean structure in (a). Here the rmsd is 1.6 Å. In (c) is shown the structure bundle calculated using PCSs, with an rmsd of 1.7 Å. The final structure bundle, shown in (d), were calculated using both PCSs and PREs and give an rmsd of 1.4 Å. The Co^{2+} and Cu^{2+} ions are shown in pink and violet respectively, and the aquamarine ribbon is the mean NMR structure for each case. Reproduced with permission from [530]. Copyright (2013) American Chemical Society.

protein, and must be combined with conventional restraints used for diamagnetic proteins. Therefore ^1H - ^1H distance restraints between the backbone $^1\text{H}^{\text{N}}$ were also measured on $(\text{Cu}^+, \text{Zn}^{2+})$ -SOD. Using the (H)NHH-RFDR sequence 297 such distance restraints were obtained. These were combined with dihedral angle restraints and ambiguous hydrogen-bond restraints in the programme Cyana. In the absence of any paramagnetic restraints the structure calculation yielding the bundle of structures shown in Figure 13.39 (a). The precision of the structure is comparatively low, having a root-mean-square deviation (rmsd) from the mean of 3.1 Å.

13.8.3 Paramagnetic relaxation enhancement as structural restraints

The precision of the calculated structure was improved by the inclusion of PREs from $(\text{Cu}^{2+/+}, \text{Zn}^{2+})$ -SOD. The resolution necessary to measure the relaxation rates was obtained from the two-dimensional (H)NH spectra of the two proteins, which are shown in Figure 12.68. Here 103 resonances were resolved, indicating that the (H)NH pulse sequence (shown in Figure 13.40 (a)) could be modified to include the necessary relaxation-measurement elements. The ^{15}N R_1 relaxation rates were measured by incorporating an inversion-recovery block after the first CP step in the (H)NH sequence as shown in Figure 13.40 (b). Measurements of the ^{13}CO R_1 values were performed using the sequence in Figure 13.40 (d), which is based on the (H)CONH sequence (shown in Figure 13.40 (c)) in which the ^{13}CO evolution time is replaced with an inversion-recovery

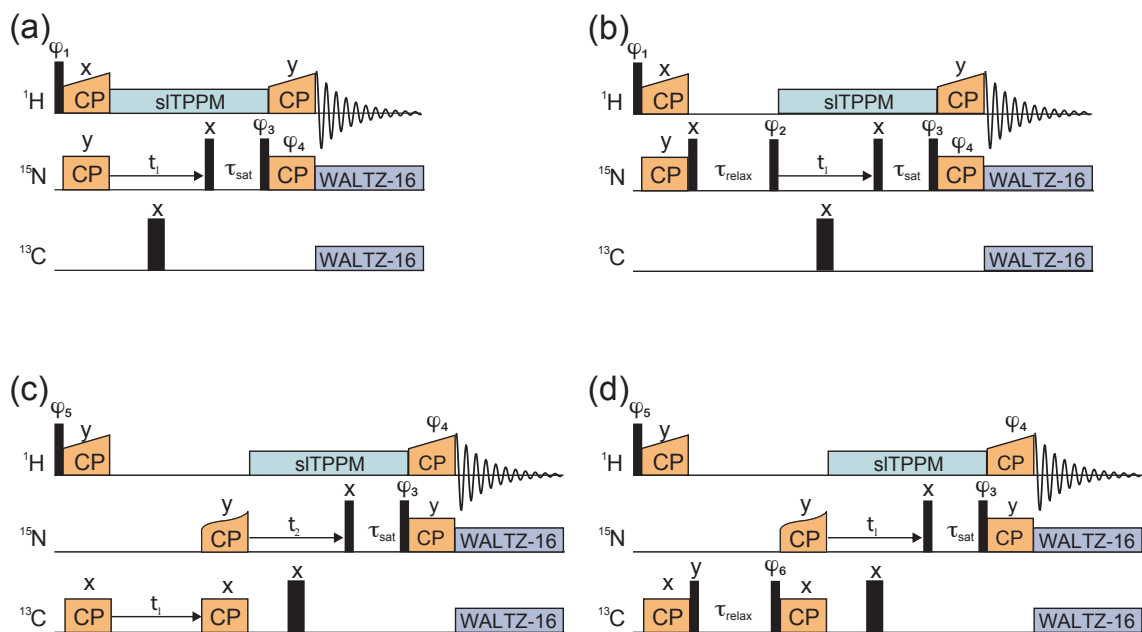


Figure 13.40: Pulse sequences used to measure relaxation rate constants of the backbone amide ^{15}N and ^{13}C spins in solid-state proteins. Measurement of the ^{15}N R_1 rate constants was performed using a sequence based on the standard (H)NH experiment shown in (a). To measure the ^{15}N R_1 values an inversion–recovery element was incorporated to give the sequence in (b). The ^{13}CO R_1 rate constants were measured using a modification of the (H)CONH pulse sequence in (c). Here the t_1 evolution time was replaced by an inversion–recovery element, giving the sequence in (d). Narrow rectangles indicate 90° pulses, and broader rectangles are 180° pulses.

block. The site-specific relaxation rates are shown in Figure 13.41. It should be noted that the measurement of these rates benefitted substantially from 60 kHz MAS and perdeuteration, as the weakening of the ^1N dipolar-coupling network reduced any coherent effects. This is particularly important for the measurement of the ^{13}CO R_1 rate constants shown in Figure 13.41 (g) and (h).

The PREs were calculated by subtracting the $(\text{Cu}^+,\text{Zn}^{2+})$ -SOD relaxation rates constants from the corresponding $(\text{Cu}^{2+},\text{Zn}^{2+})$ -SOD rate constants. This resulting in a total of 90 ^{15}N PREs and 85 ^{13}CO PREs being obtained from spins between 10 Å and 24 Å from the Cu^{2+} ion. These PREs were ascribed to the Solomon mechanism with the correlation time dominated by the electronic relaxation time, which was given the literature value of 2.5 ns [15]. The PRE varies with the distance R from the Cu^{2+} ion as $1/R^6$, enabling a distance to be calculated. In the structure calculation these distances were included with the other distance restraints, but were allowed to vary by 3 Å either side of the predicted value. In addition 25 ^1H - ^{15}N cross peaks that were observed in the (H)NH of the diamagnetic protein, but not the paramagnetic protein, were assumed to be broadened beyond detection by a PRE due to the close proximity to the Cu^{2+} ion, and so were assigned an upper distance R of 10 Å. The corresponding structure bundle is shown in Figure 13.39 (b). They show an increase in precision compared to the bundle in (a), with a lower rmsd of 1.6 Å, and particularly good definition around the metal binding sites.

This case study illustrates the utility of paramagnetic distance restraints in refining the structure of a protein. These restraints are extremely useful both in solution studies [44], and particularly in the solid state, where lower resolution and other difficulties often result in insufficient diamagnetic restraints being available for a high-precision structure calculation.

13.8.4 Pseudo-contact shifts as structural restraints

To further improve the precision of the calculated structure, PCS values from $(\text{Co}^{2+},\text{E})$ -SOD were measured and used. The initial assignment of the resonances of $(\text{Co}^{2+},\text{E})$ -SOD was achieved by comparing the (H)CANH and (H)CONH spectra with those acquired for $(\text{Zn}^{2+},\text{E})$ -SOD, and assigning those resonances that were easily identifiable, as shown in Figure 12.69 (d)–(g). From these assigned resonances PCS values were extracted by subtracting the chemical shifts of $(\text{Zn}^{2+},\text{E})$ -SOD from those of $(\text{Co}^{2+},\text{E})$ -SOD. These PCSs were then used in combination with the low-resolution structure in Figure 13.39 (a) to fit an approximate magnetic susceptibility tensor, from which the PCSs of all hitherto unassigned resonances were predicted.

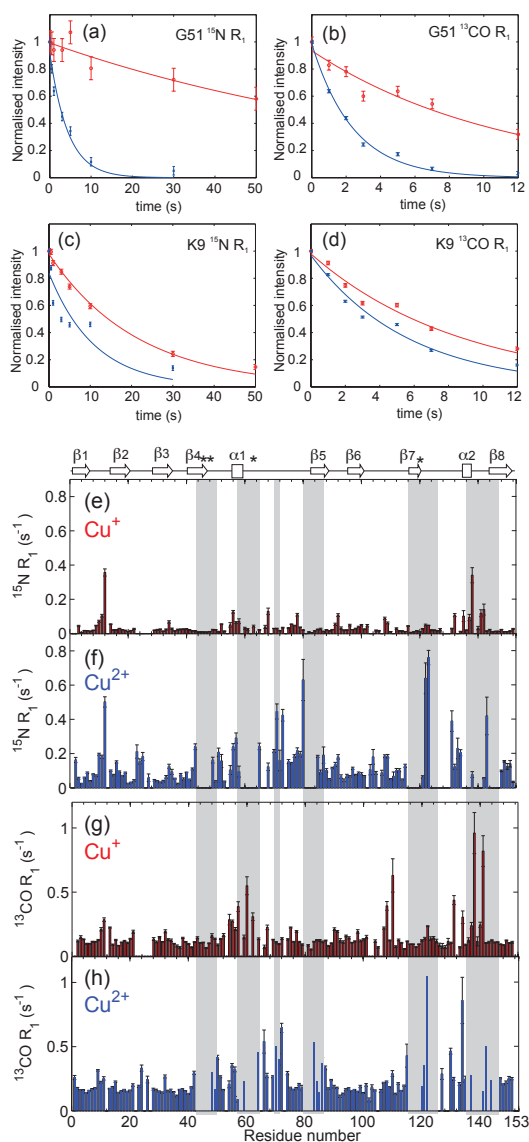


Figure 13.41: The relaxation rate constants measured for microcrystalline (Cuⁿ⁺, Zn²⁺)-SOD. Four examples of ¹⁵N and ¹³CO longitudinal relaxation decay curves are shown in (a)–(d). In all four cases the red curves are from the diamagnetic reference protein (Cu⁺, Zn²⁺)-SOD, and the blue curves showing the enhanced relaxation decay are from the paramagnetic form (Cu²⁺, Zn²⁺)-SOD. The plots in (e)–(h) show the ¹⁵N and ¹³CO R₁ values for each residue for the two proteins. The shown data are: (e) ¹⁵N R₁ of (Cu⁺, Zn²⁺)-SOD, (f) ¹⁵N R₁ of (Cu²⁺, Zn²⁺)-SOD, (g) ¹³CO R₁ of (Cu⁺, Zn²⁺)-SOD, and (h) ¹³CO R₁ of (Cu²⁺, Zn²⁺)-SOD. The secondary structure, in which the Cu-coordinating histidine residues are marked with an *, is shown at the top of the figure. The parts highlighted in grey indicate where the residues are within 12 Å of the Cu metal ion. Reproduced with permission from [530]. Copyright (2013) American Chemical Society.

The determination of the susceptibility tensor required a total of eight parameters to be fitted, namely the axial and rhombic anisotropies, the three Euler angles specifying the orientation, and the three Cartesian coordinates of the Co^{2+} ion, with the initial position estimated from the positions of the amino acids with resonances broadened by the PRE. If the predicted shifts matched those observed in the spectra the corresponding resonances were assigned. The susceptibility tensor was then refitted until all the visible peaks were assigned and a consistent susceptibility tensor obtained. The final susceptibility tensor that was obtained had axial and rhombic anisotropies of $(1.03 \pm 0.03) \times 10^{-32} \text{ m}^3$ and $(0.91 \pm 0.02) \times 10^{-32} \text{ m}^3$, and a total of 445 PCSs were assigned comprising 111 $^1\text{H}^{\text{N}}$, 223 ^{13}C , and 111 ^{15}N PCSs.

The structure calculation then proceeded by combining the 445 PCSs with the 297 ^1H - ^1H contacts and other diamagnetic restraints to obtain the structure shown in Figure 13.39 (c). The overall precision was significantly improved, as indicated by the reduction in the rmsd from 3.1 Å to 1.7 Å. In particular a substantial improvement was seen in the definition of the backbone in the vicinity of the Co^{2+} binding site.

The simultaneous use of the PRE and PCS paramagnetic restraints in combination with the ^1H - ^1H contacts was also evaluated. The final structure, which is shown in Figure 13.39 (d), showed a further increase in resolution with an rmsd that dropped to 1.4 Å. Once again particularly high definition was observed in the vicinity of the binding site of the paramagnetic metal ion.

To conclude this section we note that the work on the structure refinement of SOD described here made the assumption that the PRE and PCS structural restraints were intramolecular only. To describe it another way, the assumption was made there were no PRE or PCS effects from the metal ions of neighbouring dimers in the crystal, and that the measured restraints could therefore be interpreted as being due solely to the metal ion in the same dimer as the observed nucleus. In the case of SOD this assumption is valid, since the metal binding sites are sufficiently far from the protein surface to make any intermolecular spin-dipolar interactions negligible. However for a general microcrystalline protein the total PCS measured is the sum of the intermolecular and intramolecular parts, and it is usually necessary to account for both [531]. The concept is illustrated in Figure 13.42 [532]. It is possible to separate the intermolecular PCS from the intramolecular PCS using paramagnetic dilution, as has been demonstrated for the protein Co-MMP [12]. In order to isolate the intramolecular part one crystallizes a dilute, uniformly ^{13}C and ^{15}N labelled, paramagnetic protein in the presence of a greater concentration of the diamagnetic reference protein which has natural abundance ^{13}C and ^{15}N , as shown in Figure 13.42 [532]. The NMR spectra are therefore dominated by the labelled paramagnetic

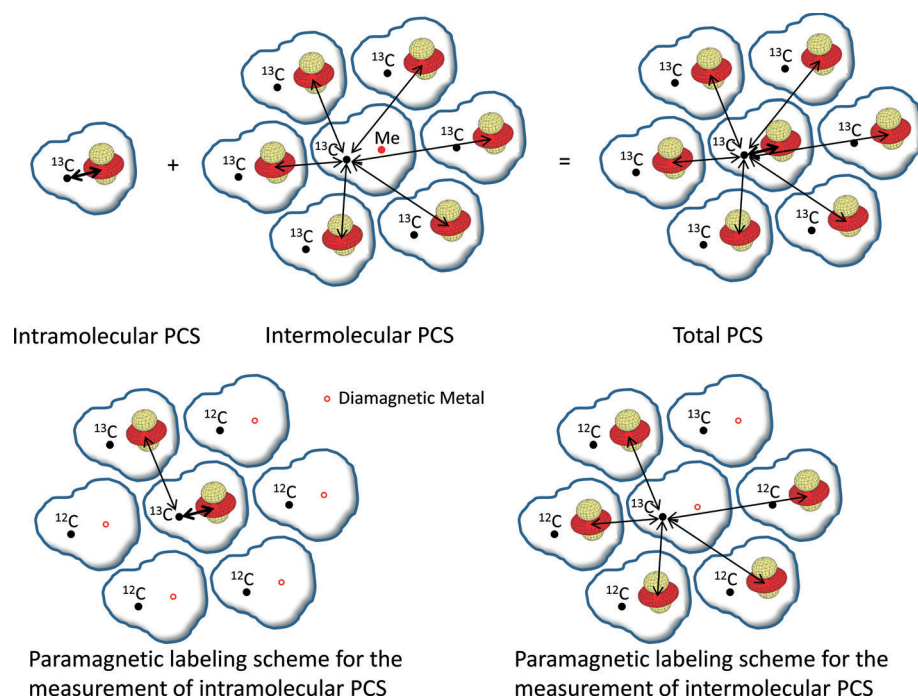


Figure 13.42: Illustration of the intra- and intermolecular contributions to the PCS in a microcrystalline protein, and how they may be separated using two different dilution schemes. Paramagnetic metal ions are indicated by the small PCS plots, and the diamagnetic reference ions are indicated by small red circles. Reproduced from Ref. [532] with permission of The Royal Society of Chemistry.

protein molecules which, for a sufficiently high degree of dilution, experience a negligible intermolecular PCS. The PCS values that are measured can therefore be ascribed entirely to the intramolecular part, and can be used to refine the tertiary structure of the protein as described in this section. If on the other hand we wish to measure the intermolecular PCSs we can adopt an alternative dilution scheme, illustrated in Figure 13.42, in which only the diamagnetic reference protein is uniformly ^{13}C and ^{15}N labelled, and is diluted in the presence of a greater concentration of the paramagnetic protein which has ^{13}C and ^{15}N at natural abundance levels. Here we observe only the diamagnetic protein molecules in the NMR spectrum, and so there are no intramolecular PCSs. The total PCSs that we do measure are entirely intermolecular, and can be used to determine the crystal structure [532]. Finally it is also possible to use PCSs containing both inter- and intramolecular contributions for structure determination without the need for dilution, as shown by Luchinat et al [12].

13.9 Lanthanide stannates $\text{Ln}_2\text{Sn}_2\text{O}_7$ in the solid state

13.9.1 Background

Lanthanide ions have unique luminescent properties which make them promising candidates for new materials for including solid-state lighting, sensing, and imaging applications [533–536]. A full understanding of their paramagnetic NMR properties is crucial both for assigning the NMR spectra, and for extracting details about the electronic structure pertaining to the unpaired electrons. As has been discussed, the understanding of the paramagnetic shifts due to lanthanide ions is less advanced than for *d*-block transition-metal ions. However the simplified theories of Golding and Halton for the contact shift [60], and Bleaney for the PCS [61], have proved very useful in this regard.

Here we present an early case study by Grey et al. who investigated a series of lanthanide stannate compounds $\text{Ln}_2\text{Sn}_2\text{O}_7$ incorporating different lanthanide ions with different concentrations [64, 65]. The contact shifts were probed by studying the compositions $\text{Ln}_2\text{Sn}_2\text{O}_7$ with 100% lanthanide content, where the paramagnetic shifts are dominated by the short-range contact interaction in the first coordination shell. In addition the effects of lower lanthanide contents were also studied in the solid-solution compositions $\text{Y}_{2-x}\text{Ln}_x\text{Sn}_2\text{O}_7$, in which shifts due to the longer-range PCS from ions in more distant coordination shells could be probed. Here we focus on the former materials, and defer a discussion of the PCS to different

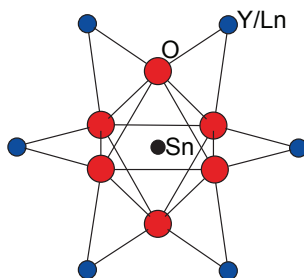


Figure 13.43: Local environment of the Sn^{4+} ion in $\text{Y}_2\text{Sn}_2\text{O}_7$. The SnO_6 octahedron of the B site coordinates to six nearest-neighbour Y atoms. The same coordination environment is expected in the lanthanide-substituted materials $\text{Ln}_2\text{Sn}_2\text{O}_7$.

systems in subsequent sections.

All the compounds $\text{Ln}_2\text{Sn}_2\text{O}_7$ adopt the pyrochlore structure with space group $Fd\bar{3}m$. These stannates are known for all lanthanides ions, with the exception of Ce^{3+} , and also for Y^{3+} . The Sn^{4+} ion is located at the B site of the structure, which is at the centre of an octahedral SnO_6 coordination environment, which is shown in Figure 13.43. The Ln^{3+} ions have a larger radius, and so occupy the larger A site which is coordinated to a distorted cubic environment of eight O ions. The SnO_6 is coordinated to six Ln^{3+} ions, which are expected to dominate the contact shift of the ^{119}Sn resonance.

13.9.2 Paramagnetic shifts

Grey et al. measured the ^{119}Sn solid-state MAS NMR spectra of the diamagnetic materials with $\text{Ln}^{3+} = \text{La}^{3+}$ and Lu^{3+} , and of the paramagnetic materials with $\text{Ln}^{3+} = \text{Nd}^{3+}$, Sm^{3+} , Eu^{3+} , and Yb^{3+} [68]. The spectra are shown in Figure 13.44. It can be seen immediately that the isotropic chemical shift is highly dependent on the nature of the lanthanide ion, varying from -4000 ppm for Nd^{3+} to 5000 ppm for Eu^{3+} . The variation of the width of the spinning-sideband manifold is also striking, with a comparatively small SA being observed for Sm^{3+} , and a particularly large value for Yb^{3+} .

The two diamagnetic materials $\text{La}_2\text{Sn}_2\text{O}_7$ and $\text{Lu}_2\text{Sn}_2\text{O}_7$ have similar isotropic chemical shifts of -642 and -641 ppm respectively, which are due entirely to the orbital contribution. The fact that there is negligible difference between these two orbital shifts indicates that there is little variation across the entire lanthanide series, and suggests that we can obtain the paramagnetic shifts simply by subtracting the average of -641.5 ppm from the total chemical shifts. In addition both $\text{La}_2\text{Sn}_2\text{O}_7$ and $\text{Lu}_2\text{Sn}_2\text{O}_7$ have a negligible SA, which

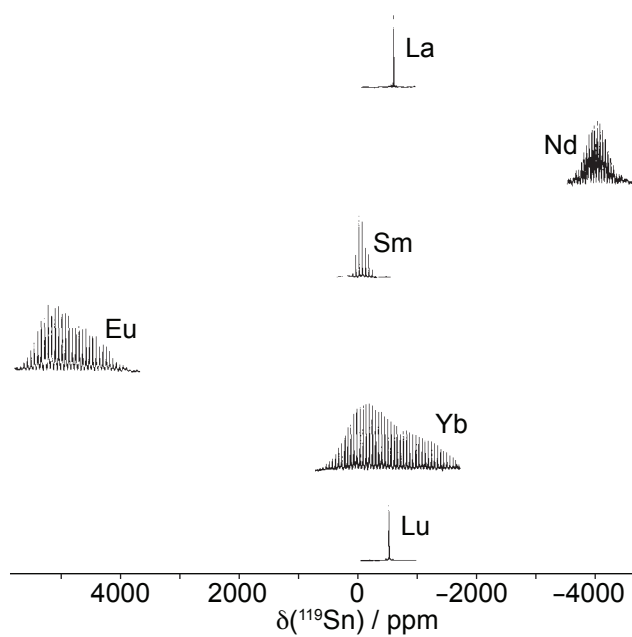


Figure 13.44: Solid-state ^{119}Sn NMR spectra of the pyrochlores $\text{Ln}_2\text{Sn}_2\text{O}_7$ at a field of 4.7 T and MAS frequencies of 3–4 kHz. The paramagnetic shifts are calculated by subtracting the chemical shifts of one of the diamagnetic systems $\text{La}_2\text{Sn}_2\text{O}_7$ or $\text{Lu}_2\text{Sn}_2\text{O}_7$. Adapted with permission from [68]. Copyright (1989) American Chemical Society.

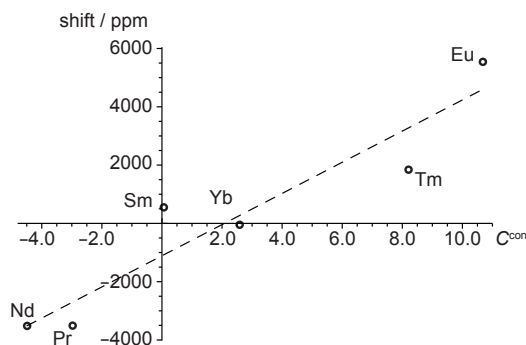


Figure 13.45: Plot of the experimental ^{119}Sn paramagnetic shifts of $\text{Ln}_2\text{Sn}_2\text{O}_7$ against the theoretical relative contact shift coefficients C^{con} in Table 6.5, calculated by Golding and Halton [60]. The experimental shifts are taken from Grey et al [68].

we can see from their spectra given that only the centreband is present under slow MAS of 3–4 kHz. This indicates that the SA observed for the paramagnetic materials is due entirely to paramagnetic effects.

We now turn to the question as to the nature of the paramagnetic shift, and whether it is dominated by the contact or pseudo-contact contributions. Close examination of Figure 13.44 indicates that shifts are mainly due to the contact interaction, as the variation of the chemical shifts relative to the mean orbital shift better matches the Golding–Halton contact coefficients in Table 6.5 than the Bleaney coefficients in Table 6.4, as noted by Grey et al [65]. This can be seen particularly for Eu^{3+} , which has the largest shift measured here, and which is predicted to have a small PCS and a large contact shift. The match is seen better in Figure 13.45, which plots the measured paramagnetic shift against the theoretical Golding–Halton contact coefficients in Table 6.5. We observe a trend that is approximately linear as expected, and so the paramagnetic shifts are dominated by the contact shift. As for the solid materials with transition-metal paramagnetic centres, we expect the contact shift to be mainly due to the short-range contact interactions from the nearest-neighbour Ln^{3+} ions in the first coordination shell. From reference to Figure 13.44 we see that there are six such contributions to the contact shift, along six pathways Ln–O–Sn . Deviations from the ideal linear trend in Figure 13.45 can be ascribed to shortcomings in the Golding–Halton theory of contact shifts.

If the spin-dipolar interaction were the sole contribution to the SA, we would expect the measured SA to correlate with the coefficients $C^{\text{SA}} = g_J^2 J(J+1)$ in Table 6.4. This provides a qualitative explanation for the increase in the SA on going from Sm^{3+} to Nd^{3+} and then to Yb^{3+} , but does not explain the very large SA seen for Eu^{3+} . It is clear that we also have to consider other contributions to the spinning-sideband manifold, such

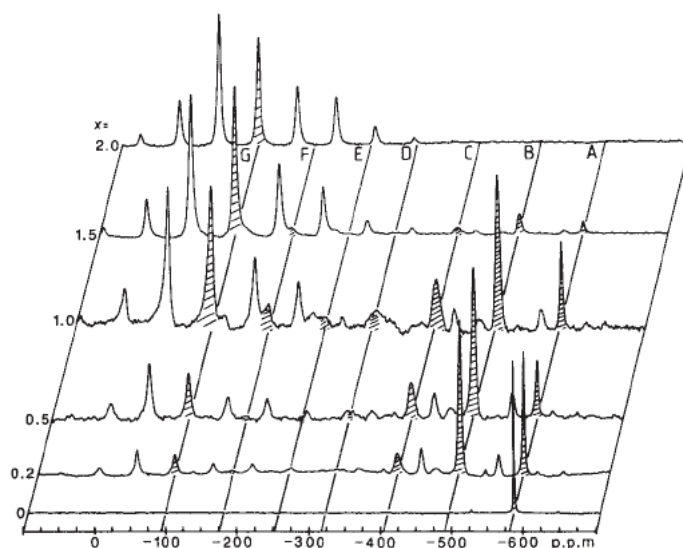


Figure 13.46: Solid-state ^{119}Sn MAS NMR spectra of $\text{Y}_{2-x}\text{Ln}_x\text{Sn}_2\text{O}_7$ with different compositions x . The six spectra collectively reveal the presence of seven main resonances at positions A–G, which are due to a number of nearest-neighbour Sm^{3+} ions that increases from zero to six, with an average contact-shift pathway contribution of 79 ppm. Adapted with permission from Springer Nature [64], copyright 1987.

as the contact shift anisotropy and BMS effects.

13.9.3 The $\text{Y}_{2-x}\text{Ln}_x\text{Sn}_2\text{O}_7$ materials with mixed composition

Grey et al. also studied the solid-solution compositions $\text{Y}_{2-x}\text{Ln}_x\text{Sn}_2\text{O}_7$ [64, 65]. Several isotropic resonances were observed in the ^{119}Sn NMR spectra, including those with paramagnetic shift contributions from the second and third coordination shells. Figure 13.46 shows a series of ^{119}Sn MAS NMR spectra for $\text{Y}_{2-x}\text{Ln}_x\text{Sn}_2\text{O}_7$ of different compositions [64]. The material with $x = 0$ gives a single sharp peak at -575 ppm (position A in Figure 13.46). This is simply the orbital contribution to the total shift, and takes a similar value to the shift for the diamagnetic materials $\text{La}_2\text{Sn}_2\text{O}_7$ and $\text{Lu}_2\text{Sn}_2\text{O}_7$ in Figure 13.44. Additionally the material with $x = 2$ has a single resonance with a broad spinning-sideband manifold and an isotropic shift of -100 ppm, which we have seen is mainly a contact shift (position G in Figure 13.46). In the mixed compositions we see additional resonances centred at positions B–F which are discretely spaced. In the light of the previous discussion of pathway contributions in sections 13.4–13.6 we can interpret the contact contributions to the shifts at positions A and G as being due to zero and six nearest-neighbour Sm^{3+} ions respectively. Therefore

the other resonances observed at B–F have contact contributions from between one and five nearest-neighbour Sm^{3+} ions. From these spectra we are able to calculate the average pathway contribution to be 79 ppm.

In addition to the dominant contact contributions the observed shifts are likely to have a substantial PCS part, giving rise to splittings in the isotropic resonances at each of the seven main positions, and which can be rationalized by the Bleaney theory. However in order to study the PCSs due to a series of lanthanide ions, we turn our attention to a different system.

13.10 The interaction between guanidinium and tris-dipicolinate lanthanide ions in solution: $(\text{Gua})_3[\text{Ln}(\text{DPA})_3]$

13.10.1 Background

The optical spectroscopy of lanthanide complexes is characterized by excited states with comparatively long lifetimes, which may be of the order of μs – ms . These long lifetimes open up the possibility of using these systems for sensitivity-enhanced bio-imaging [537]. One interesting feature of the spectroscopy of some lanthanide-containing complexes is the ability to excite an electronic transition by the simultaneous absorption of two photons, whose energies sum to the required energy of transition. The technique of two-photon absorption-induced fluorescence represented a major breakthrough in bio-imaging [538].

One class of interesting biological systems is that of anionic lanthanide tris-dipicolinate complexes $\text{Ln}(\text{DPA})_3^{3-}$ co-crystallized with proteins such as hen egg-white lysozyme, thaumatin, and urate oxidase. There is an intermolecular interaction which is particularly favourable with the guanidinium part of the amino acid arginine [539]. The nature of this interaction, and the luminescent properties of the complexes, were investigated in some detail by D'Aléo et al. who prepared a series of $\text{Ln}(\text{DPA})_3^{3-}$ complexes in aqueous solution with guanidinium cations (Gua^+) [467]. The stoichiometric composition of $(\text{Gua})_3[\text{Ln}(\text{DPA})_3]$ is shown in Figure 13.47. The interaction between $\text{Ln}(\text{DPA})_3^{3-}$ and Gua^+ was probed with ^{15}N solution NMR of the Gua^+ cation isotopically enriched with ^{15}N . The spectra were dominated by the paramagnetic effects of the unpaired $4f$ electrons of the lanthanide ions.

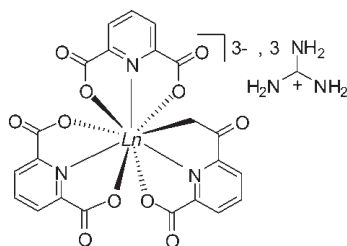


Figure 13.47: Chemical structure of the $(\text{Gua})_3[\text{Ln}(\text{DPA})_3]$ complexes. Adapted with permission from [467]. Copyright John Wiley and Sons.

13.10.2 Pseudo-contact shifts

D'Aléo et al. acquired the ^{15}N NMR spectra of $(\text{Gua})_3[\text{Ln}(\text{DPA})_3]$ with seven of the paramagnetic trivalent lanthanide ions, and the diamagnetic lanthanide ion Lu^{3+} . These spectra are shown in Figure 13.48, along with the spectrum of $\text{Gua}\cdot\text{HCl}$ for comparison. The Gua^+ cation can either be bound to the $\text{Ln}(\text{DPA})_3^{3-}$ anion through an ionic intermolecular interaction, or unbound as a free cation. We expect the Gua^+ to chemically exchange between these two environments, a hypothesis that is confirmed by all the ^{15}N NMR spectra where the presence of a single peak further indicates that we are in the fast-exchange limit and observe the average of the bound and unbound states. The substantial range of chemical shifts, from 64 to 70 ppm, is attributed to the different paramagnetic shifts of the lanthanide ions. The solution of $\text{Gua}\cdot\text{HCl}$ gives a shift at 68.5 ppm, attributed to the orbital contribution, which can be used as a diamagnetic reference to be subtracted from the other shifts to give the paramagnetic contributions. This choice is supported by the observation that the shift of $(\text{Gua})_3[\text{Lu}(\text{DPA})_3]$ is only 0.04 ppm higher than that of $\text{Gua}\cdot\text{HCl}$, which is a negligible difference and within the experimental linewidth. The linewidths are fairly uniform across the series, with the obvious exception of Gd^{3+} where the peak is broadened considerably. Therefore it appears that the transverse PRE does not add significantly to the observed broadening in the diamagnetic complexes, apart for $(\text{Gua})_3[\text{Gd}(\text{DPA})_3]$ where the long electronic relaxation times of the Gd^{3+} ion, due to the half-filled $4f$ shell and subsequent zero SO coupling strength, result in a short T_2 .

As stated above the supramolecular interaction is ionic in nature, and so we would expect the contact interaction between the ^{15}N and the Ln^{3+} ion to be zero, with the result that the shifts are entirely PCSs. One initial observation suggesting that this is indeed the case is the very small paramagnetic shift of 0.14 ppm due

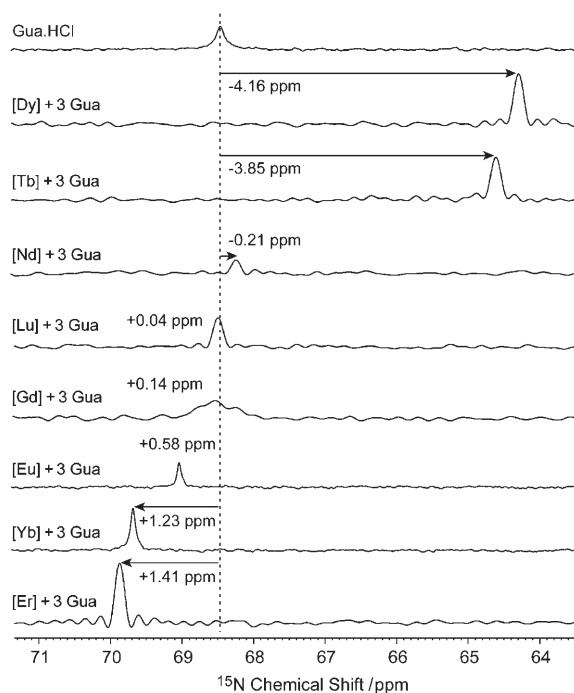


Figure 13.48: Solution ^{15}N NMR spectra of a series of $(\text{Gua})_3[\text{Ln}(\text{DPA})_3]$ complexes with different lanthanide ions in D_2O at 16.44 T. The spectra each contain a single peak due to the ^{15}N -enriched guanidinium cation. The notation $[\text{Ln}]$ is a shorthand for the $[\text{Ln}(\text{DPA})_3]^{3-}$ anion. Reproduced with permission from [467]. Copyright John Wiley and Sons.

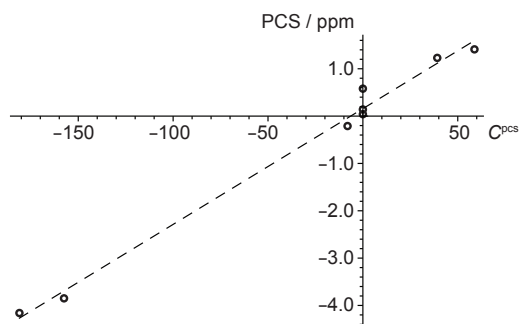


Figure 13.49: Plot of the experimental ^{15}N paramagnetic shifts of $(\text{Gua})_3[\text{Ln}(\text{DPA})_3]$ taken from Figure 13.48 against the theoretical relative PCS coefficients C_J^{PCS} in Table 6.4, calculated by Bleaney [61].

to Gd^{3+} . According to Golding and Halton the contact shift for Gd^{3+} is expected to be one of the largest in the lanthanide series [60], whereas the PCS according to Bleaney is zero [61]. We therefore ascribe the shift of 0.14 ppm to either a variation in the orbital shift, or an error that is within the experimental linewidth.

A more complete analysis is presented in Figure 13.49, in which the experimental paramagnetic shifts are plotted against the Bleaney coefficients C_J^{PCS} from Table 6.4. There is an excellent linear trend, which is expected for shifts that are entirely pseudo-contact. The one significant discrepancy is for Eu^{3+} , which is expected as the populations of the excited J -levels are neglected in the plot. Nevertheless the correlation is striking, and provides experimental evidence for the validity of the Bleaney theory in this particular case. It would be satisfying to be able to calculate the crystal-field splitting parameters from this correlation. However the slope of the line contains contributions from the crystal-field splitting, the spin-dipolar interaction, and indeed the rate of chemical exchange, which cannot be separated here. To do so would require additional information about the relative position of the ^{15}N to the metal ion and the exchange properties. This is explored in the following section.

13.11 Paramagnetic effects of lanthanide ions in the dicalcium protein calbindin D_{9k}

13.11.1 Background

In our final case study of the paramagnetic shifts due to lanthanide ions we present the work of Bertini et al. who measured the PCSs due to a series of lanthanide ions incorporated into the protein dicalcium calbindin D_{9k} , which is denoted Ca_2Cb [74]. The PCSs were used to refine the calculated structures, and the extracted susceptibility anisotropy parameters for each lanthanide ion were studied in order to gauge the quality of the agreement with the Bleaney theory.

Dicalcium calbindin D_{9k} binds two Ca^{2+} ions [540]. It is found in mammalian intestinal epithelial cells where it mediates the transport of Ca^{2+} . In the present case study the Ca^{2+} ion in the C-terminal binding site was replaced by the full series of lanthanide ions from La^{3+} to Lu^{3+} , with the exceptions of Pm^{3+} and Gd^{3+} , to give a series of 13 protein derivatives that are denoted $CaLnCb$. The chemical shifts for each amide $^1H^N$ and ^{15}N were measured for all the the derivatives, and the paramagnetic shifts were obtained by subtracting the corresponding shifts of either the $CaLaCb$ or $CaLuCb$ protein.

The advantages of using a protein such as D_{9k} to measure these paramagnetic shifts are twofold. Firstly as the NMR was performed using conventional pulse sequences the nuclei were observed outside the blind sphere, the radius of which is dependent on the particular lanthanide ion in the binding site. This means that the paramagnetic shifts could be ascribed entirely to PCSs, as the contact shifts drop to zero outside the blind sphere. Secondly the large number of PCSs available can be used to determine both the orientation and anisotropy parameters of the magnetic susceptibility tensor to a high degree of precision. Both of these points enabled a comprehensive evaluation of the Bleaney theory, which we described in section 6.5 [74].

13.11.2 Pseudo-contact shifts

The chemical shifts of the amide $^1H^N$ and ^{15}N resonances were measured by acquiring a 1H - ^{15}N HSQC spectrum for each $CaLnCb$ derivative. Four representative spectra are shown in Figure 13.50 [74]. The spectra shown are of (a) diamagnetic $CaLaCb$ ($4f^0$), (b) an example with an early paramagnetic lanthanide ($4f^2$) $CaPrCb$, (c) a 'mid' lanthanide ($4f^8$) $CaTbCb$, and (d) a late lanthanide ($4f^{12}$) $CaTmCb$. The procedure

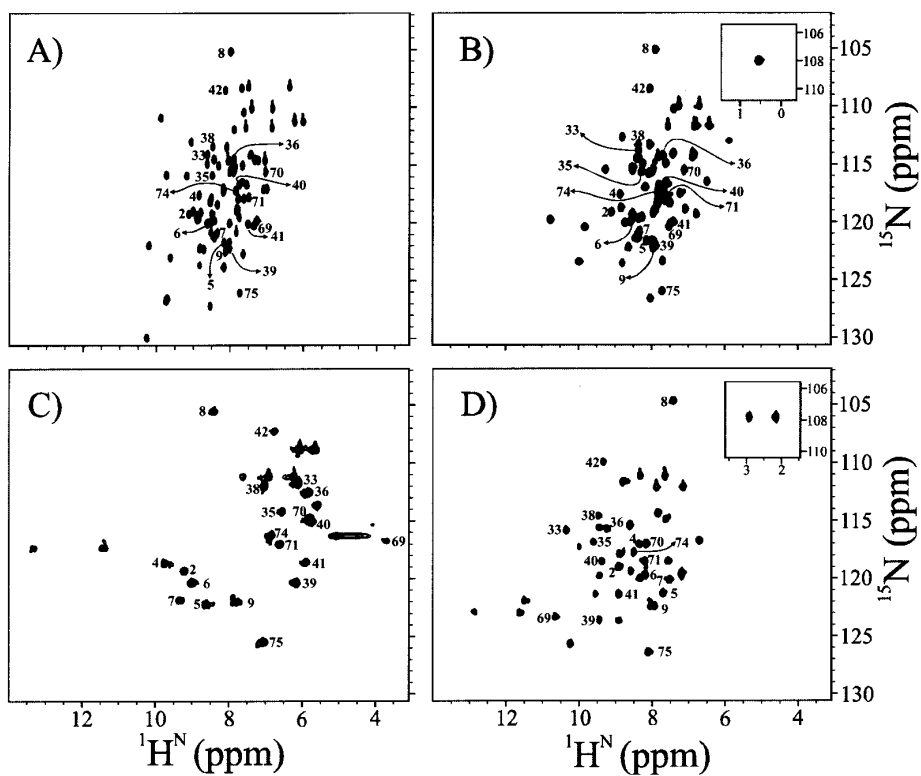


Figure 13.50: Four examples of solution ^1H - ^{15}N HSQC spectra of different CaLnCb derivatives acquired at 18.79 T and 300 K. The four derivatives are (a) diamagnetic CaLaCb, (b) CaPrCb, (c) CaTbCb, and (d) CaTmCb. Reproduced with permission from [74]. Copyright (2001) American Chemical Society.

for assigning the PCSs and calculating the magnetic susceptibility tensor was similar to that described in section 13.8.4 [45]. The PCSs themselves were calculated from the chemical shifts of each resonance by subtracting the corresponding shifts of a suitable diamagnetic reference protein. Two diamagnetic derivatives were available here, namely CaLaCb and CaLuCb, which were found to have measurably different sets of orbital shifts. It was found that a better fit of the PCSs was obtained if the former derivative CaLaCb was chosen as the reference for the early lanthanides Ce, Pr, Nd, Sm, and Eu, and if the latter reference CaLuCb was chosen as the reference for the late lanthanides Tb, Dy, Ho, Er, Tm, and Yb. This observation is consistent with the decrease in the ionic radius of the lanthanide ion across the series resulting in minor changes in the protein structure [74]. For each sample a set of 1097 $^1\text{H}^{\text{N}}$ and ^{15}N PCSs were measured. For each of these sets the susceptibility tensor was fitted to the PCS values using an initial trial structure of CaCeCb determined in solution by NOEs, using the following expression for the PCS:

$$\delta_{\text{iso}}^{\text{PCS}} = \frac{1}{12\pi R^3} \left[\Delta\chi_{\text{ax}} (3 \cos^2 \theta - 1) + \frac{3}{2} \Delta\chi_{\text{rh}} \sin^2 \theta \cos 2\phi \right], \quad (13.14)$$

where R , θ , and ϕ define the position of the nuclear relative to the PAF of the susceptibility tensor, and $\Delta\chi_{\text{ax}}$ and $\Delta\chi_{\text{rh}}$ are the axial and rhombic anisotropies of the tensor. Finally the protein structure and tensor parameters were simultaneously calculated by combining the total of 1097 PCSs for all lanthanides simultaneously with 1539 NOEs and 39 3J -coupling constants.

The axial and rhombic susceptibility anisotropy parameters $\Delta\chi_{\text{ax}}$ and $\Delta\chi_{\text{rh}}$, and the three axes specifying the orientation of the PAF, were determined for all 11 paramagnetic derivatives. It was found that all the axis orientations were within 15° of the average for all the derivatives, with the exception of CaSmCb for which a larger deviation of 20° was found. This indicates that the coordination environments for all the ions are broadly similar, with the small variations reflecting minor short-range structural changes. The values of the axial and rhombic anisotropy parameters are plotted against the Bleaney coefficients C_J^{PCS} from Table 6.4 in Figure 13.51 (a) and (b). An approximately linear correlation, indicated by the dashed best-fit lines, is observed for both anisotropy parameters. A perfect correlation would indicate firstly that the Bleaney theory is good description of the PCS of these systems, and secondly that the crystal-field splitting parameters $\langle r^2 \rangle A_2^0$ and $\langle r^2 \rangle A_2^2$ are the same for all the paramagnetic derivatives CaLnCb. Whilst there are some deviations from the ideal case, the data in Figure 13.51 nevertheless allowed the determination of the average crystal-field

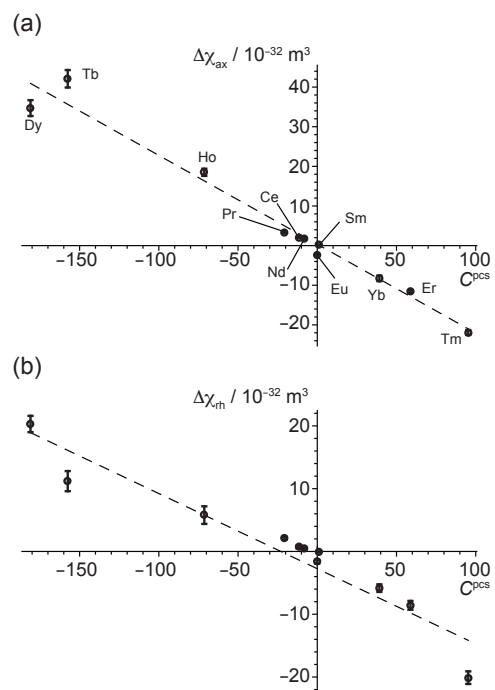


Figure 13.51: Plots of the axial and rhombic susceptibility anisotropies, and associated errors, calculated for the CaLnCb derivatives from PCSs plotted against the theoretical relative PCS coefficients C_J^{PCS} in Table 6.4, calculated by Bleaney [61]. The axial and rhombic anisotropies are plotted in (a) and (b). The susceptibility anisotropies were calculated by Bertini et al [74].

splitting parameters for the series of proteins [74].

13.11.3 Extracting the crystal-field splitting parameters

From Figure 13.51 we are in a position to calculate the average crystal-field splitting parameters. As discussed in section 6.5, the Bleaney theory gives the following expressions for the axial and rhombic susceptibility anisotropies in terms of the energy coefficients $\langle r^2 \rangle A_2^0$ and $\langle r^2 \rangle A_2^2$ of the crystal-field interaction Hamiltonian in Equation 6.51:

$$\Delta\chi_{\text{ax}} = -\frac{\mu_0\mu_{\text{B}}^2}{30(kT)^2} C_J^{\text{pcs}} \langle r^2 \rangle 3A_2^0, \quad (13.15)$$

$$\Delta\chi_{\text{rh}} = -\frac{\mu_0\mu_{\text{B}}^2}{30(kT)^2} C_J^{\text{pcs}} \langle r^2 \rangle 2A_2^2. \quad (13.16)$$

Hence the slopes of the best-fit lines to the plots of $\Delta\chi_{\text{ax}}$ against C_J^{pcs} and $\Delta\chi_{\text{rh}}$ against C_J^{pcs} in Figure 13.51 (a) and (b) yield $\langle r^2 \rangle A_2^0 = 179 \text{ cm}^{-1}$ and $\langle r^2 \rangle A_2^2 = 143 \text{ cm}^{-1}$. The corresponding crystal-field splitting parameters for each protein were found to vary within $\pm 30\%$ of these averages.

Bertini et al. performed a more sophisticated analysis than that above, from which a refined value of the axial crystal-field splitting parameter was obtained. In summary both the excited-state contributions to the PCSs in CaSmCb and CaEuCb were taken into account, and the Bleaney expression was extended to third order in $1/(kT)$. The result was an improved agreement between the experimental and calculated axial susceptibility anisotropy for each lanthanide, as shown in Figure 13.52 [74]. The average parameter $\langle r^2 \rangle A_2^0$ was refined to 169 cm^{-1} , with a variation of $\pm 15\%$ for different lanthanide ions.

This case study represents the most compelling evidence to date for the validity of the Bleaney theory for the PCS due to lanthanide ions. The reasons for this are that 11 out of 13 of the paramagnetic lanthanide ions could be incorporated into the C-terminal Ca^{2+} binding site, that a large number of PCSs that could be measured, and that the observed nuclei are sufficiently far from the lanthanide ion that only the PCS contributes to the isotropic paramagnetic shift. This study was also able to quantify the variation of the orientation of the PAF of the magnetic susceptibility tensor across the lanthanide series and the variation in the crystal-field splitting parameters, and account for higher-order terms in the Bleaney theory. These are factors that are sometimes erroneously cited as fundamental shortcomings of the Bleaney theory.

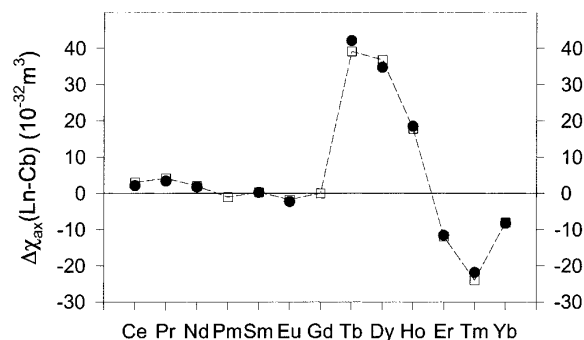


Figure 13.52: Experimental (filled circles) and calculated (open squares) axial susceptibility anisotropy values for the series of CaLnCb derivatives. The calculated values used an axial crystal-field splitting parameter of $A_2^0 \langle r^2 \rangle = 169 \text{ cm}^{-1}$ as calculated by Bertini et al [74], and correction for temperature up to terms in $1/T^3$. The right-hand vertical axis shows the expected RDC at 18.79 T and 298 K in Hz. Reproduced with permission from [74]. Copyright (2001) American Chemical Society.

13.12 Actinyl tris-carbonate complexes in solution

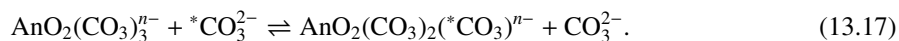
13.12.1 Background

Studies of actinide complexes and materials by NMR are currently very sparse, mainly due to the radioactivity of such systems making it difficult to obtain experimental data. Additionally, computations of the paramagnetic shifts are difficult to perform, as the heavy open-shell actinide ions require a full relativistic treatment [212]. Nevertheless such calculations have been performed very recently by Gendron et al. on small actinyl complexes containing either one or two $5f$ electrons [91, 92]. Although there are many issues still to be addressed, this work is of profound interest to theoreticians and experimentalists alike, and opens a new frontier in paramagnetic NMR.

The compounds we examine in this section are the actinyl tris-carbonates $\text{UO}_2(\text{CO}_3)_2^{5-}$, $\text{NpO}_2(\text{CO}_3)_2^{4-}$, and $\text{PuO}_2(\text{CO}_3)_2^{4-}$, all of which adopt axial symmetry within the point group D_{3h} , and for which experimental ^{13}C NMR spectra have been obtained [229, 230]. The paramagnetic centres in the first two complexes are U^{5+} and Np^{6+} respectively, each with the same open-shell configuration $5f^1$. The metal ion in the third complex is Pu^{6+} , with configuration $5f^2$.

13.12.2 Paramagnetic shifts

One point of interest for the original experimental studies of these complexes was to establish information about the kinetics of these complexes in solution. The general actinyl tris-carbonate complexes are known to exchange bound carbonate with free carbonate in aqueous solution according to the following scheme:



The experimental ^{13}C NMR spectra of the three complexes $\text{UO}_2(\text{CO}_3)_2^{5-}$, $\text{NpO}_2(\text{CO}_3)_2^{4-}$, and $\text{PuO}_2(\text{CO}_3)_2^{4-}$ in aqueous solution are shown in Figure 13.53 (a), (b), and (c). In all three spectra we observe a single peak due to the paramagnetic species $\text{AnO}_2(\text{CO}_3)_3^{n-}$ which is generally broad, with the exception of $\text{NpO}_2(\text{CO}_3)_3^{4-}$, and distinct from an additional resonance due to the $\text{CO}_3^{2-}/\text{HCO}_3^-$ species. The spectra indicate that the exchange of carbonate bound to the complex with free carbonate is in the slow exchange limit, whereas the additional exchange between the CO_3^{2-} and HCO_3^- ions is in the fast-exchange limit. As was noted during the discussion on CEST and PARACEST in section 12.4.1, the larger chemical shift dispersion of paramagnetic species in solution allows us to obtain distinct chemical shifts for such species exchanging with larger rate constants than is possible for diamagnetic complexes. Two additional peaks in the spectrum in Figure 13.53 (b) are due to the additional complex $(\text{NpO}_2)_3(\text{CO}_3)_6^{6-}$.

The paramagnetic shifts of the three actinyl tris-carbonate complexes were calculated by Gendron et al [91, 92]. They employed the general formula for the paramagnetic shielding tensor of van den Heuvel and Soncini given in Equation 4.103, which is reproduced below for convenience:

$$\begin{aligned} \sigma_{ij}^S = & \frac{2}{\hbar\gamma_I Q_0} \sum_n \exp(-\beta E_n) \sum_{m \neq n} \sum_{\nu, \mu} \frac{\langle n\nu | \hat{m}_i | m\mu \rangle \langle m\mu | \hat{\mathcal{F}}_j | n\nu \rangle}{E_m - E_n} \\ & + \frac{\beta}{\hbar\gamma_I Q_0} \sum_n \exp(-\beta E_n) \sum_{\nu, \nu'} \langle n\nu | \hat{m}_i | n\nu' \rangle \langle n\nu' | \hat{\mathcal{F}}_j | n\nu \rangle. \end{aligned} \quad (13.18)$$

They divided the shielding tensor in Equation 13.18 into two parts, with the first referred to as linear-response (LR) contribution, and the second as the Curie contribution. Here the sums are over all the electronic states, which in practice include both the ground state and any low-lying excited states. When the only significant contribution is from the electronic ground state, the shielding tensor can be written using Equation 6.24 in terms of the EPR parameters for that manifold. Gendron et al. employed that form of the EPR formalism,

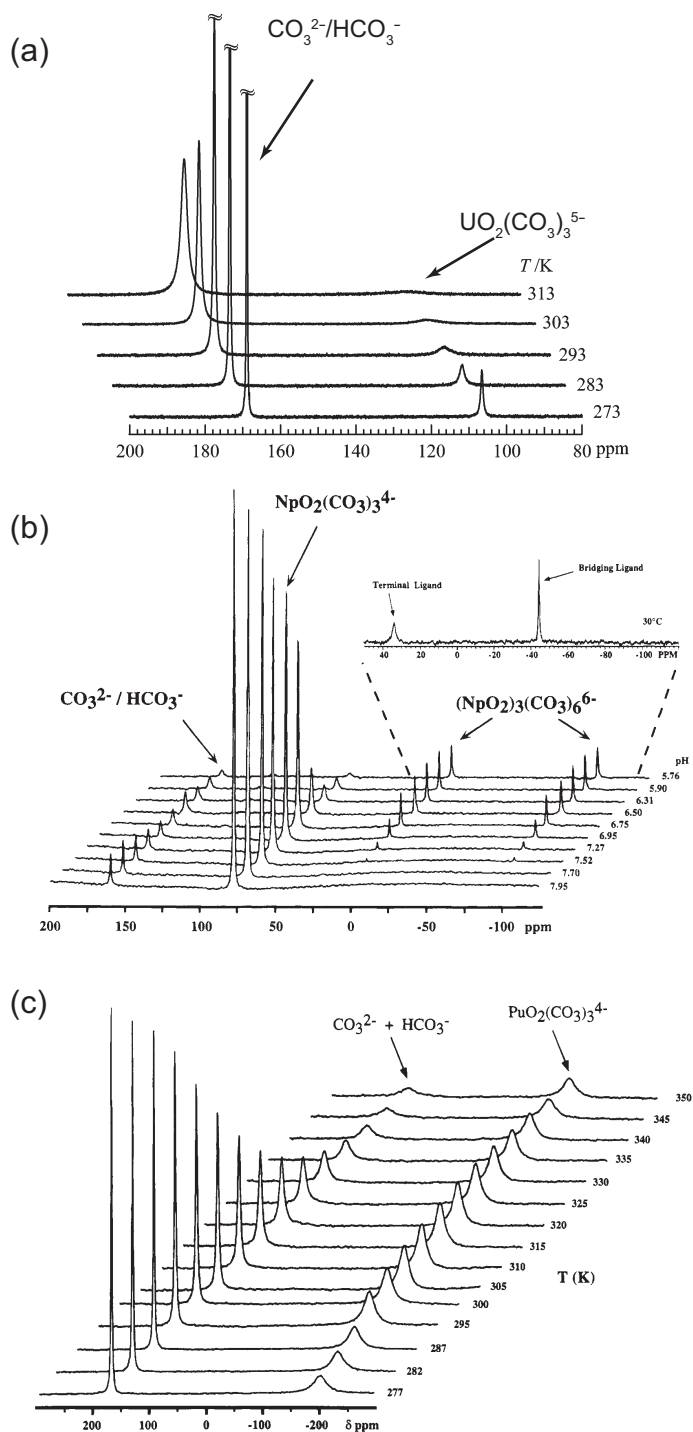


Figure 13.53: ^{13}C NMR spectra of a series of actinyl tris-carbonate complexes acquired in aqueous solution. In (a) is shown in the spectra of a 4.598×10^{-2} M solution of $\text{UO}_2(\text{CO}_3)_3^{5-}$ mixed with 1 M Na_2CO_3 , acquired at -75.45 MHz. The spectra were acquired at a series of temperatures between 273 and 313 K. The spectra of a 0.05 M solution of $\text{NpO}_2(\text{CO}_3)_3^{4-}$ mixed with Na_2CO_3 acquired at -62.9 MHz, 273 K, and variable pH are shown in (b). The inset shows the resonances due to $(\text{NpO}_2)_3(\text{CO}_3)_6^{6-}$ at 303 K. The spectra in (c) are of a 0.2 M solution of $\text{PuO}_2(\text{CO}_3)_3^{4-}$ mixed with 1 M Na_2CO_3 and 1 M NaClO_4 acquired at -62.9 MHz, a pH of 9.5, and variable temperatures between 277 and 350 K. Adapted with permission from [229, 230]. Copyright (1995 and 2005) American Chemical Society.

using the lowest-order tensor components for the g -, hyperfine, and ZFS tensors and neglecting the higher-order terms. In this case the paramagnetic shielding comprises only the Curie contribution, and the resulting shift δ^{Curie} is calculated from Equation 4.109, giving

$$\delta^{\text{Curie}} = \frac{\mu_{\text{B}}}{3\hbar\gamma_I} \text{Tr}[\mathbf{g} \cdot \mathbf{Z} \cdot \mathbf{A}], \quad (13.19)$$

where the g -, hyperfine, and ZFS tensors \mathbf{g} , \mathbf{A} , and \mathbf{D} refer to the pseudo-spin of the electronic ground state. The components of the tensor \mathbf{Z} are given by Equation 4.113, which is reproduced here:

$$\begin{aligned} Z_{kl} = & \frac{2}{Q_0} \sum_n \exp(-\beta E_n) \sum_{m \neq n} \sum_{\nu, \mu} \frac{\langle n\nu | \hat{S}_k | m\mu \rangle \langle m\mu | \hat{S}_l | n\nu \rangle}{E_m - E_n} \\ & + \frac{\beta}{Q_0} \sum_n \exp(-\beta E_n) \sum_{\nu, \nu'} \langle n\nu | \hat{S}_k | n\nu' \rangle \langle n\nu' | \hat{S}_l | n\nu \rangle. \end{aligned} \quad (13.20)$$

Finally, the description of the shift is completed by noting that if the electronic ground state has pseudo-spin 1/2, the shift simplifies to the form calculated from Equation 4.118:

$$\delta^{\text{Curie}} = \frac{\mu_{\text{B}} S(S+1)}{9\hbar\gamma_I kT} \text{Tr}[\mathbf{g} \cdot \mathbf{A}], \quad (13.21)$$

where $S = 1/2$. The contributions to the shifts were separated into the Curie and LR contributions, with each contribution further separated into the parts due to the Fermi-contact shift, PCS (due to the spin-dipolar interaction), and PSO shift.

The calculations of the paramagnetic shifts were performed using the CASSCF and RASSCF methods. The results quoted here are from calculations comprising 12 occupied orbitals and 100 unoccupied orbitals in addition to the active space, and include corrections for solvent effects.

13.12.3 Interpretation

The total calculated shifts were calculated using Equation 13.18 and are plotted, along with their individual contributions and the experimental shifts, for the three actinyl tris-carbonate complexes in Figure 13.54. For all three compounds the orbital shift was assumed to be equal to the chemical shift of 168.22 ppm of the diamagnetic isostructural analogue $\text{UO}_2(\text{CO}_3)_2^{4-}$ (containing U^{6+} ions with no $5f$ electrons). The experimental

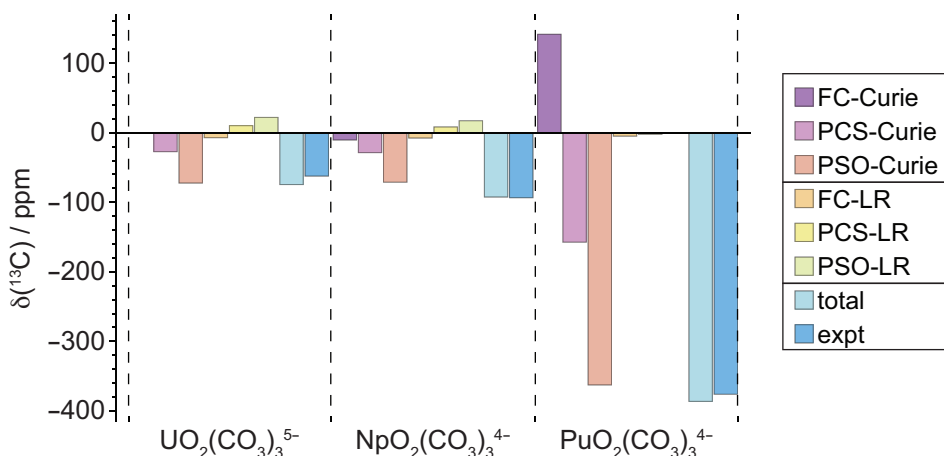


Figure 13.54: Breakdown of the contributions to the total ^{13}C chemical shifts of the three actinyl tris-carbonate complexes determined by first-principles calculations, and the comparison with the experimental shifts. The quoted shifts are for experimental temperatures of 273 K ($\text{UO}_2(\text{CO}_3)_2^{5-}$ and $\text{PuO}_2(\text{CO}_3)_2^{4-}$), and 295 K ($\text{PuO}_2(\text{CO}_3)_2^{4-}$). The calculated shifts are taken from Ref. [92], and the experimental shifts from Ref. [230] ($\text{UO}_2(\text{CO}_3)_2^{5-}$), and [229] ($\text{NpO}_2(\text{CO}_3)_2^{4-}$ and $\text{PuO}_2(\text{CO}_3)_2^{4-}$). All shifts have been referenced relative to the orbital shift of the diamagnetic complex $\text{UO}_2(\text{CO}_3)_2^{4-}$.

complex	state	energy / cm^{-1}	population / %	δ^{Curie} / ppm	total δ^{Curie} / ppm
$\text{UO}_2(\text{CO}_3)_2^{5-}$	ground, $E_{3/2}$	0	79	-94.0	-99.5
	lowest-lying excited, $E_{1/2}$	132	21	-121.2	
$\text{NpO}_2(\text{CO}_3)_2^{4-}$	ground, $E_{3/2}$	0	87	-106.5	-110.4
	lowest-lying excited, $E_{1/2}$	356	13	-136.6	

Table 13.10: Comparison of the Curie shifts obtained from the two lowest-lying doublet states of $\text{UO}_2(\text{CO}_3)_2^{5-}$ and $\text{NpO}_2(\text{CO}_3)_2^{4-}$ at 273 K. The corresponding relative energies of the states and their populations (at 273 K) are also given relative to the ground state of each molecule. Data computed by Gendron et al [92].

shifts shown in Figure 13.54 were therefore re-referenced to $\text{UO}_2(\text{CO}_3)_2^{4-}$, and therefore comprise only the contributions from paramagnetic effects. For all three complexes, it can be seen that the Curie terms are the dominant contributions to the total shift, with the LR parts representing only minor corrections.

For the two complexes with a single $5f$ electron, $\text{UO}_2(\text{CO}_3)_2^{5-}$ and $\text{NpO}_2(\text{CO}_3)_2^{4-}$, the single largest contribution to the shift is from the PSO part of the Curie shift, with the next largest terms being the Curie PCS and LR PSO. Interestingly, we see that the contact shifts are negligible in $\text{UO}_2(\text{CO}_3)_2^{5-}$. Gendron et al. also employed the EPR representation of the shift. For these two $5f^1$ complexes both the ground state and lowest-lying excited state are doublets, and can be modelled with pseudo-spin 1/2. Their Curie contributions to the shift were therefore calculated from Equation 13.21. The results are given in Table 13.10 [92]. The

pseudo-spin	g_{\parallel}	$A_{\parallel}^{\text{total}} / \text{MHz}$	$A_{\parallel}^{\text{FC}} / \text{MHz}$	$A_{\parallel}^{\text{SD}} / \text{MHz}$	$A_{\parallel}^{\text{PSO}} / \text{MHz}$	D / cm^{-1}	δ^{Curie}	$\delta_{\text{FC}}^{\text{Curie}}$	$\delta_{\text{PCS}}^{\text{Curie}}$	$\delta_{\text{PSO}}^{\text{Curie}}$
1/2	-5.687	3.76	-1.40	1.56	3.60	—	-379.0	141.6	-157.6	-363.0
1	-2.843	1.88	-0.70	0.78	1.80	3974	-379.0	141.6	-157.6	-363.0

Table 13.11: EPR parameters and Curie shifts calculated for the electronic ground state of $\text{PuO}_2(\text{CO}_3)_2^{4-}$ at 295 K. Two sets of parameters were computed, assuming either an electronic manifold of pseudo-spin 1/2 or 1. Both the hyperfine constants and their Curie shifts are also broken down into their Fermi-contact, spin-dipolar (PCS), and PSO contributions. In all cases the rhombic EPR parameters (g_{\perp} , A_{\perp}^{total} , A_{\perp}^{FC} , A_{\perp}^{SD} , A_{\perp}^{PSO} , and E) are zero. Data computed by Gendron et al [92].

paramagnetic shift is therefore well approximated in the EPR formalism, here considering only the two lowest-lying electronic states.

In the case of $\text{PuO}_2(\text{CO}_3)_2^{4-}$, the addition of the second $5f$ electron has the effect of increasing the paramagnetic shift substantially. Here the Curie contact shift and Curie pseudo-contact shift are significant, but are also of opposite sign and largely cancel, leaving the Curie PSO shift as the remaining dominant contribution. All the LR terms were found to be negligible.

The lowest-lying excited state was calculated to be 3580 cm^{-1} above the ground state, and so could be neglected in the EPR representation of the shift. The EPR parameters of the ground state were calculated twice, once assuming a pseudo-spin of 1/2 and once assuming a pseudo-spin of 1, and are tabulated in Table 13.11. We see that all the EPR parameters vary depending on which model we use for the ground state. In particular we see that the inclusion of ZFS in the pseudo-spin-1 model has the effect of reducing the magnitude of all the other parameters relative to their values in the pseudo-spin-1/2 model, as expected. Nevertheless, the two pictures give the same values for the shift in each case, and the same contributions at this temperature. However we should note that the temperature dependence of the shift, within the range where only the ground manifold is occupied, will be different for the two models. This is due to the inclusion of the tensor Z in the pseudo-spin-1 model, which does not have a simple Curie temperature dependence.

For these carbonate systems, the accurate reproduction of the experimental paramagnetic shifts sets a benchmark in computational paramagnetic NMR of actinide systems. The general trends identified for these systems suggest that (1) the Curie terms dominate the LR contributions, and (2) the most important of the Curie terms is that due to the PSO contribution. However it is currently unclear whether these trends are in fact general, or only specific to these particular types of complex. Nevertheless, it is expected that calculations of this type will become more widely employed in paramagnetic NMR of actinide complexes in the future.

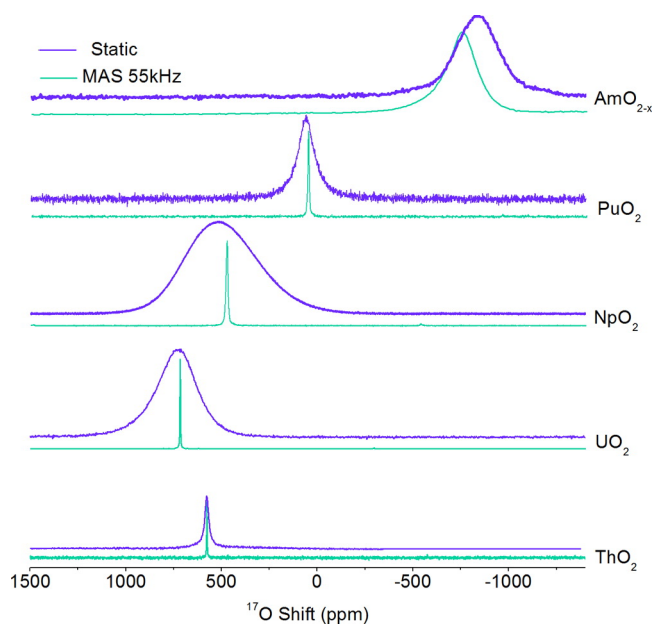


Figure 13.55: Solid-state ^{17}O NMR spectra acquired on a series of five enriched actinide oxides, at a Larmor frequency of -54.25 MHz, under both static conditions and 55 kHz MAS. Adapted with permission from [13]. Copyright (2014) American Chemical Society.

13.13 Solid actinide oxides

13.13.1 Background

The second case study of paramagnetic actinide systems we present is the ^{17}O MAS solid-state NMR study of cubic actinide oxides by Martel et al [13]. Solid actinide systems have remained elusive to NMR due both to their well-known high radiotoxicity, and to the technological challenges associated with fast spinning. This study therefore represents an impressive contribution to our understanding of the NMR properties of such solids.

13.13.2 Paramagnetic shifts

Five actinide oxides were enriched with ^{17}O , and studied with ^{17}O NMR at fast MAS of 55 kHz. The chosen oxides were ThO_2 ($5f^0$, diamagnetic), UO_2 ($5f^2$), NpO_2 ($5f^3$), PuO_2 ($5f^4$), and AmO_2 ($5f^5$). The spectra acquired under both static and MAS conditions are shown in Figure 13.55. In the spectra of the static powders

we see that the measured shifts cover a large range, from +800 ppm to –800 ppm, and depend strongly on the actinide ion. We also see that the diamagnetic oxide ThO₂ has a comparatively large shift of 576 ppm, indicating that all the oxides have substantial orbital shifts which may themselves vary considerably with the actinide ion, and which therefore complicate the interpretation of the NMR spectra. In addition, the resonances of the paramagnetic oxides are broad, each having linewidths in the range of 100–500 ppm. Since the oxides have a long-range structure that is cubic, there is no contribution from the quadrupolar interaction to the line broadening, and so the linewidths can be ascribed mainly to paramagnetic effects.

When MAS is applied, the most striking change to the spectra is the narrowing of these resonances to a few ppm, with the exception of that of AmO₂. For the other oxides the broadening observed from the static samples was therefore ascribed to the spin-dipolar shift anisotropy. The different behaviour seen for AmO₂ was shown to be due to a combination of more than one disordered phase, and oxide vacancies [13]. A second consequence of MAS is the shifting of all the resonances, with the exception of the peak from ThO₂, closer to zero. This is expected, since the increased temperature of the sample due to frictional heating reduces the Curie spin, and therefore reduces the paramagnetic contribution to the shift.

As we saw in section 13.12, the interpretation of the paramagnetic shifts due to actinide ions is complex. However in the present study, it was assumed that the cubic structure of the oxides results in a magnetic anisotropy that is zero, and as a consequence there is no contribution from the PCS. Additionally, contributions from the PSO were neglected, and the paramagnetic contribution to the shift was interpreted as a contact shift. This shift δ^S was calculated from the Curie spin using the expression in Equation 3.68:

$$\delta^S = -\frac{\langle \hat{S}_z \rangle A^{\text{FC}}}{\hbar\gamma_I B_0}. \quad (13.22)$$

However we note that the expression for the Curie spin is more complicated than that used for 3*d*-metal ions, in which only the electronic Zeeman interaction, and possibly the ZFS, is included. Martel et al. computed the Curie spin using a Hamiltonian \hat{H} that is given by [13]

$$\hat{H} = \hat{H}_{\text{FI}} + \hat{H}_{\text{CF}} + \hat{H}_{\text{Z}}. \quad (13.23)$$

Here \hat{H}_{FI} is the Hamiltonian representing all the free-ion interactions such as Coulomb repulsion, and SO cou-

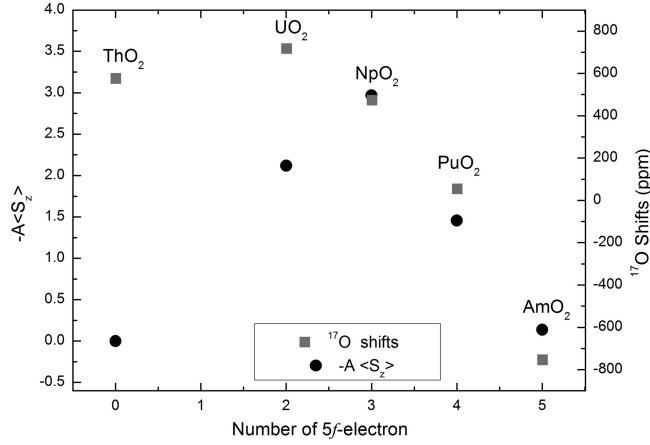


Figure 13.56: Plot of $-A\langle\hat{S}_z\rangle$ and the isotropic ^{17}O shifts against the number of $5f$ electrons for the five actinide oxides. The constant A is given by $A = -3kT/\mu_B H_0$. Adapted with permission from [13]. Copyright (2014) American Chemical Society.

pling which was here determined in the regime intermediate between the Russell–Saunders and jj schemes. The crystal-field interaction Hamiltonian \hat{H}_{CF} was written in the form of Equation 6.6. For the cubic structure of the oxides, the rank-two tensor components are zero, and we retain only a subset of the rank-four and rank-six tensors, giving a Hamiltonian of the form:

$$\hat{H}_{\text{CF}} = B_4 \left[\hat{C}_0^{(4)} + \sqrt{\frac{5}{14}} (\hat{C}_{+4}^{(4)} + \hat{C}_{-4}^{(4)}) \right] + B_6 \left[\hat{C}_0^{(6)} - \sqrt{\frac{7}{2}} (\hat{C}_{+4}^{(6)} + \hat{C}_{-4}^{(6)}) \right]. \quad (13.24)$$

The interaction is described by the operators $\hat{C}_q^{(k)}$ of rank k and order q , and the two crystal-field splitting parameters B_4 and B_6 , which indicate the strengths of the rank-four and rank-six contributions respectively. The final term is the electronic Zeeman interaction comprising both the spin and orbital parts, given by Equation 4.11.

$$\hat{H}_Z = \mu_B B_0 (\hat{L}_z + 2\hat{S}_z), \quad (13.25)$$

where it is assumed that $g_e \approx 2$. The total Hamiltonian \hat{H} was diagonalized, and the Curie spin calculated. Assuming that the Fermi-contact coupling constant is the same for all the actinides, $-3\langle\hat{S}_z\rangle kT/\mu_B B_0$ is proportional to the experimental shift. Both quantities are plotted in Figure 13.56. We see that, as an initial approximation, the variation of the Curie spin does account for the underlying trend in the variation of shift along the series of these actinides. However the quantitative agreement is comparatively poor, for example

with the Curie spin alone unable to account for the observed changes in sign of the shift on moving from PuO_2 to AmO_2 . The agreement can presumably be improved by including other relevant terms in the shift, such as the orbital contribution, which we can see is substantial for the diamagnetic oxide ThO_2 , the PSO, and higher order terms describing the magnetic anisotropy in a cubic system.

Nevertheless this study is a very interesting milestone in paramagnetic NMR of actinide materials, and is expected to encourage more work in this area. In particular, given the work described in section 13.12, it is expected that calculations of the shift in this type of solid will evolve in parallel to the experimental techniques, and provide a useful tool in the study of actinide chemistry.

13.14 Probing the nanostructure of composite materials using relayed paramagnetic relaxation enhancement

13.14.1 Background

In the final case study of this review we consider a topic that is different to those we have studied in previous sections. Previously we have highlighted studies where the system of interest contained isolated paramagnetic metal ions, or where such ions could be easily introduced, and used the paramagnetic effects to obtain both local- and long-range structural information. The effects considered were principally the paramagnetic shifts, but some insight was also obtained from measurements of the PREs. In this final study however we highlight the work of Schlagnitweit et al., who developed a new method to investigate the sizes of different domains of nm– μm length scale in multi-component materials using a paramagnetic dopant [468].

Multi-component materials are defined as comprising two or more particles or domains with different properties such as structural order and dynamics. Examples include multi-phase systems such as alloys, composites, and mixtures of polymers. The bulk properties of such systems depend on the sizes of the domains and particles, and can be altered accordingly. For this reason it is important to be able to characterize the range of size and shape of the domains in situ. Schlagnitweit proposed an NMR method for doing this utilizing the PRE of a paramagnetic dopant combined with spin diffusion [468]. This method was applied both to a model system comprising a suspension polymer nanoparticles, and then to a polymer mixture of ethyl cellulose (EC)/hydroxypropyl cellulose (HPC) in a film. This latter system is of particular interest as a

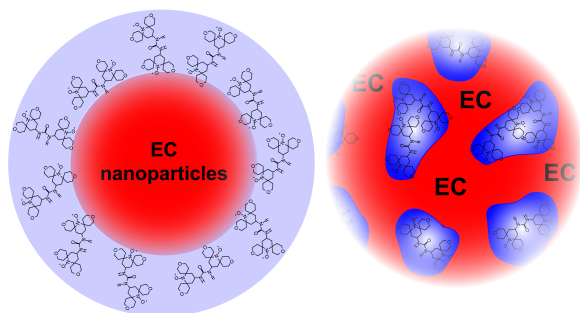


Figure 13.57: Illustration of the selective doping of a particular domain in bi-domain samples. On the left is shown a water-based suspension of EC nanoparticles. The radical is impregnated in the solution (light blue), and dopes the surface of the EC nanoparticles (red). On the right is shown a composite system containing domains of EC (red) and HPC (blue) in films covering pellets in controlled-release formulations. The radical solution impregnates the water-soluble HPC domain. This induces a PRE at the surface of the EC domains. Reproduced with permission from [468]. Copyright (2015) American Chemical Society.

coating of the film on pellets is used as a pharmaceutical controlled-release formulation.

The following two sections outline the basic method for measuring the domain sizes, and describe the application to the EC/HPC film.

13.14.2 The relay of the paramagnetic relaxation enhancement by spin diffusion

Here we briefly describe the method to measure the domain sizes of a two-component material, comprising domains A and B. Schlagnitweit et al. suggested that in order to measure the length scale of domain A we can dope the second domain B with a solution of a paramagnetic molecule of known concentration. The doping procedure is illustrated in Figure 13.57 (left panel), where the surface of an EC nanoparticle is impregnated with a solution containing an organic radical [468]. The paramagnetic centres impregnate both domain B and the surface of domain A, and therefore induce a large PRE throughout the former and at the latter. The longitudinal relaxation time of a particular nuclear site in domain A $T_1(\mathbf{r})$ becomes position dependent, decreasing as we approach the surface of A with a distance dependence $1/r^6$. We have seen that this direct PRE can be used to probe distances from the metal ion up to 100 Å, and so is not able to probe longer length scales of the order nm– μm , with the large region of the domain that is far from the surface not experiencing a measurable PRE. However spin diffusion transfers longitudinal magnetization from the centre of the domain

A to the surface, where it experiences enhanced relaxation, which is referred to as a relayed paramagnetic relaxation enhancement (R-PRE). The key to the method is that in smaller undoped domains spin diffusion transfers the magnetization to the surface more rapidly, thus resulting in a greater decrease in the apparent T_1 relaxation time from the whole domain. Hence a comparison of the longitudinal relaxation behaviour of the domain A in the impregnated sample and the undoped sample reveals information about the size and shape of domain A. In addition multiple measurements can be performed with different concentrations of paramagnetic molecules in domain B, allowing an evaluation of the uncertainty of the measurements.

The longitudinal relaxation can be measured using a saturation–recovery experiment, where the longitudinal magnetization is saturated and allowed to recover during a variable delay τ . This is followed by a 90° pulse which converts the recovered polarization into observable coherences. The signal measured during this experiment in the undoped and doped samples is denoted $S_{\text{core}}(\tau)$ and $S_{\text{doped}}(\tau)$ respectively, and the comparison between the two used to determine the domain size and shape is quantified with a R-PRE enhancement factor that is defined as $\varepsilon(\tau) = S_{\text{doped}}(\tau)/S_{\text{core}}(\tau)$.

In the undoped sample the longitudinal relaxation time constant is assumed to be constant throughout the domain A, and is referred to as T_1^{core} . In the doped sample $T_1(\mathbf{r})$ is position dependent, and takes boundary values of T_1^{core} in the centre of domain A, which is far from the surface, and a short value T_1^{surface} at the surface due to the direct PRE. In practice the value of T_1^{surface} can be taken to be the same as the corresponding value measured in the solvent in the doped domain B. Elsewhere in domain A we can calculate $T_1(\mathbf{r})$ since the direct PRE decreases with the distance r from the surface as $1/r^6$.

Spin diffusion in an extended domain is a complicated process to model rigorously using a full quantum-mechanical treatment. Fortunately it can be modelled classically using a diffusion equation which incorporates a longitudinal relaxation sink [423]. The polarization in domain A $I_z(\mathbf{r}, t)$ at position \mathbf{r} and time t is given by

$$\frac{\partial I_z(\mathbf{r}, t)}{\partial t} = D\nabla^2 I_z(\mathbf{r}, t) - \frac{I_z(\mathbf{r}, t) - I_{z,0}}{T_1(\mathbf{r})}, \quad (13.26)$$

where D is the spin-diffusion coefficient, and $I_{z,0}$ is the equilibrium polarization normalized to $I_{z,0}(\mathbf{r}) = 1$. The total polarization from the whole domain A $I_{z,A}(t)$ is found by integrating $I_z(\mathbf{r}, t)$ over all distances \mathbf{r} within the domain for each time point, i.e. $I_{z,A}(t) = V^{-1} \int_V I_z(\mathbf{r}, t) d^3r$. If the domains A are present with a distribution of sizes and shapes, it is necessary to compute the average value of $I_{z,A}(t)$ in order to obtain the

total polarization from the whole sample.

In the study of Schlagnitweit et al. the computation of the spin-diffusion dynamics was simplified by assuming that the domains A were spherical [468]. The spin-diffusion equation in Equation 13.26 was simplified by replacing \mathbf{r} with the distance r , whose origin is located at the centre of the sphere. The longitudinal relaxation time constants at the surface and centre of the sphere were set to $T_1(r_{\max}) = T_1^{\text{surface}}$ and $T_1(0) = T_1^{\text{core}}$ respectively, where r_{\max} is the radius of the sphere, and the variation of $T_1(r)$ at intermediate radii was modelled using the $1/(r - r_{\max})^6$ distance dependence of the PRE. We expect that there is a thin surface layer of domain A, of a thickness δr , which cannot be observed using conventional NMR pulse sequences and so occupies a so-called ‘blind zone’. In this study δr was assumed to be 2 Å [468]. With this condition we can write down an expression for the longitudinal relaxation time constant at arbitrary radius inside the domain as

$$\frac{1}{T_1(r)} = \left(\frac{1}{T_1^{\text{core}}} + \frac{1}{T_1^{\text{surface}}} \right) \left(\frac{\delta r}{r - r_{\max} - \delta r} \right)^6. \quad (13.27)$$

Finally the solution to the diffusion equation requires two boundary conditions, which were set to

$$I_z(r, 0) = 0, \quad \frac{\partial I_z(r_{\max}, t)}{\partial t} = 0, \quad (13.28)$$

which are interpreted as follows. The first boundary condition indicates that the polarization at time $t = 0$ is zero throughout the entire domain following saturation. The second condition indicates that the rate of change of the polarization at the domain surface is zero, so that no polarization leaves the domain.

13.14.3 Measurement of domain sizes in ethyl cellulose/hydroxypropyl cellulose film coatings in pharmaceutical controlled-release formulations

The R-PRE method was applied to a polymer mixture of EC/HPC in a film, which is used as a pharmaceutical controlled-release formulation [468]. The doping procedure is illustrated in Figure 13.57 (right panel). The paramagnetic molecule that was chosen is the organic biradical AMUPol, the structure of which is also shown in Figure 13.57. This organic molecule contains two NO· radical functional groups, which have comparatively long electronic relaxation times [166], and therefore are suitable for inducing large direct PREs. Two aqueous solutions of the biradical were prepared with concentrations of 15 mM and 30 mM, which were used to

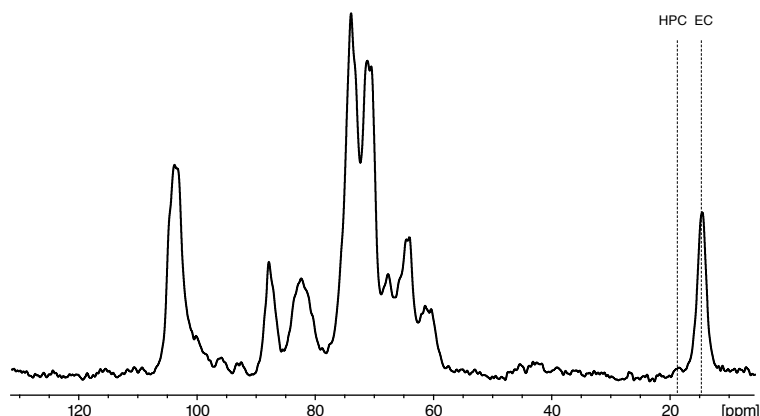


Figure 13.58: ^1H - ^{13}C solid-state CP MAS NMR spectrum of the composite EC/HPC cellulose film coatings, where the HPC domain is impregnated with a 30 mM aqueous solution of AMUPol. The spectrum was acquired at 11.74 T and 8 kHz MAS. The methyl resonance at 15 ppm is from the EC domain, and was used to measure the relaxation rates in this domain. The dashed line labelled HPC marks the expected position of the corresponding HPC resonance. Here it is not observable due to the large PRE from the paramagnetic dopant. Reproduced with permission from [468]. Copyright (2015) American Chemical Society.

impregnate the water-soluble HPC domain (B). The method was then used to determine the sizes of the EC domains (A).

The ^1H - ^{13}C CP spectrum of a doped sample acquired at 8 kHz MAS is shown in Figure 13.58. The spectrum exhibits a well-resolved methyl peak at 15 ppm from the EC domain, which was used to monitor the relaxation behaviour in this domain. Also shown in the spectrum is the expected position of the corresponding resonance in the doped HPC domain. The peak is absent due to the fast relaxation due to the direct PRE induced throughout this domain.

The longitudinal relaxation of the methyl ^{13}C in the EC domain was monitored by applying a saturation–recovery sequence following the ^1H - ^{13}C CP transfer. The recovery curves were measured for the undoped sample, and samples where the HPC domain was doped with the two radical solutions of 15 mM and 30 mM, and are shown in Figure 13.59 (a). The R-PRE enhancement curves for the two concentrations were also calculated, and are shown in Figure 13.59 (b). The spin-diffusion equation was solved for the two radical concentrations using a diffusion coefficient of $0.8 \text{ nm}^2 \text{ cm}^{-1}$, values of T_1^{surface} that were measured to be 19 ms and 13 ms for the concentrations of 15 mM and 30 mM respectively, and a value of T_1^{core} that was extracted from the saturation–recovery curve of the undoped sample. This left r_{max} as the only variable parameter in

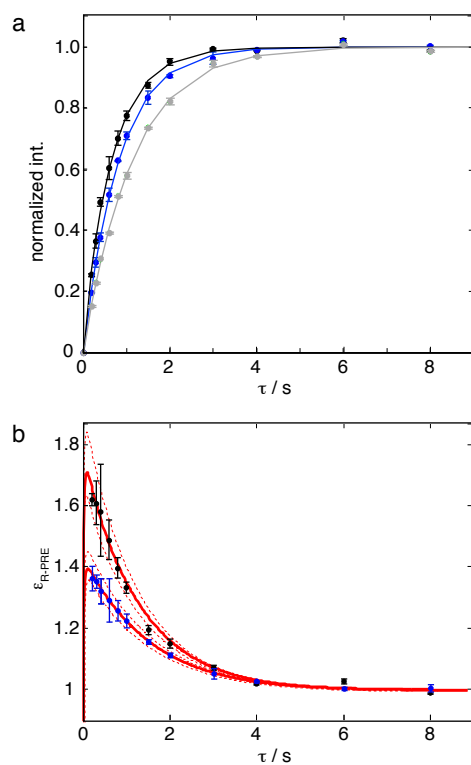


Figure 13.59: The build-up and relaxation enhancement factor curves due to the longitudinal R-PRE in the EC domain of the composite EC/HPC cellulose film coating following a saturation–recovery sequence. The curves in (a) show the build-up of the signal $S(\tau)$ as a function of the recovery delay τ of the sequence. The curves are measured from the integral of the EC methyl peak at 15 ppm in the spectrum in Figure 13.58. Three recovery curves are shown that were measured without paramagnetic doping $S_{core}(t)$ (grey), and following impregnation with 15 mM AMUPol (blue) and 30 mM AMUPol (black). In (b) are shown the relaxation enhancement curves $\epsilon(\tau) = S_{doped}(\tau)/S_{core}(\tau)$. The dashed lines indicate the margin of error. Adapted with permission from [468]. Copyright (2015) American Chemical Society.

the diffusion equation to be fitted. Following the fitting procedure the EC domain sizes d_{EC} was found to be 90 ± 10 nm and 70 ± 10 nm when calculated from the data of the samples doped at concentrations of 15 mM and 30 mM respectively [468]. Furthermore, using the EC/HPC volume ratio of 70/30 in these films and assuming spherical HPC domains allowed the determination of the HPC domain sizes d_{HPC} of 182 ± 10 nm and 142 ± 10 nm respectively.

In summary this technique represents a powerful method for measuring domain sizes of multi-component materials in situ. Although a simple spherical model for the EC domains sizes was used in this study, the method can easily be extended to more sophisticated models for the shape. Therefore this approach is expected to be widely applicable to other multi-component systems.

13.15 Key concepts

- Paramagnetic NMR is widely applicable to systems in solution or the solid state, including small molecules, proteins, and solid materials.
- Both the paramagnetic centre and the system in which it is located profoundly change the paramagnetic effects that are measured, including the shifts, shift anisotropies, paramagnetic relaxation enhancements, and inhomogeneous broadening.
- Contact shifts provide short-range structural information about the system close to a paramagnetic centre.
- Pseudo-contact shifts and dipolar-based paramagnetic relaxation enhancements provide long-range structural information.
- The shift anisotropy generally contains long-range information from the spin-dipolar interaction, and short-range information from the contact interaction.
- In small molecules both non-relativistic and spin-orbit coupling effects can be important contributions to the paramagnetic shifts, resulting in both contact and pseudo-contact contributions.
- In proteins contact shifts are important for nuclei separated from the paramagnetic centre by only a few bonds. For resonances located outside the 'blind sphere' the shifts are dominated by pseudo-contact

shifts.

- In solid materials, such as battery electrodes, the contact interaction provides information about the bonding and electron transfer between the paramagnetic centre and the observed nucleus. The shift anisotropies are dominated by the spin-dipolar interaction, but may also have an important part due to the contact interaction.
- The paramagnetic relaxation enhancement extends over a range of the order of 10–20 Å, but when combined with spin diffusion can be used to probe length scales of the order nm– μ m in multi-component materials.

Chapter 14

Concluding remarks and the future of paramagnetic NMR

To conclude this review we summarize the current state of the art in the theory and practice of paramagnetic NMR spectroscopy, as described in the earlier chapters, and outline some of the ongoing research in these areas. In recent years the amount of activity in development of theory and methods in the field of paramagnetic NMR spectroscopy has increased considerably, as has the complexity of the systems under study. The field is poised for some very exciting developments in the future, in the development of both the theory and methods, and in extending the fields of application. Improved understanding of the spin physics of these systems will also be important as the applications of dynamic nuclear polarization to an increasingly large range of systems grow, exploiting both organic and inorganic radicals.

Solution NMR studies have been conducted for several years, both on small molecules and large paramagnetic proteins. Whilst theoretical formalisms for the paramagnetic shielding tensor have also been known for many years, it has not been until relatively recently that completely general formalisms have been developed, such as those by Pennanen and Vaara, and van den Heuvel and Soncini (see chapters 3–6.) These models have, in turn, opened the door to calculations of paramagnetic shielding tensors due to first-row *d*-block metal-ions from first principles using quantum chemistry and DFT, which incorporate SO coupling effects on the hyperfine, *g*-, and ZFS tensors. In addition the PREs due to these metal ions can

be interpreted under different experimental conditions and motional dynamics. These models have increased in sophistication from incorporating only a phenomenological treatment of electronic relaxation (chapter 8) to explicit treatments (chapter 9).

Studies of paramagnetic proteins in solution have also been conducted for many years, and have reached a high level of sophistication in terms of both the methods used, and the interpretation and use of the paramagnetic effects to obtain structural information. In the latter case it has been demonstrated that PCSs, PREs, RDCs, and CCRs can all be used to supplement other distance restraints in order to obtain increasingly more accurate and precise structures (chapters 12 and 13).

In the field of solid-state NMR recent progress has been substantial. The systems being studied today cover a diverse range of fields including battery materials, surface catalysts, inorganic phosphors, pharmaceutical systems, and metalloproteins (chapter 13). The ability to study systems of increasing complexity, including compositional disorder, has been enabled by the current drive in developing new solid-state NMR methods to achieve broadband excitation and separation of the different available NMR parameters (chapters 11 and 12). The theory of the paramagnetic shielding tensor for first-row *d*-block metal-ions in the solid state has evolved in parallel to that in solution (chapter 7). Initially these methods included the effects of SO coupling and magnetic ordering in an empirical way, but more recently these properties have also been calculated from first principles. For example, the data obtained from ab-initio calculations, which generate 0 K hyperfine (Fermi contact and spin dipolar) information, can be used to predict room-temperature properties via a variety of methods, from the use of spin-only values to calculate magnetic susceptibilities and the direct use of experimental data such as magnetic susceptibility curves, to direct calculations of magnetic couplings and their use in mean field (Ising) models or Monte Carlo simulations [541], the latter proving extremely useful in disordered systems. Although by no means routine, it is now relatively straightforward to rationalize the spectra of paramagnetic materials, starting by using the often intuitive Goodenough-Kanamori rules to predict the size of the Fermi contact shifts from the nature of the overlap between metal and ligand orbitals. The shifts of the individual M-L-N sites (M = paramagnetic metal, L = ligand, N = nucleus under observation) can then be readily calculated from first principles calculations. Here, the use of a clever “flipping” method allows the contributions from different metals (and pathways) to be easily separated [54]. Although the calculations are not exact, with errors coming from the choice of functionals used and the scaling factors employed to convert 0 K data into the paramagnetic regime, they provide considerable insight into the signs

and magnitudes of the shifts. Given the inherent assumptions, further inclusion of additional terms (such as the pseudocontact shifts/spin-orbit couplings) are often not warranted, unless examining systems with very small Fermi-contact shifts. This can arise in cases where the paramagnetic ions are more than two bonds away from the NMR nucleus, in systems with competing and opposing Fermi contact shift contributions, or where the shifts are inherently small due to very weak and largely ionic bonds.

In comparison with solution NMR the PRE in the solid state is poorly understood, and this has hindered the use of the PRE for extracting structural and dynamic information. Similarly, BMS effects in solid-state NMR spectra have been studied, but have yet to be routinely exploited, for example to obtain information on crystallite shape and packing (chapter 10). They have been shown to play an extremely important role in determining the shifts of resonances in solid samples, particularly those with unusual geometries such as the planar geometries of pouch cell batteries [154]. However it remains a challenge to model the effects of magnetic inhomogeneities on, for example, sideband intensities in MAS NMR. Nonetheless, analysis of the intensities of the sideband manifolds provides a relatively straightforward way to extract structural information. Sometimes the information can be extremely simple to extract, for example, the sign of the asymmetry of the tensor being used to determine whether Li and Na ions are located within Li/Na or transition-metal layers of (Li/Na)MO₂ battery electrode materials [54, 541].

The interpretation of the shifts due to lanthanides and actinides is less advanced, with the former generally relying on theories developed in the 1970s by Golding and Halton, and by Bleaney (chapter 6). Because the ratio of the pseudo-contact to the Fermi-contact shift is generally larger than for transition metal ions, it is often more straightforward to use the PCS to extract structural information. Despite some recent progress in calculations of paramagnetic shifts of actinide complexes [91, 92, 212], actinide NMR is at a relatively early stage of development, with the experimental NMR being hampered by practical considerations (beyond those of the paramagnetism) associated with the radioactivity and toxicity of the metal ions.

The broad scope of the application of paramagnetic NMR to a number of systems in chemistry, materials science, and biology has been due to the advances in all these different areas of theory and application. In particular developments in paramagnetic solid-state NMR have opened up the field to systems in chemistry and materials science where complex compositional disorder is a key component of the properties of many materials. Further developments in NMR methods, calculations of paramagnetic shift tensor calculations and PREs, and their implementation in extracting structural and dynamic information will further increase the

ability of NMR to study more complex systems in a wider range of disciplines.

Acknowledgements

We acknowledge Prof. Lyndon Emsley (Ecole Polytechnique Fédérale de Laussane), Dr Raphaële J. Clément (University of California, Berkeley), Dr Ieuan D. Seymour, Ms Roberta Pigliapochi, Dr David M. Halat, Mr Jeongjae Lee (University of Cambridge), Dr Ladislav Benda, Mr Kevin J. Sanders, Mr Andrea Bertarello (Ecole Normale Supérieure de Lyon), Dr Judith Schlagnitweit (Karolinska Institutet), Prof. Ivano Bertini, Prof. Claudio Luchinat, Dr Giacomo Parigi (University of Florence), Prof. Martin Kaupp, Mr Arobendo Mondal (Technische Universität Berlin), Prof. Juha Vaara, Dr Jiri Mares (University of Oulu), Prof. Philip J. Grandinetti (Ohio State University), and Prof. Jozef Kowalewski (Stockholm University) for many useful discussions about various aspects of the theory and practice of paramagnetic NMR.

This work was supported by the People Programme (Marie Curie Actions Initial Training Networks (ITN)) of the European Union's Seventh Framework Programme FP7/2007-2013/ under REA grant agreement no. 317127, the "pNMR" project. AJP received funding from the Swedish Research Council (2016-03441).

Appendix A

The Wigner–Eckart theorem

The appendices in this review make extensive use of the evaluation of the matrix elements of spin operators in manifolds of particular spin states. This evaluation is greatly facilitated by use of the Wigner–Eckart theorem, which gives an expression for the matrix element of the irreducible spherical tensor operator of rank k and order q , \hat{T}_{kq} , that connects the states $|J' M'\rangle$ and $|JM\rangle$, where J and J' are the (spin, orbital, or total) angular momentum quantum numbers, and M and M' are the corresponding azimuthal quantum numbers. The version of the theorem used here employs the convention of Brink and Satchler [190], but not, for example, that of Edmonds [226]. The expression can be given either in terms of the Clebsch–Gordan coefficient $\langle JM|J' k M' q\rangle$ or the Wigner $3j$ symbol as:

$$\langle JM|\hat{T}_{kq}|J' M'\rangle = (-1)^{2k} \langle J||\hat{T}_k||J'\rangle \langle JM|J' k M' q\rangle \quad (\text{A.1})$$

$$= (-1)^{J'+k+M} \langle J||\hat{T}_k||J'\rangle \sqrt{2J+1} \begin{pmatrix} J & J' & k \\ -M & M' & q \end{pmatrix}. \quad (\text{A.2})$$

The theorem effectively separates the matrix elements into a part that is orientation-independent, and contains all the physics of the situation, and a second part that contains all the information pertaining to the orientation of the system. On the first line the Wigner–Eckart theorem is quoted in terms of the Clebsch–Gordan coefficient $\langle JM|J' k M' q\rangle$. The quantity $\langle J||\hat{T}_k||J'\rangle$ is a reduced matrix element of the rank- k tensor \hat{T}_k , which depends only on the rank k of the tensor, and the quantum numbers J and J' that define the sizes of

the angular momenta of the states. It therefore contains all the information about the system independent of orientation. The orientation dependence of the total matrix elements $\langle JM | \hat{T}_{kq} | J' M' \rangle$ depends on the magnetic quantum numbers M and M' , and the order of the tensor q , which information is contained entirely in the Clebsch–Gordan coefficient. On the second line is given the same expression in terms of the Wigner $3j$ symbol, which is the quantity in parentheses. The second expression is equivalent to the first, with the orientation dependence now being encoded in the $3j$ symbol.

A.1 The projection theorem

A special case of the Wigner–Eckart theorem is the projection theorem for vector operators, which pertains to the matrix elements of irreducible spherical tensor operators of rank one that are evaluated between states with the same value of J . For a vector operator \hat{V} the projection theorem is [190]

$$\langle JM | \hat{V} | JM' \rangle = \frac{1}{J(J+1)} \langle JM | \hat{J} (\hat{J} \cdot \hat{V}) | JM' \rangle \quad (\text{A.3})$$

$$= a_J(V) \langle JM | \hat{J} | JM' \rangle, \quad (\text{A.4})$$

where $a_J(V)$ is a scalar coefficient that depends on the reduced matrix element of \hat{V} :

$$a_J(V) = \frac{\langle J || \hat{V} || J \rangle}{\sqrt{J(J+1)}}. \quad (\text{A.5})$$

This theorem can be interpreted as follows using a classical vector model. We note that the classical equivalent of the operator in Equation A.3, $\mathbf{J} (\mathbf{J} \cdot \mathbf{V}) / (J(J+1))$, is simply the projection of \mathbf{V} along the unit vector $\mathbf{J} / \sqrt{J(J+1)}$. According to the vector model \mathbf{V} is precessing about \mathbf{J} , with the result that the component of \mathbf{V} that is perpendicular to \mathbf{J} averages to zero, leaving only the component that is parallel to \mathbf{J} . In the quantum mechanical picture the vector operator \hat{V} evolves under the action of a Hamiltonian defined by \hat{J} . The parts of the matrix elements originating from \hat{V} that do not commute with \hat{J} then average to zero.

A.1.1 Magnetic moments due to ions subject to Russell–Saunders spin-orbit coupling

The projection theorem for vector operators is important when considering the electronic magnetic moment and the corresponding Zeeman interaction of electronic spins subject to SO coupling. In the case where both S and L are non zero, the properties of the electrons are defined by the total angular momentum J , which is given by the following expression in the Russell–Saunders coupling scheme:

$$\mathbf{J} = \mathbf{L} + \mathbf{S}. \quad (\text{A.6})$$

The total magnetic moment μ_J is the sum of the electronic orbital and spin magnetic moments μ_L and μ_S :

$$\mu_J = \mu_L + \mu_S \quad (\text{A.7})$$

$$= -\mu_B (\mathbf{L} + g_e \mathbf{S}). \quad (\text{A.8})$$

Clearly \mathbf{J} and μ_J are not collinear. However we can apply the projection theorem to the vector operators corresponding to the total angular momentum and magnetic moment, $\hat{\mathbf{J}}$ and $\hat{\mu}_J$, which relates the matrix elements of the two as follows:

$$\langle JM | \hat{\mu}_J | JM' \rangle = -\mu_B g_J \langle JM | \hat{\mathbf{J}} | JM' \rangle, \quad (\text{A.9})$$

where g_J is the Landé g -factor. It is for this reason that the magnetic moment operator $\hat{\boldsymbol{\mu}}$, as defined by van den Heuvel and Soncini via the expression $-\mathbf{B}_0 \cdot \hat{\boldsymbol{\mu}}$, is taken to be $\hat{\boldsymbol{\mu}} = -\mu_B g_J \hat{\mathbf{J}}$, and the electronic Zeeman Hamiltonian is

$$\hat{H}_Z = \mu_B g_J \mathbf{B}_0 \cdot \hat{\mathbf{J}}. \quad (\text{A.10})$$

Appendix B

Relativistic corrections to the hyperfine coupling tensor

In this appendix we give expressions for the NR and SO contributions to the hyperfine coupling tensor that may be used in quantum-chemical and DFT calculations. The treatment here follows that of Arbuznikov et al., who adopt the SI convention for atomic units, and extends the presentation of the hyperfine tensor in section 4.1 [210].

B.1 The vector potential

In atomic units, the vector potential $\mathbb{A}^{(A)}(\mathbf{r}_i)$ describing the interaction between a point-like nucleus A at position \mathbf{R}_A and an electron i at position \mathbf{r}_i is given by:

$$\mathbb{A}^{(A)}(\mathbf{r}_i) = \alpha^2 \gamma_I^{(A)} \frac{\hat{\mathbf{I}}^{(A)} \times \mathbf{r}_{iA}}{r_{iA}^3}, \quad (\text{B.1})$$

where $\hat{\mathbf{I}}^{(A)}$ and $\gamma_I^{(A)}$ are the nuclear spin operator and gyromagnetic ratio of nucleus A , and $\mathbf{r}_{iA} = \mathbf{r}_i - \mathbf{r}_A$ is the position of the electron i relative to the nucleus.

B.2 The non-relativistic hyperfine interaction

The lowest-order contributions to the hyperfine interaction Hamiltonian are the Fermi-contact and spin-dipolar terms, which were discussed in section 2.8, and are of order $O(\alpha^2)$ in the fine-structure constant. The corresponding hyperfine interaction Hamiltonians $\hat{H}_{\text{FC}}^{(A)}$ and $\hat{H}_{\text{SD}}^{(A)}$ describing the coupling between nucleus A and all the electrons i have the following expressions in atomic units:

$$\hat{H}_{\text{FC}}^{(A)} = \frac{4\pi}{3} \alpha^2 g_e \gamma_I^{(A)} \sum_i \delta(\mathbf{r}_{iA}) \hat{\mathbf{s}}_i \cdot \hat{\mathbf{I}}^{(A)}, \quad (\text{B.2})$$

$$\hat{H}_{\text{SD}}^{(A)} = \frac{1}{2} \alpha^2 g_e \gamma_I^{(A)} \sum_i \hat{\mathbf{s}}_i \cdot \frac{3\mathbf{r}_{iA} \mathbf{r}_{iA} - r_{iA}^2 \mathbf{1}}{r_{iA}^5} \cdot \hat{\mathbf{I}}^{(A)}. \quad (\text{B.3})$$

If we expand the total electronic wavefunction as a superposition of molecular orbitals $|\epsilon\rangle$

$$|\psi\rangle = \sum_{\epsilon} (c_{\epsilon}^{\alpha} |\epsilon\rangle + c_{\epsilon}^{\beta} |\epsilon\rangle), \quad (\text{B.4})$$

where c_{ϵ}^{α} and c_{ϵ}^{β} are the coefficients giving the α and β spin in each orbital, we obtain the following expressions for the Fermi-contact coupling constant A^{FC} and spin-dipolar coupling tensor A_{uv}^{SD} :

$$A^{\text{FC}} = \frac{4\pi}{3} \alpha^2 g_e \gamma_I^{(A)} \frac{1}{2S} \sum_{\epsilon, \tau} P_{\epsilon\tau}^{\alpha-\beta} \langle \epsilon | \delta(\mathbf{r}_A) | \tau \rangle, \quad (\text{B.5})$$

$$A_{uv}^{\text{SD}} = \frac{1}{2} \alpha^2 g_e \gamma_I^{(A)} \frac{1}{2S} \sum_{\epsilon, \tau} P_{\epsilon\tau}^{\alpha-\beta} \left\langle \epsilon \left| \frac{3r_{A,u} r_{A,v} - r_A^2 \delta_{uv}}{r_A^5} \right| \tau \right\rangle. \quad (\text{B.6})$$

Here $P_{\epsilon\tau}^{\alpha-\beta} = \overline{c_{\epsilon}^{\alpha} c_{\tau}^{\alpha}} - \overline{c_{\epsilon}^{\beta} c_{\tau}^{\beta}}$ is the spin density matrix.

B.3 The spin-orbit-coupling correction to the hyperfine interaction

We consider second-order perturbation corrections to the hyperfine interaction from the one- and two-electron SO interaction with Hamiltonian \hat{H}_{SO} :

$$\hat{H}_{\text{SO}} = \frac{1}{4} \alpha^2 g_e \left[\sum_B Z_B \sum_i \frac{\hat{\mathbf{s}}_i \cdot \hat{\mathbf{l}}_{iB}}{r_{iB}^3} - \sum'_{i,j} \frac{(\hat{\mathbf{s}}_i + 2\hat{\mathbf{s}}_j) \cdot \hat{\mathbf{l}}_{ij}}{r_{ij}^3} \right]. \quad (\text{B.7})$$

The first term represents the one-electron interaction, and comprises a sum over all nuclei B , which have charges Z_B , and electrons i . The second term represents the two-electron SO interaction, comprises a sum over pairs of electrons i and j , and contains both the spin-same orbit and spin-other orbit parts. The two operators \hat{l}_{iB} and \hat{l}_{ij} are the orbital angular momentum operators of electron i with respect to the positions of the nucleus B and a second electron j respectively. They take the forms:

$$\hat{l}_{iB} = (\mathbf{r}_i - \mathbf{R}_B) \times (-i\hat{\nabla}_i + \mathbb{A}(\mathbf{r}_i)), \quad (\text{B.8})$$

$$\hat{l}_{ij} = (\mathbf{r}_i - \mathbf{R}_j) \times (-i\hat{\nabla}_i + \mathbb{A}(\mathbf{r}_i)), \quad (\text{B.9})$$

where $\hat{\nabla}_i$ is the gradient operator for electron i .

The field-independent parts of the one- and two-electron orbital angular momentum operators depend on $\hat{\nabla}_i$. These terms combine with the Hamiltonian $\hat{H}_{\text{PSO}}^{(A)}$ representing the paramagnetic spin-orbital interaction (PSO) of nucleus A

$$\hat{H}_{\text{PSO}}^{(A)} = \alpha^2 \gamma_I^{(A)} \sum_i \frac{\hat{l}_{iA}}{r_{iA}^3} \cdot \hat{\mathbf{I}}^{(A)}, \quad (\text{B.10})$$

to give the following one-electron $A_{uv}^{\text{SO-I}(1)}$ and two-electron contributions $A_{uv}^{\text{SO-I}(2)}$ to the hyperfine tensor:

$$\begin{aligned} A_{uv}^{\text{SO-I}(1)} + A_{uv}^{\text{SO-I}(2)} = & \frac{1}{2} \alpha^4 g_e \gamma_I^{(A)} \frac{1}{2S} \left[\sum_k^{\text{occ}(\alpha)} \sum_a^{\text{virt}(\alpha)} \frac{\langle k\alpha | \hat{h}_u^{\text{SO}} | a\alpha \rangle \langle a\alpha | \hat{l}_{A,v}/r_A^3 | k\alpha \rangle}{E_{k\alpha} - E_{a\alpha} - \Delta E_{k \rightarrow a}^{\text{xc}}} \right. \\ & \left. - \sum_k^{\text{occ}(\beta)} \sum_a^{\text{virt}(\beta)} \frac{\langle k\beta | \hat{h}_u^{\text{SO}} | a\beta \rangle \langle a\beta | \hat{l}_{A,v}/r_A^3 | k\beta \rangle}{E_{k\beta} - E_{a\beta} - \Delta E_{k \rightarrow a}^{\text{xc}}} \right]. \quad (\text{B.11}) \end{aligned}$$

Here the sums are over the occupied orbitals k , which are denoted $|k\alpha\rangle$ and $|k\beta\rangle$ for α and β electrons, and over the virtual orbitals a , denoted $|a\alpha\rangle$ and $|a\beta\rangle$. These orbitals have energies $E_{k\alpha}$, $E_{k\beta}$, $E_{a\alpha}$, and $E_{a\beta}$ respectively. The energy terms $\Delta E_{k \rightarrow a}^{\text{xc}}$ are the Malkin correction factors, which are used as semi-empirical scalings of the energy denominators when performing DFT [542]. The operator \hat{h}_u^{SO} denotes the spatial part of the SO coupling Hamiltonian in Equation B.7. We note that both the SO-I contributions to the hyperfine tensor are of order $O(\alpha^4)$, as expected, and that both have spherical rank contributions of 0, 1, and 2.

The contributions of the magnetic field to the orbital angular momenta are given by the terms containing the vector potential. These give one- and two-electron corrections to the hyperfine Hamiltonian, which are

collected together in $\hat{H}_{\text{SO}}^{(A)}$:

$$\hat{H}_{\text{SO}}^{(A)} = \frac{1}{4}\alpha^2 g_e \left[\sum_B Z_B \sum_i \hat{s}_i \cdot \frac{(\mathbf{r}_{iA} \cdot \mathbf{r}_{iB})\mathbf{1} - \mathbf{r}_{iA}\mathbf{r}_{iB}}{r_{iA}^3 r_{iB}^3} \cdot \hat{\mathbf{f}}^{(A)} - \sum_{i,j} (\hat{s}_i + 2\hat{s}_j) \cdot \frac{(\mathbf{r}_{iA} \cdot \mathbf{r}_{ij})\mathbf{1} - \mathbf{r}_{iA}\mathbf{r}_{ij}}{r_{iA}^3 r_{ij}^3} \cdot \hat{\mathbf{f}}^{(A)} \right] \quad (\text{B.12})$$

In the second-order perturbation expansion Equation B.12 gives a one-electron contribution $A_{uv}^{\text{SO-II}(1)}$ and a two-electron part $A_{uv}^{\text{SO-II}(2)}$. The former is given by

$$A_{uv}^{\text{SO-II}(1)} = \frac{1}{4}\alpha^4 g_e \gamma_I^{(A)} \frac{1}{2S} \sum_{\epsilon, \tau} P_{\epsilon\tau}^{\alpha-\beta} \left\langle \epsilon \left| \sum_B Z_B \frac{\delta_{uv}(\mathbf{r}_A \cdot \mathbf{r}_B) - r_{A,u}r_{B,v}}{r_{A'}^3 r_B^3} \right| \tau \right\rangle, \quad (\text{B.13})$$

and the latter is expected to be negligible within the validity of perturbation theory. We note that the SO-II contribution is of order $\mathcal{O}(\alpha^4)$, and has parts of spherical rank 0, 1, and 2.

The total SO coupling correction to the hyperfine coupling tensor is therefore the sum of the SO-I and SO-II parts:

$$\mathbf{A}^{\text{SO}} = \mathbf{A}^{\text{SO-I}(1)} + \mathbf{A}^{\text{SO-I}(2)} + \mathbf{A}^{\text{SO-II}(1)}, \quad (\text{B.14})$$

which we normally formulate in the following way to aid comparison with experiment:

$$\mathbf{A}^{\text{SO}} = A^{\text{FC},2} \mathbf{1} + \mathbf{A}^{\text{SD},2} + \mathbf{A}^{\text{as}}. \quad (\text{B.15})$$

Appendix C

The Pennanen–Vaara formalism for the paramagnetic shift

We now describe the Pennanen–Vaara theory for the paramagnetic chemical shift [39], which is an important recent contribution to the description of the chemical shifts of systems with SO coupling and an arbitrary electronic spin multiplicity $2S + 1$, that can be readily applied to ab initio calculations. The initial part of the derivation gives an exact expression for the chemical shielding, is valid for an arbitrary electronic spin S under high-temperature conditions, and makes no assumptions about the relative orientations of the tensors in the EPR Hamiltonian. Following this derivation, a number of assumptions are applied in order to make further progress. These assumptions are (i) that the effective electronic spin S is equal to the real spin of the ion, (ii) that the SO coupling is weak in comparison to the ligand-field interaction, (iii) that the spin system can be described by the EPR Hamiltonian in Equation 4.36, and (iv) that we need only consider contributions from the ground state spin manifold, i.e. there are no thermally-accessible excited states. Assumption (iii) effectively means that the final expression is only exact for electronic spins up to $S = 1$ and is only an approximation for larger spins, and all three assumptions limit the theory to the application to $3d$ metal ions. Nevertheless the theory has been applied successfully to $3d$ complexes with $S > 1$ [543].

We start by noting that we can model the spin system as a cloud of electrons which establish a thermal equilibrium over their states according to the Boltzmann distribution. The energies of these states are modified

by the presence of the external perturbations of the nuclear magnetic moment and the applied magnetic field, and so we can write the energy of state $|n\rangle$ E_n as a Taylor series in the components of $\hat{\mathbf{I}}$ and \mathbf{B}_0 :

$$E_n = E_n^{(0,0)} + \sum_{\alpha} E_n^{(\alpha,0)} B_{0,\alpha} + \sum_{\kappa} E_n^{(0,\kappa)} \hat{I}_{\kappa} + \sum_{\alpha,\kappa} E_n^{(\alpha,\kappa)} B_{0,\alpha} \hat{I}_{\kappa} + \frac{1}{2} \sum_{\alpha,\beta} E_n^{(\alpha\beta,0)} B_{0,\alpha} B_{0,\beta} + \dots \quad (\text{C.1})$$

In Equation C.1 $E_n^{(0,0)}$ is the part of the energy that is independent of \mathbf{B}_0 and $\hat{\mathbf{I}}$, and the coefficients $E_n^{(\alpha\beta\dots\kappa\lambda\dots)}$ are given by

$$E_n^{(\alpha\beta\dots\kappa\lambda\dots)} = \left(\frac{\partial^N E_n}{\partial B_{0,\alpha} \partial B_{0,\beta} \dots \partial \hat{I}_{\kappa} \partial \hat{I}_{\lambda}} \right)_{\mathbf{B}_0=0, \hat{\mathbf{I}}=0}, \quad (\text{C.2})$$

where N is the total number of times that E_n is differentiated. Therefore the coefficients are calculated by differentiating E_n a certain number of times with respect to the components of the magnetic field and nuclear spin, and then setting those quantities equal to zero. The significance of the terms in the Taylor series can be appreciated by referring to the EPR Hamiltonian. For example the contribution $E_n^{(0,0)}$ can be related directly to the ZFS interaction, which is independent of both \mathbf{B}_0 and $\hat{\mathbf{I}}$. The term $\sum_{\alpha} E_n^{(\alpha,0)} B_{0,\alpha}$ represents the energy contribution from the electronic Zeeman interaction as both elements are proportional to the components of the field and are independent of the nuclear spin. In addition the terms $\sum_{\kappa} E_n^{(0,\kappa)} \hat{I}_{\kappa}$ and $\sum_{\alpha,\kappa} E_n^{(\alpha,\kappa)} B_{0,\alpha} \hat{I}_{\kappa}$ originate from the hyperfine interaction, and the nuclear Zeeman and chemical shielding interactions respectively.

As we have already discussed, the electron relaxation in an open-shell (i.e. paramagnetic) system occurs on a timescale that is several orders of magnitude shorter than nuclear relaxation, and so at all relevant times the electron cloud is at thermal equilibrium, and the system is described by a Boltzmann distribution over the energy levels. Using this idea Moon and Patchkovskii stated that the chemical shielding can be determined from the part of the Boltzmann average of the energy that is linear in the applied field and the nuclear spin:

$$\hbar\gamma \sum_{ij} B_{0,i} \sigma_{ij} \hat{I}_j = \frac{\sum_n E_n \exp(-\beta W_n)}{\sum_n \exp(-\beta W_n)}, \quad (\text{C.3})$$

where $\beta = 1/kT$. Note that we distinguish between the energies that are averaged in the distribution E_n , and the energies that are used to compute the Boltzmann factors W_n . This is because the transitions that establish the thermal equilibrium of the electron cloud occur on a shorter timescale than those from which we acquire the NMR spectrum, and consequently we may omit all the terms from W_n that have a dependence on $\hat{\mathbf{I}}$. We

can therefore write W_n as a Taylor series in B_0 only:

$$W_n = W_n^{(0,0)} + \sum_{\alpha} W_n^{(\alpha,0)} B_{0,\alpha} + \frac{1}{2} \sum_{\alpha,\beta} W_n^{(\alpha\beta,0)} B_{0,\alpha} B_{0,\beta} + \dots, \quad (\text{C.4})$$

i.e. $W_n^{(\alpha,\dots,\kappa,\dots)} = 0$ for $\kappa \neq 0$. Because the ZFS is the largest term in the EPR Hamiltonian, by far the largest term in the expansion of W_n is $W_n^{(0,0)}$, and so we can write the exponential Boltzmann factors as

$$\begin{aligned} \exp(-\beta W_n) \approx \exp(-\beta W_n^{(0,0)}) & \left\{ 1 - \beta \left[\sum_{\alpha} W_n^{(\alpha,0)} B_{0,\alpha} + \frac{1}{2} \sum_{\alpha,\beta} W_n^{(\alpha\beta,0)} B_{0,\alpha} B_{0,\beta} + \dots \right] \right. \\ & \left. + \frac{\beta^2}{2} \left[\sum_{\alpha} W_n^{(\alpha,0)} B_{0,\alpha} + \dots \right]^2 + \dots \right\}. \end{aligned} \quad (\text{C.5})$$

Substituting the expansions for E_n and $\exp(-\beta W_n)$ into Equation C.3 and multiplying both sides by the denominator we obtain the following unwieldy expression:

$$\begin{aligned} & \hbar\gamma \sum_{ij} B_{0,i} \sigma_{ij} \hat{I}_j \sum_n \exp(-\beta W_n^{(0,0)}) \left\{ 1 - \beta \left[\sum_{\alpha} W_n^{(\alpha,0)} B_{0,\alpha} + \frac{1}{2} \sum_{\alpha,\beta} W_n^{(\alpha\beta,0)} B_{0,\alpha} B_{0,\beta} + \dots \right] \right. \\ & \left. + \frac{\beta^2}{2} \left[\sum_{\alpha} W_n^{(\alpha,0)} B_{0,\alpha} + \dots \right]^2 + \dots \right\} \\ = & \sum_n \left\{ E_n^{(0,0)} + \sum_{\alpha} E_n^{(\alpha,0)} B_{0,\alpha} + \sum_{\kappa} E_n^{(0,\kappa)} \hat{I}_{\kappa} + \sum_{\alpha,\kappa} E_n^{(\alpha,\kappa)} B_{0,\alpha} \hat{I}_{\kappa} + \frac{1}{2} \sum_{\alpha,\beta} E_n^{(\alpha\beta,0)} B_{0,\alpha} B_{0,\beta} + \dots \right\} \\ & \times \exp(-\beta W_n^{(0,0)}) \left\{ 1 - \beta \left[\sum_{\alpha} W_n^{(\alpha,0)} B_{0,\alpha} + \frac{1}{2} \sum_{\alpha,\beta} W_n^{(\alpha\beta,0)} B_{0,\alpha} B_{0,\beta} + \dots \right] \right. \\ & \left. + \frac{\beta^2}{2} \left[\sum_{\alpha} W_n^{(\alpha,0)} B_{0,\alpha} + \dots \right]^2 + \dots \right\}. \end{aligned} \quad (\text{C.6})$$

We obtain the expression for the chemical shielding by collecting terms of the same order in $B_{0,i}$ and \hat{I}_j . This gives

$$\sigma_{ij} = \frac{1}{\hbar\gamma} \frac{1}{Q_0} \sum_n \exp(-\beta W_n^{(0,0)}) \{ E_n^{(i,j)} - \beta W_n^{(i,0)} E_n^{(0,j)} \} \quad (\text{C.7})$$

$$= \frac{1}{\hbar\gamma} \left\{ \langle \hat{E}^{(i,j)} \rangle_0 - \beta \langle \hat{W}^{(i,0)} \hat{E}^{(0,j)} \rangle_0 \right\}, \quad (\text{C.8})$$

where Q_0 is the partition function at zero field and nuclear magnetic moment,

$$Q_0 = \sum_n \exp(-\beta W_n^{(0,0)}), \quad (\text{C.9})$$

\hat{E} and \hat{W} represent the Hamiltonian including and excluding terms depending on the nuclear magnetic moment respectively, and the notation $\langle \hat{U} \rangle_0$ refers to a Boltzmann average of the expectation value of the operator \hat{U} carried out at zero field and nuclear magnetic moment:

$$\langle \hat{U} \rangle_0 = \frac{\text{Tr} [\exp(-\beta \hat{W}^{(0,0)}) \hat{U}]}{Q_0}. \quad (\text{C.10})$$

So far this expression is exact, but unhelpful. In order to gain more insight into the factors affecting the chemical shielding we must now make the approximations (i)–(iv) above. The discrimination between \hat{E} and \hat{W} is no longer needed, having served its purpose, and we can associate both with the EPR Hamiltonian in Equation 4.36. The derivatives are given by

$$\hat{E}^{(i,j)} = -\hbar\gamma(\delta_{ij} - \sigma_{ij}^{\text{orb}}) \hat{I}, \quad (\text{C.11})$$

$$\hat{W}^{(i,0)} = \mu_B \sum_k g_{ik} \hat{S}_k, \quad (\text{C.12})$$

$$\hat{E}^{(0,j)} = \sum_l \hat{S}_l A_{lj}. \quad (\text{C.13})$$

Substituting these into the expression for σ_{ij} in Equation C.8 we obtain the Pennanen–Vaara formula for the chemical shielding:

$$\sigma_{ij} = \sigma_{ij}^{\text{orb}} - \frac{\mu_B}{\hbar\gamma kT} \sum_{kl} g_{ik} \langle \hat{S}_k \hat{S}_l \rangle_0 A_{lj}, \quad (\text{C.14})$$

which can be written as

$$\boldsymbol{\sigma} = \boldsymbol{\sigma}^{\text{orb}} - \frac{\mu_B}{\hbar\gamma kT} \mathbf{g} \cdot \langle \hat{\mathbf{S}} \hat{\mathbf{S}} \rangle_0 \cdot \mathbf{A}. \quad (\text{C.15})$$

The chemical shielding is the sum of the temperature-independent orbital shielding and the temperature-dependent paramagnetic shielding, which is given by

$$\boldsymbol{\sigma}^{\text{S}} = -\frac{\mu_B}{\hbar\gamma kT} \mathbf{g} \cdot \langle \hat{\mathbf{S}} \hat{\mathbf{S}} \rangle_0 \cdot \mathbf{A}. \quad (\text{C.16})$$

Equation C.16 is the main result of the Pennanen–Vaara theory, in which the paramagnetic shielding tensor is the product of three matrices, namely the g -tensor, hyperfine tensor, and the dyadic $\langle \hat{S}\hat{S} \rangle_0$. The information from the g - and hyperfine tensors is encoded directly, in an analogous way to that for the shielding for spin-only systems we obtained in chapter 3. This is because the g -tensor originates from the electronic Zeeman interaction, which is proportional to the applied field, and the hyperfine interaction is proportional to the nuclear spin. The ZFS tensor does not enter the expression directly, because it has no *direct* effect on the way the electron cloud is modified by the presence of the magnetic field or nuclear spins, but it is present indirectly in the Boltzmann average because it is responsible for the splittings of the energy levels at zero field and zero nuclear magnetic moment. The dyadic tensor $\langle \hat{S}\hat{S} \rangle_0$ comprises both an isotropic part and a symmetric anisotropy, but no antisymmetric part. It is worth noting that the PAF of $\langle \hat{S}\hat{S} \rangle_0$ coincides with the PAF of the ZFS tensor.

One consequence of the splitting of the electronic energy levels at zero field is to introduce a strong non-Curie temperature dependence in the shielding tensor. This is more easily appreciated by expanding the dyadic $\langle \hat{S}\hat{S} \rangle_0$ as a Taylor series in $\beta = 1/kT$:

$$\langle \hat{S}_i \hat{S}_j \rangle_0 = \frac{1}{2S+1} \text{Tr} \left[\hat{S}_i \hat{S}_j \left(1 - \beta \sum_{kl} \hat{S}_k D_{kl} \hat{S}_l \right) \right] + O(\beta^2) \quad (\text{C.17})$$

$$= \frac{1}{2S+1} \sum_n \langle n | \hat{S}_i \hat{S}_j | n \rangle - \frac{\beta}{2S+1} \sum_{kl} D_{kl} \sum_n \langle n | \hat{S}_i \hat{S}_j \hat{S}_k \hat{S}_l | n \rangle + O(\beta^2). \quad (\text{C.18})$$

The first-order term is simply [183]

$$\frac{S(S+1)}{3} \delta_{ij}, \quad (\text{C.19})$$

which is the familiar factor we encountered for spin-only systems. The corresponding first-order term in the shielding tensor is therefore

$$\sigma^S = -\frac{\mu_B S(S+1)}{3\hbar\gamma kT} \mathbf{g} \cdot \mathbf{A}. \quad (\text{C.20})$$

Incidentally this is an exact expression for the shielding with zero ZFS, as was originally derived by Moon and Patchkovskii [38]. Furthermore, if we set the g -tensor equal to g_e , we obtain the spin-only expression in Equation 3.70. In the presence of the ZFS interaction the Boltzmann average at zero field and nuclear magnetic moment is computed with the states $|n\rangle$ that are equal to the eigenstates of the ZFS Hamiltonian,

which can be written as linear combinations of the eigenstates of the Zeeman Hamiltonian $|M_S\rangle$:

$$|n\rangle = \sum_{M_S} c_{M_S} |M_S\rangle. \quad (\text{C.21})$$

The second-order term is the dyadic is more complex, but can be shown after some tedious algebra to yield

$$-\frac{\beta}{2S+1} \sum_{kl} D_{kl} \sum_n \langle n | \hat{S}_i \hat{S}_j \hat{S}_k \hat{S}_l | n \rangle = -\frac{\beta}{30} D_{ij} S(S+1)(2S-1)(2S+3). \quad (\text{C.22})$$

Note that this term is equal to zero if $S < 1$, which is a condition for the absence of the ZFS interaction. The total paramagnetic shielding tensor up to second order in β is therefore

$$\sigma^S \approx -\frac{\mu_B S(S+1)}{3\hbar\gamma kT} \mathbf{g} \cdot \mathbf{A} + \frac{\mu_B S(S+1)(2S-1)(2S+3)}{30\hbar\gamma(kT)^2} \mathbf{g} \cdot \mathbf{D} \cdot \mathbf{A}, \quad (\text{C.23})$$

which is identical to the expression originally derived by Bleaney [61]. The deviation from the Curie behaviour can be clearly seen in the second term, which varies as $1/T^2$ and is of opposite sign to the first-order term.

Finally we note that, although we could not in general apply the high-field approximation to the EPR Hamiltonian because the ZFS may be the dominant interaction, we can apply it more safely for typical $3d$ transition-metal complexes as the interaction due to the shielding tensor σ^S is dominated by the nuclear Zeeman interaction.

C.0.1 The terms in the paramagnetic shift tensor

We can break down the expression for the paramagnetic shielding tensor in Equation C.16 into a sum of individual cross terms by substituting in the expressions for the g -tensor in Equations 4.37, 4.38, and 4.39, and the hyperfine tensor in Equations 4.40, 4.41, and 4.42. The resulting terms are listed in Table C.1, up to fourth order in the fine-structure constant $O(\alpha^4)$. Truncating at $O(\alpha^4)$ means that we retain only the terms that contain at most one SO coupling term in the product $\mathbf{g} \cdot \mathbf{A}$. For example term 1 $g_e A^{\text{FC}}$ is the product of two NR parts of the g - and hyperfine tensors g_e and A^{FC} which are $O(\alpha^0)$ and $O(\alpha^2)$ respectively, and so is $O(\alpha^2)$ overall, whereas term 3 $g_e A^{\text{FC},2}$ is the product of the NR part of \mathbf{g} with an SO part of \mathbf{A} , and so is $O(\alpha^4)$ overall. Terms containing the product of two SO terms, such as $\Delta\mathbf{g} \cdot \mathbf{A}^{\text{SD},2}$ are neglected. Also included

Term	Type	Order	Without ZFS		With ZFS	
			Expression	Spherical tensor rank	Expression	Spherical tensor rank
0	orb	$O(\alpha^2)$	σ^{orb}	0, 1, 2	σ^{orb}	0, 1, 2
1	con		$g_e A^{\text{FC}}$	0	$g_e A^{\text{FC}} \langle \hat{\mathbf{S}} \hat{\mathbf{S}} \rangle_0$	0, 2
2	dip		$g_e A^{\text{SD}}$	2	$g_e \langle \hat{\mathbf{S}} \hat{\mathbf{S}} \rangle_0 \cdot A^{\text{SD}}$	0, 1, 2
3	con	$O(\alpha^4)$	$g_e A^{\text{FC},2}$	0	$g_e A^{\text{FC},2} \langle \hat{\mathbf{S}} \hat{\mathbf{S}} \rangle_0$	0, 2
4	dip		$g_e A^{\text{SD},2}$	2	$g_e \langle \hat{\mathbf{S}} \hat{\mathbf{S}} \rangle_0 \cdot A^{\text{SD},2}$	0, 1, 2
5	as		$g_e A^{\text{as}}$	1	$g_e \langle \hat{\mathbf{S}} \hat{\mathbf{S}} \rangle_0 \cdot A^{\text{as}}$	1, 2
6	con		$\Delta g_{\text{iso}} A^{\text{FC}}$	0	$\Delta g_{\text{iso}} A^{\text{FC}} \langle \hat{\mathbf{S}} \hat{\mathbf{S}} \rangle_0$	0, 2
7	dip		$\Delta g_{\text{iso}} A^{\text{SD}}$	2	$\Delta g_{\text{iso}} \langle \hat{\mathbf{S}} \hat{\mathbf{S}} \rangle_0 \cdot A^{\text{SD}}$	0, 1, 2
8	con		$A^{\text{FC}} \Delta \mathbf{g}$	1, 2	$A^{\text{FC}} \Delta \mathbf{g} \cdot \langle \hat{\mathbf{S}} \hat{\mathbf{S}} \rangle_0$	0, 1, 2
9	dip		$\Delta \mathbf{g} \cdot A^{\text{SD}}$	0, 1, 2	$\Delta \mathbf{g} \cdot \langle \hat{\mathbf{S}} \hat{\mathbf{S}} \rangle_0 \cdot A^{\text{SD}}$	0, 1, 2

Table C.1: List of the terms arising in the Pennanen–Vaara expression for the paramagnetic shielding. The terms are numbered 1–9, with their assigned terms (‘orb’ (orbital), ‘con’ (contact), ‘dip’ (dipolar), and ‘as’ (antisymmetric)) and the irreducible spherical tensor ranks with and without the ZFS. Adapted from Pennanen and Vaara [39].

in Table C.1 is an assignment of the nine paramagnetic terms according to the form of hyperfine interaction from which they originate, i.e. a contact (con), dipolar (dip), or antisymmetric (as) term. This distinction is extremely important in the interpretation of paramagnetic shifts in terms of the structural and electronic properties of the system, the contact terms providing information about through-bond transfer of unpaired electron density into the nuclear s -orbitals, and the dipolar terms providing information about the positions of metal ions with respect to the nucleus.

Appendix D

Derivation of the paramagnetic shielding tensor for arbitrary spin multiplicity to second order

This appendix details the calculation of the paramagnetic chemical shielding tensor up to second order in $1/(kT)$ in terms of the tensor parameters in the EPR Hamiltonian generalised for arbitrary spin multiplicity, starting from both the Pennanen–Vaara and van den Heuvel–Soncini formulae. The Pennanen–Vaara expression in terms of the electron magnetic moment $\hat{\boldsymbol{m}}$ and hyperfine field $\hat{\mathcal{F}}$ operators can be expanded to second order to give:

$$\sigma_{ij}^S = \frac{\beta}{\hbar\gamma_I} \langle \hat{m}_i \hat{\mathcal{F}}_j \rangle_0 \quad (\text{D.1})$$

$$= \frac{1}{\hbar\gamma_I} \left[\beta \frac{\text{Tr}_S (\hat{m}_i \hat{\mathcal{F}}_j)}{2S + 1} - \beta^2 \frac{\text{Tr}_S (\hat{m}_i \hat{\mathcal{F}}_j \hat{H}_0)}{2S + 1} \right] + O(\beta^3). \quad (\text{D.2})$$

We denote the trace of a product operator over the entire direct product spin space as Tr_S , and the trace of a one-spin operator over the manifold of states pertaining to that spin simply as Tr . Substituting in the

expressions for \hat{m} , $\hat{\mathcal{F}}$, and \hat{H}_0 gives the following expression

$$\begin{aligned} \sigma_{ij}^S = & -\frac{\mu_B}{\hbar\gamma_I} \left[\frac{\beta}{2S+1} \sum_{kk'qq'} (-1)^{q+q'} g_{kq,i} A_{k'q',j} \text{Tr}_S (\hat{S}_{k-q} \hat{S}_{k'-q'}) \right. \\ & \left. - \frac{\beta^2}{2S+1} \sum_{kk'k''qq'q''} (-1)^{q+q'+q''} g_{kq,i} A_{k'q',j} D_{k''q''} \text{Tr}_S (\hat{S}_{k-q} \hat{S}_{k'-q'} \hat{S}_{k''-q''}) \right] + \mathcal{O}(\beta^3), \end{aligned} \quad (\text{D.3})$$

where the first-order shielding contains terms that are proportional to the trace of the product of two irreducible spherical tensor spin operators, and the second-order shielding contains terms proportional to the trace of the product of three such operators.

The van den Heuvel–Soncini expression, when expanded to second-order in $1/(kT)$, is equal to

$$\sigma_{ij}^S = \frac{1}{\hbar\gamma_I} \left\langle \int_0^\beta dw \exp(w\hat{H}_0) \hat{m}_i \exp(-w\hat{H}_0) \hat{\mathcal{F}}_j \right\rangle \quad (\text{D.4})$$

$$= \frac{1}{\hbar\gamma_I} \left[\beta \frac{\text{Tr}_S (\hat{m}_i \hat{\mathcal{F}}_j)}{2S+1} - \beta^2 \frac{\text{Tr}_S (\hat{m}_i \hat{\mathcal{F}}_j \hat{H}_0)}{2S+1} + \frac{\beta^2}{2} \frac{\text{Tr}_S ([\hat{m}_i, \hat{\mathcal{F}}_j] \hat{H}_0)}{2S+1} \right] + \mathcal{O}(\beta^3), \quad (\text{D.5})$$

which is equal to the Pennanen–Vaara expression with the addition of a second-order term that depends on the trace $\text{Tr}_S ([\hat{m}_i, \hat{\mathcal{F}}_j] \hat{H}_0)$. Substituting in the EPR tensor parameters results in the following expression:

$$\begin{aligned} \sigma_{ij}^S = & -\frac{\mu_B}{\hbar\gamma_I} \left[\frac{\beta}{2S+1} \sum_{kk'qq'} (-1)^{q+q'} g_{kq,i} A_{k'q',j} \text{Tr}_S (\hat{S}_{k-q} \hat{S}_{k'-q'}) \right. \\ & - \frac{\beta^2}{2S+1} \sum_{kk'k''qq'q''} (-1)^{q+q'+q''} g_{kq,i} A_{k'q',j} D_{k''q''} \text{Tr}_S (\hat{S}_{k-q} \hat{S}_{k'-q'} \hat{S}_{k''-q''}) \\ & \left. + \frac{\beta^2}{2(2S+1)} \sum_{kk'k''qq'q''} (-1)^{q+q'+q''} g_{kq,i} A_{k'q',j} D_{k''q''} \text{Tr}_S ([\hat{S}_{k-q}, \hat{S}_{k'-q'}] \hat{S}_{k''-q''}) \right] + \mathcal{O}(\beta^3). \end{aligned} \quad (\text{D.6})$$

Both expressions are the same to first order in $1/(kT)$, and can be computed by calculating the trace of $\hat{S}_{k-q} \hat{S}_{k'-q'}$. This can be done easily by using the Wigner–Eckart theorem for the matrix elements of irreducible

spherical tensor operators [190]. The trace is therefore

$$\text{Tr}_S (\hat{S}_{k-q} \hat{S}_{k'-q'}) = \sum_{MM'} \langle S M | \hat{S}_{k-q} | S M' \rangle \langle S M' | \hat{S}_{k'-q'} | S M \rangle \quad (\text{D.7})$$

$$\begin{aligned} &= (-1)^{k+k'} (2S+1) \langle S || \hat{S}_k || S \rangle \langle S || \hat{S}_{k'} || S \rangle \\ &\quad \times \sum_{MM'} (-1)^{2S+M+M'} \begin{pmatrix} S & S & k \\ -M & M' & -q \end{pmatrix} \begin{pmatrix} S & S & k' \\ -M & M' & q' \end{pmatrix} \end{aligned} \quad (\text{D.8})$$

where the arrays in parentheses are Wigner 3j symbols. We have written the product of the phase factors from the two matrix elements as $(-1)^{S+k+M}(-1)^{S+k'+M'} = (-1)^{2S+k+k'+M+M'}$. We could equally well have written it as $(-1)^{S+k+M}(-1)^{-S-k'-M'} = (-1)^{k-k'+M-M'}$, and then simplified by noting that, from the symmetry of the first Wigner 3j symbol, the only non-zero terms in the sum satisfy $M - M' = -q$. The final phase factor is therefore $(-1)^{k-k'-q}$. The expression can now be simplified by using the orthogonality properties of the 3j symbols, and we obtain:

$$\text{Tr}_S (\hat{S}_{k-q} \hat{S}_{k'-q'}) = (-1)^{k-k'-q} (2S+1) \langle S || \hat{S}_k || S \rangle \langle S || \hat{S}_{k'} || S \rangle \sum_{MM'} \begin{pmatrix} S & S & k \\ -M & M' & -q \end{pmatrix} \begin{pmatrix} S & S & k' \\ -M & M' & q' \end{pmatrix} \quad (\text{D.9})$$

$$= (-1)^q \left(\frac{2S+1}{2k+1} \right) \langle S || \hat{S}_k || S \rangle^2 \delta_{kk'} \delta_{q-q'}. \quad (\text{D.10})$$

The operators \hat{S}_{k-q} therefore form an orthogonal basis set. The resulting expression can now be used to give the first-order paramagnetic chemical shielding, which is the same for both the Pennanen–Vaara and van den Heuvel–Soncini formalisms, and is given in Equation 6.27.

The second-order shielding tensor in both formalisms contains a trace of the product of three irreducible

spherical tensor spin operators. This trace can also be computed using the Wigner–Eckart theorem:

$$\begin{aligned}
\text{Tr}_S (\hat{S}_{k-q} \hat{S}_{k'-q'} \hat{S}_{k''-q''}) &= \sum_{MM'M''} \langle SM | \hat{S}_{k-q} | SM' \rangle \langle SM' | \hat{S}_{k'-q'} | SM'' \rangle \langle SM'' | \hat{S}_{k''-q''} | SM \rangle \\
&= (-1)^{k+k'+k''} (2S+1)^{3/2} \langle S || \hat{S}_k || S \rangle \langle S || \hat{S}_{k'} || S \rangle \langle S || \hat{S}_{k''} || S \rangle \\
&\quad \times \sum_{MM'M''} (-1)^{3S+M+M'+M''} \begin{pmatrix} S & S & k \\ -M & M' & -q \end{pmatrix} \begin{pmatrix} S & S & k' \\ -M' & M'' & -q' \end{pmatrix} \begin{pmatrix} S & S & k'' \\ -M'' & M & -q'' \end{pmatrix} \\
&= (-1)^{k+k'+k''} (-1)^{2S} (2S+1)^{3/2} \langle S || \hat{S}_k || S \rangle \langle S || \hat{S}_{k'} || S \rangle \langle S || \hat{S}_{k''} || S \rangle \\
&\quad \times \begin{pmatrix} k' & k'' & k \\ S & S & S \end{pmatrix} \begin{pmatrix} k' & k'' & k \\ -q' & -q'' & -q \end{pmatrix}. \tag{D.11}
\end{aligned}$$

To go to the last line, we have used the fact that the sum of the product of three $3j$ symbols is equal to the product of a Wigner $6j$ symbol (the array in braces) and a $3j$ symbol. The computation of this trace completes the expansion of the Pennanen–Vaara expression to $1/(kT)^2$.

All that remains is to evaluate the final term in the van den Heuvel–Soncini formula, which depends on the following trace:

$$\text{Tr}_S \left(\left[\hat{S}_{k-q}, \hat{S}_{k'-q'} \right] \hat{S}_{k''-q''} \right) = \text{Tr}_S \left(\hat{S}_{k-q} \hat{S}_{k'-q'} \hat{S}_{k''-q''} \right) - \text{Tr}_S \left(\hat{S}_{k'-q'} \hat{S}_{k-q} \hat{S}_{k''-q''} \right). \tag{D.12}$$

We have already computed the first term on the right-hand side of Equation D.12, and the second term is easily deduced by swapping the indices kq and $k'q'$. This is done simply by swapping the first and second columns in each of the $3j$ and $6j$ symbols in Equation D.11; the former acquires a phase factor of $(-1)^{k+k'+k''}$ under such an operation, whilst the latter is invariant. We therefore obtain

$$\text{Tr}_S \left(\hat{S}_{k'-q'} \hat{S}_{k-q} \hat{S}_{k''-q''} \right) = (-1)^{k+k'+k''} \text{Tr}_S \left(\hat{S}_{k-q} \hat{S}_{k'-q'} \hat{S}_{k''-q''} \right). \tag{D.13}$$

We have seen that, in order to satisfy the constraints of time reversal of the Hamiltonian, the spin operators in both the Zeeman and hyperfine terms must be of odd rank, i.e. k and k' must be odd, and the ZFS spin operators must be of even rank, i.e. k'' must be even. Therefore $k + k' + k''$ is an even number, and the trace

in Equation D.12 must be zero:

$$\text{Tr}_S \left(\left[\hat{S}_{k-q}, \hat{S}_{k'-q'} \right] \hat{S}_{k''-q''} \right) = 0. \quad (\text{D.14})$$

The Pennanen–Vaara and van den Heuvel–Soncini formalisms therefore give the same result to $1/(kT)^2$. The full second-order term is given in Equation 6.28.

Appendix E

Derivation of the paramagnetic shielding tensor for a system containing multiple, coupled paramagnetic centres of arbitrary spin multiplicity to second order

In this appendix we give the detailed calculation of the paramagnetic shielding tensor of a nucleus due to its hyperfine coupling with a cluster of interacting transition-metal ions, to second order in $1/(kT)^2$. The final result leads directly to Equation 7.53 in chapter 7.

As shown in appendix D the general van den Heuvel–Soncini formula of the paramagnetic shielding tensor to $O(\beta^2)$ is

$$\sigma_{ij}^S = \frac{1}{\hbar\gamma_I} \left[\beta \frac{\text{Tr}_S(\hat{m}_i \hat{\mathcal{F}}_j)}{\omega} - \beta^2 \frac{\text{Tr}_S(\hat{m}_i \hat{\mathcal{F}}_j \hat{H}_0)}{\omega} + \frac{\beta^2}{2} \frac{\text{Tr}_S([\hat{m}_i, \hat{\mathcal{F}}_j] \hat{H}_0)}{\omega} \right] + O(\beta^3), \quad (\text{E.1})$$

where \hat{m} and $\hat{\mathcal{F}}$ are the total electronic magnetic moment and hyperfine field operators respectively, and \hat{H}_0 is the Hamiltonian in the absence of the external magnetic field and nuclear magnetic moments, and the cluster has a total of ω electronic spin states. The cluster comprises a set of transition-metal ions A with electronic spins $S^{(A)}$, and so the electronic magnetic moment and hyperfine field operators are each a sum of terms, one for each metal ion:

$$\hat{m}_i = -\mu_B \sum_A \sum_{kq} (-1)^q g_{kq,i}^{(A)} \hat{S}_{k-q}^{(A)}, \quad (\text{E.2})$$

$$\hat{\mathcal{F}}_i = \sum_A \sum_{kq} (-1)^q A_{kq,i}^{(A)} \hat{S}_{k-q}^{(A)}, \quad (\text{E.3})$$

where $g_{kq,i}^{(A)}$ and $A_{kq,i}^{(A)}$ are the g -tensor and hyperfine tensor components, and $\hat{S}_{kq}^{(A)}$ is the irreducible spherical tensor spin operator of rank k and order q for ion A . We recall that the irreducible spherical ranks of the tensors in Equations E.2 and E.3 must be odd. The expression for \hat{H}_0 contains a part due to the ZFS interactions of each ion, and a part due to the exchange coupling interactions for all pairs of ions:

$$\hat{H}_0 = \sum_A \sum_{kq} (-1)^q D_{kq}^{(A)} \hat{S}_{k-q}^{(A)} + \sum_{A>B} \sum_{kq} (-1)^q J_{kq}^{(AB)}(k_1 k_2) \hat{T}_{k-q}^{(AB)}(k_1 k_2). \quad (\text{E.4})$$

The irreducible spherical tensor components of rank k and order q of the ZFS interaction of ion A are $D_{kq}^{(A)}$, and the exchange coupling between ions A and B is represented by the spatial tensor $J_{kq}^{(AB)}(k_1 k_2)$, and the spin tensor $\hat{T}_{k-q}^{(AB)}(k_1 k_2)$ which is formed by coupling together the two one-spin tensor operators $\hat{S}_{k_1 q_1}^{(A)}$ and $\hat{S}_{k_2 q_2}^{(B)}$:

$$\hat{T}_{k-q}^{(AB)}(k_1 k_2) = \sum_{q_1, q_2} \hat{S}_{k_1 q_1}^{(A)} \hat{S}_{k_2 q_2}^{(B)} \langle k_1 k_2 q_1 q_2 | k - q \rangle \quad (\text{E.5})$$

$$= (-1)^{k_1 - k_2 - q} \sqrt{2k + 1} \sum_{q_1, q_2} \hat{S}_{k_1 q_1}^{(A)} \hat{S}_{k_2 q_2}^{(B)} \begin{pmatrix} k_1 & k_2 & k \\ q_1 & q_2 & q \end{pmatrix}. \quad (\text{E.6})$$

We note that the ZFS tensor contains only components of even rank, which for transition-metal ions can take at most only the values $k = 2$ and 4 , with the maximum value being $2S^{(A)}$. The conventional exchange coupling tensor that is formed by coupling together two rank-one spin operators can take overall ranks $k = 0, 1$, and 2 , which represent the isotropic exchange, antisymmetric DM, and symmetric dipolar-coupling interactions respectively. If the two spins are coupled together in the opposite order, so that (AB) is replaced

by (BA) , and (k_1, k_2) by (k_2, k_1) in Equation E.6, the resulting tensor $\hat{T}_{k-q}^{(BA)}(k_2 k_1)$ is given by

$$\hat{T}_{k-q}^{(BA)}(k_2 k_1) = (-1)^{k_1+k_2+k} \hat{T}_{k-q}^{(AB)}(k_1 k_2), \quad (\text{E.7})$$

i.e. it acquires a phase factor $(-1)^{k_1+k_2+k}$ due to the symmetry properties of the $3j$ symbol. Therefore in order to maintain the same Hamiltonian, the exchange tensor parameters must satisfy

$$J_{kq}^{(BA)}(k_2 k_1) = (-1)^{k_1+k_2+k} J_{kq}^{(AB)}(k_1 k_2). \quad (\text{E.8})$$

This implies that swapping the order of the coupled spins results in a sign change for the antisymmetric DM interaction, but not for the symmetric isotropic exchange, nor the dipolar coupling interactions.

The spin operators used in the Hamiltonian are ‘product operators’ that are defined in a direct product space. Hence for example the notations $\hat{S}_{kq}^{(A)}$ and $\hat{S}_{kq}^{(A)} \hat{S}_{k'q'}^{(B)}$ are shorthand for the following direct products:

$$\hat{S}_{kq}^{(A)} \equiv \hat{S}_{kq}^{(A)} \otimes \hat{S}_{00}^{(B)} \otimes \hat{S}_{00}^{(\Gamma)} \otimes \dots, \quad (\text{E.9})$$

$$\hat{S}_{kq}^{(A)} \hat{S}_{k'q'}^{(B)} \equiv \hat{S}_{kq}^{(A)} \otimes \hat{S}_{k'q'}^{(B)} \otimes \hat{S}_{00}^{(\Gamma)} \otimes \dots, \quad (\text{E.10})$$

where $\hat{S}_{00}^{(A)}$ is the irreducible spherical tensor spin operator that is equal to the identity. The number of spin states ω in Equation E.1 is therefore given by the product of the numbers of states of each spin:

$$\omega = \prod_A (2S^{(A)} + 1). \quad (\text{E.11})$$

Using the aforementioned notation for the traces over the electronic spin states, i.e. that the trace of a product operator over the entire direct product spin space is denoted as Tr_S , and the trace of a one-spin operator over the manifold of states pertaining to that spin simply as Tr , we can write the traces Tr_S of the product operators $\hat{S}_{kq}^{(A)}$ and $\hat{S}_{kq}^{(A)} \hat{S}_{k'q'}^{(B)}$ as the products of the one-spin traces Tr :

$$\text{Tr}_S \left(\hat{S}_{kq}^{(A)} \right) = \text{Tr} \left(\hat{S}_{kq}^{(A)} \right) \text{Tr} \left(\hat{S}_{00}^{(B)} \right) \text{Tr} \left(\hat{S}_{00}^{(\Gamma)} \right) \dots, \quad (\text{E.12})$$

$$\text{Tr}_S \left(\hat{S}_{kq}^{(A)} \hat{S}_{k'q'}^{(B)} \right) = \text{Tr} \left(\hat{S}_{kq}^{(A)} \right) \text{Tr} \left(\hat{S}_{k'q'}^{(B)} \right) \text{Tr} \left(\hat{S}_{00}^{(\Gamma)} \right) \dots \quad (\text{E.13})$$

Each one-spin trace $\text{Tr}(\hat{S}_{k-q})$ can be evaluated using the Wigner–Eckart theorem [190]:

$$\text{Tr}(\hat{S}_{k-q}) = \sum_M \langle S M | \hat{S}_{k-q} | S M \rangle \quad (\text{E.14})$$

$$= (-1)^k \langle S || \hat{S}_k || S \rangle \sqrt{2S+1} \sum_M (-1)^{S-M} \begin{pmatrix} S & S & k \\ -M & M & -q \end{pmatrix}. \quad (\text{E.15})$$

Using the orthogonality relations for the Wigner 3j symbols [190] we can simplify the sum to give the simple identity

$$\text{Tr}(\hat{S}_{k-q}) = \langle S || \hat{S}_0 || S \rangle (2S+1) \delta_{k0} \delta_{q0} \quad (\text{E.16})$$

$$= (2S+1) \delta_{k0} \delta_{q0}. \quad (\text{E.17})$$

The significance of this identity is that the trace of any one-spin irreducible spherical tensor operator \hat{S}_{k-q} is zero unless the rank k is zero.

The paramagnetic chemical shielding tensor due to a system of coupled transition-metal ions with arbitrary electronic spins is given by combining Equations E.1–E.6 to give

$$\begin{aligned} \sigma_{ij}^S = & -\frac{\mu_B}{\hbar\gamma_I} \left[\frac{\beta}{\omega} \sum_{A,B} \sum_{kk'qq'} (-1)^{q+q'} g_{kq,i}^{(A)} A_{k'q',j}^{(B)} \text{Tr}_S (\hat{S}_{k-q}^{(A)} \hat{S}_{k'-q'}^{(B)}) \right. \\ & - \frac{\beta^2}{\omega} \sum_{A,B,\Gamma} \sum_{kk'k''qq'q''} (-1)^{q+q'+q''} g_{kq,i}^{(A)} A_{k'q',j}^{(B)} D_{k''q''}^{(\Gamma)} \text{Tr}_S (\hat{S}_{k-q}^{(A)} \hat{S}_{k'-q'}^{(B)} \hat{S}_{k''-q''}^{(\Gamma)}) \\ & - \frac{\beta^2}{\omega} \sum_{A,B} \sum_{\Gamma>\Delta} \sum_{kk'k''qq'q''} \sum_{k_1,k_2} (-1)^{q+q'+q''} g_{kq,i}^{(A)} A_{k'q',j}^{(B)} J_{k''q''}^{(\Gamma\Delta)}(k_1k_2) \text{Tr}_S (\hat{S}_{k-q}^{(A)} \hat{S}_{k'-q'}^{(B)} \hat{T}_{k''-q''}^{(\Gamma\Delta)}(k_1k_2)) \\ & + \frac{\beta^2}{2\omega} \sum_{A,B,\Gamma} \sum_{kk'k''qq'q''} (-1)^{q+q'+q''} g_{kq,i}^{(A)} A_{k'q',j}^{(B)} D_{k''q''}^{(\Gamma)} \text{Tr}_S ([\hat{S}_{k-q}^{(A)}, \hat{S}_{k'-q'}^{(B)}] \hat{S}_{k''-q''}^{(\Gamma)}) \\ & \left. + \frac{\beta^2}{2\omega} \sum_{A,B} \sum_{\Gamma>\Delta} \sum_{kk'k''qq'q''} \sum_{k_1,k_2} (-1)^{q+q'+q''} g_{kq,i}^{(A)} A_{k'q',j}^{(B)} J_{k''q''}^{(\Gamma\Delta)}(k_1k_2) \text{Tr}_S ([\hat{S}_{k-q}^{(A)}, \hat{S}_{k'-q'}^{(B)}] \hat{T}_{k''-q''}^{(\Gamma\Delta)}(k_1k_2)) \right]. \end{aligned}$$

This expression contains five terms. The first is of order $O(\beta)$ and contains only the g - and hyperfine tensor components. The remaining terms are all of order $O(\beta^2)$, with the second and fourth terms originating from the ZFS interactions, and the third and fifth terms originating from the exchange-coupling interactions. We now evaluate all five terms, using the Wigner–Eckart theorem to simplify the traces.

For the first term we have two situations that must be considered separately: either $A = B$ or $A \neq B$. If we set $A = B$ the trace is

$$\text{Tr}_S \left(\hat{S}_{k-q}^{(A)} \hat{S}_{k'-q'}^{(A)} \right) = \text{Tr} \left(\hat{S}_{k-q}^{(A)} \hat{S}_{k'-q'}^{(A)} \right) \prod_{B \neq A} \text{Tr} \left(\hat{S}_{00}^{(B)} \right) \quad (\text{E.18})$$

$$= (-1)^q \left(\frac{2S^{(A)} + 1}{2k + 1} \right) \langle S^{(A)} \| \hat{S}_k^{(A)} \| S^{(A)} \rangle^2 \delta_{kk'} \delta_{q-q'} \left(\frac{\omega}{2S^{(A)} + 1} \right) \quad (\text{E.19})$$

$$= (-1)^q \left(\frac{\omega}{2k + 1} \right) \langle S^{(A)} \| \hat{S}_k^{(A)} \| S^{(A)} \rangle^2 \delta_{kk'} \delta_{q-q'}. \quad (\text{E.20})$$

On substituting this into the expression for the shielding tensor we obtain the first-order shift due to a cluster of non-interacting metal ions that is similar to the expression we derived in appendix D. If we instead set $A \neq B$ the trace becomes

$$\text{Tr}_S \left(\hat{S}_{k-q}^{(A)} \hat{S}_{k'-q'}^{(B)} \right) = \text{Tr} \left(\hat{S}_{k-q}^{(A)} \right) \text{Tr} \left(\hat{S}_{k'-q'}^{(B)} \right) \prod_{\Gamma \neq A, B} \text{Tr} \left(\hat{S}_{00}^{(\Gamma)} \right) \quad (\text{E.21})$$

$$= \omega \delta_{k0} \delta_{k'0} \delta_{q0} \delta_{q'0} \quad (\text{E.22})$$

$$= 0. \quad (\text{E.23})$$

This term is equal to zero as the one-spin irreducible spherical tensor operators do not have zero ranks.

The trace of the second term only has one non-zero contribution, which is with $A = B = \Gamma$. The trace is therefore equal to

$$\text{Tr}_S \left(\hat{S}_{k-q}^{(A)} \hat{S}_{k'-q'}^{(A)} \hat{S}_{k''-q''}^{(A)} \right) = \text{Tr} \left(\hat{S}_{k-q}^{(A)} \hat{S}_{k'-q'}^{(A)} \hat{S}_{k''-q''}^{(A)} \right) \prod_{B \neq A} \text{Tr} \left(\hat{S}_{00}^{(B)} \right) \quad (\text{E.24})$$

$$\begin{aligned} &= (-1)^{k+k'+k''} (-1)^{2S^{(A)}} (2S^{(A)} + 1)^{1/2} \omega \\ &\quad \times \langle S^{(A)} \| \hat{S}_k^{(A)} \| S^{(A)} \rangle \langle S^{(A)} \| \hat{S}_{k'}^{(A)} \| S^{(A)} \rangle \langle S^{(A)} \| \hat{S}_{k''}^{(A)} \| S^{(A)} \rangle \\ &\quad \times \begin{Bmatrix} k' & k'' & k \\ S^{(A)} & S^{(A)} & S^{(A)} \end{Bmatrix} \begin{Bmatrix} k' & k'' & k \\ -q' & -q'' & -q \end{Bmatrix}, \end{aligned} \quad (\text{E.25})$$

which is again reminiscent of the second-order expression we derived in appendix D.

We have not hitherto encountered the third term. Setting $A \neq B$, $\Gamma = A$, and $\Delta = B$: we obtain the

following result for the trace:

$$\begin{aligned}
\text{Tr}_S \left(\hat{S}_{k-q}^{(A)} \hat{S}_{k'-q'}^{(B)} \hat{T}_{k''-q''}^{(\Gamma\Delta)}(k_1 k_2) \right) &= (-1)^{k_1-k_2-q''} \sqrt{2k''+1} \sum_{q_1, q_2} \begin{pmatrix} k_1 & k_2 & k'' \\ -q_1 & -q_2 & q'' \end{pmatrix} \\
&\times \text{Tr} \left(\hat{S}_{k-q}^{(A)} \hat{S}_{k_1-q_1}^{(A)} \right) \text{Tr} \left(\hat{S}_{k'-q'}^{(B)} \hat{S}_{k_2-q_2}^{(B)} \right) \prod_{\Gamma \neq A, B} \text{Tr} \left(\hat{S}_{00}^{(\Gamma)} \right) \\
&= (-1)^{k_1-k_2-q''} \sqrt{2k''+1} \sum_{q_1, q_2} \begin{pmatrix} k_1 & k_2 & k'' \\ -q_1 & -q_2 & q'' \end{pmatrix} \\
&\times (-1)^q \left(\frac{2S^{(A)}+1}{2k+1} \right) \langle S^{(A)} \| \hat{S}_k^{(A)} \| S^{(A)} \rangle^2 \delta_{kk_1} \delta_{q-q_1} \\
&\times (-1)^{q'} \left(\frac{2S^{(B)}+1}{2k'+1} \right) \langle S^{(B)} \| \hat{S}_{k'}^{(B)} \| S^{(B)} \rangle^2 \delta_{k'k_2} \delta_{q'-q_2} \\
&\times \frac{\omega}{(2S^{(A)}+1)(2S^{(B)}+1)} \\
&= \omega (-1)^{k-k'+q+q'-q''} \sqrt{2k''+1} \frac{\langle S^{(A)} \| \hat{S}_k^{(A)} \| S^{(A)} \rangle^2 \langle S^{(B)} \| \hat{S}_{k'}^{(B)} \| S^{(B)} \rangle^2}{2k+1} \frac{1}{2k'+1} \\
&\times \begin{pmatrix} k & k' & k'' \\ q & q' & q'' \end{pmatrix} \delta_{kk_1} \delta_{k'k_2}. \tag{E.26}
\end{aligned}$$

Alternatively we can also set $A \neq B$, $\Gamma = B$, and $\Delta = A$ to obtain a similar result:

$$\begin{aligned}
\text{Tr}_S \left(\hat{S}_{k-q}^{(A)} \hat{S}_{k'-q'}^{(B)} \hat{T}_{k''-q''}^{(\Gamma\Delta)}(k_1 k_2) \right) &= \omega (-1)^{k''+q+q'-q''} \sqrt{2k''+1} \frac{\langle S^{(A)} \| \hat{S}_k^{(A)} \| S^{(A)} \rangle^2 \langle S^{(B)} \| \hat{S}_{k'}^{(B)} \| S^{(B)} \rangle^2}{2k+1} \frac{1}{2k'+1} \\
&\times \begin{pmatrix} k & k' & k'' \\ q & q' & q'' \end{pmatrix} \delta_{kk_2} \delta_{k'k_1}. \tag{E.27}
\end{aligned}$$

These are the only two non-zero contributions to the third term. In both we notice that (k, k', k'') must satisfy the triangle condition. We see that Equation E.27 is the same as Equation E.26 with an extra phase factor of $(-1)^{k+k'+k''}$ due to the acyclic permutation of the first and second columns of the Wigner $3j$ symbol. The ranks k and k' are odd, so that the electronic Zeeman and hyperfine interaction Hamiltonians satisfy the time-reversal requirements, and so the sign of Equation E.27 is only changed for the terms of the exchange interaction Hamiltonian that have odd rank k'' , i.e. for the antisymmetric DM term, but not the isotropic exchange nor the dipolar coupling interactions. Combining the two contributions gives the overall expression

for the third term:

$$\begin{aligned}
& -\beta^2 \sum_{kk'k''} \sum_{qq'q''} \sum_{k_1, k_2} \sqrt{2k''+1} \begin{pmatrix} k & k' & k'' \\ q & q' & q'' \end{pmatrix} \left[\sum_{A>B} (-1)^{k-k'} g_{kq,i}^{(A)} A_{k'q',j}^{(B)} J_{k''q''}^{(AB)}(k_1 k_2) \frac{\langle S^{(A)} \parallel \hat{S}_k^{(A)} \parallel S^{(A)} \rangle^2 \langle S^{(B)} \parallel \hat{S}_{k'}^{(B)} \parallel S^{(B)} \rangle^2}{2k+1} \right. \\
& \left. + \sum_{A<B} (-1)^{k''} g_{kq,i}^{(A)} A_{k'q',j}^{(B)} J_{k''q''}^{(BA)}(k_2 k_1) \frac{\langle S^{(A)} \parallel \hat{S}_k^{(A)} \parallel S^{(A)} \rangle^2 \langle S^{(B)} \parallel \hat{S}_{k'}^{(B)} \parallel S^{(B)} \rangle^2}{2k+1} \right] \quad (E.28)
\end{aligned}$$

$$\begin{aligned}
& = -\beta^2 \sum_{kk'k''} \sum_{qq'q''} \sum_{k_1, k_2} (-1)^{k-k'} \sqrt{2k''+1} \begin{pmatrix} k & k' & k'' \\ q & q' & q'' \end{pmatrix} \sum_{A, B \neq A} g_{kq,i}^{(A)} A_{k'q',j}^{(B)} J_{k''q''}^{(AB)}(k_1 k_2) \frac{\langle S^{(A)} \parallel \hat{S}_k^{(A)} \parallel S^{(A)} \rangle^2 \langle S^{(B)} \parallel \hat{S}_{k'}^{(B)} \parallel S^{(B)} \rangle^2}{2k+1} \quad (E.29)
\end{aligned}$$

To go to the last line we have used the symmetry property of the exchange coupling tensor parameters in Equation E.8.

To evaluate the fourth term we must calculate the following trace:

$$\text{Tr}_S \left(\left[\hat{S}_{k-q}^{(A)}, \hat{S}_{k'-q'}^{(B)} \right] \hat{S}_{k''-q''}^{(\Gamma)} \right) = \text{Tr}_S \left(\hat{S}_{k-q}^{(A)} \hat{S}_{k'-q'}^{(B)} \hat{S}_{k''-q''}^{(\Gamma)} \right) - \text{Tr}_S \left(\hat{S}_{k'-q'}^{(B)} \hat{S}_{k-q}^{(A)} \hat{S}_{k''-q''}^{(\Gamma)} \right), \quad (E.30)$$

where, as for term two, the only relevant contributions are those with $A = B = \Gamma$. We have already computed the first term on the right-hand side, and the second term is easily deduced by swapping the indices kq and $k'q'$. This is done simply by swapping the first and second columns of the $3j$ and $6j$ symbols; the former acquires a phase factor of $(-1)^{k+k'}$ under such an operation, whilst the latter is invariant. We therefore obtain

$$\text{Tr}_S \left(\hat{S}_{k'-q'}^{(A)} \hat{S}_{k-q}^{(A)} \hat{S}_{k''-q''}^{(A)} \right) = (-1)^{k+k'+k''} \text{Tr}_S \left(\hat{S}_{k-q}^{(A)} \hat{S}_{k'-q'}^{(A)} \hat{S}_{k''-q''}^{(A)} \right). \quad (E.31)$$

We have seen that, in order to satisfy the constraints of time reversal of the Hamiltonian, the spin operators in both the Zeeman and hyperfine terms must be of odd rank, i.e. k and k' must be odd, and the ZFS spin operators must be of even rank, i.e. k'' must be even. Therefore $k + k' + k''$ is an even number, and the trace must be zero:

$$\text{Tr}_S \left(\left[\hat{S}_{k-q}^{(A)}, \hat{S}_{k'-q'}^{(B)} \right] \hat{S}_{k''-q''}^{(\Gamma)} \right) = 0. \quad (E.32)$$

There is therefore no contribution from the fourth term, and the second-order shift due to the ZFS interaction is contained wholly in the second term.

The fifth term contains the trace

$$\text{Tr}_S \left(\left[\hat{S}_{k-q}^{(A)}, \hat{S}_{k'-q'}^{(B)} \right] \hat{T}_{k'-q'}^{(\Gamma\Delta)}(k_1 k_2) \right). \quad (\text{E.33})$$

As we have seen for the third term, the only contributions that appear are with $A \neq B$, and so must also have $\Gamma = A$ and $\Delta = B$, or $\Gamma = B$ and $\Delta = A$. The commutator $\left[\hat{S}_{k-q}^{(A)}, \hat{S}_{k'-q'}^{(B)} \right]$ is therefore of two operators that act on different spins, and so is always zero. Hence the fifth term is trivially zero, and the effects of the exchange coupling are contained wholly in the third term.

Appendix F

Simplification of the relaxation superoperator and spectral densities in the stochastic Liouville formalism

In this appendix we provide the full derivation of two particular features of the stochastic Liouville formalism that were stated in section 9.3.1, namely the inclusion of the equilibrium nuclear-spin density operator in the expression for the relaxation superoperator, and an important symmetry property of the spectral density. The discussion closely follows that provided by Goldman [253].

F.1 The relaxation superoperator

Here we show that the expression for the Stochastic Liouville equation in section 9.3.1

$$\begin{aligned}
\frac{d\hat{\rho}^T(t)}{dt} &= -\frac{1}{\hbar^2} \sum_{m,m'} (-1)^{m+m'} \exp[i(\omega_{-m'} - \omega_{-m})t] \\
&\quad \times \int_0^\infty \left[[\hat{I}_{1-m'}, [\hat{I}_{1-m}^\dagger, \hat{\rho}^T(t)]] \text{Tr}_L \{ \hat{P}_0 \hat{L}_{1m}^T(t-\tau)^\dagger \hat{L}_{1m'}^T(t) \} \right. \\
&\quad \left. - [\hat{I}_{1-m'}, \hat{I}_{1-m}^\dagger \hat{\rho}^T(t)] \text{Tr}_L \{ [\hat{P}_0, \hat{L}_{1m}^T(t-\tau)^\dagger] \hat{L}_{1m'}^T(t) \} \right] \\
&\quad \times \exp(i\omega_{-m}\tau) d\tau,
\end{aligned} \tag{F.1}$$

can be simplified to the following

$$\begin{aligned}
\frac{d\hat{\rho}^T(t)}{dt} &= -\frac{1}{\hbar^2} \sum_{m,m'} (-1)^{m+m'} \exp[i(\omega_{-m'} - \omega_{-m})t] [\hat{I}_{1-m'}, [\hat{I}_{1-m}^\dagger, \hat{\rho}^T(t) - \hat{\rho}_0]] \\
&\quad \times \int_0^\infty \text{Tr}_L \{ \hat{P}_0 \hat{L}_{1m}^T(t-\tau)^\dagger \hat{L}_{1m'}^T(t) \} \exp(i\omega_{-m}\tau) d\tau,
\end{aligned} \tag{F.2}$$

which includes the expression $\hat{\rho}^T(t) - \hat{\rho}_0$ in the double commutator. Hence we justify the phenomenological inclusion of the equilibrium nuclear spin density operator in the semi-classical Redfield theory. In order to prove this correspondence, we need to show that the following expression in the second term of Equation F.1 can be simplified to give

$$\begin{aligned}
&[\hat{I}_{1-m'}, \hat{I}_{1-m}^\dagger \hat{\rho}^T(t)] \text{Tr}_L \{ [\hat{P}_0, \hat{L}_{1m}^T(t-\tau)^\dagger] \hat{L}_{1m'}^T(t) \} \exp(i\omega_{-m}\tau) \\
&= [\hat{I}_{1-m'}, [\hat{I}_{1-m}^\dagger, \hat{\rho}_0]] \text{Tr}_L \{ \hat{P}_0 \hat{L}_{1m}^T(t-\tau)^\dagger \hat{L}_{1m'}^T(t) \} \exp(i\omega_{-m}\tau).
\end{aligned} \tag{F.3}$$

Firstly we examine the factor that depends only on the lattice. We write the trace explicitly in terms of the sum over the lattice states $|L\rangle$, which are eigenstates of the lattice Hamiltonian \hat{H}_L with energies that are given by

$$E_L = \langle L | \hat{H}_L | L \rangle. \tag{F.4}$$

The matrix representation of the equilibrium lattice density operator is diagonal in this basis, and has the

following matrix elements:

$$\langle L | \hat{P}_0 | L \rangle = \frac{\exp(-\beta_L E_L)}{\text{Tr}_L [\exp(-\beta_L \hat{H}_L)]}. \quad (\text{F.5})$$

The trace over the lattice states is therefore equal to

$$\begin{aligned} \text{Tr}_L \left\{ \left[\hat{P}_0, \hat{L}_{1m}^T(t-\tau)^\dagger \right] \hat{L}_{1m'}^T(t) \right\} &= \sum_{LL'} \left[\langle L | \hat{P}_0 | L \rangle \langle L | \hat{L}_{1m}^T(t-\tau)^\dagger | L' \rangle \langle L' | \hat{L}_{1m'}^T(t) | L \rangle \right. \\ &\quad \left. - \langle L | \hat{L}_{1m}^T(t-\tau)^\dagger | L' \rangle \langle L' | \hat{P}_0 | L' \rangle \langle L' | \hat{L}_{1m'}^T(t) | L \rangle \right] \end{aligned} \quad (\text{F.6})$$

$$\begin{aligned} &= \sum_{LL'} \langle L | \hat{P}_0 | L \rangle \langle L | \hat{L}_{1m}^T(t-\tau)^\dagger | L' \rangle \langle L' | \hat{L}_{1m'}^T(t) | L \rangle \\ &\quad \times \left[1 - \frac{\langle L' | \hat{P}_0 | L' \rangle}{\langle L | \hat{P}_0 | L \rangle} \right] \end{aligned} \quad (\text{F.7})$$

$$\begin{aligned} &= \sum_{LL'} \langle L | \hat{P}_0 | L \rangle \langle L | \hat{L}_{1m}^T(t-\tau)^\dagger | L' \rangle \langle L' | \hat{L}_{1m'}^T(t) | L \rangle \\ &\quad \times [1 - \exp(\beta_L (E_L - E_{L'}))]. \end{aligned} \quad (\text{F.8})$$

To proceed further we note that Equation F.1 contains an integral over the time variable τ , which we now calculate. The dependence on τ is found in two factors, namely the complex exponential $\exp(i\omega_{-m}\tau)$, and the lattice operator $\hat{L}_{1m}^T(t-\tau)^\dagger$. The τ -dependence of the matrix element of the latter can be elucidated as follows:

$$\langle L | \hat{L}_{1m}^T(t-\tau)^\dagger | L' \rangle = \langle L | \exp(-i\hat{H}_L\tau/\hbar) \hat{L}_{1m}^T(t)^\dagger \exp(i\hat{H}_L\tau/\hbar) | L' \rangle \quad (\text{F.9})$$

$$= \langle L | \hat{L}_{1m}^T(t)^\dagger | L' \rangle \exp[i(\Omega_{L'} - \Omega_L)\tau], \quad (\text{F.10})$$

where $\Omega_L = E_L/\hbar$ is the angular frequency associated with the lattice energy E_L . The integral over τ is simply

$$\int_0^\infty \exp[i(\omega_{-m} + \Omega_{L'} - \Omega_L)\tau] d\tau = \pi \delta(\omega_{-m} + \Omega_{L'} - \Omega_L), \quad (\text{F.11})$$

where $\delta(\omega)$ is the Dirac delta function [189]. This integral is equal to zero unless $\omega_{-m} = \Omega_L - \Omega_{L'}$, and so we can immediately make the following replacement in Equation F.8:

$$\exp(\beta_L (E_L - E_{L'})) \rightarrow \exp(\beta_L \hbar \omega_{-m}). \quad (\text{F.12})$$

This Boltzmann factor is now independent of L and L' , and so the trace in Equation F.8 now simplifies to

$$\mathrm{Tr}_L \left\{ \left[\hat{P}_0, \hat{L}_{1m}^T(t - \tau)^\dagger \right] \hat{L}_{1m'}^T(t) \right\} \rightarrow \sum_{LL'} \langle L | \hat{P}_0 | L \rangle \langle L | \hat{L}_{1m}^T(t - \tau)^\dagger | L' \rangle \langle L' | \hat{L}_{1m'}^T(t) | L \rangle [1 - \exp(\beta_L \hbar \omega_{-m})] \quad (\text{F.13})$$

$$= \mathrm{Tr}_L \left\{ \hat{P}_0 \hat{L}_{1m}^T(t - \tau)^\dagger \hat{L}_{1m'}^T(t) \right\} [1 - \exp(\beta_L \hbar \omega_{-m})]. \quad (\text{F.14})$$

We can now partially simplify Equation F.3 by making the following replacement:

$$\begin{aligned} & \left[\hat{I}_{1-m'}, \hat{I}_{1-m}^\dagger \hat{\rho}^T(t) \right] \mathrm{Tr}_L \left\{ \left[\hat{P}_0, \hat{L}_{1m}^T(t - \tau)^\dagger \right] \hat{L}_{1m'}^T(t) \right\} \exp(i\omega_{-m}\tau) \\ \rightarrow & \left[\hat{I}_{1-m'}, \hat{I}_{1-m}^\dagger \hat{\rho}^T(t) \right] \mathrm{Tr}_L \left\{ \hat{P}_0 \hat{L}_{1m}^T(t - \tau)^\dagger \hat{L}_{1m'}^T(t) \right\} [1 - \exp(\beta_L \hbar \omega_{-m})] \exp(i\omega_{-m}\tau). \end{aligned} \quad (\text{F.15})$$

We see that the trace over the lattice operators has been written in the same format as in the right-hand side of Equation F.3.

In the second stage of the derivation we consider the nuclear-spin part of Equation F.3. We have already seen that the transformation of the spin operator \hat{I}_{1-m}^\dagger into the interaction representation is described by the following expression:

$$\hat{I}_{1-m}^\dagger(t - \tau)^\dagger = \hat{I}_{1-m}^\dagger \exp(-i\omega_{-m}(t - \tau)). \quad (\text{F.16})$$

The corresponding transformation of the matrix elements of \hat{I}_{1-m}^\dagger in the eigenbasis $|i\rangle$ of \hat{H}_I is

$$\langle i | \hat{I}_{1-m}^\dagger(t - \tau)^\dagger | j \rangle = \langle i | \exp(i\hat{H}_I(t - \tau)/\hbar) \hat{I}_{1-m}^\dagger(t - \tau)^\dagger \exp(-i\hat{H}_I(t - \tau)/\hbar) | j \rangle \quad (\text{F.17})$$

$$= \langle i | \hat{I}_{1-m}^\dagger(t - \tau)^\dagger | j \rangle \exp[-i(\omega_j - \omega_i)(t - \tau)], \quad (\text{F.18})$$

where ω_i is the angular frequency associated with the energy $\hbar\omega_i$ of state $|i\rangle$. On comparing Equations F.16 and F.18 we can write ω_{-m} as

$$\omega_{-m} = \omega_j - \omega_i. \quad (\text{F.19})$$

We now introduce the formal expression for the equilibrium nuclear-spin density operator:

$$\hat{\rho}_0 = \frac{\exp(-\beta_L \hat{H})}{\mathrm{Tr}_I [\exp(-\beta_L \hat{H})]}, \quad (\text{F.20})$$

where Tr_I is the trace taken over all the nuclear spin states. The Boltzmann factor in Equation F.15 can now be written as

$$1 - \exp(\beta_L \hbar \omega_{-m}) = 1 - \exp(\beta_L \hbar (\omega_j - \omega_i)) \quad (\text{F.21})$$

$$= 1 - \frac{\langle i | \hat{\rho}_0 | i \rangle}{\langle j | \hat{\rho}_0 | j \rangle} \quad (\text{F.22})$$

$$= \frac{\langle j | \hat{\rho}_0 | j \rangle - \langle i | \hat{\rho}_0 | i \rangle}{\langle j | \hat{\rho}_0 | j \rangle}. \quad (\text{F.23})$$

The product of the matrix element of $\hat{I}_{1-m}^\dagger \hat{\rho}^T(t)$ and the Boltzmann factor is therefore

$$\begin{aligned} \langle i | \hat{I}_{1-m}^\dagger | j \rangle \langle j | \hat{\rho}^T(t) | k \rangle [1 - \exp(\beta_L \hbar \omega_{-m})] &= \langle i | \hat{I}_{1-m}^\dagger | j \rangle \langle j | \hat{\rho}^T(t) | k \rangle \left[\frac{\langle j | \hat{\rho}_0 | j \rangle - \langle i | \hat{\rho}_0 | i \rangle}{\langle j | \hat{\rho}_0 | j \rangle} \right] \\ &= \langle i | \left[\hat{I}_{1-m}^\dagger, \hat{\rho}_0 \right] | j \rangle \langle j | \hat{\rho}_0 | j \rangle^{-1} \langle j | \hat{\rho}^T(t) | k \rangle. \end{aligned} \quad (\text{F.24})$$

Hence we make the following replacement in the nuclear-spin part of Equation F.15:

$$\left[\hat{I}_{1-m'}, \hat{I}_{1-m}^\dagger \hat{\rho}^T(t) \right] [1 - \exp(\beta_L \hbar \omega_{-m})] \rightarrow \left[\hat{I}_{1-m'}, \left[\hat{I}_{1-m}^\dagger, \hat{\rho}_0 \right] \hat{\rho}_0^{-1} \hat{\rho}^T(t) \right]. \quad (\text{F.25})$$

We are almost there. The final step is to apply the high-temperature limit to the nuclear-spin energy levels, and note that the nuclear-spin density operator at all times is equal to the sum of the identity operator and a small deviation with a leading term of order β_L . The result is that $\hat{\rho}_0^{-1} \hat{\rho}^T(t)$ approximates the identity operator $\hat{1}_I$, and we obtain

$$\left[\hat{I}_{1-m'}, \hat{I}_{1-m}^\dagger \hat{\rho}^T(t) \right] [1 - \exp(\beta_L \hbar \omega_{-m})] \rightarrow \left[\hat{I}_{1-m'}, \left[\hat{I}_{1-m}^\dagger, \hat{\rho}_0 \right] \right]. \quad (\text{F.26})$$

Substituting this into Equation F.15 we obtain Equation F.3, and therefore

$$\begin{aligned} \frac{d\hat{\rho}^T(t)}{dt} &= -\frac{1}{\hbar^2} \sum_{m,m'} (-1)^{m+m'} \exp[i(\omega_{-m'} - \omega_{-m})t] \left[\hat{I}_{1-m'}, \left[\hat{I}_{1-m}^\dagger, \hat{\rho}^T(t) - \hat{\rho}_0 \right] \right] \\ &\quad \times \int_0^\infty \text{Tr}_L \left\{ \hat{P}_0 \hat{L}_{1m}^T(t-\tau)^\dagger \hat{L}_{1m'}^T(t) \right\} \exp(i\omega_{-m}\tau) d\tau, \end{aligned} \quad (\text{F.27})$$

as required.

F.2 Symmetry properties of the spectral density

Here we derive a useful ‘symmetry-related’ identity concerning the spectral density $K_{mm'}(\omega)$, that is relevant to the application of the stochastic Liouville formalism for relaxation. We begin by writing the expression for the time-correlation function $G_{mm'}(\tau)$ in Equation 9.43 as a sum over the lattice states $|L\rangle$:

$$G_{mm'}(\tau) = \text{Tr}_L \left[\hat{L}_{1m}^\dagger \exp(i\hat{H}_L\tau/\hbar) \hat{L}_{1m'} \exp(-i\hat{H}_L\tau/\hbar) \hat{P}_0 \right] \quad (\text{F.28})$$

$$= \sum_{LL'} \langle L | \hat{L}_{1m}^\dagger | L' \rangle \langle L' | \hat{L}_{1m'} | L \rangle \langle L | \hat{P}_0 | L \rangle \exp[i(\Omega_{L'} - \Omega_L)\tau]. \quad (\text{F.29})$$

Using this in the expression for the real part of the spectral density in Equation 9.44 we obtain, for $\omega = -\omega_{-m}$:

$$\text{Re}[K_{mm'}(-\omega_{-m})] = \text{Re} \left[\int_0^\infty G_{mm'}(\tau) \exp(i\omega_{-m}\tau) d\tau \right] \quad (\text{F.30})$$

$$= \text{Re} \left[\sum_{LL'} \langle L | \hat{L}_{1m}^\dagger | L' \rangle \langle L' | \hat{L}_{1m'} | L \rangle \langle L | \hat{P}_0 | L \rangle \int_0^\infty \exp[i(\omega_{-m} + \Omega_{L'} - \Omega_L)\tau] d\tau \right] \quad (\text{F.31})$$

$$= \pi \text{Re} \sum_{LL'} \langle L | \hat{L}_{1m}^\dagger | L' \rangle \langle L' | \hat{L}_{1m'} | L \rangle \langle L | \hat{P}_0 | L \rangle \delta(\omega_{-m} + \Omega_{L'} - \Omega_L). \quad (\text{F.32})$$

We now write an expression for the time-correlation function $G_{-m'-m}(\tau)$:

$$G_{-m'-m}(\tau) = \text{Tr}_L \left[\hat{L}_{1-m'}^\dagger \exp(i\hat{H}_L\tau/\hbar) \hat{L}_{1-m} \exp(-i\hat{H}_L\tau/\hbar) \hat{P}_0 \right] \quad (\text{F.33})$$

$$= \sum_{LL'} \langle L' | \hat{L}_{1-m'}^\dagger | L \rangle \langle L | \hat{L}_{1-m} | L' \rangle \langle L' | \hat{P}_0 | L' \rangle \exp[-i(\Omega_{L'} - \Omega_L)\tau] \quad (\text{F.34})$$

$$= \sum_{LL'} \langle L | \hat{L}_{1-m} | L' \rangle \langle L' | \hat{L}_{1-m'}^\dagger | L \rangle \langle L' | \hat{P}_0 | L' \rangle \exp[-i(\Omega_{L'} - \Omega_L)\tau]. \quad (\text{F.35})$$

The lattice operators satisfy

$$\hat{L}_{1m}^\dagger = (-1)^m \hat{L}_{1-m}, \quad (\text{F.36})$$

and so the expression for $G_{-m'-m}(\tau)$ becomes

$$G_{-m'-m}(\tau) = (-1)^{m+m'} \sum_{LL'} \langle L | \hat{L}_{1m}^\dagger | L' \rangle \langle L' | \hat{L}_{1m'} | L \rangle \langle L' | \hat{P}_0 | L' \rangle \exp[-i(\Omega_{L'} - \Omega_L)\tau] \quad (\text{F.37})$$

$$= (-1)^{m+m'} \sum_{LL'} \langle L | \hat{L}_{1m}^\dagger | L' \rangle \langle L' | \hat{L}_{1m'} | L \rangle \langle L | \hat{P}_0 | L \rangle \exp[-i(\Omega_{L'} - \Omega_L)\tau] \left\{ \frac{\langle L' | \hat{P}_0 | L' \rangle}{\langle L | \hat{P}_0 | L \rangle} \right\} \quad (\text{F.38})$$

$$= (-1)^{m+m'} \sum_{LL'} \langle L | \hat{L}_{1m}^\dagger | L' \rangle \langle L' | \hat{L}_{1m'} | L \rangle \langle L | \hat{P}_0 | L \rangle \exp[-i(\Omega_{L'} - \Omega_L)\tau] \exp[\beta_L(E_L - E_{L'})]. \quad (\text{F.39})$$

This gives the following expression for the real part of the spectral density $K_{-m'-m}(+\omega_{-m})$:

$$\text{Re}[K_{-m'-m}(+\omega_{-m})] = \text{Re} \left[\int_0^\infty G_{-m'-m}(\tau) \exp(-i\omega_{-m}\tau) d\tau \right] \quad (\text{F.40})$$

$$= (-1)^{m+m'} \text{Re} \left[\sum_{LL'} \langle L | \hat{L}_{1m}^\dagger | L' \rangle \langle L' | \hat{L}_{1m'} | L \rangle \langle L | \hat{P}_0 | L \rangle \exp[\beta_L(E_L - E_{L'})] \right. \\ \left. \times \int_0^\infty \exp[-i(\omega_{-m} + \Omega_{L'} - \Omega_L)\tau] d\tau \right] \quad (\text{F.41})$$

$$= (-1)^{m+m'} \pi \text{Re} \sum_{LL'} \langle L | \hat{L}_{1m}^\dagger | L' \rangle \langle L' | \hat{L}_{1m'} | L \rangle \langle L | \hat{P}_0 | L \rangle \exp[\beta_L(E_L - E_{L'})] \\ \times \delta(\omega_{-m} + \Omega_{L'} - \Omega_L). \quad (\text{F.42})$$

The Dirac delta function on the last line indicates that $\omega_{-m} = \Omega_L - \Omega_{L'}$, and therefore the energy difference in the Boltzmann factor can be replaced by $E_L - E_{L'} = \hbar\omega_{-m}$. The final expression for $\text{Re}[K_{-m'-m}(+\omega_{-m})]$ is therefore

$$\text{Re}[K_{-m'-m}(+\omega_{-m})] = (-1)^{m+m'} \exp[\beta_L \hbar \omega_{-m}] \pi \text{Re} \sum_{LL'} \langle L | \hat{L}_{1m}^\dagger | L' \rangle \langle L' | \hat{L}_{1m'} | L \rangle \langle L | \hat{P}_0 | L \rangle \\ \times \delta(\omega_{-m} + \Omega_{L'} - \Omega_L). \quad (\text{F.43})$$

On comparing Equation F.43 with Equation F.32 we obtain the identity

$$\text{Re}[K_{-m'-m}(+\omega_{-m})] = (-1)^{m+m'} \exp[\beta_L \hbar \omega_{-m}] \text{Re}[K_{mm'}(-\omega_{-m})], \quad (\text{F.44})$$

i.e. the two spectral densities differ only by a sign and multiplicative Boltzmann factor. In the high-temperature limit, where $|\beta_L \hbar \omega_{-m}| \ll 1$, we can ignore the Boltzmann factor and the relationship between the two spectral densities simplifies to

$$\text{Re} [K_{-m'-m}(+\omega_{-m})] \approx (-1)^{m+m'} \text{Re} [K_{mm'}(-\omega_{-m})]. \quad (\text{F.45})$$

In the secular approximation the relevant terms in the relaxation superoperator have $m' = m$. The identity in Equation F.45 is then

$$\text{Re} [K_{-m-m}(+\omega_{-m})] \approx \text{Re} [K_{mm}(-\omega_{-m})]. \quad (\text{F.46})$$

Noting that $\omega_{-m} = -\omega_m$, we can write Equation F.46 in the following equivalent way:

$$\text{Re} [K_{-m-m}(-\omega_m)] \approx \text{Re} [K_{mm}(-\omega_{-m})]. \quad (\text{F.47})$$

Bibliography

- [1] M. H. Levitt. *Spin Dynamics*. Wiley and Sons, Ltd, Chichester, 2008.
- [2] L. Emsley and I. Bertini. Frontiers in solid-state NMR technology. *Acc. Chem. Res.*, 46:1912–1913, 2013.
- [3] H. Heise, F. H. Köhler, M. Herker, and W. Hiller. Inter- and intramolecular spin transfer in molecular magnetic materials. solid-state NMR spectroscopy of paramagnetic metallocenium ions. *J. Am. Chem. Soc.*, 124:10823–10832, 2002.
- [4] F. H. Köhler and R. Lescouëzec. Highly resolved spin-density distribution in the Prussian-blue precursors $\text{Cs}_2\text{K}[\text{Fe}(\text{CN})_6]$ and $\text{Cs}_2\text{K}[\text{Mn}(\text{CN})_6]$. *Angew. Chem. Int. Ed.*, 43:2571–2573, 2004.
- [5] C. P. Grey and N. Dupré. NMR studies of cathode materials for lithium-ion rechargeable batteries. *Chem. Rev.*, 104:4493–4512, 2004.
- [6] N. P. Wickramasinghe, M. Shaibat, and Y. Ishii. Enhanced sensitivity and resolution in ^1H solid-state NMR spectroscopy of paramagnetic complexes under very fast magic angle spinning. *J. Am. Chem. Soc.*, 127:5796–5797, 2005.
- [7] G. Kervern, G. Pintacuda, Y. Zhang, E. Oldfield, C. Roukoss, E. Kuntz, E. Herdtweck, J. M. Basset, S. Cadars, and L. Emsley. Solid-state NMR of a paramagnetic DIAD-Fe-II catalyst: Sensitivity, resolution enhancement, and structure-based assignments. *J. Am. Chem. Soc.*, 128:13545–13552, 2006.
- [8] A. Flambard, F. H. Köhler, and R. Lescouëzec. Revisiting prussian blue analogues with solid-state

- MAS NMR spectroscopy: Spin density and local structure in $[\text{Cd}_3[\text{Fe}(\text{CN})_6]_2] \cdot 15\text{H}_2\text{O}$. *Angew. Chem. Int. Ed.*, 48:1673–1676, 2009.
- [9] I. Bertini, L. Emsley, M. Lelli, C. Luchinat, J. F. Mao, and G. Pintacuda. Ultrafast MAS solid-state NMR permits extensive C-13 and H-1 detection in paramagnetic metalloproteins. *J. Am. Chem. Soc.*, 132:5558–5559, 2010.
- [10] J. Estephane, E. Groppo, J. G. Vitillo, A. Damin, D. Gianolio, C. Lamberti, S. Bordiga, E. A. Quadrelli, J. M. Basset, G. Kervern, L. Emsley, G. Pintacuda, and A. Zecchina. A multitechnique approach to spin-flips for $\text{Cp}_2\text{Cr}(\text{II})$ chemistry in confined state. *J. Phys. Chem. C*, 114:4451–4458, 2010.
- [11] M. J. Knight, A. J. Pell, I. Bertini, I. C. Felli, L. Gonnelli, R. Pierattelli, T. Herrmann, L. Emsley, and G. Pintacuda. Structure and backbone dynamics of a microcrystalline metalloprotein by solid-state NMR. *Proc. Natl. Acad. Sci. USA*, 109:11095–11100, 2012.
- [12] C. Luchinat, G. Parigi, E. Ravera, and M. Rinaldelli. Solid-state NMR crystallography through paramagnetic restraints. *J. Am. Chem. Soc.*, 134:5006–5009, 2012.
- [13] L. Martel, N. Magnini, J.-F. Vigier, J. Boshoven, C. Selfslag, I. Farnan, J.-C. Griveau, J. Somers, and T. Fanghänel. High-resolution solid-state oxygen-17 NMR of actinide-bearing compounds: An insight into the 5f chemistry. *Inorg. Chem.*, 53:6928–6933, 2014.
- [14] I. Bertini and C. Luchinat. Chapter 1: Introduction. *Coord. Chem. Rev.*, 150:1–28, 1996.
- [15] I. Bertini, C. Luchinat, and G. Parigi. *Solution NMR of paramagnetic molecules; application to metalloproteins and models*. Elsevier, London, 2001.
- [16] I. Bertini, C. Luchinat, and G. Parigi. Magnetic susceptibility in paramagnetic NMR. *Prog. Nucl. Magn. Reson. Spectrosc.*, 40:249–273, 2002.
- [17] J. Koehler and J. Meiler. Expanding the utility of NMR restraints with paramagnetic compounds: Background and practical aspects. *Prog. Nucl. Magn. Reson. Spectrosc.*, 59:360–389, 2011.
- [18] A. Pines, M. G. Gibby, and J. S. Waugh. Proton-enhanced NMR of dilute spins in solids. *J. Chem. Phys.*, 59:569–590, 1973.

- [19] P. Hodgkinson. Heteronuclear decoupling in the NMR of solids. *Prog. Nucl. Magn. Reson. Spectrosc.*, 46:197–222, 2005.
- [20] E. L. Hahn. Spin echoes. *Phys. Rev.*, 80:580–594, 1950.
- [21] A. W. Hing, S. Vega, and Schaefer. Transferred-echo double resonance NMR. *J. Magn. Reson.*, 96:205–209, 1992.
- [22] A. N. Clayton, C. M. Dobson, and C. P. Grey. High-resolution C-13 MAS NMR-spectra of paramagnetic lanthanide complexes. *J. Chem. Soc. - Chem. Commun.*, pages 72–74, 1990.
- [23] K. Liu, D. Ryan, K. Nakanishi, and A. McDermott. Solid-state NMR studies of paramagnetic coordination complexes: A comparison of protons and deuterons in detection and decoupling. *J. Am. Chem. Soc.*, 117:6897–6909, 1995.
- [24] D. P. Raleigh, C. P. Grey, and C. M. Soffe, N. Dobson. Multiple-frequency decoupling in magic-angle-spinning NMR of paramagnetic solids. *J. Magn. Reson.*, 97:162–170, 1992.
- [25] Y. Ishii, N. P. Wickramasinghe, and S. Chimon. A new approach in 1D and 2D C13 high-resolution solid-state NMR spectroscopy of paramagnetic organometallic complexes by very fast magic-angle spinning. *J. Am. Chem. Soc.*, 125:3438–3439, 2003.
- [26] N. P. Wickramasinghe and Y. Ishii. Sensitivity enhancement, assignment, and distance measurement in C-13 solid-state NMR spectroscopy for paramagnetic systems under fast magic angle spinning. *J. Magn. Reson.*, 181:233–243, 2006.
- [27] S. K. K. Swamy, A. Karczmarzka, M. Makowska-Janusik, A. Kassiba, and J. Dittmer. Solid-state NMR correlation experiments and distance measurements in paramagnetic metalorganics exemplified by Cu-Cyclam. *ChemPhysChem*, 14:1864–1870, 2013.
- [28] G. Kervern, G. Pintacuda, and L. Emsley. Fast adiabatic pulses for solid-state NMR of paramagnetic systems. *Chem. Phys. Lett.*, 435:157–162, 2007.
- [29] G. Kervern, S. Steuernagel, F. Engelke, G. Pintacuda, and L. Emsley. Absence of curie relaxation in paramagnetic solids yields long H1 coherence lifetimes. *J. Am. Chem. Soc.*, 129:14118, 2007.

- [30] R. J. Clément, A. J. Pell, D. S. Middlemiss, F. C. Strobridge, J. K. Miller, M. S. Whittingham, L. Emsley, C. P. Grey, and G. Pintacuda. Spin-transfer pathways in paramagnetic lithium transition metal phosphates from combined broadband isotropic solid-state MAS NMR spectroscopy and DFT calculations. *J. Am. Chem. Soc.*, 134:17178–17185, 2012.
- [31] A. J. Pell, G. Kervern, L. Emsley, M. Deschamps, D. Massiot, P. J. Grandinetti, and G. Pintacuda. Broadband inversion for MAS NMR with single-sideband-selective adiabatic pulses. *J. Chem. Phys.*, 134:024117, 2011.
- [32] A. J. Pell, K. J. Sanders, S. Wegner, G. Pintacuda, and C. P. Grey. Low-power broadband solid-state MAS NMR of ^{14}N . *J. Chem. Phys.*, 146:194202, 2017.
- [33] K. J. Sanders, A. J. Pell, S. Wegner, C. P. Grey, and G. Pintacuda. Broadband MAS NMR spectroscopy in the low-power limit. *Chem. Phys. Lett.*, 697:29–37, 2018.
- [34] A. J. Pell and G. Pintacuda. Broadband solid-state MAS NMR of paramagnetic systems. *Prog. Nucl. Magn. Reson. Spectrosc.*, 84-85:33–72, 2015.
- [35] H. M. McConnell and D. B. Chesnut. Isotropic hyperfine interactions in π -electron radicals. *J. Chem. Phys.*, 28:107–117, 1958.
- [36] H. M. McConnell and R. E. Robertson. Isotropic nuclear resonance shifts. *J. Chem. Phys.*, 29:1361–1365, 1958.
- [37] R. J. Kurland and B. R. McGarvey. Isotropic NMR shifts in transition metal complexes: The calculation of the Fermi contact and pseudocontact terms. *J. Magn. Reson.*, 2:286–301, 1970.
- [38] S. Moon and S. Patchkovskii. *Calculation of NMR and EPR Parameters: Theory and Applications*, chapter Chapter 20. First-Principles Calculations of Paramagnetic NMR Shifts. In Kaupp et al. [201], 2004.
- [39] T. O. Pennanen and J. Vaara. Nuclear magnetic resonance chemical shift in an arbitrary electronic spin state. *Phys. Rev. Lett.*, 100:133002, 2008.
- [40] J. Vaara, S. A. Rouf, and J. Mares. Magnetic couplings in the chemical shift of paramagnetic NMR. *J. Chem. Theory Comput.*, 11:4840–4849, 2015.

- [41] M. Kaupp and F. H. Köhler. Combining NMR spectroscopy and quantum chemistry as tools to quantify spin density distributions in molecular magnetic compounds. *Coord. Chem. Rev.*, 253:2376–2386, 2009.
- [42] I. Bertini and C. Luchinat. Chapter 2: The hyperfine shift. *Coord. Chem. Rev.*, 150:29–75, 1996.
- [43] I. Bertini, P. Turano, and A. J. Vila. Nuclear-magnetic-resonance of paramagnetic metalloproteins. *Chem. Rev.*, 93:2833–2932, 1993.
- [44] S. Balayssac, I. Bertini, A. Bhaumik, M. Lelli, and C. Luchinat. Paramagnetic shifts in solid-state NMR of proteins to elicit structural information. *Proc. Natl. Acad. Sci. USA*, 105:17284–17289, 2008.
- [45] M. J. Knight, I. C. Felli, R. Pierattelli, I. Bertini, L. Emsley, T. Herrmann, and G. Pintacuda. Rapid measurement of pseudocontact shifts in metalloproteins by proton-detected solid-state NMR spectroscopy. *J. Am. Chem. Soc.*, 134:14730–14733, 2012.
- [46] I. Bertini, F. Briganti, C. Luchinat, A. Scozzafava, and M. Sola. ^1H NMR spectroscopy and the electronic structure of the high potential iron-sulfur protein from *Chromatium vinosum*. *J. Am. Chem. Soc.*, 113:1237–1245, 1991.
- [47] I. Bertini and C. Luchinat. Chapter 5: Magnetic coupled systems. *Coord. Chem. Rev.*, 150:131–161, 1996.
- [48] D. Carlier, M. Ménétrier, C. P. Grey, C. Delmas, and G. Ceder. Understanding the NMR shifts in paramagnetic transition metal oxides using density functional theory calculations. *Phys. Rev. B*, 67:174103, 2003.
- [49] R. J. McCarty and J. F. Stebbins. Transition metal dopant cation distributions in MgO and CaO: New inferences from paramagnetically shifted resonances in ^{17}O , ^{25}Mg , and ^{43}Ca NMR spectra. *J. Phys. Chem. C*, 120:11111–11120, 2016.
- [50] J. F. Stebbins, R. J. McCarty, and A. C. Palke. Solid-state NMR and short-range order in crystalline oxides and silicates: a new tool in paramagnetic resonances. *Acta Cryst.*, C73:128–136, 2017.
- [51] J. F. Stebbins. Toward the wider application of ^{29}Si NMR spectroscopy to paramagnetic transition metal silicate minerals: Copper(II) silicates. *Am. Mineral.*, 102:2406–2414, 2017.

- [52] J. F. Stebbins, R. J. McCarty, and A. C. Palke. Towards the wider application of ^{29}Si NMR spectroscopy to paramagnetic transition metal silicate minerals and glasses, 2: Fe(II), Co(II), and Ni(II) silicates. *Am. Mineral.*, 2018.
- [53] J. Kim, D. S. Middlemiss, N. A. Chernova, B. Y. X. Zhu, C. Masquelier, and C. P. Grey. Linking local environments and hyperfine shifts: A combined experimental and theoretical ^{31}P and ^7Li solid-state NMR study of paramagnetic Fe(III) phosphates. *J. Am. Chem. Soc.*, 132:16825–16840, 2010.
- [54] D. S. Middlemiss, A. J. Ilott, R. J. Clément, F. C. Strobridge, and C. P. Grey. Density functional theory-based bond pathway decompositions of hyperfine shifts: Equipping solid-state NMR to characterize atomic environments in paramagnetic materials. *Chem. Mater.*, 25:1723–1734, 2013.
- [55] J. Xu, R. J. Lee, R. J. Clément, X. Yu, M. Leskes, A. J. Pell, G. Pintacuda, X.-Q. Yang, C. P. Grey, and Y. S. Meng. Identifying the critical role of Li substitution in $\text{P2-Na}_x[\text{Li}_y\text{Ni}_z\text{Mn}_{1-y-z}]\text{O}_2$ ($0 < x, y, z < 1$) intercalation cathode materials for high energy Na-ion batteries. *Chem. Mater.*, 26:1260–1269, 2014.
- [56] F. C. Strobridge, D. S. Middlemiss, A. J. Pell, M. Leskes, R. J. Clément, F. Pourpoint, Z. Lu, J. V. Hanna, G. Pintacuda, L. Emsley, A. Samoson, and C. P. Grey. Characterising local environments in high energy density Li-ion battery cathodes: a combined NMR and first principles study of $\text{LiFe}_x\text{Co}_{1-x}\text{PO}_4$. *J. Mater. Chem. A*, 2:11948–11957, 2014.
- [57] I. D. Seymour, D. S. Middlemiss, D. M. Halat, N. M. Trease, A. J. Pell, and C. P. Grey. Characterizing oxygen local environments in paramagnetic battery materials via ^{17}O NMR and DFT calculations. *J. Am. Chem. Soc.*, 138:9405–9408, 2016.
- [58] J. Lee, I. D. Seymour, A. J. Pell, S. E. Dutton, and C. P. Grey. A systematic study of ^{25}Mg NMR in paramagnetic transition metal oxides: applications to Mg-ion battery materials. *Phys. Chem. Chem. Phys.*, 19:613–625, 2017.
- [59] R. Pigliapochi, I. D. Seymour, C. Merlet, A. J. Pell, D. T. Murphy, S. Schmid, and C. P. Grey. Structural characterization of the Li-ion battery cathode materials $\text{LiTi}_x\text{Mn}_{2-x}\text{O}_4$ ($0.2 \leq x \leq 1.5$): A combined experimental ^7Li NMR and first-principles study. *Chem. Mater.*, 30:817–829, 2018.

- [60] R. M. Golding and M. P. Halton. A theoretical study of the ^{14}N and ^{17}O N.M.R. shifts in lanthanide complexes. *Aust. J. Chem.*, 25:2577–2581, 1972.
- [61] B. Bleaney. Nuclear magnetic resonance shifts in solution due to lanthanide ions. *J. Magn. Reson.*, 8:91–100, 1972.
- [62] A. M. Funk, K.-L. N. A. Finney, P. Harvey, A. M. Kenwright, E. R. Neil, N. J. Rogers, P. K. Senanayake, and D. Parker. Critical analysis of the limitations of Bleaney's theory of magnetic anisotropy in paramagnetic lanthanide coordination complexes. *Chem. Sci.*, 6:1655–1662, 2015.
- [63] B. R. McGarvey. Temperature dependence of the pseudocontact shift in lanthanide shift reagents. *J. Magn. Reson.*, 33:445–455, 1979.
- [64] A. K. Cheetham, C. M. Dobson, C. P. Grey, and R. J. B. Jakeman. Paramagnetic shift probes in high-resolution solid-state NMR. *Nature*, 328:706–707, 1987.
- [65] C. P. Grey, M. E. Smith, A. K. Cheetham, C. M. Dobson, and R. Dupree. ^{89}Y MAS NMR study of rare-earth pyrochlores: Paramagnetic shifts in the solid state. *J. Am. Chem. Soc.*, 112:4670–4675, 1990.
- [66] N. C. George, A. J. Pell, G. Dantelle, A. Llobet, M. Balasubramanian, G. Pintacuda, B. F. Chmelka, and R. Seshadri. Local environments of dilute activator ions in the solid-state lighting phosphor $\text{Y}_{3-x}\text{Ce}_x\text{Al}_5\text{O}_{12}$. *Chem. Mater.*, 25:3979–3995, 2013.
- [67] R. J. McCarty and J. F. Stebbins. Investigating lanthanide dopant distributions in yttrium aluminum garnet (YAG) using solid state paramagnetic NMR. *Solid State Nucl. Magn. Reson.*, 79:11–22, 2016.
- [68] C. P. Grey, C. M. Dobson, A. K. Cheetham, and R. J. B. Jakeman. Studies of rare-earth stannates by ^{119}Sn MAS NMR. The use of paramagnetic shift probes in the solid state. *J. Am. Chem. Soc.*, 111:505–511, 1989.
- [69] A. R. Brough, C. P. Grey, and C. M. Dobson. Structural information from NMR-studies of paramagnetic solids - Na-23 MAS spectra of sodium lanthanide salts of ethylenediaminetetraacetic acid. *J. Chem. Soc. Chem. Commun.*, pages 742–743, 1992.

- [70] A.R. Brough, C.P. Grey, and C.M. Dobson. Paramagnetic ions as structural probes in solid-state NMR: Distance measurements in crystalline lanthanide acetates. *J. Am. Chem. Soc.*, 115:7318–7327, 1993.
- [71] G. Kervern, A. D'Aleo, O. Maury, L. Emsley, and G. Pintacuda. Crystal structure determination of powdered paramagnetic lanthanide complexes by proton NMR. *Angew. Chem. Int. Ed. Engl.*, 48:3082–3086, 2009.
- [72] N. C. George, J. Brgoch, A. J. Pell, C. Cozzan, A. Jaffe, G. Dantelle, A. Llobet, G. Pintacuda, R. Seshadri, and B. F. Chmelka. Correlating local compositions and structures with the macroscopic optical properties of Ce³⁺-doped CaSc₂O₄, an efficient green-emitting phosphor. *Chem. Mater.*, 29:3538–3546, 2017.
- [73] M. Vonci, K. Mason, E. A. Suturina, A. T. Frawley, S. G. Worswick, I. Kuprov, D. Parker, E. J. L. McInnes, and N. F. Chilton. Rationalization of anomalous pseudocontact shifts and their solvent dependence in a series of *c*₃-symmetric lanthanide complexes. *J. Am. Chem. Soc.*, 139:14166–14172, 2017.
- [74] I. Bertini, M. B. L. Janik, Y.-M. Lee, C. Luchinat, and A. Rosato. Magnetic susceptibility tensor anisotropies for a lanthanide ion series in a fixed protein matrix. *J. Am. Chem. Soc.*, 123:4181–4188, 2001.
- [75] I. Bertini, C. Del Bianco, I. Gelis, N. Katsaros, C. Luchinat, G. Parigi, M. Peana, A. Provenzani, and M. A. Zoroddu. Experimentally exploring the conformational space sampled by domain reorientation in calmodulin. *Proc. Natl. Acad. Sci. USA*, 101:6841–6846, 2004.
- [76] I. Bertini, P. Kursula, C. Luchinat, G. Parigi, J. Vahokoski, M. Wilmanns, and J. Yuan. Accurate solution structures of proteins from X-ray data and a minimal set of NMR data: Calmodulin–peptide complexes as examples. *J. Am. Chem. Soc.*, 131:5134–5144, 2009.
- [77] G. Pintacuda, M. John, X.-C. Su, and G. Otting. NMR structure determination of protein-ligand complexes by lanthanide labeling. *Acc. Chem. Res.*, 40:206–212, 2007.
- [78] T. Zhuang, H.-S. Lee, B. Imperiali, and J. H. Prestegard. Structure determination of a Galectin-3–carbohydrate complex using paramagnetism-based NMR constraints. *Protein Sci.*, 17:1220–1231, 2008.

- [79] P. H. J. Keizers, A. Saragliadis, Y. Hiruma, M. Overhand, and M. Ubbink. Design, synthesis, and evaluation of a lanthanide chelating protein probe: CLaNP-5 yields predictable paramagnetic effects independent of environment. *J. Am. Chem. Soc.*, 130:14802–14812, 2008.
- [80] L. de la Cruz, T. H. D. Nguyen, K. Ozawa, J. Shin, B. Graham, T. Huber, and G. Otting. Binding of low molecular weight inhibitors promotes large conformational changes in the dengue virus NS2B-NS3 protease: Fold analysis by pseudocontact shifts. *J. Am. Chem. Soc.*, 133:19205–19215, 2011.
- [81] Y. Kobashigawa, T. Saio, M. Ushio, M. Sekiguchi, M. Yokochi, K. Ogura, and F. Inagaki. Convenient method for resolving degeneracies due to symmetry of the magnetic susceptibility tensor and its application to pseudo contact shift-based protein–protein complex structure determination. *J. Biomol. NMR*, 53:53–63, 2012.
- [82] L. Cerofolini, G. B. Fields, M. Fragai, C. F. G. C. Geraldles, G. Luchinat, C. Parigi, E. Ravera, D. I. Svergun, and J. M. C. Teixeira. Examination of matrix metalloproteinase-1 in solution. *J. Biol. Chem.*, 288:30659–30671, 2013.
- [83] J.-Y. Guan, P. H. J. Keizers, W.-M. Liu, F. Löhr, S. P. Skinner, E. A. Heeneman, H. Schwalbe, M. Ubbink, and G. Siegal. Small-molecule binding sites on proteins established by paramagnetic NMR spectroscopy. *J. Am. Chem. Soc.*, 135:5859–5868, 2013.
- [84] H. Yagi, K. B. Pilla, A. Maleckis, B. Graham, T. Huber, and G. Otting. Three-dimensional protein fold determination from backbone amide pseudocontact shifts generated by lanthanide tags at multiple sites. *Structure*, 21:883–890, 2013.
- [85] D. J. Crick, J. X. Wang, B. Graham, J. D. Swarbrick, H. R. Mott, and D. Nietlispach. Integral membrane protein structure determination using pseudocontact shifts. *J. Biomol. NMR*, 61:197–207, 2015.
- [86] W. Van den Heuvel and A. Soncini. NMR chemical shift in an electronic state with arbitrary degeneracy. *Phys. Rev. Lett.*, 109:073001, 2012.
- [87] A. Soncini and W. Van den Heuvel. Communication: Paramagnetic NMR chemical shift in a spin state subject to zero-field splitting. *J. Chem. Phys.*, 138:021103, 2013.

- [88] W. Van den Heuvel and A. Soncini. NMR chemical shift as analytical derivative of the Helmholtz free energy. *J. Chem. Phys.*, 138:054113, 2013.
- [89] B. Martin and J. Autschbach. Temperature dependence of contact and dipolar NMR chemical shifts in paramagnetic molecules. *J. Chem. Phys.*, 142:054108, 2015.
- [90] B. Martin and J. Autschbach. Erratum: “temperature dependence of contact and dipolar NMR chemical shifts in paramagnetic molecules” [*J. Chem. Phys.* 142, 054108 (2015)]. *J. Chem. Phys.*, 145:049901, 2016.
- [91] F. Gendron, K. Sharkas, and J. Autschbach. Calculating NMR chemical shifts for paramagnetic metal complexes from first-principles. *J. Phys. Chem. Lett.*, 6:2183–2188, 2015.
- [92] F. Gendron and J. Autschbach. Ligand NMR chemical shift calculations for paramagnetic metal complexes: $5f^1$ vs $5f^2$ actinides. *J. Chem. Theory Comput.*, 12:5309–5321, 2016.
- [93] J. Kowalewski, D. Kruk, and G. Parigi. NMR relaxation in solution of paramagnetic complexes: recent theoretical progress for $S \geq 1$. *Adv. Inorg. Chem.*, 57:41–104, 2005.
- [94] J. Kowalewski, L. Nordenskiöld, B. Nikolas, and P.-O. Westlund. Theory of nuclear spin relaxation in paramagnetic systems in solution. *Prog. Magn. Reson. Spectrosc.*, 17:141–185, 1985.
- [95] J. Kowalewski and Mäler. *Nuclear spin relaxation in liquids: theory, experiments, and applications*. Taylor & Francis, Boca Raton, 2006.
- [96] I. Solomon. Relaxation processes in a system of two spins. *Phys. Rev.*, 99:559–565, 1955.
- [97] N. Bloembergen. Proton relaxation times in paramagnetic solutions. *J. Chem. Phys.*, 27:572–573, 1957.
- [98] N. Bloembergen and L. O. Morgan. Proton relaxation times in paramagnetic solutions. effects of electron spin relaxation. *J. Chem. Phys.*, 34:842–850, 1961.
- [99] M. Gueron. Nuclear relaxation in macromolecules by paramagnetic ions: a novel mechanism. *J. Magn. Reson.*, 19:58–66, 1975.

- [100] A. J. Vega and D. Fiat. Nuclear relaxation processes of paramagnetic complexes. the slow motion case. *Mol. Phys.*, 31:347–355, 1976.
- [101] I. Sengupta, P. S. Nadaud, J. J. Helmus, C. D. Schwieters, and C. P. Jaroniec. Protein fold determined by paramagnetic magic-angle spinning solid-state NMR spectroscopy. *Nature Chem.*, 4:410–417, 2012.
- [102] N. Benetis, J. Kowalewski, L. Nordenskiöld, H. Wennerström, and P. O. Westlund. Nuclear spin relaxation in paramagnetic systems. The slow motion problem for electron spin relaxation. *Mol. Phys.*, 48:329–346, 1983.
- [103] N. Benetis, J. Kowalewski, L. Nordenskiöld, H. Wennerström, and P. O. Westlund. Dipole-dipole nuclear spin relaxation. A cross correlation correction to the Solomon–Bloembergen equation for T_2 . *Mol. Phys.*, 50:515–530, 1983.
- [104] N. Benetis, J. Kowalewski, L. Nordenskiöld, H. Wennerström, and P. O. Westlund. Nuclear spin relaxation in paramagnetic systems ($S = 1$) in the slow-motion regime for the electron spin. II. the dipolar T_2 and the role of scalar interaction. *J. Magn. Reson.*, 58:261–281, 1984.
- [105] T. Larsson, P.-O. Westlund, J. Kowalewski, and S. H. Koenig. Nuclear-spin relaxation in paramagnetic complexes in the slow-motion regime for the electron spin: The anisotropic pseudorotation model for $S = 1$ and the interpretation of nuclear magnetic relaxation dispersion results for a low-symmetry Ni(II) complex. *J. Chem. Phys.*, 101:1116–1128, 1994.
- [106] T. Nilsson and J. Kowalewski. Slow-motion theory of nuclear spin relaxation in paramagnetic low-symmetry complexes: A generalization to high electron spin. *J. Magn. Reson.*, 146:345–358, 2000.
- [107] P. O. Westlund, H. Wennerström, L. Nordenskiöld, J. Kowalewski, and N. Benetis. Nuclear spin-lattice and spin-spin relaxation in paramagnetic systems in the slow-motion regime for the electron spin. III. dipole-dipole and scalar spin-spin interaction for $S = 3/2$ and $S = 5/2$. *J. Magn. Reson.*, 59:91–109, 1984.
- [108] I. Bertini, J. Kowalewski, C. Luchinat, T. Nilsson, and G. Parigi. Nuclear spin relaxation in paramagnetic complexes of $S = 1$: electron spin relaxation effects. *J. Chem. Phys.*, 111:5795–5807, 1999.

- [109] D. Kruk, T. Nilsson, and J. Kowalewski. Nuclear spin relaxation in paramagnetic systems with zero-field splitting and arbitrary electron spin. *Phys. Chem. Chem. Phys.*, 3:4907–4917, 2001.
- [110] P. H. Fries and E. Belorizky. Relaxation theory of the electronic spin of a complexed paramagnetic metal ion in solution beyond the Redfield limit. *J. Chem. Phys.*, 126:204503, 2007.
- [111] S. Rast, P.H. Fries, E. Belorizky, A. Borel, L. Helm, and A. E. Merbach. A general approach to the electronic spin relaxation of Gd(III) complexes in solutions. Monte Carlo simulations beyond the Redfield limit. *J. Chem. Phys.*, 115:7554–7563, 2001.
- [112] S. M. Abernathy and R. R. Sharp. Spin dynamics calculations of electron and nuclear spin relaxation times in paramagnetic solutions. *J. Chem. Phys.*, 106:9032–9043, 1997.
- [113] N. Schaeffe and R. R. Sharp. Electron spin relaxation due to reorientation of a permanent zero field splitting tensor. *J. Chem. Phys.*, 121:5387–5394, 2004.
- [114] N. Schaeffe and R. R. Sharp. Four complementary theoretical approaches for the analysis of NMR paramagnetic relaxation. *J. Magn. Reson.*, 176:160–170, 2005.
- [115] M. Rubinstein, A. Baram, and Z. Luz. Electronic and nuclear relaxation in solutions of transition metal ions with $S = 3/2$ and $5/2$. *Mol. Phys.*, 20:67–80, 1971.
- [116] S. Rast, P.H. Fries, and E. Belorizky. Static zero field splitting effects on the electronic relaxation of paramagnetic metal ion complexes in solution. *J. Chem. Phys.*, 113:8724–8735, 2000.
- [117] P.-O. Westlund and R. M. Lynden-Bell. A study of vibrational dephasing of the A_1 modes of CH_3CN in a computer simulation of the liquid phase. *Mol. Phys.*, 60:1189–1209, 1987.
- [118] P.-O. Westlund and R. M. Lynden-Bell. The effects of pressure and temperature on vibrational dephasing in a simulation of liquid CH_3CN . *Mol. Phys.*, 61:1541–1547, 1987.
- [119] D. Kruk, J. Kowalewski, and P.-O. Westlund. Nuclear and electron spin relaxation in paramagnetic complexes in solution: Effects of the quantum nature of molecular vibrations. *J. Chem. Phys.*, 121:2215–2227, 2004.

- [120] Z. Luz and S. Meiboom. Proton relaxation in dilute solutions of cobalt(II) and nickel(II) ions in methanol and the rate of methanol exchange of the solvation sphere. *J. Chem. Phys.*, 40:2686–2692, 1964.
- [121] D. Kruk, T. Nilsson, and J. Kowalewski. Outer-sphere nuclear spin relaxation in paramagnetic systems: a low-field theory. *Mol. Phys.*, 99:1435–1445, 2001.
- [122] D. Kruk and J. Kowalewski. Nuclear spin relaxation in ligands outside of the first coordination sphere in a gadolinium (III) complex: effects of intermolecular forces. *J. Chem. Phys.*, 117:1194–1200, 2002.
- [123] T. Nilsson, G. Parigi, , and J. Kowalewski. Experimental NMRD profiles for some low-symmetry Ni(II) complexes ($S = 1$) in solution and their interpretation using slow-motion theory. *J. Phys. Chem. A*, 106:4476–4488, 2002.
- [124] D. Kruk and J. Kowalewski. Field-dependent proton relaxation in aqueous solutions of some manganese(II) complexes: a new interpretation. *J. Biol. Inorg. Chem.*, 8:512–518, 2003.
- [125] D. H. Powell, O. M. N. Dhubhghaill, D. Pubanz, L. Helm, Y. S. Lebedev, W. Schlaepfer, and A. E. Merbach. Structural and dynamic parameters obtained from ^{17}O NMR, EPR, and NMRD studies of monomeric and dimeric Gd^{3+} complexes of interest in magnetic resonance imaging: An integrated and theoretically self-consistent approach. *J. Am. Chem. Soc.*, 118:9333–9346, 1996.
- [126] E. Tóth, F. Connac, L. Helm, K. Adzamlı, and A. E. Merbach. ^{17}O -NMR, EPR and NMRD characterization of $[\text{Gd}(\text{DTPA-BMEA})(\text{H}_2\text{O})]$: A neutral MRI contrast agent. *Eur. J. Inorg. Chem.*, pages 2017–2021, 1998.
- [127] P. Caravan, J. J. Ellison, T. J. McMurry, and R. B. Lauffer. Gadolinium(III) chelates as MRI contrast agents: Structure, dynamics, and applications. *Chem. Rev.*, 99:2293–2352, 1999.
- [128] P. L. Anelli, I. Bertini, M. Fragai, L. Lattuada, C. Luchinat, and G. Parigi. Sulfonamide-functionalized gadolinium DTPA complexes as possible contrast agents for MRI: A relaxometric investigation. *Eur. J. Inorg. Chem.*, pages 625–630, 2000.
- [129] P. Caravan. Strategies for increasing the sensitivity of gadolinium based MRI contrast agents. *Chem. Soc. Rev.*, 35:512–523, 2006.

- [130] E. J. Werner, S. Avedano, M. Botta, B. P. Hay, E. G. Moore, S. Aime, and K. N. Raymond. Highly soluble tris-hydroxypyridonate Gd(III) complexes with increased hydration number, fast water exchange, slow electronic relaxation, and high relaxivity. *J. Am. Chem. Soc.*, 129:1870–1871, 2007.
- [131] D. T Schühle, J. Schatz, S. Laurent, L. Vander Elst, R. N. Muller, M. C. A. Stuart, and J. A. Peters. Calix[4]arenes as molecular platforms for magnetic resonance imaging (MRI) contrast agents. *Chem. Eur. J.*, 15:3290–3296, 2009.
- [132] E. Gianolio, S. Porto, R. Napolitano, S. Baroni, G. B. Giovenzana, and S. Aime. Relaxometric investigations and MRI evaluation of a liposome- loaded pH-responsive gadolinium(III) complex. *Inorg. Chem.*, 51:7210–7217, 2012.
- [133] M. W. Rotz, K. S. B. Culver, G. Parigi, K. W. MacRenaris, C. Luchinat, T. W. Odom, and T. J. Meade. High relaxivity Gd(III)–DNA gold nanostars: Investigation of shape effects on proton relaxation. *ACS Nano*, 9:3385–3396, 2015.
- [134] W. Nusser and R. Kimmich. Protein backbone fluctuations and NMR field-cycling relaxation spectroscopy. *J. Phys. Chem.*, 94:5637–5639, 1990.
- [135] S. H. Koenig and R. D. Brown III. Field-cycling relaxometry of protein solutions and tissue: implications for MRI. *Prog. Nucl. Magn. Reson. Spectrosc.*, 22:487–567, 1990.
- [136] I. Bertini, O. Galas, C. Luchinat, and G. Parigi. A computer program for the calculation of paramagnetic enhancements of nuclear-relaxation rates in slowly rotating systems. *J. Magn. Reson. Ser. A*, 113:151–158, 1995.
- [137] P.-O. Westlund. A low-field paramagnetic nuclear spin relaxation theory. *J. Chem. Phys.*, 108:4945–4553, 1998.
- [138] T. Nilsson and J. Kowalewski. Low-field theory of nuclear spin relaxation in paramagnetic low-symmetry complexes for electron spin systems of $S = 1, 3/2, 2, 5/2, 3$ and $7/2$. *Mol. Phys.*, 98:1617–1638, 2000.
- [139] T. Nilsson and J. Kowalewski. Erratum: Low-field theory of nuclear spin relaxation in paramagnetic

- low-symmetry complexes for electron spin systems of $S = 1, 3/2, 2, 5/2, 3$ and $7/2$. *Mol. Phys.*, 99:369–370, 2001.
- [140] J.-P. Korb and R. G. Bryant. The physical basis for the magnetic field dependence of proton spin-lattice relaxation rates in proteins. *J. Chem. Phys.*, 115:10964–10974, 2001.
- [141] R. Kimmich and E. Anoardo. Field-cycling NMR relaxometry. *Prog. Nucl. Magn. Reson. Spectrosc.*, 44:257–320, 2004.
- [142] M. F. Roberts and A. G. Redfield. High-resolution ^{31}P field cycling NMR as a probe of phospholipid dynamics. *J. Am. Chem. Soc.*, 126:13765–13777, 2004.
- [143] I. Bertini, C. Luchinat, and G. Parigi. ^1H NMRD profiles of paramagnetic complexes and metalloproteins. *Adv. Inorg. Chem.*, 57:105–172, 2005.
- [144] G. Ferrante and S. Sykora. Technical aspects of fast field cycling. *Adv. Inorg. Chem.*, 57:405–470, 2005.
- [145] C. Luchinat, G. Parigi, and E. Ravera. Can metal ion complexes be used as polarizing agents for solution DNP? A theoretical discussion. *J. Biomol. NMR*, 58:239–249, 2014.
- [146] G. Liu, M. Levien, N. Karschin, G. Parigi, C. Luchinat, and M. Bennati. One-thousand-fold enhancement of high field liquid nuclear magnetic resonance signals at room temperature. *Nat. Chem.*, 9:676–680, 2017.
- [147] D. L. VanderHart and W. L. Earl. Resolution in ^{13}C NMR of organic solids using high-power proton decoupling and magic-angle sample spinning. *J. Magn. Reson.*, 44:361–401, 1981.
- [148] M. Alla and E. Lippmaa. Resolution limits in magic-angle rotation NMR spectra of polycrystalline solids. *Chem. Phys. Lett.*, 87:30–33, 1982.
- [149] C. P. Grey, C. M. Dobson, and A. K. Cheetham. Susceptibility matching in MAS NMR. The determination of hyperfine tensors from paramagnetic stannates. *J. Magn. Reson.*, 98:414–420, 1992.
- [150] U. Schwerk, D. Michel, and M. Pruski. Local magnetic field distribution in a polycrystalline sample exposed to a strong magnetic field. *J. Magn. Reson. Ser. A*, 119:157–164, 1996.

- [151] A. Kubo, T. P. Spaniol, and T. Terao. The effect of bulk magnetic susceptibility on solid state NMR spectra of paramagnetic compounds. *J. Magn. Reson.*, 133:330–340, 1998.
- [152] R. Dickinson, A. T. Royappa, F. Tone, L. Ujj, and G. Wu. Distribution of non-uniform demagnetization fields in paramagnetic bulk solids. *J. Appl. Phys.*, 110:013902, 2011.
- [153] N. M. Trease, L. Zhou, H. J. Chang, B. Y. Zhu, and C. P. Grey. *In situ* NMR of lithium ion batteries: Bulk susceptibility effects and practical considerations. *Solid State Nucl. Magn. Reson.*, 42:62–70, 2012.
- [154] L. Zhou, M. Leskes, A. J. Ilott, N. M. Trease, and C. P. Grey. Paramagnetic electrodes and bulk magnetic susceptibility effects in the *in situ* NMR studies of batteries: Application to $\text{Li}_{1.08}\text{Mn}_{1.92}\text{O}_4$ spinels. *J. Magn. Reson.*, 234:44–57, 2013.
- [155] A. W. Overhauser. Polarization of nuclei in metals. *Phys. Rev.*, 92:411–415, 1953.
- [156] T. R. Carver and C. P. Slichter. Polarization of nuclear spins in metals. *Phys. Rev.*, 92:212–213, 1953.
- [157] T. R. Carver and C. P. Slichter. Experimental verification of the Overhauser nuclear polarization effect. *Phys. Rev.*, 102:975–980, 1956.
- [158] L. R. Becerra, G. J. Gerfen, R. J. Temkin, D. J. Singel, and R. G. Griffin. Dynamic nuclear polarization with a cyclotron resonance maser at 5 T. *Phys. Rev. Lett.*, 71:3561–3564, 1993.
- [159] M. Rosay, L. Tometich, S. Pawsey, R. Bader, R. Schauwecker, M. Blank, P. M. Borchard, S. R. Cauffman, K. L. Felch, R. T. Weber, R. J. Temkin, R. G. Griffin, and W. E. Maas. Solid-state dynamic nuclear polarization at 263 GHz: spectrometer design and experimental results. *Phys. Chem. Chem. Phys.*, 12:5850–5860, 2010.
- [160] A. B. Barnes, G. De Paëpe, P. C. A. van der Wel, K.-N. Hu, C.-G. Joo, V. S. Bajaj, M. L. Mak-Jurkauskas, J. R. Sirigiri, J. Herzfeld, R. J. Temkin, and R. G. Griffin. High-field dynamic nuclear polarization for solid and solution biological NMR. *Appl. Magn. Reson.*, 34:237–263, 2008.
- [161] T. Maly, G. T. Debelouchina, V. S. Bajaj, K.-N. Hu, C.-G. Joo, M. L. Mak-Jurkauskas, J. R. Sirigiri, P. C. A. van der Wel, J. Herzfeld, R. J. Temkin, and R. G. Griffin. Dynamic nuclear polarization at high magnetic fields. *J. Chem. Phys.*, 128:052211, 2008.

- [162] G. T. Debelouchina, M. J. Bayro, P. C. A. van der Wel, M. A. Caporini, A. B. Barnes, M. Rosay, W. E. Maas, and R. G. Griffin. Dynamic nuclear polarization-enhanced solid-state NMR spectroscopy of GNNQQNY nanocrystals and amyloid fibrils. *Phys. Chem. Chem. Phys.*, 12:5911–5919, 2010.
- [163] G. J. Gerfen, L. R. Becerra, D. A. Hall, R. G. Griffin, R. J. Temkin, and D. J. Singel. High frequency (140 GHz) dynamic nuclear polarization: Polarization transfer to a solute in frozen aqueous solution. *J. Chem. Phys.*, 102:9494–9497, 1995.
- [164] D. A. Hall, D. C. Maus, G. J. Gerfen, S. J. Inati, L. R. Becerra, F. W. Dahlquist, and R. G. Griffin. Polarization-enhanced NMR spectroscopy of biomolecules in frozen solution. *Science*, 276:930–932, 1997.
- [165] C. Song, K.-N. Hu, C.-G. Joo, T. M. Swager, and R. G. Griffin. TOTAPOL: A biradical polarizing agent for dynamic nuclear polarization experiments in aqueous media. *J. Am. Chem. Soc.*, 128:11385–11390, 2006.
- [166] C. Sauvé, M. Rosay, G. Casano, F. Aussenac, R. T. Weber, O. Ouari, and P. Tordo. Highly efficient, water-soluble polarizing agents for dynamic nuclear polarization at high frequency. *Angew. Chem. Int. Ed.*, 52:10858–10861, 2013.
- [167] C. Sauvé, G. Casano, S. Abel, A. Rockenbauer, D. Akhmetzyanov, H. Karoui, D. Siri, F. Aussenac, W. Maas, R. T. Weber, T. Prisner, M. Rosay, P. Tordo, and O. Ouari. Tailoring of polarizing agents in the bTurea series for cross-effect dynamic nuclear polarization in aqueous media. *Chem. Eur. J.*, 22:5598–5606, 2016.
- [168] A. Zagdoun, G. Casano, O. Ouari, G. Lapadula, A. J. Rossini, M. Lelli, M. Baffert, D. Gajan, L. Veyre, W. E. Maas, M. Rosay, R. T. Weber, C. Thieuleux, C. Copéret, A. Lesage, P. Tordo, and L. Emsley. A slowly relaxing rigid biradical for efficient dynamic nuclear polarization surface-enhanced NMR spectroscopy: Expeditious characterization of functional group manipulation in hybrid materials. *J. Am. Chem. Soc.*, 134:2284–2291, 2012.
- [169] A. Zagdoun, G. Casano, O. Ouari, M. Schwarzwälder, A. J. Rossini, F. Aussenac, M. Yulikov, G. Jeschke, C. Copéret, A. Lesage, P. Tordo, and L. Emsley. A slowly relaxing rigid biradical for

- efficient dynamic nuclear polarization surface-enhanced NMR spectroscopy: Expedient characterization of functional group manipulation in hybrid materials. *J. Am. Chem. Soc.*, 135:12790–12797, 2013.
- [170] D. J. Kubicki, G. Casano, M. Schwarzwälder, S. Abel, C. Sauvé, K. Ganesan, M. Yulikov, A. J. Rossini, G. Jeschke, C. Copéret, A. Lesage, P. Tordo, O. Ouari, and L. Emsley. Rational design of dinitroxide biradicals for efficient cross-effect dynamic nuclear polarization. *Chem. Sci.*, 7:550–558, 2016.
- [171] P. C. A. van der Wel, K.-N. Hu, J. Lewandowski, and R. G. Griffin. Dynamic nuclear polarization of amyloidogenic peptide nanocrystals: GNNQQNY, a core segment of the yeast prion protein Sup35p. *J. Am. Chem. Soc.*, 128:10840–10846, 2006.
- [172] M. L. Mak-Jurkauskas, V. S. Bajaj, M. K. Hornstein, M. Belenky, R. G. Griffin, and J. Herzfeld. Energy transformations early in the bacteriorhodopsin photocycle revealed by DNP-enhanced solid-state NMR. *Proc. Natl. Acad. Sci. USA*, 105:883–888, 2008.
- [173] V. S. Bajaj, M. L. Mak-Jurkauskas, M. Belenky, J. Herzfeld, and R. G. Griffin. Functional and shunt states of bacteriorhodopsin resolved by 250 GHz dynamic nuclear polarization-enhanced solid-state NMR. *Proc. Natl. Acad. Sci. USA*, 106:9244–9249, 2009.
- [174] G. T. Debelouchina, G. W. Platt, M. J. Bayro, and R. G. Griffin. Magic angle spinning NMR analysis of β_2 -microglobulin amyloid fibrils in two distinct morphologies. *J. Am. Chem. Soc.*, 132:10414–10423, 2010.
- [175] M. J. Bayro, T. Maly, N. R. Birkett, C. E. MacPhee, C. M. Dobson, and R. G. Griffin. High-resolution MAS NMR analysis of PI3–SH3 amyloid fibrils: Backbone conformation and implications for protofilament assembly and structure. *Biochemistry*, 49:7474–7484, 2010.
- [176] K. Jaudzems, A. Bertarello, S. R. Chaudhari, A. Pica, D. Cala-De Paepe, E. Barbet-Massin, A. J. Pell, I. Akopjana, S. Kotelovica, D. Gajan, O. Ouari, K. Tars, G. Pintacuda, and A. Lesage. Dynamic nuclear polarization enhanced biomolecular NMR spectroscopy at high magnetic field with fast magic-angle spinning. *Angew. Chem. Int. Ed.*, in press, 2018.

- [177] A. Lesage, M. Lelli, D. Gajan, M. A. Caporini, V. Vitzthum, P. Miéville, J. Alauzun, A. Roussey, C. Thieuleux, A. Mehdi, G. Bodenhausen, C. Copéret, and L. Emsley. Surface enhanced NMR spectroscopy by dynamic nuclear polarization. *J. Am. Chem. Soc.*, 132:15459–15461, 2010.
- [178] M. A. Hope, D. M. Halat, P. C. M. M. Magusin, S. Paul, L. Peng, and C. P. Grey. Surface-selective direct ^{17}O DNP NMR of CeO_2 nanoparticles. *Chem. Commun.*, 53:2142–2145, 2017.
- [179] M. F. Delley, G. Lapadula, F. Núñez-Zarur, A. Comas-Vivas, V. Kalendra, G. Jeschke, D. Baabe, M. D. Walter, A. J. Rossini, A. Lesage, L. Emsley, O. Maury, and C. Copéret. Local structures and heterogeneity of silica-supported M(III) sites evidenced by EPR, IR, NMR, and luminescence spectroscopies. *J. Am. Chem. Soc.*, 139:8855–8867, 2017.
- [180] B. Corzilius, A. A. Smith, A. B. Barnes, C. Luchinat, I. Bertini, and R. G. Griffin. High-field dynamic nuclear polarization with high-spin transition metal ions. *J. Am. Chem. Soc.*, 133:5648–5651, 2011.
- [181] M. Kaushik, T. Bahrenberg, T. V. Can, M. A. Caporini, R. Silvers, J. Heiliger, A. A. Smith, H. Schwalbe, R. G. Griffin, and B. Corzilius. Gd(III) and Mn(II) complexes for dynamic nuclear polarization: small molecular chelate polarizing agents and applications with site-directed spin labeling of proteins. *Phys. Chem. Chem. Phys.*, 18:27205–27218, 2016.
- [182] K. R. Thurber and R. Tycko. Perturbation of nuclear spin polarizations in solid state NMR of nitroxide-doped samples by magic-angle spinning without microwaves. *J. Chem. Phys.*, 140:184201, 2014.
- [183] A. Abragam. *Principles of Nuclear Magnetism*. Oxford University Press, Oxford, 1961.
- [184] A. Abragam and B. Bleaney. *Electron Paramagnetic Resonance of Transition Ions*. Oxford University Press, Oxford, 1970.
- [185] J. A. Weil and J. R. Bolton. *Electron Paramagnetic Resonance: Elementary Theory and Practical Applications*. John Wiley & Sons, Inc., Hoboken, New Jersey, 2007.
- [186] J. D. Jackson. *Classical Electrodynamics: Third Edition*. John Wiley & Sons, Inc., Hoboken, New Jersey, USA, 1999.
- [187] S. Blundell. *Magnetism in condensed matter*. Oxford University Press, Oxford, 2001.

- [188] N. W. Ashcroft and N. D. Mermin. *Solid State Physics*. Thomson Learning, London, UK, 1976.
- [189] K. F. Riley, M. P. Hobson, and S. J. Bence. *Mathematical Methods for Physics and Engineering*. Cambridge University Press, Cambridge, 1997.
- [190] D. M. Brink and G. R. Satchler. *Angular Momentum*. Clarendon Press, Oxford, 1993.
- [191] N. F. Ramsey. Magnetic shielding of nuclei in molecules. *Phys. Rev.*, 78:699–703, 1950.
- [192] U. Haeberlen and J. S. Waugh. Coherent averaging effects in magnetic resonance. *Phys. Rev.*, 175:453–467, 1968.
- [193] S. E. Ashbrook, J. McManus, M. J. Thrippleton, and S. Wimperis. Second-order cross-term interactions in high-resolution MAS NMR of quadrupolar nuclei. *Prog. Nucl. Magn. Reson. Spectrosc.*, 55:160–181, 2009.
- [194] M. Mehring. *Principles of High-Resolution NMR in Solids*. Springer Verlag, Berlin, 1983.
- [195] C. P. Bean and J. D. Livingston. Superparamagnetism. *J. Appl. Phys.*, 30:120S–129S, 1959.
- [196] S. Bedanta and W. Kleemann. Superparamagnetism. *J. Phys. D: Appl. Phys.*, 42:013001, 2009.
- [197] L. Bordonali, Y. Furukawa, M. Kraken, F. J. Litterst, C. Sangregorio, M. F. Casula, and A. Lascialfari. ^1H NMR study of the spin dynamics of fine superparamagnetic nanoparticles. *Phys. Rev. B*, 85:174426, 2012.
- [198] S. E. Ashbrook and M. J. Duer. Structural information from quadrupolar nuclei in solid state NMR. *Concept. Magn. Reson. A*, 28A:183–248, 2006.
- [199] B. J. Walder, K. K. Dey, M. C. Davis, J. H. Baltisberger, and P. J. Grandinetti. Two-dimensional NMR measurement and point dipole model prediction of paramagnetic shift tensors in solids. *J. Chem. Phys.*, 142:014201, 2015.
- [200] J. Autschbach, S. Patchkovskii, and B. Pritchard. Calculation of hyperfine tensors and paramagnetic NMR shifts using the relativistic zeroth-order regular approximation and density functional theory. *J. Chem. Theory Comput.*, 7:2175–2188, 2011.

- [201] M. Kaupp, M. Bühl, and V. G. Malkin, editors. *Calculation of NMR and EPR Parameters: Theory and Applications*. Wiley-VCH, Weinheim, 2004.
- [202] A. C. Hennum, W. Klopper, and T. Helgaker. Direct perturbation theory of magnetic properties and relativistic corrections for the point nuclear and Gaussian nuclear models. *J. Chem. Phys.*, 115:7356–7363, 2001.
- [203] E. Malkin, I. Malkin, O. L. Malkina, V. G. Malkin, and M. Kaupp. Scalar relativistic calculations of hyperfine coupling tensors using the Douglas–Kroll–Hess method with a finite-size nucleus model. *Phys. Chem. Chem. Phys.*, 8:4079–4085, 2006.
- [204] J. Autschbach. Magnitude of finite-nucleus-size effects in relativistic density functional computations of indirect nmr nuclear spin–spin coupling constants. *ChemPhysChem*, 10:2274–2283, 2009.
- [205] J. Autschbach. Relativistic effects on electron–nucleus hyperfine coupling studied with an exact 2-component (X2C) Hamiltonian. *J. Chem. Theory Comput.*, 13:710–718, 2017.
- [206] P. Atkins and R. Friedman. *Molecular Quantum Mechanics*. Oxford University Press, Oxford, 2005.
- [207] R. Boca. Zero-field splitting in metal complexes. *Coord. Chem. Rev.*, 248:757–815, 2004.
- [208] C. J. Pickard and F. Mauri. First-principles theory of the EPR *g*-tensor in solids: Defects in quartz. *Phys. Rev. Lett.*, 88:086403, 2002.
- [209] T. O. Pennanen, J. Vaara, and M. Kaupp. Density-functional calculations of relativistic spin-orbit effects on nuclear magnetic shielding in paramagnetic molecules. *J. Chem. Phys.*, 123:174102, 2005.
- [210] A. V. Arbuznikov, J. Vaara, and M. Kaupp. Relativistic spin-orbit effects on hyperfine coupling tensors by density-functional theory. *J. Chem. Phys.*, 120:2127–2139, 2004.
- [211] F. Neese. Calculation of the zero-field splitting tensor on the basis of hybrid density functional and Hartree-Fock theory. *J. Chem. Phys.*, 127:164112, 2007.
- [212] J. Autschbach. NMR calculations for paramagnetic molecules and metal complexes. *Annu. Rep. Comput. Chem.*, 11:3–36, 2015.

- [213] M. Gerloch and R. F. McMeeking. Paramagnetic properties of unsymmetrical transition-metal complexes. *J. Chem. Soc. Dalton Trans.*, pages 2443–2451, 1975.
- [214] I. Bertini and C. Luchinat. Appendices. *Coord. Chem. Rev.*, 150:265–292, 1996.
- [215] E. A. Suturina and I. Kuprov. Pseudocontact shifts from mobile spin labels. *Phys. Chem. Chem. Phys.*, 18:26412–26422, 2016.
- [216] L. Benda, J. Mares, E. Ravera, G. Parigi, C. Luchinat, M. Kaupp, and J. Vaara. Pseudo-contact NMR shifts over the paramagnetic metalloprotein CoMMP-12 from first principles. *Angew. Chem. Int. Ed.*, 55:14713–14717, 2016.
- [217] F. H. Köhler and O. Storcheva. Paramagnetic prussian blue analogues $\text{CsM}^{\text{II}}[\text{M}^{\text{III}}(\text{CN})_6]$. the quest for spin on cesium ions by use of ^{133}Cs MAS NMR spectroscopy. *Inorg. Chem.*, 54:6801–6806, 2015.
- [218] B. Henderson and G. F. Imbusch. *Optical Spectroscopy of Inorganic Solids*. Oxford University Press, Oxford, 1989.
- [219] K. W. H. Stevens. Matrix elements and operator equivalents connected with the magnetic properties of rare earth ions. *Proc. Phys. Soc. A*, 65:209–215, 1952.
- [220] H. A. Buckmaster, R. Chatterjee, and Y. H. Shing. The application of tensor operators in the analysis of EPR and ENDOR spectra. *Phys. Stat. Sol. A*, 13:9–50, 1972.
- [221] C. Rudowicz and M. Karbowski. Terminological confusions and problems at the interface between the crystal field Hamiltonians and the zero-field splitting Hamiltonians—Survey of the CF14ZFS confusion in recent literature. *Physica B*, 451:134–150, 2014.
- [222] J. S. Griffith. Some investigations in the theory of open-shell ions Part I. the spin-Hamiltonian. *Mol. Phys.*, 3:79–89, 1960.
- [223] H. A. Buckmaster and Y. H. Shing. A survey of the EPR spectra of Gd^{3+} in single crystals. *Phys. Stat. Sol. A*, 12:325–361, 1972.
- [224] S. A. Marshall and R. A. Tilton. Zeeman interaction for the ^8S term of Gd^{3+} in ThO_2 . *Phys. Lett. A*, 30:216–217, 1969.

- [225] H. A. Buckmaster, R. Chatterjee, and Y. H. Shing. Determination of the generalized spin-hamiltonian parameters of Gd^{3+} in lanthanum ethylsulphate at 290 K. *J. Magn. Reson.*, 4:85–89, 1971.
- [226] A. R. Edmonds. *Angular Momentum in Quantum Mechanics*. Princeton University Press, Princeton, New Jersey, 1957.
- [227] C. Görller-Walrand and K. Binnemans. *Handbook on the physics and chemistry of rare earths*, volume 23. Elsevier, 1996.
- [228] T. Marks and A. M. Seyam. Stable uranium(IV) alkyl and aryl complexes. *J. Am. Chem. Soc.*, 94:6545–6546, 1972.
- [229] D. L. Clark, D. E. Hobart, and M. P. Neu. Actinide carbonyl complexes and their importance in actinide environmental chemistry. *Chem. Rev.*, 95:25–48, 1995.
- [230] K. Mizuoka, I. Grenthe, and Y. Ikeda. Structural and kinetic studies on uranyl(V) carbonate complex using ^{13}C NMR spectroscopy. *Inorg. Chem.*, 44:4472–4474, 2005.
- [231] H. Xiang, C. Lee, H.-J. Koo, X. Gong, and M.-H. Whangbo. Magnetic properties and energy-mapping analysis. *Dalton Trans.*, 42:823–853, 2013.
- [232] H.-J. Koo, H. J. Xiang, C. Lee, and M.-H. Whangbo. Effect of magnetic dipole–dipole interactions on the spin orientation and magnetic ordering of the spin-ladder compound $Sr_3Fe_2O_5$. *Inorg. Chem.*, 48:9051–9053, 2009.
- [233] D. Dai, H. J. Xiang, and M.-H. Whangbo. Effects of spin-orbit coupling on magnetic properties of discrete and extended magnetic systems. *J. Comput. Chem.*, 29:2187–2209, 2008.
- [234] I. Dzyaloshinskii. A thermodynamic theory of “weak” ferromagnetism of antiferromagnetics. *J. Phys. Chem. Solids*, 4:241–255, 1958.
- [235] T. Moriya. New mechanism of anisotropic superexchange interaction. *Phys. Rev. Lett.*, 4:228–230, 1960.
- [236] D. S. Middlemiss, F. Blanc, C. J. Pickard, and C. P. Grey. Solid-state NMR calculations for metal oxides and gallates: Shielding and quadrupolar parameters for perovskites and related phases. *J. Magn. Reson.*, 204:1–10, 2010.

- [237] F. Neese. Metal and ligand hyperfine couplings in transition metal complexes: The effect of spinorbit coupling as studied by coupled perturbed Kohn–Sham theory. *J. Chem. Phys.*, 118:3939–3948, 2003.
- [238] J. B. Goodenough. Theory of the role of covalence in the perovskite-type manganites $[\text{La},\text{M}(\text{II})]\text{MnO}_3$. *Phys. Rev.*, 100:564–573, 1955.
- [239] J. Kanamori. Superexchange interaction and symmetry properties of electron orbitals. *J. Phys. Chem. Solids*, 10:87–89, 1959.
- [240] J. B. Goodenough. An interpretation of the magnetic properties of the perovskite-type mixed crystals $\text{La}_{1-x}\text{Sr}_x\text{CoO}_{1-\lambda}$. *J. Phys. Chem. Solids*, 6:287–297, 1958.
- [241] S. Lee, S. Choi, J. Kim, H. Sim, C. Won, S. Lee, S. A. Kim, N. Hur, and J.-G. Park. Antiferromagnetic ordering in Li_2MnO_3 single crystals with a two-dimensional honeycomb lattice. *J. Phys. Condens. Matter*, 24:456004, 2012.
- [242] E. J. Lee, C. and Kan, H. J. Xiang, R. K. Kremer, S.-H. Lee, Z. Hiroi, and M.-H. Whangbo. Spin reorientation in the square-lattice antiferromagnets RMnAsO ($\text{R} = \text{Ce}, \text{Nd}$): Density functional analysis of the spin-exchange interactions between the rare-earth and transition-metal ions. *Inorg. Chem.*, 51:6890–6897, 2012.
- [243] C. H. Townes, C. Herring, and W. D. Knight. The effect of electronic paramagnetism on nuclear magnetic resonance frequencies in metals. *Phys. Rev.*, 77:852–853, 1950.
- [244] J. P. Yesinowski. Solid-state NMR of inorganic semiconductors. *Top. Curr. Chem.*, 306:229–312, 2012.
- [245] C. P. Slichter. *Principles of magnetic resonance*. Harpeter & Row, New York, Evanston, and London, 1963.
- [246] A. G. Redfield. The theory of relaxation processes. *Adv. Magn. Reson.*, 1:1–32, 1965.
- [247] I. Bertini and C. Luchinat. Chapter 3: Relaxation. *Coord. Chem. Rev.*, 150:77–110, 1996.
- [248] D. Kruk. *Theory of Evolution and Relaxation of Multi-spin Systems*. Arima Publishing, Bury St Edmunds, UK, 2007.

- [249] D. Kruk. *Understanding spin dynamics*. Pan Stanford Publishing Pte Ltd, Singapore, 2016.
- [250] R. K. Harris and R. Wasylshen, editors. *Paramagnetic Relaxation in Solution*. John Wiley, Chichester, 2011.
- [251] E. Belorizky, P. H. Fries, L. Helm, J. Kowalewski, D. Kruk, R. R. Sharp, and P.-O. Westlund. Comparison of different methods for calculating the paramagnetic relaxation enhancement of nuclear spins as a function of the magnetic field. *J. Chem. Phys.*, 128:052315, 2008.
- [252] M. Goldman. *Quantum Description of High-Resolution NMR in Liquids*. Oxford University Press, Oxford, 1991.
- [253] M. Goldman. Advances in magnetic resonance: Formal theory of spin–lattice relaxation. *J. Magn. Reson.*, 149:160–187, 2001.
- [254] J. Keeler. *Understanding NMR Spectroscopy Second Edition*. Wiley and Sons, Ltd, Chichester, 2010.
- [255] J. H. Van Vleck. Paramagnetic relaxation times for titanium and chrome alum. *Phys. Rev.*, 57:426–447, 1940.
- [256] R. Orbach. Spin-lattice relaxation in rare-earth salts. *Proc. R. Soc. London, Ser. A*, 264:458–484, 1961.
- [257] R. R. Ernst, G. Bodenhausen, and A. Wokaun. *Principles of nuclear magnetic resonance in one and two dimensions*. Oxford University Press, Oxford, 1987.
- [258] M. Goldman, P. J. Grandinetti, A. Llor, Z. Olejniczak, R. J. Sachleben, and J. W. Zwanziger. Theoretical aspects of higher-order truncations in solid-state nuclear magnetic resonance. *J. Chem. Phys.*, 97:8947–8960, 1992.
- [259] I. Bertini, A. Donaire, C. Luchinat, and A. Rosato. Paramagnetic relaxation as a tool for solution structure determination: *Clostridium pasteurianum* ferredoxin as an example. *Proteins: Struct., Function, Genet.*, 29:348–358, 1997.
- [260] L. X. Ma, A. M. M. Jorgensen, G. O. Sorensen, J. Ulstrup, and J. J. Led. Elucidation of the paramagnetic R-1 relaxation of heteronuclei and protons in Cu(II) plastocyanin from *anabaena variabilis*. *J. Am. Chem. Soc.*, 122:9473–9485, 2000.

- [261] L. Nordenskiöld, A. Laaksonen, and J. Kowalewski. Applicability of the Solomon–Bloembergen equation to the study of paramagnetic transition metal–water complexes. An *ab initio* SCF-MO study. *J. Am. Chem. Soc.*, 104:379–383, 1982.
- [262] E. Toth, L. Helm, K. E. Kellar, and A. E. Merbach. Gd(DPTA-bisamide)alkyl copolymers: a hint for the formation of MRI contrast agents with very high relaxivity. *Chem. Eur. J.*, 5:1202–1211, 1999.
- [263] P.-O. Westlund. A generalised Solomon–Bloembergen–Morgan theory for arbitrary electron spin quantum number S — the dipole–dipole coupling between a nuclear spin $I = 1/2$ and an electron spin system $S = 5/2$. *Mol. Phys.*, 85:1165–1178, 1995.
- [264] S. Wimperis and G. Bodenhausen. Relaxation-allowed cross-peaks in two-dimensional N.M.R. correlation spectroscopy. *Mol. Phys.*, 66:897–919, 1989.
- [265] I. Bertini, C. Luchinat, and D. Tarchi. Are true scalar proton–proton connectivities ever measured in COSY spectra of paramagnetic macromolecules? *Chem. Phys. Lett.*, 203:445–449, 1993.
- [266] K. Pervushin, R. Riek, G. Wider, and K. Wüthrich. Attenuated T_2 relaxation by mutual cancellation of dipole–dipole coupling and chemical shift anisotropy indicates an avenue to NMR structures of very large biological macromolecules in solution. *Proc. Natl. Acad. Sci. USA*, 94:12366–12371, 1997.
- [267] R. C. Wilson and R. J. Myers. Electron paramagnetic resonance spectrum and spin relaxation for $\text{Ti}(\text{H}_2\text{O})_6^{3+}$ in aqueous solution and in frozen glass. *J. Chem. Phys.*, 64:2208–2211, 1976.
- [268] I. Bertini, C. Luchinat, and Z. Xia. Electronic relaxation of the titanium(III) hexaaqua complex detected by solvent water ^1H NMRD spectroscopy. *Inorg. Chem.*, 31:3152–3154, 1992.
- [269] R. N. Rogers and G. E. Pake. Paramagnetic relaxation in solutions of VO^{++} . *J. Chem. Phys.*, 33:1107–1111, 1960.
- [270] D. Kivelson. Electric-field fluctuations and spin relaxation in liquids. *J. Chem. Phys.*, 45:1324–1332, 1966.
- [271] D. C. McCain and R. J. Myers. Spin-lattice and spin-spin relaxation times for VO^{2+} in aqueous solution. *J. Phys. Chem.*, 71:192–200, 1967.

- [272] D. R. Eaton. The nuclear magnetic resonance of some paramagnetic transition-metal acetylacetonates. *J. Am. Chem. Soc.*, 87:3097–3102, 1965.
- [273] A. M. Chmelnick and D. Fiat. Hydration of the vanadium (III) ion by oxygen-17 and proton magnetic resonance. *J. Magn. Reson.*, 8:325–331, 1972.
- [274] G. L. McPherson, R. C. Koch, and G. D. Stucky. Electron spin resonance spectra of V^{2+} , Mn^{2+} , and Ni^{2+} in single crystals of $CsMgBr_3$ and $CsMgI_3$. *J. Chem. Phys.*, 60:1424–1431, 1974.
- [275] B. R. McGarvey. Line widths in the paramagnetic resonance of transition ions in solution. *J. Phys. Chem.*, 61:1232–1237, 1957.
- [276] G. N. La Mar and F. A. Walker. Proton nuclear magnetic resonance and electron spin resonance investigation of the electronic structure and magnetic properties of synthetic low-spin ferric porphyrins. *J. Am. Chem. Soc.*, 95:1782–1790, 1973.
- [277] G. N. La Mar and G. R. Van Hecke. Proton nuclear magnetic resonance studies of spin delocalization in low-spin chelates of chromium (II) and iron (III) with symmetrically substituted *o*-phenanthrolines and α, α' -bipyridines. *J. Am. Chem. Soc.*, 91:3442–3450, 1969.
- [278] S. H. Koenig, R. D. Brown III, and M. Spiller. The anomalous relaxivity of $Mn^{3+}(TPPS_4)$. *Magn. Reson. Med.*, 4:252–260, 1987.
- [279] M. Grant, H. W. Dodgen, and J. P. Hunt. Water exchange between solvent and aquomanganese(II) and aquophenanthroline manganese(II) complexes. *Inorg. Chem.*, 10:71–72, 1971.
- [280] I. Bertini, F. Capozzi, C. Luchinat, and Z. Xia. Nuclear and electron relaxation of $Fe(OH_2)_6^{3+}$. *J. Phys. Chem.*, 97:1134–1137, 1993.
- [281] I. Bertini, O. Galas, C. Luchinat, L. Messori, and G. Parigi. A theoretical analysis of the 1H nuclear magnetic relaxation dispersion profiles of diferric transferrin. *J. Phys. Chem.*, 99:14217–14222, 1995.
- [282] L. P. Yu, G. N. La Mar, and K. Rajarathnam. 1H NMR resonance assignment of the active site residues of paramagnetic proteins by 2D bond correlation spectroscopy: Metcyanomyoglobin. *J. Am. Chem. Soc.*, 112:9527–9534, 1990.

- [283] L. Banci, I. Bertini, S. Marconi, R. Pierattelli, and S. G. Sligar. Cytochrome P450 and aromatic bases: A ^1H NMR study. *J. Am. Chem. Soc.*, 116:4866–4873, 1994.
- [284] Y. Ducommun, K. E. Newman, and A. E. Merbach. High-pressure ^{17}O NMR evidence for a gradual mechanistic changeover from i_a to i_d for water exchange on divalent octahedral metal ions going from manganese(II) to nickel(II). *Inorg. Chem.*, 19:3696–3703, 1980.
- [285] L. Banci, I. Bertini, S. Marconi, and R. Pierattelli. ^1H -NMR study of reduced heme proteins myoglobin and cytochrome P450. *Eur. J. Biochem.*, 215:431–437, 1993.
- [286] M. T. Werth and M. Kurtz Jr. ^1H -NMR spectra of rubredoxins: New resonances assignable to α -CH and β -CH₂ hydrogens of cysteinate ligands to iron(II). *J. Am. Chem. Soc.*, 109:273–275, 1987.
- [287] A. M. Chmelnick and D. Fiat. Magnetic resonance studies of ion solvation. the hydration of the cobaltous ion. *J. Chem. Phys.*, 47:3986–3990, 1967.
- [288] L. Banci, I. Bertini, and C. Luchinat. ^1H NMRD studies of solutions of paramagnetic metal ions in ethyleneglycol. *Inorg. Chim. Acta*, 100:173–181, 1985.
- [289] I. Bertini, C. Luchinat, M. Mancini, and G. Spina. The electron–nucleus dipolar coupling. the effect of zero-field splitting of an $S = 3/2$ manifold. *J. Magn. Reson.*, 59:213–222, 1984.
- [290] C. Chachaty, A. Forchioni, J. Virlet, and J. C. Ronfard-Haret. Spin densities, ligand exchange and ^{13}C relaxation in aniline-Ni II complexes. *Chem. Phys. Lett.*, 29:436–440, 1974.
- [291] G. N. La Mar. Electron spin relaxation in pseudo-tetrahedral cobalt(II) and nickel(II) complexes in solution. *J. Am. Chem. Soc.*, 87:3567–3571, 1965.
- [292] L.-J. Ming, L. Banci, C. Luchinat, I. Bertini, and J. S. Valentine. Characterisation of copper–nickel and silver–nickel bovine superoxide dismutase by ^1H NMR spectroscopy. *Inorg. Chem.*, 27:4458–4463, 1988.
- [293] U. E. Steiner and Bürßner. Theoretical treatment of magnetic field dependent in-cage backward electron transfer during photooxidation of Ru(II) complexes. *Z. Phys. Chem. N. F.*, 169:159–180, 1990.

- [294] A. Paulo, A. Domingos, A. P. de Matos, and I. Santos. Synthesis, characterization, and study of the redox properties of rhenium(V) and rhenium(III) compounds with tetrakis(pyrazo1-1-y1)borate. *Inorg. Chem.*, 33:4729–4737, 1994.
- [295] S. Aime, M. Botta, and G. Ermondi. NMR study of solution structures and dynamics of lanthanide(III) complexes of DOTA. *Inorg. Chem.*, 31:4291–4299, 1992.
- [296] I. Bertini, F. Capozzi, C. Luchinat, G. Nicastro, and Z. Xia. Water proton relaxation for some lanthanide aqua ions in solution. *J. Phys. Chem.*, 97:6351–6354, 1993.
- [297] G. P. Vishnevskaya and B. M. Kozyrev. Effect of solvent on the paramagnetic relaxation constants in liquid solutions of gadolinium nitrate. *J. Struct. Chem.*, 7:20–24, 1966.
- [298] A. Hudson and J. W. E. Lewis. Electron spin relaxation of 8S ions in solution. *Trans. Faraday Soc.*, 66:1297–1301, 1970.
- [299] V. M. Malhotra, H. A. Buckmaster, and J. M. Dixon. Estimation of τ_1 for Yb^{3+} ions from the temperature variation of the EPR linewidths for Gd^{3+} in $\text{YbCl}_3 \cdot 6\text{H}_2\text{O}$ single crystals. *J. Phys. C: Solid St. Phys.*, 13:3921–3931, 1980.
- [300] G. Hernandez, M. F. Tweedle, and R. G. Bryant. Proton magnetic relaxation dispersion in aqueous glycerol solutions of $\text{Gd}(\text{DTPA})^{2-}$ and $\text{Gd}(\text{DOTA})^-$. *Inorg. Chem.*, 29:5109–5113, 1990.
- [301] S. Aime, L. Barbero, and M. Botta. Trends in NMR studies of paramagnetic Gd(III) complexes as potential contrast agents in MRI. *Magn. Reson. Imag.*, 9:843–847, 1991.
- [302] S. H. Koenig. From the relaxivity of $\text{Gd}(\text{DTPA})^{2-}$ to everything else. *Magn. Reson. Med.*, 22:183–190, 1991.
- [303] S. K. Misra and U. Orhun. Spin-lattice relaxation time of Yb^{3+} in $\text{YbCl}_3 \cdot 6\text{H}_2\text{O}$. *Solid State Commun.*, 63:867–869, 1987.
- [304] L. P. Hwang and C.-Y. Ju. Proton spin relaxations in solutions of paramagnetic complex with $S = 3/2$ in slow motion region. *J. Chem. Phys.*, 83:3775–3789, 1985.

- [305] P. L. Wang, J.-H. Lee, S.-M. Huang, and L. P. Hwang. Proton spin relaxation in solutions of the complex tris(acetylacetonato)chromium(III). *J. Magn. Reson.*, 73:277–286, 1987.
- [306] D. Kruk and J. Kowalewski. Nuclear spin relaxation in paramagnetic systems ($S \geq 1$) under fast rotation conditions. *J. Magn. Reson.*, 162:229–240, 2003.
- [307] D. Kruk, A. Kubica, W. Masierak, A. F. Privalov, M. Wojciechowski, and W. Medycki. Quadrupole relaxation enhancement—application to molecular crystals. *Solid State Nucl. Magn. Reson.*, 40:114–120, 2011.
- [308] W. Masierak, M. Florek-Wojciechowski, I. Oglodek, R. Jakubas, A. F. Privalov, B. Kresse, F. Fujara, and D. Kruk. Dynamics of $[\text{C}_3\text{H}_5\text{N}_2]_6[\text{Bi}_4\text{Br}_{18}]$ by means of ^1H NMR relaxometry and quadrupole relaxation enhancement. *J. Chem. Phys.*, 142:204503, 2015.
- [309] S. A. Al'tshuler and K. A. Valiev. On the theory of longitudinal relaxation of paramagnetic salt compounds. *Sov. Phys. JETP*, 35:661–668, 1958.
- [310] J. Korringa. Nuclear magnetic relaxation and resonance line shift in metals. *Physica*, 16:601–610, 1950.
- [311] G. Mozurkewich, H. I. Ringermacher, and D. I. Bolef. Effect of demagnetization on magnetic resonance line shapes in bulk samples: Application to tungsten. *Phys. Rev. B*, 20:33–38, 1979.
- [312] T. M. Barbara. Cylindrical demagnetization fields and microprobe design in high-resolution NMR. *J. Magn. Reson. Ser. A*, 109:265–269, 1994.
- [313] C. H. Durney, J. Bertolina, D. C. Ailion, R. Christman, A. G. Cutillo, A. H. Morris, and S. Hashemi. Calculation and interpretation of inhomogeneous line broadening in models of lungs and other heterogeneous structures. *J. Magn. Reson.*, 85:554–570, 1989.
- [314] S. N. Hwang and F. W. Wehrli. The calculation of the susceptibility-induced magnetic field from 3D NMR images with applications to trabecular bone. *J. Magn. Reson. Ser. B*, 109:126–145, 1995.
- [315] J. H. van Vleck. The dipolar broadening of magnetic resonance lines in crystals. *Phys. Rev.*, 74:1168–1183, 1948.

- [316] H. Primas. Generalized perturbation theory in operator form. *Rev. Mod. Phys.*, 35:710–712, 1963.
- [317] M. Goldman, P. J. Grandinetti, A. Llor, Z. Olejniczak, J. R. Sachleben, and J. Zwanziger. Theoretical aspects of higher-order truncations in solid-state nuclear-magnetic-resonance. *J. Chem. Phys.*, 97:8947–8960, 1992.
- [318] M. Leskes, P. K. Madhu, and S. Vega. Floquet theory in solid-state nuclear magnetic resonance. *Prog. NMR. Spectrosc.*, 57:345–380, 2010.
- [319] P. J. Grandinetti, J. T. Ash, and N. M. Trease. Symmetry pathways in solid-state NMR. *Prog. Nucl. Magn. Reson. Spectrosc.*, 59:121–196, 2011.
- [320] G. Bodenhausen, H. Kogler, and R. R. Ernst. Selection of coherence-transfer pathways in NMR pulse experiments. *J. Magn. Reson.*, 58:370–388, 1984.
- [321] S Antonijevec and G. Bodenhausen. Quadrupolar transfer pathways. *J. Magn. Reson.*, 180:297–304, 2006.
- [322] M. M. Maricq and J. S. Waugh. NMR in rotating solids. *J. Chem. Phys.*, 70:3300–3316, 1979.
- [323] M. H. Levitt, D. P. Raleigh, F. Cruzet, and R. G. Griffin. Theory and simulations of homonuclear spin pair systems in rotating solids. *J. Chem. Phys.*, 92:6347–6364, 1990.
- [324] M. H. Levitt. Why do spinning sidebands have the same phase? *J. Magn. Reson.*, 82:427–433, 1989.
- [325] E. R. Andrew, A. Bradbury, and R. G. Eades. Removal of dipolar broadening of nuclear magnetic resonance spectra of solids by specimen rotation. *Nature*, 183:1802–1803, 1959.
- [326] D. T. Edmonds and M. R. Wormald. Theory of resonance in magnetically inhomogeneous specimens and some useful calculations. *J. Magn. Reson.*, 77:223–232, 1988.
- [327] L. F. Fuks, F. S. C. Huang, C. M. Carter, W. A. Edelstein, and P. B. Roemer. Susceptibility, lineshape, and shimming in high-resolution NMR. *J. Magn. Reson.*, 100:229–242, 1992.
- [328] L. E. Drain. The broadening of magnetic resonance lines due to field inhomogeneities in powdered samples. *Proc. Phys. Soc.*, 80:1380–1382, 1962.

- [329] J. Cavanagh, W. J. Fairbrother, A. G. Palmer III, M. Rance, and N. J. Skelton. *Protein NMR spectroscopy: principles and practice*. Academic Press, London, 2007.
- [330] M. J. Duer. *Introduction to solid-state NMR spectroscopy*. Blackwell, Oxford, 2005.
- [331] R. Tycko. BIOMOLECULAR SOLID STATE NMR: Advances in structural methodology and applications to peptide and protein fibrils. *Annu. Rev. Phys. Chem.*, 52:575–606, 2001.
- [332] I. Bertini and C. Luchinat. Chapter 7: Two-dimensional spectra and beyond. *Coord. Chem. Rev.*, 150:185–220, 1996.
- [333] I. Bertini and C. Luchinat. Chapter 9: Hints on experimental techniques. *Coord. Chem. Rev.*, 150:243–264, 1996.
- [334] S. L. Patt and B. D. Sykes. Water eliminated Fourier transform NMR spectroscopy. *J. Chem. Phys.*, 56:3182–3184, 1972.
- [335] T. Inubushi and E. D. Becker. Efficient detection of paramagnetically shifted NMR resonances by optimizing the WEFT pulse sequence. *J. Magn. Reson.*, 51:128–133, 1983.
- [336] K. L. Bren, H. B. Gray, L. Banci, I. Bertini, and P. Turano. Paramagnetic ^1H NMR spectroscopy of the cyanide derivative of Met80Ala-iso-1-cytochrome c. *J. Am. Chem. Soc.*, 117:8067–8073, 1995.
- [337] J. Hochmann and H. Kellerhals. Proton NMR on deoxyhemoglobin: Use of a modified DEFT technique. *J. Magn. Reson.*, 38:23–39, 1980.
- [338] P. J. Chmielewski, L. Latos-Grazynski, and T. Glowiak. Reactions of nickel(II) 2-Aza-5,10,15,20-tetraphenyl-21-carbaporphyrin with methyl iodide. The first structural characterization of a paramagnetic organometallic nickel(II) complex. *J. Am. Chem. Soc.*, 118:5690–5701, 1996.
- [339] I. Bertini, A. Coutsolelos, A. Dikiy, C. Luchinat, G. A. Spyroulias, and A. Troganis. Structural and dynamic information on double-decker Yb^{3+} and Dy^{3+} porphyrin complexes in solution through ^1H NMR. *Inorg. Chem.*, 35:6308–6315, 1996.
- [340] L. Banci, I. Bertini, C. Luchinat, and M. S. Viezzoli. A comment on the proton NMR spectra of cobalt(II)-substituted superoxide dismutases with histidines deuteriated in the .epsilon.1-position. *Inorg. Chem.*, 29:1438–1440, 1990.

- [341] J. T. J. Lecomte, S. W. Unger, and G. N. La Mar. Practical considerations for the measurement of the homonuclear overhauser effect on strongly relaxed protons in paramagnetic proteins. *J. Magn. Reson.*, 94:112–122, 1991.
- [342] L. Di Bari, G. Pintacuda, and P. Salvadori. Solution equilibria in YbDOTMA, a chiral analogue of one of the most successful contrast agents for MRI, GdDOTA. *Eur. J. Inorg. Chem.*, pages 75–82, 2000.
- [343] M. A. Smith, H. Hu, and A. J. Shaka. Improved broadband inversion performance for NMR in liquids. *J. Magn. Reson.*, 151:269–283, 2001.
- [344] S. Ciofi-Baffoni, A. Gallo, R. Muzzioli, and M. Piccioli. The IR-¹⁵N-HSQC-AP experiment: a new tool for NMR spectroscopy of paramagnetic molecules. *J. Biomol. NMR*, 58:123–128, 2015.
- [345] I. Bertini, C. Luchinat, G. Parigi, and R. Pierattelli. NMR spectroscopy of paramagnetic metalloproteins. *ChemBioChem*, 6:1536–1549, 2005.
- [346] P. H. J. Keizers and M. Ubbink. Paramagnetic tagging for protein structure and dynamics analysis. *Prog. Nucl. Magn. Reson. Spectrosc.*, 58:88–96, 2011.
- [347] M. Sattler, J. Schleucher, and C. Griesinger. Heteronuclear multidimensional NMR experiments for the structure determination of proteins in solution employing pulsed field gradients. *Prog. Nucl. Magn. Reson. Spectrosc.*, 34:93–158, 1999.
- [348] W. Bermel, I. Bertini, I. C. Felli, R. Kümmerle, and R. Pierattelli. ¹³C direct detection experiments on the paramagnetic oxidized monomeric copper, zinc superoxide dismutase. *J. Am. Chem. Soc.*, 125:16423–16429, 2003.
- [349] W. Bermel, I. Bertini, L. Duma, I. C. Felli, L. Emsley, R. Pierattelli, and P. R. Vasos. Complete assignment of heteronuclear protein resonances by protonless NMR spectroscopy. *Angew. Chem. Int. Ed.*, 44:3089–3092, 2005.
- [350] W. Bermel, I. Bertini, I. C. Felli, Y.-M. Lee, L. Luchinat, and R. Pierrattelli. Protonless NMR experiments for sequence-specific assignment of backbone nuclei in unfolded proteins. *J. Am. Chem. Soc.*, 128:3918–3919, 2006.

- [351] W. Bermel, I. Bertini, I. C. Felli, R. Kümmerle, and R. Pierattelli. Novel ^{13}C direct detection experiments, including extension to the third dimension, to perform the complete assignment of proteins. *J. Magn. Reson.*, 178:56–64, 2006.
- [352] I. Bertini, F. Briganti, C. Luchinat, and A. Scozzafava. ^1H NMR studies of the oxidized and partially reduced 2(4Fe–4S) ferredoxin from *clostridium pasteurianum*. *Inorg. Chem.*, 29:1874–1880, 1990.
- [353] I. Bertini, F. Briganti, C. Luchinat, L. Messori, R. Monnanni, A. Scozzafava, and G. Vallini. 2D ^1H NMR studies of oxidized 2(4Fe–4S) ferredoxin from *clostridium pasteurianum*. *FEBS. Lett.*, 289:253–256, 1991.
- [354] S. C. Busse, G. N. La Mar, and J. B. Howard. Two-dimensional NMR investigation of iron-sulfur cluster electronic and molecular structure of oxidized *clostridium pasteurianum* ferredoxin. Interpretability of contact shifts in terms of cysteine orientation. *J. Biol. Chem.*, 266:23714–23723, 1991.
- [355] I. Bertini, F. Capozzi, C. Luchinat, M. Piccioli, and A. J. Vila. Applications of COSY to paramagnetic heme-containing systems. *J. Magn. Reson.*, 95:244–252, 1991.
- [356] G. Pintacuda, M. A. Keniry, T. Huber, A. Y. Park, N. E. Dixon, and G. Otting. Fast structure-based assignment of ^{15}N HSQC spectra of selectively ^{15}N -labeled paramagnetic proteins. *J. Am. Chem. Soc.*, 126:2963–2970, 2004.
- [357] E. Babini, I. Bertini, F. Capozzi, I. C. Felli, M. Lelli, and C. Luchinat. Direct carbon detection in paramagnetic metalloproteins to further exploit pseudocontact shift restraints. *J. Am. Chem. Soc.*, 126:10496–10497, 2004.
- [358] I. Bertini, B. Jiménez, and M. Piccioli. ^{13}C direct detected experiments: Optimization for paramagnetic signals. *J. Magn. Reson.*, 174:125–132, 2005.
- [359] I. Bertini, L. Duma, I. C. Felli, M. Fey, C. Luchinat, R. Pierattelli, and P. R. Vasos. A heteronuclear direct-detection NMR spectroscopy experiment for protein-backbone assignment. *Angew. Chem. Int. Ed.*, 43:2257–2259, 2004.
- [360] W. Bermel, I. Bertini, I. C. Felli, R. Pierattelli, and P. R. Vasos. A selective experiment for the sequential protein backbone assignment from 3D heteronuclear spectra. *J. Magn. Reson.*, 172:324–328, 2005.

- [361] W. Bermel, I. Bertini, I. C. Felli, M. Piccioli, and R. Pierattelli. ^{13}C -detected *protonless* NMR spectroscopy of proteins in solution. *Prog. Nucl. Magn. Reson. Spectrosc.*, 48:25–45, 2006.
- [362] M. Kostic, S. S. Pochapsky, and T. C. Pochapsky. Rapid recycle ^{13}C , ^{15}N and ^{13}C , $^{13}\text{C}'$ heteronuclear and homonuclear multiple quantum coherence detection for resonance assignments in paramagnetic proteins: Example of Ni^{2+} -containing acireductone dioxygenase. *J. Am. Chem. Soc.*, 124:9054–9055, 2002.
- [363] I. Bertini, F. Capozzi, C. Luchinat, M. Piccioli, and A. J. Vila. The Fe_4S_4 centers in ferredoxins studied through proton and carbon hyperfine coupling. Sequence-specific assignments of cysteines in ferredoxins from *clostridium acidi urici* and *clostridium pasteurianum*. *J. Am. Chem. Soc.*, 116:651–660, 1994.
- [364] R. Krishnamoorthi, J. L. Markley, M. A. Cusanovich, C. T. Przywiecki, and T. E. Meyer. Hydrogen-1 nuclear magnetic resonance investigation of high-potential iron-sulfur proteins from *Ectothiorhodospira halophila* and *Ectothiorhodospira vacuolata*: a comparative study of hyperfine-shifted resonances. *Biochemistry*, 25:60–67, 1986.
- [365] I. Bertini, A. Donaire, B. A. Feinberg, C. Luchinat, M. Piccioli, and H. Yuan. Solution structure of the oxidized 2[4Fe-4S] ferredoxin from *Clostridium pasteurianum*. *Eur. J. Biochem.*, 232:192–205, 1995.
- [366] S. Aono, D. Bentrop, I. Bertini, A. Donaire, C. Luchinat, Y. Niikura, and A. Rosato. Solution structure of the oxidized Fe_7S_8 ferredoxin from the thermophilic bacterium *Bacillus schlegelii* by ^1H NMR spectroscopy. *Biochemistry*, 37:9812–9826, 1998.
- [367] R. O. Louro, I. J. Correia, L. Brennan, I. B. Coutinho, A. V. Xavier, and D. L. Turner. Electronic structure of low-spin ferric porphyrins: ^{13}C NMR studies of the influence of axial ligand orientation. *J. Am. Chem. Soc.*, 120:13240–13247, 1998.
- [368] I. Bertini, C. Luchinat, G. Parigi, and F. A. Walker. Heme methyl ^1H chemical shifts as structural parameters in some low-spin ferriheme proteins. *J. Biol. Inorg. Chem.*, 4:515–519, 1999.
- [369] F. A. Walker. Magnetic spectroscopic (EPR, ESEEM, Mössbauer, MCD and NMR) studies of low-spin ferriheme centers and their corresponding heme proteins. *Coord. Chem. Rev.*, 185-186:471–534, 1999.

- [370] L. Banci, I. Bertini, G. Cavallaro, and C. Luchinat. Chemical shift-based constraints for solution structure determination of paramagnetic low-spin heme proteins with bis-His and His-CN axial ligands: the cases of oxidized cytochrome b(5) and Met80Ala cyano-cytochrome c. *J. Biol. Inorg. Chem.*, 7:416–426, 2002.
- [371] I. Bertini, S. Ciurli, A. Dikiy, R. Gasanov, C. Luchinat, G. Martini, and N. Safarov. High-field NMR studies of oxidized blue copper proteins: The case of spinach plastocyanin. *J. Am. Chem. Soc.*, 121:2037–2046, 1999.
- [372] I. Bertini, C. O. Fernández, B. G. Karlsson, J. Leckner, C. Luchinat, B. G. Malmström, A. N. Nersissian, R. Pierattelli, E. Shipp, J. S. Valentine, and A. J. Vila. Structural information through NMR hyperfine shifts in blue copper proteins. *J. Am. Chem. Soc.*, 122:3701–3707, 2000.
- [373] D. F. Hansen and J. J. Led. Determination of the geometric structure of the metal site in a blue copper protein by paramagnetic NMR. *Proc. Natl. Acad. Sci. USA*, 103:1738–1743, 2006.
- [374] R. Ghose and J. H. Prestegard. Electron spin–nuclear spin cross-correlation effects on multiplet splittings in paramagnetic proteins. *J. Magn. Reson.*, 128:138–143, 1997.
- [375] J. Boisbouvier, P. Gans, M. Blackledge, B. Brutscher, and D. Marion. Long-range structural information in NMR studies of paramagnetic molecules from electron spin–nuclear spin cross-correlated relaxation. *J. Am. Chem. Soc.*, 121:7700–7701, 1999.
- [376] I. Bertini, J. Kowalewski, C. Luchinat, and G. Parigi. Cross correlation between the dipole–dipole interaction and the curie spin relaxation: The effect of anisotropic magnetic susceptibility. *J. Magn. Reson.*, 152:103–108, 2001.
- [377] G. Pintacuda, K. Hohenthanner, G. Otting, and N. Müller. Angular dependence of dipole-dipole-Curie-spin cross-correlation effects in high-spin and low-spin paramagnetic myoglobin. *J. Biomol. NMR*, 27:115–132, 2003.
- [378] J. R. Tolman, J. M. Flanagan, M. A. Kennedy, and J. H. Prestegard. Nuclear magnetic dipole interactions in field-oriented proteins: Information for structure determination in solution. *Proc. Natl. Acad. Sci. USA*, 92:9279–9283, 1995.

- [379] L. Banci, I. Bertini, J. G. Huber, C. Luchinat, and A. J. Rosato. Partial orientation of oxidized and reduced cytochrome b₅ at high magnetic fields: Magnetic susceptibility anisotropy contributions and consequences for protein solution structure determination. *J. Am. Chem. Soc.*, 120:12903–12909, 1998.
- [380] S. W. Fesik, G. Gemmecker, E. T. Olejniczak, and A. M. Petros. Identification of solvent-exposed regions of enzyme-bound ligands by nuclear magnetic resonance. *J. Am. Chem. Soc.*, 113:7080–7081, 1991.
- [381] T. Madl, W. Bermel, and K. Zangger. Use of relaxation enhancements in a paramagnetic environment for the structure determination of proteins using NMR spectroscopy. *Angew. Chem. Int. Ed.*, 48:8259–8262, 2009.
- [382] G. Otting. Protein NMR using paramagnetic ions. *Annu. Rev. Biophys.*, 39:387–405, 2010.
- [383] T. Madl, T. Guttler, D. Gorlich, and M. Sattler. Structural analysis of large protein complexes using solvent paramagnetic relaxation enhancements. *Angew. Chem. Int. Ed.*, 50:3993–3997, 2011.
- [384] K. M. Ward, A. H. Aletras, and R. S. Balaban. A new class of contrast agents for MRI based on proton chemical exchange dependent saturation transfer (CEST). *J. Magn. Reson.*, 143:78–87, 2000.
- [385] S. Zhang, P. Winter, K. Wu, and A. D. Sherry. A novel Europium(III)-based MRI contrast agent. *J. Am. Chem. Soc.*, 123:1517–1578, 2001.
- [386] S. Zhang and A. D. Sherry. Physical characteristics of lanthanide complexes that act as magnetization transfer (MT) contrast agents. *J. Solid State Chem.*, 171:38–43, 2003.
- [387] S. Aime, A. Barge, D. Delli Castelli, F. Fedeli, A. Mortillaro, F. U. Nielsen, and E. Terreno. Paramagnetic lanthanide(III) complexes as pH-sensitive chemical exchange saturation transfer (CEST) contrast agents for MRI applications. *Magn. Reson. Med.*, 47:639–648, 2002.
- [388] J. Zhou and P. C. M. van Zijl. Chemical exchange saturation transfer imaging and spectroscopy. *Prog. Nucl. Magn. Reson. Spectrosc.*, 48:109–136, 2006.
- [389] S. Aime, D. Delli Castelli, and E. Terreno. A paramagnetic MRI-CEST agent responsive to lactate concentration. *J. Am. Chem. Soc.*, 124:9364–9365, 2002.

- [390] S. Aime, C. Carrera, D. Delli Castelli, S. Geninatti Crich, and E. Terreno. Tunable imaging of cells labeled with MRI-PARACEST agents. *Angew. Chem. Int. Ed.*, 44:1813–1815, 2005.
- [391] S. Zhang, A. D. Sherry, and C. R. Malloy. *Proceedings of the 13th Annual Meeting ISMRM Miami*, page 2707, 2005.
- [392] S. Antonijevic and S. Wimperis. Separation of quadrupolar and chemical/paramagnetic shift interactions in two-dimensional $^2\text{H } I = 1$ nuclear magnetic resonance spectroscopy. *J. Chem. Phys.*, 122:044312, 2005.
- [393] J. T. Ash, N. M. Trease, and P. J. Grandinetti. Separating chemical shift and quadrupolar anisotropies via multiple-quantum NMR spectroscopy. *J. Am. Chem. Soc.*, 130:10858–10859, 2008.
- [394] A. J. Pell, R. J. Clément, C. P. Grey, L. Emsley, and G. Pintacuda. Frequency-stepped acquisition in nuclear magnetic resonance spectroscopy under magic angle spinning. *J. Chem. Phys.*, 138:114201, 2013.
- [395] S. W. Sparks and P. D. Ellis. ^{195}Pt shielding tensors in potassium hexachloroplatinate(IV) and potassium tetrachloroplatinate(II). *J. Am. Chem. Soc.*, 108:3215–3218, 1986.
- [396] M. T. Sananes, A. Tuel, and J. C. Volta. A study by ^{31}P NMR spin-echo mapping of VPO catalysts: I. characterization of the reference phases. *J. Catal.*, 145:251–255, 1994.
- [397] M. T. Sananes, A. Tuel, and J. C. Volta. Characterization of different precursors and activated vanadium phosphate catalysis by ^{31}P NMR spin echo mapping. *J. Catal.*, 148:395–398, 1994.
- [398] M. T. Sananes and A. Tuel. Magnetic properties of vanadium phosphorus oxide catalysts studied by spin echo mapping ^{31}P nmr. *J. Chem. Soc., Chem. Commun.*, pages 1323–1324, 1995.
- [399] Y. Y. Tong. Nuclear spin-echo Fourier-transform mapping spectroscopy for broad NMR lines in solids. *J. Magn. Reson., Ser. A*, 119:22–28, 1996.
- [400] L. Canesson and A. Tuel. The first observation of ‘NMR-invisible phosphorus in cobalt-substituted aluminophosphate molecular sieves. *Chem. Commun.*, pages 241–241, 1997.

- [401] L. Canesson, Y. Boudeville, and A. Tuel. Local environment of phosphorus atoms in $\text{CoAPO}_4 - n$ molecular sieves: A ^{31}P NMR study. *J. Am. Chem. Soc.*, 119:10754–10762, 1997.
- [402] G. Mali, A. Ristic, and V. Kaucic. ^{31}P NMR as a tool for studying incorporation of Ni, Co, Fe, and Mn into aluminophosphate zeotypes. *J. Phys. Chem. B*, 109:10711–10716, 2005.
- [403] D. Massiot, I. Farnan, N. Gautier, D. Trumeau, A. Trokiner, and J. P. Courures. ^{71}Ga and ^{69}Ga nuclear magnetic resonance study of $\beta\text{-Ga}_2\text{O}_3$: resolution of four- and six-fold coordinated Ga sites in static conditions. *Solid State Nucl. Magn. Reson.*, 4:241–248, 1995.
- [404] R. W. Schurko, S. Wi, and L. Frydman. Dynamic effects on the powder line shapes of half-integer quadrupolar nuclei: A solid-state NMR study of XO_4^- groups. *J. Chem. Phys. A*, 106:51–62, 2002.
- [405] J. Ash and P. J. Grandinetti. Solid-state NMR characterization of ^{69}Ga and ^{71}Ga in crystalline solids. *Magn. Reson. Chem.*, 44:823–831, 2006.
- [406] L. A. O’Dell, A. J. Rossini, and R. W. Schurko. Acquisition of ultra-wideline NMR spectra from quadrupolar nuclei by frequency-stepped WURST-QCPMG. *Chem. Phys. Lett.*, 468:330–335, 2009.
- [407] L. A. O’Dell and R. W. Schurko. Fast and simple acquisition of solid-state ^{14}N NMR spectra with signal enhancement via population transfer. *J. Am. Chem. Soc.*, 131:6658–6659, 2009.
- [408] M.-H. Thibault, B. E. G. Lucier, R. W. Schurko, and F.-G. Fontaine. Synthesis and solid-state characterization of platinum complexes with hexadentate amino- and iminophosphine ligands. *Dalton Trans.*, pages 7701–7716, 2009.
- [409] A. W. MacGregor, L. A. O’Dell, and R. W. Schurko. New methods for the acquisition of ultra-wideline solid-state NMR spectra of spin-1/2 nuclides. *J. Magn. Reson.*, 208:103–111, 2011.
- [410] K. Harris, A. Lupulescu, B. E. G. Lucier, L. Frydman, and R. W. Schurko. Broadband adiabatic inversion pulses for cross polarization in wideline solid-state NMR spectroscopy. *J. Magn. Reson.*, 224:28–47, 2012.
- [411] L. A. O’Dell. The WURST kind of pulses in solid-state NMR. *Solid State Nucl. Magn. Reson.*, 55-56:28–41, 2013.

- [412] J. Cabana, J. Shirakawa, G. Chen, T. J. Richardson, and C. P. Grey. MAS NMR study of the metastable solid solutions found in the $\text{LiFePO}_4/\text{FePO}_4$ system. *Chem. Mater.*, 22:1249–1262, 2010.
- [413] D. M. Halat, R. Dervisoglu, G. Kim, M. T. Dunstan, F. Blanc, D. S. Middlemiss, and C. P. Grey. Probing oxide-ion mobility in the mixed ionic–electronic conductor $\text{La}_2\text{NiO}_{4+\delta}$ by solid-state ^{17}O MAS NMR spectroscopy. *J. Am. Chem. Soc.*, 138:11958–11969, 2016.
- [414] O. Pecher, D. M. Halat, J. Lee, Z. Liu, K. J. Griffith, M. Braun, and C. P. Grey. Enhanced efficiency of solid-state NMR investigations of energy materials using an external automatic tuning/matching (eATM) robot. *J. Magn. Reson.*, 275:127–136, 2017.
- [415] H. Y. Carr and E. M. Purcell. Effects of diffusion on free precession in nuclear magnetic resonance experiments. *Phys. Rev.*, 94:630–638, 1954.
- [416] S. Meiboom and D. Gill. Modified spin-echo method for measuring nuclear magnetic relaxation times. *Rev. Sci. Instr.*, 29:688–691, 1958.
- [417] G. Metz, X. Wu, and S. O. Smith. Ramped-amplitude cross polarization in magic-angle-spinning NMR. *J. Magn. Reson. Ser. A*, 110:219–227, 1994.
- [418] R. H. van Eck and W. S. Veeman. Spin density description of rotational-echo double-resonance, transferred-echo double-resonance and two-dimensional transferred-echo double-resonance solid state nuclear magnetic resonance. *Solid State Nucl. Magn. Reson.*, 2:307–315, 1993.
- [419] T. Gullion, D. B. Baker, and M. S. Conradi. New, compensated Carr–Purcell sequences. *J. Magn. Reson.*, 89:479–484, 1990.
- [420] Z. Yao, H.-T. Kwak, D. Sakellariou, L. Emsley, and P. J. Grandinetti. Sensitivity enhancement of the central transition NMR signal of quadrupolar nuclei under magic-angle spinning. *Chem. Phys. Lett.*, 327:85–90, 2000.
- [421] N. M. Trease, K. K. Dey, and P. J. Grandinetti. Optimum excitation of “enhanced” central transition populations. *J. Magn. Reson.*, 200:334–339, 2009.

- [422] S. Prasad, H.-T. Kwak, T. Clark, and P. J. Grandinetti. A simple technique for determining nuclear quadrupole coupling constants with RAPT solid-state NMR spectroscopy. *J. Am. Chem. Soc.*, 124:4964–4965, 2002.
- [423] N. Bloembergen. On the interaction of nuclear spins in a crystalline lattice. *Physica*, 15:386–426, 1949.
- [424] A. E. Bennett, J. H. Ok, R. G. Griffin, and S. Vega. Chemical shift correlation spectroscopy in rotating solids: radio frequency-driven dipolar recoupling and longitudinal exchange. *J. Chem. Phys.*, 96:8624–8627, 1992.
- [425] N. P. Wickramasinghe, M. A. Shaibat, C. R. Jone, L. B. Casabianca, A. C. de Dios, J. S. Harwood, and Y. Ishii. Progress in ^{13}C and ^1H solid-state nuclear magnetic resonance for paramagnetic systems under very fast magic angle spinning. *J. Chem. Phys.*, 128:052210, 2008.
- [426] Y. Ishii and R. Tycko. Multidimensional heteronuclear correlation spectroscopy of a uniformly N-15- and C-13-labeled peptide crystal: Toward spectral resolution, assignment, and structure determination of oriented molecules in solid-state NMR. *J. Chem. Am. Soc.*, 122:1443–1455, 2000.
- [427] L. J. M. Davis, I. Heinmaa, and G. R. Goward. Study of lithium dynamics in monoclinic $\text{Li}_3\text{Fe}_2(\text{PO}_4)_3$ using ^6Li VT and 2D exchange MAS NMR spectroscopy. *Chem. Mater.*, 22:769–775, 2010.
- [428] L. J. M. Davis, B. L. Ellis, T. N. Ramesh, L. F. Nazar, A. D. Bain, and G. R. Goward. ^6Li 1D EXSY NMR spectroscopy: A new tool for studying lithium dynamics in paramagnetic materials applied to monoclinic $\text{Li}_2\text{VPO}_4\text{F}$. *J. Phys. Chem. C*, 115:22603–22608, 2011.
- [429] O. N. Antzutkin, S. C. Shekar, and M. H. Levitt. Two-dimensional sideband separation in magic-angle-spinning NMR. *J. Magn. Reson. Ser. A*, 115:7–19, 1995.
- [430] J. Z. Hu, D. W. Alderman, C. Ye, R. J. Pugmire, and D. M. Grant. An isotropic chemical shift–chemical shift anisotropy magic-angle slow-spinning 2D NMR experiment. *J. Magn. Reson. Ser. A*, 105:82–87, 1993.

- [431] M. Crozet, M. Chaussade, M. Bardet, L. Emsley, B. Lamotte, and J.-M. Mouesca. Carbon-13 solid-state NMR studies on synthetic model compounds of [4Fe-4S] clusters in the 2+ state. *J. Phys. Chem. A*, 104:9990–10000, 2000.
- [432] I. Hung, L. Zhou, F. Pourpoint, C. P. Grey, and Z. Gan. Isotropic high field NMR spectra of Li-ion battery materials with anisotropy > 1 MHz. *J. Am. Chem. Soc.*, 134:1898–1901, 2012.
- [433] M. Garwood and L. DelaBarre. The return of the frequency sweep: Designing adiabatic pulses for contemporary NMR. *J. Magn. Reson.*, 153:155–177, 2001.
- [434] J. Baum, R. Tycko, and A. Pines. Broad-band and adiabatic inversion of a 2-level system by phase-modulated pulses. *Phys. Rev. A*, 32:3435–3447, 1985.
- [435] T. L. Hwang, P. C. M. van Zijl, and M. Garwood. Fast broadband inversion by adiabatic pulses. *J. Magn. Reson.*, 133:200–203, 1998.
- [436] E. Kupce and R. Freeman. Adiabatic pulses for wide-band inversion and broad-band decoupling. *J. Magn. Reson. Ser. A*, 115:273–276, 1995.
- [437] M. Deschamps, G. Kervern, D. Massiot, G. Pintacuda, L. Emsley, and P. J. Grandinetti. Superadiabicity in magnetic resonance. *J. Chem. Phys.*, 129:204100, 2008.
- [438] S. Conolly, G. Glover, D. Nishimura, and A. Macovski. A reduced power selective adiabatic spin-echo pulse sequence. *Magn. Reson. Med.*, 18:28–38, 1991.
- [439] T. L. Hwang and A. J. Shaka. Water suppression that works. excitation sculpting using arbitrary wave-forms and pulsed-field gradients. *J. Magn. Reson. Ser. A*, 112:275–279, 1995.
- [440] K. Stott, J. Stonehouse, J. Keeler, T. L. Hwang, and A. J. Shaka. Excitation sculpting in high-resolution nuclear magnetic resonance spectroscopy: Application to selective NOE experiments. *J. Am. Chem. Soc.*, 117:4199–4200, 1995.
- [441] M. Bini, S. Ferrari, C. Ferrara, M. C. Mozzati, D. Capsoni, A. J. Pell, G. Pintacuda, P. Canton, and P. Mustarelli. Polymorphism and magnetic properties of Li_2MSiO_4 (M = Fe, Mn) cathode materials. *Sci. Rep.*, 3:3452, 2013.

- [442] A. Bertarello, T. Schubeis, C. Fuccio, E. Ravera, M. Fragai, G. Parigi, L. Emsley, G. Pintacuda, and C. Luchinat. Paramagnetic properties of a crystalline iron–sulfur protein by magic-angle spinning NMR spectroscopy. *Inorg. Chem.*, 56:6624–6629, 2017.
- [443] B. Burcher, K. J. Sanders, L. Benda, G. Pintacuda, E. Jeanneau, A. A. Danopolous, P. Braunstein, H. Olivier-Bourbigou, and P.-A. R. Breuil. Straightforward access to stable, 16-valence-electron phosphine-stabilized Fe⁰ olefin complexes and their reactivity. *Organometallics*, 36:605–613, 2017.
- [444] E. Mitoudi-Vagourdi, W. Papawassiliou, S. Müllner, A. Jaworski, A. J. Pell, P. Lemmens, R. K. Kremer, and M. Johnsson. Synthesis and physical properties of the oxofluoride Cu₂(SeO₃)F₂. *Inorg. Chem.*, in press, 2018.
- [445] R. Siegel, T. T. Nakashima, and R. E. Wasylshen. Sensitivity enhancement of NMR spectra of half-integer spin quadrupolar nuclei in solids using hyperbolic secant pulses. *J. Magn. Reson.*, 184:85–100, 2007.
- [446] K. K. Dey, S. Prasad, J. T. Ash, M. Deschamps, and P. J. Grandinetti. Spectral editing in solid-state MAS NMR of quadrupolar nuclei using selective satellite inversion. *J. Magn. Reson.*, 185:326–330, 2007.
- [447] T. T. Nakashima, R. E. Wasylshen, R. Siegel, and K. J. Ooms. Sensitivity enhancement of solid-state NMR spectra of half-integer spin quadrupolar nuclei: Double- or single-frequency sweeps? Insights from the hyperbolic secant experiment. *Chem. Phys. Lett.*, 450:417–421, 2008.
- [448] T. T. Nakashima, R. Teymoori, and R. E. Wasylshen. Using hyperbolic secant pulses to assist characterization of chemical shift tensors for half-integer spin quadrupolar nuclei in MAS powder samples. *Magn. Reson. Chem.*, 47:465–471, 2009.
- [449] P. Caravatti, G. Bodenhausen, and R. R. Ernst. Selective pulse experiments in high-resolution solid-state NMR. *J. Magn. Reson.*, 55:88–103, 1983.
- [450] G. Pintacuda, N. Giraud, R. Pierattelli, A. Böckmann, I. Bertini, and L. Emsley. Solid-state NMR spectroscopy of a paramagnetic protein: Assignment and study of human dimeric oxidized Cu^{II}–Zn^{II} superoxide dismutase (SOD). *Angew. Chem. Int. Ed.*, 46:1079–1082, 2007.

- [451] S. Parthasarathy, B. Yoo, D. McElheny, W. Tay, and Y. Ishii. Capturing a reactive state of amyloid aggregates. *J. Bio. Chem.*, 289:9998–10010, 2014.
- [452] N. P. Wickramasinghe, S. Parthasarathy, C. R. Jones, C. Bhardwaj, F. Long, M. Kotecha, S. Mehboob, L. W.-M. Fung, J. Past, A. Samoson, and Y. Ishii. Nanomole-scale protein solid-state NMR by breaking intrinsic ^1H t_1 boundaries. *Nature Meth.*, 6:215–218, 2009.
- [453] I. Bertini, L. Emsley, I. C. Felli, S. Laage, A. Lesage, J. Lewandowski, A. Marchetti, R. Pierattelli, and G. Pintacuda. High-resolution and sensitivity through-bond correlations in ultra-fast magic angle spinning (MAS) solid-state NMR. *Chem. Sci.*, 2:345–348, 2011.
- [454] S. Laage, A. Lesage, L. Emsley, I. Bertini, I. C. Felli, R. Pierattelli, and G. Pintacuda. Transverse-dephasing optimized homonuclear j -decoupling in solid-state NMR spectroscopy of uniformly ^{13}C -labeled proteins. *J. Am. Chem. Soc.*, 131:10816–10817, 2009.
- [455] E. Barbet-Massin, A. J. Pell, M. J. Knight, A. L. Webber, I. C. Felli, R. Pierattelli, L. Emsley, A. Lesage, and G. Pintacuda. ^{13}C -detected through-bond correlation experiments for protein resonance assignment by ultra-fast MAS solid-state NMR. *ChemPhysChem*, 14:3131–3137, 2013.
- [456] V. Chevelkov, B. J. van Rossum, F. Castellani, K. Rehbein, A. Diehl, M. Hohwy, S. Steuernagel, F. Engelke, H. Oschkinat, and B. Reif. ^1H detection in MAS solid-state nmr spectroscopy of biomacromolecules employing pulsed field gradients for residual solvent suppression. *J. Am. Chem. Soc.*, 125:7788–7789, 2003.
- [457] E. K. Paulson, C. R. Morcombe, V. Gaponenko, B. Dancheck, R. A. Byrd, and K. W. Zilm. Sensitive high resolution inverse detection NMR spectroscopy of proteins in the solid state. *J. Am. Chem. Soc.*, 125:15831–15836, 2003.
- [458] L. Zheng, K. W. Fishbein, R. G. Griffin, and J. Herzfeld. Two-dimensional solid-state proton NMR and proton exchange. *J. Am. Chem. Soc.*, 115:6254–6261, 1993.
- [459] V. Chevelkov, K. Rehbein, A. Diehl, and B. Reif. Ultrahigh resolution in proton solid-state NMR spectroscopy at high levels of deuteration. *Angew. Chem. Int. Ed.*, 45:3878–3881, 2006.

- [460] U. Akbey, S. Lange, W. T. Franks, R. Linser, K. Rehbein, A. Diehl, B. J. van Rossum, B. Reif, and H. Oschkinat. Optimum levels of exchangeable protons in perdeuterated proteins for proton detection in MAS solid-state NMR spectroscopy. *J. Biomol. NMR*, 46:67–73, 2010.
- [461] M. J. Knight, A. L. Webber, A. J. Pell, P. Guerry, E. Barbet-Massin, I. Bertini, I. C. Felli, L. Gonnelli, R. Pierattelli, L. Emsley, A. Lesage, T. Herrmann, and G. Pintacuda. Fast resonance assignment and fold determination of human superoxide dismutase by high-resolution proton-detected solid-state MAS NMR spectroscopy. *Angew. Chem. Int. Ed.*, 50:11697–11701, 2011.
- [462] E. Barbet-Massin, A. J. Pell, K. Jaudzems, W. T. Franks, J. S. Retel, S. Kotelovica, I. Akopjana, K. Tars, L. Emsley, H. Oschkinat, A. Lesage, and G. Pintacuda. Out-and-back ^{13}C – ^{13}C scalar transfers in protein resonance assignment by proton-detected solid-state NMR under ultra-fast MAS. *J. Biomol. NMR*, 56:379–386, 2013.
- [463] E. Barbet-Massin, A. J. Pell, J. S. Retel, L. B. Andreas, K. Jaudzems, W. T. Franks, A. J. Nieuwkoop, M. Hiller, V. Higman, P. Guerry, A. Bertarello, M. J. Knight, M. Felletti, T. Le Marchand, S. Kotelovica, I. Akopjana, K. Tars, M. Stoppini, V. Bellotti, M. Bolognesi, S. Ricagno, J. J. Chou, R. G. Griffin, H. Oschkinat, A. Lesage, L. Emsley, T. Herrmann, and G. Pintacuda. Rapid proton-detected NMR assignment for proteins with fast magic angle spinning. *J. Am. Chem. Soc.*, 136:12489–12497, 2014.
- [464] L. B. Andreas, K. Jaudzems, J. Stanek, D. Lalli, A. Bertarello, T. Le Marchand, D. Cala-De Paepe, S. Kotelovica, I. Akopjana, B. Knott, S. Wegner, F. Engelke, A. Lesage, L. Emsley, K. Tars, T. Herrmann, and G. Pintacuda. Structure of fully protonated proteins by proton-detected magic-angle spinning NMR. *Proc. Natl. Acad. Sci. USA*, 113:9187–9192, 2016.
- [465] S. A. Rouf, J. Mares, and J. Vaara. ^1H chemical shifts in paramagnetic Co(II) pyrazolylborate complexes: A first-principles study. *J. Chem. Theory Comput.*, 11:1683–1691, 2015.
- [466] M. C. Tucker, M. M. Doeff, T. J. Richardson, R. Fiñones, E. J. Cairns, and J. A. Reimer. Hyperfine fields at the Li site in LiFePO_4 -type olivine materials for lithium rechargeable batteries: A ^7Li MAS NMR and SQUID study. *J. Am. Chem. Soc.*, 124:3832–3833, 2002.

- [467] A. D'Aléo, G. Pompidor, B. Elena, J. Vicat, P. L. Baldeck, L. Toupet, R. Kahn, C. Andraud, and O. Maury. Two-photon microscopy and spectroscopy of lanthanide bioprobes. *ChemPhysChem*, 8:2125–2132, 2007.
- [468] J. Schlagnitweit, M. Tang, M. Baias, S. Richardson, S. Schantz, and L. Emsley. Nanostructure of materials determined by relayed paramagnetic relaxation enhancement. *J. Am. Chem. Soc.*, 137:12482–12485, 2015.
- [469] Z.-F. Xu, Y. Xie, W.-L. Feng, and H. F. Schaefer III. Systematic investigation of electronic and molecular structures for the first transition metal series metallocenes $M(C_5H_5)_2$ ($M = V, Cr, Mn, Fe, Co,$ and Ni). *J. Phys. Chem. A*, 107:2716–2729, 2003.
- [470] B. P. Pritchard, S. Simpson, E. Zurek, and J. Autschbach. Computation of chemical shifts for paramagnetic molecules: A laboratory experiment for the undergraduate curriculum. *J. Chem. Educ.*, 91:1058–1063, 2014.
- [471] H. M. McConnell and C. M. Holm. Proton resonance shifts in nickelocene. *J. Chem. Phys.*, 27:314–315, 1957.
- [472] H. M. McConnell and C. M. Holm. Proton resonance shifts in paramagnetic metal aromatic complexes. *J. Chem. Phys.*, 28:749–750, 1958.
- [473] F. Aquino, B. Pritchard, and J. Autschbach. Scalar relativistic computations and localized orbital analyses of nuclear hyperfine coupling and paramagnetic NMR chemical shifts. *J. Chem. Theory Comput.*, 8:598–609, 2012.
- [474] F. H. Köhler and W. Proßdorf. Metallocenes: first models for nuclear magnetic resonance isotope shifts in paramagnetic molecules. *J. Am. Chem. Soc.*, 100:5970–5972, 1978.
- [475] F. H. Köhler, K.-H. Doll, and W. Proßdorf. Extreme ^{13}C -NMR data as information on organometal radicals. *Angew. Chem. Int. Ed.*, 19:479–480, 1980.
- [476] N. Hebandanz, F. H. Köhler, and G. Müller. Electron spin adjustment in manganocenes. Preparative, paramagnetic NMR and X-ray study on substituent and solvent effects. *J. Am. Chem. Soc.*, 108:3281–3289, 1986.

- [477] H. Eicher and F. H. Köhler. Determination of the electronic structure, the spin density distribution, and approach to the geometric structure of substituted cobaltocenes from NMR spectroscopy in solution. *Chem. Phys.*, 128:297–309, 1988.
- [478] N. Hebandanz, F. H. Köhler, F. Scherbaum, and B. Schlesinger. NMR spectroscopy of paramagnetic complexes. Part 36— $^2/1\text{H}$ NMR of paramagnetic metallocenes: Primary and secondary isotope effects and signal narrowing. *Magn. Reson. Chem.*, 27:798–802, 1989.
- [479] F. H. Köhler and X. Xie. Vanadocene as a temperature standard for ^{13}C and ^1H MAS NMR and for solution-state NMR spectroscopy. *Magn. Reson. Chem.*, 35:487–492, 1997.
- [480] J. Blümel, M. Herker, W. Hiller, and F. H. Köhler. Study of paramagnetic chromocenes by solid-state NMR spectroscopy. *Organometallics*, 15:3474–3476, 1996.
- [481] H. Heise, F. H. Köhler, and X. Xie. Solid-state NMR spectroscopy of paramagnetic metallocenes. *J. Magn. Reson.*, 150:198–206, 2001.
- [482] S. Altmannshofer, E. Herdtwerk, F. H. Köhler, R. Miller, R. Möller, E.-W. Scheidt, W. Scherer, and C. Train. Crystal-packing-induced antiferromagnetic interactions of metallocenes: Cyanonickelocenes, -cobaltocenes, and -ferrocenes. *Chem. Eur. J.*, 14:8013–8024, 2008.
- [483] P. Hrobárik, R. Reviakine, A. V. Arbuznikov, O. L. Malkina, V. G. Malkin, F. H. Köhler, and M. Kaupp. Density functional calculations of NMR shielding tensors for paramagnetic systems with arbitrary spin multiplicity: Validation on 3d metallocenes. *J. Chem. Phys.*, 126:024107, 2007.
- [484] R. Prins, J. D. W. van Voorst, and C. J. Schinkel. Zero-field splitting in the triplet ground state of nickelocene. *Chem. Phys. Lett.*, 1:54–55, 1967.
- [485] P. Baltzer, A. Furrer, J. Hulliger, and A. Stebler. Magnetic properties of nickelocene. A reinvestigation using inelastic neutron scattering and magnetic susceptibility. *Inorg. Chem.*, 27:1543–1548, 1988.
- [486] S. Li, Y. M. Hamrick, R. J. Van Zee, and W. Weltner Jr. Far-infrared magnetic resonance of matrix-isolated nickelocene. *J. Am. Chem. Soc.*, 114:4433–4434, 1992.
- [487] J. Hulliger, L. Zoller, and J. H. Ammeter. Orientation effects in EPR powder samples induced by the static magnetic field. *J. Magn. Reson.*, 48:512–518, 1982.

- [488] J. Voitländer and E. Schimitschek. Paramagnetische Resonanzuntersuchungen an einem Mangan-dicyclopentadienylkomplex. *Z. Elektrochem.*, 61:941–943, 1957.
- [489] M. E. Switzer, R. Wang, M. F. Rettig, and A. H. Maki. Electronic ground states of manganocene and 1,1'-dimethylmanganocene. *J. Am. Chem. Soc.*, 96:7669–7674, 1974.
- [490] V. P. Desai, E. König, and B. Kanellakopulos. Magnetic susceptibility and electron paramagnetic resonance of chromocene and 1,1'-dimethyl-chromocene: Evidence for the dynamic Jahn–Teller effect. *J. Chem. Phys.*, 78:6299–5306, 1983.
- [491] E. König, R. Schnakig, B. Kanellakopulos, and R. Klenze. Magnetism down to 0.90 K, zero-field splitting, and the ligand field in chromocene. *Chem. Phys. Lett.*, 50:439–441, 1977.
- [492] R. Prins, P. Biloen, and J. D. W. van Voorst. Electron spin resonance of vanadocene. *J. Chem. Phys.*, 46:1216–1217, 1967.
- [493] R. Prins and J. D. W. van Voorst. Bonding in sandwich compounds. *J. Chem. Phys.*, 49:4665–4673, 1968.
- [494] H. H. Dearman, W. W. Porterfield, and H. M. McConnell. Paramagnetic resonance of bis-cyclopentadienyl vanadium in ferrocene. *J. Chem. Phys.*, 34:696–697, 1961.
- [495] H. M. McConnell. Indirect hyperfine interactions in the paramagnetic resonance spectra of aromatic free radicals. *J. Chem. Phys.*, 24:764–766, 1956.
- [496] B. Martin and J. Autschbach. Kohn–Sham calculations of NMR shifts for paramagnetic 3d metal complexes: protocols, delocalization error, and the curious amide proton shifts of a high-spin iron(II) macrocycle complex. *Phys. Chem. Chem. Phys.*, 18:21051–21068, 2016.
- [497] B. Pritchard and J. Autschbach. Theoretical investigation of paramagnetic NMR shifts in transition metal acetylacetonato complexes: Analysis of signs, magnitudes, and the role of the covalency of the ligand–metal bonding. *Inorg. Chem.*, 51:8340–8351, 2012.
- [498] R. Pigliapochi, A. J. Pell, I. D. Seymour, C. P. Grey, D. Ceresoli, and M. Kaupp. DFT investigation of the effect of spin-orbit coupling on the NMR shifts in paramagnetic solids. *Phys. Rev. B*, 95:054412, 2017.

- [499] A. Mondal, M. W. Gaultois, A. J. Pell, M. Iannuzzi, C. P. Grey, J. Hutter, and M. Kaupp. Large-scale computation of NMR shifts for paramagnetic solids using CP2K. *J. Chem. Theory, Comput.*, 14:377–394, 2018.
- [500] A. J. Cohen, P. Mori-Sánchez, and W. Yang. Challenges for density functional theory. *Chem. Rev.*, 112:289–320, 2012.
- [501] K. Długopolska, T. Ruman, M. Danilczuk, and D. Pogocki. Analysis of NMR shifts of high-spin cobalt(II) pyrazolylborate complexes. *Appl. Magn. Reson.*, 35:271–283, 2008.
- [502] K. Mizushima, P. C. Jones, P. J. Wiseman, and J. B. Goodenough. Li_xCoO_2 ($0 < x < 1$): A new cathode material for batteries of high energy density. *Mater. Res. Bull.*, 15:783–789, 1980.
- [503] C. Pan, Y. J. Lee, B. Ammundsen, and C. P. Grey. ^6Li MAS NMR studies of the local structure and electrochemical properties of Cr-doped lithium manganese and lithium cobalt oxide cathode materials for lithium-ion batteries. *Chem. Mater.*, 14:2289–2299, 2002.
- [504] M. Carewska, S. Scaccia, F. Croce, S. Argumugam, Y. Wang, and S. Greenbaum. Electrical conductivity and $^{6,7}\text{Li}$ NMR studies of $\text{Li}_{1+y}\text{CoO}_2$. *Solid State Ionics*, 93:227–237, 1997.
- [505] C. Marichal, J. Hirschinger, P. Granger, M. Ménétrier, A. Rougier, and C. Delmas. ^6Li and ^7Li NMR in the $\text{LiNi}_{1-y}\text{Co}_y\text{O}_2$ solid solution ($0 \leq y \leq 1$). *Inorg. Chem.*, 34:1773–1778, 1995.
- [506] J. Woodward. Praeparatio Caerulei Prussiaci Ex Germania Missa. *Philos. Trans. R. Soc. London*, 33:15–17, 1724.
- [507] S. S. Kaye and J. R. Long. Hydrogen storage in the dehydrated Prussian blue analogues $\text{M}_3[\text{Co}(\text{CN})_6]_2$ ($\text{M} = \text{Mn}, \text{Fe}, \text{Co}, \text{Ni}, \text{Cu}, \text{Zn}$). *J. Am. Chem. Soc.*, 127:6506–6507, 2005.
- [508] A. Karyakin, E. Karyakin, and L. Gorton. Amperometric biosensor for glutamate using Prussian blue-based artificial peroxidase as a transducer for hydrogen peroxide. *Anal. Chem.*, 72:1720–1723, 2000.
- [509] M. T. G. Valentini, R. Stella, L. Maggi, and G. Ciceri. Copper hexacyanoferrate(II) and (III) as trace cesium adsorbers from natural waters. *J. Radioanal. Nucl. Chem.*, 114:105–112, 1987.

- [510] G. Boxhoorn, J. Moolhuysen, J. G. F. Coolegem, and R. A. Van Santen. Cyanometallates: an underestimated class of molecular sieves. *J. Chem. Soc. Chem. Commun.*, pages 1305–1307, 1985.
- [511] A. Eftekhari. Potassium secondary cell based on Prussian blue cathode. *J. Power Sources*, 126:221–228, 2004.
- [512] J. J. Alexander and H. B. Gray. Molecular orbital theory for metal complexes: ferrocyanide and cobalticyanide ions. *Coord. Chem. Rev.*, 2:29–43, 1967.
- [513] S. Ferlay, T. Mallah, R. Ouahes, P. Veillet, and M. Verdaguer. A room-temperature organometallic magnet based on Prussian blue. *Nature*, 378:701–703, 1995.
- [514] A. Flambard, F. H. Köhler, R. Lescouëzec, and B. Revel. Probing spin density and local structure in the Prussian blue analogues $\text{CsCd}[\text{Fe}/\text{Co}(\text{CN})_6] \cdot 0.5\text{H}_2\text{O}$ and $\text{Cd}_3[\text{Fe}/\text{Co}(\text{CN})_6]_2 \cdot 15\text{H}_2\text{O}$ with solid-state MAS NMR spectroscopy. *Chem. Eur. J.*, 17:11567–11575, 2011.
- [515] N. Baumgärtel, A. Flambard, F. H. Köhler, and R. Lescouëzec. Paramagnetic hexacyanometalates. The diversity of spin distribution studied by ^{13}C and ^{15}N MAS NMR spectroscopy. *Inorg. Chem.*, 52:12634–12644, 2013.
- [516] A. K. Padhi, K. S. Nanjundaswamy, and J. B. Goodenough. Phospho-olivines as positive-electrode materials for rechargeable lithium batteries. *J. Electrochem. Soc.*, 144:1188–1194, 1997.
- [517] H. Ehrenberg, N. N. Bramnik, A. Senyshyn, and H. Fuess. Crystal and magnetic structures of electrochemically delithiated $\text{Li}_{1-x}\text{CoPO}_4$ phases. *Solid State Sci.*, 11:18–23, 2009.
- [518] N. A. Chernova, G. M. Nolis, F. O. Omenya, H. Zhou, Z. Li, and M. S. Whittingham. What can we learn about battery materials from their magnetic properties? *J. Mater Chem.*, 21:9865–9875, 2011.
- [519] S. L. Wilcke, Y.-J. Lee, E. J. Cairns, and J. A. Reimer. Covalency measurements via NMR in lithium metal phosphates. *Appl. Magn. Reson.*, 32:547–563, 2007.
- [520] A Mondal and M. Kaupp. Quantum-chemical approach to NMR chemical shifts in paramagnetic solids applied to LiFePO_4 and LiCoPO_4 . *J. Phys. Chem. Lett.*, 9:1480–1484, 2018.
- [521] A. J. Thompson. *Metalloproteins*. Verlag Chemie, Weinheim FRG, 1985.

- [522] R. K. Thauer. CO₂ reduction to formate in *clostridium acidi-urici*. *J. Bacteriol.*, 114:443–444, 1973.
- [523] I. Bertini, F. Capozzi, S Ciurli, C. Luchinat, and M. Messori, L. Piccioli. Identification of the iron ions of high potential iron protein from *Chromatium vinosum* within the protein frame through two-dimensional NMR experiments. *J. Am. Chem. Soc.*, 114:3332–3340, 1992.
- [524] L. Banci, I. Bertini, F. Capozzi, P. Carloni, S. Ciurli, C. Luchinat, and M Piccioli. The iron-sulfur cluster in the oxidized high-potential iron protein from *Ectothiorhodospira halophila*. *J. Am. Chem. Soc.*, 115:3431–3440, 1993.
- [525] M. Karplus. Vicinal proton coupling in nuclear magnetic resonance. *J. Am. Chem. Soc.*, 85:2870–2871, 1963.
- [526] C. Heller and H. M. McConnell. Radiation damage in organic crystals. II. Electron spin resonance of (CO₂H)CH₂CH(CO₂H) in β -succinic acid. *J. Chem. Phys.*, 32:1535–1539, 1960.
- [527] E. W. Stone and A. H. Maki. Hindered internal rotation and ESR spectroscopy. *J. Chem. Phys.*, 37:1326–1333, 1962.
- [528] J. M. McCord and I. Fridovich. Superoxide dismutase. an enzymic function for erythrocyprein (hemocuprein). *J. Biol. Chem.*, 244:6049–6055, 1969.
- [529] H. E. Parge, R. A. Hallewell, and J. A. Tainer. Atomic structures of wild-type and thermostable mutant recombinant human Cu, Zn superoxide-dismutase. *Proc. Natl. Acad. Sci. USA*, 89:6109–6113, 1992.
- [530] M. J. Knight, I. C. Felli, R. Pierattelli, L. Emsley, and G. Pintacuda. Magic angle spinning NMR of paramagnetic proteins. *Acc. Chem. Res.*, 46:2108–2116, 2013.
- [531] S. Balayssac, I. Bertini, M. Lelli, C. Luchinat, and M. Maletta. Paramagnetic ions provide structural restraints in solid-state NMR of proteins. *J. Am. Chem. Soc.*, 129:2218–2219, 2007.
- [532] A. Bhaumik, C. Luchinat, G. Parigi, E. Ravera, and M. Rinaldelli. NMR crystallography on paramagnetic systems: solved and open issues. *CrystEngComm.*, 15:8639–8656, 2013.
- [533] D. Parker. Luminescent lanthanide sensors for pH, pO_2 and selected anions. *Coord. Chem. Rev.*, 205:109–130, 2000.

- [534] S. Faulkner, S. J. A. Pope, and B. P. Burton-Pye. Lanthanide complexes for luminescence imaging applications. *Appl. Spectrosc. Rev.*, 40:1–31, 2005.
- [535] T. Gunnlaugsson and J. P. Leonard. Responsive lanthanide luminescent cyclen complexes: from switching/sensing to supramolecular architectures. *Chem. Commun.*, pages 3114–3131, 2005.
- [536] S. Pandya, J. Yu, and D. Parker. Engineering emissive europium and terbium complexes for molecular imaging and sensing. *Dalton Trans.*, pages 2757–2766, 2006.
- [537] N. Weibel, L. J. Charbonnière, M. Guardigli, A. Roda, and R. Ziessel. Engineering of highly luminescent lanthanide tags suitable for protein labeling and time-resolved luminescence imaging. *J. Am. Chem. Soc.*, 126:4888–4896, 2004.
- [538] W. Denk, J. H. Strickler, and W. W. Webb. Two-photon laser scanning fluorescence microscopy. *Science*, 248:73–76, 1990.
- [539] G. Pompidor, A. D’Aéo, J. Vicat, L. Toupet, N. Giraud, R. Kahn, and O. Maury. Protein crystallography through supramolecular interactions between a lanthanide complex and arginine. *Angew. Chem. Int. Ed.*, 47:3388–3391, 2008.
- [540] H. J. Vogel, T. Drakenberg, S. Forsen, J. D. J. O’Neill, and T. Hofmann. Structural differences in the two calcium binding sites of the porcine intestinal calcium binding protein: a multinuclear NMR study. *Biochemistry*, 24:3870–3876, 1985.
- [541] J. Billaud, R. J. Clément, A. R. Armstrong, J. Canales-Vázquez, P. Rozier, C. P. Grey, and P. G. Bruce. β -NaMnO₂: A high-performance cathode for sodium-ion batteries. *J. Am. Chem. Soc.*, 136:17243–17248, 2014.
- [542] V. G. Malkin, O. L. Malkina, M. E. Casida, and D. R. Salahub. Nuclear magnetic resonance shielding tensors calculated with a sum-over-states density functional perturbation theory. *J. Am. Chem. Soc.*, 116:5898–5909, 1994.
- [543] J. Mares, H. Liimatainen, T. O. Pennanen, and J. Vaara. Magnetic properties of Ni²⁺(aq) from first principles. *J. Chem. Theory Comput.*, 7:3248–3260, 2011.

Glossary

LS Russell–Saunders.

ABMS anisotropic bulk magnetic susceptibility.

aMAT adiabatic magic-angle turning.

An actinide.

AO atomic orbital.

AP anti-phase.

BMS bulk magnetic susceptibility.

CA alpha carbon (protein).

CASSCF complete active space self-consistent-field method.

CB beta carbon (protein).

CCR cross-correlated relaxation.

CEST chemical exchange dependent saturation transfer.

CO carbonyl carbon (protein).

COASTER correlation of anisotropies separated through echo refocusing.

COSY correlation spectroscopy.

CP cross polarization.

CPMG Carr–Purcell–Meiboom–Gill.

CSA chemical shift anisotropy.

CT central transition.

DFT density functional theory.

DHSQC dipolar heteronuclear single-quantum correlation.

DINEPT dipolar insensitive nucleus enhanced by polarization transfer.

DIPAP double in-phase anti-phase.

DIPSI decoupling in the presence of scalar interactions.

DM Dzyaloshinskii–Moriya.

DNA deoxyribonucleic acid.

DNP dynamic nuclear polarization.

DQF-COSY double-quantum-filtered correlation spectroscopy.

EC ethyl cellulose.

EDTA ethylenediamine tetraacetic acid.

EFG electric-field gradient.

EPR electron paramagnetic resonance.

ESR electron spin resonance.

EXSY exchange spectroscopy.

FC Fermi contact.

FID free-induction decay.

FWHM full-width at half-maximum.

GGA generalized gradient approximation.

H^{CA} alpha proton (protein).

H^N amide proton (protein).

HETCOR heteronuclear correlation.

HF hyperfine.

HMQC heteronuclear multiple-quantum correlation.

HOMO highest-occupied molecular orbital.

HPC hydroxypropyl cellulose.

HS high-spin.

HSQC heteronuclear single-quantum correlation.

IBMS isotropic bulk magnetic susceptibility.

IP in-phase.

IPAP in-phase anti-phase.

IS inner-sphere.

LCAO linear combination of atomic orbitals.

LF ligand field.

Ln lanthanide.

LR linear-response.

LS low-spin.

LUMO lowest-unoccupied molecular orbital.

MAS magic-angle spinning.

MAT magic-angle turning.

MATPASS magic-angle turning phase-adjusted spinning sidebands.

MATPASS nuclear magnetic resonance dispersion.

MMP metalloproteinase.

MO molecular orbital.

MODEFT modified driven equilibrium Fourier transform.

MRI magnetic resonance imaging.

NH amide nitrogen (protein).

NMR nuclear magnetic resonance.

NOE nuclear Overhauser effect.

NOESY nuclear Overhauser effect spectroscopy.

NQR nuclear quadrupole resonance.

NR non-relativistic.

OM oncomodulin.

OS outer-sphere.

PAF principal axis frame.

PARACEST paramagnetic chemical exchange dependent saturation transfer.

PASS phase-adjusted spinning sidebands.

PBA Prussian Blue analogue.

PCS pseudo-contact shift.

PDSD proton-driven spin diffusion.

PRE paramagnetic relaxation enhancement.

PSD proton spin diffusion.

PSO paramagnetic spin orbital.

R-PRE relayed paramagnetic relaxation enhancement.

RAPT rotor-assisted population transfer.

RDC residual dipolar coupling.

RF radio-frequency.

RFDR radio-frequency driven recoupling.

RKKY Ruderman–Kittel–Kasuya–Yosida.

ROE rotating-frame Overhauser enhancement.

ROESY rotating-frame Overhauser effect spectroscopy.

S³AP single-sideband-selective adiabatic pulse.

S³E selective-spin-state excitation.

SA shift anisotropy.

SC sidechain (protein).

SD spin-dipolar.

SHAP short high-power adiabatic pulse.

SHAP-CPMG short high-power adiabatic pulse Carr–Purcell–Meiboom–Gill.

SO spin orbit.

SOD superoxide dismutase.

SS spin-spin.

ST satellite transition.

TEDOR transferred-echo double resonance.

TM transition metal.

TOCSY total correlation spectroscopy.

TROSY transverse relaxation-optimized spectroscopy.

VASP Vienna ab initio Simulation Package.

VOCS variable offset cumulative spectroscopy.

WEFT water eliminated Fourier transform.

WURST wideband, uniform rate, smooth truncation.

Z Zeeman.

ZFS zero-field splitting.

ZQ zero-quantum.